Editors:

Meho Sasa Kovacevic

Lovorka Libric

Mario Bacic

EURO
ENGEO

2024

Engineering Geology & Geotechnics:

Building for the Future

Proceedings of the 4th European Regional Conference of IAEG

Dubrovnik, Croatia, 8-12 October 2024

ENG IAEG
AIGI GEOL

Engineering Geology and Geotechnics: Building for the Future

Proceedings of 4th European Regional Conference of IAEG
Dubrovnik, Croatia, 8-12 October 2024

Editors:

Meho Sasa Kovacevic

Lovorka Libric

Mario Bacic

University of Zagreb, Faculty of Civil Engineering
Zagreb, 2024.

Organization

CHAIRMEN

Ivan Kosović, Croatian Geological Survey

Lovorka Librić, University of Zagreb, Faculty of Civil Engineering

ORGANIZING COMMITTEE

Meho Saša Kovačević, University of Zagreb, Faculty of Civil Engineering

Danijela Jurić Kaćunić, University of Zagreb, Faculty of Civil Engineering

Lovorka Librić, University of Zagreb, Faculty of Civil Engineering

Mario Bačić, University of Zagreb, Faculty of Civil Engineering

Ivan Kosović, Croatian Geological Survey

Stratis Karantanellis, University of Michigan

Staša Borović, Croatian Geological Survey

Laszlo Podolszki, Croatian Geological Survey

Kosta Urumović, Croatian Geological Survey

Helen Reeves, Jacobs

Janusz Wasowski, National Research Council – Research Institute for Geo-hydrological Protection

Leo Matešić, University of Rijeka, Faculty of Civil Engineering

Alan Vranjković, INA d.d.

Ines Vlahov, INA d.d.

Nikša Marković, IN Stria d.o.o.

Foreword

This volume contains the proceedings of the 4th European Regional Conference of the International Association for Engineering Geology and the Environment. The conference took place from October 8-12, 2024 in the beautiful city of Dubrovnik, Croatia, and brought together leading experts, researchers, practitioners and students not only from Europe but from all over the world to discuss the latest advances, challenges and opportunities in the field of engineering geology and geotechnics. The conference was themed "Engineering Geology and Geotechnics: Building for the Future" and provided a forum for dialogue on issues and recent developments in a variety of topics, including: Site investigation and characterization for sustainable infrastructure development, Engineering geology and cultural heritage protection, Emerging technologies and applications in engineering geology and geotechnics, Geohazard assessment and risk mitigation for infrastructure projects, Engineering geology for society, Geological and geotechnical challenges in urban development and construction, Environmental geology and geotechnics for natural resource management, Advances in geological modelling for engineering applications, Geo-aspects of earthquake engineering, and Advances and innovations in landslide and engineering geology research. Therefore, the written papers included in these proceedings reflect the breadth and depth of the topics covered at the conference.

It is a special honor to host the conference and publish these proceedings, which mark the 60th anniversary of the founding of the International Association for Engineering Geology and the Environment (IAEG), an association dedicated to promoting and supporting the advancement of engineering geology through technological activities and research. Bringing together different but complementary fields of engineering geology and geotechnics under the umbrella of this conference promotes interdisciplinary collaboration, knowledge sharing and a comprehensive approach to tackling complex engineering challenges. By working together, the two fields can ensure that engineering projects are not only technically sound, but also safe, sustainable and environmentally responsible. This is especially important in today's world where urbanization and population growth are progressing at an unprecedented rate and the demands on our built environment are greater than ever.

The success of this conference would not have been possible without the tireless efforts of the organizing committee, the scientific committee and the many reviewers who worked hard to ensure the quality of the papers presented. The organizers would also like to thank all the companies and institutions that have provided valuable support for this conference. Finally, we would like to thank all the participants whose enthusiasm and commitment made this conference a truly enriching experience. We are particularly proud of the contributions from young researchers and emerging professionals whose fresh perspectives and innovative ideas will shape the future of our disciplines.

We hope that the knowledge shared in these proceedings will inspire further research and collaboration, contributing to the advancement of engineering geology and geotechnics.

Zagreb, October, 2024.

The Editors

Content

Topic 1

Site Investigation and Characterization for Sustainable Infrastructure Development

GEOLOGICAL-GEOTECHNICAL CHARACTERIZATION OF A RESERVOIR AREA

ISABEL FERNANDES [1], MARIA DOS ANJOS RIBEIRO [2], JORGE NEVES [3], MÁRIO QUINTA-FERREIRA[4]

[1] *Departament of Geology/FCUL & IDL, Instituto Dom Luiz, Campo Grande, 1749-016 Lisbon, Portugal, mifernandes@fc.ul.pt*

[2] *DGAOT/FCUP, Rua do Campo Alegre, 4169-007 Porto, Portugal, maribeir@fc.up.pt*

[3] *EDP Produção, Rua Ofélia Diogo da Costa 39, 4149-022 Porto, Portugal, jorgepacheco.neves@edp.pt*

[4] *Dep. Ciências da Terra, Universidade de Coimbra. Rua Sílvio Lima. 3030-790 Coimbra, Portugal, mqf@dct.uc.pt*

Abstract

The construction of a large dam demands that an accurate study of the rock mass be performed. Besides the aspects related to the foundation, the geologic and geotechnical characteristics of the reservoir area gained increasing importance due to the possibility of slope instability which might, eventually, affect the serviceability of the dam.

Slope instability in rock masses is a complex phenomenon that can be manifested by different types of mechanisms often controlled by the geologic structure, namely the joint system. The present work presents the geological mapping performed in the area covered by the reservoir of a large dam to be built on a rock mass composed of metasedimentary rocks. To assess the stability of the reservoir slopes, the geotechnical assessment included desk study and field survey, as well as the use of digital elevation modeling (DEM) aiming to obtain a set of maps of susceptibility factors. These included the geological map of the area, altimetry, slope angle maps, slope strikes, and land use mapping complemented with stereographic projection of the joint system in different locations for kinematic analysis. The combination of susceptibility factors led to the identification of the more problematic areas.

Keywords

metasedimentary rocks, geologic mapping, joints sets, kinematic analysis, digital elevation modeling

1 Introduction

The construction of a large dam is usually controversial due to several factors from the high cost of construction and river diversion to the social and environmental impacts. The construction involves several geotechnical problems in particular those related to the permeability and the mechanical properties of the rock mass foundation. However, the study of the reservoir has shown in the past to be of utmost importance as landslides in natural slopes may be induced by the increase or variation of the groundwater level or by earthquakes (Aydan, 2016). In the worst scenario, landslides in the reservoir area cause the overtopping of the dam with catastrophic consequences, as in the Vajont dam (Muller, 1964; Semenza and Ghirotti, 2000). Also, the planes of contact between different lithologies can promote the occurrence of slope failure as referred to in Ayan (2016) for the Aratozawa Dam landslide. The author explains the influence of the different mechanical properties of rocks outcropping in the area and refers to the splitting of the rocks along the bedding planes, in which mica laminations were parallel to the bedding orientation.

Following the work of Cruden (1991), and published in Fell et al (2008) landslide is defined as "the movement of a mass of rock, debris or earth down a slope", with designations defined in Varnes (1978).

The definition of landslide susceptibility is "the quantitative or qualitative assessment of the classification, volume (or area), and spatial distribution of landslides which exist or potentially may occur in an area" (Fell et al., 2008). Regarding the factors that control the occurrence of landslides and their importance in landslides susceptibility assessment for different landslide mechanisms, a summary can be found in Corominas et al. (2014) although it seems that there is no generally agreed method for producing landslide susceptibility maps (Guzzetti et al., 2000).

The instability problems around and above the rim of the reservoir depend on several factors, namely: a) Type of soil/rock forming the slope, b) Geometry of the slope, c) Vegetation cover, and d) Human interference within the reservoir rim boundary (Anbalagan and Kumar, 2015). The assessment of the area includes, usually, the analysis of historical records, geological mapping, the study of the joints and major faults, and the evaluation of the slope stability which can be made by qualitative or quantitative methods. The inventory of landslides is traditionally performed by the visual interpretation of aerial photographs, possibly with the aid of automated methods, aiming to reduce the manual interpretation. However, information about historical records is usually scarce or not available at all. Anbalagan and Kumar (2015) state that future landslides will occur under similar conditions as past and present landslides (Lee and Talib, 2005). Pourghasemi et al. (2013) study states that the mapping of actual landslides in the study area is essential for describing the relationship between the landslide distribution and the conditioning factors. However, in the present work, there is no knowledge of multi-temporal inventories leading to the use of only the current distributional pattern to identify susceptible areas.

According to Jaedicke et al. (2014) topography is a key factor for landslide susceptibility which increases with the inclination of the slopes. The author defines different thresholds of slope angles for mass movements to occur: natural loose geological materials are stable up to slope angles of 27º; in terrain steeper than 30º, rocks and other loose materials fall continuously; and above 45º, usually only rockfalls and large rock avalanches occur.

In Pourghasemi et al. (2013) four categories of slope gradient are considered, namely: (1) 0–5º, (2) 6–15º, (3) 16–30º and (4) > 30º. In the present work, the classes in Gupta and Albalagan (1997) were followed: Escarpment/cliff (>45º), steep slope (36-45º), moderately steep slope (26-35º), gentle slope (16-25º), very gentle slope (≤15º). For the analysis, also the findings of Braathen et al. (2004) were taken into account. The authors state that in rock masses sliding can occur for slopes with angles lower than 45º and that rock falls, eventually with backstepping, take place for angles of 60-75º, in special when sub-vertical joints are present.

Regarding the elevation map, also the classes of relative relief used in Gupta and Albalagan (1997) were considered, namely: low (≤100 m), medium (101-300 m), and high (>300 m).

By the end of 2000's first decade, studies were developed to evaluate the viability of a large dam in the centre of Portugal equipped with a hydraulic tunnel and an underground power plant. The dam site is located in an asymmetric V-shaped valley with the abutment on the left bank steeper than the right bank. The dam is planned to be a roller-compacted concrete gravity dam with 89 m maximum height, and 400 m width at its crest.

The present work summarizes the results obtained by the geological-geotechnical assessment of the reservoir covering an area of about 70 km^2 and presents the methods used for the preliminary assessment of the stability of slopes around and above the rim of the reservoir.

2   Methods

The geological-geotechnical study of the area affected by the reservoir involved the combination of different methodologies to assess the stability of the reservoir slopes: a) in-situ investigation of mass movements and historical inventory; b) analysis of aerial photographs and satellite images with draft of the structural map of the area; c) production of the geological map based on field survey; d) production of thematic maps of the triggering factors (altimetry, slope angle maps, and slope strikes), using digital elevation modeling (DEM); e) land use mapping; f) stereographic projection of the joint system in a different location to perform the kinematic analysis.

The characterization of the area, with the predominant orientation of the river of NNE-SSW, included a preliminary desk study in which all the available maps for the region were collated and orthophoto maps analyzed. Aerial photographs on 1:6,667 scale were observed to define the structure of the rock mass

and to identify the main faults and tectonic alignments; register historic landslide scars; and delineate the roads and paths to be used during the field survey.

The field survey included extensive mapping at the scale 1:10,000 of the area covered and surrounding the future reservoir and the establishment of joint survey stations. The recommendations in ISRM (1979) were followed in what concerns the characteristics of the joints, namely, the dip/dip direction, spacing, aperture, persistence, and roughness. The rock mass was classified according to the degree of weathering (W1 to W5) and fracturing (F1 to F5). The dip/dip direction data were plotted on a stereonet projection using the software DIPS (Rocscience) to define the main sets of joints and to prepare histograms for each characteristic assessed. The roughness of each discontinuity was evaluated by comparison with roughness profiles to attribute a JCR value.

3   Results

3.1 Historic record

The study area has a low density of population concentrated in small villages with most of the area uninhabited. In consequence, the possible effects of landslides on the property and the few occurrences have not been registered. To prepare the landslide inventory map, the aerial photograph and the satellite images were analyzed and orthophotographic maps were interpreted. The information about past landslides was complemented during the field survey for geological mapping. The observation in situ allowed the identification of very small volume mass movements related to the manmade walls for agricultural use and the accumulation of debris at the river banks in restricted areas (Figure 1).

Figure 1. Mass movement features interesting very restricted areas

3.2 Morphology and land use

The fluvial network follows the main structural alignments in the region, namely NE-SW and N-S. The valley walls contain rare terracing as well as alluvial deposits plains. The hills show flattened summit surfaces. The area is characterized by very low population density (7.8 to 11 inhabitants per km^2). The small villages are situated at the top of the hills, far from the rim surrounding the reservoir, which will have its maximum water level at 227 m elevation.

The geomorphology of the area shows smooth slopes and occasional cliffs, relief variation from 100 to 300 m, and a low longitudinal profile. Vegetation covers most of the valleys and hills in the wide valley extending for 24 km along the river and tributaries. The dense fluvial network defines a rectangular drainage pattern with some entrenched meanders, in which the steepest cliffs are observed.

The slopes are steeper close to the confluence of the main river and the two larger tributaries. The observation of the slope angle map shows that the slopes have dominantly angles <25º. Slopes >45º are scarce and occur in restricted areas, more commonly close to the meanders of the river. In Figure 2 two areas of the reservoir are shown to exemplify the topography and inclination of the river banks.

In the area, the land use is divided between agricultural land and fallow land. There used to be olive-rich agriculture but with the aging of inhabitants and desertification, most of these are now abandoned. They were arranged in terraces along the slopes, limited by ancient armor stone walls. The recent agriculture terraces with olives are more abundant in the NW bank of the river, dipping to S and SE. The most recent agricultural use is dedicated to eucalyptus which is planted at higher elevations on the

river banks, in special where the morphology becomes smoother. It is more common in the upstream extremity of the reservoir. The outcrops of rock are more common on the SE bank of the river, coinciding with the slopes oriented to N and NW.
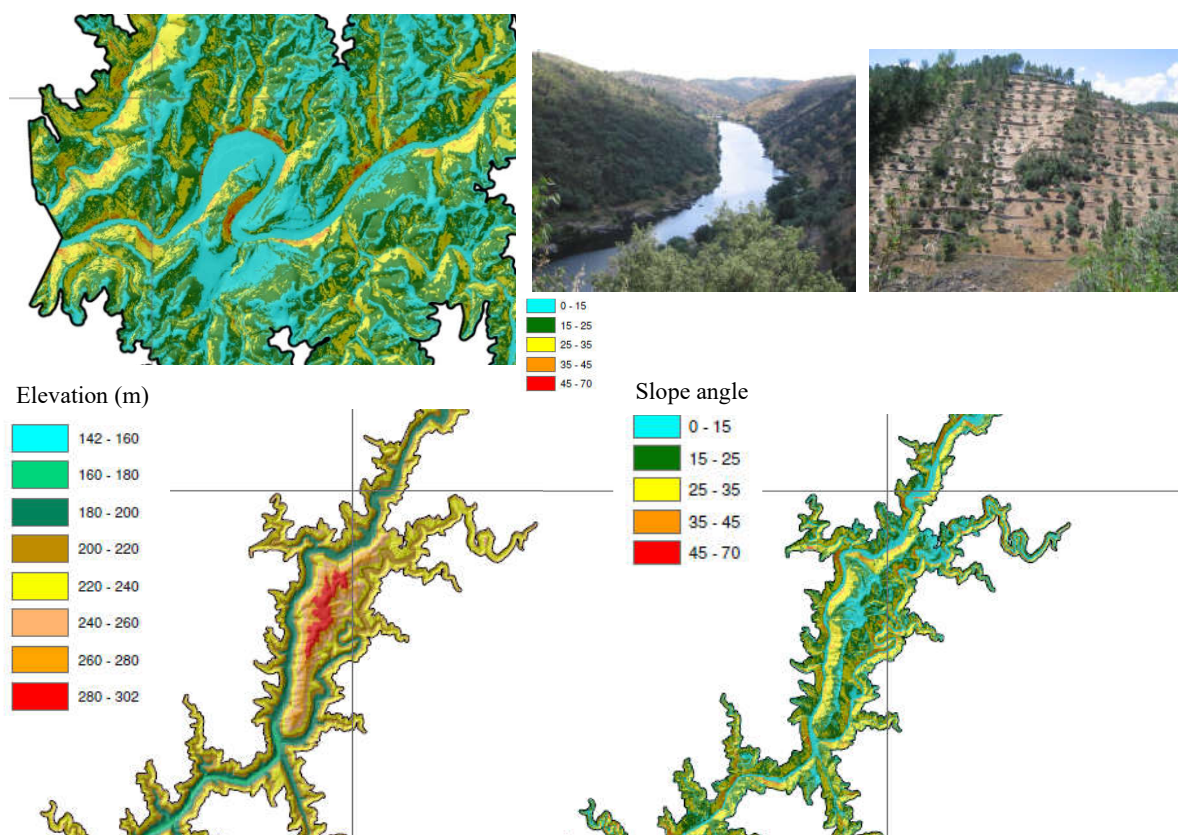
Figure 2. Aspects of the geomorphology of the valley, showing dominantly smooth slopes (<20º): the area of the larger meander, located 2 km upstream of the dam site, the highest elevation area, and examples of the land use

3.3 Geologic mapping of the reservoir

In the area, a sequence of metasedimentary rocks outcrops formed by layers of variable thickness of metagreywacke (quartz-rich rock) and phyllite. This formation outcrops in a wide area of the country and is named the Schist-Greywacke Complex (SGC) (Medina et al., 1998; Pereira et al., 2012). The works published about the rock mass of the area of study refer to the Beiras Group of the Schist-Greywacke Complex dated from the late Proterozoic to the Cambrian period which is composed of metasedimentary rocks of the greenschist facies, in the chlorite zone and, locally, in the biotite zone. Some small areas of fluvial terraces occur along the river banks. They contain conglomeratic deposits with an abundant matrix of ferruginous sandy clay and are 2 to 3 m in height.

Along the area, three slightly different formations were found, namely Perais, Malpica, and Rosmaninhal. All these formations were affected by the Variscan orogeny which imposed folding and low-grade metamorphic features. The geological contacts are aligned NE-SW to WNW-ESE.

Rosmaninhal formation outcrops in the upper part of the reservoir area, where the valley is wider and the slopes smoother. It is characterized by the dominance of pelitic layers with some millimetric to centimetric layers of metagraywacke and rare conglomerate intercalations.

The Malpica formation is the basal unit of the SGC. It occupies a narrow part of the reservoir, coinciding with the highest elevation and steeper slopes in the area. It is characterized by the predominance of metagreywacke with minor phyllite intercalations.

Perais formation occurs in the dam emplacement site and is composed of thin layers of turbiditic meta-siltite and meta-argillite and centimetric to decimetric layers of meta-greywacke.

At the surface, the rock mass is weathered to heavy weathered (W3 to W4), mainly in the phyllite layers,

and shows close to very close joints (F4-F5). Foliation, the main anisotropic feature of the rock mass, defines very small blocks that tend to produce localized rock fall and toppling. Drill cores obtained for the study of the dam foundation rock mass show that the rocks are dark grey to black in color when sound (W1), and moderately spaced (F3). In the quartz-rich layers, the foliation is not well marked whilst in the phyllite it imprints a strong anisotropy to the rock. The surficial soil forms a thin layer mainly composed of clay. Figure 3 presents the main aspects of the three formations and the surficial soil.
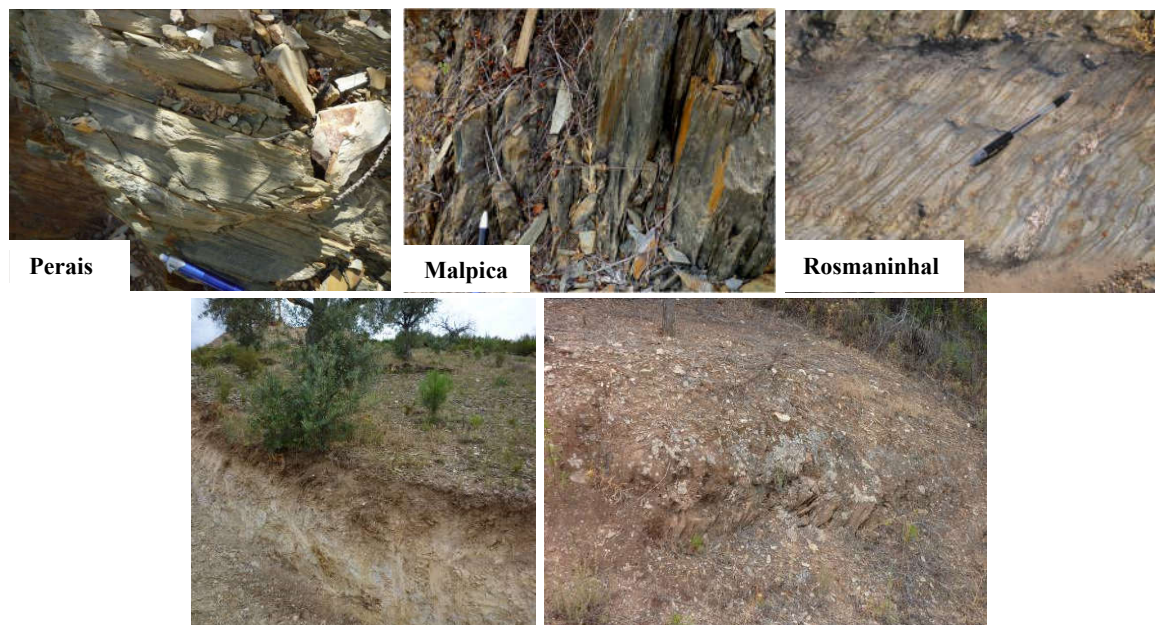
Figure 3. General features of the three geological formations identified and of the surficial soils. The thin surface soil is composed of poor quality highly weathered rock, silt, and clay.

3.4 Structure and geomechanical characteristics

The main alignments were identified by the analysis of the aerial photographs and Google Earth, and plotted on the topographic map to prepare the fieldwork. The outcrops are rare and the places to assess the rock mass structure are limited. The choice was conditioned to the locations where enough measurements (tens) could be made. At the surface, the rock mass is heavily cracked by the foliation planes which are open due to weathering, giving place to tiny blocks of rock which cause small-scale rock falls.

The foliation is oriented NW-SE, parallel to the stratification, which agrees with the regional alignments (Figure 4). It constitutes the main set of discontinuities in the three formations outcropping. Besides this NW-SE sub-vertical set, there are subhorizontal joints that define centimetric blocks of rock by the intersection with the main set. The regional fractures also include ENE-WSW to NE-SW and N-S to NNE-SSW. The major faults are NE-SW, sub-vertical and many of the rivers and tributaries follow the sub-vertical faults alignments. The quartz veins are usually associated with the faults and the fault gauge is formed of fragments of rock, intensely tectonized quartz, clay, and iron oxides.

The section of the valley closer to the dam site is oriented E-W to ENE-WSW and shows a narrow meander with steep slopes, influenced by a major fault parallel to the valley. Upstream, NW-SE faults are dominant, which is approximately perpendicular to the NE-SW valley orientation.

Table 1 presents the characteristics of the main faults identified during the fieldwork performed for the geologic mapping.
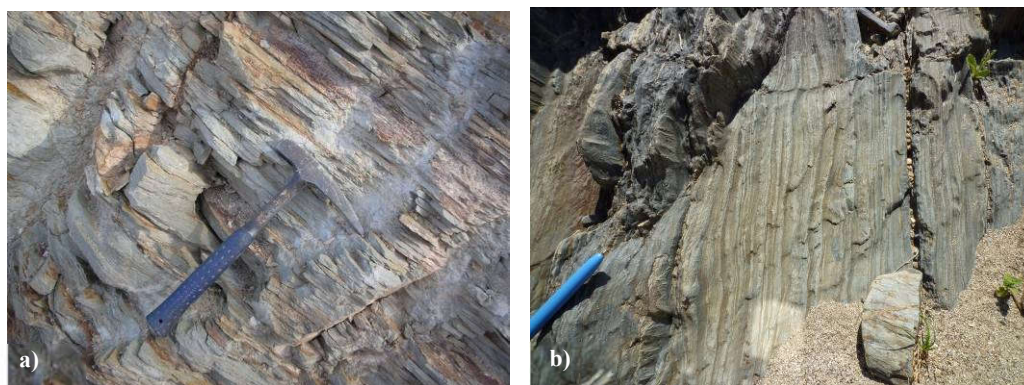
Figure 4. Perais formation, close to the dam site, composed of grey phyllite and greywacke thin layers, S0//S1: N150º; 60ºSW to N140º; 80ºSW

Table 1. Characteristics of the main faults mapped in the area

Fault	Orientation	Gauge (m)	Description of the fault gouge
A	N110º; 90º	4,5	Fragments of quartz and schist with clay
B	N60º; 80ºW	6,5	Fragments of quartz and schist with clay
C	N0º; 90º	4,0	Fragments of quartz and schist with clay; several fractures parallel
D	N35º; 90º	4,0	Ferruginous fragments of quartz and schist with clay;
E	N0º; 90º	5,0	Fragments of quartz and schist
F	N45º a 50º; 90º	10,0	Brecciated fault gauge
G	N135º; 65ºSW	9,0	Fragments of quartz with clay
H	N115º; 90º	5,0	Fragments of quartz and schist with clay

The metasedimentary rocks that form the rock mass both of the dam foundation and the reservoir were characterized by laboratory tests elsewhere (Loureiro et al., 2014; Quinta Ferreira et al., 2015). The values obtained for the sound velocity (V_P) of un-weathered rock cores vary from as low as 561 m/s, for the phyllite layers, to 3378 m/s, for the quartz-rich layers, with an average of 1657 m/s. The unconfined strength ranges from 4 to 78 MPa, being lower for the phyllite layers than for the quartz-rich layers (meta-greywacke). The drill cores, however, mostly show the axis subparallel to the foliation, which may affect the results of the UCS tests.

Regarding the visual characterization of the rock mass *in situ*, the values of GSI are 30-45 for the phyllite layers and 40-55 for the quartz-rich layers, assuming 30 and 40 as the worst scenario, respectively, and m_i of 10. Table 2 shows the mechanical parameters of the rock mass obtained using Hoek-Brown et al. criterion (2002) for a slope of 30 m maximum height, which seldom occurs and assumes the worst scenario for the value of GSI.

Table 2. Properties of the rock mass based on GSI analysis and laboratory test results (using RSdata software)

	Phyllite layers	Quartz-rich layers (Meta-greywacke)
UCS (MPa)	31	48
GSI	30	40
mi	10	10
E (MPa)	880	1948
Cohesion (MPa)	0.080	0.146
Ø (º)	23	33

3.4 Kinematic analysis

The results obtained with DIPS software defined the main sets of discontinuities. The kinematic analysis included the assessment of four types of mass movements: planar sliding, wedge sliding, and direct and

flexural toppling (Hudson and Harrison, 1995). The analysis was carried out considering the possibility of having a slope of 60º, which constitutes the worst possible scenario, and a friction angle of 30º. Table 3 summarizes the results of the kinematic analysis for each formation using the main orientations of the valley for each formation.

The results obtained confirm the site observation that the main mass movement is due to direct toppling and flexural toppling. These movements may occur at the lower levels of the rover banks, where the river excavated steep slopes, and in the manmade excavations for agriculture. The sub-vertical foliation causes the toppling but the dimensions of the blocks are smaller than 50 cm due to the intense fracturing of the rock mass at the surface. The foliation planes and the joints are smooth and show iron oxides due to water percolation and exposition to the weathering elements.

Table 3. Evaluation of the different types of mass movements (%) obtained by kinematic analysis (DIPs)

	Valley	Planar sliding	Wedge sliding	Direct toppling	Flexural toppling
Rosmaninhal	N-S, 60ºE	0	4	8	0
	N-S, 60ºW	6	12	100 (set 2)	2
	N20º, 60ºSE	0	4	10 (oblique)	93 (set 1)
	N20º, 60ºNW	2	14	94 (set 2)	0
	N120º, 60ºNE	0	0	1	6
	N120º, 60ºSW	3	3	94 (set 2)	93 (set 1)
Malpica	N-S, 60ºE	1	18	6	0
	N-S, 60ºW	0	9	75 (set 2)	0
	N30º, 60ºSE	3	19	7	6
	N30º, 60ºNW	32 (set 2)	14	100 (set 2)	0
Perais	N-S, 60ºE	0	3	42 (set 2)	0
	N-S, 60ºW	0	3	70 (set 2)	12
	N40º, 60ºSE	0	4	12	0
	N40º, 60ºNW	0	5	87 (set 2)	100 (set 3)

4   Conclusion

A field survey was carried out to elaborate the geological mapping of the area. The lithology is similar in all the area covered by the reservoir. The river and tributaries have a smooth longitudinal profile. The river flows in a V-valley with rare alluvial deposits.

The structure of the rock mass was assessed to map the main faults and to define the joint sets. Foliation is the main feature, mainly sub-vertical. It is parallel to the stratigraphic contacts (S0//S1) between materials that vary from very fine-grained phyllites to medium-grained quartz-meta-greywackes. The mechanical characteristics of both lithologies are different but the layers are very thin and limits cannot be defined at the scale of the study.

The definition of the joint sets and the use of kinematic analysis performed allow to understand that toppling is the most probable type of mass movement. As observed in the fieldwork, there are localized manifestations of toppling due to the dip/dip direction of the schistosity. However, the spacing of the fractures defines small blocks (F4-F5) which are visible at the lower levels of the river banks and along excavations prepared for agriculture.

Acknowledgments

References

Anbalagan, R.; Kumar, R. Reservoir induced landslides –A case study of reservoir rim region of Tehri Dam. *TIFAC-IDRIM Conference* 28th –30th October 2015 New Delhi, India, 2015.

Aydan, O. Some considerations on a large landslide at the left bank of the Aratozawa Dam caused by the 2008 Iwate–Miyagi intraplate earthquake. *Rock Mech Rock Eng*, 2016, 49, 2525–2539. DOI 10.1007/s00603-016-0977-1

Corominas, J.; van Westen, C.; Frattini, P.; Cascini, L.; Malet, J.-P.; Fotopoulou, S.; Catani, F.; van Den Eeckhaut, M.; Mavrouli, O.; Agliardi, F.; Pitilakis, K.; Winter, M. G.; Pastor, M.; Ferlisi, S.; Tofani, V.; Herva´s, J.; Smith J. T. (2014). Recommendations for the quantitative analysis of landslide risk. *Bull Eng Geol Environ*. 2014, 73, 209–263.

Cruden, D.M. A simple definition of a landslide, *Bulletin of the International Association of Engineering Geology*, 1991, 43, 27-29.

Gupta, P.; Anbalagan, R. Slope stability of Tehri Dam Reservoir Area, India, using landslide hazard zonation (LHZ) mapping, *Quarterly Journal of Engineering Geology and Hydrogeology,* 1997, 30 (1): 27–36. https://doi.org/10.1144/GSL.QJEGH.1997.030.P1.03

Guzzetti, F.; Cardinali, M.; Reichenbach, P.; Carrara, A. Comparing Landslides Maps: A case study in the Upper Tiber Basin, Central Italy, *Environmental Management*. 2000, 25/ 3, 247-263.

Hoek. E.; Carranza-Torres, C.; Corkum, B. Hoek-Brown failure criterion-2002 edition, in *Proc. The 5th North American Rock Mechanics Symp*, Toronto, Canada. 2002, 1, 267-273.

ISRM. Suggested Methods for the Quantitative Description of Discontinuities in Rock Masses, *Int. J. Rock Mech. Min. Sci. & Geomech. Abstr.*, 1979, 15, 319-368.

Jaedicke, C.; Van Den Eeckhaut, M.; Nadim, F. et al. Identification of landslide hazard and risk 'hotspots' in Europe. *Bull Eng Geol Environ*, 2014, 73, 325–339. https://doi.org/10.1007/s10064-013-0541-0

Lee, S.; Talib, J. A. Probabilistic landslide susceptibility and factor effect analysis. *Environ. Geol.,* 2005, 47, 982-990.

Loureiro, F.; Fernandes, I.; Ribeiro, M. A; Neves, J.; Quinta-Ferreira, M. Characterization of a schist using laboratory tests. *SGEM*, Albena, Bulgaria, 2015, 1(2):171-178.

Medina, J.; Sequeira, A.; Silva, F.; Oliveira, J.T.; Rodriguez Alonso, M.D. O complexo Xisto-Grauváquico (CXG) da região de V.N. de Poiares-Arganil- Mortagua. In: Oliveira, J.T., Dias, R.P. (Eds.), Livro Guia das Excursões, *V Congresso Nacional de Geologia*. Lisboa, Portugal. 1998, 137–158.

Muller, L. The rock slide in the Vaiont Valley. *Rock Mech Eng, Geol*, 1964, 2, 148–212.

Pereira, M.F.; Linnemann, U.; Hofmann, M.; Chichorro, M.; Solá, A.R.; Medina, J.; Silva; J.B. The provenance of Late Ediacaran and Early Ordovician siliciclastic rocks in the Southwest Central Iberian Zone: Constraints from detrital zircon data on northern Gondwana margin evolution during the late Neoproterozoic. *Precambrian Research,* 2012, 166– 189.

Pourghasemi, H. R.; Goli Jirandeh, A.; Pradhan, B.; Xu, C.; Gokceoglu, C. Landslide susceptibility mapping using support vector machine and GIS. *J. Earth Syst. Sci.*, 2013, 122: 349–369.

Fell, R.; Corominas, J.; Bonnard, C.; Cascini, L.; Leroi, E.; Savage, W.Z. *Guidelines for landslide susceptibility, hazard and risk zoning for land use planning*, on behalf of the JTC-1 Joint Technical Committee on Landslides and Engineered Slopes. 2008a, 102, Issues 3–4, 85-98.

Quinta-Ferreira, M., Fernandes, I., Loureiro, F., Alves, J., Perdigão, R., Ribeiro, M.A., Santarém Andrade, P., Neves, J. Geologia de Engenharia de rochas xistosas: os xistos negros da EN17 em Coimbra e os filitos de Vila Velha de Ródão. *Comunicações Geológicas*, 2015, 12/102, Issue 1, 89-96, *Atas do VIII Seminário Recursos Geológicos, Ambiente e Ordenamento do Território*, UTAD, Vila Real. DOI: 10.13140/RG.2.1.2214.8569.

Semenza, E.; Ghirotti, M. History of the 1963 Vaiont slide: the importance of geological factors. *Bull Eng Geol Environ*, 2000, 59, 87–97

Varnes, D. J. *Slope Movement Types and Processes*, In: Landslides Analysis and Control, (Ed. R.L. Schuster and R.J. Krizek), Transportation Research Board, National Academy of Sciences, Special Report, 1978, 176, 12-33.

CORRELATION OF ROCK MASS RATING (RMR), TUNNELLING QUALITY INDEX (Q) AND GEOLOGICAL STRENGTH INDEX (GSI) IN PRE-CAMBRIAN DOLOMITE BASED ON FIELD DATA

PUSKER RAJ JOSHI[1], MILAN KHAREL[2], ASHOK POUDEL[2], GANESH RAJ JOSHI[3], DIPAK SAPKOTA[3]

[1] *SKJV-Tanahu Hydropower project*

[2] *SKJV-Tanahu Hydropower project*

[3] *Geo-Environment Nepal,*

[3] *Tanahu Hydropower Project*

Abstract

Over the recent decades, several authors have documented empirical associations among rock mass classification systems, which derive from extensive measurements and observations under particular site conditions and in various geological regimes. This underscores how important the reliability of a correlation equations is, and how critical is the apprehension of each systems objective. Consequently, none of these formulas can claim universal applicability in the contemporary context. Further to this, to ensure effective design and evaluation of an underground opening, it is essential to possess a comprehensive understanding of the geological, structural geological, hydrogeological, and geotechnical attributes of the excavated rock. In the context of Tanahu Hydropower Project (Nepal), diversion tunnels and auxiliary galleries are being excavated in dolomite. 642 tunnel profiles were mapped, and rock mass was classified using three empirical systems; GSI, RMR and Q. After processing and plotting the in-situ data, correlation equations for the three indices were analyzed using regression modeling aiming to identify the most optimal equation and to present a precise relationship between RMR, Q and GSI in the particular Lesser Himalaya formation. These relationships were then compared with those found in existing literature. The developed regression models reveal reliable correlations between RMR, Q, and GSI indices, enabling the engineering geological evaluation for a broad range of rock mass qualities. These formulations of geo-mechanical indices will serve as valuable tools for tunnelling professionals during decision-making processes, preliminary design phases, stability assessments, and estimates of temporary support systems.

Key words

Rock mass classification, RMR, Q system, GSI, Dolomite, Empirical correlation

1   Introduction

The classification of rock masses has evolved into an indispensable tool for the underground excavation industry, particularly in the design and construction of tunnels and caverns. It plays a crucial role in predicting the necessary support structures for underground spaces. Among the rock mass classification systems used in underground work worldwide, the RMR system [1] the RMi system [2] the NGI-index Q-system [3] and the GSI [4]. Tunnelling Quality index (Q) [3] and RMR[1] system are the most commonly and frequently employed system in the all the countries [5-9]. In the context of the Nepal Himalaya, Q [3] and RMR [1] systems have been prevalent in underground excavation design and support activities[10]. Most existing classification systems have their roots in civil engineering case studies from Europe and America [4,7,11-13]. The attention to detail that various classification systems take on various factors and the rating levels for these parameters vary from one classification system to

another. Due to the varying nature of classification system, at least two methods should be used at any site during the early stages of a project [1,14]. The multiple classification systems offers a comprehensive understanding of rock mass characteristics, enabling the estimation of strength and deformation properties, and thus, contributing to a more accurate initial and final support strategy. Detailed calculations for all parameters in both classification systems are not always feasible. Therefore, correlations between these systems are invaluable for the quick determation of various design parameters. Numerous correlations have been developed by researchers and scientists at different stages for different rock mass classification systems. These correlation equations provide a rapid verification of resulting rock mass rating values without the need for extensive recalculations. Despite of having correlation between two systems, from the start of the origin to till date, an efficient correlation between these classification systems has always been felt by researcher and the rock engineering practitioner in Nepal. This is associated with the fact that each previously generated phrase was the result of a set of particular data and site conditions. The accuracy of the base data from which these expressions were derived is critically important to their validity [15].

2 Description of Projects

In recent times, within the realm of Himalayan geology, there has been a surge in underground construction activities, driven primarily by the construction of hydropower projects, water supply infrastructure, and irrigation systems. The utilization of underground spaces for various purposes has been steadily on the rise. Within this context, the need for correlations between different classification systems has become paramount, particularly in the Nepal Himalaya. To contribute to the evaluation of tunnelling cases with respect to the himalayan geology, Tanahu Hydropower Project, currently under construction (Figure 1), was selected as a focal point.
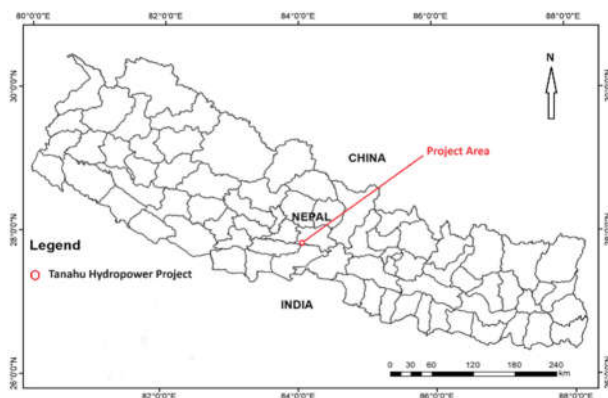
Figure. 1 Location map of the project

Figure. 2 Dolomite Rock present in the study area

3 Geology and Geomorphology of Projects

With respect to the geomorphology, Nepal divided into eight distinct geomorphic regions spanning from the east to the west: the Terai, Churia Range, Dun Valley, Mahabharat Range, Midland, Fore Himalaya, Higher Himalaya, and Inner and Trans Himalaya[19, 20]. Similarly, Nepal features five divisions within the primary tectonic zone, including the Gangetic Plain (Terai), the Sub-Himalayan Zone (Siwaliks), the Lesser Himalayan Zone, the Higher Himalayan Zone, and the Tibetan-Tethys Himalayan Zone [20, 21]. These primary Himalayan thrusts and faults demarcate the aforemention tectonic zones and include the Main Frontal Thrust (MFT), the Main Boundary Thrust (MBT), the Main Central Thrust (MCT), and the South Tibetan Detachment System (STDS), arranged from south to north [22].Tanahu Hydropower Project site is situated 150 km west of Kathmandu on Seti River,Tanahu District, Gandaki Provionce. The project comprise a reservoir storage type project designed with a targeted installed capacity of 140 MW [16]. The geological composition of the area primarily consists of low-grade

metamorphic rock units encompassing slate, intercalations of Phyllite, Quartzite, and Dolomite (see figure 2). A concrete gravity dam with a maximum height above foundation level of 140m and an estimated total concrete volume (including dam body, spillway, and appurtenant structures) of over 920,000 m³ will form [17]. 25km long reservoir with a total volume of 295 million m³.River water is diverted by two diversion tunnel having total length 1167m (inner diameter 11.4 m). The reservoir will feed the concrete lined head race tunnel (1469.6 m long, 7.4m internal diameter)[16-18]. Before reaching the underground powerhouse, the headrace tunnel intersects with a restricted Orifice type surge shaft (61.5 m height, 25.5 m diameter)[18].

4   Literature Review

4.1   Rock Mass Classification System

The Rock Mass Classification System is an important tool in the field of geotechnical engineering which is widely used to evaluate the quality and stability of rock masses for different project development. This system categorizes rock masses based on specific properties and parameters, which enables geotech engineers to make better decisions of the project design, development, and safety measures. There are different rock mass classification systems which have distinct and unique methodology and applications. However, the most commonly used rock mass classification systems include the Rock Mass Rating (RMR), the Geological Strength Index (GSI) and the Q-system.

4.1.1 Tunnelling Quality Index (Q) System

Nick Barton of the Norwegian Geotechnical Institute (NGI) developed a Tunnelling Quality Index, Q-system, based on around 200 tunnels and caves case histories [3]. This system is primarily used to characterize rock mass and estimate the necessary tunnel support. It classifies rock mass quality into different categories based on six parameters: rock quality designation (RQD), joint number (Jn), joint roughness number (Jr), joint alteration (Ja), joint water reduction factor (Jw), and stress reduction factor (SRF). The Q value, which indicates the quality of the rock mass in an underground opening, is calculated as the product of the ratios of these six parameters. The Q value is determined by the product of the ratios of above six parameters which provides a quantitative measure of rock mass quality for underground openings. The Q value is widely used to determine an appropriate support system for tunnels and other underground excavations. It predicts the behavior of the rock mass and helps to select suitable support measures such as rock bolts, shotcrete, and steel sets. which ensure the safety and stability of underground projects.The formula of the Q value is derived from the following equation:

$$Q = (\text{RQD}/Jn) \times (Jr/Ja) \times (Jw/\text{SRF}) \qquad (1)$$

4.1.2 Rock mass rating (RMR) System

The Rock Mass Rating (RMR) System is one of the widely used classification methods for identifying the quality of rock masses. Z.T. Bieniawski established the Rock Mass Rating (RMR) system or Geomechanics classification during the 1970s in South Africa in the 1970s [1]. The system has been revised several times with the increments of additional case data since its first variant.Significant changes were made over the years with revisions in 1974, 1975, 1976 and 1989. In the beginning, the system was established only for tunnels but with time, the system was also introduced for foundations, rock slopes and mining cases [5]. For the classification of rock mass, this approach uses six fundamental factors.The RMR system provides a systematic way to evaluate the rock mass characteristics and determine the necessary support systems for tunnels, mines, and foundations. Moreover, by providing a reliable and systematic approach to classifying rock mass quality, the RMR system helps engineers to make decisions about excavation methods, support systems, and safety measures. This system is particularly valuable in preliminary design phases and for assessing the stability and performance of rock masses in various geological conditions. For the classification of rock mass, this approach uses six fundamental factors. RMR value is calculated from equation (2).

$$RMR = R1+R2+ R3+R4+ R5+ B \tag{2}$$

R1 corresponds to rating related to the intact rock strength, R2 relates to RQD, R3 refers to the spacing of discontinuities, R4 comprises a series of joint surface condition parameters (i.e. persistence, aperture, roughness, infill material and weathering), R5 represents groundwater conditions, and B is the rating adjustment for joint orientations. The derivative value range from 0 to 100, and with reference to the excavation span. The system defines specific stand-up times, a recommendation for optimal excavation strategy, and recommends estimated rock support measures.

4.1.3 Geological Strength Index (GSI)

Hoek, E. (1994). "Strength of rock and rock masses." ISRM News Journal, 2(2), 4-16. In this paper, Hoek introduced a more practical index, the Geological strength index (GSI) . The GSI is effective for both weak and hard rock masses. GSI is less time consuming than the aforementioned existing classification system. GSI links qualitative observational assesment of rock mass to geotechnical engineering values, ie. Mohr–Coulomb, Hoek–Brown strength parameters or rock [23]. In 1999, and aiming to introduce surface condition rating (SCR) and structure rating (SR) Sonmey and Ullusay, [24] attempted to a more quantitative numerical basis for evaluating GSI.
Cai et al. (2004) enhanced the GSI system by providing a more detailed and quantitative approach to classifying and evaluating rock mass structures. Their work allows for a more precise estimation of rock mass properties, which is crucial for various engineering applications.
According to V. Marinos et al. (2005), There are some limitations of GSI which are Subjectivity (visual) in Assessment, Experience Dependency, Scale and Sampling Issues, Sampling Bias, Surface Conditions (Weathering Effects) Variability, Infill Material, Complex Geological Settings (Heterogeneity), Anisotropy, Empirical Nature, Lack of Theoretical Foundation, Quantitative to Qualitative Transition, Integration with Other Systems (Compatibility)**.** These highlighted limitations that need to be addressed for more accurate and reliable assessments. Overcoming these limitations involves improving.
Hoek et al. (2013) made significant advancements in the Geological Strength Index (GSI) system particularly in the linearization and quantification of the axes used in GSI charts. These improvements aimed to enhance the reliability and ease of use of the GSI system in practical engineering applications. The refined GSI charts and enhanced empirical relationships contributed to a better understanding and prediction of rock mass behavior, ultimately supporting more effective and safe engineering practices.
Day et al. (2019) introduced the composite GSI which represents a significant advancement in rock mass classification for heterogeneous conditions. By integrating individual GSI values from multiple domains and using a weighted average approach, composite GSI provides a more accurate and holistic assessment of rock mass quality. This method enhances the reliability of geotechnical evaluations and supports better-informed engineering decisions in complex geological settings.
V. Marinos in 2017 significantly advanced the application of the Geological Strength Index for flysch formations. By developing a specific GSI chart and detailed guidelines tailored to the unique characteristics of flysch, Marinos provided a more accurate and practical tool for assessing rock mass quality in these complex geological settings. The adapted GSI for flysch improves the reliability of geotechnical evaluations and supports better-informed engineering decisions, ultimately enhancing the safety and effectiveness of engineering projects involving flysch.

4.1.4 Existing Relationship

Various researchers have developed several relationships between rock mass classification systems. Most of the relationships have from research cases in individual yet different regimes, in terms of geological formations, tectonic regimes, and geomorphology, stress enviroments etc. Existing correlation equations between RMR and Q, RMR and GSI and GSI and Q which are presented in Table 1.

Table 1 Literature correlation equation between RMR, Q and GSI

Existing correlations	Proposed by	Existing correlations	Proposed by
RMR = 9InQ + 44	Bieniawski [1] 1989	RMR = 8.15lnQ + 44.88	Laderian and Abaspoor [46] 2012
RMR = 5.9InQ + 43	Rutledge and Perston [25] 1978	RMR = 6.3lnQ + 43	Ranasooriya and Nikraz [47] 2012
RMR = 5.4lnQ + 55.2	Moreno [26] 1980	RMR = 8.09lnQ + 43.08	Rafiee [48] 2013
RMR = 5InQ + 60.8	Cameron-Clerke and Budavari [27] 1981	RMR = 5.7lnQ+ 43.65	Castro Caicedo and Pe´rez Pe´rez [49] 2013
RMR = 7.5InQ + 42	Baczynski [28] 1983	RMR = 2.87lnQ +48.71	Ali et al. [50] 2014
RMR = 10.5InQ + 41.8	Abad et al. [29]1983	RMR = 4.52lnQ + 43.635	Sayeed and Khanna [51] 2015
RMR = 43.89–9.19InQ	Celada Tamames [30] 1983	RMR = 6.55lnQ + 59.53	Senra [52] 2016
RMR = 5.3InQ + 50.81	Udd and Wang [31] 1983	RMR = 8.8832InQ + 43.26	Rezaei and latifi [53] 2018
RMR = 8.7lnQ +38	Kaiser and Gale [32] 1985	RMR = 12.334InQ+ 26.01	Sadeghi et al. [54] 2020
RMR = 6.8 InQ + 42	Sheorey [33] 1993	GSI = RMR-5	Hoek and Brown [4] 1997
RMR = 9lnQ + 49	Al-Harthi [34] 1993	GSI = 0.42RMR + 23.07	Cosar [44] 2004
RMR = 12.11lnQ + 50.89	Choquet and Hadjigogiu [35] 1993	GSI = 0.687RMR +4.714	Morales et al. [55] 2004
RMR = 7lnQ + 44	El-Naqa [36]1984	GSI = 6^{e}0.05RMR	Osgoui and Unal [56] 2005
RMR = 6.1 InQ + 53.4	Rawlings et al. [37] 1995	GSI = 0.692RMR + 22.32	Hashemi et al. [45] 2010
RMR = 15lnQ + 50	Barton [38] 1995	GSI = 1.35RMR – 16.4	Irvani et al. [57] 2013
RMR = 7lnQ + 36	Tugrul [39] 1998	GSI = 0.73RMR – 4.38	Singh and Tamrakar [58] 2013
RMR = 5.97 InQ + 49.5	Sunwoo and Hwang [40] 2001	GSI = 0.99RMR – 4.9	Ali et al. [50] 2014
RMR = 4.2 InQ + 50.6	Asgari [41] 2001	GSI = 1.21RMR – 18.61	Zhang et al. [59] 2019
RMR = 3.7lnQ + 53.1	Sari and Pasamehmetoglu [42] 2004	GSI = 0.9143RMR + 6.132	Sadeghi et al. [54] 2020
RMR = 6.4lnQ + 49.6	Kumar et al. [43] 2004	GSI = 1.61In Q+ 42.99	Cosar [44]
RMR = 2.8lnQ + 45.19	Cosar [44] 2004	GSI = 5.96InQ+ 47.85	F. Deak et al. [60]
RMR = 5.37lnQ + 40.48	Hashemi et al. [45] 2010	GSI = 12.638InQ + 28.538	Sadeghi et al. [54]

5   Methodology

To establish correlations between RMR, Q, and GSI, an extensive face mapping was undertaken. This encompassed the examiation of each chainage, covering a total of 1.63 kilometers in the Diversion tunnels and grouting gallery tunnels. 643 tunnel segments were assessed and mapped. The excavation methodology employed was drill and blast. The RMR system used for this classification, referred to as RMR89 (1989 version), account for the correction of discontinuity orientation, while the Q system denoted as Q94, incorporate the latest updates pertaining to the Support Requirement Factor (SRF) aiming phenomena such as sliding, cracking, and rock burst. Following the processing and refinement of raw data, a comprehensive assessment was conducted to determine the accuracy of the existing

expressions. A series of mathematical expressions with particular formats (i.e, linear, exponential, logarithmic, and power), were scrutinized to pinpoint the most suitable equation of the highest correlation coefficient and the minimal error margin. Subsequently, a thorough accuracy analysis was performed using key metrics including the Mean Absolute Error (MAE), the Mean Absolute Percentage Error (MAPE), the Root-Mean-Square Error (RMSE), the Pearson's Coefficient for Correlation (R), and the Coefficient of Determination (R2), in order to ascertain the reliability of the derieved expressions. Every individual analysis method possesses its own distinct characteristics and significance for comprehending and interpreting results. The correlation coefficient, denoted by R, measures the strength and direction of a linear relationship between two variables. Its value ranges from -1 to 1, means perfect positive and negative linear relationship and R=0, means no linear relationship. R helps in understanding how strongly two variables are related linearly. R-squared (R^2) represents the proportion of the variance in the dependent variable that is predictable from the independent variable(s). Its value ranges from 0 to 1, where $R^2 = 1$, The model explains all the variability of the response data around its mean. $R^2 = 0$, The model explains none of the variability of the response data around its mean.

 A higher R^2 means a better fit of the model to the data. MAE is the average of the absolute differences between predicted values and observed values. It measures the average magnitude of the errors in a set of predictions, without considering their direction. It gives a clear indication of how close the predictions are to the actual outcomes. RMSE is the square root of the average of squared differences between predicted and observed values. It measures the average magnitude of the error. It gives a higher weight to larger errors compared to MAE, which can be useful if larger errors are particularly undesirable in the application context. MAPE is the average of the absolute percentage errors between predicted and observed values. It expresses the accuracy of the forecasting system as a percentage and useful for understanding the error relative to the size of the actual values, making it easier to interpret in percentage terms. They were expressed as follows:

$$r = n \sum xy - (\sum x)(\sum y) \div \sqrt{n(\sum x^2) - (\sum x)^2} \sqrt{n(\sum y^2) - (\sum y)^2}$$
(3)

$$R^2 = \frac{1}{N}\{\sum(x_i - x) \times (y_i - y)/\sigma_x - \sigma\}^2$$
(4)

$$MAE = \frac{1}{n}\sum_{i=1}^{n}|x_i - x|$$
(5)

$$RMSE_{fo} = [\sum_{i=1}^{N}(z_{fi} - z_{oi})^2/N]^{\frac{1}{2}}$$
(6)

$$MAPE = \frac{100}{N} \times \sum_{i=1}^{N}|\frac{xi - \hat{x}i}{xi}|$$
(7)

6   Results

The primary goal of this research constitutes an attempt to present a new, precise relationship between RMR, Q and GSI in the Dolomite rock of Nepal Himalaya [61]. For this purpose, the data obtained from Diversion tunnels and different Grouting Gallery tunnels of the Tanahu Project were analyzed. Each tunnel has its own specific geology, and characterised by individual geomorphological and stress conditions. For reference, the data range of rock mass qualities based on the geological mapping records along with highest, lowest, mean and frequent values of Q system, RMR and GSI is shown in Table 2, below.

Table 2: Actual RMR, Q and GSI based on lithology of THP (642 data)

	Highest value	Lowest value	Mean value	Frequent value
Q-value	7.5	0.2	1.465	0.5
RMR	64	36	52	62
GSI	65	20	51	48

The first attempt in this study was made to correlate RMR versus Q, GSI versus RMR and GSI versus Q within the project area [61]. The correlation derivatives between RMR, Q and GSI of the Tanahu project were developed from 642 tunnel segments (1.63 km) respectively, and are presented in Table 3. The analysis of different mathematical expressions [61] for Dolomite rock is presented in Table 3., It is evident that the logarithmic relationships represent the most suitable expressions for RMR versus Q, GSI versus RMR and GSI versus Q.

Table 3: Comparison of various relationship between RMR, Q and GSI of Tanahu hydropower project

Approach	Expression (RMR Vs Q)	R2	Expression (GSI Vs RMR)	R2	Expression (GSI Vs Q)	R2
Linear	RMR = 4.579Q + 46.129	0.4654	GSI = 0.8155RMR + 7.6732	0.7516	GSI = 3.208Q + 46.065	0.2619
Power	RMR= 51.27Q0.1952	0.7505	GSI= 1.5598RMR$^{0.8773}$	0.7523	GSI= 49.346Q0.1688	0.5261
Exponential	RMR = 45.732e0.0881Q	0.3752	GSI= 20.537e0.0168RMR	0.7469	GSI= 45.311e0.0674Q	0.2119
Logarithmic	RMR = 10.057 ln Q + 52.079 (8)	0.7891	GSI = 42.203 ln RMR – 116.02 (9)	0.7557	GSI = 8.0311 ln Q + 50.161 (10)	0.5688

The best-fit regression models resulting from RMR versus Q, GSI versus RMR and GSI versus Q were further analyzed with the utilization statistical matrix in order to evaluate the accuracy of the results [61]. The results obtained in table 4 from analyzing R, MAE, RMSE and MAPE indicate very good implementation . To generate the relationship for the whole data set, correlation was conducted [61]with Dolomite, i.e., lesser Himalaya rock mass. The coefficient of determination R^2 ranges from 0.3752 to 0.7891 for RMR versus Q (Figure. 3), 0.7469 to 0.7557 for GSI versus RMR (Figure. 4) and 0.2119 to 0.5688 for GSI versus Q (Figure. 5), with all best-fit relationships corresponding to logarithmic regression lines for all of the combinations. (Table 4).

Table 4: Evaluation of accuracy of relationship between RMR,Q and GSI of Precambrian Dolomite at THP

Relationship	Approach	R2	MAE	RMSE	MAPE(%)	R
RMR vs Q	Logarithmic	0.7891	3.799	5.055	6.22%	0.8883
GSI vs RMR	Logarithmic	0.7557	3.22	4.43	322.40%	0.8693
GSI vs Q	Logarithmic	0.5688	4.25	5.62	1.39%	0.7541

$$RMR = 10.057 \ln Q + 52.079 \qquad (8)$$
$$GSI = 42.203 \ln RMR - 116.02 \qquad (9)$$
$$GSI = 8.0311 \ln Q + 50.161 \qquad (10)$$

Therefore, from this particular research, equation (8) and (10), having MAPE is 6.216%, 1.39% (MAPE provides a clear and understandable measure of prediction accuracy. By expressing the error as a percentage, it allows for easy comparison across different datasets and scales. A lower MAPE value indicates a more accurate forecasting equation, while a higher MAPE value suggests less accuracy) which shows minimum percentage than other equations and it is proposed as the preferred formulae for estimating relation between RMR versus Q, and GSI versus Q but for equation (9) , the percentage of MAPE is very high ie. 322.4% which suggest less accuracy so it is not reliable (see Table 5).
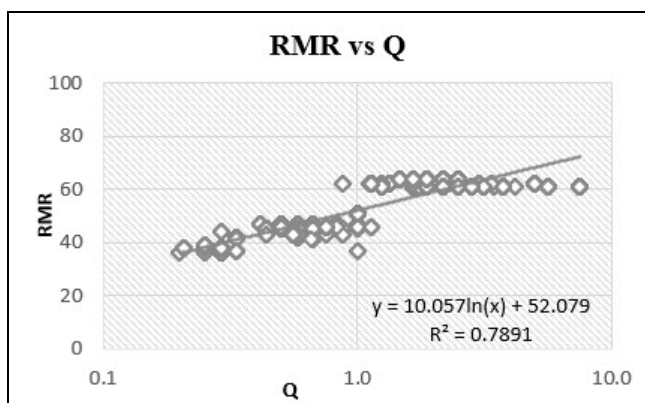
| **Figure 3**: Relation between RMR and Q system (best-fit graph) | **Figure 4**: Relation between GSI and RMR (best-fit graph) |
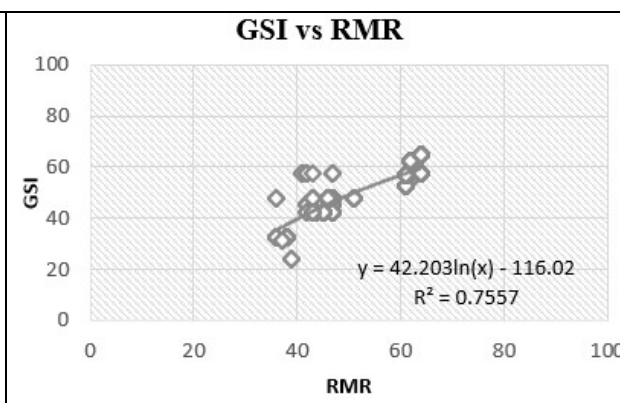
Table 5: Best suitable relationship between RMR, Q and GIS of Precambrian Dolomite

Approach	Equation		R^2	Relationship
Logarithmic	RMR = 10.057 ln Q + 52.079	(8)	0.7891	RMR vs Q (Best)
Logarithmic	GSI = 42.203 ln RMR - 116.02	(9)	0.7557	GSI vs RMR (not reliable)
Logarithmic	GSI = 8.0311 ln Q + 50.161	(10)	0.5688	GSI vs Q

The results obtained from the analysis of RMR versus Q has been compared with some of the existing equations from various researchers (Table 1). The research equation indicates a similar trend to the equation proposed by Choquet and Hadjigogiu (1993) [35] for Q values ranging from 1 to 3. For Q < 2, Mereno (1993) [26] predicts lower RMR values than the research equation, whereas for Q > 2, it predicts higher RMR values. Barton (1995) predicts lower RMR values than the research equation for Q < 1.5 and higher RMR values for Q > 1.5.The comparison of derived trend-line with previous research works is shown in Figure. 6.
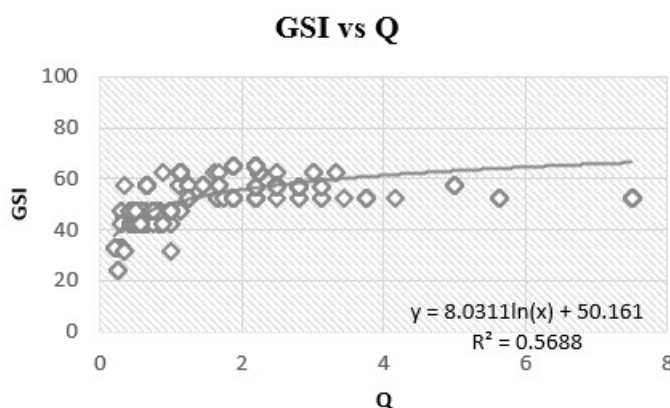
Figure 5: Relation between Q and GSI (best-fit graph)

The results obtained from the analysis of GSI versus RMR were compared with the Hoek and Brown [4], Cosar [44], Singh and Tamarkar [58], and Hashemi et al.[45] equations (Fig. 7). From RMR values of 35 to 65, Hoek and Brown (1997) [4] and Morales et al. (2004) [55] predict a similar pattern to the research equation with the same values of GSI. In contrast, Cosar [44] and Hashemi et al. [45] predict higher GSI values than the research equation for RMR > 50, and lower GSI values for RMR < 50. Additionally, Chaulagai and Dahal (2023) [61] and Zhang et al. (2019) [59] equations consistently predict higher GSI values than the research equation.

 The results obtained from the analysis for GSI versus Q were compared with the existing equations proposed by Cosar [44], F. Deak [60] and Sadeghi et al. [54]. The equation proposed by F. Deak [60] follows a similar pattern but predicted higher values. As illustrated in Figure 8, the highest variability

between these equations occurs when Q values lies in between 0.4 and 0.6, i.e., poor to fair rock mass.The equation proposed by Cosar[44] and Sadeghi et al. [54] predicted higher values as compared to the research equation and does follow the proposed equation pattern.
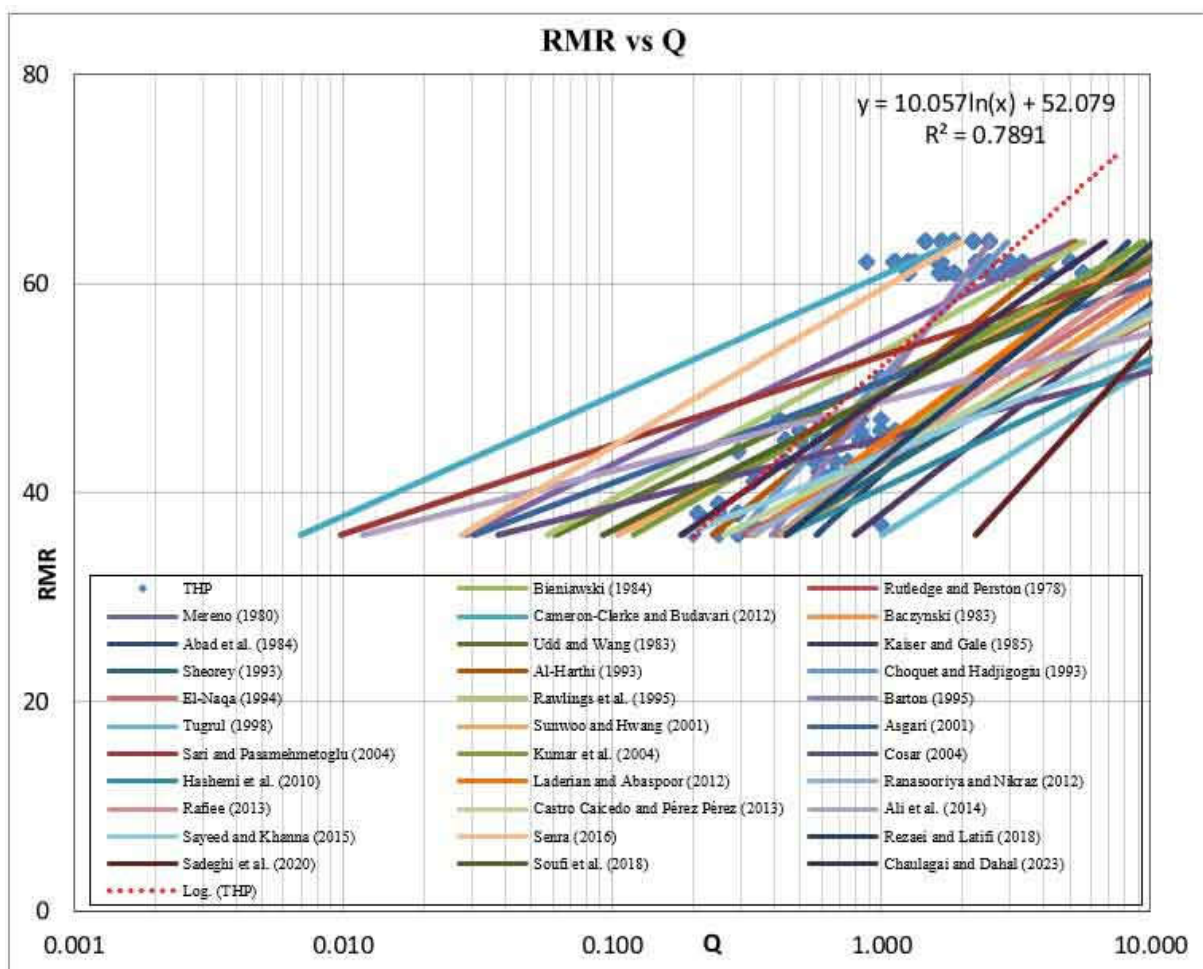
Figure. 6: Comparison of trend line of existing research with previous research works for RMR versus Q
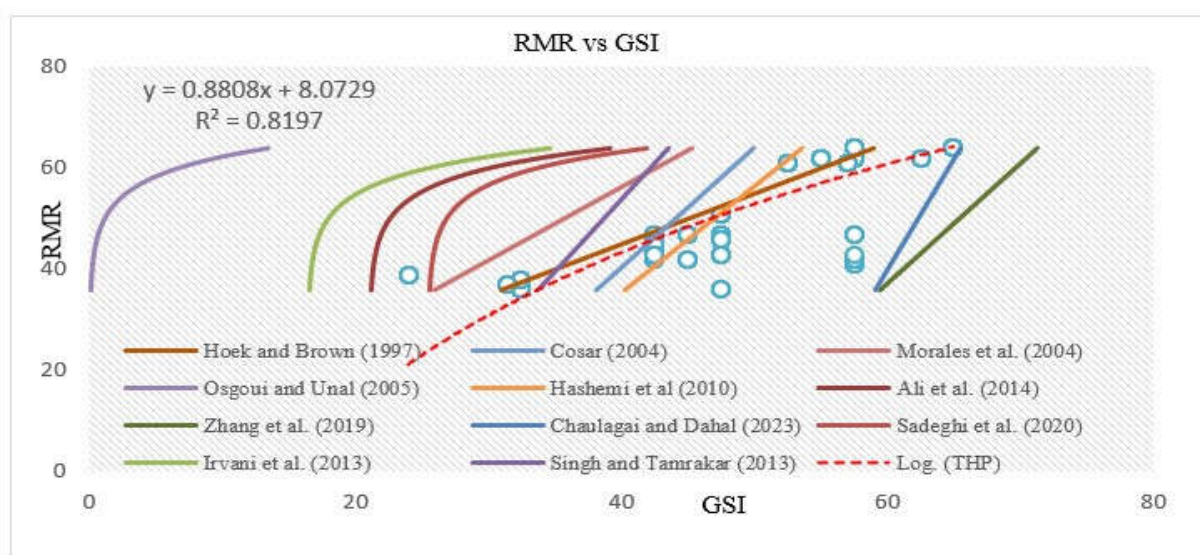
Figure. 7: Comparison of trend line of existing research with previous research works for RMR versus GSI
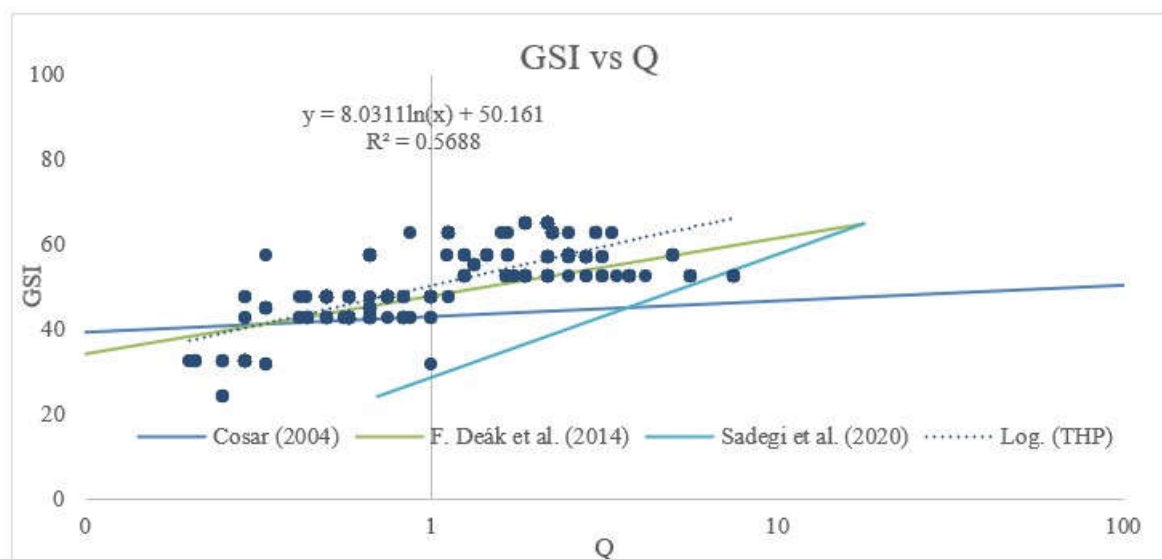
Figure. 8: Comparison of trend line of existing research with previous research works for GSI versus Q

7   Conclusion

Exponents in the field of rock engineering often rely on correlation equations between classification systems, particularly when multiple classification systems are required. The ongoing development of correlation equations between rock mass classifications is driven by the evolving needs of specific site conditions and the accumulation of extensive local data. The significant volume of construction activities in the Lesser Himalayan region, particularly in tunneling projects, has intensified the demand for tailored correlation equations between the most commonly applied classification systems.

To address this, a comprehensive evaluation and analysis of data from 642 tunnel profiles from Project, underground excavations was undertaken. Statistical analysis revealed that results obtained from the project data sets outperforms the results from equations available in relevant literature by previous researchers. This underscores the importance of accounting for specific geological conditions when applying previously established relationships. Upon comparing the relationships developed in this study with existing equations, it is evident that some exhibited similar trends to one or more previous relations [35] [55] [4] [60]. However, the majority of the compared equations did not display such similarities.

In light of the numerous equations [8] [9] and [10] generated from the analysis of the entire tunnel data set, it is recommended to utilize the equation [8] that demonstrates the strongest relationship derived from this data set. This suggested equation offers a practical and efficient solution for the preliminary and final stage studies, as well as the site selection process, particularly within the Precambrian Dolomite Rock in the lesser Himalayan region. It is important to note that the research relationship is generated from data sets of the Lesser Himalaya rock unit, so the researched equation [8] functions well in the Lesser Himalaya. However, caution should be exercised when applying this relationship to the Higher Himalaya and Sub-Himalayan Zone (Siwaliks), and it is advised to avoid using these relationships outside the scope of this study's geological conditions.

Acknowledgements

References

1. Bieniawski ZT (1989) Engineering rock mass classifications.Wiley, New York
2. Palmstro¨m A (1995) RMi-A for rock mass characterization system for rock engineering purposes. The University of Oslo, Norway, p 400

3. Barton N, Lien R, Lunde J (1974) Engineering classification of rock masses for the design of tunnel support. Rock Mech 6:189–236

4. Hoek E, Brown ET (1997) Practical estimates of rock mass strength. Int J Rock Mech Min Sci 34:1165–1186

5. Akram MS, Mirza K, Zeeshan M, Jabbar MA (2018) Assessment of rock mass quality and deformation modulus by empirical methods along Kandiah River, KPK, Pakistan. Open J Geol 08:947–964. https://doi.org/10.4236/ojg.2018.810057

6. Stille H, Palmstro¨m A (2003) Classification as a tool in rock engineering. Tunn Undergr Sp Technol 18:331–345. https://doi.org/10.1016/S0886-7798(02)00106-2

7. Barton N, Bieniawski ZT (2008) RMR and Q - setting records straight. Tunn Tunn Int, pp 26–29

8. Pells PJ, Bieniawski ZT, Hencher SR, Pells SE (2017) Rock quality designation (RQD): time to rest in peace. Can Geotech J 54:825–834. https://doi.org/10.1139/cgj-2016-0012

9. Rehman H, Naji AM, Kim JJ, Yoo HK (2018) Empirical evaluation of rock mass rating and tunneling quality index system for tunnel support design. Appl Sci 8. https://doi.org/10.3390/app8050782

10. Sunuwar SC (2006) Rock support in hydropower projects of Nepal: case studies. J Nepal Geol Soc 34:29–38

11. Hoek E (2007) Practical rock engineering, p 341

12. Hoek E, Diederichs MS (2006) Empirical estimation of rock mass modulus. Int J Rock Mech Min Sci 43:203–215.
https://doi.org/10.1016/j.ijrmms.2005.06.005

13. Goel RK, Jethwa JL, Paithankar AG (1996) Correlation between Barton's Q and Bieniawski's RMR—a new approach. Int J Rock
Mech   Min   Sci   Geomech   33:179–181.
https://doi.org/10.1016/0148-9062(95)00057-7

14. Bieniawski ZT (1978) Determining rock mass deformability: experience from case histories. Int J Rock Mech Min Sci
15:237–247. https://doi.org/10.1016/0148-9062(78)90956-7

15. Castro-Fresno D, Diego-Carrera R, Ballester-Mun˜oz F, A´lvarezGarcı´a J (2010) Correlation between Bieniawski's RMR and Barton's Q index in low-quality soils. Rev la construccio´n 9:107–119. https://doi.org/10.4067/s0718-915x2010000100012

16. Annual report-Tanahu Hydropower project (2079/2080 B.S.) pp 1-90

17. Tanahu Hydropower Project. Social Safeguard Monitoring Report, Project No. 43281-013 Quarterly Report April –June 2023 pp 1-47

18. Tanahu Hydropower Project. Social Safeguard Monitoring Report Project No. 43281-013 Quarterly Report October 2023 pp 1-43.

19. Hagen T (1969) Report on the geological survey of Nepal pre liminary reconnaissance. u¨rich, Memoires de la soc. Helvetique des sci. naturelles 185

20. Upreti BN (1999) An overview of the stratigraphy and tectonics of the Nepal Himalaya. J Asian Earth Sci 17:577–606. https://doi.org/10.1016/S1367-9120(99)00047-4

21. Ganser A (1964) Geology of the Himalaya. Inter Sci John Wiley, London

22. Tiwari RK, Paudyal H (2023) Fractal characteristics of the seismic swarm succeeding the 2015 Gorkha Earthquake, Nepal. Indian Geotech J. https://doi.org/10.1007/s40098-022-00704-1

23. Cai M, Kaiser PK, Uno H, Tasaka Y, Minami M (2004) Estimation of rock mass deformation modulus and strength of jointed hard rock masses using the GSI system. Int J Rock Mech Min Sci 41:3–19. https://doi.org/10.1016/S1365-1609(03)00025-X

24. Sonmez H, Ulusay R (1999) Modifications to the geological strength index (GSI) and their applicability to stability of slopes. Int   J   Rock   Mech   Min   Sci   36:743–760.
https://doi.org/10.1016/S0148-9062(99)00043

25. Rutledge JC, Preston RL(1978) Experience with engineeringclassifications of rock. Proc Int Tunnel Symp Tokyo A:3.1– A3.7

26. Moreno TE (1980) Application de las c1assificaciones geomechnicas a los tuneles de parjares. 11st Cursode Sostenimientos Activosen Galeriasy Tunnels, Found Gomez Parto, Madrid, Spain

27. Cameron-Clarke IS, Budavari S (1981) Correlation of rock massclassification parameters obtained from borecore and In-situ observations. Eng Geol 17:19–53. https://doi.org/10.1016/0013-7952(81)90019-3

28. Baczynski NRP (1983) Application of various rock mass classifications to unsupported openings at Mount Isa, Queensland: A case study. In: Proceeding 3rd Australia- New Zealand Conference on Geomechanics, Wellington, 12–16 May, 1980, vol 2, pp 137– 143

29. Abad J, Celada B, Chacon E, Gutierrez V, Hidalgo E (1983) Application of geomechanical classification to predict the convergence of coal mine galleries and to design their supports. In:

    5th ISRM Congr, Melbourne, Australia. https://doi.org/10.1016/0148-9062(84)92847-x

30. Celada Tamames B (1983) Fourteen years of experience on rockbolting in Spain. In: Stephansson O (ed) Proceedings international symposium on rock bolting, Abisko 1983, , pp 295–311

31. Udd JE, Wang HA (1985) A comparison of some approaches tothe classification of rock masses for geotechnical purposes. In: Ashworth E (ed) Proceedings 25th U.S. symposium on rock mechanics, rapid city, SD, Balkema, Rotterdam, pp 69–78

32. Kaiser TK, Gale AD (1985) Evaluation of cost and empricalsupport design at BC Rail Tumbler Ridge tunnels. Canadian Tunnelling, Tunnelling Association of Canada, Wiley, New York, pp 77–106

33. Sheorey PR (1993) Experience with the application of modernrock classifications in coal mine roadways.Comprehensive rock engineering, principles practice and projects, Editor in Chief J. A. Hudson, Pergamon 5:411–431

34. Al-Harthi AA (1993) Application of CSIR and NGI classificationsystems along tunnel no. 3 at Al-Dela descent, Asir Province, Saudi Arabia. In: Cripps JC, Coulthard JM, Culshaw MG (eds) The engineering geology of weak rock, Balkerma, Rotterdam

35. Choquet P, Hadjigogiu J (1993) Design of support for underground excavations. In: Hudson JA (ed) Comprehensive rock engineering, principles practice and projects. Pergamon Press, Oxford, vol 4, pp 313–348.

36. El-Naqa A (1994) Rock mass characterisation of Wadi Mujibdam site. Central Jordan Eng Geol 38(1–2):81–93

37. Rawlings CG, Barton N, Smallwood A, Davies N (1995) Rockmass characterisation using the Q and RMR systems. In: 8th ISRM Congress (Tokyo), Balkema, Rotterdam, vol, pp 29–31

38. Barton N (1995) The influence of joint properties in modellingjointed rock masses. In: 8th ISRM Congress, Tokyo, Japan, pp 25–29

39. Tugrul A (1998) The application of rock mass classificationsystems to underground excavation in weak limestone, Ataturk dam. Turkey Eng Geol 50(3–4):337–345

40. Sunwoo C, Hwang S (2001) Correlation of rock mass classification methods in Korean rock mass. In: 2nd Asian rock mechanics symposium, Beijing. A. A. Balkema, Rotterdam, pp 631–633

41. Asgari AR (2001) New correlation between ''Q & RMR'' and ''N& RCR''. In: Proceedings of 5th Iranian Tunnelling Conference,Tehran (in Persian). http://www.civilica.com/EnPaper-ITC05-003_0871148829.html.

42. Sari D, Pasamehmetoglu AG (2004) Proposed support design,Kaletepe tunnel. Turkey Eng Geol 72(3–4):201–216.https://doi.org/10.1016/j.enggeo.2003.08.003

43. Kumar N, Samadhiya NK, Anbalagan R (2004) Application ofrock mass classification systems for tunneling in Himalaya, India. Int J Rock Mech Min Sci 41:852–857. https://doi.org/10.1016/j.ijrmms.2004.03.147

44. Cosar S (2004) Application of rock mass classification systemsfor future support design of the Dim tunnel near Alanya. Master of Science thesis in mining engineering, Middle East Technical University, Ankara Turkey, p 217

45. Hashemi M, Moghaddas S, Ajalloeian R (2010) Application ofrock mass characterization for determining the mechanical properties of rock mass: a comparative study. J Rock Mech Geotech Eng 43(3):305–320. https://doi.org/10.1007/s00603-009-0048-y

46. Laderian A, Abaspoor MA (2012) The correlation between RMRand Q systems in parts of Iran. Tunn Undergr Sp Technol 27(1):149–158. https://doi.org/10.1016/j.tust.2011.06.001

47. Ranasooriya J, Nikraz H (2012) Reliability of the linear correlation of rock mass rating (RMR) and tunnelling quality index (Q). Aust Geomech J 44(2):47–54

48. Rafiee R (2013) Tunnels stability analysis using binary andmultinomial logistic regression (LR). J Geol Min Res 5(4):97–107. https://doi.org/10.5897/jgmr2013.0176

49. de Castro Caicedo A´ J, Pe´rez Pe´rez DM (2013) Correlation between the RMR and Q geomechanical classifications at'' LA LI´NEA'' exppratory tunnel. Colombian Centeral Andes Earth Sci Bull 34:42–50

50. Ali W, Mohammad N, Tahir M (2014) Rock mass characterization for diversion tunnels at Diamer Basha Dam, Pakistan—a design perspective. Int J Sci Eng Technol 3:1292–1296

51. Sayeed I, Khanna R (2015) Empirical correlation between RMRand Q systems of rock mass classification derived from Lesser Himalayan and Central. In: International conference on engineering geology in new millennium. New Delhi, India, pp 1–12

52. Senra K (2016) Correlations between geomechanical propertiesto amphibolites and schists from south of Minas Gerais state, Brazil. Master of Science Thesis in Civil Engineering, Universidade Federal de Vic¸osa, Vic¸osa, Brazil, p 160

53. Rezaei M, Latifi Sh (2018) Development of a new empiricalrelation between RMR and Q rock mass classification systems. Iranian J Eng Geol 12(2):100–103

54. Sadeghi S, Sharifi Teshnizi E, Ghoreishi B (2020) Correlationsbetween various rock mass classification / characterization systems for the Zagros tunnel-W Iran. J Mt Sci 17. https://doi.org/10.1007/s11629-019-5665-7

55. Morales T, Uribe-Etxebarria G, Uriarte JA, Valderrama IF (2004) Geomechanical characterisation of rock masses in Alpine regions: the Basque arc (Basque-Cantabrian basin, northern Spain). Eng Geol 71(3–4):343–362. https://doi.org/10.1016/S0013-7952(03)00160-1

56. Osgoui R, U¨ nal E (2005) Rock reinforcement design for unstable tunnels originally excavated in very poor rock mass. In: 31st ITAAITES World Tunnel Congress, Istanbul, Turkey, 291–296

57. Irvani I, Wilopo W, Karnawati D (2013) Determination ofNuclear Power Plant Site in West Bangka Based on Rock Mass Rating and Geological. J SE Asian Appl Geol 5(2):78–86. https://doi.org/10.22146/jag.7210

58. Singh JL, Tamrakar NK (2013) Rock mass rating and geologicalstrength index of rock masses of Thopal-Malekhu River areas, Central Nepal Lesser Himalaya. Bull Dep Geol 16:29–42. https://doi.org/10.3126/bdg.v16i0.8882

59. Zhang Q, Huang X, Zhu H, Li J (2019) Quantitative assessmentsof the correlations between rock mass rating (RMR) and Geological Strength Index (GSI). Tunn Undergr Sp Technol 83:73–81. https://doi.org/10.1016/j.tust.2018.09.015

60. Deak F, Kovacs L, Vasarhelyi B (2014) Geotechnical rock massdocumentation in the Bataapati radioactive waste repository. CentEurGeol 57:197–211.

61. Correlation of Bieniawski's RMR and Barton's Q System in the Nepal Himalaya Kanchan Chaulagai, ,Ranjan Kumar Dahal,   Indian Geotech J https://doi.org/10.1007/s40098-023-00762-z

PARAMETERS OF OVERCONSOLIDATION OF JURASSIC CLAY SOILS IN THE MOSCOW REGION

VLADIMIR MATVEEV [1,2], VIOLETTA SHANINA [1]

[1] *Lomonosov Moscow State University, Russia, violettav@inbox.ru*

[2] *Geotechnical Graduate Lab LLC, Russia, vladimir@matveev.email*

Abstract

Jurassic clay deposits are distributed almost everywhere in the Moscow region. Overconsolidation parameters characterize the initial stress-strain state of the soil. Jurassic deposits may be in the zone of influence of the designed structures, for the calculation of settlements of which nonlinear models of soil behaviour are used. As a result of the study, the behaviour of these soils was studied and processed using various graphical constructions. Soil samples were collected from various sites in Moscow, at depths ranging from 7.7 to 23.8 m, belong to the Jurassic system, being marine sediments. The mineral composition is dominated mainly by smectites (38.5-46.5%). The soils under study are classified as non-saline to slightly saline stiff clays (degree of salinity D_{sal} 0.40-0.71%, plasticity index I_p 15-58%, liquidity index I_L from 0.07-0.26). The overconsolidation ratio *OCR* for Jurassic clays at Desenovskoye ranged from 2.1 to 8.1, which corresponds to overconsolidated and highly overconsolidated soils, and in Fadeev street 1.2-1.9, classifying them as normally consolidation soils according to GOST 25100-2020 standards. The preoverburden pressure *POP* ranged from 115 to 831 kPa and from 69 to 372 kPa, respectively. Thus, the data obtained indicate that historical stresses exceeded modern ones and large thickness of the eroded soils is due to the proximity to the river.

Key words

preconsolidation pressure, salinity, swelling, Jurassic clays, Moscow

1 Introduction

To Jurassic clay deposits are distributed almost everywhere in the Moscow region, with the exception of river valleys and its southern and western sides. Jurassic deposits may be in the zone of influence of the designed structures, for the calculation of settlements of which nonlinear models of soil behaviour are used. Due to the history of geological development of the Moscow region, which includes several glaciations, an important characteristic of clayey rocks is their degree of overconsolidation.

Approaches to studying the effects of overconsolidation vary in stratigraphy, oil and gas geology, soil mechanics, and engineering geology. Meanwhile, the study of overconsolidation using engineering geology methods can provide interesting and important information for other branches of geology, for example, for stratigraphy (Kudryashova, 2002).

Soils are considered overconsolidated if their overburden stresses are less than the historical ones, which were maximum during the existence of the soil; the tested stresses are called preconsolidation stresses σ'_p. For the formation of the properties of pre-Quaternary clay, their density, strength and deformability, the depth of occurrence and position within certain geological structures or zones are of great importance, i.e. the duration of the impact of gravitational, geochemical and tectonic compaction during lithification (Kudryashova, 2002). Such soils differ greatly from similar ones in genesis and composition in their physical and mechanical properties.

The main quantitative indicators of soil overconsolidation are preoverburden stress *POP* and overconsolidation ratio *OCR*. Preoverburden stress *POP* is the difference between the effective preconsolidation stress σ'_p and the vertical effective overburden stress σ'_{vo}. The overconsolidation ratio *OCR* is the ratio of the effective preconsolidation stress σ'_p to the existing vertical effective overburden stress σ'_{vo}. Preconsolidation stress σ'_p is the conditional maximum effective stress on the soil during its existence (GOST R 58326-2018). Thus, this is a pseudo-elastic limit which separates 'elastic' pre-yield from 'plastic' post-yield behaviour of a soil (Umar, Sadrekarimi, 2016). The estimation of the preconsolidation stress σ'_p is usually carried out on the basis of the results of one-dimensional consolidation tests. According to Kudryashova (2002), for Jurassic clay of the Moscow region, *OCR* varies from 2 to 12.6.

2   Methods

The tests were carried out in general according to ASTM D 2435 and GOST R 58326-2018 with some deviations from the standard, since the current edition does not apply to swelling and saline soils. The dimensions of the cutting rings for oedometers were 50×20 mm and 42×13.5 mm (according to ASTM D 2435 no less than 50×12 mm, GOST 12248.4-2020 no less than 71×20 mm), which made it possible to carry out tests on equipment of Geotek standard series up to higher maximum values of vertical stress 5.0 and 7.2 MPa (according to GOST R 58326-2018 no less than 8.0 MPa). The loading scheme was compiled with a step increment coefficient *LIR* of 0.75 (according to GOST 12248.4-2020 *LIR* is 1.0), which allows one to obtain more experimental points and, therefore, more accurately carry out graphical constructions. The criterion for conditional stabilization was 0.01 mm in 4 hours; the completion of filtration consolidation was monitored using a graph of deformation versus the square root of time, excluding creep deformation (ASTM D 2435, Method B and GOST 12248.4-2020). A total of 18 compression tests were carried out. Graphic processing. The compression curves were processed by seven graphical methods for determining the preconsolidation stress (Table 1).

Table 1. Brief description of methods for determining preconsolidation stress and principles of their construction (Matveev, Shanina, 2022)

Method	Principle of the method
Group of semilogarithmic methods	
Casagrande	Constructions are carried out in the space of the porosity coefficient and the logarithm of stresses e — $\log \sigma$. A tangent and horizontal line is drawn to the point of maximum curvature of the compression curve. Next, a bisector is drawn between them. The point of intersection of the bisector and the tangent to the final segment determines σ_p (Casagrande, 1936)
Pacheco Silva	The construction space is e — $\log \sigma$. A horizontal line will be drawn through the initial porosity coefficient e_0 until it intersects with the tangent to the final section. Next, a vertical line is lowered from the intersection point until it intersects with the compression curve, after which another horizontal line is drawn, the intersection of which with the tangent to the final section determines σ_p (Pacheco Silva, 1970).
Burland	Constructions are carried out in the space of the porosity index and the logarithm of stress I_V — $\log \sigma$, which is equivalent to the space e — $\log \sigma$. The σ_p is determined by the intersection of the tangents to the initial and final sections of the compression curve (Burland, 1990).
Boone	The construction space is e — $\log \sigma$. This method uses an unloading loop. The σ_p is determined by the intersection of the tangent to the end section and a line parallel to the unloading loop passing through the overburden pressure point (Boone, 2010).
Group of bilogarithmic methods	
Butterfield, Oikawa, Sridaran, Onitsuka	Logarithmic methods have been proposed by many researchers (Butterfield, 1979; Oikawa, 1987; Onitsuka, 1995). The methods use logarithmic space for the dependence of $e+1$ on stress σ. The difference between the methods is in the choice of the logarithm base. The methods offer the same designs that do not depend on the scale of the axes.

Energy Methods Group	
Tavenas, Becker	The strain energy is used as a criterion for determining σ_p. The constructions are carried out in the bilinear space of the dependence of the accumulated strain energy W on the effective stress σ. The preconsolidation stress σ_p is determined by the simple intersection of the tangents to the start and end sections (Becker et al, 1987).
Wang and Frost	Similar to Becker's method, but uses an unloading loop during construction. To obtain the line of dissipated strain energy, the decompression line is graphically subtracted from the primary compression line (Wang, Frost, 2004).

Previously conducted studies show (Matveev, Shanina, 2021) that the most reliable data are obtained by the Boone method, because the unloading branch is used for construction, which does not affect the effects of the non-expressed inflection of the compression curve. The bend is not expressed due to the disturbance of the soil structure during sampling and the predominance of the mixed nature of structural connections over cementation ones in the studied soils.

3   Results

Characteristics of the studied soils. Soil samples were collected from various sites in Moscow: Fadeev street (55.77°N, 37.60°E) and Desenovskoe village (55.52°N, 37.38°E) at depths ranging from 7.7 to 23.8 m and belong to the Jurassic system, being marine sediments. For the selected samples, the particle size distribution, chemical and mineral composition, and physical properties were determined. The mineral composition is dominated mainly by smectites (from 38.5% to 46.5%). In accordance with the classification according to GOST 25100-2020 according to the degree of salinity D_{sal}, the studied soils are distinguished from non-saline to slightly saline (from 0.40% to 0.71%), the type of salinity is marine. Based on the relative swelling strain without load ε_{sw}, soils are classified from moderately swelling to highly swelling (from 10.6% to 38.9%). The soils under study are classified as stiff clays (I_p from 15 to 58%, I_L from 0.07 to 0.26). In general, the property indicators correspond to the literature data (STO 36554501-020-2010; Kudryashova, 2002). The compression curves were processed by seven graphical methods for determining the preconsolidation stress, the results are presented in Table 2.

Table 2. Values of preconsolidation stress of the studied Jurassic clays

Sample ID	Degree of salinity D_{sal}	Plastisity index I_p (%)	Liquidity index I_L	Void ratio e	Overvurden pressure, kPa	Preconsolidation stress σ_p, kPa determined by graphical method						
						Casa-grande	Pacheco Silva	Becker	Wang, Frost	Bilog.	Burland	Boone
Desenovskoe village (55.52°N, 37.38°E)												
HMC745	0.40	51	0.11	1.30	194	975	783	916	937	935	829	846
HMC746	0.43	51	0.12	1.33	206	501	330	562	538	477	352	340
HMC747	0.61	52	0.10	1.30	224	917	669	956	955	800	682	696
HMC748	0.65	56	0.09	1.31	268	1178	775	1294	1295	1011	820	846
HMC749	0.77	58	0.20	1.42	280	1276	1215	1449	1318	1031	816	714
HMC750	0.55	47	0.06	1.24	306	1258	926	1218	1305	1067	1028	1137
HMC751	0.03	54	0.11	1.34	336	873	534	1032	1026	821	621	627
HMC752	0.55	44	0.24	1.58	154	499	374	368	384	522	402	412
HMC753	0.68	45	0.17	1.57	186	722	492	676	654	652	505	493
HMC754	0.71	45	0.14	1.38	260	565	397	513	487	607	393	375
HMC755	0.16	42	0.20	1.75	280	1147	922	1117	1093	994	882	867
Fadeeva street (55.77°N, 37.60°E)												

HMC608	21	0.23	0.93	450	1521	555	1534	481	1404	1430	822
HMC609	15	0.20	0.64	460	714	388	763	368	784	647	529
HMC610	22	0.24	0.86	476	1257	696	1345	646	1276	1121	842
HMC621	24	0.23	0.77	406	936	456	1026	289	1184	940	712
HMC622	29	0.22	0.83	426	936	456	1026	343	1108	940	724
HMC623	15	0.26	0.73	446	1754	406	1902	231	1465	1662	717
HMC624	27	0.13	1.22	466	1254	573	1291	592	1135	1072	663

The grahical methods give different results, and the methods themselves have a high variation due to the inaccuracy of graphical constructions. Of particular interest is the HMC750 sample, which has an abnormally high value of the preconsolidation stress to other samples. Since this sample does not differ from neighboring samples in other properties, this is most likely due to the peculiarities of graphical constructions.

The overconsolidation parameters were also evaluated by correlation dependencies with index tests. The following formulas were used:
Stas, Kulhawy, 1984

$$\sigma'_p = p_a 10^{1,11 - 1,62\, IL}$$

DeGroot et al., 1999

$$\sigma'_p = 10^{2,9 - 0,96\, IL}$$

Kootahi, Mayne, 2016

$$\begin{cases} \log(\sigma'_p/p_a) = 0.17 + 0.86\log(\sigma'_p/p_a) - 0.09\log LI\,, OCR < 3 \\ \log(\sigma'_p/p_a) = 0.62 + 0.73\log(\sigma'_p/p_a) - 0.24\log LI\,, OCR \geq 3 \end{cases}$$

In order to avoid a sharp jump, in our study, the transition between formulas was provided by a weight sigmoid (logistic) function.

The overconsolidation parameters were also evaluated by correlation dependencies with cone penetration tests (CPT). The following formulas were used:
Mayne, 2009

$$\sigma'_c = 0,33(q_t - \sigma_{zg})^{m_{IC}}$$
$$m_{IC} = 1 - \frac{0,28}{1 + (I_c/2,65)^{25}}$$
$$I_C = \sqrt{(3,47 + \lg Q)^2 + (1,22 + \lg F)^2}$$

Ladd, Foot, 1974 (SHANSEP)

$$\left(\frac{c_u}{\sigma_0}\right)_{OC} = \left(\frac{c_u}{\sigma_0}\right)_{NC} OCR^m$$
$$c_u = \frac{(q_c - \sigma_{zg})}{N_k}$$

We believe that $\left(\frac{c_u}{\sigma_0}\right)_{NC} \approx 0,22$; $m \approx 0,8$; $N_k \approx 14$

Figure 1 shows the change of overburden stress and preconsolidation stress of Jurassic clays in Desenovskoe village with depth. Preconsolidation stress were determining by oedometer test with Boone interpretation method (red markers; the maximum and minimum estimates of preconsolidation stress are marked with segments, since graphical methods are subjective) and correlation dependencies with index tests: Stas, Kulhawy, 1984 (blue markers), DeGroot et al., 1999 (orange markers), Kootahi, Mayne, 2016 (green markers, left bound for NC clay, right bound for OC clay, middle point with logistic smoothing procedure).
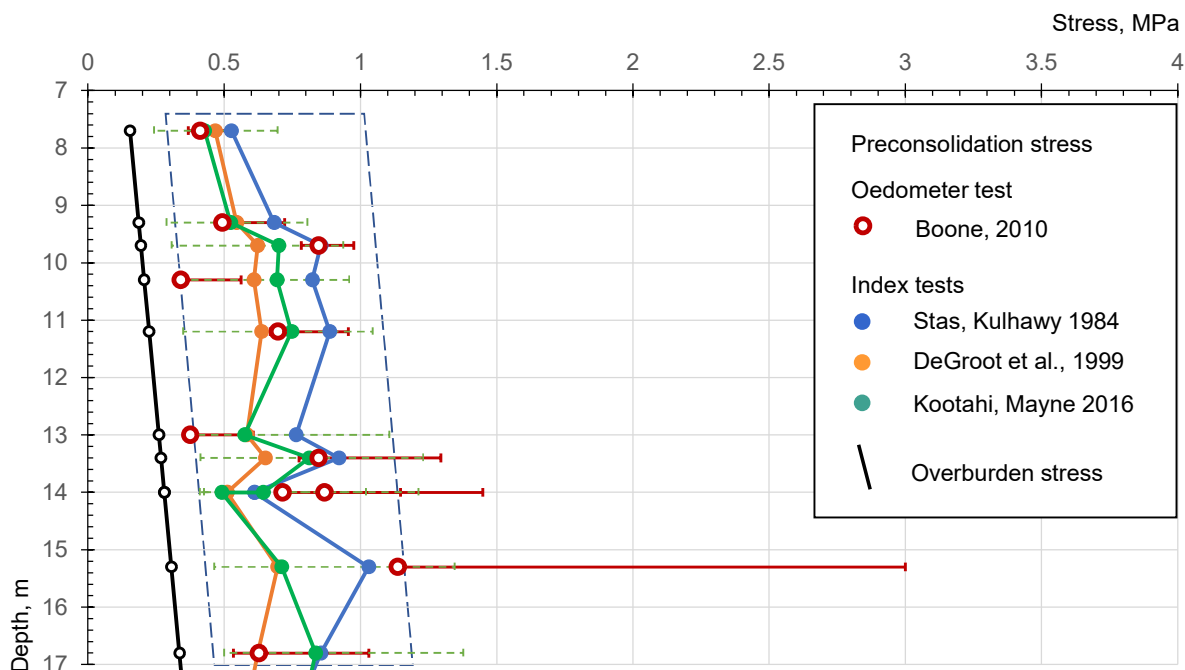
Figure 1. Variation with depth of overburden stress and preconsolidation stress of Jurassic clays, determining by oedometer and index tests in Desenovskoe village.

It is easy to see that the data obtained from various empirical formulas and experimental values generally correspond to each other, forming a 700 kPa wide band along the overburden pressure line. The preoverburden stress *POP* ranged from 115 to 831 kPa, average value 650 kPa

Figure 2 shows the change of overburden stress and preconsolidation stress of Jurassic clays in Desenovskoe village with depth. Preconsolidation stress were determining by oedometer test with Boone interpretation method and correlation dependencies with cone penetration test (CPT): Mayne, 2009 and SHANSEP.
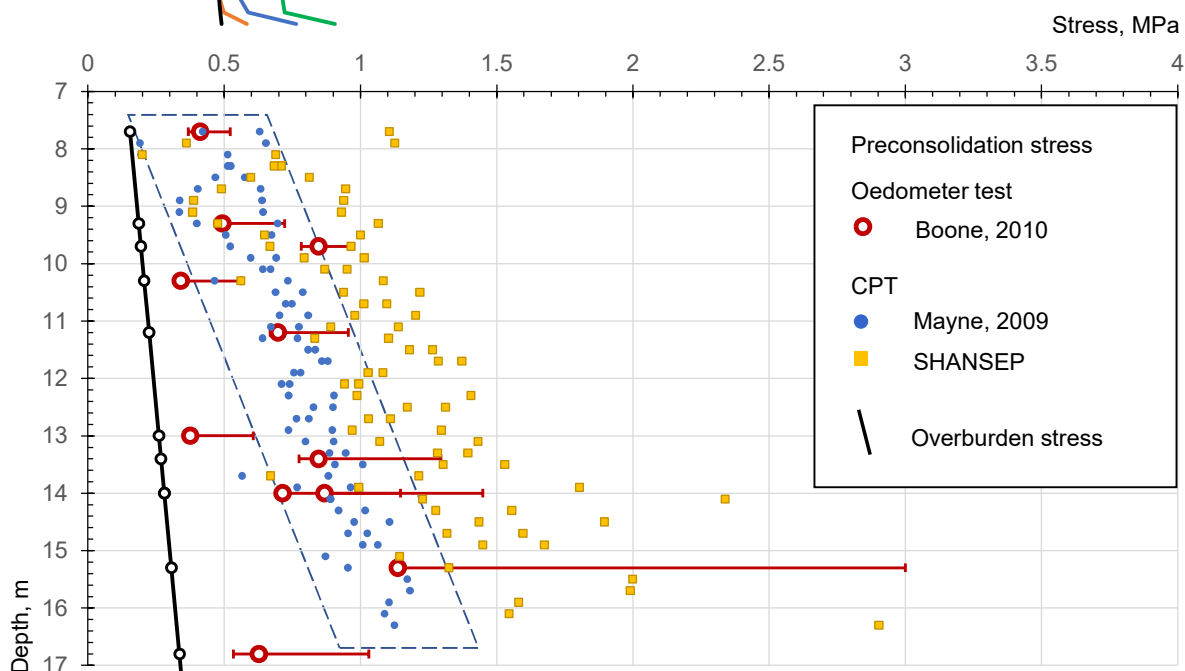
Figure 2. Variation with depth of overburden stress and preconsolidation stress of Jurassic clays, determining by oedometer and CPT tests in Desenovskoe village.

The Mayne method matches the experimental data better than SHANSEP. At the same time, there is an increase in *POP* with a depth of 300 to 900 kPa, while the *OCR* equal 4 remains almost constant. This is probably due to the peculiarity of the interpretation of CPT data.

Figure 3 and 4 shows the change of overburden stress and preconsolidation stress of Jurassic clays in Fadeev street with depth. The data obtained from various empirical formulas and experimental values generally correspond to each other, forming a 500 kPa wide band along the overburden pressure line. The preoverburden stress *POP* ranged from 69 to 372 kPa, average value 250 kPa.
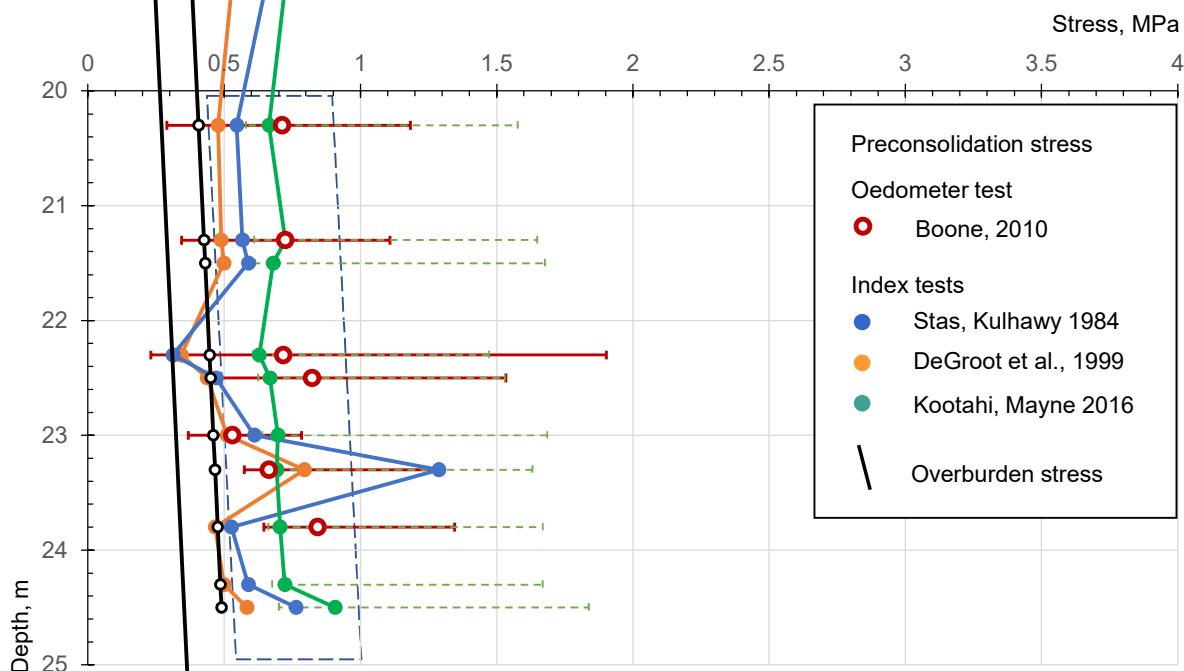
Figure 3. Variation with depth of overburden stress and preconsolidation stress of Jurassic clays, determining by oedometer and index tests in Fadeev street.
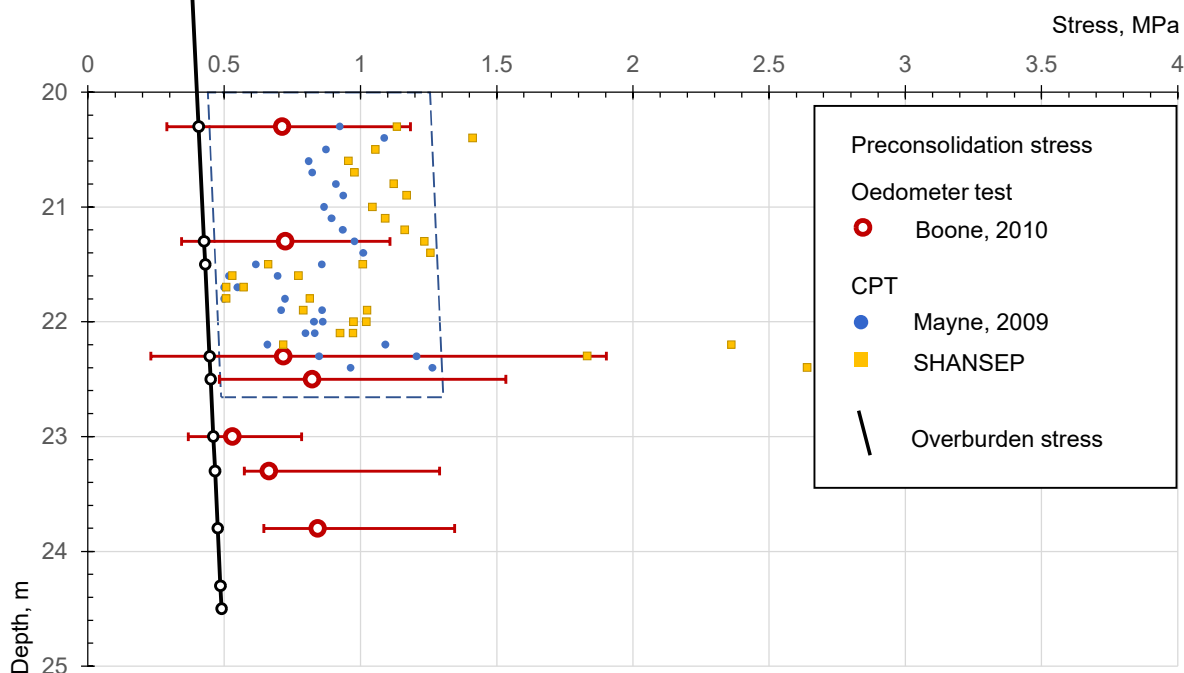
Figure 4. Variation with depth of overburden stress and preconsolidation stress of Jurassic clays, determining by oedometer and CPT tests in Fadeev street.

The CPT data form a wide band, which nevertheless corresponds to the experimental data. Average value of *POP* and *OCR*, obtained by CPT, equal 400 kPa and 1.8.

The *OCR* and *POP* of the samples taken in Desenovsky are higher than those on Fadeev Street. This is probably due to the proximity to the Desna River (less than 0.5 km), and as a result, the greater thickness of the eroded soils. On Fadeev Street, the distance to the nearest Moscow River is at least 3 km, and *OCR* is 1.2-1.9.

4   Conclusion

Overconsolidation ratio *OCR* for Jurassic clays at Desenovskoye ranged from 2.1 to 8.1, which corresponds to overconsolidated and highly overconsolidated soils, and in st. Fadeev from 1.2 to 1.9, that is, normally consolidation soils according to the GOST 25100-2020 classification. The preoverburden stress *POP* ranged from 115 to 831 kPa and from 69 to 372 kPa, respectively. Thus, the data obtained indicate that historical stresses exceeded modern ones and large thickness of the eroded soils is due to the proximity to the river.

References

Becker, D.E., Crooks, J.H.A., Been, K., Jefferies, M.G. Work as a criterion for determining in situ and yield stresses in clays. *Canadian Geotechnical Journal*. 1987, 4, 549–564.

Boone, S.J. A critical reappraisal of "preconsolidation pressure" interpretations using the oedometer test. *Canadian Geotechnical Journal.* 2010, vol. 47, no. 3, pp. 281–296.

Burland, J. B. On the compressibility and shear strength of natural clays. *Géotechnique.* 1990, 40(3), 329-378.

Butterfield, R. A natural compression law for soils (an advance on e — log p'). *Géotechnique.* 1979, 24(4), 469-480.

Casagrande, A. The determination of the preconsolidation load and its practical significance. *Proceedings of the 1st International Conference on soil mechanics and foundation engineering.* Cambridge, UK: Harvard Printing Office, 1936, vol. 3, 60–64.

GOST 12248.4-2020 *Soils. Determination of deformability characteristics using the compression method*. Moscow, Standartinform, 2020.

GOST 25100-2020 *Soils. Classification*. Moscow, Standartinform, 2020.

GOST R 58326-2018 *Soils. Method for laboratory determination of overconsolidation parameters*. Moscow, Standardinform. 2018.

Kootahi, Karim & Mayne, Paul. (2016). Index Test Method for Estimating the Effective Preconsolidation Stress in Clay Deposits. Journal of Geotechnical and Geoenvironmental Engineering. 142. 04016049. 10.1061/(ASCE)GT.1943-5606.0001519.

Kudryashova, E.B. *Patterns of formation of overconsolidated clayey soils*. Ph.D. Thesis, Lomonosov Moscow State University, Moscow, Russia, 2002.

Matveev, V.V., Shanina, V.V. The influence of subjective factors on the accuracy of graphical constructions to interpret the preconsolidation pressure in IL-tests. *Proceedings of 3rd European Regional Conference of IAEG*, Athens, Greece, 6-10 October 2021. — Vol. 2. — National Group of Greece of IAEG Athens, Greece, 2021.

Matveev, V.V., Shanina, V.V. Systematization of factors influencing the accuracy of graphical constructions for determining pre-compaction stress. *Sergeevskie readings. Fundamental and applied issues of modern soil science*. Issue 23. Moscow, GeoInfo, 2022.

Mayne, P.W. 2014a. Generalized CPT method for evaluating yield stress in soils. Geocharacterization for Modeling and Sustainability (GSP 234), ASCE, Reston, Virginia: 1336-1346.

Oikawa, H. Compression curve of soft soils. *Journal of the Japanese Geotechnical Society, Soils and*

Foundations. 1987, vol. 27, no. 3, pp. 99–104.

Onitsuka, K., Hong, Z., Hara, Y., Yoshitake, S. Interpretation of Oedometer Test Data for Natural Clays. *Soils and foundations.* 1995, 35(3), 61–70. doi:10.3208/sandf.35.61

Pacheco Silva, F. A new graphical construction for determination of the preconsolidation stress of a soil sample. *Proceedings of the 4th Brazilian Conference on soil mechanics and foundation engineering.* Rio de Janeiro, Brazil, 1970, vol. 2, no. 1, pp. 225–232.

STO 36554501-020-2010 *Deformation and strength characteristics of Jurassic clay soils in Moscow.* Moscow, OJSC "National Research Center "Construction", 2010.

Umar, M. Sadrekarimi, A. Accuracy of determining pre-consolidation pressure from laboratory tests. *Canadian Geotechnical Journal.* 2016, vol. 54, no. 3, pp. 441–450. https://doi.org/10.1139/cgj-2016-0203.

Wang, L., Frost, J.D. Dissipated strain energy method for determining preconsolidation pressure. *Canadian Geotechnical Journal.* 2004, vol. 41, no. 4, pp. 760–768.

COLLAPSE OF THE SCHIEBURG TUNNEL IN LUXEMBOURG: GEOLOGICAL CAUSES AND EMERGENCY SECURING WORKS

STEVE GRUSLIN [1], TIFFANY HENNEBAUT [2]

[1] *GEOCONSEILS, Luxembourg, steve.gruslin@geoconseils.lu*

[2] *GEOCONSEILS, Luxembourg, tiffany.hennebaut@geoconseils.lu*

Abstract

On 27 August 2022, a collapse occurred in the Schieburg tunnel during repairs on the vault. Around $400m^3$ of debris flowed out in a matter of seconds, completely blocking the tunnel and the only railway line serving the north of Luxembourg towards Belgium. The rockfall occurred 60m from the southern entrance, at a point where the overburden above the tunnel is 31m. The geological and geotechnical studies carried out included reconnaissance boreholes with parameter recording to a length of 80m, geophysical prospecting using electrical and seismic tomography, and a structural study of outcrops in the vicinity of the tunnel. These investigations revealed a highly complex geological situation, with the rockfall zone located at the intersection of a system of conjugate faults not recorded on the geological maps. The results made it possible to estimate the volume and shape of the deconsolidated zone above the collapse, and to propose safety measures to reinforce the deconsolidated zone above the tunnel, safely remove the cone of scree and repair the vault. Geotechnical monitoring of the safety works was carried out from start to finish, enabling the tunnel to be reopened less than one year after the collapse, despite very difficult access conditions.

Key words

Tunnel, collapse, rock slump, geological investigations, emergency works, Luxembourg

1   Introduction

A collapse occurred in the Schieburg tunnel (built in the 19th century) in Luxembourg on 27/08/2022 during repair works on the vault, completely blocking the tunnel and traffic on the only railway line linking the north of Luxembourg to Belgium (Figure 1). The rockfall occurred approximately 60m from the southern entrance of the tunnel, at a point where the overburden above the tunnel is 31m, and under a forest canopy.

In the first phase, in order to understand the causes of the rockfall and, on that basis, to be able to restore traffic in the tunnel while guaranteeing its integrity, a geotechnical study was carried out, including reconnaissance boreholes with parameter recording, geophysical investigations using electrical and seismic tomography, as well as camera passes inside the boreholes. At the same time, a geological and structural analysis was carried out on all the rock outcrops around the tunnel.

In a second phase, once the principle of making the tunnel safe again had been established, geotechnical monitoring was carried out throughout the works. Additional electrical tomography was also used throughout the injection phase to monitor the filling of the deconsolidated zone above the tunnel and check the effectiveness of the reinforcement measures. The results of these tomographies were also used to refine the initial geological and hydrogeological model.

Figure 1. Rock slump seen from the southern part of the tunnel

This paper presents the results of the 2 phases mentioned above, as well as the safety measures implemented. These measures enabled the tunnel to be reopened less than one year after the collapse, despite very difficult access conditions, both for reconnaissance boreholes and for carrying out the work.

2 Geological context and investigations carried out

2.1 Geological contexte

The Schieburg tunnel, located to the north of Luxembourg near Kautenbach, is underlain by Lower Devonian (Emsian) formations forming what is known as the "Our Formation - Schuttbourg Member", which is characterised by alternating sandstone, clayey sandstone, sandy phyllite and phyllite. The geological map also shows a regionally significant NNW-SSE trending fault approximately 250m to the east of the tunnel. This fault is subvertical, oriented 151.4° to the north and appears to have a dextral offset (see Figure 6 right).

2.2 Investigations

To understand the geological and geotechnical situation and explain the causes of the rockfall, a geotechnical study was carried out. This included in a first step 10 inclined reconnaissance boreholes drilled from the surface with parameters recorded up to 80m in length, geophysical surveys using electrical tomography and seismic techniques, and camera passes inside the boreholes. At the same time, a structural and stereographic analysis was carried out on all the rock outcrops around the tunnel. The geophysical profiles had the following characteristics: 2 refraction seismic profiles of 100 m with a spacing of 4m between the geophones, 2 seismic profiles of 50m with a spacing of 2m between the geophones and 3 electrical tomographies with a spacing of 3m between the electrodes for 2 of them, and 2.5m for the last one.

In a second phase, additional electrical tomography was carried out to refine the data from the initial study, but also to follow the grout injections through the deconsolidated zone and check the effectiveness of the reinforcement measures. The 2 additional geoelectric profiles, each 315m long, with a spacing of 5m between the electrodes, were perpendicular to each other and oriented at 45° to the axis of the tunnel in line with the rockfall. In addition, geotechnical monitoring was carried out throughout the works, and the geological and structural study has been refined.

3   Results of the investigations

3.1 Geological and structural situation and faults

After the collapse, and while the first geotechnical study was in preparation, the priority was to understand the geological and structural situation of the area. The rock in the area around the tunnel consists of alternating sandstone and quartzite beds of decimetre to multi-decimetre thickness, with intercalations of shale beds. These beds (particularly the more competent sandstone and quartzite beds) are intersected by 2 families of diaclases perpendicular to each other and perpendicular to the bedding planes, which helps to break up the rock into roughly parallelepiped blocks of varying dimensions. The dip of the stratification planes is generally subvertical and oriented to the SE. Several erratic discontinuities also intersect these beds in a more random fashion, favouring the appearance of dihedrals.

Analysis of the scree cone inside the tunnel shows the presence of blocks and boulders of widely varying sizes, as well as elements that can be assimilated to soils. We also noted the presence of banks that had been completely altered in clay, but still had a remnant of sheets, or even folds and quartz inclusions. Completely transformed and vitrified-looking beds were noted, either in the form of rocky pieces, or in the form of veneers on sandstone beds. Striations indicating displacement (following the passage of a fault, for example) were observed. The clay alterations intercalated between the rock banks can act like a soap layer between the blocks and are very sensitive to variations in water content.

Structural and stereographic analysis revealed a steeper dip (70°) for the stratification near the scree cone than near the northern exit of the tunnel (48°). Two outcrops are directly accessible at the southern entrance to the tunnel, on either side of the train track. At this point, the stratification on the outcrop on the east side dips to the south at 70° to 75°, while the stratification on the outcrop on the west side dips more steeply at 86° to 89°. This variation in the dip of the stratification over such a short distance could be linked to the influence of a fault. Along the logging road above the tunnel, we see that the dip of the stratification decreases from west to east as we approach the tunnel, and then increases sharply directly east of the northern entrance to the tunnel, from 57° to 23° and then increasing to 51° directly east of the tunnel. There is also a change in the strike for the least inclined beds. This trend was also observed just above the northern entrance to the tunnel, where the dip of the stratification varies between 57° to the west and 17° to the east. Several fault planes were observed along the access path to the northern entrance of the tunnel. Directly to the east of the tunnel, the rock mass is no longer visible, and a zone covered with vegetation and soft ground can be observed. This zone corresponds to the supposed passage of a fault plane. Beyond this zone along the road, the dip of the stratification increases again to 51°.

The various observations mentioned above (see also Figure 2) have clearly revealed a variation in the orientation (strike and dip) of the stratification over very short distances, suggesting the presence of a fault or a fault system probably associated with the main fault shown on the geological map. These fault systems in this kind of rocks are generally linked to folds close to the fault planes and bank-to-bank slides. The presence of beds completely transformed into clay, vitrified elements and the mixture of blocks of variable dimensions in a clay matrix also suggest the influence of a zone crushed by a fault.
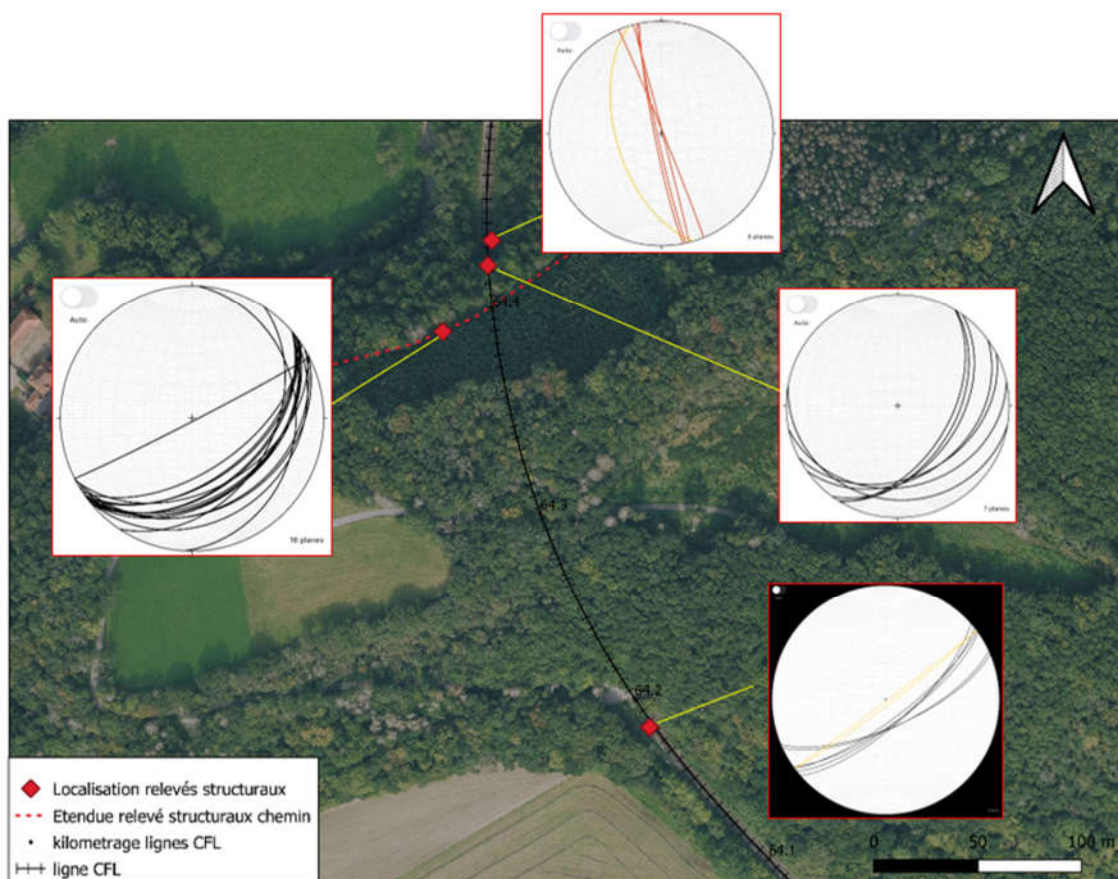
Figure 2. Variation of the strike and the dip of the stratification (black) all around the tunnel. The fault planes observed to the north of the tunnel are shown in red and yellow on the stereogram in the top center

Several camera passes were made in the boreholes. In the deconsolidated zone, the images obtained show the presence of more or less angular blocks and boulders in a clay matrix, as well as numerous voids between the blocks following the rearrangement after the rock slump. The nature of the material is compatible with an area that was crushed following the passage of a fault and subsequently altered by water circulation.
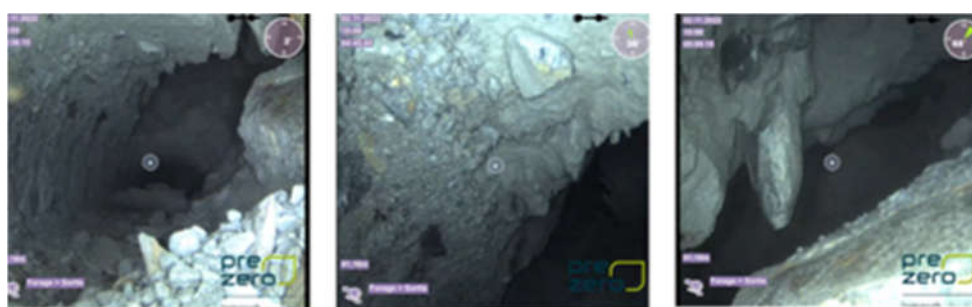
Figure 3. Camera pass through borehole 2 showing blocks and boulders of varying sizes in a clay matrix

Finally, the data from the reconnaissance boreholes and the geophysical studies are compatible with observations suggesting the presence of a faulted/deconsolidated zone located to the east of the tunnel and intersecting it close to the collapsed zone (NE-SW direction). The boreholes also show that the funtis resulting from the collapsed zone rises upwards in the form of a "chimney" rather than spreading laterally. This is compatible with a slide that would have occurred along weathered, clay-filled planes that would have been destabilised by the removal of the vault. In addition, the works on the vault were carried out just after a long period of dry weather, which led to the clay joints being transformed into cohesionless dry joints. Figure 4 summaries the results that can be interpreted from the reconnaissance boreholes.
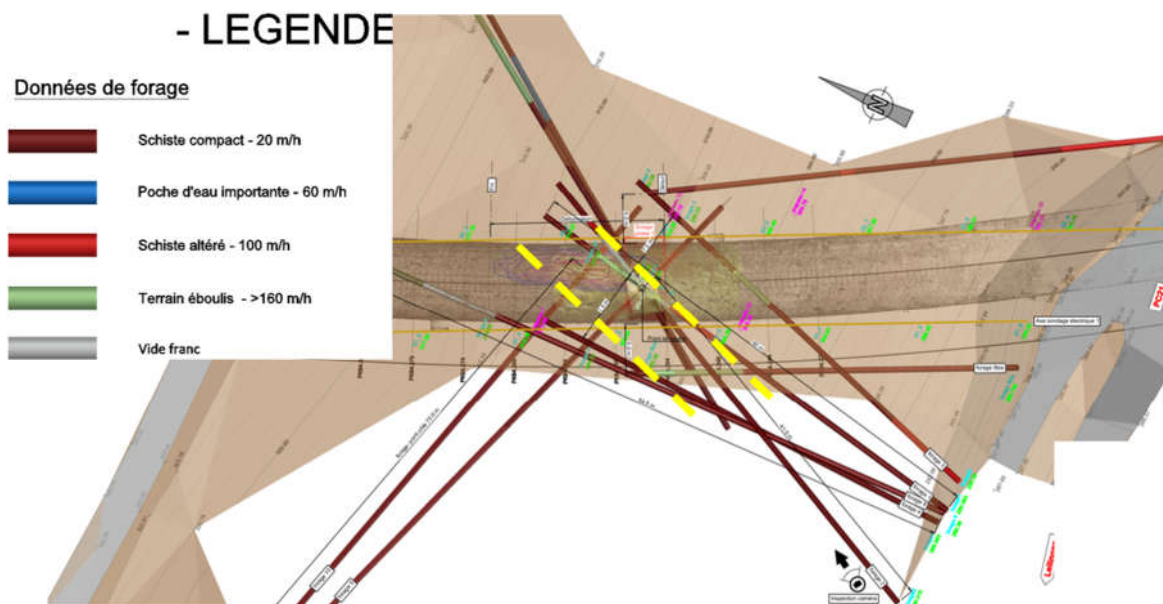
Figure 4. Possible orientation of the deconsolidated/faulted zone (in yellow) based on reconnaissance boreholes

The geophysical measurements carried out during phase 1 of the study confirm the existence of an altered and/or highly fractured zone in line with and around the collapsed zone. This zone is not punctual, has an irregular geometry and appears to be expanding eastwards and possibly northwards.

Additional geophysical measurements (electrical tomographies) have enabled us to refine our understanding of the structural situation at the study site. The various results of the geophysical studies suggest the presence of several deconsolidated zones (one in the immediate vicinity of the tunnel and another further east), probably linked to the presence of one or more faults.
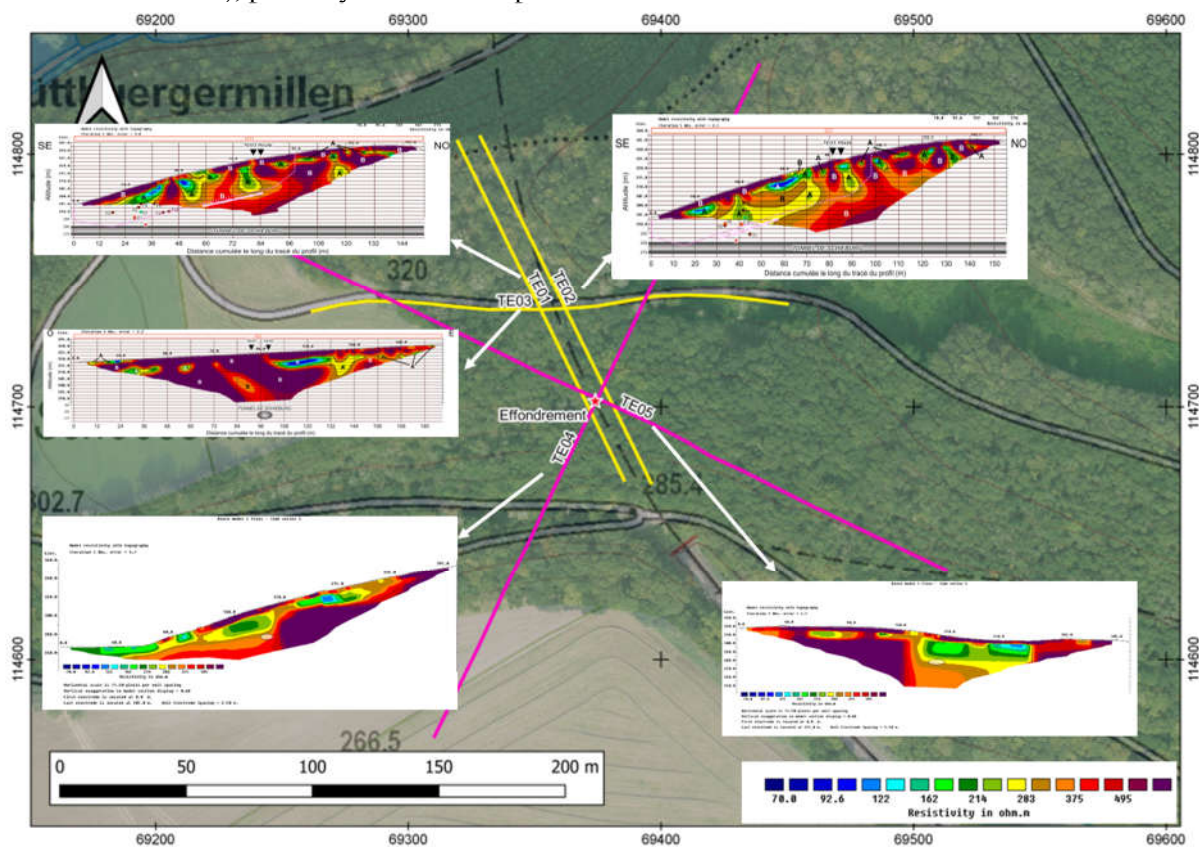
Figure 5. Location of electrical tomographies (yellow lines: 1st phase, magenta lines: 2nd phase) and results obtained

By linking these results with field observations, as well as the position and orientation of the fault shown on the geological map, geomorphological evidence of the presence of fault zones in the vicinity of the tunnel, and the orientation of the deconsolidated zone, which can be estimated on the basis of the results of reconnaissance boreholes, the interpretations shown in Figure 6 left can be made.

We thus have both a fault parallel to the main fault shown on the geological map and passing to the east of the tunnel (fault shown in red in Figure 6) and a fault perpendicular to the above-mentioned fault, which was also revealed by drilling (see Figure 4), and which intersects the axis of the tunnel in the collapse zone (fault shown in black in Figure 6). These 2 faults are thought to form part of a system of strike-slip faults (although it cannot be ruled out that they are also vertically dipping) linked to the various faults shown and supposed on the regional geological map, as illustrated in Figure 6, right.
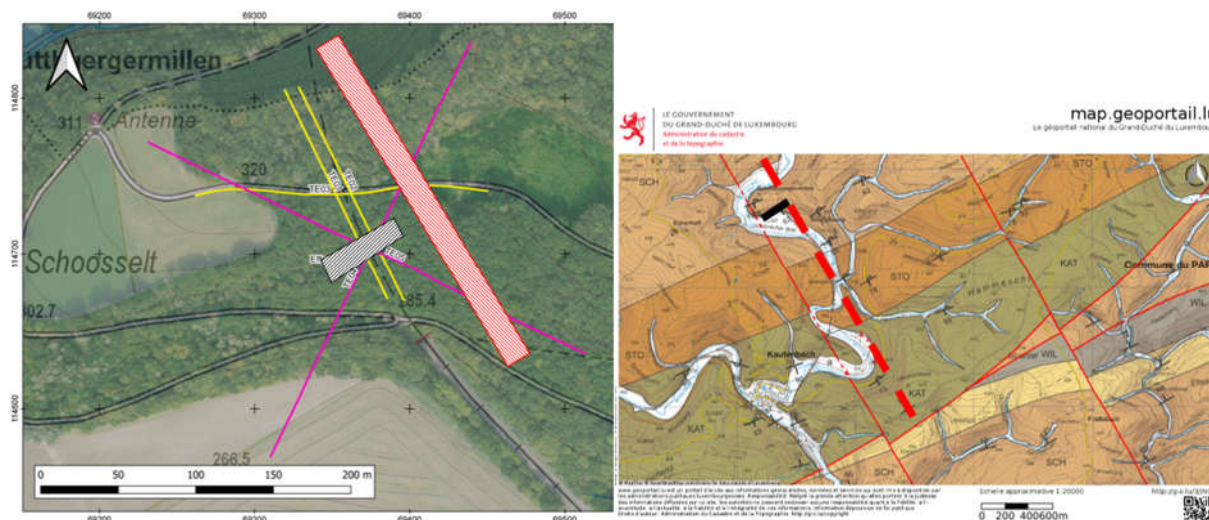
Figure 6. On the left: interpretation of the position of potential faults (red and black) based on electrical tomography and field observations. The yellow and magenta lines represent the axes of the electrical tomographies (see Figure 5). On the right: transfer of these faults (red and black dashes) on an extract of the geological map (faults are represented on the geological map by red lines)

3.2 Conclusions of the geological and geotechnical investigations

Taking into account all the results obtained, the causes that can be retained to explain the rockslide are as follows.

Firstly, the presence of a local geological event combining a zone intersected by 2 fault zones and a folded zone responsible for the alteration of certain banks into clay and the deconsolidation of the rock marked by numerous blocks of very variable dimensions. The division into relatively small blocks is accentuated by the existence of several families of discontinuities (stratification, diaclases, schistosity, fractures, etc.).

Secondly, the stratification is very upright (> 70° in the area of the collapse), which is conducive to instability if the support is removed (by removing the vault for example) and if alteration (water) or drying due to a period of drought greatly reduces the cohesion between the stratification planes.

The rockfall would be the result of a slide along these clay-filled planes (soap layer in the case of water, or loss of cohesion through shrinkage in the case of drying). The extremely dry period prior to the works resulted in a sharp reduction in the cohesion of the clay planes.

The rockfall was probably initiated by the collapse of the banks that had been transformed into clay, which broke away, accentuating the deconfinement of the rest of the altered/decomposed zone. The incident was therefore the result of a combination of geological, tectonic and climatic factors.

4   Emergency securing works

4.1 Securing principle

Based on the complicated topographical situation, the presence of the cone of scree in the tunnel and the technical capabilities of the companies involved, the following methodology was adopted, in consultation with the Lux Ouvrages d'Art design office:

1. Injection of the extrados of the vault on either side of the cone of scree (north and south sides) to fill the voids between the vault and the ground.

2. Injections through the cone of scree to ensure its stability during excavation, and gunning with anchors of the walls of the cone.

3. Injections of cement grout into boreholes drilled from the top of the ground (31m above the tunnel) to fill the voids between the destabilised blocks and boulders above the vault. The injections were carried out in several planes: 0.5m, 1.5m, 3m, 5m, 7.5m, 10m and 15m above the vault.

4. Placement of anchor bars from above in order to hold the injected zone in place (bars of sufficient length to cross the entire deconsolidated zone and anchor in the sound rock beyond it).

5. Anchoring and injections from the tunnel to create a kind of forepole umbrella system and hold the injected soil in place above the hole in the vault.

6. Complete removal of the scree heap.

7. Definitive securing of the vault around the collapsed area using arches formed from galvanised steel "T" sections embedded in the existing vault, between which galvanised steel plates have been welded.

8. Injection of a cement grout behind the welded plates to ensure contact between the arch and the old vault.

9. Drilling of drainage boreholes all around the final arches.
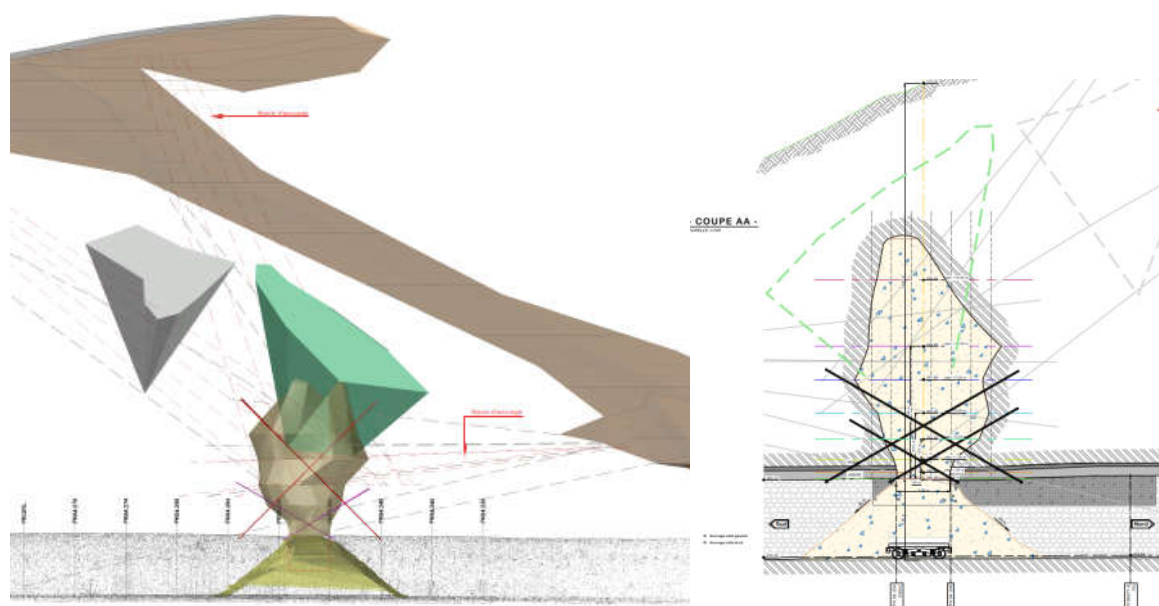
Figure 7. Principle of injection from above (left) and anchoring the injected heap (right)

Figure 8. On the left: drilling from above ton inject the grout. On the right: drilling from the tunnel for anchoring the deconsolidated soil injected above the hole in the vault

Figure 9 shows the situation at the end of the safety works, with the final belts in place.

Figure 9. Situation at the end of the safety works (same point of view as Figure 1)

4.2 Geotechnical and geophysical monitoring

Geotechnical assistance was provided throughout the safety worksite. This was done by checking the injections using electrical tomography and core sampling from the tunnel at various key stages once the works inside the tunnel were possible under safe conditions. For the geophysical monitoring, the 325m tomographic profiles mentioned above were used, applying 2 different analysis protocols (Wenner and Schlumberger), with an initial intervention serving as a "0" measurement and control measurements at different time intervals. A comparison between the initial and final measurements clearly shows an increase in resistivity in the vicinity of the tunnel. This is particularly evident in the profile shown in Figure 10. The increase was most noticeable after the injection work from the vault inside the tunnel.
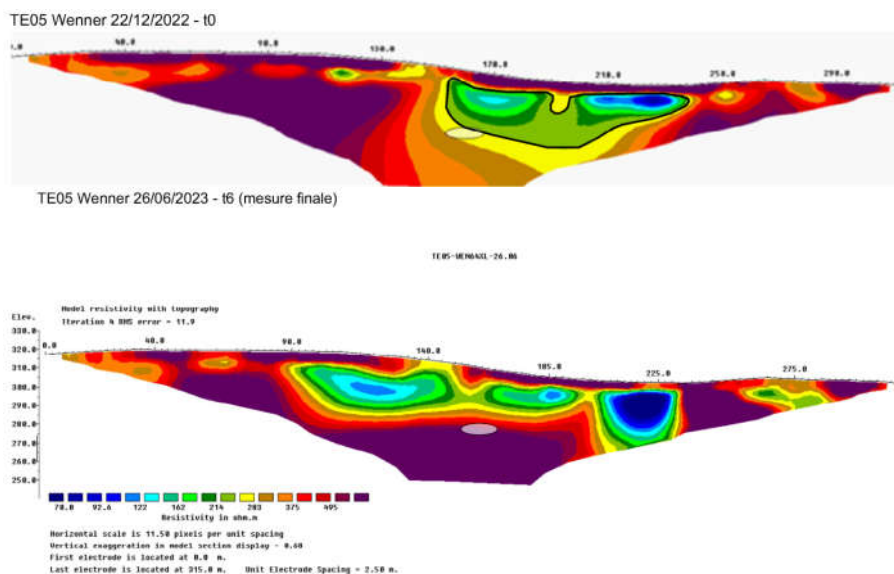
Figure 10. Comparison between the initial measurement and the final measurement showing the increase in resistivity around the tunnel

The geophysics also confirms that the injections did not remain localised to the boreholes, but that the grout probably spread over a fairly large area around the tunnel, which is also confirmed by grout spills observed along the path rising above the tunnel.

In addition to the monitoring by electrical tomography, several phases of control coring were carried out: coring of the vault and pedestals to check the grouting of the interface between the masonry and the ground in place, coring from the tunnel to check the injections carried out from above and coring to disassociate the gunite between the scree heap and the vault, which also enabled the injections to be checked and improved. The various check cores confirmed the low permeability of the ground and scree (significant presence of clay materials in which boulders of varying sizes are embedded), with grout concentrated mainly in the voids between blocks and boulders or along discontinuity planes. This left a number of areas in which the grout was unable to penetrate, and which were therefore not grouted. Nevertheless, the grouted areas provided sufficient overall stability, which was ensured by the installation of anchor bars (from the surface, but also from the tunnel on the north and south sides), the purpose of which was to hold the plug thus created in place so that the scree cone could be removed, and the final arches installed.

Grout was also found further to the south than the area targeted by the injection boreholes drilled from the surface, indicating that the relatively fluid grout initially used by the company tended to follow the planes of discontinuities present in the massif (stratification/schistosity planes dipping to the SE, fault planes or cracks in the rock beds) and to spread over a larger volume than the volume to be treated initially.

In total, 450m^3 of grout was injected. Additional evidence confirming the presence of a fault (striations and quartz crystallisations) was also found in the drill cores.

4.3 Hydrogeological situation

From a hydrogeological point of view, the following observations were made following the study carried out prior to the safety works: a relatively large amount of water at a depth of 25m in borehole 1, an equally large amount of water at a depth of 26m in borehole 6, a verbal indication from the project owner of the presence of a diverted spring near the southern entrance to the tunnel, traces of dampness in several places in the tunnel, traces of dampness in several places in the tunnel, especially on the east side (the side of the supposed fault), traces of dampness at the top of the scree cone on the north side

and just before it on the east side of the tunnel and, lastly, circulations of water observed along planes of discontinuities along a path below the tunnel.

A number of indications suggesting a change in flow conditions in the massif were noted as the work progressed. This change in flow could be linked either to the drains created by the boreholes creating preferential flow zones, or to a change in the permeability of the massif by the clogging of certain discontinuities by the injection grout, or to a combination of these 2 influencing factors. The following signs were observed: the locations of the moisture zones visible in the tunnel at vault level have been moved north and south (on either side of the grouted zone) and are present in greater numbers; more water has entered the tunnel, even partially flooding the track at one point in the absence of pumping; a great deal of water was entering the scree heap; water entering the eastern masonry retaining wall at the southern entrance to the tunnel, which had previously remained relatively dry; water arriving in several places on the paths around the tunnel, which had previously remained dry; and lastly, water seeping into the embankment bordering the path passing over the tunnel, one of which is linked to the presence of a reconnaissance borehole that is also bringing back water, confirming the creation of a preferential flow zone linked to the boreholes.

All these findings led to the decision to drill drainage boreholes in the vault and pedestals all around the area secured by the arches. This drainage system is all the more important given that the protection is mainly made of steel.

5   Conclusion

The geological, geotechnical and geophysical investigations carried out determined that the collapse was the result of a local combination of several factors: the presence of 2 faults (one of which runs right through the collapse) and a folded zone responsible for strong fracturing and clay alteration of certain rock banks, the division into relatively small blocks due to the existence of several families of discontinuities, as well as a very upright stratification (> 70° in the area of the fallen zone), which is conducive to instability if the support is removed and if alteration (water) or drying due to a period of drought greatly reduces the cohesion of the stratification planes. The extremely dry period prior to the works certainly had an influence on the cohesion of the clay planes. The incident is therefore the result of a combination of geological, tectonic and climatic factors.

Monitoring of the works and additional investigations carried out in parallel with the work to make the Schieburg tunnel safe have enabled the hypotheses put forward at the end of the initial study phase to be refined and clarified. Geophysical measurements confirmed the presence of suspected faults. These measurements, combined with the observations made during the initial study, provided a better understanding of the situation and suggested the presence of 2 faults, one of which would actually intersect the tunnel at approximately right angles to it. The extent of the deconsolidated zone linked to this presumed fault could be determined.

These conclusions, in relation to the extent of the deconsolidated zone and the faulted geological context, show that extensive safety work was necessary to enable the tunnel to be reopened, and enhance the importance to realise a geological and structural investigations in such a complicated geological or work context. This allowed the tunnel to be reopened less than one year after the collapse, despite very difficult access conditions for both the exploratory drilling and the safety work.

INTACT ROCK STRENGTH AND ELASTIC PARAMETERS FOR ROCK TYPES IN KIRUNA AND MALMBERGET MINES

NIKOLAOS GRENDAS [1], MATTHEW MAWSON [2], THOMAS WETTAINEN [3], ANNA KYRIAKIDOU [4]

[1] *LKAB (Luossavaara-Kiirunavaara Aktiebolag (publ)), Sweden, nikolas.grendas@lkab.com*

[2] *LKAB (Luossavaara-Kiirunavaara Aktiebolag (publ)), Sweden, matthew.mawson@lkab.com*

[3] *LKAB (Luossavaara-Kiirunavaara Aktiebolag (publ)), Sweden, thomas.wettainen@lkab.com*

[4] *LKAB (Luossavaara-Kiirunavaara Aktiebolag (publ)), Sweden, anna.kyriakidou@lkab.com*

Abstract

This study aims to analyse the correlation between intact strength and elastic parameters of Kiruna and Malmberget rock masses with their geological and alteration characteristics. Recent geotechnical programs in these mines have identified intact rock strength and elastic parameters for various rock masses. Key rock mass classification systems like IRMR, RMR89, or Q use both subjective assessments (IRS - Intact Rock Strength) and objective point load tests to evaluate intact rock strength. Accurate measurements are essential for estimating in situ geotechnical conditions and stresses in deep mine designs. Ongoing UCS (Unconfined Compressive Strength) and TCS (Triaxial Compressive Strength) campaigns have provided valuable additional data for geotechnical models. Numerous studies have demonstrated that Kiruna rock masses generally exhibit greater strength than Malmberget. This study reveals that Malmberget rock types have intact strengths ranging from 100 to 300 MPa, with various types and intensities of alteration for granites, rhyodacites and trachyandesites sometimes exceeding 300 MPa, while biotite schist and massive magnetite may fall below 90 MPa. In Kiruna, intact strength varies between 100 and 350 MPa, including massive magnetite, with the strongest types such as quartz porphyries and tuff, exceeding 350 MPa. Although alteration settings are observed to have a negligible impact on UCS, however, they play a significant role in influencing the elastic parameters. These findings enhance the geotechnical understanding of these mines and lead to more efficient strategic mine planning.

Key words

Intact rock strength, Elastic parameters, Unconfined compressive strength (UCS), Young's modulus, Poisson's ratio, Lithology, Alteration

1.   Introduction

Understanding the geotechnical properties of rock masses is critical for the design and safety of deep mining operations. The rock masses in Kiruna and Malmberget mines, the two largest iron ore underground mines in Sweden (Figure 1), present a unique opportunity to study these properties due to their extensive geotechnical programs. In recent years, these programs have focused on identifying the intact rock strength and elastic parameters for various rock types, essential for realistic estimation of in situ geotechnical conditions and stress distribution.

The importance of accurate measurements of intact rock strength and elastic parameters cannot be overstated, particularly in the context of deep mine designs where the structural integrity and stability of rock masses are paramount. Traditional rock mass classification systems, such as the In-situ Rock Mass Rating (IRMR), Rock Mass Rating 1989 (RMR89), and the Q-system (Bieniawski 1985, Laubscher 1990) often rely on subjective assessments of IRS. These assessments can also be complemented by more objective methods, such as point load tests, which provide a more reliable basis for classification and subsequent engineering decisions (ISRM 1985).

Figure 1 A map of Northern Europe showing the Scandinavia peninsula where Kiruna and Malmberget mines in Sweden are spotlighted

Ongoing Uniaxial Compressive Strength (UCS) and Triaxial Compressive Strength (TCS) testing campaigns have been instrumental in yielding valuable data that contribute significantly to geotechnical models (Bieniawski & Bernede 1979, Deere & Miller 1967, Hoek & Brown 2019). This study's comprehensive analysis based on geotechnical borehole logging and laboratory testing not only corroborates previous findings but also provides new insights into the mechanical behaviour of these rock masses. By expanding the geotechnical knowledge base, this research supports the development of more accurate and reliable geotechnical models, ultimately enhancing the safety and efficiency of mining operations in these regions.

This study leverages the latest data from extensive geotechnical investigations conducted in Kiruna and Malmberget mines. By examining the correlation between the intact strength, elastic parameters, and lithological - alteration characteristics, this research aims to enhance the understanding of these rock masses. The findings indicate notable differences between the two regions.

1.1.   Geological settings of Kiruna mine

The Kiruna iron ore deposit, one of the largest and most significant in the world, is an apatite iron oxide deposit formed around 1.9 billion years ago during the Precambrian era (Hallberg et al. 2012). The iron ore is hosted within a sequence of metavolcanics and metasedimentary rock, known as Porphyry Group. The primary minerals in the Kiruna deposit are magnetite and hematite (less abundant), with significant amounts of apatite (a calcium phosphate mineral) and minor amounts of other minerals such as actinolite, albite, scapolite, quartz and carbonates. The ore body is generally steeply dipping and tabular to lens-shaped, extending for almost 5 kilometres along strike, up to 100 m thick and more than 1300 m down dip. The surrounding rocks have experienced extensive hydrothermal alteration, including albitisation, silicification, sericitization, and the introduction of various hydrothermal minerals (Bergman et al. 2001). The origin of the Kiruna ore is debateable, linked to either direct magmatic activity lead crystallization of iron minerals or hydrothermal processes that concentrated the iron and phosphate minerals (Geijer 1910, Troll et al. 2019). The mine operates primarily as an underground mine using sublevel caving, a method well-suited to the steeply dipping and extensive ore bodies of the Kiruna deposit.

1.2.   Geological settings of Malmberget mine

The Malmberget iron ore deposit, located in the Gällivare municipality in northern Sweden, is an important iron oxide-apatite (IOA) type ore body, similar to the Kiruna deposit. Formed around 1.9 billion years ago during the Precambrian era, the iron ore is hosted within a sequence of felsic and mafic metavolcanic and metasedimentary rocks, predominantly of volcanic origin, which have undergone significant metamorphism and deformation (Bergman et al. 2001, Hallberg et al. 2012, Sarlus et al. 2020). The primary minerals in the Malmberget deposit are magnetite and hematite, with significant amounts of apatite and other accessory minerals such as amphiboles, pyroxenes, quartz, and feldspar. The ore structure is complex compared to Kiruna, consisting of multiple steeply dipping ore bodies in a fold structure that vary significantly in size and shape, extending for almost 5 kilometres along strike, more than 1800 m down dip while thickness varies between 30 to 200 m depending on the ore zone. The surrounding rocks have experienced extensive hydrothermal alteration, including silicification, chloritization, and the introduction of various hydrothermal minerals. The origin of the Malmberget ore is linked to volcanic activity, with iron-rich sediments being deposited on the sea floor and later concentrated by hydrothermal processes. The mine operates primarily as an underground mine using sublevel caving and sublevel stopping methods, which are well-suited to the complex and extensive ore bodies of the Malmberget deposit.

2   Methods

This study employed a comprehensive approach to present and analyse the intact strength and elastic parameters of rock material for the Kiruna and Malmberget mines, with geotechnical laboratory testing being the primary methodology. Samples from various rock types were collected through drilling campaigns and subjected to Uniaxial Compressive Strength (UCS) tests to determine the maximum axial compressive stress they could withstand before failure. Additionally, Triaxial Compressive Strength (TCS) tests were conducted to assess the rock's strength under confining pressure, simulating in situ stress conditions and providing insights into the rock's behaviour under different stress regimes. Secant elastic parameters such as Young's modulus and Poisson's ratio were measured using strain gauges during UCS and TCS tests, which are crucial for understanding the deformation characteristics of the rock masses. Point load tests were also performed as a supplementary method to quickly estimate the intact rock strength. Alongside laboratory testing, geotechnical borehole logging was conducted to gather continuous records of rock properties along the drilled holes, including Rock Quality Designation (RQD), and detailed geological characterization such as RMR89, IRMR and Q.

The data collected from laboratory tests and borehole logging were systematically analysed to establish correlations between intact rock strength, elastic parameters, and geological characteristics. Statistical methods were used to evaluate the distribution of strength and elastic parameters, investigate the influence of lithology and alteration on rock behaviour, and compare the geotechnical properties of Kiruna and Malmberget rock material. This methodological framework ensured a robust and comprehensive assessment, contributing significantly to the geotechnical understanding necessary for safe and efficient deep mining operations in these regions.

In this study, only the uniaxial compressive strength (UCS) results for Kiruna and Malmberget mines are presented accompanied with core logging characteristics including lithology and alteration. The triaxial compressive strength (TCS) results are excluded due to their complexity, necessitating a more detailed and comprehensive analysis, which will be addressed in a subsequent study. In Table 1 an inventory of the samples used is presented and in **Error! Reference source not found.** the geospatial distribution of the samples is visualised in plan view perspective for both sites. As becomes prominent in Figure 2, the geospatial distribution of testes samples is notably sparse, particularly in Kiruna region. Consequently, further sampling is required to enhance the geotechnical investigation in subsequent studies.

Table 1 Inventory about the type, amount and date for the samples used for both sites

Test type	Site	Samples	Boreholes	Testing date From	Testing date To
UCS	Kiruna	192	21	Sep-23	Feb-24
UCS	Malmberget	218	21	Oct-22	Nov-23
Total		**410**	**42**		
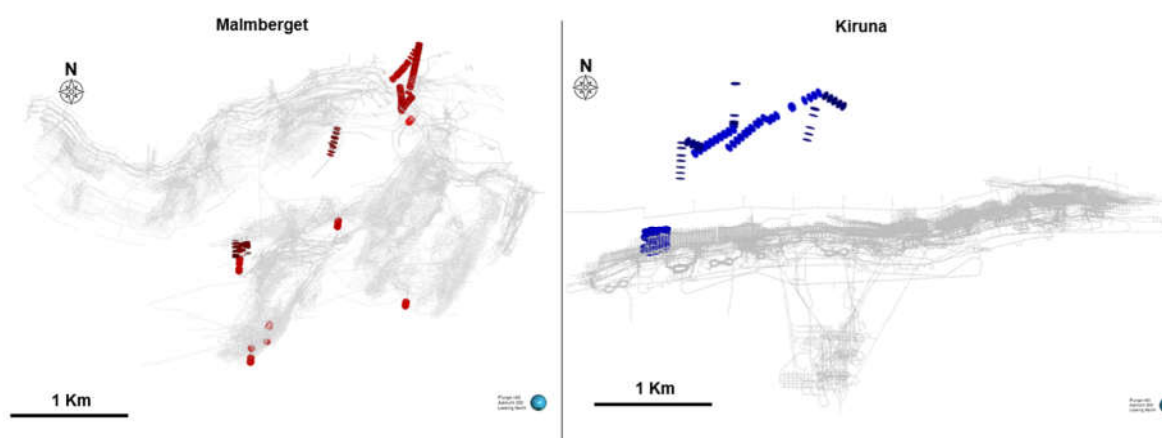
Figure 2 The geospatial distribution of UCS samples used in the present study is presented in a plan view perspective for Malmberget and Kiruna sites, looking north with a plunge of +60°. The mine layouts are presented in grey colour.

3   Results

The results of this study provide a detailed understanding of the intact strength and elastic parameters of rock material from the Kiruna and Malmberget mines. The findings are based on extensive geotechnical laboratory testing, supplemented by borehole logging. Here, we present the key results for each mine and discuss their implications.

A comparative analysis of the two mining regions revealed distinct differences in geotechnical properties, which correlate with their geological characteristics. In Figure 3, the overall distribution of all tested samples for UCS, Young's modulus and Poisson's ratio is presented in box plot form. Although

in Kiruna the highest concentration of data is lower than in Malmberget, strength results are obtained above 300 MPa and greater Young's modulus is observed which highlights that more competent rocks are present in Kiruna than in Malmberget. Moreover, in Kiruna, higher elastic modulus is attributed due to the predominance of syenite and quartz porphyry and massive magnetite, which are less altered and more structurally competent. Conversely, the higher elasticity of Malmberget rocks is associated with the presence of more altered rock types and the existence of biotite schist and the high concentration of biotite mineral in the matrix of rocks.

Figure 3 Summarised distribution of all tested samples for UCS, Young's modulus and Poisson's ratio.

In Kiruna site the lithologies analysed encompasses syenite porphyry, magnetite, quartz porphyry, tuff, and dyke porphyry. In contrast, Malmberget site includes trachyandesite, rhyodacite, trachybasalt, pegmatite, granite, magnetite, and biotite schist. It is noteworthy that the lithologies of Malmberget are identified by local names, which are extensively used by mine geologists and engineers and are based on colour. The correspondence is the following: Trachyandesite is known as grey-red leptite (GRL), rhyodacite as red-grey leptite (RGL) and trachybasalt as grey leptite (GLE). Also, magnetite is considered an alteration for Malmberget by the means of magnetite minerals enrichment in the hanging and footwall wall rock masses due to hydrothermal fluids. Figures included in the following subchapters 3.1 and 3.2, present statistical analyses using box plots to compare UCS (Figure 4, Figure 7), Young's modulus (Figure 5, Figure 8), and Poisson's ratio (Figure 6, Figure 9) across different lithologies and alteration states for the Kiruna and Malmberget sites. It should be noted that the black boxes appearing in the box plots serve two purposes: they either delineate areas of denser distribution for different alterations within the same lithology or highlight multiple data concentrations for the same lithology and alteration.

3.1 Kiruna rock mass

The geotechnical laboratory tests revealed that the intact rock strength in the Kiruna mine exhibits significant variability depending on the rock type. Kiruna rock material exhibit UCS values ranging from 50 to nearly 400 MPa, with most values falling between 100 and 270 MPa. Notably, magnetite shows UCS values from 100 to 200 MPa, whereas higher values are observed for quartz porphyry and tuffs. The lithology of tuff material warrants further analysis due to the variability observed in its uniaxial compressive strength (UCS) results. For a total of 55 UCS tests conducted on tuff with a quartz porphyry matrix, the values range from 50 to 400 MPa, with a denser distribution between 100 and 250 MPa. Young's modulus generally ranges between 40 and 80 GPa, except for magnetite, which varies from 40 to 120 GPa, with some extreme values exceeding 120 GPa or falling below 40 GPa. The high elastic modulus reflects the rocks' ability to withstand significant stress without deforming, which impacts stability in deep mining operations. Similarly, Poisson's ratio ranges from 0.15 to 0.3, with magnetite displaying a broader range of 0.15 to 0.4, and occasional extreme values above 0.4 or below 0.15. The primary alteration observed in Kiruna is the "pervasive albite with hematite staining," which appears to impact nearly all the tested lithologies. In this context, several alterations specifically affect magnetite and quartz porphyry. Actinolite mineral significantly influences both lithologies by generally increasing their strength, whereas chlorite exclusively affects quartz porphyry by reducing its strength. Regarding elastic parameters, a more pronounced influence is obvious. Specifically, actinolite and calcium minerals increase Young's modulus in magnetite, whereas apatite enrichment decreases it.

Chlorite minerals, on the other hand, tend to lower Poisson's ratio in quartz porphyry.
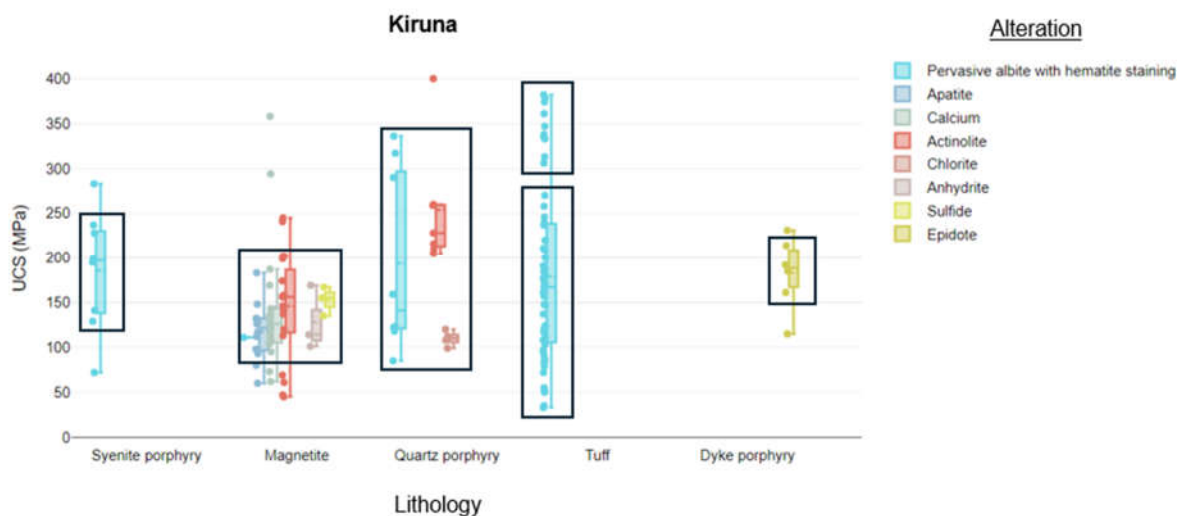
Figure 4 UCS visualization for Kiruna in comparison with Lithology and Alteration units.
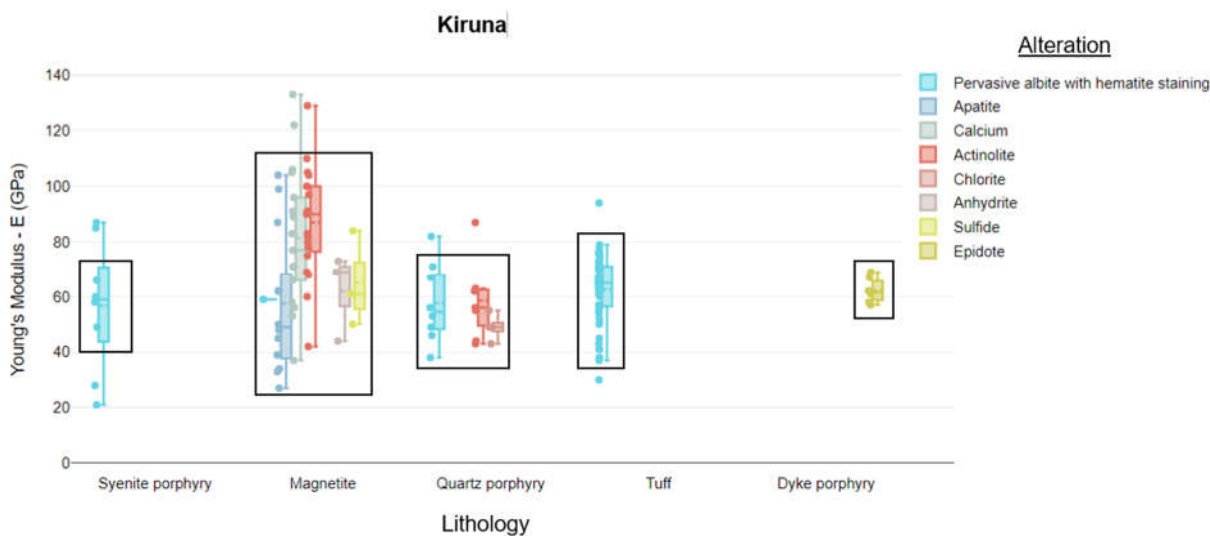
Figure 5 Young's Modulus visualization for Kiruna in comparison with Lithology and Alteration units.
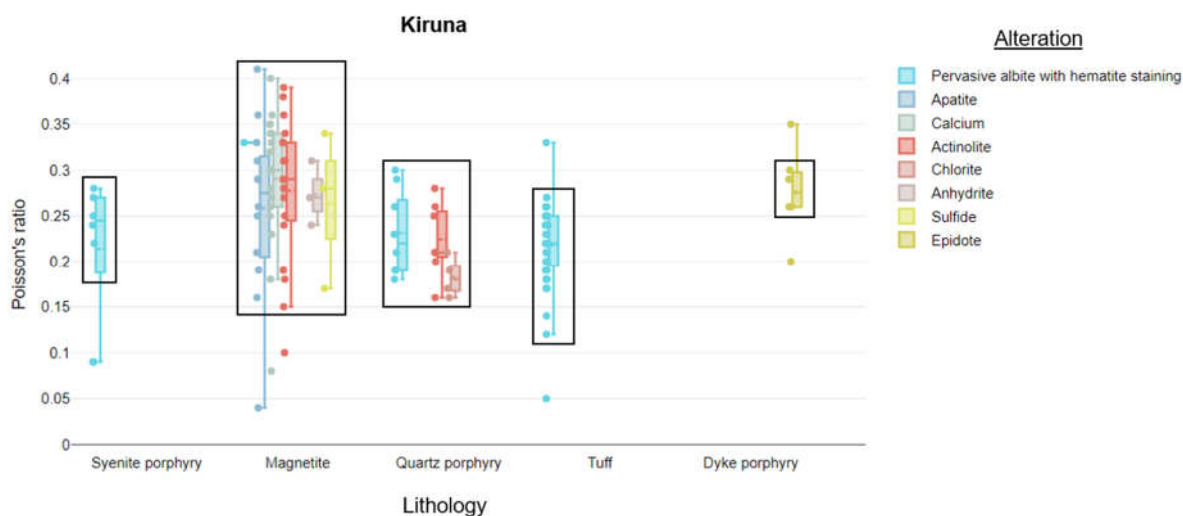
Figure 6 Poisson's ratio visualization for Kiruna in comparison with Lithology and Alteration units.

3.2 Malmberget rock mass

For the Malmberget mine, UCS values range between 70 and 300 MPa, with some extreme cases exceeding 300 MPa. Notably, rhyodacite, trachyandesite and granite exhibit higher UCS values, often surpassing 200 MPa, whereas biotite schist records the lowest values, typically under 90 MPa. Magnetite demonstrates UCS values ranging from 75 to 150 MPa, with the majority clustering around 100 MPa. Further sampling is required to establish reliable UCS data for pegmatite. As there is not an official scale for Young's modulus, the presented results could be categorized into four observed classes: 20-40 GPa, 40-80 GPa, 80-100 GPa, and above 120 GPa, with most test results falling between 40-80 GPa. Magnetite generally exhibits Young's modulus values above 80 GPa, regardless of skarn or apatite alteration, although some specific readings fall below 40 GPa, warranting further investigation. For biotite schist, Young's modulus is consistently below 60 GPa. Poisson's ratio generally ranges from 0.15 to 0.3, with a few samples, including magnetite, exceeding 0.3 or dropping below 0.15. Alteration minerals do not significantly impact UCS results as they do Young's modulus and Poisson's ratio. Biotite alteration notably reduces Young's modulus in trachyandesite and trachybasalt, whereas magnetite enrichment increases it, except in rhyodacite where it decreases. Additionally, biotite alteration raises the Poisson's ratio in trachyandesite, while magnetite enrichment lowers it. This lower Poisson's ratio indicates a higher propensity for deformation under stress, which must be accounted for in geotechnical analysis. Unaltered granite shows a higher Poisson's ratio, and magnetite exhibits two distinct groups, with most values around 0.2.
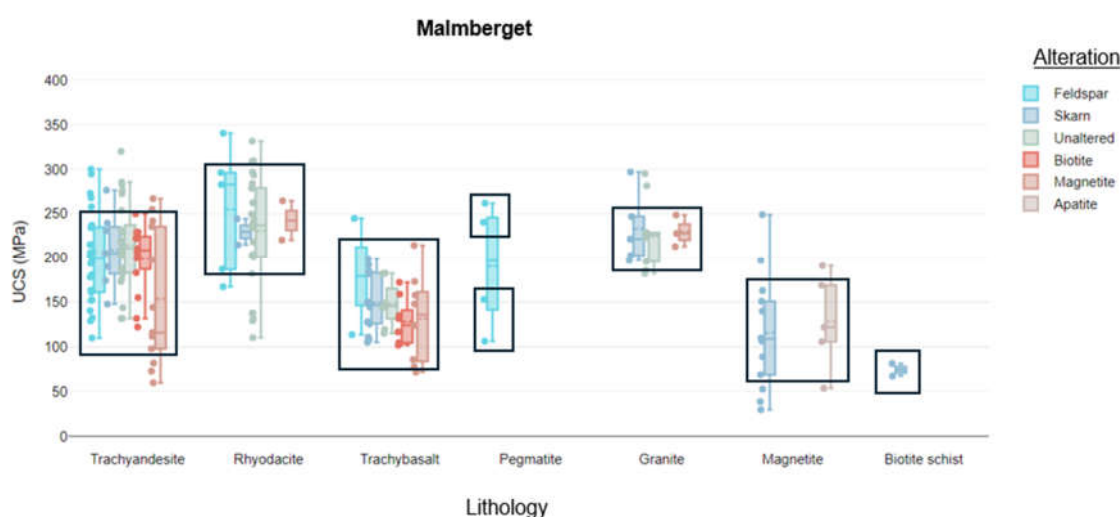
Figure 7 UCS visualization for Malmberget in comparison with Lithology and Alteration units.
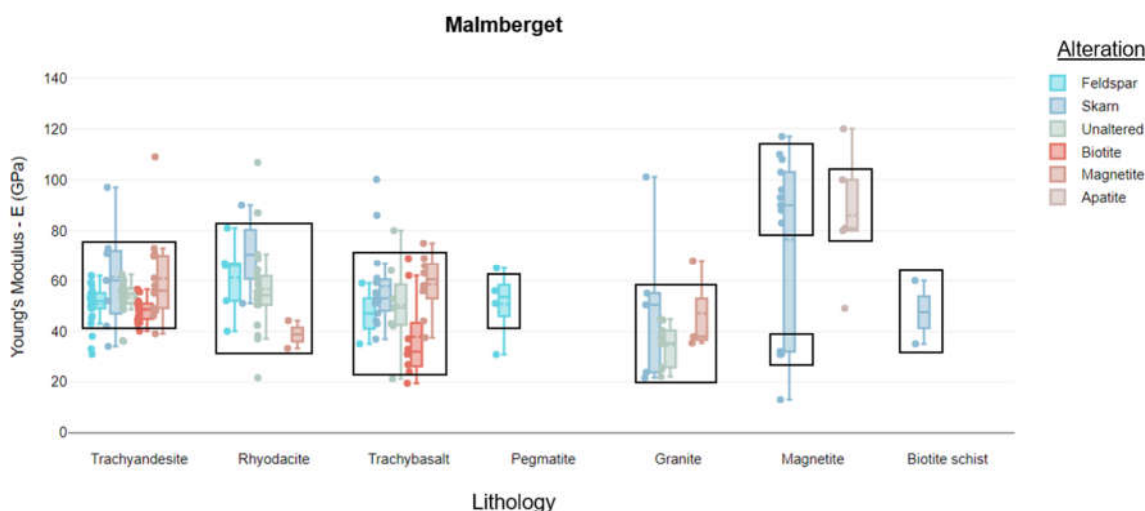
Figure 8 Young's Modulus visualization for Malmberget in comparison with Lithology and Alteration units.
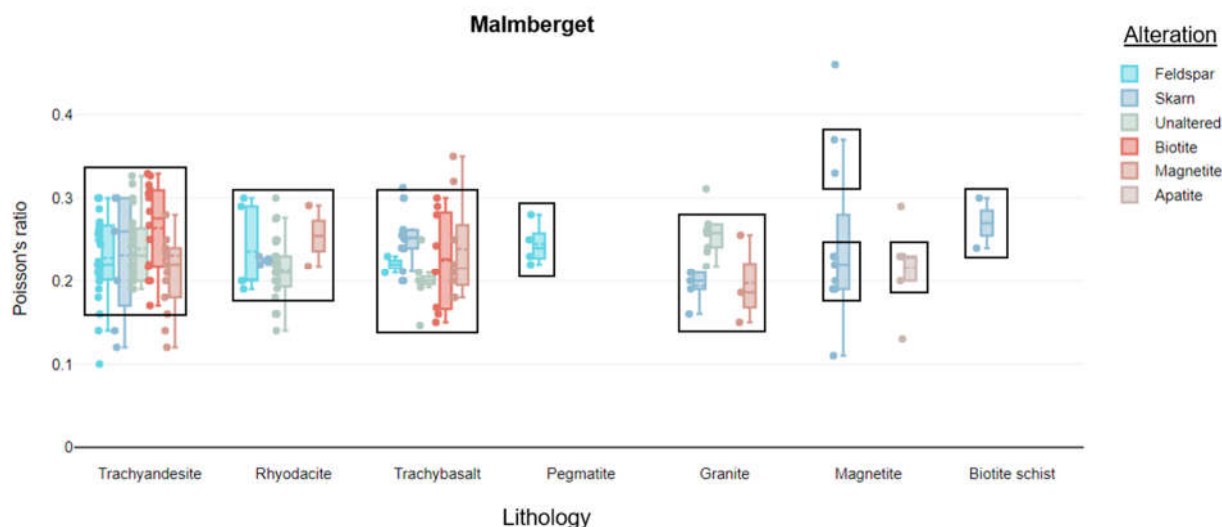
Figure 9 Poisson's ratio visualization for Malmberget in comparison with Lithology and Alteration units.

4   Conclusion

This study has provided a statistical analysis of the intact strength and elastic parameters of rock material in the Kiruna and Malmberget mines, offering a comprehensive understanding of their correlation with geological and alteration characteristics. The current study demonstrates that alteration minerals significantly impact the elastic parameters more than the intact strength, and this must be considered during geotechnical analysis. Through extensive geotechnical programs, including borehole logging and laboratory testing, we have established significant differences in the mechanical properties of the rock types in these regions.

Moreover, the study underscores the necessity of accurate and objective measurements of intact rock strength and elastic parameters for the realistic estimation of in situ geotechnical conditions. The findings highlight the limitations of relying solely on traditional rock mass classification systems that depend on subjective assessments. Instead, integrating objective test results, such as those from point load, UCS, and TCS tests, enhances the reliability of geotechnical models.

The results of this study have important implications for the design and safety of mining operations in Kiruna and Malmberget. The higher strength and stiffness of Kiruna rocks (especially magnetite) suggest that different strategy on support systems may be required compared to Malmberget, where lower strength and higher deformability necessitate more robust support measures. These findings highlight the need for region-specific geotechnical models that account for the unique properties of the rock material in each mine.

To enhance the reliability of the results and comparability of the mines, a greater number of samples must be collected from both sites, particularly in Kiruna, where the geospatial distribution of the data is currently limited. Overall, this study enhances the geotechnical knowledge base for Kiruna and Malmberget, providing valuable data for improving mine design, safety, and efficiency in these significant mining regions.

Acknowledgements

References

ASTM Designation; *Standard method of test for elastic moduli of rock core specimens in uniaxial compression.* American Society for Testing and Materials, D 3148-72.

Bergman, S.; Kübler, L.; Martinsson, O. *Description of regional geological and geophysical maps of northern Norrbotten County (east of the Caledonian orogen)*. Sveriges geologiska undersökning Ba 56, 110 pp., 2001.

Bieniawski, Z.T. *Engineering Rock Mass Classifications*. Wiley, New York, 1989.

Bieniawski, Z.T.; Bernede, M.J. *Suggested methods for determining the uniaxial compressive strength and deformability of rock materials: Part 1. Suggested method for determining deformability of rock materials in uniaxial compression,* International Journal of Rock Mechanics and Mining Sciences & Geomechanics Abstracts, Volume 16, Issue 2, Pages 138-140, ISSN 0148-9062, 1979, Available online: https://doi.org/10.1016/0148-9062(79)91451-7

Deere, D.U.; Miller, R.P. *Engineering classification and index properties for intact rocks*. Tech. Rep. No. AFWL-TR-65-116. University of Illinois, Urbana. 229p., 1967.

Geijer, P. *Igneous rocks and iron ores of Kiirunavaara, Luossavaara and Tuollavaara.* Economic Geology, 5 (8): 699–718., 1910, Available online: https://doi.org/10.2113/gsecongeo.5.8.699

Hallberg, A.; Bergman, T.; Gonzalez, J.; larsson, D.; Morris, G. A.; Perdahl, J. A.; Ripa, M.; Niiranen, T.; Eilu, P. *Metallogenic areas in Sweden.* Geological Survey of Finland, Special Paper 53, 139–206, 2012.

Hoek, E.; Brown, E. T. *The Hoek–Brown failure criterion and GSI – 2018 edition.* Journal of Rock Mechanics and Geotechnical Engineering, Volume 11, Issue 3, Pages 445-463, ISSN 1674-7755, 2019.

ISRM; *Suggested methods for determining point load strength.* Int J Rock Mech Min Sci Geomech Abstr 22(2):51–60, 1985.

Jürgen, H., Schön; *Chapter 6 - Elastic Properties*, Editor(s): Jürgen H. Schön, Developments in Petroleum Science, Elsevier, Volume 65, Pages 167-268, ISSN 0376-7361, ISBN 9780081004043, 2015, Available online: https://doi.org/10.1016/B978-0-08-100404-3.00006-8

Laubscher D.H. *A geomechanics classification system for the rating of rock mass in mine design*. J. S. Atr. Inst. Min. Metall., vol. 90, no. 10, pp. 257-273. 1990.

Sarlus, Z.; Andersson, U.; Martinsson, O.; Bauer, T.; Wanhainen, C.; Andersson, J.; Whitehouse, M. *Timing and origin of the host rocks to the Malmberget iron oxide-apatite deposit*, Sweden. Precambrian Research, Volume 342, 105652, ISSN 0301-9268, 2020, Available online: https://doi.org/10.1016/j.precamres.2020.105652

Troll, V.R.; et al. *Global Fe–O isotope correlation reveals magmatic origin of Kiruna-type apatite-iron-oxide ores*. Nat Commun 10, 1712, 2019. Available online: https://doi.org/10.1038/s41467-019-09244-4

CHARACTERIZING THE CPT RESPONSE AND PARTICLE SIZE DISTRIBUTION OF FLUVIALLY DEPOSITED PLEISTOCENE SAND IN THE NETHERLANDS

FENNA VAN AARLE [1], KEVIN DUFFY [2], KAY KOSTER [3], DOMINIQUE NGAN-TILLARD [4], RONALD HARTING [5], FREEK BUSSCHERS[6]

[1] *Delft University of Technology, The Netherlands, fennavaarle@gmail.com*

[2] *Delft University of Technology, The Netherlands, k.duffy@tudelft.nl*

[3] *TNO Geological Survey of the Netherlands, The Netherlands, kay.koster@tno.nl*

[4] *Delft University of Technology, The Netherlands, d.j.m.ngan-tillard@tudelft.nl*

[5] *TNO Geological Survey of the Netherlands, The Netherlands, ronald.harting@tno.nl*

[6] *TNO Geological Survey of the Netherlands, The Netherlands, freek.busschers@tno.nl*

Abstract
Understanding the geological and geotechnical characteristics of the shallow subsurface is crucial for engineering decisions in densely populated regions like the Netherlands. Urban areas are for a large part built on a complex stack of sand, clay, silt, gravel and organics that were deposited over the last hundreds of thousands of years under gradually subsiding tectonic conditions. One of these units, a fluvially deposited sand known as the Kreftenheye Formation, is widespread across the western part of the country and is vital for foundation design and groundwater dynamics. The Kreftenheye Formation is therefore well described by geotechnical and geological tests, yet integrating both types of data has rarely been done on a nationwide scale. This paper focuses on 76 pairs of Cone Penetration Tests and boreholes that include Kreftenheye, out of a full database of nearly 200 pairs from TNO - Geological Survey of the Netherlands, generally reaching depths up to 40 meters. The study reveals significant spatial variations and depositional patterns within the Kreftenheye Formation, illustrating how overlying or interlayered flood plain or soft channel lag sediments influences the response of the CPT. Furthermore, CPT response and borehole samples have helped with making geological distinctions between the upper, Weichselian part of the Kreftenheye Formation and the lower Saalian part, showing how integrating both datasets can give both geological and geotechnical insights.

Key words
CPT, soil variability, granular soil, particle size distribution, Late Pleistocene, fluvial sand

1   Introduction

In the Netherlands, a fluvially deposited Middle and Late Pleistocene sand, known as the Kreftenheye Formation, is widespread across the country and the Dutch North Sea Sector (Busschers et al., 2007; TNO-GSN, 2024). In the heavily populated coastal and river areas of the Netherlands, the formation is typically overlain by clay and peat of Holocene age (Ngan-Tillard et al., 2010; Koster et al., 2018). Consequently, most infrastructure and buildings are founded on piles. These foundation piles are driven through the overlying soft sediment, transferring most of the load to the stiff sands of the Kreftenheye Formation.

Nevertheless, the formation poses some engineering challenges. The formation is generally dense to very dense, with Cone Penetration Test (CPT) tip resistances reaching more than 80 MPa in parts. Getting piles to their target depth whilst avoiding refusal and pile damage can therefore be challenging (de Gijt et al., 2019; Duffy et al., 2024). Furthermore, weak zones within this layer can bring unexpected changes in the pile installation resistance, as well as affecting the ultimate capacity of the pile.

Traditionally, many studies focus on the geological characterization of formations, often missing out on important patterns revealed by geotechnical data such as CPTs (Busschers et al., 2005; TNO-GSN, 2024). Conversely, CPT focused research and industry practices may disregard the geological origin of deposits and overlook essential insights into the formation's history and potential risks (Robertson, 2016;Mayne, 2017). By integrating both geological and geotechnical perspectives, a more comprehensive understanding of subsurface conditions can be achieved, leading to better-informed engineering decisions.

This research addresses this integration gap by analysis of a dataset of nearly 200 CPTs and borehole pairs from the TopIntegraal drilling and measurement program provided by TNO – Geological Survey of the Netherlands (Buma et al., 2024), generally penetrating the shallow subsurface up to depths of ~40 meters. This paper presents this analysis, showing the geological and geotechnical patterns and variations within the Kreftenheye Formation and how the integration of geological and geotechnical knowledge can lead to more effective engineering designs.

2   Depositional history of the Kreftenheye Formation

The Kreftenheye Formation was deposited by the river systems Rhine and Meuse in the Netherlands, commencing during the late Middle and Late Pleistocene, spanning approximately 160,000 to 12,000 years ago (Busschers, 2008; Peeters et al, 2015; Verbraeck, 1983; Weerts and Busschers, 2003). This timeframe encompasses the late Saalian (cold climate, glaciation), Eemian (warm climate), Weichselian (cold and temperate climate), and Holocene (warm climate) periods, each characterized by distinct climate conditions and sea levels (Figure 1).
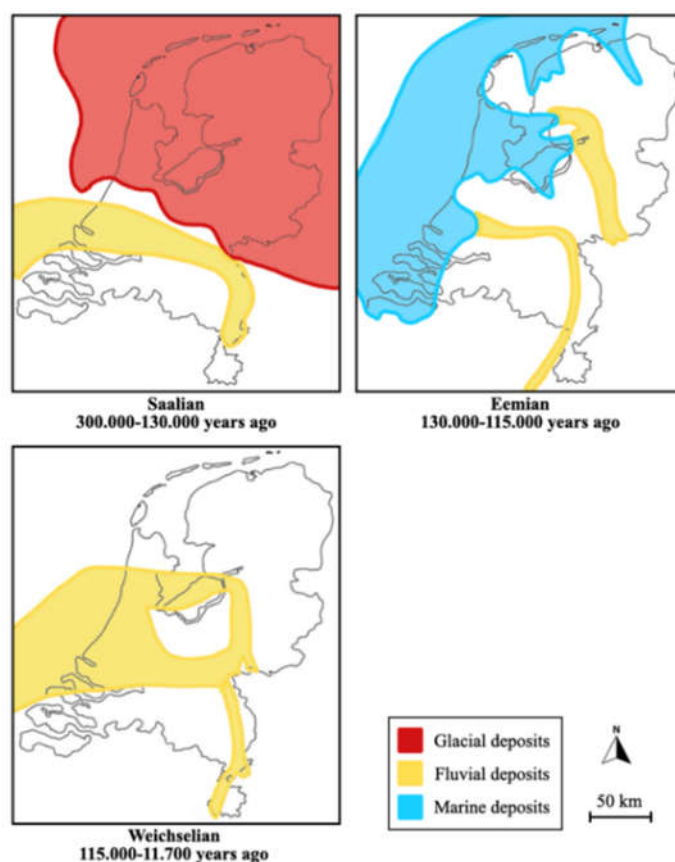
Figure 1. Simplified paleogeographical maps of the Netherlands during the late Saalian, Eemian, and Weichselian periods. Adapted from Busschers et al. (2007) and Wong (2007).

During the late Saalian glaciation, which occurred approximately 160.000 to 130.000 years ago, the northern region of the Netherlands experienced extensive glaciation with the ice sheet prograding into the Netherlands up-to the Haarlem – Utrecht – Nijmegen – Dusseldorf line. Along the ice front ice-pushed ridges were formed and fluvial sediments of the Rhine-Meuse were deposited in front, depositing the older part of the Kreftenheye Formation. During the late Saalian deglaciation the Rhine took a new course into the former glaciated area and the Meuse remained in a position south of the former ice line. During the Eemian (130.000 to 115.000 years ago), the climate warmed, tree vegetation developed and sea-level rose to elevations similar to or above present day values, hereby submerging major part of the Netherlands. The encroaching coastline reduced the energy of the river systems, with dominance of deposition in meandering rivers, estuaries and shallow marine environments (Peeters et al., 2016). In the subsequent Weichselian period (115.000 to 11.700 years ago), the Netherlands experienced a return to generally colder conditions with a strong drop in sea-level, formation of (temporal) permafrost and opening of the vegetation cover. Colder periods alternated with warmer climatic periods although especially the last 20.000 years of the Weichselian experienced most cold climatic conditions with large scale development of permafrost and supply of coarse-grained sediments into the Rhine-Meuse system, hereby depositing the upper part of the Kreftenheye formation. During the second half of the Weichselian, the branch of the Rhine through the northern Netherlands became entirely abandoned and the Rhine retook a course south of the former late Saalian ice line, merging with the Meuse.

To summarize, the diverse climatic and environmental conditions over this timescale resulted in fluvial deposits that include a wide range of sediment types. Consequently, the Kreftenheye Formation is characterized by fine to coarse-grained sand and gravel, interspersed with five characteristic Members and Beds (TNO-GSN, 2024), although we do note that most of the Kreftenheye Formation is not subdivided into Beds and/or Members:

- **Wijchen Bed**: Silty clay from meandering rivers and wind-blown fine grained sands, deposited during the late Weichselian .
- **Ockenburg Mb.**: Coarse sand with reworked marine fossils from the Eemian sea, deposited during the Weichselian.
- **Zutphen Mb.**: Clay, silt, peat and sand, deposited during the Eemian.
- **Twello Mb.**: Medium fine to coarse sand, and stiff clay, deposited during late Saalian and early Eemian.
- **Well Mb.**: Medium to coarse sand, deposited during the late Weichselian.

3   Methods

The dataset used in this research is provided by TNO – Geological Survey of the Netherlands and is collected as part of the drilling and measurement program TopIntegraal (e.g. Buma et al 2024, Harting et al., 2023; Bosch et al 2014; Vernes et al., 2010). The dataset serves as a resource for characterizing subsurface conditions up to a depth of 30–50 meters in the Netherlands.

The objective of the TopIntegraal program is to provide detailed insights into subsurface characteristics to support for instance geological mapping, hydraulic assessments, and infrastructure planning. This is achieved through the integration of lithological, geochemical, geotechnical, and hydraulic data obtained from borehole trajectories and CPTs in the Netherlands. The dataset targets all the lithostratigraphic units defined in the shallow subsurface of the Netherlands and is running since 2006.

Figure 2. Map of the Netherlands showing the locations of the CPT and borehole pairs, including a subset of locations within the Kreftenheye Formation used in this study.

Figure 2 shows an overview of the data locations in the Netherlands and the area of deposition of the Kreftenheye Formation. Each data point comprises two main components: a CPT sounding and a borehole. The CPT includes measurements of cone resistance, sleeve friction, and excess pore water pressure. The boreholes are sampled at different frequencies and intervals to capture the formation and its members. Data points are limited in the central eastern region of the Netherlands, as not all areas have been targeted yet in the ongoing TopIntegraal program. The acquisition and - in time - release of this data by TNO is expected in the future. The distance between the CPT and the borehole is intended to be limited as the CPT is performed first as an exploratory CPT before the drilling is performed. Three-quarters of the data points have the two main components lying within a 10-meter distance of each other. The bar chart in Figure 3 displays the number of data points (CPT and borehole pairs) for the Kreftenheye Formation, indicating the number datapoints for the members. Additionally, the chart highlights in green the number of grain size measurements available within the formation and its individual members. CPT data for the formation and its members were selected based on the lithostratigraphic interpretations of the associated boreholes by TNO.
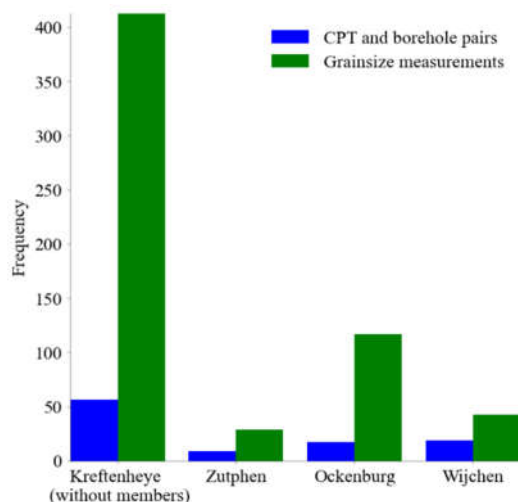
Figure 3. Overview of the dataset of the Kreftenheye Formation used in this study.

4   Results

4.1   CPT and borehole integration

Laboratory research (Ahmadi and Robertson 2005; de Lange 2018; Tehrani et al. 2018) as well as numerical research (van den Berg 1994) has shown that the CPT tip resistance is affected by soil not

just at the CPT tip, but in a zone several diameters above and below the CPT tip. Figure 4 shows this effect in a field measurement context: in this case, the Wijchen Bed of approximately 25 cm thickness overlying the Kreftenheye Formation. The transition zone is indicated in the borehole picture by a red circle. First, the CPT data identifies the presence of the Wijchen Bed. Following this, the transition to the underlying layer, characterized by the higher cone resistance of the Kreftenheye Formation sand, extends over a considerable depth of more than a quarter of a meter. This suggests that the influence of the overlying soil on the CPT tip resistance affects a significant vertical range. This extended transition is unlikely to represent a gradual mixing of clay and sand over such a distance within the Wijchen Bed, given its distinct depositional environment compared to the undifferentiated Kreftenheye Formation sand. This observation suggests that the CPT cone is likely influenced by the Wijchen Bed, even after it has physically passed the boundary due to its sensing distance. Consequently, this result indicates that caution is needed when interpreting CPT data for the first interval of the Kreftenheye Formation because of the sensing distance.
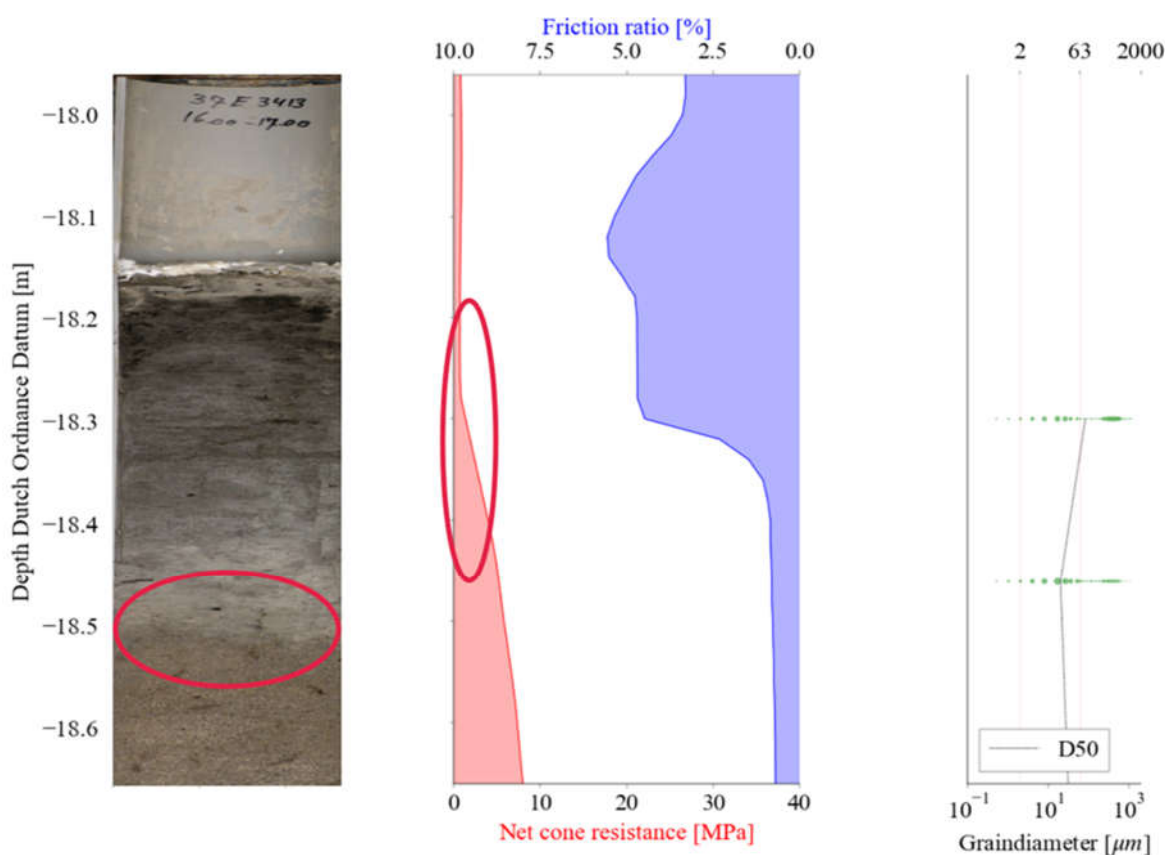
Figure 4. Influence of sensing distance on the Wijchen Bed. Left pane: photo taken from the borehole (B37E3413), central panel: CPT of the same interval (CPT000000012746), right panel: grainsize measurements for the interval.

Interlayered floodplain or soft channel lag deposits occur within the undifferentiated fluvial Kreftenheye Formation and can significantly affect the response of foundation piles, as studied by Chai et al. (2022). Their research underscores the importance of identifying weak zones and understanding their extent. Figure 5 illustrates an example of an intermediate weak zone in the CPT response within the undifferentiated Kreftenheye Formation, indicated by a red circle. However, the borehole picture shows no clear weak zone that can be linked to the CPT response. In other borehole pictures, small clay pebbles are visible, indicating that channel lag deposits described by Busschers (2008) may be present, and it is possible the CPT cone encountered one. This example demonstrates the importance of understanding the geological context when interpreting a CPT profile, as it can provide additional information on the spatial variability of weak zones.
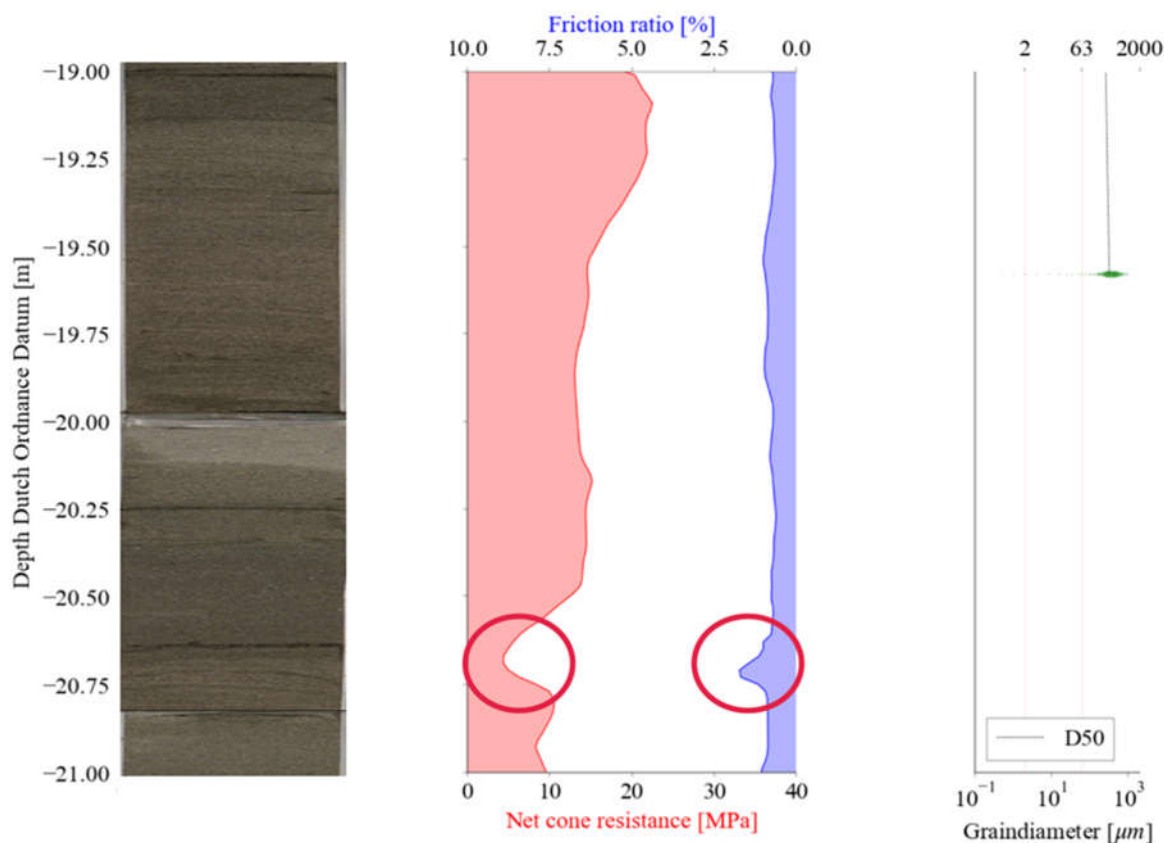
Figure 5. Intermediate soft layer within the Kreftenheye Formation. Left pane: photo taken from the borehole (B14E0952), central panel: CPT of the same interval (CPT000000043211), right panel: grainsize measurements for the interval.

4.2   Kreftenheye Area A and B

The second result presented in this article is the identification of differences between two regions within the Kreftenheye Formation. Busschers (2008) distinguished two areas within the Kreftenheye Formation based on the region and age: Area A, the upper/northern branch of the river system, deposited during the Weichselian and Eemian periods, and Area B, the lower/southern branch of the river system, deposited during the Saalian and Weichselian glacial period (see Figure 1). Busschers (2008) described the differences between these areas based on continuous core samples; however, a detailed analysis based on CPT measurements has not yet been conducted.

Figure 6 illustrates all the CPT data for the undifferentiated Kreftenheye Formation without the members, categorized into Areas A and B, plotted on a Robertson (1990) classification chart for translating CPT sounding into soil types. The CPT data is selected based on the borehole descriptions. The plot reveals a significant difference between the regions: Area A exhibits a wider range of cone resistances and friction ratios compared to Area B, with Area A having a higher proportion of low cone resistance soils. Additionally, the grain size distribution plot for Areas A and B shows a similar pattern, with Area B comprising more uniform and coarser material compared to the more variable and fine grained material in Area A.

The coarser and more uniform sediments in Area B can possibly be explained by the colder climate and low vegetation of the Saalian glacial period compared to the more variable Weichselian period (Peeters et al 2015). These conditions contribute to a more energetic river system, which deposits coarser and more uniform sediements.
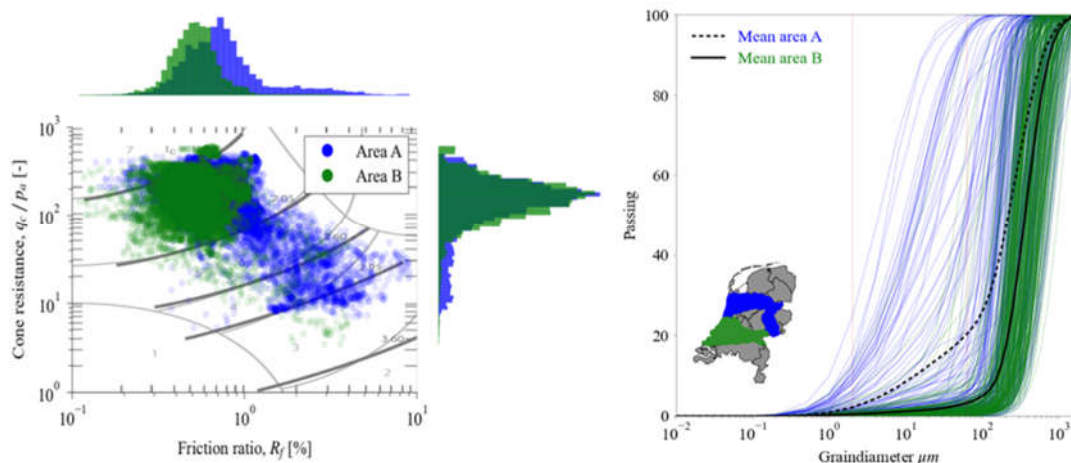
Figure 6. Robertson (1990) soil classification chart and the cumulative grain size distribution for Areas A and B of the undifferentiated Kreftenheye Formation. 27 CPTs and 157 grain size distributions for Area A, 26 CPTs and 256 grain size distributions for Area B.

4.3   Ockenburg Member

The Ockenburg Member is characterized by the presence of reworked marine fossils from Eemian tidal and coastal deposits by the Rhine-Meuse river during the Weichselian (Busschers et al., 2005; 2007; Peeters et al., 2016). The dataset of this study is used to find other distinguishing features within the Ockenburg Member to differentiate it from the Kreftenheye Formation, motivated by its mixed characteristics and location underneath major cities such as Rotterdam.

Figure 7 provides an overview of the CPT data and grain size measurements for both the Ockenburg Member and the Kreftenheye Formation. The CPT data shows a more centred distribution of data points compared to the Kreftenheye Formation. A region for the Ockenburg Member is visible (indicated by a red circle), consisting of two outlier data points from locations near the present-day coastline. The grain size data indicates that the Ockenburg Member is slightly more uniform and coarser on average compared to the Kreftenheye Formation.
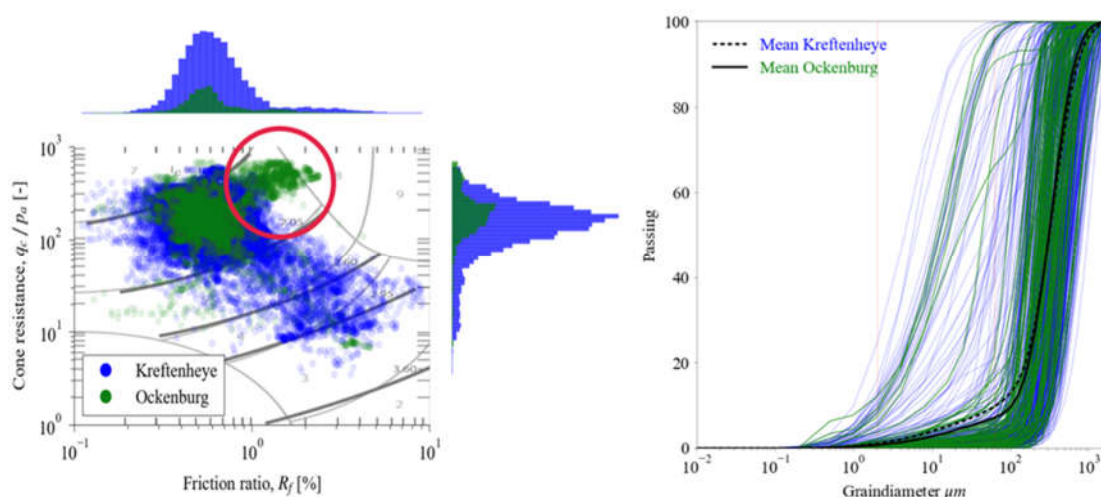
Figure 7. Robertson (1990) soil classification chart and the cumulative grain size distribution for the undifferentiated Kreftenheye Formation and the Ockenburg Member. 53 CPTs and 413 grain size distributions for the Kreftenheye Formation, 18 CPTs and 117 grain size distributions for the Ockenburg Member.

5   Implications for geotechnical engineering

The findings of this study have several signification implications for geotechnical engineering practices, particularly in the context of ground modelling and probabilistic analysis.

From a geotechnical perspective, the stratigraphic changes within the Kreftenheye Formation can affect how the formation is modelled at both a site-specific and regional level. CPT-based ground models are used to infer the soil properties between investigation points and—in the context of deep sand formations—are used for both stochastic and probabilistic modelling of deep excavations (Roubos 2019), as well as for offshore and onshore piled foundations (Peuchen et al. 2022; Vanneste et al. 2022). Ground models can be qualitative or quantitative and are developed using various methods, including geostatistical methods (Vanneste et al. 2022; Vessia et al. 2020) and machine learning methods (Peuchen et al. 2022; Vanneste et al. 2022; Xie et al. 2022). Ground models should accurately reflect the stratigraphical and lithological variation within each formation. A thorough understanding of the depositional processes and the resulting stratigraphical and lithological differences, is crucial for this purpose.

Lithological heterogeneity, such as the thin zones embedded within the Kreftenheye Formation, significantly affects how piles respond based on their location, relative strength, and thickness (Boulanger and DeJong, 2018; de Lange, 2018; Tehrani et al., 2018). Recognizing the likelihood of encountering these thin zones can help designers anticipate unexpected changes in a pile's installation response or performance under loading. This understanding enables more accurate predictions and adjustments during the design and construction phases, ultimately enhancing the reliability and safety of geotechnical structures.

6   Conclusion

A combined dataset was used of nearly 200 CPTs and borehole pairs provided by TNO – Geological Survey of the Netherlands, penetrating the shallow subsurface up to depths of ~40 meters, was used to study the Kreftenheye Formation. This formation is vital for geotechnical engineering applications such as foundation design and groundwater dynamics.

The data analysis revealed the influence of a weak layer in the formation on the CPT response, highlighting the importance of understanding the sensing and development distance from a CPT cone, as well as the geological context, when interpreting CPT measurements within this formation. Additionally, the dataset has improved the distinction between a northern and southern geographical area within the undifferentiated Kreftenheye, demonstrating coarser and more uniform sediment in the southern area compared to the northern area. Finally, the research has shown the challenge of identifying the Ockenburg Member from the undifferentiated Kreftenheye data using only CPT data, as both exhibit resemblance and overlap. However, the Ockenburg Member exhibited an additional cluster that did not overlap with the undifferentiated Kreftenheye. Additional research is recommended to further understand this cluster.

Acknowledgements

References

Ahmadi, M. M.; Robertson P. K. 2005. Thin-layer effects on the CPT qc measurement. *Canadian Geotechnical Journal*. 42 (5): 1302–1317.

Bosch, J. H. A.; Harting, R.; Gunnink, J.T*.; Lithologische karakterisering van de GeoTOP van Noord-Nederland (Hoofdgebied 5).* TNO-report 2014 R10680

Boulanger, R. W.; DeJong, J. T. 2018. Inverse filtering procedure to correct cone penetration data for thin-layer and transition effects*. In Proceedings of the 4th International Symposium on Cone Penetration Testing,* CPT18, CRC Press, pp. 24–44.

Buma, J. T.; de Heer, E.; Bus, S. A. R.; Harting, R.; Booltink, W. *TopIntegraal, het boor- en meetprogramma van de ondiepe ondergrond van Nederland - Deelrapport 1. Meetgegevens en kentallen verzadigde doorlatendheid,* versie 1.0. TNO-rapport TNO 2023 R10561, TNO - Geologische Dienst Nederland, Utrecht, 2024.

Busschers, F. S.; Weerts, H. J. T.; Wallinga, J.; Cleveringa, P.; Kasse, C.; de Wolf, H.; Cohen, K. M. Sedimentary architecture and optical dating of Middle and Late Pleistocene Rhine-Meuse deposits - fluvial response to climate change, sea-level fluctuation and glaciation. *Netherlands Journal of Geosciences - Geologie En Mijnbouw.* 2005, 84(1), 25–41.

Busschers, F. S.; Kasse, C.; van Balen, R. T.; Vandenberghe, J.; Cohen, K. M.; Weerts, H. J. T.; Wallinga, J.; Johns, C.; Cleveringa, P.; Bunnik, F. P. M. Late Pleistocene evolution of the Rhine-Meuse system in the southern North Sea basin: imprints of climate change, sea-level oscillation and glacio-isostacy. *Quaternary Science Reviews.* 2007, Vol. 26, 25–28.

Busschers, F. S. *Unravelling the Rhine: Response of a fluvial system to climate change, sea-level oscillation and glaciation*. Ph.D. Thesis, Vrije Universiteit Amsterdam, the Netherlands, 2008.

Chai, J.; Tehrani, F. S. Effect of Weak Zones on Foundation Pile Response*. In Proceedings of the International Symposium on Geotechnical Safety and Risk*, Newcastle, Australia, 14-16 December 2022; Research Publishing, Singapore, 2022

De Gijt, J. G.; Brassinga, H. E.; Roubos, A. A. Some learning cases in the Port of Rotterdam*. In IOP Conference Series: Materials Science and Engineering*, 2019, October, Vol. 615, No. 1, p. 012052, IOP Publishing.

de Lange, D. A. 2018. *CPT in thinly layered soils: validation tests and analysis for multi thin layer correction.* Nederlandse Aardolie Maatschappij, 120.

Duffy, K. J.; Gavin, K. G.; Korff, M.; De Lange, D. A.; Roubos, A. A. Influence of installation method on the axial capacity of piles in very dense sand. *J. Geotech. Geoenviron. Eng.* 2024, 150 (6): 04024043.

Harting, R.; Buma, J.; van Leer, M. *Hydraulic conductivity measurements of aquitard sediments in the Netherlands*. Mendeley Data, V1, 2023.

Koster, K.; De Lange, G.; Harting, R.; de Heer, E.; Middelkoop, H. Characterizing void ratio and compressibility of Holocene peat with CPT for assessing coastal–deltaic subsidence. *Quarterly Journal of Engineering Geology and Hydrogeology.* 2018, 51 (2): 210–218.

Mayne, P. W. Stress history of soils from cone penetration tests. *Soils Rocks.* 2017, 40, 203-218.

Ngan-Tillard, D. J. M.; Venmans, A. A. M.; Slob, E. Total engineering geology approach applied to motorway construction and widening in the Netherlands: Part I: A pragmatic approach. *Engineering Geology,* 2010, 114, 3-4.

Peeters, J.; Busschers, F. S.; Stouthamer, E. Fluvial evolution of the Rhine during the last interglacial-glacial cycle in the southern North Sea basin: a review and look forward. *Quaternary International*, 2015, 357, 176-188.

Peeters, J.; Busschers, F. S.; Stouthamer, E.; Bosch, J. H. A.; Van Den Berg, M. W.; Wallinga, J.; Versendaal, A. J.; Bunnik, F. P. M.; Middelkoop, H. Sedimentary architecture and chronostratigraphy of a late Quaternary incised-valley fill: A case study of the late Middle and Late Pleistocene Rhine system in the Netherlands. *Quaternary Science Reviews*, 2016, 131(A), 211-236.

Peuchen, J.; van Kesteren, W.; Vandeweijer, V.; Carpentier, S.; van Erp, F. Upscaling 1 500 000 synthetic CPTs to voxel CPT models of offshore sites. *In Proceedings of the Conference, Bologna*, Italy, 2022; CRC Press: Bologna, Italy, 2022; pp. 641–645.

Robertson, P. K. Soil classification using the cone penetration test. *Canadian Geotechnical Journal*, 1990, 27(1):151–158.

Robertson, P. K. Cone penetration test (CPT)-based soil behaviour type (SBT) classification system — an update. *Canadian Geotechnical Journal.* 2016, 53(12): 1910-1927.

Roubos, A. *Enhancing reliability-based assessments of quay walls.* Ph.D. Thesis, Delft University of Technology, the Netherlands, 2019.

Tehrani, F. S., M. I. Arshad, M. Prezzi, and R. Salgado. 2018. Physical Modeling of Cone Penetration *in Layered Sand. J. Geotech. Geoenvironmental Eng.* 144(1): 04017101. American Society of Civil Engineers. https://doi.org/10.1061/(ASCE)GT.1943-5606.0001809.

TNO-GSN. *Online portal for subsurface information of the Netherlands.* www.dinoloket.nl/en

Van den Berg, P. *Analysis of soil penetration.* Ph.D. Thesis, Delft University of Technology, the Netherlands, 1994

Vanneste, M.; Sauvin, G.; Dujardin, J. R.; Forsberg, C. F.; Klinkvort, R. T.; Forsberg, C. S.; Hansen, R. C. 2022. Data-Driven Ground Models: The Road to Fully-Integrated Site Characterization and Design. *In Proceedings of the 2nd Vietnam Symposium on Advances in Offshore Engineering*, edited by D. V. K. Huynh, A. M. Tang, D. H. Doan, and P. Watson, Singapore, Springer, 2022, pp. 3–21.

Verbraeck, A. Sedimentation in the mid-Netherlands river area during the Late Weichselian. *Geologie en Mijnbouw,* 1983, 62: 487-491.

Vernes, R. W.; Bosch, A. J.; Harting, R.; de Heer, E.; Griffioen, J. Towards a physical and chemical characterization of the shallow subsurface of the Netherlands. *In First International Conference on Frontiers in Shallow Subsurface Technology*. cp-150-00020; European Association of Geoscientists & Engineers, 2010.

Vessia, G.; Di Curzio, D.; Castrignanò, A. 2020. Modeling 3D soil lithotypes variability through geostatistical data fusion of CPT parameters. *Sci. Total Environ.* 698: 134340. https://doi.org/10.1016/j.scitotenv.2019.134340.

Weerts, H.; Westerhoff, W.; Cleveringa, P.; Bierkens, M.; Veldkamp, J.; Rijsdijk, K. Quaternary geological mapping of the lowlands of The Netherlands, a 21st century perspective. *Quaternary International.* 2005, 133–134, 159–178.

Wong, T. E.; Batjes, D. A. J.; de Jager, J. *Geology of the Netherlands*. Royal Netherlands Academy of Arts and Sciences, Amsterdam, 2007.

Xie, J.; Huang, J.; Lu, J.; Burton, G. J.; Zeng, C.; Wang, Y. 2022. Development of two-dimensional ground models by combining geotechnical and geophysical data. *Eng. Geol.* 300: 106579. https://doi.org/10.1016/j.enggeo.2022.106579.

Topic 2

Engineering Geology and

Cultural Heritage Protection

GEOTECHNICAL INVESTIGATION FOR RECONSTRUCTION OF ŽUPANIJSKI COMPLEX POŽEGA

IVAN BARANAŠIĆ[1], IVAN ALIVOJVODIĆ[1], DINO POSARIĆ[1]

[1] *Institut IGH d.d., Croatia, dino.posaric@igh.hr*

Abstract

Geotechnical investigation was conducted during February and March 2023, and has included four exploratoray boreholes, SPT testing, CPTu testing on three microlocations, laboratory testing , geophysical surveys with MASW and seismic refraction method. Investigation methods were conducted to determine soil conditions of the location and provide values for future design purposes. Results of field investigation and laboratory testing were used to create basic soil model, which will serve as guideline to aid designers for determining foundation depth, excavation method, construction pit shielding technology and dewatering operations.

Key words

Geotechnical report, Exploratory drilling, Laboratory testing, SPT testing, CPTu testing, Seismic refraction method MASW

1. Introduction

Institut IGH was commissioned for conducting geotechnical investigation inside the centre of the main complex of Požeško-slavonska županija. The center of the main complex is situated between the Palača velikog župana and Županijska palača on the east and a medieval building on the west. The buildings of the main complex were build in 18th century during the rain of Austro-Hungarian empire, except the medieval building on the west. Palača velikog župana and Županijska palača including the town hall were consistently upgraded until the end of 19th century. During the 18th century the palaces were headquarters of the Barun Trenk.

Geotechnical investigation was conducted on the basis of conceptual architectural design, Rusanov ured d.o.o., Zagreb, 2022. The modern reconstruction includes two new buildings and an underground garage. The underground garage will be leaning on the old cellar beneath Županijska palača, and the new buildings will be also leaning on the Županijska palača and on the Palača velikog župana.

Inside the complex itself there are several basic administrative buildings, parking lot with sheds and maintenance buildings. Geotechnical investigation was adapted to free space inside the complex and with intention not to interfere into daily administrative operations inside the complex.

Geotechnical investigation was conducted during February and March 2023. Geotechnical exploration included four exploratory boreholes depth of 15m, SPT testing approximetly every 2m, CPTu testing on three micro locations, laboratory testing on undisturbed and disturbed samples and geophysical surveys. The goal of the investigation was to determine geological and geotechnical characheristics of soil on the location. The results of the investigation were presented in the geotechnical report which will provide guidelines for designers.

2. Methods

2.1. Geological characteristics of the location

General geological characteristics of the location were determined from main geological maps, sheet Orahovica (D. Jamičić, et al. 1987) scale 1:100000 and from sheet Nova Kapela scale 1:100000 (M. Šparica, et al. 1980).
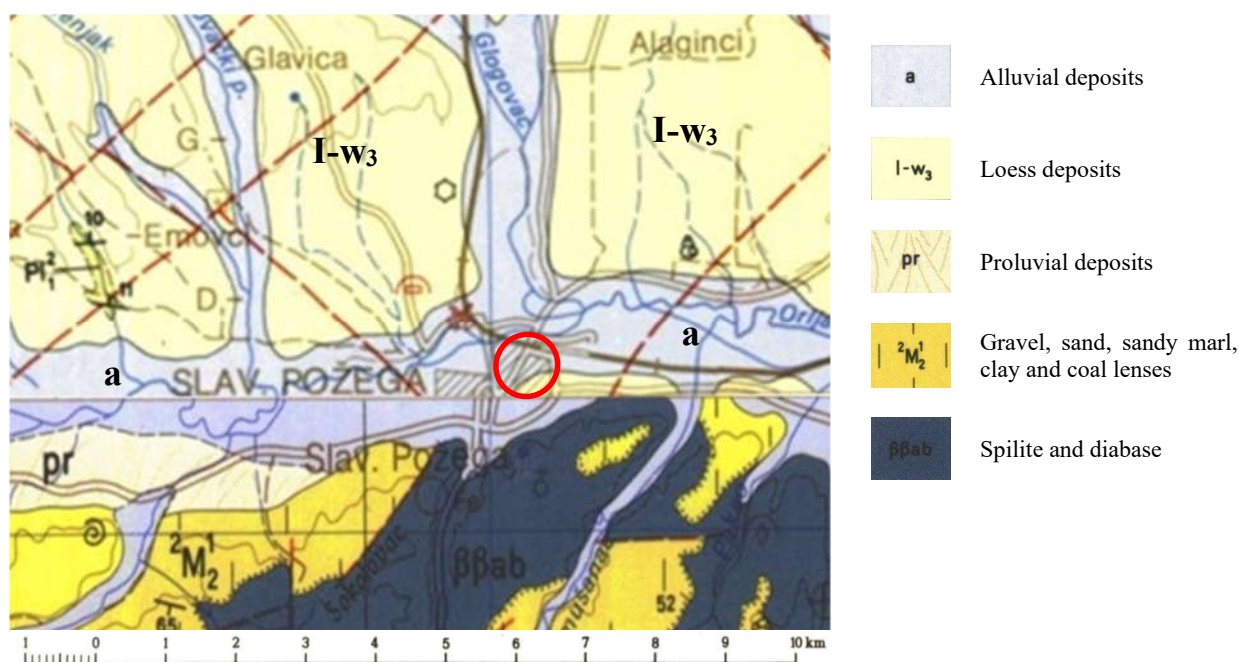
Figure 1. Main complex location of Požeško-slavonska županija on geological maps sheet Orahovica (D. Jamičić, et al. 1987) (up) and sheet Nova Kapela (M. Šparica, et al. 1980) (down).

According to the data from geological maps location of the complex is situated on alluvial deposits (a). Alluvial deposits are represented by gravels, sandy gravels and silts. Thickness of these deposits is aproximetly 10m.

Loess deposits (I-w$_3$) cover a wide area of city of Požega and Požeška kotlina. Loes deposits were created by wind in upper pleistocene in multiple stages depending on the climate conditions. During colder periods silt with sand was percipitated, while during warmer periods under the influence of atmospheric and underground water clay beds were formed. Thicknes of these deposits does not exceed 20 meters.

2.2. Geotechnical investigation

For the purpose of geotechnical exploration following methods were used:
- Exploratory drilling on four locations, each location 15m in depth;
- SPT testing;
- Field USCS soil classification;
- Pocket penetrometar and torvane testing on drilled core;
- CPTu testing with measurement of pore pressure on three locations;
- Geophisycal surveys using seismic refraction and MASW method.

2.2.1. Exploratory drilling with SPT testing

Drilling was conducted with a drill rig Geotech 605D using rotation technique on four locations (Figure 3.). During drilling undisturbed samples were taken and SPT testing was conducted approximately every 2 to 3 meters. After the drilling of the final depth of 15 meters drilled core was photographed, USCS soil classification was conducted along with in situ testing with a pocket penetrometer and torvane. Undisturbed samples were also taken for laboratory testing. During and after the drilling occurrence and level of ground water was measured.

Figure 2. Location of borehole B-3 with Geotech 605D drill rig.

2.2.2. CPTu testing

Table 1. SBT_n (Normalized Soil Behaviour type) soil classification (Robertson, 1990)

SBT_n zone (soil type)	Soil Behaviour Type
1	Sensitive, fine grained
2	Organic soils - clay
3	Clay – silty clay to clay
4	Silt mixtures- clayey silt to silty clay
5	Sand mixtures – silty sand to sandy silt
6	Sands – Clean sand to silty sand
7	Gravelly sand to dense sand
8	Very stiff sand to clayey sand
9	Very stiff fine grained

Soil testing using static penetrometer with pore pressure measurement on three (Figure 3.) micro locations was conducted using the caterpillar rig Geotech AB-200, which depending on anchoring conditions provides maximum force of 200kN. The speed of penetration was maintained within range of 20 ± 5 mm/s. While adding rods and during measurement of pore pressure dissipation penetration was stopped. Interpretation of field data was conducted using CPT-PRO software (Geotech Ltd.) and with recommendations given from Cone Penetration Testing in Geotechnical Practice, Lunne T., Robertson P.K. and Powell J.J.M. (1997). Soil classification was done using normalized CPTu parameters according to Robertson method Soil classification using the cone penetration test, Canadian Geotechnical Journal (1990). This method distinguishes nine soil types.

Table 2. Depth of CPTu testing

CPTu marking	Planned depth of penetration (m)	Executed depth of penetration (m)
CPTU-1	15	15,18
CPTU-2	15	13,60
CPTU-3	15	15,24

2.2.3. Laboratory testing

Testing on undisturbed and disturbed samples was done in geotechnical laboratory of Institut IGH d.d. Zagreb. These test were conducted: liquid and plasticity limits (BS 1377:1990, P2-4.5;5) sieve analysis (ASTM D422-63(2007)e2), moisture content (ASTM D2216-19), oedometer testing – one-dimensional consolidation (ASTM D2435/D2435M-11(2020)), direct shear (ASTM D3080/D3080M-23), uniaxial

strength (BS EN ISO 17892-7:2018) and permeability testing in oedometer under variable hydraulic loading (HRN U.B1.034)

2.3. Geophysical survey

Geophysical survey inside the complex was done using two methods, seismic refraction and MASW method.

Seismic refraction utilizes the spreading speed of S-waves and their spatial disposition, for the purpose of determening physical and mechanical properties of subsoil. Based on the results of seismic refraction survey it is possible to determine depth and thickness of soil, lateral contacts and fault positions. Seismic refraction measurement was done along four profiles 33 meters in length. For the survey the geophone array was three meters with thirteen seismic source points. For the purpose of data recording TERRALOC ABEM PRO 2 digital seismograph was used. The results of seismic refraction are represented as a depth cross section with longitudinal waves.

MASW method was used on four line profiles. Multichannel Analysis of Surface Waves is a method which utilizes disperzive charachteristics of surface waves (Rayleighs waves) to determine the spreading speed of S-waves by depth (Park et al., 1999). Spreading of Rayleighs waves is a combination of longitudinal and transverzal movement between their phase movement. The speed of Rayleighs waves depends on the speed of S-waves and the properties of the media (density, Poissons count) in which they are spreading. Poissons count is important for determining the relationship between the spreading speed of Rayleighs and S-waves. Value of Poissons count 0.25 defines the spreading speed of Rayleighs waves which have a value of 92% according to the speed of S-waves (Stokoe et al.,1994). MASW method was utilized alongside seizmic refraction profiles and the results are represented as the spreading speed of S-waves by depth.

3. Results of geotechnical investigation

On the basis of data provided by exploratory drilling and laboratory testing borehole logs were created. Geotechnical profiles were also drawn on the basis of borehole logs and CPTu testing. On the basis of these results geological model of soil was created and it is consisting from six layers (Figure 4.). The first layer consists from low plasticity clay (CL) and granular materials gravel (GM), sand (SC) and it represents filling material. Below the filling material the second layer is represented by low plastic clay (CL). The third layer is represented by granular materials, sandy and silty gravel (GM) and with silty and clayey sand (SM, SC). Low plastic clay (CL) represents fourth layer, while the fifth layer consists of low (CL) and high plastic (CH) clay. The final sixth layer is represented with silty sand (SM) with variable gravel content.

Results that came from geotechnical exploration gave a clearer picture about the relationship of alluvial (a) and loess (I-w_3) deposits. This relationship is represented as a interval layer change of gravel and sand with clay (Figure 4.). The created geological model was used as preliminary geotechnical soil model, which contains six geotechnical units. First geotechnical unit was dived into two blocks a and b. Cohesive material (CL) presents block a, while block b consists from granular materials (GM, SC). The main aquifer was established at the depth of approximately 12,50 meters.
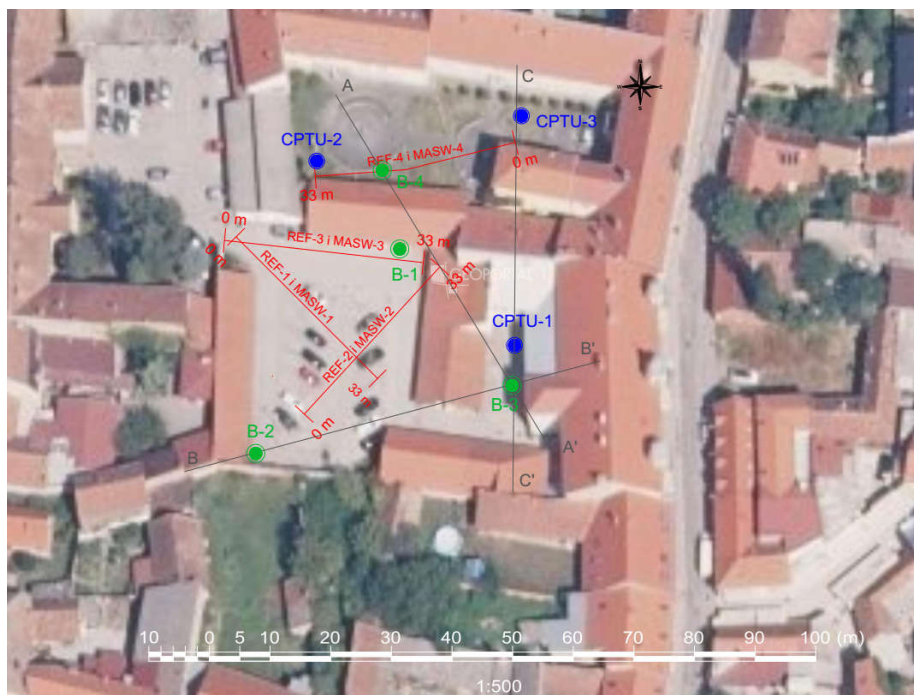
Figure 3. Positions of geotechnical investigation
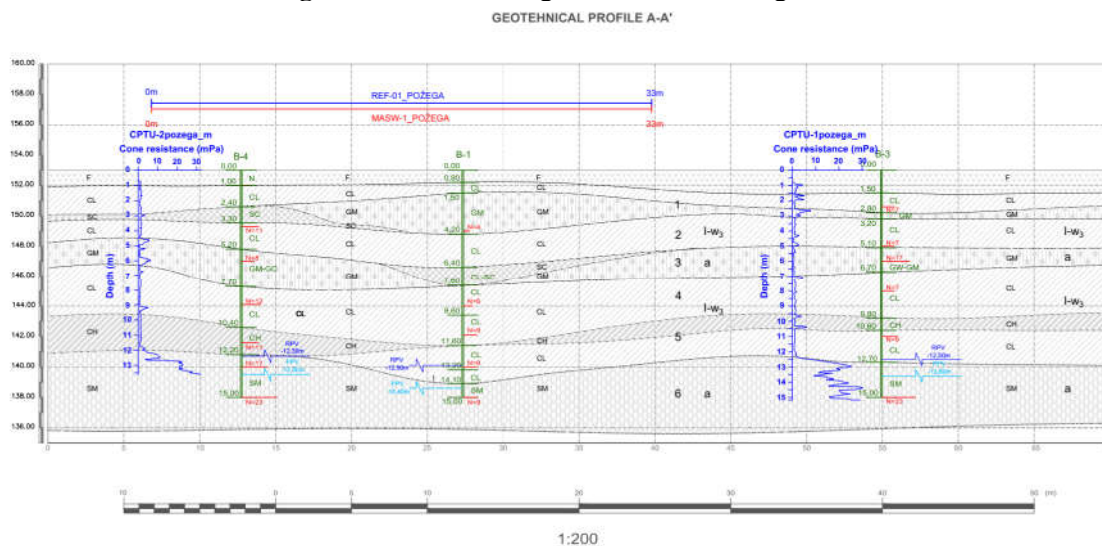
Figure 4. Geotechnical profile with six geotechnical units from results of exploratory drilling,CPTu testing and geophysical survey.
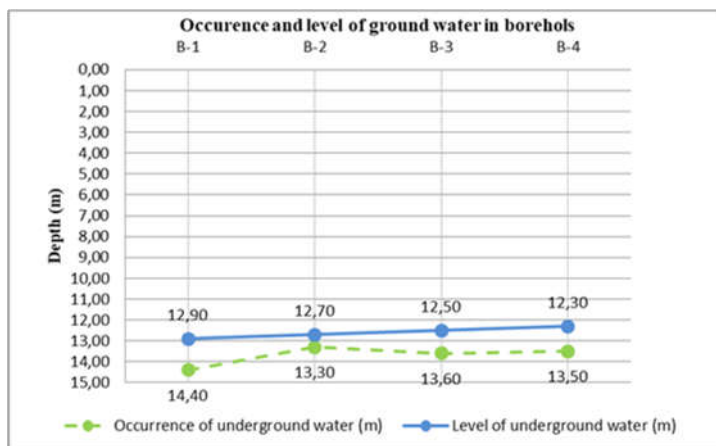
Figure 5. Occurrence and measured level of underground water

Because of the previously defined layer change and on the basis of sieve analysis results in all layers of granular materials permeability coefficient k was determined using the USBR method. Permeability of clay layers was determined from undisturbed samples using permability testing in oedometer under variable hydraulic loading.

$$k = c * d_{20}^{2,3} \text{ (cm/s)} \tag{1}$$

Where
c=0,36
d_{20}- grain size at 20% passing (mm)
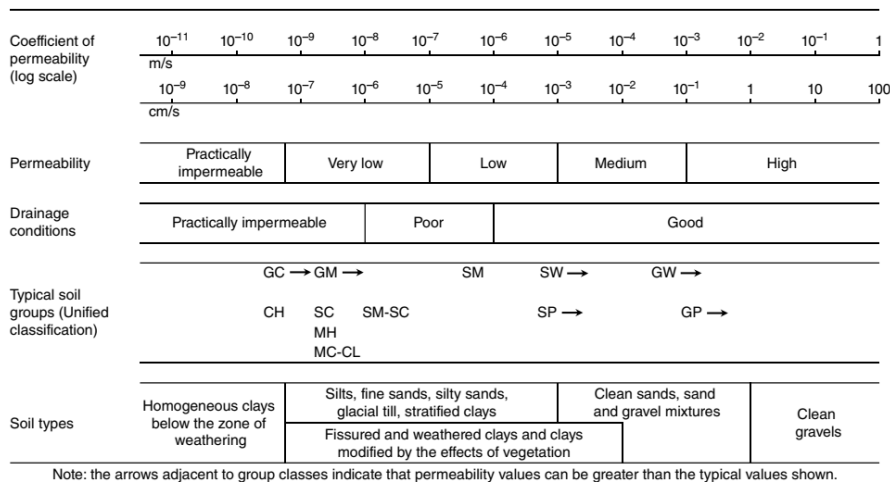
Figure 6. Typical permeability values for soils (Casagrande et al., 1940) (from Carter et al., 2016)

Based on the results of sieve analysis and permeability testing in oedometer, permeability values were determined. Cohesive materials represented by low (CL) to high (CH) plasticity clay have permeability coefficient values from $1,05 \cdot 10^{-7}$cm/s to $7,05 \cdot 10^{-9}$cm/s, and are classified as materials with low permeability. Granular materials silty sandy gravel (GM) and clayey to silty sand (SC, SM), have permeability coefficient values from $1,23 \cdot 10^{-5}$cm/s to $7,82 \cdot 10^{-8}$ cm/s and are characterized as materials with very low permeability.

Seismic refraction survey results are relatively well coincided with the results from exploratory drilling, especially in zones of slower speeds from 600m/s to 800m/s which were defined as a filling material during exploratory drilling.
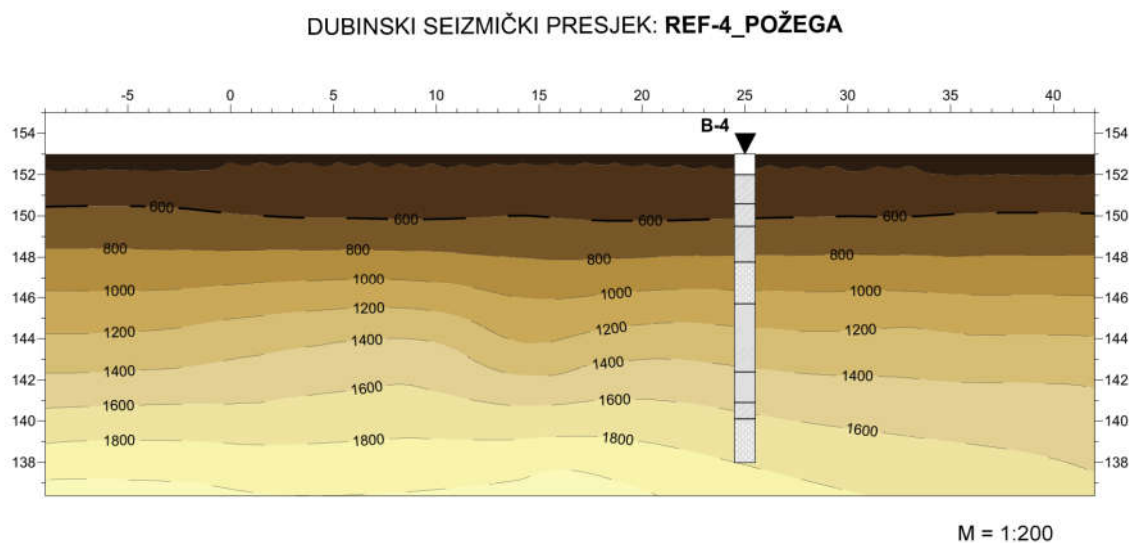
Figure 7. Seismic refraction profile REF-4_POŽEGA with borehole B-4

Results from MASW survey (Table 4.) determined material zones C and D according to EUOROCODE

8 document HRN EN 1998-1 :2011, which also showed good correlation values with SPT testing during exploratory drilling. (Figure 9.)

Table 3. Length of MASW profiles with EUROCODE 8 soil classification

MASW profile	Length of profile (m)	$V_{S(30)}$ (m/s)	EUROCODE 8 soil category
MASW-1	33	159 m/s	D
MASW-2	33	135 m/s	D
MASW-3	33	193 m/s	C
MASW-4	33	140 m/s	D
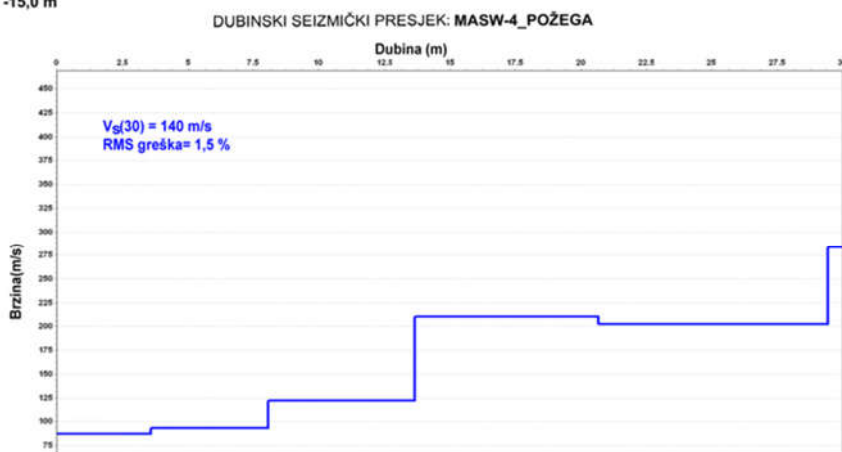
Figure 8. MASW profile MASW-4_Požega
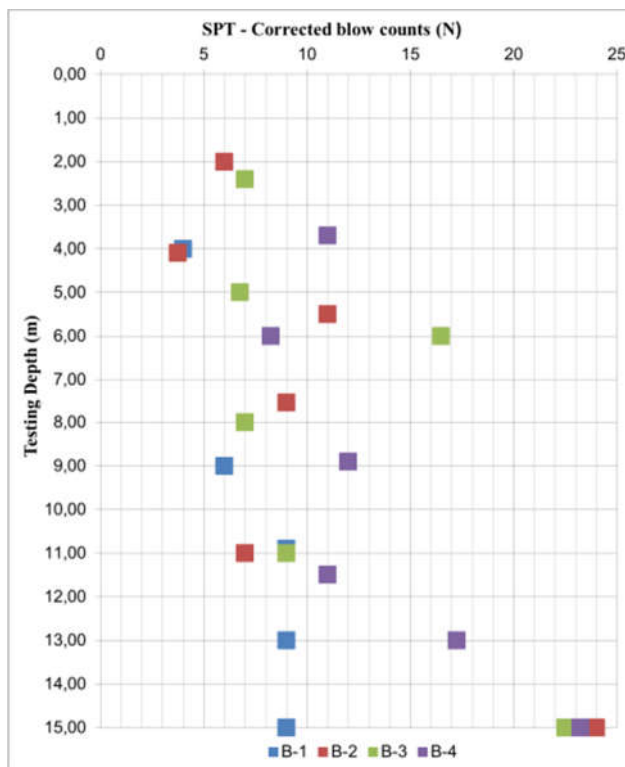
Figure 9. Results of SPT blow counts per borehole

4. Conclusion

In accordance with the results of geotechnical investigation soil model was created. Geotechnical soil model is composed from six geotechnical units, which were defined as a layer change of cohesive and granular materials. Cohesive materials are represented by low (CL) to high (CH) clays, while granular materials are characterized with clayey silty sands (SC, SM) and silty sandy gravel (GM).

Boreholes and CPTu testing data were used in creating geotechnical profiles (Figure 3.) of the site. Exploratory drilling alongside data provided by CPTu testing gave a good insight of subsoil structure of the site. These results have provided guidelines to determine relationship between alluvial (a) and loess (I-w_3) deposits. The main aquifer depth was established at approximately 12,50m.

The data provided by seismic refraction was used to confirm the depth of filling material layers defined in goetechnical soil model. Values of average shear wave velocity $V_{s(30)}$ confirmed soil types category C i D with values from SPT data.

Results from SPT and CPTu testing can be used for determening geotechnical soil parameters. From the results of geotechnical investigation several recommendations were given.

Foundation depth of the new buildings must be determined in accordance with foundation depth of an underground garage. Before any excavation activities begin the monitoring of the nearby buildings must be defined. All excavation for foundations must be conducted with construction pit shielding technology. Excavated material must not be deposited inside the complex area. Dewatering operations must also be prepared in case of ground water occurence in layers of granular materials.

References

ASTM D 2487-93. Standard Classification of Soils for Engineering Purposes (Unified Soil Classification System). Soil and Rock. 1995, 04.08.

ASTM D 2488-93. Standard Practice for Description and Identifacation of Soils (Visual Manual Procedure). Soil and Rock. 1995, 04.08.

Bačani, A. Hidrogeologija I, Sveučilište u Zagrebu, 2006.

Carter, M.; Bentley, Stephen P. Correlations of Soil Properties, London, John Wiley & Sons, Ltd, 2nd Ed. 2016.

Mance, M.; Cvetković, M.; Jurić Kačunić, D. Laboratorijsko i terensko određivanje koeficijenata propusnosti, Simpozij doktorskog studija građevinarstva, 2019, 35-46.

Park, C.B.; Miller, R.D.; Xia, J. Multichannel analysis of surface waves. Geophysics. 1999, 64, 800-808.

Robertson, P.K. Interpretation of Cone Penetration Tests – a unified approach. Canadian Geotechnical Journal. 2009, 46, 1-19.

Robertson, P.K. Soil Classification using the cone penetration test. Canadian Geotechnical Journal. 1990, 27(1), 151-158.

Robertson, P.K.; Cabal, K.L. Guide to cone Penetration Testing for Geotechnical engineering, Gregg Drilling & Testing, Inc, 6th Ed.

TOWARDS A RAPID AND PRACTICAL DETERMINATION OF THE PIN-ROCK INTERACTION PARAMETERS OF THE CERCHAR ABRASIVITY TEST

MARKUS KASPAR [1], THOMAS FRÜHWIRT [2], CHRISTINE LATAL [1], MANFRED BLÜMEL [3]

[1] *Institute of Applied Geosciences, TU Graz, Austria, markus.kaspar@tugraz.at; christine.latal@tugraz.at*

[2] *Chair of Mining Engineering and Mineral Economics, Montanuniversität Leoben, Austria, thomas.fruehwirt@unileoben.ac.at*

[3] *Institute of Rock Mechanics and Tunnelling, TU Graz, Austria, bluemel@tugraz.at*

Abstract

The CERCHAR test is a widely used index test for evaluating rock abrasiveness and associated tool wear in rock excavation. However, routine testing only assesses the wear on the pin itself. To evaluate the advancement rates in rock cutting during excavation, it is also crucial to consider the material removal of the rock. Recent studies have begun to include this aspect by developing advanced methods, automated testing devices, or using customized equipment for test evaluation. However, these methods are too time-consuming and specialized to be used in routine laboratory testing. This study investigates the correlation between traditional CAI and associated material removal by complementary measurements of the scratch groove on the rock specimen using a stereomicroscope. The presented approach enables the straight forward determination of additional parameters, such as rock volume removal and pin tip loss, based on the inherent pin tip geometry and associated scratch groove geometry. These parameters are then used to calculate the CERCHAR Abrasion Ratio, which serves as a proxy for the excavability of different rock types. Despite some minor limitations, this approach can deliver values that are comparable to those obtained using specialized equipment. Therefore, it has the potential to be a practical method for assessing abrasion and excavation on job sites.

Key words

Rock excavation, CERCHAR Abrasivity Index, CERCHAR Abrasivity Ratio.

1   Introduction

The CERCHAR test was developed over 50 years ago as a quick way to assess abrasivity on job sites (Valantin, 1974; Thuro 2002, Rostami et al., 2005). Since then, numerous studies have presented more comprehensive and sophisticated methods to characterize the processes associated with rock and pin properties during this test. The CERCHAR Abrasivity Ratio (CAR), as well as testing devices equipped with real-time monitoring sensors were recently proposed to address these issues (Hamzaban et al. 2014, Zhang and Konietzky 2020, Zhang et al. 2020, Karrari et al. 2024). Although these studies offer valuable insight into rock excavation, the methods presented require specialized equipment, such as scanning electron microscopes, 3D high-resolution microscopes and/or real-time sensors. The aim of this study is to extend the evaluation of the CERCHAR test to apply these methods outside of academic institutions. This is achieved by addressing rock-pin interaction through the use of intrinsic geometric properties of the stylus and straightforward measurements of the scratch groove on the tested rock specimen. The pin tip wear (CAI) and material removal is linked based on these measurements and the CERCHAR pin geometry. Results are related to other parameters used in the industry such as the Rock Abrasivity Index (RAI) and uniaxial compressive strength (UCS). The method is tested on a wide range

of sedimentary rocks (Alpine Flysch Zone, Karawanke Mountains), metamorphic rocks (Austro-Alpine basement) and igneous rocks (Bohemian Massif), to assess its potential applicability and limitations.

2   Methods

In total, 60 specimens of metamorphic, sedimentary and igneous rocks were investigated for their abrasive behavior and excavability. The rocks cover a broad range of fabric characteristics, such as grain size, anisotropy, strength and mineralogical composition. The rocks were tested using a CERCHAR device with a fixed, stationary steel pin while the sample is being moved by a handwheel (West 1989). The pins and testing procedure comply with AFNOR and ASTM standards, and ISRM and DGGT recommendations (AFNOR 2000, Alber et al. 2014, Käsling and Plinninger 2016, ASTM 2022). The pins are 10 mm in diameter and have a Rockwell hardness of HRC 55±1 with a 90° conical tip. Specimens are formatted into blocks of approximately 50 x 50 x 100 mm. The rocks are cut with a diamond saw to ensure uniform test surface conditions (ÖBV 2013). Metamorphic and sedimentary rocks are tested perpendicular to their foliation and bedding, respectively. The pin tip wear of 5 pins for each sample is measured under a transmitted light microscope (80x magnification). From the average of these 5 measurements the CERCHAR Abrasivity Index (CAI) is calculated. The cross diameter of the corresponding scratch grooves produced by the pins on the rock sample are measured under the same microscope in reflected light mode. The uniaxial compressive strength (UCS) tests are conducted load and/or strain controlled with a minimum duration of 5 minutes following the recommendation No. 1 of the Commission on Rock Testing of the German Geotechnical Society (Mutschler 2004) and the standard ON B 3124-9 (Austrian Standards International 1986) using an MTS model 815. Bulk mineral compositions were determined by x-ray powder diffraction analyses (XRD) using a PANalytical X´Pert PRO diffractometer. Based on the mineralogical composition of the samples, the equivalent quartz content (F_{EQu}) is calculated using the quartz normalised factors of recommendation No. 25 of the Commission on Rock Testing of the German Geotechnical Society (Plinninger et al., 2021). The Rock Abrasivity Index (RAI) is calculated as the product of UCS and F_{EQu} (Plinninger 2002).

3   Results

3.1 Parameters of pin-rock interaction

The 90° conus geometry of the pin tip and the associated scratch groove exhibit certain intrinsic relations that are used to extend the evaluation of the standard CERCHAR test. The volumetric wear volume of the pin tip (V_s in Fig. 1) can be obtained from the CAI by either using the conical volume (Eq. 1) where the height and radius are equal (i.e. 0.05 CAI, or pin tip wear height) or the exponential relationship (Eq. 2). The amount of material removed from the rock during the test is indirectly inferred by measuring the scratch width (Sw) produced on the sample (Fig. 1). The pin geometry is directly related to the scratch width, i.e. the deeper the indentation, the wider the scratch. Knowing the CAI and the scratch width (Sw), it is possible to calculate the pin penetration depth into the rock (P_x) and the vertical pin displacement (A_x) using Eq. 3 and 4. Depending on the tested rock type, different scenarios are realized for these geometric parameters. The proportion of P_x varies greatly, being close to zero for hard rocks like granite, or equal to A_x for very soft rocks (Fig. 1a-c).

$$V_s\ [mm^3] = \frac{1}{3}\pi * 0.05CAI^3 \tag{1}$$

$$V_s[mm^3] = 0.00013 * CAI^3 \tag{2}$$

$$P_x\ [mm] = \frac{(Sw - 0.1CAI)}{2} \tag{3}$$

$$A_x\ [mm] = P_x + 0.05CAI \tag{4}$$

From the CAI, P_x and Sw the corresponding idealized removed rock volume over a testing distance of 10 mm can be calculated as a trapezoid (Eq. 5):

$$V_m \ [mm^3] = (Sw + 0.1CAI) * \frac{P_x}{2} * 10 \tag{5}$$

The ratio between the volume of the removed rock material (V_m) and the abraded pin tip volume (V_s) is the CERCHAR Abrasion Ratio (CAR), providing information on the excavability associated with the abrasivity of a rock (Zhang and Konietzky, 2020). The formula for calculating the CAR is given in Eq. 6.

$$CAR \ [-] = \log_{10}\left(\frac{V_m}{V_s}\right) \tag{6}$$
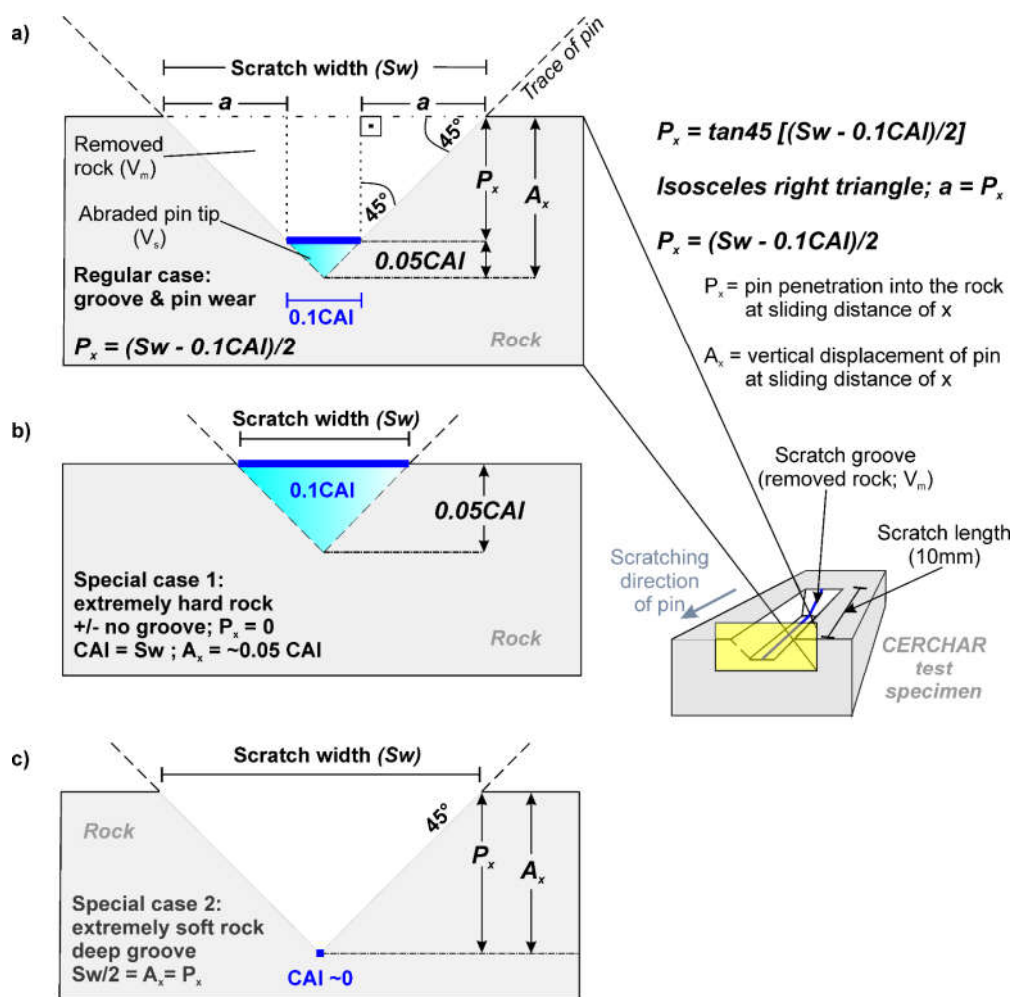
Figure 1. Concept and scenarios of CAI and associated removal of rock material, i.e. excavation. a) regular case: the pin abrasion and rock excavation occur at the same time. b) extremely hard rock: the pin is abraded without significantly penetrating into the rock. c) soft rock: the pin deeply penetrates into the rock with only minor abrasion taking place at the pin tip.

The groove is identified by the color difference to the surrounding diamond saw cut surface and exhibits a prominent edge (Fig. 2). This edge is best developed in fine grained, sedimentary rocks or marbles (Fig. 2a,b). The Sw is measured by applying tangent lines at the edges without incorporating breakout moulds in order to account for an idealized V-shaped groove (Fig. 2c). In hard, coarse grained crystalline rocks the groove is sometimes poorly developed, irregular or almost invisible (Fig. d-g). This may be attributed to the skating effect (Al-Ameen and Waller 1994, Macias et al., 2016) known to occur in these

types of rocks (Fig. 2h). Whenever possible the Sw is measured in the last 25 % of the scratch groove where pin tip wear is already close to the final CAI. Plinninger et al. (2003) showed that about 85 % of the final pin tip wear already occurs within the first two millimeters of the scratch (Fig. 3a). Thus, as the pin loses material at the tip and simultaneously penetrates the rock, the vertical displacement (A_x) also increases and follows a similar pattern (Fig. 3b). The actual removed material corresponds to the area top of the P_x–sliding distance curve recorded during the CERCHAR test (Karrari et al. 2024).

For uniformly shaped scratch grooves one representative cross diameter was measured at each scratch. For irregular shaped grooves (i.e. varying penetration depths), a mean value of multiple cross diameters was determined. Similar to determining the CAI, the mean value of 5 scratch width measurements is calculated for each rock sample.
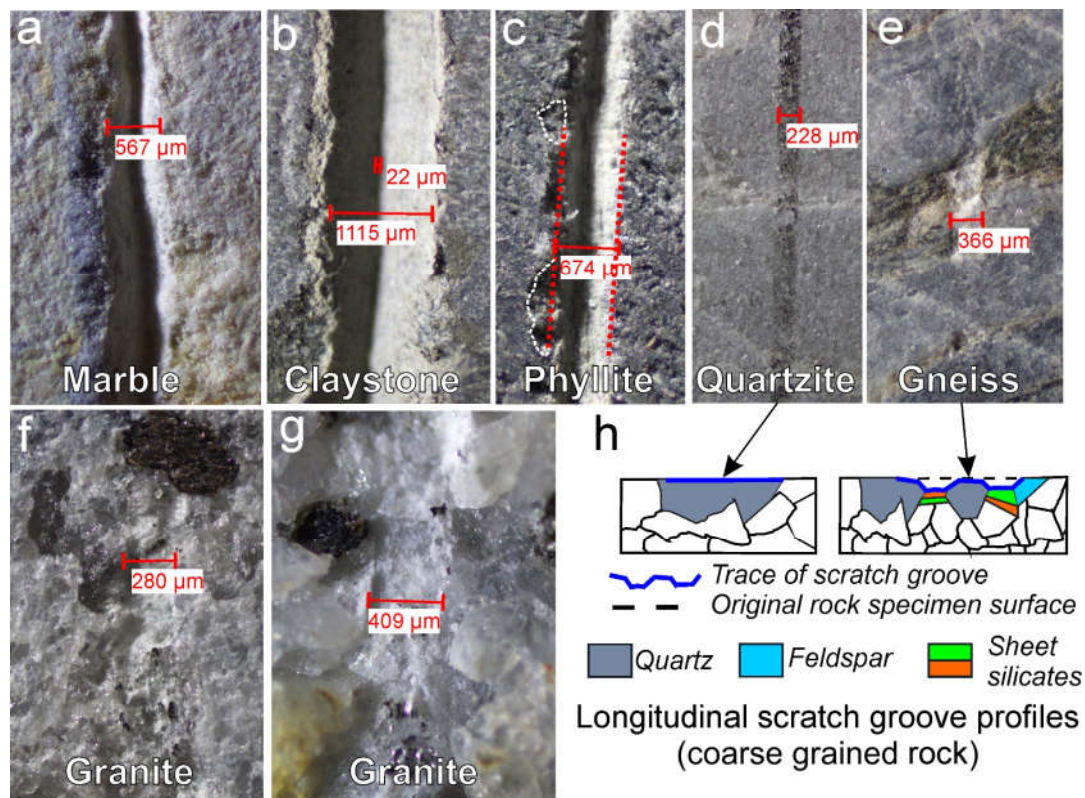
Figure 2. CERCHAR test scratch grooves of different rock types. a) Marble with a distinct v-shaped scratch groove profile. b) Sharply defined scratch groove in a claystone penetrating deeply into the rock. The groove base is close to the actual CAI measured at the pin tip. c) Phyllite with minor breakout moulds (white dashed outlined areas) and applied tangent line at the edge of the scratch groove. d) Extremely hard quartzite with only a surficial trace of the scratch. e) Gneiss exhibiting differential pin indentation due to mineral hardness differences. f) poorly developed scratch groove in a granite. g) granite with quartz grains ripped out of the fabric. h) schematic drawing of a scratch groove with varying P_x on hard, coarse grained rock.
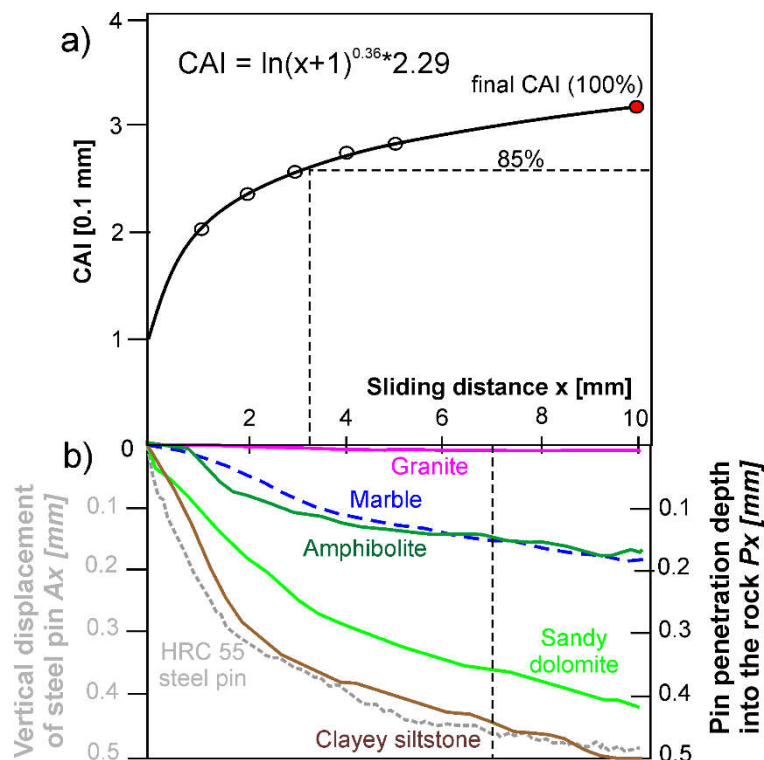
Figure 3. Relation between pin tip wear and penetration depth for different rock types as a function of the sliding distance of the pin. a) CAI vs. sliding distance (modified after Plinninger et al. 2003). b) Vertical displacement and pin penetration depth as a function of the sliding distance (compiled and modified after Hamzaban et al. 2014). Absolute pin penetration depths (P_x) depend on the rock type, but patterns are similar and the pin penetration depth is already close to its final level after 75 % of the sliding distance. The vertical pin displacement (A_x) approaches P_x for very soft, non-abrasive rocks (e.g. clayey siltstone) and is equal to 0.05CAI for very hard rocks (i.e. only pin tip wear with no penetration into the rock; see special cases shown in figure 1b and c).

3.2 Concept evaluation

In general, the penetration depth into the rock decreases with increasing abrasivity. With coarse grained crystalline rocks (granite) there can be a discrepancy between the scratch width and the CAI value, i.e. negative P_x (Fig. 4a). This may be due to the measuring technique for the pins if abrasion is uneven at the tip. Therefore, the measured CAI is higher than the actual contact area of the pin with the rock surface. Especially rocks falling into the classes CAI<3 exhibit a wide range of material removal for rocks falling into one CAI category. Interestingly, the relative range is very similar for the first four abrasivity classes and lies between V_m 2.16 – 2.76 mm³. For the classes CAI>3, the values are between V_m 0.79 – 0.01 mm³. This boundary roughly coincides with the transition from sedimentary to crystalline metamorphic and magmatic rocks (Fig. 4a). Figure 5 shows a compilation of the pin tip wear height and P_x and the associated CAR for the six investigated rock groups.
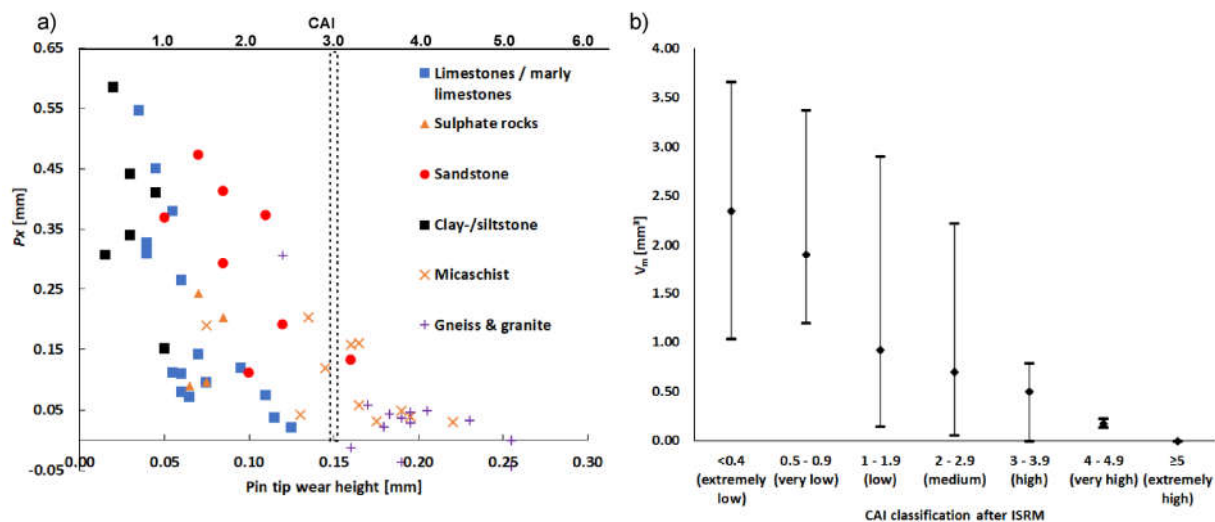
Figure 4. Range of excavability. a) pin tip wear height (or corresponding CAI) versus pin penetration depth P_x. Sedimentary rocks are found at CAI<3. The majority of crystalline rocks exhibits values CAI>3. b) The range of removed rock material (V_m) within the different CAI classes.
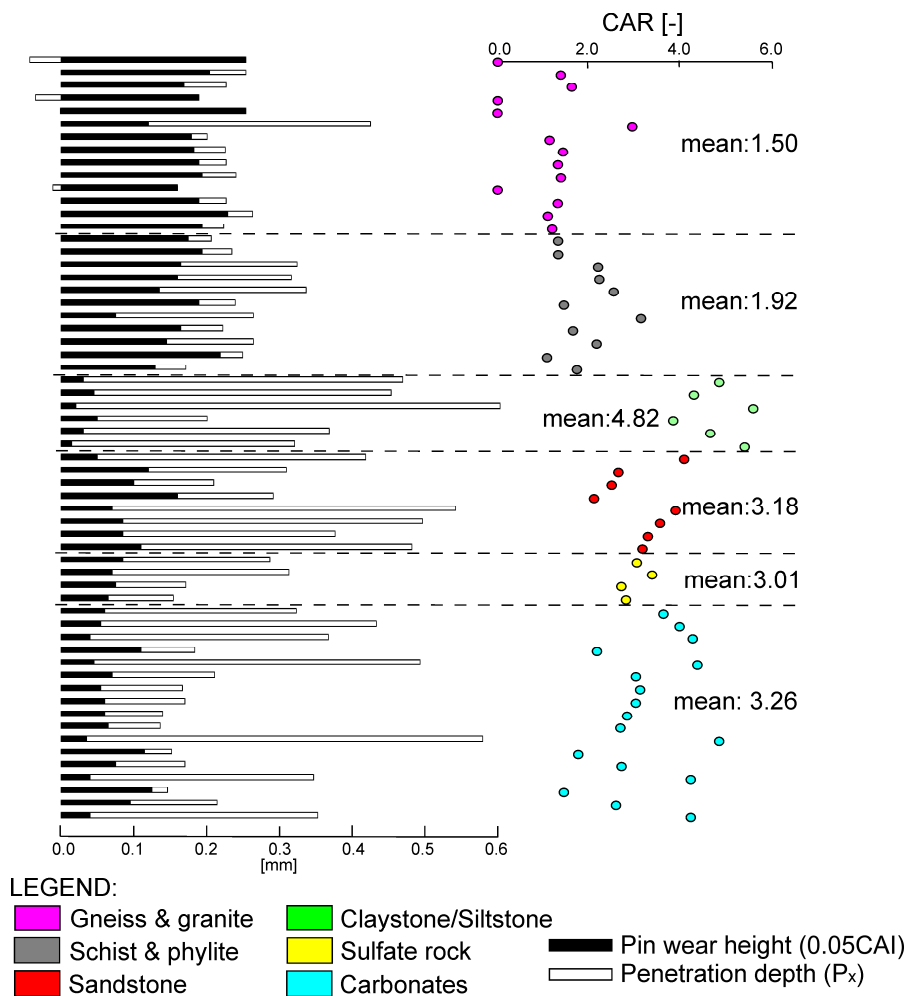
Figure 5. Compilation of the pin wear height, pin penetration depth into the rock and associated CAR for the investigated rock types. Note that negative values for the penetration depth are obtained for some very hard rocks and thus CAR cannot be determined, i.e. becomes zero.

The penetration depth cannot be attributed to a single rock property. P_x is rather controlled by factors such as porosity, grain size and the fabric of the rock type. There seems to be a limitation in penetration depth above a certain threshold of UCS of approximately 60 MPa, where no deep penetrations are realized. This value corresponds to the value reported by Kaspar et al. (2023) above which the CAI can most reliably be predicted from mineralogical analyses using reference values from single crystal scratch tests. Penetration depths higher than 0.25 mm are only observed for sedimentary rocks, while low values (approx. 0.15 mm) are observed for crystalline rocks. However, there are also sedimentary rocks with small P_x. These are dominated by massive, fine grained, relatively pure limestones. In fact, an increase in other components than carbonates (i.e. quartz, feldspars and sheet silicate) seems to have an adverse effect on the penetration depth. The marly limestones, for example, plot in the upper region of the diagram in Fig. 6. Weakly cemented rocks and fine grained rocks such as sandstones and clay-/siltstones exhibit the highest penetration rates and their CAI does not exceed 2. In such cases, mineral grains are probably more easily removed from the rock fabric. The content of hard, abrasive minerals (Mohs hardness >5.5; Plinninger 2008) alone does not serve as a proxy for abrasion or resistance against penetration. The sandstone in Fig. 6, for example, has a quartz content of 84 %, but a very high penetration depth, pointing to a microstructural control rather than mineralogical control. The only crystalline rock with higher penetration depth is a chlorite rich green schist plotting between the two clusters.
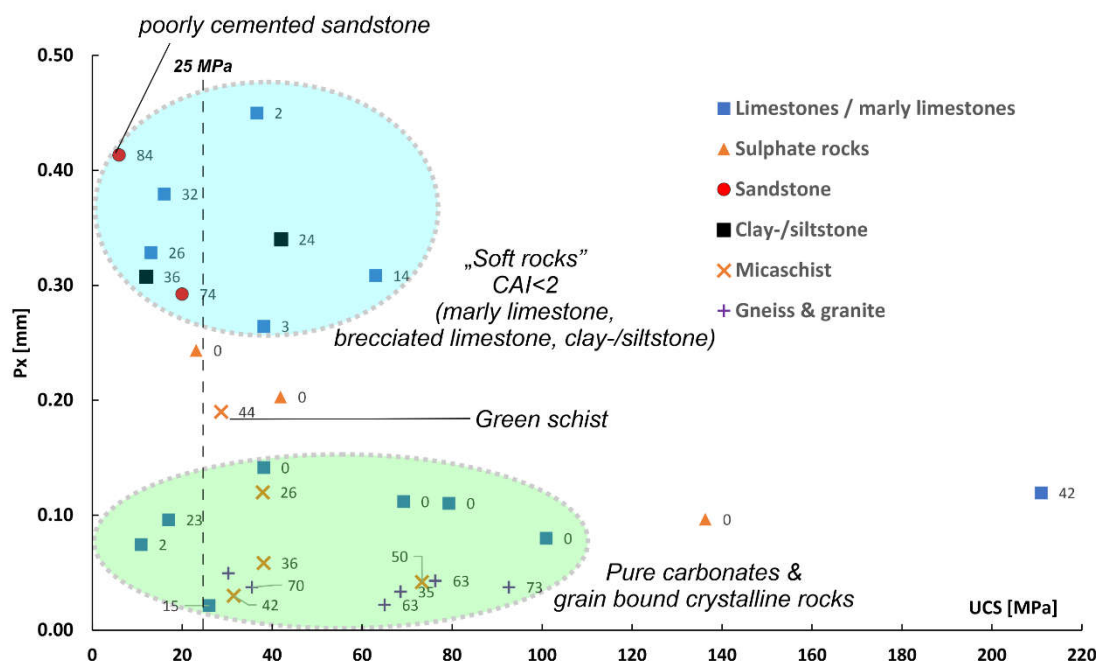
Figure 6. Plot of penetration depth (P_x) and UCS. The cluster in the upper, light blue region comprises weakly cemented sedimentary rocks and impure carbonates (marls) and clay-/siltstones, commonly referred to as soft rocks. The lower, light green cluster comprises well interlocked, pure carbonates and grain bound crystalline rocks. The traditional limit for defining soft rocks by means of UCS = 25 MPa is shown for reference. The numbers next to the symbols indicate the content (percent) of abrasive minerals with a Mohs hardness >5.5.

There is a negative linear correlation between CAI and CAR with the overall regression coefficient being consistent with the one published by Zhang and Konietzky (2020) (Fig. 7). A weak correlation is found for the CAR and RAI (Fig. 8a). It roughly reflects the pattern that rocks with a high CAR have a low RAI and are less abrasive and thus easier to excavate. The fitting for all rock types is slightly lower than for RAI and CAR (Plinninger and Thuro 2004) (Fig. 8b). Crystalline rocks tend to have higher ranges of RAI with low CAR, while the opposite is the case for sedimentary rocks. This supports the general hypothesis that sedimentary rocks can be excavated more efficiently while being less abrasive on the tool. Crystalline rocks on the other hand are less efficiently excavated and cause more damage on the tools. However, there are limestones with low CAR and low RAI. Such rocks might be less efficient to drill/excavate, but are not abrasive on the tool. This points to a mineralogically controlled

abrasivity for this kind of rocks.
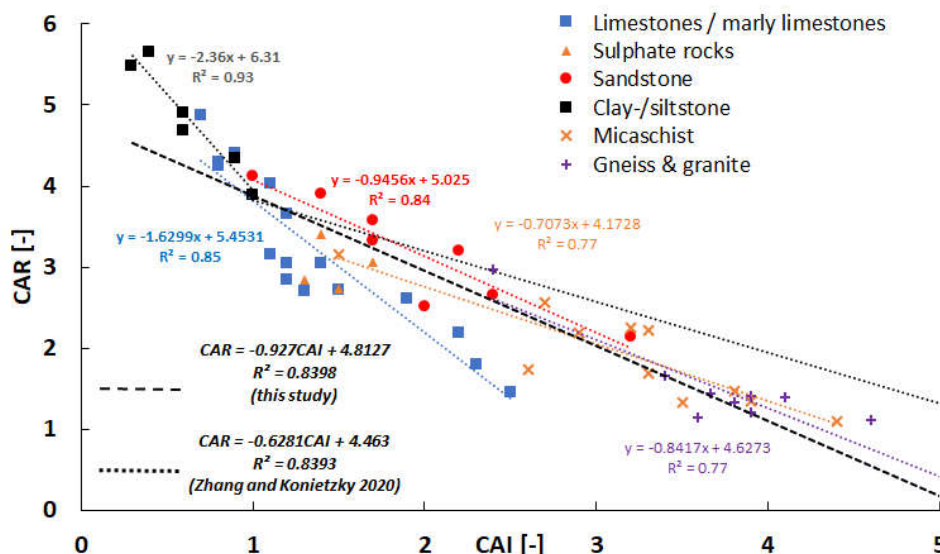
Figure 7. Correlation between CAI and CAR for the different rock types. Overall regression line and formula of Zhang and Konietzky (2020) is shown for comparison.
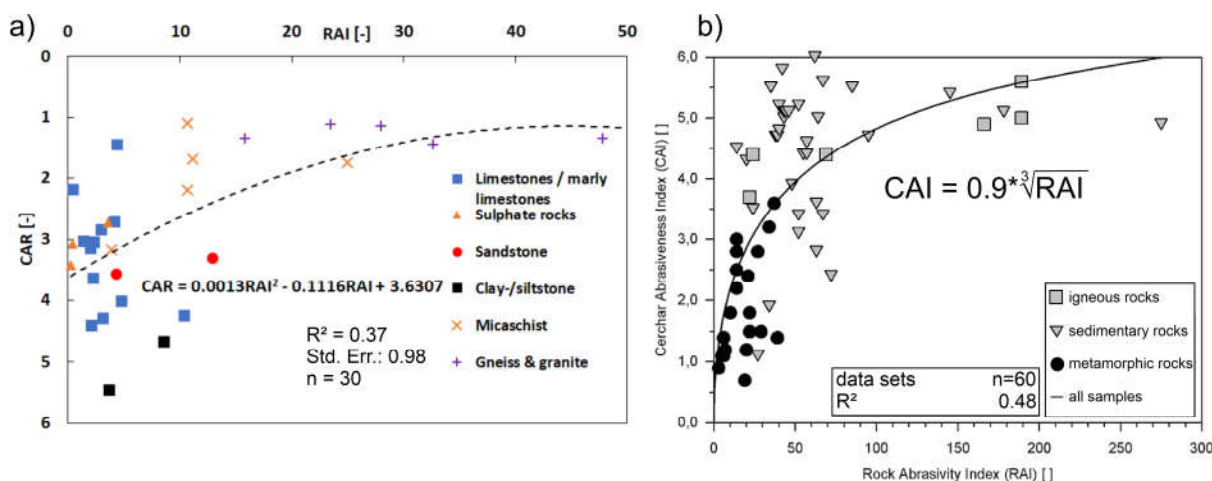
Figure 8. The CAI in relation to other parameters. a) correlation between CAR and RAI obtained for the used dataset. b) correlation between RAI and CAI (after Plinninger and Thuro 2004, Schumacher 2004).

The details of the statistical analysis for Fig.8a is given in Tab.1 and Tab.2. The significance level from the F-test is essentially 0 and the p-values from the t-test are lower than 0.05, fulfilling the conditions for a significant correlation between CAR and RAI.

Table 1. Variance analysis and F-test

Parameters	Degrees of freedom	Sum square	Mean square	F	Sign.-level.
Regression	2	15.23	7.62	7.95	0.002
Residue	27	25.88	0.96	1.5/1	
Total	29	41.11			

Table 2. Regression coefficients and t-test

Parameter	Coefficient	Std. err.	t	p
Intercept	3.6307	0.2732	13.2885	0.0000
RAI	-0.1116	0.0301	-3.7058	0.0010
RAI²	0.0013	0.0004	2.9338	0.0068

4   Conclusion

The presented approach individualizes the assessment of the CAI and associated material removal irrespective of the tested lithology. So far, the CAI only provided information for the tool wear, but not on the excavation progress. Instead of utilizing a high-resolution 3D model of a scratch groove obtained from specialized instruments, the basic 2D scratch dimensions are measured under the same microscope used for determining the CAI. This is less time consuming and can be performed in a second step at the rock specimen after measuring the pin tip wear. There are limitations such as irregular groove profiles so that only approximations of the actual groove volume are possible. Nevertheless, it provides additional information on the excavability behavior in rock dredging projects. Even though the presented approach uses idealized and simplified geometries the results reflect those obtained from other more laborious methods. The CAR results, for example, are consistent with the findings of Zhang and Konietzky (2020) and show similar patterns and fittings. The absolute values vary, probably as a result of natural variations in rock composition and fabric. Limitations occur for very abrasive rocks with little to almost zero material removal leading to unrealistic negative P_x values. This effect was also observed by Hamzaban (2014) where abnormal curves occurred with very little P_x values. The reason lies in the measurement of the CAI. If the wear flat is not perfectly flat, the contact area of the steel pin with the rock can be smaller than the measured CAI. In combination with very little penetration into the rock, Sw is also close to the CAI, so that the method might not be reliably applicable in such extreme cases. For the evaluation presented here, saw cut rock surface should be used to eliminate the uncertainties due to height changes of rough surfaces. Furthermore, the additional information on the penetration depth (P_x) and the associated removed rock volume (V_m) can be used to refine the traditional understanding of soft rocks. Kaspar et al. (2022) highlighted the heterogeneity of natural stone materials and that both, strength and mineralogical composition influence to varying degrees the abrasivity of different rock types. The presented approach in this study adds information on the excavability to the solely UCS based definition of soft rocks.

References

AFNOR. *Norme Française P94-430-1 Rock – Determination of the rock abrasiveness – Part 1: Scratching test with a pointed tool,* Paris, Association Française de Normalisation, 2000.

Al-Ameen, S.I.; Waller, M.D. The influence of rock strength and abrasive mineral content on the CERCHAR Abrasive Index. *Engineering Geology.* 1994, 36, 293–301.

Alber, M.; Yarali, O.; Dahl, F.; Bruland, A.; Kasling, H.; Michalakopoulos, T.N.; Cardu, M.; Hagan, P.; Aydin, H.; Ozarslan, A. ISRM suggested method for determining the abrasivity of rock by the CERCHAR Abrasivity Test. *Rock Mechanics and Rock Engineering.* 2014, 47, 261–266.

ASTM. *Designation 7625 Standard test method for laboratory determination of abrasiveness of rock using the CERCHAR abrasiveness index method.* West Conshohocken, ASTM International, 2022

Hamzaban, M-T.; Memarian, H.; Rostami J. Continuous monitoring of pin tip wear and penetration into rock surface using a new Cerchar abrasivity testing device. *Rock Mechanics and Rock Engineering.* 2014, 47, 689–701.

Karrari, S.S.; Heidar, M.; Hamidi, J. K.; Teshnizi, E.S. New Cerchar device used for evaluating Cerchar abrasivity parameters. *International Journal of Geomechanics.* 2024, 24, 3, 04024005.

Käsling, H.; Plinninger, R. J. Determining the abrasivity of rock using the CERCHAR test – Recommendation No. 23 of the Commission on Rock Testing of the German Geotechnical Society. *Bautechnik.* 2016, 93, 6, 409–415.

Kaspar, M., Latal, C., Pittino, G., Blümel, M. Hardness, strength and abrasivity of rocks:Correlations and predictions. *Geomechanics and Tunnelling*. 2023, 16, 2, 184–192.

Kaspar, M., Latal, C., Blümel, M., Pittino, G. Is soft rock also non-abrasive rock? An evalua-tion from lab testing campaigns. *In Proceedings of the EUROCK conference, Espoo, Finland, 12 – 15 September 2022*; IOP Conference Series: Earth and Environmental Science, 1124, Rock and Fracture Mechanics in Rock Engineering and Mining, 012019.

Macias, F.J.; Dahl, F.; Bruland A. New rock abrasivity test method for tool life assessments on hard rock tunnel boring: The Rolling Indentation Abrasion Test (RIAT). *Rock Mechanics and Rock Engineering*. 2016, 46, 1679–1693.

Mutschler, T. Uniaxial compression tests on rock samples – Recommendation No. 1 (revised) of the Commission on Rock Testing of the German Geotechnical Society. *Bautechnik*. 2004, 81, 10, 825–834.

ÖBV *Merkblatt Abrasivitätsbestimmung von grobkörnigem Lockergestein*, Vienna, Österreichische Bautechnikvereinigung, 2013.

ON B 3124-9 *Testing of natural stone; mechanical properties of rock; modulus of elasticity, stress-strain curve and poisson's ratio under uniaxial compressive loading*, Vienna: Austrian Standard International, 1986.

Plinninger, R.J. Klassifizierung und Prognose von Werkzeugverschleiß bei konventionellen Gebirgslösungsverfahren im Festgestein. *Münchner Geologische Hefte*. 2002, 17

Plinninger, R.; Kasling, H.; Thuro, K.; Spaun, G. Testing conditions and geo-mechanical properties influencing the CERCHAR abrasiveness index (CAI) value. *International Journal of Rock Mechanics & Mining Sciences*. 2003, 40, 259–263.

Plinninger R.J.; Thuro, K. Wear prediction in hardrock excavation using the CERCHAR Abrasiveness Index (CAI). *In Proceedings of the 53rd Geomechanics Colloquy & ISRM Regional Symposium Eurock, Salzburg, Austria, 7–8 October 2004*; Glückauf, Essen, Germany, 2004.

Plinninger R.J. Abrasiveness assessment for hard rock drilling. *Geomechanics and Tunnelling*. 2008, 1, 38–46.

Plinninger, R.J.; Käsling, H.; Popp, T. Determination of rock abrasivity using mineralogical-petrographical methods – Recommendation No. 25 of the Commission on Rock Testing of the German Geotechnical Society. *Geotechnik*. 2021, 44, 2, 123–135.

Rostami, J.; Ozdemir, L.; Bruland, A.; Dahl, F. Review of issues related to Cerchar abrasivity testing and their implications on geotechnical investigations and cutter cost estimates. *In Proceedings of the Rapid Excavation and Tunneling Conference, Seattle (WA), USA, 25–27 June 2005;* Society for Mining Metallurgy & Exploration: Englewood (CO), USA, 2005.

Schumacher, L. Design parameters and operating conditions for hard-rock tunnelling machines. *Felsbau*. 2004, 22, 3, 21–28.

Thuro, K. Geologisch-felsmechanische Grundlagen der Gebirgslösung im Tunnelbau. *Münchner Geologische Hefte*. 2002, 18.

Valantin, A. Test CERCHAR pour la mesure de la dureté et de l'abrasivité des roches. *In Proceedings of the Conference on Development and Exploratory Techniques in Coal Mines, Luxembourg, 28–30 November 1973;* Commission of the European Communities: Luxembourg, Luxembourg, 1974.

West, G. Technical note – Rock abrasiveness testing for tunnelling. *International Journal of Rock Mechanics and Mining Sciences & Geomechanics Abstracts*. 1989, 26, 2, 151–160.

Zhang, G.; Konietzky, H. CERCHAR Abrasion Ratio (CAR) as a new indicator for assessing rock abrasivity, rock–stylus interaction and cutting efficiency. *Rock Mechanics & Rock Engineering*. 2020, 53, 3363–3371.

Zhang, G.; Konietzky, H.; Frühwirt, T. Investigation of scratching specific energy in the Cerchar abrasivity test and its application for evaluating rock-tool interaction and efficiency of rock cutting. *Wear*. 2020, 448–449, 203218.

THREE-DIMENSIONAL MODELLING FOR THE DELINEATION OF HAZARD ZONES ON ROCKY SLOPES IN AREAS OF ARCHAEOLOGICAL INTEREST

EMMANOUIL CHATZIANGELIS[1], NIKOLAOS DEPOUNTIS[2], PANAGIOTIS PELEKIS[3]

[1] *University of Patras, Department of Geology, Greece, up1089644@upatras.gr*

[2] *University of Patras, Department of Geology, Greece, ndepountis@upatras.gr*

[3] *University of Patras, Department of Civil Engineering, Greece, ppelekis@upatras.gr*

Abstract

With the development of technology and the ever-increasing needs in infrastructure projects, the application of new technology in all technical branches, as well as in the field of Engineering Geology and Rock slope engineering, is becoming more and more imperative. The use of drones for mapping large areas and slopes is now imperative and particularly useful. Also, the creation of a 3-d terrain model in the form of a point cloud data set is particularly useful for a large number of geotechnical analyses. This paper analyzes the process and parameters for the creation of a high-resolution 3-d terrain model, with the use of highly sophisticated programs (UgCS and ArcGIS-Drone2Map), which can be used for the delineation of hazard zones on rocky slopes and discontinuity kinematic analysis in sites of particular interest. Towards this scope several programs can be used (e.g. DSE and Rocscience's dips and rocfall3) to assess the quality of the rock-mass and its discontinuities, as well as the probability of rock falls. The process of performing all the above is not complex but requires familiarity. The study area of assessing this type of modelling is Acrocorinth, one of the most important archaeological sites in Greece, at which is necessary to analyse its vulnerability to rockfalls and design hazard zones.

Key words
Rockfalls, 3D terrain model, slope, disconinuities, rock mass.

1   Introduction

Acrocorinth is a 575 meter high cliff that dominates the plain of the modern and ancient city of Korinthos in Greece and is the largest and oldest fortress in the Peloponnese peninsula. It was constructed during the classical years and it played an important role through the ages due to its strategic position. The entrance area of the archaeological site is located at the entrance point of the Castle, where for defensive reasons it was originally built in a position particularly exposed to all kinds of natural hazards. It was continuously occupied from archaic times to the early nineteenth century (Athanasoulis, 2014). Today it is one of the most important archaeological sites in Greece, with many visitors and it is very important to analyse its vulnerability to rockfalls.
The current research analyzes the potentiality of rockfalls at the entrance of the archaeological site, the footbridge and the visitor access road and examines the wider area which is an active geomorphological field, where rockfalls have been occurring for centuries (Fig1). The phenomenon of rocks and boulders falling from the steep slopes of Acrocorinth is considered diachronic, while evidence of rockfalls already exists since ancient times. In the present research, due to the steep morphology and the difficulty of recording all discontinuities that prevail along the site's slopes, a drone with rtk and high-definition camera was used to survey the high and steep slopes. Purpose of this, was to create a high-resolution 3D terrain model that can clarify in detail the geometric features of the discontinuities of the rock mass as they have been described by Bieniawski (1989) as well as to detect rockfall seeders and characterise them based on the work of Volkwein et al (2011). Similar works, but not on archaeological sites, have

been carried out by Saro et al (2018), Guzzetti et al (2002) and others.

Figure 1. The steep rocky slopes of Acrocorinth in Greece and the area of study

2   Methods

2.1   Synopsis

The methodology used in the curerent reserach is based on the creation of a high-resolution terrain model from which all necessary information is derived for further analyses. This results in fewer file conversions, using core programs rather than using intermediate programs to convert files where errors occur and data reliability is lost. To achieve this, a planned drone flight is carried out through UgCS with flight data that give a GSD value<0.5cm, then the 3d terrain model is created with ESRI's ArcGIS-Drone2Map software, which is directly connected to ArcGISPro for further processing and filling in data without conversions. Having the high-resolution 3D model, the data is imported into the DSE software (Riquelme et al, 2015) to extract the rock mass characteristics (slope inclination and dip/dip direction of discontinuities). Data extracted from DSE are compared with measurements derived in the field with conventional methods (geological compass) and assessed with the use of Rocscience Dips program (licensed academic version 8.027) to check if further improvements are necessary in the digital proposed methodology. Moreover, the 3d terrain model is imported into the Rocscience RocFall3 program (licensec academic version 1.014) to determine the kinetic energy and bounce heigth of potential rockfalls in the entire area. Therefore, a complete digitized method is created to assess all potential risks arising from rock masses and their discontinuities, regardless of their accessibility.

2.2   Geological setting of the study area

Acrocorinth is a prominent tectonic structure, located WSW of the canal of Corinth representing a typical horst. The exposed alpine formations are believed to belong to the Pelagonian zone (Internal Hellenides). The stratigraphy includes Middle Jurassic limestones and various-colored shales with cherts (Collier et al, 1991). These shales either intercalate or lie on top of Middle Triassic-Lower Jurassic limestones. The alpine formations have been initially deformed by thrust faulting that was active in the

Pelagonian zone during Eocene – Latest Cretaceous. A north – south trending thrust fault, bounds the Acrocorinth to the west. Shales and Jurassic limestones occupied respectively the footwall and the hanging wall of this thrust. Generally, east-dipping low-angle thrust faults affect the Middle Jurassic limestones. Due to the latest extensional phase, high- angle normal faults were formed, affecting the pre-existing alpine structures. As a result, a series of neotectonic structures, such as horsts and grabens have been formed. A typical example of the above-mentioned structures is the Acrocorinth horst (Fig.2). This structure is bounded by two west – east trending normal faults downthrown to the north and to the south respectively. Thick Upper Pliocene-Pleistocene to Quaternary clastic sediments cover uncomfortably the alpine formations in the adjacent areas.
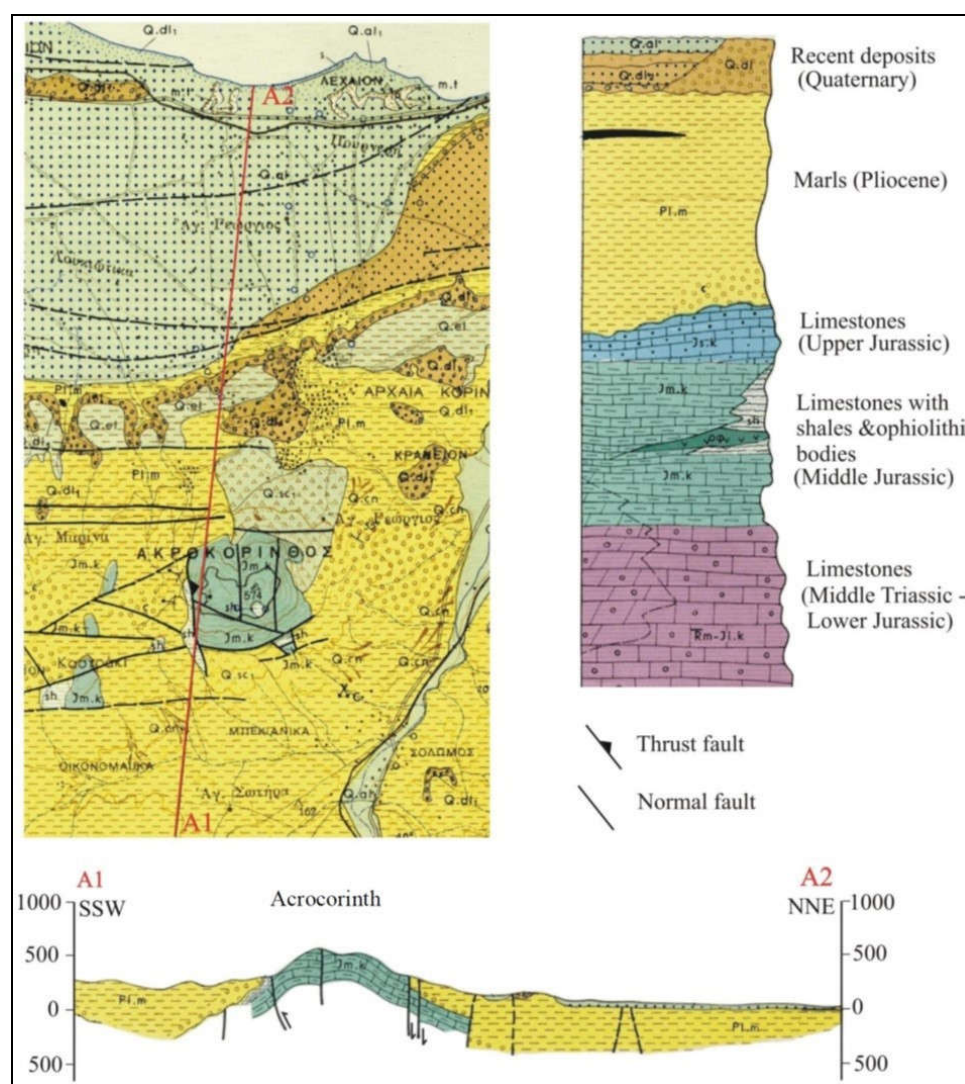
Figure 2. Geological setting of the Acrocorinth horst accompanied with a cross-section based on the Korinthos geological sheet (I.G.M.E, 1971)

2.3   Drone setting and flight planning

In order to achieve a correct and accurate 3D terrain model, some preparation is required in the field. Especially in this case, where through the terrain model conclusions and evidence about the discontinuities of the rock mass are exploited, it is very important to create a high-resolution terrain model with aerial photographs. With the rtk module that exists in the drone and the use of the UgCS program the flight is planned with the correct paths to ensure the necessary overlap between the photos, constant distance between drone and slope, accuracy in shooting position, and constant shooting angle.

All the above parameters contribute to the small value of the GSD index, which concerns the sharpness of the photos. It is worth noting that DJI provides a program for horizontal flight planning, but in this case, due to the existing steep slopes, a vertical flight was performed. Overall, through programming with the UgSC software the flight time was minimized and the minimum possible value of GSD for the accuracy of the 3d terrain model was achieved. Figure 3 shows the planned flight with the calculated data, flight time, number of photos, GSD, and area covered.

Figure 3. Scheduled flight with calculated data, flight time, number of photos, GSD, and area covered

2.4   3D terrain model

Agisoft Metashape and cloud compare programs are used in many corresponding tasks for similar works. However, in this research ESRI's drone2map software was used for two main reasons. Initially, it is a similar program to Agisoft Metashape but it communicates directly with Arcgis Pro where an advanced analysis can be carried out using directly additional data from other sources, such as cartographic, geological, climatic data, etc. Also, the type of file that is generated can be directly imported into other software programs related to discontinuity analysis like the DSE and Rocfall3, that are used for further stability and rockfall analysis.

After completing the flight all the aerial photos and flight data are imported into the drone2map software and the 3d terrain model is created having a high resolution and clarity for further extraction of the discontinuity characteristics of the examined rock mass. Because of the original flight design, there is no need for a higher resolution or sharpness than the existing, so that time and computing power is saved. Figure 4 shows the generated 3d terrain model of Acrocorinth, the drone's flight path and shooting locations and Table 1 presents the types of files created by the drone2map software.
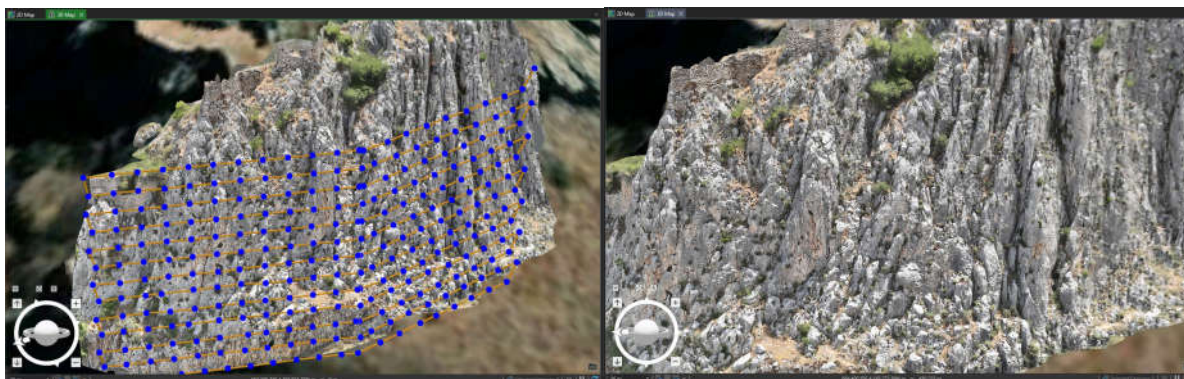
Figure 4. 3D terrain model of Acrocorinth with the drone's flight path and shooting locations

Table 2. Types of files created by the drone2map software

3D Products of Drone2Map		
Create point clouds	**Create DSM Texture Meshes**	**Create 3D Texture Meshes**
SLPK	SLPK	SLPK
LAS	DAE	DAE
Merge LAS Tiles	OBJ	OBJ
	OSGB	OSGB
	3D Tiles	3D Tiles

3   Results

3.1   Discontinuity analysis from field data

As mentioned before field measurements were took place in the research area of Acrocorinth with a detailed recording of 65 discontinuity planes along with their features (orientation in dip/dip direction, aperture, spacing, continuity, etc). All the recorded data were imported into the Rocscience Dips program (version 8.027) for further analysis. From the analysis perfromed the resulting stereodiagram was produced in which it is obvious that one major (1m: 79/189) and two minor discontinuity set planes (2m: 75/28 and 3m: 86/216) seem to prevail in the entire area (Fig 5).
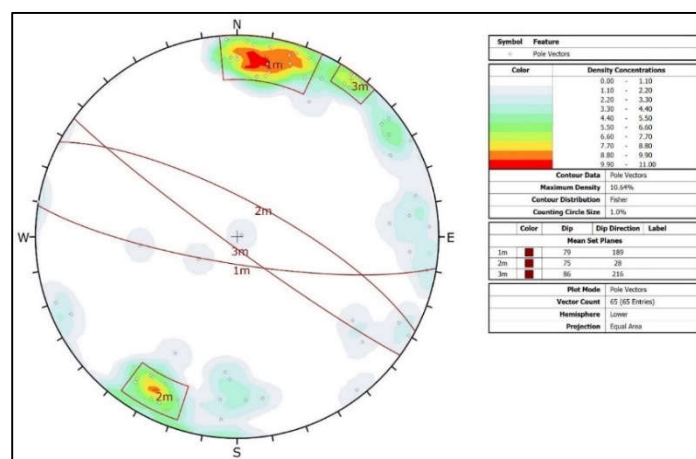
Figure 5. Stereodiagram of the discontinuity pole vectors (1m, 2m, 3m) and the major planes in the study area

3.2   Discontinuity analysis from digital data

As mentioned before the 3d terrain model created with ESRI's ArcGIS-Drone2Map software was imported into the DSE software (Riquelme et al, 2015) to extract the slope inclination and the dip/dip direction of discontinuities. The density and the percentage of the principal poles extraction from DSE are presented in Table 2. By comparing the field (Fig.5) and digital data (Table 2) it seems that there is a coincidence among the discontinuities 1m and J1, 2m and J6, 3m and J2. However, the major plane from both sets (1m and J1) gives a significant difference in the dip direction of 57[0], so that a further analysis of the digital data set is necessary to understand the reason of this difference.

Table 3. Density and principal poles extraction fron DSE

No	Dip⁰	Dip Dir⁰	Density	%
J1	76	246	2.09	48
J2	82	224	1.23	12
J3	56	318	0.55	14
J4	59	102	0.21	1
J5	89	339	0.20	3
J6	88	31	0.12	10
J7	89	92	0.11	10

3.3 Rock fall simulation

In the Acrocorinth cliff the three systems of discontinuities, as examined before, are the main factor in potential failures, with overturns and falls of rectangular pieces of small-medium size that can reach a size of 1-1.3 m^3. For this reason, the 3d terrain model that was created was particularly useful to simulate rockfalls in the entire research area (Fig 6).

Figure 6. Panoramic view of the Acrocorinth cliff in which the 3d terrain model was created

For this purpose, the Rocscience RocFall3 program (version 1.014) was used with several trajectories simulating the travelling of the detached rock blocks along the steep slopes of the research area. The results of the simulation were converted into raster-geotiff format files and imported into the ArcGIS Pro software for further processing and rendering of the required information (kinetic energies and rock bounce heights) at all points of the research area (Fig 7).
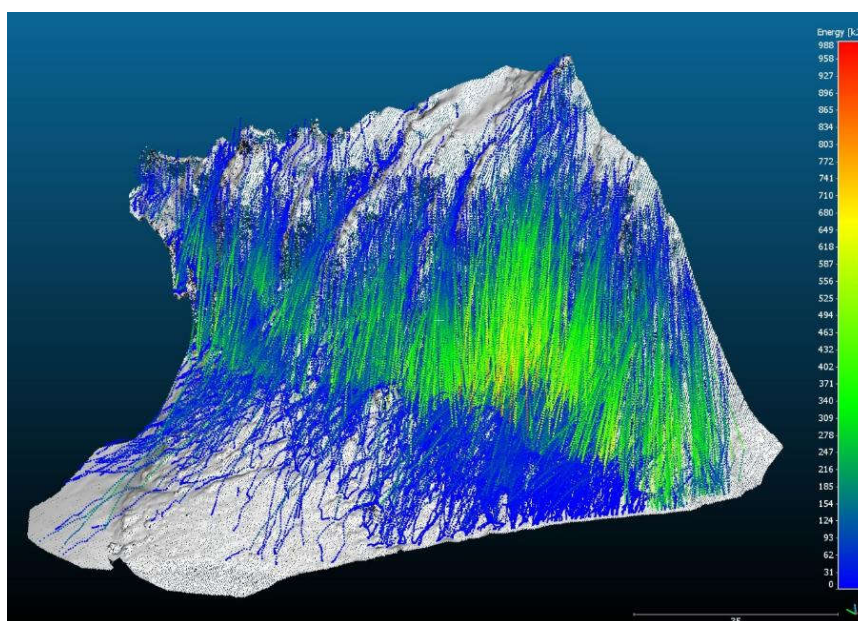
Figure 7. Image fragment (raster) of the distribution of kinetic energy in various trajectories of the rocks because of the simulations

The generated data in asci format can be processed as raster files and used as overlay information in 2D

and 3D models of the topography across the survey area (Fig 8), so that it is possible to determine the kinetic energy and rock bounce height values for the selection of the most appropriate rock fall protective system at the most suitable location.
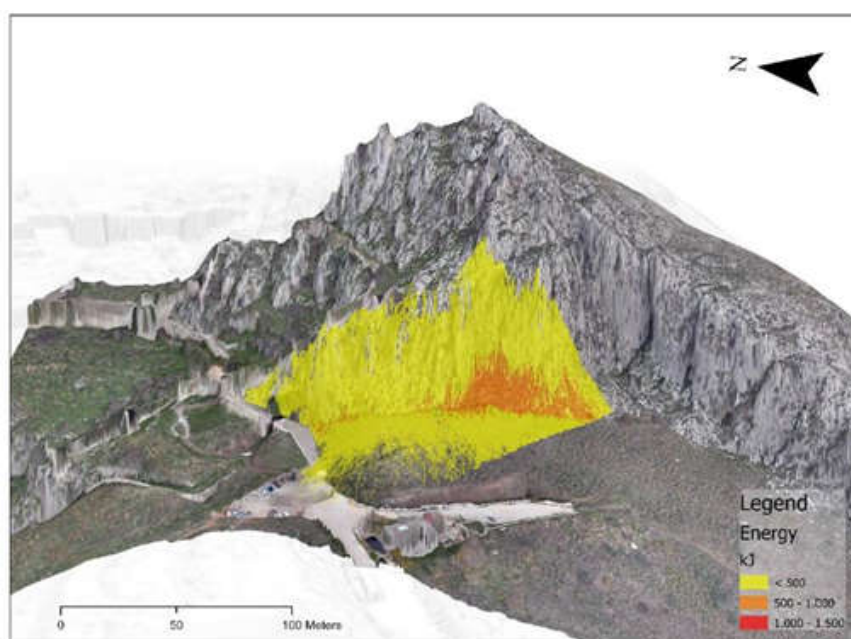
Figure 8. Distribution of the rockfall kinetic energy in the survey area with three zones of kinetic energy

The simulation discussed can be extended to the entire area of Acrocorinth, so that it is possible to identify hazard and risk zones and decide on the most appropriate protection measures in each zone, saving valuable time and money.

4 Conclusion

The classic process of discontinuity measurements through the geological compass is particularly time-consuming and requires direct access to the slope, which in many cases is not possible. Through the process of drone flight and the extraction of the characteristics of rock mass discontinuities, work time is significantly reduced, and data are obtained from hard-to-reach areas. In this procedure flight preparation and planning plays an important role, because it gives high-precision data that is useful in the later digital processing. Moreover, not many programs are used, so there is no need for many file conversions and the resulting data is considered highly reliable and useful for many purposes. The methodology presented in this paper was applied to the Acrocorinth cliff in Greece, an area of particular archaeological interest and the data collected in the field provided important information regarding the discontinuity features that control the kinetics of the cliff.

With reference to the discussed methodology, a 3D terrain model of high definition and precision was created with the correct use of photogrammetry methods, equipment and programs, to obtain reliable data for the discontinuities of the rock mass in question. The orientations (dip/dip direction) of three discontinuity planes extracted by the DSE software program through the specific high-resolution 3D terrain model were like those derived by the geological compass, but with a significant difference in the value of the dip direction in on one of the three discontinuity planes. It is a fact that the discontinuity data extracted from the proposed procedure need further investigation to minimize any errors, as well as the fact that the proposed procedure is promising and will solve many problems of rockmass kinetic analysis in areas where access is not feasible.

This method has all the necessary properties to be applied to various rocky slopes and infrastructure projects and to create hazard zones, as Depountis et al (2019) did on a major road in western Greece. This can be achieved by delineating different hazard zones in the 3D model created with the rockfall

simulations performed in the entire study area, which distinguish the distribution of rock kinematics across the surface of the relief in different categories.

References

Athanasoulis, D. The castle of Acrocorinth and its enhancement project (2006-2009), Greece. *Hellenic Ministry of Culture and Tourism/ 25th Ephorate of Byzantine Antiquities*, 2014, 9-16.

Bieniawski, Z.T. Engineering Rock Mass Classifications: A Complete Manual for Engineers and Geologists in Mining, Civil, and Petroleum Engineering. *JohnWiley & Sons: Hoboken, NJ, USA*, 1989.

Collier, R.; Dart, C. Neogene to Quaternary rifting, sedimentation and uplift in the Corinth Basin, Greece. *Journal of the Geological Society of London*, 1991, 148, 1049-1065.

Depountis, N.; Nikolakopoulos, K.; Kavoura, K.; Sabatakakis, N. Description of a GIS-based rockfall hazard assessment methodology and its application in mountainous sites. *Bulleting of Engineering Geology and the Environment,* 2020, 79, 645–658

Guzzetti, F.; Crosta, G.; Detti, R.; Agliardi, F. STONE: A computer programm for the three-dimensional simulation of rock-falls. *Computers and Geosciences*, 2002, 28, 1079–1093.

I.G.M.E., Geological map of Korinthos, 1971.

Riquelme, A.J.; Abellán, A.; Tomàs, R. Discontinuity spacing analysis in rock masses using 3D point clouds. *Engineering Geology*, 2015, 195, 185–195.

Rocscience Inc., Toronto, Canada. *Academic Bundle License Software No.:21832-001*, 2024, issued to the Laboratory of Engineering Geology, University of Patras, Greece.

Sarro, R.; Riquelme, A.; García-Davalillo, J.C.; Mateos, R.M.; Tomás, R.; Pastor, J.L.; Cano, M.; Herrera, G. Rockfall simulation based on UAV photogrammetry data obtained during an emergency declaration: Application at a cultural heritage site. *Remote Sensing*, 2018, 10, 1923.

Scavia, C.; Barbero, M.; Castelli, M.; Marchelli, M.; Peila, D.; Torsello, G.; Vallero, G. Evaluating Rockfall Risk: Some Critical Aspects. Geosciences 2020, 10, 98.

Volkwein, A.; Schellenberg, K.; Labiouse, V.; Agliardi, F.; Berger, F.; Bourrier, F.; Dorren, L.K.A.; Gerber, V.; Jaboyedo, M. Rockfall characterisation and structural protection—A review. *Natural Hazards and Earth Systems Sciences, 2011*, 11, 2617–2651.

ROCKFALL RISK ASSESSMENT USING 3D ANALYSES, A CASE STUDY FROM A CULTURAL HERITAGE SITE IN GREECE

CHARALAMPOS SAROGLOU [1,2], VASILEIOS KALLIMOGIANNIS [1]

[1]*School of Civil Engineering, NTUA, Greece, e-mail:* vkallim@central.ntua.gr

[1]*School of Civil Engineering, NTUA, Greece, e-mail:* saroglou@central.ntua.gr

[2]*School of Earth Science & Environment, University of Leeds, UK*

Abstract
Rockfalls pose a significant risk to human activities and infrastructure. The assessment of rockfall risk is critical in delineating zones of higher risk and mitigating the potential impact from such events in inhabited areas. This paper presents an example of how 3D rockfall modelling has been utilised to assess the risk from rockfalls at a cultural heritage site in Central Greece. The site is characterised by an Acropolis situated at the crest of a promontory, which is formed by steep limestone slopes. Following detailed UAV surveying, engineering geological mapping of rockfall prone areas, discontinuity mapping using different techniques and field measurements to identify the prevailing conditions on the slope, the analyses were performed using two dimensional and three-dimensional methods to calculate the rockfall trajectories under different scenarios. The 3D analyses results were compared to 2D rockfall analyses, to evaluate the accuracy of the two approaches. It was concluded that the 2D analysis predicted well the rockfall trajectories, in relation to the 3D analyses, but the zoning of high-risk zones was only possible when the 3D analyses where utilised. Different scenarios (i.e., earthquake, allocation of source areas) were assessed to determine the appropriate mitigation measures and zone areas where no further development should take place.

Key words
Risk, Rockfall, Rock, Slope, Cultural Heritage

1 Introduction

Rockfalls are types of ground failures that involve the detachment of rock blocks from rocky slopes followed by a rapid downhill movement. This movement is characterized as rolling, bouncing, sliding or free-falling (Varnes, 1978) and the trajectories of the rock blocks travel variable distances. Even through their economic impact is lower compared to large-scale landslides, rockfalls result in similar fatalities (same order of magnitude) as all other landslide types due to their sudden trigger mechanism coupled with the high velocities that the rock blocks travel (Hoek, 2000). During the last 2 decades, an increase in the number of rockfalls was noticed in Greece, due to intense rainfall events and earthquakes. A significant number of sites prone to rockfalls near inhabited areas and archaeological sites have been identified in Greece but rockfall protection measures have been applied in relatively few cases (Saroglou, 2013).

Risk assessment relies heavily on predicting accurately the trajectories of falling rocks, considering various factors such as the rock slope characteristics, the properties of the falling rocks, the triggering mechanism and others. Risk assessment is currently performed more frequently using three dimensional rockfall analysis allowing for a more robust assessment. The case study is located in Voiotia prefecture, central Greece and is characterised by an Acropolis (built around 4th century BC) situated at the crest of a limestone promontory. The Acropolis still preserves a 400-meter-long fortification that surrounds the

north and east side of the promontory and persists into the sea. The slopes on which the Acropolis is founded are generally high and steep. The area is characterized as high risk regarding rockfall vulnerability due to the fragmentation of the limestone rock mass and the presence of overhanging rock blocks. In addition, a settlement is located around the perimeter of the hill at the base of the steep slopes, hence, the risk of rockfalls to human activity is very high.

In 2019, a rockfall event occurred after heavy rainfall and affected a house located at the base of the slope putting also into risk the integrity of the archaeological site. Site investigation proved that there have been more rockfall incidents formerly. Therefore, it is estimated that if stabilization measures are not applied, it is very likely that a potential rockfall may impact the area down slope, especially in the event of a heavy rainfall or an earthquake.

Figure 1. Left: An aerial photograph showing the location of the 2019 rockfall detachment (marked in red color) and the area of rock blocks deposition (marked in blue color); Right: A photograph of the rockfall event retrieved from the crest of the slope.

The paper assesses the risk from rockfalls by determining the trajectories and impact energy on the surrounding area of the promontory. Detailed UAV surveying of the study area, engineering geological mapping of rockfall prone areas, discontinuity mapping and field measurements have been undertaken as presented in Saroglou et al (2021).

2   Geology of the studied area

The area of interest comprises the following geological formations: The hill on which the Acropolis is located, consists of thick limestones and dolomites (T-Jik,d) which are underlain by a schist-chert formation (Jm-s.sh) at the base of the slope. This formation spreads to the north, northeast and the south (Figure 2). The western region in the area of interest consists of alluvial deposits.

Limestones and dolomites (T-Jik, d): The limestones and dolomites in the area are thick to massive with dip angle of bedding of 60^0 towards the northern slope of the promontory. The formation is intersected by three to four discontinuity sets resulting in a blocky-very blocky rockmass (GSI between 55 and 65). The discontinuities are moderately weathered, open to very open and partially filled with clay.

Schists and cherts (Jm-s.sh): This formation consists of shales alternating with radiolarites. They are interspersed with or impend (tectonically) ultramafic rocks, and they are locally strongly serpentinized. Inclusions of limestone blocks are often observed, and their thickness is between 50 and 80 m.
A geological map of the region is provided in Figure 2.
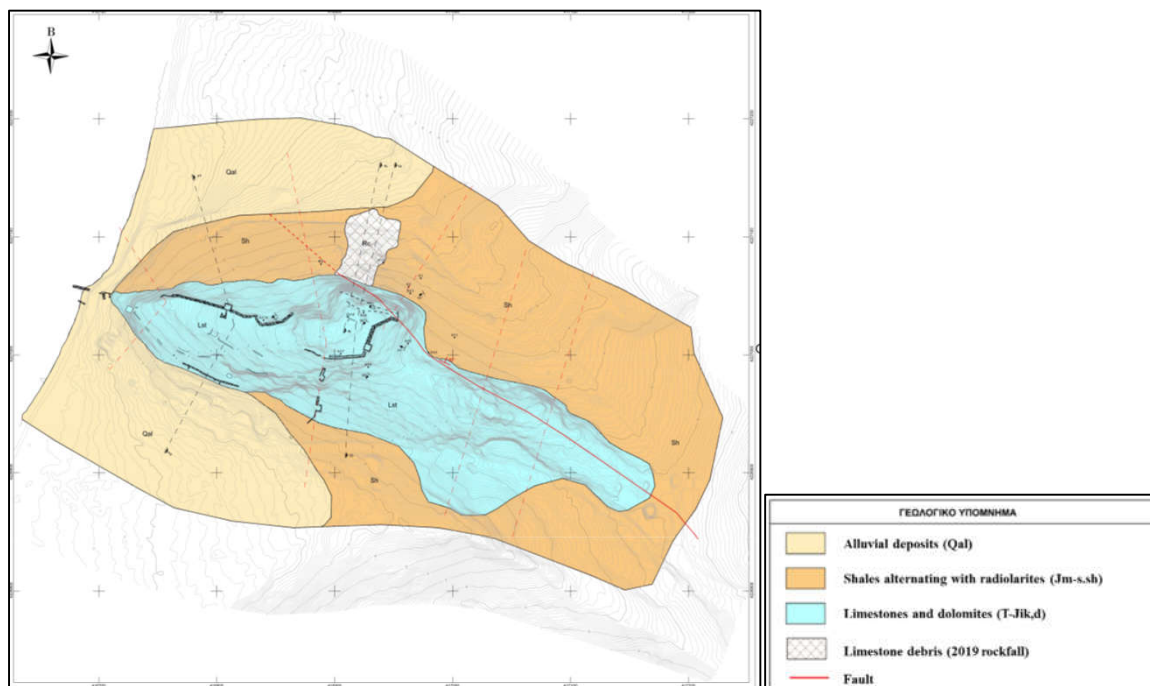
Figure 2 Geological map of the studied area (1:1000).

3   2D rockfall analyses

3.1 Methodology

The rockfall analyses (Rocfall2, Rocscience) determine the trajectory of the rock blocks, as well as the resulting total kinetic energy and the bouncing height. At a later stage of the analysis, the position of the rockfall barrier, which has a specific energy absorption capacity and a specific height, is selected.
After selecting the position and characteristics of the barrier, an additional analysis is carried out in which the effectiveness of the proposed barrier is confirmed. The analyses were performed in eight (8) characteristic cross-sections (Figure 3).
The following parameters are required to accurately calculate the trajectories of the falling rock blocks:
1. Starting position
2. Initial velocity (transport and angular)
3. Falling mass
4. Geotechnical parameters of geological materials along the slope.

The starting position of the rock blocks is generally considered by the highest point of the slope, close to its crest. In places where the relief of the slope has site specific characteristics (e.g. a terrace or a change in inclination) that may significantly affect the trajectory of the blocks, a second starting position at lower elevation of the slope was selected.

To take into account the seismic shaking impact on the initial velocity of the rock blocks, an initial horizontal velocity is assumed:

$$m \times \gamma \times s = \frac{1}{2} m \times \upsilon^2 \Rightarrow \upsilon = \sqrt{2 \times \gamma \times s} \qquad (1)$$

where m (kg) is the mass of the rock block, s (m) is the block's displacement to trigger the fall, u is the initial velocity (m/s) and γ is the pseudostatic acceleration acting on the block. According to the Seismic Hazard map of Greece (OASP, 2003) the research area belongs to seismic zone 2 (out of 3). The seismic acceleration factor for zone 2 is γ=0.24 g. However, due to the proximity of the area to active faults of the Corinthian Gulf a 50% increase is introduced and the design coefficient γ is 0.36g. Therefore, according to Eq. (1), an initial velocity of 0.2m/s is used for all the rockfall cases.

3.2 Geotechnical parameters for rockfall analysis

The friction angle and the normal and tangential restitution coefficients for the geomaterials along the slope are selected based on literature results on similar formations (Robotham et al., 1995 και Saroglou et al, 2012, Saroglou et al., 2018). These are summarised in Table 1.

Table 1. Geotechnical parameters for rockfall analysis.

Formation	Friction angle φ / standard deviation (^{0})	Normal restitution coefficient R_n / standard deviation	Tangential restitution coefficient R_t / standard deviation
Limestone	32/2	0.45/0.04	0.85/0.04
Schist	30/2	0.35/0.04	0.80/0.04
Limestone debris (2019 rockfall)	34/2	0.45/0.04	0.80/0.04
Talus with vegetation	30/2	0.32/0.04	0.80/0.04
Talus cover	30/2	0.32/0.04	0.82/0.04

In addition, based on the photogrammetric documentation of the slope as well as the recordings of fallen rock blocks in situ, the predominant volume of overhanging blocks was between 2 and 6 m^3. Based on this evidence the volume of a single block was assumed equal to 4 m^3 in the analyses.

3.3 Results

The results of the 2D rockfall analyses prove that the region in the vicinity of the promontory is characterized as high risk with regard to rockfall impact. In most cases, the rockfall trajectories reach the houses situated at the toe of the slope. In Figure 3, the orange circles mark the initial position of the rock blocks and the green ones their final position along each cross-section. The north-eastern part (cross-sections 7 and 8) is less affected since the width of the promontory is reduced and the length between the settlement and the promontory is high enough for the rock blocks to stop. Figure 4 illustrates two characteristic examples of rock fall trajectories along cross-sections 1-1 and 6-6.

Figure 4 Trajectories (initial and final positions) of the rock blocks simulated in the 2D analyses.
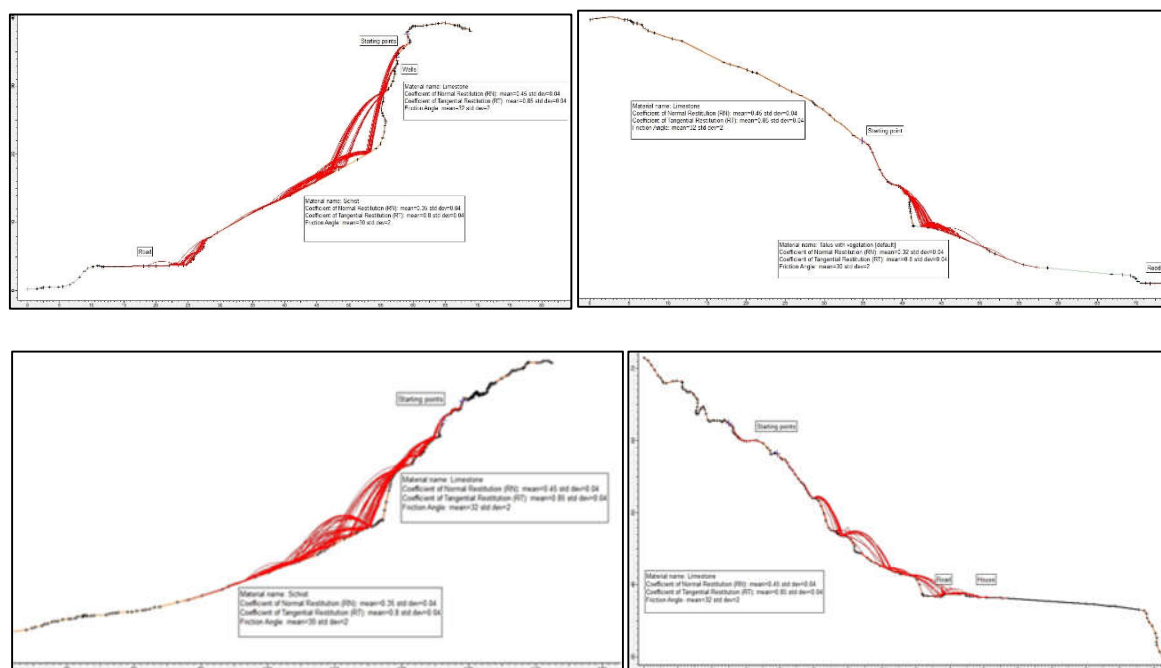
Figure 11 Typical trajectories of rock blocks along cross-section 1-1' (top) and 7-7' (bottom). Left: Northern slopes, Right: Southern slopes.

4   3D rockfall analyses

4.1 Methodology

To investigate thoroughly the risk of rockfall in the area, three-dimensional analyses were performed using Rockyfor3D (Dorren, 2016). Rockyfor3D simulates trajectories of individual rock blocks using deterministic models. The trajectories are simulated using vectors in three dimensions, and two equations of motion are applied, free fall and rolling. The input geotechnical parameters in Rockyfor3D include the geometry of the falling rocks blocks and the characteristics of the geological formations. Those are described below:

Soiltype: The soiltype is directly linked to the normal coefficient of restitution (R_n). Eight soiltypes are introduced: 1. Fine soil material >1.00m; 2. Fine soil material <1.00m; 3. Scree ($\emptyset < \sim10$ cm), or medium compact soil with small rock fragments, or forest road; 4. Talus slope ($\emptyset > \sim10$ cm), or compact soil with large rock fragments, 5. Bedrock with thin weathered material or soil cover; 6. Bedrock, 7. Asphalt road and 8. River, or swamp, or material in which a rock could penetrate completely.

Roughness (rg10,20,70): Each of these classes corresponds to the height of a representative obstacle that a falling block encounters 70%, 20%, and 10% of the cases during a rebound, respectively. The surface roughness is used to calculate the tangential coefficient of restitution (R_t). The roughness should be determined in the field by identifying homogenous zones in the study area or obtain data from similar formations.

Dimensions, shape and density of falling rock blocks: The height, width, length and shape are defined. As in the case of 2D analyses, the volume of a single block was assumed equal to 4 m³. Based on the in-situ investigation, a rectangular shape (2m x 2 m x 1m) was selected. The density of the limestone rock blocks was estimated at 2500kg/m³, meaning that the weight of a single block is 10 tons. The initial velocity of the rock blocks was set equal to 0.20m/s (as in the case of the 2D analyses).

4.2 Geotechnical parameters of the terrain

The geotechnical input parameters of the studied area are given in Table 2.

Table 2. Geotechnical input parameters for 3D rockfall analysis

Input parameters	Limestone	Schist	Alluvial deposits	Limestone debris (2019 rockfall)
Density (kg/m^3)	2500	-*	-	-
Shape of falling blocks	Rectangular	-	-	-
D_1 (m)	2	-	-	-
D_2 (m)	2	-	-	-
D_3 (m)	1	-	-	-
RG_{70} (m)	0	0.03	0	0.50
RG_{20} (m)	0.05	0.03	0	0.75
RG_{10} (m)	0.10	0.03	0.05	1.50
Soiltype (See Section 4.1)	6	3	2	6
*No source areas exist in these formations hence the corresponding input parameters do not need to be defined				

4.3 Results

The main parameters assessed to evaluate the 3D analyses results are:

-The trajectories of the simulated rock blocks: These determine whether the rock blocks reach or not a location in the area of interest.

-The Reach Probability (RP): The probability of a rock block to reach the location of interest.

-The Kinetic Energy (E$_{95CI}$): The mean kinetic energy (kJ) of the falling rock blocks in a specific location increased by 2 standard deviations (95% confidence interval assuming a normal distribution of energies).

-The Passing height (Ph$_{95CI}$): To mean height (m) of the falling rock blocks in a specific location increased by 2 standard deviations (95% confidence interval assuming a normal distribution of passing heights)

The results of these four (4) metrics are plotted on the map of the studied area as illustrated in Figure 5 and Figure 6. The probability of the rock blocks approaching a location close to the source areas is high and decreases downstream as the blocks are scattered or the trajectories stop. The kinetic energies of the rock blocks range between 200-1600 kJ in most parts of the map, but in some places (especially in the central, southern part) exceed 1600 kJ and in very few cases 3200 kJ. Finally, the passing heights Ph95CI rarely exceed 4 to 6 m.
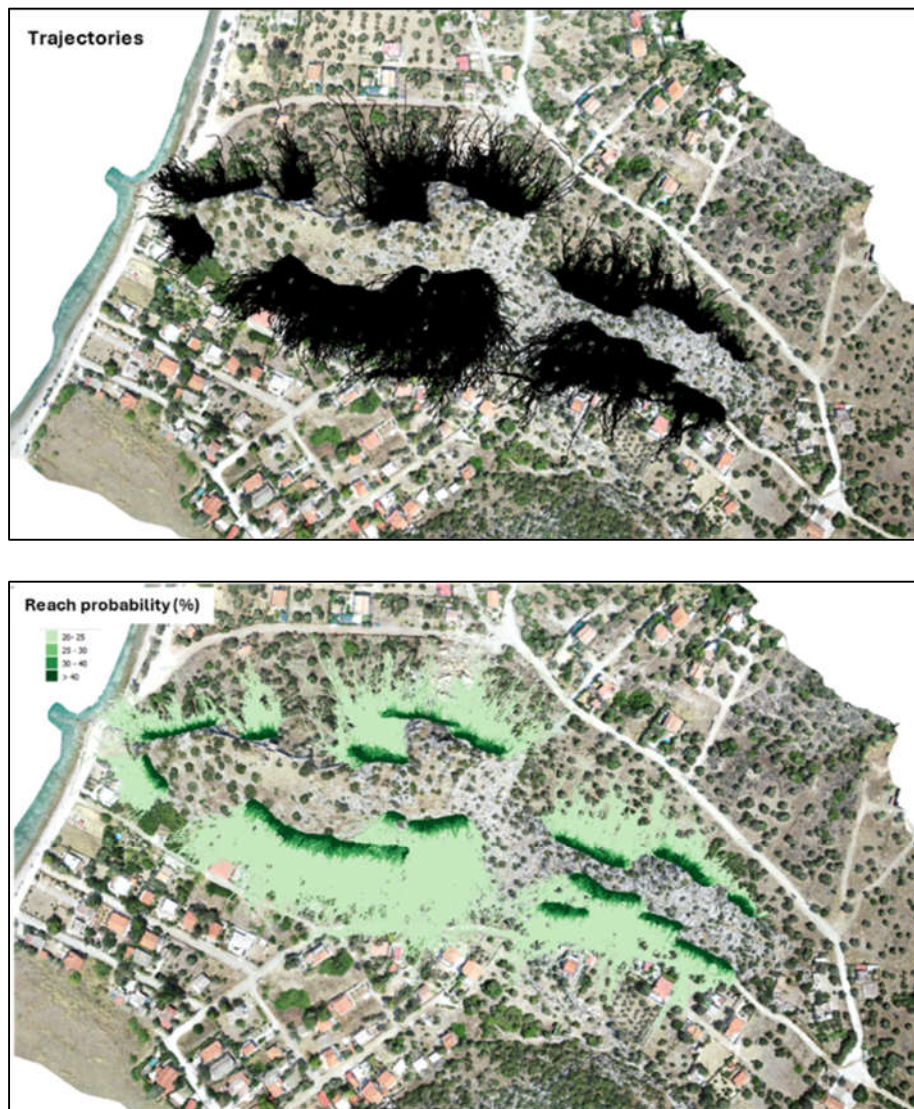
Figure 6 3D rockfall analyses results; Top:Trajectories of the simulated rock blocks, Bottom: Distribution of Reach probability (RP) of rock blocks/ on the area of interest.
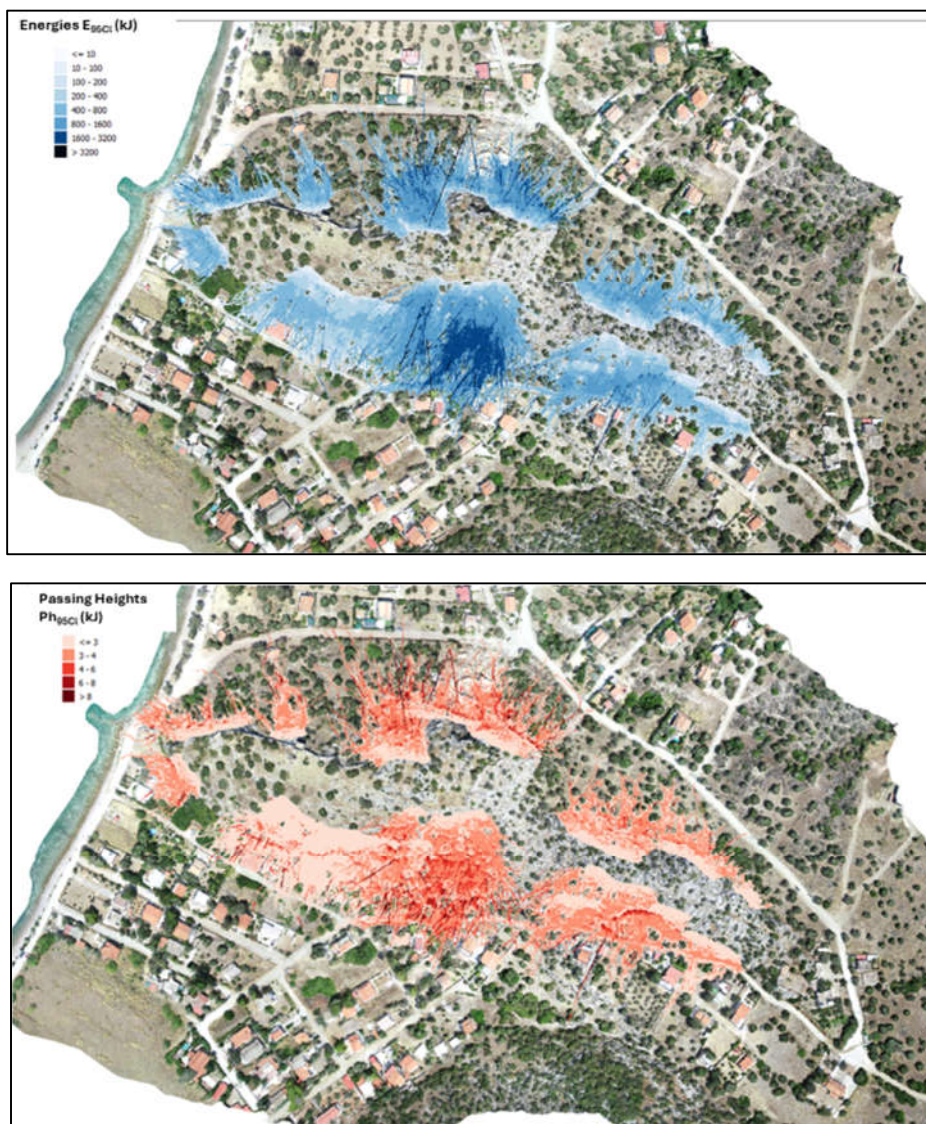
Figure 7 Top: Distribution of kinetic Energies E_{95CI} on the area of interest, Bottom: distribution of Passing heights Ph_{95CI} on the area of interest.

The data interpretation in the Figures above prove that rockfalls pose a significant risk to the houses as a significant number of rock blocks reach the residential area and thus, protection measures are necessary. The 3D and 2D analyses results match well and furthermore they allow the evaluation of the rock blocks' lateral deviation which facilitates the optimum dimensioning of protective barriers.

5 3D analyses with protective measures

To address the potential risk of rockfalls impacting the houses, it was proposed that rockfall barriers are installed at specific locations to stop the trajectories. The barrier design kinetic energy ranges between 500 kJ and 2000 kJ at maximum, dimensioned at the 95% percentile of kinetic energy distribution while their height is equal to 5 m. The optimum location and length are determined based on the 3D analyses as shown in Figure 8a. Figures 8b-d illustrate the distribution of the Reach Probabilities (RPs), kinetic Energies (E_{95CI}) and Passing Heights (Ph_{95CI}) for the analyses considering the mitigation with rockfall barriers.
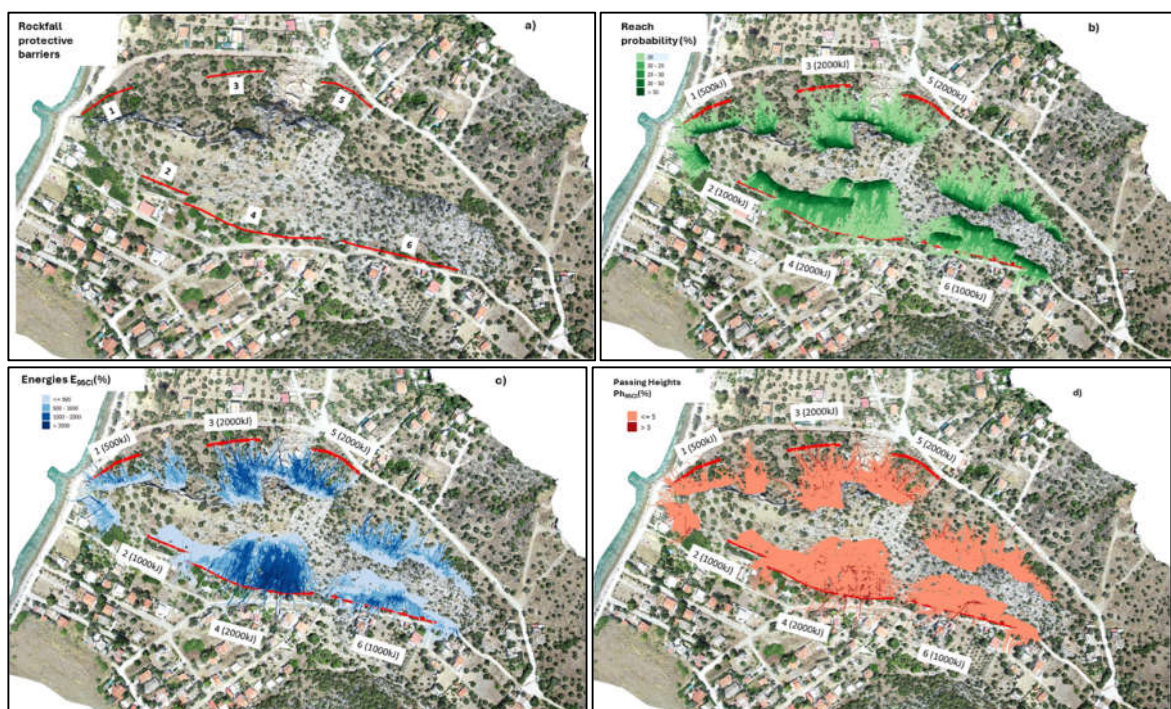
Figure 8 3D rockfall analyses results with protective barriers: a) Location of the rockfall protective barriers, b) Distribution of Reach probability (RP) of rock blocks, c) Distribution of kinetic Energies E_{95Cl}, d) Distribution of Passing heights Ph_{95Cl}.

The protective rockfall barriers stop the trajectories of the falling rock blocks and protect the residential area at the base of the limestone promontory. Some outliers exist (i.e., rock blocks that surpass the protective barriers), but their impact with the barriers decreases their kinetic energy hence their trajectories do not reach the houses.

6   Conclusions

The present study evaluates the rockfall risk of a cultural heritage site in Central Greece using both 2D and 3D rockfall analyses. It is concluded that the 2D analysis predicted well the rockfall trajectories, in relation to the 3D analyses, but the identification of high-risk zones was feasible only through more robust 3D analyses. 2D rockfall analyses neglects the effect of the topography whilst 3D analyses account for the lateral dispersion of rockfall trajectories (Crosta and Agliardi, 2004), i.e., the ratio of the lateral distance separating the trajectories to the slope length.

The studied area is vulnerable to rockfalls, a fact that was confirmed recently (2019) as a rockfall event impacted a house located at the base of the promontory. Based on the results from 3D rockfall modelling, protective measures consisting from rockfall barriers were proposed, and further analyses were carried out to assess their performance which was found to be sufficient to protect the residential area and the cultural heritage site.

References

Crosta, G.B., Agliardi, F. Parametric evaluation of 3D dispersion of rockfall trajectories, Natural Hazards Earth System Sciences, v.4(4), pp.583-598. 2004.

Dorren, L.K.A. Rockyfor3D (v5.2) revealed – Transparent description of the complete 3D rockfall model. 2016.

Hoek, E. Analysis of rockfall hazards. In: Hoek E (ed) Practical rock engineering, pp 117–136. 2000.

Ministry of Environment Planning and Public Works. "Greek Earthquake Resistant Design Code," Athens, Greece (In Greek). 2003.

Robotham, M. E., Wang, H., and Walton, G. Assessment of risk from rockfall from active and abandoned quarry slopes, I.M.M., Section A., 104, 25–33, 1995.

Saroglou, H., Marinos, V., Marinos, P., and Tsiambaos, G. Rockfall hazard and risk assessment: an example from a high promontory at the historical site of Monemvasia, Greece, Nat. Hazards Earth Syst. Sci., 12, 1823–1836, https://doi.org/10.5194/nhess-12-1823-2012, 2012.

Saroglou, H. Rockfall Hazard in Greece. Bulletin of the Geological Society of Greece, vol. XLVII 2013. Proceedings of the 13th International Congress, Chania, 2013.

Saroglou, C., Asteriou, P., Zekkos, D., Tsiambaos, G., Clark, M., and Manousakis, J.: UAV-based mapping, back analysis and trajectory modeling of a coseismic rockfall in Lefkada island, Greece, Nat. Hazards Earth Syst. Sci., 18, 321–333, https://doi.org/10.5194/nhess-18-321-2018 , 2018.

Saroglou C., Kong D., Wu F., Kallimogiannis V., Tsirogianni A., Bar N.: Rock mass characterisation for rock slope instabilities using aerial photogrammetry and 3D Point Cloud Model interpretation. Proc. of 3rd European Regional Conference of IAEG, Athens, 2021.

Varnes, D.J. Slope movement types and processes. In: Schuster RL, Krizek RJ (eds) Landslide analysis and control. Transportation Research Board, Special report 176. National Academy Sciences, Washington, DC, pp 11–33. 1978.

Topic 3

Emerging Technologies and Applications in Engineering Geology and Geotechnics

A MECHANICALLY STABILIZED EARTH WALL DESIGN IN A HIGH SEISMIC REGION (TURKIYE)

CEREN DEMIREL DELIKTAS [1], ABDULLAH ONUR USTAOGLU [2], CANDAN GOKCEOGLU [3]

[1] *Su-Yapı Engineering and Consultancy Inc., Türkiye, ceren.demirel@suyapi.com.tr*

[2] *Progeo Project Engineering Consultancy Limited Company, Türkiye, o.ustaoglu@progeo.com.tr*

[3] *Hacettepe University, Türkiye, cgokce@hacettepe.edu.tr*

Abstract

This paper presents the performance assessment of a mechanically stabilized earth (MSE) wall in highly seismic region for the design earthquake with peak ground acceleration value of 0.533g in Türkiye. Wall performance under static and seismic conditions was searched with finite element and limit equilibrium analysis. Performance results of static case were compared with the lateral displacement limitations stipulated by some standards and specifications. On the other hand, lateral movement of wall after extreme seismic event was evaluated depending on post-earthquake investigation and shaking table testing due to the lack of deformation analysis-based regulations. The analysed wall section in 23.95 m height is expected to experience no damage to moderate damage level without collapse with 2.1 cm for static case and 50.9 cm for seismic situation. This case study shows that the performance of high single-tiered MSE walls is satisfactory even under high seismic actions.

Key words
MSE wall, displacement, FEM, LEM, Plaxis, seismic

1   Introduction

Mechanically stabilized earth (MSE) wall is the generic term for the combination of soil mass and reinforcement including steel strips, welded wire meshes, or geotextiles. Although the French architect and engineer Henri Vidal introduced the modern steel strip reinforced wall technology in USA in the early 1960s (Christopher, 2005), the concept of reinforced soil is dated back to the end of the third millennium B.C (en.Wikipedia.org). with the use in the construction of the temple towers in ancient Mesopotamia. In Türkiye, it has been an alternative to conventional reinforced concrete and gravity walls since the 80s owing to the advantages it provides.

The fundamental reasons why mechanically stabilized earth walls are preferred to the conventional type of walls are the ability to tolerate differential settlement under poor foundation conditions and the deformations created by both static and seismic lateral forces such as earthquake and earth pressure. Moreover, it has been possible to reach heights exceeding 30 m with MSE walls (FHWA-NHI-10-024, 2009).

Sandri (1998) performed some observations on eleven reinforced soil structures exceeding 4.6 m to 24.0 m in height shaked by a 6.7 magnitude Northridge earthquake whose horizontal maximum acceleration varying between 0.5g~0.1g and vertical accelerations equal to 1.5 times of horizontal maximum acceleration values. None of the reinforced soil structures shows any signs of movement although significant structural crack formation occurred at cantilever walls.
The seismic performance of the reinforced wall bridge approach in 10 m height along the Trans-

European Motorway was evaluated as satisfactory after the Kocaeli (Izmit) earthquake with a magnitude of 7.4. The bridge decks were collapsed totally while damage to MSE walls was just limited to panel cracks and separation due to liquefaction-induced bearing capacity problems and differential settlement (Pamuk et al., 2004).

Wartman et al. (2006) reported that upper layers of reinforcement, peak ground acceleration more than twice the design value, and perpendicular effects in the ground motion were in charge of the permanent displacement experienced by four MSE wall bridge approaches in 8.2 m maximum height after the 2003 Tecoman, Mexico earthquake.

The tallest four-tiered 45.7 m MSE wall, constructed for the aim of Seattle-Tacoma International Airport expansion was numerically modeled by Lindquist (2008). For the time history finite element analysis made, 0.09 m horizontal displacement and a bi-linear type of shear surface extending reinforced zone were observed, which is evaluated as well performing wall during ground shaking.

Rajoor et al. (2018) studied the deformation and stability behavior of a four-tiered 44 m MSE wall with finite element analysis by using accelerograms of the Van, Turkiye earthquake, the Chile earthquake, and the Northridge earthquake. At the end of the study, it was observed that 3.14 m of maximum total deformation develops and there is direct relationship between magnitude and total displacement whereas the relation between total displacement and epicenter distance is inverse.

As can be seen from the literature review, although analysis and seismic performance of tiered or single-tiered but relatively short MSE walls were investigated in the literature, the performance of high and single-tiered MSE walls in seismically active regions has not been studied. For this reason, this study presents the static and pseudo-static analysis of a single-tiered MSE wall of 23.95 m high in a seismically active region. The aim is to share the satisfactory performance of high, single-tiered MSE wall designed in seismically active region and to show the alternative way for this kind of walls with the literature. Therefore, it can be accepted as an interesting case study for the international geotechnical engineering community.

2   Project Background and MSE Wall Selection Reasons

Sakarya, the province located in the northwest of Türkiye, is a seismically active region, which is the project site on the North Anatolian Fault Zone (NAFZ) (Figure 1). NAFZ is one of the most active seismic regions, and this zone is responsible for many destructive earthquakes in Türkiye. The length of the NAFZ is approximately 1200 km and it forms the plate boundary between Eurasia and Anatolia.
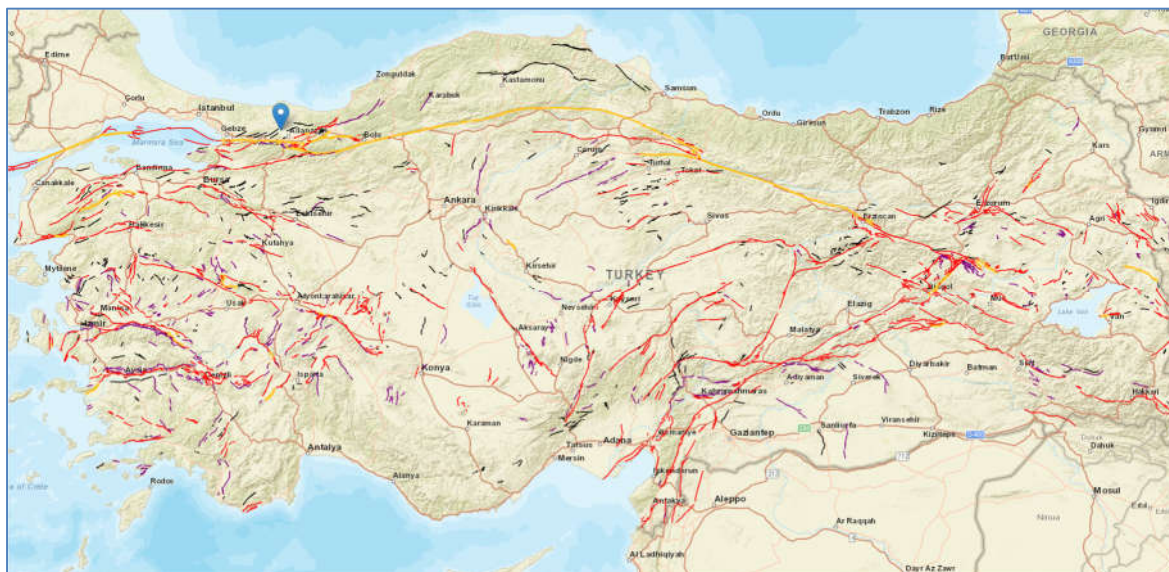
Figure 1. The active faults of Türkiye and the project location (Mineral Research and Exploration General Directorate, 2021)

In the scope of public private partnership projects of Ministry of Health, City Hospital with 1000 Beds in Sakarya was designed with seismic isolation. The placement of seismic isolation at the first basement level of the main hospital building raised a retaining problem changing 6.48~23.95 m in height to create a seismic gap of 1.65 m as stated in Figure 2. This seismic gap needs to be maintained at the ground level due to architectural restrictions and safety issues. Therefore, single-tiered MSE walls were designed for heights taller than 6.0 m to take advantage of flexibility and durability under high seismic loads while reinforced concrete retaining walls were planned to be constructed for smaller heights than 6.0 m. In this study, the analysis procedure and results were given for the most critical section, i.e. for the height of 23.95 m wall.
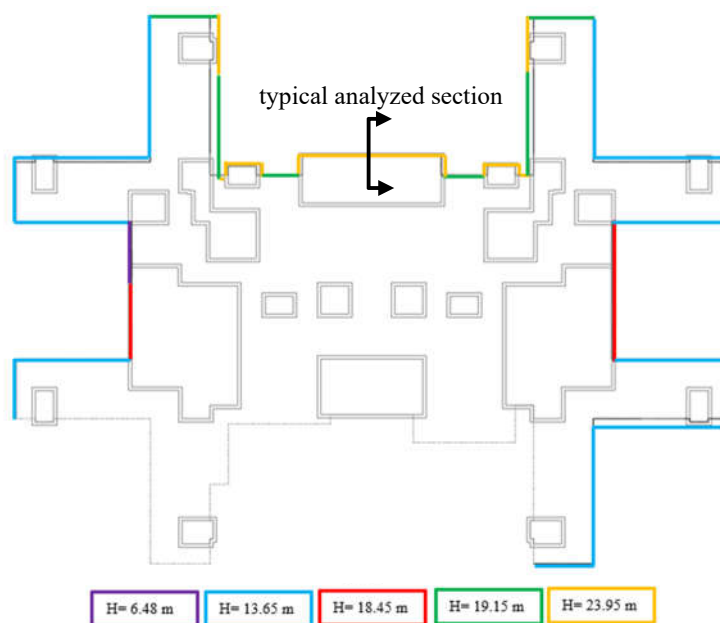
Figure 2. Foundation formwork plan of main hospital and MSE wall layout

3   Geotechnical Conditions of the Project Site

The lithological units in the region, at 40°50'17.53"N and 30°17'16.22"E, are divided into 3 zones from north to south: the Western Pontide Zone, the Armutlu-Almacık Arkotdag Zone, and the Sakarya Zone as given in Figure 3.
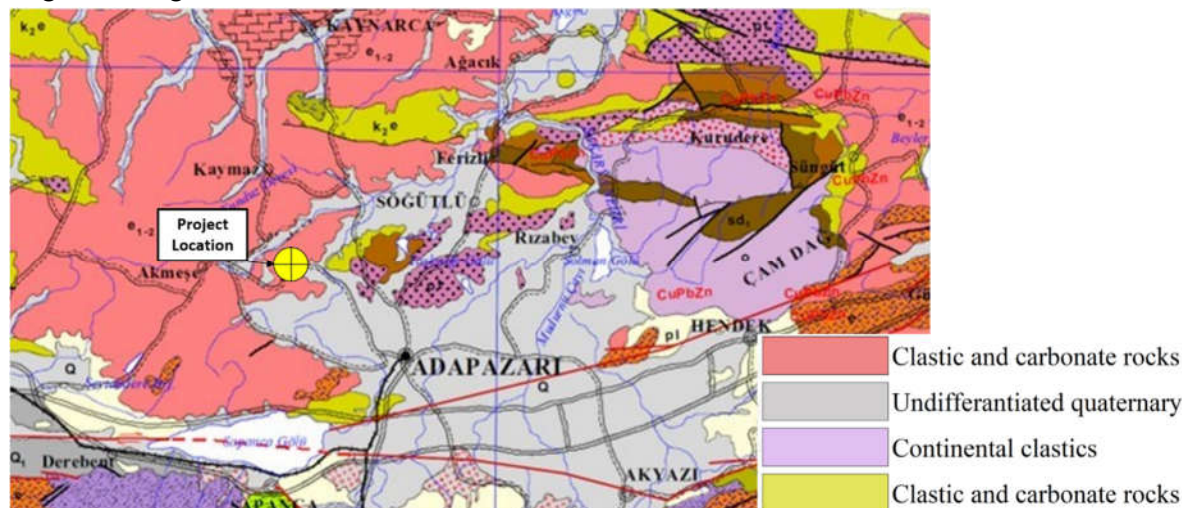
Figure 3. Geological map in 1/25000 scale (General Directorate of Mineral Research and Exploration)

The geology of the project site shows the same engineering geology characteristics throughout the site. It was observed that there is topsoil in 0.5 m thickness from the surface underlain by stiff clay and claystone. The MSE walls are constructed at the same level with the foundation bottom layer of the main hospital building coincides with a claystone layer.

The seismic wall design was performed with the peak ground acceleration value of 0.533g and spectral acceleration coefficient of 1.568 taken from the Turkish Building Earthquake Code (TBDY, 2018) for ZC-type soil conforming to the earthquake with a return period of 475 years.

4   Design Procedure and Analysis

AASHTO LFRD Bridge Design Specifications (AASHTO 2020 and interim updates) was selected as the basis for the design of MSE walls. Overall wall performance objectives and considerations related to displacement of soil reinforcement constituted the challenges in the project. Since the walls are located on the same lithological unit with the foundation bottom level of the main hospital building, which is claystone, no bearing capacity, and settlement problems are expected.

Both reinforced fill and backfill soil shall satisfy the criteria of plasticity index less than 6 and uniformity coefficient higher than 5. Gradation of fill materials shall conform to the condition given in KTŞ (2013), which matches AASHTO A-1 and A-3 class soils.

5 kPa dead load and 15 kPa live load due to carpark were acted on MSE walls in addition the seismic actions. In TBDY (2018), it is stated that the horizontal and vertical static equivalent earthquake coefficients, symbolized with k_h and k_v respectively, for retaining structures, can be calculated from Eq. (1). Here, "r" stands for the coefficient and was taken as 2 conforming to the walls allowed to deform to a maximum $120S_{DS}$ (mm) displacement.

$$k_h = 0.4 * S_{DS} / r \text{ and } k_v = 0.5 * k_h, \text{ (TBDY, 2018)} \tag{1}$$

Internal stability including pull-out and breakage of soil reinforcement as well as external stability with eccentricity, bearing capacity, and sliding were checked following the load and resistance factors given in AASHTO (2020 and interim updates) for both static and seismic conditions. Geosynthetic strips were used as reinforcement elements with the aim of developing friction and passive resistance between the compacted fill and the strips. In the design of geosynthetic reinforcing strips, reduction factors for damaging effects of placement and compaction of soil, strength loss caused by chemical degradation, and the effect of creep resulting from long-term sustained tensile load throughout 100 years of design life were taken into consideration. Figure 4 shows the configuration of strips in 75 cm vertical spacing, whose length is equal to 70% of the overlying wall height and stretches to 1.1~0.8 times of wall height for the 3 upper layers, due to pull-out considerations.
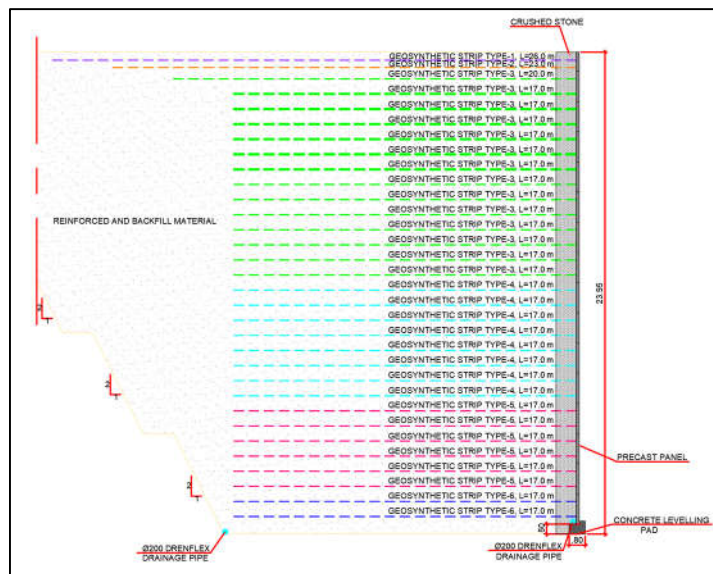
Figure 4. Typical cross section of MSE wall (dimensions are in meters)

4   Results

In order to examine potential failure surfaces passing behind and under the reinforced zone, limit equilibrium static and pseudo-static stability analyses were performed with Slide2 by searching minimum factor of safety of 1.5 under static conditions and 1.1 under seismic conditions (Elias et al., 2001). Geosynthetic strips were modeled as support by defining coverage ratio, long-term design strength, and interface shear strength parameters, which are given in Table 1. Mohr-Columb and Generalized Hoek-Brown material models were utilized for soils and rock mass, respectively, whose geotechnical design parameters are given as Table 2. As the result of the calculation with the Spencer Method (1967), the minimum factor of safety values for global stability were attained as stated in Figure 5.

Table 1. Design parameters of geosynthetic strips

Strip Type No	Coverage Ratio (%)	Long Term Tensile Strength (kN/m)	Adhesion (kPa)	Friction Angle (°)
1	48	139		
2	36	208		
3	24	346	3.5	26
4	24	485		
5	30	485		
6	36	485		

Table 2. Design parameters of soils layers

Soil Type	Cohesion (kPa)	Internal Friction Angle (°)	Unit Weight (kN/m³)	Elasticity Modulus (kPa)
Drained clay	20	29	19	50000
Undrained clay	200	-	20	85000
Reinforced fill	5	36	21	50000
Backfill	5	30	20	50000

Rock Type	UCS (kPa)	GSI	mi	D	Elasticity Modulus (kPa)
Claystone	5000	50	4	0.7	134100
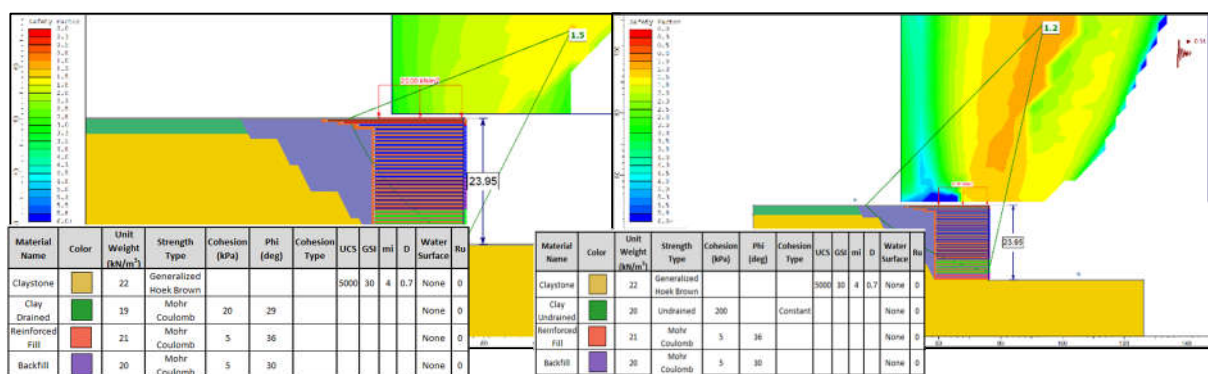
Figure 5. Global stability analysis result for static (on the left-hand side) and seismic (on the right-hand side) case

Deformations were checked with finite element static, and pseudo-static analysis performed in Plaxis-2D by reflecting stage construction phases into the analysis. For the modelling of soils, same material models were accepted with Slide2 analysis while geosynthetic strips were modelled as geogrid elements without any bending and compression capacity with an Elastic-Perfectly Plastic model by defining axial stiffness. Figure 6 and Figure 7 show the expected displacement behaviour as well as minimum and maximum horizontal displacement values for static and seismic conditions, respectively.
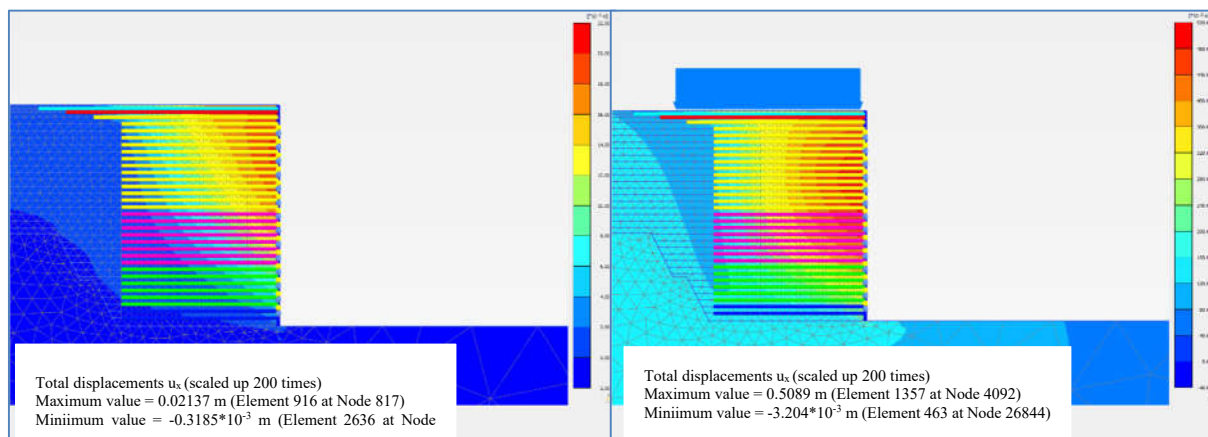
Figure 6. Horizontal deformation behavior of MSE wall under static (on the left hand-side) and seismic (on the right hand-side) conditions
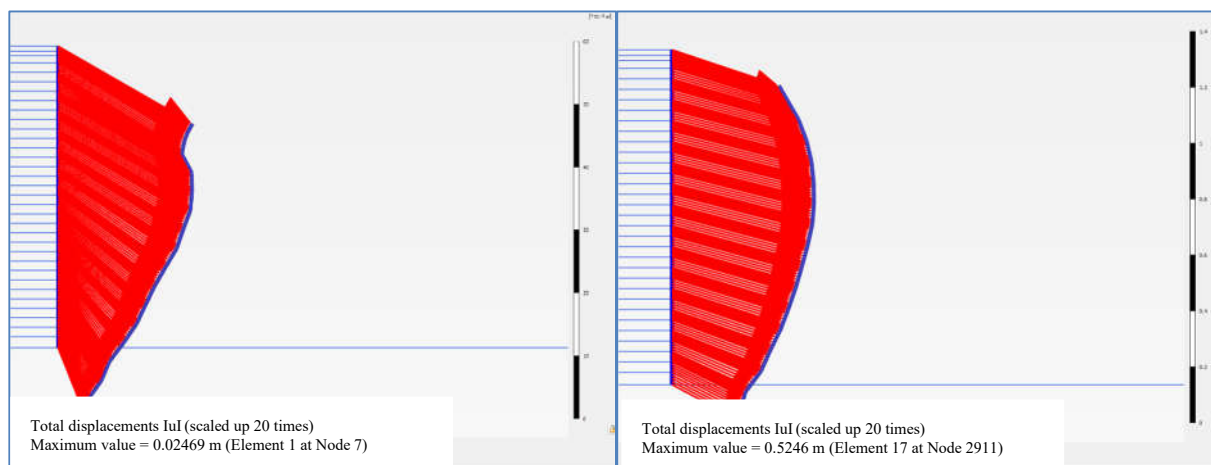
Figure 7. Deformation behavior of MSE wall under static ((on the left hand-side) and seismic (on the right hand-side) conditions

An amount of lateral displacement is required for the composition of friction and passive resistance between geosynthetic strips and compacted fill. However, design of MSE walls must be performed to check excessive deformations causing possible structural damage. Lateral displacement limitations for concrete panel faced reinforced soil walls stipulated by some standards and specifications under static conditions was shown as Table 3.

Table 3. Guidelines on lateral displacement limitations for concrete panel faced reinforced soil walls (Li et al., 2021)

Standards/Specifications	Maximum lateral displacements (m)
WSDOT (2005)	0.012 m for 3 m height
FHWA (2008) and AASHTO 2009)	0.9%-0.4% of wall height
EN 14475 (2006)	0.025
BS8006 (2010)	0.5% of wall height
NGG (2005)	0.1%-0.3% of wall height
New Zealand Bridge Handbook	0.15 for daily traffic>2500
	0.20 for (daily traffic<2500

The relation between obtained horizontal displacement value and the guidelines on it was shown as Figure 8 and Figure 9. Expected horizontal displacement of the analysed wall section was obtained as 21.4 mm as presented in Figure 6 and Figure 7, which is smaller than maximum horizontal displacement boundary as per each standard summarized in Figure 8 and Figure 9. Guidelines given in NGG, EN14475 and WSDOT were evaluated as so close to the ones obtained from the analysis; whereas, New Zealand Bridge Handbook, BS8006 and FHWA allow the wall to move more laterally.
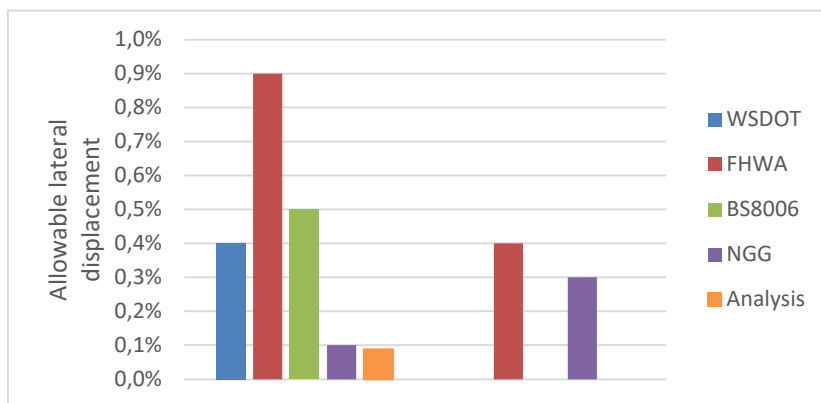
Figure 8. Comparison of horizontal displacement values between guidelines given some standards and obtained with analysis
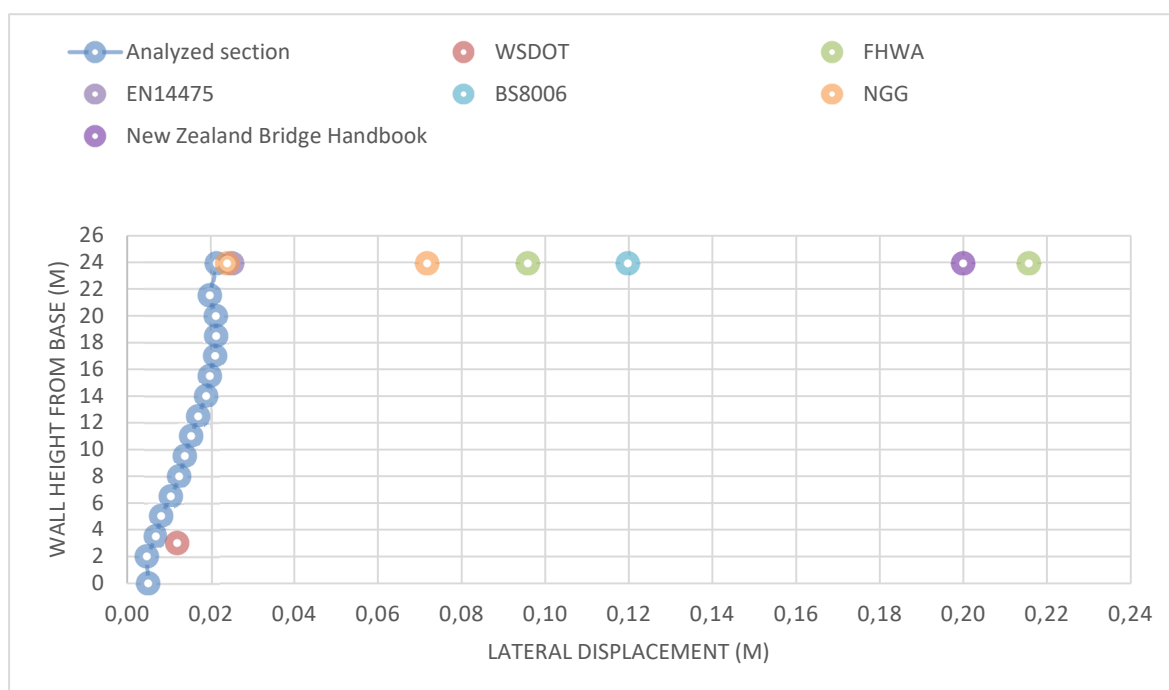
Figure 9. Horizontal displacement distribution along the wall

Stuedlain et al. (2010) measured lateral displacements by establishing inclinometers approximately 2 m behind the top tier face of a 46 m high MSE wall. Maximum lateral displacement within the reinforced soil mass was determined as 45 mm and was evaluated as not excessive. When compared the analysed wall section, maximum horizontal displacement of 21.4 mm under static cases with finite element analysis makes sense.

Since there are few regulations following displacement control design under seismic loads, seismic

performances depending on post-earthquake investigation and shaking table testing were utilized in the evaluation of the studied wall section. Zhang et al. (2009) categorized a three-level seismic fortification standard by considering Sichuan Earthquake, and classifying the damage as follows: "no damage" for lateral displacement smaller than 1.0% of wall height, "repairable damage" for lateral displacement smaller than 3.5% of wall height; and "not fall" for lateral displacement smaller than 6.0% of wall height. Kuwano et al. (2011) set the horizontal displacement limit of 3% of wall height as a step between ultimate and serviceability limit state under Tohoku Earthquake. In contrast, Zhu et al. (2012) evaluated the wall exhibiting deformation bigger than 4.0% of the wall height as partial damage without leading to a complete collapse. Given the maximum permissible lateral displacements for both two-tiered and single-step MSE Walls, adopting 3.8% of the wall height as the control index for lateral displacement in the initial post-earthquake damage assessment is advised (Li et al., 2021).

According to the studies depending on post-earthquake investigation and shaking table testing, the analysed section was expected to experience no damage to moderate damage without collapse with 50.9 cm lateral displacement as given in Figure 6 and Figure 7, which coincides with 2.12%H.

Once the deformation behaviour was examined given in Figure 7, it was seen that maximum expected horizontal displacement occurred at 70% and 65% height above base of wall in static and seismic conditions, respectively. Won et al. (2021) reported that the maximum lateral displacement observed at 0.58~0.75H from the base of the wall after making a series of small-scale models on MSE walls with a full-height rigid facing and a segmental panel type wall facing.

5   Conclusion

In this study, static and seismic performance of single-tiered MSE wall in 23.95 m height were evaluated by performing LEM for global stability and FEM for lateral displacement. Maximum horizontal displacement values in static and seismic case were obtained as 21.4 mm and 50.9 cm, respectively. Expected horizontal displacement is below allowable limits stipulated by the guidelines (NGG, EN14475, WSDOT, New Zealand Bridge Handbook, BS8006 and FHWA). On the other hands, post-earthquake investigation and shaking table testing were utilized in the assessment of maximum horizontal displacement in seismic case due to lack of regulations following displacement control design under seismic loads. The seismic performance of the designed MSE wall is found satisfactory, which is important in terms of being single-tiered, 23.95 m high reinforced soil wall such a seismically active region.

References

Berg, R.; Christopher, B.; Samtani, N. *Design and Construction of Mechanically Stabilized Earth Walls and Reinforced Soil Slopes – Volume 1, Report No: FHWA-NHI-10-024*. U. S. Department of Transportation Federal Highway Administration, Arlington, VA, 2009.

Elias, V.; Christopher, B.R.; Berg, R.R. *FHWA-NHI-00-043: Mechanically stabilized earth walls and reinforced soil slopes – Design and construction guidelines*. Federal Highway Administration, Washington, D.C., 2001.

Hongwei, Z.; Lingkan, Y.; Xuhai, Z. Comparison of dynamic characteristics between netted and packaged reinforced soil retaining walls and recommendations for seismic design. *Chinese Journal of Geotechnical Engineering*. 2012, 34.

Jianjing, Z.; Jun, F.; Shiguo, X.; Chanqing, L. Discussions on Two Key Technical Problems for Seismic Design of Retaining Structures. *Journal of Southwest Jiaotong University*. 2009, 22, 321-326.

Kuwano, J; Miyata, Y; Koseki, J. Performance of reinforced soil walls during the 2011 Tohoku earthquake. *Geosynthetics International*. 2014, 21, 179-196.

Li, S.; Cai, X.; Jing, L.; Xu, H.; Huang, X.; Zhu, C. Lateral dipslecement control of modular-block reinforced soil retaining walls under horizontal seismic loading. *Soil Dynamics and Earthquake Engineering.* 2021, 141.

Lindquist, D. D. Seismic Modeling of a 135-Foot-Tall MSE Wall. *In Proceedings of Geotechnical Earthquake Engineering and Soil Dynamics IV,* 20 June 2020.

Mechanically stabilized earth. Wikipedia. Available online:

 https://en.wikipedia.org/wiki/Mechanically_stabilized_earth (accessed on 23 December 2023)

Pamuk, A.; Ling, H.I.; Leshchinsky, D.; Kalkan; E.; Adalier, K. Behavior of Reinforced Wall System During the 1999 Kocaeli (Izmit), Turkey, Earthquake. *In Proceedings of Fifth International Conference on Case Histories in Geotechnical Engineering*, New York, 13-17April 2004.

Rajoor, R.; Rajput, V; Bharadwaj, G. A Study on Behavior of MSE wall under Different Earthquake Conditions. *Journal of Engineering Reseacrh adn Application.* 2018, 8, 62-64.

Sandri, D. A Performance Summary of Reinforced Soil Structures in the Greater Los Angeles Area after the Northridge Earthqauke. *Geotextiles and Geomemebranes*. 1997, 15, 235-253.

Stuedlein, A. W.; Bailey, M.; Lindquist, D.; Sankey, J.; Neely, W.J. Design and Performance of a 46-m-High MSE Wall. *Journal of Geotechnical and Geoenvironmental Engineering.* 2010, 136.

Turkish Building Earthquake Code (TBDY). Disaster and Emergency Management Presidency, 2018.

Technical Specification for Highways (KTŞ). General Directorate of Highways, 2013.

Wartman, J.; Rondinel-Oviedo, E.A.; Rodriguez-Marek, A. Peformance and Analyses of Mechnically Stabilized Earth Walls in the Tecoman, Mexico Earthquake. *Journal of Performance of Constructed Facilities*. 2006, 20.

Won, M.S.; Langcuyan, C.P.; Choi, G.H. Experimental study on the behavior of MSE wall having full-height rigid facing and segmental panel-type wall facing. *Open Geosciences*. 2021, 13, 932-943.

PLANNING AND METHODOLOGY ADOPTED TO DEAL WITH ADVERSE GEOLOGICAL PROBLEMS ENCOUNTERED DURING HRTS EXCAVATION OF TEESTA VI HYDROELECTRIC PROJECT (500MW), SIKKIM, INDIA.

ANIL KUMAR DASH [1], MANOJ KUMAR LAKRA [2], SAILENDRA SINGH BARIHA [3], MOHINDER PAL SINGH [4,] ANOOP KUMAR PATEL [5]

[1] *NHPC Limited (A Govt. of India Enterprise), India, akdash@nhpc.nic.in*

[2] *NHPC Limited (A Govt. of India Enterprise)*, Ind*ia, manojlakra@nhpc.nic.in*

[3] *NHPC Limited (A Govt. of India Enterprise)*, India*, sailendrabariha@nhpc.nic.in*

[4] *NHPC Limited (A Govt. of India Enterprise), India, mohinder@nhpc.nic.in*

[5] *NHPC Limited (A Govt. of India Enterprise)*, India, *anooppatel@nhpc.nic.in*

Abstract
Tunnelling and Underground excavations in the Himalayan mountains is a formidable task in itself. The challenges in such a condition are further amplified if a project which was under execution by one agency due to financial issues came to complete halt. Further after a considerable time lapse, these partially constructed projects under ageing conditions are taken over by other agencies towards its completion. Teesta VI HEP, is one of such projects, which was partially constructed by M/s. Lanco Teesta Hydropower Limited (LTHPL), promoted by the Lanco Group but could not be completed due to financial crunch by scheduled completion time of May 2012 and the construction works were in standstill position since Dec 2012. Subsequently, acquisition of M/s LTHPL and execution of balance works of Teesta IV HEP was entrusted to NHPC by NCLT bench in Oct 2019. After taking over the partially constructed project by NHPC, excavation activities of the tunnel for balance stretches were resumed during June 2021 under challenging global pandemic period. This paper elaborated on the various geological challenges faced by NHPC during resumption and fresh HRTs excavations. Methodology, geological studies/ monitoring protocols followed to achieve the project's goal has been described in detail. As the execution of the tunnels were typically planned with precise deadlines to achieve the project excavation schedule, so this paper also expounded various measures taken during Re-strengthening of tunnel support, restoration of collapsed tunnel areas, precaution taken at low cover zone and adverse geology during excavation of tunnels.

Key words
Re-investigation*,* Re-strengthening, Restoration, Reassessment, Rehabilitation, Pipe roofing, Fore poling.

1   Introduction

The Himalayan mountains are the youngest mountain range and exhibit active plate tectonics that result in high stresses leading to common occurrences of folding, faulting, and shearing in the rock mass (KC Diwakar et al. 2022). These challenges further intensify in the Sikkim Himalayan range, due to its complicated geological settings and presence of highly deformed and fragile rock strata. That's why surface as well as underground excavation in the Sikkim region has become a much more challenging, time consuming, costly affair for project authorities. Very often geological problems pose significant obstacles that go beyond the expertise and scope of the developers. Not addressing these geological issues timely, results in a massive setback for the developer, as the project may be delayed or even abandoned in worst cases during any stage of the project's construction lifetime. In Sikkim state itself, many hydropower projects had been stalled for various reasons with delays ranging from few years to

even a decade.

Similarly, Teesta VI HEP located on River Teesta is such a project which remained undeveloped for about 9 years without any progress at the project site. NHPC- *A Govt of India enterprise* has taken up the task of completion of this project during the year 2019. The project is located on river Teesta in the Himalayan state of Sikkim in India. It is a Run of River (RoR) scheme with a Barrage located about 3 Km downstream of Teesta - V Powerhouse at Sirwani upstream of Singtam town. It envisages construction of 26.5m high barrage which shall facilitate diversion of river water by means of 02 Nos. of HRTs each of ±13.7Km long to an underground powerhouse located near Pamphok village to generate 500MW. Each pressurised headrace tunnel is modified horse shoe shape, with 9.8m finished dia of about 78 square metres cross-sectional area. The Head Race Tunnel will be concrete lined for its entire length. The minimum rock pillar thickness between wall to wall is ±30m between both the HRTs.

This paper highlights the primary geological adversities that concerned NHPC during restoration works and during excavation of balance span of HRTs. The Authors have drawn special attention to how adverse geological conditions encountered during tunnelling excavation have been dealt with in a professional way to achieve the project excavation schedule.
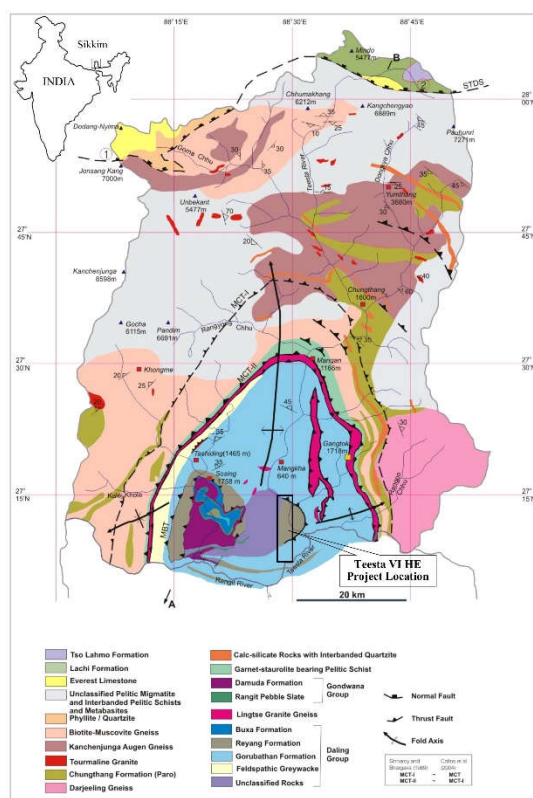
Figure 1. Geology and Stratigraphy of Teesta Basin in Sikkim, India (modified after Acharya, 1989; Ray, 1989; Neogi et al., 2000; GSI, 2001; Catlos et al., 2002, 2004).

2   Geological and Topographical seting of the Project

The Project area falls in the Lesser Himalayas consisting of low grade meta-sedimentary rocks belonging to Gorubathan formation of Daling Group. The Lesser Himalayan orographic tract in Sikkim area is found on both the sides of river Teesta and encircled by Main Central Thrust (MCT). Due to this thrust the Daling Group of rock mass underwent intense folding and faulting in the form of several anticlinal and synclinal deformational structures. In general, the distribution of the Daling Group of rocks shows a broad sweep in a north-south antiformal axis plunging gently due north resulting in divergent dips

varying in directions from NW in western sector to NE in eastern sector through almost north in the central part. In the eastern and western sectors, broad warps with easterly and westerly axial plunges respectively are also responsible for local variation in attitude.

The rock types exposed in the project area are mainly interbedded sequences of Quartzite, Phyllite with their variants. Quartzite is usually coarse grained, medium strong to strong and highly jointed in nature except in HRT intake area, where it was completely crushed due to its vicinity to the regional anticlinal fold axis. Whereas, Phyllites show a complete wide range of compositional, strength variations, weathering grades, and deformation magnitude. The Phyllitic rock mass found in the project area displays variation in composition with Quartzitic, Chloritic, Sericitic, Carbonaceous and Slaty in nature along with layers of Quartzite bands in between. As the composition of Phyllite varies considerably and so are the strength and other geotechnical parameters. The ridges, which stand out along the HRTs alignment are predominantly of competent lithounit, while the phyllite rich portion make out gently sloping landforms. It is the natural landforms on the surface which determine geological conditions at the tunnel grade.

As per seismic zoning map of India, the project area falls within Seismic Zone-IV and has records of seismicity in adjacent areas. As per Seismotectonic atlas, GSI (2000), two major tectonic features viz. MBT & MCT are located about ±36Km South and ±15 Km East of the project location respectively.

Topographicaly both the HRTs are running almost North to South on Right bank of River Teesta. The tunnel alignments span having rugged topography with low to high mountains with altitude varying from EL: ±360M to EL: ±1300M, with 05 Nos. of prominent deep cut perennial streams. The maximum superincumbent cover over the tunnel is to the order of 900m while it is 55m-60m in the nala reaches.
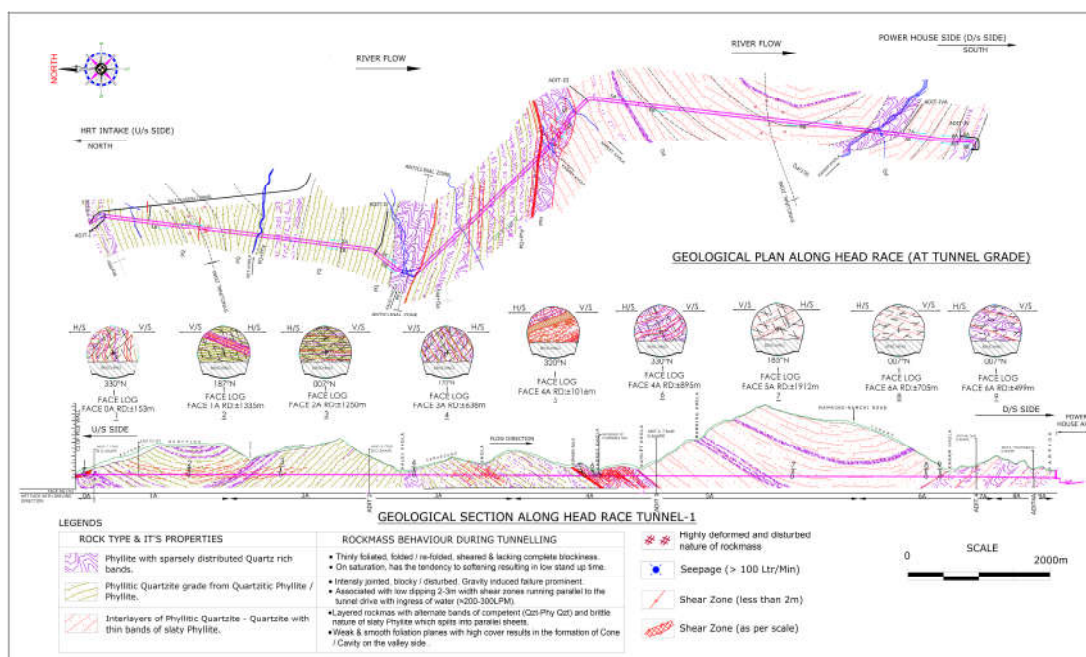
Figure 2. Geological Plan & section along Head race Tunnel (HRT) at Tunnel Grade of Teesta VI H.E. Project.

3   Hindrances faced prior to start of fresh excavation

Heading excavation of approx.10.8Km out of total 27.5Km, Benching excavation of ±4.27Km and Overt Lining of ±1.55Km was completed by the previous developer. To facilitate construction of the HRTs five numbers of Adits had already been constructed.

However, due to a long hiatus of the project, the primary support that had been provided by previous developer had developed with age various defects that had distorted the tunnel cross section and were vulnerable to failure. This vulnerable span of the tunnel was thoroughly investigated and identified. The major hindrances/challenges faced by the NHPC were as follows.

- Project had witnessed lots of urbanisation above the tunnel alignment which was once covered with dense forest. Now, the tunnel alignments span mostly traversing below private properties, public roads, NH, pharmaceutical companies, high power transmission towers, etc. Human activities have impacted slope stability and increased the risk of landslides mainly during the rainy season.
- Without any dewatering arrangement, Adit-1, 2 & 3 were flooded with seepage water and further access to HRTs were blocked.
- HRT Faces 0A and 0B from Adit-1 were in collapsed state due to encounterance of crushed quartzite in the form of sugar cube and bands of sheared Phyllite.
- HRT Faces 1A & 1B from Adit-1and Faces 2A & 2B from Adit-2 were in fairly good condition except some areas where Ribs and LGs were either twisted, deteriorated or cracked, wire mesh and shotcrete were detached and rock mass at crown areas were exposed.
- A big cavity was formed at 400m inside Adit-2 during restoration works due to prolonged exposure of rock mass to saturation conditions.
- HRT Faces 3A & 3B from Adit-2 and passing below Kalej Khola were in completely collapsed state. Furthermore, a surface cave-in was observed on the surface above face-3A.
- The already excavated tunnel behind HRT Face 4A and 4B from Adit-3 were collapsed due to encounterance of highly weathered and sheared Phyllite. Further, the reported incidence of a surface cave-in had compelled fear among the local public. Also, downstream Faces 5A & 5B of HRTs from this Adit had encountered a maximum number of collapses/cavities formations at various locations especially where Steel rib support was not provided.
- From Adit-4A two faces Face 7A & 7B were already excavated and partial lining work was also completed. But the upstream faces 6A and 6B were partially excavated and Face 6A was in a collapsed state 100m behind the Face.

Figure 3. Showing Photographs of Hindrances faced during resumption of Underground works. (a) Water accumulation at Tunnels. (b) Twisting and Buckling in Lattice girder. (c) & (d) Rockfall and cavity formation in allready excavated tunnel portion (e), (f), (g) & (h) huge cavities and collapsed tunnel area in allready excavated tunnel portion. (i) & (j) Collapsed tunnel face and surface cave-in above the tunnel at Kalej Khola (k) & (i) Collapsed tunnel below Kamlet Khola.

3   Challenges & Mitigation Measures

During fresh excavation carried out by NHPC, several adverse problems have been encountered due to adverse geological conditions. These difficulties have been dealt with utmost care and giving attention to geological details. The various challenges faced along with mitigation measures taken while tackling these hindrances are as follows.

3.1 Archived Geological data acquisition

The acquisition of progressive geological data gathered by the previous developer during the course of tunnelling works was the first & most challenging task faced by NHPC. Most of the geological drawings were non digital or paper documents had deteriorated with time. Beside this, some of the geological data related to underground excavation was either missing or partial. So, the organisation of archived geological logs, reports, Lab test reports etc were done and studied for understanding the geological conditions of the area.

Figure 4. Showing Photographs of Confirmatory Surface Geological and Geophysical studies. (a) Geological survey along HRT alignment. (b) Assessing rock strength using Schmidt Hammer. (c) Drilling activity (d) Topographical survey (e) Resistivity Imaging. (f) Cross hole P-wave Tomography.

3.2 Reassessment of geological condition

COVID-19 paved the way towards subsequent nationwide lockdowns which had restricted NHPC to carry out additional geological exploration in time. Despite this restriction, confirmatory surface geological mapping, exploratory drill holes and geophysical survey along the vulnerable nala stretches was carried out particularly along the HRT alignment with much difficulties. The surface geological mapping was done along the road cut, nala sections, few sporadic rock exposures with the help of mobile based GPS & also through geodetic instruments at low cover / nala stretch to understand regional geological set up, litho contact & their engineering characteristics that might adversely affect the excavation works of tunnels. Geophysical investigations like Resistivity Imaging & Seismic Tomography surveys carried out at site specific locations for assessment of subsurface geological conditions. These geophysical techniques successfully delineated the geological conditions at Intake area and vulnerable nala stretches. Most of the collapsed face, cave in location at low cover zone, nala stretch was successfully dealt with utmost care and giving attention to geological details gathered through additional exploration, mapping and geophysical studies. Reassessment of geological conditions has helped in tackling many geological problems that were anticipated initially. Along with these geological and geophisical survey Pre conditional survey prior to the restart of the tunnelling works was also done for the existing buildings above the tunnel alignment. Structural integrity of the individual buildings, owner name etc was recorded during inspection.

3.3 Water accumulation / dewatering of tunnels

Seepage water accumulation at HRT tunnels and Adits had greatly influenced the stability of the tunnel support system and with time weakened making it vulnerable to collapse. Structural instability, corrosion of steel structures, chipping out of shotcrete, loosening of rock reinforcement etc were few of the major safety concerns during restoration works. To address this issue, a comprehensive drainage system and effective dewatering arrangements were established before resuming excavation activities. In low cover nala stretch, attempts were made to channelize / divert the surface water away from the vicinity of the tunnel alignments to avoid percolation down onto the collapsed or active work area at tunnel grade.

3.4 Re-strengthening of tunnel support measures

During construction by the previous developer, primary support in the form of shotcrete, rock bolts, dominantly Lattice Girder etc. were provided in HRTs / Adits that had the initial support for the opening. Consequently, many stretches of the already excavated HRTs by previous developer had developed with age various defects like chipping out of shotcrete, distressing in rock bolts, buckling of LG / Ribs, distortion of the tunnel cross section which has been associated with huge cavity / cone formation. Accordingly, more than 300 working days have been consumed for additional restoration and strengthening measures for most of the already excavated portion of the HRTs to avoid threat of further instability which has facilitated advancement in excavation from established faces. The additional protection measures included application of Steel Fibre Reinforced Shotcrete (SFRS) and anchored rock bolts and replacement of buckled LG/Steel ribs with new ones. Bracing support through MS beam / plate along with additional Rock bolts/ Self-Drilling Anchor (SDA) were provided which was completely embedded with fibre shotcrete. Afterward, extensive grouting activities were carried out on potentially vulnerable zones for consolidating the poor rock mass behind the rib supports.

Figure 5. Showing Photographs of rectification works and additional support measures (a) restoration work under progress, skin to skin ribs were embedded under SFRS (b) Rectified tunnel (c) Fore poling to stabilise the crown of the Tunnel. (d) & (e) Pipe roofing created an umbrella-like structure above the crown to prevent collapses. (f) Multisegmental excavation.

3.5 Rehabilitation of collapsed tunnel Face

Prior to the fresh excavation, most of the tunnel face was in collapsed conditions as these were excavated either in lower Class III or in Class IV & V rockmass. The restoration of these collapsed faces had hindered the start of underground activities of the project to a greater extent. Additional drawings and directives were issued to deal with these collapsed faces. Before the start of the activities, it was ensured that adequate resources viz, manpower, machineries and materials were readily available at site.

Specialised manpower were deployed for specialised works like pipe roofing, grouting activities etc. Pipe roofing was carried out with 21 m long, 89mm dia pipes @ 15-20 degree with an overlap of 10m length.

3.6 Restoration works

Vulnerable stretches of tunnel span that were excavated by the previous developer were identified and monitoring of these areas was done with instruments. Additional rectification works were carried out before restarting of the fresh heading excavation where the tunnel's structural integrity was uncertain. Beside this, some of the tunnel section excavated by the previous developer was in the undercut section and not as per design specification. To achieve the specified tunnel section, it was required to strip rock mass by removing already erected ribs /LGs to accommodate Gantry. This has necessitated strengthening of in-situ rock mass, cautious excavation by non-explosive method, additional support measures, systematic instrumentation programme etc.

4   Geological challenges encountered during fresh excavation

After re-strengthening and restoration of the collapsed tunnel faces, balanced underground excavation work was carried out by using suitable Drill Blast methodology or by Mechanical means of excavation as per the condition of rock mass. During progressive excavation of balance works, project had encountered several hindrances due to adverse geology conditions as given below:
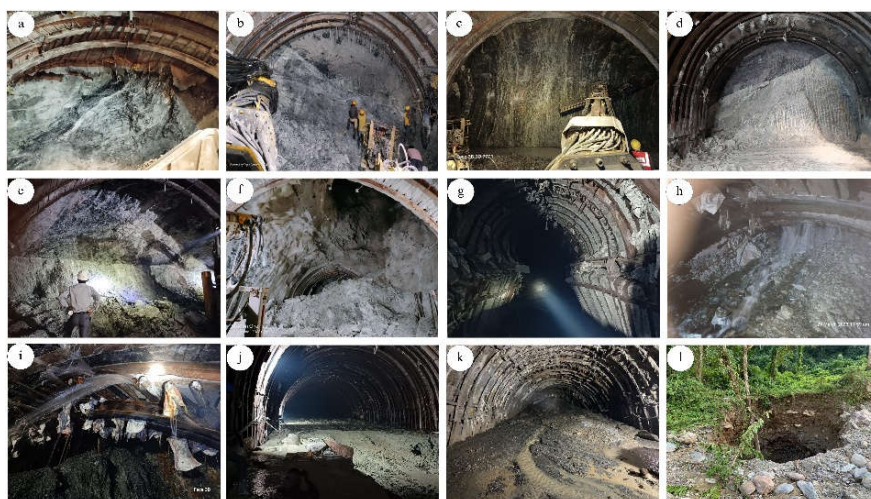
Figure 6. Showing Photographs of Geological hindrances faced during fresh excavation (a) Shear seams Parallel to foliation plane. (b) Shear zone at the hinge of synclinal fold. (c) vertical Shear seams at the hinge of Anticlinal fold. (d) & (e) Shear zones manifested along Fault planes. (f) Cone formation due to subparellel folaition plane (g) Squeezing in the tunnel. (h) & (i) Flowing water condition. (j) Tunnel filled with slush (k) &(l) Collapsed tunnel face & Surface Cave-in above the tunnel face.

4.1 High overburden and low rock cover zone:

The HRT intake is located in high overburden cover to the tune of 50m which mainly consists of highly saturated, unconsolidated and heterogeneous in nature. During excavation by the previous developer, local instability problems were reported at the surface due to the unconsolidated overburden mass. Although instability problems were observed at the surface, it also posed an immediate threat of instability at the tunnel during the excavation works of HRTs. The rock mass at tunnel grade in this zone was highly weathered and crushed Quartzite in the form of sugar cube along with bands of sheared and deformed Phyllite. Due to these adverse geological conditions, tunnelling activities at the intake area was a very challenging and difficult task. Knowing the geological conditions, the tunnelling in this span

was done through non explosive means by providing a sequence of pipe roofs along with multi-segmental methodology. This area was further closely monitored by providing suitable monitoring instruments such as Load cell, MPBX, SPBX, Convergence metre and survey targets.

4.2 Sequence of Anticline & Syncline Structures

In the project area, Teesta River is flowing along a major antiformal structure and the effect of this has rendered the rock mass to be fractured, highly jointed with intermittent shear seams/zones particularly between Intake to Adit III. Thus, the closer the tunnel alignment nearer to the river, the more the adverse nature of rock mass has been encountered. In addition, sequence of anticline & syncline folds, passes throughout the HRTs alignment, causing the rock mass to be extremely deformed and under stressed condition. Beside this, the same litho-units are encountered repeatedly having variable physical and mechanical properties worsen the tunnelling in this area. Overall, the synclinal & anticlinal zones displayed increased jointing leading to more fracturization, intrafolial folds, shear zones, minor faults and other associated structures which are also variably-oriented. Overall, the weak rock masses produced by such regional tectonic features are present throughout the whole tunnel length. It is generally observed that the competency of the rock mass changed dramatically in a few metres and in such cases; frequent removal of rock support, particularly steel ribs proved to be dangerous if temporarily a better quality of the rock mass appeared for the shooter stretch of the tunnel.

4.3 Shear Seams/Zone

These geological features are associated with multiple shear seams of varying thickness from few cm to tens of metres had continuously hampered the tunnelling activities to a greater extent. The rock mass along these shear seams/zones are strongly deformed, crushed, cohesionless and showing substantial heterogeneity. Encountering these shear zones during tunnelling results in the form of face instability/collapse, excessive over break, cavity/chimney formation, running ground condition, mud inrush, squeezing and/or swelling of rock mass etc. Tunnelling through this type of shear zone was extremely challenging and difficult which required additional support measures in the form of pregrouting, pipe roofing, fore poling along with steel ribs support were completely embedded in SFRS.

4.4 Interception of Groundwater

With the increase in blocky nature of rock and at the boundary of anticline-Syncline boundaries, frequency of joints in the surrounding rock is noticed to be increased. The risks of hitting large quantities of high-pressure ground water during advancement was dealt by conducting advance probing. At times, the seepage encountered was acceptable and at times, it was unacceptable which was dealt with by providing drainage holes and pre grouting activities.

Also when Tunnels were driven below perennial streams through highly sheared, soft nature of Phyllite under a cover varying from 55m to 70m had initially presented considerable difficulty in terms of face stability due to seepage of water. Large inflows of pressurised water to the order of 700-1000 LPM was captured during tunnel excavation in HRT Face 3B below Kalej Khola and face 4B that caused surface subsidence. This difficulty was tackled by sequential excavation involving partial excavation of top heading leaving a core (rock ledge at the centre of face) at the face with pipe roofing techniques.

4.5 Occurrences of Flammable Gas

During initial excavation of HRT Face 4B at RD: ±41m by previous developer in the month of Nov 2009, release of flammable gas was detected at the contact of competent Quartzite-Phyllitic Quartzite with soft nature of Phyllite which eventually burst into flame. Similarly, during excavation by NHPC, incidence of concentration of flammable gases was initially reported when the HRT Face 4A was entering Kabrey Khola. The gas was releasing particularly from the tunnel arch section. The measurement of Lower Explosive Limit (LEL) recorded through the handheld equipment was up to 30% resulting in incidence of fire during heading excavation at this tunnel face. Accordingly, improvement

of ventilation and strengthening monitoring measures were done. Additionally, 02 Nos., 30m to 24m long of probe holes were also done at the working face wherein LEL was detected to the order of 1-5% and tunnel advancement was attempted safely with the help of mechanised equipment.

5   Methods adopted for tunnel stability

Project had adopted various additional support measures which minimizing hindrance during progressive tunnelling. These additional support measures are as follows:

Advance Probing: Probe holes up to 20m long were conducted to explore the competency of strata and also to assess stored water ahead of the tunnel face. This method has greatly benefited in difficult ground conditions towards avoiding potential risk and was the best option to control sudden water inflows during excavation.

Pre-drainage holes: 45mm dia, 20m long, drilled in crown periphery at 10-15° upwards, followed by installation of perforated pipes. These helped in reduction of hydrostatic pressure and minimising seepage from face ahead. It was always ensured to divert the water from the face towards its rear side to facilitate smooth excavation works.

Pre-excavation grouting: 45mm dia, 10m long, 10-15° upwards in crown periphery and at face was drilled from the tunnel excavation face towards the advancement. The grout was pumped in and allowed to set before advancing. The activities were performed ensuring 3m overlapping with the next round of pre-grouting. Microfine cement grouting in addition to normal cement grouting was provided during pre-grouting / consolidation grouting. In Kalej Khola nala stretch, permeason grouting was also executed from the ground surface. The risk of unexpectedly running of water ingress into extremely poor and unstable ground ahead of the face was avoided through these activities and also stand-up time of the rock face was improved considerably.

Fore-poling: 32mm dia reinforcing bars, 10m long, at a close interval of 200-300mm, 10-15° upwards in crown periphery were provided at the tunnel periphery by hammering or by drilling. In case of drilling, the holes were grouted after installation of forepoles. The activities were performed ensuring 3m overlapping with the next round of forepoling.

Pipe Roofing: 89mm dia, 21m long, casing perforated pipes using sacrificial drill bits were inserted around the arch section of the tunnel face. The pipes are spaced 300-400mm c/c and inclined 10-15° upwards from the periphery of the tunnel face. The perforated pipes are then grouted in stages with a maximum pressure of 4bars. So, the arrangement of overall grout pipes was ensured to form an umbrella around the roof of the tunnel and its advancement zone. This methodology was adopted where Class V (very poor) rock was anticipated at the advancement zone.

Face sealing: When full face heading excavation of the tunnel was being done against the dip in sheared nature and soft nature of Phyllite, frequent collapse of the rock face has hampered the progress. Without any perceptible movement and before any kind of alarm could be given, the exposed tunnel rock face often collapsed which posed a threat to the workers. Subsequently, this adverse incidence was controlled by application of layers of fibre shotcrete on the rock face timely. The advancement of the tunnel was restricted to 1-2m in each cycle with concurrent support measures.

6   Conclusion

Tunnelling in Himalayan regions presents numerous challenges due to the presence of adverse geological conditions. Most of the problems in Himalayan tunnelling are attributed due to lack of knowledge of the adverse geological features of the area and their potential risk and resulted in time and

cost overruns of the project. The excavation of HRTs in Teesta VI HE Project was challenging due to encountering weak, fragile and sheared rocks. As the alignment of the HRTs passes through a series of folds, sheared rock mass with varied lithology, low cover, flammable gas etc, the tunnelling so far has required more steel rib support, Pipe roofing and forepoling arrangement than expected. Accumulation of progressive geological data; both surface and subsurface has helped in tackling many geological problems that were anticipated initially. Almost all the nala stretch had been successfully crossed with utmost care and giving attention to geological details.

Acknowledgements

References

Acharyya, S.K., Ghosh, S., Mandal, N., Bose, S., Pande, K. Pre-Himalayan tectono-magmatic imprints in the Darjeeling-Sikkim Himalaya (DSH) constrained by 40Ar/39Ar dating of muscovite. *J. Asian Earth Sci.* 2017, 146, 211-219.

Acharyya, S. K., The Daling Group, its nomenclature, tectono stratigraphy and structural grain : with notes on their possible equivalents. *Spec. Publ. Geol. Surv. India*, 1989, 22, 5-13.

Goel, R.K. Challenges of Tunnelling in Fragile Rocks of Himalaya. *researchgate*, 2015, 1-8.

KC, D.; Gautam, K.; Dangi, H.; Kadel, S.; Hu, L. Challenges in Tunneling in the Himalayas: A Survey of Several Prominent Excavation Projects in the Himalayan Mountain Range of South Asia. *Geotechnics*, 2022, 2, 802–824.

Kumar, M.V.; Kumar, Y.P.; Kumar, A.V. Challenges and Strategies for Tunnelling in the Himalayan Region. Indian Geotechnical Conference, *IGS Mumbai Chapter & IIT Bombay*, 2010.

Mathur, N.K. Speedy development of hydropower project in Sikkim Himalaya by optimization of head race tunnel layout: A case study of Teesta V HE project (510 MW), *East Sikkim, India. Journal of Engineering Geology*, 2014, XXXIX (2), 143-153.

Mehra, A. Effect of Discontinuity Orientation and Geological Overbreak in Tunnels: Case study of Tunnel T 74 R (A). *International Journal for Research in Applied Science & Engineering Technology (IJRASET),* 2021, 9, 1104-1108.

Ministry of Environment & Forest, Government of India. Carrying capacity study of Teesta Basin in Sikkim. *Centre for Interdisciplinary studies of Mountain & Hill Environment (CISMHE),* University of Delhi, Delhi, India.

Naithani, A.k.; Nawani, P.C. Engineering geological investigations of Dik Chhu Hydroelectric Project, Sikkim Himalaya, *India. Journal of Nepal geological society*, 2011, 43, 317-326.

NHPC Limited. *Detailed Project Report (Revised)-Teesta Stage VI HE Project*, 2021.

NHPC Limited. *Report on Geophysical investigations involving resistivity imaging and Seismic tomography at Teesta-VI hydroelectric project, Sikkim*, April 2021.

Schubert, w.; Mendez, J.M.D. Influence of Foliation Orientation on Tunnel Behavior. *Procedia Engineering*, 2017, 191, 880-885.

Sharma, H. R.; Tiwari, A. N. Challenges of Tunnelling in Adverse Geology. *Eurock 2015 & 64th Geomechanics Colloquium. Schubert & Kluckner*. 2015,100 - 106.

Sharma, H. R.; Tiwari, A. N. Tunnelling in the Himalayan Region: geological problems and solutions. *International Water Power & Dam Construction*. September 2012, 14 - 19.

Terzaghi, K. Rock defects and loads on tunnel support. Introduction to Rock Tunnelling with Steel Supports. *Commercial Sheering and Stamping Co., Youngstown, Ohio, U.S.A.*1946, 27.

ENGINEERING PROTECTION OF RECREATIONAL FACILITIES

SERGEY MATSIY [1], ULIANA SIDARAVICHUTE [2], VLADIMIR MATSIY [3]

[1] *Trubilin Kuban State Agrarian University, Krasnodar, Russia, e-mail: matsiy@mail.ru*

[2] *Trubilin Kuban State Agrarian University, Krasnodar, Russia, e-mail: dd600902@gmail.com*

[2] *Trubilin Kuban State Agrarian University, Krasnodar, Russia, e-mail: vmatsiys@gmail.com*

Abstract

Based on empirical evidence from field surveys, morphometric parameters of mudflows were determined. In laboratory conditions, data on the geological structure of slopes, physical and mechanical properties of soils, etc. were obtained. On the site, three mudflow basins were identified, which in case of prolonged heavy rainfall and snowmelt form mudflows causing damage to various-purpose structures, including the ropeway, ski track No.1, engineering protection facilities, haul road, antenna-mast structure No.2, and pedestrian crossing. Based on field surveys, it was established that the existing mudflow protection structures were insufficient to ensure full safety of the existing facilities and adjacent structures. Based on these calculations, the following measures were recommended to stabilise the situation, namely along the Sulimovsky Creek: installation of flexible anti-mudflow barriers, arrangement of a network of drainage ditches, and erosion control. Thus, the structure type recommended for Section Line No. 3 was unsupported mudflow barrier 5-6 m high and 15 m wide. The structure type for Section Line No. 4 was unsupported mudflow barrier 4-5 m high and up to 15 m wide.

Key words

mudflow protection structures, mudflow, load on protective barrier, hydraulic engineering, morphometric parameters.

1 Introduction

Mudflows are widespread throughout the Russian Federation [1]. In order to protect buildings and structures from mudflows, anti-mudflow facilities and structures are erected, with preliminary calculations of the mudflow load on the barrier and the capacity of the mudflow-retaining structure [2]. The analysis of mudflow risk for the territory of the North-West Caucasus, which included probability of the event and its possible consequences, has shown that the highest value of mudflow risk of the territory (R) is found in the Central region (R=78%), followed by the Southern region (R=56%), then the Maritime and Eastern regions, respectively (R=36% and R=29%) [3]. Our research object is located within the boundaries of the Maritime District of the North-West Caucasus.

2 Brief overview of the issue

Over a half of the area within the boundaries of the studied site is covered by forests with evergreen species. There is a widespread undergrowth of Caucasian rhododendron (Rhododendron caucasicum) throughout the area, which prevents mudflows, but dense vegetation does not provide complete protection from mudflows (Figure 1) [4]. Mudflow control structures belong to engineering protection structures, which should ensure reliability and the possibility of systematic observations [5]. For

mudflow-directing and mudflow-preventing structures, the structure category is determined depending on the type of the soils and their height: mudflow-directing and mudflow-preventing structures located in unpopulated areas are assigned class IV; those located in populated areas are assigned class III. Stabilising structures are assigned class IV. Thus, the channels of watercourses contain coarse clastic material of wood origin, as well as various fractions of geological elements.

Figure 1. The Rzhanoi Creek course with boulders and fragmental material (debris).

The aim of this research was to substantiate the need to take measures to stabilise the situation with regard to possible mudflows at the site, and to select optimal engineering protection structures.

3   Materials and methods

In the course of the mudflow hazard assessment process, mudflow basins were identified within the alpine resort's recreational complex. During the field surveys, the boundaries of mudflow basins and their parameters were clarified, and erosion and mudflow activity at the site was examined.

The site is located on the left slope of the Mzymta River valley near the village of Esto-Sadok. Sixty-five mudflow channels were identified in the basin of the Mzymta River. The area affected by mudflows is 510 km^2 [6]. When assessing the mudflow potential of an area, one of the factors was the lithological composition of the rocks as the source of the solid component of mudflows. The area under study lies within the evolution of rocks of the Jurassic and Cretaceous age. The northern half of the area is represented by the Lower and Middle Jurassic clay shale, siltstones, mudstones, and their interbedding packages, i.e. rocks of low anti-denudation stability, which form a large amount of clayey matter. The main basins of the right tributaries of the Mzymta River are located within the limits of these rocks. Dense limestone, dolomites, marls of the Middle and Upper Jurassic eras are known to be resistant to degradative agents. These rocks form the rocky Achishkho Ridge and the Aibga Ridge, from where the Mzymta's left tributaries originate. The valleys of these watercourses have the form of gorges, with channel gradients up to 400 ppm. According to archival data, among the Quaternary formations are landslide and deluvial-landslide deposits over 10 m in thickness, and alluvial fan deposits up to 20 m in thickness. The various-age alluvial fan deposits are represented by pebbly-rubbly, grussy-gravelly masses with inclusion of boulders with loamy filler. The alluvium of the Mzymta River terraces is composed by 80% gravel, pebbles and boulders and 20% sandy-clayey rock. The presence of thick friable (soft) deposits on the slopes of the site determines favourable conditions for mudflow formation in the middle and lower parts of the slope.

The North-West Caucasus is characterised by poorly developed mudflow processes and a low level of knowledge about them. The mudflow processes emerged after deforestation [7] (Figure 2). In the region, rainfall is the main factor of soil erosion, leading to the splitting of the Mzymta River into a system of deep basins, which are leftovers of millennia-old depressions before turning into an elongated marshy depression [8, 9]. The study site is located in the Krasnodar Territory, the village of Estosadok (Russia).

* Note: Category I areas are characterized by the presence of medium-sized mudflows and medium-active runoff-forming surfaces; In areas of category II, small mudflows and weakly active runoff-forming surfaces are noted; Category III areas are characterized by rare or absent mudslides, but due to environmental changes they may occur
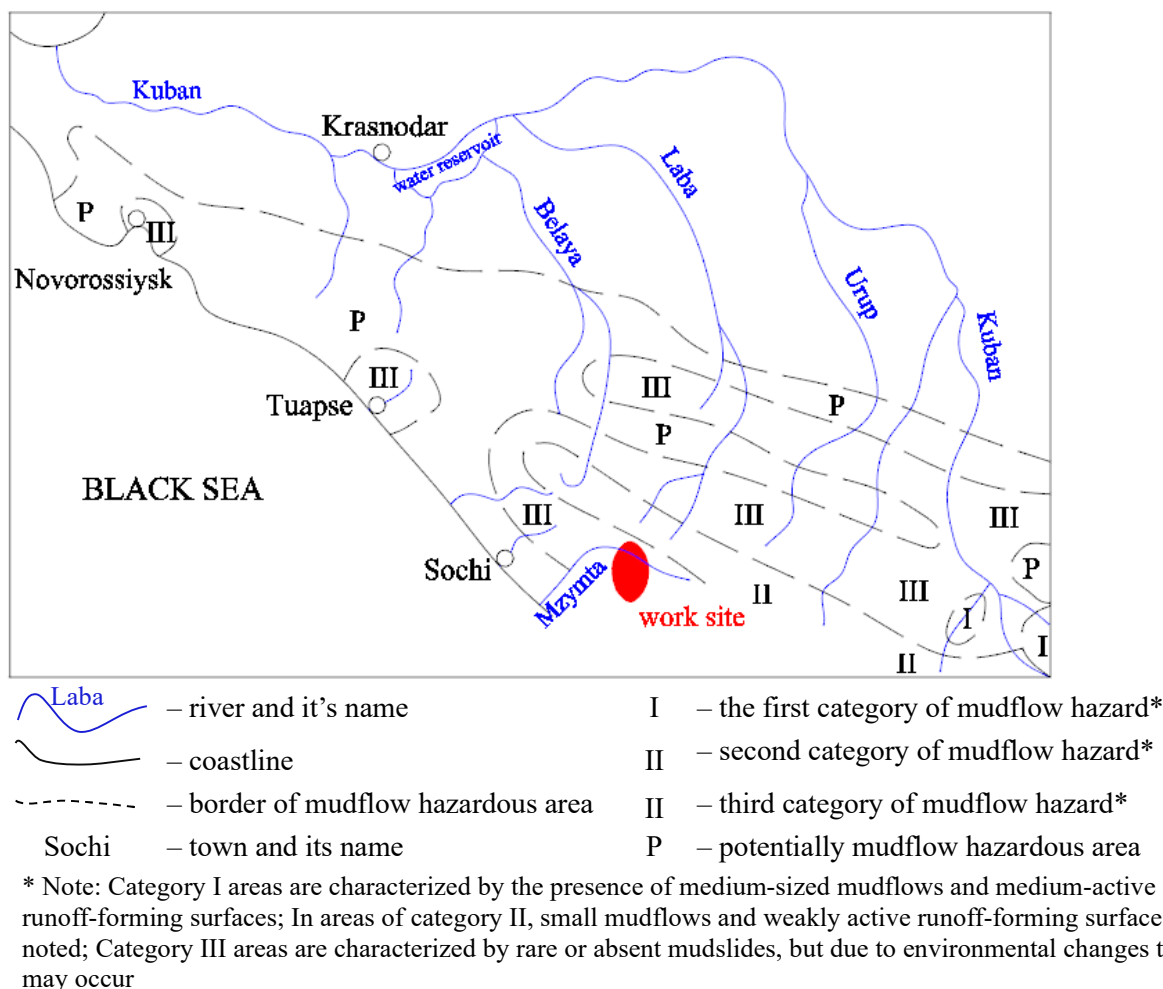
Figure 2. Location of the work site combined with the map of mudflow-prone areas

Thus, 3 permanent watercourses and 13 temporary water catch basins were identified in the area of survey, the latter of which were becoming more active during incessant rainfall.

Based on the results of field surveys of the area, the following morphometric characteristics of the mudflow basins of the Rzhanoi, Shumikhinsky and Sulimovsky Creeks were computed: channel length, water catchment area, and general slopes; the data are presented below in Table 1. The length of temporary watercourses varied from 0.11 km to 4.58 km.

Table 1. Morphometric parameters of mudflow basins of alpine resorts

Watercourses	Mean watercourse slope, ‰	Weighted average channel slope angle, ‰	Water catch area, km^2	Channel length, km
Rzhanoi Creek, Ski piste No.1	357	321	2.35	4.58
Shumikhinsky Creek, Ski piste No.1	425	321	1.77	2.89
Water Intake No.2, Shumikhinsky Creek	425	321	1.77	2.89
Water Intake No.1, Sulimovsky Creek	405	398	1.18	2.07

The quantitative parameters of mudflows were identified in accordance with the instruction for determination of rain mudflow calculated characteristics and the mudflow study guide. Based on that, conclusions were made about the spread of mudflows and their hazard within the construction site and measures were proposed to reduce the mudflow hazard.

The existing mudflow protection structure protects the transformer box from mudflows at the Alpika-Service railway station. It is located in the basin of the Rzhanoi Creek. The mudflow protection structures serve to attenuate and detain possible mudflows in case of their passage along the streambed [10]. Additionally, the channel is being reinforced downstream both sides of the barriers with gabion meshy products [11].

Results and discussion. According to Special Technical Specifications (VSN 03-76 «Instruction for Determination of Rain Mudflow Characteristics»), mudflow barriers should be calculated for the maximum mudflow volume with a 1% exceedance probability. The mudflow velocity ν, m/s, was determined for each gabion mesh (Table 2):

Table 2. Calculation of mudflow velocity of 1% probability

Section Line	$Q_{1\%}$, m^3/sec.	I_y, ‰	$W_{1\%}$	ν, m/sec.
No.2	4.1	299	0.053	2.28
No.3	6.6	298	0.175	3.18
No.4	6.5	298	0.175	3.17

The mudflow load calculation was performed using «DEBFLOW» design software for flexible mudflow protection systems. «DEBFLOW» software provides design solutions for mudflow protection structures. The mudflow load calculation for Barrier I in the Sulimovsky Creek is shown in Table 3 below.

Table 3. Mudflow load calculation for Barrier I (Section Line No. 2)

Parameter	Identifier	Value	Measurement unit
Mudflow type and density			
Type of mudflow	Typ	typical	–
Density of mudflow mass	ρ	2300	kg/m^3
Weight of mudflow mass	γ	22.6	kN/m^3
Liquid phase content	ω	0.21	–
Mudflow volume and number of mudflow waves			
Aggregate mudflow volume (water included)	V_{tot}	1600	m^3
Number of waves	H	3	–
Average wave volume	V_H	533	m^3
First wave volume	V_{N1}	800	m^3
Peak discharge			

Parameter	Identifier	Value	Measurement unit
Peak discharge	Q_p	7	m^3/sec.
Reliability factor			
General reliability factor	SF	1.5	

The load calculations for Section Lines Nos. 3 and 4 were carried out similarly.

According to the calculation of mudflow retention volume, the total volume was 1866 m^3, the required volume was 1600 m^3; hence the reserve was 266 m^3.

According to point 2.16.8 of Special Technical Specifications VSN 03-76, when determining the height of the structure, the equalising slope of mudflow deposits should be taken into account. For the site under consideration, this slope was 22°. When choosing the type of structures, the following were taken into account: calculations of retained material; calculations of mudflow velocity; mudflow load on mudflow protection structure. Once the initial data were entered, the optimal types of structures to protect alpine resort facilities from mudflows were determined (Table 4).

Table 4. Construction type selection for Barrier I

Parameter	Identifier	Value	Measurement unit
Section line geometry			
System height	$H_{0,1}$	5	m
Channel width at ground rope	$b_{u,1}$	5	m
Channel width at head rope	$b_{o,1}$	22	m
Distance to overlying barrier	$L_{0,1}$	65	m
Channel slope and volume of retained material			
Height of filled system	$H_{1,1}$	3.8	m
Average channel slope upstream barrier	$l_{c.1}$	40	%
Surface slope of barrier-retained material	$l'_{c.1}$	27	%
Angle between wire net and channel talweg	ξ	73.2	°
Length of barrier-retained material	L_1	31.7	m
Volume retained	$V_{r.1}$	768	m^3
Front velocity and flow height			
Front velocity	V_{str}	3.7	m/sec.
Impact velocity at barrier site	V_1	2.3	m/sec.
Flow height	h	0.6	m
Maximum height of lower section line	$h_{d.1}$	0.4	m

Construction type – mudflow barrier with support, height – 5-6 m, width – up to 25 m.

The choice of the type of structures required for structures Nos. 3 and 4 was done by analogy.

The construction type for Section Line No. 3 is an unsupported mudflow barrier 5–6 m high and up to 15 m wide. The construction type for Section Line No. 4 is an unsupported mudflow barrier 4–5 m high and up to 15 m wide. Unsupported structures are applicable for narrow valleys and streambeds of small mountain rivers [12]. Thus, according to the calculation of the capacity of the mudflow retention structures: for Section Line No. 2: length of the retained material – 31.7; retained volume – 0.768 m^3; for Gate No. 3: length of the retained material – 31.7; retained volume – 0.725 m; for Section Line No. 4: length of the retained material – 20.0; retained volume 0.373 m.

The total volume of mudflow retention facilities capacity is 1,866,000 m^3 for the total mudflow volume of 1,600,000 m^3.

4   Conclusion

According to the study, the most typical for the North-West Caucasus are debris mudflows of up to 10,000 m3 in volume. In the process of mudflow surveys, the following facilities were found to be exposed to mudflow hazard:

- Alpine ski track No. 1 at the points where it is crossed by the Shumikhinsky and Rzhanoi Creeks. To protect it, it is necessary to design mudflow protection nets in the narrow part of the valley of the Shumikhinsky Creek; strengthen the bottom and the banks of the Shumikhinskiy Creek upstream of the projected Water Intake No.1. Protection of the ski piste No. 1 from mudflows along the Rzhanoi Creek can be realised by construction of a mudflow-deflecting dam.
- Structures of the main water intake located within the Shumikhinsky Creek impact area.
- Formation of low-volume mudflows is possible in the Sulimovsky Creek, but it has mudflow protection.

Other facilities are not exposed to mudflows.

To reduce the level of mudflow hazard in the territory of the mountain resort, installation of mudflow barriers is planned as part of engineering protection, for which calculations have been made in this paper. According to their results, two barriers 5 metres high and one barrier 4 metres high are to be installed there. The total capacity of these barriers is sufficient to ensure the protection of the Olympic infrastructure from possible destructive mudflows.

In addition to engineering anti-mudflow measures, it is recommended to perform the following works on reducing the occurrence of mudflow processes in the study area: embankment of the beds of small streams, including temporary watercourses, to prevent the occurrence of erosion and mudflow processes, and reclamative afforestation – soil reclamation in areas with open soils, including along the routes of roads and ski trails. In addition, for forecasting purposes, it is necessary to organise constant monitoring of the state of the slopes and watercourse beds [13].

References

A Quantitative Assessment of Mudflow Intensification Factors on the Aibga Ridge Slope (Western Caucasus) over 2006–2019. S. V. Shvarev, S. V. Kharchenko, V. N. Golosov, M. I. Uspenskii, 2021, Vol. 42, No. 2, pp. 122-130, DOI 10.1134/S1875372821020128.

Bandurin M. A., Prikhodko I. A., Bandurina I. P., Rudenko A. A. Analysis of Impact of Urbanization Development on the Deterioration of Ecological State of Rivers. *IOP Conference Series: Earth and Environmental Science, Virtual, Online, 10–12 January 2022, Virtual, Online, 2022*, P. 042044, DOI 10.1088/1755-1315/988/4/042044.

Baljyan, P. H., Baljyan V. P. Development of the method of analysis for determining the coordinates of terminal surface of mudflow sediments. *Bulletin of high technology*, 2020, No. 3(14), pp. 3-13.

Bogdanov I.S. Mudflow protection constructions design experience at the transport infrastructure facilities in dumped conditions. *Mudflow Flows: Catastrophes, Risk, Forecast, Protection: Proc. of the 6th International Conference. Dushanbe – Khorog, Tajikistan, 20–26 September 2021.* Ed. by: S.S. Chernomorets, K.S. Viskhadzhieva. Vol. 1. – Dushanbe – Khorog, Tajikistan: Promotion Publ., 2020, pp. 363-370.

GEOBRUGG. Geobrugg AG: website. – URL: https://www.geobrugg.com/ru/Geobrugg-Safety-is-our-nature-114436.html (Accessed on: 19 December 2023.)

Ghetto O.N., Belov V.A. On the reliability and safety of structures for engineering mudflow protection. *Land Reclamation and Water Management: Proc. of All-Russian Scientific-Practical Conf., Dedicated to the 145th Anniversary of the Formation of «Donleskhoz»* (GBU RO "Directorate of Specially Protected Natural Territories of Regional Significance"). Iss. 19, Novocherkassk, Lik Publ., 2021, pp. 88-94.

Ghetto O.N., Belov V.A., Anokhin A.M. Assessment of the reliability of mudflow-retaining structures. *Land Reclamation and Water Management: Proc. of All-Russian Scientific-Practical Conf.* (Shumakov Readings), Dedicated to the 95th Birthday of Prof. V.S. Lapshenkov. Iss. 18, Novocherkassk, Lik Publ., 2020, pp. 124-127.

Ghetto O. N., Belov V. A. Organisational and technical measures to ensure mudflow protection. *Land Reclamation and Water Engineering.* 2022. No. 3. P. 264-276.

Golosov V.N., Kuznetsova Yu.S., Ivanova N.N., [et al.] Geomorphological consequences and hydrometeorological conditions of extreme flood in the Tsanyk river basin, Greater Sochi area. *Mudflow Flows: Catastrophes, Risk, Forecast, Protection: Proc. of the 6th International Conference. Dushanbe – Khorog, Tajikistan, 20–26 September 2021*, Ed. by: S.S. Chernomorets, K.S. Viskhadzhieva. Vol. 1. – Dushanbe – Khorog, Tajikistan: Promotion Publ., 2020, pp. 438-445.

Kondratieva N.V., Adzhiev A.Ch., Bekkiev M.Yu., Geduyeva M.M., Perov V.F., Razumov V.V., et al. *Cadastre of Mudflow Hazard in the South of the European Part of Russia*, Moscow, Feoriya Publ., Nalchik, Pechatny Dvor Publ., 2015, 148 p.

Panina O.V., Dontsova *O.L.* Main geological and ecological forecasting of mudflow risks in the North-Western Caucasus, Geology, *Geography and Global Energy*, no. 3(70), 2018, pp. 201-207.

Volosukhin V.A., Bandurin M.A., Prikhodko I.A. Theoretical justification for reducing the risks of operation of hydraulic structures and the use of flexible dams for engineering protection of the territory from flooding, *Proceedings of Lower Volga Agro-University Complex: Science and Higher Education*, no. 4(68), 2022, pp. 407-418, DOI: 10.32786/2071-9485-2022-04-49.

Zharashuev M.V., Terekulov Z.M., Akshayakov Z.T., Battaev A.Sh. Development of a method for floods and mudflows monitoring in hard-to-reach areas, Proc. of Dagestan State Pedagogical University. *Natural and Exact Sciences*, 2021, Vol. 15, no. 1, pp. 68-73, DOI: 10.31161/1995-0675-2021-15-1-68-73.

DEVELOPMENT OF A MEDICANE-INDUCED LANDSLIDE INVENTORY; CASE STUDY OF 2023 CYCLONE DANIEL, CENTRAL GREECE

SOTIRIS VALKANIOTIS [1], MARIA TAFTSOGLOU [1], GEORGE PAPATHANASSIOU [2], DOMNA SAMARA [2], CATERINA ZEI [3], THEMISTOKLIS CHATZITHEODOSIOU [4]

[1] *Dept. Civil Engineering, Democritus University of Thrace, Greece,* valkaniotis@yahoo.com, mtaftsog@civil.duth.gr

[2] *School of Geology, Aristotle University of Thessaloniki, Greece,* gpapatha@geo.auth.gr, domnasamara@geo.auth.gr

[3] *Department of Physics and Earth Science, University of Ferrara, Italy,* caterina.zei@unife.it

[4] *School of Civil Engineering, National Technical University of Athens, Greece,* themisto123@gmail.com

Abstract

Cyclone (Medicane) Daniel was a devastating Mediterranean tropical-like cyclone that affected Greece during September 4-8 2023. Severe rainfall in central and southern Greece led to widespread landslides and flooding that caused more than 2 billion euros in damages. Flooding in Thessaly region surpassed 1 million hectares, the largest recorded flood event in recent history. The areas most affected by landslides and debris flows was Pilio mountain range along the Aegean coast and the mountainous part of Western Thessaly, along Pindos Mountain range, where severe mass wasting was also documented during Medicane Ianos in September 2020. Using post-event satellite imagery (WorldView, Planet and Copernicus Sentinel-2), and field surveys a detailed inventory of more than 3,000 landslides was recorded within an area of 2,7000 km^2 in the mountainous part of Western Thessaly. Numerous damaging debris flows and debris floods were also mapped along most of the major rivers and streams of this area. Most landslides were shallow landslides of few meters up to 20-30 meters, but also a major number of large (up to 0.2 km^2) earth and rock slides were also mapped. The largest rock slide (Pirra landslide), documented in detail by a field and UAS survey, occurred at the ridgeline above Pirra settlement, Trikala region. Pirra slide created a landslide dam that blocked a small ephemeral stream and led to the creation of a small ~7,000 m^2 lake that persists seven months after the event. The detailed landslide inventory shows a narrow concentration that is interpreted to be related with the significant local variations of heavy rainfall, and also a strong correlation with either highly susceptible geological formations or prehistoric/inactive large/giant landslides. The Daniel landslide inventory (2023) is also compared with the inventory of Medicane Ianos (2020), as they have a similar distribution along the same area, and also have a significant overlap.

Key words

Landslides, inventory, Medicane, Daniel, remote sensing, Greece,

1 Introduction

Severe meteorological phenomena such as storms, hurricanes and cyclones have devastating impact on the population, infrastructure but also the natural environment. Apart from flooding, these events usually trigger numerous landslides along the impacted areas (Larsen 2008). Mapping and studying of these landslide are necessary steps towards understanding and mitigating these types of natural disasters.
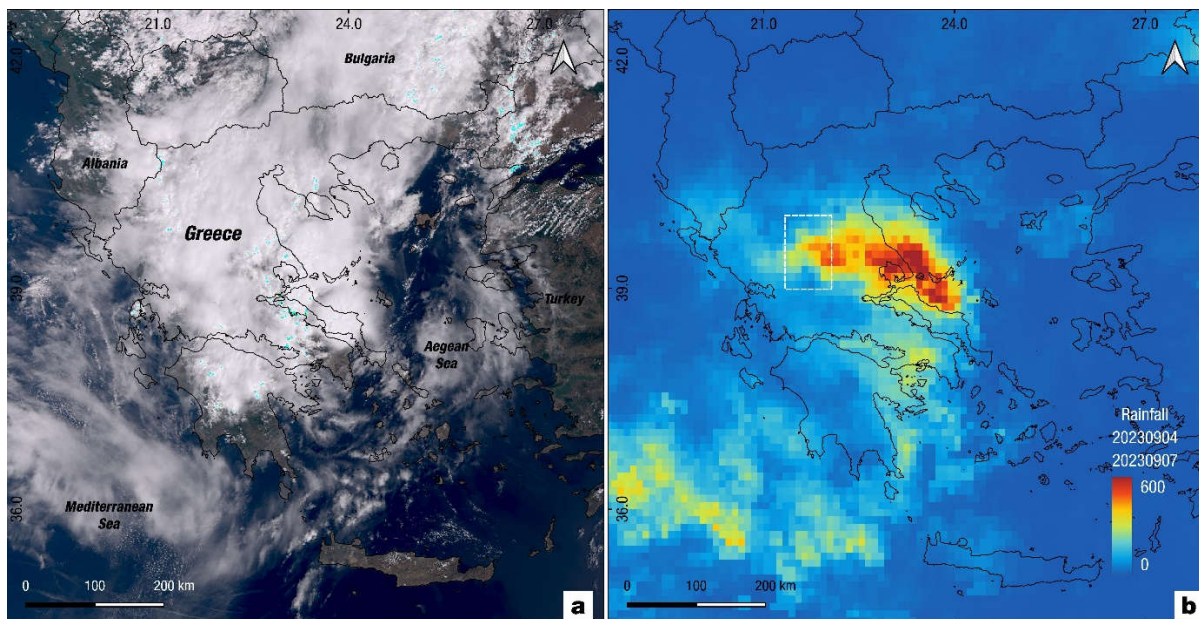
Figure 1. a) Copernicus Sentinel-3 satellite image from Cyclone Daniel landfall, September 4 2023. b) Accumulated rainfall from satellite measurements (NASA GPM) from September 4 to September 7 2023. White dashed rectangle marks the study area in western Thessaly.
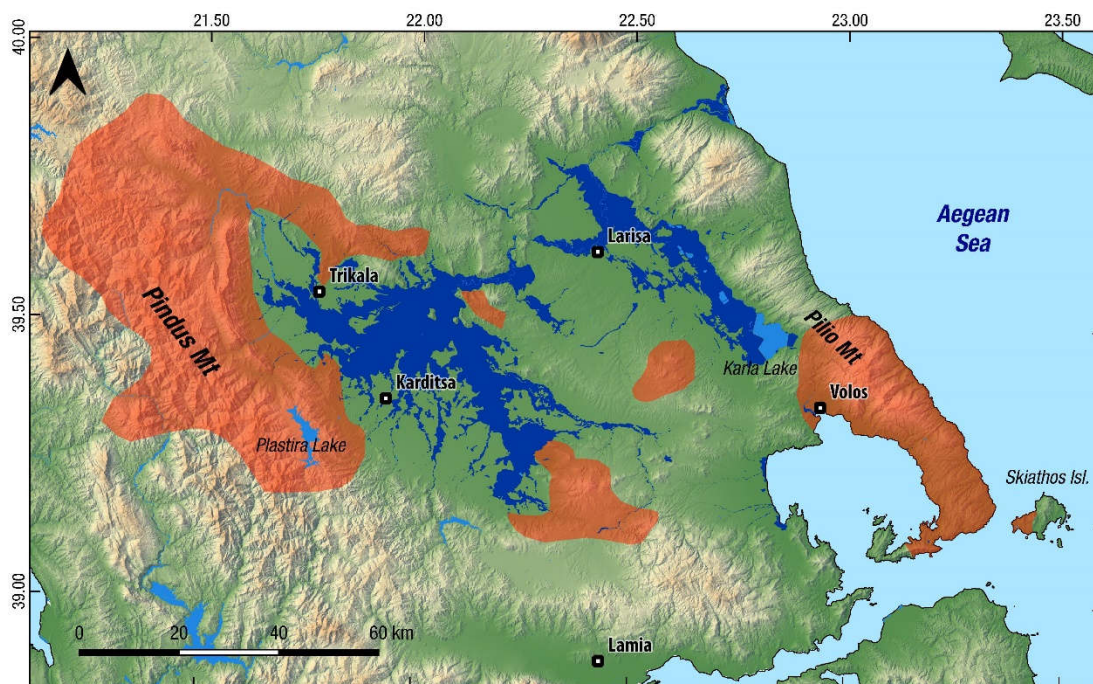
Figure 2. Overview of the effects of Medicane Daniel in Thessaly region. Dark blue color marks the cumulative flooded areas during and shortly after the landfall (September 2023), mapped from Landsat 8 and Sentinel-2 satellite imagery. Total flooded area exceeds 1400 square kilometers. Major landslide affected areas are marked with orange polygons, based on satellite mapping.

The Mediterranean Basin is one of the most cyclogenetic regions worldwide as a result of its characteristic morphology. Medicanes (Mediterranean hurricanes), a concatenation of Mediterranean Sea with hurricanes, resemble tropical cyclones but present certain differences like much shorter expected lifespan (Miglietta 2019).

Medicane Ianos (September 2020) was the first devastating event that led to extensive destruction in Greece, including flooding, serious damages to infrastructure and numerous landslides (Lekkas et al

2020; Zekkos et al 2020; Lagouvardos et al 2022). A large number (>2000) of landslides were triggered by Ianos in the mountainous area of western Thessaly (Valkaniotis et al 2022). Cyclone (Medicane) Daniel, three years after Ianos, landed on Greece in September 2023. From September 4 up to September 7 2023, central Greece and especially Thessaly region, experienced severe rainfall exceeding 1000 mm at places (Figure 1). More than 1400 km² of Thessaly were flooded during this event (Figure 2). Debris flows and floods in mountainous watersheds and torrents led to serious damages of property and infrastructure in most parts of Thessaly. Southern Pilio mountain and the mountainous area of western Thessaly (Pindos mountain range) experienced thousands of landslides triggered by Cyclone Daniel (Lekkas et al 2023; Qiu et al 2023). We focused on the landslides triggered in the western Thessaly region, in order to develop an event-based landslide inventory.

2 Data and Methods

2.1 Remote sensing data

We acquired all available USGS Landsat 8/9 (15 meters ground resolution) and Copernicus Sentinel-2 (10 meters ground resolution) satellite imagery after the event, covering the dates of September 8 up to September 15 2023. Additional frames of Planet imagery (3-4 meters ground resolution) was acquired over the study area with multiple dates (September 8 – September 14). Parts of the study area were covered by early post-event very high resolution (<2 meters ground resolution) satellite imagery (WorldView-3, SPOT, GeoEye-1) that were acquired through Copernicus Data Archive.

A series of post-event field surveys in the study area (Trikala – Karditsa, Thessaly) were performed in the days following the event. During these surveys, satellite imagery rapid mapping was verified and checked in the field. In more than 15 locations, UAS photogrammetric surveys were executed in sites where major landslides occurred.
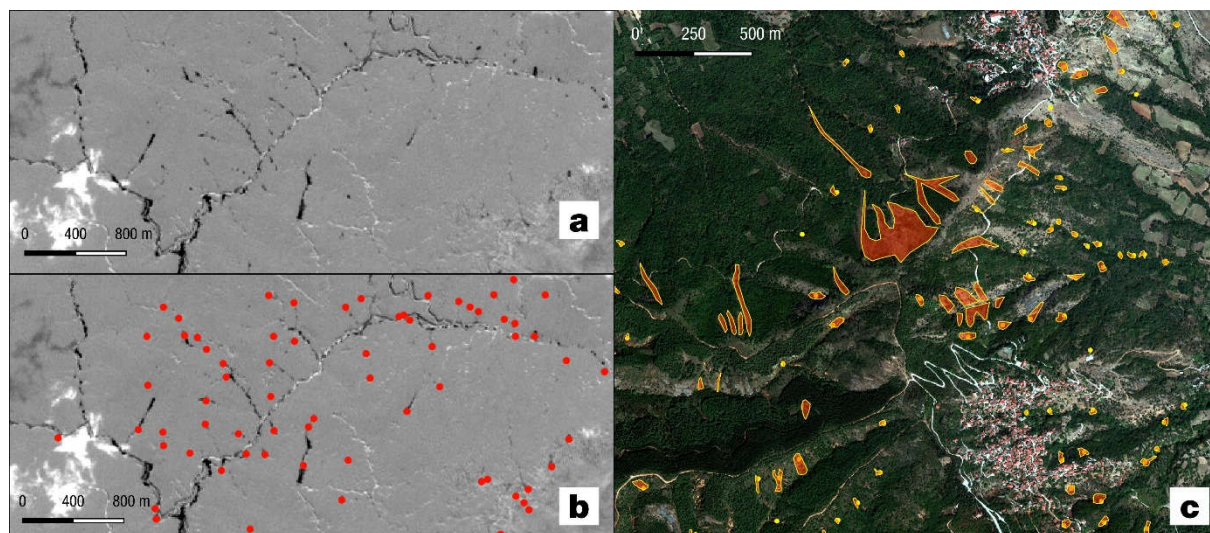
Figure 3. a) Example of landslide mapping using Sentinel-2 band 04 normalized difference index as an aid. Dark colors are areas that changed between the two dates and can mark the location of landslides. b) Same view with mapped landslide locations as red dots. c) Mapped landslide polygons (orange) over a WorldView-3 image (Fanari/Kanalia settlements, Karditsa).

2.2 Landslide inventory mapping

A preliminary landslide inventory was compiled using high resolution Copernicus Sentinel-2 multispectral imagery (Figure 3). Landslides were mapped using visual inspection, with comparison of

pre- and post-event images. Manual process was assisted by using semi-automatic methods (Valkaniotis et al 2022) such as normalized band differencing (Figure 3).
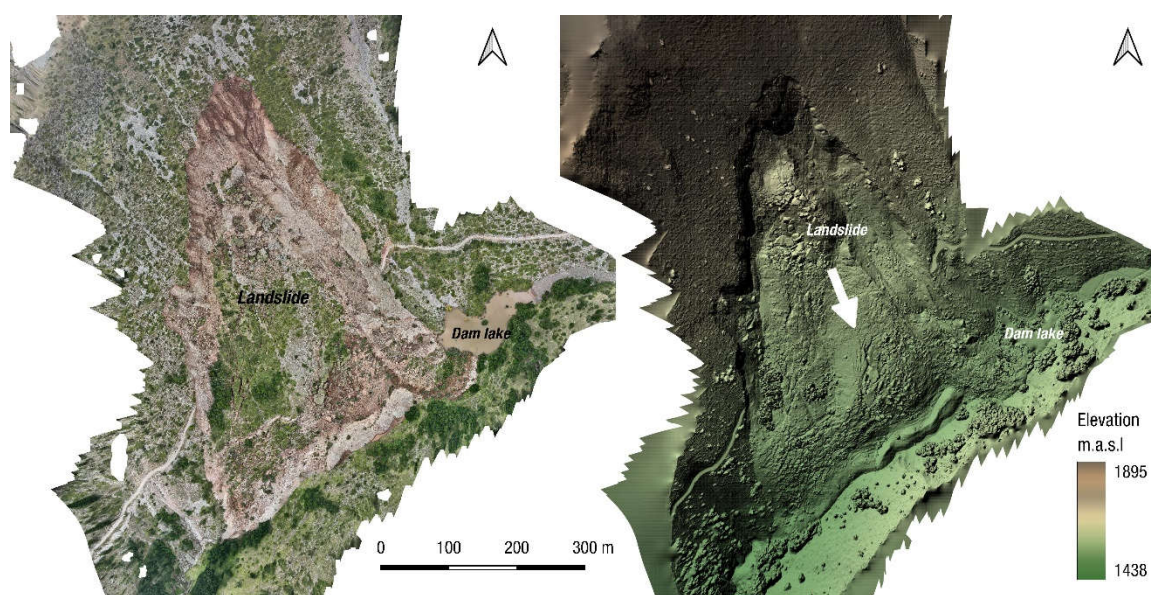
Figure 4. The large landslide dam that was triggered near Pirra settlement, Trikala. Orthophoto map (a) and digital surface model (b) from UAS photogrammetric post-event survey.

After the development of the preliminary rapid mapping landslide inventory, we proceeded with the final event inventory, using Planet and VHR satellite imagery for more detailed mapping of landslide locations and polygons. UAS orthophotos and digital elevation models of major deep-seated landslides were also used for detailed delination. One of the largest landslides with length exceeding 500m was triggered at the Pindos mountain range, near Pirra settlement, Trikala region, and created a small landslide dam lake that persists up to this date (Figure 4).

3   Results

The preliminary landslide inventory of 3,278 landslides is presented in Figure 5. Most of the landslides are found along the Pindos Mountain range, with additional concentrations in the hilly areas north of Trikala and near Mouzaki. A significantly increased number of landslides is expected after the completion of the detailed landslide inventory.

Studying the distribution of landslides, we can estimate the area of peak rainfall on the mountainous part of the affected region (Figures 5 & 6) as the one that encloses most of the landslides. A comparison with the Medicane Ianos inventory (Figures 6 & 7) shows the more severe intensity of the Daniel event, that led to more landslides in the same region but also triggered a large number of rockslides and large deep-seated landslides that were quite uncommon for the Ianos inventory. Distribution and density of landslides show a correlation with geological formations susceptible to landslides, but also with local rainfall amount and rain intensity during the three days Daniel event.
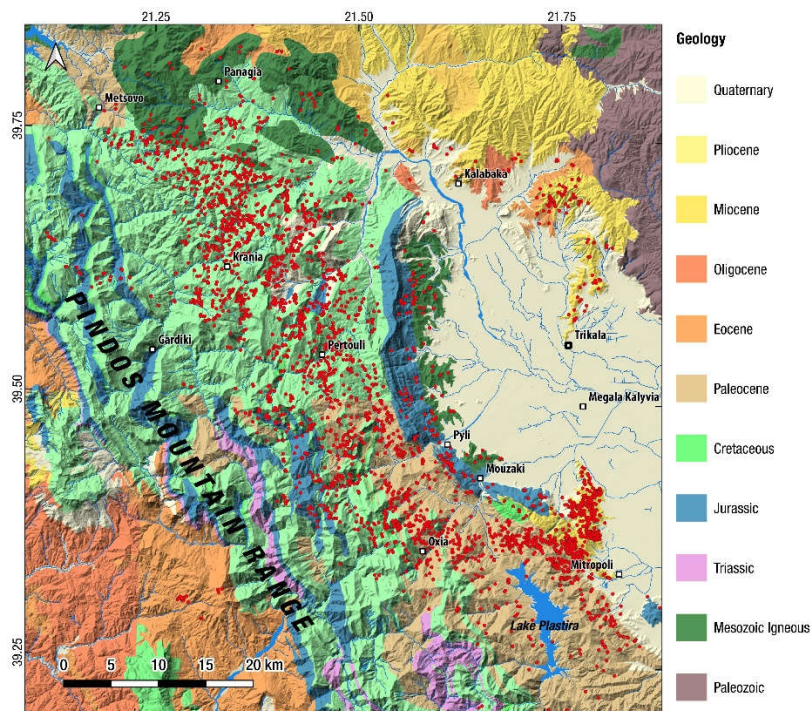
Figure 5. Preliminary landslide inventory (red dots). Simplified geology from Hellenic Survey of Geology & Mineral Exploration (HSGME) geological map sheets.
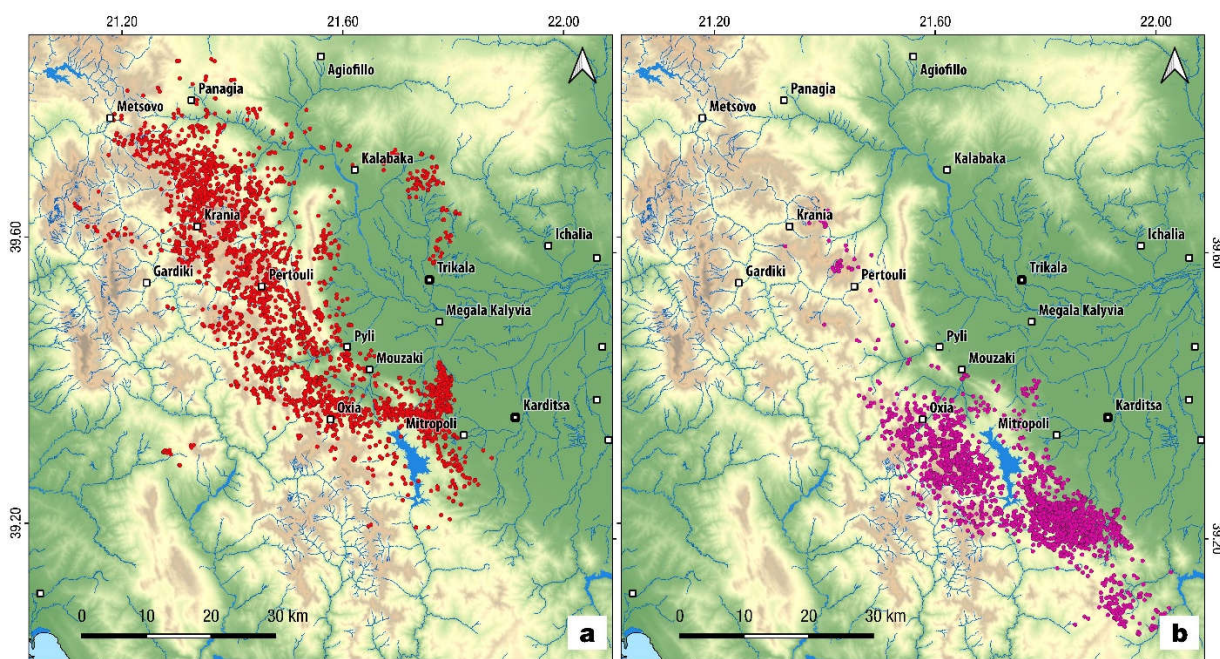
Figure 6. a) Landslides triggered by Cyclone Daniel (red dots, September 2023). b) Landslides triggered by Cyclone Ianos (purple dots, September 2020). Modified after original inventory from Valkaniotis et al. (2022).
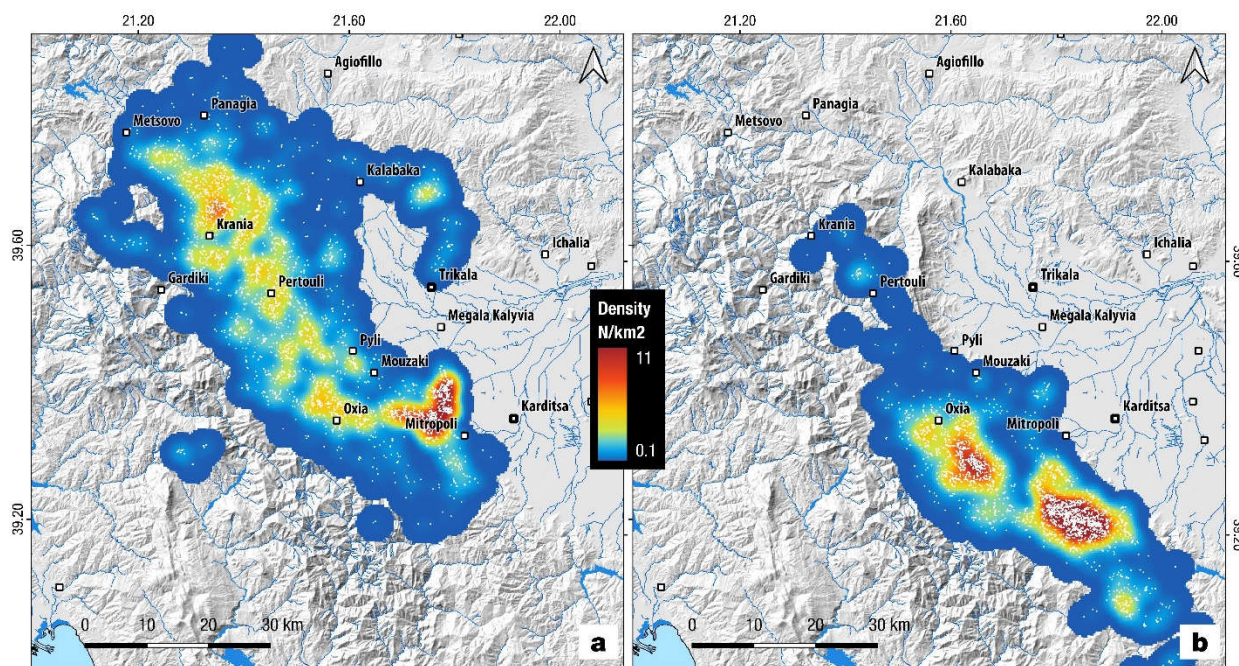
Figure 7. a) Landslide density of Cyclone Daniel (September 2023). b) Landslide density of Cyclone Ianos (September 2020). Landslide locations as white dots. Modified after original inventory from Valkaniotis et al. (2022).

4   Conclusion

We developed a detailed landslide inventory related to Cyclone Daniel (September 2023) at the region of western Thessaly, Greece. More than 3000 landslides were mapped using remote sensing data (Copernicus Sentinel-2 and Planetscope imagery) and also verified and enriched from a series of field surveys after the event. This area was also affected by Cyclone Ianos in September 2020 (Valkaniotis et al. 2022), that triggered ~2000 landslides with a significant areal overlap in both inventories. Even without including the numerous landslides that were simultaneously triggered by Cyclone Daniel in eastern Thessaly (Magnesia, southern Pilio Mountain range and Sporades islands), the western Thessaly inventory alone classifies this as the most severe landslide event documented in detail in modern Greece. The detailed landslide inventories developed for both Cyclones (Ianos and Daniel) are a valuable tool to study Medicane effects in SE Europe and especially assessing future hazard from similar weather-related events in Thessaly region, Greece.

References

Lagouvardos, K.; Karagiannidis, A.; Dafis, S.; Kalimeris, A.; Kotroni, V. Ianos—A hurricane in the Mediterranean. *Bull. Am. Meteorol. Soc*. 2022, 103, E1621–E1636

Larsen M.C. Rainfall-triggered landslides, anthropogenic hazards, and mitigation strategies. *Adv. Geosci.* 2008, 14, 147–153

Lekkas E.; Nastos P.; Cartalis C.; Diakakis M.; Gogou M.; Mavroulis S.; Spyrou N.-I.; Kotsi E.; Vassilakis E.; Katsetsiadou K.-N.; et al. Impact of medicane "IANOS" (September 2020) on Cephalonia and Ithaki Islands. *In Newsletter of Environmental, Disaster and Crises Management Strategies*; National Capodistrian University of Athens: Athens, Greece, 2020; ISSN 2653-9454

Lekkas E.; Diakakis M.; Mavroulis S.; Filis Ch.; Bantekas Y.; Gogou M.; Katsetsiadou K-N.; et al. The early September 2023 Daniel storm in Thessaly region (central Greece). *In Newsletter of Environmental, Disaster and Crises Management Strategies*; National Capodistrian University of Athens: Athens, Greece, 2023; ISSN 2653-9454

Miglietta, M.M. Mediterranean tropical-like cyclones (Medicanes). *Atmosphere* 2019, 10, 206.

Qiu J.; Zhao W.; Brocca L.; Tarolli P. Storm Daniel revealed the fragility of the Mediterranean region. *The Innovation Geoscience*, 2023, 1(3), 100036

Scheip C.M.; Wegmann K.W. HazMapper: A global open-source natural hazard mapping application in Google Earth Engine. *Nat. Hazards Earth Syst. Sci*. 2021, 21, 1495–1511

Scheip C.; Wegmann K. HazMapper v1.0 Source Code (Version 1.0). *Zenodo,* 2020. Available online: https://zenodo.org/record/4103348#.Y43JIX3MJPY

Valkaniotis S.; Papathanassiou G.; Marinos V.; Saroglou C.; Zekkos D.; Kallimogiannis V.; Karantanellis E.; Farmakis I.; Zalachoris G.; Manousakis J.; Ktenidou O-J. Landslides Triggered by Medicane Ianos in Greece, September 2020: Rapid Satellite Mapping and Field Survey. *Geosciences*, 2022. 12(23), 12443, https://doi.org/10.3390/app122312443.

Zekkos D.; Zalachoris G.; Alvertos A.E.; Amatya P.M.; Blunts P.; Clark M.; Dafis S.; Farmakis I.; Ganas A.; Hille M.; et al. The September 18–20 2020 Medicane Iaonos Impact on Greece—Phase I Reconnaissance Report; *Geotechnical Extreme Events Report–Reconnaissance Report*, GEER-068; Geer Association: San Francisco, CA, USA, 2020

CORRELATION BETWEEN JOINT ROUGHNESS COEFFICIENT (JRC) AND STATISTICAL ROUGHNESS PARAMETERS

NIKIEMA TEGAWENDE [1], GONZE NICOLAS [2], DESCAMPS FANNY [3]

[1] *University of Mons, Belgium, tegawende.nikiema@umons.ac.be*

[2] *University of Mons, Belgium, nicolas.gonze@umons.ac.be*

[3] *University of Mons, Belgium, fanny.descamps@umons.ac.be*

Abstract

Rocks are heterogeneous anisotropic media containing discontinuities that influence their mechanical behavior through their surface morphology, aperture, and filling material. Surface morphology is generally characterized by roughness, which is used as an input parameter in analytical or numerical models of rock mass stability.

Quantifying the roughness of discontinuities is a complex operation that requires appropriate methodologies and tools. Barton's Joint Roughness Coefficient (*JRC*) is widely used due to its simplicity for quantifying roughness and addressing joint shear strength. However, the visual comparison method is subjective and may cause biases in the *JRC* estimates. Several authors proposed to rely on statistical estimators to eliminate such bias.

On this basis, the current study examines the added value of 3D optical profilometry for roughness quantification. Typical *JRC* profiles were digitized, and a 3D printer was used to create surfaces reproducing the roughness state of the profiles. These surfaces were analyzed with a 3D optical profilometer to determine statistical estimators. The most relevant estimators are identified and correlations with the *JRC* are proposed. When investigating the mechanical behavior of rock joints, such correlations will help converting statistical roughness estimates from fractures tested in laboratory into comprehensive *JRC* values to address joint shear strength.

Keywords

Discontinuity, Joint Roughness Coefficient (*JRC*), 3D printed surface, optical profilometer, statistical roughness estimates.

1 Introduction

Rock masses are often crossed by joints that significantly influence their mechanical properties and deformation behavior. Particularly, the shear strength of rock joints depends on their surface irregularities, also called roughness. Barton's empirical criterion (Barton, 1973) obtained from shear tests on various types of rock joints; it is known for estimating rock joints shear strength:

$$\tau = \sigma_n \tan\left[JRC \log_{10}\left(\frac{JCS}{\sigma_n}\right) + \phi_b \right] \tag{1}$$

where τ represents the peak shear stress, σ_n is the effective normal stress, *JRC* is the joint roughness coefficient, *JCS* is the joint compressive strength, and ϕ_b is the basic friction angle. Among those parameters, *JRC* is traditionnally estimated by comparison to standard profiles (Barton & Choubey, 1977). This method is widely used in rock engineering, geotechnics and rock mechanics.

The visual assessment method for *JRC*, however, introduces subjectivity depending on operator's estimation and experience (Hsiung et al., 1993; Beer et al., 2002; Grasselli & Egger, 2003). This has led to an increasing interest in finding more objective and reproducible methods to quantify joint roughness. Methods such as standard profiles digitizing or profilometry allow to compute statistical estimators and led to several correlations (Tse & Cruden, 1979; Maerz et al., 1990; Yu & Vayssade, 1991; Tatone & Grasselli, 2010). Good correlations are generally established with the root mean square slope (Z_2) and the structure function (*SF*). These estimators, while effective, are sensitive to sampling intervals, introducing variability in relationships (Yu & Vayssade, 1991). Other correlations involving fractal dimensions have been explored, but deriving distinctive fractal dimensions for roughness profiles with self-affine characteristics remains challenging (Huang et al., 1992; Li & Huang, 2015).

In the current study, two methods are proposed to analyze *JRC* profiles. The first method is the digitization of profiles in order to analyze them in terms of statistical estimators. The second method deals with optical profilometry on 3D printed profiles in order to automate fracture roughness quantification for laboratory samples. Results are compared to literature data to validate the proposed methodologies.

2   Methods

Barton & Choubey (1977) used a comb with a set of teeth estimated at 1 mm diameter over a length of 10 cm to fit the joint surface and draw the corresponding 2D roughness profile. A total of 136 rock joint surface specimens were profiled, in most cases 3 profiles per surface, to obtain the ten standard profiles. The *JRC* values obtained by back-calculation were classified in intervals of two from 0 (lowest roughness) to 20 (highest roughness).

Several parameters have been used by other authors (Tse & Cruden, 1979; Maerz et al., 1990; Yu & Vayssade, 1991; Hsiung et al., 1993; Tatone & Grasselli, 2010; Jang et al., 2014) and the most common are considered in this study: the root means square slope (Z_2), the structure function (*SF*) and the linear roughness (R_L) or roughness profile index (R_p). They are defined as follows:

$$Z_2 = \left[\frac{1}{L}\int_0^L \left(\frac{dz}{dx}\right)^2 dx\right]^{1/2} \approx \left[\frac{1}{N-1}\sum_{i=1}^{N-1}\left(\frac{z(x_{i+1}) - z(x_i)}{x_{i+1} - x_i}\right)^2\right]^{1/2} \qquad (2)$$

$$SF = \frac{1}{L}\int_0^L [z(x_{i+1}) - z(x_i)]^2 dx \approx \frac{1}{N-1}\sum_{i=1}^{N-1}(z_i - z_{i+1})^2 \qquad (3)$$

$$R_P = \frac{\sum_{i=1}^{N-1}[(z_{i+1} - z_i)^2 - (x_{i+1} - x_i)^2]^{1/2}}{L} \qquad (4)$$

where *L* is the length of the profile, *z* is the height of the profile, *x* is the x-coordinate, *N* is the number of *z* differential points.

2.1 Digitization of standard *JRC* profiles

Several steps are required to analyse the *JRC* profiles in terms of statistical estimators. First of all, the ten standard profiles (ISRM, 1978) were scanned with a 100dpi resolution, providing images with 440 pixels for 10 cm and a pixel size of 0.227 mm. This resolution is chosen to comply with the physical roughness determination from profile combs (1mm diameter teeth on a 10 cm length). Every image file is saved in black and white format. A Python code was developed for digitizing the images. X-coordinates are taken at the center of each pixel, while y-coordinates are computed as the median of all

black pixels corresponding to a given x-value (Figure 1). Then, the roughness profile is shaped by linking consecutive points by a linear segment. Other researchers also digitized standard *JRC* profiles with different methodologies and sampling intervals. Their work is summarised in Table 1.

Standard profiles have different horizontal lengths. This observation is similar to that made by Jang et al. (2014). The 7th profile (*JRC 12–14*) is the shortest (95.89 mm) and the 8th profile (*JRC 14–16*) is the longest (100.10 mm). In addition, they are not horizontal, i.e. their reference best-fit straight line is not horizontal (Tatone & Grasselli, 2010) and a rotation is performed in order to align the best-fit line with the horizontal axis. Figure 2 shows the digitized *JRC* 14–16 profile (original profile) and the corresponding one after rotation. After that, a Python code was used to compute roughness estimators for different sampling intervals. The value of each interval was determined from the highest point in the interval to simulate the use of a Barton's comb.

Table 1. Some *JRC* digitizing methods and proposed correlations with statistical estimators.

Digitizing method	Sampling interval [mm]	Proposed correlation	R²	Reference
Profile enlarged 2.5 x X-sampling = 1.27 mm Y-sampling = smooth curve Reference line = mean of all the amplitudes	1.27	$JRC = 32.47 log(Z_2) + 32.20$	0.986	Tse & Cruden (1979)
		$JRC = 16.58 log(SF) + 37.28$	0.984	
Shadow profilometry X-sampling 0.20 mm Y-sampling = center line	0.50	$JRC = 411(R_P - 1)$	0.984	Maerz and al. (1990)
		$JRC = 401(R_P - 1)$	0.973	
Philips digital A3 plotter Profile enlarged 2.4 x X-coordinates 0.6, 1.2 and 2.4 mm Y-sampling = center line	0.25	$JRC = 60.32(Z_2) - 4.51$	0.968	Yu & Vayssade (1991)
		$JRC = 239.27(\sqrt{SF}) - 4.51$	0.968	
		$JRC = 558.68(R_P) - 557.13$	0.951	
	0.50	$JRC = 61.79(Z_2) - 3.47$	0.973	
		$JRC = 121.13(\sqrt{SF}) - 3.28$	0.972	
		$JRC = 559.73(R_P) - 597.46$	0.974	
	1.00	$JRC = 64.22(Z_2) - 2.31$	0.983	
		$JRC = 63.69(\sqrt{SF}) - 2.31$	0.983	
		$JRC = 702.67(R_P) - 699.99$	0.951	
AutoCAD Scanned image in black and white at 1 200 dpi X-sampling: 0.5 mm Y-sampling: manual Reference line = fit-line of all the amplitudes	0.50	$JRC = 51.85(Z_2)^{0.60} - 10.37$	0.960	Tatone & Grasselli (2010)
		$JRC = \left[3.36x10^{-2} + \dfrac{1.27x10^{-3}}{\ln(R_P)}\right]^{-1}$	0.972	
	1.00	$JRC = 55.03(Z_2)^{0.74} - 6.10$	0.977	
		$JRC = \left[3.38x10^{-2} + \dfrac{1.07x10^{-3}}{\ln(R_P)}\right]^{-1}$	0.972	
Origine software Scan image at 1 200 dpi (black and white) X-sampling: 0.1, 0.5, 1.0 and 2.0 mm Y-sampling: center line	0.50	$JRC = 51.16(Z_2)^{0.531} - 11.44$	0.972	Jang et al. (2014)
		$JRC = 73.95(SF)^{0.226} - 11.38$	0.972	
		$JRC = 65.9(R_P - 1)^{0.302} - 9.61$	0.973	
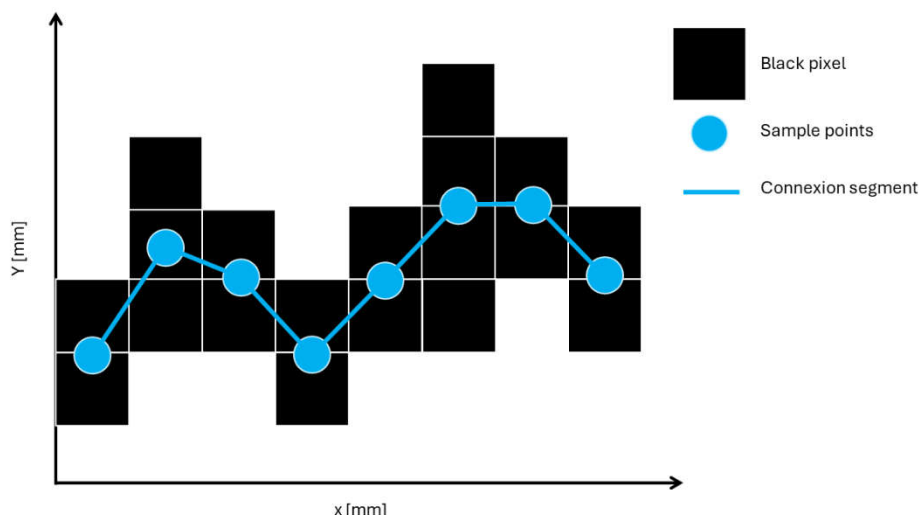
Figure 1. Illustration of the digitization methodology.
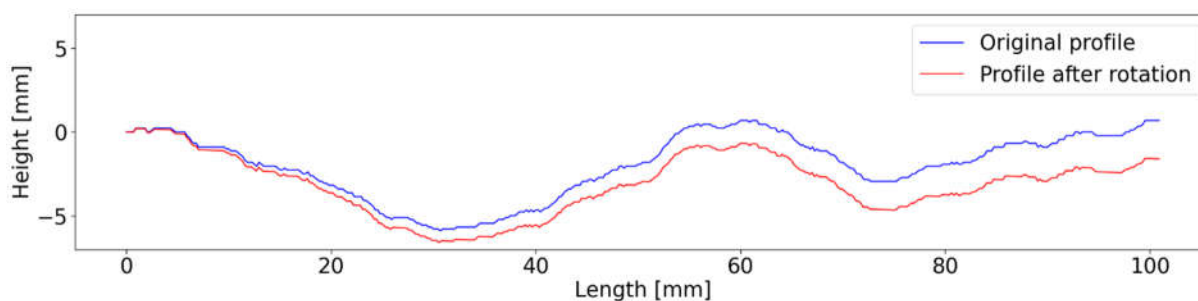
Figure 2. Digitized *JRC* 14-16 profile in its original orientation (blue) and after rotation (red).

2.2 Three-dimensional printing and profilometry

The ten digitized profiles were also printed as 3D surfaces by Elegoo Mars 3 resin printing device, with a resolution of 10 μm in z and 0.035 μm in x and y.

The 3D optical profilometer Keyence VR-6200 has been used to scan the 3D printed surfaces. The profilometer has a resolution of ± 4 μm in z and ±5 μm in x and y directions. It uses optics to create linear fringe projection light through built-in high intensity light-emitting diodes (LED). The light impinges the object diagonally with a precise angle. When there are height differences on the surface of the object, the fringe projection image is distorted in relation to the height difference of the object. The distorted fringe projection image is captured by complementary metal–oxide–semiconductor (CMOS) monochrome cameras from straight above, and the object height is measured from the distortion. When there are no height differences on the impinge surface, the fringe projection light remains undistorted. The profilometer applies the light from both right and left projection units to minimize the influence of the object's shape and orientation. An example of a 3D printed surface and a 3D scanned surface is shown in Figure 3.

The analysis module provided with the profilometer proposes more than 30 statistical estimators, most of them proposed in ISO 4287 (1997), which were examined to look for relation with the *JRC*. These estimators can be determined either from raw measured data or using the stylus mode. The purpose of this mode is to mimic the operation of a mechanical profilometer by simulating the displacement of a stylus along the profile to analyze. This mode enables the user to change the tip radius (from 1 to 500 μm) and the tip angle (from 1 to 120°) of the stylus. Increasing the radius, as discussed below, has the effect of smoothing the profile and eliminating minor vertical variations.

In this study, in order to compare methodologies, Z_2 and R_P are considered. The raw data profiles were also processed by the Python code developed for the scanned profiles to compare and validate the different approaches (Barton's comb and stylus mode).
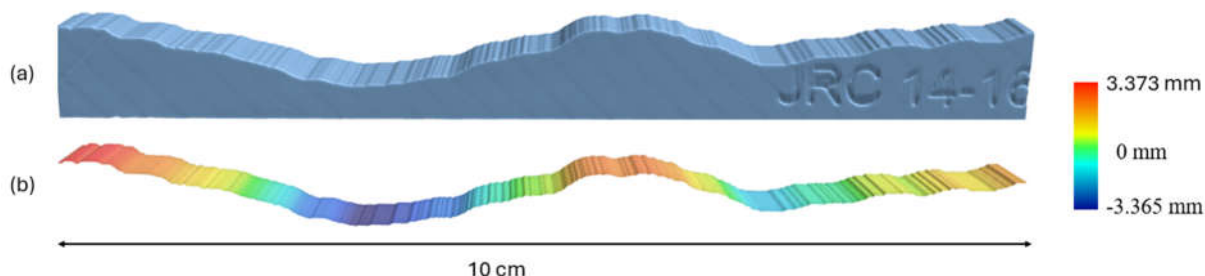
Figure 3. Illustration of 3D printed *JRC* 14-16 profile (a) and the corresponding scanned profile (b).

3   Results

First, the dependency on the sampling interval is investigated. All the estimators vary according to the sampling interval, as illustrated for Z_2 (Figure 4a) and R_P (Figure 4b). The variation is non-linear and statistical estimators tend to decrease when the sampling interval increases. The influence of the sampling interval decreases significantly as the interval increases, and becomes negligible for an interval close to 1 mm. The values of *JRC* 6–8 are similar to those of *JRC* 8-10.
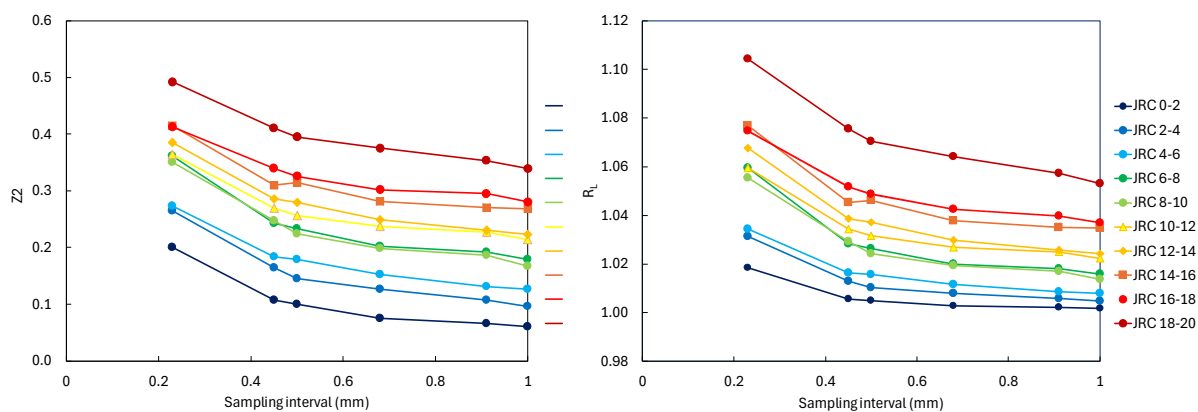
Figure 4. Influence of sampling interval on statistical estimators of JRC. (a) Z_2. (b) R_P.
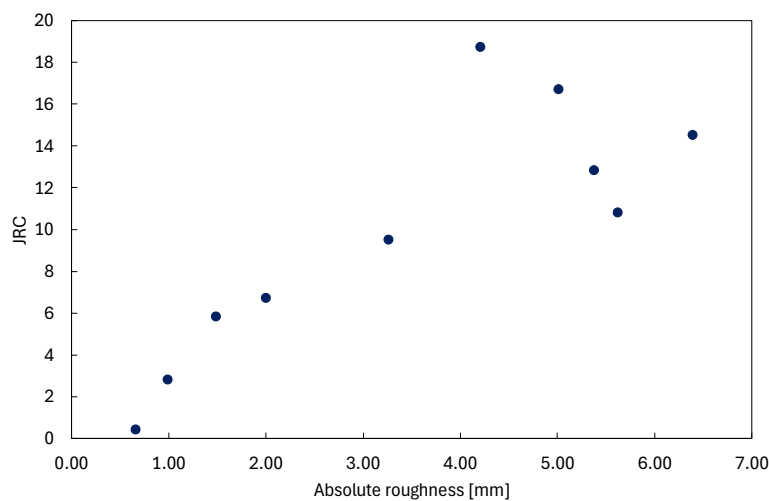
Figure 5. Absolute roughness of the standard *JRC* profiles.

The parameters that do not consider the differential of the amplitude z (e.g. absolute roughness, arithmetic roughness) are poorly correlated with *JRC*. We observe that the absolute roughness of the *JRC* 12–14, *JRC* 16–18, and *JRC* 18–20 profiles is smaller than those of the immediately preceding profiles (Figure 5).

In agreement with the geometry of profile combs and as proposed by many authors, sampling intervals of 0.5 mm and 1.0 mm are considered for further analysis of roughness estimates. In stylus mode, stylus diameters of 0.5 and 1.0 mm respectively are considered.

Z_2 is probably the most used estimator for *JRC* (Tse & Cruden, 1979; Yu & Vayssade, 1991; Tatone & Grasselli, 2010). The relationship between *JRC* and Z_2 is illustrated in Figure 6a and b. Z_2 estimated from digitized profiles and from profilometry give consistent results and are also very close to previously published data. For a 1.0 mm sampling interval, data from both methods even overlap each other. On those graphs, Z_2 is also obtained from the stylus mode of the profilometer. In this case, data are shifted to the right. The offset is about 0.1 for all profiles and whatever the sampling interval and can be explained by the implementation of the stylus mode on the profilometer which does not reproduce the physical principle of a profile comb. Linear correlations are proposed between Z_2 and *JRC* (Table 2).

Similarly, *JRC* vs R_P plots are proposed in Figure 6c and d. Again, R_P computed from digitized profiles and from profilometer are consistent with literature data and overlap on Figure 6d. R_P is linearly correlated with JRC (Table 2). The stylus method gives slightly different results and, in this case, the regression lines are not parallel to the others.

SF is addressed in Figure 6e and f. This statistical estimator has not been used by many authors and literature data show some discrepancy. Our results fit quite well with Yu & Vayssade's ones (1991). Similarly to them, we observe a linear correlation between $\sqrt{SF}$ and *JRC*. For the digitized and the profilometric calculating method, the regression curves are close to each other when the sampling interval is 0.50 mm, and they even overlap when the sampling interval is 1.00 mm.

Table 2. Correlation equation between JRC and Z_2, SF and R_p for sampling intervals 0.50 mm and 1.00 mm.

	Sampling interval = 0.50 mm		Sampling interval = 1.00 mm	
Methodology	Correlation	R^2	Correlation	R^2
Digitized profiles	$JRC = 66.20Z_2 - 6.38$	0.966	$JRC = 67.49Z_2 - 3.32$	0.967
	$JRC = 132.06\sqrt{SF} - 6.376$	0.966	$JRC = 67.154\sqrt{SF} - 3.324$	0.967
	$JRC = 290.7R_P - 290$	0.932	$JRC = 354(R_P) - 351.75$	0.919
Optical profilometer	$JRC = 64.79Z_2 - 5.09$	0.966	$JRC = 66.14Z_2 - 2.93$	0.967
	$JRC = 129.59\sqrt{SF} - 5.091$	0.966	$JRC = 66.138\sqrt{SF} - 2.927$	0.967
	$JRC = 302.18R_P - 300.86$	0.924	$JRC = 349.27R_P - 346.76$	0.908
Optical profilometer (Stylus mode)	$JRC = 65.25Z_2 - 11.21$	0.935	$JRC = 64.87Z_2 - 9.36$	0.949
	$JRC = 238.6R_P - 240.57$	0.924	$JRC = 248.38R_P - 249.39$	0.929
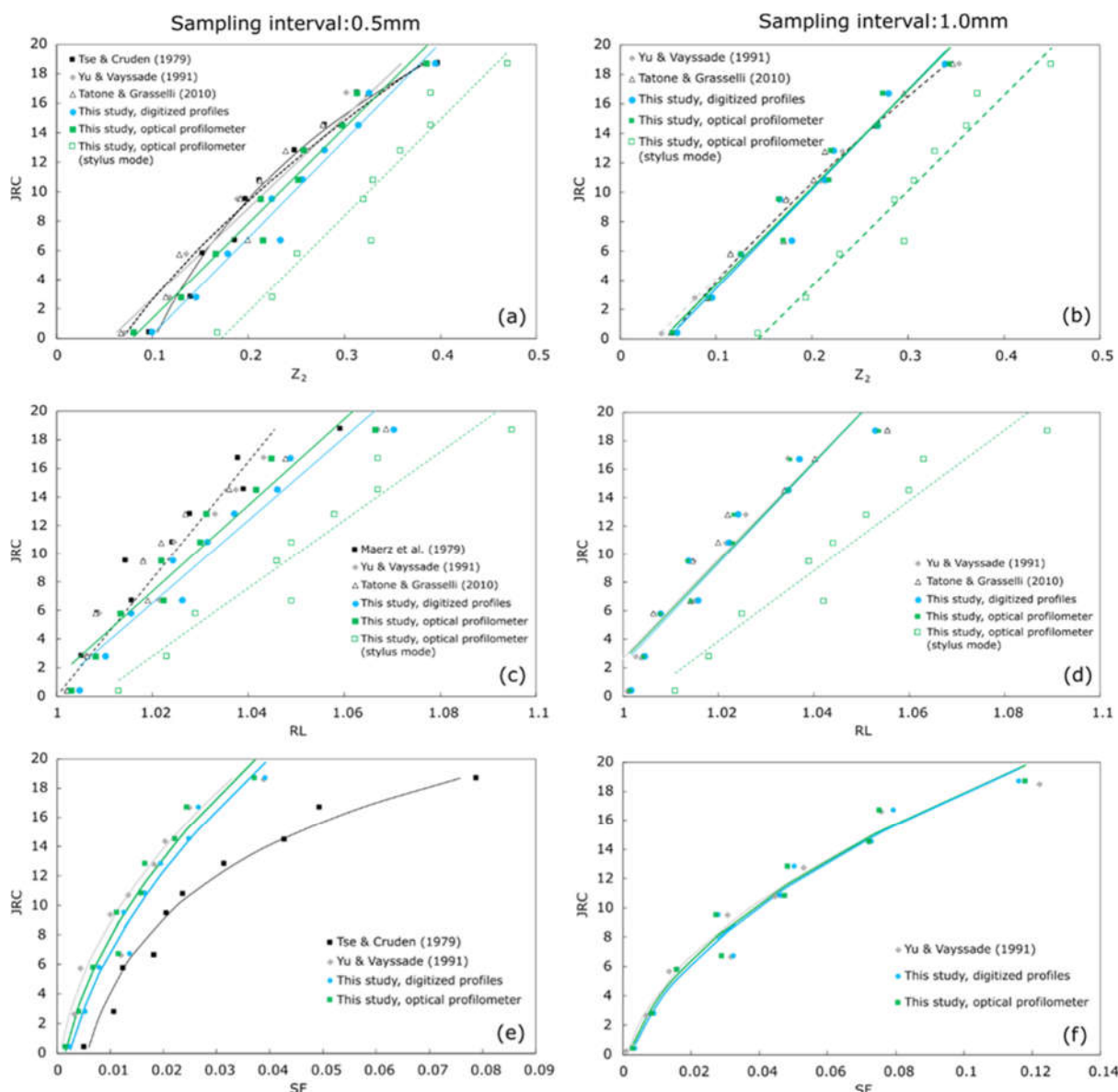
Figure 6. Relationships between statistical estimators and *JRC* for sampling intervals of 0.5mm (a, c and e) and 1.0mm (b, d and f). Estimators are computed from digitized profiles (blue dots) and from profilometry (green squares). For profilometry, stylus mode values are also considered when available (Z_2 and R_P only).

4   Conclusion

This study addresses the quantification of joint roughness using advanced methodologies to overcome the subjectivity and enhance the reproducibility of the *JRC* estimation. The ten Barton' standard profiles have been digitized, printed into 3D surfaces and scanned with an optical profilometer. The most common statistical estimators (Z_2, R_P and *SF*) have been calculated in order to explore for correlation with *JRC*. Our results generally fit with the ones proposed in literature (Tse & Cruden, 1979; Yu & Vayssade, 1991; Tatone & Grasselli, 2010; Maerz et al. 1990). For Z_2 and R_P, a stylus mode is available with profilometric measurement. This method gives slightly different results but the data are still well correlated with *JRC*. In future work on geometric characterization of fracture roughness, such statistical estimates from profilometer can be considered as an efficient tool for automated description of laboratory fracture surfaces.

References

Barton, N. Review of a new shear-strength criterion for rock joints. *Engineering Geology*. 1973, *7* (4), 287–332. DOI: 10.1016/0013-7952(73)90013-6

Barton, N., & Choubey, V. The shear strength of rock joints in theory and practice. *Rock Mechanics Felsmechanik Mécanique Des Roches*. 1977, *10* (1–2), 1–54. DOI: 10.1007/BF01261801

Beer, A. J., Stead, D., & Coggan, J. S. Technical Note Estimation of the Joint Roughness Coefficient (JRC) by Visual Comparison. *Rock Mechanics and Rock Engineering*. 2002, *35* (1), 65–74. DOI: 10.1007/s006030200009

Grasselli, G., & Egger, P. Constitutive law for the shear strength of rock joints based on three-dimensional surface parameters. *International Journal of Rock Mechanics and Mining Sciences*. 2003, *40* (1), 25–40. DOI: 10.1016/S1365-1609(02)00101-6

Hsiung, S. M., Ghosh, A., Ahola, M. P., & Chowdhury, A. H. Assessment of conventional methodologies for joint roughness coefficient determination. *International Journal of Rock Mechanics and Mining Sciences & Geomechanics Abstracts*. 1993, *30* (7), 825–829. DOI: 10.1016/0148-9062(93)90030-H

Huang, S. L., Oelfke, S. M., & Speck, R. C. Applicability of fractal characterization and modelling to rock joint profiles. *International Journal of Rock Mechanics and Mining Sciences & Geomechanics Abstracts*. 1992, *29* (2), 89–98. DOI: 10.1016/0148-9062(92)92120-2

ISO 4287. *Geometrical Product Specifications (GPS) - Surface texture: Profile method - Terms, definitions and surface texture parameters*. 1997

ISRM. *Suggested methods for the quantitative description of discontinuities in rock masses*. 1978.

Jang, H. S., Kang, S. S., & Jang, B. A. Determination of Joint Roughness Coefficients Using Roughness Parameters. *Rock Mechanics and Rock Engineering*. 2014, *47* (6), 2061–2073. DOI: 10.1007/s00603-013-0535-z

Li, Y., & Huang, R. Relationship between joint roughness coefficient and fractal dimension of rock fracture surfaces. *International Journal of Rock Mechanics and Mining Sciences*. 2015, *75* , 15–22. DOI: 10.1016/j.ijrmms.2015.01.007

Maerz, N. H., Franklin, J. A., & Bennett, C. P. Joint roughness measurement using shadow profilometry. *International Journal of Rock Mechanics and Mining Sciences & Geomechanics Abstracts*. 1990, *27* (5), 329–343. DOI: 10.1016/0148-9062(90)92708-M

Tatone, B. S. A., & Grasselli, G. A new 2D discontinuity roughness parameter and its correlation with JRC. *International Journal of Rock Mechanics and Mining Sciences*. 2010, *47* (8), 1391–1400. DOI: 10.1016/j.ijrmms.2010.06.006

Tse, R., & Cruden, D. M. Estimating joint roughness coefficients. *International Journal of Rock Mechanics and Mining Sciences & Geomechanics Abstracts*. 1979, *16* (5), 303–307. DOI: 10.1016/0148-9062(79)90241-9

Yu, X., & Vayssade, B. Joint profiles and their roughness parameters. *International Journal of Rock Mechanics and Mining Sciences & Geomechanics Abstracts*. 1991, *28* (4), 333–336. DOI: 10.1016/0148-9062(91)90598-G

EVALUATING TECHNICAL AND ECONOMICAL ASPECTS OF CONVENTIONAL AND MTBM METHODS FOR DAM DIVERSION TUNNELS - THE CASE OF THE TRIANTAFYLLIA DAM

CHRISTINA NTEMIROGLOU [1], VASSILIS MARINOS [2], SERA LAZARIDOU [3]

[1] *National Technical University of Athens, Greece, christidem@gmail.com*

[2] *National Technical University of Athens, Greece, marinosv@civil.ntua.gr*

[2] *Hydroexigiantiki Consulting Engineers, Greece, slazaridou@hydroex.gr*

Abstract

Hydraulic tunnels and particularly diversion tunnels are crucial for dam operations, since they ensure dry conditions during construction and served as water intakes or evacuators during operation. It is undeniable that the dam type and construction rate significantly affect diversion tunnel design which is highly related with the hydrological and hydraulic calculations. This paper aims to evaluate technical and economical aspects of either conventional or mechanized by microTBM excavation methods. The case study of this research is the Triantafyllia dam in Greece, which is built on gneissic rock masses. Key components included analysing hydrological processes and designing the hydraulic and geotechnical aspects of the diversion tunnel, considering the rock mass qualities. Tunnel diameter alternatives were determined based on the dam type, construction time, and failure mechanisms. Engineering geological sections were created from ground investigation data, while deformations and support measures requirements were assessed using software for critical areas. The suitability of several microTBM machines was also examined. Finally, costs for each scenario were examined.

Key words

Conventional and Micro-Tunneling methods, Dam Diversion Tunnels, Gneiss rock masses, GSI, TBC, Technical – economical comparison, TBM selection, Hydrology, Hydraulics.

1   Introduction

Hydraulic tunnels are among the most significant components in the suite of projects associated with a dam. These tunnels are categorized into intake tunnels, reservoir drainage tunnels, and diversion tunnels, whose functions overlap and complement each other upon the completion of construction works. According to Afshar et al. (1994) diversion systems significantly impact the construction timeline, and its cost constitutes a substantial portion of the overall project budget. Typically, the choice of diversion system capacity and the dimensions of its components involves both socioeconomical and technical considerations. This kind of tunnels, have a special interest as their proper design and efficient operation ensure the required dry conditions for the optimal construction of the dam. It is observed that the diameter of the diversion tunnel is directly dependent on the hydraulic design of the upstream area, a critical factor of which is the parameter of the return period. This, in turn, is heavily dependent on the type of dam as it is related to the risk of failure and the required construction time of dam. However, it is widely accepted that in the scientific community, there has been a lack of research comparing the technical and economical aspects of tunnel excavation methods and the consequent excavation time, while considering the type of dam and its effect on the hydraulic design of the upstream area.

The purpose of this paper is to further examine the dependency of these factors and additionally to conduct a technical and economical comparison of conventional and mechanical tunnel excavation

methods, using microTBM, for various diversion tunnel diameters. This framework is applied to the case of the Triantafyllia dam in Northern Greece, which is founded on a gneissic rock masses, slightly to moderately fractured.

2   Methods

2.1 Input data and utilized software

The primary data for this study were collected from the preliminary and final design reports of the Triantafyllia dam (Hydroexygiantiki L. S. Lazaridis & Co., 1999) which were processed and utilized for the geotechnical evaluation with the aim of proposing new alternative design scenarios for the diversion tunnel.
More specifically, the primary data included drawings such as the horizontal layouts and typical cross-sections of the dam and the diversion tunnel in order understand the current location and the dimensions. Moreover, through the evaluation of the ground investigation program, and particularly photographic material from the geological core boxes, useful data were obtained for designing the geotechnical longitudinal section of the diversion tunnel. Additionally, the results of laboratory tests, such as point load tests, uniaxial compression tests, tensile tests (Brazilian test) as well as the results of on-site tests, specifically permeability tests (Lugeon, Maag) were included to examine the appropriate type of microTBM, for the geotechnical assessment and also for the study of tunnel failure mechanism. Finally, the hydrological and hydraulic calculation reports of the project, along with its technical report, were particularly useful for the up-to-date hydrological and hydraulic design.
In our study, advanced geotechnical software played a pivotal role in the analysis and assessment of key parameters. Geotechnical software, specifically Unwedge by Rocscience Inc., was employed to evaluate the stability of wedges, while also RS2, another software by Rocscience Inc., was utilized for conducting geotechnical simulations. These simulations were conducted to investigate the resistance provided by the support system and to calculate the convergence and ultimate deformations following excavation. Regarding the subject of the hydrological study, the QGIS software was used in order to calculate the basic geometrical characteristics of the basin of Triantafillia and also the HEC-HMS software from the U.S. Army Corps of Engineers was used, while for the flood wave routing through the diversion tunnel, an appropriate programming environment in R was developed.

2.2 Methodology

In order to investigate the engineering geological background, we evaluated the boreholes that were executed as part of the geological study and we compared this information with the Geological Map of Greece by the Institute of Geological and Mining Research. The Geological Strength Index (GSI) system to classify the rocky formations of gneiss and granitic gneiss (V. Marinos, 2007) was used. Based on the combination of these data, we separated three engineering-geological units, TS I, TS II and TS III, as elaborated bellow. Moreover, considering the height of the overburden and the uniaxial compressive strength σ_{ci}, we determined the tunnel behavior modes, based on the Tunnel Behavior Chart (TBC) (Marinos, V. 2012) for each geological section.
The hydrological study was conducted for a return period of 100 years, in accordance with the Greek specifications for the development of flood protection projects and international and Greek common practice, as well as the engineering judgment depending on the required construction time of the tunnel. Based on the method named Soil Conservation Service (SCS) and utilizing software HEC-HMS, we calculated the final design flood hydrograph for a range of return periods. For the same range, we examined the effect of the diameter of diversion tunnel at the appropriate function of diversion tunnel. The return period is related with the type of the dam and the required construction time.
Following, we examined three different scenarios based both on the method of excavation and on the type of the dam. More specifically, the scenarios I, II, and III were examined, corresponding to an earthen dam with a 3-meter diameter tunnel excavated by conventional method, an earthen dam with a 3-meter diameter tunnel excavated using a micro-Rock TBM, and an RCC dam with a 2-meter diameter diversion tunnel excavated similarly using a micro-Rock TBM, respectively. Also, firstly we examined

the construction of an earthfill dam and the conventional excavation, secondly an earthfill dam and the mechanized excavation method using Micro-TBM and finally a RCC dam and the mechanized excavation method using Micro-TBM. For these cases we determined the required support systems and the suitability of the appropriate Micro-TBM types. We also calculated the cost for each scenario.

3   Case study – Triantafyllia Dam

The Triantafyllia dam is constructed on the homonymous river, approximately 2 km upstream from its outlet to the plain of Florina and about 1.5 km northwest of the settlement of Ano Ydrousa (Figure 1). The purpose of the project is water storage for the irrigation and water supply needs of the plain of Florina, as well as ecological provision, amounting to a volume equivalent to 1 hm³ annually during the irrigation months.

Figure 1. Project location map

The complex of the dam of Triantafyllia consists of individual projects. More specifically, the dam is constructed by stones, its central core is impermeable and it is distinguished into specific main zones. The height of the dam is 75 meters from the foundation of the core, with a crest length of 510 meters and a crest width of 16 meters. Dam reservoir has a dual role in order to provide water for irrigation and water supply. The maximum operating level of the reservoir is 838 m, corresponding to a surface area of 0.486 km² and a volume of 10.08 hm³, while the usable volume is 9.56.Furthermore there is a spillway, which width is 31.5 m and its capacity is up to 375 m³/s). Also, there is a diversion tunnel with a horseshoe cross-section, which diameter is 3 m and its length is up to 705 m.

3.1 Geological background

In the context of the geological study, there were drilled 19 sampling boreholes (Figure 2) from which we mainly evaluated 4, G-12, G-1, G-6 and G-10 at the area of diversion tunnel, two at the right abutment of the dam and one near the ending point of the diversion tunnel.

Figure 2. General layout of the diversion tunnel of the Triantafyllia dam (in red). In dots the sampling boreholes.

According to the geological report of the Preliminary Study and the reports of the consultant, Professor P. Marinos, the wider area is composed of metamorphic, Paleozoic-aged rocks of the Pelagonian Zone.

The gneiss-schist bedrock is extensively covered by weathered lateral colluvium and older fluvial deposits. Specifically, the rocky bedrock at the dam site consists of gneisses-granite gneisses with intercalations of amphibolitic and biotite schists, while aplite veins and lens-shaped concentrations are also present. On the right abutment, the percentage and thickness of amphibolitic-biotite schists increase, while the rocky bedrock is overlain by a thin weathering mantle. Gneiss is characterized by high strength, heterogeneity from its texture, irregular weathering, and shear zones that create fragmented and weathered areas up to 10 meters thick, composed of residual weathered gneiss and clay materials. The area's tectonic structure features folding and faulting. Specifically, a longitudinal fault with a disturbance zone up to few meters wide is present at the lower right abutment, addressed with typical remediation and reinforced with a cement grouting diaphragm. The gneissic rock mass generally has moderate fracturing, resulting in high strength, low deformability, and low permeability. RQD values vary from moderate to high but are lower in intensely fractured zones.

3.2 Engineering geological conditions

In order to evaluate the quality of the formations and to proceed with the longitudinal geotechnical section, and to determine the failure mechanisms, the assessment of RQD, GSI, weathering degree, and σci was conducted.

The degree of fragmentation of the gneiss varies throughout the depth examined. The condition of the rock mass on the right abutment is characterized as compact to fractured, with RQD values ranging from 25% to 98%, and locally fragmented (RQD<25%). The fragmentation zones either have significant thickness (G1), or finally, have small thickness but are frequently interchanged with zones of lesser fragmentation (G6). The fragmentation is less apparent at the toe of the right abutment, although the presence of fragmented zones cannot be entirely ruled out.

Based on the results from the borehole analysis, the rock mass appears slightly to moderately fragmented with an average RQD of 60%. Representative samples are shown in Figure 3 .

a   b
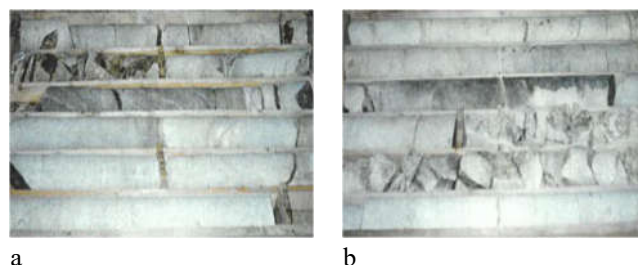
Figure 3. Samples from the drill cores showing that the rock mass is moderately fractured and slightly weathered
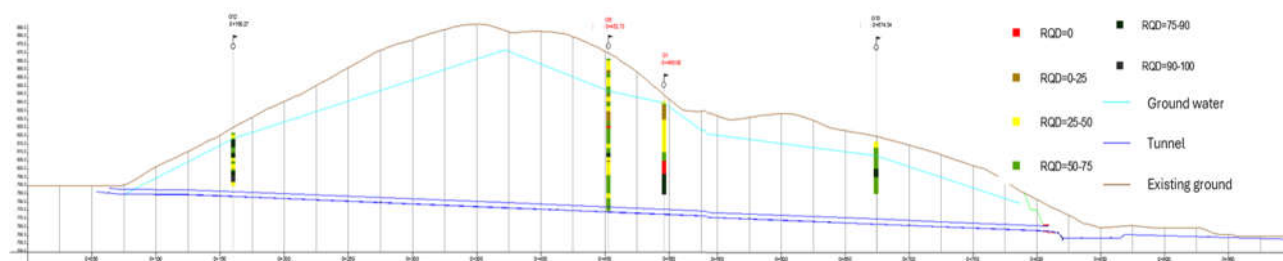
Figure 4. Longitudinal Section of RQD Distribution

Based on the geological map of the Institute of Geological and Mineral Exploration, the site specific geological conditions as well as the data from the boreholes, the geological section of the examined tunnel was evaluated. During the excavation of the diversion tunnel, good-quality rock masses of gneissic and granitic-gneissic nature are expected to be encountered, while at 0+495, a fault is expected

to be encountered, as evident from the geological map and the reduced mechanical characteristics of the rock mass.

For the classification of the rocky formations of gneiss and granitic-gneiss along the tunnel, the Geological Strength Index (GSI) method was used since both gneissic and granitic-gneissic rocks have a clear rocky structure. The GSI for gneissic rock masses was used based on diagram of Figure 5**5**, considering the structure and degree of weathering of the rock mass (V. Marinos, 2007). Specifically, it was considered that a higher degree of weathering occurred in the portal area (category III), while in the rest of the tunnel length, weathering was considered to be of category II. Regarding the structure of the rock mass, it was generally considered blocky-disturbed-seamy and slightly fragmented-undistorted-stratified in areas outside the portals, gneiss and granitic-gneiss outcrops, and the fault zone.

Based on the above, three engineering geological units were considered for the design of this tunnel, depending on the structure and the mechanical properties of the respective rock mass.

In the portal area, a higher degree of weathering (category III) and disturbed/stratified/faulted rock mass were considered, hence the category TSI. In the TSII, i.e., in sections where healthy gneiss and granitic-gneiss are encountered, weathering is significantly lower (category II), while the structure is considered intact to slightly blocky. Finally, in the TSIII where gneissic and granitic-gneissic rocks are present on the surface and in the fault zone area, weathering is again moderate (category II), lower than that of TSII, while in terms of structure, it was characterized as blocky-disturbed-seamy rock mass. The projections of each engineering geological unit appear at Figure 5
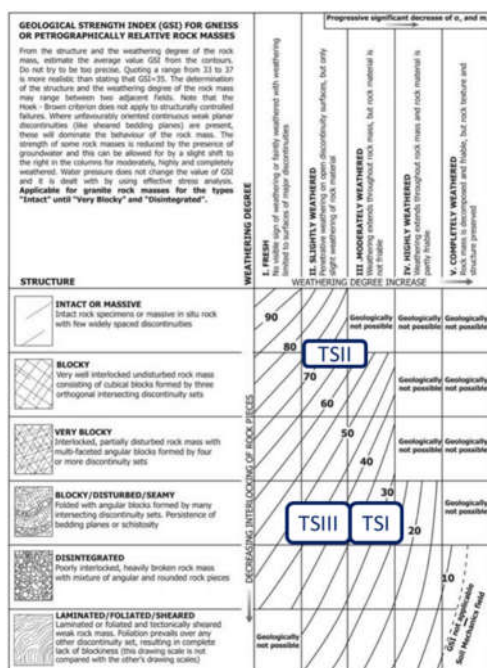
Figure 5. Geological Strength Index (GSI) for Weathered Gneiss Rock Masses (V. Marinos, 2007)

Table 1. Geological properties

Variable	T.S. II	T.S. III
Special Weight (γ) (MN/m³)	0.026	0.026
Rock mass disturbance (D)	0.5	0.5
Elasticity measure of rockmass (E_m)(MPa)	2187.2	192.2
Strenth of intact rock (σ_{ci}) (MPa)	110	30
Strenth of rockmass (σ_{cm}) (MPa)	34.2	2.9
GSI	70	40
m_i	28	28
Poisson ratio (ν)	0.25	0.25
Coefficient of lateral earth pressure (K_o)	0.8	0.8
Friction angle (φ)	40	35
Dilatancy (δ)	10	8.75

To complete the geotechnical assessment process, the magnitude of uniaxial compressive strength σ_{ci} per geological section was determined based on laboratory tests (point load test) conducted during the final study. From the data of the final study approximate values of uniaxial compressive strength σ_{ci} were considered equal to 40, 110, and 60 MPa for TSI, TSII, and TSIII, respectively.

An additional essential characteristic necessary for the geotechnical assessment of the rock mass is the intact rock properties of the geomaterials along the tunnel. Constant m_i, which is related to the frictional properties of the geological formation, and its value is associated with its fabric and the interlocking of its particles. Its determination was based on the method of Hoek and Marinos (2000) which considers results from laboratory tests. More specifically, for the TSI (tunnel portal area), was considered to be 23 (28-5) as the mechanical properties of the gneiss there are more weakened, for the TSII (healthy gneiss and healthy granodiorite), m_i was assumed to be 28, and finally, for the TSIII (fault zone area), a value

of m_i equal to 23 was adopted again due to the diminished mechanical properties.
The deformation modulus Ei of the intact rock was evaluated 12, 5, and 2.5 GPa for TSI, TSII, and TSIII. Finally, the measure of elasticity, the specific weight of the rock mass, was considered to be 0.026 MN/m³, based on the results of the geotechnical study.

3.3 Tunnel behavior and failure modes

Taking into account the structure, the maximum height of the overburden, and the uniaxial compressive strength of the intact rock, potential failure mechanisms per TS were determined based on the TBC chart failure mechanism diagram shown in Figure 6
In general, structurally controlled failures can be only expected along the tunnel. Specifically, the failure type Ch – Wg involves the collapse of a chimney type in combination with wedge-like slides or falls of blocks due to gravity. The rock mass is heavily jointed, maintaining its structure in most cases, while usually exhibiting an open cross-section without good interlocking. This structure, combined with small lateral stresses, may progressively lead to collapses and progressively to over-excavations of the chimney type. The failure type Wg – St is encountered in stable sections with local gravitational failures, which may be characterized by wedge-like slides or falls of blocks due to gravity. Finally, the mechanism Ch – Sh includes chimney-type failure combined with small to moderate deformations and the occurrence of shear failures in small areas around the tunnel. The correlation between each engineering geological unit and the failure mode is shown in Figure 6.
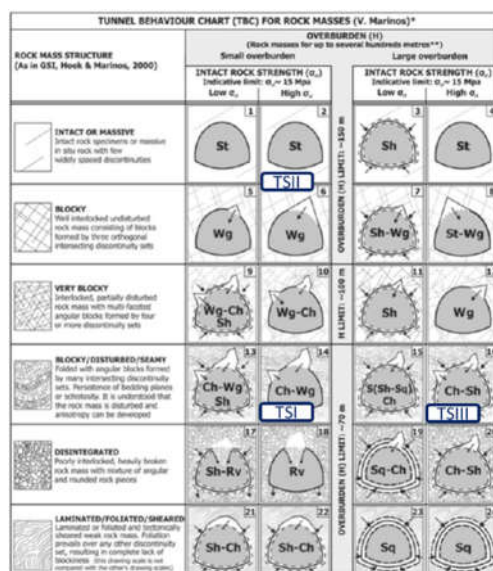
Figure 6: Failure modes (Marinos, V., 2012) – Wg: Wedge failure ,Ch: Chimney failure ,Sh: Shearing failures in shallow zone around the tunnel perimeter ,St: Stable
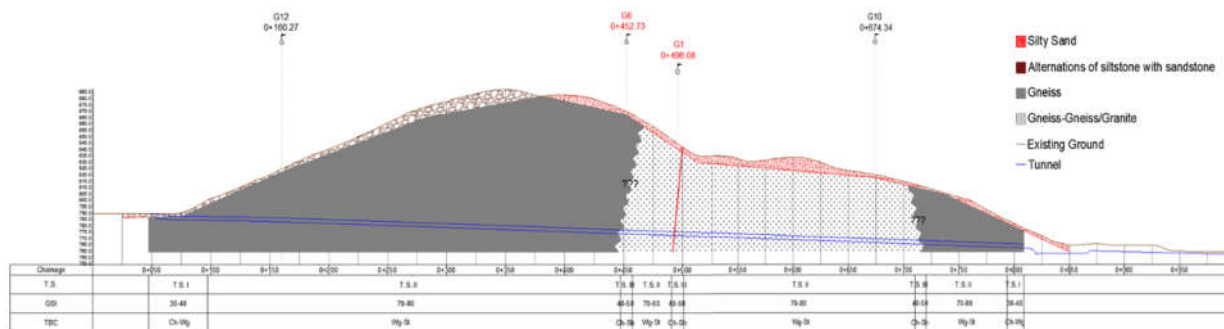
Figure 7: Engineering geological longitudinal section added with tunnel behavior appraisal.

4   Impact of hydraulics on tunnel diameter

Due to the advancements in the science of hydrology since the period when the final study of the Triantafyllia dam was conducted (1999), it was deemed necessary to reevaluate the input flood hydrographs for various return periods according to the construction time of the diversion tunnel, based on new and improved methods.

First of all, the design hydrograph was calculated based on the updated rainfall intensity-duration-frequency curves of the Flood Risk Management Plans of the Ministry of Environment and Energy for the Western Macedonia Hydrological District (EL09), to which the Triantafyllia dam belongs. Following the use of the HEC-HMS software by the US Army Corps of Engineers, the watershed hydrographs were determined for return periods of 10, 20, 50, and 100 years using the PRF 484-unit hydrograph, and the characteristics previously mentioned. The design flood hydrographs for return periods of 10, 20, 50, and 100 years, the effect of the diameter of the diversion tunnel on the routing of the flood volume through it was examined. Specifically, key characteristics were collected, such as the peak outflow ($Q_{max\,out}$), the maximum water height upstream of the tunnel entrance (h_{max}), and the height of the forebay, in an R programming environment. In Figures 8 and 9**Error! Reference source not found.**, the correlation between the return period (T) and the peak outflow ($Q_{max\,out}$) and the maximum water height upstream of the tunnel (h_{max}) is presented for various tunnel diameters (1.5, 2.0, and 3.0 meters).
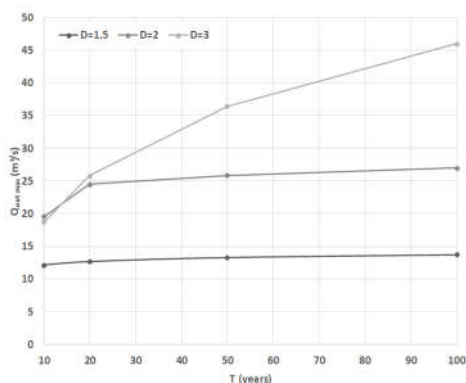
Figure 8. $Q_{max\,outflow}$ as size of return period
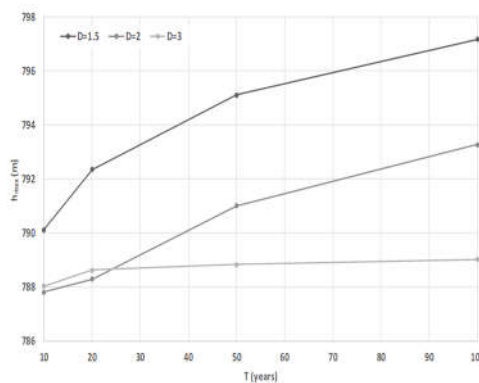
Figure 9. $h_{max\,outflow}$ as size of return period

A crucial factor in selecting the diameter of the diversion tunnel is the required construction time of the dam. More specifically, considering the daily construction rate of the dam depending on its type, a design flood hydrograph is selected with a suitable return period so that the risk of exceedance falls within certain acceptable limits. This risk is calculated according to Equation 1, where N is the expected completion time of the project and T is the return period.

$$r = 1 - \left(1 - \frac{1}{T}\right)^N \tag{1}$$

In the case of an earthen dam, the construction rate typically amounts to around 10 cm/day, while for an RCC dam, this is significantly higher, approximately 30 cm/day. Therefore, for a dam with a height of 75 m, the required time is expected to be 4 years for the earthen type and 2 years for the RCC type, considering an additional year in both cases for unforeseen issues. Based on the above information, it was calculated that considering a design flood return period of 100 years, for an earthen dam, a risk level of 3.9% is within acceptable limits. Similarly, to achieve the same risk level for an RCC dam, a return period of 50 years was chosen, corresponding to a risk level of 4.0%.

The calculations for the maximum peak discharge and the height of the cofferdam were carried out for the various return periods and different diameters of the diversion tunnel in order to understand the correlation between the individual parameters. Considering Figures 8 and 9 it was deemed reasonable to select a diversion tunnel diameter of 3.0 m and a return period of 100 years for an earthen dam. Additionally, for an RCC dam, a diversion tunnel diameter of 2.0 m was selected instead of 1.5 m since, as demonstrated in the right figure, in this case, the forebay height is 4 m lower, thus preferable from an

economical point of view. It is noted that for the RCC dam, the design flood return period was selected as 50 years. All these data are required for the hydraulic calculations and geotechnical design of the diversion tunnel.

5   Comparing conventional and mechanized excavation methods

5.1 Scenario I

Given that the rock mass exhibits distinct joint patterns, it was deemed appropriate to assess their stability using the Unwedge software by RocScience Inc. As evident from the tunnel's layout, this does not maintain the same direction along its entire length. Therefore, the stability of wedges was examined in two sections, A and B, at chainages 0+000 to 0+375 and 0+375 to 0+780, respectively. The orientation in each section was measured at 130° and 55°, respectively, while the gradient along the length is common and equal to 2°. The friction angle was taken as 32°, and the cohesion as 0.06 MPa, according to the data from the final study of the trial tunnel. The details of the discontinuities studied are summarized in Table 2. Additionally, the length of the discontinuities was considered equal to one excavation step, which is 3 m in this case.

Table 2. Elements of Discontinuities

Discontinuities	Orientation
J1	55/025
J2	75/195
J3	80/300
J4	75/115

From the analysis, the discontinuities J1J2J3 and J2J3J4 on the roof in both sections A and B were considered unstable so we proposed the placement of Swellex bolts, with a tensile strength of 0.12 MN, and a length of 2 m, installed in a 2 x 3 pattern (2 m perimeter spacing every 3 m step), as it is showed at Figures 10 to 12.
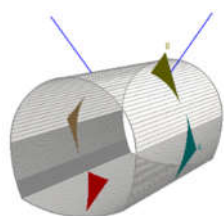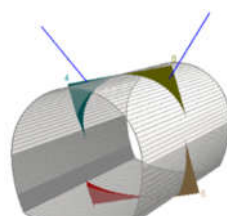
Figure 10. A – J1J2J3   **Figure 11**. A –J2J3J4   **Figure 12**. B –J2J3J4
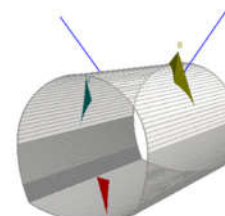
We can expect mainly wedge problems but we also check places where deformations can develop, especially in fault zones and strong disintegration, where GSI, sci and mi are the smallest and the overburden are the highest. Specifically, the cases of maximum overhangs on healthy schist (0+350 – Analysis 1), maximum overhangs on healthy granite-schist (0+475– Analysis 2), and the fault zone in a granite-schist environment (0+495– Analysis 3) were examined. For these areas, longitudinal displacement profiles) and longitudinal development profiles of the failure degree were formed, based on the Chern et al. (1998) method.
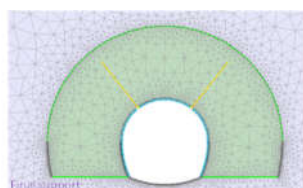
Figure 13. 1 – Final support   **Figure 14**. 2 – Final support   **Figure 15**. 3 – Final support
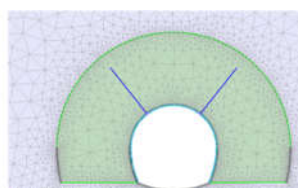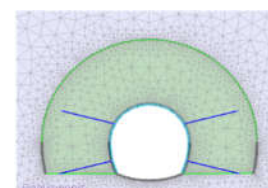
In the simulations, certain basic assumptions were adopted. Specifically, regarding the soil, the rock

mass was simulated as elasto-plastic, assuming isotropic linear elasticity. For simulating the behavior of the geological structure, the Generalized Hoek & Brown failure criterion (2002) was utilized. The parameters used are summarized in Table 1. According to the operation mode of the RS2 software, the disturbance degree D due to excavation is applied across the entire extent of the geological structure. As evident, this does not make sense since the impact of excavation and the subsequent disturbance of the rock mass are concentrated within a disturbance zone, approximately 2.5 m thick around the excavation area (Georgiou et al., 2023), as depicted in Figures 13 to 15.

The support of the underground opening is achieved through the combination of two support sections, A and B. Specifically, section A includes a shotcrete lining with a thickness equal to the minimum recommended by Guidelines for road project studies standards, along with type Swellex expandable rock bolts. Additionally, section B comprises a shotcrete lining and steel lattice girders, along with full-length grouted rock bolts. The properties of the support measures for both proposed sections A and B are presented in Table 3.

The total displacements developed during excavation were calculated to be 3 mm at the crown and 1 mm at the sidewalls, in case of analysis 1 (0+350), 2 mm at the crown and 1 mm at the sidewalls in case of analysis 2 (0+475) and 1.4 at the crown and 0.7 mm at the sidewalls.

Table 3. Recommended support measures

	Analysis 1 & 2 - T.S. II	Analysis 3 – T.S. III
Opening phases	1	1
Excavation step	3	1.5
Shotcrete - C20/25 (cm)	5	15
Bolts	Swellex, 320 kN, L=2 m, 1.0 x 3.0 m	Fully bonded, 160 kN, L=2 m, 1.0 x 1.5 m
Steel sets	-	Lattice Girder, 3 bar, #50, 18.26 mm / Excavation step

Based on the descriptive pricing of public works according to Law 4412/2016 (Government Gazette 147 A / 8-8-2016), the total cost for excavating the tunnel, considering the loading and unloading of rocky materials, excavation, support measures, and labor, was evaluated to be around 8.1 million euros.

5.2 Scenario II

In this scenario, the excavation of the tunnel was examined using a micro-TBM. In order to ensure hydraulic consistency between scenarios I and II and to make the results comparable, the equivalent hydraulic radius of the tunnel was calculated assuming a circular cross-section with a diameter of 3.1 m.

It's worth mentioning that unlike scenario I, where excavation is carried out using the drill and blast method, resulting in rock mass disturbance (D=0.5), in scenario II, excavation is done using micro-TBM, hence the rock mass is undisturbed (D=0). The support of the underground opening is achieved with the direct support section type C, consisting of a shotcrete shell, the properties of which are summarized in Table 4.

The selection of the micro-TBM machine for the excavation of the tunnel of interest is a fundamental aspect. A fundamental element in determining immediate support is the selection of the micro-TBM machine chosen for the excavation of the tunnel in question. For this purpose, an investigation into the applicability of each micro-TBM was conducted, as presented in the longitudinal section in figure 16. From this investigation and based on the characteristics of each tunneling machine, the micro-Rock TBM was considered the most suitable, as it shows good performance over the majority of the tunnel length. The area of particular interest is the fault zone at Station 0+495, where there is a possibility of encountering water. In this area, it is deemed necessary to perform horizontal drilling (prop drilling) and carefully monitor the water flow. For this purpose, it is recommended to locally install piezometers and

subsequently pump the water,or construct reservoirs in the case of low pressure. These horizontal drillings can be carried out either adjacent to the excavation after constructing an appropriate auxiliary tunnel or along the axis of the excavation using the micro-TBM itself.

Figure 16. 1 – Micro-TBM feasibility

The total displacements developed during excavation were calculated to be 1.3 mm at the crown and 0.6 mm at the sidewalls, in case of analysis 1 (0+350), 1 mm at the crown and 0.5 mm at the sidewalls in case of analysis 2 (0+475) and 6 at the crown and 3 mm at the sidewalls.

Table 4. Recommended support measures

	Analysis 4-9
Opening phases	1
Excavation step	1.50
Shotcrete – C20/25(cm)	30

Based on the descriptive pricing of public works according to Law 4412/2016 (Government Gazette 147 A / 8-8-2016), the total cost for excavating the tunnel, considering the loading and unloading of rocky materials, excavation, support measures, and labor, was determined to be 1.9 million euros.

5.3 Scenario III

In this scenario, the alternative case of constructing an RCC (Roller Compacted Concrete) dam was examined. These types of dams are characterized by their high construction speed as they do not require the use of formwork or reinforcement. This significantly affects the diameter of the diversion tunnel, as we expect a lower flood discharge over a shorter period of time, leading to a smaller diameter. Among their advantages are the impermeable nature of the dam body, the minimization of cooling and vibration requirements compared to conventional concrete, and the reduction in cement usage due to the possibility of using industrial by-products. A typical construction rate for RCC dams is approximately 30 cm per day. To achieve a comparable risk level to that of constructing an earthfill dam, the design flood event chosen was a 50-year recurrence interval, and it was deemed reasonable to examine the construction of a tunnel with a diameter of 2 m instead of 1.5 m, due to the significantly smaller height of the headworks. Therefore, in this scenario, the construction of a 2 m diameter diversion tunnel along with the simultaneous construction of an RCC dam is being considered. Moreover, the excavation of the tunnel was examined using a micro-TBM.
The total displacements developed during excavation were calculated to be 0.9 mm at the crown and 0.5 mm at the sidewalls, in case of analysis 1 (0+350), 0.7 mm at the crown and 0.4 mm at the sidewalls in case of analysis 2 (0+475) and 4.8 at the crown and 2.4 mm at the sidewalls at analysis 3 (0+495). Based on the descriptive pricing of public works according to Law 4412/2016 (Government Gazette 147 A / 8-8-2016), the total cost for excavating the tunnel using micro-Rock TBM, considering the loading and unloading of rocky materials, excavation, support measures, and labor, was determined to be 1.0 million euros.

5   Results and Discussion

This study presents a technical and economical comparison of conventional (drilling and blasting) versus mechanical (microtunneling) excavation methods for diversion tunnels, with a focus on how dam type affects tunnel diameter through hydrological and hydraulic considerations. Using the Triantafyllia dam in Florina as a case study, the "as built" design employed the drill and blast method for the diversion tunnel on the right abutment, and an earthen dam was selected. The new approach evaluated literature and project data to develop revised geotechnical conclusions and propose an updated geotechnical design for the tunnel.

Regarding the geotechnical conclusions initially drawn, the surrounding rock mass was categorized into three engineering geological units TSI, TSII, and TSIII, around the portals, in the section of the tunnel where gneiss and granite-gneiss were characterized by good mechanical properties, and in the area around the gneiss and granite-gneiss interface points as well as in the fault area, respectively. As for the main geotechnical characteristics of the individual geotechnical units, we distinguish that overall, it is about a good-quality rock mass except for the fault area and the gneiss and granite-gneiss interface area, where the rock mass is more weakened and has poorer mechanical properties.

Regarding on the behavior of the rock mass in the tunnels and the possible failure modes depending on the maximum height of the overburden, the structure, and the uniaxial compressive strength of the intact rock, the potential failure modes of the rock mass were predicted. More specifically, the dominant failure modes are Ch-Wg, Ch-Sh and St.

Regarding the hydrological aspect, considering the influence of the construction rate of each type of dam, suitable return periods were selected for hydrological and hydraulic calculations. Specifically, with the reasonable assumption of a construction rate of 10 cm/day in the case of an earthen dam and 30 cm/day in the case of an RCC dam, and accounting for delays due to unforeseen problems during construction amounting to 1 year, the completion time was determined to be 4 and 2 years, respectively. With the goal of equalizing the risk considered for design with a return period T and a completion time N, it was deemed appropriate to select return periods of 100 and 50 years for the earthen and RCC dams, respectively.

Subsequently, hydrological calculations were carried out starting from the rainfall curves of nearby stations, from which the design rainfall for each return period was determined and transformed into runoff using the HEC-HMS software. Then, to investigate the influence of the return period on the diameter of the diversion tunnel, an R programming environment model was developed to route the inflow hydrograph, yielding output parameters such as the maximum outflow discharge, the required height of the cofferdam, and the maximum water level at the tunnel entrance. From this investigation for various return periods, the selection of a diameter of 2 and 3 meters and return periods of 50 and 100 years was deemed reasonable for the RCC and earthen dam types, respectively.

Subsequently, the geotechnical design was implemented considering the peculiarities of the surrounding rock mass, while the analyses, both in the case of the drill and blast method and the microtunneling method, were carried out using the RS2 software. All the support measures of the typical sections A, B, C, and D were proved to be sufficient as demonstrated using the RS2 software.

The main criteria for selecting the optimal scenario are the feasibility of support measures, time, and cost. The relevant results for each scenario are presented in Table **5**. It is evident that, based on the assumptions, the excavation of the 2m diameter diversion tunnel using microtunneling with micro-Rock TBM and the construction of an RCC dam are clearly more cost-effective. It is noted that in the technical and economic comparison, only the costs related to the excavation of the diversion tunnel were considered, not the construction of the respective types of dams (earthfill and RCC) and their peculiarities, as this issue does not correspond to the objectives of this study.

Table 5. Results – Scenarios I, II, III

	Scenario I	Scenario II	Scenario III
Diameter	3.0	3.1	2.0
Excavation method	Drill & Blast	Micro-TBM	Micro-TBM
Cost (millions)	8	1.9	1.8
Required time	251 days	21 days	21 days

Obviously, the choice to construct an RCC (Reinforced Cement Concrete) dam as opposed to another type of dam, such as an earthen dam or another type of concrete dam, is also determined by geotechnical conditions and the suitability of construction materials in the surrounding area. Therefore, there is the cost of the diversion tunnel as well as the cost of the dam itself, which is affected by its type and construction materials. The calculation of the cost of the dam itself is not within the scope of this paper. Moreover, although the conventional method appears more time-consuming and costly, it is often chosen because the equipment is already available from previous construction projects, and it does not require more specialized personnel for the excavation and support sequence.

The present study marks the initial steps in developing a methodology for comparing the technical and economical aspects of conventional and Micro-TBM methods for dam diversion tunnels. To enhance its comprehensiveness, it is suggested to parameterize the characteristics of the rock mass, dam embankment, and reservoir area for a more accurate selection of dam type. This would move beyond purely economical and time-based criteria. Additionally, there's a need to focus on peripheral stations to better understand their influence on reducing surface runoff from rainfall curves, thus improving the accuracy of data representation. Further investigation and improvement of the stochastic framework regarding flood event categorization and correlation to flood risk levels is recommended. This could involve generating multiple synthetic hydrographs for each return period instead of selecting individual flood events.

Acknowledgements

References

Afshar A., Barkhordary A., Marino M., Optimizing River Diversion under Hydraulic and Hydrologic Uncertainties, Journal of Water Resources Planning and Management, Volume 120, Issue 1, https://doi.org/10.1061/(ASCE)0733-9496(1994)120:1(36)

Georgiou, D., Benardos, A., & Nomikos, P. (2023). *Effect of the rock mass disturbance due to the tunnel excavation on the tunnel loading, based on numerical simulation. Expanding Underground - Knowledge and Passion to Make a Positive Impact on the World*- Proceedings of the ITA-AITES World Tunnel Congress, WTC 2023, 569–577. https://doi.org/10.1201/9781003348030-69

Hydroexigiantiki S.A., L. S. Lazaridis, Final design of Triantafyllia dam, Florina, 1999

Marinos V. 2007. Geotechnical classification and engineering geological behavior of weak and complex rock masses in tunneling, Doctoral thesis, School of Civil Engineering, Geotechnical Engineering Department, National Technical University of Athens (NTUA), Athens. (In greek)

Marinos V. Assessing rock mass behavior for tunneling. Environmental and Engineering Geoscience. 2012;18(4):327-341Marinos V., M. Benissi, G. Rovolis, K. Korkaris, G. Stoumpos, N. Syrtariotis, K. Aggelidaki, I. Papadatos, M. Panteliadou, D. Papouli, *Innovative assessment methodologies to introduce rock mass behavior into tunnelling - The legacy of Professor Paul Marinos in the Athens Metro*, World Tunnel Congress, Greece, Athens, 2023

Special Secretariat for Water, Flood Risk Management Plans of River Basins in the Western Macedonia Hydrographic District, 2023

Soil Conservation Service, National Engineering Handbook, section 4, Hydrology, U.S. Dept. of Agriculture, U.S. Government Printing Office, Washington, D.C., 197

PREDICTING ROCK TYPE AND QUALITY FROM MWD DATA IN EXPLORATORY DRILLHOLES - FOCUSING ON GEOLOGIC TRANSITION ZONES AND UNCERTAINTY ASSESSMENTS

TOM F. HANSEN [1,2], ZHONGQIANG LIU [1]

[1] *Norwegian Geotechnical Institute, Norway, tom.frode.hansen@ngi.no*

[2] *University of Oslo, Norway*

Abstract

Measure While Drilling (MWD) data, a high-resolution sensor dataset collected during rock tunnel excavation worldwide, is underutilised, mainly serving for geological visualisation. Recent studies have demonstrated that MWD-data can identify rock type and rock mass quality for data from short blasting holes. Currently, there are no reliable, efficient methods in tunnelling to accurately predict rock mass characteristics in advance, which limits planning of advance rock support, excavation design, and the logistical planning for reuse of excavated rock. Traditional exploratory methods, such as geophysics, core drilling, or subjectively interpreted hammer holes, suffer from being time-consuming, costly, and offering insufficient resolution. To overcome these limitations, we employed ensemble machine learning models on MWD sensor data from 24 m exploratory holes in infrastructure tunnels with diverse geology. This approach enables accurate predictions of rock type and rock mass quality, providing a planning horizon of several days. We provide confidence metrics for the predictions, enhancing decision support by identifying areas of uncertainty. Our approach, particularly focusing on the challenging geological transition zones, achieved balanced accuracies above 0.9 for rock type and 0.8 for rock quality (Q-class). This advancement significantly improves the planning and execution of rock tunnelling projects.

Keywords

Machine learning, MWD, rock mass characterisation, geological transition zones, uncertainty assessment.

1   Introduction

Measure While Drilling (MWD) data, a high-resolution sensor dataset collected during tunnel excavation, is currently underutilised, primarily serving for geological visualisation. Recent studies have demonstrated that MWD data can be translated into rock type and rock mass quality for short blasting holes (Hansen, Erharter, et al., 2024; Hansen, Liu, & Torresen, 2024). There are arguably no reliable, efficient methods in tunnelling to accurately predict rock mass characteristics several blasting rounds ahead, which does not limit the excavation process (Liu & Gan, 2023). Traditional exploratory methods, such as geophysics and core drilling, are time-consuming, costly, and typically offer insufficient resolution. Another common method involves drilling exploratory hammerholes and subjectively interpreting the penetration rate and colour of flushing water, which is subjective and provides no detailed information about rock type and rock mass quality. Existing methods exhibit high uncertainties, and the communication of these uncertainties is not well developed.

Accurately predicting rock type and rock mass quality over twenty meters in advance of tunnelling can optimise decisions about advance support, excavation design, and the reuse of excavated rocks, days before the rock mass is excavated. This capability is valuable for efficient tunnel construction and resource management. Previous attempts to predict from MWD-data have been hindered by the lack of

a big dataset of high-quality drilling data, inadequate methods to capture the complexity of drilling data, and the computational demands of processing such data. To the author's knowledge, no studies have systematically evaluated the uncertainty of these predictions. For predicting rock type, several studies have employed machine learning algorithms with varying degrees of success (Kadkhodaie-Ilkhchi et al., 2010; Leung & Scheding, 2015; Silversides & Melkumyan, 2022). Despite their promising results, these studies are further limited by the narrow range of rock types considered, small datasets, and a focus on single holes, which restricts their applicability and generalizability. In the realm of predicting rock mass quality, recent research has explored the relationship between MWD data and rock mass metrics that describe overall stability or soundness, primarily through rock mass classification approaches (Fernández et al., 2023; Galende-Hernández et al., 2018; van Eldert et al., 2020, 2021). However, these studies also grappled with issues of small datasets, subjective human intervention, and limited representativeness for large-scale tunnelling projects

This study aims to leverage Measure While Drilling (MWD) data to provide accurate predictions of rock type and rock mass quality from long exploratory drillholes through geological transition zones, using data from infrastructure tunnels with diverse geology in Norway.
We introduce confidence metrics for the predictions, enhancing decision support by identifying areas of uncertainty. Our study focuses explicitly on challenging geological transition zones. From existing studies we know that such ensemble models and MWD-data work well for predicting rock type and rock mass quality from short blasting holes (Hansen, Erharter, et al., 2024; Hansen, Liu, & Torresen, 2024). In this study we extend the planning horizon significantly and provide uncertainty assessments through zones of rapidly changing geology. This way we provide a more comprehensive decision support system.

The structure of this paper is organised as follows: Section 2 details the methodology, including the dataset description, experimental setup, and evaluation metrics. Section 3 presents the results, covering prediction outcomes, communicating uncertainty, and evaluating the precision-recall trade-off. Finally, Section 4 provides conclusions and outlook.

2 Methods

2.1 Dataset

The dataset includes MWD data (features) and rock mass classification (labels) for 4,408 blasting rounds from 15 geologically diverse hard rock tunnels across four Norwegian infrastructure projects: UDK, UNB, RV4, and E39. The construction and pre-processing of the dataset are described in detail in a separate paper (Hansen, Liu, & Torressen, 2024). Precambrian Gneisses, Permian Basalt and Granite, Permian Rhomb porphyry, Cambro-Silurian shales, limestone, and claystone are key rock types. Figure describes a geological profile of the Permian rocks in the Drammens tunnel. Prediction results and confidence metrics will specifically be evaluated in this tunnel's geologic transition zones.

Figure illustrates the data collection process conceptually for shorter drillholes. For every 15 m of tunnelling, the 24 m exploratory holes are drilled inside the profile and some holes with a five-degree inclination out from the tunnel profile. Pre-processed values from all drillholes within a 1 m tunnel section (approximately 5000 values) were used to compute mean, median, standard deviation, variance, skewness, and kurtosis for each MWD parameter, resulting in 48 MWD-feature values plus three geometrical parameters (overburden, tunnel width, and Jn-mult), totalling 51 feature values per sample. Mapped to the Q-systems'(reference) Q-class labels and rock type, resulting in 23,277 samples, enriching the dataset with feature variations to enhance model performance and generalizability. Q-values, grouped into stability classes from "Exceptionally good" (class A) to "Exceptionally poor" (class G), recommend specific measures for Q-values under 1.0, such as Reinforced Ribs of Shotcrete (RRS) and spiling bolts. An accurate binary prediction model identifying this threshold has significant practical and economic benefits.
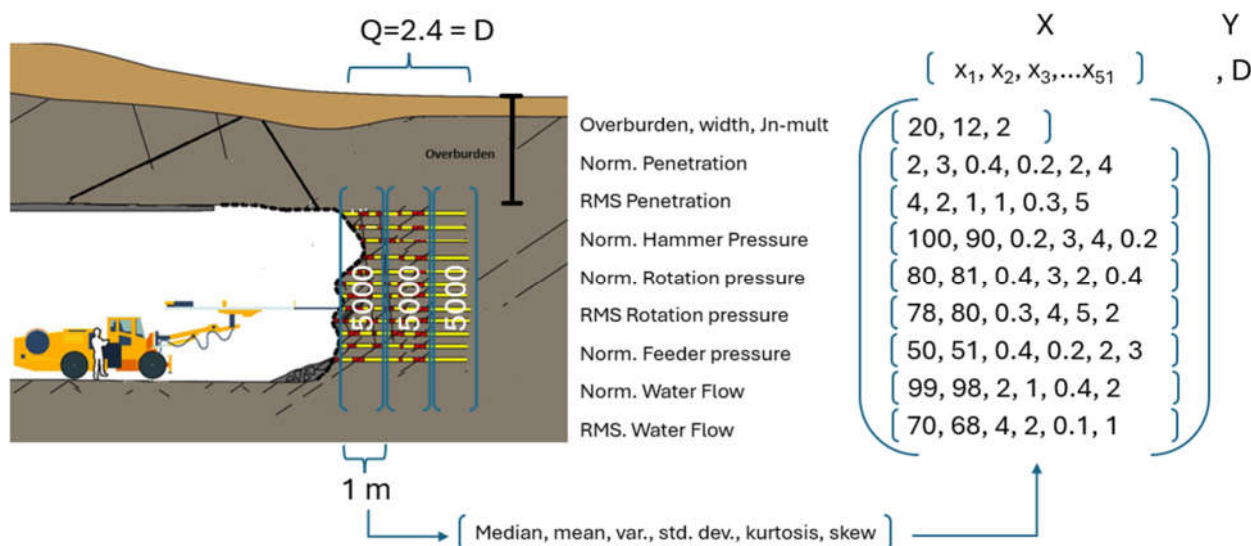
Figure 1. Illustrating the collection of MWD values for 1 m tunnel sections.
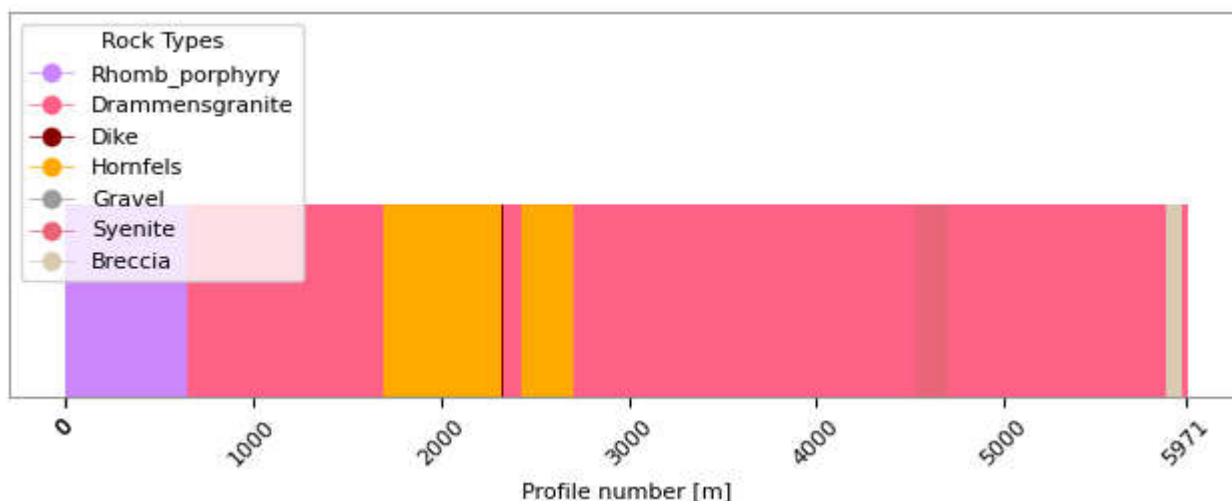
Figure 2. The geologic profile of the Permian rocks in the Drammens tunnel.

2.2 Experimental setup

Sample values of features and Q-class or rock type were trained and evaluated by several classifiers implemented in Scikit-learn (Random Forest, Extra Trees, KNN, logistic regression, MLP), LGBM, and XGBOOST (Pedregosa et al., 2011). Despite efforts to balance the dataset, medium Q-classes naturally had more samples. The SMOTE package (Chawla et al., 2002) was used to balance the training dataset before feeding it into the ML algorithms. Except for tree models, all tested models performed best when features were scaled to the [0,1] range using a MinMax scaler. To avoid data leakage, the pipeline functionality in Scikit-learn ensured scaling and balancing were based only on training data. The training and evaluation process followed the process outlined in Hansen et al. (Hansen, Liu, & Torresen, 2024) to ensure reproducibility. The dataset was split into 75% training and 25% test sets. Hyperparameters were tuned using Bayesian optimisation with the Optuna package (Akiba et al., 2019). Each new hyperparameter run used 5-fold cross-validation with random splits of the training set into training and validation sets. Final training used the entire set with optimised parameters before testing on the untouched test set and performing a 5-fold cross-validation on the full dataset. This process classified both Q-classes and rock types. The pipeline of processes used to train both target labels is illustrated in Figure .
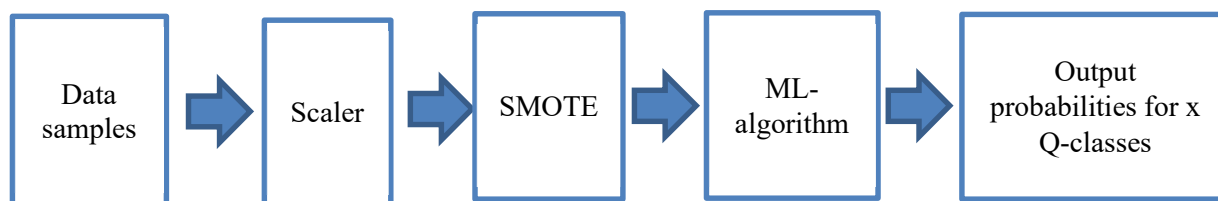
Figure 3. Defining the pipeline for the training process used to classify both target labels.

2.3 Metrics

To ensure robust analysis and mitigate misleading conclusions, we report several performance metrics (James et al., 2013). Each metric highlights different aspects of model performance, focusing on classifying rock masses into six categories.

Balanced Accuracy (Avg Recall Macro): Recall for a single class is defined as the ratio of true positives (correctly predicted instances of the class) to all actual instances of that class (sum of true positives and false negatives). Our primary metric, Balanced Accuracy, is the average recall across all classes, which is crucial for our unbalanced dataset. It ensures that larger classes do not disproportionately influence performance, vital for detecting weaker rock classes and preventing safety hazards.
Standard Accuracy: We include standard accuracy for comparison, measuring the proportion of correct predictions out of all predictions, providing an overall performance view.
Average Precision Macro: Avg. Macro Precision complements our recall focus by measuring the ratio of true positives to all instances identified as that class. This metric helps understand the false positive rate, which is critical in preventing the overestimation of rock strength.
F1 Score Macro: The F1 Macro Score combines recall and precision, offering a balanced view. It is essential for balancing recall and precision, acknowledging future insights that may highlight its importance.
Confusion Matrix: The confusion matrix provides an overview of precision and recall for each class, visualising class imbalances and prediction leakage. We present it in three versions: recall, precision, and non-normalized, showing correct and incorrect predictions.

2.4 Calibrating probabilities

To investigate model uncertainty in class predictions, we use the confidence information represented by the probabilities for each class. The class with the highest probability is predicted. A probability threshold can classify an instance as "unsure" if no class exceeds that threshold. In this study, we use a threshold of 0.8. However, existing probability scores often have flaws. Probabilities from several machine learning algorithms, such as tree-based models and KNN, tend to be biased, especially for imbalanced datasets (Niculescu-Mizil & Caruana, 2005; Zadrozny & Elkan, 2002). For tree-based models, this bias is due to the variance in the underlying base-trees, leading to less confident predictions. Conversely, Logistic Regression provides true probabilities as it directly optimises maximum likelihood based on cross-entropy loss. To address biased probabilities, one can calibrate them using isotonic and sigmoid calibration methods available in Scikit-learn. By comparing the true frequency of the positive label against its predicted probability, these methods transform probability values into interpretable statistical probabilities. For example, a probability of 0.85 for class B means that 85% of samples with similar feature values are correctly classified as class B.

We have constructed precision-recall graphs to visualise how we can adjust the probability threshold to vary the predictions of specific classes. To build a precision-recall graph for each class, we begin by splitting the dataset into training and testing sets, ensuring the testing set represents all classes. The classification model is trained using the training set, and the trained model then predicts probabilities for each class in the testing set. By varying the decision threshold from 0 to 1, we calculate precision

and recall at each threshold level for each class. Precision is calculated as the ratio of true positives to the sum of true positives and false positives, while recall is the ratio of true positives to the sum of true positives and false negatives. These values are then plotted with recall on the x-axis and precision on the y-axis, using different line styles and colours to distinguish between classes. This results in a precision-recall curve for each class, visualising the trade-off between precision and recall across different thresholds.

3 Results

3.1 Predicting rock type and rock quality from long exploratory holes

The results for predicting Q-class and rock type from long holes closely aligned with existing prediction results from blastholes, albeit with approximately 4% lower scores for rock (Hansen, Erharter, et al., 2024; Hansen, Liu, & Torresen, 2024). This alignment was anticipated, given the comparability of data from long exploratory holes and shorter blast holes. We achieved the best performance by using a voting classifier in a pipeline that included Min-Max scaling and SMOTE for data balancing. For predicting rock type, the voting classifier combined KNN, Extra Trees, and LightGBM algorithms, while for predicting rock quality, it combined KNN, Extra Trees, and CatBoost algorithms. This ensemble approach excelled by enhancing recall and precision, improving balanced accuracy to 0.92, up from 0.87 with KNN alone, while maintaining the precision score of Extra Trees. Each algorithm was trained separately with its scaler in the voting classifier, and a majority vote determined the final classification. By leveraging the distinct advantages of KNN's non-parametric, lazy learning approach and the diverse strengths of both bagging (Extra Trees) and boosting (CatBoost for rock quality, LightGBM for rock type) methods, we were able to enhance the predictive performance for both rock type and rock quality.

In Figure , we present confusion matrices and metrics for a model trained to predict rock type and rock quality on the test set for all tunnels. The numbers are based on concatenating the results from the test sets for all splits in a 5-fold cross-validation run. The lower value for limestone seems to be caused by similarities in signature with the MWD signature from shale, "leaking" predictions to this rock type.
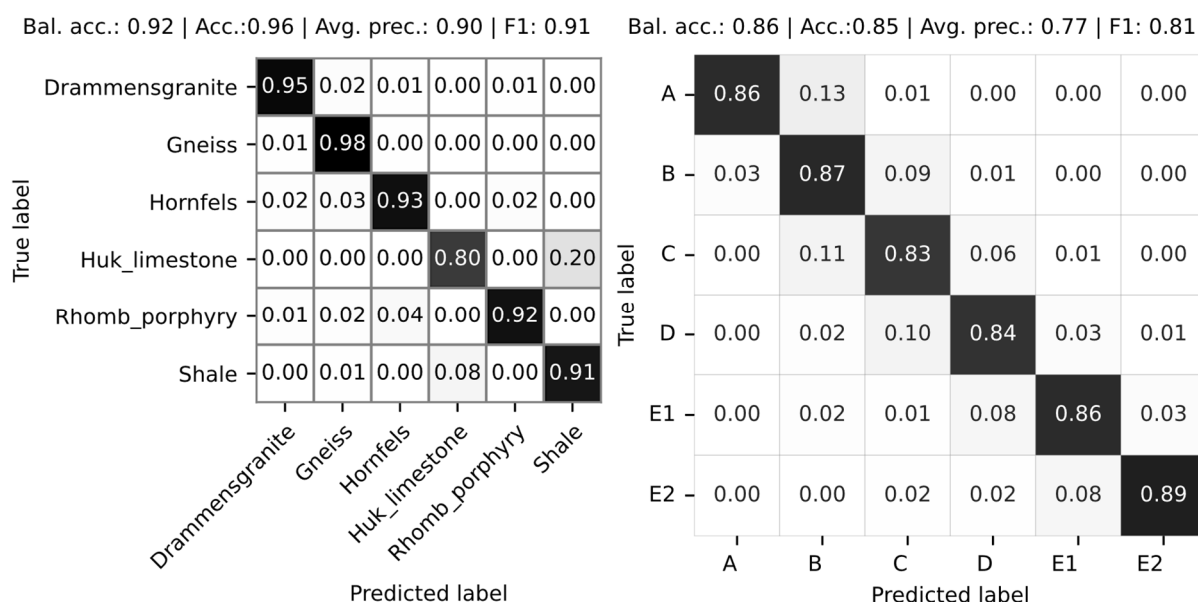
Figure 4. Confusion matrixes for predicting rock type and rock quality with a voting classifier.

3.2 Communicating uncertainty

Communicating uncertainty in predictions is crucial for a transparent AI-model. Transparency is

considered one of the key factors in frameworks for ethical AI (Prem, 2023). When humans use ML models for decision-making, it is crucial to assess how confident the model is about its predictions. This assessment allows humans to determine how the prediction should be incorporated into their final decision-making process. By effectively conveying the uncertainty associated with ML predictions, we can ensure more informed, transparent, and responsible use of AI systems. This study emphasises assessing the uncertainty of predictions, expressed as probabilities, in geologic transition zones. Figure illustrates the calibration of probability values for predictions. In this figure, probabilities for the predicted class are plotted in a histogram of uncalibrated and calibrated probabilities using sigmoid and isotonic techniques. The calibrated values generally shift to the right, indicating increased confidence in the predicted class. Since the uncalibrated probabilities were biased towards extreme values for several samples, we chose sigmoid calibration for further analysis.
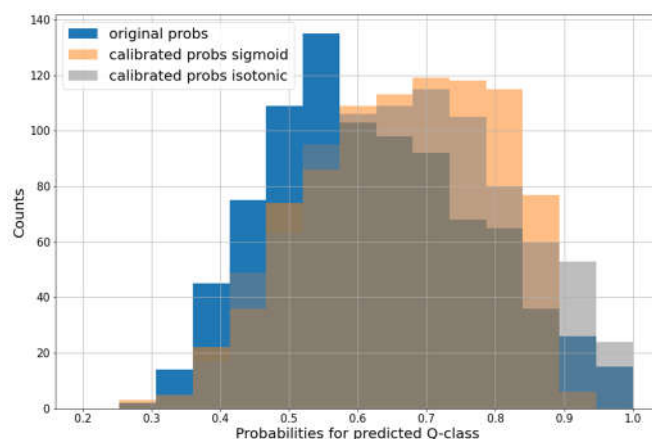
Figure 5. Comparison of ML probabilities with two types of calibrated probabilities.

To communicate the calibrated prediction-uncertainty in geologic transition zones, we selected two zones in the Drammen tunnel (see geologic profile in Figure). The plots show predicted rock types in five-meter sections along the exploratory holes drilled from the tunnel face. The y-scale indicates prediction probability. The tunnel face is on the left in the plot. Predictions below a 0.8 threshold are classified as "unsure". The pie charts below illustrate the distribution of probability values for each class for a specific prediction. In Figure , the correct prediction should be three Rhombporphyry followed by three Drammen Granite, indicating one incorrect prediction. For section 3, the model predicts Drammen Granite (60%) and Rhombporphyry (30%) but chooses incorrectly. This is consistent with the nearby rocks, suggesting that section 3 might be a mixture of Rhomb porphyry and Drammen granite.

In Figure , the true predictions should be three rounds of Drammen granite and three rounds of Hornfels, indicating one error. The incorrect prediction of Rhombporphyry in the transition zone with high probability is problematic. The reason for this is unknown but could be due to a mislabelled sample.

In Figure , the correct labels are three Hornfels and three Drammen granite, resulting in three incorrect and three uncertain predictions. The most significant error in this plot is the high probability prediction of Drammen granite in section 3, where the correct label was Hornfels. An incorrect prediction due to uncertainty is less concerning and reflects the changing geology. In all sections with incorrect predictions, the choice is between two logical rock types. Notably, there is no sudden high probability of Rhombporphyry within the Hornfels zone.
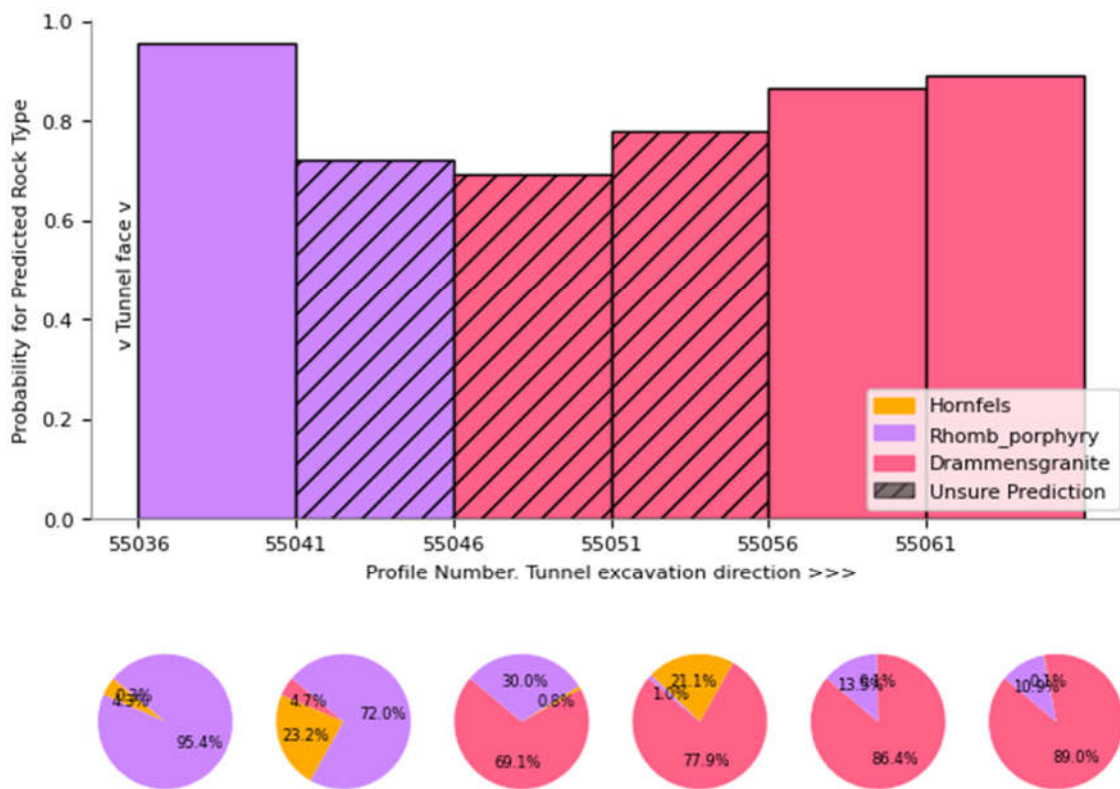
Figure 6. Prediction and uncertainty assessment in a geologic transition zone in Drammen tunnel, zone 1
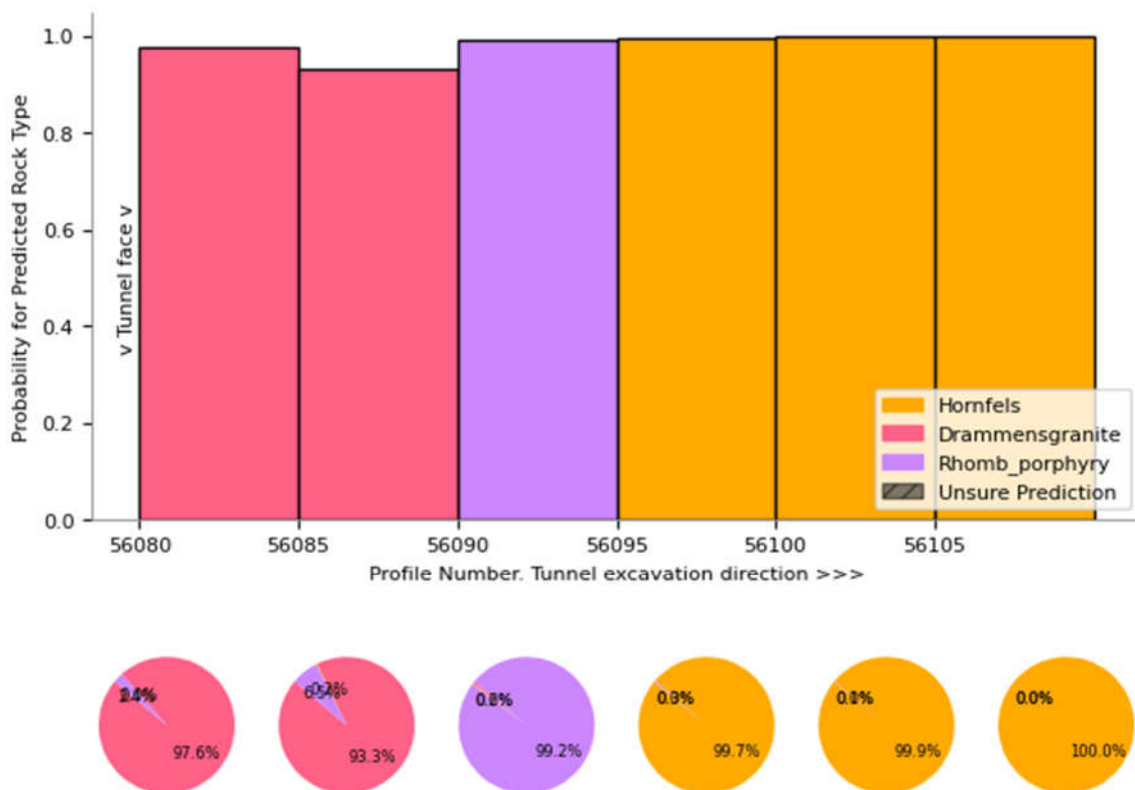
Figure 7. Prediction and uncertainty assessment in a geologic transition zone in Drammen tunnel, zone 2
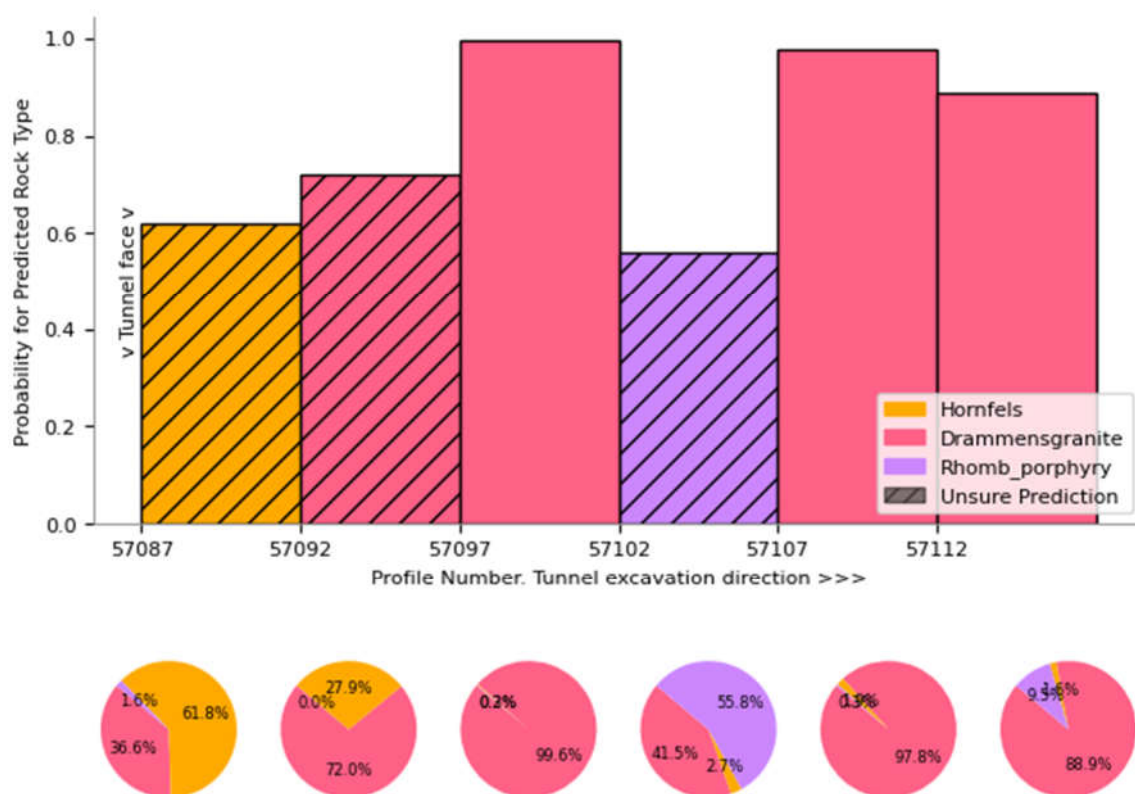
Figure 8. Prediction and uncertainty assessment in a geologic transition zone in Drammen tunnel, zone 3

Figure 12 illustrates prediction uncertainty conveyed through feature values and bar plots for rock mass classification. This visualisation aims to demonstrate alternative methods of communicating uncertainty in machine learning models, including providing feature values. Figure 12 presents plots of four random blasting rounds detailing feature values, true labels, predicted labels, and probabilities for each class within the Q-class labels A, B, C, D, E1, E2. In the figure, blasting rounds three and four are correctly predicted as class E2 and C with high confidence. Round one is incorrectly predicted as class E1 instead of C. This prediction should be considered uncertain, given the medium-sized probabilities for several classes. In round two, probabilities for classes B and C are observed. High probabilities for two neighbouring classes suggest a borderline sample between classes B and C. This is analogous to human physical mapping. For decision support, this should be conservatively interpreted as class B.

This leads to a suggested approach for handling prediction uncertainty in ML predictions:

- When only one class has a high probability, the prediction confidence is high.
- When two neighbouring classes have similar probabilities, the sample is likely a border case and should be conservatively interpreted as the class with the poorest ground.
- When several classes have significant probabilities (typically over 0.1), the classifier is uncertain, and the prediction should not be trusted.

The classifier can programmatically implement such probability-based confidence interpretation by adding simple target-based logic as the final prediction step. Thus, predictions strengthened with confidence information should significantly contribute to a data-driven decision support system for face engineers. In the next section, we will explore how to tune the precision-recall trade-off towards detecting certain classes, by varying the probability threshold for predictions.
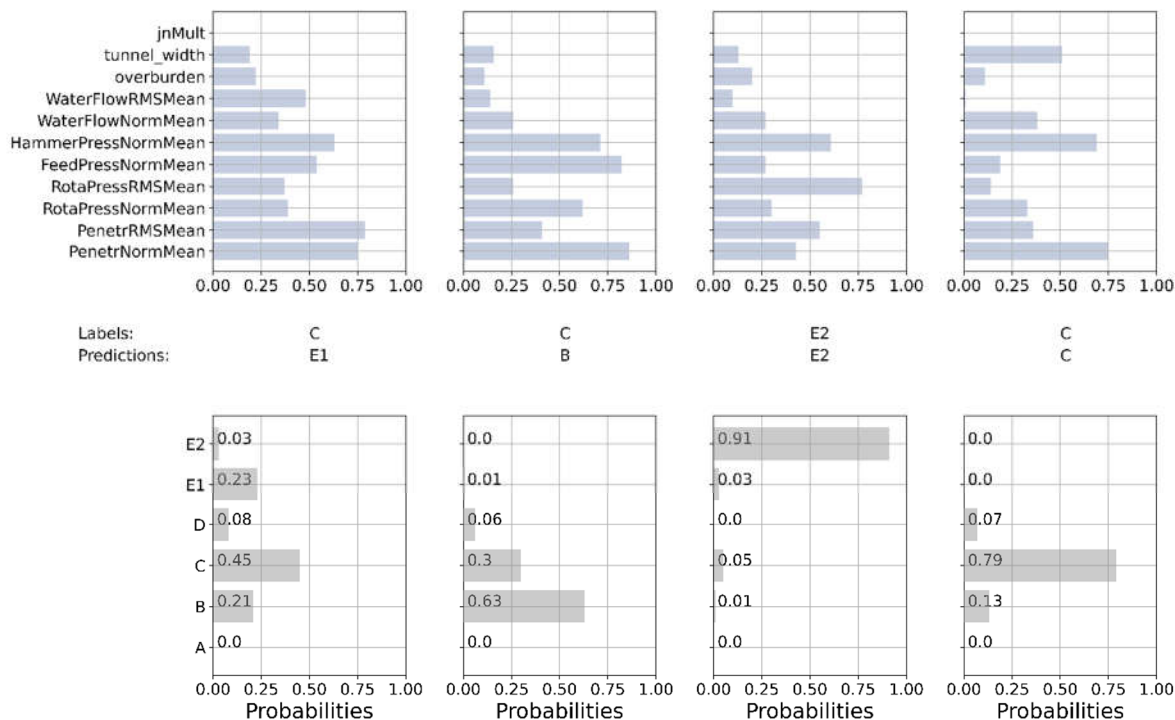
Figure 12. Calibrated probability plot of 4 Q-class predictions. Feature values are scaled to a 0-1 interval.

3.3 Tuning the prediction threshold
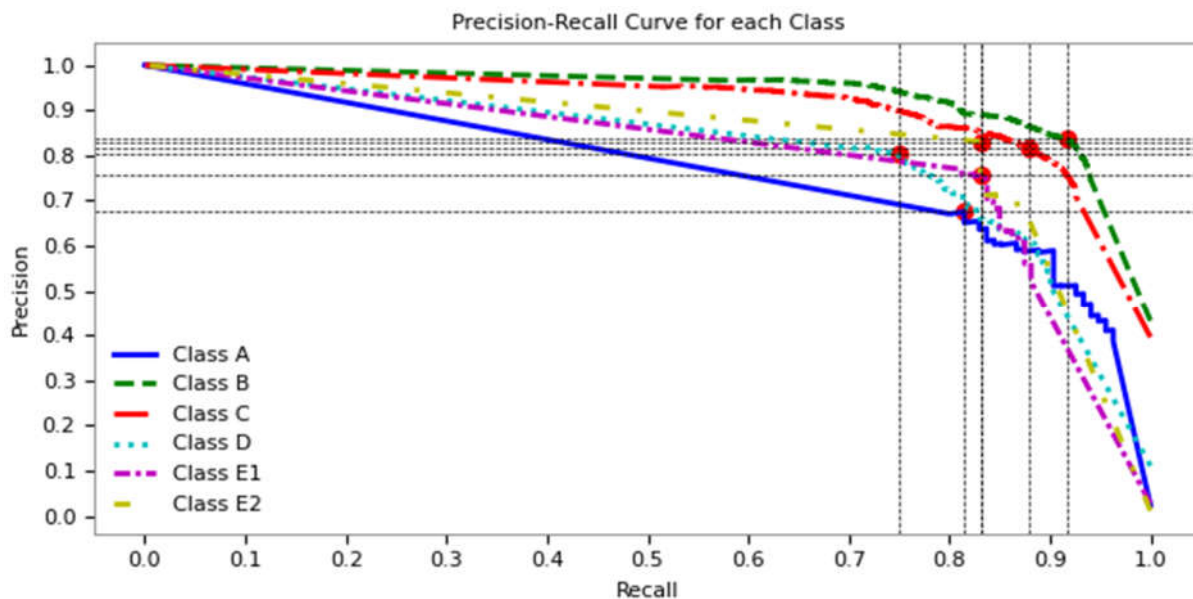
Figure 13. Precision - recall curves for rock quality classes

The plot in Figure 13 illustrates the precision-recall curves for six rock quality classes within our dataset, with each curve representing a different class. The red dots indicate the optimal trade-off points between precision and recall for each class, showing where we achieve the best balance of these metrics. For instance, examining Class E1 (represented by the magenta dashed line), we observe that adjusting the probability threshold for prediction can shift the balance between precision and recall. Specifically, lowering the threshold can increase recall, allowing us to detect more E1 samples. This adjustment would, however, come at the expense of precision, leading to a greater number of false positives. The implications of such an adjustment are significant in practical applications. In scenarios where detecting

all instances of Class E1 is critical (e.g., identifying high-risk rock formations), it may be preferable to prioritise recall over precision. This approach ensures that most, if not all, E1 samples are identified, even if it means accepting a higher rate of incorrect predictions. Conversely, maintaining a higher precision may be more desirable in situations where the cost of false positives is high, even at the expense of missing some true E1 instances.

Balancing these metrics according to the specific requirements of the application can enhance the effectiveness and reliability of the predictive model, making it more suited to the practical needs of tunnelling and mining operations.

4 Conclusion and outlook

This study demonstrates the potential of using Measure While Drilling (MWD) data from long exploratory holes combined with ensemble machine learning models to predict rock type and rock mass quality in infrastructure tunnelling. The findings highlight the value of leveraging high-resolution sensor data to improve the planning and execution of rock tunnelling projects. Key findings:

- **Accurate Predictions**: Achieved balanced accuracies above 0.9 for rock type and 0.8 for rock quality (Q-class).
- **Extended Planning Horizon**: Enabled predictions several days in advance, providing critical information for logistical planning and support design.
- **Ensemble Models**: Ensemble machine learning models, including KNN, Extra Trees, and LightGBM/CatBoost, demonstrated the best performance.
- **Uncertainty Assessment**: Confidence metrics were introduced to enhance decision support, particularly in geological transition zones, ensuring more reliable and transparent predictions.
- **Tuning predictions**: Demonstrated how to tune predictions by varying the probability threshold illustrated by the consequences in the precision-recall trade-off and classifying to a class "unsure" below a certain threshold.
- **Practical Application**: Demonstrated practical benefits by predicting rock mass characteristics in advance, optimising excavation strategies, and improving resource management.

Future research should focus on refining these predictive models, particularly in the challenging geologic transition zones, to handle a broader range of geological conditions and extend their applicability to other tunnelling projects. Enhancing the dataset with more diverse geological samples and improving uncertainty assessment methods will be crucial. Integrating these predictive capabilities into real-time decision support systems for tunnelling projects can significantly enhance operational efficiency and safety.

Acknowledgements

References

Akiba, T., Sano, S., Yanase, T., Ohta, T., & Koyama, M. (2019). *Optuna: A Next-generation Hyperparameter Optimization Framework*. arXiv. https://doi.org/10.48550/ARXIV.1907.10902

Chawla, N. V, Bowyer, K. W., Hall, L. O., & Kegelmeyer, W. P. (2002). SMOTE: Synthetic minority over-sampling technique. *Journal of Artificial Intelligence Research*, *16*, 321–357. https://doi.org/10.1613/jair.953

Fernández, A., Sanchidrián, J. A., Segarra, P., Gómez, S., Li, E., & Navarro, R. (2023). Rock mass structural recognition from drill monitoring technology in underground mining using discontinuity

index and machine learning techniques. *International Journal of Mining Science and Technology*, *33*(5), 555–571. https://doi.org/10.1016/j.ijmst.2023.02.004

Galende-Hernández, M., Menéndez, M., Fuente, M. J., & Sainz-Palmero, G. I. (2018). Monitor-While-Drilling-based estimation of rock mass rating with computational intelligence: The case of tunnel excavation front. *Automation in Construction*, *93*(May), 325–338. https://doi.org/10.1016/j.autcon.2018.05.019

Hansen, T. F., Erharter, G. H., Liu, Z., & Torresen, J. (2024). A comparative study on machine learning approaches for rock mass classification using drilling data. *Http://Arxiv.Org/Abs/2403.10404*. http://arxiv.org/abs/2403.10404

Hansen, T. F., Liu, Z., & Torresen, J. (2024). Predicting rock type from MWD tunnel data using a reproducible ML-modelling process. *Tunnelling and Underground Space Technology*, *152*, 105843. https://doi.org/10.1016/j.tust.2024.105843

Hansen, T. F., Liu, Z., & Torressen, J. (2024). Building and analysing a labelled measure while drilling dataset from 15 hard rock tunnels in Norway. *Available at SSRN: Https://Ssrn.Com/Abstract=4729646 or Http://Dx.Doi.Org/10.2139/Ssrn.4729646*. https://doi.org/http://dx.doi.org/10.2139/ssrn.4729646

James, G., Witten, D., Hastie, T., & Tibshirani, R. (2013). *An Introduction to Statistical Learning* (Vol. 103). Springer New York. https://doi.org/10.1007/978-1-4614-7138-7

Kadkhodaie-Ilkhchi, A., Monteiro, S. T., Ramos, F., & Hatherly, P. (2010). Rock recognition from MWD Data: A comparative study of boosting, neural networks, and fuzzy logic. *IEEE Geoscience and Remote Sensing Letters*, *7*(4), 680–684. https://doi.org/10.1109/LGRS.2010.2046312

Leung, R., & Scheding, S. (2015). Automated coal seam detection using a modulated specific energy measure in a monitor-while-drilling context. *International Journal of Rock Mechanics and Mining Sciences*, *75*, 196–209. https://doi.org/10.1016/j.ijrmms.2014.10.012

Liu, M., & Gan, Q. (2023). Applied research of comprehensive advance geological prediction in Daluoshan water diversion tunnel. *Scientific Reports*, *13*(1). https://doi.org/10.1038/s41598-023-36090-8

Niculescu-Mizil, A., & Caruana, R. (2005). Predicting good probabilities with supervised learning. *ICML 2005 - Proceedings of the 22nd International Conference on Machine Learning*, *1999*, 625–632. https://doi.org/10.1145/1102351.1102430

Pedregosa, F., Varoquaux, G., Gramfort, A., Michel, V., Thirion, B., Grisel, O., Blondel, M., Prettenhofer, P., Weiss, R., Dubourg, V., Vanderplas, J., Passos, A., Cournapeau, D., Brucher, M., Perrot, M., & Duchesnay, E. (2011). Scikit-learn: Machine Learning in {P}ython. *Journal of Machine Learning Research*, *12*, 2825–2830.

Prem, E. (2023). From ethical AI frameworks to tools: a review of approaches. *AI and Ethics*, *3*(3), 699–716. https://doi.org/10.1007/s43681-023-00258-9

Silversides, K. L., & Melkumyan, A. (2022). Machine learning for classification of stratified geology from MWD data. *Ore Geology Reviews*, *142*, 104737. https://doi.org/10.1016/j.oregeorev.2022.104737

van Eldert, J., Funehag, J., Saiang, D., & Schunnesson, H. (2021). Rock support prediction based on measurement while drilling technology. *Bulletin of Engineering Geology and the Environment*, *80*(2), 1449–1465. https://doi.org/10.1007/s10064-020-01957-x

van Eldert, J., Schunnesson, H., Johansson, D., & Saiang, D. (2020). Application of Measurement While Drilling Technology to Predict Rock Mass Quality and Rock Support for Tunnelling. *Rock Mechanics and Rock Engineering*, *53*(3), 1349–1358. https://doi.org/10.1007/s00603-019-01979-2

Zadrozny, B., & Elkan, C. (2002). Transforming classifier scores into accurate multiclass probability estimates. *Proceedings of the ACM SIGKDD International Conference on Knowledge Discovery and Data Mining*, *x*, 694–699. https://doi.org/10.1145/775047.775151

REVIEW OF THE CONCEPT OF SMART LEVEES

NICOLA ROSSI [1], MEHO SAŠA KOVAČEVIĆ [2], MARIO BAČIĆ [3], GORAN GRGET [4]

[1] *University of Zagreb, Faculty of Civil Engineering, Croatia, nicola.rossi@grad.unizg.hr*

[2] *University of Zagreb, Faculty of Civil Engineering, Croatia, meho.sasa.kovacevic@grad.unizg.hr*

[3] *University of Zagreb, Faculty of Civil Engineering, Croatia, mario.bacic@grad.unizg.hr*

[4] *Geokon-Zagreb d.d., Croatia, goran.grget@geokon.hr*

Abstract

Monitoring of structures during construction and their exploitation is a common practice, often required by investors and/or national standards, to ensure that the performance of the structure is satisfactory with regards to the specified limit states. For this purpose, various quantities are measured, all related and most indicative of problems arising from approaching a specified limit state. In geotechnical practice, these usually include pore-water pressures, deformations, stresses, and temperatures. All the mentioned measurements can be either conducted and collected manually at discrete time intervals, or automatically such that data is collected remotely almost continuously. When equipment to measure and collect these quantities automatically is installed into a levee, a so-called Smart Levee is established. Its purpose should be to provide real time data to existing prediction models which can then predict any critical behaviour of the levee before failure occurs. Since most of commonly used the equipment for gathering the mentioned quantities is designed to collect data in a single point along the levee, the monitored sections should be spaced such that each is representative of a longer reach. Alternatively, equipment that allows for gathering data along a line should be used, to be placed along the whole stretch of levees which need to be monitored. Examples of such equipment mostly include fibre optic cables for strain and temperature measurements, and stationary or UAV-mounted terrain surveying equipment. This paper gives a review of the practices in constructing Smart Levees throughout the world, discussing the most commonly used equipment and monitored quantities, with the expected results and their application.

Key words

monitoring, smart levee, real-time data, early warning system (EWS)

1 Introduction

Monitoring of levees as flood protection structures is an activity of repeated and frequent measurements, used for early detection of potential failure to avoid fatal consequences. The terms "frequent" and "early" are relative terms – they can be conducted multiple time across the span of multiple hazardous events (floods) or be practically continuous within a single event. In the first case, the results could indicate a slow degradation of the levee, which can be used to detect sections that need to be strengthened before the next floods. In the second case the data is searching for the initiation of failure mechanisms during a single event, which require immediate action to prevent complete failure, meaning they must be detected as soon as possible by ensuring continuous measurements in time. The commonly used term for detection of potential failure from the sensor data is "anomaly detection", and is usually done by statistical analysis of time series or machine learning procedures (Balis et al., 2017). In the realm of possible failures of levees, we can identify several mechanisms, as described by Wolff (2008) to be

overtopping, slope stability, external erosion, underseepage and through-seepage, with the latter two being also collectively called internal erosion mechanisms. To detect the correct failure mode/mechanism that is initiating, the appropriate quantities must be measured. Traditionally, though, regular assessments are done by visual inspection (Hopman et al., 2011), which offers only very limited type of data to work with, and only at the levee surface without much insight into the physical state of the soil within the levee. The state of the interior can be inferred from what is seen on the surface, but only qualitatively, which may be good for sensitivity type of analyses. Visual inspection, if frequent enough, can help detect anomalies due to long-term degradation of materials. Measurements with instruments offer what visual inspection cannot and can be categorized according to various criteria. The broadest division is made by local/in-situ or remote/ex-situ measurements (van Vliet et al., 2012). The former refers to the measurement of a quantity at any point on or inside the levee with a sensor placed at the exact location of measurement, while the latter refers to any measurement taken away from the sensor, regardless of whether the instrument is on land, airborne or in space (e.g. geophysics, LiDAR, satellite). Measurements can further be categorized by being used to measure a property directly or indirectly, by their spatial coverage (single point, along a line or over a surface), and by their frequency/density (spatial). Due to the scale of the various failure mechanisms, it is advised to keep the frequency/density within 1-30 m (Cundill, 2016). In that sense, "continuous" measurements in the longitudinal direction can be considered as having any density that could detect the relevant failure mode. Such categorizations offer a useful tool for selecting the appropriate instruments for the specific case, during the design phase of the monitoring system.

When any combination of sensors on/in a levee is incorporated into an automated system for collecting data, the result is called a "smart levee". Technological advances offer development of smaller, lighter, cheaper and more energy-efficient sensors in the form of micro electro-mechanical systems (MEMS), such as piezometers, thermal sensors, inclinometers and accelerometers (Cundill, 2016), which make smart levees more viable in practice. Such sensors can also become smart sensors themselves, by including individual information processing functions that can perform various calculations and make decisions. This functionality is not a requirement for smart levees, as the data can still be collected in its entirety and analysed by a separate computer. However, the aspiration for all smart levees is to not only collect data, but also implement an automatic data processing structure that combines data from multiple sensors, and which detects anomalies, calculates risks, and alarms the competent authorities. This, however, requires that the development time of the failure modes is long enough, and that the failure initiation is detected early enough, to leave enough time for reaction – otherwise the effort may be in vain. Nevertheless, even without immediate processing, the data collected is useful, especially in newly monitored levees, to investigate their behaviour after one or more hazardous events, to then improve the understanding and employ more efficient management measures and improved design of future levees. When enough data is collected, the system can then be extended with models that automatically perform all the necessary calculations, to become a functioning part of an early warning system.

To achieve a better understanding of the failure mechanism, instruments can also be installed in experimental levees constructed only for learning and calibration purposes, just like the IJkdijk in the Netherlands (Bersan et al., 2015; de Vries et al., 2012; Koelewijn et al., 2014, 2013) or the ISMOP project in Poland (Balis et al., 2017; Sekuła et al., 2017).

2   Overview of the relevant projects

In this paper we collected and analysed several case studies involving the instrumentation of levees, to review the current best practices. A review of the available literature showed that several existing levees have been instrumented to assess their stability in real time in the Netherlands, the USA, Italy and Croatia, and some for experimental purposes in the Netherlands and Poland. When designing monitoring for experimental levees whose purpose is to deepen the understanding of the failure mechanisms and test the applicability of individual instruments, then many combinations of sensors are installed for a comprehensive and exhaustive analysis. The sensors can be of any type, depending on the goal of the

experiments. When instrumenting real levees and dikes, the first obstacle is the amount of equipment that needs to be installed along the whole protected area, so only sensors that have been proven to work for specific (expected) failure mechanisms, are installed and relied upon. Studies regarding the application of individual instruments in the monitoring process with respect to one or more failure mechanisms are abundant, e.g. (Inaudi, 2019; Inaudi et al., 2013; Niederleithinger et al., 2012; Sjödahl et al., 2011), but their incorporation into an autonomous unit for levee monitoring requires more considerations.

The idea of having a functional smart levee is to monitor its state ideally along the whole structure, which may prove unfeasible due to the required amount of equipment needed to be installed to cover the whole levee while ensuring appropriate density to cover the scale of the various failure mechanisms. A compromise is thus often required, where only "weak spots" are monitored (Hopman et al., 2011). This implies that weak spots are known in advance, prior to instrumentation, which may be indicated by visual inspection. A weak spot is comprised of a specific cross-section with specific material properties, which lead to its "weak" behaviour. Rossi et al. (2023) have shown that to define a cross-section uniquely, over 100 distinct parameters are required, regarding geometry, physical, mechanical and hydraulic characteristics of the levee, the foundation soil and the immediate surroundings. However, not all of them have considerable effect on stability, so the list can be reduced while still accurately defining a cross-section. By gathering sensor data at the selected weak spots, predictive models can be created that pertain to levees with similar characteristics. Then, such models can be utilized at other sections similar to the monitored one, identified from investigation works that should be available for most existing levees from project documentation. This approach requires more time to fully implement, as it needs a period of data collection and model development, as well as exhaustive review of the available investigation works to identify the similar sections, but it also requires only one characteristic cross-section to be instrumented. Usually though, similar cross-sections are found in the vicinity of each other, within the same "reach". A reach being defined as the length of levee for which the geometry and subsurface conditions are sufficiently similar that they can be represented for analysis and design by a single two-dimensional cross-section and foundation profile (Wolff, 2008). Consider we add another condition to this definition – that a reach should also be characterized by equal consequences were the levee to fail anywhere within that reach – such that the morphology of the protected area is now also considered. This means that by carefully dividing a levee into reaches, we can instrument one cross-section within that reach, and the monitoring results would be representative of the whole thing. Of course, failure can be triggered by unforeseen circumstances at other sections, which is why special attention must be given to identifying the section with the highest probability of failure.

To evaluate local conditions on found weak spots, emphasis is often placed on monitoring of pore pressures within a levee, to assess seepage, even though recently other physical measurements have been made within and on top of levees (Hopman et al., 2011). Pore pressure measurements are conducted by piezometers which take measurements at a single point. As an indirect alternative, temperature measuring is increasingly being used to monitor seepage through dams, levees and dikes (Bersan et al., 2015), and is considered to be one of the most effective methods of assessing seepage (Sekuła et al., 2017). Temperature measurements can be conducted most efficiently by fibre optic sensors, which makes measurements continuous in the direction of installation, but can also be made by individual sensors installed together with other types of sensors, like inclinometers or piezometers. Electromagnetic methods (such as GPR – ground penetrating radar, and EMI – electromagnetic induction) have also been shown to have good application for detecting water in the soil (Santamarina et al., 2005), however they are somewhat more scarce in the practice of smart levees. Seismic methods have also been used for water detection, among other useful design parameters (Lorenzo et al., 2014). The reader is directed to Niederleithinger et al. (2012) for an insightful discussion on the various geophysical methods for dike inspection.

2.1 Experimental embankments

The IJkdijk experiments utilize various combinations of equipment to detect different failure modes on the four constructed embankments (east, west, north, south). Bersan et al. (2015) used piezometers, flow metres, fibre optics for temperature, infrared cameras with visual inspection for validation using high definition cameras, at frequency of two measurements per hour. All of these instruments are utilized to assess changes in seepage due to underseepage (piping) failure mode in the west embankment. According to the measured data, they show that the pipes during internal erosion in the initial stage have much smaller area of influence than 1 m, and that a higher density than that would be beneficial for detecting this type of failure, and that a higher data collection frequency is required for implementation of an early warning system (EWS). Koelewijn et al. (2013, 2014) performed analyses (AIO-SVT, all in one sensor validation test) on three of the four embankments (east, west, south), to their respective design failure modes – piping, micro-instability and overtopping for the east and west, and deep sliding for the south embankment. Piezometers, fibre optics for temperature and strain (installed vertically and horizontally), fast ground-based SAR (synthetic aperture radar) system (for displacement), infrared camera, flow meters, ERT (electrical resistivity tomography) system and inclinometers were used in an automated manner, while GPR has been used manually, also with visual inspection by HD cameras. The authors emphasize the performance of the infrared cameras, SAR system and the vertically installed fibre optics for strain and temperature measurements. Of note is a proposed and tested automatic prevention measure, in the form of drainage tubes which can automatically open to drain water from the levee based on measurements, whose performance was also shown to be satisfactory. de Vries et al. (2012) performed piping experiments on the IJkdijk embankments, and used plastic and glass fibre optics for deformation, vibration and temperature monitoring, acoustic sensors for dynamic imaging, self-potential to detect leakage, infrared cameras for deformations and well locations, MEMS piezometers and inclinometers with temperature sensors, and conventional piezometers for their respective uses. Even though pore pressure measurements have been shown to be quite good at predicting piping, temperature measurements within the layer of potential failure give more detailed information, and given their relative cost compared to piezometers, are a good alternative to be implemented.

As part of the ISMOP project, Balis et al. (2017) and Sekuła et al. (2017) instrumented a levee in the Lesser Poland region, using piezometers, individual temperature sensors as well as fibre optic cables for temperature measurement, weather stations, earth pressure sensors and inclinometers. Their measurement frequency adapts dynamically to the current situation, and the instruments are placed at each 2.5 m along the levee where the permeability was higher, and 5 m where it was lower. They discuss many practical considerations regarding installation and operation of the instruments during levee exploitation, as well as the architecture required for implementing an automated failure detection and warning (support) system, which includes data collection in a shared database and processing using "urgent computing" (e.g. Leong and Kranzlmüller, 2015) services, and decision making processes. The latter being divided into three phases – anomaly detection, threat estimation on section where anomalies are detected, and risk assessment when the threat exceeds a certain threshold.

2.2 Operational embankments

When instrumenting operational dikes and levees for practical implementation of an early warning system, only a fraction of the instruments is viable for monitoring of larger stretches of embankments unless a large financial commitment is possible. As part of the planned iLevee project in the USA, 10 section of the flood protection system, from I- and T-walls to earthen embankments, have been instrumented as a demonstration. Inclinometers and extensometers have been installed on all sections with interferometric SAR for monitoring, while additional fibre optics for strain measurements and tiltmeters have been installed along the walls, and additional piezometers and shape acceleration arrays

(SAA) were installed on the levee sections (Dunbar et al., 2017). In Italy, Cola et al. (2019) instrumented a 350 m long section along the Adige river affected by piping. They utilized piezometers and ERT, along with standard field and laboratory investigation techniques to identify the area most prone to piping, which has then been additionally instrumented with fiber optics for temperature measurement and traditional temperature sensors at or near the land side toe of the levee, at three depths. The sensors operate remotely while communicating data to a server every hour. It is noted that the one-hour frequency is enough to detect seepage paths, but not for the implementation of an early warning system. The fiber optics were shown to be an efficient methods of monitoring temperature variations connected with seepage through the soil. An instrumented cross-section is shown in Figure 1. In the Netherlands, as part of the UrbanFlood FP7 project, Melnikova et al. (2011) have instrumented an operating dike with piezometers and inclinometers, at four sections deemed critical. The gathered data was used to calibrate numerical and empirical models, whose performance was later compared with the actual data. The models have been implemented into an EWS for levee stability, breaching and flood propagation calculations by Krzhizhanovskaya et al. (2011), with a thorough discussion of all the constituent parts of an EWS, and considerations for its implementation at local and larger scales. For the test site with four cross-sections instrumented with piezometers and inclinometers, the simulations implemented in the EWS have been shown to perform in less than one minute with the usage of supercomputers, which would otherwise take much longer to run. If supercomputers are available through an urgent computing system, such models are a viable option. However, when instrumenting large levee stretches which require hundreds of models to run to detect failure mechanisms which are short to occur, and urgent computing is not available, machine learning models can be trained in advance on collected data, to be run within seconds or minutes when needed.
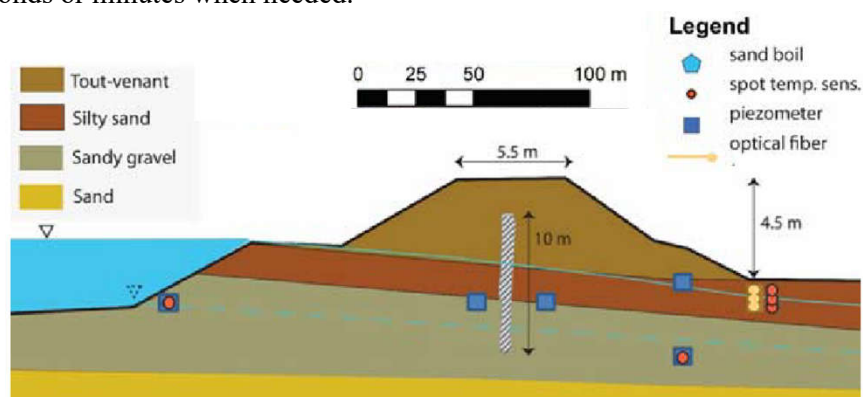
Figure 1. Instrumented cross-section along the Adige river, from (Cola et al., 2019).

In Croatia, the VEPAR project (Grget et al., 2023) instrumented a levee on one cross-section next to the Sava river. As part of the project, a suitable location is found, ground investigation performed, a numerical model established, instruments installed and a system for automatic data gathering and transfer employed, and the response of the system is tested. The used instruments included inclinometers with MEMS technology and piezometers with thermal sensor at three cross section in a stretch of 100 m of levee, and linear thermal sensors along the stretch with sensors every ~9m. The cross-sections consists of levees 4-5 meters high, with a high and wide land-side berm for the service road, only approx. 1 m from the crest height (Figure 2). Due to such geometry, the berm height was not exceeded in either of the two recorded flood events, even though one of them was the second highest event ever recorded. For this reason, most of the inclinometers located near the crown did not register any displacements. One inclinometer installed on the slope within the inundation of the river showed lateral movements in both directions, during the increasing phase of the water wave and the receding phase respectively. This location has been previously known for soil creep, and some parts have been subjected to reinforcement measures (Mihaljević and Gagro, 2010). Still, the inclinometer shows that the displacements continue to increase slightly as the water wave recedes. The registered pore pressures corresponded nicely with

the incoming water wave with a time delay of one day, therefore the smaller fluctuations in water height were not registered, but only the main events. The thermal sensors within the inclinometers and piezometers did not manage to detect the water waves per se, except for some variations in some of them, but the linear sensors placed at the toe showed a continuous increase in temperature from their installation, with much more fluctuations during the measurements. These fluctuations are not evidently correlated with the water wave, but information from the weather station could be used to analyse the data more deeply.
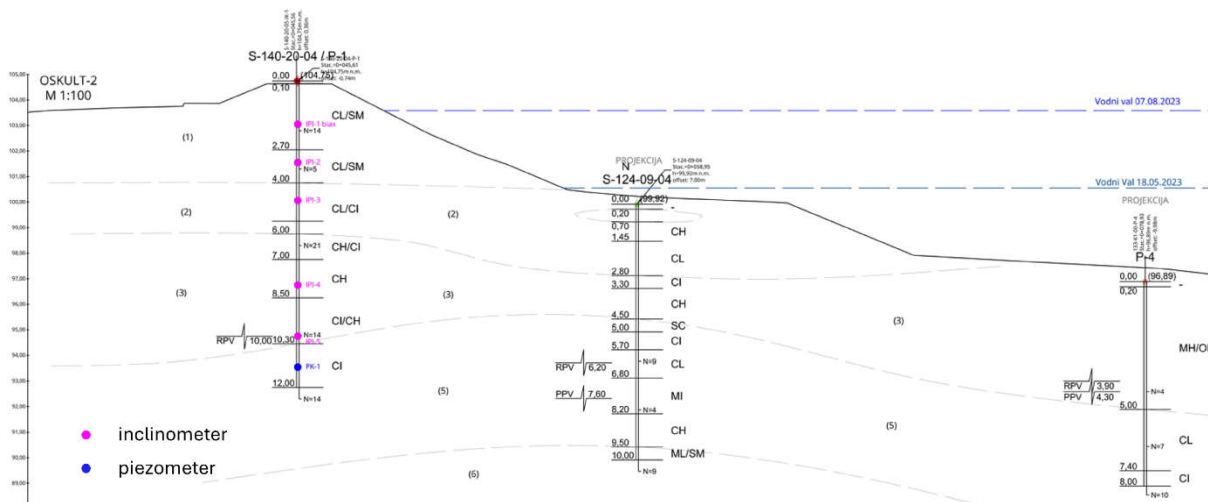
Figure 2. One of the cross-sections with installed equipment as part of the VEPAR project.

3   Analysis

Many instruments are being tested for their applicability in monitoring of embankments, either manual or autonomous, on experimental embankments as well real operational ones. However, some state-of-the-art instruments are always present and still widely used, even though there are objectively better options among the newer technologies. Such instruments include inclinometers and piezometers, with now the already widely used thermal sensors, and recently more and more of fibre optics for temperature and strain measurements. Remote sensing is also an emerging type of measurements, mostly from seismic and electromagnetic methods, as well as airborne and space measurements like SAR. To facilitate the selection of suitable methods, Table 1 divides the instruments mentioned in this paper into different categories.

4   Conclusion

Currently, visual inspection is still the most common type of monitoring for most levees, and that will likely remain the case until competent authorities are able to allocate more funds towards monitoring of levees, in order to develop early warning systems. As discussed by various authors referenced in the paper, developing such a system consists of several segments which require additional funds and personnel to maintain across the thousands of kilometres of levees under the jurisdiction of a single competent authority. In any case, advanced monitoring equipment is essential for the early prediction of failure and the assessment of the state of the embankments. Since failure prediction is mainly interested in the occurrences within the soil body, instruments for in-situ measurements have been widely used. However, most of the in-situ measurements weaken the levee by installation, by creating seepage paths, especially if they are later removed. Furthermore, by definition, in-situ methods can only measure at a

single point or at several points along a line. For these reasons, remote sensing methods which do not damage the embankments and can measure continuously across areas, are becoming increasingly more interesting ways for performing geotechnical monitoring in smart levees. In-situ measurements are often direct measurements, which is more favourable than indirect ones, while remote sensing mostly relies on indirect measurements which requires correlations with the desired quantities.

Table 1. Commonly used instruments in smart levees with their categorization and typical usage

Instrument	in-situ / remote	spatial coverage	direct / indirect	measured params.	indirect quantity
piezometer	IS	point	D	water pressure	
thermal sensor	IS	point	I	temperature	water content
fibre optics	IS	line	D/I	temperature, strain, vibration	water content
inclinometer	IS	line	D	inclination (deformations)	
GPR	R	area	I	backscatter of electromagnetic waves	soil layers, structures
EMI	R	area	I	electrical conductivity	soil layers, water content
seismic methods	R	area	I	seismic waves velocity	soil layers, mechanical properties
flow meter	IS	point	D	discharge	
infrared camera	R	area	I	temperature	water content
SAR	R	area	I	backscatter of electromagnetic waves	deformations
ERT	R	area	I	electrical resistivity	soil layers, water content
HD camera	R	area	I		
acoustic sensors	R	point	I	acoustic signal	soil layers, mechanical properties
self potential	R	area	I	electric potential	water velocity, salinity, water content
weather station	IS	point	D	weather conditions	
earth pressure sensor	IS	point	D	pressure	
extensometer	IS	point	D	strains	
tiltmeter	IS	point	D	inclination	
SSA	IS	line	D	inclination (deformations)	

Of the geotechnical monitoring methods available, MEMS inclinometers play an important role in smart levees, as they provide lateral displacements in a line usually installed vertically inside the levee. Alternatives include SAA and vertically places fibre optics. However, these are all in-situ measurements that provide deformation data from within the levee, which cannot be obtained by other remote sensing methods. Instead, remote sensing methods, like the commonly used SAR, are able to cover large areas, but take measurements only at the embankments. Regarding seepage, various methods of temperature measurement are the most popular, but electromagnetic and even seismic methods have been shown to have applications in that regard. Still, one of the most used methods of water detection are piezometers, even though they are in-situ instruments which take measurements only at a single point. When designing a monitoring plan for a smart levee, it is important that adequate instruments are selected in accordance with the expected failure modes at each cross-section/reach, such that a combination of their data can detect the onset of each failure mode early enough.

Acknowledgments

warning system and population awareness for multi hazard cascading events).

References

Balis, B., Bartynski, T., Bubak, M., Harezlak, D., Kasztelnik, M., Malawski, M., Nowakowski, P., Pawlik, M., Wilk, B., 2017. Smart levee monitoring and flood decision support system: reference architecture and urgent computing management. Procedia Computer Science, International Conference on Computational Science, ICCS 2017, 12-14 June 2017, Zurich, Switzerland 108, 2220–2229. https://doi.org/10.1016/j.procs.2017.05.192

Bersan, S., Koelewijn, A.R., Simonini, P., 2015. Application of distributed temperature sensors in piping-prone dikes, in: Ninth International Symposium on Field Measurements in Geomechanics. Australian Centre for Geomechanics, Sydney, Australia.

Cola, S., Simonini, P., Bossi, G., Schenato, L., Polo, F., 2019. Geotechnical Analysis and Optical Fiber Based Monitoring of an existing river levee affected by piping. Presented at the ICONHIC 2019, 2nd International Conference on Natural Hazards & Infrastructure, Chania, Greece.

Cundill, S.L., 2016. Investigation of Remote Sensing for Dike Inspection (Ph.D.). University of Twente, The Netherlands.

de Vries, G., Koelewijn, A.R., Hopman, V., 2012. IJkdijk Full Scale Underseepage Erosion (Piping) Test: Evaluation of Innovative Sensor Technology 649–657. https://doi.org/10.1061/41147(392)63

Dunbar, J.B., Galan-Comas¸, G., Walshire, L.A., Wahl, R.E., Yule, D.E., Corcoran, M.K., Bufkin, A.L., Llopis, J.L., 2017. Remote Sensing and Monitoring of Earthen Flood-Control Structures (final report No. ERDC/GSL TR-17-21). USACE, Vicksburg, MS.

Grget, G., Mihaljević, I., Šindler, D., Kaić, M., Rubčić, I., Ivoš, H., Pećina, I., 2023. Pilot projekt "Pametni nasip". Elaborat o provedenim geotehničkim mjerenjima. (Geotehnički elaborat No. E-140-20-03). Geokon-Zagreb d.d., Zagreb.

Hopman, V., Kruvier, P., Koelewijn, A., Peters, T., 2011. How to create a Smart Levee, in: 8th International Symposium on Field Measurements in GeoMechanics. Berlin, Germany, pp. 12–16.

Inaudi, D., 2019. Optical Fiber Sensors for Dam and Levee Monitoring and Damage Detection, in: Lorenzo, J., Doll, W. (Eds.), Levees and Dams: Advances in Geophysical Monitoring and Characterization. Springer International Publishing, Cham, pp. 91–120. https://doi.org/10.1007/978-3-030-27367-5_5

Inaudi, D., Cottone, I., Figini, A., 2013. Monitoring Dams and Levees with Distributed Fiber Optic Sensing. Presented at the The 6th International Conference on Structural Health Monitoring of Intelligent Infrastructure.

Koelewijn, A.R., de Vries, G., van Lottum, H., 2013. Full-scale field validation of innovative dike monitoring systems. Presented at the 18th International Conference on Soil Mechanics and Geotechnical Engineering, Paris, France.

Koelewijn, A.R., De Vries, G., Van Lottum, H., Förster, U., Van Beek, V.M., Bezuijen, A., 2014. Full-scale testing of piping prevention measures: three tests at the Ijkdijk, in: 8th International Conference on Physical Modelling in Geotechnics, Proceedings. Presented at the 8th International Conference on Physical modelling in Geotechnics, CRC Press - Taylor and Francis Group, pp. 891–897.

Krzhizhanovskaya, V.V., Shirshov, G.S., Melnikova, N.B., Belleman, R.G., Rusadi, F.I., Broekhuijsen, B.J., Gouldby, B.P., Lhomme, J., Balis, B., Bubak, M., Pyayt, A.L., Mokhov, I.I., Ozhigin, A.V., Lang, B., Meijer, R.J., 2011. Flood early warning system: design, implementation and computational modules. Procedia Computer Science 4. https://doi.org/10.1016/j.procs.2011.04.012

Leong, S.H., Kranzlmüller, D., 2015. Towards a General Definition of Urgent Computing. Procedia Computer Science, International Conference On Computational Science, ICCS 2015 51, 2337–2346. https://doi.org/10.1016/j.procs.2015.05.402

Lorenzo, J.M., Hicks, J., Vera, E.E., 2014. Integrated seismic and cone penetration test observations at a distressed earthen levee: Marrero, Louisiana, U.S.A. Engineering Geology 168, 59–68. https://doi.org/10.1016/j.enggeo.2013.10.019

Melnikova, N.B., Shirshov, G.S., Krzhizhanovskaya, V.V., 2011. Virtual Dike: multiscale simulation of dike stability. Procedia Computer Science, Proceedings of the International Conference on Computational Science, ICCS 2011 4, 791–800. https://doi.org/10.1016/j.procs.2011.04.084

Mihaljević, I., Gagro, M., 2010. Sanacije dijela lijeve obale rijeke Save uzvodno od ustave Prevlaka. (Građevinski projekt No. E124- 09– 03). Geokon-Zagreb d.d., Zagreb.

Niederleithinger, E., Weller, A., Lewis, R., 2012. Evaluation of Geophysical Techniques for Dike Inspection. JEEG 17, 185–195. https://doi.org/10.2113/JEEG17.4.185

Rossi, N., Bačić, M., Librić, L., Kovačević, M.S., 2023. Methodology for Identification of the Key Levee Parameters for Limit-State Analyses Based on Sequential Bifurcation. Sustainability 15, 4754. https://doi.org/10.3390/su15064754

Santamarina, J.C., Rinaldi, V.A., Fratta, D., Klein, K.A., Wang, Y.-H., Cho, G.C., Cascante, G., 2005. A survey of elastic and electromagnetic properties of near-surface soils, in: Butler, D.K. (Ed.), Near-Surface Geophysics. Society of Exploration Geophysicists, Tulsa, OK, pp. 71–88.

Sekuła, K., Borecka, A., Kessler, D., Majerski, P., 2017. Smart levee in Poland. Full-scale monitoring experimental study of levees by different methods. Computer Science 18, 357–384.

Sjödahl, P., Johansson, S., Dahlin, T., 2011. Investigation of shallow leakage zones in a small embankment dam using repeated resistivity measurements in Internal erosion in embankment dams and their foundations: Internal Erosion in Embankment Dams and Their Foundation. [Host publication title missing] 13, 165–172.

van Vliet, L., Koelewijn, A.R., van der Vat, M., 2012. Sensors, Deltafacts. Foundation for Applied Water Research (STOWA), Deltares.

Wolff, T.F., 2008. Reliability of levee systems, in: Phoon, K.-K. (Ed.), Reliability-Based Design in Geotechnical Engineering. CRC Press, London, England, pp. 448–496.

Topic 4

Geohazard Assessment and Risk Mitigation for Infrastructure Projects

PREDICTING SHALLOW RAINFALL-INDUCED LANDSLIDES IN ETHEKWINI MUNICIPALITY, SOUTH AFRICA: UTILISING THE TRIGRS MODEL

SIBONAKALISO GOODMAN CHILIZA [1,2], EGERTON HINGSTON [2], MOLLA DEMLIE [2]

[1] *Council for Geoscience, South Africa, gchiliza@geoscience.org.za*

[2] *University of KwaZulu-Natal, South Africa, hingstone@ukzn.ac.za; demliem@ukzn.ac.za*

Abstract

This study investigates the application of the TRIGRS model for predicting rainfall-induced shallow landslides in the eThekwini Municipality, South Africa. TRIGRS simulates transient infiltration and slope stability to assess landslide susceptibility. The model was applied to a 1 km² block in a landslide-affected area. Rainfall scenarios with varying intensity and duration were modelled. Scenario A, simulating high-intensity rainfall, predicted widespread instability in the southern block, which coincides with a zone of weaker geotechnical properties, including areas covered by the Berea red sand (landslide-prone soil). This aligns with observed landslides that occurred in this area following a high-intensity rainfall event. Scenario B, simulating lower intensity but longer duration rainfall, predicted overall stability across the research area. This highlights the critical influence of peak rainfall intensity on slope stability in this specific case. The minimum Factor of Safety (FOS) depth (0 m and 2.9 m) varied between scenarios, indicating a higher risk of shallow surface erosion under high-intensity rainfall.

The TRIGRS model effectively identified areas susceptible to landslides. Rainfall intensity is a key factor influencing slope stability, with peak intensity being more critical than total rainfall duration in this case. The study emphasises the importance of considering both geotechnical properties and rainfall intensity for robust slope stability assessments and hazard mitigation strategies.

Keywords

Early warning system, landslide prediction, landslide susceptibility assessment, shallow landslide, spatially distributed slope stability models, TRIGRS.

1 Introduction

Rainfall-induced landslides significantly threaten life and property in the eThekwini Metropolitan Municipality (eThekwini Metropol) of KwaZulu-Natal, South Africa. The devastating 2022 event, resulting in hundreds of fatalities and billions of Rand in damages, underscores the critical need for improved prediction capabilities. Thus, to minimise the landslide hazard risk in the eThekwini Metropolitan Municipality, knowledge of how rainfall influences landslide susceptibility in this region is necessary. Various methods are currently being used in space and time prediction of shallow landslides at the catchment scale. Among them, physically based models, such as SHALSTAB (Montgomery and Dietrich, 1994), SINMAP (Pack et al., 1998), GEOtop-FS (Rigon et al., 2006), TRIGRS (Baum et al., 2008), SLIP (Montrasio and Valentino, 2008), HIRESSS (Rossi et al., 2013), SHIA_landslide (Aristiz´abal et al., 2016), STEP-TRAMM (Lehmann and Or, 2012), SCOOPS 3D (Reid et al., 2015), R.ROTSTAB (Mergili et al., 2014) and FSLAM (Medina at al., 2021). This study investigates the application of TRIGRS, a spatially distributed shallow landslide prediction model, in the eThekwini Municipality located in Eastern South Africa. By integrating a transient infiltration model with slope stability analysis, TRIGRS offers a physically based approach to simulating soil hydrology and slope response under various rainfall scenarios. This work is part of a research that aims to predict

the timing and location of shallow landslides within the study area, ultimately contributing to landslide susceptibility assessment and early warning system development through (i) assessing the variation of the Factor of Safety, (ii) the soil depth for the minimum Factor of Safety in a grid based on variable rainfall intensity and duration, and (iii) locate/map the location of unstable areas/grids.

2   Methods

The TRIGRS Model (Transient Rainfall Infiltration and Grid-Based Regional Slope-Stability) is a Fortran program based on the association between a hydrologic and a stability model that predicts shallow landslides induced by rainfall events by computing transient pore-pressure changes and their effects on the Safety of Factor (FOS) at different depths (Baum et al., 2008). The model works by associating a hydrological model (Richards equation for infiltration and transient-type and three-dimensional flow for heterogeneous, isotropic and unsaturated medium) to a stability model Eq. (1) proposed by Iverson (2000). Eq. (1) has been coded into a software program by means of a Fortran language.

$$FS = \frac{\tan\phi\prime}{\tan\delta} + \frac{c - \psi(Z,t)\gamma w \tan\phi\prime}{\gamma s Z \sin\delta \cos\delta} \tag{1}$$

Where, "*Fs*" is the Factor of Safety [dimensionless]; "*φ or ϕ*" is the angle of internal friction [∘]; "*θ or δ*" is the angle of the slope [∘]; "*c*" is the effective cohesion [kPa]; "*ψ (Z, t)*" is the pressure head [kPa]; "*Z*" is the soil depth [m]; "*t*" is the time [s]; "*ρw or γw*" is the water density [kg/m3] and "*ρs or γs*" is the soil density [kg/m3].

The input data requirements and the process flow in TRIGRS are outlined in Figure 1. The data input into the TRIGRS is initially done using a Digital Elevation Model to construct the slope angle and flow direction maps (contributing area). Since the Factor of Safety of a slope depends on various factors like geotechnical and hydrological properties (cohesion, internal friction angle, depth, hydraulic conductivity and others as indicated in Table) and time-varying rainfall intensity, obtaining these soil and rainfall data is crucial (Baum et al., 2002). The parameters used in the TRIGRS model were divided into topographical properties, rainfall and soil properties (geotechnical) depicted in Figure which for corresponding property zones were kept the same for scenarios A and B. These are herein referred to as scenarios A and B, which pertain to rainfall intensity and duration parameters of two events as 2,40E+01mm/h and 8,00E+00 mm/h after 12 and 48 hours of rainfall durations, respectively. These are also in agreement with rainfall intensity recordings reported by Bell and Maud (2000).
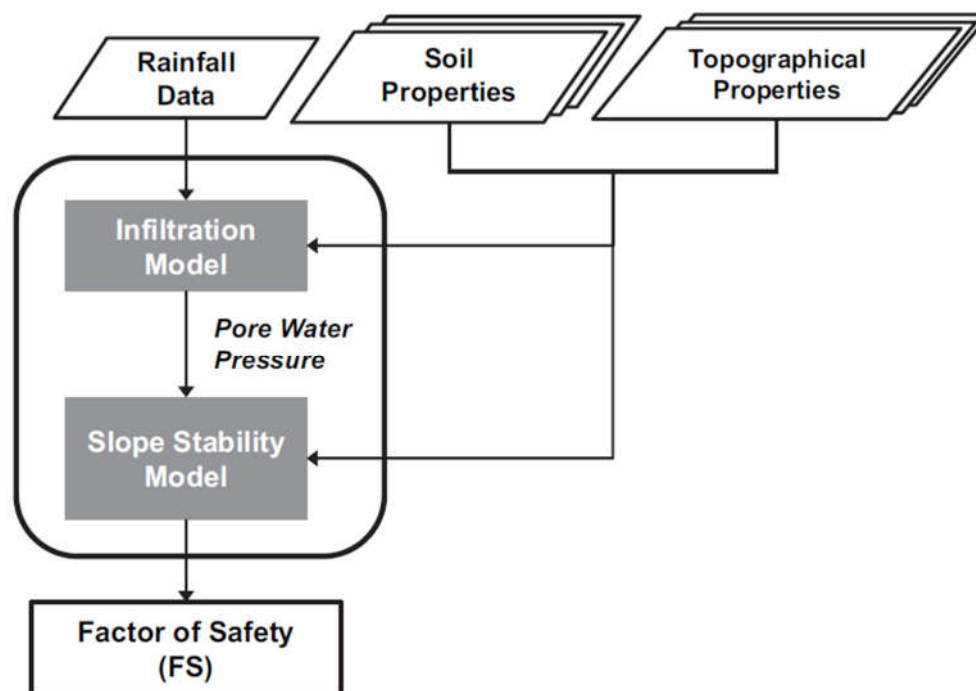
Figure 1. TRIGRS data and process flow (Kim et al.,2013).

In both scenarios, geotechnical values were derived from soil samples collected in the field from the landslide scars and analysed, pursuant to the applicable South African National Standard SANS634(2012) and ASTM ASTM D422-63(2007). The commercial laboratories commissioned for the purposes of this study and existing consultant reports provided the required soil properties values.

This study tests the application of TRIGRS modelling for eThekwini Municipality where rainfall intensity data is limited as only daily rainfall data was available. Therefore, a series of TRIGRS simulations were undertaken by specifying a range of rainfall intensities and durations that result in reasonable predictions of the shallow landslide occurrence in the study area. The soil thickness is also an essential parameter in the TRIGRS model (Baum et al., 2008). Soil thickness affects infiltration and soil cohesion in deterministic shallow landslide models. Soil thickness data was limited to the central business district of Durban and could not be interpolated satisfactorily using the IDW interpolation method in Arc GIS. As a result, in this study, simulations were made using an average 3 m scenario for Zmax to simulate the maximum thickness of the soil. The same scenario was used for the initial height of the water *(d)* as proposed by Baum et al. (2002).

The study area was subdivided into four property zones based on the regional geological and topographic map (Table). To identify property zones which are used to simplify inputting physical properties (soil strength parameters and hydraulic properties)into the model, first, the analysis included topographic position and landform analysis (Weiss, 2001) to create landforms using the Topographic Position Index (TPI). The methodology involves generating a multi-scale TPI, classifying it into slope position and landform types, and characterising watersheds based on TPI values. By incorporating additional metrics such as elevation variance and slope, the analysis can reveal detailed topographic features like ridges, valleys, slopes, and flat areas (Weiss, 2001). Secondly, a weight overlay analysis using geology, slope and landforms was conducted in ArcGIS Pro to produce property zones and these are Zone A (Residual Dolerite, Residual granite in local ridges and hilly valleys, mountain top, high ridges; Zone B (Residual Shales, alluvium, dune and beach sand in mountain tops, high ridges and mid slopes); Zone C (residual sand and hillslope colluvium, recent sand deposits in mountain tops, high ridges, local ridges and hilly valleys, upper slopes and mesas); and Zone D (residual granite in mountain tops, high ridges and mid

slopes).

The Saturated hydraulic conductivity K_{sat} (m/s) was determined using the empirical equation proposed by Hazen (1911), as shown in Eq. (2). The hydraulic conductivity value in Eq. (2) is determined based on grain size distribution analysis of soil samples taken across the study area. The results were also compared with published and in situ test results from this research.

$$K = Cx(d10)^2 \qquad (2)$$

Where K is hydraulic conductivity (cm/s), d10 is the effective grain size in cm (i.e. 10 % of particles are finer or 90% of particles coarser) and C is a constant that ranges from 40 to 150 (cm/s)-1. The range of values of C are as follows, but one can use the median value from the range given to each grain size and sorting category:

- Very fine, poorly sorted sand   40-80
- Fine sand with appreciable fines   40-80
- Medium sand, well sorted   80-120
- Coarse sand, poorly sorted   80-120
- Coarse sand, well sorted, clean   120-150

Table 1. Geotechnical and hydrological parameters used in Zmax = d (3 m) scenarios for FoS calculations in TRIGRS.

Property zones	Effective cohesion, c (kPa)	Effective friction angle phi (°)	Unit weight *(ps)* (kN/m³)	Maximum thickness of the soil (Z_{max}) [m]	Initial height of the water table (d) [m]	Saturated hydraulic conductivity K_{sat} (m/s)	Infiltration rate I_{LT}(m/s)	Hydraulic diffusivity D_0 (m²/s)	Vertical saturated hydraulic conductivity (K_{sat}) [m/s]
1	30	35	17	3	3	1,E-07	1,00E-09	1,E-05	1,E-06
2	15	28	17	3	3	1,E-07	1,00E-09	1,E-05	1,E-06

Initially, challenges were encountered while utilising the TRIGRS program due to limitations in the data used for the analysis. To overcome the challenges and improve the computational efficiency of the analysis, the study area was discretised into smaller, more manageable units. Previously, the entire eThekwini metropolitan area, encompassing a data grid of 621 columns and 858 rows, was analysed. In this revised approach, the area is segmented into a grid of 1 km² blocks, each consisting of 100-meter x 100-meter resolution grids. This discretisation reduced the data volume to a more manageable 11 x 11 grid while still capturing the spatial variability of the phenomenon timing and distribution of shallow, rainfall-induced landslides.

Figure shows an example of a 1 km² block elevation grid (DEM) around the uMgababa Church Landslide of 11/12 April 2022.
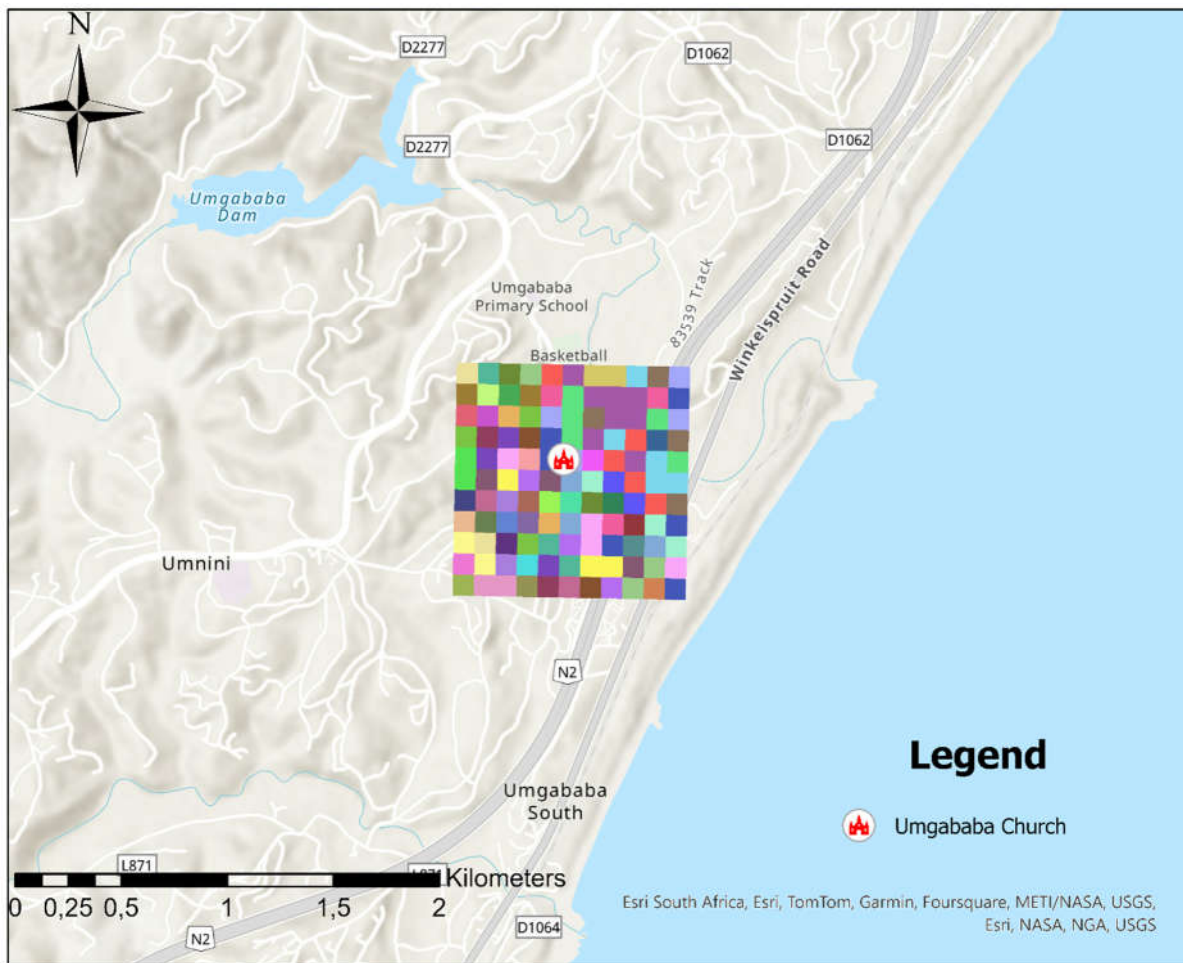
Figure 2. A 1 km² block elevation grid (DEM) with uMgababa Church Landslide approximately in the middle.

3　TRIGRS Modelling Test Site Characteristics

The TRIGRS model was applied to a landslide threatening a sizable church property near Durban, South Africa (Figure 2 & 3). The site, located 350 m west of the N2 highway crossing the uMgababa River (S30°9′32.97″; E30°48′56.97″), is underlain by Vryheid Formation sandstones and shales, which are, in turn, overlain by Berea Formation silty sands, with no mapped regional faults.

Figure 3. Local geology is characterised by Vryheid Formation mudrocks and siltstone overlain by Berea-type sands.

The 22 415 m^2 landslide that occurred around the focus area has a width of 115 m and a runout distance of 185 metres downslope. Preliminary observations revealed that the failure surface may have involved translational and rotational failure mechanisms. Multiple soil slumps observed in the Berea Formation silty sands point to a curved failure plane. Due to the slope failure, existing roads that crossed the slope were moved approximately 25 metres downslope. Several residential buildings within and near the landslide's margins were destroyed or severely damaged. However, the St John's Apostolic Faith Mission Church and other structures on the church property were moved downslope without collapsing, garnering media attention.

4   TRIGRS Modelling Results and Discussion

The results of the TRIGRS slope stability modelling for the test site i.e. the minimum Factor of Safety (FOS) and soil depth distribution across the research area for Scenarios A and B, respectively are presented and discussed. The minimum FOS represents the most critical location within each 100 x 100 m grid cell for potential slope failure. TRIGRS also generates additional output files including the depth of minimum FOS and the pressure head at that depth. The conventional interpretation of the FOS value in slope stability analysis is adopted in this study. A stable slope is characterised by FS greater than 1.0, indicating sufficient resisting forces to counteract destabilising forces. Conversely, a FOS value less than 1.0 signifies an unstable slope susceptible to failure (Wad, 1978). Notably, areas with a FOS significantly below 1.0 are considered highly susceptible to landslides.

TRIGRS model results for Scenario A:

A significant concentration of unstable cells (FOS < 1. 0) is evident (Figure), predominantly distributed across the southern block of the 1 km² test site. This southern region coincides with Property Zone 2, which is characterised by lower shear strength parameters. Specifically, Zone 2 exhibits an effective cohesion (c) of 15 kPa and a friction angle (ϕ) of 28°. These weaker geotechnical properties contribute to the inherent instability of this zone. Furthermore, the predominant soil type in Zone 2 is Berea red sand, a material known for its erodibility and susceptibility to landslides (Richards, 2009).

The TRIGRS output for Scenario A reveals two distinct FOS values: 0 and 11. This binary distribution suggests that the entire southern block (Property Zone 2) is predicted to be unstable under the high-intensity rainfall conditions of Scenario A. This prediction aligns with the observed landslides that occurred in this region on April 11th and 12th, 2022, following the high-intensity rainfall event. These landslides caused significant damage, including the destruction of houses and the displacement of residents.
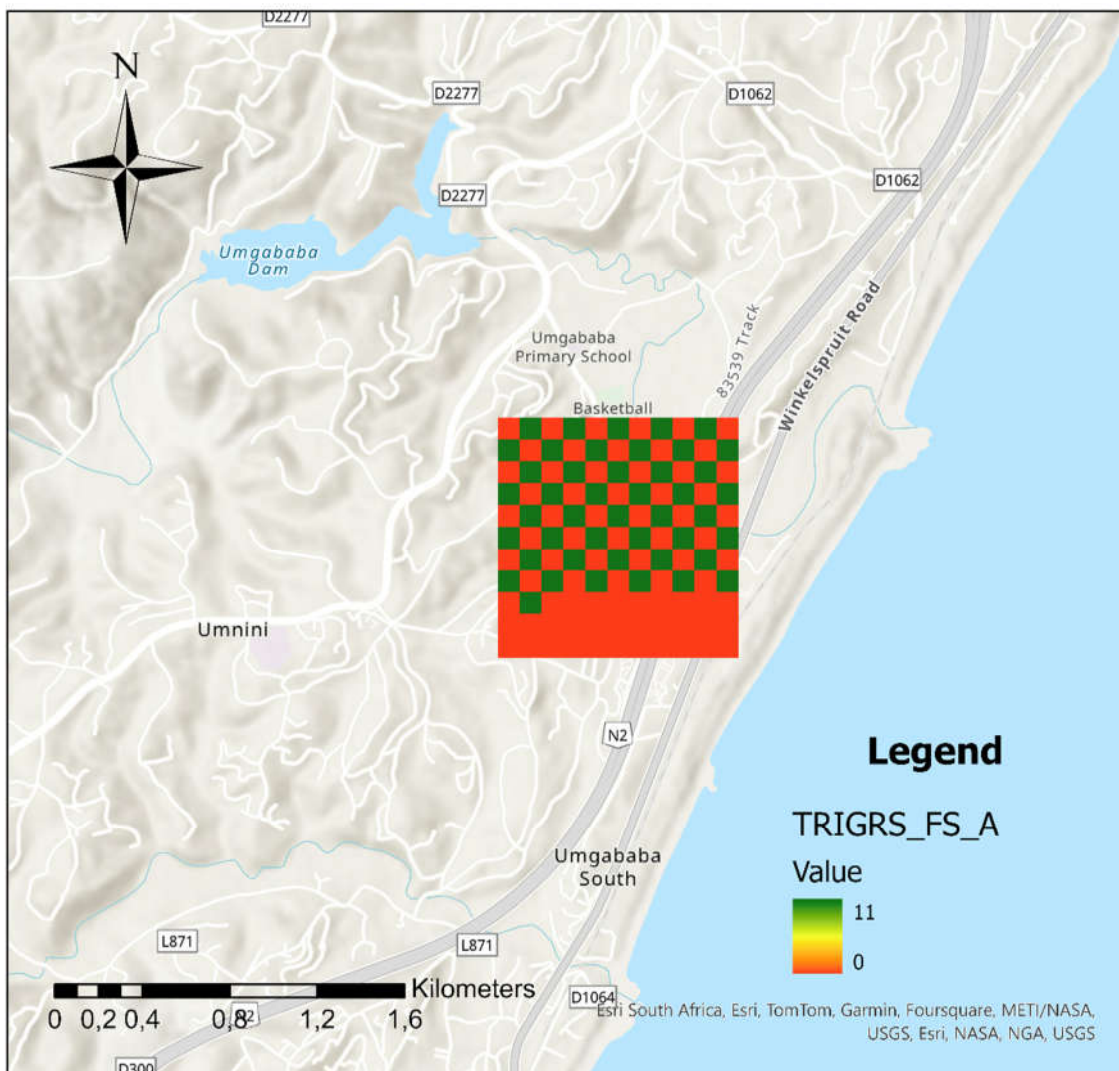
Figure 4. Display of TRIGRS output file for the minimum Factor of Safety for scenario A in ArcGIS Pro.

TRIGRS model results for Scenario B:

Figure presents the minimum FOS distribution for Scenario B, which simulates a lower rainfall intensity (8 mm/h) but with a longer duration (48 hours). As shown in the figure and the accompanying table, the minimum FOS values across the grid range from 2.432 to 11. This result indicates that the entire research area remains stable under the less severe rainfall conditions of Scenario B, despite the extended rainfall duration. A critical observation from comparing the results of Scenarios A and B is the dominant influence of rainfall intensity on slope stability in the study area. While Scenario A with its high-intensity rainfall resulted in widespread instability, Scenario B with its lower intensity rainfall maintained overall slope stability despite the longer duration. This finding suggests that the critical factor for slope failure in this specific case is the peak intensity of the rainfall event rather than the total rainfall duration.
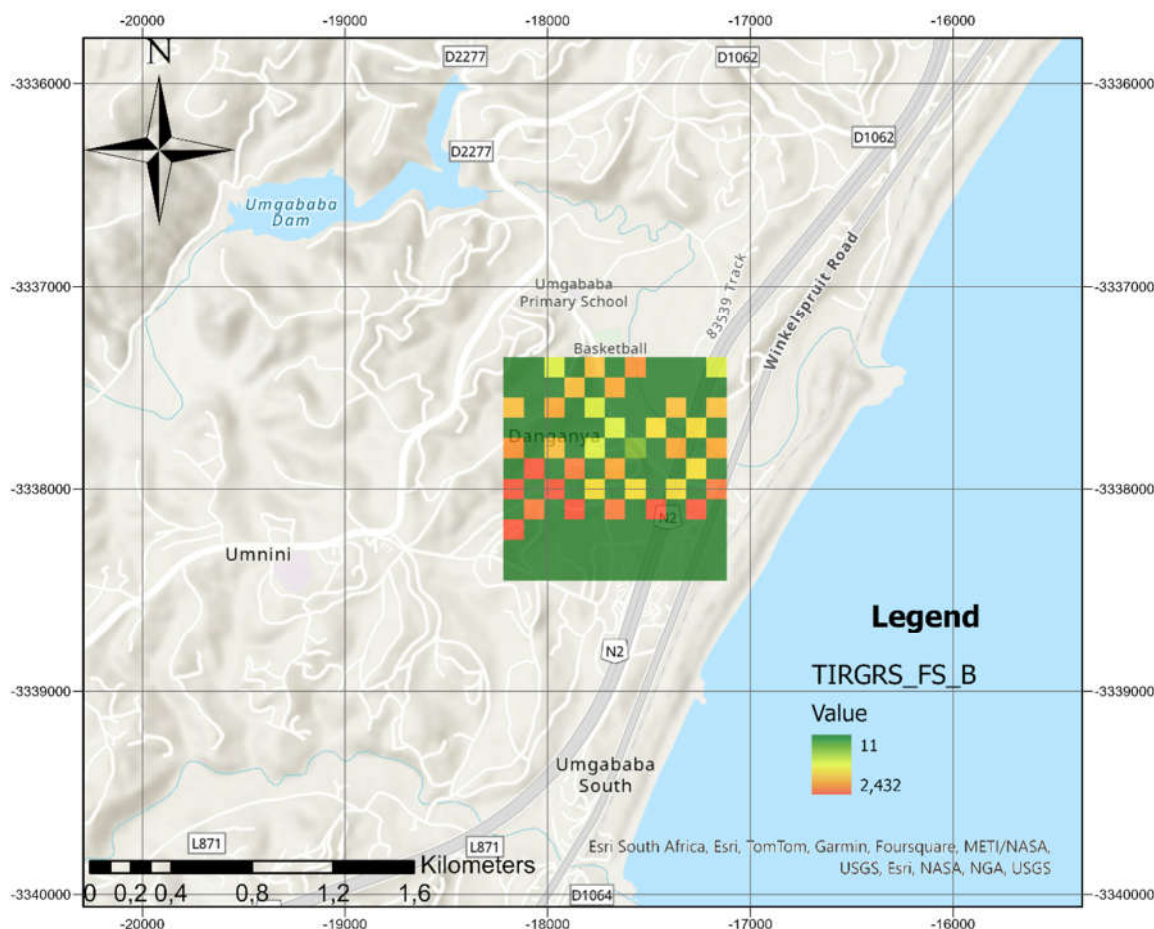
Figure 5. Display of TRIGRS output file for the minimum Factor of Safety for scenario B in ArcGIS Pro.

The minimum Factor of Safety was computed at various soil depths, indicating possible rapture (failure) surfaces. For scenario A, the soil depths with a minimum FOS were computed at 0 m in TRIGRS for all grids. This means that the minimum FoS might be at a very shallow depth within the soil, close to the surface, indicating an inherent risk of surface erosion or sloughing, where a thin layer of soil peels away. In scenario B, the minimum Factor of Safety was found at soil depths of around 0.4 m in several locations/grids. In some locations, the minimum Factor of Safety was also found at a depth of around 2.96 m. This could be due to several factors, such as the presence of a weak layer of soil at this depth, or changes in the pore water pressure distribution (Figure). The southern zone has the lowest FS in Scenario A and the highest in Scenario B which highlights the significant dependence of stability on scenario conditions and material properties.
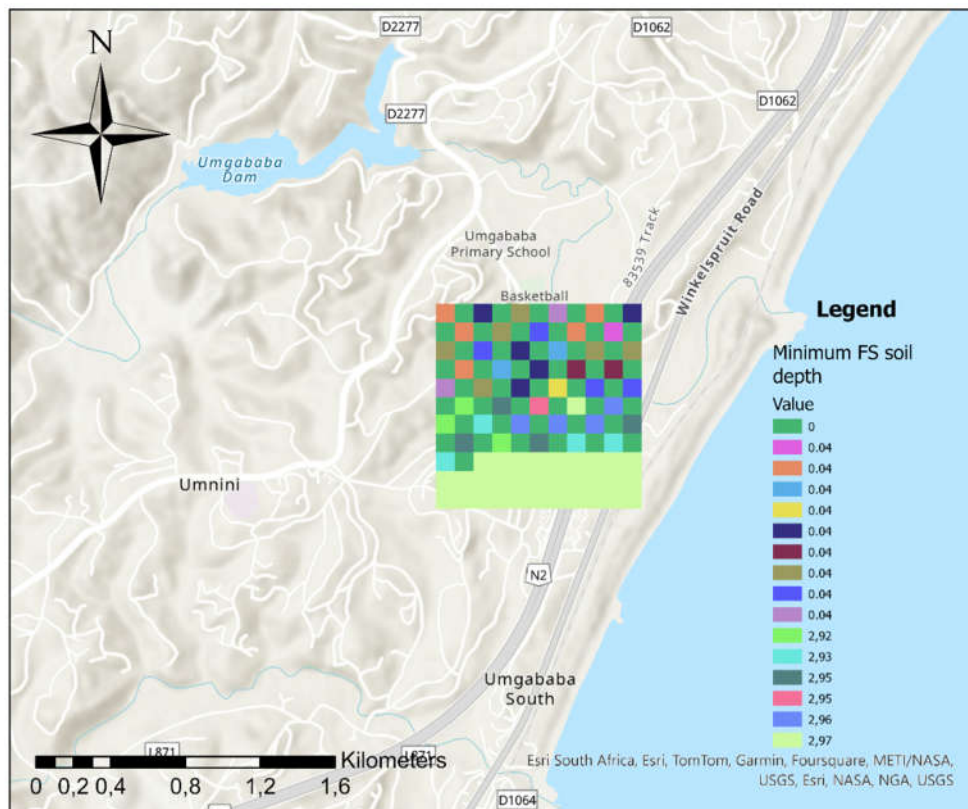
Figure 6. Soil depths with the minimum FS for each grid.

5   Conclusions

The TRIGRS model effectively identified areas susceptible to slope failure in the 1 km² test site near Durban, South Africa. Scenario A, simulating high-intensity rainfall, predicted widespread instability (FOS < 1.0) concentrated in the southern block. This coincides with Property Zone 2, characterised by weaker geotechnical properties and Berea red sand, a landslide-prone soil type. This aligns with observed landslides that occurred in this region following a high-intensity rainfall event in April 2022. Conversely, Scenario B, simulating lower rainfall intensity for a longer duration, resulted in overall stability (FOS > 1.0) across the entire research area. This highlights the critical influence of peak rainfall intensity on slope stability, suggesting that, in this specific case, the total rainfall duration was less important than the intensity for triggering landslides.

The stability of the South zone is highly dependent on the rainfall scenario, i.e. intensity and duration, as shown by Scenario A conditions. The southern zone's material properties exhibit sensitivity to the type of rainfall conditions applied with Scenario B's loading conditions seem to be more favourable for the South zone, resulting in a higher FS. These conclusions highlight the importance of considering different rainfall scenarios and material properties when evaluating slope stability.

The minimum Factor of Safety (FOS) depths varied between scenarios. In Scenario A, the minimum FOS occurred at a very shallow depth (0 m), indicating a high risk of surface erosion or sloughing. Scenario B displayed minimum FOS depths of around 0.4 m and 2.96 in some locations, potentially due to weaker soil layers or pore water pressure changes. The findings highlight the importance of considering both geotechnical properties and rainfall intensity for robust slope stability assessments.; and provide valuable insights for hazard mitigation strategies in the study area.

References

ASTM D. 422-63. Standard test method for particle-size analysis of soils. Annual book of ASTM standards. 2007;4:10-6.

Aristizábal E, Vélez JI, Martínez HE, Jaboyedoff M. SHIA_Landslide: a distributed conceptual and physically based model to forecast the temporal and spatial occurrence of shallow landslides triggered by rainfall in tropical and mountainous basins. Landslides. 2016 Jun;13:497-517.

Baum RL, Savage WZ, Godt JW. TRIGRS: a Fortran program for transient rainfall infiltration and grid-based regional slope-stability analysis, version 2.0. Reston, VA, USA: US Geological Survey; 2008.

Bell FG, Maud RR. Landslides associated with the colluvial soils overlying the Natal Group in the greater Durban region of Natal, South Africa. Environmental geology. 2000 Jul;39:1029-38.

Hazen, A. "Discussion of Dams on sand foundations by A. C. Koenig", Trans. Am. Soc. Civ. Eng., 73, pp. 199–203, 1911.

Iverson RM. Landslide triggered by rain infiltration. Water resources research. 2000 Jul;36(7):1897-910.

Kim D, Im S, Lee C, Woo C. Modeling the contribution of trees to shallow landslide development in a steep, forested watershed. Ecological Engineering. 2013 Dec 1;61:658-68.

Lehmann P, Or D. Hydromechanical triggering of landslides: From progressive local failures to mass release. Water Resources Research. 2012 Mar;48(3).

Medina V, Hürlimann M, Guo Z, Lloret A, Vaunat J. Fast physically-based model for rainfall-induced landslide susceptibility assessment at regional scale. Catena. 2021 Jun 1;201:105213.

Mergili M, Marchesini I, Rossi M, Guzzetti F, Fellin W. Spatially distributed three-dimensional slope stability modelling in a raster GIS. Geomorphology. 2014 Feb 1;206:178-95.

Montgomery DR, Dietrich WE. A physically based model for the topographic control on shallow landsliding. Water resources research. 1994 Apr;30(4):1153-71.

Montrasio L, Valentino R. A model for triggering mechanisms of shallow landslides. Natural Hazards and Earth System Sciences. 2008 Oct 21;8(5):1149-59.

Pack RT, Tarboton DG, Goodwin CN. SINMAP, a stability index approach to terrain stability hazard mapping. SINMAP user's manual, Terratech Consulting Ltd. 1998.

Reid ME, Christian SB, Brien DL, Henderson ST. Scoops3D: software to analyze 3D slope stability throughout a digital landscape. US Geological Survey; 2015.

Richards, N.P. (2009). Explanation of the engineering geological and geotechnical conditions for the 1:50 000 scale map sheet 2930 DD & 2931 CC Durban. Council for Geoscience.

Rigon R, Bertoldi G, Over TM. GEOtop: A distributed hydrological model with coupled water and energy budgets. Journal of Hydrometeorology. 2006 Jun 1;7(3):371-88.

Rossi G, Catani F, Leoni L, Segoni S, Tofani V. HIRESSS: a physically based slope stability simulator for HPC applications. Natural Hazards and Earth System Sciences. 2013 Jan 25;13(1):151-66.

South African Bureau of Standards (SABS). Geotechnical investigations for township development [SANS 634]. SABS Standards Division. ISBN 978-0-626-27636-2. 2012.

Ward TJ. Factor of Safety Approach to Landslide Potential Delineation. Colorado State University; 1976.

Weiss A. Topographic position and landforms analysis. InPoster presentation, ESRI user conference, San Diego, CA 2001 Jul 9 (Vol. 200).

GEOHARZARDS TRAPS ENCOUNTERED ON THE ROUTE OF THE HIGHWAY PITEŞTI-SIBIU, ROMANIA

MIHAELA STĂNCIUCU [1], ADRIAN M. DIACONU [2], IULIANA G. DOGARU [2], RAMONA A. MIHAI[2]

[1] *University of Bucharest, Romania, mihaela.stanciucu@unibuc.ro*

[2] *Geotesting CI, Romania, office@geotesting.ro*

Abstract

The architecture of the geological structure is very often an intricate composition of structural rock and soil masses, affected by divers and independently or simultaneously discontinuities syn, or post genetic, which sustain one or more local and regional aquifers, and is continuously submitted to gravitational, and seismically hazardous actions. Usually, all large infrastructure projects invariable pass through one or more complex areas in which objectives are affected by geohazards at various scales. This is also the case of the route of the highway Pitesti-Sibiu, Romania, which was investigated in several field campaigns to decrypt the complex geological and hydrogeological structure. The paper elaborates and details, one by one, all enounced geohazards, which were studied by diverse and numerous investigation methods: geological, geotechnical, hydrogeological, and geophysical, by a multidisciplinary team.

Key words

Landslides, faults, expansive soils, erosional process, geohazard.

1   Geologic and tectonic frame

Along 50km sections of the route, the highway steps over four large geologic structures (from South-East to North -West): Getic Depression, Subcarpathian thrust belt, and Post-tectonic Cover of South Carpathians, and effectively cut up a stratigraphic column starting from Palaeocene sandstones and claystone, up to Quaternary alluvial, deluvial or terrace deposits. All structures, which are situated less than 150 km from the Vrancea Seismic Zone, are affected by a few deep intra-Moesical faults and more recent and superficial thrust faults which turn into blocky fractured shapes in the upper deposits.
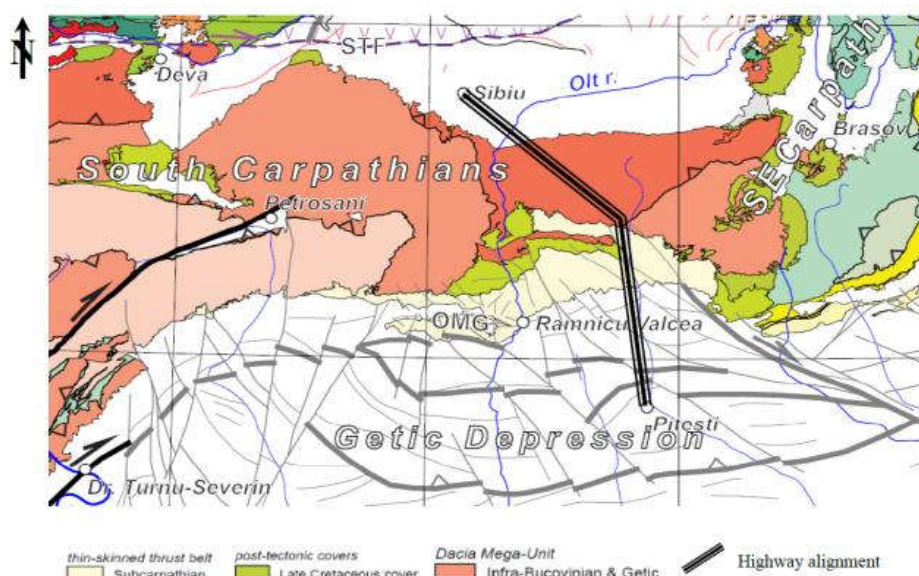
Figure 1. Geologic frame of the project (RGI, 2023)

2. Investigations

The field investigation program at the current stage of the study included geotechnical drilling, standard drilling penetration tests (*SPT*), heavy dynamic penetration tests (*DPH*), ~~and,~~ static cone penetration tests (*CPT*), *ERT* electrical resistivity tomographies and *MASW* seismic measurements. On the route of the studied highway section, a total of 208 boreholes with a total length of 4525 m was executed.

3. The Northern area

3.1. Geological frame of the Northern area
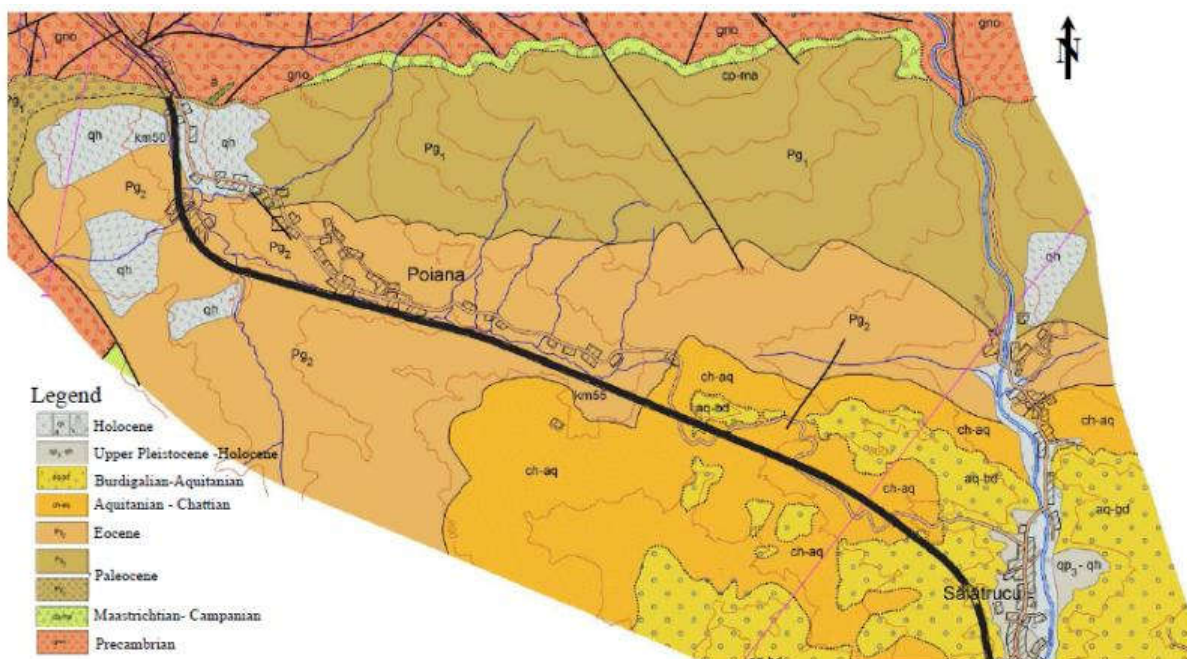
Figure 2. Geologic frame of the Northern area (RGI, 2021)

The oldest bedrock we encountered in the Northern area of investigation is Lower Paleocene (*Pg₁*) which are represented by polymictic conglomerates, or by grey and reddish marls with sandstones. This package appears at the surface on the extreme Northern frame of the investigated area, but is uncovered in all torrential valleys encountered in the highway alignment.

The Eocene deposits (*Pg₂*) are very extended at the surface in this area, and have large thicknesses what exceeds 100m. The basic level is represented by polygenic conglomerates containing crystalline shale, Jurassic limestone and coarse sandstone, followed by marls and sandstones.

The next layer is represented by the specific Pucioasa formation (*ch-aq*) consisting in dark-grey clays and thin layers of fine sand.

The newest bedrock we encountered in the area is the aquitanian-burdigal deposits (*aq-bd*) which are lithologically constituted of „*erratic*" polygenic conglomerates, sometimes poorly cemented by a sandy clay matrix, which includes elements from the most varied formations (crystalline shales, mesozoic rocks, etc, eocene organogenic limestones, as well as soft buckets of oligocene rocks), gravels and sands that comprise frequent intercalations of gray marl.

The shallow formations are mainly composed in thick, unconsolidate deluvial deposits (*qp₃-qh*) as in extended sliding masses of debris or landslides, both being predominantly constituted by elements coming from submerged deposits.

3.2. Geohazard traps encountered in the Northern area

3.2.1. Geomorphological hazards

As the topographical alignment of the highway, it's opening up on the top of the hills, between 800m and 700m height, it passes over numerous torrential valleys and ravines. All of them are thus open to erosional processes due to superficial spillage of rainfalls, which may attain 130mm/month in winter or 200mm/month in summer. In consequence, most of them (more than 15 positions) are found in various stages of evolution manifested by the presence of frequent faces of detachment and various stages of instability. Considering all above, the geomorphological hazard present in this area derives from the fragmentation of the general slope by torrential erosion of the water from surface runoff in the context of a predominantly non-cohesive substrate of the bedrock and of shallow deposits.

3.2.2. Hydrogeological hazards

In the Northern part of the Northen area, due to the high position of the site, the groundwater was intercepted at depths ranging from 1 m to 9 m, usually as an aquifer with a free level cantoned in the non-cohesive levels of the complex of quaternary deluvial deposits. Due to the lithological variability of the deluvial structure (is recognized that the existence of a minimum percentage of 20% of fine fractions <0.063mm, transforms a granular layer from aquifer into aquitard), it was frequently encountered the situation in which the cohesive levels from the surface of the land, locally bring the aquifer under pressure, fact demonstrated by the presence in several drillings of a piezometric level in a completely cohesive quaternary sequence.

In the Southern part of the Northen area, the groundwater was sporadically intercepted on the investigated route, only in 20% of executed boreholes, as a partial free-level aquifer, partial under pressure, located at depths ranging from 0 m to 22 m, either in the deluvial deposits or in non-cohesive layers of the base rock. Likewise, deluvial deposits, the non-cohesive deposits of the base rock have variable percentages of fine fractions, creating the premises that they become locally aquitard, and thus delimiting multiple discontinuous "*suspended*" aquifers, feed from precipitation.

Overlaid over the general regional aquifer situated at deeper depths, these local "*suspended*" aquifers are non-permanent, but temporary, during periods of strong rainfalls when they can enter under pressure, generating (also temporarily) the loss of internal resistance of non-cohesive deposits.

3.2.3. Geological and geomechanical hazards

From geologic point of view, hazards that may occur in this part of the project is related both on the bedrock formations and on the shallow deposits, as we describe below.

The bedrock formations, regardless of petrography / lithology or age, is found in boreholes with the specific characteristics of an overconsolidated rock, intensely fragmented by relaxation and sometimes with one or more intense shearing intervals. This situation may explain by the fact that in this specified area, all bedrocks formations were and still are subject to the following fields of efforts (Figure 2 a, b, c):

- Overall tectonic stress applied to the entire sedimentary structure, which manifests in long term (compressions and shears with extremely low deformation speeds occurring in geological time, but which by summing up the effects can generate such deformations);
- actual and local stresses, due to sliding forces acting in time at a perceptible human scale; in the preliminary phases of sliding phenomena, the entire sliding forces generate plastic or brittle deformations (depending on the degree of saturation of the clays / degree of cementation of sandstones or conglomerates) which are not (yet) generalized along a unique sliding surface to facilitate the movement of a large mass of rocks, or in final stages assembled on a proper shear surface which allows displacements of the upper deposits on limited distances to a position with lower potential energy.
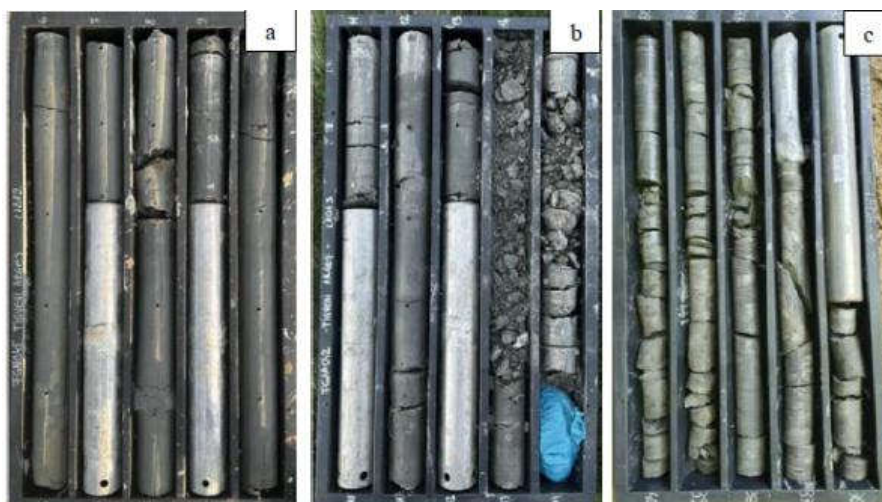
Figure 3. Aspects of hazadous geologic characteristics of cohesive bedrock:
(a) undisturbed; (b) sheared ; (c) intensely fragmented by relaxation Pucioasa formations(*ch-aq*);
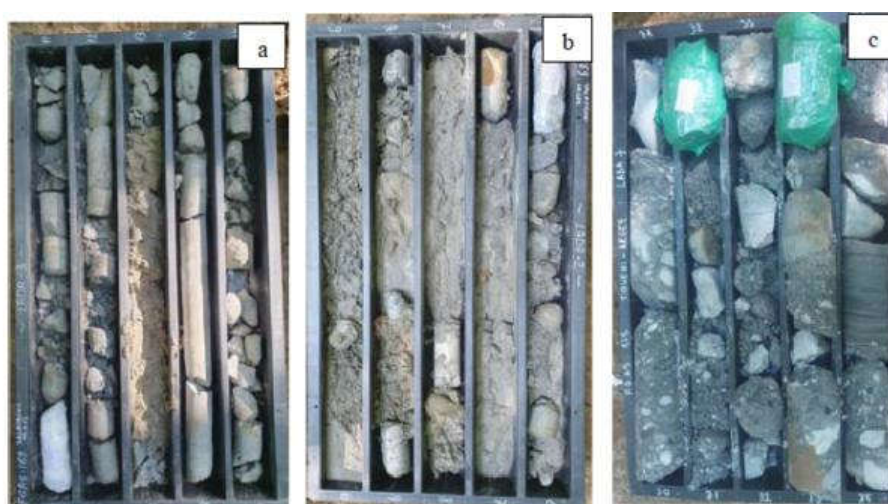
Figure 4. Aspects of hazadous geologic characteristics of un-cohesive bedrock:
(a) Variable degree of cementation of sandstone; (b) immersed sands and fragments of Eocene sanstone (Pg_2);
(c)) „*erratic*" polygenic conglomerates with variable degree of cementation *(aq-bd)*

Most of the time, the non-cohesive bedrock deposits are either fine and very homogeneous or coarse and extremely inhomogeneous, containing numerous rock fragments of various sizes and petrographic types. In many positions the fine - non-cohesive deposits are found in a partially/apparently cemented state (Figure 4, a), generating levels of sandstone with cementing levels ranging from uncementing to very well cemented. But there are also situations where these deposits contain intercalations of conglomerates, core samples with lengths >0.50m of compact rocks or fragments of hard rocks which are more or less ~~desegregated~~ (disaggregated?) (Figure 4, c).

The shallow formations in this part of the project are exclusively Holocene deluvial type (*qh*) which are always unconsolidated and consists either of weakly cohesive matrix (in soft or very soft plastic state) mixed with elements of the bedrock, or more frequently they are made up mainly of non-cohesive soils, is loose state.

Even that the uncohesive bedrock formations or shallow deposits are found in predominantly dry state, another hazard that may affect these soils is related to the genetic or postgenetic hererogenity of these deposits which promote the formation of temporary, discontinuous "*suspended*" aquifers, that we described above, during or after every strong precipitation. In consequence, in short time sequences, the entrapped areas of uncohesive deposits may develop temporary excessive water pressures which destroy

the natural sedimentary structure and leave the volume of the affected slope with near nul shear resistance. As mark of this geomechanical process, we found in boreholes, in both formations frequently "immersed sands", as presented in Figure 4. b.

Due to the limited and discontinuous extensions of these suspended aquifers, displacements do not generate a well-defined area of yielding, however, it is very likely that this fact is one of the primary causes of multiple lithological disturbances and discontinuities of the non-cohesive deposits that subject the slopes constantly and continuously to some "incremental" displacement downstream, over short distances. These cumulative manifestations over time, or amplified by seismic events (that may generate even local liquefaction areas) can lead to significant instability as is confirmed by geophysical investigations executed in these areas, two of them being presented in Figure 5.
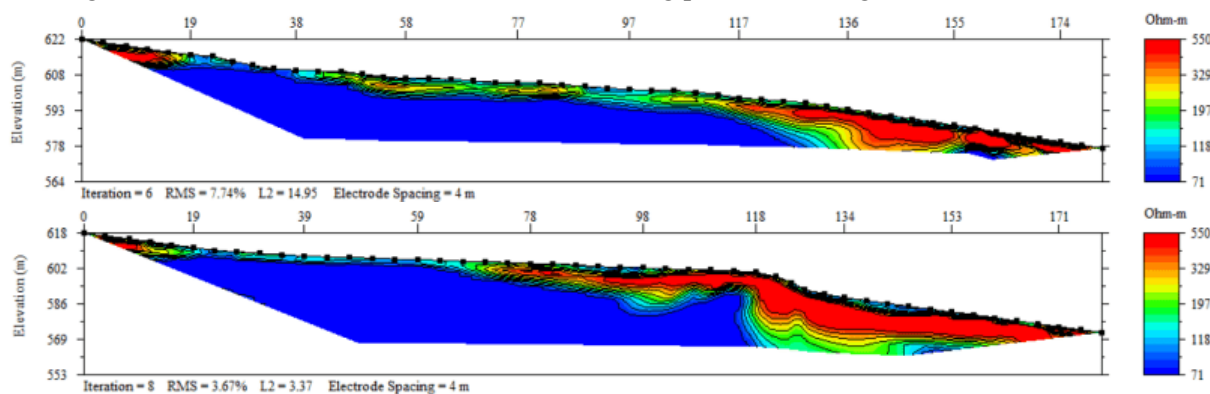
Figure 5. Geophysical investigations (*ERT*) wich confirm the instability of deluvial shallow deposits (Geotesting C.I, 2023)

4. The Southern area

4.1. Geological frame of the Southern area
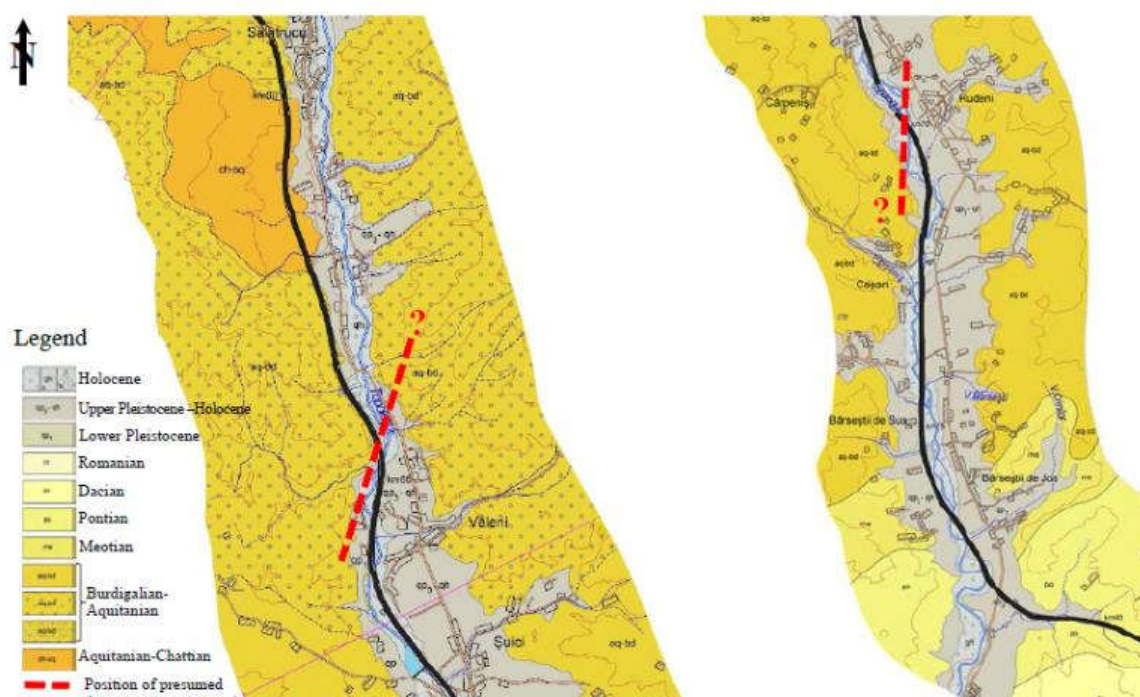
Figure 6. Geologic frame of the Southern area (RGI, 2021)

The oldest bedrock we encountered in the Southern area of investigation is Pucioasa formation (*ch-aq*) consisting in dark-grey clays and thin layers of fine sand, which is exposed at the surface in the North part of the Southern area, but is spread in depth in all the rest of the project.

It is covered by a thick package of aquitanian-burdigal deposits (*aq-bd*) which were mainly described in the previous section 3.2., but here a new member completes the succession, respectively a reddish layer of clays or marls.

The next lithologic complex is attributed to Miocene epoch and is composed mainly by marls (*me, po, ro*) or marls alternated with sands (*dc*).

The shallow formations are mainly composed in alluvial gravels which are regionally spread, namely Cândești Strata (*qp₁*), followed by unconsolidated deluvial deposits (*qp₃-qh*) and actual alluvial sediments (*qh*).

4.2. Geohazard traps encountered in the Southern area

4.2.1. Geomorphological and anthropic hazards

In this Southern part of the project, the route alternately crosses the both banks of the Topolog river.

On the right side of the river, which have a limited extension, the route traverses both the terrace and the meadow units, encountering the following geomorphologic features which generate hazardous aspects that may affect the embankment:

- The position on the highway is often situated on the first level of the terrace, in the area of connection with the base of the hill slope, which reach higher altitudes between 550m and 750m, and are cut by numerous torrential valleys and ravines. Locally, in several positions it approaches very close to the slopes, which in some places already manifests instability phenomena under various stages of development;
- these critical positions favors also the temporary the accumulation of the flows from surface runoff of precipitation, which are prevented from infiltration in deep by the presence of impermeable river bed, or the accumulations of permanent springs that emerges at the base of the slopes, and are obstructed from discharge in river by the embankment itself;
- Also, on this side of the river the phenomena of instability of the connection between the terrace deposits (3m-15m height) and lower alluvial banks, as of the erosional processes of the latter, are quasi permanent presented;
- finally, we mention here, as an important anthropic hazard, the presence of the exploitation career of sand and gravel in Salatrucu, Arges County, which is subjected to continuous regressive erosion processes under the action of rainwater, accentuated on the background of poor cementing of conglomerate formations (Figure 7).

Figure 7. Aspects of the perimeter of the exploitation of sand and gravel quarry in Salatrucu

On the left side of the Topologu river, mainly extend the alluvial plain on 2km-3km wide and in consequence the embankment will encounter only:

- erosional processes of alluvial banks, which is active along the entire length (Figure 8);
- fewer torrential valleys affluents on the left that discharges the waters coming from the surface of the terrain and water leakages on the forehead of the alluvial plain. In one position, namely Vãleni location, it develops a limited area of terraced deposits that are shattered by an important left affluent;
- some instability phenomena at the level of connection between the minor and the major riverbed;
- finally, an important anthropic hazard on this side represents the presence of numerous and extensive bumps (positive and negative) due to chaotic exploitation of alluvial deposits or landfills, as the presence of a small concrete dam.

Figure 8. Undisturbed (left) and instable deposits (right) of riverbanks

4.2.2. Hydrogeological hazard

In this Southern part of the project, we encounter two superficial aquifers located on both sides of the Topolog river:

- on the right side, the phreatic aquifers develop according to the morphological unit in which they are quartered. These aquifers are located in terraces and deluvial deposits that are generally coarse, consisting of sands, gravels and boulders;
- on the left side, the meadow of Topolog has between 2 km and 3 km wide, and the groundwater level is situated between 0.5 m-2 m deep, in aluvial porous permeable layer deposits which are covered by a thin waterproof roof. During periods of intense rainfall, the regime of flow can temporarily enter under pressure and under high hydraulic load, the aquifer can become artesian at the base of the embankment. In the discharge sections of this aquifer, due to temporary rise of hydraulic gradient of water flow, pipping and internal regressive errosions may occur, causing extensive landslides as is the case of above mentioned Vãleni area.

Bellow all these phreatic aquifers lays a huge structure, namely the "Cândești Layer". From hydrogeological perspective, it is defined as a large multistat-aquifer structure characterized by hydraulic conductivity of up to 100m/day and transmissivity of less than 1000m^2/day, with a thin supply front in the North, which ends at contact with the Carpathian chain and the main directions of groundwater flow from North to South (Palcu et. al., 2008).

This regional hydrogeological configuration is in hydraulic contact with deeper regional aquifers and can develop water pressures on the coatings up to 40 Barr. The entire package of multilayer aquifers (from the Jurassic to the Upper Pleistocene) operates under a pressure regime that becomes uneven artesian. These deep (regional) aquifer horizons defined as the "Dacian Artesian Basin", is located under the erosion base and is supplied by infiltration of the surface waters of the main valleys and atmospheric precipitation through the border areas of these formations, which sometimes are situated far away. In consequence, all these structures are therefore in hydraulic communication with the groundwater levels

generating vertical drainage phenomena when the developmental pressures are high (Figure 9).

Figure 9. Artezian well and swamping areas created by vertical ascensional drainage of Cândeşti aquifer

4.2.3. Presence of expansive soils

On this Southern part of the project, the foundation ground consists mainly of weakly consolidated or normally consolidated alluvial quaternary formations (maximum 15m thick), followed in depth by bedrock formations which include alternations of cohesive and non-cohesive complexes (Figure 10). The main risk factor is the quasi-continuous presence of soils with large swelling and contractions, both in the case of bedrock formations framed in the cohesive complex and sporadically in the fine-cohesive levels of the quaternary deposits. An extensive study of these swelling formations was based on more than 660 samples that have been tested both mineralogical and geotechnical.

Figure 10. Cohesive bedrock in the Sothern part of the project

From mineralogic point of view, these swelling soils are made mainly of hydrous phyllosilicate, especially of smectite clays (60%-80%), followed by illite (20%-30%) and subordinate kaolinite and chlorite. The main geotechnical characteristics include the predominance of fine granulometric composition (*Cl* and *siCl* in proportion >72%), of high and very high plasticity (I_p >20% in the proportion 95%). In the purpose of a better interpretations, the results have been divided into three classes according to the plasticity index and range values of swelling pressure (p_u), as presented in Table 1.

Table 1. Classification system according to plasticity indices and swelling pressures results

Class of swelling pressures		C1		C2		C3		Total number of samples	[%]
		No	[%]	No	[%]	No	[%]		
(I)	p_u<200kPa	28	100	203	91	254	62	485	73
(II)	200≤ p_u<400kPa	-	-	16	7	114	28	130	20
(III)	p_u ≥400kPa	-	-	4	2	44	11	48	7

Figure 11 presents the variation in depth of the swelling pressure as the corresponding distribution of differences between inflation pressures and geological load at the level of sampling of the respective sample (p_u-s_g).

We appreciate that these values must to be regarded as estimative but expressing a real geotechnical risk that can manifest both in the areas specified by this investigation, as well as in the syngenetic areas that have not been tested yet, especially due to the intricate occurrence of these soils in the vicinity or inside the Cândești Strata.
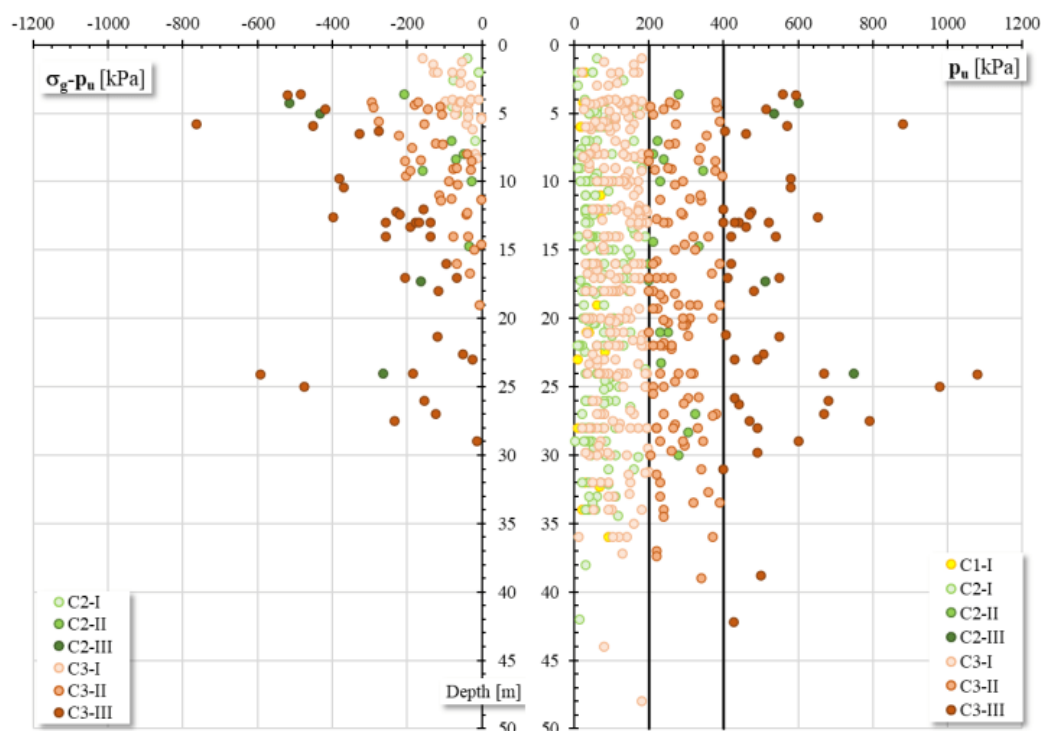
Figure 11. The variation in depth of p_u (right) and of the potential heave of Cândești Layers (left).

4.2.4. Tectonic hazard

In this Southern area, we found some geomorphological aspects that suggests that the entire geological structure is possibly affected by tectonic disturbances. More precisely, in at least two locations in this area, the river suffers a sudden change of the course direction, both dextro-roughing, with displacements of about 100m (Fig.6). These aspects are consistent with the tectonic compression frame of this sector where other systems of parallel fault with NE-SV direction are already pointed out. In these two locations, these presumptions are also sustained by the findings in the cores of the boreholes situated on both sides of the presumed fractures, mainly by the following aspects whose explanation can only be one of tectonic nature:

- in the areas of the roughest of the river, the continuity of the geologic and hydrogeologic structure is broken on short distances, by the development of different members of the bedrock (cohesive/noncohesive) respectively, by the disappearance of the underground water table level on several meters distances;

- usually, the non-cohesive complex of the bedrock consists of fine to coarse granular deposits, which often also contain significant percentages of fine fractions, which are found in a partially/apparently cemented state, generating levels of soft rocks. In the positions we mention above, these deposits contain many intercalations or fragments of hard rocks, allogeneic as marbles, gneiss, or tuffs;

- the same situation is encountered also in cohesive complex of the bedrock, which usually contains levels of fine particles, generally in the stiff state, but the areas we reffer too these deposits contains frequently hard allogeneic rock fragments imbedded, and the soil matrix was found in a soft consistency.

5   Conclusion

The complex investigations – geomorphologic, hydrogeologic, geologic, mineralogic and geophysical-performed on the alignment of about 20km length between Poiana and Tigveni, part of Piteşti-Sibiu highway, revealed several natural and anthropic aspects that may become truly traps for the further large project.

Geomorphologically, in the Northern part, the route is situated on the slopes and alternately crosses climbs, promontories and torrential valleys, with west-east orientation. Here, instability phenomena are already manifested in various stages of evolution, most of them along torrential valleys which fragmented the continuity of the slope and eroded the base thereof, constituting preliminary factors of the instability re-appearances. In the Southern part, the route is situated on the terrace level and on the alluvial plain of the main watercourse Topolog, and the main geomorphologic traps consist in the development of the erosional processes both of the river at the base of the terrace as of runoff precipitations on very neighbouring slopes.

From hydrogeological perspective, in the highlands of the Northern part, heterogeneity of deluvial deposits favours the formation of non-permanent suspended aquifers, which temporarily during periods of precipitation, may enter under pressure, generating loss of internal resistance of non-cohesive deposits. Consequently, these are subject to downstream "incremental" displacements on short distances, in a process that occurs without the formation of a well-defined area of disposal, but are uncovered by superficial deformations. In the Southern part, hydrogeological traps refer to the artesian manifestation of both superficial (alluvial) and regional (Cândeşti) aquifers that may induce pipping and internal regressive erosions in foundation terrains, or the wetting of the base of the future embankment.

The specific geological features consist, in the Northern part, in the prevalence in the foundation terrains of the over-consolidated rocks which have been affected by tectonic and neo-tectonic processes of folding, cutting or even bending over other formations, and now during the project excavation, may be easier affected by sliding processes due to relaxation deformations. In the Southern part, the main geologic trap is the presence and the discontinuous spreading of expansive soils, with a very hight content of smectite minerals (60%-80%). Here, the recorded values of the swelling pressures are also sometimes exceptional ($p_u<1080kPa$), and are associated with very high free swelling values ($U_L<600\%$). This feature is even more hazardous, as these layers are prone to wetting by ascensional vertical drainage phenomena of the regional Cândeşti aquifer.

Apart from the major seismic hazard which derives from the vicinity with one of the strongest seismic epicentral areas of Europe (less than 160 km from Vrancea), the tectonic network of main and secondary faults has been proved denser than the official tectonic architecture, some of them being revealed by newest investigations and still pending for geophysical seismic endorsement.

References

Geotesting C.I: Geotechnical study for the purpose design and execution of the Sibiu-Pitesti highway. Section 3: Cornetu - Tigveni, Sector 2, km 61+740 – km 81+879. 2023, ST-A-3-PT-SG-S1-001.

Palcu, M., Melinte, M.C., Jurkiewicz, A., Witek Gh. şi Rotaru, A. Preliminary inventory of aquifer structures in the southern part of Romania. *Geo-Eco-Marina*. 2008; 17: 7-16

Romanian Geologic Institute (RGI), *Geologic map of Romania*, scale 1:1000000, 2023

Romanian Geologic Institute (RGI), *Geologic map of highway Cornet-Piteşti*, scale 1:50000, 2021

RESTORATION OF DAMAGE TO A PROVINCIAL ROAD IN THE REGION OF ATTICA (GREECE) AFTER A DISASTROUS WEATHER EVENT

NIKOLAOS TAVOULARIS [1], AGGELIKI KONSTANTARA [1], AGGELIKI ZIAVRA [1], LEONIDAS SOTIROPOULOS [2]

[1] *Region of Attica, Directorate of Technical Works, Piraeus & Islands Regional Unit, Greece,* ntavoularis@patt.gov.gr, akonstan2002@gmail.com, aziavra@patt.gov.gr,

[2] *EDAFOS Engineering Consultants, Greece,* lsotiropoulos@edafos.gr

Abstract

This paper describes soil instabilities and rockfalls that occurred during the heavy rainfall of September 2023, named "Daniel," in a total length of 4.8 km of the Provincial Road Old Epidaurus-Galata belonging to the Region of Attica in Greece. The Department of Technical Works of the Piraeus & Islands Regional Unit (Attica, Greece) oversaw the restoration of the damage manifested in the above-mentioned area. On the rocky slopes of the road, instability phenomena were activated during the occurrence of intense rainfall in September 2023.

In the present study, the geological and geotechnical characteristics of the instabilities problems which activated after the extreme weather phenomena are briefly described and proposals and immediate measures to address them are presented.

Furthermore, two well-known assessment methodologies were implemented, which confirm the hazard and risk respectively in selected part of the area under consideration. Since this section of the Provincial Road had been closed after the occurrence of "Daniel" and because this road is connected with tourist resorts as well as many towns and villages in the Piraeus & Islands Regional Unit, the immediate and secure restoration of the described damage and removal of risk were of major importance for the Regional Authority of Attica.

Key words

Rockfalls, Old Epidaurus – Galata Provincial Road, Daniel rainfall, mitigation measures, hazard estimation

1 Introduction

On 5-7 September of 2023, a very heavy rainfall (maximum daily rainfall recorded: 754 mm), named as "Daniel" manifested in many areas of Greece, resulting in tremendous damages to infrastructure and losses of people lives. One of those areas that suffered from this devastating event was part (e.g. 4.8 km) of the Provincial Road Old Epidaurus - Galata belonging to the municipality of Troizinia-Methana of the Region of Attica (e.g., the biggest regional government authority in Greece). The Provincial Road Old Epidaurus - Galata junction, which is a main transit route to Galata, Troizina, Kalloni, etc (Figure 1), closed for restoration works (EDAFOS S.A, Region of Attica, 2024).

For the section from ch. 4+370 to ch. 9+170, with a total length of 4,8 km, the geological and geotechnical conditions are presented and evaluated, in order to record and determine problems of soil instabilities and rockfalls that occurred on 5-7 September of 2023.

Rockfalls and soil instabilities of small and large scale occurred in the studied section of the road, which were mainly related to but not limited to the occurrence of extreme weather conditions. The instability phenomena are more pronounced during the winter months and pose a risk to the safe movement of passing vehicles along the road. During the extreme weather events of September 2023, but also previously, in December 2021, rock falls and sliding of soil materials occurred in some locations of the Provincial Road, resulting in its disconnection, without damages. Due to severe flooding phenomena of

September of 2023 and to avoid accidents, the road had been closed from 7 September 2023 till 30 April 2024 as a precautionary measure.

Ten (10) general areas of soil instability with uniform characteristics (geological conditions, type, size and mechanism) and a total of twenty-nine individual locations of activated or potential instabilities were identified (EDAFOS S.A, Region of Attica, 2024).

On the rocky slopes of the road, as well as in the wider area, during the occurrence of intense rainfall and flooding events in September 2023, instability phenomena were activated such as:

• Rock blocks failures of toppling and wedge mechanisms (Tavoularis et al., 2021),
• Flows and slides of scree and talus cone materials,
• Planar failure of the rock mass along unfavorable oriented bedding or discontinuities

In the area of interest (Figure 1), apart from the manifested failures, the presence of a significant number of large rock blocks has been noted, most of which are in marginal equilibrium, with a risk of toppling, sliding and falling within the road.
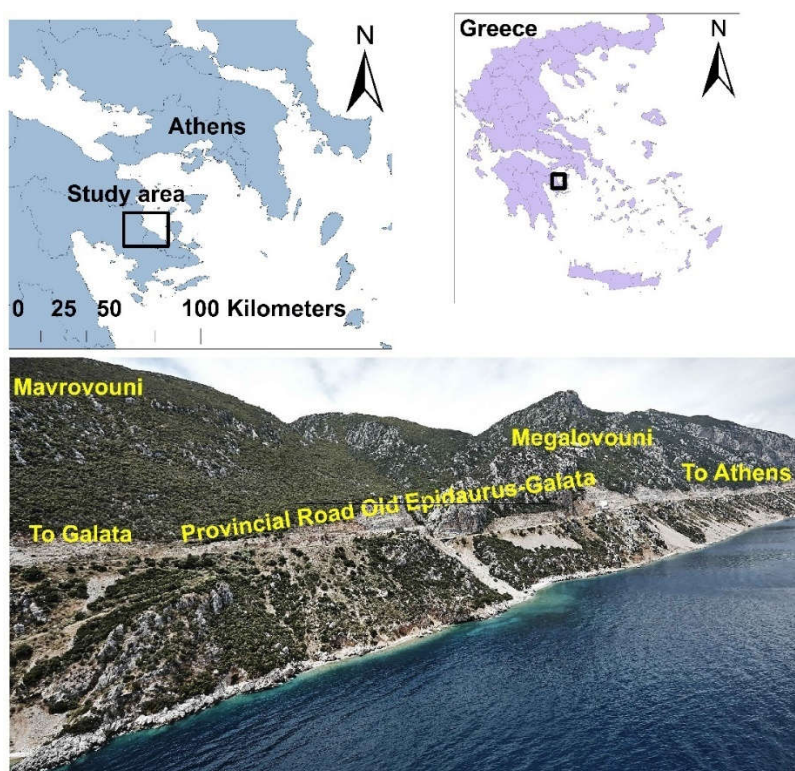
Figure 1. Overview of the study area of the Provincial Road Old Epidaurus-Galata (view from Trip in View site)

As previously mentioned, the road was closed from the beginning of this event (e.g. 7 September of 2023) till the end of April of 2024, where restoration works fulfilled. During this period, the Department of Technical Works of the Piraeus & Islands Regional Unit (Regional Authority of Attica, Greece) supervised the restoration of the damage and the removal of risks manifested in the above-mentioned area.

In this paper, the geological and geotechnical characteristics of the conditions and issues of potential instabilities that were activated after the extreme weather phenomena, and proposals and immediate measures to address them are presented (so that road conditions are restored and made safer than the previous operational state). Furthermore, the paper implements two well-known existing rockfall hazard assessment methodologies; a qualitative (Rock Hazard Rating System) and a quantitative one (Quantitative Risk Assessment) that attempted to validate the hazard in selected part of the area under consideration.

Since this section of the provincial road is connected with important tourist resorts as well as being the basic road line to many towns and villages in the Piraeus & Islands Regional Unit, the immediate and secure restoration of the described damage and removal of risk was of major importance for the Regional Authority of Attica.

1.1 Geomorphological setting

The study area is developed between Old Epidaurus and the settlement of Kalloni and is morphologically located on the foothills of the mountain ranges Megalovouni and Mavrovouni with peaks at approximately +850 m and +600 m respectively and is characterized by a basically mountainous terrain with moderate to steep slopes of natural slopes. The absolute altitude along the road varies between +85 m and +135 m (Figure 1). The morphology of the wider area reflects the combined effect of geological structure, recent tectonic evolution and erosion processes and largely determines the processes involved in the activation of soil instabilities (EDAFOS S.A, Region of Attica, 2024).

Based on the geological structure and the composition of the rocks, the area is placed in a mountainous terrain zone, within the limestone formations that dominate the entire area.

The hydrographic network is generally sparse, locally more frequent in places where mainly tectonic structures such as faults, fault lines, fault zones, etc. pass through and its branches are mainly oriented NE - SW with a west to east flow direction. At the locations of the streams and gullies, the accumulation and transport of large amounts of debris from recent rainfall was found to have accumulated and transported on the slopes and inside the road.

The infiltration, estimated to be in excess of 50-60 %, occurs primarily by underground seepage, but it is also estimated that surface runoff is similarly significant due to the pronounced dolomitization of the formation. The watercourses have a significant flow and are characterized by their high carrying capacity, particularly during heavy rainfall events.

The main geomorphological features observed that affect the occurrence of soil instabilities are a) the steep overhanging slopes and b) the intense erosions and gullies within the streams and torrents that flow into the road (Figure 2).

Figure 2. Debris cone and alluvial material at the base of the slope and within the road, from material accumulated through the two talweg - gullies.

Due to the intense flooding events of recent years, the carrying capacity of watercourses (solid flow) has increased which directly affects the activation of slides. Three (3) such locations were identified in the study section which constitute those with the highest accumulation of unstable materials.

1.2. Geological setting

According to the geological map (Sheet LIGURIO, 1:50.000) of Greek Institute of Geological and Mining Exploration (IGME), the following geological formations were identified in the area of interest (EDAFOS S.A, Region of Attica, 2024):

- Fill materials
- Debris flows and gully materials (Tavoularis, 2023). The flows of soil and rock materials that have accumulated in the rock traps and / or on the road deck are associated with the presence of slope debris and alluvial materials, loose and unconsolidated, which during the recent floods moved in the form of saturated material flows, downstream and the outlet of the watercourses to the Provincial Road.

- Rock blocks - Products of rockfalls occurred in rocky limestone formations.
- "Pantokratoras" Limestones»: (a) Brecciated "Pantokratoras" Limestones, (b) Highly fractured and moderately to very weathered "Pantokratoras" Limestones, (c) Slightly fractured and weathered "Pantokratoras" Limestones.

The detachments of large sized rock blocks from slopes consisted of scree matrices and / or from the crowns of steep slopes.

1.3 Geotechnical setting

Twenty-nine segments were identified with geotechnical issues (existing and potential geotechnical instabilities) during the fieldwork and attributed to the severe weather phenomena that took place on 05-07/09/2023. It is noted that some of these may existed prior to the recent flooding, however it is considered that they need to be resolved for the safe operation of the road and its return to its previous condition. For the necessity of the upcoming described methodologies, one particular segment of the road is briefly presented (EDAFOS S.A, Region of Attica, 2024).

Section from ch. 5+490 km to ch. 5+590 km

There is a predominant occurrence of "Pantokrator" limestone, a formation which, as has been reported, constitutes the geological background throughout the section under consideration. The slope has a maximum height of about 50 – 55 m and a bench at a height of about 22-23 m from its base. At the area of interest, two grades of rock mass qualities were distinguished; one with fair characteristics that corresponds to thin bedded limestone, intensely fractured, with presence of secondary infilling materials and moderately to highly weathered discontinuities' surfaces by fine-stratified structure, intense fractured, presence of secondary soil fills and moderate - high discontinuity weathering, and one with good characteristics that correspond to medium to very thin bedded limestone, moderately fractured to widely spaced discontinuities, with no infilling and slightly weathered discontinuities' surfaces. The bedding planes inclined towards NW/NE with a dip angle of about 30° - 35°.
Apart from bedding planes, five (5) sets of discontinuities were encountered. According to the evaluation of the Schmidt diagrams, two common failure mechanisms were identified: rock toppling and rock wedge sliding. In actual conditions, locations of rock fragment detachment, mainly large-size rock 'wedges', and the occurrence of toppling or falling/detachment of overhangs were found. A typical rock wedge failure that caused serious damages to the existing metal barrier is presented in Figure 3.

Figure 3. Falling of an individual boulder of 8m^3 (maximum bolder size of the rockfall) that bounced off the existing protection measures and ended up on the road deck within the provincial road, at about Ch. 5+525 km. Close-up view of debris flow (on the right)

In order to optimize the available budget allocation for this project, two systematically used hazard and risk assessment methodologies were applied.

2 Methods

2.1 Rockfall Hazard Rating System (RHRS)

The instability events manifested in the Old Epidaurus- Galata Provincial Road after "Daniel" event, represent a major hazard because they can cause severe damage to infrastructure and loss to human lives. An efficient way to reduce potential future damage, is to improve land-use planning using, qualitative as well as quantitative hazard assessment approaches at the local and site-specific scales for one main reason, which is the recent dramatic climatic changes that have totally increased the frequency of slope instability events (Ferrari et al. 2016).

In this paper, a qualitative method, the well-known Rockfall Hazard Rating System (RHRS) is used, firstly developed from Oregon Department of Transportation (USA) in the late 1980s in order to set rockfall project priorities and allocate limited funds (Pierson, 1992). RHRS is a slope rating system, typically adopted to provide a relative ranking of potentially unstable slopes. The main goal is to obtain consistent and comparable information for a series of locations to plan for safety improvements. As a planning tool, RHRS facilitates a proactive approach, but it can also be used in response to a rockfall event on a single slope to both describe the event and compare it to other rockfall events in a consistent manner. Since, for the restoration of the study area a similar economic constraint existed, the use of an economical tool such as RHRS can be used, in order to prioritize the slopes most at risk of collapsing. According to this, nine parameters – categories are necessary to identify rock cuts that require a detailed geological - geotechnical analysis (Table 1). The description and explanation of using these parameters can be found on Pierson (1992) and Ferrari et al. (2016) research findings.

Table 1. Application of the RHRS (Pierson et al., 2005). Bold indicates the score of the study section.

Parameter - Category	Rating criteria and scores				
	3 points	9 points	27 points	81 points	Estimated value from: 5+490 - 5+590
1. Slope height (m)	7.6	15.2	22.9	**30.5**	**81**
1. Ditch effectiveness	Good catchment	Moderate catchment	**Limited catchment**	No catchment	**27**
2. Average vehicle risk	**25% of the time**	50% of the time	75% of the time	100% of the time	**3**
3. Percent of decision sight distance	Adequate, 100 % of low design value	**Moderate, 80 % of low design value**	Limited, 60 % of low design value	Very limited, 40 % of low design value	**9**
5. Paved road width (m)	13.4	**11**	8.5	6.1	**9**
6. Geologic character					
Case 1:					
Structural condition	Discontinuous joints, favorable orientation	Discontinuous joints, random orientation	Discontinuous joints, adverse orientation	Continuous joints, adverse orientation	
Rock friction	Rough, irregular	Undulating	Planar	Clay infilling or slickensided	
Case 2:					
Structural condition	Few erosion features	Occasional erosion features	Many erosion features	**Major erosion features**	**81**
Difference in erosional rates	Small difference	**Moderate difference**	Large difference	Extreme difference	**9**
7. Block size (m)	0.3	0.6	0.9	**1.2**	**81**
8. Volume per event (m³)	2.3	**4.6**	6.9	9.2	**9**
9. Climate and presence of water on slope	Slow to moderate precipitation or no freezing periods or no water on slope	Moderate precipitation or short freezing periods or intermittent water on slope	**High precip. or long freezing periods or continual water on slope**	High precip. and long freezing periods or continual water on slope and long freezing period	**27**
10. Rockfall history	**Few falls**	Occasional falls	Many falls	Constant falls	**3**
				Total Score	**339**

According to Hoek (1999), RHRS classification is based on a set of simple visual observations, most of which can be carried out from a slow-moving vehicle as would be required for the preliminary evaluation of miles of mountain highway. The system also contains all the components required for a complete engineering evaluation of the risks to the public. These include highway design factors as well as geometrical and geotechnical factors, all presented in clear and unambiguous terms.

According to Ferrari et al. (2016), the detailed ratings rank the slopes from least to most hazardous, using nine categories, scored exponentially from 3 to 81, with the intention of maximum allowable score for all categories being 100. Thus, slopes with higher scores are associated with greater hazards.

Once the score has been attributed to each parameter/category, the sum is the overall score. In the selected case study (ch. 5+490 – ch. 5+590), the ultimate final score is equal to 339 and as Hoek (1999) mentions, this score justifies the hazard of the segment and explains the reason why appropriate mitigation measures should be taken.

However, even though RHRS system laid the foundations for modern rockfall hazard assessments and inspired several successive methods (Ferrari et al., 2016), its main disadvantage is that it depends on the capabilities of the expert – evaluator, since the scores may be estimated differently and the final RHRS score is hardly reproducible (Vandewater et al. 2005).

2.2 Quantitative Risk Assessment (QRA)

The previously mentioned disadvantage can be solved by using additionally a quantitative method where it takes a step further the initial screening level of RHRS evaluation of the most dangerous areas. In particular, **Q**uantitative **R**isk **A**ssessment (QRA) has been developed to quantify the probability of potential losses that are related to the occurrence of a hazardous incident by estimating the number of destroyed belongings, and losses of human lives. Some of the benefits of the use of quantitative risk assessment in landslide risk management include (Fell et al., 2005):

- It allows comparison of risks across for example cut slopes on highways, and thereby allows prioritization of remedial works, and potentially setting of risk-based standards for acceptable designs.
- It provides a framework to insert uncertainties and engineering judgement into a system, resulting in an awareness to consider what can go wrong, and their potential consequences, together with how the uncertainties can be best managed.

In the following example, certain elements of landslide risk assessment are presented. The main scope is to calculate the risk to persons travelling on the Provincial Road of Old Epidaurus – Galata as shown in the Figure 4.
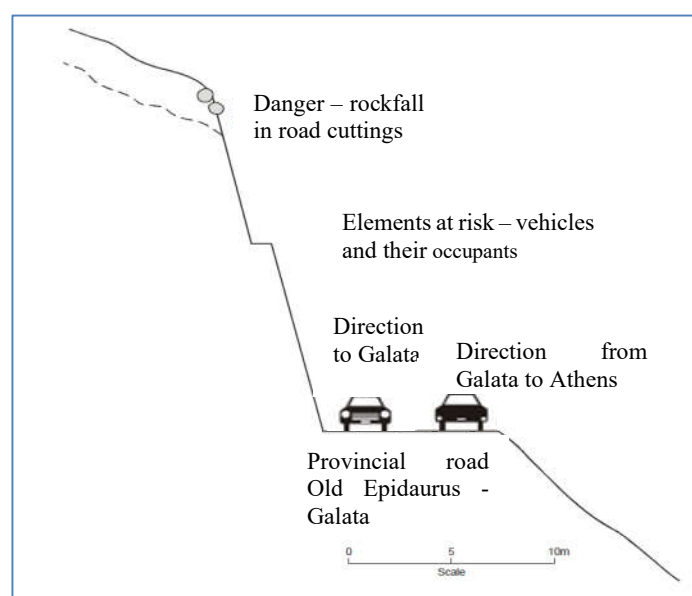
Figure 4. Characteristic segment of the Provincial Road Old Epidaurus – Galata which is part of the suburban road network of Attica Region.

Risk Analysis

The annual probability that a particular person may lose his/her life can be calculated from (Fell et al., 2005): $P_{(LOL)}=P_{(L)} * P_{(T:L)} * P_{(S:T)} * V_{(D:T)}$, where

$P_{(LOL)}$ is the annual probability that the person will be killed

$P_{(L)}$ is the frequency of the landsliding

$P_{(T:L)}$ is the probability of the landslide reaching the element at risk

$P_{(S:T)}$ is the temporal spatial probability of the element at risk

$V_{(D:T)}$ is the vulnerability of the person to the landslide event

(a) Danger characterization

This road was constructed at the beginning of the first decade of millennium. The 31 cuts in the road were constructed at relatively steep slopes. The last at least twenty years, in many parts of the slopes, there are remnant effects of poor blasting practices used in excavating rock slopes as well as stress relief following excavation. According to historical recordings from the Directorate of Technical Works of Regional Unit of Piraeus & Island, there have been occasionally rockfall incidents per year with boulders ranging in size from 25 cm diameter to 1.2 m diameter. The cuttings are in similar climatic conditions, geological background and topographical characteristics. Based on the recorded boulder impacts on the road surface, it is assessed that 50 % of rock falling from the slope will impact on lane with direction to Galata and 50 % of rock falling from the slope will impact on Lane with direction to Athens (Figure 4).

(b) Frequency analysis

The average frequency of rockfalls for each cutting is 1 per year. There are a total of 31 cuts along the provincial road Old Epidaurus-Galata, giving a total of 1/31 rockfalls per year or 0.000088/day, the average frequency (N_R) of rockfalls onto lane with direction to Galata is $N_{GALATA}=0.5*0.000088=0.000044$/day, and on lane with direction to Athens is $N_{Athens}=0.5*0.000088=0.000044$/day.

(c) Consequence analysis

(i) Temporal spatial probability ($P_{(S:T)}$) of vehicles

The probability of a vehicle occupying the length of road onto which the rockfalls is given by:

$P(S:T)=Nv/24 * L/1000*1/Vv$, where

N_v= average number of vehicles/day

L= average length of vehicles (metres)

V_v= velocity of vehicle (km/hour)

For each lane, the estimated (based on empirical basis) average number of vehicles per day over the year is 1000*, the average length of the vehicles is 6 metres, and they are travelling at 70 km/hr, ignoring the width of the boulder:

Figure 5. Illustration of the Induction Loops on a road (Federal Highway Administration, U.S. Department of Transportation, 2006)

---

* The Department of Technical Works of Piraeus & Islands Regional Unit is about to install in a particular segment of the Provincial Road Old Epidaurus-Galata, a system named "Induction loops". These are sensors placed next to each other on all lanes of the road. Their task is to record the flow of traffic on the road. The sensors record the volume and other information

about each vehicle that passes over the induction loop: what kind of vehicle it is (e.g. motorcycle, passenger car, truck), when it passed and at what speed it passed. The useful data collected by the inductive loops will be transmitted to the Traffic Management Centre of the Region of Attica for analysis and evaluation (Figure 5).

For each lane, the temporal probability is: $P_{(S:T)}=1000/24 * 6/1000 * 1/70 = 41.66*0.006*0.014=0.0035$
For a particular vehicle travelling once each day in one direction: $P_{(S:T)}=1/24 * 6/1000 * 1/70 =0.0416*0.006*0.014=0.0000035$.

(d) Vulnerability of the persons in the vehicles
Based on empirical judgement, it is estimated that the vulnerability of persons in vehicles in two lanes is 0.15.

(e) Risk estimation
The annual probability of the person most at risk losing his/her life by driving along the provincial road is:

$P_{(LOL)}=P_{(L)} * P_{(T:L)} * P_{(S:T)} * V_{(D:T)} = 0.000044 * 0.5 * 0.0000035 * 0.15 = 1.155*10^{-11}$ per year for each vehicle for each lane.

where $P_{(T:L)}$, which is the probability of the landslide reaching the element at risk (e.g., vehicle), is estimated from empirical methods calculating travel distance equal to 0.5.

For a person who only travels on the road once per year in each direction, $P_{(LOL)} = 3.164*10^{-14}$/annum $(1.155*10^{-11}/365)$.
The total annual risk assuming each of the 1000 vehicles/day carries an average of 4 persons is:
$1000*365*4*3.164*10^{-14}$ per year $=4.62*10^{-8}$ persons/year.

Risk Assessment
From Table 2 (Fell et al., 2005), the tolerable individual risk for existing slopes is $1*10^{-4}$ persons/year. Thus, for the individual most at risk, with $P_{(LOL)}= 1.155*10^{-11}$, the risk is within the tolerable limit.

Table 2. AGS (2000) suggested tolerable risk criteria

Situation	Suggested tolerable risk for loss of life
Existing engineered slopes	10^{-4}/annum person most at risk
	10^{-5}/annum average of persons at risk
New engineered slopes	10^{-5}/annum person most at risk
	10^{-6}/annum average of the persons at risk

Taking into account the outcomes of the above risk assessment approach, risk mitigation options should not be considered. However, due to the fact that the Provincial Road Old Epidaurus-Galata constructed 20 years ago, remnant effects of poor blasting practices used in excavating rock slopes have been noticed, the appearance of stress relief following excavation is evident along the road, not to mention the importance of the safe operation of the provincial road for the economic development of the wider region, appropriate mitigations measures must be taken.

3 Results

Along the study area, technical works have been constructed during the last 20 years to prevent rockfall phenomena, most of which have functioned adequately during the recent flooding events. However, during the fieldwork that followed "Daniel" incident, locations with rock slope failures and erosion issues were identified, which may be exacerbated in the event of heavy rainfall and/or dynamic (seismic) loading. Furthermore, taking into consideration the outcomes of the two previous described hazard assessment methodologies, additional interventions - mitigation works were prioritized to ensure the safe operation of the Provincial Road, such as:
1.   In some locations, precarious rock blocks perched on the top of slopes were identified. Their potential failure risked the subsequent accumulation of a significant volume of material in the rock fences, rock traps and road deck. For these reasons, scaling and rock removal works took place to improve the stability of the existing slopes and to safely perform further the interventions.

2.   The accumulation of debris flow materials was found on the benches and behind the rock traps and metal fences along almost the entire section of the road, which were removed to ensure their proper function and to allow collection of similar future phenomena.

3.   Permanent deformation and/or complete failure of existing measures was observed in several locations. At these locations, their functionality was checked and the repair and/or replacement of existing structures that have been deformed or completely failed (Rock barriers, rock fences, steel meshes, reinforced concrete walls, etc.) was required.

4.   Repair works of embankments and deck sections of the road were executed.

5.   Anchoring of free meshes was implemented.

6.   In some locations, the scaling of "keyblocks" was considered ineffective due to the potential precipitation of larger scale failures. In these cases, spot bolting of individual rock blocks was carried out.

In the Figure 6, characteristic views from the restoration works are presented in contrast to the ones before mitigation measures and after the occurrence of Daniel.

Figure 6. Characteristic views after the devastating heavy rainfall "Daniel" (left side) and restoration works (right side)

4 Conclusion

The purpose of this study is to present the soil instabilities and rockfalls that occurred on the slopes of part of the Provincial Road Old Epidaurus-Galata during the period of 05 to 07 September 2023 with the occurrence of extreme weather events (e.g., "Daniel") and briefly describe the appropriate measures implemented in order to address and avoid future such phenomena.

In addition, two hazard assessment methodologies were presented at a specific location of the road

alignment that confirmed quantitatively (QRA) and qualitatively (RHRS) the value of the preliminary examination and prioritization of the planned measures to address existing and potential instability issues.

It must be noted that the above interventions (e.g., scaling and rock removal works, restoration of rock barriers, rock fences, steel meshes, reinforced concrete walls, anchoring of free meshes, spot bolting of individual rock blocks) were aimed at restoring the road to its previous condition (i.e., before the flooding events of "Daniel" taken place), so that it could be re-opened as soon as possible. It is highlighted that in order to eliminate the hazard to minimum, the correct sizing of interventions requires additional specialized studies (e.g. geological, geotechnical, structural and road design), something that the Department of Technical Works of the Piraeus & Islands Regional Unit has already planned to implement.

It is emphasized that because the phenomena occurring in the study area are dynamic, it is necessary to constantly monitor the behavior of the slopes. This necessity increases during the winter period. It is therefore proposed to monitor the condition of the slopes and the possible development of failures during rainy periods, so that it will be possible to extend the monitoring to other locations, if it is necessary, through the use of early warning systems.

References

EDAFOS Engineering Consultants S.A., Region of Attica, Directorate of Technical Works, Piraeus & Islands Regional Unit. *Geological study for the evaluation of the condition of the slopes of the Old Epidaurus – Kalloni junction (new axis) using new technologies (e.g. Drone, etc), 2024.* Technical Report.

EDAFOS Engineering Consultants S.A., Region of Attica, Directorate of Technical Works, Piraeus & Islands Regional Unit. *Geological & Geotechnical Identification of Unsafe Sections & Proposals for Immediate Measures - Technical Report (ch. 4+370 – ch. 9+170), 2024*. Technical Report.

Federal Highway Administration, U.S. Department of Transportation (2006). Chapter 2, Traffic Detector Handbook: Third Edition—Volume I. Publication Number: FHWA-HRT-06-108.

Fell, R., Ho, K.K.S., Lacasse, S., Leroi, E. A framework for landslide risk assessment and management. *Proceedings of the International Conference on Landslide Risk Management*. Vacouver, Canada, 3-25. 31 May – 3 June 2005.

Ferrari, F.; Giacomini, A.; Thoeni, K. Qualitative Rockfall Hazard Assessment: A Comprehensive Review of Current Practices. *Rock Mech Rock Eng (2016) 49:2865–2922*, DOI 10.1007/s00603-016-0918-z.

Hoek, E. Putting numbers to geology – an engineer's viewpoint. *The Second Glossop Lecture – presented to the Geological Society, London. Quarterly Journal of Engineering Geology,* Vol. 32, No. 1, 1999, pages 1 – 19.

Pierson LA. The rockfall hazard rating system. Transportation research record: rockfall prediction and control and landslide case histories. 1992, no 1343, pp. 6–13.

Tavoularis, N. Soil Erosion and Landslide Susceptibility Mapping in Western Attica, Greece: A Rock Engineering System Approach. *Geosciences* 2023, 13(11), 338; https://doi.org/10.3390/geosciences13110338.

Tavoularis, N.; Papathanassiou, G.; Ganas, A.; Argyrakis, P. Development of the Landslide Susceptibility Map of Attica Region, Greece, Based on the Method of Rock Engineering System. *Land 2021, 10(2), 148*; https://doi.org/10.3390/land10020148.

Vandewater, C.; Dunne WM.; Mauldon, M. ; Drumm EC, ;Bateman, V (2005) Classifying and assessing the geologic contribution to rockfall hazard. *Environ Eng Geosci.* 11(2):141–154.

COMPARISON OF PREDICTED OR DESIGNED WITH ACTUAL OR EXECUTED CONDITIONS USING THE EXAMPLE OF RECENTLY CONSTRUCTED TUNNELS "PODMURVICE" AND "DEBELI BRIJEG" IN THE REPUBLIC OF CROATIA

FILIP VUKIČEVIĆ[1], NIKOLA ŠEGEDIN[2], SUAD JULARDŽIJA[3], LEO MATEŠIĆ[1]

[1] *Geokon-Zagreb d.d., Croatia, info@geokon.hr*

[2] *Institut igh, d.d., Croatia, nikola.segedin@igh.hr*

[3] *Institut igh, d.d., Croatia, suad.julardzija@igh.hr*

Abstract

During the period from 2019 to 2023, as part of the project to construct the state road D403 from junction Škurinje to the Port of Rijeka and the construction of access roads to the Pelješac Bridge, geological supervision was carried out over the excavation of the "Podmurvice" tunnel with a total length of L=1237.00 m and the "Debeli Brijeg" tunnel with a total length of L=2443.00 m. The role of geological supervision over tunnel excavation involved actively participating in the process of determining the actual engineering geological profile along the tunnel route and the process of verifying the stability of underground excavation. During the design phase, geotechnical classification of rock mass was applied using the RMR and Q-system. During the excavation phase, in coordination with the supervisory authority, RMR geomechanical classification was adopted as the main and leading classification method of rock mass, all with the purpose of determining the actually executed category of rock mass excavation, which served as the main basis for determining the type of primary substructure assembly. The main goal of this article is to compare the predicted or designed conditions (engineering geological profile along the tunnel route, rock mass quality (excavation categories), types of primary substructure assembly, etc.) with the actually executed conditions at the mentioned locations of two recently constructed tunnels in the Republic of Croatia.

Key words

Tunnels "Podmurvice" and "Debeli brijeg", construction phase (underground excavation), geological supervision, RMR classification, excavation categories, comparison predicted – actual executed state

1 Introduction

From 2019 to 2023, as part of the construction project of the state road D403 from the Škurinje interchange to the port of Rijeka and the construction of the access road to the Pelješac Bridge, geological supervision was carried out over the excavation of the three-lane "Podmurvice" tunnel and the two-lane "Debeli Brijeg" tunnel, with total lengths of L=1237.00 m and L=2443.00 m, respectively. Along the routes and corridors of both tunnels, geotechnical investigation works (GIW) were performed according to the research program agreed upon between the chief designer of the structure and the investor. The results of the investigative works were used as the main foundational basis for creating the predicted engineering geological (geotechnical) models, upon which the projects for the mentioned tunnel structures were developed.

The role of geological supervision during the tunnel excavation (execution phase) was to actively participate in the process of determining the actual engineering geological profile along the tunnel route

and in the verification process of underground excavation stability (together with the specialist supervisory team) using a jointly agreed methodology. The main objectives of this article are to compare the predicted or designed state with the actual executed state at the specified locations of two recently constructed tunnels in the Republic of Croatia and to demonstrate, through practical examples, the identified shortcomings in the investigation phase, which consequently affected the deviations between the predicted and actual executed state.

2 General overview of the location, structure, and geological features

2.1 Tunnel "Podmurvice" – D403 (City of Rijeka)

The main tunnel tube "Podmurvice" is the longest and most complex structure on the D403 route, consisting of three traffic lanes and passing under the densely built-up urban area of "Podmurvice". In plan view, the main tunnel tube has a specific curvature. The tunnel grade line is a uniform ascent of 4.5% for almost the entire length of the tunnel. The underground excavation of the main tube was carried out over a length of 1237.00 m, starting at chainage km 0+589 and ending at chainage 1+826.00 m. The elevation at the entrance portal is +78.26 m above sea level, and the exit portal is at +22.09 m above sea level, which corresponds to a height difference of 56.17 m between the two portals. The maximum overburden of the Podmurvice tunnel is approximately 50 m, and the minimum is approximately 2.00 m (IGH d.d. 2011a, IGH d.d. 2011b, Rijekaprojekt d.o.o. 2018). Within the main tunnel tube "Podmurvice", emergency pedestrian exits were constructed at an axial distance of approximately 30 m, connected to the main tunnel tube by 4 cross-passages designed exclusively for pedestrian use (Figure 1).

Figure 1. Tunnel "Podmurvice"

The excavation work on the main tunnel tube started on November 27, 2020, and finished on February 4, 2022, achieving an average progress of 3.50 meters per day. Considering the extremely complex geotechnical conditions (urban environment, zones with low overburden, poor rock mass quality, etc.) along the entire tunnel route, the excavation was carried out using the principles of the New Austrian Tunneling Method (NATM). The general principle of this method is that the rock mass itself is the main load-bearing element of the tunnel, with primary and secondary supports used only to establish a load-bearing ring within the rock mass. Excavation methods included drilling and blasting (D&B), mechanical excavation (rock hammer), and combination of these methods. The contractor for the works was EUROASFALT Sarajevo d.o.o., while the supervision was performed by IGH d.d. and Geokon Zagreb d.d (EURO-ASFALT d.o.o. 2022). Topographically, the area of the city along which the tunnel route passes is highly rugged, predominantly steep, and part of a highly developed karst region.

The basic relief has been significantly altered by intensive city construction, filling, and cutting. Geologically, the tunnel route traverses an area composed of six lithostratigraphic units, ranging in age from the lower cretaceous to the paleogene. Table 1 provides the registered percentage share of lithostratigraphic units along the tunnel route.

Table 1. Lithostratigraphic units along the the "Podmurvice" tunnel route

LITHOSTRATIGRAPHIC UNITS TUNNEL "PODMURVICE" (City of Rijeka)		
Lithology	**Stratigraphy**	**%**
Foraminiferal limestones	^{3+4}Pg Paleogene	13,58
Transgressive boundary		
Limestones	$K_2^{2,3}$ Upper Cretaceous	63,22
	K_2^{2}	
Limestones and dolomites	$^2K_2^{1,2}$	
Transgressive boundary		
Carbonate breccia (flysch)	^2E Eocene	20,86
Transgressive boundary		
Limestones with inserts of limestone breccias	K_1^{3-5} Lower Cretaceous	2,34

2.2 Tunnel "Debeli brijeg" – access roads to the bridge (Pelješac peninsula)

The access roads to the Pelješac Bridge are part of a project to connect Southern Dalmatia, which has strengthened the connectivity of the national territory in the far south of the Republic of Croatia. As part of the construction of the access roads to the Pelješac Bridge, the two-lane "Debeli Brijeg" tunnel was built, consisting of a main tunnel tube and a service tunnel tube, which are interconnected by cross passages for pedestrian passage (9) and emergency vehicles (2). The "Debeli Brijeg" tunnel predominantly runs in a northeast-southwest direction, passing under an uninhabited area. The underground excavation of the main tube was carried out over a length of 2443.00 m. The elevation at the entrance portal (km 10+927) is +243.56 m above sea level, and at the exit portal (km 13+370) it is +240.435 m above sea level, which corresponds to a height difference of 3.12 m between the two portals. The tunnel grade line rises for the first 1100 m from the entrance portal, after which the slope decreases until the end of the tunnel structure (IGH d.d. 2016, IGH d.d. 2018). The maximum overburden of the "Debeli Brijeg" tunnel is approximately 158 m, and the minimum overburden outside the portal zones is approximately 7.5 m (Figure 2).

Figure 2. Tunnel "Debeli Brijeg"

The excavation work on the main tunnel tube (MTT) "Debeli Brijeg" began on April 1, 2020, and was completed on December 16, 2020, achieving an average progress of 5.69 m/day from the exit portal side and 4.87 m/day from the entrance portal side (HGI-CGS, 2007). The excavation was carried out using the principles of the New Austrian Tunneling Method (NATM), where the rock mass itself is the main load-bearing element of the tunnel, with primary and secondary supports used only to establish a load-bearing ring within the rock mass. Excavation methods included drilling and blasting (D&B), mechanical excavation (rock hammer), and a combination of these methods. The contractor for the works was ZGS STRABAG AG/STRABAG d.o.o., while the supervision was performed by Investinženjering d.o.o., Centar za organizaciju građenja d.o.o., and Geokon Zagreb d.d. as the subcontractor for geological supervision.

The investigated area represents an elevated carbonate massif in the northeastern part of the Pelješac Peninsula, with a Dinaric direction extending northwest-southeast (NW-SE). The "Debeli Brijeg" tunnel was constructed in well-layered carbonate deposits of the Pelješac Peninsula mountain massif. The tunnel route area is built from two lithostratigraphic units of Upper Cretaceous age (Cenomanian-Turonian-Senonian). Cenomanian deposits are represented by well-layered, monoclinally positioned dolomites with a dip direction towards the northeast (NE). The dolomites are typically dark gray, fine to medium-grained, and of late diagenetic type. Turonian and Senonian deposits are represented by well-layered limestones. These are light gray or light brown mudstones, wackestones, and packstones, often recrystallized. The geological structure is monoclinal with a dip of the layers towards the northeast (ZGB Strabag AG/Strabag d.o.o. 2021). Table 2 provides the registered percentage share of lithostratigraphic units along the tunnel route.

Table 2. Lithostratigraphic units along the "Debeli Brijeg" tunnel route

LITHOSTRATIGRAPHIC UNITS TUNNEL "DEBELI BRIJEG" (Pelješac peninsula)		
Lithology	**Stratigraphy**	**%**
Limestones	$K_2^{2,3}$ Upper Cretaceous (turonian-senonian)	16,23
Dolomites	K_2^1 Upper Cretaceous (cenomanian)	77,28
Thrust fault contact		
Limestones	$K_2^{2,3}$ Upper Cretaceous (turonian-senonian)	6,49

3 Methodology of work

Considering that tunnels are linear structures, it is very challenging to optimize a geotechnical investigation program that reliably defines the characteristics and conditions of the rock mass or soil in the subsurface. These characteristics can vary significantly along the tunnel route depending on the complexity of the underground geological conditions. The stabilization systems for the underground excavation, as described in the main geotechnical design, provide excavation technology and support system solutions that are of a predictive nature. During construction phase, these design solutions need to be verified or modified as necessary, which constitutes the second phase of design. Observations, measurements, tests, and analyses conducted during the second phase of design are an integral part of the tunnel project documentation and are recorded through the as-built tunnel documentation.

The primary objectives of the second phase of designing the stabilization of the underground excavation were:

- Determining the actual engineering-geological profile along the tunnel route, i.e., the actual stress-strain parameters of the rock mass along the tunnel route;
- Geotechnical observations and measurements;
- Optimizing all stabilization measures given in the first phase of design;
- Verifying the stability of the underground excavation

For determining the actual engineering geological profile and the quality of rock masses along the tunnel route during the construction of the tunnel, the following was carried out:

- Engineering-geological mapping;
- Classifying the rock mass;
- Determining all relevant rock mass parameters.

Engineering geological mapping was conducted parallel to the tunnel excavation after each advancement step, necessitating the constant presence of a geologist on the construction site. The purpose of engineering geological mapping is classifying or categorizing the rock mass along the tunnel excavation. This mapping of tunnel excavations determines lithological, structural, and physical-mechanical characteristics, degree of weathering, and spatial position of structural elements relative to the tunnel axis. In addition, mapping determines hydrogeological conditions (presence of groundwater and its impact on construction and later tunnel operation), justified over-excavation in zones with unfavourable geological conditions. The contractor's geologist and the supervising geologist were responsible for the quality of the mapping performed.

Considering that the tunnels "Podmurvice" and "Debeli brijeg" are classified among those where the behavior of underground excavation during excavation and stabilization is primarily conditioned by structural defects in the rock mass, the RMR geomechanical classification (Bieniawski, 1989) and the Q system (Barton, Lien, Lunde, 1974; Barton, Grimstad, 1993) were applied during the design phase. During the construction phase, at the suggestion of the supervising engineer for excavation (geological supervisor), the RMR geomechanical classification (Bieniawski, 1989) of the rock mass was accepted as the main and leading method applied throughout the excavation of the "Podmurvice" and "Debeli brijeg" tunnels. Therefore, within the framework of engineering geological mapping, it was necessary to define geological parameters for classifying the rock masses for categorization purposes. The parameters needed to be recorded after every change in geotechnical conditions to determine the quality and category of the rock mass.

The recording and determination of parameters were conducted in accordance with ISRM recommendations (ISRM 1978).

During the tunnel excavation, zones were identified where, in addition to the rock mass quality determined by the RMR (Rock Mass Rating) geomechanical classification, it was necessary to consider the overall geotechnical characteristics affecting the stability of the underground excavation. These factors could result in different excavation categories and support systems compared to those derived solely from the rock mass quality determined through RMR parameter mapping. Examples of such zones include:

- **Portal zones**: Areas at the tunnel entrance where ground conditions often change rapidly;
- **Zones with low overburden (H < B)**: Areas where the depth of cover is less than the tunnel span, posing stability challenges;
- **Fault zones**: Areas with significant geological discontinuities;
- **Zones with unstable blocks in the tunnel crown (calotte)**: Areas where blocks are prone to instability and could fall;
- **Cavernous and speleological features**: Presence of cavities and caves, which, depending on their size and position relative to the main tunnel axis, required special treatment for stabilization.

These complex zones demanded tailored solutions to ensure the stability of the underground excavation. The standard support systems and excavation categories based on the RMR classification needed to be adjusted to account for the additional geotechnical features, ensuring safe and effective tunnel construction.

4. Brief overview of the investigation works

Geotechnical investigation works (GIW) along the routes of the "Debeli brijeg" and "Podmurvice" tunnels were the basic basis for the creation of the main geotechnical projects of the tunnel. The GIW included exploratory drilling, engineering-geological mapping of the tunnel corridors, and geophysical surveys (seismic refraction and shallow reflection seismics). Along the corridor of the "Podmurvice" tunnel, a total of 4 exploratory boreholes were drilled with individual depths of 30.00 m (TP-1, 0+621 km), 60.00 m (TP-2, 1+141 km), 30.00 m (TP-3, 1+620 km), and 12.15 m (TP-4, 1+810 km). Along the

corridor of the "Debeli brijeg" tunnel, a total of 5 exploratory boreholes were drilled with individual depths of 15.00 m (MPT-4, 10+937 km), 60.00 m (MPT-5, 11+172 km), 110.00 m (MPT-6, 12+026 km), 95.00 m (MPT-7, 12+873 km), and 20.00 m (MPT-8, 13+330 km). It is important to note that during the investigation works, the design axis of the "Debeli brijeg" tunnel was partially redesigned, shifted such that only one (MPT-4) of the five boreholes lies in the designed axis of the tunnel, while the others are located within the mapped corridor of the tunnel. Based on all the conducted investigations and their office processing, two lithostratigraphic units and two engineering-geological blocks were identified in the researched area of the planned "Debeli brijeg" tunnel. In contrast to the "Debeli brijeg" tunnel, six lithostratigraphic units and four engineering-geological blocks were identified in the area of the planned "Podmurvice" tunnel. The criteria for this division were: lithostratigraphic characteristics of the rock mass, physical and mechanical properties of intact rock, the degree of tectonic fracturing, the intensity of karstification, and the characteristics of the main structural pattern.

5   Comparison of predicted and executed excavation categories

By comparing the predicted and executed engineering geological model along the routes of both tunnels, it was established that the spatial position of the elements of the basic structural assembly and the lithostratigraphic representation of the units along the routes were sufficiently accurately predicted in the research phase at the level of the tunnel level. However, the prediction of the representation of rock mass quality categories along the same routes significantly deviates from the executed one, which can be clearly seen in the diagrams of the comparison (Figure 5).

Along both tunnels, during the creation of the predictive engineering-geological profile (report on the conducted investigation works) along the corridor of the tunnels, the predicted share of rock mass quality categories along the corridors was not provided, which significantly influenced and complicated the comparison and represents the main drawback of the investigation works. Considering all the above, the statistical comparison of predicted versus executed was made based on the data of the predicted cumulative share of rock mass quality categories taken from the main tunnel projects.

In addition to the cumulative predicted data, all qualitative and quantitative descriptive data on the quality of the rock mass were used in the engineering-geological comparison between predicted and executed , which were integral parts of the report on the conducted investigation works. These data were used in the design to determine the predicted representation of rock mass quality categories along the routes of both tunnels and to select the appropriate type of primary substructure.
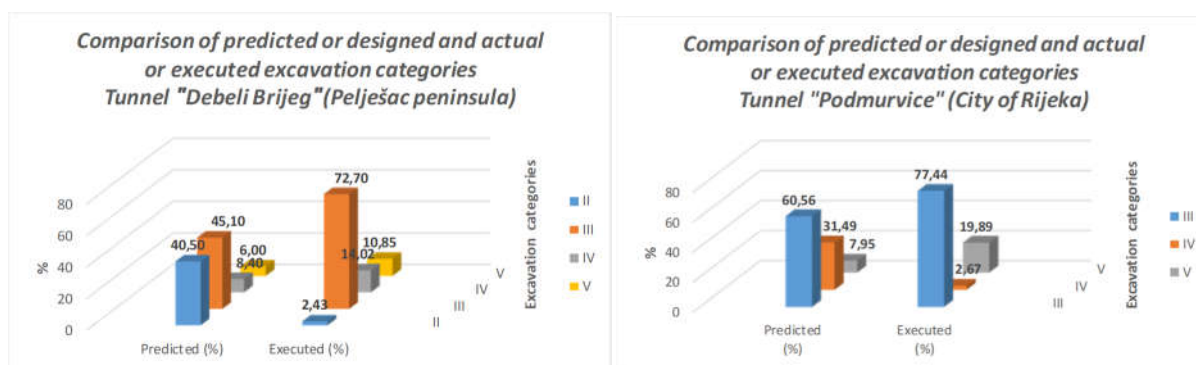
Figure 5. Comparasion of predicted and executed mass quality categories

The deviations in the representation of predicted and executed excavation categories are evident. Compared to the predicted share, the percentage share of II. excavation category is lower by 38.07%, the share of III. excavation category is higher by 27.60%, the share of IV. excavation category is higher by 5.62%, and the share of V. excavation category is higher by 4.85%. In contrast to the Debeli brijeg tunnel, in the Podmurvice tunnel (Figure 5), the absence of II. excavation category is evident, which was accurately predicted. Compared to the predicted share, the percentage share of III. category is higher by 16.88%, the share of IV. category is lower by 28.82%, and the share of V. category is higher by 11.94% compared to the predicted.

Such significant deviations between the predicted and actual categories of rock mass quality, and consequently the corresponding types of primary support structures, can be attributed to several key factors. The most important factor is the insufficient amount of geotechnical investigation works (GIW), which was evidently inadequately optimized during the development of the GIW. This ultimately had an undeniable impact on the registered significant differences between the predicted rock mass quality and the actual executed quality. Considering the small and insufficient amount of GIW, mainly based on exploratory drilling, which provides point data, and taking into account that the underground tunnel excavation represents continuous linear data, it is concluded that it is very difficult to accurately predict the distribution of excavation categories and types of primary support system along the tunnel route. The above examples from practice indicate the crucial role of geological supervision over the construction of tunnels. Primarily, the geological supervision compares the predicted and realized engineering geological profile, corrects the predicted profile as necessary and informs the chief supervising engineer in a timely manner. In situations of significant deviations from the predicted and actually executed state, according to personal assessment, the chief supervising engineer informs the chief engineer of the construction site and the chief designer. All these efforts aim to ensure the stability of the underground excavation.

In the following text, several characteristic photographs of the tunnel faces of "Podmurvice"(Figure 6) and "Debeli brijeg"(Figure 7) tunnels are highlighted. These images show registered engineering geological occurrences during tunnel construction, which represented weak geotechnical zones (caverns with and without soil infill, fault-cavernous zones, zones of rock mass mylonitization at thrust contact, etc.). Based on their occurrence, dimensions, and spatial position relative to the tunnel axis, these features directly impacted the stability of the underground excavation. However, they were not predicted during the investigation or design phase.

The photographs on Figure 6. show significant geologically interesting occurrences that were registered during the excavation of the "Podmurvice". Due to the specificity of the environment (urban area) in which the underground excavation was conducted, special emphasis was placed on unpredicted geological phenomena registered in the chainage interval km 1+732-1+718 (L= 14.00 m) during the excavation on the southern (exit) side of the "Podmurvice" tunnel. This manifested on the surface as large quantities of sandy material with interlayers of low to high plasticity clay of exceptionally hard consistency, yellow in color. Spatially, the sandy material affected the upper half of the tunnel face, including the sides of the tunnel and the entire crown (calotte) of the tunnel, as clearly seen in the provided images. It is assumed that the registered material continues to extend in the direction of the calotte or the surface of the terrain. In that part of the tunnel, the thickness of the upper layer of the tunnel was only 16-17 m, which is close to the width of the tunnel. There are buildings and roads on the surface. All together, it represented a demanding and dangerous section, and strict measures had to be applied to ensure the stability of the underground excavation.

The excavation progress dynamics in this part were adapted to the actual geological conditions along the excavation with a maximum allowed advancement step of 0.50 - 1.00 m, using only an excavation hammer or bucket as the most optimal excavation technology, and timely and efficient support of the same. The second occurrence was registered during the excavation on the northern (exit) side of the same tunnel, in the chainage interval 0+652-0+672 (L=20.00 m), represented by a subvertical cavernous zone without fill, 4-5 m wide at the center of the tunnel face. Cavernous zone is spatially extending from the center of the excavation profile towards the right side where it ends (km 0+672).

Considering the registered chainage location of the mentioned geological occurrences and the registered lithostratigraphic type of material after 'exiting' these occurrences in the direction of excavation progress, they are geologically interpreted as parts of the transgressive boundary. On the southern (exit) side of the tunnel (km 1+732-1+718) they are interpreted as parts of the transgressive boundary between lower cretaceous limestones (K_1^{3-5}) and eocene carbonate breccia (^2E), while on the northern (entrance) side of the tunnel (km 0+652-0+672) they are interpreted as parts of the transgressive boundary between paleogene foraminiferal limestones (^{3+4}Pg) and upper cretaceous ($K_2^{2,3}$) limestones.

The presumed transgressive contact between the Lower Cretaceous and the Eocene

1+732 km

1+730 km

1+727 km

1+726 km

1+725 km

1+724 km

The presumed transgressive contact between the Upper Cretaceous and the Paleogene -

0+656 km

0+660 km

Figure 6. Tunnel Podmurvice (City of Rijeka)

The photographs on Figure 7. show significant engineering-geological occurrences registered during the excavation of the "Debeli brijeg" tunnel. Photos are mark by the chainage location. Photo marked 11+142 km represent chainage interval from km 11+121 to 11+186 (L=65.00) where is material of the fault zone. Photos marked with 11+409 km, and 12+155 km, 12+719,50 km represent six chainage intervals from km 11+377.50 to 12+726 where are caverns without fill. Lenght of those intervals are varied fom 10 to 40 meters. Photo marked 13+212 km represent chainage interval from km 13+172 to 13+212 (L=40.00) where is fault-overthrust contact zone – rock mass mylonitization zone.

Considering that all the mentioned materials belong to soil and unfilled caverns for which the RMR classification was not applicable, the excavation was automatically classified and executed in the V category according to the GTS (general technical specifications for tunnel works). All the mentioned engineering-geological occurrences, in the context of the prognosis of poorer rock mass quality, were not predicted, which proved to be one of the significant disadvantages in the research phase

Figure 7. Tunnel Debeli brijeg (Pelješac peninsula)

6. Discussion and Conclusion

During the execution of underground tunnel excavation, numerous challenges and difficulties engineers may encounter become evident. These issues represent significant challenges for engineers, largely attributable to deviations between predicted and actual engineering geological models. These deviations are observed in both subject tunnels and are presumably the result of several key factors, including:

- Insufficient optimization of geotechnical investigation work quantity (GIW program): A limited number of boreholes were conducted, which are the most reliable data points along the tunnel route. The area between boreholes is partially 'covered' by geophysics, which provides second and higher-order data compared to borehole data. Additionally, the quality of geophysical survey results depends on the quality of the field measurements and the subsequent interpretation.

- Lack of predictive percentage share of rock mass quality categories: The prognostic engineering geological profile of the tunnel (report on GIW and engineering geological works) does not show the predicted percentage distribution of rock mass quality categories along the tunnel routes, which is a crucial conclusion of the geotechnical investigation works (GIW).
- Actual field conditions (difficult terrain): The inability to access the planned positions of boreholes and geophysical profiles with drilling equipment leads to deviations from the main tunnel axis.

Considering that tunnels are linear structures, and underground excavation is a continuous linear activity while boreholes provide point data, it is challenging in practice to accurately predict the percentage distribution of excavation categories and types of primary support structures along the tunnel route. Therefore, during the tunnel excavation phase, it is crucial to have the continuous presence of geological engineers on-site to monitor the excavation continuously. This ensures the determination of the actual engineering geological profile along the tunnel route and timely registration of significant deviations from the predicted to the actual state, promptly informing all key participants in the tunnel construction process, from the main supervising engineer to the main site engineer and the main designer. This is all aimed at ensuring the stability of the underground excavation and ultimately the quality and safety of the construction work. The deviations and their causes observed in the "Podmurvice" and "Debeli Brijeg" tunnels serve as practical examples for all future participants (investor, designer, supervisor, and contractor) in tunnel construction , aiming for safer and higher quality execution of such projects.

References

Barton, N.R., Lien, R., Lunde, J., *Engineering classification of rock masses for the design of tunnel support*, Rock Mechanics and Rock Engineering. 6 (4). Springer: 189–236. 1974

Barton, N.R., Grimstad, E., *Updating the Q-system for NMT*, In Kompen, C.; Opsahl, S.L.; Berg, S.L. (eds.). Proc. of the International Symposium on Sprayed Concrete - Modern Use of Wet Mix Sprayed Concrete for Underground Support, Fagernes, 1993.

Bieniawski, Z.T., *Engineering Rock Mass Classification*, 1989

EURO-ASFALT d.o.o., *Final report on engineering geological mapping of the main tunnel tube of tunnel "Podmurvice"*, 2022

HGI-CGS, *Mainland-Pelješac bridge with access roads on D8 and D414 Engineering Geological Investigation Works - basis for the main project*, 2007

IGH d.d., *Mainland-Pelješac Bridge with Access Roads on D8 and D414 - Geotechnical Investigation Works - Overview of Investigation Works for tunnels*, 2016

IGH d.d., *Mainland-Pelješac bridge with access roads on D8 and D414 - Main geotechnical project for tunnel "Debeli Brijeg",* Sheet G30, 2018

IGH d.d., *State Road D403 from Škurinje junction to port of Rijeka - Geotechnical Investigation Works (Engineering Geological Investigation) - basis for the main project*, 2011a

IGH d.d., *State Road D403 from Škurinje junction to port of Rijeka- Geotechnical Investigation Works (Report on Geotechnical Investigation Works) - basis for the main project*, 2011b

ISRM, *Suggested methods for the quantitative description of discontinuities in rock masses*, 1978

Rijekaprojekt d.o.o., *State road D403 from Škurinje junction to port of Rijeka - Main geotechnical project for tunnel "Podmurvice"*, Sheet 4, 14-045, 2018

ZGB Strabag AG/Strabag d.o.o., *Final engineering geological report - Main tunnel tube and cross connections of tunnel "Debeli Brijeg"*, GPC-120/2021, 2021

SOIL INVESTIGATIONS AS A CORNERSTONE FOR GEOTECHNICAL DESIGN OF LIQUEFACTION MITIGATION MEASURES BELOW LEVEES

MARIO BACIC[1], KATARINA ANDACIC[2], KENNETH GAVIN[3], KOSTA URUMOVIC[4]

[1] University of Zagreb, Faculty of Civil Engineering, Croatia, mbacic@grad.hr,

[2] Center of Faculty of Civil Engineering ltd, Croatia, kandacic@grad.hr

[3] TU Delft, the Netherlands, K.G.Gavin@tudelft.nl

[4] Croatian Geological Survey, Croatia, kurumovic@hgi-cgs.hr

Abstract

Levees are particularly susceptible to damage during seismic events, and failure mechanisms can involve large deformations due to soil liquefaction within and below the levee. To assess the liquefaction potential below the levees, and for the purpose of planning liquefaction mitigation measures, in-situ and/or laboratory investigations must be carried out. This is a challenge, especially due to the great length of the levees, and the limited financial and time resources available for carrying out the investigations. This paper provides an insight into two examples of investigation work carried out to determine the liquefaction potential and gives an overview of the design measures to remediate the underlying soil. These are the Pušćine levee in Međimurje County, which was reconstructed due to insufficient height in terms of flooding, and the Hrastelnica levee in Sisak-Moslavina County, which was damaged in the 2020 Petrinja earthquake. While numerous dynamic penetration tests were carried out on the Pušćine levee to assess the liquefaction potential, Hrastelnica levee assessments relied on the static (cone) penetration tests. The paper further discusses step forward in mapping the spatial variability of liquefaction potential under the levees, through the efforts of ongoing LeveeLiq project.

Key words

liquefaction, levee, soil investigation works, remediation design, LeveeLiq project

1 Introduction

As one of the consequences of the strong Petrinja earthquake in 2020, liquefaction occurred in large parts of Sisak–Moslavina County, whose geology is generally characterized by saturated, poorly graded sands and silty sands (Pollak et al., 2021). In the Rapid Damage Assessment Report (Republic of Croatia, 2021), it was estimated that liquefaction occurred on almost 1600 ha of the county area at varying depths from 3 to 15 m. All liquefaction zones are located in the alluvial deposits of the Kupa, Sava, Glina and Maja rivers at a maximum distance of about 1 km from the riverbanks. About 7% of the area affected by liquefaction is located under the levees. This was detected by numerous cracks in the ground surface and erupted sand, as well as numerous cracks and deformations of the levees (Figure 1).

The levee deformations shown correspond well with the levee damage patterns D-2 and D-3 of Oka et al. (2012) (Figure 2), which were detected after the magnitude 9.0 Tohoku earthquake in 2011 in Japan, where damage to the levees was recorded at 2,115 locations. These patterns include longitudinal cracking and lateral expansion of the levee slope near the toe, as well as settlement of the levee crest. The authors state that the associated damage is due to liquefaction of the foundation soil, liquefaction of the soil in the levees as the water-saturated area was above ground level, and the long duration of this huge earthquake, or a combination of the above factors.

Figure 1. Deformed levees as a consequence of earthquake - induced liquefaction in Sisak – Moslavina County
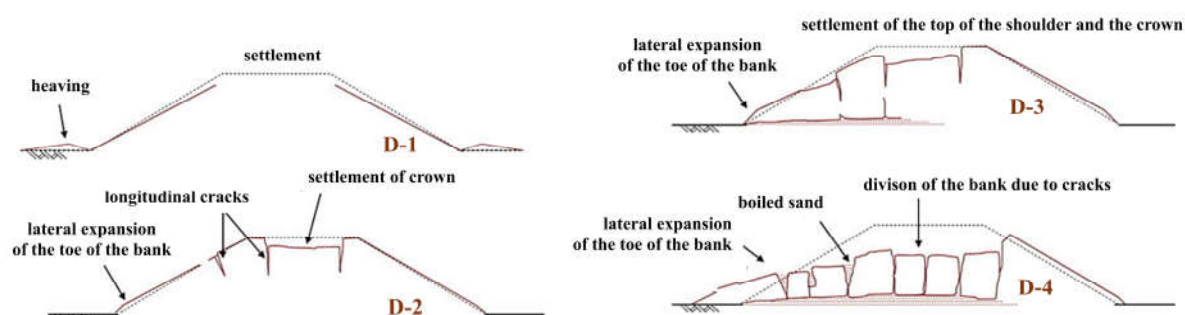
Figure 2. Typical damage and failure patterns of river embankments, modified from Oka et al. (2012)

Even though the water levels of adjacent rivers were not high enough to flood a large area, the likelihood of a cascade of earthquakes and floods put those responsible for flood protection infrastructure on alert. Therefore, in the aftermath of the earthquake, much attention was focused on how to mitigate the risks associated with liquefaction for future earthquake events. It was soon recognized that the focus should be on adequate and comprehensive investigations that would provide mitigation designers quantitative information on the liquefaction potential of the soil below the levees. The interest of geotechnical practitioners in an optimal soil investigation campaign arose not only for the reconstruction of the levees damaged by the 2020 Petrinja earthquake, but also for levees in other seismically active regions of Croatia, as the high risks of levee failure increase the need for reliable assessments. This raises the crucial question of the type and frequency of investigation methods to assess the liquefaction potential below the network of existing or future levees. This paper presents the efforts to assess the liquefaction potential below the two levees - Pušćine in Međimurje County and Hrastelnica in Sisak – Moslavina County. While the Pušćine levee is being reconstructed because it does not meet the requirements for extreme water height, the Hrastelnica levee is one of the levees that was severely damaged in the aforementioned earthquake in Petrinja in 2020.

2   Methods for assessing the liquefaction potential

Conducting soil investigations along levees to assess liquefaction potential is both expensive and time consuming due to a combination of technical, logistical and legal factors. Because the inherent variability of soil makes it difficult to predict the behavior of each individual layer during an earthquake, interpreting the data and results of various tests often requires a high degree of engineering judgment, leading to subjectivity and variability in assessment outcomes. Therefore, it is desirable to use a combination of different methods to gain a more complete insight into the liquefaction risk in a given area.

This chapter does not provide an exhaustive list of methods for assessing liquefaction potential, but rather a brief overview of the possibilities. The number and variety of methods for assessing liquefaction potential results from different theoretical considerations about which factors are decisive for the activation of liquefaction potential. Barua et al. (2023) highlight several methods for evaluating liquefaction potential, as shown in Table 1. The table is complemented by the geophysical tests, as this method is increasingly used despite the conflicting opinions on the use of the small strain-based in situ method to estimate liquefaction resistance, with which large strains are associated (Bačić et al., 2024).

Table 1. Comparison among liquefaction potential assessment methods, modified from Barua et al. (2023)

Assessment method	Data requirement	Complexity	Usefulness for Mapping of Liquefaction Potential
Topographical and geological – feature analysis	Topographical and geological data	Simple	Useful for wide areas
Penetration in-situ tests	Direct use of geotechnical data: blow count value (i.e. SPT or BPT) / cone resistance (CPT) and grain size distribution data with estimates of peak surface acceleration	Simple	Useful for wide areas
Geophysical in- situ tests	Direct use of geophysical data: soil shear wave velocities with estimates of peak surface acceleration	Simple	Useful for wide areas
Laboratory cyclic shear testing of undisturbed samples	Geotechnical data: laboratory cyclic shear testing of undisturbed samples in light of dynamic – response analyses	Complex: too tedious and costly	Rigorous estimation at single site
In-situ blasting or laboratory shake table testing	Geotechnical data: in-situ cyclic or blasting tests, or laboratory shake table tests	Complex: too tedious and costly	Rigorous estimation at single site

For the estimation of the liquefaction potential, which serves as the basis for data-driven selection of mitigation measures, a choice is usually made between geotechnical/geophysical in-situ tests and the laboratory cyclic shear tests. Although laboratory tests, with controlled shear strain or controlled shear stress, can provide a more detailed insight into the liquefaction potential of a material, i.e. its cyclic undrained behavior, a simplified method based on the aforementioned in-situ tests is usually used for routine assessments. These assessments are based on empirical correlations derived from historical data for which liquefaction charts are developed and periodically updated.

3   Pušćine levee in Međimurje County: a dynamic penetration approach

3.1   Description of the site and investigation works

The Pušćine levee is located on the left bank of the Drava River in northern Croatia, Međimurje County, Figure 3, and is 3.4 km long. Initially built in 1966 to protect the settlements of Pušćina and Gornji Hrašćan from flooding, the levee does not have a sufficient safety height. This was demonstrated in November 2012, when the largest recorded water wave led to severe flooding in the area. It was decided to reconstruct the levee so that it meets the flow rate requirements of 2900 m³/s, which in turn means an increase of up to 1.5 m compared to the existing crest level. However, the raising and construction of the access road will shift the levee 12 to 20 m towards the water side to fit into the existing Croatian Waters' cadastral parcel.

Figure 3. The layout and the current condition of the Pušćine levee

The investigation works were carried out in several phases. For the main design (Elektroprojekt, 2020), the initial reconnaissance campaign comprised six boreholes, each 8 m' deep, together with the SPT tests and laboratory investigations (FCEZG, 2013). The subsurface was found to consist mainly of alluvial Quaternary deposits dominated by sandy and gravelly material, with silts and clays also present. The upper layer with a thickness of 1.0 to 5.0 m consists mainly of loose to medium-dense silty sands with a uniform grain size distribution. These are underlaid by relatively dense, well-graded gravels, some of which are mixed with clays. Four seismic refraction profiles were investigated, each with a length of 240 m'. However, in order to better assess the thickness and locations of the sandy soils, additional investigations were carried out by drilling 35 shallow boreholes with a depth of 5 m along the levee toe (CFCE, 2016). These showed that the levee rests on potentially liquefiable soil for around 60% of its length. The investigation campaign is supplemented by 21 light dynamic penetrometer (DPL) tests (Premur, 2022) with a depth of 3 to 4.6 m in the identified sandy formations.

3.2 Liquefaction evaluation and mitigation measures

The main design analyzed the liquefaction potential by determining the minimum number of SPT blows necessary for the soil to resist liquefaction. In this case, the cyclic-stress ratio was calculated using the following equation:

$$CSR = 0{,}65 \times \frac{a_{max}}{g} \times \frac{\sigma_{v0}}{\grave{\sigma}_{v0}} \times r_d \qquad (1)$$

where the r_d is stress reduction factor, a_{max} is the peak horizontal ground acceleration, while σ_{vo} and σ'_{vo} represent total and effective vertical stress, respectively. The liquefaction resistance CRR parameter is the CSR value required to activate liquefaction, which happens when $CSR \geq CRR$. Using the a_{max} of 0.14g which corresponds to the seismic event of 475-year return period, and applying the stress-reduction, the calculated CSR is 0.156. For the silty sands with 15% of fines, which form soil just below the levee, the critical SPT blow number is 9 (without groundwater) to 11 (with groundwater), Figure 4. Therefore, main design identifies two criteria which should be fulfilled in order to consider the liquefaction mitigation measures: (1) the material of the surface soils are uniformly to poorly graded sand or silty sand; (2) SPT blow number in sand or silty sand should be lower than 9 or 11. When the obtained DPL blow numbers (Premur, 2022) are correlated with the SPT values, the associated SPT values range from 2 to 7 in sandy formations, followed by the significant increase in number of blows in lower gravel layers.
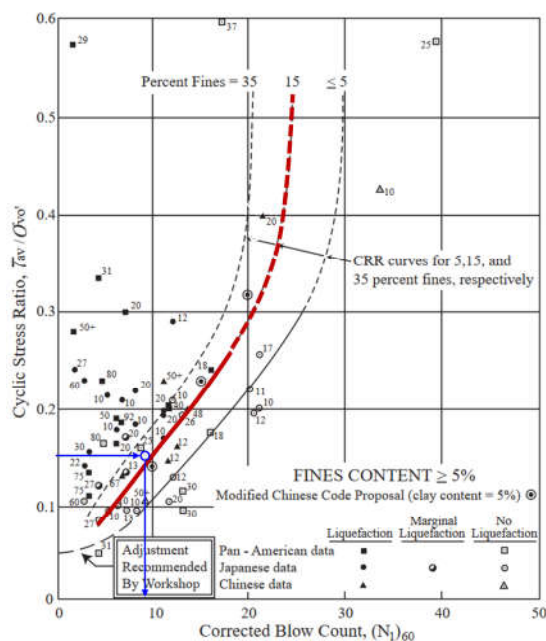
Figure 4. An SPT-based soil liquefaction chart, modified from Seed et al. (1984)

As an optimal liquefaction mitigation solution, a replacement of upper, liquefaction-prone, layer is chosen. It is done in such a way that the excavated layer, which consists mainly of silty sands, is mixed with coarse-grained gravel in a ratio of 70 % (sand) – 30 % (gravel). This increases the liquefaction resistance of the sands, while at the same time meeting the hydraulic (seepage) requirements of the design. The typical cross-section of the reconstructed Pušćine levee is shown in Figure 5.
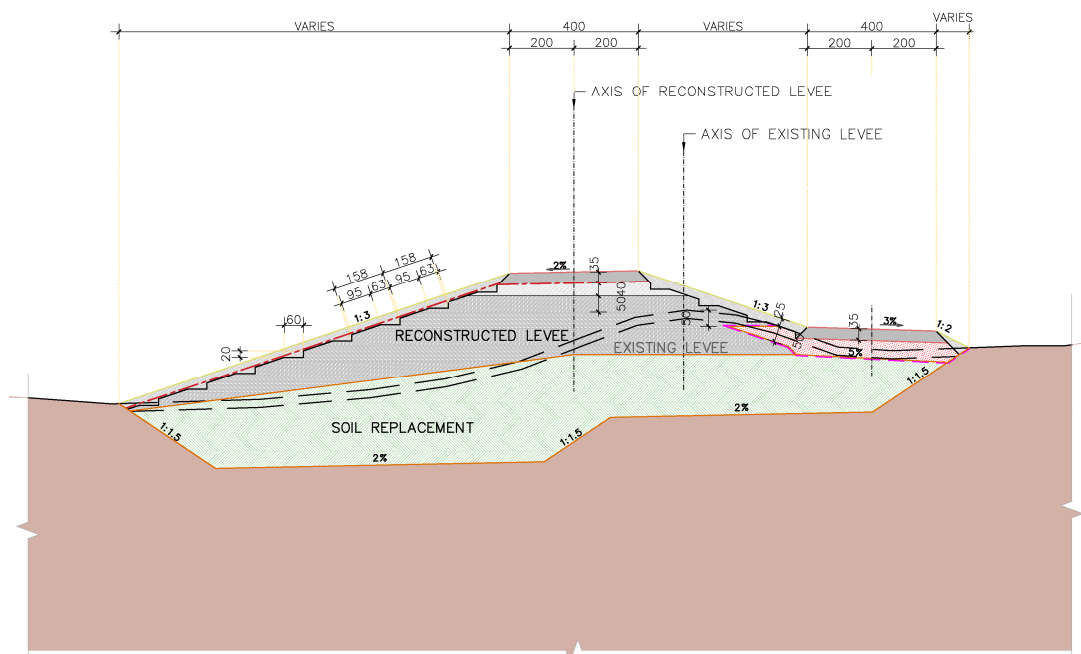
Figure 5. A cross section of reconstructed Pušćine levee (CFCE, 2022)

Advanced numerical simulations were used to test the influence of different replacement depths on the behavior of the levees by calculating the levee settlements in the event of liquefaction. If no replacement is carried out, the expected liquefaction-induced settlements are between 100 and 150 cm, which is considered unsatisfactory. If the replacement is carried out to the depth of the lower gravels, the expected

settlements are between 6 and 10 cm. However, as 60% of the length of the levee lies on soils at risk of liquefaction and both the financial and technical aspects of such large-scale soil replacement need to be considered, it was decided to replace the soil to a depth of 2 m or lower if gravels are encountered. This solution leads to settlements in the range of 30 to 40 cm, which is considered acceptable as it is assumed that the levee will retain its function as flood protection during the subsequent remediation works.

4   Hrastelnica levee in Sisak - Moslavina County: a CPT approach

4.1 Description of the site and investigation works

As a result of the 2020 Petrinja earthquake, a levee on the left bank of the Sava River in Hrastelnica, Sisak-Moslavina County, showed significant deformations and cracks on the crest, slopes and surrounding soil. The length of the damaged section is 400 m, from km 106+200 to km 106+600 (Figure 6). The damage is largely due to liquefaction, with a large amount of sand ejecta observed.

Figure 6. The layout of the damaged section of Hrastelnica levee with observed sand ejecta

To assess the condition of the soil as a starting point for the levee remediation, the soil investigation campaign (CFCE, 2021a) comprised four boreholes, each with a depth of 15 m', laboratory testing of samples, 4 cone penetration tests with PWP measurements (CPTU) with depths of 8 to 18 m and a geophysical campaign with electrical tomography (ERT), seismic refraction and multi-channel analysis of surface waves (MASW).

The investigation shows that the existing levee consists largely of low plasticity clays, while the subsurface soil profile consists of low plasticity clays underlain by a clayey sand layer. The thickness of the upper clayey materials varies between 7 and 10 meters, while the lower clayey sand with low levels (up to 17%) of fine particles is associated with the liquefaction that has occurred.

3.2   Liquefaction evaluation and mitigation measures

The liquefaction assessment for the design of the mitigation measures for Hrastelnica levee rely on is the CPTU tip resistance and associated liquefaction chart for silty sand, Figure 7a. For the calculation of CSR, the equation (1) is used, with the a_{max} of 0.30g which corresponds to a seismic event of 475-year return period.

The calculated values of the factor of safety to liquefaction, i.e. the ratio of CRR to CSR, are shown in Figure 7b for one CPTU at the location. All CPTUs show similar consistent results, with the high probability of liquefaction calculated for the layers identified as clayey sand layers during drilling. In addition, customised software (Librić et al., 2022) is used to calculate the probability of liquefaction (PL) along the depth based on the methodology proposed by Juang et al. (2002) with the governing equation:

$$PL = \frac{1}{\left[1 + \left(FS/_A\right)^B\right]} \tag{2}$$

where A = 1.0 and B = 3.3 are selected as regression coefficient.

(a)

(b)
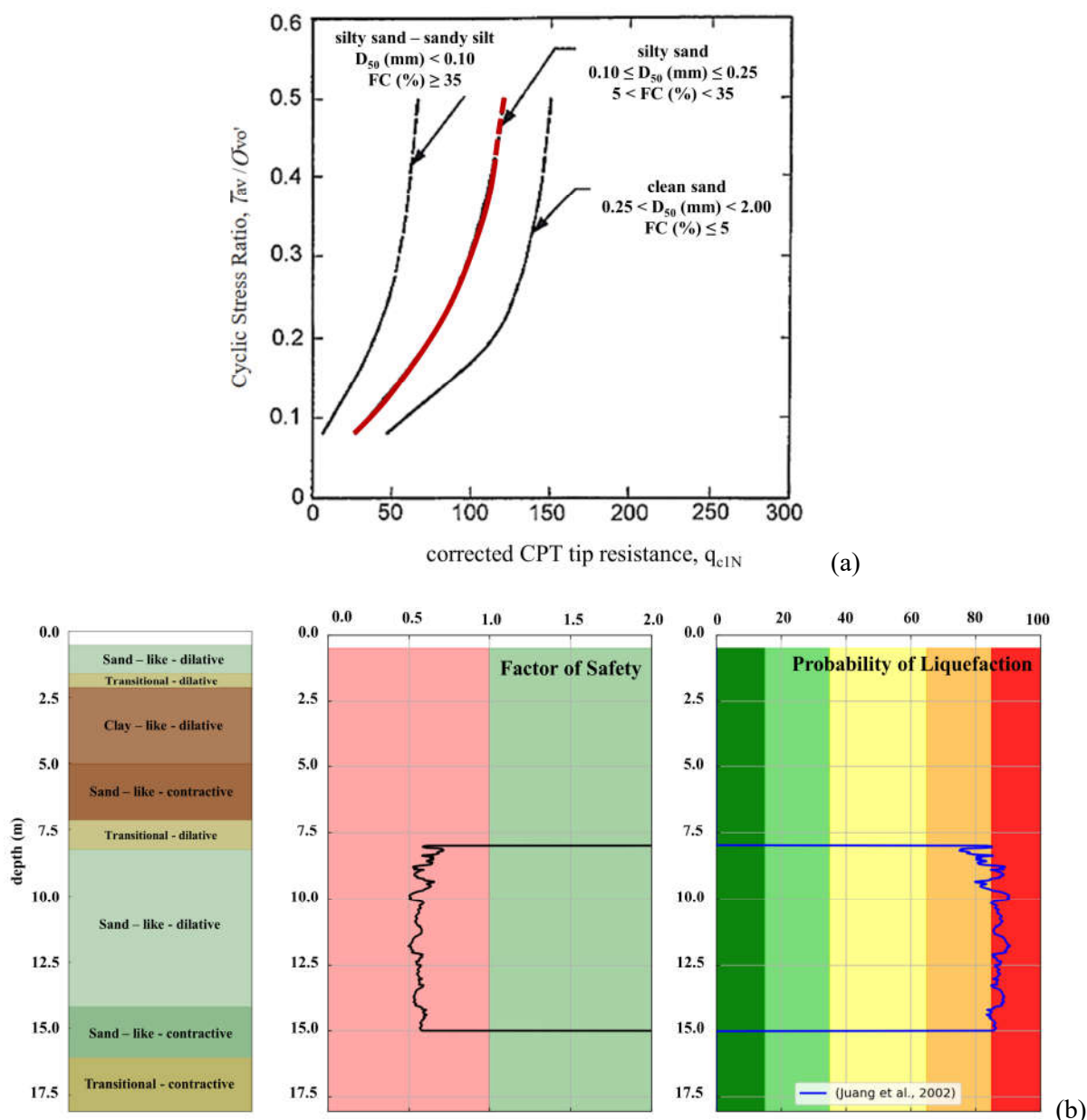
Figure 7. Assessing the soil liquefaction potential through the CPTU tests: (a) An CPT-based soil liquefaction chart, modified from Stark and Olson (1995), (b) results of one CPTU test showing the estimated soil profile with calculation of factor of safety and probability of liquefaction occurrence

Considering the greater depth of the liquefiable layers, deep soil improvement by means of jet grouting

is chosen. Jet grouting is a soil improvement method in which a binding agent is injected into the soil under high pressure to form a compact "soil concrete" with better mechanical properties. The grouting columns are to be installed in a 3 x 3 m arrangement with an expected diameter of 80 cm and a variable length depending on the depth of the sands at risk of liquefaction. By applying the procedure proposed by Özsoy and Durgunoğlu (2003) with the CSR reduction coefficient based on the selected improvement arrangement, the factors of safety increase due to jet grouting implementation is significant (values > 4), so that the probability of liquefaction occurrence decreases to < 2 %. In places where sand layers are encountered in the upper part of the soil profile, the reconstructed levee is "deepened" so that the upper soil profile is replaced by material with the same properties as that used for the levee reconstruction, with geogrids being installed at several levels. The typical cross-section of the reconstructed Hrastelnica levee is shown in Figure 8.
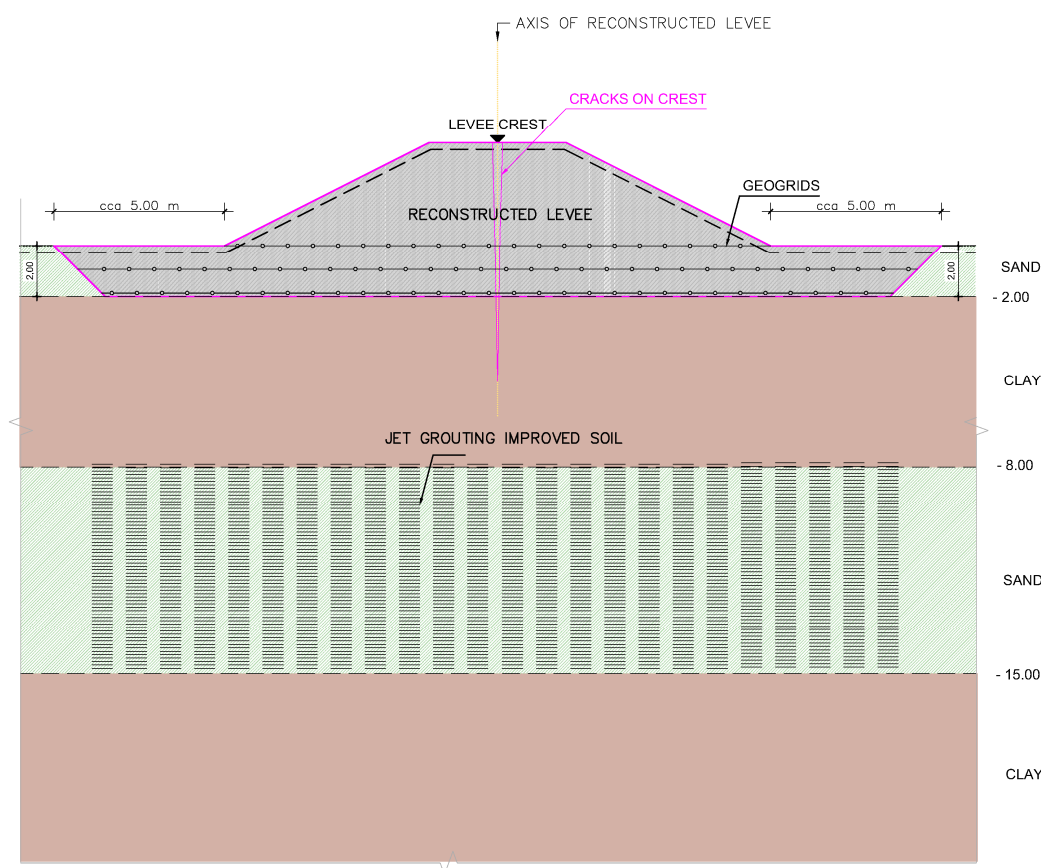
Figure 8. A cross section of reconstructed Hrastelnica levee (CFCE, 2021b)

5   LeveeLiq approach towards the mapping of liquefaction potential below levees

Considering that the commonly used "simplified" approach to liquefaction assessment, as shown in the examples of the Pušćine levee and the Hrastelnica levee, is based on the discrete nature of the in-situ investigations, there is a great need to optimize these investigations along the linear levee network. Such discrete information obtained by means of dynamic or static penetration tests neglect the inherent spatial variability of the soil. Therefore, the ongoing efforts of LeveeLiq (Mapping of the spatial variability of liquefaction potential below the levees and modelling of optimal mitigation techniques) project investigates the assessment of the spatial distribution of liquefaction potential at the asset - level (i.e. levee - level) as a result of the vertical and horizontal variability of the soil. Therefore, LeveeLiq goes a step further by introducing an assessment methodology that accounts for inherent soil variability by correlating the results of different in-situ investigation techniques, focusing on methods that provide fast

yet reliable information. The focus is on the CPT method for the assessment of liquefaction along with MASW geophysical method. Although the MASW method has several disadvantages, such as - (1) the fact that the shear wave velocity correlates more directly with the void ratio of the soil than the relative density of the soil, the latter being a better indicator of liquefaction potential; (2) the lack of sensitivity of the shear wave velocities to the stress-deformation history of the soil, which has a major influence on liquefaction resistance; (3) thinner layers with low shear wave velocities that can potentially be liquefied may not be detected if the measurement resolution is not sufficient - the method provides consistent information on liquefaction resistance, while the investigations can capture a larger volume of soil beneath the levee in a relatively short time. Therefore, using the CPT and MASW data as well as sporadic borehole data, an algorithm is developed to automatically determine the spatial probability of liquefaction under a levee. In doing so, the detrending of the CPT data will be conducted, followed by statistical data processing that includes the identification of statistical parameters (mean value, standard deviation, coefficient of variation, autocorrelation functions and fluctuation scale), all with the purpose of developing a spatial Gaussian log-normal random field. This ultimately leads to the calculation of the spatial distribution of the probability of liquefaction. By having this quantified spatial information, mitigation measures could be identified and optimized in a more comprehensive manner.

6   Conclusions

When constructing new or reconstructing existing levees in seismically active areas, it is of utmost importance to consider the possibility of liquefaction occurring. This requires careful and engineering decisions on appropriate methods to assess liquefaction, which are usually hampered by a combination of technical, logistical and legal factors. The usual compromise is to conduct in-situ geotechnical tests that provide relatively reliable but discrete information about the liquefaction potential of the soil profile under investigation. Such an estimation of liquefaction potential is presented in this paper using the example of two levees in Croatia – the Pušćine levee in Međimurje County, which was reconstructed due to its insufficient height and for which the dynamic penetration tests SPT and DPL were used, and the Hrastelnica levee in Sisak – Moslavina County, which was reconstructed due to its severe damage after the 2020 Petrinja earthquake and where the liquefaction assessments were based on cone (static) penetration tests. In both cases, the methods enabled a quantified, data-driven selection of optimal liquefaction protection measures. To account for the inherent soil variability and its influence on liquefaction potential along the linear levee network, the LeveeLiq research project will take a step forward by correlating the results of different optimized in situ investigation techniques.

References

Bačić, M.; Kovačević, M.S.; Rossi, N.; Librić, L. Assessing the Soil Liquefaction Susceptibility: A Comparative Study of CPT and MASW Techniques in the Aftermath of Road Failure. *In Proceedings of Road and Rail Infrastructure VIII (CETRA 2024)*. Lakušić, S. (ed) ., Zagreb: University of Zagreb Faculty of Civil Engineering, 2024. doi: 10.5592/CO/CETRA.2024

Barua, U.; Ansary, M.A.; Islam, I.; Munawar, H.S.; Mojtahedi, M. Multi-Criteria Earthquake Risk Sensitivity Mapping at the Local Level for Sustainable Risk-Sensitive Land Use Planning (RSLUP). *Sustainability,* 2023, 15 (7518). doi: https://doi.org/10.3390/su15097518

CFCE. Center of Faculty of Civil Engineering. *Additional geotechnical investigations for the purpose of reconstruction of Pušćine levee*. Geotechnical investigation report, no. GIZ-009/2016, 2016.

CFCE. Center of Faculty of Civil Engineering. *Left bank embankment in km 106+200 to km 106+600 in Hrastelnica, Sisak-Moslavina County*. Geotechnical investigation report, no. GLP-059/2021, 2021a.

CFCE. Center of Faculty of Civil Engineering. *Left bank embankment in km 106+200 to km 106+600 in Hrastelnica, Sisak-Moslavina County*. Detailed design, no. GLP-059/2021, 2021b.

CFCE. Center of Faculty of Civil Engineering. *Reconstruction of th levee on the left bank of the Drava River near Pušćine from km 0+000 to km 3+476*. Detailed design, no. IZP-034/2022, 2022.

Elektroprojekt. *Reconstruction of th levee on the left bank of the Drava River near Pušćine from km 0+000 to km 3+476*. Main design, no. G3-A30.00.01-G03.0, 2020.

FCEZG. University of Zagreb, Faculty of Civil Engineering. Geotechnical investigation works for the reconstruction of Pušćine levee. Geotechnical investigation report, GIZ-110-149/2013, 2013.

Juang, C.H.; Jiang, T.; Andrus, R.D. Assessing probability-based methods for liquefaction evaluation. *Journal of Geotechnical and Geoenvironmental Engineering*. 2002 128 (7), 580-589.

Librić, L.; Bačić, M.; Kovačević, M. S. Utilization of CPTU for evaluation of liquefaction probability below the flood protection embankment in Croatia. *In Proceedings of the 3rd International Conference on Natural Hazards and Infrastructure*. 5-7 July, 2022. Athens, Greece 2022.

Oka, F.; Tsai, P.; Kimoto, S.; Kato. R. Damage patterns of river embankments due to the 2011 off the Pacific Coast of Tohoku Earthquake and a numerical modelling of the deformation of river embankments with a clayey subsoil layer. *Soils and Foundations*. 2012, 52 (5), 890-909. doi: https://doi.org/10.1016/j. sandf.2012.11.010

Özsoy, B.; Durgunoğlu, H.T. The mitigation of liquefaction by means of high modulus columns. *Fifth Turkish National EEC*, Istanbul, May 2003.

Pollak, D.; Gulam, V.; Novosel, T.; Avanić, R.; Tomljenović, B.; Hećej, N.; Terzić, J.; Stipčević, J.; Bačić, M.; Kurečić, T. et al. The preliminary inventory of coseismic ground failures related to December 2020 – January 2021 Petrinja earthquake series. *Geologia Croatica: journal of the Croatian Geological Survey and the Croatian Geological Society*. 2021, 74 (2), 189-208. doi:10.4154/gc.2021.08

Premur. *Geotechnical investigations for the purpose of reconstruction of Pušćine levee – DPL investigations*. Geotechnical investigation report, no. 109/22-D, 2022.

Republic of Croatia. *Croatia December 2020 Earthquake - Rapid Damage and Needs* Assessment, 2021.

Seed, H. B.; Tokimatsu, K.; Harder, L. F.; Chung, R. M. *The influence of SPT procedures in soil liquefaction resistance evaluation.,* Earthquake Engineering Research Center Rep. No. UCB/EERC-84/15, Univ. of California, Berkeley, California, 1984.

Stark, T.D.; Olson, S.M. Liquefaction Resistance Using CPT and Field Case Histories. Journal of Geotechnical Engineering. 1995, 121 (12), 856-869. doi 10.1061/(ASCE)0733-9410(1995)121:12(856)

INVESTIGATION AND REINFORCEMENT OF A WEATHERING INDUCED ROCK FALL EVENT

ÖMER ÜNDÜL[1], MOHAMMAD MANZOOR NASERY[2], GÖKHAN ŞANS[3]

[1] *İstanbul Technical University, Mining Faculty Geological Engineering. Dept. Türkiye, undul@itu.edu.tr*

[2] *Dynamica Mühendislik Co., 61010 Trabzon, dynamicamuhendislik@gmail.com*

[3] *İstanbul Technical University, Mining Faculty Geological Engineering. Dept. Türkiye, sansg@itu.edu.tr*

Abstract

Increasing population and demand on housing increases the interaction of geo-environment and human settlements. Thus, the rate of natural events effecting daily human life surges for highly populated areas. A rock fall event occurred in a highly populated area in İstanbul (Türkiye). The source rock blocks belong to the Paleozoic sequence of İstanbul composed of nodular limestone with sandy-clay interlayers. These rock masses slided and fall a day after heavy rains. The study initiated by the examination of the dimensions of rock blocks and their paths and continued with the investigation of discontinuity and weathering properties. Geomatic studies established numerical 3D view of the area based on drone views. Field observations showed the effect of the growing roots of trees within discontinuities. This weathering effect exerted stresses along discontinuities. Laboratory studies showed that the rock has moderate uniaxial compressive strength (40-51MPa). Numerical models obtained from various cross sections demonstrated the most critical sections to be considered and reinforced. Study advices pre-cleaning of risky blocks after a fence production on the potential falling paths, rock anchors in some localities with varying lengths. These mitigation processes were then re-assessed with numerical models showing that the factor of safety increased to desired levels.

Key words
FEM Analysis, Mitigation, Rock fall, Urban Areas, Weathering

1 Introduction

Rock falls are natural events that mostly occurs in rugged and mountainous terrain, cut-slopes and open-pit mines. These events have impact on human life and engineering structures. As well-known rockfall is defined by Varnes (1978) as the very rapid and sudden movement of rock blocks separated along discontinuity surfaces on slopes due to gravity. The fundamental reason for these sudden instabilities in rock masses is that the peak shear strength on the discontinuity surfaces can easily drop to the residual shear strength as a result of a few millimeters of displacement (Wyllie and Mah, 2002). This event can be triggered under various effects such as freeze-thaw, wetting-drying cycle of water along discontinuities, heavy rains, growth of tree roots, weathering and seismic effect etc. exhibiting a free fall down steep slopes, rolling and/or jumping of blocks depending on the steepness of the slope (Ritchie, 1963; Wyllie, 2015). Blocks that remain stable for years in rock slopes can suddenly separate from the mass and tend to move downwards. In order to properly design reinforcement and/or landslide mitigation works techniques, engineers need data including dimensions of rock blocks, impact loads, travel distances, jump heights etc.

Such an event occurred in the flanks of Bosphorus strait on 02.10.2023 (Figure 1 and Figure 2). Rock fall initiated in an area approximately of 20x10m. It was observed that the rocks were distributed laterally for 40 meters at a distance of approximately 80 meters away from the detachment zone. The

site comprises many priceless historical buildings. On the other hand, unfortunately there are some buildings constructed without any engineering design and any approval from authorities. Thus, these latter buildings have huge potential even to collapse without any major impact (rockfall, seismic event etc.). Some of these buildings were already damaged during the rockfall event (Figure 2). Along the Bosphorus strait, due to official, visual and environmental restrictions engineers force to define environmentally friendly designs. This research and engineering application define a systematic reinforcement methodology especially for such steep slopes in densely populated area where environmental and visual expectations should be considered.

Figure 1. Location Map of the Study Area (İstanbul-Türkiye).

The trend of the slopes in study area are north-east and south-west direction (Figure 1). Since there are actively used pedestrian paths and dense settlements under the risky slope, rock falls threaten the safety of life and property. To analyse different risk situations regarding the potentially unstable rock geometries the study area was analysed in three zones (Figure 3).

i.   Block Rockfall (Zone A - area with relatively large blocks - approximately more than 1m^3)
ii.   Rocks with relatively smaller dimensions and debris slides (Zone A and Zone B - area with relatively smaller rock blocks and potential of debris flow of varying natural and man-made material)
iii.   Rubble due to risky structures and building components (Zone B - area with structures and building components)

It is clear that the collapsed building component are suspended in different positions on the slope, which has a potential risk to slide (Figure 2 c and d).

Figure 2. Views of a) failed blocks b) closer view of nodular limestone c) damaged building d) risky natural and man-made debris material.

2. Methods

The initial stage of the study comprises generating surface model and base maps of the study area using photogrammetric methods. Simultaneously, geological and engineering geology properties were determined following the definition of physical and mechanical properties of the rocks by laboratory studies. Index and mechanical results were determined according to ISRM (1981 and 2007) suggestions. In addition, kinematic analyses were performed based on discontinuity measurements of the slopes. Depending on these data geotechnical numerical model of study area was prepared and slope stability analyses were carried out using finite element method (FEM). With the help of 1,200 different probabilities on the sections prepared from the digital terrain model of the study area, the jump height, speed and total kinetic energy possibilities of the possible falling rock blocks were calculated and evaluated. Reinforcements and precautions were than proposed.

3. Numerical 3D Model of the Area

Detailed topographic data are very important in rock fall events both in analyzing the rock fall event and stability analysis before and after precautions. The aerial photographs obtained from an unmanned drone were evaluated with the stereoscopic method. Point cloud and vector data were compiled to generate 3D numerical model with contour lines (Figures 3).
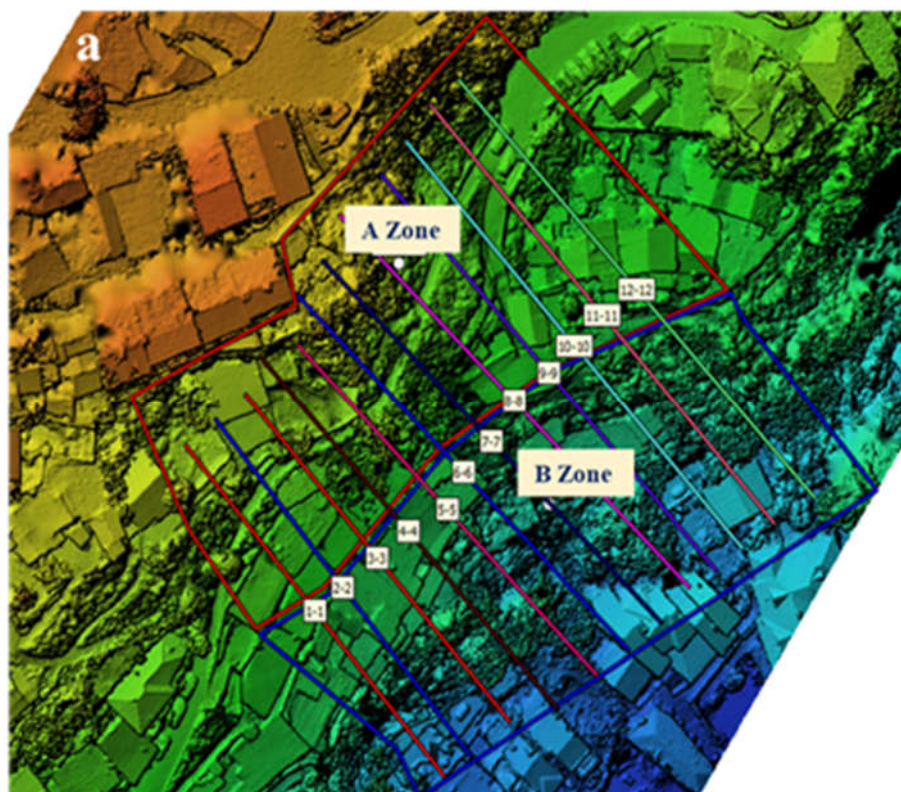
Figure 3. Digital elevation view on the 3D terrain model showing studied zones and critical rockfall routes (e.g. 1-1, 2-2 etc. in varying colors) (note that the resolution of the orthophoto is 1.35cm/px).

4. Geological and Engineering Geological Properties

The rocks in the study area belong to the Istanbul Paleozoic. The unit is known in the region as Ayineburnu Member (Dcda) of Denizli Köyü formation (DCd). Upper Devonian aged Dcda is a limestone-claystone succession of different strengths. The unit gained a lumpy appearance with a boudinage structure during the diagenesis process (Figure 2) thus named basically as nodular limestone. The rock mass was fractured by tectonic events and weathering. The effect of root on discontinuities are very evident. The growing roots within the apertures of discontinuities decreases the shear strength. This process is unfortunately very common on the site (Figure 4). These biological and physical weathering effects play a major role in the stability of the rock mass.
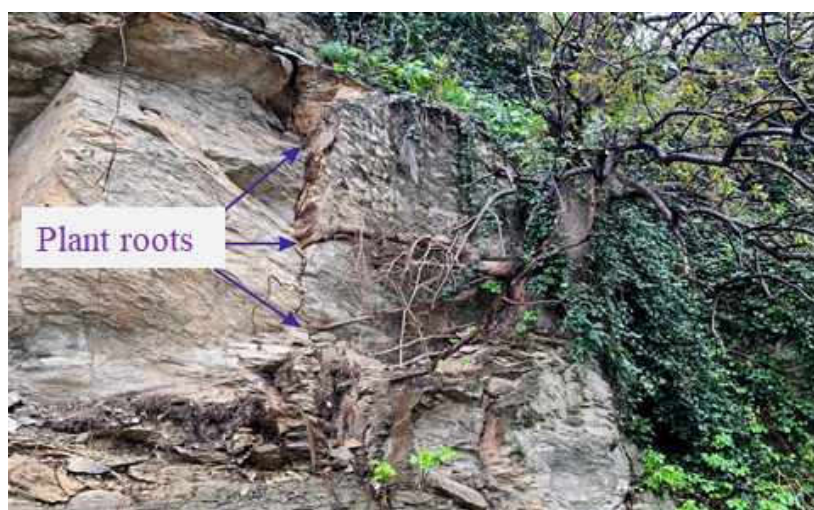
Figure 4. View of the effects of plant roots along discontinuities.

The distance between the discontinuities is approximately 200cm on average (varying between 80-400cm) and the discontinuities are mostly closed. Open discontinuities range from millimeters to 10 cm, especially in areas where plant roots penetrate deeply. The continuity of almost all of the discontinuities, except for discontinuities due to weathering in the sections close to the surface, can be observed throughout the outcrop. Discontinuities are wavy-smooth and slightly rough (JRC 6-8). Water seepage has been observed in areas close to the surface along the discontinuities during rainy periods. The rock mass can be considered as slightly and moderately weathered according to ANON (1995).

The effective ground acceleration value of the study area was obtained from the Turkey Earthquake Hazard Map, and the maximum ground acceleration value was determined as 0.325 g and was considered in the calculations.

Field studies and observations reveal that some blocks on the slope had previously fallen and some risky blocks are standing with a potential of a fall or slide. Thus, further studies were carried out and their results are given below.

5. Kinematic Analysis

Kinematic analyses were performed with Rocscience Dips (2024) software. Both field observations and discontinuity orientations in the study area show that planar and wedge-type movements may develop. The kinematic analysis of the rock mass considered planar and wedge type instabilities (Figure 5). The safe slope angle is 32° for planar shear and 37° for wedge type instability. Reducing the general slope angle of the rock mass to 37° will completely prevent from possible instabilities. However, since this is not possible due to the surrounding construction, risks must be eliminated with local intervention and protection structures in risky blocks and areas.
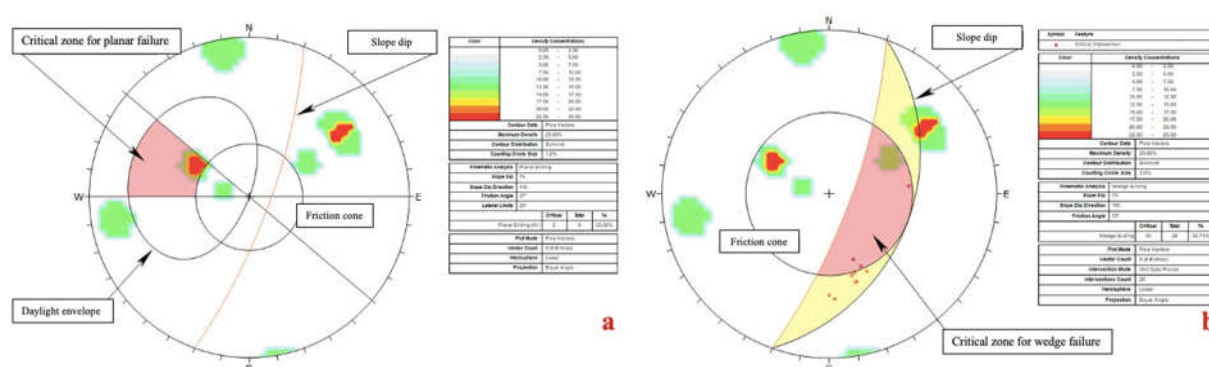
Figure 5. Kinematic analysis a) Plane type stability analysis of rock mass, b) wedge type stability analysis of rock mass.

6. Slope Stability Analysis by Using Finite Element Method

In order to determine the stability condition, the finite element method "RS2 v.11.023" (Rocscience, 2024) program was used and total displacement analyses were performed with the critical SRF (Stress reduction factor) value. Stress-strain analyses were performed using the failure criterion suggested by (Hoek et al. 2002) and plastic failures were investigated. Seismic loads were also considered in the numerical analyses and the horizontal ground acceleration value was determined as 0.325g.

For geomechanical conditions, the horizontal vertical stress ratio was chosen as 0.4 in both static and dynamic calculations. Geotechnical parameters calculated according to Hoek-Brown (2018) Failure Condition and GSI are presented using field observations and laboratory test results. The parameters used in the numerical analysis are given in Table 1.

Table 1. Geotechnical parameters for nodular limestone

Geomechanical Parameter	Value
Unit Weight (MN/m^3)	0.025
Young Modulus (MPa)	596.52
Poisson Ratio	0.3
Uniaxial Compression Strength (MPa)	30
Geological Strength Index (GSI)	41
D (Disturbance Factor)	0.7
m_b	0.274
s	0.0002
a	0.511

Critical slopes of the study area were evaluated with the finite element analysis method, and the total displacements are given in Figures 6a-c-e under static loads, and in Figures 6b-d-f under dynamic condition. Long-term slope stability analysis was carried out under current state and dynamic loads by applying the Shear Strength Reduction (SSR) shear stress reduction method in numerical calculations.
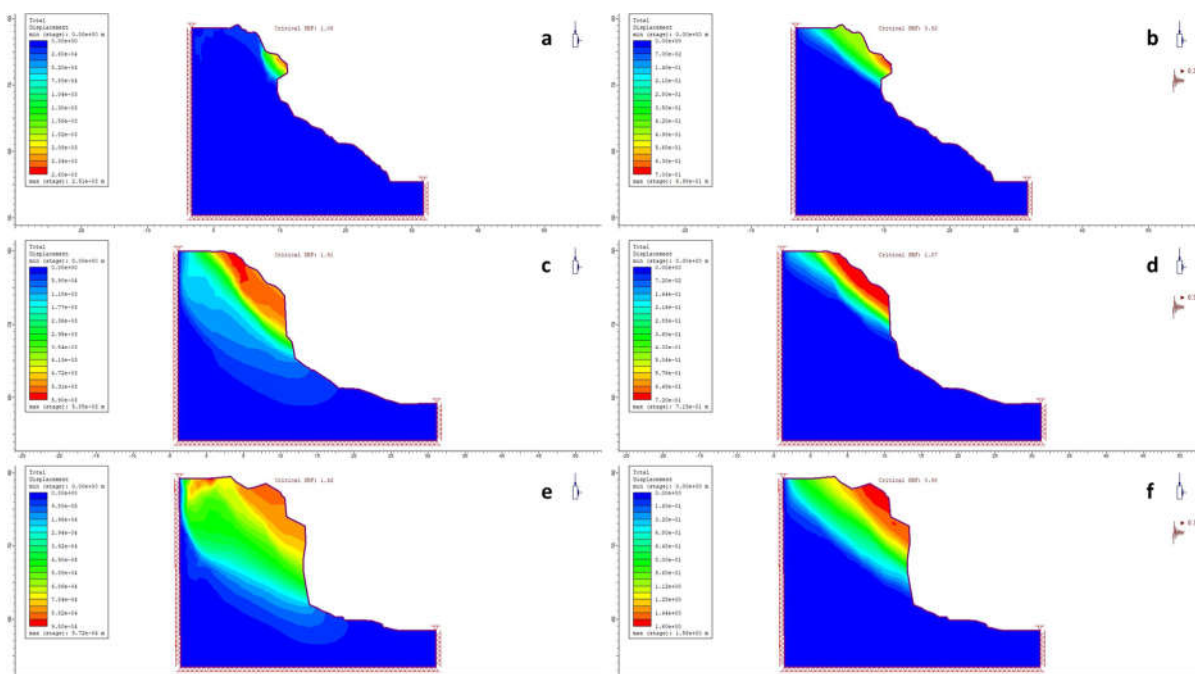
Figure 6. Total displacement a) for static condition along section K1-1 b) under dynamic conditions along section K1-1 c) for static condition along section K2-2. d) under dynamic conditions along section K2-2 e) for static condition along section K3-3 f) under dynamic conditions along section K3-3 (Please refer to Figure 3 for cross section routes)

The analyses showed that the slopes have SRF over "1" under static conditions. But decreases below "1" in dynamic conditions. Under static conditions the displacement is expected to be less than 0.26cm whereas it may rise to 70cm under dynamic conditions. This shows that some parts of the study area will be unstable in the event of an earthquake. In this study, SRF values obtained for static and dynamic situations are accepted as Safety Factor (SF).

7. Rock Fall Analysis

As a result of preliminary analysis, the 12 most critical routes for rocks that may fall were determined on the 3D numerical model prepared with photogrammetric methods. Figure 3 shows the most critical routes of rockfall. Rock fall analyses were carried out in the RocScience RockFall (2024) program by taking cross-sections of the determined routes.

In rock fall analyses, material parameters were determined depending on the geological structure of the slope along the route (Table 1). The factors that directly affect rock fall analysis results are the recovery coefficients (Rn, Rt) and friction angle. Coefficient of normal and tangential restitutions Rn and Rt values, which control the energy dissipation at the points where the falling block contacts the topography, were defined in the sections in accordance with the lithological situation on the slope. Clean hard bedrock feature and parameters were defined for the routes in the RocFall program, depending on the land situation nodular limestone surfaces. In the software, bedrock outcrops (weathered limestone) feature and material parameters were defined in areas with weathered nodular limestone surfaces, depending on the terrain along the route.

7.1. 2D Rock Fall Analysis

During site investigation, it was observed that the risky rock blocks and previously failed rock blocks exhibit varying volumes (0.25-6m³). In addition, the risky blocks in Zone A has volumes of approximately 15-20m³. The slope geometry and discontinuity properties along routes 1-1 and 3-3 reveal that risky blocks have a volume of approximately 1m³ and a mass of 2450 kg. Considering discontinuity properties along remaining nine routes, the largest block size was determined as 6m³. and an average weight of 14700 kg. A totally of 1200 different rock fall analysis scenarios were calculated by solving the jump height of rock blocks, total kinetic energy and the maximum distance. Results revealed that rocks can reach with 100 different possibilities for each route. Maximum jump height and total kinetic energy values obtained from rock fall analyses are given in Table 2.

Table 2. Block Weight, Initial Speed, Maximum Jump Height and Total Kinetic Energy Values in Rock Fall Analyses along the Route.

	Section No:	1-1	2-2	3-3	4-4	5-5
1 m³ and 2,450 kg Block	Risky Block Mass (kg)	2,450	2,450	2,450	2,450	14,700
	Initial Fall Speed (m/s)	1.00	1.00	1.00	1.00	1.00
	Maximum Bounce Load Upon Impact with the Road (m)	1.96	2.48	2.68	3.14	3.80
	Total Kinetic energy at the moment of hitting the Road (kJ)	83.35	150.05	114.30	449.32	2132.2
	Section No:	6-6	7-7	8-8	9-9	10-10
6 m³ and 14,700 kg Block	Risky Block Mass (kg)	14.700	14.700	14.700	14.700	14.700
	Initial Fall Speed (m/s)	1.00	1.00	1.00	1.00	1.00
	Maximum Bounce Load When Hitting the Barrier (m)	5.51	5.59	5.93	3.05	2.05
	Total Kinetic energy at the moment of hitting the barrier (kJ)	4,219.7	1,708.2	3,639.4	3,175.1	4,516.3
	Section No:	11-11	12-12			
6 m³ and 14,700 kg Block	Risky Block Mass (kg)	14,700	14,700			
	Initial Fall Speed (m/s)	1.00	1.00			
	Maximum Bounce Load When Hitting the Barrier (m)	3.38	8.46			
	Total Kinetic energy at the moment of hitting the barrier (kJ)	4,414.3	4,489.5			

The analyses reveal that 90% of the falling blocks can reach the settlements. Although the rock block reaching the residences at the most critical section in the rock fall analysis has a kinetic energy of approximately 4,500 kJ, and average speed of 24.10 m/sec and a maximum jump height of 10 m and an average of 3-4 m height along the routes. The geometry of the slope hinders the work of some large vehicles. For these reasons some risky blocks should be broken and removed from the slope with a fully controlled rock crushing application and then supported with reinforced combined nets and rock bolts.
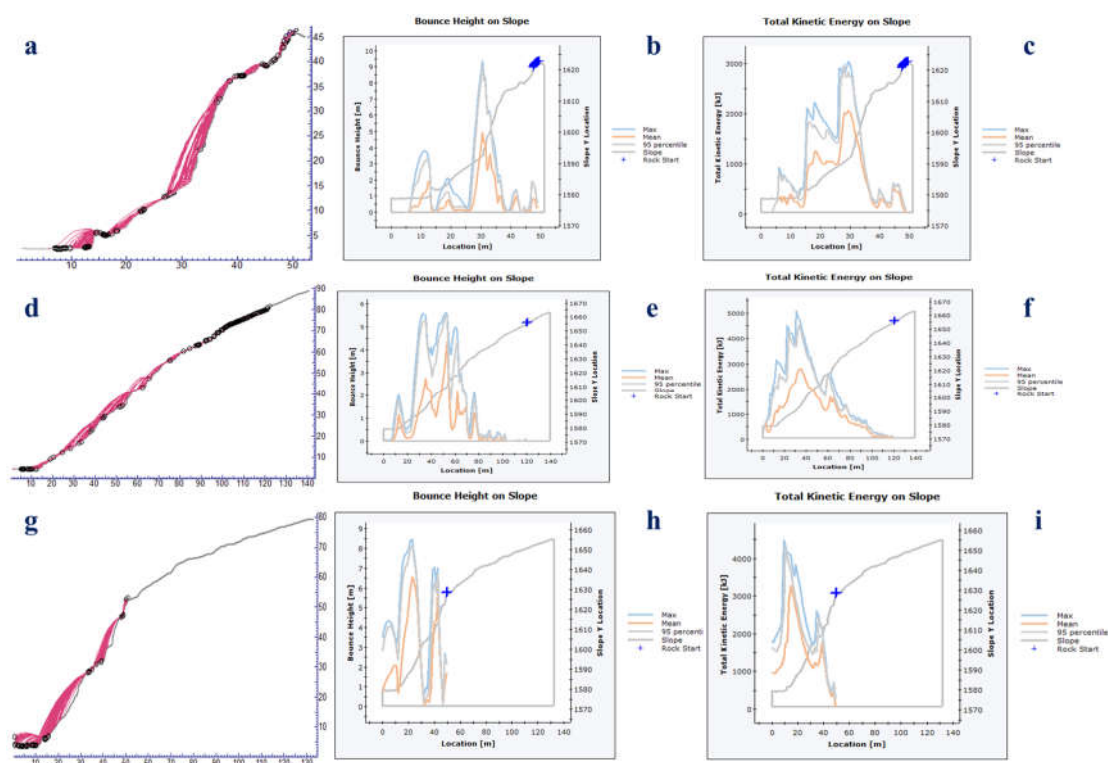
Figure 7. Scenarios that may occur during rock fall along routes No 5, 10 and 12 (left column show the calculated jump heights, mid-columns show the bounce heights, right column shows the kinetic energies).

8. Conclusions

The study investigated a rock fall event on 02.10.2023. The rocks belong to Paleozoic sequence of İstanbul. These old rocks were deformed under tectonic stresses. Besides, these nodular limestones are subjected to biological and physical weathering. Thus, discontinuities of varying properties exist.

The investigation initiated with the construction of precise digital surface model of the study area utilizing orthoimages. Stability analysis exhibit the kinematic admissibility. Rock fall analyses utilizing 3D model defined major rock fall paths, speed, impact energy and the jump height of potential falling rocks. According to these findings five stage reinforcement methodology was proposed for the site as follows;

- *Construction of fens barrier,* rockfall analysis reveal that 90% of falling blocks reach the settlements. This is unfortunately confirmed by the event occurred in 02.10.2023. Prior to any reinforcement works fence barriers was proposed as a must in order to ensure the security during construction. Fence barrier will remain as a permanent precaution thus will play an important role in any instabilities that may occur in time.
- *Fully controlled rock breaking and detailed slope cleaning,* all risky rock blocks that has potential to fail (i.e. highly weathered, deeply penetration of roots etc.) must be broken or cleaned and removed from the slope in a controlled manner.
- *Reinforced combined net,* the investigated entire slope will be fixed with a reinforced combined net. The nets will be anchored to the deeper and durable rock slope.
- *Supporting Risky Blocks with Rock Bolts,* in addition to previous reinforcements blocks with considerably higher volumes (volume of 96.52 m³ and total weight as 236.48 tons) will be anchored to the rock mass with rock bolts.
- *Monitoring.* After applying the precautions, the reinforced slope was reevaluated with numerical models concluding the increase (the recalculated safety factor is at least 1.1 in dynamic condition and the static safety factor will be at least 3). At the latest stage, due to the importance of the study area it is strongly recommended to monitor the reinforcement system and the slope stability.

References

ANON The description and classification of weathered rocks for engineering purposes. *Q J Eng Geol*. 1995, 28:207–242.

Hoek, E., Carranza –Torres, C.T., and Corkum, B., Hoek-Brown failure criterion:2002 edition. *Proceedings of the North American Rock Mechanics Society Meeting*. Toronto, Canada, 2002, 1-6.

Hoek, E. and Brown, E.T. 2018. The Hoek-Brown criterion and GSI -2018 edition. *Journal of Rock Mechanics and Geotechnical Engineering*. 2019; 6(3): 445-463.

ISRM (International Society for Rock Mechanics) Rock Characterization, Testing and Monitoring. *International Society of Rock Mechanics Suggested Methods*. Pergamon Press, Oxford, 211 p., 1981.

ISRM (International Society for Rock Mechanics) *The complete ISRM suggested methods for rock characterization*. In: Ulusay, R., Hudson, J.A. (Eds.), Testing and Monitoring. 1974-2006. p. 628., 2007.

Ritchie, A.M. Evaluation of rockfall and its control. *Highw Res Board Rec*.1963, 17,13–27.

Rocscience Dips. *Graphical and Statistical Analysis of Orientation Data*. V. 8.027, Rocscience Inc., Toronto, 2024.

Rocscience RS2. *2D Geotechnical Finite Element Analysis*. V. 11.023, Rocscience Inc., Toronto, 2024.

Rocscience RocFall2. *Statistical Analysis of Rockfalls*. V. 8.024, Rocscience Inc., Toronto, 2023.

Turkey Earthquake Hazard Map. Available online: https://tdth.afad.gov.tr/TDTH/main.xhtml. accessed on (24 December 2023).

Varnes, D. J. Slope movement types and processes, In: R. L. Schuster and R. J. Krizek, Eds. *Landslides, Analysis and Control*. National Academy of Sciences, pp. 11-33, 1978.

Wyllie, D.C. *Rock Fall Engineering*. CRC Press, Taylor & Francis Group. 270 pp., 2015.

Wyllie, D.C., Mah, C.W. *Rock Slope Engineering*, 4th edition. Taylor & Francis, London, 422 pages, 2002.

THE USE OF COMPUTATIONAL FLUID DYNAMICS (CFD) IN THE VENTILATION-BASED REMOVAL OF TOXIC GASES LEAKING FROM GEOTHERMAL SOURCES IN INFRASTRUCTURE PROJECTS

C. OKAY AKSOY[1], G. GÜLSEV UYAR AKSOY [2], H. BERKER SARISAN [3]

[1]*Dokuz Eylül University Mining Engineering Department, Turkey, okay.aksoy@deu.edu.tr[1]*

[2]*Hacettepe University Mining Engineering Department, Turkey, gulsevaksoy@hacettepe.edu.tr*

[2] *GOA Mining, Turkey, berkersarisan@gmail.com*

Abstract

The ventilation-based removal of toxic gases leaking from geothermal sources in infrastructure projects is crucial for both human health and environmental protection. In this process, Computational Fluid Dynamics (CFD) simulations are highly valuable for modeling and analyzing complex physical processes related to the transport and distribution of gases. During infrastructure projects in geothermal areas, various gases can leak from underground geothermal sources. These gases may include toxic and/or combustible gases such as hydrogen sulfide (H_2S), carbon dioxide (CO_2), and methane (CH_4). Effective design of a ventilation system is crucial for removing toxic gases through ventilation. Computational Fluid Dynamics (CFD) simulations can be used to evaluate the design and performance of ventilation systems. Modeling the gases leaked from geothermal sources using CFD simulations can help understand how gases move throughout infrastructure projects and their environmental impacts. CFD simulations can assist in optimizing factors such as the placement of ventilation systems, duct design, air flow rates, and filtration efficiency. This optimization ensures effective removal of toxic gases and minimizes environmental impacts. CFD simulations can be used to assess the effectiveness and safety of ventilation systems for removing toxic gases. Additionally, simulating the operation of ventilation systems during potential emergencies can help evaluate risks.

Key words
Calculational Fluid Dynamics, tunnel, fan, geothermal source, infrastructure

1   Introduction

Infrastructure projects may encounter geothermal gas leaks, which can have serious effects on the environment. These gases are often toxic and/or combustible. The most common ones include hydrogen sulfide (H_2S), carbon dioxide (CO_2), and methane (CH_4). The release of these gases into the environment can lead to various harmful consequences.

Firstly, these gases can directly harm human health. Hydrogen sulfide can cause serious effects on the respiratory system with short-term exposure and can lead to severe health problems with long-term exposure. Carbon dioxide in high concentrations can cause respiratory problems and even death. Methane is a flammable gas and can increase the risk of explosions.

Additionally, geothermal gas leaks can also negatively impact natural habitats. Damage to vegetation and soil by these gases can disrupt ecosystems' balance. High concentrations of carbon dioxide can negatively affect plant growth and lead to soil acidification. Methane leaks can contribute to climate change by creating a greenhouse effect in the atmosphere.

In cases where geothermal gas leaks are not cleaned through ventilation, serious risks can arise. Especially in enclosed spaces or tunnels, gas concentrations can reach dangerous levels. This situation can endanger the health of workers and increase the risk of explosions or poisoning in emergencies.

Therefore, it is crucial to effectively clean geothermal gas leaks through ventilation. Ventilation systems help to extract these gases and release them outside, thus protecting the environment and the health of workers. Additionally, proper design and regular maintenance of these systems are of critical importance.

In conclusion, the environmental effects of geothermal gas leaks and the risks associated with not cleaning them through ventilation should be taken seriously. Without effective measures, potential dangers to both the environment and human health may arise. Therefore, managing gas leaks and ensuring the effectiveness of ventilation systems are crucial in geothermal infrastructure projects.

2 Methods

2.1 The Importance Of Using The CFD Method

In the analysis of ventilation systems for managing geothermal gas leaks, Computational Fluid Dynamics (CFD) plays a pivotal role. CFD is a powerful computational tool used to simulate and analyze the behavior of fluids and gases in complex systems. It employs numerical methods and algorithms to solve the governing equations of fluid flow, heat transfer, and other related phenomena.

CFD allows engineers and researchers to model and visualize the distribution and movement of gases within infrastructure projects, such as tunnels or enclosed spaces. By dividing the domain into discrete computational cells, CFD simulates the interactions between fluid particles and boundary surfaces, providing insights into flow patterns, turbulence, temperature distributions, and gas concentrations.

In the context of ventilation analysis for geothermal gas management, CFD enables detailed simulations of airflow dynamics, helping to optimize the design and performance of ventilation systems. By inputting parameters such as fan characteristics, duct geometries, environmental conditions, and gas properties, CFD simulations can predict how gases disperse and are removed through ventilation.

One of the key advantages of CFD is its ability to assess multiple design scenarios rapidly and cost-effectively, allowing engineers to iterate and refine ventilation system designs before implementation. This iterative process helps identify potential issues and optimize system parameters to achieve efficient gas removal while minimizing energy consumption and environmental impacts.

Moreover, CFD can simulate various operating conditions and emergency scenarios, providing valuable insights into the effectiveness and safety of ventilation systems under different circumstances. This predictive capability is crucial for ensuring the reliability and resilience of ventilation systems in mitigating the risks associated with geothermal gas leaks.

CFD simulations provide powerful tools for understanding and predicting complex fluid dynamics, but they also come with certain limitations and uncertainties. Factors such as model simplifications, grid resolution, turbulence models, and boundary conditions can affect the accuracy of simulation results. Therefore, collecting experimental data and validating simulations with this data is critical for ensuring the reliability of the models. Accurate data collection and continuous model calibration enhance the accuracy of CFD simulations and ensure the reliability of the results obtained. In this type of study, the detection of gases seeping from the ground and the rate at which they are seeping are of great importance.

Additionally, identifying leaks or seepages in the existing ventilation structure, as well as permeable areas in the tunnel structure that could affect ventilation, will enhance the accuracy of the simulation

In summary, Computational Fluid Dynamics (CFD) plays a crucial role in the analysis and optimization of ventilation systems for managing geothermal gas leaks in infrastructure projects. By providing detailed insights into airflow dynamics and gas dispersion, CFD enables engineers to design effective and reliable ventilation systems that protect both human health and the environment.

In this study, an example tunnel geometry and fan duct structure were analyzed using the Computational Fluid Dynamics (CFD) method to investigate the optimization of a ventilation system in the event of a potential geothermal gas leak.

2.2 Geometry

To perform CFD analyses, the three-dimensional geometry of the structure must first be created in a computer-aided design program. In this project, the ANSYS program's SpaceClaim module was utilized as the design tool. The created tunnel geometry has a length of 815 meters and a surface area of 130 m². Within the tunnel geometry, a fan duct geometry with a diameter of 2200 millimeters and a length of 765 meters was constructed (ANSYS Education Tutorials, 2016).
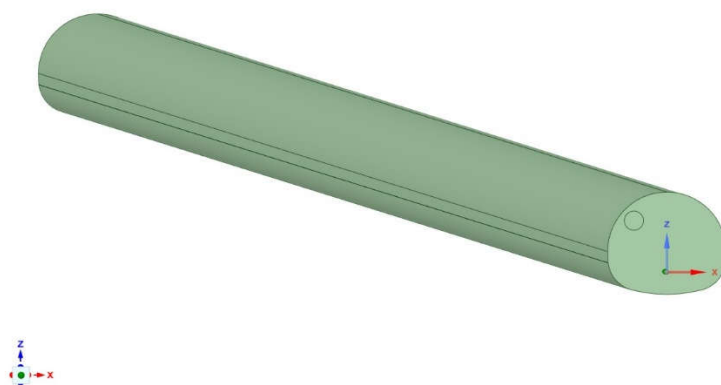
Figure 1. Sample tunnel geometry

2.3 Meshing

Meshing is the process of dividing a physical domain into smaller intervals. The purpose of meshing is to facilitate the solution of a differential equation. In this study, the Cutcell Mesh method was used as the meshing technique. Cutcell Mesh is an efficient mesh model due to its high orthogonal quality and low number of resulting elements. On the geometry, a high-quality mesh with 2,426,253 elements and an orthogonal quality value of 0.07 was created.

Boundary names were defined on the mesh, including inlet, internal_fantup1, outlet, wall_fantup1, and fluid_source. The inlet boundary name represents the entrance of the fan duct, internal_fantup1 represents the surface where the fan duct opens into the tunnel, outlet represents the tunnel exit, wall_fantup1 represents the walls of the fan duct, and fluid_source represents the areas on the tunnel floor where gas is released (ANSYS Education Tutorials, 2016).
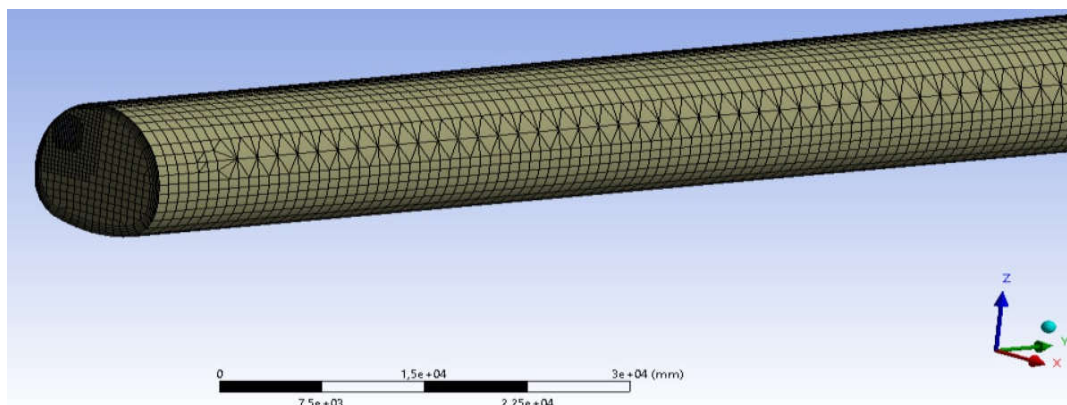
Figure 2. Mesh structure created on tunnel geometry
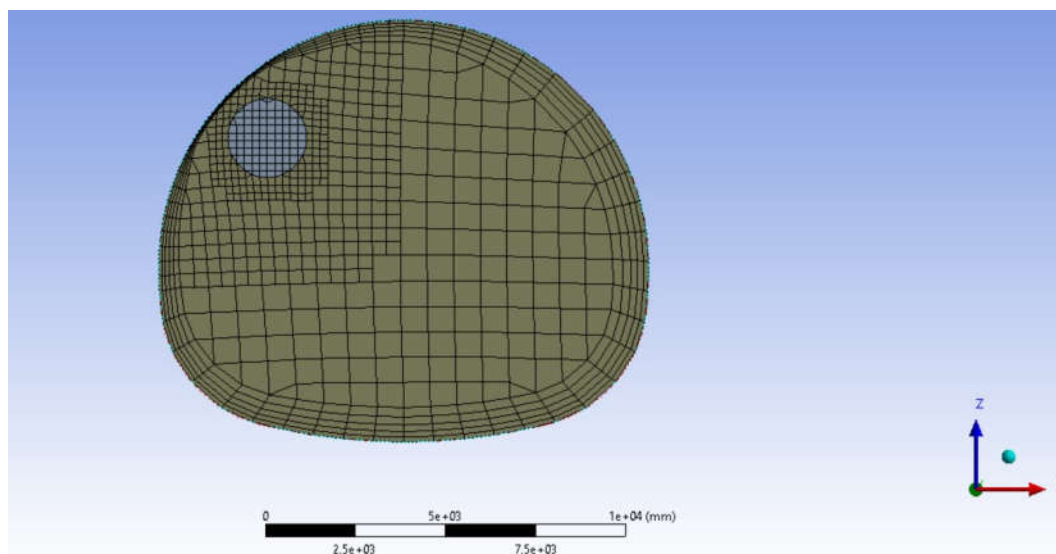
Figure 3. Cross-sectional view of the mesh structure

2.4 CFD Analyses

Computational Fluid Dynamics (CFD) is an engineering tool used to analyze the movement and interactions of fluids (typically liquids and gases) using computer-based numerical methods. CFD analyses utilize computer programs and mathematical methods to model and simulate fluid flow, temperature distributions, pressure differences, and other physical properties.

CFD analysis involves mathematically modeling the geometry of a system or device and conducting equation-based simulations of fluid behavior consistent with this model. Fundamental equations such as the Navier-Stokes equations, momentum equations, and energy equations form the basis of the analysis. These equations are solved using numerical methods such as finite element method, finite volume method, finite difference method, etc., to model fluid behavior (ANSYS Education Tutorials, 2016).

In this study, 8000ppm CO_2 and 40ppm H_2S gases are assumed to leak from a geothermal source for 400 meters from the tunnel mirror. It is also assumed that the fan tubes used are sealed and that there are no other factors affecting the air flow inside the tunnel.

2.4.1 Analysis No 1

The air flow rate supplied from the fan to the tunnel is 39 m^3/s. The surface area of the fan is 3.8013 m^2. The cross-sectional area of the tunnel is 130 m^2, and the average air flow velocity inside the tunnel is 0.3 m/s, directed towards the tunnel exit (-Y direction).

The following analyses were conducted with a fan and fan duct with a length of 765 meters and a diameter of 2200 mm, achieving an airflow rate of 39 m³/s. The fan's air blowing velocity to achieve the 39 m³/s flow rate was calculated (Goodfellow, 2020).

$$39 \text{ m}^3/\text{s} = (3{,}8013 \text{ m}^2) * (V1) \tag{1}$$

$$V1 = 10{,}2596 \text{ m/s} \tag{2}$$

The airflow velocity of the fan has been determined to be 10.2596 m/s.

In the analyses conducted, starting from the mirror and extending to a distance of 400 meters, a release of 8000 ppm CO_2 and 40 ppm H_2S has been made from the fluid_source boundary.

The following results have been obtained:

When examining the mass contours of CO_2 and H_2S gases for the last 400 meters, it is observed that approximately 100 meters from the tunnel exit, the concentrations of CO_2 range between 800 ppm and 1600 ppm, and for H_2S, they range between 4 ppm and 8 ppm. It is evident that the gas density, which is higher in the middle of the tunnel, decreases towards the tunnel exit. Although not very efficient, it can be seen from the shapes formed by the mass contours that the gases are being swept towards the tunnel exit (Figure 4, Figure 5).
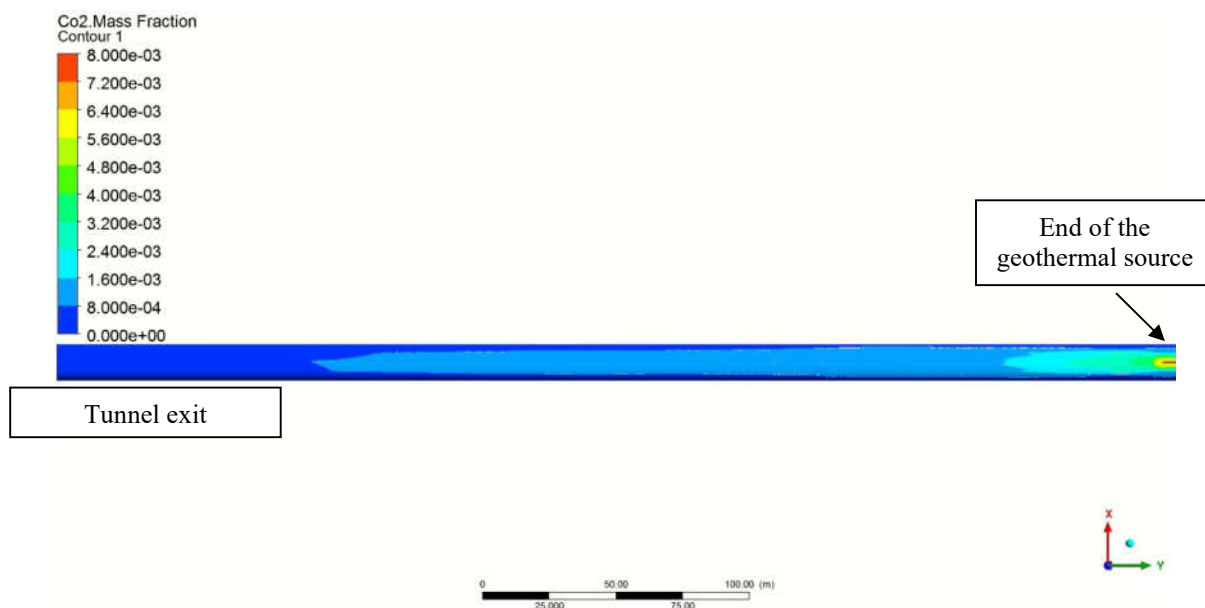
Figure 4. CO_2 mass contour view of the section from the end of the geothermal source to the exit of the tunnel
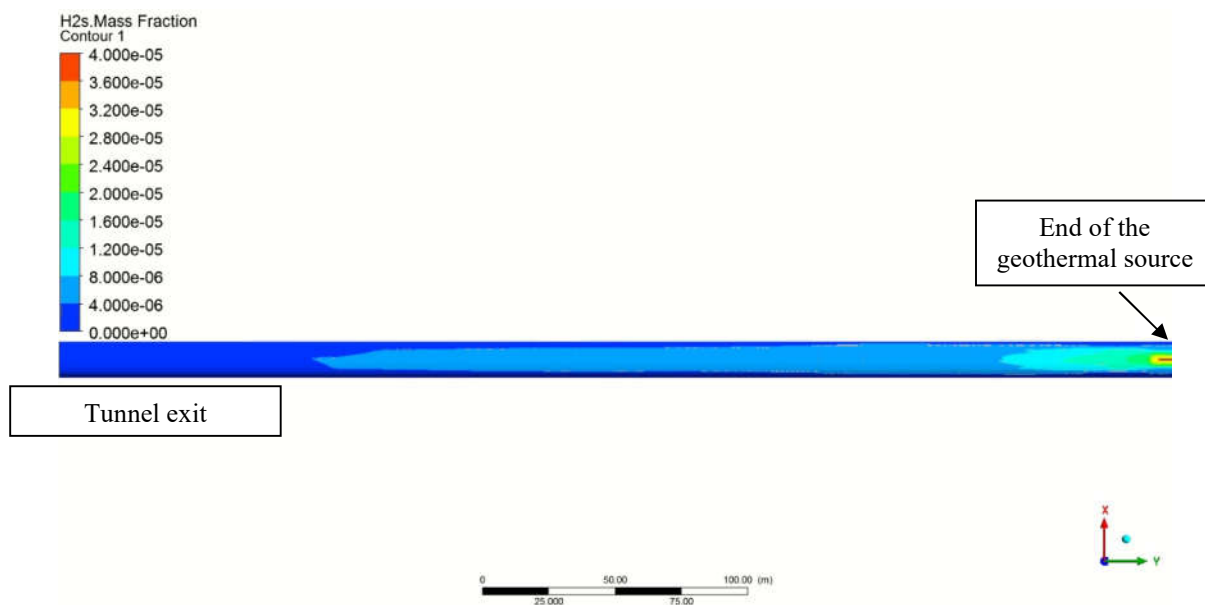
Figure 5. H₂S mass contour view of the section from the end of the geothermal source to the exit of the tunnel

2.4.2 Analysis No 2

In addition to the first analysis, a fan has been placed at the 100th meter of the tunnel, and a fan duct has been defined from its end to the tunnel exit, similar to the first fan duct. The diameter of the fan duct is 2200 mm. Like the first fan, the second fan also intakes the airflow inside the tunnel with a flow rate of 39 m³/s.
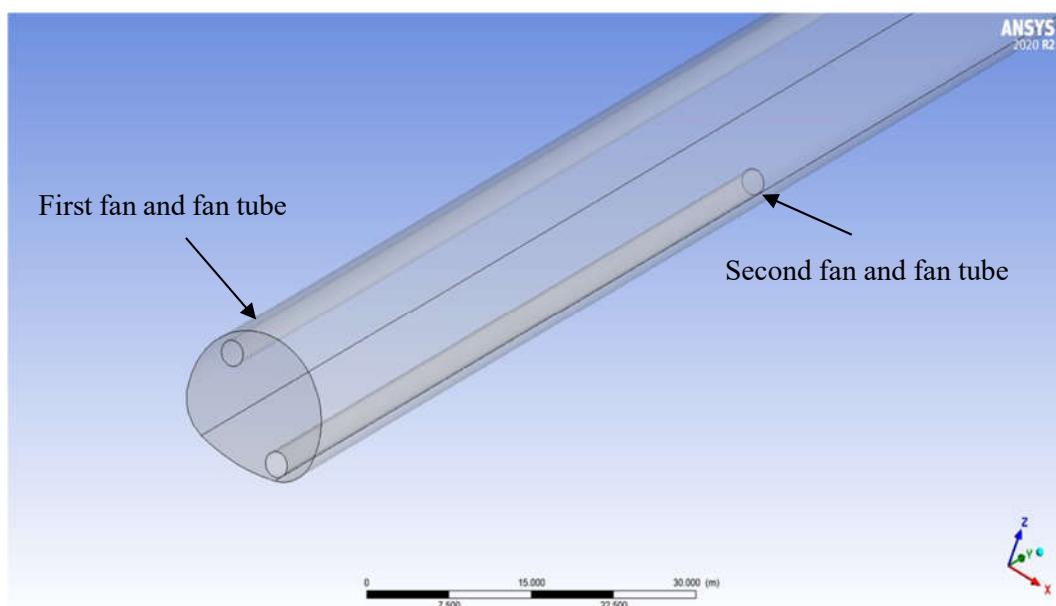
Figure 6. Second fan and fan tube defined in the tunnel geometry for ventilation optimization

When examining the mass contours for CO_2 and H_2S gases for the last 400 meters, similar results to the first analysis have been obtained. However, the placement of the second fan at a distance of 100 meters from the exit, where the emitted gases are at 0 ppm and the airflow is weak, has not been effective in removing the gases (Figure 7, Figure 8).
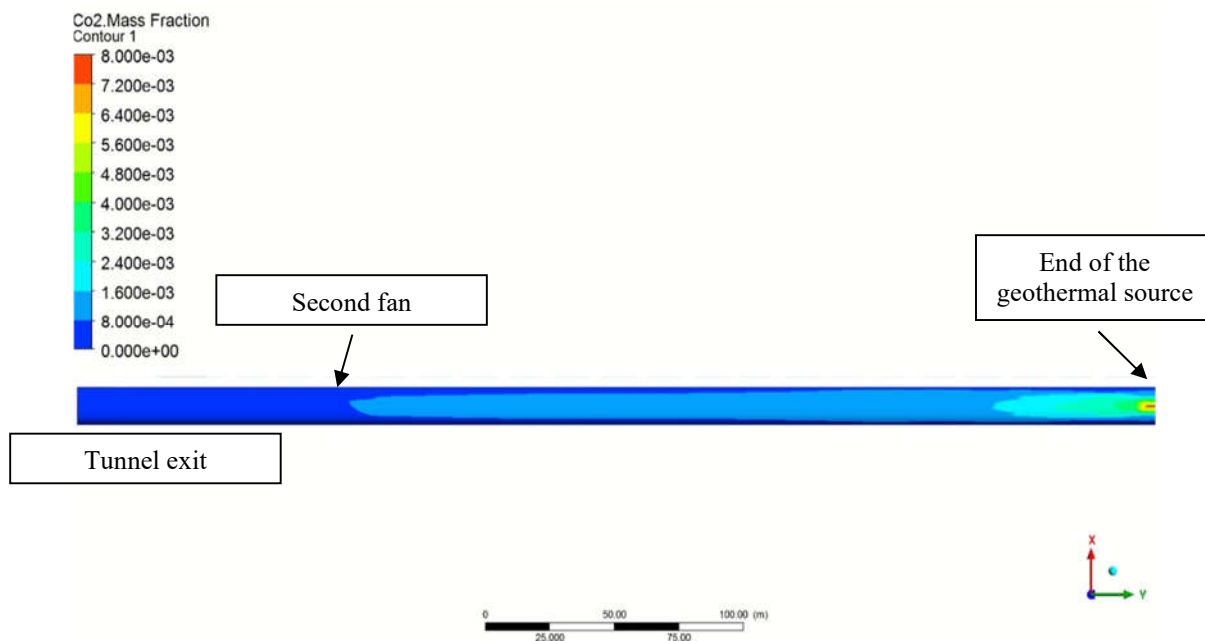
Figure 7. CO_2 mass contour view of the section from the end of the geothermal source to the exit of the tunnel
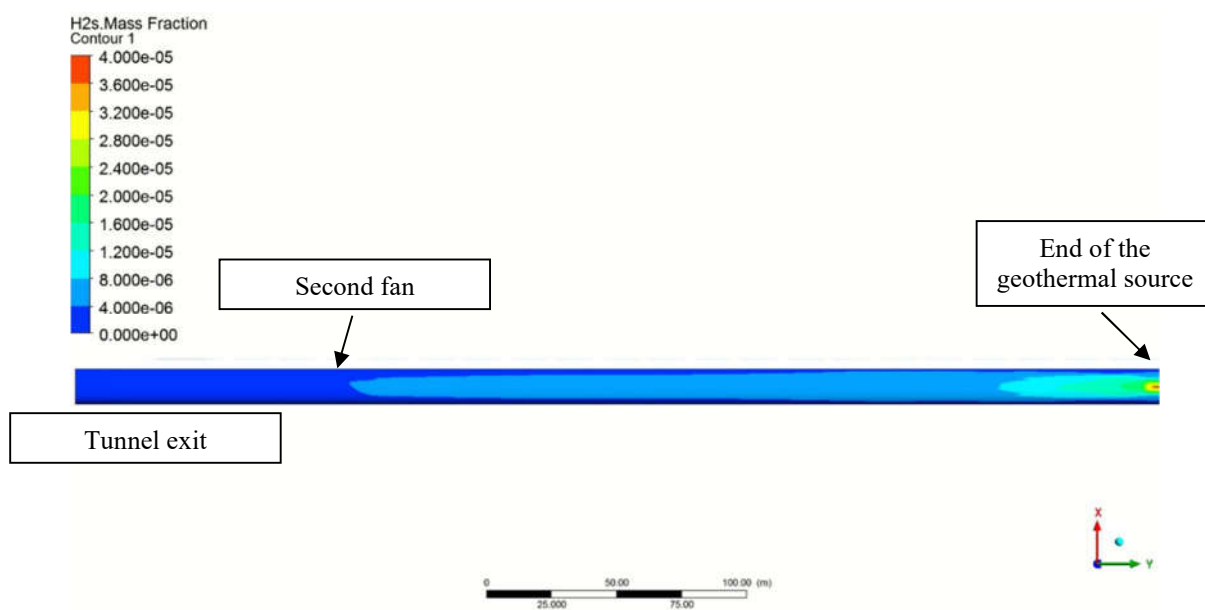
Figure 8. H_2S mass contour view of the section from the end of the geothermal source to the exit of the tunnel

2.4.3 Analysis No 3

In this scenario, the length of the fan duct, which was initially 765 meters, has been increased to 790 meters. The second fan has not been used.

The structure observed in the mass contours for the last 400 meters is similar to the results obtained in the first analysis. While 0 ppm values are observed for both gases in the last 100 meters, accumulations of 2400 ppm for CO_2 and 12 ppm for H_2S have formed from the end of the source (Figure 9, Figure 10).
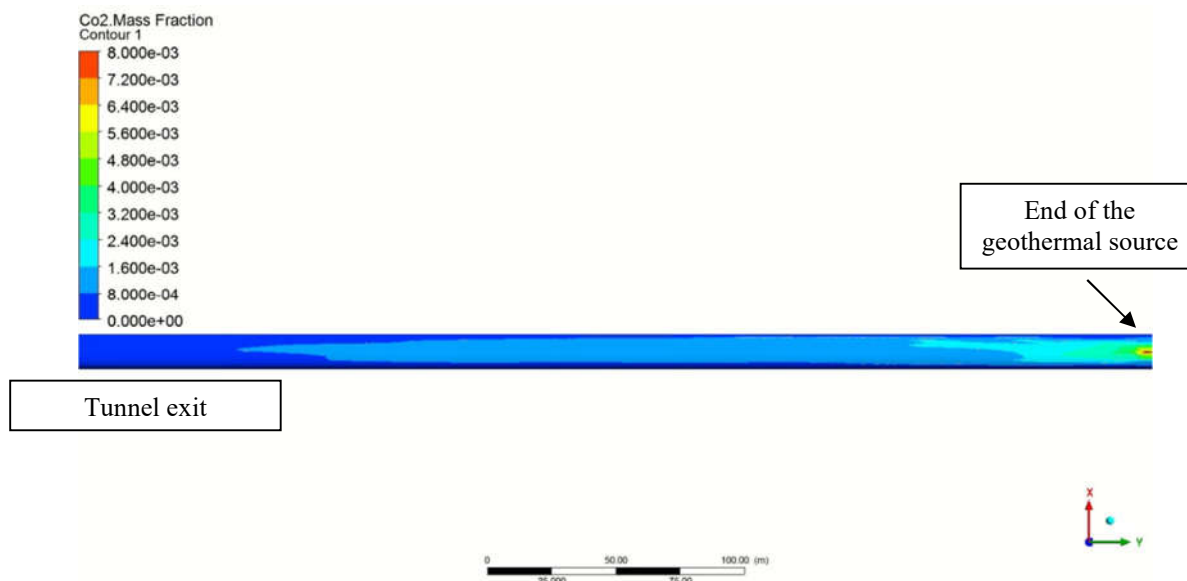
Figure 9. CO_2 mass contour view of the section from the end of the geothermal source to the exit of the tunnel
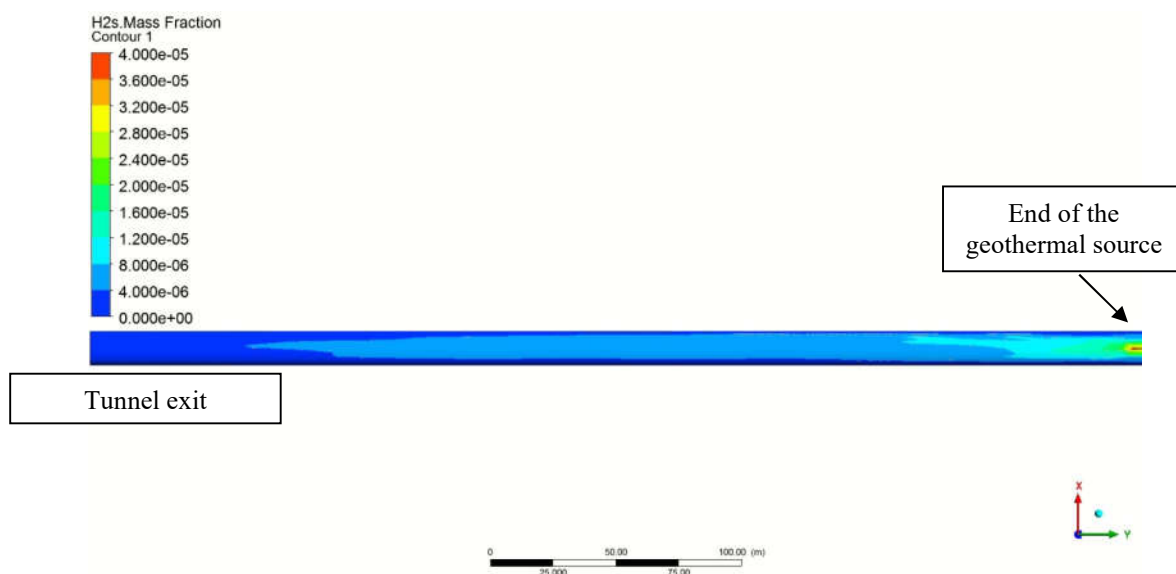
Figure 10. H_2S mass contour view of the section from the end of the geothermal source to the exit of the tunnel

2.4.4 Analysis No 4

In the 4th analysis, there is a second fan. The diameter of this fan is 2200 mm. The fan is defined at a distance of 375 meters from the tunnel exit. A fan duct with a diameter of 2200 mm is defined for this fan up to the tunnel exit. Similar to the first fan, an airflow intake rate of 39 m^3/s is defined.

When examining the mass contours of the gases, the effect of the second fan is clearly visible. When the emitted gases reach the influence area of the second fan, they are vacuumed and discharged. As a result, CO_2 and H_2S gases are at 0 ppm values after the second fan towards the tunnel exit. However, accumulations of 1600 ppm to 6400 ppm for CO_2 and 8 ppm to 32 ppm for H_2S are observed above the source, as in previous analyses (Figure 11, Figure 12).
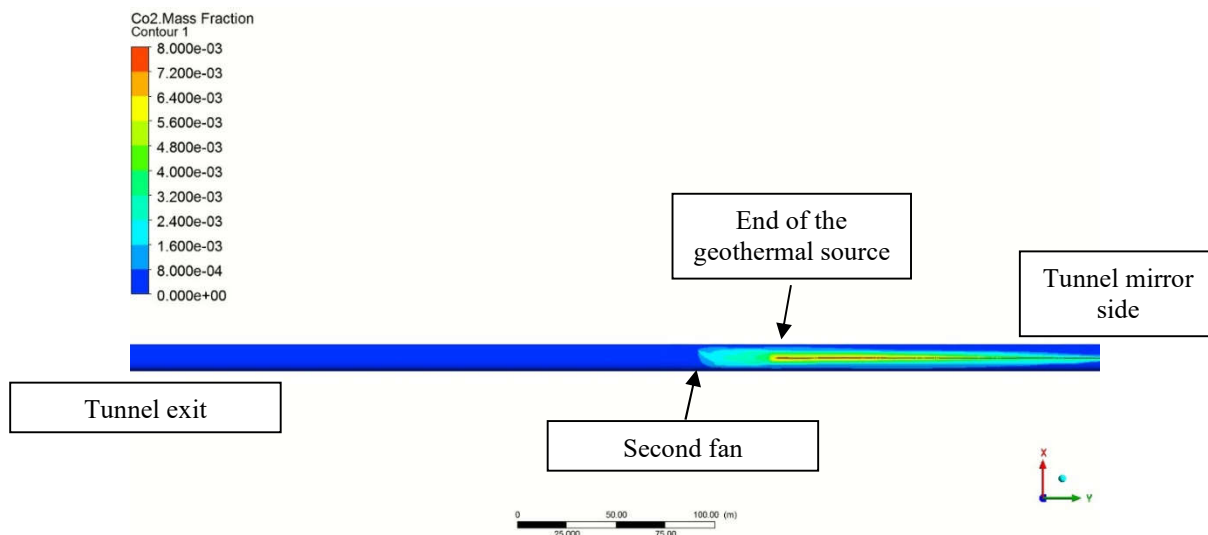
Figure 11. CO_2 mass contour view of the section from the mirror side of the tunnel to the exit of the tunnel
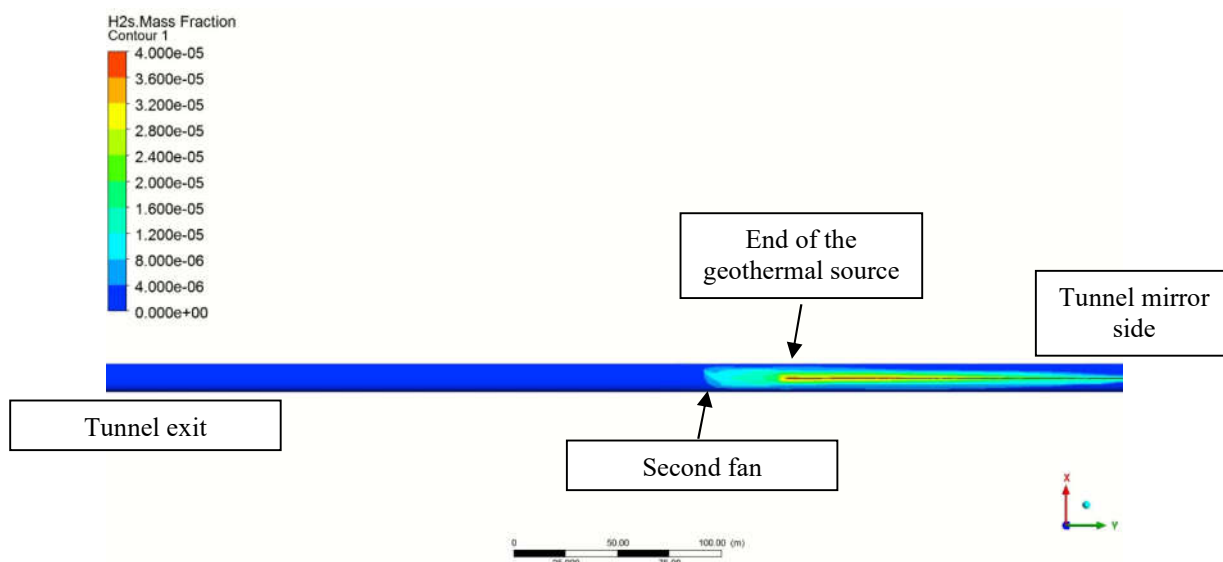
Figure 12. H_2S mass contour view of the section from the mirror side of the tunnel to the exit of the tunnel

3   Results

It is observed that CO_2 and H_2S gases near the mirror are at 0 ppm values. This is because the airflow is strong in the areas close to the mirror, effectively sweeping the gases.

In the first analysis, accumulations of CO_2 and H_2S gases of up to approximately 8000 ppm and 40 ppm, respectively, were observed in the tunnel at approximately 400 meters from the mirror.

The second fan added in the 2nd analysis, positioned near the tunnel exit where the gases are at 0 ppm values (100 meters from the tunnel exit), did not contribute positively to the evacuation of gases.

By moving the position of the second fan closer to the source (375 meters from the tunnel exit) and extending the fan duct it is connected to, the performance of gas sweeping has noticeably improved. From the second fan defined in the 4th analysis onwards, the CO_2 and H_2S gases in the tunnel are at 0 ppm values.

4   Conclusion

The results of the analyses highlighted the importance of proper ventilation design in the effective removal of geothermal gases from infrastructure projects. By optimizing fan placement, duct configurations, and airflow rates, CFD simulations demonstrated the potential to minimize the accumulation of geothermal toxic gases in tunnel environments.

This study demonstrates that the use of CFD methodology provides valuable information on the dynamics of geothermal gas distribution and facilitates the development of efficient ventilation systems to protect both human health and the environment in infrastructure projects. The analyses performed in this study underline the importance of CFD in addressing the challenges posed by geothermal gas leaks and highlight its role in ensuring the safety and sustainability of such projects. Likewise, the analysis and testing of different removal methods for geothermal gas and liquid leaks that may occur in different geometries, structures, resource types can be performed with the CFD method. Thus, time and resource management can be realized efficiently.

References

ANSYS Training Courses (2016). SpaceClaim Introduction, Meshing Introduction, Fluent Introduction.

Çengel Y. A., Cimbalak J. M. (2004). Fluid Mechanics: Fundamentals and Applications.

Goodfellow H. D., Kosonen R. (2020). Industrial Ventilation Design Guide: Volume 1: Fundamentals.

Liu C., Yeoh G. H., Tu J. (2007). Computational Fluid Dynamics: A Practical Approach.

Ferziger, J.H., & Perić, M. (2002). *Computational Methods for Fluid Dynamics*.

MINIMIZATION OF BLASTING-INDUCES VIBRATIONS IN A METAL MINE USING SURFACE WAVE MITIGATION

G. GÜLSEV UYAR AKSOY [1], C. OKAY AKSOY [2], OZAN SAVAŞ [3]

[1]*Hacettepe University Mining Engineering Department, Turkey, gulsevaksoy@hacettepe.edu.tr*

[2]*Dokuz Eylül University Mining Engineering Department, Turkey, okay.aksoy@deu.edu.tr*

[3]*GOA R&D Mining and Environment Technologies Ltd.Co Ankara/ Turkey, ozansavas@goamining.com.tr*

Abstract

In rock excavations using blasting, the effects of seismic waves propagating into the environment are very important. Severe seismic vibrations can cause damage to nearby structures, buildings and even open pit slopes within the quarry, as well as to the leach fields, if any. Vibrations can affect structural integrity and lead to cracks. In this study, a different approach from conventional methods is adopted to reduce blasting-induced vibrations. The new method is based on the principle of surface wave mitigation and aims to minimize vibrations by considering the interaction of seismic waves with each other. Within the scope of the study, two group blasts were carried out in a metal mine in Turkey using an electronic ignition system to compare the traditional method with the innovative, novel method, and a pilot blast was carried out to be used in the developed method. Since the seismic signal obtained from the pilot blast contains geological information throughout the area it passes through, no geological data is needed for group blasting modeling. When the recorded data is analyzed, the positive contribution of the method based on the principle of surface wave mitigation to the environmental impact and blasting efficiency of the detonation whose delays are determined by the method based on the principle of surface wave mitigation is clearly evident.

Key words

Electronic initiation system, seismic waves, blasting, vibration,fly rock

1   Introduction

Crushing rock masses by blasting is one of the most powerful and economical methods in mining, quarrying, road, tunnel, dam, construction and infrastructure works. However, increasing competition, environmental protection requirements and safety measures have necessitated the development of new blasting techniques. Along with these developments, environmental impacts caused by blasting such as stone blasting, air shock, dust emission and vibrations have also come to the fore. Among these impacts, vibrations caused by blasting cause the most complaints. This is because while stone blasting and air shock are effective in areas close to the blasting point, blasting vibrations can be felt even at much greater distances. For this reason, conscious and sensitive enterprises should carry out or have the necessary measurement and evaluation studies carried out to minimize the negative effects of blasting and to prevent damage to the environment.

As it is known, electronic detonation systems have been used in the world for more than 30 years. These systems enable the design and implementation of highly successful blasts in mines to prevent ore contamination, ensure slope stability, obtain the desired fragment size, minimize vibration and air shock problems. In this study, it is aimed to see the application of electronic firing systems in the field and to compare the results with similar blasting with a non-hand firing system. As known from the literature,

electronic igniters provide more accurate timing than conventional pyrotechnic igniters based on the burning rate of a pyrotechnic composition. (Cardu, 2013).

In this study, delay values that aim to minimize vibrations by taking into account the principle of surface wave attenuation and the interaction of seismic waves with each other are used against the conventional delays in blasting using an electronic firing system. The aim is to compare these delay values with the vibrations that occur as a result of blasting. In this context, the mentioned delay values, which aim to minimize vibrations by taking into account the principle of surface wave attenuation and the interaction of seismic waves with each other, were processed into our patented software Seisblast Promax with the signal received from a single hole blasted representing the group one day before the group blasts and the delays were determined.

Electronic capsules, which have been used globally for more than 30 years, have not yet achieved widespread use in our country except for special applications. One of the main reasons for this is the lack of sufficient studies on this subject. For this reason, it is aimed to shed light on the subject by researching and revealing the advantages of electronic ignition systems in order to popularize the use of electronic ignition systems by enterprises and to raise our country to the level of global technology in the field of mining.

2   Methods

As part of an experimental study, 1 pilot blast and 2 group blasts were conducted in a metal mine. In order to determine the electronic delays in the 30-hole group blast, a single-hole pilot blast was first performed. Seismic data from the pilot blast were subjected to signal analysis with the Seisblast Promax program and electronic delays were determined. A total of 3 blasts were conducted, one group of 30 holes in which the delays determined as a result of seismic wave analysis from the pilot blast were applied and another group of 30 holes in which the delays were given classically. The aim here is to use the delays determined using Seisblast Promax software and compare the results with similar blasting with conventional (17-25 ms) delays using electronic firing system.

Group blasting locations and seismograph locations are given in Figure 1.

Figure 1. Group blasting locations and seismograph locations (Seismographs: micro,14465,12269,13638,12270)

Seismic waves from the pilot blasting were recorded with 4 seismographs and seismic waves from the group blasting were recorded with 5 seismographs. Thus, it was possible to analyze and analyze the seismic waves generated by the blasts with electronic capsule and to compare them with the results of previous blasts in the same area with conventional delays (17-25 ms) and seismic recordings made by us using Seisblast Promax software. For group blasts, the nearest seismograph (micro) was placed 60 m away from the blasting location and the farthest seismograph (12270) was placed 182 m away.

The delays were determined using Seisblast Promax software using micro-coded seismograph data located 51 m from the blast location in the pilot blast.
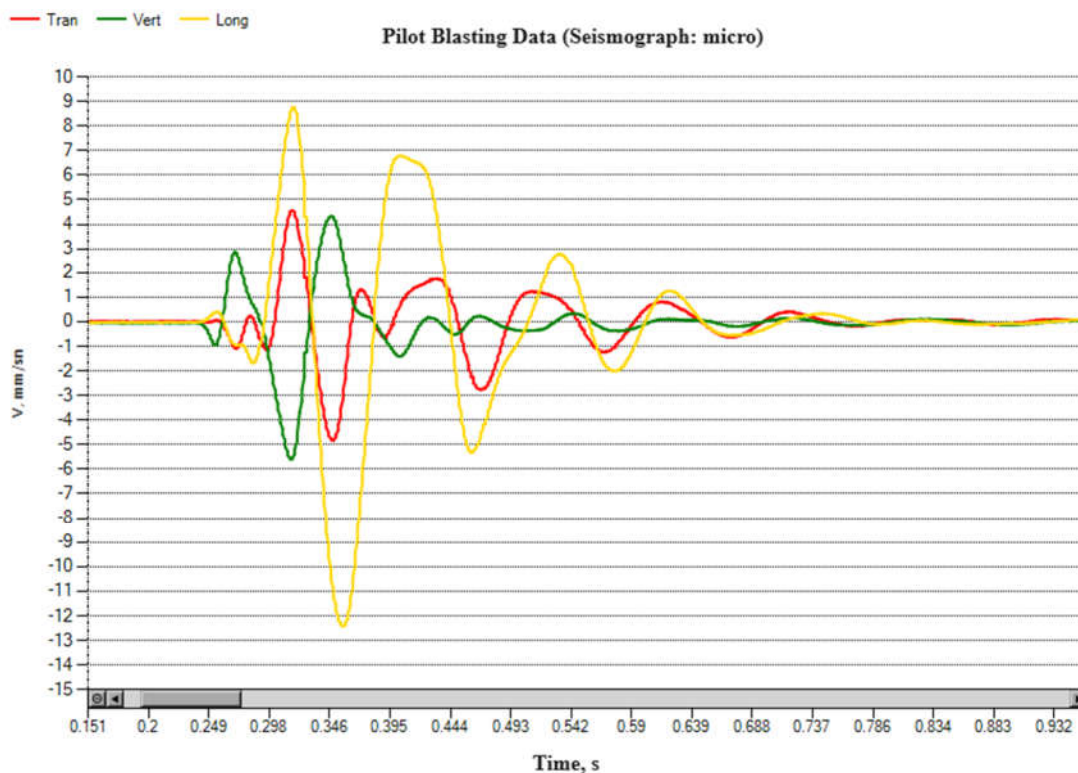
Figure 2. Pilot blasting data recorded from seismograph micro

Electronic capsule delays were determined by us, uploaded to the logger and defined to the capsules in the field (Figure 3).

Figure 3. An image from the field application of electronic capsules

Information on the blast geometry of the group and pilot blast holes is given in Table 1.

Table 1. Information on the blast geometry of the group and pilot blast holes

Blasting Location	Hole Diameter, mm	Average Hole Length, m	Blasting Geometry	Explosive Quantity, kg	Detonating Element	Number of Holes
Pilot	102	5.5	-	Emulsion: 10 Anfo: 12.5 Dynamite: 0.5	Nonel Capsule	1
Group-1 (17-25ms) Classical Delays Applied	102	5.5	Burden: 3.1 Spacing: 3.6	Emulsion: 10 Anfo: 12.5 Dynamite: 0.5	Electronic Capsule	30
Group-2 SeisBlast Promax Delays Applied	102	5.5	Burden: 3.1 Spacing: 3.6	Emulsion: 10 Anfo: 12.5 Dynamite: 0.5	Electronic Capsule	30

Group blast holes are shown in figure 4.

Figure 14. Group blast holes

Figure 5 shows the delays applied to the holes for conventional blasting and Figure 6 shows the delays applied to the holes using Seisblast Promax software, respectively.

Figure 5. Delays applied to the holes for conventional blasting system

Figure 6. Delays applied to the holes using Seisblast Promax software

The reason for choosing these delays is to minimize the effects of blasting-induced seismic waves on the slopes and the surrounding residential areas. With the data obtained from the pilot blasting, the designs were made through SeisBlast_Plus software, and in this way, it was aimed to control and minimize the vibration values at the specified distances. The number of holes, hole geometry and seismograph locations are the same for both electronic capsule group blasts.

3 Results

Table 2 presents the results of measurements using different seismograph instruments (Micro, 14465, 12269, 13638, 12270). For each seismograph, pilot and two separate groups (Group 1 and Group 2) data are included. These data show particle velocity readings and dominant frequencies in the lateral (T), vertical (V), longitudinal (L) and peak particle velocity (PPV) components of the seismic waves.

Table 2 shows the particle velocity and frequency values of seismic waves generated by pilot and group blasts measured on seismographs.

Table 2. Vibration and frequency values recorded from pilot and group blasts

Seismograph	Groups	Measurement Distance, m	T mm/s	V mm/s	L mm/s	PPV mm/s	Dominant Frequency Hz
Micro	**Pilot**	51	4.839	5.588	12.43	13.36	9.75
	Group 1	60	10.3	6.936	11.97	13.55	12.75
	Group 2	63	5.029	4.658	8.859	9.335	6.69
14465	**Pilot**	92	1.397	1.016	3.302	3.665	7.5
	Group 1	90	4.826	3.429	4.572	5.242	6
	Group 2	96	2.667	1.27	3.048	3.391	5.25
12269	**Pilot**	120	1.143	0.381	1.27	1.356	7
	Group 1	130	2.286	1.778	3.937	4.042	6
	Group 2	140	2.794	0.762	1.905	3.314	5.25
13638	**Pilot**	97	0.635	1.016	2.413	2.646	9.25
	Group 1	158	1.651	1.397	3.429	3.657	5.75
	Group 2	161	1.778	1.016	1.778	2.044	5.25
12270	**Pilot**	-	-	-	-	-	-
	Group 1	182	0.635	1.651	2.667	2.814	4.88
	Group 2	192	1.143	1.143	1.27	1.571	5.25

The vibration values caused by Group 2 blasting, which is done by assigning electronic delays determined using Seisblast Promax software to the holes, are below the vibration values caused by Group 1. Electronic capsules were used in both groups of detonations, but the main difference here is that in group 2, in addition to the classical delays, they were determined by the principle of seismic wave analysis. When the longitidunal component values of seismographs 12269 and 13638 are examined, it is seen that the 2nd group minimizes the vibration by about 1/3.
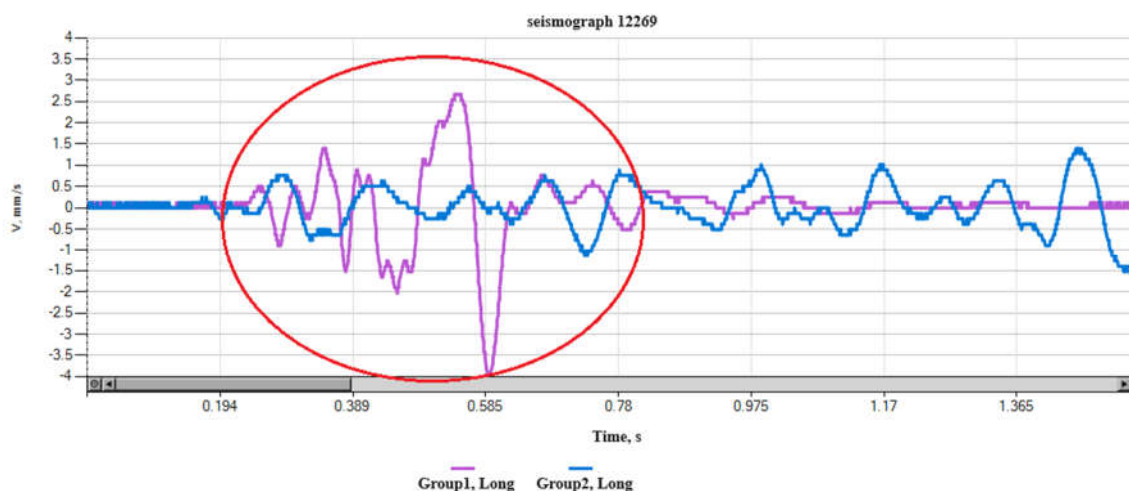
Figure 7. Comparison of group1 and group2 from seismograph 12269 in the longitidunal component

Figure 7 shows that for seismograph 12269, the seismic signal in the long component of Group 1 (purple color) has higher amplitudes than Group 2 (blue color). Especially during the main seismic activity period between 0.389 and 0.585 seconds, the velocity values of Group 1 are up to ±3.5 mm/s, while the velocity values of Group 2 remain around ±2 mm/s. This suggests that the blast or seismic event in Group 1 was stronger and produced a larger velocity change. Both groups stabilized in the period after the main seismic activity.
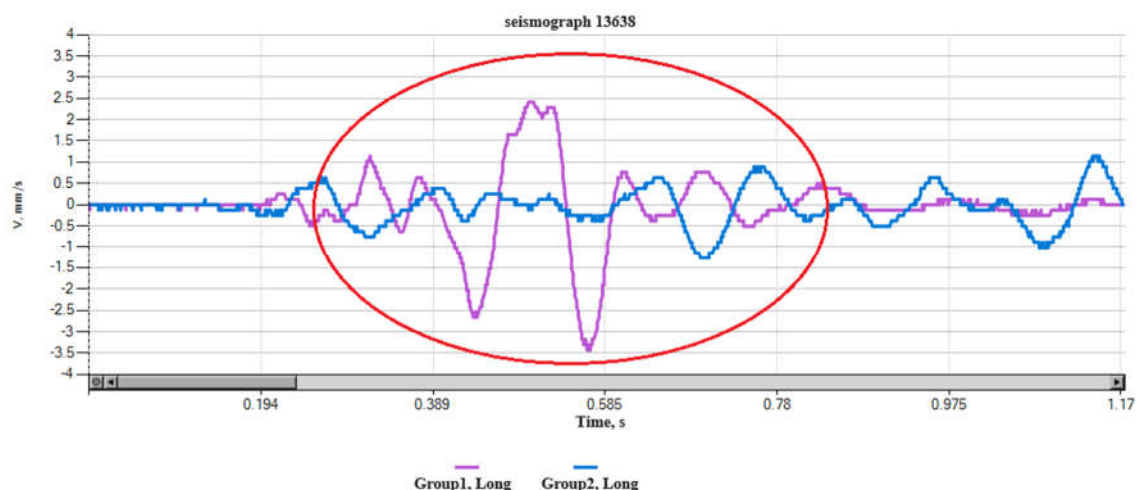
Figure 8. Comparison of group1 and group2 from seismograph 13638 in the longitidunal component

Figure 8 shows that for seismograph 13638, the seismic signal in the long component of Group 1 (purple color) has higher amplitudes than Group 2 (blue color). Especially during the main seismic activity period between 0.389 and 0.585 seconds, the velocity values of Group 1 are up to ±3.5 mm/s, while the velocity values of Group 2 remain around ±2 mm/s. Both groups stabilized in the period after the main seismic activity.

4   Conclusion

In modern mining and civil engineering applications, the use of electronic delay systems in blasting processes is becoming increasingly common. Electronic delay systems offer a number of advantages by giving the user precise control over the timing of the blasting process. Electronic delay systems offer much more flexibility than traditional mechanical and chemical delays. These systems allow users to customize blasting layouts and timings to suit their needs. For example, where vibrations during blasting need to be minimized or fracturing needs to be optimized with a specific orientation, electronic delays can be used to create ideal timing combinations. This leads to more controlled and targeted blasting results. The use of electronic delay systems in blasting processes significantly improves both safety and operational efficiency with their user-friendly features and flexibility. The possibilities offered by this technology allow blasting operations to be carried out in a more controlled, safe and environmentally friendly manner in modern mining and civil engineering applications. In this context, the use of electronic delays is considered an important development in blasting design and applications.

In this study, we used Seisblast Promax software to analyze the seismic waves and determine the delays that will dampen each other as a result of this signal analysis. Group 2 blasting with the delays we determined using Seisblast Promax software reduced the vibration by one third compared to Group 1 blasting with conventional delays. In addition, there was no heave and the fragmentation was more homogeneous.

Contrary to what is known, by modeling the seismic signals received from the blasting of a single hole, group blasts of 400-500 holes can be planned that will not harm the environment. International patents and international publications on this scientific fact are abundant in the literature. What is important here is not the number of holes, but the right blasting design and the implementation of this design with the right blasting elements.

References

Alejano, L.R., Ferrero, A.M., Oyanguren, P.R., Fernandes, M.I.A. (2011). Comparison Of Limit Equilibrium, Numerical And Physical Models Of Wall Slope Stability. International Journal Of Rock Mechanics And Mining Sciences

Cardu M. (2013). A Review Of The Benefits Of Electronic Capsüls, Remrevistaescola De Mines

Cardu M, Muccı A., Uyar GG. (2015). Investigating The Effects Of Benchgeometry And Delaytimes On The Blastinducedvibrations İn An Open-Pitquarry

DIN 4150-3. (1999). Structural Vibration-Effects Of Vibration On Structures

IME. (2017). EBIS Guideline, Electronic Blast Initiation System

DEFORMATION FORECASTING AND STABILITY ANALYSIS OF SOFT ROCK TUNNEL FORM MICROSESMIC SOURCE PROBABILISTIC LOCALIZATION

YUEPENG SUN [1], NUWEN XU [2], BIAO LI [3], PEIWEI XIAO [4], ZHIQIANG SUN[5]…

[1] *Sichuan university, China, People's Republic of, ypsun1997@163.com*

[2] *Sichuan university, China, People's Republic of, xunuwen@scu.edu.cn*

[3] *Southwest Petroleum University, China, People's Republic of, libiaoscu@163.com*

[4] *Sichuan university, China, People's Republic of, xpwsl@163.com*

[5] *Sinohydro Bureau 7 Co., Ltd., China, People's Republic of, 345178218@qq.com*

Abstract

Surrounding rock deterioration and large deformation have always been a significant difficulty in designing and constructing tunnels in soft rock. The key lies in real-time perception and quantitative assessment of the damaged area around the tunnel. An in-situ microseismic (MS) monitoring system is established in the plateau soft tock tunnel. In this paper, the probability density field of MS source based on probability mapping is proposed, which lays a foundation for accurately revealing the progressive damage characteristics of soft rock tunnel. The spatial distribution of MS dissipative energy is established. The morphological evolution of tunnel with multiple damage degrees in axial and radial direction is analyzed. Based on the basics MS energy parameter,a three-dimensional model was created to visualize the damage zone of the tunnel surrounding rock. The model depicted varying degrees of damage, and three high damage zones were identified. The rapid increase of the depth and extent of high damage area can be used as the criterion of dynamic warning of large deformation of surrounding rock of tunnel. This paper provides valuable insights for damage and dynamic warning of surrounding rock of high-stress soft rock tunnel.

Key words

Soft rock tunnel, MS monitoring, Seismic source location, Excavation damage zone.

1 Introduction

With the growth of the global economy and the increasing demand for modernization, tunnels have emerged as a highly favorable option for constructing transportation infrastructure in intricate topographical conditions (Yu et al., 2022). China's road transport network has extended tunnels to high mountainous areas in recent years, resulting in long lines (length exceeding 10 km) and deep burial (depth exceeding 500 m), making it impossible to avoid complex geological features and poor ground layers (Du et al., 2023; Zhu et al., 2019). When a tunnel passes through soft rock, such as carbonaceous slate, mudstone, etc., with high in-situ stress, the surrounding rock mass experiences time-dependent extrusion deformation and fracturing due to intense internal extrusion and excavation loading; this phenomenon of the surrounding rock in the tunnel is characterized by long-term non-convergence of deformations, leading to issues such as spray concrete cracking, arch distortion, and deformation invading limit (Figure 1). These problems significantly impede the safety and efficiency of tunnel construction, resulting in substantial economic losses and delays in project completion (Kang et al., 2022; Yu et al., 2023; He et al., 2022). For soft rock tunnels, investigating the progressive deformation and failure mechanism in soft rockmass around the tunnel is crucial for predicting, evaluating, and ensuring the safety of soft rock tunnels subjected to high-ground stress.

Figure 1. Large deformation and typical failure characteristics of supporting structure of tunnel project.

The railway tunnel studied in this research is located on the edge of the Qinghai-Tibet Plateau and the Sichuan Basin, one of the world's most active areas of neotectonic movement (Wang and Barbot, 2023). Tectonically, due to the collision between the Indian Ocean plate and the Eurasian plate, the geological tectonic activity in the tunnel's location is intense, the geological conditions are complex, and the in-situ stress is high. (Chen et al., 2023). The area studied in this research is the No.4 auxiliary tunnel. Figure 1a shows the longitudinal profile of the No.4 auxiliary tunnel by approximately 1600 m. The exit chainage (vertical projection distance of the route) is 0+000 m, and the entrance chainage is 1+642 m, and the longitudinal slope is 0.67%. The cross-sections of the No.4 auxiliary tunnel are both in the shape of a city gate. A combination of the micro bench cut method and traditional drilling and blasting excavates the auxiliary tunnels. The lithology of the strata traversed by the tunnel is mainly carbonaceous phyllite, sandstone, with thin layered structure distribution and distorted rock formation. Due to internal and external geological dynamic disturbance and the influence of excavation unloading, the stability of fractured carbonaceous phyllite is weak. The average uniaxial compressive strength of the carbonaceous slate obtained from the field point load testing ranges from 1.60 to 10.83 MPa (Hathway, 2009). The uniaxial compressive strength measured in different regions varies greatly, and the standard deviation of data is 2.739 MPa. The stability of tunnel's surrounding rock is adversely affected by a combination of intricate geological conditions, the presence of thin layers of surrounding rock, elevated ground stress, and the presence of soft rock mass.

A comprehensive understanding of the internal structure of the surrounding rock mass and its dynamic evolution, including fracture field, displacement field, and stress field, is challenging due to the complexity and invisibility of the interior. MS monitoring technology, a three-dimensional and non-destructive monitoring method, can monitor real-time micro-fracture initiation, development, expansion, and failure in the rock mass. This technology also helps in understanding the weakening of mechanical properties caused by the accumulation of rock damage (Mngadi et al., 2019). Feng et al. (2022) recognized deep engineering rock mass's internal aging deformation and failure process through in-situ MS monitoring. Chen et al. (2018) identified the time, intensity and extent of initial crack and breakage in soft rock tunnel by analyzing the frequency and energy evolution of MS events. Regrettably,

the authors have not adequately elucidated soft rock tunnels' fracturing expansion and squeezing deformation. Consequently, current research aims to employ MS monitoring to comprehensively investigate the precise geographic extent and configuration of failure in soft rock tunnels. Additionally, authors seek to forecast and monitor significant deformations within soft rock tunnels.

This paper presents a practical application of MS monitoring in the safety management of large deformations caused by fracturing and squeezing the surrounding rock in a soft rock tunnel in Southwest China. A real-time MS monitoring system was utilized to analyze the initiation, propagation, and the disparities and expansion characteristics of fractured and damaged zones during various construction periods. This study integrates DEM simulation method with quantification of MS source mechanisms to elucidate the mechanism behind significant deformation disasters resulting from fracture development in surrounding rocks during intense unloading conditions. The findings provide an important case study that can contribute to predicting massive deformation accurately as well as implementing precise support measures in soft rock tunnels.

2   Methods

2.1 MS monitoring scheme and performance test

The MS monitoring system manufactured by the Engineering Seismology Group (ESG), Canada, was installed on December 7, 2022 and has been in operation since then. The MS monitoring network is composed of six single-axis accelerometers with natural frequency of 10khz, Paladin digital signal acquisition system and Hyperion digital signal processing system. All accelerometer cables are connected to a Paladin digital signal acquisition system. The Paladin data acquisition component gathers data in real-time and sends it to the Hyperion digital signal processing system via a communication cable. Figure 2 shows a multi–channel MS monitoring in plateau soft tock tunnel following the suggested approach by the in-situ investigations and the ISRM suggested method (Feng et al., 2019). Due to space, staffing, and safety equipment constraints, the MS sensor was distributed on the two junctions behind the working face, 30m apart. The first row of sensors was 30 meters from the tunnel's working face. When the working face moved 30 m forward, the row of sensors farthest from the work area were recycled and then put in a place 30 m away from later working face.
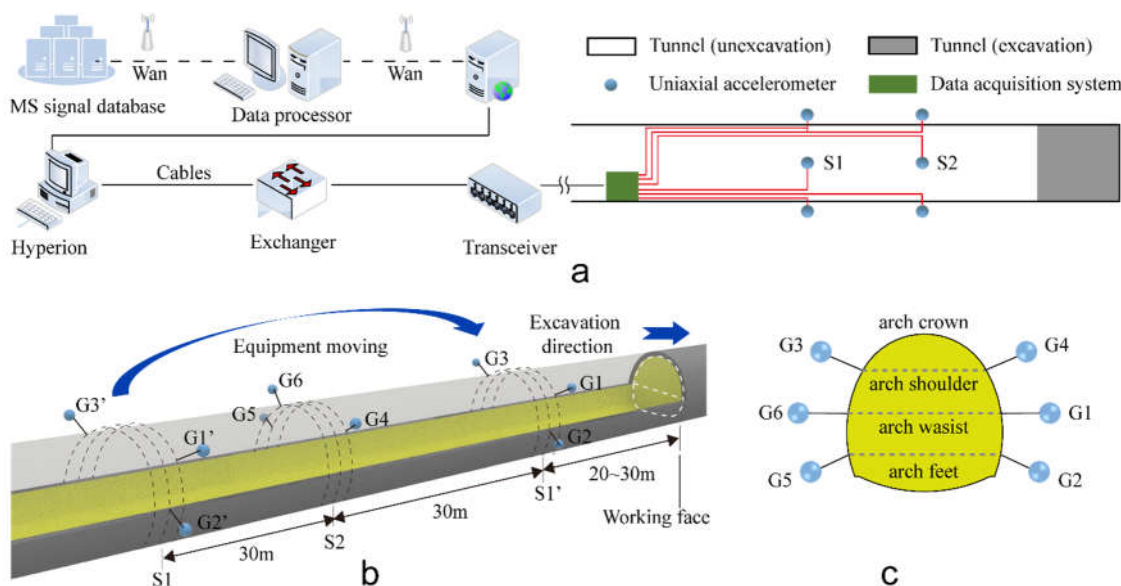
Figure 2. The MS monitoring system configuration. (a) Topology of MS monitoring network. (b) Moving diagram of field accelerometer sensor. (c) Front view of the layout of accelerometer sensors.

Figure 3 illustrates the signals the MS monitoring system acquired within the monitored area.

Identification of the effective MS signal requires detailed waveform analysis in both the time and frequency domains. Fig. 4a illustrates working face excavation blasting on March 4, 2023. The signal lasted 0.4 seconds and had a maximum amplitude of 4 volts. In the time-frequency domain, MS events have a significant frequency distribution from 100 to 1500 Hz, with a concentration from 200 to 900 Hz. The dominant frequency is 476.667 Hz. G6 sensor (The sensor closest to the source in the array during monitoring) data from April 4, 2023, shows an average MS soft rock signal in Fig. 4b. Signal duration is 65 ms. The frequency distribution in the time-frequency domain is centered between 234 and 522 Hz. The dominant frequency is 299.333Hz, and the frequency domain curve is smooth with a low peak frequency. The waveform and signal composition are simple. The sensor's sample frequency exceeds two times the monitoring object's primary MS signal's highest frequency, meeting on-site MS monitoring standards.
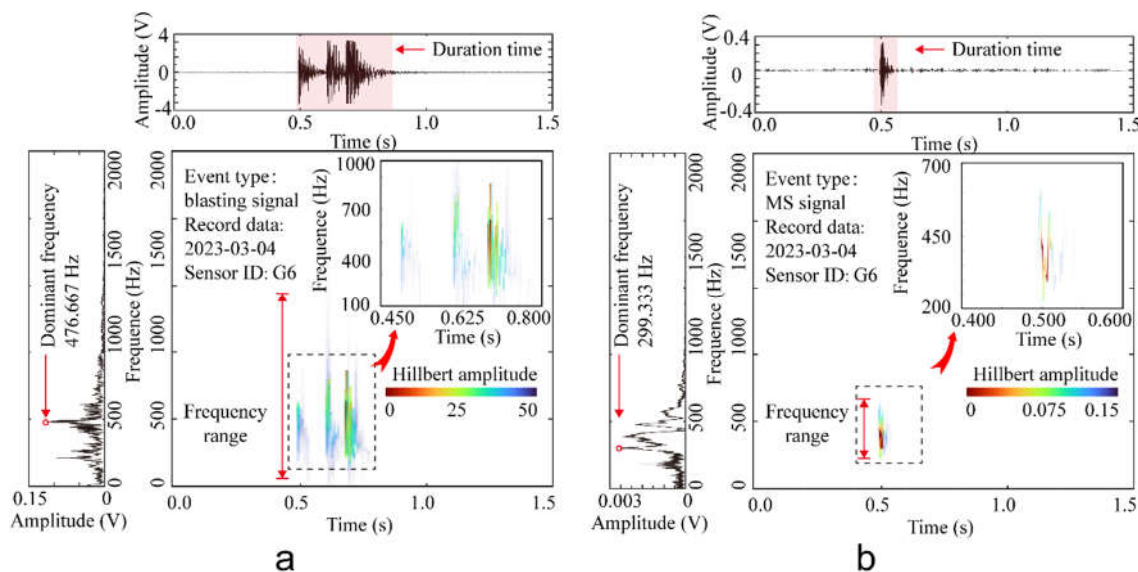
Figure 3. Elastic wave signal time domain, frequency domain and spectrum diagram: (a) Typical burst signal. (b) Typical MS signal.

While blasting and MS signal wave shapes are similar, their creation methods differ. a MS signal recognition and classification method combining ensemble empirical mode decomposition (EEMD), singular value decomposition (SVD) and extreme learning machine (ELM) are used to detect microfracture signals automatically in soft rocks (Zhang et al, 2019). This technology gives engineering-useful real-time rock mass fracture data. The study tracked the soft rock tunnel's surrounding rock damage, fracture, and dilatation using real-time online rock micro-fracture data. This MS signal database supports dynamic early warning and analyzes the gradual damage development mechanism of substantial deformation in the soft rock tunnel surrounding rock.

2.2 Relationship of the source parameters and Positioning probability density field

Energy transformation is essential to physical changes, and energy drive can cause rock collapse. The energy perspective makes damage evolution analysis evident throughout the rock compression failure. Radiated MS energy comes from elastic waves emitted during rock fracture and sliding due to the transfer of elastic strain energy to inelastic strain energy. Radiated MS energy can show rock microfracture location, intensity, and strain energy storage and release in the focused area. The radiated MS energy [E] can be calculated as follows:

$$E = 4\pi\rho v F_c^2 R^2 \int_0^2 \dot{u}_{\text{corr}}^2(t)\mathrm{d}t \tag{1}$$

Where E is the radiated MS energy, ρ is the density of rock mass in the monitoring area, v is the density

of rock mass in the monitoring area, F_c is the root-mean-square radiation pattern factor, R is the focal distance, t is the duration of the MS shape in the time domain, $\ddot{u}_{corr}^2(t)$ is the function of the square of the far-field velocity spectrum corrected according to the radiation path.

When more MS events occur during monitoring, the probability density field of each event can be added, resulting in a probability density field of multiple AE events. For all MS events that occur in the measuring time and space range, the probability density at a random location x is calculated as

$$p_A(x) = \sum_{a \in A} f(x, x_{g,a}) = \sum_{a \in A} \frac{1}{(\sqrt{2\pi})} \frac{1}{\sigma^k} e^{-\|x - x_{g,a}\|^2 / 2\sigma^2}, k \in \{1, 2, 3\} \tag{2}$$

where, A is a set of all MS events that occurred in the measuring time and space range, $x_{g,a}$ is the estimated location of event a, and other parameters are defined same as before. Figure 4 illustrates the whole approach. The required variables/inputs are the arrival times t_r, the sensor locations x_r, the wave speed c and the standard deviation of the error component σ. The first three inputs are required for a deterministic source localization, and the last one is needed additionally for a probabilistic source localization.
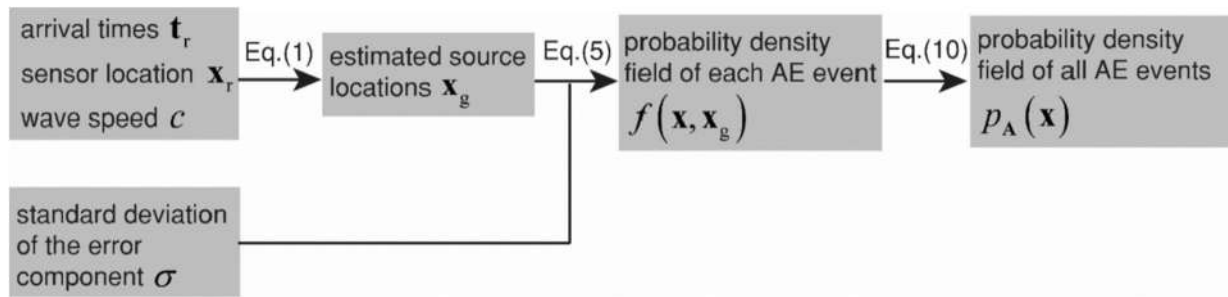
Figure 4. Derivation of probability density field of AE events. (Zhang et al., 2022)

3   Results

Figure 5a illustrates the temporal-spatial distribution of MS events and deformation at chainage 0+865m–chainage 0+885m section of auxiliary tunnel #4. MS events and deformation of tunnel showed a significant correlation with the advancement of tunnel excavation. The time series is divided into four phases based on three-time points: tunnel step excavation, inverted arch initial support closed loop, and inverted arch pouring. The deformation and MS parameters of all phases are shown in Table 1.

Table 1. Deformation parameters and cumulative MS event of all phases

Parameters	April 1 to 8, 2023 (Phase I)	April 9 to 16, 2023 (Phase II)	April 17 to May 1, 2023 (Phase III)	May 2 to 15, 2023 (Phase IV)
Vertical deformation of arch crown / mm	37.55	66.395	111.29	114.01
horizontal deformation of the arch shoulder / mm	167.62	257.42	281.36	286.26
horizontal deformation of the arch wasist / mm	365.99	475.10	528.44	534.69
horizontal deformation of the arch feet / mm	-	170.07	245.71	263.40
Cumulative MS event / count	61.00	50.00	77.00	3.00

Phase I corresponds to April 1 to 8, 2023. The deformation data reveals that, following the excavation of the upper partition, the maximum deformation of the tunnel reached 321.7mm in while the average

deformation rate was 40.2 mm/d, located on the arch shoulder. The overall trend of red and blue curve (horizontal deformation of the arch waists and arch feet, respectively) indicates that the surrounding rock has undergone a quick deformation phase, with a few measurement points experiencing abrupt variations. For instance, on April 8, 2023, a peak deformation rate of 70mm/d was detected in a single day. Each day, an average of 7 MS events were recorded, with a maximum of 27 events on the highest day.

Phase II corresponds to April 9 to 16, 2023. The maximum deformation of the tunnel arch waist was 490.9mm, and the average rate was 24.8 mm/d (with a maximum single-day deformation rate of 51.3 mm/d). The average daily MS events were 7, indicating frequent micro- fractures occur. The count of MS events was closely associated with blasting excavation frequency, rock unloading strength, and geological conditions in phase I and II. From April 1 to 16, 2023, the tunnel's internal stress state changed sharply during excavation and unloading in the segment between chainage 0+865 and chainage 0+885, undergoing blasting and mechanical excavation. The excavation would decrease the minimum principal stress in the surrounding rock, causing stress loss and concentrating the maximum principal stress, destroying the surrounding rock of the tunnel and inducing numerous rock micro-fractures.

Phase III corresponds to the time between April 17 to May 1, 2023. The surrounding rock displacement rate reduced dramatically during this stage, and the deformation only reached 40.4 millimeters, averaging 2.7 millimeters per day (maximum 14.7 mm/day). Compared to phase I and II, the frequency of MS activity during phase III has notably decreased, as only an average of 5 MS events were recorded daily. At the same time, the occurrence of MS events decreased progressively over time. It can be inferred from this feature that on the gradual advancement of the excavation working face, the intensity of excavation disturbance lessened, and the associated induced rock fracture activity became relatively weak, resulting in a relatively small count of accompanying MS events.

Phase IV corresponds to the time between May 1 to 15, 2023. This phase has 1.7 mm deformation and 533 mm cumulative deformation. The average daily deformation rate is 0.1 mm. The site construction is mainly supported; the stress of the rock mass tends to be stable, and the whole shows low MS activity. In summary, the convergence deformation growth trend of the surrounding rock is consistent with the time distribution of MS events.

The analysis of the spatial distribution characteristics of AE/MS events offers valuable information about the deformation and damage zone of the surrounding rock resulting from tunnel excavation and unloading (Feng et al., 2023). The spatial distribution of MS events of auxiliary tunnel #4 throughout the monitoring period (April 1 - May 15, 2023) is depicted in Figures 5b and c. The MS events are primarily distributed within a 10m radius of the working face, which indicates that the occurrence of MS events is related to the unloading of tunnel excavation. According to the findings of the tunnel section investigation, it was observed that most MS occurrences tend to concentrate on the east-side wall of the tunnel. Compared to the horizontal convergence deformation data from sections D-E at chainage 0+865m–chainage 0+885m section of auxiliary tunnel #4, the deformation on the west side of the tunnel measures 147.4mm. In comparison, the east side exhibits a displacement of 364.0mm. The deformation failure region of the east side tunnel revealed by MS aggregation agrees with the convergence deformation location (Figure 5c).

Additionally, Figure 5d depicts the measurement of the shortest distance between the center of MS events and the tunnel wall at different phases of tunnel construction. The distance between an MS event and the tunnel wall is considered the shortest distance between an MS source center and the tunnel wall. This approach allows for the analysis of the impact of various MS events on the tunnel wall in space to some extent. In correlation with Figures 5b and c, it can be seen that the excavation of the upper partition leads to the dispersion of MS event throughout the superficial layer of the surrounding rock of the tunnel,

primarily concentrated in the arch crown of tunnel. As the excavation of the upper partition progressed and the initial branch of the invert was sealed, fractures intensified, resulting in notable energy events that propagated from the deep surrounding rock mass and expanded toward the shallow surrounding rock mass.
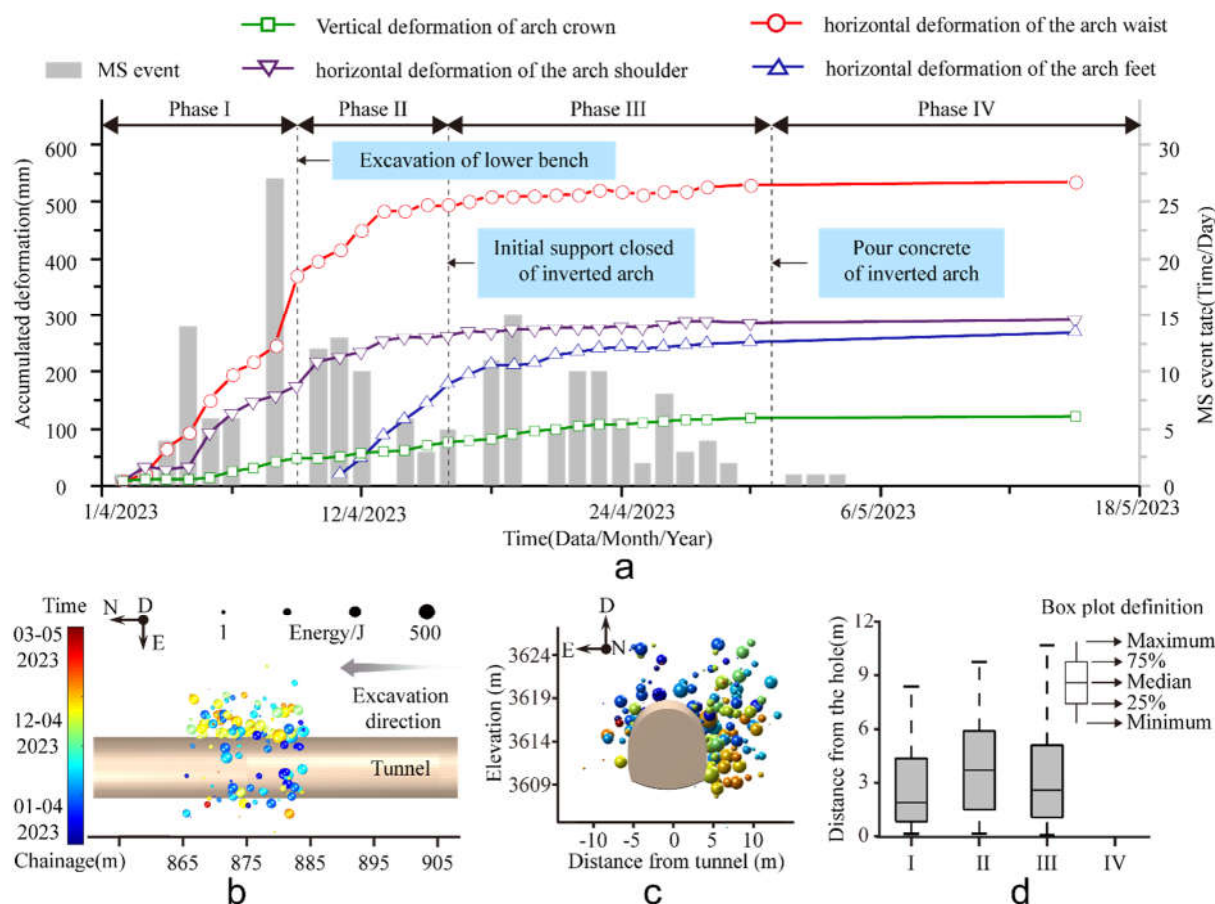
Figure 5. Spatial–temporal evolution of the distribution of the MS events: (a) Temporal evolution of MS and deformation of initial support surface. (b) Top view of MS spatial distribution. (c) Front view of MS spatial distribution (the sphere illustrated in the diagram represents the MS event. The different hues represent the temporal occurrence of micro-ruptures, while the magnitude of the sphere is proportional to the radiated MS energy). (d) Statistical rule of MS aggregation.

To further explore the stability of the soft tunnel and forewarn the large deformation caused by stress expansion and structural deformation, author correlate the spatial distribution of radiated MS energy with the damage state of rock mass. The envelope for the radiated MS energy is depicted in Figure 6. The three-dimensional analysis provides spatial distribution and morphological characteristics of the surrounding rock with different damage degrees around the tunnel. Therefore, we can further infer damage areas for potential strong deformation in the soft tunnel rockmass that could be induced by radiated MS energy anomalies. The damage zone of the surrounding rock is asymmetrical in the radial direction of the tunnel, and the damage of the surrounding rock varies in the direction of the tunnel axis with different chainage. This observation is consistent with the results obtained from in-situ deformation monitoring.

The prestressed anchorage support system has achieved a remarkable control effect in soft rock tunnels. This study applies mass spectrometry monitoring to construct three-dimensional models of rock masses with varying degrees of damage. Three high-damage zones are delineated comprehensively, and the depth of deformation zones is generally 4 ~ 12 m. This helps to determine the length of the support (the

length of the anchorage zone passes through the high damage zone) to avoid excessive support strength or insufficient support effectiveness. This approach will aid in managing deformation during the first excavation process and effectively mitigate the resistance encountered by the shotcrete layer's wall support. in addition, based on the visualization of micro-fracture intensity within the surrounding rock's three-dimensional space, the surrounding rockmass damage zone can be specifically targeted using high-strength restrained concrete support to achieve accurate and robust reinforcement for weak surrounding rock.
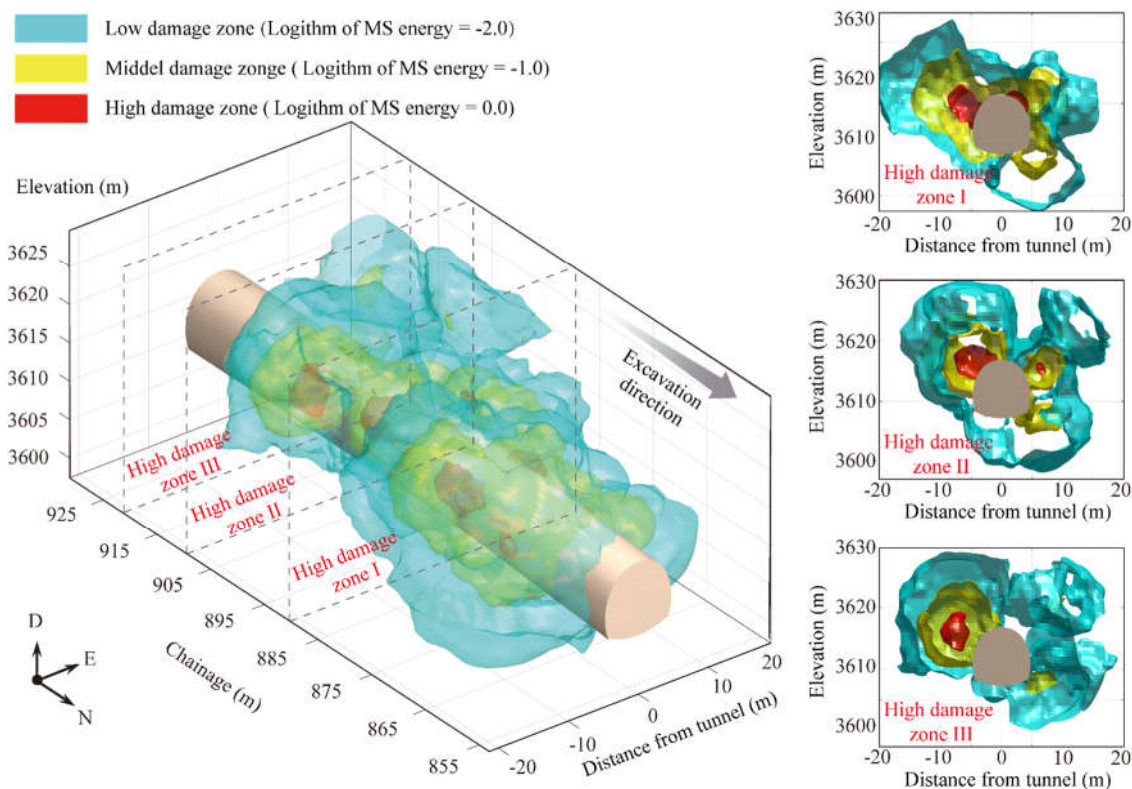
Figure 6. The 3D envelope for the radiated MS energy provides spatial distribution and morphological characteristics of the surrounding rock with different damage degrees around the tunnel.

4   Conclusion

This paper presents a case study on the plateau soft rock tunnel's progressive deformation and failure mechanism. A comprehensive method integrating the MS monitoring, the numerical simulation, and moment tensor inversion, is applied for a quantitative description of the progressive failure evolution of soft rock tunnel, which involves the fracturing expansion and squeezing deformation of the surrounding rock mass. The conclusions can be drawn.

(1) The aggregation of MS activity, which reflects the progressive damage of the surrounding rock, can better reveal and delineate the deformation and failure area of the soft rock tunnel. During excavation and unloading, MS is distributed throughout the shallow area of the rock surrounding the tunnel, most of it in the top arch region. With excavating the lower partition, the high energy MS event is generated from the deep layer and then propagated shallow.

(2) The research utilizes MS monitoring to create 3D models of rock masses that display different levels of damage. Three regions with significant damage are identified in both the radial and axial directions surrounding the tunnel, with deformation depths typically ranging from 4 to 12 meters.

Acknowledgements

References

Chen, F., Ma, T.H., Tang, C.A., Du, Y.H., Li, Z.C., Liu, F. Research on the Law of Large-Scale Deformation and Failure of Soft Rock Based on Microseismic Monitoring. *Advances in Civil Engineering*. 2018, 9286758.

Chen, X.Y., Liu, J.L., Burg, J.P., Yan, J.X., Zhou, B.J., Shan, H.S., Bao, X.X., Fan, W.K., Zhang, J., Hou, C.R. Lateral middle-lower crustal flow in response to continental collision: New insights from the metamorphic complexes in the southeastern Tibetan Plateau. Earth-Science Reviews.2023, 247: 104604.

Du, Y.L., Yi, T.H., Li, X.J., Rong, X.L., Dong, L.J., Wang, D.W., Gao, Y., Leng, Z. Advances in Intellectualization of Transportation Infrastructures. *Engineering*. 2023, 24(5): 240-253.

Feng, X.T., Young, R.P., Reyes-Montes, J.M., Aydan, Ö., Ishida, T., Liu, J.P., Liu, H.J. ISRM Suggested Method for In Situ Acoustic Emission Monitoring of the Fracturing Process in Rock Masses. *Rock Mechanics and Rock Engineering*. 2019, 52: 1395-1414.

Feng, X.T., Yang, C.X., Kong, R., Zhao, J., Zhou, Y.Y., Yao, Z.B., Hu, L. Excavation-induced deep hard rock fracturing: Methodology and applications. *Journal of Rock Mechanics and Geotechnical Engineering*. 2022, 14: 1-34.

Hathway, A.W. The Complete ISRM Suggested Methods for Rock Characterization, Testing and Monitoring; 1974–2006. *Environmental & Engineering Geoscience*.2009, 15 (1): 47–48.

He, M.C., Sui, Q.R., Li, M.N. Compensation excavation method control for large deformation disaster of mountain soft rock tunnel. *International Journal of Rock Mechanics and Mining Sciences*. 2022, 32: 951-963.

Kang, Y.S., Geng, Z., Liu, Q.S., Liu, B., Zhu, Y.G. Research progress on support technology and methods for soft rock with large deformation hazards in China. *Rock and Soil Mechanics*. 2022, 43(8): 2035-2059.

Mngadi, S.B., Durrheim, R.J., Manzi, M.S.D., Ogasawara, H., Yabe, Y., Yilmaz, H., Wechsler, N., Van Aswegen, G., Roberts, D., Ward, A.K., Naoi, M. Integration of underground mapping, petrology, and high-resolution microseismicity analysis to characterise weak geotechnical zones in deep South African gold mines. *International Journal of Rock Mechanics and Mining Sciences*. 2019, 114, 79-91.

Wang, L.F., Barbot, S. Three-dimensional kinematics of the India–Eurasia collision. *Communications Earth & Environment*. 2023, 4: 16.

Yu, M.Y., Cheng, F., Liu, J.P., Peng, D.C., Tian, Z.J. Frequency-Domain Full-Waveform Inversion Based on Tunnel Space Seismic Data. *Engineering*. 2022, 18(11): 197-206.

Yu, W., Wang, B., Zi, X., Guo, X.X., Wang, Z.Y. Effect of prestressed anchorage system on mechanical behavior of squeezed soft rock in large-deformation tunnel. *Tunnelling And Underground Space Technology*. 2023, 131: 104782.

Zhang, F.Q., Yang, Y.G., Naaktgeboren, M., Hendriks, M.A.N. Probability density field of acoustic emission events: Damage identification in concrete structures. *Construction and Building Materials* 2022, 327(11): 126984.

Zhang, J.Y., Jiang, R.C., Li, B. An automatic recognition method of microseismic signals based on EEMD-SVD and ELM. *Computers & Geosciences*. 2019, 133:104318.

Zhu, H.H., Yan, J.X., Liang, W.H. Challenges and Development Prospects of Ultra-Long and Ultra-Deep Mountain Tunnel. *Engineering*. 2019, 5(3): 384-392.

Topic 5

Engineering Geology for the Society

TEMPERATURE DEPENDENCE OF THE RESIDUAL SHEAR STRENGTH: THE ROLE OF CLAY FRACTION

OM PRASAD DHAKAL [1], MARCO LOCHE [1], RANJAN KUMAR DAHAL [2], GIANVITO SCARINGI [1]

[1] *Institute of Hydrogeology, Engineering Geology and Applied Geophysics, Faculty of Science, Charles University, Prague, Czech Republic; gianvito.scaringi@natur.cuni.cz (corresponding author)*

[2] *Central Department of Geology, Tribhuvan University Kirtipur, Kathmandu, Nepal*

Abstract

The residual shear strength is a key parameter in slope stability. It can depend on temperature according to the material's composition and hydro-mechanical boundary conditions. However, landslide materials are often heterogeneous and anisotropic, and the role of thermo-mechanical coupling in their behaviour remains poorly understood. We conducted ring-shear experiments on landslide soil samples from the Melamchi catchment in central Nepal, where a large-scale disaster occurred in 2021. We tested water-saturated specimens under normal stresses of 50–150 kPa and a rate of shearing of 0.1 mm/min. After attaining the residual shear condition, we increased the temperature to 50 °C to evaluate a new steady-state value of shear resistance. We explored the role of the clay fraction by progressively removing the coarsest particles according to different cutoff sizes (125, 62, and 20 μm). We observed thermal sensitivity – and, in particular, weakening upon heating – only in specimens with a clay fraction higher than 10%. This finding is consistent with mechanisms of thermal sensitivity observed in fine-grained soils, which are related to physico-chemical interactions in clay minerals.

Keywords

Residual shear strength, temperature, shear rate, landslide, thermo-hydro-mechanical coupling.

1   Introduction

The shear strength is a fundamental parameter governing the stability of soil and rock slopes, as well as the triggering and propagation of landslides. The residual shear strength – a minimum, steady-state value of shearing resistance – is especially relevant in reactivated landslides, where a well-defined shear zone or slip surface has formed and has already undergone large strains or displacements (Skempton, 1964, 1985). In sheared soil or regolith containing clay minerals, the residual shear strength can be significantly lower than the critical state or fully softened shear strength owing to the progressive alignment of clay particles along the direction of shearing. In fact, in face-to-face arrangements, the shearing resistance of water-saturated clay minerals is minimal, and very low values of drained residual friction angle (lower than 5°) can be attained, especially if highly active clays such as smectites are abundant (Mesri and Olson, 1970). Such a low friction angle can promote landslide activity even along gentle slopes and discontinuities (Hu et al., 2018).

The residual shear strength depends on a number of factors, including the normal stress and rate of shearing, the mineral composition, the size and shape of the sheared particles, the chemical composition of the pore fluid, and temperature (Di Maio and Scaringi, 2016; Scaringi et al., 2018; Scaringi and Loche, 2022; Duque et al., 2023; Loche and Scaringi, 2023). Coupled processes of thermo-chemo-hydro-mechanical nature are complex and often lead to counterintuitive responses, such as heating-induced consolidation despite thermal expansion of both water and mineral grains or enhanced hydraulic

conductivity upon exposure to saline solutions despite an important decrease in overall porosity (Mitchell, 1991; Di Maio, 1996). The role of the rate of shearing has been explored extensively in recent years (e.g., Tika et al., 1996; Scaringi et al., 2018; Duque et al., 2023), and significant "rate effects" have been observed for rates above 0.1–1 mm/min (i.e., for strain rates above 10^{-3}–10^{-1} s^{-1}) in usual experimental setups. In the presence of a large proportion of clay minerals, an increase in strength that scales roughly linearly with the logarithm of the rate of shearing is often observed (Scaringi and Di Maio, 2016; Scaringi et al., 2018; Kohler et al., 2023). However, the application of these insights to real-scale problems remains challenging owing to the difficult evaluation of the thickness of the shear zone (and hence the strain rate), its composition, and spatial heterogeneity. Both basal and distributed shearing (internal plastic deformation) can characterise landslide kinematics (Di Maio et al., 2015; Massey et al., 2016).

Few studies have focused on evaluating the effect of temperature on the residual shear strength, and the published results are insufficient for a comprehensive understanding; however, the role of clay minerals has been recognised, and coupling between rate-dependent and temperature-dependent responses has been suggested (Shibasaki et al., 2016, 2017; Garcia et al., 2023; Loche and Scaringi, 2023). More specifically, the largest thermal sensitivity seems to be observed at rates of shearing below the threshold for significant rate effects (0.1–1 mm/min), that is, in a condition of laminar shearing that is likely drained. Notably, very important thermal effects also arise under very large rates of shearing (>0.1 m/s, out of the scope of this work), where frictional heating and, possibly, thermal pressurisation dominate the response (e.g., Goren and Aharonov, 2007).

In the realm of stable or potentially unstable slopes and slow-moving landslides – and in non-freezing conditions – temperature is usually accounted for in models only if slope-vegetation-atmosphere interaction is considered. These models focus on thermo-hydraulic coupling to define the slope hydrology and hydraulics (e.g., water content, infiltration, suction, pore water pressure, seepage) at and near the slope-atmosphere interface (e.g., Guglielmi et al., 2023; Badakhshan et al., 2024). This coupling can affect the stability of a slope by changing the effective stress state while the material's friction angle remains unaffected. However, in the light of the experimental evidence briefly introduced above, the direct thermo-mechanical coupling can also affect the stability of a slope – and the kinematics of an active landslide – by modifying the frictional resistance of the sheared material (Scaringi and Loche, 2022, 2024). The potential magnitude of this coupling has been quantified numerically (Loche and Scaringi, 2023) and field evidence of slow-moving landslides responding to seasonal changes in temperature has been found (Shibasaki et al., 2016). Climate change may alter the temperature distribution in slopes, particularly in proximity to the surface, where climate extremes and enhanced seasonal excursions may affect slope stability also through thermo-mechanical coupling (Scaringi and Loche, 2022).

In this contribution, we discuss some recent experiments conducted on natural materials sampled from an area that featured widespread landsliding in Nepal. The materials were sheared and exposed to controlled changes in temperature. In the experimental campaign, we focused, in particular, on evaluating the importance of the mineral composition and identifying a threshold clay fraction below which the role of temperature in the residual shear strength can be considered negligible and could be safely excluded from modelling.

2   Materials and methods

2.1 Study area

The Melamchi Valley in central Nepal (**Fig. 1**) experienced a severe flood in 2021 as a result of the propagation of a chain of geohazards. The event was probably initiated by the outburst of a rather small glacial lake (~2500 m-) in the upper reaches of the catchment and amplified by the important runoff

resulting from monsoon rainfall, the entrainment of soil and regolith, and fifteen simultaneously triggered landslides.

Geologically, the Melamchi catchment lies on the southern front of the higher Himalayan sequence that comprises the higher Himalayan crystalline rocks (Dhital, 2015). The catchment extends northwards to the moderately (35–45°) northwest dipping main central thrust that runs in the NW-SE direction. The sequence from the main central thrust is followed by the kyanite-garnet schist of the Talamarang Fm. The overlying Gyalthum Fm. features quartzite mica interlayered by feldspar-garnet-biotite schist. This is followed by a band of Bolde quartzite and finally by the Timbu Fm., where the majority of the landslides took place. The maximum thickness of this formation is 1.1 km and comprises light to dark grey intensely deformed migmatites, banded gneisses, schists, and quartzite. The Timbu Fm. is followed by the overlying Golphu Fm., consisting of dark fray feldspar-garnet-biotite schist, banded gneiss, and laminated quartzite bands.

In the region, the precipitation pattern identifies three seasons: pre-monsoon from January to May, monsoon from June to September, and post-monsoon from October to December. The average annual precipitation for the whole catchment varies from 1200 to 3000 mm, and ~80% of the precipitation occurs during the monsoon season (Shrestha et al., 2016). The average annual temperature ranges from 4 to 33 °C. The average annual discharge measured at the Helambu station until 2021 (when the station was swept away) was ~10 m^3/s, with peaks of ~30 m^3/s during the monsoon season and values as low as ~2.5 m^3/s during the driest month.
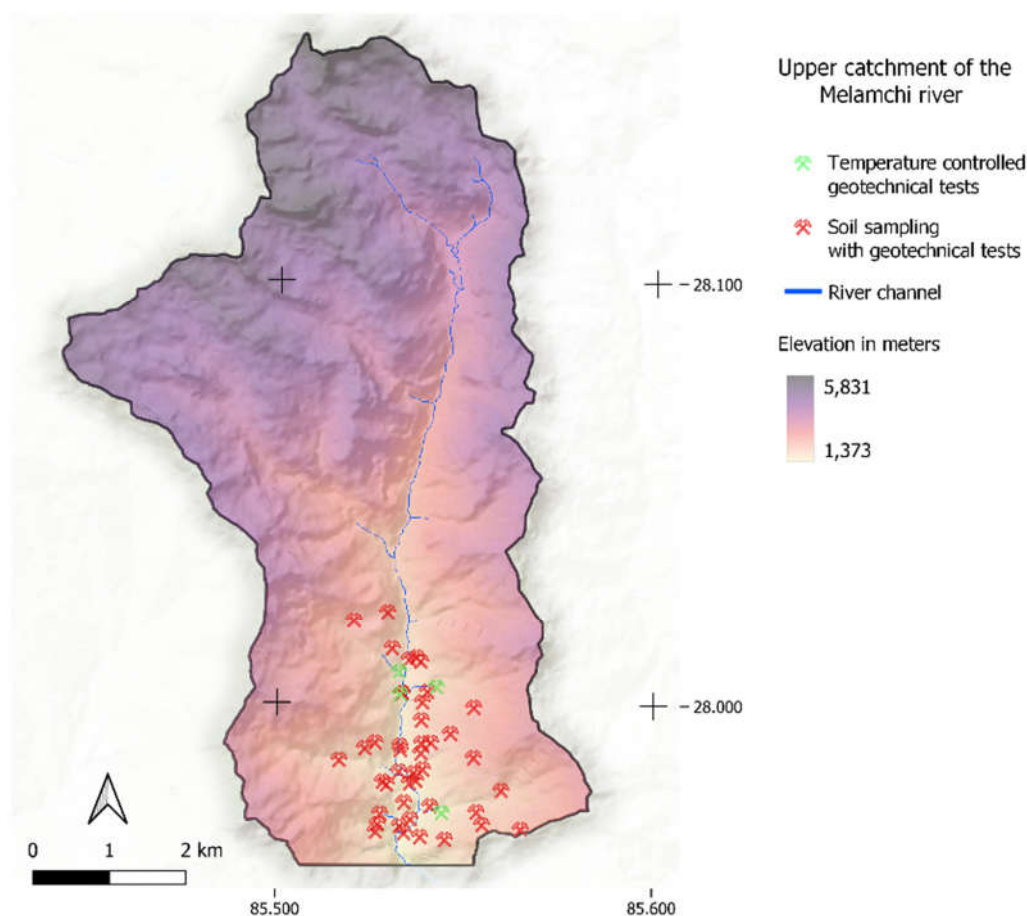
Figure 1. Digital elevation model of the study area with the indication of the sampling sites. Locations marked in green are where the samples for the experiments described in this work were taken.

2.2 Materials

After the 2021 event, an extensive survey was conducted, which included sampling at 70 locations affected by the landslides. Owing to the impossibility of bringing heavy machinery to the sites, sampling was performed using a manual tool and reached depths of ~1 m. We selected four samples for our experimental campaign, which featured different properties and compositions (**Table 1**). The samples were crushed, oven-dried, and sieved, and from each sample, four specimens were obtained by eliminating the coarsest fraction according to different cutoff sizes (125, 62, and 20 µm). Therefore, the specimens submitted to the experiments featured distinct clay fractions (**Table 2**).

Table 1. Basic properties and mineral composition (according to X-ray powder diffraction analysis) of the samples from the Melamchi catchment in Nepal.

Sample	A68	A71	A69	A31
Natural water content (%)	9	9	8	32
Unit weight (g cm^{-1})	1.38	1.65	1.34	1.51
Dry density (g cm^{-1})	1.27	1.52	1.25	1.16
Liquid limit (%)	36	23	35	23
Cohesion (kPa)	12	7	14	14
Friction angle (°)	27	29	30	32
Quartz (%)	57	36	59	64
Plagioclase (%)	19	11	16	15
Chlorite (%)	4	0	4	3
Muscovite (%)	4	20	4	3
Kaolinite (%)	4	5	3	3
Other minerals (%)	12	28	14	12

Table 2. Cutoff grain size and clay fraction (i.e., fraction smaller than 2 µm) of the tested samples.

Sample	Cutoff grain size (µm)	Clay fraction (%)
	125	12
A68	62	16
	20	17
	125	16
A71	62	21
	20	23
	125	12
A69	62	16
	20	21
	125	11
A31	62	14
	20	19

2.3 Methods

A Bromhead-type ring-shear device manufactured by Controls S.p.A. was used (Fig. 2). The device is equipped with computerised control of the normal load and rate of shearing and monitoring of the shearing resistance and vertical settlement. The annular box accommodating the material has an inner diameter of 70 mm, an outer diameter of 100 mm, and a height of 5 mm (Fig. 2). Drainage is ensured by two roughened porous brass platens placed at the top and bottom bases. Lateral confinement is provided by a stiff metal frame. The box rotates, powered by an electric motor able to provide a wide range of angular speeds. The top platen, screwed to a metal cap through which the normal load is applied, remains still as it is contrasted by two stiff load cells, installed with opposite orientations and both perpendicular to a stiff arm extending from the top cap. The box is placed in a bath of deionised water that is topped up periodically to prevent desaturation of the material. The device was modified to control the temperature of the water bath (Loche and Scaringi, 2023). Water from a 3 L thermostatic bath was circulated in a metal pipe, which was thermally insulated except for the portion immersed in the bath.

A thermocouple was installed in the proximity of the top porous platen, as close as possible to the material, to monitor the temperature during the experiments.
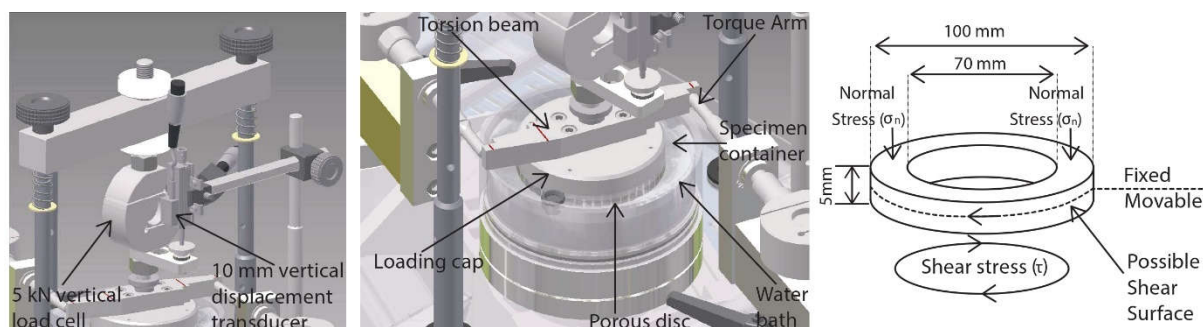
Figure 2. Schematics of the Bromhead-type ring-shear device used for the experiments with the indication of key elements and sample dimensions (mod. from Loche & Scaringi, 2023).

A thick paste was prepared by mixing the dry sieved material with deionised water to reach a water content less than the liquid limit in order to limit the settlement during consolidation. This was verified by repeatedly performing fall cone tests during sample preparation. However, no systematic measurement of the consistency index was made. Similarly, the water content and bulk density prior to the experiments were not measured as they are not expected to influence the shear behaviour of the soil once it reaches the residual shear condition.

After preparation, the paste was left to hydrate for at least 24 hours under a plastic cover so as to ensure full water saturation. It was then placed in the shear box, carefully filling gaps and removing air bubbles. Overconsolidation of the specimens was achieved by stepwise loading to 600 kPa and then unloading to 150, 100, or 50 kPa according to needs. Dissipation of the pore water pressure excess, not tracked directly, was ensured by monitoring the consolidation curve.

The specimens were then sheared at a rate of 0.1 mm/min until the residual shear condition was achieved. Further shearing for at least 10 mm was performed prior to increasing the temperature of the water bath from room temperature, 20 °C, to about 50 °C with the shearing ongoing. About 30 min elapsed from the beginning of heating until a steady value of temperature was recorded in the bath. To attain a steady state within the material and allow for the dissipation of any transient condition that may have arisen, such as thermal pressurisation, the temperature of the bath was kept elevated for up to 8 hours or until a steady value of shearing resistance could be evaluated. Finally, the thermostatic bath and circulation pump were turned off, and the system was allowed to cool down to room temperature. Meanwhile, the specimen was sheared further, and the shearing resistance after the heating-cooling cycle was recorded. In total, 36 experiments were conducted, exploring 3 values of normal stress × 3 grain size cutoffs × 4 samples.

3   Results

A representative result is shown in Fig. 3a, where the shearing resistance before, during, and after the phase at elevated temperature is plotted vs. the shearing distance for the 9 specimens obtained from sample A68 (3 normal stress values × 3 grain-size cutoffs). Tests conducted with a larger cutoff size (lower clay fraction) did not show significant changes in steady-state resistance with temperature, while some weakening emerged for smaller cutoff sizes and larger normal stresses. The larger normal stress facilitates the formation of a shear zone with preferential particle orientation; this is conducive to lower resistance, as confirmed by the decrease in friction coefficient with the normal stress increasing. Particle alignment has a more pronounced effect on the shearing resistance of clay minerals, which, moreover, tend to exhibit lower friction than non-clay minerals. In fact, as the cutoff grain size decreases, the resistance decreases, and the dependence on the normal stress becomes more pronounced.

In Fig. 3a, a transient response to heating is shown in the form of a rapid increase in resistance, followed by a more gradual drop to the steady-state value. This could be explained by a rapid decrease in pore water pressure in (a portion of) the shear zone as a consequence of the rapid heating, which dissipates according to the soil's hydraulic conductivity. The phenomenon is not easy to interpret owing to the transient and non-uniform heating, which proceeds through the steel and brass elements as well as directly through the cell water in both radial and axial directions. Furthermore, the material is not homogeneous and has an anisotropic structure, with a softened top layer (the shear zone) and an overconsolidated underlying layer. In principle, this should not affect the residual shear strength but could play a role in the thermal response. In fact, the two layers should have different porosity and arrangements of the solid skeleton, with different thermal, mechanical, and hydraulic properties. In principle, a homogeneous soil sample undergoing rapid heating should exhibit a transient thermal pressurisation (and hence a decrease in shearing resistance) owing to positive pore water pressures arising from the larger thermal expansion of water compared to that of the mineral grains.

As for the steady-state response, the decrease in shearing resistance could be related to a decrease in water viscosity and/or to more efficient lubrication provided by the clay minerals against the larger and bulkier non-clay grains. Given the comparatively low clay fraction, even under the smallest cutoff size, it may be reasonable to hypothesise that grain-to-grain shearing of bulky particles mainly occurs, facilitated by the hydrated clay minerals, rather than clay-to-clay shearing. This is supported by the comparatively high value of friction coefficient in all tests (see also Fig. 3b), corresponding to friction angles around 25°, which are lower than typical friction angles of sands but are higher than residual friction angles attainable in clay-rich soils and gouges under the explored normal stress.

A summary of the effect of the clay fraction on the residual friction angle and the steady-state response to heating is provided in Fig. 4. Here, the friction angle is evaluated from the slope of the Mohr-Coulomb failure envelope calculated from the steady-state values of shearing resistance under the three normal stresses (50, 100, 150 kPa), assuming no cohesion intercept. The heterogeneity of the samples does not allow for a clear trend to be observed. However, an increase in the thermal effect (difference between the residual friction angle evaluated at 20 °C and at 50 °C) with the clay fraction can be intuited. This effect is, however, small (up to ~1° of friction angle or ~4% loss of resistance upon 30 °C of heating) and may not be significant in the stability of slopes or kinematics of landslides, where the amplitude of thermal forcing is comparable to that applied in the experiments only close to the ground surface.
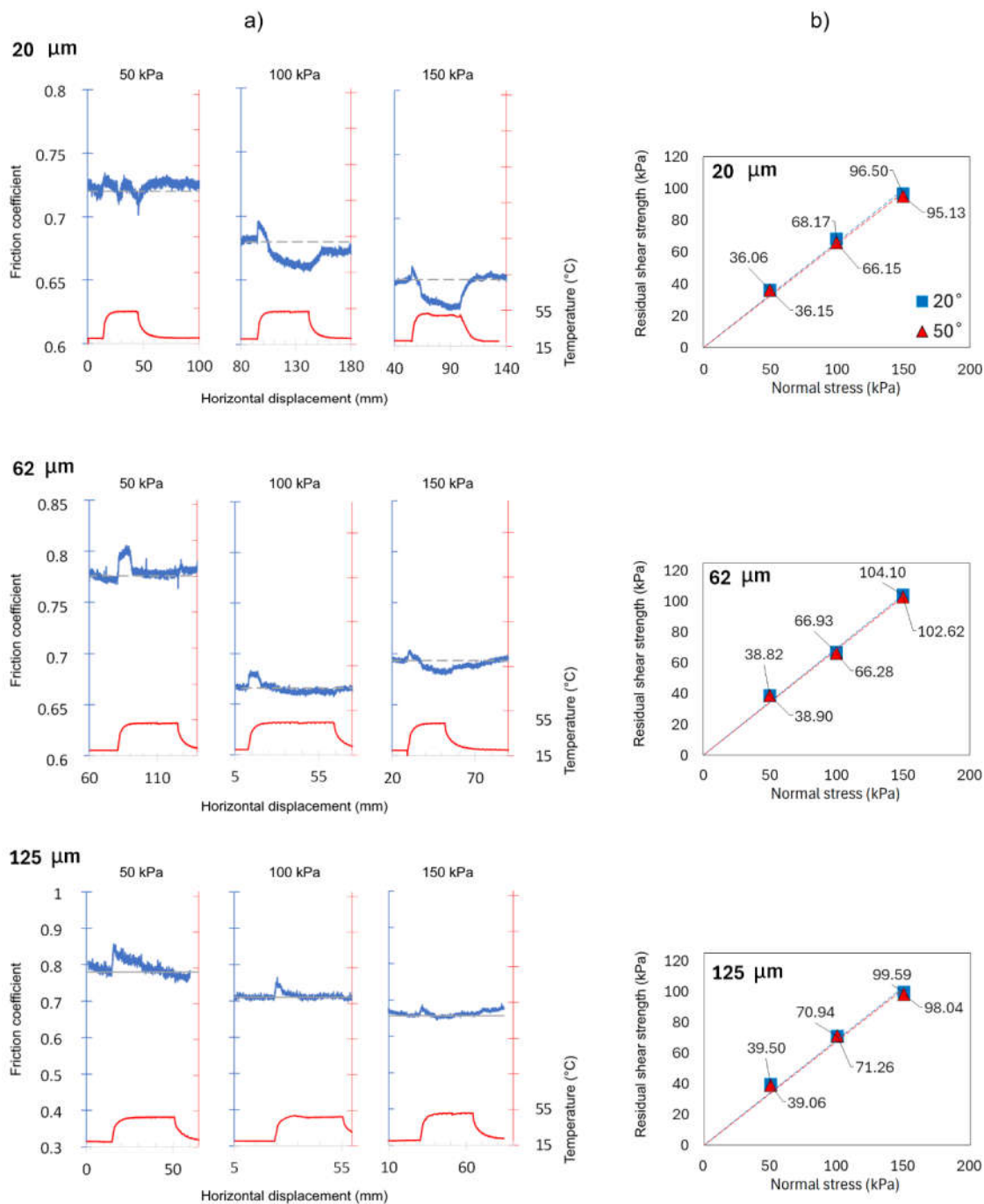
Figure 3. a) Frictional resistance (residual shear strength) and temperature (measured in the water bath) vs. shear displacement for one of the samples (A68). The experiments were conducted on specimens prepared at different cutoff grain sizes (20, 62, and 125 μm), sheared at a rate of 0.1 mm/min under normal stresses of 50, 100, and 150 kPa. b) Failure envelopes obtained from the experiments shown in a).
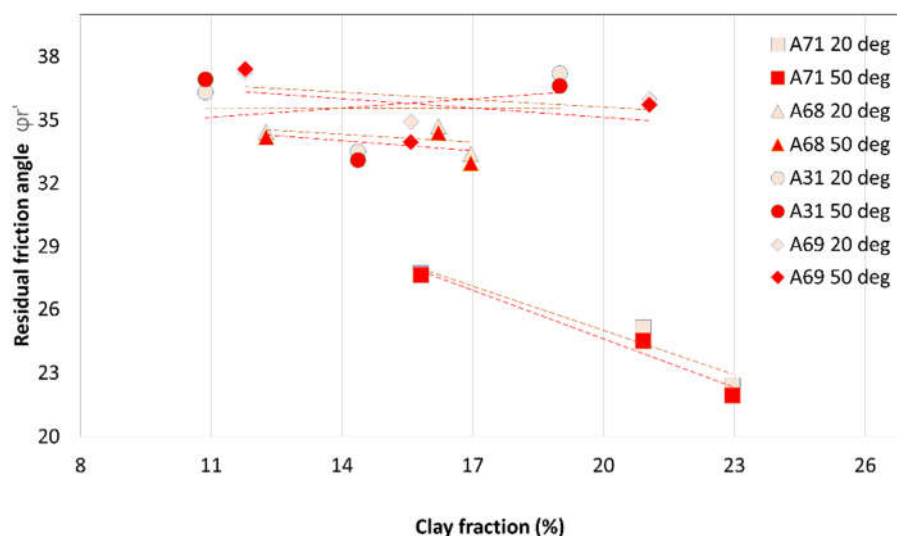
Figure 4. Residual friction angle as a function of clay fraction and temperature for the four samples investigated in this study. The values of residual friction angle were computed by linearly interpolating the results obtained under normal stresses of 50, 100, and 150 kPa for each sample and cutoff grain size, assuming no cohesion intercept. The coefficient of determination R^2 for all interpolations was >0.98.

4   Conclusion

The purpose of this study was to evaluate how temperature affects the residual shear strength of natural landslide soils containing a small proportion of clay minerals. This study complements previous research that focused on pure clays or artificial mixtures and demonstrated that temperature may have a measurable effect on the residual shear strength for values of clay fraction of ~10% and above. Considering the low-plasticity nature of the clay minerals in the tested samples and, particularly, the likely absence of smectites, this threshold value may be smaller for the generality of soils. The magnitude of the effect was, however, small and unlikely to affect the global slope stability. Yet, the effect may be significant in the shallow portion of the ground, where seasonal and even daily thermal excursions can be large and may contribute to deformation phenomena in both soil covers and exposed rock. In future research, we will be using a larger number of natural samples from diverse landslide sites in order to explore the effects of clay fraction and clay minerals content on the thermal sensitivity of the residual shear strength without the need to rework the samples through successive sieving. This way, we aim to obtain charts that will be more representative of the natural variety of clay properties.

References

Badakhshan, E., Vaunat, J., Veylon, G., 2024. Meteorological and vegetation effects on the thermal analysis of slopes. Renewable and Sustainable Energy Reviews 196, 114352. https://doi.org/10.1016/j.rser.2024.114352

Dhital, M.R., 2015. Geology of the Nepal Himalaya: Regional Perspective of the Classic Collided Orogen. Springer.

Di Maio, C., 1996. Exposure of bentonite to salt solution: osmotic and mechanical effects. Géotechnique 46, 695–707. https://doi.org/10.1680/geot.1996.46.4.695

Di Maio, C., Scaringi, G., 2016. Shear displacements induced by decrease in pore solution concentration on a pre-existing slip surface. Engineering Geology 200, 1–9. https://doi.org/10.1016/j.enggeo.2015.11.007

Di Maio, C., Scaringi, G., Vassallo, R., 2015. Residual strength and creep behaviour on the slip surface of specimens of a landslide in marine origin clay shales: influence of pore fluid composition. Landslides 12, 657–667. https://doi.org/10.1007/s10346-014-0511-z

Duque, J., Loche, M., Scaringi, G., 2023. Rate-dependency of residual shear strength of soils: implications for landslide evolution. Géotechnique Letters 13, 1–8. https://doi.org/10.1680/jgele.23.00004

Garcia, L.M., Pinyol, N.M., Lloret, A., Soncco, E.A., 2023. Influence of temperature on residual strength of clayey soils. Engineering Geology 323, 107220. https://doi.org/10.1016/j.enggeo.2023.107220

Goren, L., Aharonov, E., 2007. Long runout landslides: The role of frictional heating and hydraulic diffusivity. Geophysical Research Letters 34. https://doi.org/10.1029/2006GL028895

Guglielmi, S., Pirone, M., Dias, A.S., Cotecchia, F., Urciuoli, G., 2023. Thermohydraulic Numerical Modeling of Slope-Vegetation-Atmosphere Interaction: Case Study of the Pyroclastic Slope Cover at Monte Faito, Italy. Journal of Geotechnical and Geoenvironmental Engineering 149, 05023005. https://doi.org/10.1061/JGGEFK.GTENG-11240

Hu, W., Scaringi, G., Xu, Q., Van Asch, T.W.J., Huang, R., Han, W., 2018. Suction and rate-dependent behaviour of a shear-zone soil from a landslide in a gently-inclined mudstone-sandstone sequence in the Sichuan basin, China. Engineering Geology 237, 1–11. https://doi.org/10.1016/j.enggeo.2018.02.005

Kohler, M., Hottiger, S., Puzrin, A.M., 2023. Rate, Water Pressure, and Temperature Effects in Landslide Shear Zones. Journal of Geophysical Research: Earth Surface 128, e2023JF007220. https://doi.org/10.1029/2023JF007220

Loche, M., Scaringi, G., 2023. Temperature and shear-rate effects in two pure clays: Possible implications for clay landslides. Results in Engineering 20, 101647. https://doi.org/10.1016/j.rineng.2023.101647

Massey, C.I., Petley, D.N., McSaveney, M.J., Archibald, G., 2016. Basal sliding and plastic deformation of a slow, reactivated landslide in New Zealand. Engineering Geology 208, 11–28. https://doi.org/10.1016/j.enggeo.2016.04.016

Mesri, G., Olson, R.E., 1970. Shear Strength of Montmorillonite. Géotechnique 20, 261–270. https://doi.org/10.1680/geot.1970.20.3.261

Mitchell, J.K., 1991. Conduction phenomena: from theory to geotechnical practice. Geotechnique 41, 299–340.

Scaringi, G., Di Maio, C., 2016. Influence of Displacement Rate on Residual Shear Strength of Clays. Procedia Earth and Planetary Science 16, 137–145. https://doi.org/10.1016/j.proeps.2016.10.015

Scaringi, G., Hu, W., Xu, Q., Huang, R., 2018. Shear-Rate-Dependent Behavior of Clayey Bimaterial Interfaces at Landslide Stress Levels. Geophysical Research Letters 45, 766–777. https://doi.org/10.1002/2017GL076214

Scaringi, G., Loche, M., 2024. Temperature and Rate Effects on the Residual Shear Strength of Clays: A State of the Art, in: Proceedings of the 6th Regional Symposium on Landslides in the Adriatic-Balkan Region, ReSyLAB2024 (Eds. Marjanović and Đurić). Belgrade (Serbia), pp. 247–251.

Scaringi, G., Loche, M., 2022. A thermo-hydro-mechanical approach to soil slope stability under climate change. Geomorphology 401, 108108. https://doi.org/10.1016/j.geomorph.2022.108108

Shibasaki, T., Matsuura, S., Hasegawa, Y., 2017. Temperature-dependent residual shear strength characteristics of smectite-bearing landslide soils: Temperature-Dependent Residual Strength. Journal of Geophysical Research: Solid Earth 122, 1449–1469. https://doi.org/10.1002/2016JB013241

Shibasaki, T., Matsuura, S., Okamoto, T., 2016. Experimental evidence for shallow, slow-moving landslides activated by a decrease in ground temperature: Landslides Affected by Ground Temperature. Geophysical Research Letters 43, 6975–6984. https://doi.org/10.1002/2016GL069604

Shrestha, S., Shrestha, M., Babel, Mukand.S., 2016. Modelling the potential impacts of climate change on hydrology and water resources in the Indrawati River Basin, Nepal. Environ Earth Sci 75, 280. https://doi.org/10.1007/s12665-015-5150-8

Skempton, A.W., 1985. Residual strength of clays in landslides, folded strata and the laboratory. Geotechnique 35, 3–18.

Skempton, A.W., 1964. Long-term stability of clay slopes. Geotechnique 14, 77–102.

Tika, T.E., Vaughan, P.R., Lemos, L.J.L.J., 1996. Fast shearing of pre-existing shear zones in soil. Géotechnique 46, 197–233. https://doi.org/10.1680/geot.1996.46.2.197

SURFACE DEFORMATION OF THE LANDSLIDE OF HATTARO PASS CAUSED BY THE 2024 NOTO PENINSULA EARTHQUAKE

TERUYUKI KIKUCHI [1], KEIJI CHIDA [2], JUN TAJIKA [3], KENTARO KANAYAMA [4], KOSUKE OTSU [5], TERUYOSHI HATANO [6], SHIN ANDO [7], NOBUSUKE HASEGAWA [7], HIDEKI INAGAKI [8], MASAHIKO OSADA [9]

[1] *Suwa University of Science, Japan, kikuchi_teruyuki@rs.sus.ac.jp*

[2] *Hassu Co., Ltd., Japan, k-chida@hasshu.co.jp*

[3] *Geo-technical Research Co. Ltd., Japan, tajika@geo-tech.co.jp*

[4] *Dia Nippon Engineering Consultants Co., Ltd., Japan, kanayama_kentaro@dcne.co.jp*

[5] *Docon Co., Ltd., Japan, ko1974@docon.jp*

[6] *Nakanihon Air Co. Ltd., Japan, teruyoshi.hatano@nnk.co.jp*

[7] *Oyo Co. Ltd, Japan, ando-shin@oyonet.oyo.co.jp, hasegawa-nobu@oyonet.oyo.co.jp*

[8] *Kankyo Chishitsu Co., Ltd., Japan, inagaki@kankyo-c.com*

[9] *Saitama University, Japan, osada@mail.saitama-u.ac.jp*

Abstract
This study aimed to confirm that the occurrence of specific surface deformations is consistent with actual geological structures. Although it is difficult to obtain an overall understanding of large-scale land surface deformations, particularly from field surveys alone, the interpretation of land surface deformations through vector analysis can lead to a correct understanding. This makes the role of estimations based on topography, geology, and history more important for predicting and forecasting landslides and slope failures. In this study, we focused on a landslide that occurred west of the *Hattaro* Pass on the boundary between *Wajima* and *Suzu* cities during the 2024 *Noto* Peninsula Earthquake (Mj7.6) on January 1, 2024. The results of the multitemporal vector analysis and the views obtained from the field survey are summarized.

Key words
Noto Peninsula Earthquake, Landslide, Displacement vector analysis, Syncline

1   Introduction

In recent years, disasters associated with extreme weather events and large-scale earthquakes have occurred frequently and are expected to continue in the future. In such large-scale disasters, slope disasters of various sizes and forms, such as deep and surface failures, have been reported (Yin et al., 2009; Wartman et al., 2013; Karakas et al., 2021).

After a disaster, it is effective to quickly identify land surface changes and prevent the occurrence of secondary disasters for the stability of social infrastructure. Furthermore, it is difficult to understand the mechanism of disaster occurrence when the target area and number of sites are large (Osanai et al., 2019). In particular, when many landslides and collapses occur simultaneously, they are impossible to monitor using ordinary extensometers and inclinometers in terms of securing materials and costs, and multiple locations over a wide area must be monitored in detail. Aerial laser surveying, a quality-controlled method, can be used to measure land surface changes during a disaster by processing data from two different periods. For example, sediment change maps and volume calculations can be created by calculating the elevation range of the same coordinates from two periods of digital elevation model

(DEM) data. Vector analysis has been used to study landslides and mass movements associated with earthquakes and heavy rainfall disasters (Mukoyama, 2010; Kikuchi et al., 2017). Using the same precision laser measurement results obtained before and after a disaster, this method can examine the process of change in a target area and obtain results that can lead to the prediction of future changes. Vector analysis is useful for understanding geological structures and landslide mechanisms.

Landslide sliding has been linked to geological structures. The Monte Tok landslide movement that caused the 1963 Vaiont Dam failure highlights the importance of structural folding (Massironi et al., 2013). Landslide behavior is also related to sensitivity to crustal deformation, and structural conditions can indirectly influence landslides (Damm et al., 2010).

The aim of this study was to confirm whether the specific landslide locations obtained from the analysis of the variation vectors of bi-period aerial laser surveys were consistent with the actual geological phenomena in the area. Although it is difficult to understand the entirety of a land surface change, particularly at a large-scale, using field surveys alone, the interpretation of the land surface change can lead to a correct understanding by performing a variation vector analysis (Takami et al., 2019). Increasing the number of case studies makes the role of estimations based on topography, geology, and past history more important in the prediction of landslides, slope failures, and their occurrence.

In this study, we examined a landslide that occurred west of the *Hattaro* Pass on the boundary between *Wajima* City and *Suzu* City during the 2024 *Noto* Peninsula Earthquake (Mj7.6) on January 1, 2024 (Figure 1). The results of the multitemporal vector analysis and the views obtained from the field survey are summarized.
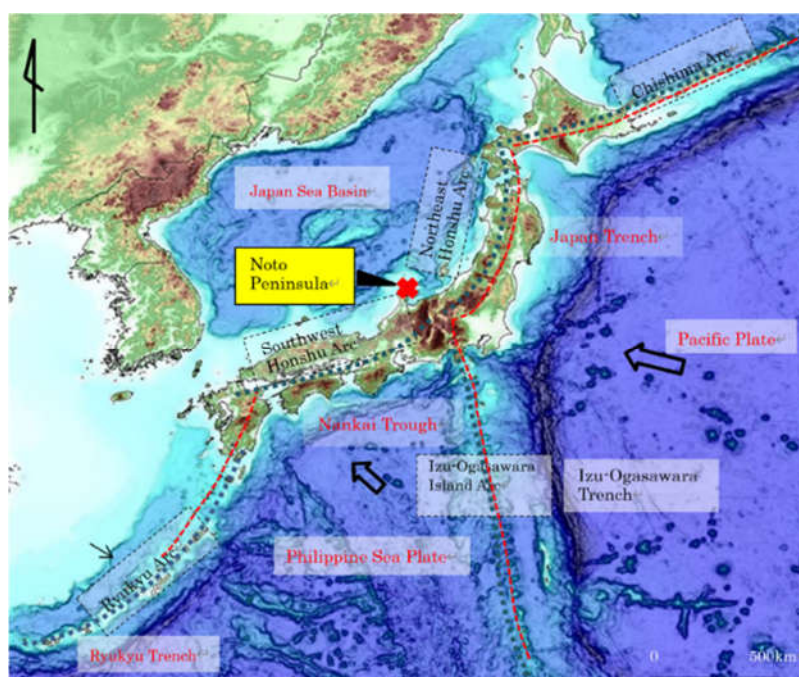
Figure 1. General topographic view around Japan

2 Disaster Event

The 2024 *Noto* Peninsula Earthquake occurred on January 1st, 2024, with a maximum intensity of VII in northwestern Japan. The earthquake had a magnitude of 7.6 at a depth of approximately 15 km in the *Noto* region of *Ishikawa* Prefecture. The seismic mechanism of this earthquake was a reverse fault type with maximum principal stress axis in northwest-southeast direction, and the earthquake occurred within the crust. Figure 1 presents a general view of Japan. The Japanese Archipelago comprises five island arcs. The Philippine Sea Plate moves in the NW direction at 4 cm/yr and subducts into the *Nankai*

Trough. Conversely, the Pacific Plate moves in the WNW direction at 9 cm/yr on average and subducts in the Japan and *Izu-Ogasawara* trenches. Moreover, the *Izu-Ogasawara* Island Arc collided with the Honshu Arc and intruded to the north. These continuous movements in the subduction zones at the boundaries of the plates are the main causes of large earthquakes and tsunamis. Many active faults are distributed in the island arcs.

3   Topography and Geology

The target site is located west of *Hattaro* Pass, approximately 4 km northwest of *Horyu-san* (471 m), at the boundary between *Wajima* City and *Suzu* City, *Ishikawa* Prefecture, in the northeastern *Noto* Peninsula, as shown in Figure 2. This mountain range has a summit approximately 400 m above sea level and many gentle slopes. The area is composed of siliceous Neogene mudstones. The oblique axis of the *Wakayama-gawa* syncline gently west-southwest from the *Wakayama* River to the *Suzuya* River via the *Hattaro* Pass (Yoshikawa et al., 2002). This area was the site of many landslides caused by the 2024 *Noto* Peninsula Earthquake (Geospatial Information Authority of Japan, 2024).

Legend Ip: Siliceous siltstone, Dg: Glauconite Sandstone, At: rhyolitic pyroclastic rock,
Hs: Coarse-grained sandstone, Rt: Dacitic pyroclastic rock
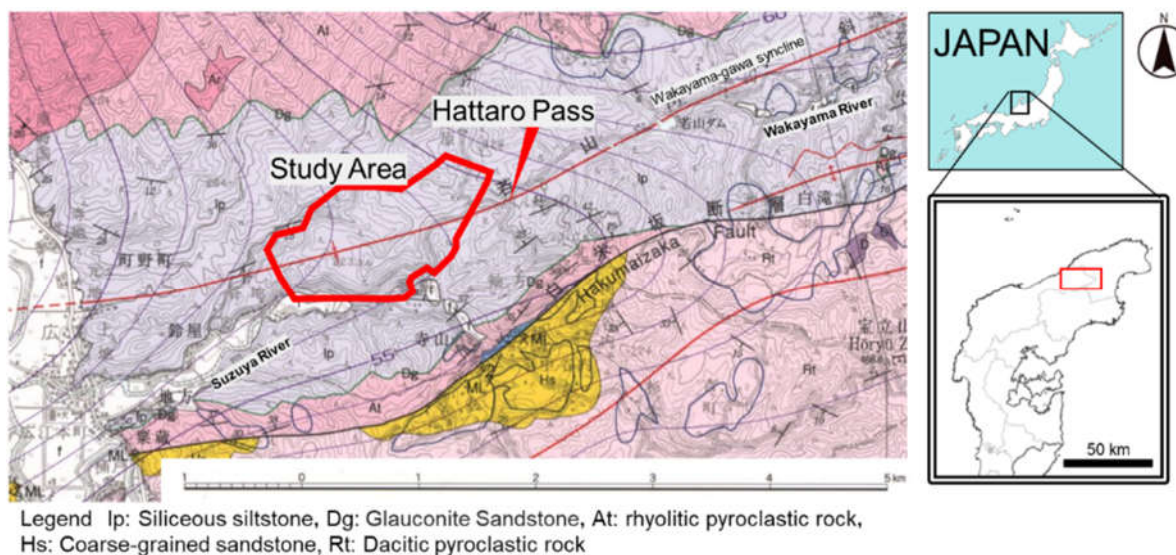
Figure 2. Geological map and survey location map: Geology of the *Suzumisaki, Noto-iida* and *Horyuzan* district., in: Quadrangle Series, 1:50,000 (Yoshikawa et al., 2002)

4   Displacement Vector Analysis Method and Results

In this study, displacement vector analysis was conducted using the pre- and post-earthquake point-cloud data shown in Table 1. Compared to the usual difference analysis for height, the variation vector analysis method provides a concrete understanding of the direction of variation and has been increasingly used in recent years (Fey et al., 2015). The displacement vector analysis method is based on a point cloud-matching process in which the point clouds of the lower model (Substratum-DEM) are compared directly without meshing (Kikuchi et al., 2017). Pre-earthquake data for 2020/2022 were used as the first period, and post-earthquake data were used as the second period. The point with the highest agreement was used as the final displacement (Figure 3). For locations where the displacement is greater than 10 m, that is where the land surface has changed to the extent that matching is not possible, the displacement vector cannot be calculated. Therefore, the results of the height difference analysis, shown in Figure 4, were used to confirm the results.

The size of the landslide variation area reached approximately 1.6 km east-west and 1.1 km north-south

in the analysis area, which is comparable in scale to the *Aratosawa* seismic landslide of the *Miyagi-Iwate Nairiku* Earthquake (2008, Mj7.2) (Kinoshita et al., 2012), although the magnitude of the variation differs. The displacement of the moving body exceeded 5 m in many locations, and the direction of displacement was in the southern direction; however, westward and eastward displacements were also observed at several locations, reflecting the complex ground deformation during the earthquake. Based on the results of displacement vector analysis, the moving body, including the collapse site, can be divided into multiple blocks. The results of the displacement vector analysis were classified using the same trend vectors. As a result, they can be summarized into nine blocks, as shown in Figure 5. These blocks are predominantly moved from south to south-southwest, though several are moved west to southwest.

Table 1. List of data used for aerial laser surveys

Type of data	pre-earthquake	post-earthquake
Time of survey	2020, 2022	1/11/2024
Average point density	18 point/m^2	18 point/m^2
Provider	APIGD*	Nakanihon Air Co. Ltd.

* Association for Promotion of Infrastructure Geospatial information Distribution
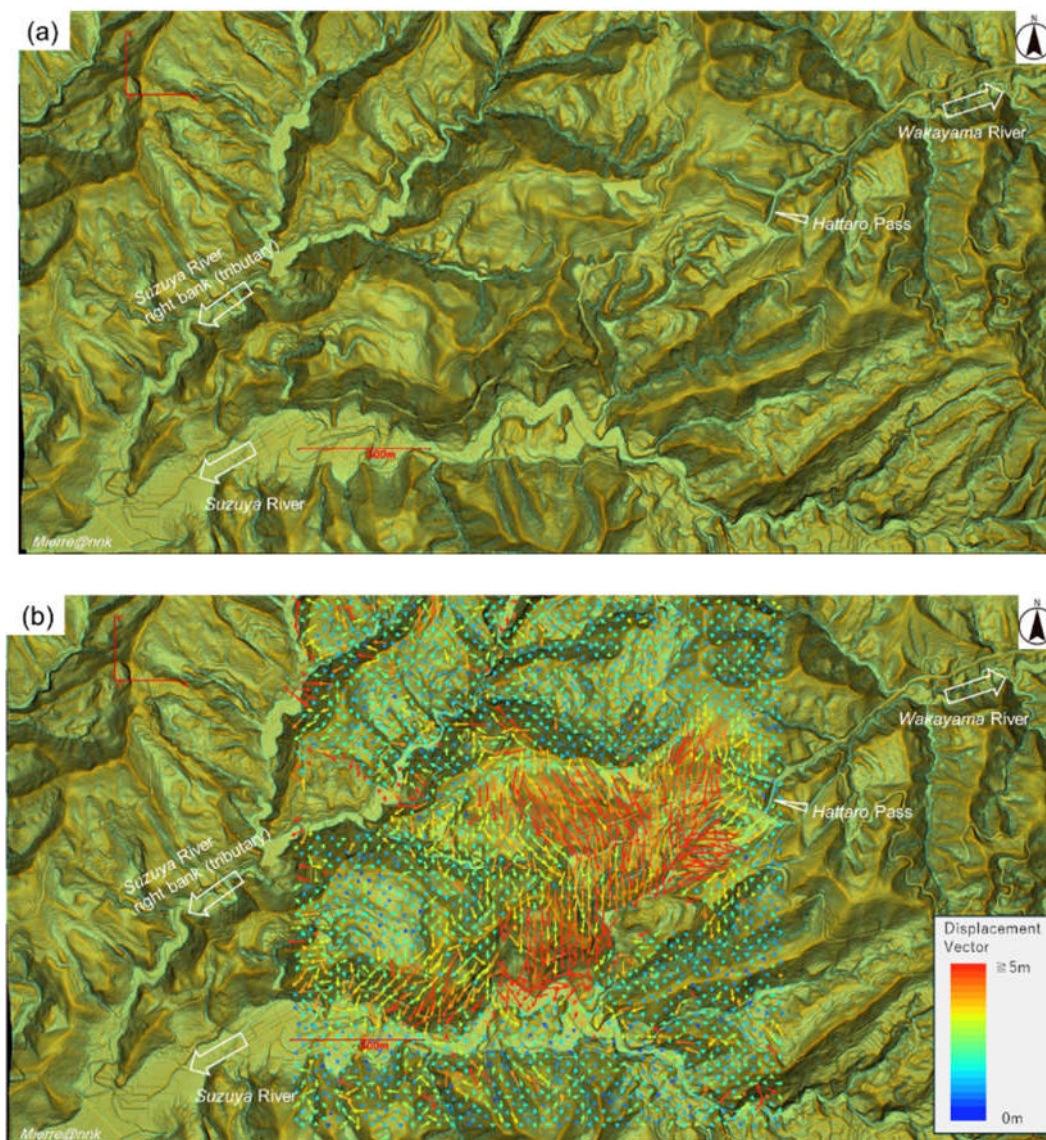
Figure 3. (a) Terrain relief image post- earthquake and (b) Result of displacement vector analysis
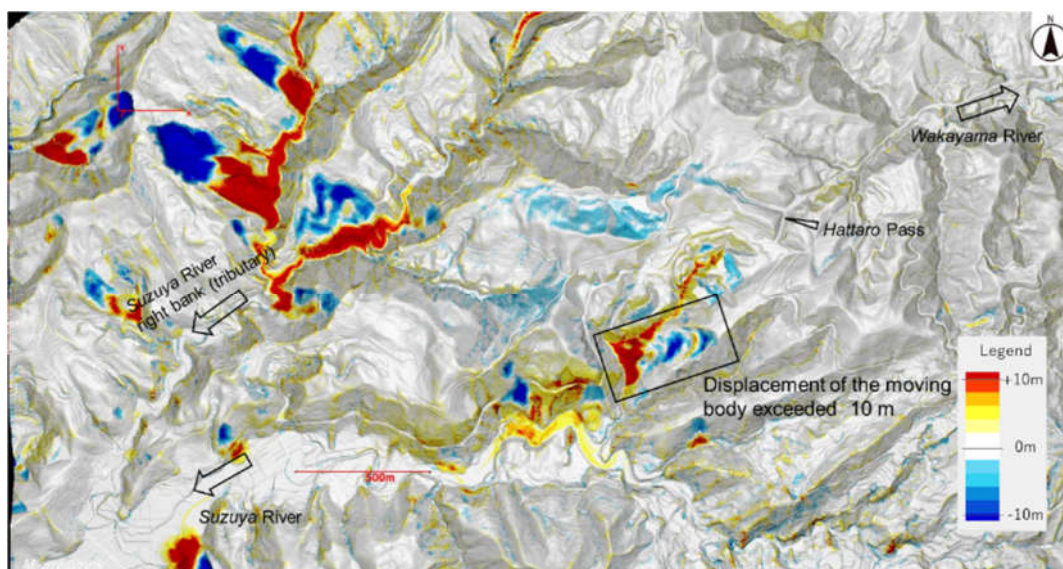
Figure 4. Height difference analysis results and locations where variation of 10 m or more occurred

Figure 5. Classification of vectors based on results of displacement vector analysis

5   Field Survey

The field survey was conducted from May 25 to 28, 2024, by members of the Disaster Geology Research Group of the Japan Society of Engineering Geology (JSEG). The route from the *Suzuya* River in *Wajima* City to *Wakayama* Dam via *Hattaro* Pass was surveyed to determine the topographical and geological conditions of the surrounding area. The survey was conducted efficiently after obtaining the results of the analysis of the variation vectors in advance and deciphering the topography (Figure 3). The survey results are shown in Figure 6 and summarized below.

- Loc.I The terrain is a south-falling terrace with a scarps (4 m) behind it (Figure 7).
- Loc.II South-falling terrace crossing a rice paddy field site. The terrain is a south-falling terrain that crosses a paddy field site, suggesting repeated activity. The valley was dammed, and a suitable site for rice paddies was created (Figure 8).
- Loc.III The depression is extensive, reaching a maximum width of 30 m with a step topography of 2.5 m on the north side and 1 m on the south side (Figure 9).

- Loc.IV Multiple terraces are distributed on the steps in the south-falling terrain. Multiple terraces are distributed on the step, and openings were observed at 0.2–1.0 m on each terrace (Figure 10).
- Loc.V Deformed topography (vertical offset of 1.2 m and right lateral offset of 1.6 m) was observed inside the mobile unit (Figure 11).
- Loc.VI The prefectural road overlooking the Suzuya River was completely collapsed (Figure 12).
- Loc.VII A strange slope extrusion phenomenon was observed in the upper part of the prefectural road (Figure 13).
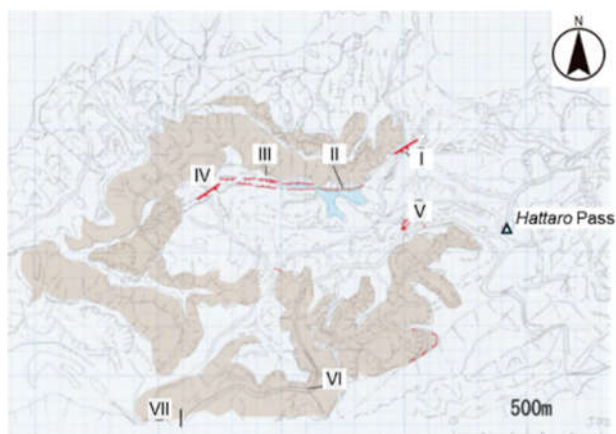
Figure 6. Topographic interpretation map and surveyed locations; red line indicates faults, and red bold line indicates step-like terrain, with the direction of fall indicated by the caption and the direction of movement indicated by the arrow. I-VII: Location number

Figure 7. Image at Loc. I, showing the southward lowering of a step on the west side of *Hattaro* Pass, which occurred approximately 5 m in front of a small cliff topography (4 m high).

Figure 8. Image at Loc. II. Vertical displacement of former rice paddy approximately 2 m W-E, south lowering "fault," the boundary with the rise behind is a small cliff topography. It is believed that repeated activities dammed the valley and created a suitable area for rice paddy fields.
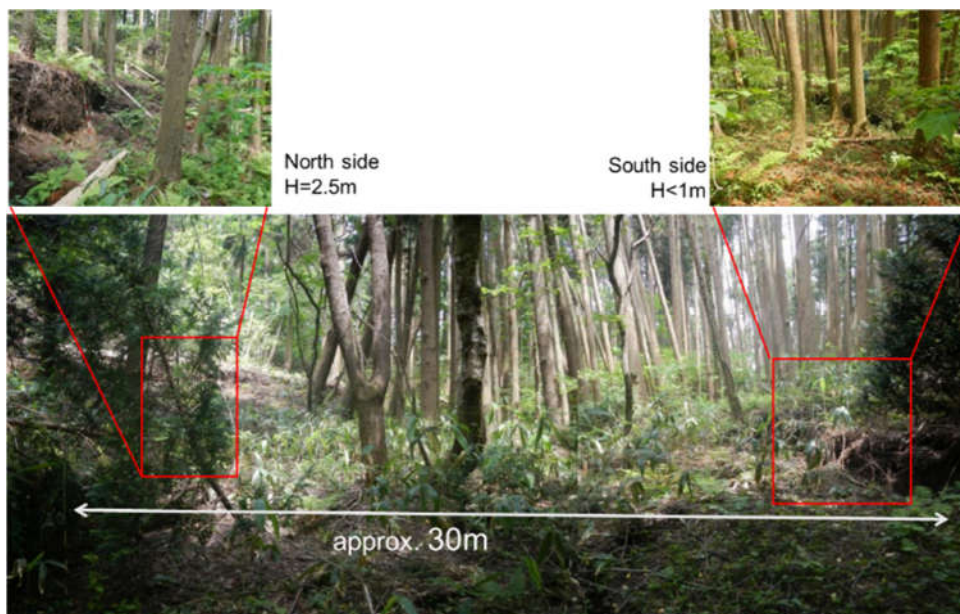
Figure 9. Image at Loc. III. Graben structure is observed.
The north side of the depression is tilted south, and the south side is tilted north.

Figure 10. Image at Loc. IV. Step-fault like deformation of north side of depression and scarps extending to WNW direction

Figure 11. Image at Loc. V. Internal deformation of mobile unit, with 1.2 m longitudinal displacement and 1.6 m horizontal displacement on the right side.

Figure 12. Image at Loc.VI. Collapse of a prefectural road.

Figure 13. Image and Simplified sketch (cross-section) at Loc. VII.
Extruded area at the southern end of the landslide

6   Discussion

Based on the results of the variation vector analysis and survey, the plan, geological structure, and results of the variation vector analysis can be summarized, as shown in Figure 14. The movement trend was significant to the south, orthogonal to the Wakayama-gawa syncline.

Based on a field survey, a series of slip cliffs and graben structures appeared at the northern end of the landslide. These structures have good continuity in the east-west direction, and both are at the edge of the moving landslide body because of the low deformation on the south side. The maximum width of the graben structure was 30 m, and a maximum drop of 2.5 m was observed on the north side. This drop is larger than the 1 m drop on the south side of the graben structure and is the basis for the main slide cliff. Various deformations are observed in the internal structure of the landslide. On the southern side facing Suzuya-River no terraced topography corresponding to a slip cliff was observed. Instead, as shown in Figure 13, extrusion and collapse were observed on many slopes.

The results of vector analysis and field survey were compiled into a cross-sectional map. As shown in Figure 15, the landslide occurred along the stratigraphic plane (10–15°), indicating that the landslide extended from the 30-m wide section of the depression (Loc. III) via the Wakayama-gawa syncline to

the steep slope on the right bank of the Suzuya River (Loc. VII). The movement trend also supports this phenomenon. The field survey revealed multiple traces of sliding. This suggests that the site may be subject to repeated fluctuations owing to the influence of the Wakayama-gawa syncline.
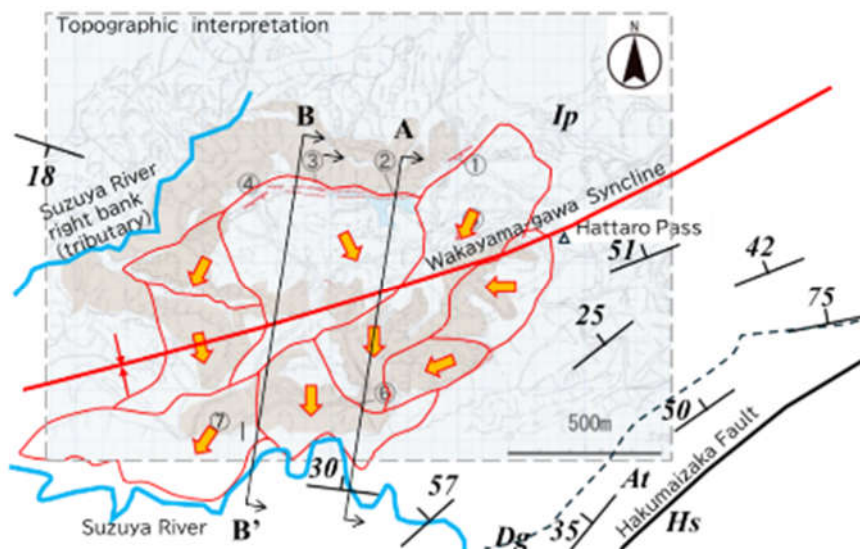
Figure 14. Integrated plan, A-A' and B-B' are cross-sectional locations, legends are same as Figure 3, and red thin line is based on the variation area (Figure 6).
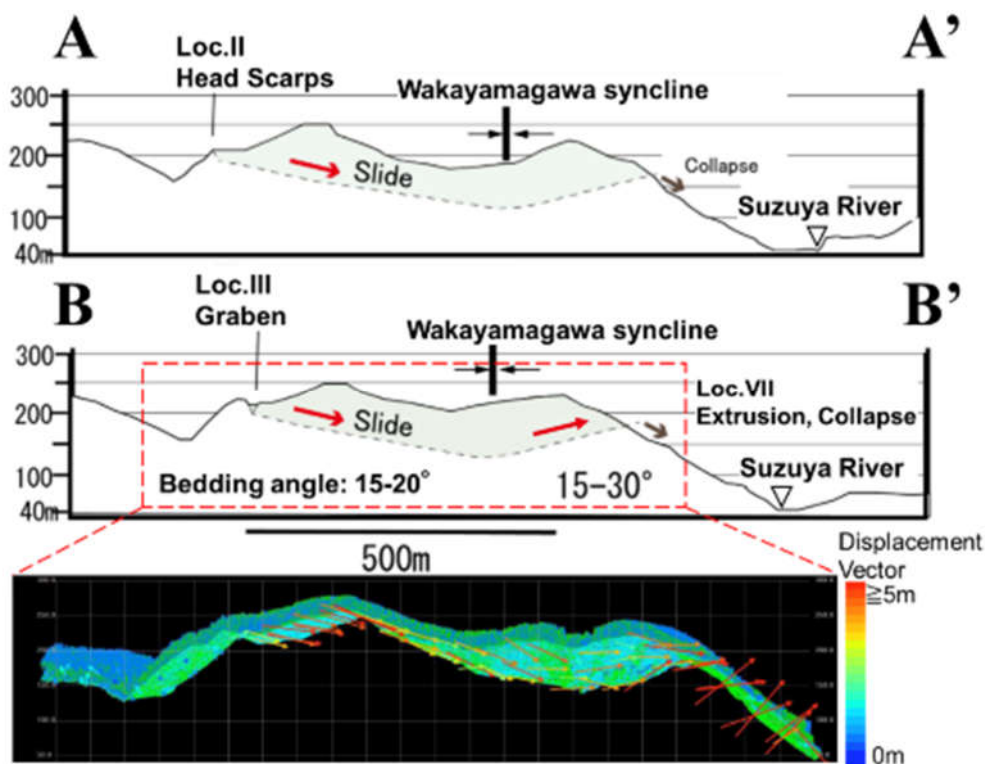
Figure 15. Cross sections of A-A' and B-B' and surrounding area (projected width 100 m)

7   Conclusion

This study confirmed that landslide locations identified through displacement vector analysis from aerial laser surveys matched actual geological phenomena observed after the 2024 Noto Peninsula Earthquake. The displacement vector analysis revealed significant, complex ground deformations. Field surveys

validated these findings. The integration of high-precision aerial data and on-ground surveys is essential for understanding and predicting landslide behaviors, enhancing disaster preparedness and infrastructure stability.

Acknowledgements

References

Association for Promotion of Infrastructure Geospatial information Distribution: Front Geospatial, https://front.geospatial.jp/ (accessed on 4 July 2024).

Damm, B.; Becht, M..; Varga, K.; Heckmann, T. Relevance of tectonic and structural parameters in Triassic bedrock formations to landslide susceptibility in Quaternary hillslope sediments. *Quaternary International*. 2010, 222(1–2), 143–153.

Fey, C.; Rutzinger, M.; Wichmann, V.; Prager, C.; Bremer, M.; Zangerl, C. Deriving 3D displacement vectors from multi-temporal airborne laser scanning data for landslide activity analyses. *GIScience & Remote Sensing*. 2015, 52(4), 437–461.

Geospatial Information Authority of Japan: Slope Failure and Deposition Distribution Data and Slope Failure and Deposition Distribution Map, https://www.gsi.go.jp/BOUSAI/20240101_noto_earthquake.html (accessed on 4 July 2024).

Karakas, G.; Nefeslioglu, H. A.; Kocaman, S.; Buyukdemircioglu, M.; Yurur, T.; Gokceoglu, C. Derivation of earthquake-induced landslide distribution using aerial photogrammetry: the January 24, 2020, Elazig (Turkey) earthquake. *Landslides*. 2021, 18(6), 2193–2209.

Kikuchi, T.; Hatano, T.; Senda, Y.; Nishiyama, S. Development of analytic method for landslide measurement by movement vectors using S-DEM data obtained from airborne laser point clouds. *Journal of The Japanese Society of Engineering Geology*. 2017, 57(6), 277–288.

Kinoshita, A.; Shibasaki, T.; Hashimoto, J.; HASEGAWA, Y.; SAMMORI, T.; OKADA, Y. Geotechnical characteristics of collapsed slope triggered by the 2008 Iwate-Miyagi Nairiku earthquake in the Koei district, Kurihara City, Miyagi Prefecture, Japan. *Journal of the Japan Society of Erosion Control Engineering*. 2012, 65(2), 3.

Massironi, M.; Zampieri, D.; Superchi, L.; Bistacchi, A.; Ravagnan, R.; Bergamo, A. ; Ghirotti, M. ; Genevois, R. Geological structures of the Vajont landslide. *Italian Journal of Engineering Geology and Environment*. 2013, 573–582.

Mukoyama, S. Estimation of ground deformation caused by the Earthquake（M7.2）in Japan,2008,from the Geomorphic Image Analysis of high resolution LiDAR DEMs. *Journal of Mountain Science*. 2010, 8(2), 239–245.

Osanai, N.; Yamada, T.; Hayashi, S. I.; Kastura, S. Y.; Furuichi, T.; Yanai, S.; ... Miyazaki, M. Characteristics of landslides caused by the 2018 Hokkaido Eastern Iburi Earthquake. *Landslides*. 2019, 16, 1517–1528.

Takami, T.; Mukoyama, S.; Homma, S.; et al. Evaluation and analysis of slope movements using multi-temporal LiDAR DEM. *Journal of the Japan Landslide Society*. 2019, 56(6),295.

Wartman, J.; Dunham, L.; Tiwari, B.; Pradel, D. Landslides in eastern Honshu induced by the 2011 Tohoku earthquake. *Bulletin of the Seismological Society of America*. 2013, 103(2B), 1503–1521.

Yin, Y.; Wang, F.; Sun, P. Landslide hazards triggered by the 2008 Wenchuan earthquake, Sichuan, China. *Landslides*. 2009, 6, 139–152.

Yoshikawa, T.; Kano, K.; Yanagisawa, Y.; Komazawa, M.; Joshima, M.; Kikawa, E. Geology of the Suzumisaki, Noto-iida and Horyuzan district. *in: Quadrangle Series, 1:50,000, Geological Survey of Japan, AIST*. 2002, 76 (in Japanese with English abstract).

DEVELOPMENT OF THE NEW ZEALAND LANDSLIDES DATABASE

ROSS ROBERTS [1]

[1] *Auckland Council, New Zealand, ross.roberts@aucklandcouncil.govt.nz*

Abstract

There have been over 1,500 recorded landslide-related fatalities in New Zealand (more than from earthquakes and tsunami combined) since 1760. No single organisation in New Zealand has overall responsibility for landslides. As a result, landslide data has been stored in multiple discrete locations, often in widely varying formats, with no ability to compile the data to get an overall understanding of the distribution of landslide risk across the country. The New Zealand Landslides Database enables multiple organisations including the public to deposit factual information about every landslide into a single repository, and users to be able to access the data for their own purposes. Co-funded by the Earthquake Commission (EQC) and Auckland Council, with support from GNS Science, the beta version of the database went live in 2022. By sharing this data organisations gain significant benefits by understanding how landslides might affect their people and assets. This paper describes the development of the database and its use in a recent emergency event. It highlights the need for a consistent data schema to enable integration of multiple landslide inventories, describes the benefits, and proposes approaches to deliver the schema.

Key words

landslide, database, data, New Zealand

1   Introduction

Landslides are one of New Zealand's most significant natural hazards. Since 1760 there have been at least 1,500 deaths from landslides in New Zealand. More fatalities have occurred from landslides than from earthquakes (501), volcanic activity (179) and tsunami (1) combined over the last 160 years (de Vilder et al, 2024). A lower estimate of the national annual cost associated with landslides is NZ $250–$300 M/year (Rosser et al, 2017).

Before the losses from landslides can be reduced, the hazard must be recognised and the risk assessed appropriately. Risk, for the purposes of landslide risk management, is commonly defined as "*The potential for adverse consequences, loss, harm or detriment as a result of landsliding, as viewed from a human perspective within a stated period and area.*" (Lee & Jones, 2023).

Risk is generally considered to be a function of the hazard (a landslide) and the consequences (in most cases, impact on people or property). A landslide susceptibility, hazard and/or risk analysis, commonly in the form of a map, provides a way to identify areas where landslides exist or could occur, what they may impact and therefore the risk that they pose (de Vilder et al, 2023).

Understanding the spatial and temporal distribution of previous landslides is required to inform susceptibility studies and risk assessment. A comprehensive landslide inventory provides this data. A landslide inventory is defined as "an inventory of the location, classification, volume, activity and date of occurrence of individual landslides in an area" (AGS, 2007). A landslide inventory is the most important information source for quantitative zoning of landslide susceptibility, hazard and risk (Van Den Eeckhaut & Hervás, 2012). However, no single organisation in New Zealand has overall

responsibility for landslides, so data about the spatial and temporal distribution of landslides is fragmented and incomplete. This creates several challenges:

- It is challenging to undertake landslide susceptibility studies because the key input data, the landslide inventory, is incomplete.
- Members of the public struggle to identify who to report landslides to in emergencies. As a result, landslide reports are often directed to an inappropriate organisation, and by the time they get to the appropriate responders they lack key information like location and criticality.
- Homes and infrastructure are sometimes built in inappropriate locations because a history of land instability has been lost.

These challenges can be overcome by the creation of a robust and accessible landslide inventory. New Zealand already has several landslide databases, the most well-known of which is owned and operated by GNS Science, a government owned research institute. Although a valuable resource, GNS staff note some limitations that prevent it from being more widely used (pers. com.) including:

- It is only editable by GNS staff, meaning that utilities, territorial authorities and insurers are unable to add landslides they have identified.
- It is unfunded, meaning that GNS staff are unable to add many records.
- Quality assurance is not built in, meaning that some records are of questionable validity.
- User groups outside of GNS were not included in the database design, so it does not capture all the data they might need.

Because of these limitations, other databases have been developed. These include several landslide databases created by GNS and others for data relating to slow moving landslides, the Kaikoura earthquake triggered landslides and landslides in Wellington, the Bay of Plenty and others. There are also records of landslides held by the Natural Hazards Commission (NHC Toka Tū Ake, New Zealand's land insurance entity) in claims information, as well as many local authorities and infrastructure owners in a range of formats. This proliferation of data sources means that there is no way to produce a national map of landslides, and that compiling data is challenging due to the variable formats and standards used.

Without this consolidated, consistent and quality assured landslide inventory any efforts to assess spatial landslide hazard or risk will be flawed. Landslide hazard assessments are greatly enhanced if they include information on the magnitude, encompassing the distribution, type, density, size and impacts of landslides, and temporal frequency of past landslide events. The on-going capture of landslide records provides the magnitude and temporal frequency of landslide activity and its relationship with terrain types and individual triggering events, and this increases the reliability of landslide hazard assessment (Rosser et al., 2017).

2   Development of the New Zealand Landslides Database

2.1 Scoping
The NZ Landslides Database was developed to resolve the problems described above. The long-term goals for the Landslide Database are that it will, over time:
- Enable data to be standardised and consistent across all organisations that manage and use landslide information
- Replace legacy systems with improved and current technology and functionality
- Improve quality of landslide data
- Increase availability of landslide data to interested parties
- Improve public engagement relating to the reporting and viewing of landslide information
- Provide a source of landslide information for other related systems

- Become the national database for landslide data

2.2 Funding and development

Funding for the database development was obtained through the NHC Toka Tū Ake Biennial Grants programme, while hosting and staff time was funded by Auckland Council. Beca was engaged to refine the scope and develop the online tool. Development was undertaken in a series of ten two-week sprints, with testing and improvements happening in parallel. Ongoing improvements are underway in response to user needs, currently funded by Auckland Council.

2.3 Fundamental Principles

The database was built based on the following key principles defined by the steering group:

2.3.1 Unique identifiers

Each landslide has a unique identifier automatically assigned to it which never changes, allowing easy referencing. A URL for each landslide allows it to be linked from other sources.

2.3.2 One source of the truth

Landslide data can be easily entered in a single location by all the relevant organisations. An API (Application Programming Interface) is available to allow one-way information transfer from the NZ Landslides Database into other organisations internal systems in real time. This presents spatial information about each landslide which can be overlain on internal datasets such as asset locations or claims information without those commercially sensitive data being shared externally. Each landslide has a unique identifier (which is automatically assigned to each landslide by the database) that never changes. The Landslide ID can be used within organisations to link the landslide to internal information.

2.3.3 Internationally recognised data schema

To maximise compatibility with other datasets, data entry is limited to drop-down options aligned with the Hungr et al (2014) update to the Varnes classification scheme and the IAEG Commission 37 working group (Corominas et al, 2023).

2.3.4 Factual, non-confidential information

As the database is an open, shared resource, it would not be appropriate to hold private or confidential information. Instead, each record holds only factual information about the landslide and provides a unique identifier which can be referenced within organisations internal private systems. Private, commercially sensitive or organisation-specific information is held on those internal systems which reference the landslide unique identifier from the NZ Landslides Database.

2.3.5 Allow for increasing knowledge

When a landslide is first identified, it is often the case that relatively little is known about it. The database was structured to allow minimal information to be entered at first, and for additional information to be added over time.

2.3.6 Track change over time

Many landslides evolve over time. Some will re-activate and change shape or size. Others may be altered by human interventions (e.g. stabilisation works). The database was designed to record these changes without losing the history of the landslide. A time-slider allows change over time to be reviewed. This includes spatial mapping, which can be edited and added to over time, and these changes will all be tracked (Fig 4).

2.3.7 Allow landslides to be grouped (parent features)

As new information is collected, or as landslides evolve, it is common to identify that two previously mapped landslides are part of a larger feature. To manage this, each landslide can have a parent. This parent-child relationship allows small landslides to be linked to a record representing the larger feature. These links can be added at any time as new information becomes available. One parent record can have many child records, but each child can have only one parent.

2.3.8   Track all edits

To help ensure quality data, every change made to the database is recorded in a change log alongside the name of the user who made the edits (Figure 3). The history tracking described above allows a clear, documented trail of all changes (change log), records who made each change and the reason for the change (e.g. the change may be that new information became available, or the landslide reactivated and physically changed, or to correct an older error in the data).

2.3.9   Open to qualified users

Data can be added by any suitably qualified person, regardless of their organisation, once they have been approved as having the appropriate skills and experience. This allows a 'crowd- sourcing' approach to gain the maximum amount of data without compromising quality.

In general the level of knowledge and skill needed is that of an Engineering New Zealand Professional Engineering Geologist (PEngGeol) or equivalent. Users are expected to have a robust understanding of landslide classification schema, and to understand the importance of reliable quality data management.

2.3.10   No duplication

Where related (but not landslide specific) data is already held in other locations, it is not duplicated in the NZ Landslides Database. For example, borehole data already has a host in the NZ Geotechnical Database. The NZ Landslides Database instead references this data held elsewhere.

2.3.11   Allow for remediation

A common problem in urban areas is experienced when a landslide is partially or fully remediated. Landowners, worried about the stigma of having a landslide record on their property, often request that database entries relating to the landslide be deleted as they may mislead future purchasers. Allowing remedial works to be recorded enables the landslide record to be maintained while still satisfying the needs of the landowner.

2.3.12   Allow for public reporting

An unusual element of the database was the inclusion of a public reporting tool. This tool, presented as a simple online form, allows any individual to start a landslide record in the database. A screenshot of the public reporting tool is shown in Figure 1. Previously reported landslides are shown in the interface so that users can identify if the landslide has already been reported.

Figure 1. The public reporting tool showing existing reported landslides in Auckland.

This enables any individual to create a basic landslide record, represented as a single point on a map,

with key data associated with it. The record can then be expanded upon by suitably qualified users once the landslide is investigated further, or it can be marked as invalid if there are errors or inconsistencies in the record.

Once submitted, the record is summarised as a simple PDF report (with personally identifiable information removed) and automatically forwarded on to a pre-determined list of email addresses. These can be set spatially, enabling asset owners (e.g. roading authorities) to be notified of landslide reports on their network without being overwhelmed with notifications from outside their area of interest.

2.4 Database structure

The core data about each landslide is stored in the master data table, which creates one source of truth for the landslide.

Table 1. Landslide data which can be assigned to master landslide record

Data Group	Data fields	Format
0. Public submission	0.1 Reported by (email)	email
	0.2 Reported by (Name)	Text
1. Identifiers	1.1 Parent landslide	Choice
	1.2 Landslide name	Text
2. Location	2.1 Location description	Text
	2.2 Location recording method or device	Text
	2.3 Estimated error in location recording method	Choice
	2.4 X Coordinate (NZTM)	Number
	2.5 Y Coordinate (NZTM)	Number
3. Description and setting	3.1 Physical setting	Choice
	3.2 Geological Setting	Text
	3.3 Geomorphological Setting	Text
	3.4 Landslide Description	Text
	3.5 Up-Slope Catchment Description	Text
4. Movement	4.1 Primary movement type	Choice
	4.2 Primary movement type subclass	Choice
	4.3 Secondary movement type(s)	Choice
	4.4 Complexity of mass movement	Choice
5. Date and activity	5.1 Has the landslide been active in the last 1000 years?	Choice
	5.2 Landslide activity	Choice
	5.3 Velocity class / rate of movement	Choice
	5.4 Estimated date of first movement	Date/time
	5.5 Accuracy of dating method of first movement	Choice
	5.6 Accuracy of dating method of most recent movement	Choice
	5.7 Estimated date of most recent movement	Date/time
6. Shape and dimensions	6.1 Slope angle prior to landslide	Number
	6.2 Slope angle of displaced material	Number
	6.3 Angle of rupture surface (translational)	Number
	6.4 Aspect (direction of movement)	Choice
	6.5 Length along ground zone of depletion	Number
	6.6 Length along ground zone of accumulation	Number
	6.7 Maximum height of main scarp	Number
	6.8 Maximum width of landslide perpendicular to direction of movement	Number
	6.9 Maximum depth from original surface to surface of rupture	Number
	6.10 Travel angle	Number
	6.11 Estimate of landslide area (min)	Number
	6.12 Estimate of landslide area (max)	Number
	6.13 Estimate of landslide volume (min)	Number
	6.14 Estimate of landslide volume (max)	Number
	6.15 Volume/area estimation method	Text
7. Materials	7.1 Materials in landslide	Choice
	7.2 Debris type	Choice

Data Group	Data fields	Format
	7.3 Vegetation cover	Choice
8. Triggers	8.1 Primary causal triggering factor	Choice
	8.2 Other factors influencing instability	Multi-choice
	8.3 Estimated magnitude of earthquake causing landslide	Number
	8.4 Rainfall Description	Number
	8.5 Rainfall total in preceding 24 hours	Number
	8.6 Rainfall total in preceding 3 days	Number
	8.7 Rainfall total in preceding 7 days	Number
9. Consequences	9.1 Damage description	Text
	9.2 Approximate number of injured people	Number
	9.3 Approximate number of fatalities	Number
	9.4 Approximate damage cost (NZ$)	Number
	9.5 Environmental damage	Text
	9.6 Features and assets impacted by the landslide	Multi-choice
10. Legacy data links		
11. Information sources	11.1 Source of landslide information (description)	Text
	11.2 Bibliographic reference of landslide information source	Text
	11.3 Project name / number	Text
	11.4 Original database (for bulk uploaded files)	Text
12. Quality assurance	12.3 QA Person Name	Text
	12.4 QA Person email	Email
	12.5 QA level	Choice
	12.6 QA status	Choice
	12.7 Comments	Text

Further details of the structure are presented in the database manual, available online (LandslidesNZ website), including guidance on content details which are also shows as pop-up tool tips in the database. A careful balance was struck between allowing a large range of data to be recorded, and relatively simple functionality which requires fewer fields. No fields are mandatory other than a unique ID and information about when the record was created, and by who. This enables a landslide to be created when little is known about it, and for data to be added as it becomes available. This overcomes a major shortcoming of some other databases that a landslide can only be recorded once it has been investigated in detail. Further information can be added at any stage by suitably qualified registered users.

In addition to the core metadata, an unlimited number of spatial features can be assigned to each landslide. These are entered graphically and are summarised in Table 2.

Table 2. Geospatial features which can be attached to the basic landslide record. Detailed definitions of each feature type are provided in the online manual to ensure consistent use.

Feature class	Types	Typical content
Landslide features	Points, Lines, Polygons	Landslide area, zone of depletion, zone of accumulation, hummocky ground, sinkholes, springs, scarp lines, cracks, damaged structures, breaks of slope, streams, landslide dammed lakes, etc.
Corrective features	Points, Lines, Polygons	Drains, retaining walls, anchors etc.
Photographs	Points	Images
Investigations & monitoring	Points	Links to NZ Geotechnical Database boreholes etc.

An example of a single landslide mapped at a basic level is shown in Figure 3.
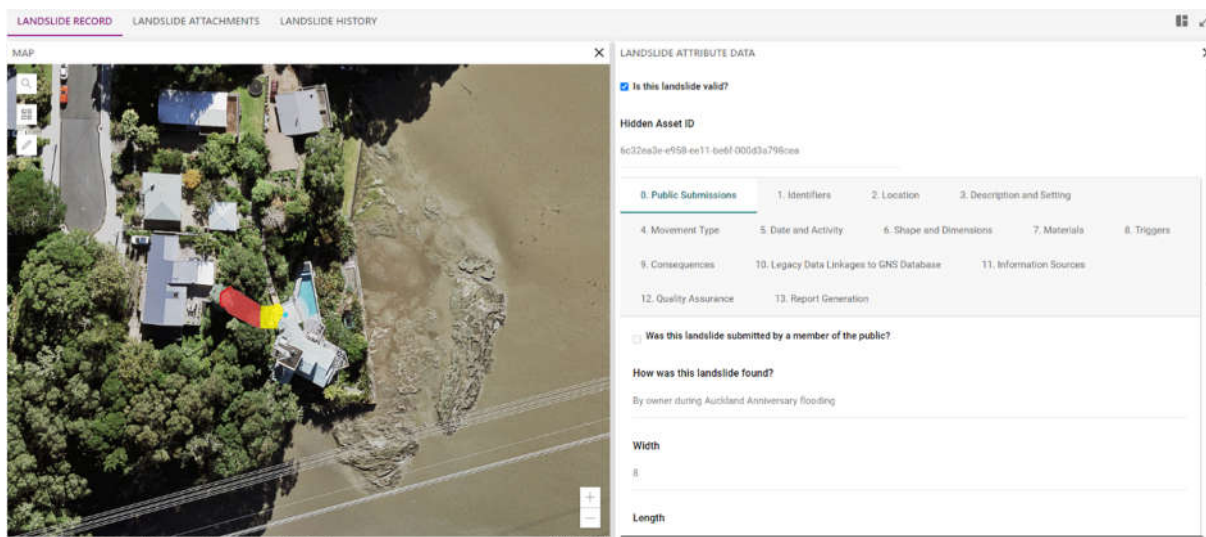
Figure 2. View of the NZ Landslide Database, showing the overview map of a single landslide. Red is zone of depletion, yellow is zone of accumulation. (OpenStreetMap / Auckland Council).
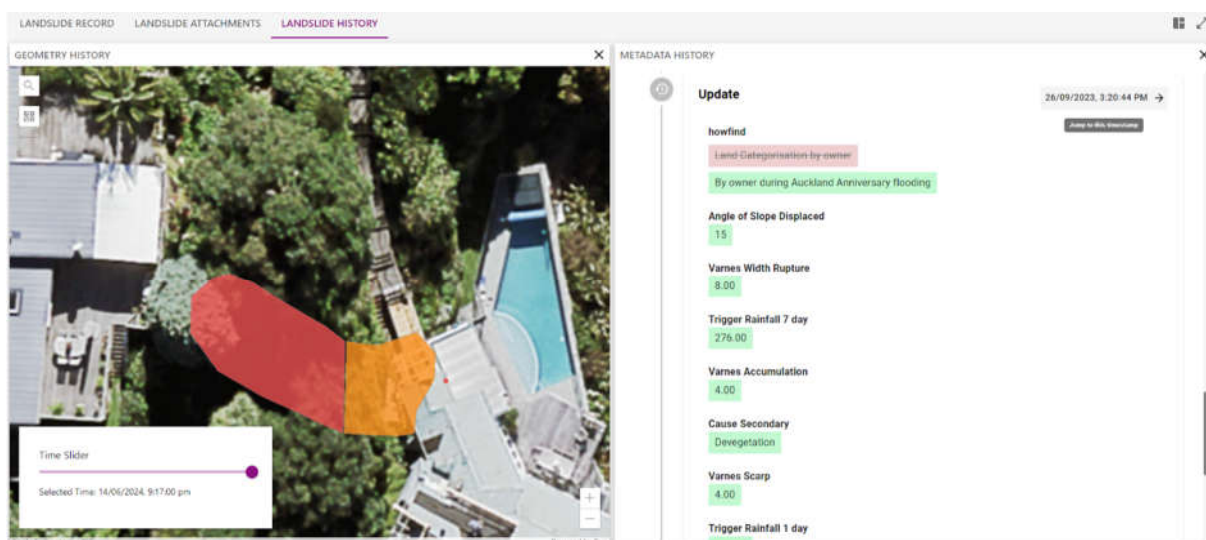
Figure 3. An example of the history log showing tracked changes. New data in fields is shown in green, and old/amended data in red. The data, including GIS shapes, can be tracked over time and rolled-back to previous versions. The time slider shows how geospatial features have changed.

3   Use in Emergency Response and Recovery

The NZ Landslides Database went live in late 2022. January 2023 was Auckland's wettest month since records began. The heaviest rainfall produced widespread flooding across Auckland on Friday 27 January, which the National Institute of Water and Atmospheric Research (NIWA) described as at least a 1-in-200-year event. On that day, Auckland's Albert Park recorded 280 mm of rain in under 24 hours and 211 mm in under 6 hours. Central Auckland experienced over 45% of its yearly rainfall in just one month, over 8.5 times the January average (NIWA, 2023). Two weeks later in the early hours of 14 February 2023, a second weather event, Cyclone Gabrielle, hit Auckland. The storm continued south, affecting many other areas along the east coast of the North Island of New Zealand. A National State of Emergency was declared on 14 February (Roberts et al, 2024). During the Auckland floods in January and February 2023 the database was fully functional and provided a critical intelligence gathering function.

Figure 4. NZ Landslide Database feed on an Emergency Control Centre display during emergency response.

A live data feed from the NZ Landslides Database provided through an API enabled a map to be shown in the Auckland Emergency Management Emergency Control Centre (Fig 4). This displayed public reports of landslides in real time. Members of the public submitted 118 landslides through the public reporting tool during the 27 January to 14 February period in the Auckland region.

Figure 5. Example NZ Landslide Database automatically generated report.

This feed greatly added to situational awareness in the control centre, enabling prioritisation of emergency response and allowing the Controller to understand which areas were worst affected.

Once the emergency response was completed, more comprehensive data collection commenced. A combination of satellite imagery, aerial photography, LiDAR, and detailed on-site assessments are being used to validate public reports, to add technical detail to these reports, and to add landslides where no report was made. Detailed assessments were made of over 250 landslide affected homes. Each of these was mapped directly into the database, and the reports automatically generated from the database to ensure consistency and improve efficiency (Fig 5).

4   Need for an international data schema

There are few international landslide databases available. A prime example is the NASA Cooperative Open Online Landslide Repository (e.g. Juang et al, 2019) (Fig 6).
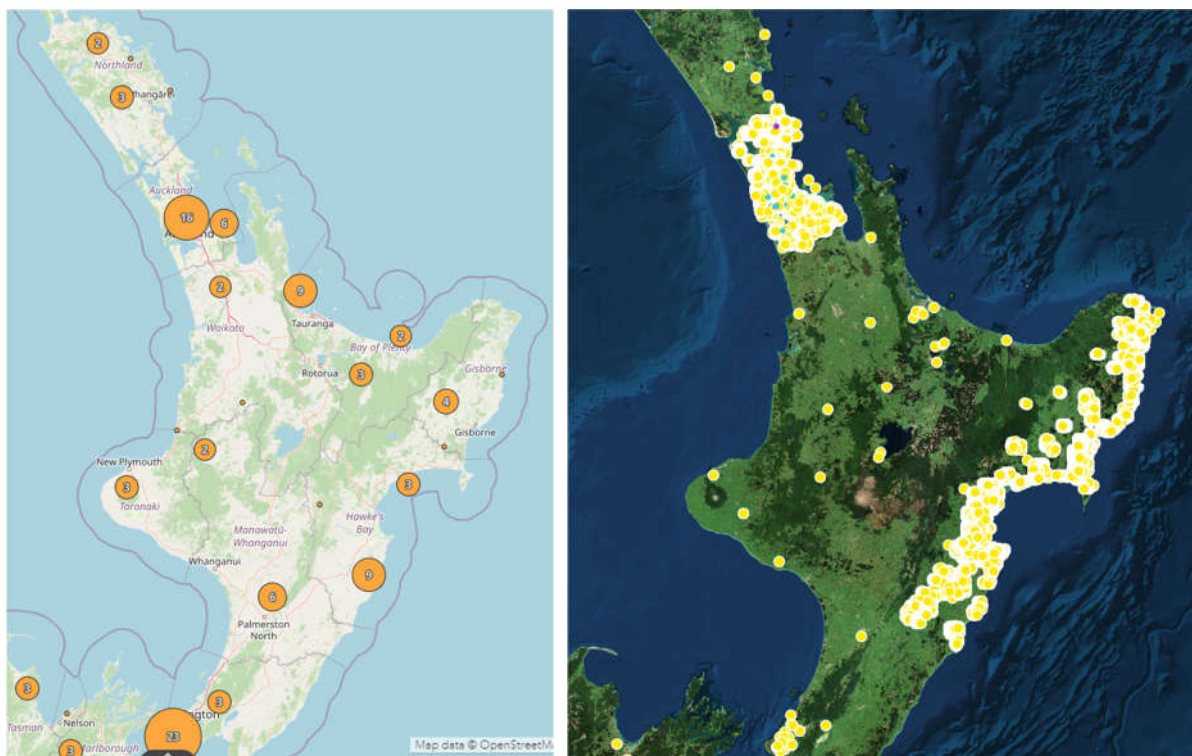
Figure 6. Comparison of the NASA Landslide Viewer (left) showing 56 landslides on the North Island of New Zealand and the NZ Landslide Database showing 150,000 landslides in the same area.

Efforts to develop landslide susceptibility and risk maps, and to eventually forecast landslides, will reply on reliable, consistent and comprehensive landslide inventories. Current approaches result in fragmented databases which suit the needs of the creators of those databases but may hamper these broader risk management needs. Experience from the geotechnical sector suggests that the benefits of these customised databases can be maintained while still allowing data to be transferred between databases by use of a standardised data transfer format such as AGS4.0 (NZGS, 2017 and AGS, 2017).

5   Conclusions

The New Zealand Landslides Database went live in 2022, and has already proved to be extremely valuable through the flooding and cyclone events in Auckland in early 2023. The database enables the crowd-sourcing of information from the public, with robust follow-up quality assurance, and the ability for input from skilled and experienced geo-professionals regardless of their organisation. This information has already proven valuable in emergency response and is showing great promise for recovery. It is anticipated that the comprehensive coverage that it provides will prove to be an extremely valuable tool in future landslide susceptibility, hazard and risk studies.

It is expected that the data collected through the Auckland flooding and cyclone events will be used to inform rainfall induced landslide modelling by GNS Science that will result in a landslide forecasting tool for use in emergency preparation (pers. comm.). However, international attempts to develop similar tools will be hindered until a consistently used data format or data transfer format is developed and adopted.

- Sally Dellow, Brenda Rosser & Chris Massey of GNS Science for their advice and support.
- The steering committee and technical advisory group members: Daniel Rodriguez (KiwiRail), Stuart Finlan (Waka Kotahi NZTA), Steve Raynor (Tauranga City Council), Susan Tilsley (Beca), Tracy Howe (University of Auckland / NZ Geotechnical Database), Claudia Harford (Auckland Council), David Barrell (GNS Science), Kiran Saligame (MBIE), Lukas Janku (KiwiRail), Phil Mourot (Waikato Regional Council) and Roger Fairclough (NZ Lifelines Council / NZ Landslide Advisory Group).

References

AGS (2007). *Australian Geomechanics Society Guideline for Landslide Susceptibility, Hazard and Risk Zoning for Land Use Planning*. Australian Geomechanics Vol 42 No 1 March 2007. ISSN 0818-9110.

AGS (2017). *Saving Time and Money: AGS Data Transfer Format*. Association of Geotechnical & Geoenvironmental Specialists. https://www.ags.org.uk/item/saving-time-and-money-ags-data-transfer-format/

Cormominas, J., Guzzetti, F., Lan, H., Macciotta, R., Marunteranu, C., McDougall, S., Strom, A. (2023). Revisiting landslide risk terms: IAEG commission C-37 working group on landslide risk nomenclature. Bulletin of Engineering Geology and the Environment (2023) 82:450. doi: 10.1007/s10064-023-03474-z

de Vilder SJ, Kelly SD, Buxton R, Allan S, Glassey PJ. 2023. *Landslide planning guidance: reducing landslide risk through land-use planning*. Lower Hutt (NZ): GNS Science. (GNS Science miscellaneous series; 144). doi:10.21420/R2X8-FJ49

Hungr, O., Leroueil, S. & Picarelli, L. *The Varnes classification of landslide types, an update*. Landslides 11, 167–194 (2014). https://doi.org/10.1007/s10346-013-0436-y

Juang CS, Stanley TA, and Kirschbaum DB (2019) *Using citizen science to expand the global map of landslides: Introducing the Cooperative Open Online Landslide Repository (COOLR)*. PLOS ONE. 14(7): e0218657. doi: 1371/journal.pone.0218657.

LandslidesNZ website. https://landslides.nz/nz-landslides-database-manual/

Lee, E.M., & Jones, D.K.C. 2023. *Landslide Risk Assessment 3rd Edition*. ICE Publishing. ISBN 987-0-7277-5801-9. https://doi.org/10.1680/lra.58019.001

NIWA . 2023. *Website news article: Auckland suffers wettest month in history*. 2 February 2023. https://niwa.co.nz/news/auckland-suffers-wettest-month-in-history

NZGS (2017). *Electronic transfer of geotechnical and geoenvironmental data*. AGS4NZ v1.0.1. https://fl-nzgs-media.s3.amazonaws.com/uploads/2022/06/AGS-NZ-V4.0.1-October-2017-3.pdf

Roberts R, Lee K, McLelland R, Brook M (2024). *The 2023 landslides and engineering geological response in Auckland, New Zealand*. In proceedings of 4th European Regional Conference of IAEG, Dubrovnik.

Rosser, B., Dellow, S., Haubrock, S. and Glassey, P. 2017. *New Zealand's National Landslide Database*. Landslides 14, 1949–1959 (2017). https://doi.org/10.1007/s10346-017-0843-6

Van Den Eeckhaut, M. and Hervás, J. 2012. *Landslide Inventories in Europe and Policy Recommendations for Their Interoperability and Harmonisation*. In: Margottini, C., Canuti, P. and Sassa, K., Eds., Landslide Science and Practice, Springer, Berlin, Heidelberg, 35-42. https://doi.org/10.1007/978-3-642-31325-7_4

THE 2023 LANDSLIDES AND ENGINEERING GEOLOGICAL RESPONSE IN AUCKLAND, NEW ZEALAND

ROSS ROBERTS [1], KUANJIN LEE [2], REBEKAH MCLELLAND [3], MARTIN BROOK [4]

[1-3] *Auckland Council, New Zealand, ross.roberts@aucklandcouncil.govt.nz*

[4] *University of Auckland, New Zealand*

Abstract

Auckland is the largest urban area of New Zealand's North Island with a population of ~1.7M. Auckland has a sub-tropical climate, with warm and humid summers which can be associated with intense rainfall. January 2023 was Auckland's wettest month since records began. The heaviest rainfall produced widespread flooding across Auckland on Friday 27 January described as at least a 1-in-200-year event. Two weeks later Cyclone Gabrielle hit Auckland. West Auckland recorded 248 mm of rain. Tragically these events resulted in six deaths in Auckland, three of which occurred when landslides hit buildings. Two volunteer firefighters lost their lives while undertaking search and rescue operations, and tens of thousands of landslides were triggered. This paper describes the storm events, the landslides they triggered, and the emergency response work undertaken by engineering geologists and geotechnical engineers.

Key words

landslides, Auckland, New Zealand, risk, emergency response

1   Introduction

Auckland is the largest city in New Zealand (Fig 1). Home to around a third of the 5 million New Zealanders, it contributes almost 40 per cent of the nation's gross domestic product. "Tāmaki Makaurau", the Māori name for Auckland, means Tāmaki desired by many. This name reflects the abundance of natural resources, strategic vantage points, portage routes, and food-gathering places which first attracted Māori, and then other settlers. Set between the Tasman Sea and the Pacific Ocean, Auckland has 3,200 km of coastline, many hills and rivers, and numerous sandy beaches backed by volcanoes of the Auckland Volcanic Field. Auckland has a sub-tropical climate, with warm and humid summers which can be associated with intense rainfall.

The geology of Auckland is relatively young. Much of the area is underlain by relatively poorly cemented Miocene sandstones and mudstones, and volcanics of the same age or younger (Fig 2). These weather relatively rapidly to sensitive residual clays and silts. In addition, colluvium deposits from reworking of residual soils and former landslides exist on slopes, while late Pleistocene and Holocene fluvial deposits occupy valley floors (Edbrooke et al. 2003).

Landslides are one of New Zealand's most significant natural hazards. Since 1760 there have been at least 1,500 deaths from landslides in New Zealand. More fatalities have occurred from landslides than from earthquakes (501), volcanic activity (179) and tsunami (1) combined over the last 160 years (de Vilder et al, 2024). A lower estimate of the national annual cost associated with landslides is NZ \$250–\$300 M/year (Rosser et al, 2017).
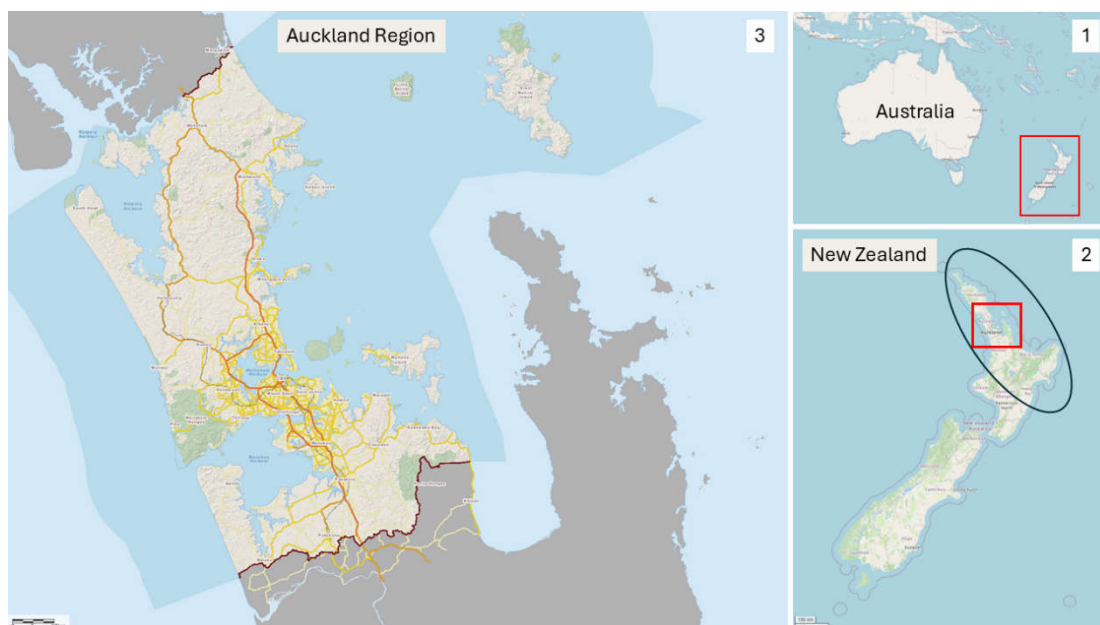
Figure 1. Location. 1.1 Shows New Zealand (red box) relative to Australasia. 1.2 Shows Auckland (red box) relative to New Zealand, with Cyclone Gabrielle affected areas in blue oval. 1.3 Shows Auckland Region with surrounding areas in grey. The damage encompased the full region (OpenStreetMap / Auckland Council).

Landslides across Auckland generally are of shallow depth (<10 m), commonly forming in the weathered soil mantle or along the soil/rock interface. Typically in this region, surface materials become saturated, decreasing effective stress and causing failure shallow landslides across more competent underlying bedrock (Palma et al. 2020). Tens of thousands of landslides can occur across a region in a single storm, causing fatalities and damaging property and infrastructure. Such events create particular challenges for disaster response agencies (e.g. Roberts 2023).
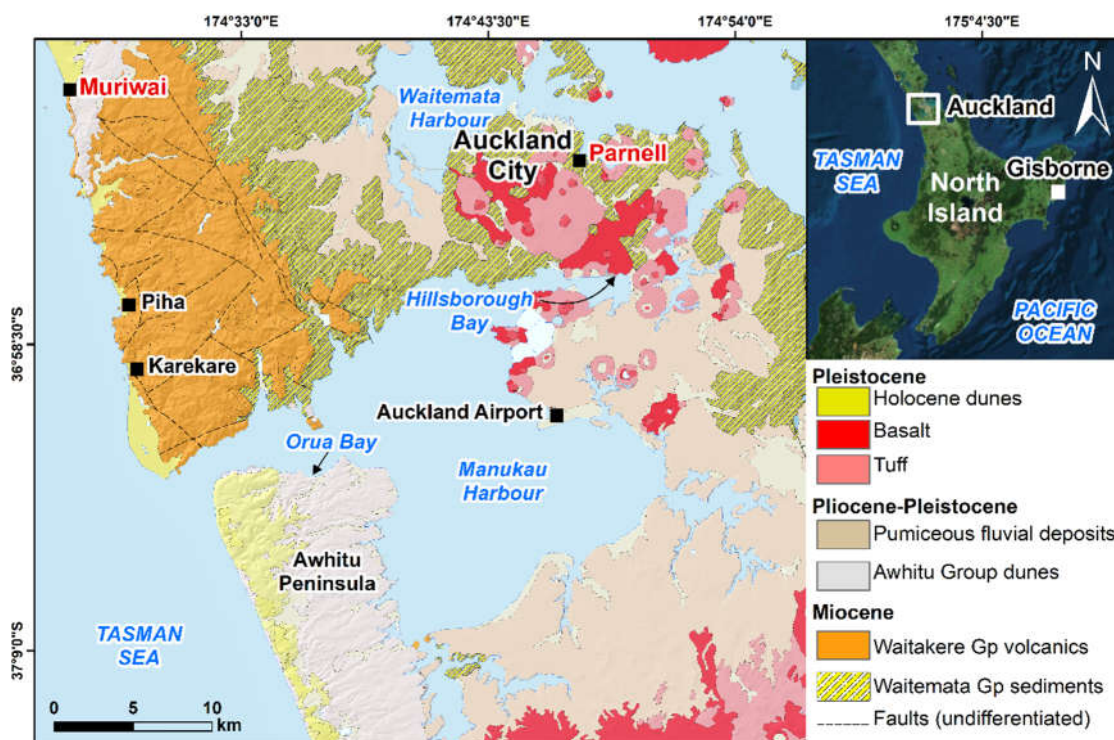
Figure 2. Generalized regional geology of Auckland with locations of fatal landslides in Parnell (January 27, 2023) and Muriwai (February 13, 2023) highlighted in red font.

2   The Auckland Flood and Cyclone Gabrielle

2.1 Meteorological summary

January 2023 was Auckland's wettest month since records began, with 539 mm recoded at a central Auckland rain gauge at Albert Park (Fig 3). The heaviest rainfall produced widespread flooding across Auckland on Friday 27 January, which the National Institute of Water and Atmospheric Research (NIWA) described as at least a 1-in-200-year event. On that day, Auckland's Albert Park recorded 280 mm of rain in under 24 hours and 211 mm in under 6 hours. Central Auckland experienced over 45% of its yearly rainfall in just one month, over 8.5 times the January average (NIWA, 2023).
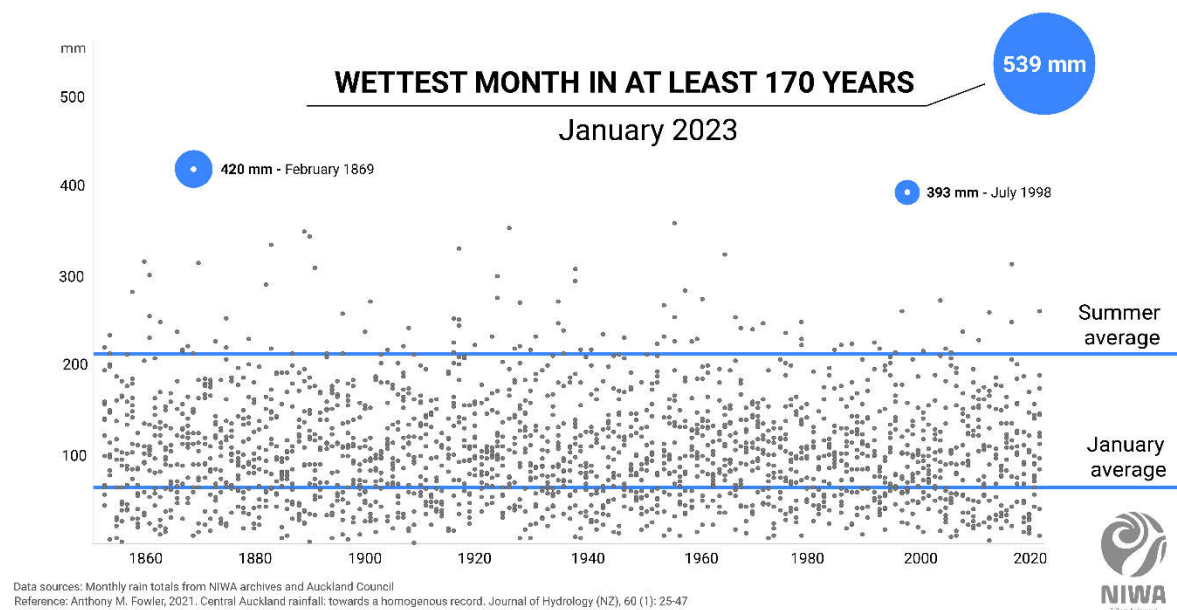
Figure 3. Central Auckland monthly rainfall (1853-2023). NIWA graphic: https://niwa.co.nz/news/auckland-suffers-wettest-month-in-history

The wet month resulted in extremely high groundwater levels. A central Auckland monitoring location at Mt Eden gave the highest groundwater level recorded since the station was installed in 1997, 2.5m above the average winter high level (Auckland Council internal data). New and reactivated springs formed across the central city, causing additional flooding.

Just two weeks later in the early hours of 14 February 2023, a second weather event, Cyclone Gabrielle, hit Auckland. West Auckland recorded 248 mm of rain and winds gusting up to 150 kph (Fig 4). The storm continued south, affecting many other areas along the east coast of the North Island of New Zealand. A National State of Emergency was declared on 14 February, applying to the six regions most impacted by the cyclone: Northland, Auckland, Tairāwhiti, Bay of Plenty, Waikato, Hawke's Bay and Tararua District. This was only the third time a National State of Emergency had been declared.
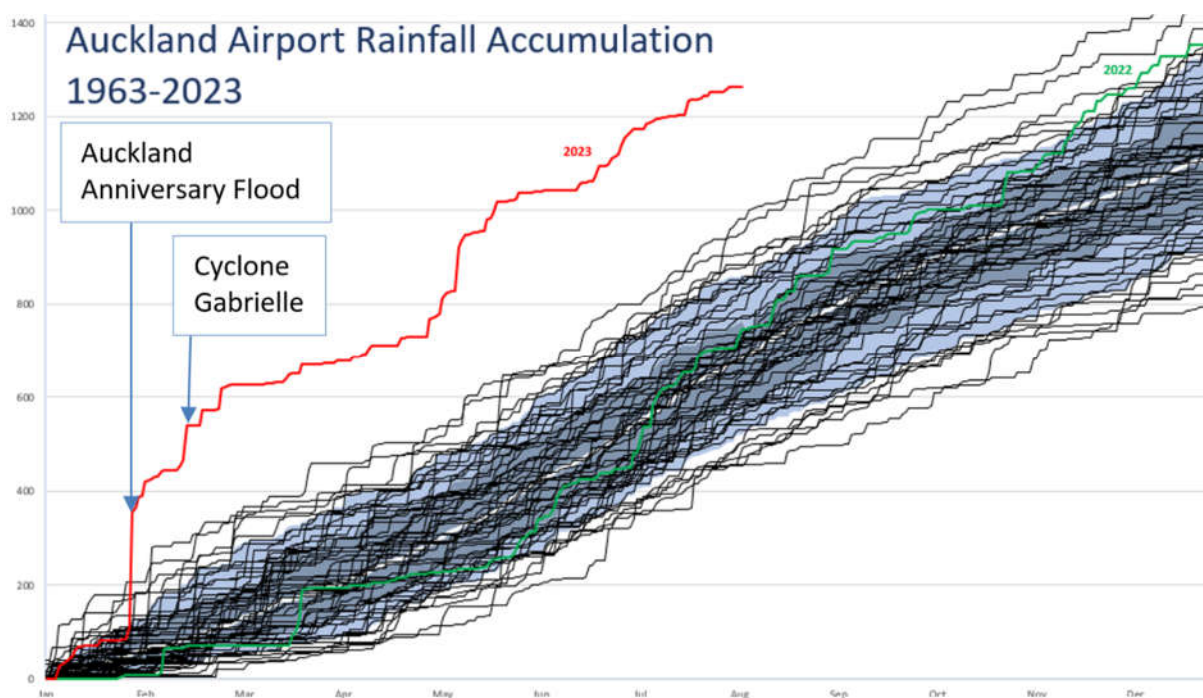
Figure 4. Auckland Airport cumulative annual rainfall. White line is 1991-2020 normal annual rainfall. Green = 2022 rainfall accumulation, dark grey shading shows 25-75th interquartile range, light grey shading shows 10-90th interquartile range. (G Griffiths, MetService, personal communication, Aug 2023)

2.2 Impacts

The intense rainfall on 27 January and 14 February resulted in thousands of landslides, including many on coastal cliffs and populated inland areas (Fig 5). While the impacts of the January storm were generally limited to Auckland, Cyclone Gabrielle also hit other regions in New Zealand. Nationwide over 140,000 landslides triggered by these two events have been mapped. Eleven people lost their lives and nearly 2,000 people were injured during the cyclone (Public Health Communications Centre Aotearoa, 2023). In Auckland the two events caused three fatalities due to landslides. One occurred on 27 January in Parnell when a landslide hit a home, and two volunteer firefighters tragically lost their lives to landslides in Cyclone Gabrielle while rescuing residents in the coastal settlement of Muriwai.

In Auckland most landslides were shallow. Highly mobile flows occurred in Awhitu Group sands where they were commonly triggered by smaller shallow rotational or translational landslides. Similarly mobile flows occurred in Waitemata Group East Coast Bays Formation residual soils where these were on longer steep hills, in one case damaging the North Auckland main trunk line near Wellsford (Fig 6.2). Translational landslides in residual soils and colluvium formed on Waitakere Group Volcanics at Karekare. Around central Auckland, hundreds of landslides occurred on the Waitemata Group East Coast Bays Formation residual soils and weathered rocks, particularly on clifftops around Manukau Harbor and Waitemata Harbour (Fig 6.1). Many houses around the coastal cliffs often have minimal "setback" (<10 m) from cliff edges (Brook and Nicoll, 2024).

Many homes were rendered uninhabitable by the landslides and flooding, with nearly 2,000 families displaced from their homes in Auckland in the immediate aftermath of the storms. Over 6,000 tonnes of waste was generated, creating a significant hazard as much of it was contaminated with sewerage. There were over 1,300 landslides on the roading network in Auckland, and an estimated $2.5 billion in private insurance claims. 8,500 vehicles in Auckland were damaged, mostly by flooding.
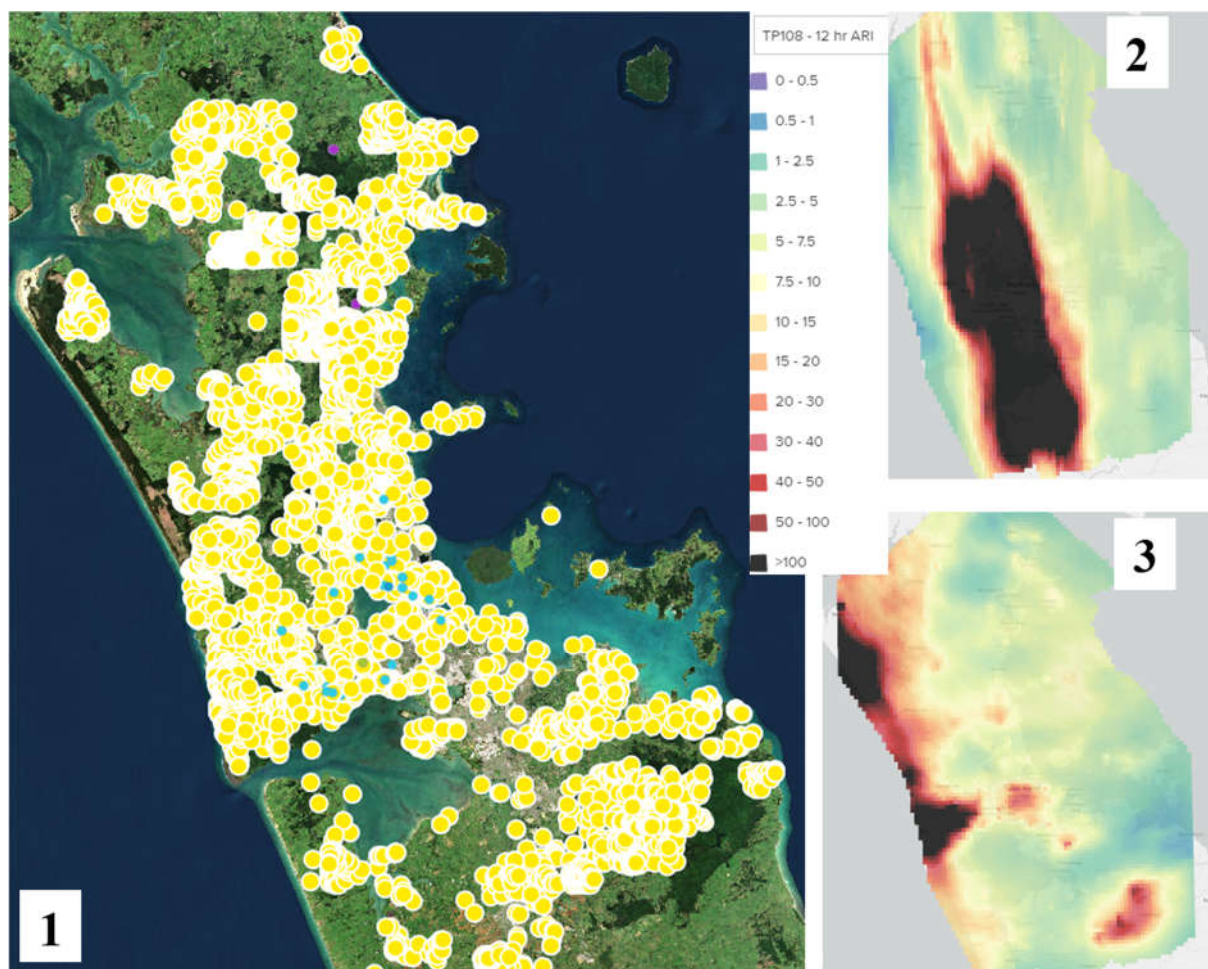
Figure 5. 1) Landslides mapped in the Auckland region after Cyclone Gabrielle and the Auckland Anniversary Floods, showing spatial distribution covering the full region (NZ Landslides Database, extracted 16 May 2024). 2) Rainfall intensity distribution for Auckland Anniversary Flood (12hr ARI maximum between 12:00 on 27 Jan and 12:00 on 28 Jan). 3) Rainfall intensity distribution for Cyclone Gabrielle (12hr ARI maximum between 12:00 on 13 Feb and 12:00 on 14 Feb). Areas with ARI>100 years shown in black.

3   Engineering Geological Response

Engineering geologists and geotechnical engineers (geo-professionals) from the public and private sectors volunteered extensive hours to serve their communities during the emergency response. In general practice in New Zealand the following stages occur, in series or in parallel, during a response:

1.   Initial response / Rapid Impact Assessment
2.   Infrastructure assessments
3.   Rapid Building Assessment
4.   Interim Use Evaluation
5.   Detailed Damage Evaluation
6.   Insurance Assessments
7.   Private Remedial Assessments

Further explanation is available in Chapter 11 of the New Zealand Geotechnical Society Slope Stability Guidance Unit 1 (NZGS, 2023). In this event, an additional phase of risk categorisation was added following a mandate from central government to identify which homes were not appropriate for ongoing occupation, and should be bought out by the government (Roberts et al, 2024).

3.1 Initial response and infrastructure assessments

When a local or national state of emergency has been declared, emergency services (including Urban Search and Rescue and Civil Defence Emergency Management) complete initial assessments on the ground and from the air, and collate information on overall impacts. Priority was given to homes where there may be casualties or vulnerable residents, then to life-critical infrastructure. These first responders were exposed to natural hazards such as landslides. To manage this risk, geo-professionals provided on-call support, acting as spotters and proving advice for any works around and near landslides.
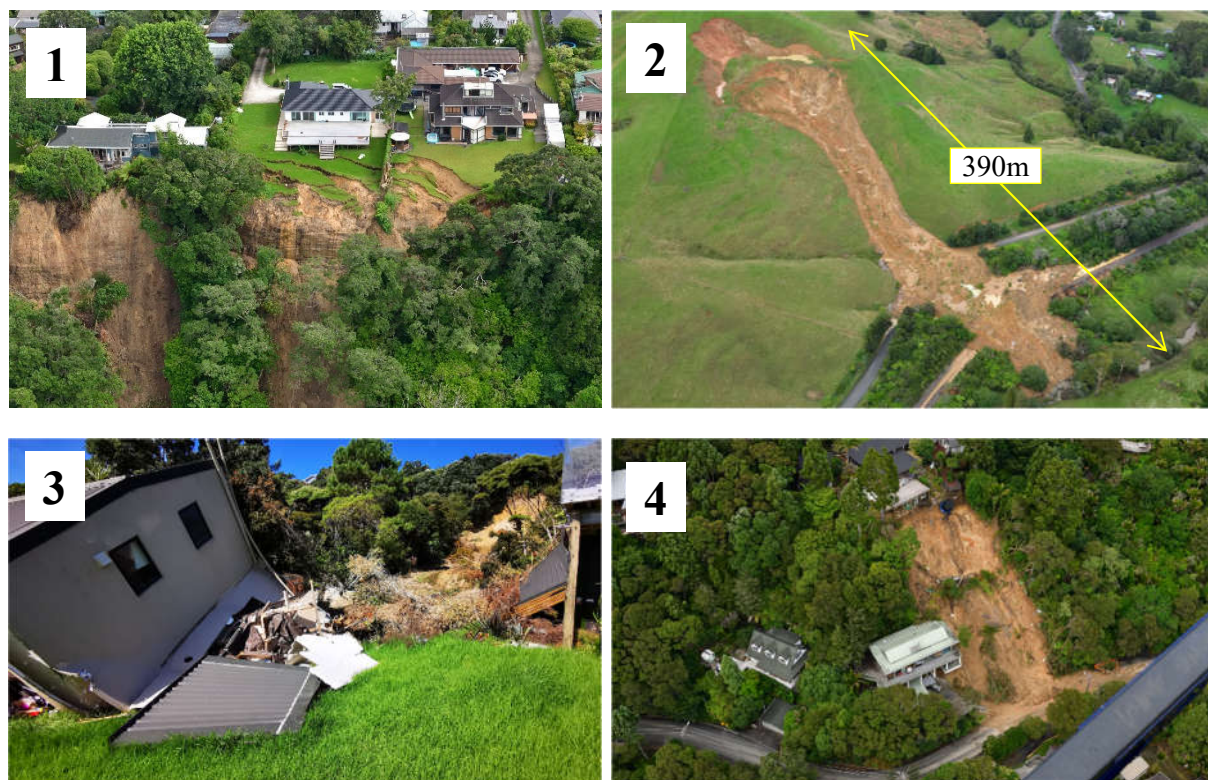
Figure 6. Examples of Auckland landslides triggered in 2023 which affected homes and infrastructure. 1) Typical cliff-top failure in residual deposits of the East Coast Bays Formation. 2) Rotational failure of residually weathered clay transitioning to a flow inundating a road and main railway line in north Auckland. 3) A two-storey home pushed about 20 m off its foundations in Muriwai. 4) Shallow translational slide common on steep slopes in west Auckland.

Initial helicopter reconnaissance (e.g. Fig 6.4) allowed the extent of the damage to be quickly confirmed, vulnerable areas identified and enable responders to focus efforts on the areas of greatest need.

3.2 Rapid Building Assessments

Rapid Building Assessments (RBA) are a brief evaluation of individual buildings and their immediate surrounds for damage, usability and hazards exposure. The goal is to assess immediate risk to public safety. The key purpose of the RBA is to determine a building is safe to occupy, land instability poses a potential risk and if the building itself poses a potential risk to people and other property. The assessment is carried out quickly (typically 20 mins per building) to allow a larger number and coverage of affected properties be able to be assessed. Placards were placed on the properties assessed. Placards are a legal notice which cannot be lawfully removed or changes without expressed permission from the building consent authority.

In Auckland, about 7,000 homes were assessed for damage and of these over 600 homes were given "Red Placards" meaning they were unable to be accessed and over 2,000 were given "Yellow Placards"

meaning access was restricted. The remainder received "White Placards" meaning that the building has suffered light or no damage and could be used (Auckland Council, 2023). Geo-professionals provided technical input to provide their opinion on geohazards and their risk to properties. These informed the decision made on the placard given. In New Zealand many geo-professionals are trained for this function, and follow guidance set out in the Field Guide: Rapid Post Disaster Building Usability Assessment – Geotechnical (Ministry of Business, Innovation & Employment, 2018).

3.3 Drone surveys, LiDAR and remote imagery

Auckland Council was fortunate to have access to skilled in-house drone operators, and to be in the middle of a LiDAR campaign using helicopter-based equipment. These were re-deployed into emergency response and collected very valuable data from the hardest hit areas.

Figure 7. Example 3D model from drone from Muriwai, collected and published three days after the landslides.

Pix4D Mapper cloud was used for 2D orthomosaic stitching and 3D model reconstruction from drone data, enabling very rapid model production and sharing. These datasets were published online (https://landslides.nz/data/) to allow free access for infrastructure providers, emergency services and others, and proved very useful in assessing geomorphology, landslide run-out and the Fahrböschung (F) angle.

Repeat LiDAR surveys were conducted in areas of greatest concern at weekly intervals to identify any ongoing movement and determine if homes at the margins of landslides, or in potential run-out impact zones, could be re-occupied by changing their RBA placard. This high-quality data was essential in supporting this high-consequence decision making.

Satellite imagery was also procured but was less valuable than anticipated. High levels of cloud cover meant that getting cloud-free images took several months. The end products were useful for retrospectively mapping 150,000 landslides across New Zealand, but were not available in time for meaningful use in response. The resolution and georeferencing was lower than images collected using helicopters or fixed-wing aircraft.

3.4 Communication with community

Communication with affected homeowners proved to be a key challenge. In Muriwai, because it was the community with the highest concentration of affected homes, Auckland Council held a series of public meetings to explain what was happening, and issued 24 newsletters between March and August 2023 (Auckland Council, 2023). An example of the type of communications that were particularly well received is available at https://www.aucklandcouncil.govt.nz/recovery-extreme-weather-disasters/Documents/8-march-muriwai-community-newsletter.pdf

When new technical results were ready, they were issued to the community in draft for feedback, and a combination of public presentations and one-on-one meetings with geotechnical specialists were held to explain the implications and gather feedback. Local community groups provided a valuable sounding board and helped liaise with members of the community that were hard to reach. The public sessions were supported by other disciplines such as experts in RBA placarding, insurance, mental health, and financial advisors. Early frustration, anger and fear was broadly alleviated by this approach, and a good degree of trust was built, although there were some exceptions.

For other areas of Auckland, communications were less consistent. Because the affected homes were widely distributed, public meetings were not very effective and it was hard to create newsletters that were relevant. This led to people feeling isolated and ignored. The most successful channel was through webinars and pre-recorded YouTube videos. These were used to explain the technical approaches and to answer frequently asked questions while providing time flexibility to the audience, allowing them to view the content at their convenience.

Later, "Recovery Navigators" were employed to provide a single point of contact for each affected homeowner. These non-technical customer facing staff were supported by the in-house geotechnical team to be able to give some technical support, and to triage questions from homeowners so they could be efficiently answered without delaying other risk assessments. This was more successful than the earlier approaches, it took some time for the Recovery Navigators to be knowledgeable enough about the process to add significant value, and some early interactions with homeowners did not go as well. Detailed, early technical training for these communications staff is essential to success. Direct contact between affected homeowners and technical specialists gave by far the best outcome in most cases, but was challenging to resource. It is recommended that in significant recovery efforts that engineers and scientists with good communication skills are engaged to undertake this role.

3.5 Building a response team

In addition to the standard response, two elements were added to the team. Firstly, in April 2023 a geotechnical advisory panel of five technical experts was engaged. Their role was to review the methodologies being used, the scopes given to suppliers, and key deliverables. They also provided ad-hoc advice which was particularly valuable on more controversial decisions. The panel was technically balanced with two geotechnical engineers, two engineering geologists, and an engineering geologist/hydrogeologist. The panel was convened as required and worked together to compile advice for the Council team.

Secondly, in May 2023 external project managers were procured. It had quickly become apparent that the scale of mobilisation needed to implement the government direction would exceed the capacity of in-house project managers, and that using geo-professionals for project management would distract them from delivering the important technical work.

4 Conclusions and lessons
4.1 Systems and processes

Local Authorities can position themselves to manage situations like these by ensuring that business-as-usual systems are designed with disaster response and recovery as part of their core functionality, and have in place the right processes to enable these systems to be scaled up.

This particularly applies to the rapid collection of data, including aerial photography and remote sensing. The ability to quickly collect, process, interpret and share this data is highly valuable. It is challenging to set up the appropriate contracts and systems during an emergency response, so these need to be planned in advance.

4.2 Communications

Clear, frequent communications explaining the technical decisions will be needed to bring members of the community on the journey as information becomes available. Having technical experts available to support communities (alongside other disciplines offering support for mental health, financial advice etc.) creates much better outcomes.

4.3 Resources and expertise

Access to the right skills at the right time can make a significant difference to the recovery effort. Auckland was fortunate to have access to skilled geo-professionals, many of whom were trained in RBA. In particular, the setting up of a Geotechnical Advisory Panel and engaging project managers added significant value.

4.4 'Gut-feel' and data-led decision-making

Many early decisions made with limited information proved to be remarkably accurate such as the application of the Fahrböschung (F) angle in Muriwai. In the immediate response rapid decisions were needed to determine which homes to evacuate through the RBA process. The extent of the seven main landslides in Muriwai were mapped, and the maximum and minimum F-angle ascertained. This was then mapped across the remainder of the affected area and each home assigned an RBA placard reflecting the risk.
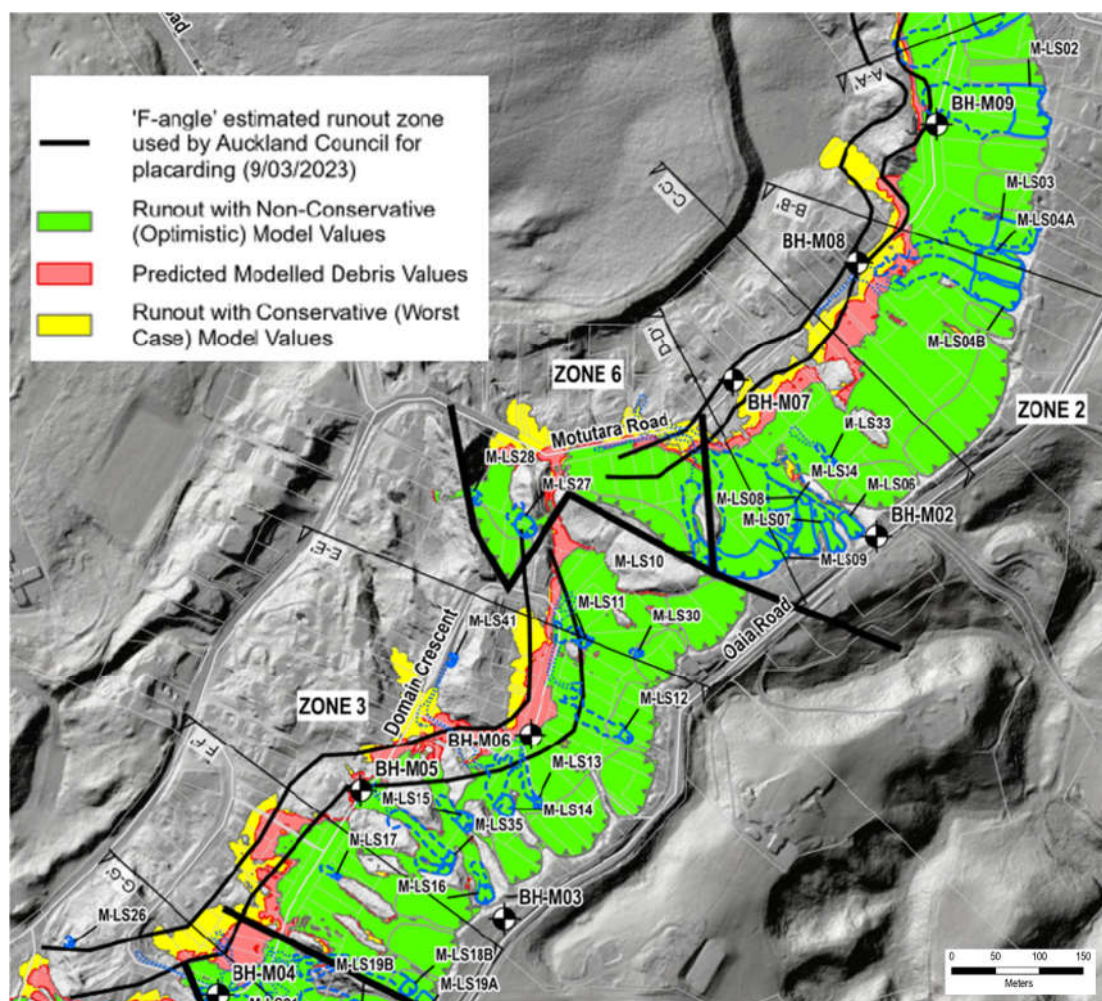
Figure 8. Best-case and worst-case F-angle (parallel black lines) mapped over one weekend shortly after Cyclone Gabrielle, compared with results of detailed RAMMS modelling (coloured zones). Mapped landslides shown in blue (GHD, 2023). Oaia Road follows the edge of the steep, northwest-facing escarpment.

Later, detailed geotechnical assessments and RAMMS modelling was undertaken. This took nearly six months but gave broadly similar results. Additional rigour provided by more detailed analyses was essential to give confidence to homeowners and politicians, but the similarity in outcome highlights the value of rapidly applied expert judgement in emergency situations (Fig 8).

Acknowledgements

References

Auckland Council (2023). *Previous Muriwai recovery community newsletters*. https://ourauckland.aucklandcouncil.govt.nz/news/2023/11/previous-muriwai-community-newsletters

Brook, M.S. and Nicoll, C. (2024). *Brief report of fatal rainfall-triggered landslides from record-breaking 2023 storms in Auckland, New Zealand*. Landslides. DOI 10.1007/s10346-024-02258-0

Edbrooke SW, Mazengarb C, Stephenson W (2003) *Geology and geo- logical hazards of the Auckland urban area, New Zealand*. Quaternary International 103:3–21

Ministry of Business, Innovation & Employment (2018). *Field Guide: Rapid Post Disaster Building Usability Assessment – Geotechnical*. https://www.building.govt.nz/assets/Uploads/managing-buildings/post-emergency-building-assessment/building-usability-assessment-geotechnical.pdf

NIWA (2023). *Website news article: Auckland suffers wettest month in history*. 2 February 2023. https://niwa.co.nz/news/auckland-suffers-wettest-month-in-history

NZGS (2023). Slope Stability Geotechnical Guidance Series – Unit 1 – General Guidance. Draft for Comment, December 2023. https://fl-nzgs-media.s3.amazonaws.com/uploads/2023/12/NZGS-Slope-Stability-Guidance-Draft-For-Comment.pdf

Palma A, Garrill R, Brook MS, Richards N, Tunnicliffe J (2020) *Reactivation of coastal landsliding at Sunkist Bay, Auckland, following ex-Tropical Cyclone Debbie, 5 April 2017*. Landslides 17:2659–2669

Pullar-Strecker T. (2023). *Website news article: Repair bill from cyclone and Auckland floods at least $9b, Treasury estimates*. https://www.stuff.co.nz/business/131883544/repair-bill-from-cyclone-and-auckland-floods-at-least-9b-treasury-estimates

Roberts R (2023) *Use of the New Zealand Landslides Database in Auckland for emergency response*. Proceedings of the 14th Australia and New Zealand Conference on Geomechanics, Cairns 2023 (ANZ2023) 1–6

Roberts R, Lee K, McLelland R, Chakravorty N (2024). *A Case Study on Reactive Managed Retreat from Landslide Risk – Lessons Learned in Auckland, New Zealand*. In proceedings of 4th European Regional Conference of IAEG, Dubrovnik.

Rosser, B., Dellow, S., Haubrock, S. and Glassey, P. (2017). *New Zealand's National Landslide Database*. Landslides 14, 1949–1959 (2017). https://doi.org/10.1007/s10346-017-0843-6

SEISMIC ZONE "KRESNA" IN SOUTH-WESTERN BULGARIA AND THE INFRASTRUCTURE PROJECTS IN THE AREA

KIRIL ALEXANDROV ANGUELOV[1], DOBRIN DENEV DENEV[2], KIRIL KIRILOV ANGUELOV[3]

[1] *Todor Kableshkov University of Transport, angelov@bondys.bg*

[2] *University of Architecture, Civil Engineering and Geodesy, dobrin_denev@yahoo.com*

[3] *University of Mining and Geology St. Ivan Rilski, office@bondys.bg*

Abstract

On April 4th, 1904, an earthquake with a magnitude of 7.9 on the Richter scale occurred on the territory of the Kresna Gorge (southwestern Bulgaria). The earthquake is a consequence of activity along a fault (Krupnishki Fault), which crosses almost perpendicularly the meridional Struma fault zone along which the Struma River flows. As a result of the earthquake, several deep cracks were formed, and the waters of the Struma River were completely drained in a few hours. At the moment, designers and builders stands the significant goal for the construction of the last highway section of the Struma Highway. The highway is built almost entirely between Sofia and the border with Greece ("Kulata – Promachonas" customs). Considering the complex seismic situation, the question about the best and safest construction remains the part of the highway near the Kresna Gorge. There are several options for the construction of this section - with a long tunnel, with short tunnels and bridges or with the construction of one-way high-speed road sections in both directions. In the following report, we will make a comparative assessment of the proposed options.

Key words

Earthquake, Struma Highway, Seismic risk, Bridge, Tunnel, Safety assessment

1. Introduction

The Struma motorway is one of the most important motorways in the Republic of Bulgaria, and it has almost entirely been constructed (from Sofia city to Kulata-Promahon), except a section of 15km (from Simitli town to Kresna town), which goes through a very complicated geomorphological structure, called the Kresna gorge (*Figure 1*). Three alternatives have been designed for going through that section: Alternative One – tunnel 15 km long, Alternative Two – speed road near the Struma River (short tunnels, bridges and open road sections); Alternative Three – eastern alternative – along the higher sections of the eastern slope of the gorge. Engineering-geological investigations have been carried out for all the above alternatives to meet the requirements of the "concept design" phase and have an environmental impact assessment. The selection of the best, economically most efficient alternative, however, proved to be very difficult.
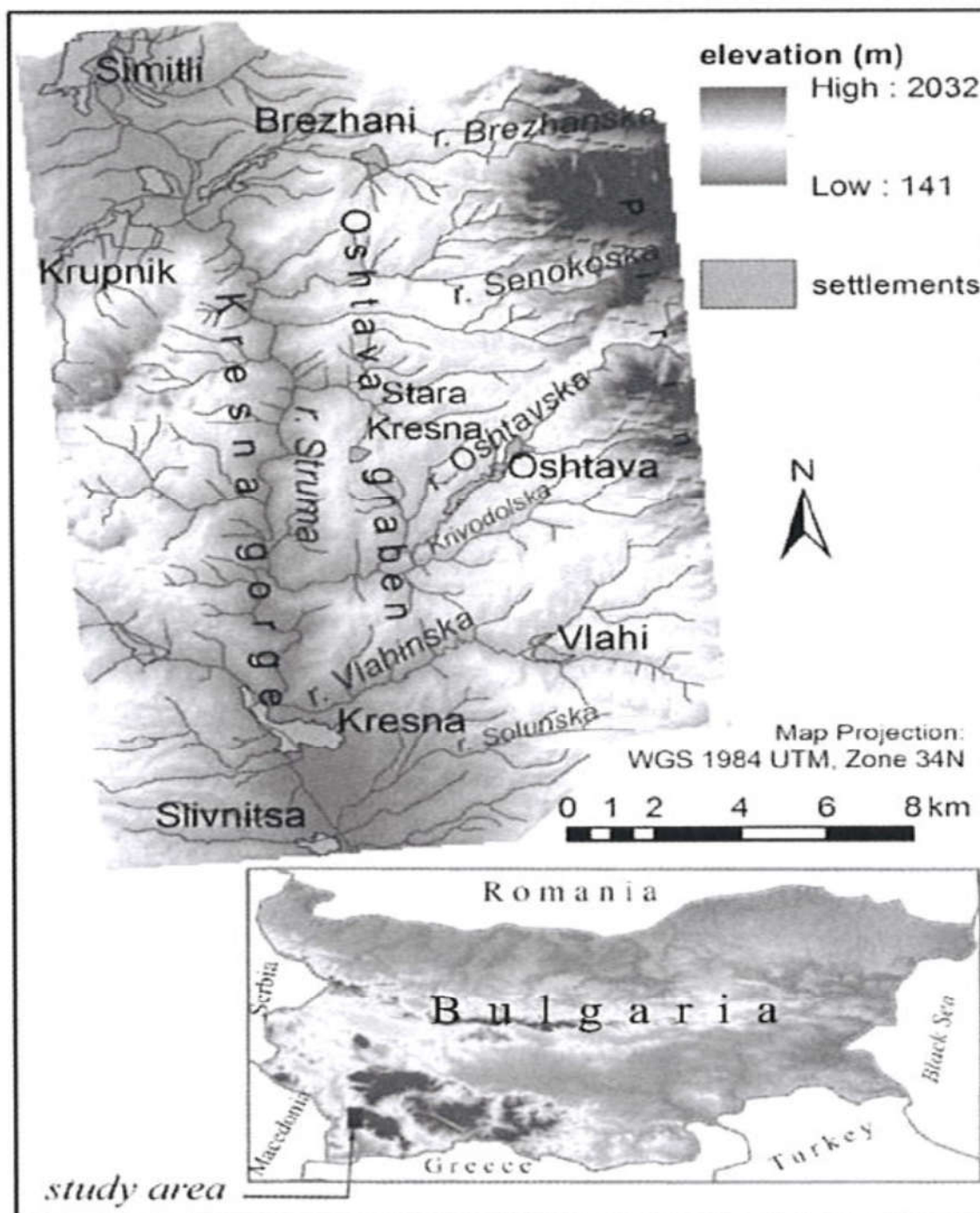
Figure 1. Location of study area in Bulgaria.

1.1 Geological conditions

The investigated section of the "Struma-Lot 3.2" motorway goes through the Kraishte structural zone, through its southern block, in particular the Belasitsa-Ograzhden block.

The rocks of the Ograzhden group compose almost entirely the Ograzhden block and the Lisiiski horst of the Vlahina block. These are amphibolites, mica gneisses and migmatites. The slopes, situated northward from the town of Kresna, are composed of the rocks of the so-called "gneiss-migmatite complex" (Marinova, Zagorchev, 1993). They are composed of biotite and two-mica gneisses and migmatites, noted by Zagorchev (1984) as the "Maleshevska" Group. It is characterized by complicated tectonic structure – almost isoclinal folds and development of zones of shearing.

After km 394+800 the route of the motorway goes into the zone of the Struma (Sandanski) graben. The graben is filled with Neogene, Plio-Pleistocene and Quaternary sediments. The lithostratigraphy of the Neogene sediments, filling the graben within the scope of the freeway, includes the Sandanski Formation and Kalimanska Formation. The Sandanski Formation outcrops as a stripe of different width between Kresna town and Gradeshnitsa village. The sediments of the Kalimanska Formation occur above it. The Kalimanska Formation is composed of sandy, alleurolites, sandy clays, irregularly alternating one with another or laterally adhering.

The Kalimanska Formation is widely distributed, according to Kojumdjgieva et al. (1982). It outcrops eastward from the valley of the Struma River. Monogenic marble breccia, composing the Ilinden Member, occurs at the Gorna Gradeshnitsa. Conglomerates in alternation with sands of 4-5 m thickness (lower sandy-conglomerate formation) follow upward in the section of the Kaliman Formation, northward from the Gorna Gradeshnitsa village. The upper conglomerate-sandy formation is also composed of breccia-conglomerates, with sandy-gravel filling. The age of the Kaliman Formation has been defined as Pondok (Kojumdjgieva et al. 1982). (*Figure 2*)

Quaternary sediments are characterized by different lithogenetic types. However, the alluvial and delluvial-prolluvial sediments are prevailing. The delluvial-prolluvial sediments (dpQ) include blocks, boulders, clays, sands, gravel) and they are observed at many locations along the route.

1.2 Tectonic structures and faults, crossing the Lot 3.2 of the "Struma" motorway

The tectonic conditions of the investigated section of the motorway are defined as a complicated geotectonic complex on the territory of the Republic of Bulgaria. The route of the highway (including tunnels) either crosses or goes in parallel, but very close to multiple faults, which refer to two groups, according to their direction: Kraishtidna group (150 -1700) and Tvardishka group (40-600).

Prevailing are the faults of the first group (Kraishtidna group), which belong to a fault bunch of nearly 5 km width, noted as the Struma fault zone. The route of Lot 3.2 of the Struma Motorway (including the tunnels at the beginning of the gorge) goes in parallel to that fault zone, and at some locations, it crosses some of the composing fault structures (*Figure 2*). In regional aspect, formation of the grabens along the river and its general direction (1700) is pre-defined by that fault zone.

The second fault group defines the crosswise fragmentation of the section. That group is most clearly shown in the Krupnishka fault zone, where the Oranovo-Simitli graben is formed (*Figure 2*)

In the section composed of the metamorphites of the gneiss-migmatite complex, the main fault is the Yavorovski fault. It is presented by a group of faults following a NW-SE direction (120-1350) and dipping predominantly to SW. It is most properly shown on the south bank of the Struma River. The fault has indicated the southern boundary of the Kresna horst, Vrablianski and Milev (1973) and it has defined the rate of vertical rise of +3.4mm/year at Yavor, and then at the Kresna village, the rate sharply falls down to +1.4mm/year.

1.3 Estimate of the seismic risk

The seismic risk is defined by the endogenous processes and phenomena in the investigated region; earthquakes and slow tectonic movements refer to the above processes and phenomena.

The first estimates of the magnitude of the bigger earthquake of the two earthquakes, which took place on 4th April 1904 are as follows: Ms=7,5 (Gutemberg and Rickter, 1954), Ms= 7,85 (Christoskov and Grigorova, 1968) and M= 7,75 (Karnik, 1969). Lower estimates were made later, presented by Abe and Noguchi (1983), who estimated it as Ms = 7,1.

Different authors came to similar estimates for the magnitudes of both the earthquakes on 4th April 1904. (for example Pacheco and Sykes, 1992; Ambraseys, 2001, Dineva et al., 2002; Papazachos and Papazachos, 2002; Meyer et al., 2002, 2007; Pavlides and Caputo, 2004; Ganas et al., 2005; Bayliss and Burton, 2007), which were much lower that the estimates of the 1950s and the 1960s.

We will not comment on those estimates of our colleagues seismologists. We would like to mention that we do not have similar data. According to Eurocode 8, the coefficient of seismicity for that region is Re= 0,32. That coefficient is extremely important for sizing all the structures and slopes.

Three (3) alternatives for the route of Struma Motorway Lot 3.2 were proposed under the above complicated geomorphological, engineering-geological and seismological conditions.

2. Overview of the alternatives

2.1 Alternative One

This alternative presents a tunnel, 15 km long, going through two highly active seismic zones (Krupnishka zone, M 7,9 – the earthquake in 1904 and the Yavorovska zone, with an expected magnitude 6,2. Faults that are almost perpendicular and/or skew to the tunnel axis as well as the very fracturing and weathering of the rocks were the reasons for rejecting that alternative at a large forum, organized by the Bulgarian Construction Chamber some time ago. Nevertheless that, it was approved in the previous year by environmental organizations (non-profit organizations).

An important factor for rejecting that alternative was the radioactivity of the rocks as well as the potential hazard of accidents inside the tunnel. Evacuation and rescue of people in such unfavourable cases inside the tunnel would be almost impossible, unless there are evacuation openings at every 100-200 m. However, the seismicity of the area around Kresna is a decisive factor. Strong earthquakes (which have already taken place in the Kresna gorge) may result in faults that will cause failure and (vertical and lateral) displacement of the tunnel tube. That will make the tunnel unusable – without an option for future repair. A similar example of an abandoned tunnel after an earthquake with a magnitude M=7,5 is the tunnel at Shenzhen, China (*Figure 3*) (*2008 Sichuan earthquake Wikipedia*). It is possible that the factors mentioned above may be the reasons for drivers to start avoiding passing through the long tunnel, which will make the investment unnecessary. With respect to the environment, the tunnel alternative is also arbitrary – the tunnel will bring a change in the hydrodynamics of groundwater flow. For example, drying of streams or changing their course and appearance in the tunnel. An appropriate location for depositing immense excavated rock masses will be needed – with the accompanying factor that some of the rock masses are radioactive. The tunnel alternative needs continuous forced ventilation and artificial lighting, which may be a decisive financial argument for not accepting it. The tunnel alternative also involves a long period of construction, the use of expensive equipment for excavation of the tunnel and complicated operation later. Inside the tunnel, traffic speed is reduced to 50-70 km/h – therefore, the road will not be a speed road – another fact that makes the investment inadvisable. The long tunnel will evidently be avoided by drivers, who have even a slight form of claustrofoby, eye-seeing difficulties and orientation, and other reasons, as well. The above means that the old road through the gorge will continue to be used with all its unfavourable consequences (such as the ones recently observed).

According to preliminary estimates (reduced estimates, in our opinion), the value of that alternative will account to 0,6 – 0,7 billion EUR. We do not know whether operational cost estimates have been prepared, but they will not be low (*Figure 2*).
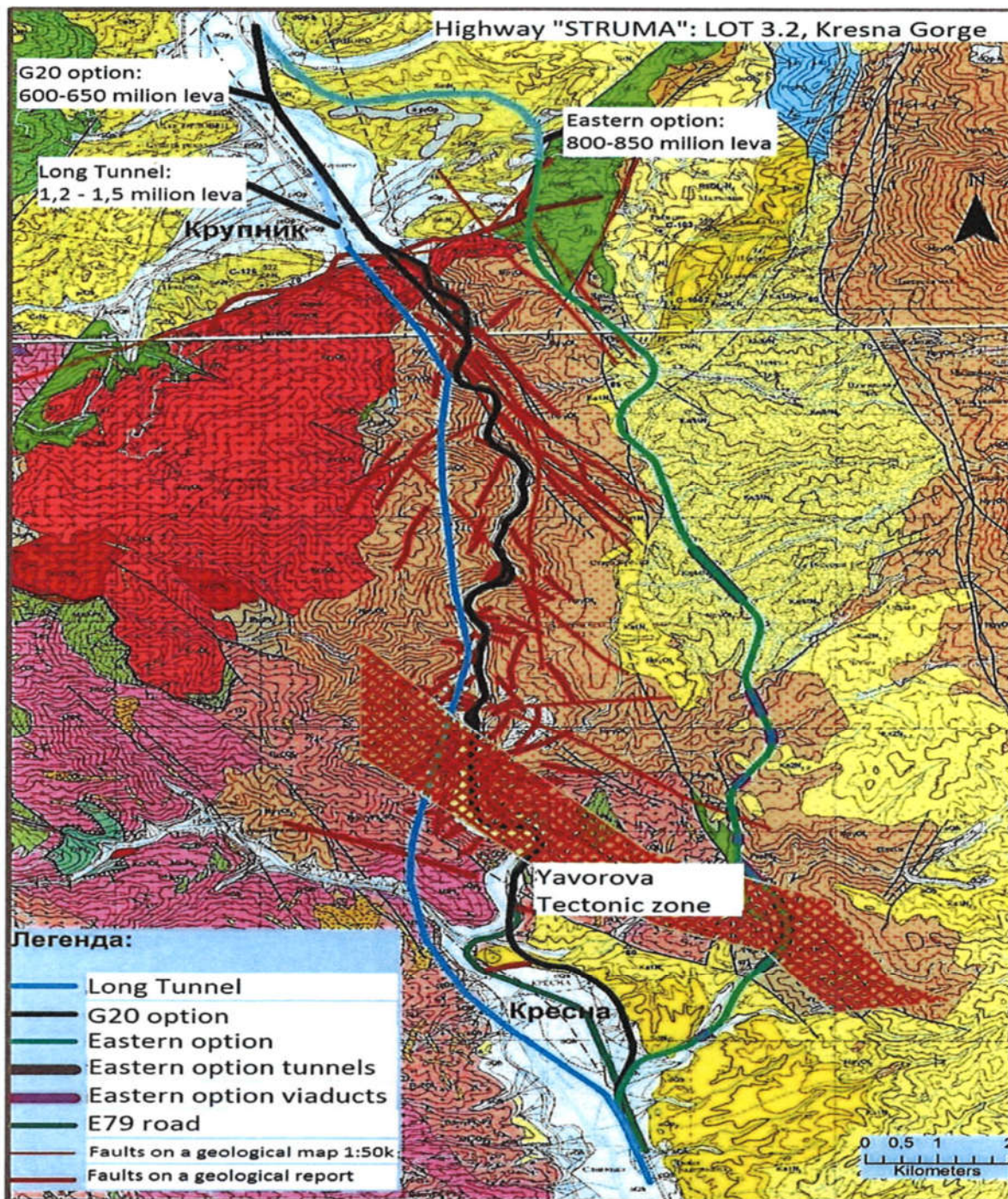
Figure 2 Priced alternatives for the Lot 3.2 of the Struma Motorway-placed on geological map

TO CLARIFY: Prices in EUR G20 option – 300-350 million EUR; Long tunnel – 0.6 -0.7 billions EUR; Eastern option – 400-425 million EUR
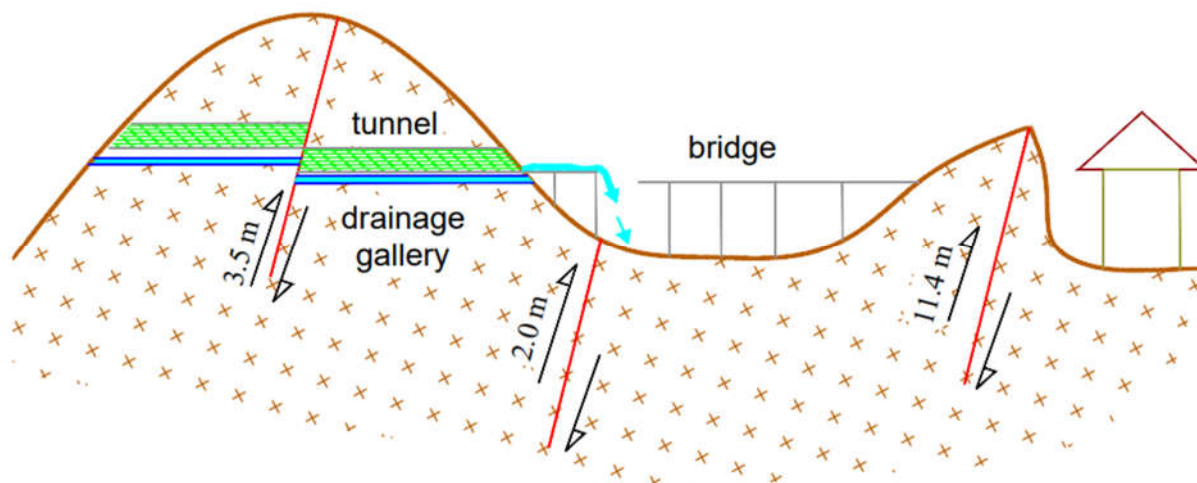
Figure 15 Abandoned tunnel after an earthquake of magnitude 8,0 at Shenzhen, China .Schematic cross-section of displacement during the earthquake in 2008

2.2 Alternative Two

This alternative presents an option to preserve the existing road through the gorge in the direction Sofia – Thessaloniki and construction of a second carriageway along the so-called "eastern alternative" at the slopes of the Pirin mountain – for the direction Thessaloniki – Sofia. Regarding that alternative, from an altitude of 350 m at Krupnik village, the vertical alignment goes up to 750-800 m altitude and then falls steeply down to the Dolna Gradeshnitsa village (elevation nearly 175 m). Therefore, the alignment involves long and critical gradients, which are not allowed, according to the standards for a high-speed road (gradient of 5.2%) between Krupnik and Stara Kresna, and between Stara Kresna and Dolna Gradeshnitsa (*Figure 4*).
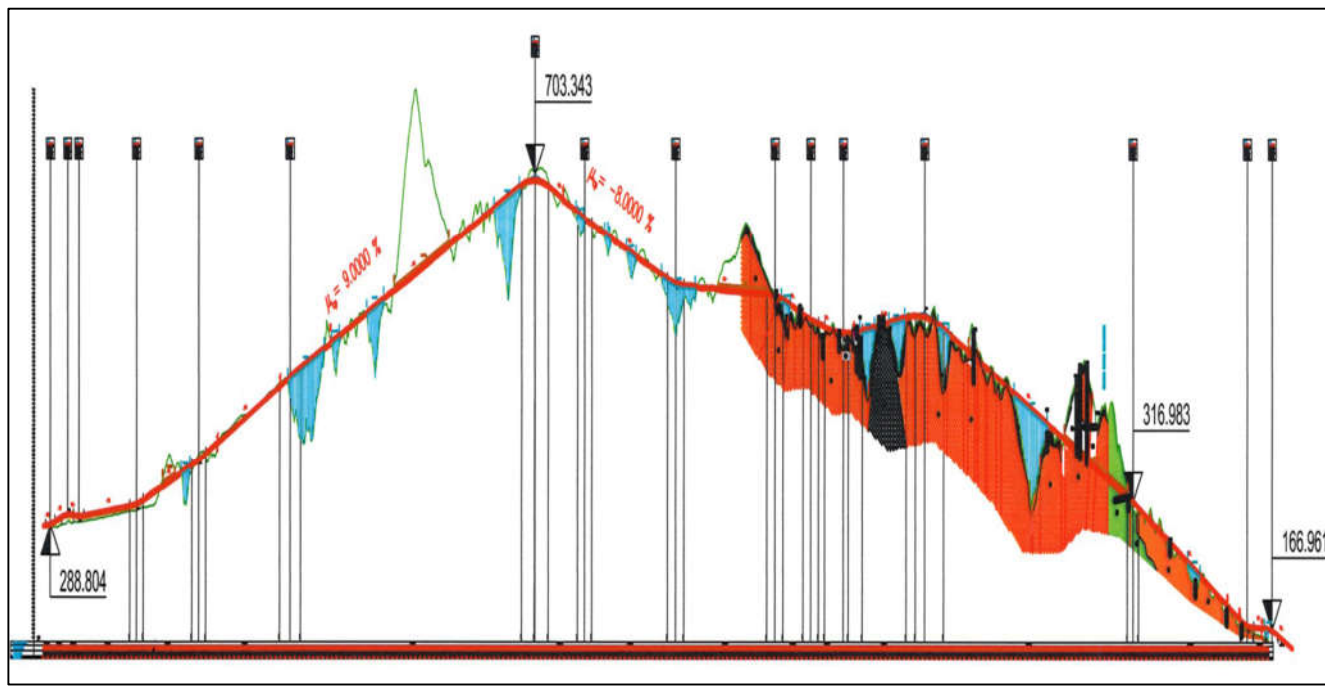
Figure 4 Summary profile of an eastern variant LOT 3.2 – AM Struma, Mx= 5000, My= 1000

The above means that a high probability of accidents during the exploitation of the road section will be incorporated into the phase of the design. In addition, this alternative involves complicated construction works within unfavorable geological conditions (the foundations would be placed in highly weathered and fractured rock varieties, where foundation of structures and arching of tunnels will be a problem). This will result in an even more complicated maintenance and repair of the system "bridge-tunnel, bridge-tunnel" in extremely unfavorable engineering-geological and climatic conditions. In addition to the above circumstances is the existence of the two seismic zones (Krupnishka zone and Yavorovska zone). It will require complicated and expensive winter maintenance – due to the high level of weathering and fracturing of the rocks and high temperature amplitude within the road section. A large bridge structure is also presented in the section – a bridge structure with the largest span in Bulgaria. The value of that alternative has been estimated at 490 million EUR.

A substantial disadvantage of that alternative is the fact that environmental issues will not recover – traffic in the gorge will continue, even with a reduced intensity, however with time it will again become the same as nowadays.

There is an additional option – two highways along the same route (i.e. achieving a full highway width), and completely liberate the Kresmna gorge from transit traffic. As far as we know, such a technical decision has not been investigated yet. However, it is evident that it will be much more expensive than the already designed one - with one carriageway.

2.3   Alternative Three

That alternative present upgrading of the existing road along the Struma River and the section immediately close to it, i.e. the construction of a speed road with four active lanes is envisaged, short bridges and seismic-proof bridges. This alternative is technically possible for construction. All the requirements of environmental scientists shall be strictly followed, namely preserving the unique landscape of the Kresna gorge, preserving the protected vegetation and animal species (their habitats, migration paths etc.) and preserving the "Tisata" natural reserve. Regarding that alternative, the highway may pass through environmentally sensitive zones with road widths, longitudinal gradients and radians of curves etc. The road gradients are minimal, there is no danger of frosting of pavement and drainage systems in winter etc. The construction of bridge structures at two levels is advisable. The alternative is defined as comparatively less expensive, nevertheless the special nature-protection measures, which will be applied in the design phase, in the construction and in the operation. Speed in the gorge may be reduced to 100 km/h, and zones for short-time recreation and platforms for nature observation may be segregated in the section between Krupnik and Kresna. The estimated value of the alternative is nearly 300 million EUR.

3.   Conclusion

Based on the analysis of the engineering geological condition and seismological factors, we propose the alternative three to be selected for financing – an alternative that goes along the Struma River valley, the most effective one from a feasibility point of view, and in addition, its construction may improve the environmental conditions in the area.

An almost completely finalized technical design is available, so probably a more detailed Environmental Impact Assessment will be needed (will be amended, respectively) to indicate the requirements of environmental scientists regarding designs for execution.

References

Abe, K. and Noguchi, S. (1983). Revision of magnitudes of large shallow earthquakes, 1897- 1912, *Physics of the Earth and planetary intenors*, 33(1):1—11.

Ambraseys, N. N. (2001). The Kresna earthquake of 1904 in Bulgaria. *Annals of Geophysics,* 44(1):95-117.

Bayliss, T. J. and Burton, P. W. (2007). A new earthquake catalogue for Bulgaria and the conterminous Balkan high hazard region. *Natural Hazards and Earth System Science,* 7(3):345-359. https://hal.archives-ouvertes.fr/hal-00299430/.

Christoskov, L. and Grigorova, E. (1968). Energetic and space-time characteristics of the destructive earthquakes in Bulgaria after 1900. *Bulletin Institute of Geophysics, Sofia,* 12:79-107.

Dineva, S., Batllo, J., Mihaylov, D., and Van Eck, T. (2002). Source parameters of four strong earthquakes in Bulgaria and Portugal at the beginning of the 20th century. *Journal of seismology,* 6(1):99—123.

Gutenberg, B. and Richter, C. (1954). *Seismicity of the Earth and Associated Phenomena.* Princeton University Press. 310 p.

Meyer, B., Armijo, R., and Dimitrov, D. (2002). Active faulting in SW Bulgaria: possible surface rupture of the 1904 Struma earthquakes. *Geophysical Journal International,* 148(2):246-255.

Kojumdjieva, E. I. Nikolov, P. Nedjalkov, A. Busev. Stratigraphy of the Neogene in Sandanski Graben,12.31982.62-81

Milovanov, I. Petrov, V. Valev, A. Marinova, I. Klimov, D. Sinyovsky, M. Ichev, S. Pristavova, E. Ilieva, B. Banushev. *Explanatory note to the Geological Map of the Republic of Bulgaria in scale 1:50 000. Map sheet K- 34-70-G (Vaksevo)* Consortium Geocomplex, 2009.

Milovanov, I. Petrov, V. Valev, A. Marinova, I. Klimov, D. Sinyovsky, M. Ichev, S. Pristavova, E. Ilieva, B. Banushev. *Explanatory note to the Geological Map of the Republic of Bulgaria in scale 1:50 000. Map sheet K-34-82-G (Berovo) and K-34-83-V (Kresna).* Consortium Geocomplex, 2009.

Pacheco, J. F. and Sykes, L. R. (1992). Seismic moment catalog of large shallow earthquakes, 1900 to 1989. *Bulletin of the Seismological Society of America,* 82(3):1306-1349.

Papadimitriou, E., Karakostas, V., TYanos, M., Ranguelov, B., and Gospodinov, D. (2007). Static stress changes associated with normal faulting earthquakes in the South Balkan area. *International Journal of Earth Sciences*, 96(5):911-924.

Pavlides, S. and Caputo, R. (2004). Magnitude versus faults' surface parameters: quantitative relationships from the aegcan region. Tectonophysics, 380(3): 159-188.

Zagorchev, I. Neogene fluviolacustrine systems in the northern PeriAegian Region – Geolocica Balcanica, 32.2-4:2002

2008 Sichuan earthquake (2024) Wikipedia. Available at:
https://en.wikipedia.org/wiki/2008_Sichuan_earthquake (Accessed: 31 July 2024).

A CASE STUDY ON REACTIVE MANAGED RETREAT FROM LANDSLIDE RISK – LESSONS LEARNED IN AUCKLAND, NEW ZEALAND

ROSS ROBERTS [1], KUANJIN LEE [2], REBEKAH MCLELLAND [3], NIKKI CHAKRAVORTY [4]

[1-4] *Auckland Council, New Zealand, ross.roberts@aucklandcouncil.govt.nz*

Abstract

New Zealand is a geologically diverse group of islands on a plate boundary with a high exposure to natural hazards including landslides. Since 1760 there have been over 1,500 recorded landslide-related fatalities in New Zealand (more than from earthquakes and tsunami combined), averaging an economic impact of at least NZ $250–$300 M/year. In January and February 2023, a series of severe storms caused flooding and triggered over 150,000 landslides, tragically killing fifteen people (six of whom were in Auckland), and ultimately costing New Zealand over NZ$15 billion in recovery effort. Historically, Central and Local Government in New Zealand held a limited role in supporting homeowners after events of this magnitude; typical involvement would be to manage imminent risk to life, while leaving private insurance to deal with remaining issues. However, in 2023 the New Zealand Government recognised that the scale and impacts of the Auckland Anniversary Storm and Cyclone Gabrielle weather events required additional support. They saw an opportunity to reduce future risk to human life by enabling a form of managed retreat. They developed a categorisation scheme for residential properties, which was implemented by local councils to classify properties by their risk level and remove people from intolerable risk. This paper describes the development and implementation of the scheme and some of the lessons learned that may be applicable to future scenarios of this scale.

Key words

landslides, Auckland, New Zealand, risk, managed retreat, policy

1   Introduction

Situated near an active plate boundary, New Zealand is exposed to many natural hazards. Auckland is New Zealand's largest city. Home to around a third of the 5 million New Zealanders, it contributes almost 40 per cent of the nation's gross domestic product. Auckland has 3,200 km of coastline, many marginally stable hills and flood-prone rivers, and its numerous sandy beaches are backed by volcanoes of the Auckland Volcanic Field. Auckland has a sub-tropical climate, with warm and humid summers which can be associated with intense rainfall.

January 2023 was Auckland's wettest month since records began (Roberts et al, 2024). The heaviest rainfall produced widespread flooding across the region during Auckland's Anniversary weekend on Friday 27 January, which the National Institute of Water and Atmospheric Research (NIWA) described as at least a 1-in-200-year event. Central Auckland experienced over 45% of its yearly rainfall in just one month, which is over 8.5 times the January average (NIWA, 2023). Two weeks later in the early hours of 14 February 2023, a second weather event, Cyclone Gabrielle, hit Auckland. The storm continued south, affecting many other areas along the east coast of the North Island of New Zealand. A National State of Emergency was declared on 14 February.

This series of severe storms triggered over 150,000 landslides, killed fifteen people (six in Auckland), and cost New Zealand over NZ$15 billion (Roberts et al, 2024). Infrastructure was destroyed, with many roads closed for month to years. Thousands of homes were damaged, and in some cases destroyed by a

combination of flooding and landslides. In the following months, many residents mobilised to demand some form of managed retreat, sparking a debate across academic and political realms (e.g., Stuff, 2023).

2   Central Government policy response

In March 2023 the New Zealand government set up a Cyclone Recovery Unit to lead, coordinate and monitor the severe weather recovery across government. This included a Cyclone Recovery Taskforce (CRT), chaired by Sir Brian Roche, which operated until February 2024 (Mitchell, 2024).

On 2 April 2023, a new Act of Parliament was passed (Severe Weather Emergency Recovery Legislation Act 2023) to assist affected communities and local authorities to respond to, and recover from, the impacts of the severe weather events. This Act enabled faster decision making through Orders in Council, which are tools used to amend existing laws. For example, an Order in Council was used to allow temporary accommodation to be built for displaced families which would otherwise have breached planning rules (Department of the Prime Minister and Cabinet, 2023).

The CRT identified that the scale of the event required a new approach to disaster recovery and risk management. Key issues included:
- The number of displaced people would have overwhelmed normal support mechanisms.
- The number of homes destroyed would have put at risk the insurability of property in future.
- Insurance payouts would not have covered the costs for risk reduction requirements, leaving people unable to leave/sell their homes while remaining exposed to an intolerable level of risk to life.

To manage these issues the Taskforce developed a non-statutory scheme to categorise residential property affected by landslides or flooding. These were announced by the Cyclone Recovery Minister Grant Robertson on 1 May 2023 (New Zealand Government, 2023).

Table 1. Categories for residential properties

Category	Definitions	Examples
1	Repair to previous state is all that is required to manage future severe weather event risk.	Minor flood damage to repair but no need for significant redesign/retrofitting.
2C	Community level interventions are effective in managing future severe weather event risk.	Local government repairs and enhances flood protection schemes to adequately manage the risk of future flooding events in the face of climate change effects.
2P	Property level interventions are needed to manage future severe weather event risk, including in tandem with community level interventions.	Property specific measures are necessary e.g., improved drainage, raising houses is necessary. Benefits accrue to property owners but some may face affordability issues.
2A	Potential to fall within 2C/2P but significant further assessment required.	Interventions may be required / possible but insufficient information to provide initial categorisation (these may subsequently move between "2" categories or to categories 1 / 3).
3	Future severe weather event risk cannot be sufficiently mitigated. In some cases some current land uses may remain acceptable, while for others there is an intolerable risk of injury or death.	In the face of enhanced climate risks the property may face unacceptable risk of future flooding. Other property could be subject to unstable land that poses an ongoing risk.

On 1 June 2023 the government announced that it would enter into a funding arrangement with councils in affected regions to support them to offer a voluntary buyout for owners of Category 3 designated residential properties, and would co-fund work needed to protect Category 2 properties. Minister Grant Robertson expressed support for a locally-led response and delegated the next steps to local councils.

The division of responsibility is shown in Fig 1.
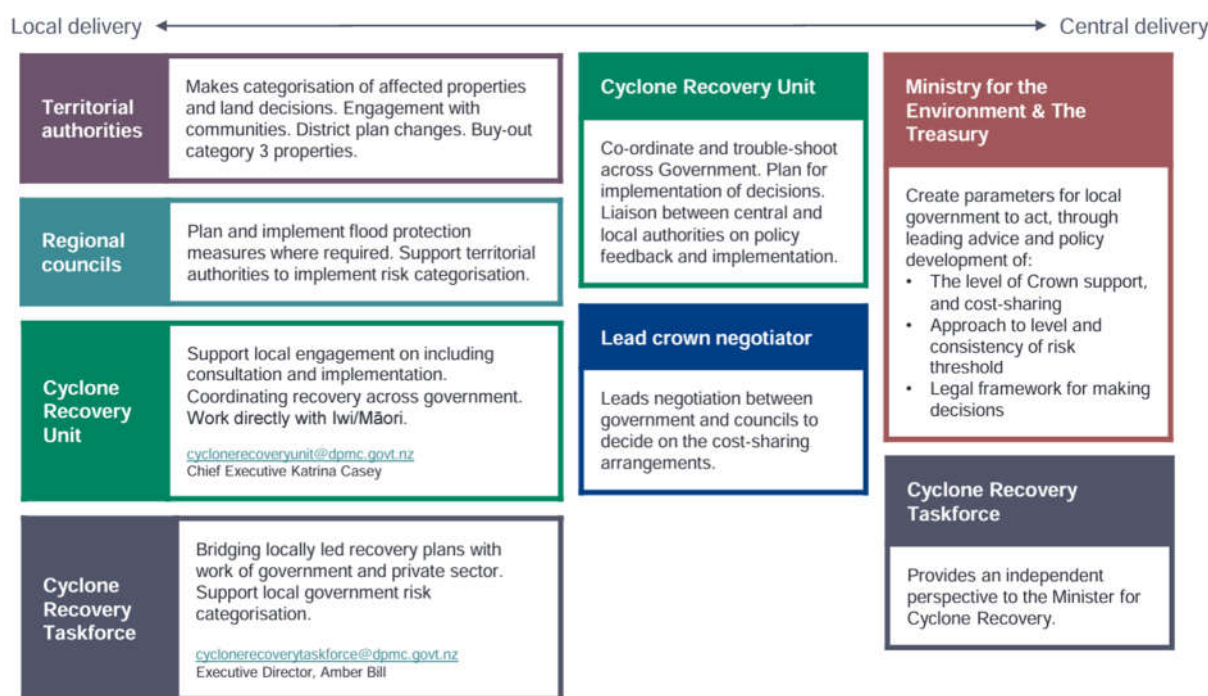
Figure 1. Roles and responsibilities set out by the CRT in the Future of Severely Affected Land (FOSAL) information pack (Cyclone Recovery Unit, 2023). Auckland Council is a Unitary Authority, so takes on the responsibilities of Territorial Authorities and Regional Councils.

3   Auckland Council response

To implement the government policy, each Territorial Authority needed to determine how to categorise the affected homes. Key considerations by Auckland Council included:

- Identifying the scale of the problem and which properties were affected.
- Creating technical definitions of the terms provided by the Taskforce to allow consistent and fair categorisation of properties. In particular, the following terms from Table 1 were challenging:
  - *"... cannot be sufficiently mitigated"*
  - *"Intolerable risk of injury or death"*
- Negotiating the split of costs for Categories 2 and 3 with Treasury (Central Government) and finding a funding source for the council component (including community consultation).
- Developing detailed policies enabling decisions to be made transparently, quickly and equitably.

3.1 Assessment of number of affected properties
In April 2023, the CRT asked for initial estimates of the possible number of Category 3 properties in Auckland to inform their policy advice to central government. At this stage there was no clearly defined policies, so Auckland Council staff used data from Rapid Building Assessments and expert judgement to establish how many homes would be extremely challenging to mitigate the risks. The initial assessment was that there would be in the order of 700 homes in this category, of which 200 would be due to landslide risk and 500 would be due to flood risk (Roberts et al, 2024).

3.2 Technical definitions
Auckland Council focused on defining two technical terms: "*Intolerable risk*" and "*Feasible mitigation*". These were required to develop the policies which would ensure that each case was assessed fairly, and to enable the scale of the response and funding requirements to be more accurately defined.

New Zealand has no formal risk tolerance settings. Despite this, intolerable risk was relatively easy to define for landslide affected properties. The Australian Geomechanics Society Guidelines for Landslide

Risk Management were already used in New Zealand and provided a relatively simple mechanism for assessing the Annual Individual Fatality Risk in a way that is appropriate for residential housing (Australian Geomechanics Society, 2007). An annual individual fatality risk of 10^{-4} was taken as the boundary between tolerable and intolerable risk, based on Table 1 of the guidelines. This boundary value had the benefit of having been used and tested in New Zealand for rockfall risk after the Canterbury earthquake sequence (Canterbury Earthquake Recovery Authority, 2011). This risk boundary value was presented to, tested by, and supported by the Independent Hearings Panel at the time (Independent Hearings Panel, 2015). It also had the benefit of being relatively easy to explain to the public and elected officials since it is broadly comparable with the risk of dying each year on the roads in New Zealand (Ministry of Transport, 2024), a risk that our society tolerates but tries to reduce.

It was more challenging to provide a technical definition for the phrase "*Future severe weather event risk cannot be sufficiently mitigated*". The first problem was deciding what counts as sufficient mitigation. Having defined a risk tolerance, it would seem reasonable to take any reduction in risk to below this threshold as having 'sufficiently mitigated' the risk. However, this fails to consider the requirements of the Building Act which could impose a higher standard. Although the Building Act does not explicitly give risk tolerances, it is suggested in the New Zealand Building Code Handbook (Ministry of Business, Innovation & Employment, 2014) that residual risk would need to be acceptable, which it defines as "*the level of risk the public is prepared to accept without further management*".

The second problem was the word "*cannot*". With the application of unlimited time and money, most natural hazard risks can be mitigated. However, this would probably not be socially or politically acceptable. To resolve this issue, Auckland Council used the "locally-led" mandate from central government to redefine Category 3 by changing this part of the definition to "*There are no feasible mitigation solutions (either property-based or community-based) that would reduce that risk to tolerable levels*". This allowed a more balanced approach to be taken, as the word "*feasible*" could encompass several factors. Auckland Council's definition of "*feasible*" for the work required to reduce the risk can be paraphrased as:

- **Expected to comply with legislative requirements.** This allowed the exclusion of potentially cheaper mitigation measures that would fail to get consent for construction.
- **Under normal circumstances would take less than two years to implement from the time of categorisation.** This avoided the risk of people having to live in a home which was exposed to an intolerable risk for a significant period of time.
- **Would cost less than 25% of the value of the property they protect.** This balanced the costs with the likely benefits, considering optimism bias in preliminary costings, construction cost inflation in a very constrained post-disaster market, and the potential that the risk reduction would not be to the level of an equivalent newly built home with the same value. Capital Value (CV) is known for all properties in New Zealand as it is the basis for local taxes, and was used in preference of a formal valuation to significantly speed up the decision-making process.
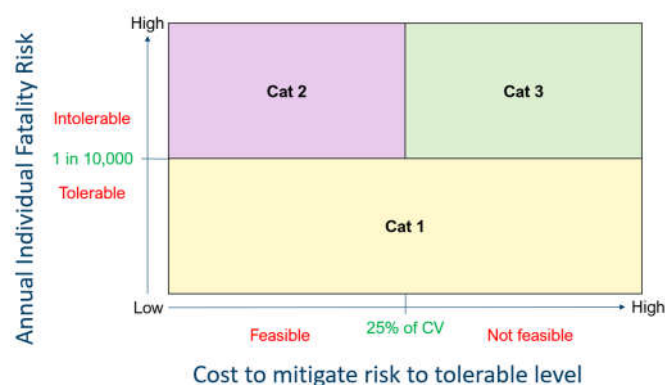
Figure 2. Graphical representation of the risk categories. CV = Capital Value of the home.

A range of options were presented to elected officials. These options included costs ranging from 10% to 75% of the value of the property protected were presented. The benefits and risks associated with the various options were discussed in depth, and the policy settings described above were developed from these debates. These definitions allowed a relatively simple decision-making process by comparing the outcomes of a risk assessment and feasibility-level design for mitigation costs (Fig 2).

3.3 Policy development

A clear policy was written to ensure that people were treated fairly, and that decision-makers have endorsed the process through which individual decisions are made. The overarching objective was "*to support Aucklanders to voluntarily relocate from residential housing situations on properties that pose an intolerable risk to their lives*". The terms were guided by the following considerations:

- **Effective** – the speed and uptake of buy-out to remove the intolerable risk to life posed to households from their property.
- **Affordable** – the amount of funding available across the number of properties that need to be purchased to remove intolerable risk to life. Affordability assumptions and scenarios have been used to help make an assessment against this criterion as a high level of uncertainty exists.
- **Fair and consistent with policy intent** – our legal obligations to be fair and for the scheme to be consistent with the stated policy intent.
- **Equitable** – scheme equity for those most in need and those who fund the scheme (Auckland Council, 2023a).

3.4 Negotiations

The anticipated local government cost for recovery in Auckland was NZ$2 billion, making it a very significant cost relative to the annual budget of $3.7 billion. The negotiated agreement allowed for over $1 billion contribution from central government with the remaining funds provided by Auckland Council (Auckland Council, 2023b). Key elements funded by central government were:

- 50% of the cost of buying the Category 3 homes ($774 million total)
- 62% of the cost of implementing Category 2C risk reduction measures ($820 million total)
- 79% of the cost of transport recovery costs ($390 million total)

Significant costs remained with Auckland Council including all costs associated with assessing risk, identifying impacted or at-risk properties, transaction and demolition/deconstruction costs, and ongoing operational cost associated with the land. These were consulted on with the public and approved in the Annual Budget.

3.5 Property assessments

In many cases where properties were subject to both landslide and flooding impacts, property assessments involved both flooding assessments and landslide assessments. The focus of this paper covers landslide assessments only. Because of the nature of the landslide risk, which generally comprised small landslides affecting one or a small cluster of homes, risk assessments had to be undertaken at an individual property level (Fig 3). A balance needed to be struck between accuracy and speed. A swift outcome for owners was crucial. Many affected residents were suffering significant financial and mental health challenges, either living in a potentially risky location or being displaced from their home and community (although some government support was available). However, accuracy was also important; the assessments would have significant cost implications and affect the lives of the homeowners for years to come. To balance these competing demands a two-stage process was set up whereby properties that were clearly not subject to intolerable risk could be identified through a desk study, while resources could be diverted towards the more detailed studies required for riskier properties.

Homeowners who had their properties assessed in the Rapid Building Assessment stage of the response were asked if they wanted to be considered in the voluntary buy-out process. Media involvement through published news articles inviting homeowners to register increased awareness of the categorisation scheme and insurance companies sent letters to their customers. Affected homeowners were asked to

submit information through a Survey123 online form with GIS capabilities. This form allowed rapid collection of information about affected homes, their owners, and the damage. The ability for owners to attach photographs, videos, and reports was particularly useful in the desktop assessment process.
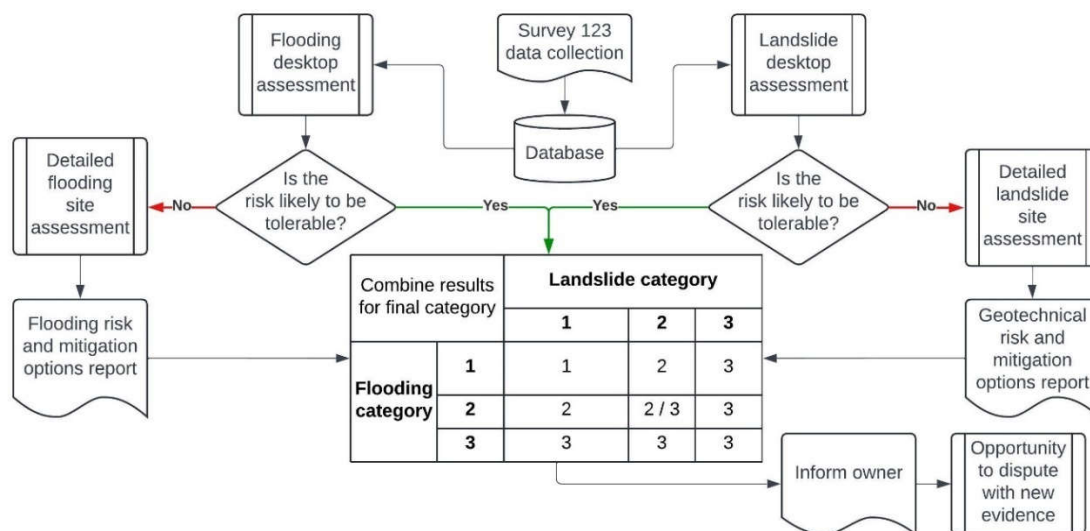
Figure 3. Process to assess final risk category.

The form was operational from 14 June 2023 and within two weeks over 800 submissions were received. By the end of 2023 this increased to 2,385. The property categorisation scheme is set to conclude on 30 September 2024, when there is predicted to be between 3,000 and 3,500 applications submitted (Fig 4).

Submitted data was extracted for analysis, initially into Microsoft Excel and later into a SharePoint list where the results of detailed assessments could be added. In the case of multiple submissions, each property has a unique identifier separate from the Submission ID that ensured management of information entered through duplicate entries. In later stages of the recovery this process is being transitioned into a fully featured Customer Relationship Management (CRM) platform to enable better case tracking and integration into other council systems.
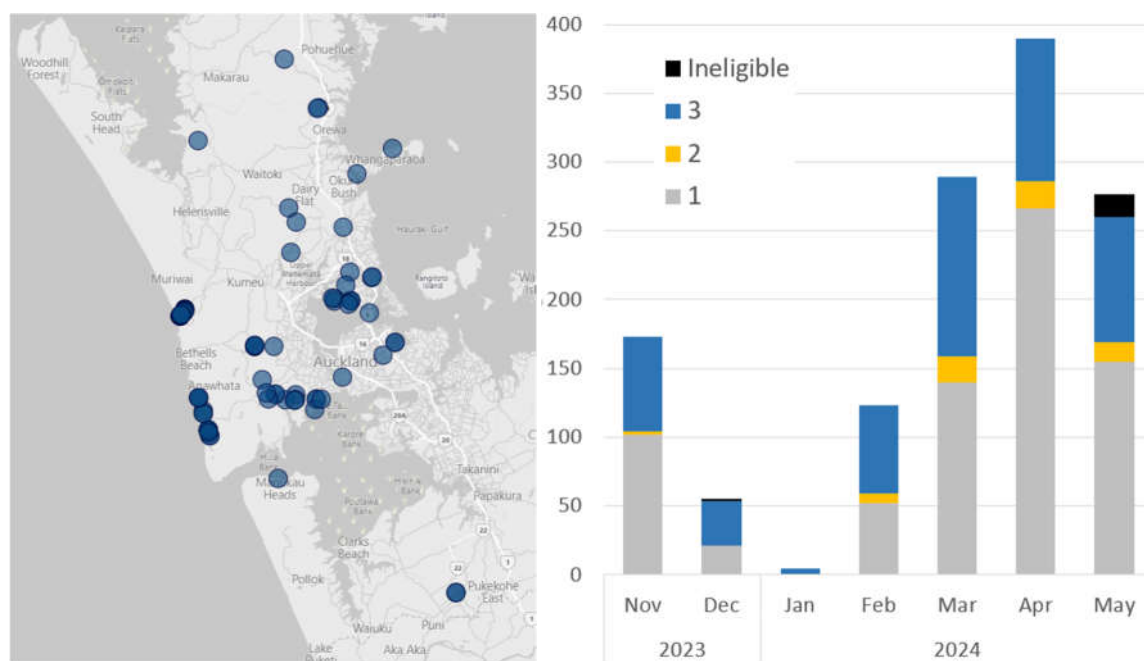
Figure 4. Left: Map of properties assigned Category 3 for landslide risk (to mid-May 2024). Right: rate of progress assigning categories (combined flooding and landslide risk). By the end of April 2023, 1,287 categories had been assigned to homes. A total of 900 Category 3 homes are forecast.

For properties that needed a detailed landslide risk assessment, Auckland Council engaged a panel of nine local supplier consultancies. A standardised reporting template was developed for them to use along with incident-specific guidelines for the application of the AGS2007 methodology to help deliver consistency between assessors. Peer review was undertaken in Australia to reduce the burden on local suppliers who were already stretched in the emergency response. The reporting template was also made freely available to the public should they wish to get alternative advice (Auckland Council, 2023c). Training was provided to these geotechnical suppliers at project initiation and repeated approximately six months later as a refresher and to build upon lessons learned. Input from the authors of AGS 2007 guidelines was also gathered as part of the refresher exercise.

The assessment process in the west coast communities of Muriwai, Piha and Karekare was carried out differently in that initially an area-wide lens to the risk assessment was adopted as opposed to the property-specific approach taken for majority of categorisation scheme applications . This was due to the large number of homes affected (many of which were evacuated and therefore vulnerable to looting), the fatalities that occurred, and the severe damage to roads and other lifeline utilities. Strict cordons were placed around these communities limiting access these areas. As owners were unable to easily get access to geotechnical advice, an area-wide risk assessment was undertaken on their behalf.

4   Conclusions and lessons

4.1 'Gut-feel' and data-led decision-making

Many early decisions made with limited information proved to be remarkably accurate. For example, the initial estimate that there would be about 700 category 3 homes, made before policy had been developed or detailed site assessments had been started, appears to be broadly correct. Best estimates (as of May 2024) range from 650 to 900 homes.

4.2 Policy and policy development

The clearly documented policy (Auckland Council, 2023a) was valuable in guiding and justifying decisions made throughout the process of categorisation. As a non-statutory form of managed retreat without underpinning legislation, having these rules clearly set out and approved by the appropriate political body significantly reduced the risk of scope creep and disputes.

The evolution and development of policy after the disaster introduced several challenges. The methodology initially used in Muriwai, Piha and Karekare only evaluated the risk and did not quantify the cost of mitigating the risk. This was because at the time these west coast community areas were being assessed, it was not Auckland Council's role to complete this. Thirdly, due to categorisation decisions being issued on the cumulative risk consequences from both flooding and landslides, alignment of assessment programmes and outcomes between different technical teams proved challenging in communicating expected timelines for assessment completion to homeowners. Once the policy settings changed, additional work was required to assess mitigation costs. This could have caused serious delays if the underlying approach Auckland Council had taken had been incompatible with the central government policy. This was avoided by working closely with the CRT. By helping guide their direction the risk assessment approaches already commenced in the west coast communities were continued and the definitions given by the government were compatible, meaning there was no need to re-do any of the risk assessment work.

In the response to the weather events of 2023, it took approximately six months to develop policy, negotiate funding, develop systems, and fully implement a process for managed retreat. Figure 4 shows that the first Category 3 homes were formally categorised in November 2023, eight months after the disaster. The technical process of undertaking the assessments can take only a few months if a system is set up and functioning, although more complex cases will always take longer. Similar properties could be categorised much more quickly in future events if appropriate advanced planning and policy work

has been completed, and data management systems and structures are in place to track and manage risk assessment cases.

4.3 Communication and evolving opinions

Communication with affected homeowners proved to be a key challenge. In Muriwai, because it was the community with the highest concentration of affected homes, Auckland Council held a series of public meetings to explain what was happening. 24 newsletters were issued by Council between March and August 2023, which were well received by the community. A similar approach was taken in Piha and Karekare. For other areas of Auckland, communications were less consistent. Because the affected homes were widely distributed, public meetings were not very effective and it was hard to create newsletters that were relevant. This led to people feeling isolated and ignored. The most successful communication channel was through webinars and pre-recorded YouTube videos.

The opinions of many homeowners changed, sometimes multiple times, through the year. The majority of these were initially adamant that they would never leave their home, and over time changed their position. This was most apparent in Muriwai, where the frequent detailed technical communications to the community and with individuals helped them to understand the risk. In other areas where communications weren't so detailed, the transition from rejection to acceptance was less successful.

4.4 Timeframes

The most commonly asked questions in response and recovery were about timeframes. Homeowners wanted to know when information would be available, and when decisions would be made. From the experiences in Auckland, four main lessons stood out.

1   In an emergency response tasks takes longer than usual. Even with a clear plan and good management, delays will occur.
2   Technical staff will often apply business-as-usual thinking, giving promises that in the circumstances they cannot meet.
3   If policy isn't defined in advance, or is altered through the recovery, timeframes will change. When this happens it is essential to communicate this quickly and widely. The community will find this frustrating, and it may be seen as a breach of trust, but it is better than having to justify a delay later.
4   There will be significant pressure to resolve all issues quickly. However, it is much better to under-promise and over-deliver. The impact (particularly financial and on mental health) for the community of a series of broken promises on timeframes should not be underestimated. It may also result in a loss of trust in the technical outcomes.

If in doubt, it is recommended to double any estimates before communicating this to the community, and to be transparent about uncertainties. Saying "I don't know" in a public meeting is hard but earns trust. Regular updates and explanations around programme constraints assisted in alleviating worry.

4.5 Data and reporting issues

In a large-scale emergency it is vital that data is managed sensitively and carefully. There will be many problems to manage, and without robust and reliable data sources there is a serious risk that cases can be lost or forgotten. Some of the data issues encountered are summarised below:

1   Public submissions will vary significantly in quality and detail. A plan to fill in the gaps for people who can't (or won't) engage through defined channels is essential. These must consider the range of needs in the community, such as the need for interpreters or dealing with people who are not capable of managing their own affairs.
2   Reporting tools will be used in ways you might not envisage. Auckland Council's Survey123 tool was used by some people to request further information. Others made multiple submissions, sometimes to add new information and in some cases to raise the profile of their case seeking a faster resolution. This meant that there were more submissions than there were affected properties. Some included very specific requests which the system wasn't set up to follow up on.
3   There is not a one-to-one relationship between people and homes. Care needs to be taken to set up a database to reflect this. Auckland Council's database was set up to have unique datasets for each

home, which best aligned with the government policy settings. This became problematic where there were multiple parties involved (e.g. a landlord and tenant) or where people moved house during the process. Eventually Auckland Council migrated to a fully-featured CRM tool that could deal with more complex data relationships.

4   Careful decisions need to be made about data governance and security. There will be an obligation to keep personal information private while sharing other information, and for data that is held to be kept on record in perpetuity. Some tools are flexible and quick, but are not ideal long-term data repositories and may have limitations around security and quality assurance.

5   Visibility and transparency between datasets and different recovery teams is key to minimise time querying reporting status and progress to both internal and external stakeholders, and ensure each discipline can prioritise the completion and review of assessments over information-gathering.

Best outcomes can be achieved when existing business-as-usual systems can be scaled up for use in emergency situations. New systems developed in response can be faster to align with new policies, but will cause problems later. Agencies involved in emergency response and recovery should build appropriate functionality into systems before events occur. This should include the ability to rapidly add many additional users, including from external agencies, to support the recovery.

4.6 Systemic gaps and issues
It is apparent from the need to create the categorisation system in the aftermath of a disaster that New Zealand's approach to natural hazard risk management has gaps. For example, there are cases of individuals whose homes are severely damaged (or at risk), but are not eligible for buy-out because the risk to life is not intolerable. In some of these cases the insurance payout for the damage is not sufficient to cover the costs of the mitigation, and the homeowners are unable to borrow additional funds to do the work because banks will not lend on these homes. These owners are trapped in homes they can't afford to fix, but are unable to sell, insure or remortgage. Further work is needed to identify and investigate these gaps, and to determine how people in these situations can be supported in a way that is fair and equitable for them and other members of society who may be providing the underlying funding, for example through taxes and rate payments.

4.7 Reactive managed retreat is achievable in recovery
Experience in Auckland shows that in the aftermath of a disaster, managed retreat can be achieved, and may well be called for by communities. For this to be implemented effectively it is essential that there is a clearly defined and easily understood policy explaining how decisions will be made. Clear, frequent communications explaining the technical decisions will be needed to bring members of the community on the journey as information becomes available. Having technical experts available to support communities (alongside other disciplines offering support for mental health, financial advice etc.) creates much better outcomes.

New Zealand can be better prepared for managed retreat in future by continuing work started under the last government to develop cross-party consensus, and matching legislation, building on Action 4.1 of the National Adaptation Plan (Ministry for the Environment, 2022). An important debate needs to be held as a nation to determine what our risk tolerance is, and how much we are prepared to pay (individually and collectively) for greater safety from natural hazards.

Acknowledgements

References

Auckland Council (2023a). *Category 3 Voluntary Buy-out Support Scheme Homeowner handbook*. https://www.aucklandcouncil.govt.nz/recovery-extreme-weather-disasters/Documents/category-3-voluntary-buy-out-homeowner-handbook.pdf

Auckland Council (2023b). *Auckland Council and Crown agree to cost sharing agreement for storm recovery and resilience work*. News story published on Auckland Council website, 10 October 2023. https://ourauckland.aucklandcouncil.govt.nz/news/2023/10/auckland-council-and-crown-agree-to-cost-sharing-agreement-for-storm-recovery-and-resilience-work

Auckland Council (2023c). Geotechnical engineer report template and guidelines. On Auckland Council website page "Get your own geotechnical report". https://www.aucklandcouncil.govt.nz/recovery-extreme-weather-disasters/property-categorisation-resolution/Pages/get-own-geotechnical-report.aspx

Australian Geomechanics Society (2007). *Practice Note Guidelines for Landslide Risk Management 2007, AGS(2007c)*. Journal and News of the Australian Geomechanics Society Volume 42 No 1 March 2007. ISSN 0818-9110.

Cyclone Recovery Unit (2023). *Future of Severely Affected Land (FOSAL) Information Pack – 10 July 2023*. In Cyclone Recovery Unit newsletter for 17 July 2023. Department of Prime Minister and Cabinet. https://www.dpmc.govt.nz/publications/cyclone-recovery-unit-newsletter-17-july-2023

Canterbury Earthquake Recovery Authority (2011). Port Hills White Zone Update and Decision Process. Memo addressed to the Minister for Canterbury Earthquake Recovery, 28 October 2011, report no M/11/0133. https://www.dpmc.govt.nz/sites/default/files/2024-04/port-hills-white-zone-update-and-decision-making-process.pdf

Department of the Prime Minister and Cabinet (2023). *Severe Weather Events Recovery Review Panel releases*. https://www.dpmc.govt.nz/our-programmes/special-programmes/severe-weather-events-recovery-review-panel-releases

Independent Hearings Panel (2015). *Proposals notified for incorporation into a Christchurch Replacement District Plan – Decision 6 – Natural Hazards (part)*. 17 July 2015. https://chchplan.ihp.govt.nz/wp-content/uploads/2015/03/Natural-Hazards-part.pdf

Ministry of Transport (2024). *Death on NZ roads since 1921*. Live website report, retrieved on 18 May 2024. https://www.transport.govt.nz/statistics-and-insights/safety-road-deaths/death-on-nz-roads-since-1921

Ministry for the Environment (2022). *Aotearoa New Zealand's first national adaptation plan*. Wellington. Ministry for the Environment publication ME1660. ISBN 978-1-99-102549-4

Mitchell, M. (2024). *Cyclone Recovery Taskforce concludes*. NZ Government Press Release, 20 February 2024 https://www.beehive.govt.nz/release/cyclone-recovery-taskforce-concludes

New Zealand Government (2023). *Update on assessment of affected properties post Cyclone and flooding*. Press release issued 1 May 2023. https://www.beehive.govt.nz/release/update-assessment-affected-properties-post-cyclone-and-flooding

Roberts R, Lee K, McLelland R, Brook M (2024). *The 2023 landslides and engineering geological response in Auckland, New Zealand*. In proceedings of 4th European Regional Conference of IAEG, Dubrovnik.

Stuff (2023). *Managing the retreat: Is there political will for buying out flood victims, and how might it work?* 29 March 2023. https://www.stuff.co.nz/business/the-monitor/131500489/managing-the-retreat-is-there-political-will-for-buying-out-flood-victims-and-how-might-it-work

THE LAST 10 YEARS OF GEOSCIENCES ENGINEERING EDUCATION IN TÜRKIYE

G. GÜLSEV UYAR AKSOY[1], C. OKAY AKSOY[2], A. ALPER UYAR[3]

[1]*Hacettepe University Mining Engineering Depatment*, Ankara /Türkiye

[2]*Dokuz Eylül University, Mining Eng. Department*, İzmir/ Türkiye

[3]*GOA R&D Mining and Environment Technologies Ltd.Co* Ankara/ TÜRKİYE

Abstract

This study explains how geosciences engineering departments in Türkiye have entered a painful process in the last 10 years due to wrong education policies and mine accidents, and reveals the fact that the decreasing interest in these departments is due to the prejudices of the Turkish people and that these prejudices are a natural consequence of the events.There is no doubt that interest in geoscience engineering is on the decline worldwide. However, the situation in Türkiye is serious enough to be the subject of this article. The study aims to draw conclusions on two cases. The political failure of the education system and the effects of social prejudices, reinforced by mining accidents, on the psychology of students.

Key words

*G*eosciences Engineering ,Mining , Geophysical, Geological ,Education

1. Introduction

Mining is a field of activity that is not fully realized to be present in every area of our lives, except for the generally known mines. In developing countries such as Türkiye, there are situations where the sensitivity and oppositional spirit can be mixed with lack of knowledge and ignorance. It is known that the role of accidents in the mines is an undeniable fact that the societies are so biased in their view of mining activities under the title of sensitivity. Mining, geology and geophysics engineers have a special place and importance in mining and other underground resource activities. In recent years, some universities in Türkiye as well as in the world have opened departments of Petroleum and Natural Gas Engineering, Earth Science Engineering and Mineral Processing Engineering and have taken important steps towards the specialization of the sector. At this point, another starting point of our study, the complexity and meaninglessness of the education system in Türkiye, comes into play. On the one hand, the geosciences are pregnant with the formation of new faculties and are trying to recruit students; on the other hand, the mining, geology and geophysics departments themselves are forced to fill their quotas, let alone many of them are facing the unpleasant consequences of not being able to accept even one student.

Trying to exclude critical approaches, our study presents statistics from the global and Turkish context and focuses on the problems that can be solved in these environments. It then offers suggestions and solutions that may be useful. Finally, it tries to shed light on how to produce graduates who love mining, which is one of the most important professions of today and the future for Türkiye and the world, who are conscious, selected with preferences and who have completed their education with an idealistic mindset.

2.   Overview of Universities in Türkiye and Status of Engineering Education

We can say that the history of universities in the Republic of Türkiye started with the University Revolution in 1933. Following the establishment of Istanbul University in 1933, Istanbul Technical University in 1944 and Ankara University in 1946, Karadeniz Technical University and Ege University were opened in 1955, becoming the first universities established in the Republican era.

In 1956, Middle East Technical University (as Middle East Institute of Technology) was opened in Ankara, Atatürk University in Erzurum in 1957, Anadolu University (as Eskişehir Academy of Economic and Commercial Sciences) in Eskişehir in 1958, and Hacettepe University in Ankara in 1967, marking, in the words of our Founder and National Hero Mustafa Kemal Atatürk, the most important beginnings of the young Republic of Türkiye on the road to reaching the level of Contemporary Civilization. Middle East Technical University became the first university in Türkiye to offer education in English. As of 2000, there were 70 universities operating in 39 provinces in Türkiye (Table I).

It can be said that the history of engineering faculties in Türkiye, which are considered to be underground sciences (mining, geology, geophysics, petroleum, earth sciences), began in 1915 with the establishment of the "İlmü'l Arz ve Maadin Dar-ül Mesaisi", now known as the "Institute of Geology and Mineralogy" at Dârülfünûn-ı Şahane, and was the predecessor of today's Istanbul University. In 1924, Zonguldak hosted the establishment of the Higher School of Mining Engineering, which was created in response to the need for mining engineers. The first studies in the field of geophysics were recognized with the establishment of the Rasathane-i Amire in 1868, which was established after the great Istanbul earthquake. The first academic education in Mining Engineering started with the establishment of the "Faculty of Mining" at Istanbul Technical University in 1953. In 1953, with the establishment of the Maçka Faculty of Mining Engineering, geophysical engineering started at Istanbul Technical University. Geology was the first department to award the degrees of Geological Engineer and Petroleum Engineer, and did so as early as 1961.

The tables below provide a comprehensive overview of the total number of universities in Türkiye, the engineering faculties within these universities and the presence of geoscience departments within these faculties. The before and after analyses, chosen as the methodology, are divided into two periods: until 2000 and from 2000 to the present. Academic quality and world university rankings are included in these tables, which constitute the core of the studies that form the subject of our article, in order to increase the impact of the analysis. Both the world university rankings and the university quotas and academic statuses shown in the tables have been updated according to the 2023-2024 data. After 2000, especially after 2004 when political stability was achieved, new universities were rapidly established in Türkiye with the slogan "A University in Every Province". By 2014, the number of universities in Türkiye had more than doubled to 157. Ten years later, in 2024, 48 new universities were opened, bringing the total number of universities to 205.

The attached tables provide a comprehensive overview of Turkish universities as well as a detailed analysis of their global position in the QS World University Rankings. QS World University Rankings, a leading authority on global university rankings, is based on a comprehensive database of 1,500 universities each year. Among the QS World data, four Turkish universities are ranked in the top 550. METU (ranked 336th), Istanbul Technical University, Boğaziçi University and Koç University. With the exception of Istanbul University, Hacettepe University, Ankara University and Yıldız Technical University, all other universities are ranked in the 1200+ range. Another statistical observation is that all 133 Turkish universities that became operational after 2000 are ranked in the 1500+ range and are therefore not included in the above list. It is clear that the number of universities in Türkiye has almost tripled in the last two decades. However, despite these considerations, without even going into details, it is clear that we have become a country with a significant number of unqualified universities. University planning should be one of the most comprehensive and detailed plans in a state's government program. Just as the number of schools in a neighborhood should be determined according to the population and the number of students, and new schools should be built when necessary, just as the number of mosques in a neighborhood should be determined according to the population and the number of congregations.

Table 1. Universities in Türkiye before 2000

NO	CITY	Institution Name	YEAR	Y/N	QS Ranking
1.	İstanbul	Istanbul University	1933	N	711-720
2.	ANKARA	Police Academy	1937	N	1501+
3.	İstanbul	Istanbul Technical University	1944	Y	=404
4.	ANKARA	Ankara University	1946	Y	901-950
5.	İzmir	Ege University	1955	Y	1001-1200
6.	Trabzon	Karadeniz Technical University	1955	Y	1501+
7.	Erzurum	Ataturk University	1957	Y	1401+
8.	ANKARA	Middle East Technical Universit	1959	Y	=336
9.	ANKARA	Hacettepe University	1967	Y	761-770
10.	İstanbul	Boğaziçi University	1971	Y	=514
11.	ADANA	Cukurova University	1973	Y	1401+
12.	Diyarbakır	Dicle University	1973	Y	1501+
13.	Sivas	Sivas Cumhuriyet University	1974	Y	1501+
14.	Bursa	Bursa Uludag University	1975	Y	1501+
15.	Elazığ	Fırat University	1975	Y	1501+
16.	Konya	Selcuk University	1975	Y	1501+
17.	Samsun	Ondokuz May University	1975	Y	1501+
18.	Malatya	Inonu University	1975	Y	1501+
19.	Kayseri	Erciyes University	1978	Y	1201-1400
20.	ANKARA	Gazi University	1982	Y	1001-1200
21.	Antalya	Akdeniz University	1982	Y	1401+
22.	Edirne	Trakya University	1982	Y	1501+
23.	Eskişehir	Anadolu University	1982	N	1201-1400
24.	İstanbul	Marmara University	1982	N	1201-1400
25.	İstanbul	Mimar Sinan Fine Arts Universit	1982	N	1501+
26.	İstanbul	Yildiz Technical University	1982	Y	951-1000
27.	İzmir	Dokuz Eylul University	1982	Y	1201-1400
28.	Van	Van Yüzüncü Yıl University	1982	Y	1501+
29.	ANKARA	İhsan Doğramacı Bilkent Univer:	1984	Y	1501+
30.	Gaziantep	Gaziantep University	1987	Y	1501+
31.	Afyonkarahisa	Afyon Kocatepe University	1992	Y	1501+
32.	Aydın	Aydin Adnan Menderes Universi	1992	Y	1501+
33.	Balıkesir	Balıkesir University	1992	Y	1501+
34.	Bolu	Bolu Abant Izzet Baysal Universi	1992	Y	1501+
35.	Çanakkale	Canakkale Onsekiz Mart Univers	1992	Y	1501+
36.	Denizli	Pamukkale University	1992	Y	1501+
37.	Hatay	Hatay Mustafa Kemal University	1992	Y	1501+
38.	Isparta	Süleyman Demirel University	1992	Y	1201-1400
39.	İstanbul	Galatasaray University	1992	Y	1501+
40.	İzmir	Izmir Institute of Technology	1992	Y	1201-1400
41.	K.Maraş	K.Maraş Sütçü İmam University	1992	Y	1501+
42.	Kars	Kafkas University	1992	Y	1501+
43.	Kırıkkale	Kirikkale University	1992	Y	1501+
44.	Kocaeli	Kocaeli University	1992	Y	1501+
45.	Kütahya	Kutahya Dumlupinar University	1992	Y	1501+
46.	Manisa	Manisa Celal Bayar University	1992	Y	1501+
47.	Mersin	Mersin University	1992	Y	1501+
48.	Muğla	Muğla Sıtkı Koçman University	1992	Y	1501+
49.	Niğde	Nigde Omer Halisdemir Univers	1992	Y	1501+
50.	Sakarya	Sakarya University	1992	Y	1401+
51.	Şanlıurfa	Harran University	1992	Y	1501+
52.	Tokat	Tokat Gaziosmanpasa Universit	1992	Y	1501+
53.	Zonguldak	Zonguldak Bülent Ecevit Univers	1992	Y	1501+
54.	Eskişehir	Eskisehir Osmangazi University	1993	Y	1501+
55.	İstanbul	Koç University	1993	Y	=431
56.	ANKARA	Baskent University	1994	Y	1501+
57.	İstanbul	Isik University	1996	Y	1501+
58.	İstanbul	Istanbul Bilgi University	1996	Y	1201-1400
59.	İstanbul	Sabancı University	1996	Y	1501+
60.	İstanbul	Yeditepe University	1996	Y	1501+
61.	ANKARA	Atilim University	1997	Y	1501+
62.	ANKARA	Cankaya University	1997	Y	1501+
63.	İstanbul	Beykent University	1997	Y	1501+
64.	İstanbul	Dogus University	1997	Y	1501+
65.	İstanbul	Istanbul Kultur University	1997	Y	1501+
66.	İstanbul	Kadir Has University	1997	Y	1501+
67.	İstanbul	Maltepe University	1997	Y	1501+
68.	Mersin	Çağ University	1997	N	1501+
69.	İstanbul	Bahcesehir University	1998	Y	1501+
70.	İstanbul	Golden Horn University	1998	Y	1501+
71.	ANKARA	Ufuk University	1999	N	1501+
72.	İstanbul	Istanbul Okan University	1999	Y	1501+

Table 2. Universities opened in Türkiye after 2000

NO	CITY	Institution Name	YEAR	Y/N	NO	CITY	Institution Name	YEAR	Y/N
1.	İstanbul	Istanbul Commerce University	2001	Y	67.	İstanbul	Bezmialem Vakıf University	2010	N
2.	İzmir	Izmir University of Economics	2001	Y	68.	İstanbul	Fatih Sultan Mehmet University	2010	Y
3.	İzmir	Yasar University	2001	Y	69.	İstanbul	Istanbul 29 May University	2010	N
4.	ANKARA	TOBB University of Economics and Technol	2003	Y	70.	İstanbul	Istanbul Gedik University	2010	Y
5.	Adıyaman	Adiyaman University	2006	Y	71.	İstanbul	Istanbul Sabahattin Zaim University	2010	Y
6.	Aksaray	Aksaray University	2006	Y	72.	İzmir	Izmir Kâtip Çelebi University	2010	Y
7.	Amasya	Amasya University	2006	Y	73.	Kayseri	Abdullah Gul University	2010	Y
8.	Burdur	Burdur Mehmet Akif Ersoy University	2006	Y	74.	Konya	Necmettin Erbakan University	2010	Y
9.	Çorum	Hitit University	2006	Y	75.	Trabzon	Eurasia University	2010	Y
10.	Düzce	Duzce University	2006	Y	76.	ADANA	Alparslan Turkesh University of Science and Techno	2011	Y
11.	Erzincan	Erzincan Binali Yıldırım University	2006	Y	77.	ANKARA	Turkish Aeronautical Association University	2011	Y
12.	Giresun	Giresun University	2006	Y	78.	Antalya	Alanya University	2011	Y
13.	İstanbul	Demiroglu Science University	2006	N	79.	İstanbul	Istanbul Gelisim University	2011	Y
14.	Kastamonu	Kastamonu University	2006	Y	80.	İstanbul	Uskudar University	2011	Y
15.	Kırşehir	Kırşehir Ahi Evran University	2006	Y	81.	İstanbul	MEF University	2012	Y
16.	Ordu	Ordu University	2006	N	82.	ANKARA	Ankara Social Sciences University	2013	N
17.	Rize	Recep Tayyip Erdoğan University	2006	Y	83.	ANKARA	Yüksek İhtisas University	2013	N
18.	Tekirdağ	Tekirdag Namik Kemal University	2006	Y	84.	Gaziantep	Sanko University	2013	N
19.	Uşak	Usak University	2006	Y	85.	İstanbul	Istanbul Esenyurt University	2013	Y
20.	Yozgat	Yozgat Bozok University	2006	Y	86.	Konya	Konya Food and Agriculture University	2013	Y
21.	Ağrı	Agri Ibrahim Chechen University	2007	N	87.	İstanbul	Biruni University	2014	Y
22.	Artvin	Artvin Coruh University	2007	Y	88.	Kocaeli	Gebze Technical University	2014	Y
23.	Batman	Batman University	2007	Y	89.	Antalya	Alanya Alaaddin Keykubat University	2015	N
24.	Bilecik	Bilecik Şeyh Edebali University	2007	Y	90.	Antalya	Belek University	2015	Y
25.	Bingöl	Bingöl University	2007	Y	91.	Balıkesir	Bandirma 17 Eylül University	2015	Y
26.	Bitlis	Bitlis Eren University	2007	Y	92.	Hatay	Iskenderun Technical University	2015	Y
27.	Çankırı	Çankırı Karatekin University	2007	Y	93.	İstanbul	University of Health Sciences	2015	N
28.	İstanbul	Acibadem University	2007	Y	94.	İstanbul	Ibn Haldun University	2015	N
29.	İstanbul	Istanbul Arel University	2007	Y	95.	İstanbul	Istanbul Rumeli University	2015	Y
30.	İstanbul	Istanbul Aydin University	2007	Y	96.	İstanbul	Istinye University	2015	Y
31.	İstanbul	Ozyegin University	2007	Y	97.	Ankara	Gendarmerie and Coast Guard Academy (Military)	2016	N
32.	Karabük	Karabuk University	2007	Y	98.	İstanbul	National Defense University (Military)	2016	N
33.	Karaman	Karamanoglu Mehmetbey University	2007	Y	99.	İstanbul	Fenerbahçe University	2016	Y
34.	Kırklareli	Kirklareli University	2007	Y	100.	İstanbul	Beykoz University	2016	Y
35.	Kilis	Kilis 7 Aralık University	2007	Y	101.	İstanbul	Istanbul Kent University	2016	N
36.	Mardin	Mardin Artuklu University	2007	Y	102.	İstanbul	Istanbul Topkapi University	2016	Y
37.	Muş	Mus Alparslan University	2007	Y	103.	İzmir	Izmir Bakircay University	2016	Y
38.	Nevşehir	Nevsehir Haci Bektas Veli University	2007	Y	104.	İzmir	Izmir Democracy University	2016	Y
39.	Osmaniye	Osmaniye Korkut Ata University	2007	Y	105.	ANKARA	Ankara University of Music and Fine Arts	2017	N
40.	Siirt	Siirt University	2007	Y	106.	ANKARA	Ostim Technical University	2017	Y
41.	Sinop	Sinop University	2007	Y	107.	İstanbul	Turkish-Japanese University of Science and Techno	2017	N
42.	Ardahan	Ardahan University	2008	Y	108.	Nevşehir	Cappadocia University	2017	Y
43.	Bartın	Bartın University	2008	Y	109.	Afyon	Afyonkarahisar University of Health Sciences	2018	N
44.	Bayburt	Bayburt University	2008	Y	110.	ANKARA	Ankara Hacı Bayram Veli University	2018	N
45.	Gaziantep	Hasan Kalyoncu University	2008	Y	111.	ANKARA	Ankara Medipol University	2018	Y
46.	Gümüşhane	Gumushane University	2008	Y	112.	ANKARA	Lokman Hekim University	2018	N
47.	Hakkâri	Hakkari University	2008	Y	113.	Eskişehir	Eskisehir Technical University	2018	Y
48.	Iğdır	Iğdır University	2008	Y	114.	Gaziantep	Gaziantep Islamic University of Science and Techno	2018	Y
49.	İstanbul	Altinbas University	2008	Y	115.	Isparta	Isparta University of Applied Sciences	2018	N
50.	İstanbul	Piri Reis University	2008	Y	116.	İstanbul	Istanbul University-Cerrahpasa	2018	Y
51.	Şırnak	Sirnak University	2008	Y	117.	İstanbul	Istanbul Atlas University	2018	Y
52.	Tunceli	Munzur University	2008	Y	118.	İstanbul	Istanbul Health and Technology University	2018	Y
53.	Yalova	Yalova University	2008	Y	119.	İzmir	Izmir Tınaztepe University	2018	N
54.	ANKARA	TED University	2009	Y	120.	K.Maraş	Kahramanmaras Istiklal University	2018	Y
55.	İstanbul	Nisantasi University	2009	Y	121.	Kayseri	Kayseri University	2018	Y
56.	İstanbul	Istanbul Medipol University	2009	Y	122.	Konya	Konya Technical University	2018	Y
57.	İstanbul	Yeni Yüzyıl University	2009	Y	123.	Kütahya	Kutahya University of Health Sciences	2018	Y
58.	Kayseri	Nuh Naci Yazgan University	2009	Y	124.	Malatya	Malatya Turgut Özal University	2018	Y
59.	Konya	KTO Karatay University	2009	Y	125.	Mersin	Tarsus University	2018	Y
60.	Mersin	Toros University	2009	Y	126.	Sakarya	Sakarya University of Applied Sciences	2018	N
61.	ANKARA	Ankara Yıldırım Beyazit University	2010	Y	127.	Samsun	Samsun University	2018	Y
62.	Antalya	Antalya Science University	2010	Y	128.	Sivas	Sivas University of Science and Technology	2018	Y
63.	Bursa	Bursa Technical University	2010	Y	129.	Trabzon	Trabzon University	2018	N
64.	Erzurum	Erzurum Technical University	2010	Y	130.	İstanbul	Istanbul Galata University	2019	N
65.	İstanbul	Istanbul Medeniyet University	2010	Y	131.	ANKARA	Ankara Science University	2020	Y
66.	İstanbul	Turkish-German University	2010	Y	132.	Kocaeli	Kocaeli University of Health and Technology	2020	Y
					133.	Bursa	Mudanya University	2022	Y

[1]Note: The "Y/N" column indicates whether the universities in question have engineering faculties. [2]Note: The 2024 edition of the QS World University Ranking lists Istanbul Aydın University and Gebze Technical University in the 1201-1400 range, while all other universities are ranked above 1500.

It has been argued that the university program should be one of the most sensitive areas of state planning, given that universities represent the leading educational and training institutions of a state. The university program, the units within it, and the professions needed by the state should be planned together, which I refer to as the optimal form of planning. Rather than proposing the immediate establishment of mining faculties, it would be more prudent to first determine the appropriate mining policies and to provide the requisite training for miners .In parallel with the analysis of Türkiye's universities mentioned above, our geosciences engineering programs have proliferated in an unplanned and unprogrammed manner. Although there are exceptions, such as the opening of Petroleum and Natural Gas Engineering Faculties at Iskenderun Technical University or Batman University, and faculties that have been opened and put into operation - within a program - based on the needs and foundations of the region, we are faced with a picture in which the number of quotas and the number of students settled in general is constantly decreasing. 53% of universities with earth sciences faculties programs could not admit any students in 2023. The universities that had quotas but were able to place students were able to fill 76% of these quotas. The reason for the increase in this rate was again due to the fact that well-established universities admitted students with 100% occupancy. In other words, the old ones continued to be good, while the new ones could not find a place in the preference rankings. To summarize, 39 of the 74 faculties with earth science engineering programs have passed the year, while only 11 faculties have been able to reach the number of students deserving to be a class and start their education without any problems.

A review of historical data reveals that, ten years ago, the number of quotas and students enrolled had more than doubled. In the current decade, 52 new universities have been established in Türkiye. In addition to being unable to fill the student quota, the universities were unable to train sufficient numbers of qualified academics. This deficiency in quality is also evident in the academic structure. A similar phenomenon has occurred in the academic community. Graduates of earth sciences departments at major universities have left the country to pursue their professions in Africa or Australia or elsewhere in the world, rather than accept the academic opportunities offered to them. This is due to the fact that the earth sciences departments have reached a point where they are no longer preferred in student recruitment.

Table 3. Geosciences Engineering quotas and placements in 2023

2023	TOTAL NUMBER OF FACULTIES	FACULTIES NOT RECEIVING QUOTAS	NUMBER OF FACULTIES FILLING ALL QUOTAS	THE RATIO OF FACULTIES NOT RECEIVING QUOTAS %		TOTAL NUMBER OF PLACES AT QUOTA FACULTIES	TOTAL NUMBER OF STUDENTS PLACED IN FACULTIES WITH QUOTA	PLACEMENT RATIO %
GEOLOGY	33	23	6	70%		293	236	81%
GEOPHISICS	11	5	2	45%		136	85	63%
MINERAL PROCESSING	1	0	1	0%		41	41	100%
MINES	24	11	5	46%		403	291	72%
PETROLEUM	5	0	3	0%		160	136	85%
TOTAL	**74**	**39**	**17**	**53%**		**1033**	**789**	**76%**

Table 4. 2013 Geosciences Engineering quotas and placements.

2013	TOTAL NUMBER OF PLACES AT QUOTA FACULTIES	TOTAL NUMBER OF STUDENTS PLACED IN FACULTIES WITH QUOTA	PLACEMENT RATIO %
GEOLOGY	1157	820	71%
GEOPHISICS	403	255	63%
MINERAL PROCESSING	30	30	100%
MINES	877	584	67%
PETROLEUM	145	145	100%
TOTAL	2612	1834	70%

Table 5. Comparison between the year 13/23

2013-2023	TOTAL NUMBER OF PLACES AT QUOTA FACULTIES RATIO	TOTAL NUMBER OF STUDENTS PLACED IN FACULTIES WITH QUOTA RATIO
GEOLOGY	-75%	-71%
GEOPHISICS	-66%	-67%
MINERAL PROCESSING	37%	37%
MINES	-54%	-50%
PETROLEUM	10%	-6%
TOTAL	-60%	-57%

Table 6. Presents the general status of Geosciences Engineering in 2023.

DIVISIONS	Institution Name	ACADEMICS				STUDENTS	QUOTA 2023	PLACED 2023	PLACED %	BASE SCOR
		PROF.	ASS.PRF	DR.LECT	TOT					
MINERAL PROCESSING	1. ISTANBUL TECHNICAL UNIVERSITY	8	2	3	13	360	41	41	100%	398,7
GEOPHISICS	2. ANKARA ÜNİVERSİTY (ENG)	6	1	3	10	47	21	21	100%	324,9
GEOPHISICS	3. DOKUZ EYLÜL UNIVERSITY	7	6	4	17	74	21	5	24%	308,9
GEOPHISICS	4. ISTANBUL TECHNICAL UNIVERSITY	7	4	2	13	325	41	41	100%	402,0
GEOPHISICS	5. İSTANBUL UNIVERSITY-CERRAHPAŞA	9	4	7	20	134	21	16	76%	307,8
GEOPHISICS	6. KARADENİZ TECHNICAL UNIVERSITY	5	4	6	15	23	16	0	0%	
GEOPHISICS	7. KOCAELİ UNIVERSITY	4	3	3	10	40	16	2	13%	310,5
		38	22	25	85	643	136	85	63%	
GEOLOGY	8. ANKARA ÜNİVERSİTY (ENG)	11	2	2	15	152	41	41	100%	332,9
GEOLOGY	9. ÇUKUROVA UNIVERSITY	9	3	1	13	58	26	5	19%	308,3
GEOLOGY	10. DOKUZ EYLÜL UNIVERSITY	14	8	4	26	165	20	20	100%	308,0
GEOLOGY	11. FIRAT UNIVERSITY	9	2	7	18	61	14	0	0%	
GEOLOGY	12. HACETTEPE UNIVERSITY	16	6	5	27	363	52	52	100%	351,8
GEOLOGY	13. ISTANBUL TECHNICAL UNIVERSITY	20	4	9	33	412	41	41	100%	411,0
GEOLOGY	14. İSTANBUL UNIVERSITY-CERRAHPAŞA	9	1	6	16	201	31	31	100%	310,0
GEOLOGY	15. KARADENİZ TECHNICAL UNIVERSITY	15	1	8	24	78	16	4	25%	309,2
GEOLOGY	16. NİĞDE ÖMER HALİSDEMİR UNIVERSITY	3	2	7	12	28	11	1	9%	369,0
GEOLOGY	17. MIDDLE EAST TECHNICAL UNIVERSITY (ENG)	9	4	2	15	457	41	41	100%	455,0
		115	33	51	199	1975	293	236	81%	
MINES	18. AFYON KOCATEPE UNIVERSITY	4	4	2	10	75	11	4	36%	312,4
MINES	19. ÇUKUROVA UNIVERSITY	7	1	3	11	57	26	9	35%	310,4
MINES	20. DOKUZ EYLÜL UNIVERSITY	17	8	3	28	338	41	41	100%	318,5
MINES	21. ESKİŞEHİR OSMANGAZİ UNIVERSITY	13	4	5	22	202	31	31	100%	319,2
MINES	22. HACETTEPE UNIVERSITY (ENG)	9	7	6	22	356	52	52	100%	378,2
MINES	23. İNÖNÜ UNIVERSITY	4	3	0	7	33	39	3	8%	312,6
MINES	24. ISTANBUL TECHNICAL UNIVERSITY	8	4	1	13	399	52	52	100%	422,6
MINES	25. İSTANBUL UNIVERSITY-CERRAHPAŞA	6	2	4	12	276	41	38	93%	307,7
MINES	26. KARADENİZ TECHNICAL UNIVERSITY	11	5	0	16	118	21	11	52%	308,6
MINES	27. MUĞLA SITKI KOÇMAN UNIVERSITY (ENG)	3	4	0	7	60	21	6	29%	312,3
MINES	28. NİĞDE ÖMER HALİSDEMİR UNIVERSITY	2	4	2	8	19	11	0	0%	0,0
MINES	29. MIDDLE EAST TECHNICAL UNIVERSITY (ENG)	3	1	2	6	439	41	41	100%	460,7
MINES	30. ZONGULDAK BÜLENT ECEVİT UNIVERSITY	3	1	3	7	93	16	3	19%	308,5
		90	48	31	169	2465	403	291	72%	
PETROLEUM - NAT.GAS	31. BATMAN UNIVERSITY (ENG)	2	2	5	9	17	21	12	57%	308,5
PETROLEUM - NAT.GAS	32. İSKENDERUN TECHNICAL UNIVERSITY	4	0	2	6	93	26	11	42%	310,6
PETROLEUM - NAT.GAS	33. ISTANBUL TECHNICAL UNIVERSITY (ENG)	2	3	5	10	375	41	41	100%	451,0
PETROLEUM - NAT.GAS	34. İZMİR KATİP ÇELEBİ UNIVERSITY	2	0	3	5	228	31	31	100%	347,0
PETROLEUM - NAT.GAS	35. MIDDLE EAST TECHNICAL UNIVERSITY (ENG)	7	7	7	21	446	41	41	100%	470,0
		17	12	22	51	1159	160	136	85%	

3. A comparison of the global ranking of universities and the ranking of Turkish universities in the field of geosciences.

It is evident that the challenges associated with the expansion of our existing faculties and the establishment of new faculties in earth sciences warrant serious consideration. However, it is also crucial to recognize the remarkable growth of our earth sciences departments in the Republic of Türkiye and the impressive global position of our successful universities.

The tables below illustrate the university rankings of Turkish universities in Mining, Geology,

Geophysics and Petroleum in the QS World Ranking 2024. Upon analysis of the ten-year period, it becomes evident that our universities have undergone a series of changes. In the rankings determined by these organizations, our universities have either maintained or lost their positions over the years. These organizations utilize various criteria, including academic publications, citations, employment status of graduates, and quality standards, to evaluate universities. It is evident that these organizations are primarily focused on maintaining their current positions. Consider the achievements of Middle East Technical University, which is ranked 11th in the world in Petroleum and Natural Gas Engineering, and Istanbul Technical University, which is ranked in every department. As we will reiterate in our conclusions and recommendations, in addition to focusing on the academic careers and subsequent productivity of our graduates, it is essential to focus on the productivity and research and development capabilities of our current academics.

Table 7. University Rankings of Geosciences (QS World Rankings)

TOP 240 Universities GEOLOGY	NUMBER OF UNIVERSITIES OF COUNTRIES	Top 240 Universities GEOPHYSICS	NUMBER OF UNIVERSITIES OF COUNTRIES	Top 70 Universities Engineering - MINERAL & MINING	NUMBER OF UNIVERSITIES OF COUNTRIES	Top 160 Universities PETROLEUM Engineering	NUMBER OF UNIVERSITIES OF COUNTRIES
United States	62	United States	62	United States	14	United States	17
United Kingdom	27	United Kingdom	26	Australia	11	United Kingdom	13
China (Mainland)	17	Germany	18	Canada	6	Russia	10
Germany	17	China (Mainland)	14	India	6	India	8
Australia	13	France	13	United Kingdom	4	Australia	7
Canada	12	Australia	12	China (Mainland)	3	Malaysia	6
France	12	Canada	12	Türkiye	2	Brazil	5
Italy	9	Italy	9	Chile	2	Egypt	5
Japan	8	Japan	8	Germany	2	Canada	4
Netherlands	7	Netherlands	7	Italy	2	China (Mainland)	4
Switzerland	5	Switzerland	6	Japan	2	Germany	4
Hong Kong SAR	4	Hong Kong SAR	4	Malaysia	2	Iran, Islamic Republic of	4
New Zealand	4	New Zealand	4	Russia	2	Japan	4
Spain	4	Spain	4	South Africa	2	Pakistan	4
Sweden	4	Sweden	4	Other Countries	1	Türkiye	3
Belgium	3	Belgium	3			Colombia	3
Denmark	3	Denmark	3			Denmark	3
India	3	India	3			Italy	3
Norway	3	Norway	3			Lebanon	3
Chile	2	South Korea	3			Norway	3
Ireland	2	Chile	2			Saudi Arabia	3
South Africa	2	Greece	2			South Korea	3
South Korea	2	Ireland	2			Spain	3
Taiwan	2	Portugal	2			United Arab Emirates	3
Türkiye	1	Saudi Arabia	2			Ecuador	2
Other Countries	12	Taiwan	2			France	2
		Türkiye	1			Mexico	2
		Other Countries	11			Other Countries	26

Table 8. The university rankings for the departments of geology, geophysics, mining, and petroleum, and An analysis of Türkiye's status.

Top 240 Universities -GEOLOGY					Top 240 Universities - GEOPHYSICS			
2024	2023	Institution	Location		2024	2023	Institution	Location
1	1	ETH Zurich - Swiss Federal Institute of Technology	Switzerland		1	1	ETH Zurich - Swiss Federal Institute of Technology	Switzerland
2	2	Harvard University	United States		2	2=	Harvard University	United States
3	5	University of Oxford	United Kingdom		3	6	University of Oxford	United Kingdom
4	6	University of Cambridge	United Kingdom		4	4	University of Cambridge	United Kingdom
5	7	Massachusetts Institute of Technology (MIT)	United States		=5	2=	California Institute of Technology (Caltech)	United States
6	4	University of California, Berkeley (UCB)	United States		=5	7	Massachusetts Institute of Technology (MIT)	United States
7	3	California Institute of Technology (Caltech)	United States		=5	5	University of California, Berkeley (UCB)	United States
8	10	University of Washington	United States		8	8=	Columbia University	United States
9	8	Stanford University	United States		9	8=	Stanford University	United States
10	9	Columbia University	United States		10	10	University of Washington	United States
****	*****	**********************************	**********		****	*****	**********************************	**********
****	*****	**********************************	**********		****	*****	**********************************	**********
201-240		Istanbul Technical University	Türkiye		201-240		Istanbul Technical University	Türkiye
****	*****	**********************************	**********		****	*****	**********************************	**********
****	*****	**********************************	**********		****	*****	**********************************	**********

Top 70 Universities - Engineering - Mineral & Mining			
2024	2023	Institution	Location
1	1	Colorado School of Mines	United States
2	2	Curtin University	Australia
3	4	The University of New South Wales (UNSW Sydney)	Australia
4	5	The University of Queensland	Australia
5	6	McGill University	Canada
6	3	Saint-Petersburg Mining University	Russia
7	7	The University of Western Australia	Australia
8	9	King Fahd University of Petroleum & Minerals	Saudi Arabia
9	8	Universidad de Chile	Chile
10	21	University of Toronto	Canada
*****	*****	***********************************	***********
51-70	51-70	Istanbul Technical University	Türkiye
51-70		Middle East Technical University	Türkiye
*****	*****	***********************************	***********
*****	*****	***********************************	***********

Top 160 Universities - Petroleum Engineering			
2024	2023	Institution	Location
1	1	University of Texas at Austin	United States
2	2	Stanford University	United States
=3		Technical University of Denmark	Denmark
=3	3	Texas A&M University	United States
5	4	King Fahd University of Petroleum & Minerals	Saudi Arabia
6	5	University of Alberta	Canada
7	7	The University of Adelaide	Australia
8	6	Imperial College London	United Kingdom
9	13	The University of New South Wales (UNSW Sydney)	Australia
10		The University of Tokyo	Japan
11	10	Middle East Technical University	Türkiye
*****	*****	***********************************	***********
51-100	51-100	Boğaziçi University	Türkiye
51-100	45=	Istanbul Technical University	Türkiye
*****	*****	***********************************	***********

4. A Brief Overview of the Past Decade in the Turkish Republic.

A decade ago, we conducted a comparative analysis of the status of our universities and earth science engineering faculties. The objective of this analysis was to identify potential areas for improvement. In order to achieve the desired results, it is also necessary to examine the process by which these results were reached. In 2013, the unemployment rate in Türkiye was 9.7%, while inflation stood at 7.4%. In 2023, the unemployment rate remained at 9.4%, while inflation reached a staggering 64.77%.. Over the past decade, the Republic of Türkiye has experienced a significant social upheaval (Gezi Park Events in 2013), a major coup attempt (FETO coup attempt on July 15, 2016), and a fundamental shift in the system of governance (transition to the Presidential System of Governance following the April 16, 2017 referendum and the June 24, 2018 transition to a partisan presidential system). It is evident that these three events had a profound impact on Turkish political history, both in terms of their causes and consequences. However, there is another commonality between them. This is the difficulty that young masses, whose brains are still developing and who are therefore unable to distinguish between truth and reality, face in making professional choices in the midst of a complex and uncertain world. Each event was observed not only in the year in which it occurred, but its consequences were felt in economic and political situations for many years. Türkiye, rightly or wrongly, has been evaluated based on the reality and effects of these events, which has resulted in unfavourable outcomes and perceptions in various fields, including education. The imbalance between supply and demand in earth sciences departments is consistent with this situation, but it has also been significantly affected by the negative publicity surrounding the related professional groups following the successive mining accidents. Furthermore, this phenomenon does not confirm the adage that there is no such thing as good or bad publicity. In the new mining areas, industry constituents that have been the subject of criticism from environmental groups have come to the forefront with projects rife with negligence and rent-seeking. Consequently, a number of legitimate mining operations have also been subject to criticism. In addition to the aforementioned political events, the Republic of Türkiye has also experienced two significant tragedies over the past decade. One of these is the Manisa/Soma mining accident, which resulted in the death of 301 miners and was described as "the biggest mining disaster in the history of the Republic". It is also a fact that this accident is one of the most important mining accidents in recent world history (Manisa/Soma, May 13, 2014). Another disaster, which occurred with such recent temporal proximity that its wounds are still bleeding, was the Kahramanmaraş earthquakes, which buried 50,000 people. Unfortunately, this earthquake also ranks as the deadliest disaster in our historical record (February 6-7, 2023).

5. Mining accidents in Türkiye and their effects on Geosciences Engineering Education

Türkiye has a reputation for mining accidents that are not generally regarded as positive. In particular, 301 miners lost their lives in the coal mine accident in Soma district of Manisa on May 13, 2014. The causes of this accident are still debated, and it has been recorded as the deadliest mining accident in the world in the 21st century. Although the number of accidents and related fatalities in mining has decreased in developed countries due to technological developments, increased occupational health and safety awareness, and the implementation of mining regulations, large-scale accidents in coal mines still occur, particularly in developing countries. As illustrated in Table VI, many years have passed since the world's most significant mining accidents, and countries have learned valuable lessons from major mining accidents.

Table 9. Most Fatal Mining Accidents in the World

THE MOST DEADLY MINING ACCIDENTS IN THE WORLD				
	YEAR	COUNTRY/ PLACE	DEATH TOLL	CAUSE
1.	1942	BENXIHU/CHINA	1549	EXPLOSION
2.	1906	COURRIERES/FRANCE	1099	EXPLOSION
3.	1914	KYUSHU/JAPAN	687	EXPLOSION
4.	1960	DATONG/CHINA	684	EXPLOSION
5.	1963	OMUTA/JAPAN	458	EXPLOSION
6.	1913	CAERPHILLY/UNITED KINGDOM	439	EXPLOSION
7.	1960	CLYDESDALE/SOUTH AFRICA	435	MIGRATION
8.	1972	WANKIE/ZIMBABWE	426	EXPLOSION
9.	1866	YORKSIRE/UNITED KINGDOM	388	EXPLOSION
10.	1965	DHANBAD/INDIA	375	EXPLOSION
11.	1975	CHASNALA/INDIA	372	EXPLOSION
12.	1907	MONONGAH/USA	362	EXPLOSION
13.	2014	SOMA/TÜRKİYE	301	BURNING
14.	1956	BOIS DU CAZIER/BELGIUM	267	BURNING
15.	1992	ZONGULDAK/TÜRKİYE	263	EXPLOSION

In countries with significant coal production (China 50.8%, Indonesia 9%, India 8% of the total world production), mining accidents are inevitable. In these countries, statistics are recorded as the number of deaths per 100 million tons of production. Between 2012 and 2023, 3200 people lost their lives in coal mine accidents in the People's Republic of China. A review of the last 10 years of mining accident statistics in Türkiye, which has a production of 0.4%, reveals that a total of 411 people lost their lives in mining accidents between 2013 and 2023.

The statistical data, when compared with the figures from other mining-producing countries around the globe, reveals a concerning trend in Türkiye. The mining accidents that occur in Türkiye are not only of a poor quality but also result in severe consequences.

Following the occurrence of fatal mining accidents, a negative public opinion about the sector is formed in Türkiye, as is the case in other countries. However, the impact of strong opposition discourses, regardless of their veracity, on public opinion is significantly more pronounced in Türkiye than in other countries. This is due to the fact that, despite the advent of the 21st century, a considerable number of mines continue to be operated using techniques and methods that date back a century.

The negative public opinion inevitably affects the preferences of university candidates, with many young people regarding the mining and underground sciences sector with trepidation. While it is challenging to demonstrate this determination with figures, feedback from students and prospective students in academic daily life corroborates this determination.

6. Conclusion and Recommendations

In our country, where lack of planning has become a dominant feature in every field, one of the most damaging consequences of this is observed in higher education and geoscience engineering education/training, which is a part of it. Universities that have been teaching in geosciences engineering disciplines for years are accepting students well below their capacity and are facing closure due to young people not choosing them.

Nowadays, it is seen that the opportunities available in geosciences engineering departments are gradually shrinking, the quality of education is decreasing, and the infrastructure opportunities are not adequately created. At this point, by directing the lens of state policies in this direction, central planning should be made, and education policies based on social needs, production, employment and lifelong education, and strengthening the country's science and technology competence should be implemented in universities. In this context, geoscience engineers should be trained in the quantity and quality required by the country. Studies should be carried out to improve the educational quality of existing departments.

In order to solve the unemployment problems of geoscience engineers, legal initiatives should be increasingly continued to provide employment by expanding the business areas that concern geoscience engineers. In an environment where unemployment is increasing, departments related to sub-branches of earth sciences engineering should not be opened.
Similarly, new geosciences engineering departments should not be opened, and existing ones should be provided with equal and sufficient opportunities. Course curricula in relevant departments should be rearranged according to changing needs, soil mechanics, occupational health and safety, computer applications in earth sciences and environment, etc. courses should be included in the curriculum as compulsory courses. In addition to all these, in order to purify the negative thoughts in the minds of the Turkish society, state support should be given to technological investments, and mines and earth sciences research should be brought to the standards of developed countries. In this sense, the state should be brought from a dimension where criticism is made a lot but solution suggestions are not emphasized, to a position where non-governmental organizations increase their activities and have a sufficient say for a solution-oriented struggle. The state should support these organizations with all its units, handle all the mentioned problems together with the committees formed by academic boards, and all responsible people should act with merit. In order to prevent accidents in mines, hundreds of articles written on these issues and dozens of solution projects should be examined, and state contributions should be increased with positive discrimination due to the impossibilities in their execution, although Tubitak (The Scientific and Technological Research Council of Türkiye) support has been received. It should be ensured that the referees appointed for the projects developed related to earth sciences should be from the branches appropriate to the project, and finally, if the issue is human life and employee life, commercialization concerns should be put aside and focus should be placed on the correct and reliable execution of the project.

References

Avşarağlu N , (2017) Ülkemizde Yerbilimleri Mühendislikleri Profili ve Mevcut Durum Analizi. The Profile of Geosciences and Engineering in our Country and the Analysis of the Current Situation.

Özdemir C, TUNCA B, ÇÖL M (2023) Mining Accidents in the World and in Türkiye.

QS World University Rankings 2024: Top global universities www.topuniversities.com.

Kaymakoğlu B, Tombal Kara T.D, (2022)Problems of mining education at Turkish universities: past, present and future

Zhao Y. , Yan Y. , Liu K., Zhao X, Li H., Cao J., Zhang S., Ma K. (2022) Analysis of coal mine safety accident features in China, 2017–2022 . https://doi.org/10.1016/j.ghm.2024.03.002

Council of Higher Education (YÖK) https://yokatlas.yok.gov.tr/lisans-anasayfa.php

Topic 6

Geological and Geotechnical Challenges in Urban Development and Construction

REMEDIATION OF THE LANDSLIDE AND RETAINING WALL SUČEVIĆ

NIKOLA TRBOVIĆ [1], BORIS KEREŠ [2]

[1] *Geolog savjetovanje d.o.o., Croatia, nikola.trbovic@geolog.hr*

[2] *Monterra d.o.o., Croatia, boris.keres@monterra.hr*

Abstract

This paper presents remediation works of the landslide and retaining wall at Sučević, located on the state road DC1, section Gračac – Knin. The remediation of the landslide provided by the design includes the construction of a supporting structure made of reinforced embankment with facing of concrete modular blocks. Stabilization of the existing retaining wall involves the installation of geotechnical self-drilling anchors with a diameter of 38 mm and a length of 15 m. The supporting structure is divided into six cascades, each of which consists of the mentioned system: concrete modular blocks, geogrids, and embankment. Displacements of the structure during construction were measured with inclinometers. Each level of the supporting structure has its own line foundation with dimensions of 0.60×0.20 m, while the lowest level has a line foundation with dimensions of 0.80×0.40 m, under which there are micropiles with a diameter of 180 mm and a length of 6 m, at an axial distance of 2 m. In this project, 11,375 pieces of concrete blocks were installed, with a total mass of 227.5 tons. In total, 4300 m³ of stone material with a granulation of 0-75 mm and 4300 m² of geogrid were installed inside the reinforced soil structure.

Key words
landslide, reinforced earth, stabilization, micropiles, rock anchor

1 Introduction

On the state road DC 1, section Gračac - Knin, instability appeared under the existing reinforced concrete retaining wall in the form of a translational landslide. The landslide covered an area with a width of 60-65 m, a length of 90-115 m, and the sliding surface is at an average depth of 6 m. In total, about 35,000 m³ of material was removed. As a result of this instability, the foundation of the existing reinforced concrete wall was undermined, reducing the stability of the wall and the entire road above it.

This paper presents the initial condition of the landslide, geotechnical investigation works and calculations, and describes each phase of the landslide remediation. The focus of the work is on presenting all phases of the work on the landslide. Additionally, the paper shows the inclinometer measurements that were carried out at the position of the existing reinforced concrete wall during the execution of the works.

Figure 1. The initial state of the landslide, March 2023

The landslide occurred in the spring of 2018 during extreme rainfall.

2 Methods

This chapter presents the chronological sequence of activities for the purpose of landslide remediation: geotechnical investigation works, landslide remediation design, and implementation of landslide remediation works. The focus of this work is on presenting the performance of works on the remediation of the landslide, along with the challenges that arise during the remediation of landslides, especially on inaccessible terrain.

2.1 Geotechnical investigation works

Geotechnical investigations were carried out at the location of the landslide in October 2020. The list of geotechnical investigation works and the number of locations where they were carried out can be found in Table . Geophysical surveys were conducted as part of the research for the development of the landslide remediation project and retaining wall. From the results of seismic and geoelectrical geophysical tests, it is possible to determine and evaluate: the depth and configuration of the bedrock, lateral and vertical material changes, the positions of more fractured zones in the bedrock, and the appearance of caverns in such zones (Highland & Bobrowsky, 2008; Mihalić Arbanas & Arbanas, 2015).

Geotechnical investigation work	Number of locations on the landslide
Geological prospecting	over the entire surface
Measurement with a Schmidt hammer	4 locations, 10 measurements per location
Measurement with a geological compass	over the entire surface
Terrain profiling with georadar (GPR, P)	6 profiles
Shallow refraction seismic captures	2 profiles
Geoelectric point recordings	2 locations
Machine drilling	3 drillhole, 20 m depth

During the field investigation work, field AC soil classification was performed, soil samples were taken, and "in situ" tests were carried out on rocks. Additionally, the occurrence and level of underground water were monitored during drilling. For the purpose of conducting geostatic stability analyses, based on the results of geotechnical investigations, the geotechnical profile is divided into two layers: embankment and heavily weathered limestone. The strength parameters of the layers are shown in Table (Hoek & Marinos, 2007).

Table 2 . Strenght parameters of the layers

Layer number	Layer name	φ_{ef}	c_{ef} (kPa)	γ (kN/m^3)
1	Embankment	36°	1,0	20,0
2	Heavily weathered limestone	35°	93,0	24,0

2.2 Landslide remediation design

For the purpose of creating the entire structure of the reinforced soil and ensuring the stability of the retaining wall, the designers conducted geotechnical stability analyses. A global stability analysis was carried out for the initial state of the landslide and for each phase of the construction of the structure. Furthermore, the dimensioning of micropiles, head beams of micropiles, rock anchors, and foundations of each floor of the structure was performed. The usability of the slope, defined as the ratio between destabilizing forces (active forces) and stabilizing forces (passive forces), is 95%. That is a calculation with implemented EN 1997-1, PP3. The maximum foreseen lateral displacement at the top of the structure is 5 mm.
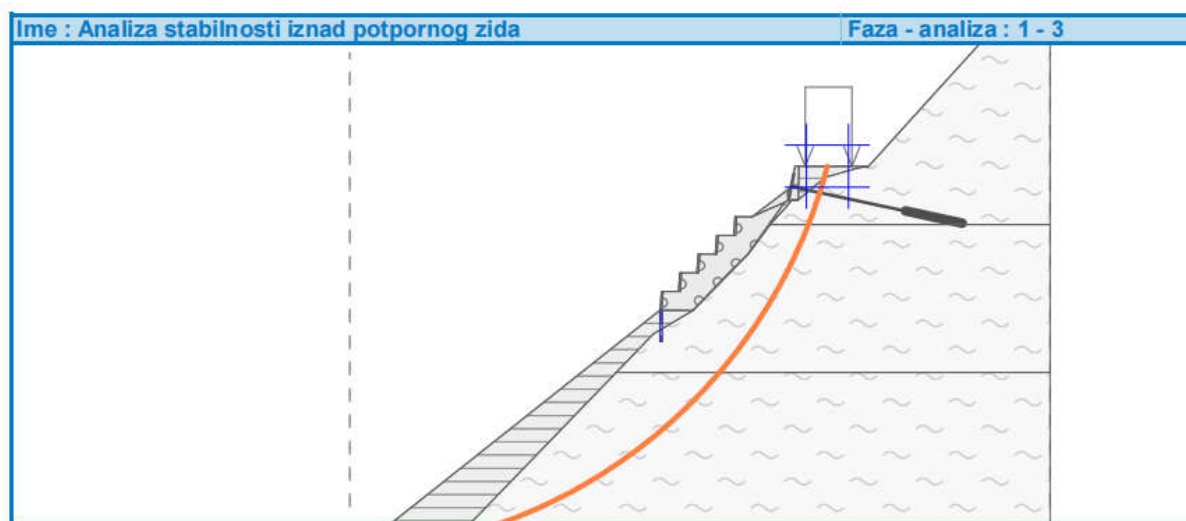
Figure 3. Global stability analyses in Geo5 software Slope Stability

The calculations were carried out using the geotechnical software Geo5, specifically the Slope Stability and MSE Wall software, which are part of the Geo5 software package. The global stability of the landslide was verified using the Slope Stability software. This software is used to perform slope stability analysis for various structures such as embankments, earth cuts, anchored retaining structures, and MSE walls. The slip surface is considered circular or polygonal and analyzed using several general methods. The dimensioning of the component parts of the reinforced soil construction was performed using the MSE Wall software. This program is used for the verification of mechanically stabilized earth walls and segmental retaining walls reinforced by geogrids (georeinforcements). The Slope Stability software enables calculation of global stability using several calculation methods, including Bishop, Fellenius/Petterson, Spencer, Janbu, and Morgenstern – Price (Popescu, 2001). Figure 2 shows global stability analyses in Geo5 software Slope Stability on one of the cross-sections. Figure 3 shows the cross-section of the structure with all elements of reinforced soil, micropiles, rock anchors, geotechnical profile, and the intended inclinometer.
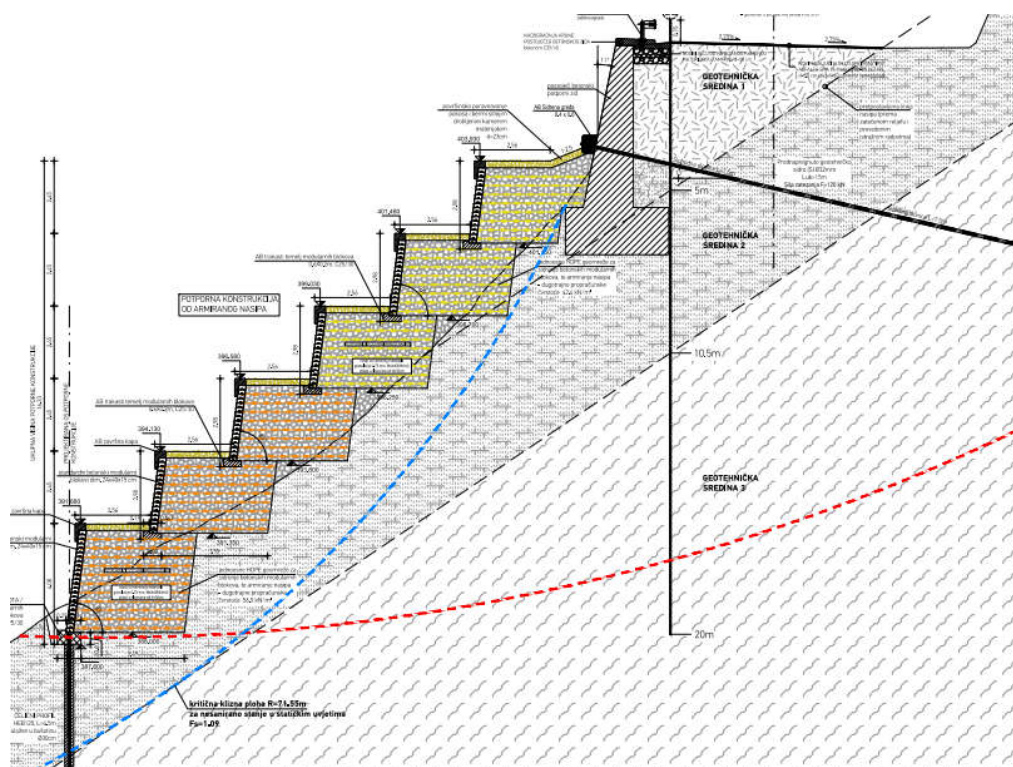
Figure 3. Cross section of the construction

2.3 Implementation of landslide remediation works

In this chapter, each phase of landslide remediation is described in detail. The description of the work chronologically follows the order of execution. All figures show work from the mentioned construction site.

2.3.1 Installation of rock anchors

Before any work on the remediation of the landslide, it was necessary to ensure the stability of the existing reinforced concrete wall with self-drilling rock anchors. Self-drilling rock anchors are installed because there is a layer of fill material behind the existing wall, followed by a layer of heavily weathered limestone.

A total of 34 rock anchors were installed, at an axial distance of 1.50 m. Each anchor is 15 m long and

38 mm in diameter. The diameter of the borehole is 90 mm, and the injection is carried out along the entire length of the anchor. Table 4 shows technical characteristics of self-drilling rock anhors.

Table 4. Technical characteristics of rock anchors

Type of rock anchor	Self-drilling rock anchor
Thickness (mm)	7,1
Ultimate load, (kN)	440
Yield point $f_{y0,2}$, (kN)	360
Average cross section (mm^2)	680
Weight (kg/m')	5,5
Nominal diameter (mm)	38
Thread type	left

Each anchor was tensioned to a force of 130.0 kN, 7 days after injection. The anchors were tensioned using a hydraulic press while monitoring the applied force and displacement in the anchor. Three anchors were tested with a force of 185.0 kN. The anchors are grouted with cement suspension, with a water-cement ratio of 0.42 and 1% swelling additive based on the mass of cement.

Figure 4. Installing of rock anchors

After the anchors have been tensioned and tested, it is allowed to proceed with the remediation works.

2.3.2 Construction of access road

To facilitate work on the sliding body, an access road was constructed from the state road to the lowest elevation of the structure. This road served for the transportation of machinery and delivery of materials. As construction progressed to the level of the state road, adjustments to the access road were necessary. It was always extended to the bottom level of each floor's foundation to provide maneuvering space for machinery.

In total, 840 m³ of excavation and 50 m³ of embankment were carried out for the construction of the access road.

Figure 5. The beginning of the construction of the access road

2.3.3 Micropiles instalation

The foundation of the lowest floor of the structure, made of reinforced soil, was constructed in combination with micropiles with a diameter of 180 mm and a length of 6.0 m. The micropiles were installed at an axial distance of 2.0 m, covering a total length of 58.0 m, resulting in the installation of 30 micropiles.

Figure 6. Installation of micropiles

After drilling a borehole with a diameter of 180 mm, HE 120 A steel profiles, 6 m long, are inserted into the borehole. The entire borehole is then injected with a cement suspension with a water-cement ratio of 0.42 and 1% swelling additive per cement mass. Seven days after the completion of grouting, a pile integrity test is conducted, which is a prerequisite for proceeding with the construction of the head beam.

2.3.4 Construction of head beam

The head beam is 60 m long with a cross-sectional dimension of 80×40 cm. For its construction, 19.50 m³ of concrete of compressive strength class C30/37 and 1500 kg of reinforcement were utilized. The main challenge was the delivery of fresh concrete to the beam's position, accomplished by using an excavator bucket. Concrete was transported to the beginning of the access road by a concrete mixer, and then loaded into the excavator's bucket. The installation with concrete pumps was not feasible due to the considerable distance from the state road to the bottom of the beam, which exceeds 40 m.
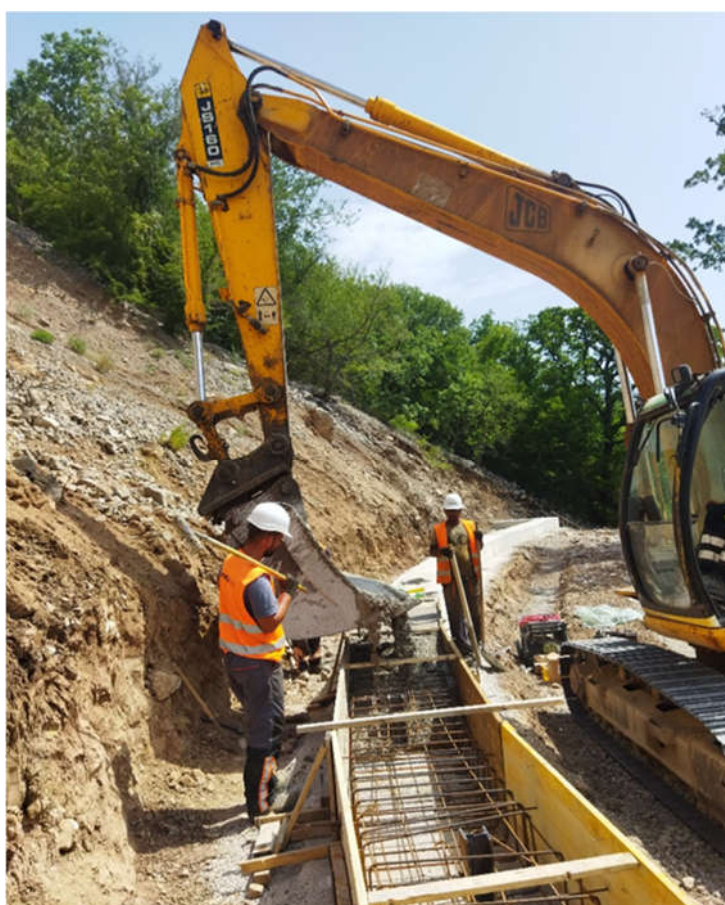
Figure 7. Construction of head beam

2.3.5 Construction of reinforced earth

The reinforced earth construction comprises three main elements: the face element, the tensile element, and the backfill material. The construction consists of a total of six floors. Five out of the six floors are 2.56 m high, while the lowest floor is 3.52 m high. Each floor is offset by 2.50 m towards the existing wall compared to the previous floor. Consequently, the total height of the structure is 16.32 m, and its length is 60 m.

The face of the wall comprises concrete blocks measuring 60×20×16 cm. Each block weighs 20 kg, and a total of 11,375 blocks were incorporated into the structure, resulting in a mass of 227.5 tons.

Longitudinal reinforcement, consisting of bars with a diameter of 6 mm, is positioned in each row of blocks. In every other row, a geogrid, serving as a tensile element, is attached around the longitudinal reinforcement. The geogrid is placed 3 m wide behind the wall, with an overlap of 0.50 m over the longitudinal reinforcement. The longitudinal reinforcement is inserted into slots within the blocks.

At an axial distance of 2.40 m, or in every fourth block, a reinforcing bar with a diameter of 20 mm is inserted to vertically stiffen the face of the wall. The rod is anchored into the foundation of each floor by 20 cm, and the rods are continued by overlapping for a length of 50 cm. After the vertical bars are installed, the cavity inside the block is injected with a cement mixture for rock anchor injection. Figure 8 illustrates the components of the reinforced soil construction: wall face, longitudinal reinforcement, geogrid, vertical stiffener, and embankment.

Figure 8. Reinforced earth elements

Stone material with a granulation of 0-75 mm was used as the filling material. The material was compacted using vibrating plates, ensuring a compressibility modulus (Ms) greater than 40 MPa. In total, 4,300 m³ of stone material was installed. Figure illustrates the completed construction after finishing the works.

Figure 9. Completed construction, October 2023

3   Results of inclinometer monitoring

In order to verify the remediation solution, an inclinometer was installed to monitor displacement. An inclinometer tube was positioned near the top of the reinforced concrete wall to monitor displacement on the landslide. An initial measurement was taken in the inclinometer, with two additional measurements conducted during the execution of the works, and a final measurement made after the works were completed. The largest displacement recorded was 1.07 mm, measured after all work had been completed.
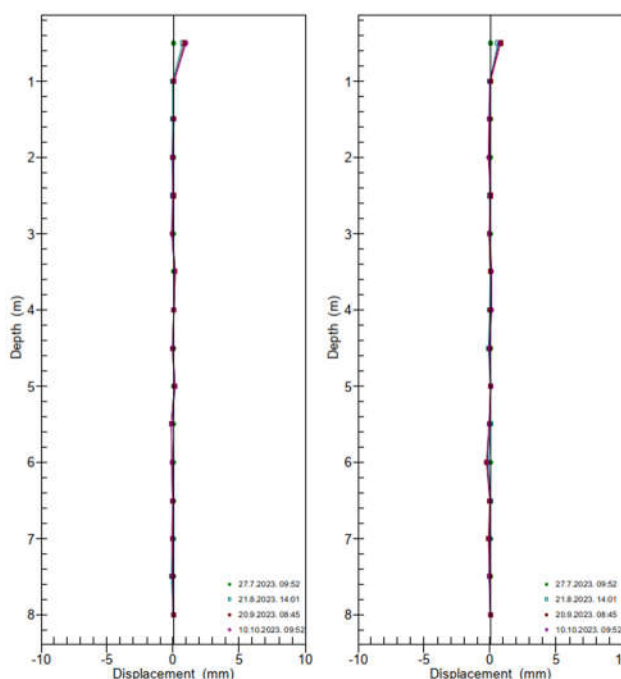
Figure 10. The results of inclinometer measurements

4   Conclusion

Reinforced soil support structures, as a type of backfilled support structures, base their stability on the interaction of tensile elements and the surrounding backfilled soil. They are constructed in such a way that the embankment behind the front face of the supporting structure is combined with tensile elements

such as geogrids, tensioners, and the like. The front face of the structure serves to prevent local erosion and has an aesthetic function but does not significantly contribute to the stability of the entire structure.

By undertaking the remediation of the Sučević landslide, it was demonstrated that the construction of reinforced soil is feasible even in highly inaccessible areas with steep slopes. The results of the inclinometer measurements, which will continue to be conducted annually for the next three years, confirm the success of the landslide remediation.

By constructing with reinforced soil, it is possible to utilize materials available on-site, particularly those generated from excavation.

References

Cruden, D. M., Varnes D. J. Landslide types and processes. *National Academy Press, Special Report 247*. 1996, 36-75.

Highland, L., Bobrowsky, P.T. (2008), The landslide handbook – A guide to understanding landslides, *U.S. Geological Survey.* 2008

Hoek, E.; Marinos, P. A brief history of the development of the Hoek-Brown failure criterion. *Soils and Rocks.* 2007, 30, 85-92.

Mihalić Arbanas, S., Arbanas, Ž. Landslides: A Guide to Researching Landslide Phenomena and Processes. *IGI Global.* 2015, 474-510.

Popescu, M. A suggested method for reporting landslide remedial measures. *Bulletin of Engineering Geology and the Environment.* 2001, 69-74.

Varnes, D. J. Slope movement types and processes. *National Research Council, Special Report 176.* 1978, 11-33.

COMPARATIVE STUDY ON STRENGTH CHARACTERISTICS OF CARBONATE ROCKS FROM AL AIN, ABU DHABI, UNITED ARAB EMIRATES (UAE)

HASAN ARMAN [1], ABDULAZIZ KHALID KHALIFA ALAZZANI [2], MANSOOR SALEH AYEDH AL HARTHI [3], AHMED QAYED MOSAAD ALHARBI [4], MULHAM ABDALLA AL MANSOUR [5], SAFWAN PARAMBAN [6]

[1] *United Arab Emirates University, United Arab Emirates, harman@uaeu.ac.ae*

[2] *United Arab Emirates University, United Arab Emirates, 201915039@uaeu.ac.ae*

[3] *United Arab Emirates University, United Arab Emirates, 201883204@uaeu.ac.ae*

[4] *United Arab Emirates University, United Arab Emirates, 201931725@uaeu.ac.ae*

[5] *United Arab Emirates University, United Arab Emirates, 202050912@uaeu.ac.ae*

[6] *United Arab Emirates University, United Arab Emirates, p.safwan@uaeu.ac.ae*

Abstract

Rock strength determination, whether in-situ or in laboratory, generally requires time consuming processes. Various testing methods, such as uniaxial compressive strength (UCS), point load index PLI ($I_{s(50)}$), indirect tensile strength (ITS), and Schmidt hammer (on core, SHV_C or rock block samples, SVH_{RB}) tests are commonly used to measure rock strength in the laboratory. In this study, sixty representative blocks of carbonate rock were collected from three different locations of the study area. Of these, forty-three blocks were selected for Schmidt hammer tests (SHV_{RB}). NX size (54 mm) core samples from the same blocks were prepared, and the UCS, PLI ($I_{s(50)}$), and ITS tests were carried out according to ASTM (American Society for Testing and Materials) standards. The results indicate that variable correlations, strong to very weak, or absent, exist between the rock strength parameters. The best correlations found were between the mean UCS and the mean PLI ($I_{s(50)}$) ($R^2 = 0.70$), and between the mean PLI ($I_{s(50)}$) and the mean ITS ($R^2 = 0.62$). The obtained rock strength parameters may be specific to the arid environment of the investigated carbonate rocks. However, the results are useful as a guide to decision makers and engineers.

Key words

carbonate rocks, rock strength, uniaxial compressive strength (UCS), point load index (PLI ($I_{s(50)}$)), indirect tensile strength (ITS), Schmidt hammer on rock block sample (SHV_{RB})

1   Introduction

Measurements of rock strength are critical data in various engineering applications. Rock strength may be defined as the inherent strength of an isotropic rock under various conditions (Hawkins, 1998). Due to the variability of carbonate rocks structures, textures and mineralogical compositions, even on the meter scale, the generalizing of an overall bulk mechanical property, such as rock strength, is a regular problem. Therefore, it is crucial to measure the rock strength through in-situ and laboratory studies (Erguler, 2009; Yilmaz, 2010; Arman et al., 2014; 2017; 2021). Rock strength measurement, either in-situ or in the laboratory environment, is a comparatively costly and time-consuming process that involves substantial efforts in rock sampling, preparation and laboratory tests. Furthermore, a large number of rock specimens must be tested in order to arrive at a representative value for a large rock exposure.

The study areas are located at the north and east of Jabal Hafit mountain, which lies southeast of Al-Ain city, Abu Dhabi, UAE. The geologic and tectonic features of Jabal Hafit are well-documented in terms of local lithology, structural features and major stress-strain fields (Arman et al., 2014; 2017; 2021; Warrack, 1996; Boukhary et al., 2003; 2005; Styles et al., 2006) (Fig. 1).
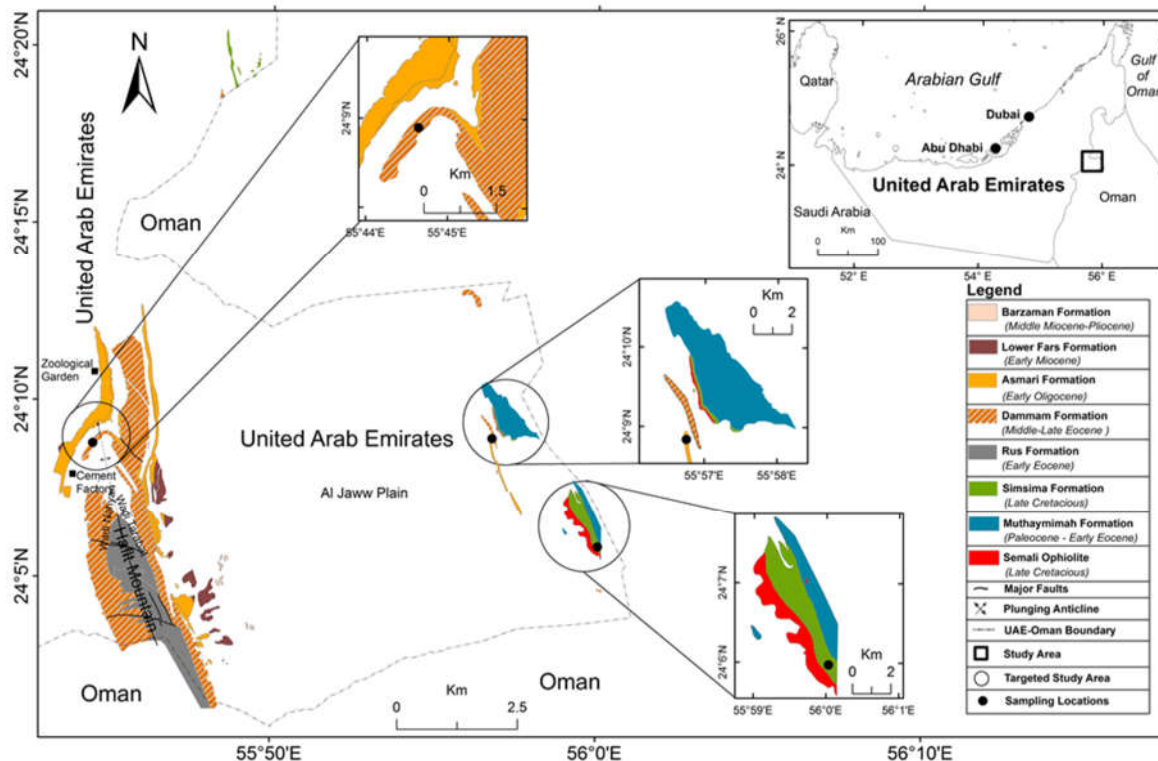
Figure 1. Geological map of the rock block sampling sites and surroundings.

Certain geo-engineering problems, such as slope instability, common occurrences of landslides, rock falls, paleo-karstic cavitation, etc., have been reported in Al-Ain. Carbonate rocks from the Simsima Formation (Late Cretaceous 73-65 Myr), Dammam Formation (Middle to Late Eocene 49-34 Myr) and Asmari Formation (Early Oligocene 34-29 Myr) were chosen for strength analyses, since they represent the commonest exposures of rock masses in the Al-Ain area (see Fig. 1).

In the literature, there are detailed specifications for the various available strength testing methods, including unconfined compressive strength (UCS), point load index PLI ($I_{s(50)}$), indirect tensile strength (ITS), Schmidt hammer (either on core, SHV_C or rock block samples, SVH_{RB}). This study intends to perform laboratory strength tests of the UCS, PLI ($I_{s(50)}$), ITS and SVH_{RB} on rock blocks and core samples, and derive empirical equations to describe the relations between the mean UCS and mean PLI ($I_{s(50)}$); the mean ITS and mean SHV_{RB}; the mean PLI ($I_{s(50)}$) against mean ITS and mean SHV_{RB}; and between the mean ITS and mean SHV_{RB}.

2 Experimental Studies and Results

Field trips were conducted to obtain sixty representative carbonate rock blocks samples (approximately 30x30x30 cm size) from the Simsima, Dammam and Asmari Formations from the study areas (Fig. 1, Fig. 2, and Fig. 3a). After a quality inspection of the blocks to eliminate any with visible discontinuities, fractures, filling material, etc., a subset of forty-three blocks, comprising twelve, sixteen and fifteen

from the Simsima, Dammam, and Asmari Formations, respectively, were used for Schmidt hammer tests (SHV_{RB}) (Fig. 3b). NX size (54 mm) core samples from the same rock blocks were drilled, trimmed, measured (sample preparations), and different strength tests of the UCS, PLI ($I_{s(50)}$), and ITS were carried out on the core samples according the suggested ASTM (American Society for Testing and Materials) standards (ASTM D5873-95, 1996; ASTM D2938-95, 1995; ASTM D5731-02, 2003; ASTM D3967-95a, 2001; ASTM D4543, 2019) (Fig. 3c-h).

Figure 2. A typical rock blocks from sampling sites.
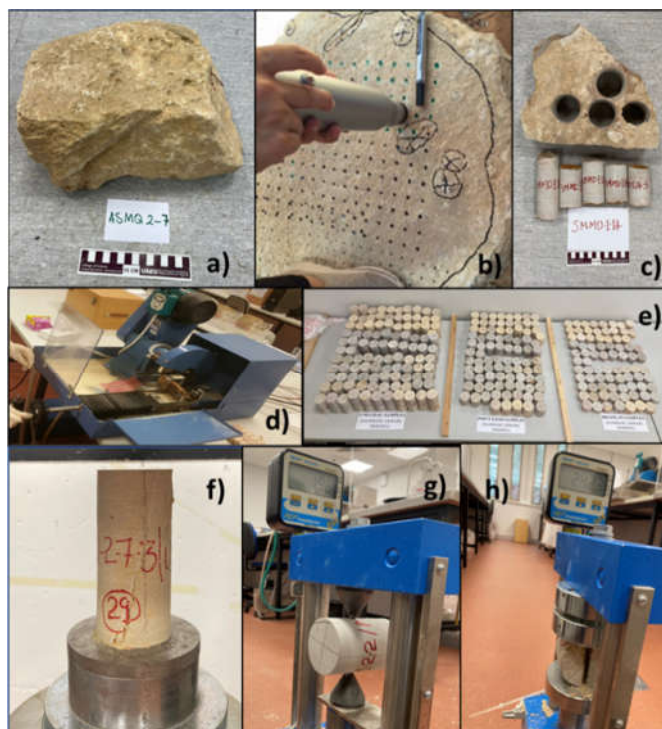
Figure 3. a) Rock block sample, b) Schmidt Hammer test on rock block (SHV_{RB}), c) Core samples with rock block, d) Core sample trimming, e) Prepared test samples, f) Uniaxial compressive strength (UCS) test, g) Point load index (PLI ($I_{s(50)}$)) test and h) Indirect tensile strength (ITS) test.

Core test samples were prepared with Length (L) / Diameter (D) ratio of 2.0 to 2.5 (for UCS), greater

than 1 (for PLI ($I_{s(50)}$)), and 0.2 to 0.75 (for ITS). The loading rate for the UCS tests was 0.75 (MPa/sec) and a strain gage was not used during the test. In addition, the failure modes of the UCS tests ranged from tension, to shear, to tension + shear, and the failures were in general through the matrix. For the PLI ($I_{s(50)}$) tests, the coefficient of 1.03 was used to convert the peak load to strength. For the Schmidt hammer tests, the orientation of the rock block and hammer was 90-degree angle and the rock blocks were placed on a concrete floor that had a similar high degree of stiffness. The number of strikes that were delivered to a single point on the block to collect the Schmidt hammer data depended on the surface area of the block and was about 10 according to related standards. After collection of the strength data, the relations between the mean UCS and mean PLI ($I_{s(50)}$), the mean ITS and mean SHV_{RB}; the mean PLI ($I_{s(50)}$) against the mean ITS and the mean SHV_{RB}; and the mean ITS against the mean SHV_{RB}, were represented by empirical equations (Fig. 4a-f). In addition, the descriptive statistics of carbonate rocks strength tests are listed in Table 1.

Figure 4. a) Mean UCS vs. mean PLI ($I_{s(50)}$), b) Mean UCS vs. mean ITS, c) Mean UCS vs. mean SHV_{RB}, d) Mean PLI ($I_{s(50)}$) vs. mean ITS, e) Mean PLI ($I_{s(50)}$) vs. mean SHV_{RB} and f) Mean ITS vs. mean SHV_{RB}.

Table 1. Descriptive statistics of carbonate rock's strength tests

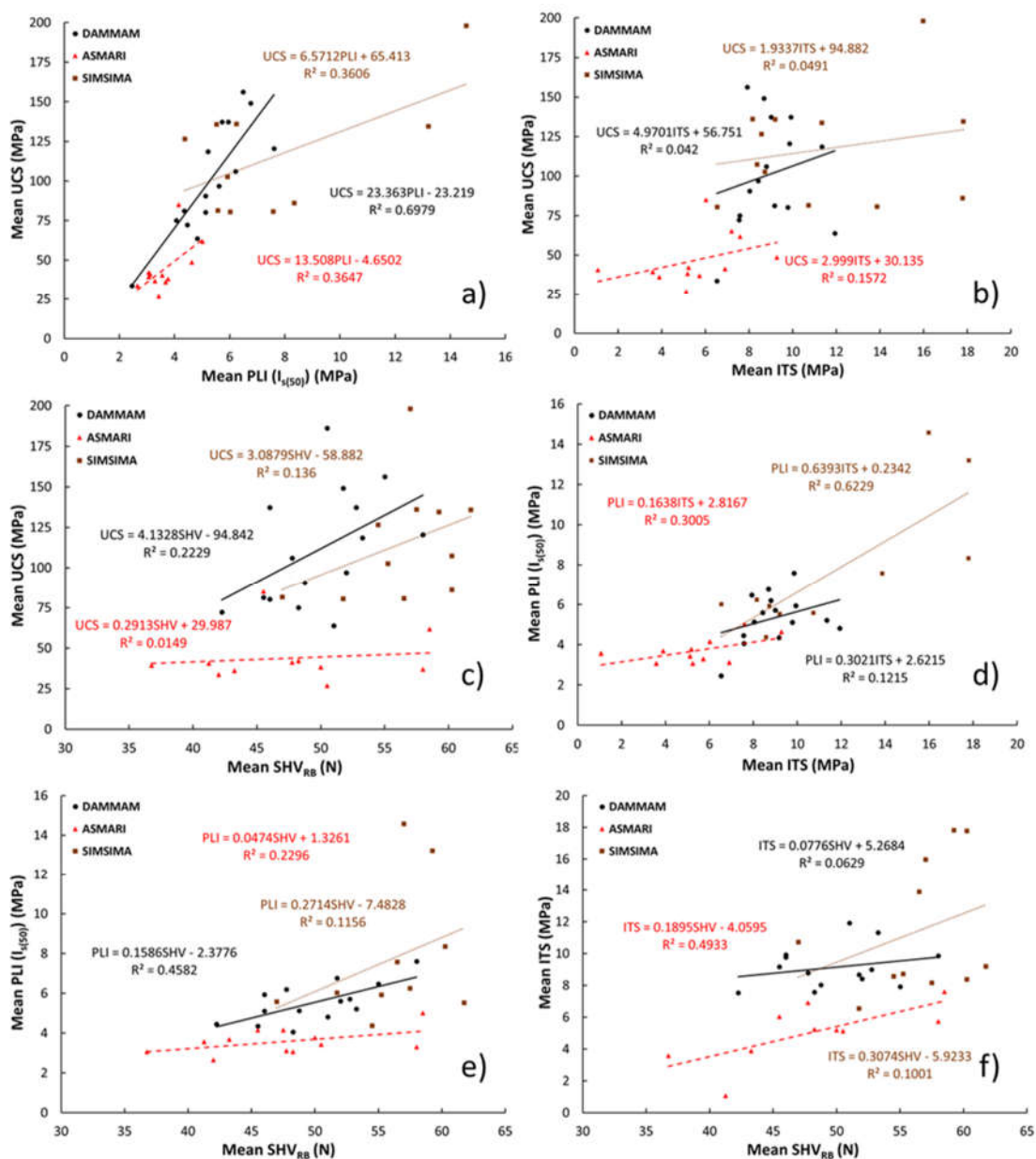| Dammam Formation					
Test types	Number of samples	Minimum (MPa)	Maximum (MPa)	Mean (MPa)	Standard deviation
UCS	51	33.81	186.14	106.60	39.86
PLI ($I_{s(50)}$)	45	1.69	7.60	5.15	1.50
ITS	39	4.90	13.48	9.05	1.92
Asmari Formation					
UCS	31	25.25	84.96	44.19	14
PLI ($I_{s(50)}$)	25	2.34	5.24	3.58	0.84
ITS	23	1.07	9.27	5.58	1.98
Simsima Formation					
UCS	22	42.91	216.41	126	46.65
PLI ($I_{s(50)}$)	18	4.11	15.07	7.28	2.92
ITS	18	6.54	23.87	11.21	4.37

The results revealed a full spectrum of covariances, from strong to very weak correlation, to no correlation, between the mean values of rock strength parameters with specific determination of coefficient (R^2) values ranging from 0.70 and 0.02. The best correlations were found to be between the mean UCS and mean PLI ($I_{s(50)}$) ($R^2 = 0.70$), and between the mean PLI ($I_{s(50)}$) and mean ITS ($R^2 = 0.62$) (see Fig. 4a and 4d). Moreover, in general, carbonate rocks from the three formations exhibited a broad range of strength behavior from moderate to strong (Simsima), weak to moderate (Dammam) and weak (Asmari) in terms of the measured various strength parameters in the study areas.

3   Discussions and Conclusions

This work presents a comparative study of strength characteristics for carbonate rocks of the Simsima, Dammam, and Asmari Formations, which are well-exposed in the Al Ain region, UAE. In general, the study shows that the carbonate rocks from the Simsima Formation have the highest strength value compared to carbonate rocks from the Dammam and Asmari Formations, in term of the strength tests of the UCS, PLI ($I_{s(50)}$), ITS and SHV_{RB}. The carbonate rocks from the three formations indicate significant variations in the various strength tests. The findings of this experimental study are unique and may provide valuable information for local authorities and engineers to guide decision-making in engineering applications, such as buildings, roads, tunnels, etc. around Al Ain city. Furthermore, this study will help to minimize or prevent environmental risks and hazards affecting the study areas and surroundings for the present and in the future. Eventually, such reliable and practical information should be considered as a preliminary study and may enable the site managers, engineer, researchers and scientists to implement more detailed investigations along the studied areas and the regions.

References

Arman, H.; Hashem, W.; El Tokhi, M.; Abdelghany, O.; Al Saiy, A. Petrographical and geomechanical properties of the Lower Oligocene Limestones from Al Ain City, United Arab Emirates. *Arabian Journal Science and Engineering.* 2014, 39, 261–271.

Arman, H.; Hashem, W.; Abdelghany, O.; Aldahan, A. Effects of lithofacies and environment on in situ and laboratory Schmidt hammer tests: a case study of carbonate rocks. *Quarterly Journal of Engineering Geology and Hydrogeology.* 2017, 50, 179–186.

Arman, H.; Abdelghany O.; Abu Saima, M.; Aldahan, A.; Mahmoud, B.; Hussein, S.; Fowler, A. Petrological control on engineering properties of carbonate rocks in arid regions. *Bulletin of Engineering Geology and the Environment.* 2021, 80, 4221–4233.

ASTM D2938-95. Standard test method for unconfined compressive strength of intact rock core specimens. 1995, 279–281.

ASTM D5873-95. Standard test method for determination of rock hardness by rebound hammer method. 1996, 693–695.

ASTM D3967-95a. Standard test method for splitting tensile strength of intact rock core specimens. 2001, 1–3.

ASTM D5731-02. Standard test method for determination of the point load strength index of rocks. 2003, 1–7.

ASTM D4543-19. Standard practices for preparing rock core as cylindrical test specimens and verifying conformance to dimensional and shape tolerances. 2019, 1–13.

Boukhary, M.; Abdelghany, O.; Bahr, S. Nummulites alsharhani n.sp. (Late Lutetian) from Jabal Hafit and Al Faiyah: Western side of the Northern Oman Mountains, United Arab Emirates. *Revue Paleobiol Geneve.* 2002, 21(2), 575-585, 1–3.

Boukhary, M.; Abdelghany, O.; Bahr, S; Hussein-Kamel, Y. Upper Eocene larger foraminifera from the Dammam Formation in the border region of United Arab Emirates and Oman. *Micropaleontology.* 2005, 51(6), 487–504.

Erguler, Z. A.; Ulusay, R. Water-induced variations in mechanical properties of clay-bearing rocks. *International Journal of Rock Mechanics and Mining Sciences.* 2009, 46, 355–370.

Hawkins, A. B. Aspects of rock strength. *Bulletin of Engineering Geology and Environment.* 1998, 57, 17–30.

Sytles, M. T.; Ellison, R. A.; Arkley, S. L. B.; Crowley, Q.; Farrant, A.; Goodenough, K. M.; Ckervey, J. A.; Pharaoh, T. C.; Philips, E. R.; Schofield, D.; Thomas, R. J. The geology and geophysics of the United Arab Emirates. Geology. *Ministry of Energy, United Arab Emirates.* 2006, 2, 1–351.

Yilmaz, I. Influence of water content on the strength and deformability of gypsum. *International Journal of Rock Mechanics and Mining Sciences.* 2010, 47, 342–347.

Warrak, M. Origin of the Hafit structure: implication for timing the Tertiary deformation in the northern Oman Mountains. *Journal of Structural Geology* 1996, 803–818.

ASSESSMENT OF ROCK-MASS GROUTABILITY IN HIGH-STRESS METAMORPHICS; SEEPAGE CONTROL AND RESILIENCE INTERVENTION – THE UPPER TAMAKOSHI HEADRACE TUNNEL CASE STUDY, NEPAL

EIRINAIOS CHRISTAKIS [1], SANJIB SAPKOTA [2]

[1] *Tractebel Engineering GmbH, Germany,* renos.christakis@tractebel.engie.com

[2] *Tractebel Engineering GmbH, Germany,* sanjib.sapkota@tractebel.engie.com

Abstract

The underestimation of geomechanical properties and any possible misinterpretation of the anticipated rock-mass behaviour during dynamic hydraulic operation of pressurised underground structures, can either influence the performance of a hydropower scheme or even undermine the resilience and stability of the structure. This becomes apparent for tunnels constructed in complex geological environments; influenced by active tectonics, subjected to high external stress, or intersected by adverse geological features. A well-known record of hydropower tunnel failures underline the necessity for pro-active measures, in order to mitigate geological risk, control tunnel's performance, and optimise their resilience.

High-pressure barrier grouting constitutes a key-intervention method to contain sections of low-quality rock-mass, control internal seepage, mitigate out-leakage, address blast induced damage of the surrounding profile, and achieve synergy with the concrete lining segments. Aiming to optimise grouting schemes, the authors discuss the role of barrier grouting as intervention technique, and analyse the groutability of Gneiss under high-stress environment. The analysis focuses on correlating the intrinsic rock-mass properties with the permeability measurements and the injection output (i.e. grouting data), in order to develop a preliminary tool for the pre-estimation of grouting requirements and the subsequent optimisation of grouting programme, tailored to the needs of the project.

Key words

Grouting, Ground improvement, Permeability, Gneiss, Pressure tunnel, Anisotropy

1   Introduction

The stability, the performance and the serviceability of a pressurised water conveyance tunnel in hydropower projects are essential parameters for efficient power generation and the sustainability of the entire project. Tunnel resilience relates to several aspects of a hydropower plant such as the realistic parametrisation, the adherence to quality standards, the structural integrity, the continuous monitoring, regular inspection and maintenance strategy, and the emergency preparedness. All these contribute to risk reduction for possible deteriorations or defects that can result in leak, reduced flow rates, or even a structural failure. Pressure tunnels can be either unlined -where stress, rock mass and the hydrogeological regime permit so; or lined with steel ferules and concrete or the combination of both. Unlined structures may be also supplementary supported by shotcrete layers, rock bolts, steel ribs and other conventional tunnelling support elements or techniques. Should the anticipated rock mass behaviour during operation, the stress regime, and hydrogeological conditions necessitate so, pressure tunnels can be partially lined along certain stretches.

The primary design factors for the construction of a pressure tunnel, i.e. its geometry (dimensions, inclination, and alignment), the excavation method (mechanical or conventional), and its permanent support (lined, partially lined, or unlined), are summarised as follows:

- Intrinsic permeability related to the surrounding rock mass.
- Anticipated hydraulic induced permeability during operation.
- Geostructural characteristics of rock mass (e.g. jointing degree).
- Presence of tectonic features that intersect the structure or exist in the vicinity (e.g. faults, sheared zones, etc.).
- Rock mass quality with respect to anisotropy, erodibility, deformability, and joint conditions.
- In-situ stresses and the geo-tectonic regime.
- Geomorphology and the surrounding hydraulic network.
- Internal stresses during operation (dynamic pressure or hammering, driving pressure, pressure fluctuations cycles).

A long record of failure of pressurised underground waterways during the last decades (e.g. La Higuera 2011, Glendoe 2009, Shuakhevi 2017, etc.) indicates that their construction and operation entail risks associated with the design and the construction quality (Brox, 2019; Hencher, 2019; Shrestha, 2021). The majority of recorded incidents directly relate to design flaws due to inadequate geological information, and the misconception of geomechanical/hydraulic characteristics of the broader area, especially in complex geological environments. The synergy of such misconceptions could result in tunnel failure incidents that involve uncontrolled leakage (due to unaddressed permeability or hydrojacking during operation), zones of poor rock mass quality (i.e. inadequate support of weak zones, mitigation of lineaments, etc.), excessive hydraulic effects, or a combination of the aforementioned. The hydraulic effect becomes more apparent in run-of-river schemes which, according to Brox (2019), these are typically "*subjected to seasonal fluctuations of run-off with associated significant pressure variations*".

2   Optimisation towards resilience

2.1 Upper Tamakoshi Hydropower Project & Geological Regime

Upper Tamakoshi is a peaking run-of-river hydroelectric scheme in NNE Nepal, located close to the border with China, which generates 456 MW power output. The gross head is 822m, with a design discharge 66 m³/sec, and a reservoir of 0.9 million m³ storage capacity. The main project components comprise: a) a 22m high concrete dam with twin settling basins; b) the 7.9km long partially lined headrace tunnel; c) two vertical penstock shafts (373m and 311m); d) a 695m vertical surge system; e) an underground valve chamber; f) a powerhouse complex that hosts six units (l:142m x b:13m x h:25m); g) a transformer cavern (l:167m x b:13m x h:19m); and h) a 2.9km long tailrace tunnel. The headrace tunnel (HRT) was excavated with conventional method (drill & blast) in inverted-D shape (6m height, 6m span; 32.1 m² cross-sectional area). 15% of the tunnel is concrete lined (1.2 out of 7.9km), in five sections due to design modifications; principally related to deviations from the anticipated geomechanical and geohydrological conditions.

The project area is situated 20 km north of the Main Central Thrust (MCT) tectonic zone, allocated in the metamorphic units of the Higher Himalayas, represented mainly by micaceous Schists and banded Gneiss with abundant mica contents. The surrounding rock-mass is characterized by light grey to dark grey, fine to coarse grained Gneiss, intercalated with biotite-muscovite Schists and quartz & Pegmatitic veins. The massif is truncated by major lineaments, mainly trending towards NNE to NN. With reference to the geomorphology, some of the major tributaries run along prominent lineaments of the catchment area, mostly coinciding with the joint systems of the rock mass, and especially with the Gneiss' foliation. The regional geomorphological map illustrates an extensive well-developed dendritic network which

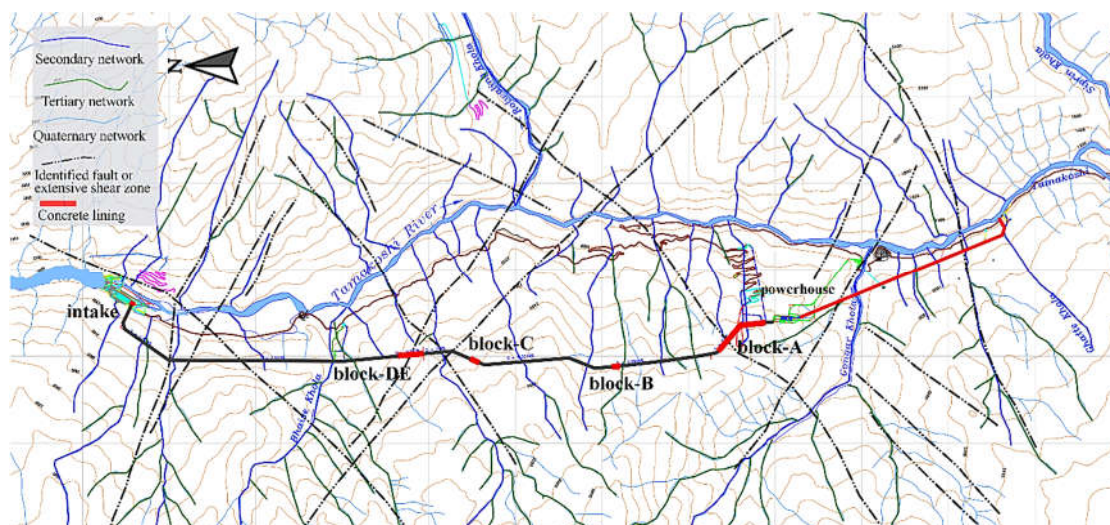covers the catchment area of Tamakoshi river (Figure 1).

Figure 1. Regional geomorphological map of Project area

Based on seismicity records along the Main Frontal Thrust (MFT) of the Himalaya, the tunnel aligns parallel to sub-parallel to the trend of tectonic horizontal stress (NNE) (Basnet and Panthi, 2019).

2.2 Conceptual Design & Optimisation

The integrity of the investigation phase and the adequacy of the acquired hydrogeological and geomechanical information are pivotal for the selection of an optimal and safe tunnel alignment. However, the geomorphology and the steep terrain of the area limited the accessibility and therefore, the accuracy of the engineering geological information. During the design stage, the alignment was based on the Norwegian criterion, aiming to construct an inclined and unlined waterway (~7° slope, supported with shotcrete, rock bolts, and steel ribs). However, in-situ stress measurements which were conducted during the excavation revealed a low horizontal stress regime, and an indicative anisotropic regime; a fact that based on Panthi & Basnet (2017) results in a decrease in the confinement of rock mass and anisotropic in-situ stress conditions. The minor principal stress was measured as low as 1.9-1.2 MPa, a range of values that under a high overburden (>500m) could be associated with areas of weak rock mass or sheared zones. In line with the test results, and in order to eliminate hydrojacking risk, the alignment was revised to slightly horizontal (<1° slope); and in order to increase the overburden, the downstream part was also shifted further away from the slope (i.e. the valley side). The encountered rock mass quality along certain stretches in conjunction with the groundwater behaviour during the excavation stage differed from the design assumptions (i.e. the anticipated conditions). Consequently, for stretches where rock mass was defined incompetent to deal with long-term stability, and to bear hydraulic fluctuations; the design concept was revised, and these stretches were lined with reinforced concrete.

Tunnel sections were casted in order to confine vulnerable and incompetent areas with respect to the inferior quality and the poor hydraulic performance of the surrounding rock mass. Nevertheless, a residual risk still remains within the transition areas at the contact between unlined and concrete lined stretches, along cold joints, and adjacent to the intersection areas with access adits. For these areas, systematic high-pressure barrier grouting was conducted at transitions between lined and unlined sections aiming to contain such zones by:

- establishing a radial low-permeability buffer,
- improving the major intrinsic rock-mass properties of the transition sections, and

- addressing localised human-induced fragmentation and stress issues which in principle relate to the excavation of the structure (i.e. excavation damage zone and the redistribution of stresses).

2.3 Geology of Headrace Tunnel

The entire tunnel was excavated through Gneiss. The engineering geological characteristics of the formation based on the ISRM standards (Barton, 1978) are described as follows.

Light grey to dark grey, fine to coarse grained, strong to very strong (R4-R5) and locally medium strong (R3), fresh to moderately weathered (F-MW) and locally highly to completely weathered (HW-CW), thin to very thick foliated, GNEISS, with pegmatite & quartz veins. The joint surfaces are smooth to rough, planar (class VII, VIII) and locally slickensided (III), tight to open (0.1-1mm) with occasionally extremely wide (20-80cm) apertures. The apertures are either empty, or filled with sand or clay. The joint spacing ranges between close to wide (0.08m to 2.0m), with very low to medium persistence (0.8m to 10.0m). The predominant geostructural features are expressed by three main joint sets and random joints (class VII), signified by gneissosity. The overall geometry is blocky, and seepage during excavation was mainly insignificant with occasional dripping and minor inflows (class I-II), and localised major inflows (class IV). Small-scale mild spalling effects were observed between chainage 0+500 and 1+500 km.

The Norwegian Geotechnical Institute's empirical classification Q-system (NGI, 2022) was utilised for the assignment of temporary support measures. The rock mass quality based on the actual mapped values covers a vast range from exceptionally poor (<0.01) sections to extremely good (>100) (mean value: 6.8; most frequent value: 11.2). The summary of Q parameters is portrayed in Table 1. Due to the aforementioned localised extremely poor to very poor rock mass quality four stretches were concrete lined and contained with high pressure barrier grouting fans. The characteristics of the lined sections and the main grounds for the design modifications, are summarized in Table 2.

Table 1. Encountered rock mass quality (Q-system; NGI standards, 2022)

Parameter	Description	Range	Frequent value
RQD	Very poor to excellent	10-98	90
Joint set number J_n	Crushed rock to two sets and random joints	20-0.5	6
Joint roughness J_r	Slickensided planar to discontinuous joints	0.5-4.0	1.5
Joint alteration J_a	Strong overconsolidated thick bands of clay to tightly healed	10-0.75	3.0
Water reduction J_w	High pressure inflow to dry conditions	0.33-1.0	1.0
Stress reduction SRF	Moderate spalling to medium stress	10-1.0	1.0

Table 2. Concrete lined stretches

Concrete block	Chainage		Q-value		Grounds of modification
	from	to	min	max	
Intake	0+000	0+020	7.5	12.0	Low overburden (<60m)
DE	3+552	3+835	0.007	0.03	Extremely to exceptionally poor rock mass, moderate inflows (12-14 lit/min)
C	4+390	4+508	0.02	0.28	Very poor to extremely poor rock mass
B	6+046	6+134	0.5	>1.0	Very poor rock mass & extreme ingress (locally >150 lit/min)
A	7+284	7+940	0.02	0.75	Very poor to extremely poor rock mass, high hydrostatic pressure (>110m)

3   Methodology of Grouting Programme

Considering the principal objectives of the grouting programme, stable cement mixes were injected for the improvement of rock mass properties, for the control of groundwater flow, aiming to form a watertight buffer before and after the concrete lined tunnel sections. The grouting rounds comprised systematic radial staggered grout-fans, drilled perpendicular to the periphery, all tested, injected, in two sequential stages based on the grouting target depth; i) the deep, and ii) the shallow stage. All holes were finally plugged with non-shrinking mortar.

The grouting programme commenced with the execution of the deep stage, with a varying target depth between 12 and 25m, and varying maximum injection pressures between 10, 30 and 45bar; values that should not exceed the minimum rock stress (hydrojacking risk)) (Sapkota et al., 2021). The maximum applied pressure and the injection depths are dependant of, and proportional to the measured stress, the overburden, and the seepage conditions. The primary round consisted of two closely spaced fans (3.0m longitudinal spacing, 8 holes each), with the permeability criterion set to 0.5 Lu. This constitutes an iterative procedure which comprises supplementary rounds (i.e. supplementary full fans at 1.0m longitudinal spacing or split holes), until criteria were met in all drilled holes.

The subsequent stage consisted of shallow injections, to a 5m target depth, and varying maximum injection pressures between 10 and 30bar; with applied pressures been proportional to the seepage and stress conditions, as well. The testing and injection strategy adopted the principles of the deep stage (i.e. supplementary rounds and 0.5 Lu permissible limit). The entire process is described in Figure 2, below.
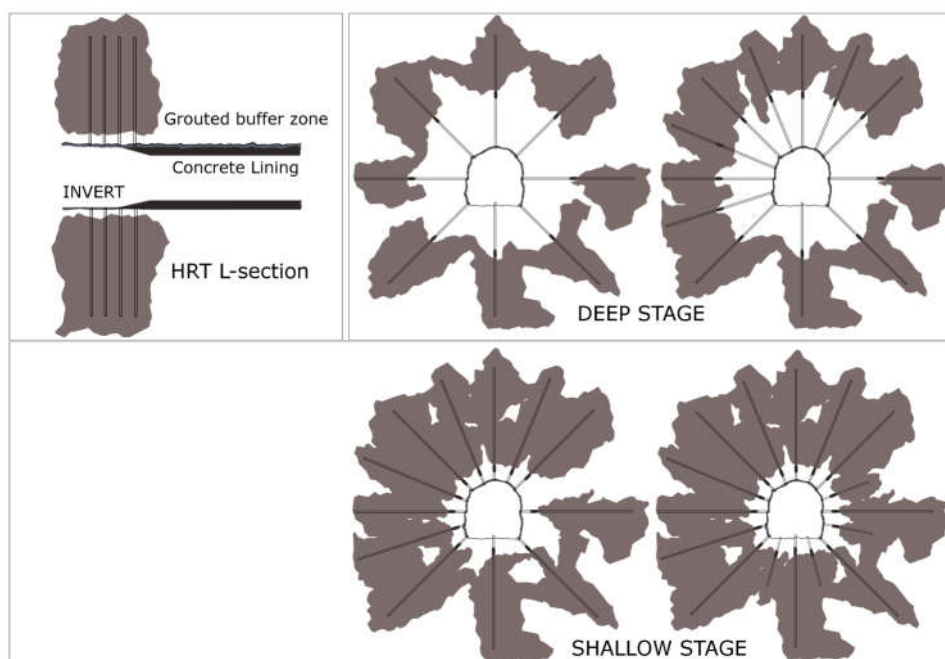
Figure 2. Barrier grouting drilling & injection process

The cement suspensions enhanced with chemical admixtures were used for all stages. Groutability can be influenced by large scale lineaments and tectonic features, rock mass geomechanical properties and joint characteristics, the excessive groundwater pressure, and the blasting performance. To optimise groutability, two cement types were used; ordinary Portland cement (OPC) for holes of permeability higher than 3 Lu, and microfine cement (MFC) for those of lower value. The maximum injection volume for holes with permeability measured below 8 Lu was set to 2000 litres, and for holes exceeding 8 Lu to 3000 litres. The injection adopted a gradual ascending density strategy. i.e. from thin to thick mixes,

according to the grout take behaviour of each hole. Therefore, holes of low permeability (<3 Lu) were injected with MFC grouts ranging from 1.2 to 0.6 water/cement ratio and the addition of superplasticiser (2.0-1.0%); holes of moderate permeability (3-8 Lu) were injected with OPC grouts ranging from 1.2 to 0.6 water/cement ratio and the addition of superplasticiser (2.0-1.0%); and holes of higher permeability (>8 Lu) were injected with OPC grouts ranging from 1.0 to 0.5 water/cement ratio and the addition of superplasticiser (1.5%). Figure 3 illustrates the process flowchart.
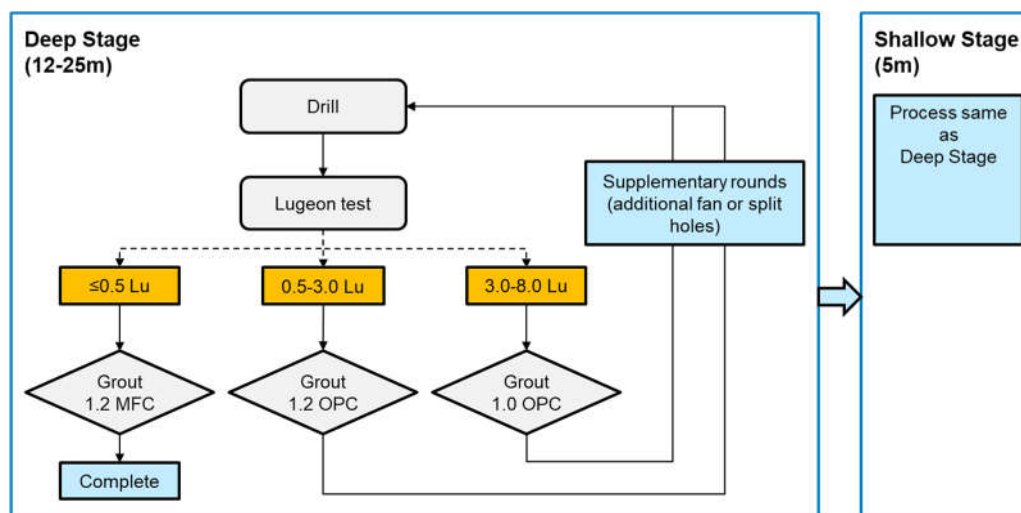
Figure 3. Barrier grouting process flowchart

Grouting can employ normal cements, very fine binders, chemical grouts, and enhancement admixtures. Nonetheless, variations in the mix with respect to cement quality (specific surface), water/cement ratio, the presence of admixtures (e.g. bentonite, silica, superplasticiser, etc.), and the temperature influence the behaviour and the performance of the injected mix in terms of yield stress, viscosity and binding time (Håkansson, 1993). Consequently, quality control during the entire operation is an integral factor for efficient operation. Given the fact that grouting necessitates tailor-made designs, only quality control can assure the stability and the groutability of the mix, and primarily verify the suitability of grouts.

4   Grouting Programme Evaluation and Analysis

Aiming to satisfy the main objectives of the tunnel optimisation programme and establish an impermeable buffer zone at the boundaries of the concrete lined sections, 692 grout holes in eight tunnel sections (total tunnel length: 54m) were drilled, tested, and grouted. In total, 237.9 m³ of grouts were injected through 5372 metres of grout holes.

As already stated, water pressure tests were carried out for all holes, prior to grouting. The measured permeability for the majority of holes (78.2%) is characterised "very low", with values between 0 and 1.0 Lu, whereas 11.3% of holes exhibited permeabilities between 1 and 5.0 Lu, i.e. "low", 8.1% between 5 and 15 Lu, i.e. "moderate", and 2.4% between 15 and 50 Lu, i.e. "medium". Apart from the majority of holes (78.2%) where permeability values indicated very tight and dry conditions (Lu<1.0), 14.7% of tested holes featured turbulent behaviour, 1.7% laminar behaviour, 1.6% "dilation", 2.6% "washout", and 1.2% "void-filling". To achieve the design criteria (0.5 Lu max permeability) of the eight buffer zones, for the 434 primary holes another 258 supplementary holes were drilled tested and grouted. According to the design criteria for the selection of grout mix, 592 holes (85.5%) were injected with microfine cement mixes (Lu<3.0), 49 holes (7.1%) were injected with Portland mixes of 1.2-0.8 water/cement ratio (Lu 3.0-8.0), and 51 holes (7.4%) with Portland mix of 1.0-0.6 water/cement ratio (Lu >8.0). The testing and injection summary is illustrated in a set of graphs (Figure 4 and Figure 5).
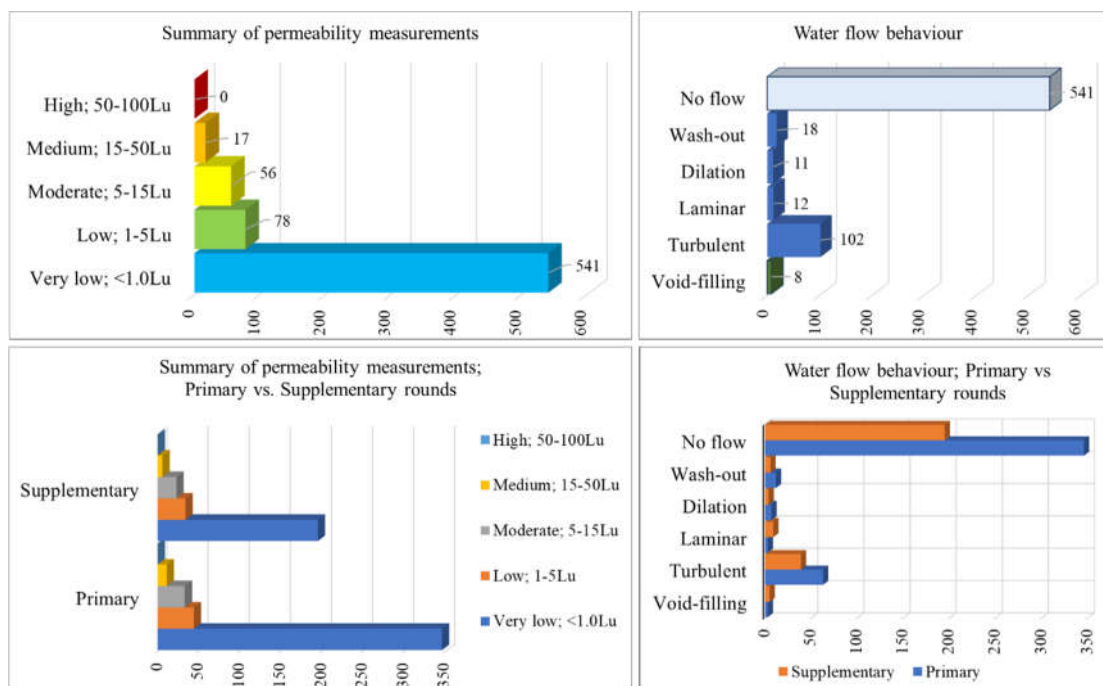
Figure 4. Summary of permeability and water flow behaviour
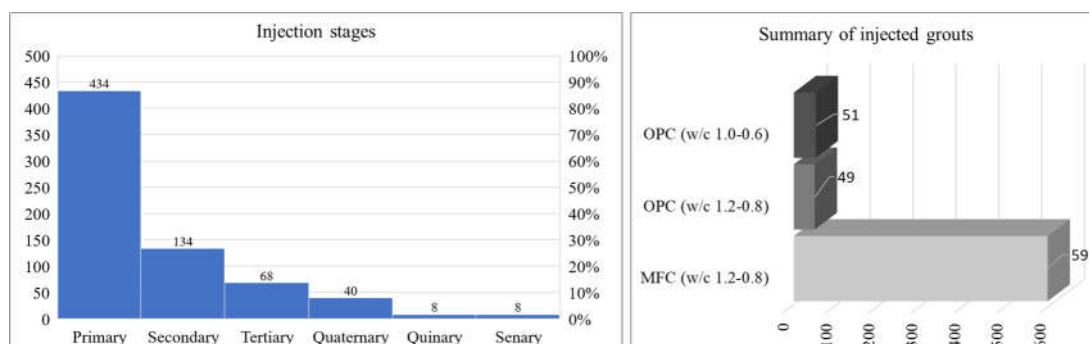
Figure 5. Summary of grouting stages and injected grout mixes

For the evaluation of the grouting outcome, and for research purposes, the authors considered the following parameters:

- Consumption rate (Q_g) corresponds to the injected volume in a 1m grout-hole segment (litres/m). The unit provides direct information about the groutability of the injected segment.
- Consolidation ratio (*CR*) corresponds to the ratio between the injected volume and the theoretical rock mass volume of the grouted tunnel zone (%). The unit reflects the theoretical void space (primary and secondary) within the grouted block.
- Drilling factor (D_f) is the ratio of the drilled metres of the supplementary holes required to achieve the design criteria (0.5 Lu) divided by the drilled metres of primary holes. The unit provides an indication for the required grouted metres to control residual permeability, and an estimate regarding the geometry of the anticipated fissures, joints, voids, and their interconnection.
- Volume factor (V_f) is the ratio of the injected volume of the supplementary holes required to achieve the design criteria (0.5 Lu) divided by the injected volume of primary holes. The factor constitutes a preliminary index for the necessary volume consumed to form an impermeable

    barrier within the grouted target zone.

- Consumption factor (C_f) is the ratio of the consumption rate of supplementary holes required to achieve the design criteria (0.5 Lu) divided by the consumption rate of primary holes. The factor can provide information about the residual "*absorptive*" capacity of the rock mass.

The majority of holes for both primary and supplementary stages was injected with low rates (Q_g) which did not exceed 20 lit/m, with filtered mean rates (5% filtering of extreme low and extreme high volumes) 23.7 lit/m for the primary and 24.4 lit/m for the supplementary stages. The consumption rates are illustrated in Figure 6.
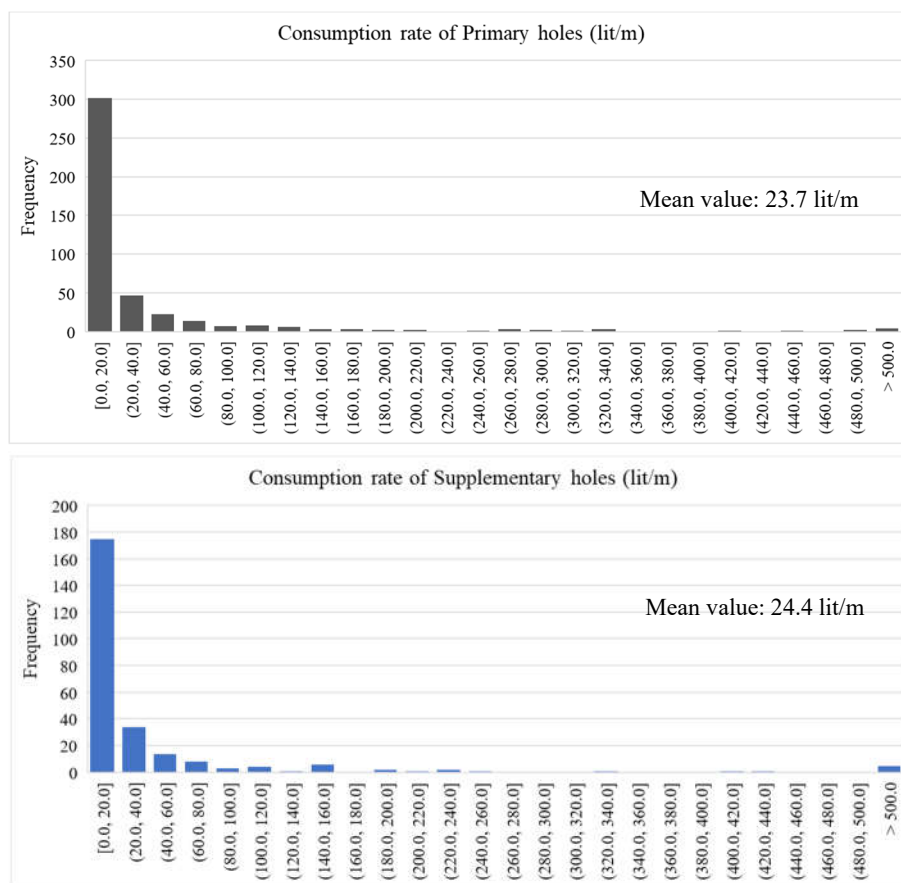
Figure 6. Summary of consumption rates (Q_g) per grout stage

The range of the consumption rate for all blocks varied between 23.3 and 110.8 lit/m, with the highest rates been measured closer to the intake area of the tunnel (block DE-u/s and Intake block). In a similar pattern, the highest consolidation rates were measured in the same upstream blocks, with *CR* values for all blocks ranging between 0.3% and 2.12%. Contrarywise, the highest drilling factors (D_f) were recorded at the most downstream block (block A) with values ranging between 0.63 to 3.54. The volume factor (V_f) ranged between 0.15 and 1.05, without showing any characteristic behaviour with respect to the tunnel's alignment; whereas the consumption factor (C_f) also did not show any normalised behaviour along the tunnel and ranged between 0.14 and 1.24.

The aforementioned parameters were correlated with the actual geomechanical parameters of the tunnel, i.e. the overburden (H), the as-mapped Q-values, and various combinations of the assigned individual Q factors (i.e. block factor: RQD/Jn, joint factor: Jr/Ja, the normalised Q value by excluding the stress deduction factor SRF, and several combinations with the parallel use of experimental constants). The summary of input and grouting output values for each grouted block is illustrated in Table 3.

Table 3. Summary of basic injection parameters

Block	Overburden (m)	Q-value	Q_{norm}	Q_g (lt/m)	CR %	D_f	V_f	C_f
A-u/s	569	25.3	12.50	23.6	0.30	3.54	0.90	0.25
B-d/s	681	4.1	9.63	46.7	0.75	2.06	0.75	0.36
B-u/s	681	3.9	6.04	26.4	0.30	1.13	0.15	0.14
C-u/s	917	1.1	5.83	45.7	0.39	0.63	0.77	1.24
C-d/s	830	7.1	2.78	39.3	0.44	1.06	1.05	0.99
DE-u/s	680	1.5	4.67	36.5	0.42	1.19	0.60	0.51
DE-d/s	532	11.9	12.50	107.4	1.55	1.69	0.75	0.44
Intake	61	7.5	9.38	110.8	2.12	1.68	0.82	0.99

With respect to the correlation between output parameters, the correlation between the injection rate (Q_g) and the consolidation ratio (CR) indicate and exponential ascending trend of high reliability ($R^2=0.944$). Among the correlated parameters, the drill factor (D_f) produced an exponential reliable ascending correlation (coef. of determination $R^2=0.806$) against the actual Q-value, and the overburden produced an exponential reliable descending correlation (coef. of determination $R^2=0.724$) against consolidation ratio (CR). The corresponding graphs are shown in Figures 7 and 8.
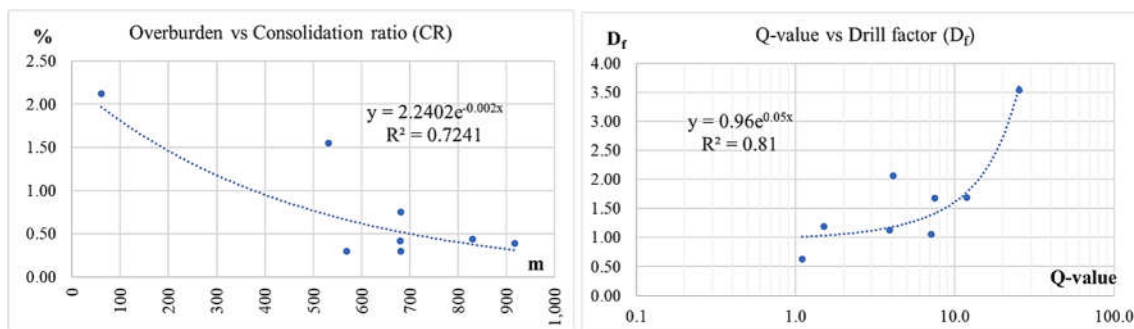
Figure 7. Correlation graphs between input and output grouting parameters
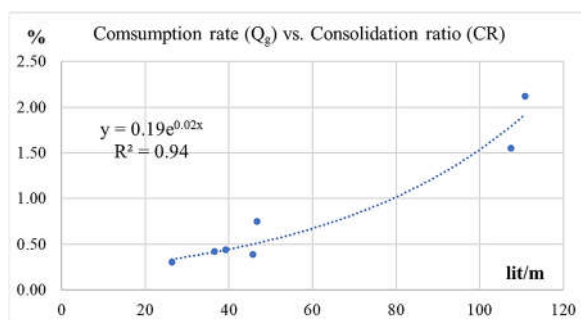
Figure 8. Correlation graph between output grouting parameters (Q_g per m of grout hole vs. CR)

5 Conclusions

Based on the available test data, the major fraction of primary holes (77.4%) met the established permeability criteria (0.5 Lu), whereas a larger fraction (~90%) of all primary and supplementary holes is characterised by very tight to tight conditions (<5 Lu). The permeability tests for the 14.5% of primary holes and the 15.2% of the supplementary holes indicate turbulent flow. Turbulent flow relates to partly open to moderately wide cracks. In line with these observations, the overall structure of the grouted

zones mainly indicate the presence of small-scale localised fractured zones, or isolated areas of inferior quality rock mass which have been addressed by the high-pressure barrier grouting programme; but not extensive interconnected features or significant water flow conduits. In addition, the barrier grouting programme managed to form and integrate impermeable and improved rock mass buffer zones to the concrete lining segments. Headrace tunnel was filled with water and the project was set into operation in August 2020. After 25 months of operation, the authors inspected the entire tunnel during the first dewatering. The subsequent conjecture was in practice verified by the seepage behaviour of the grouted zones in comparison to the zones' behaviour prior to water filling and after the execution of the grouting programme; as well as the state of the concrete lining. In brief, no changes in seepage conditions were measured and observed, and no defects were found in the casted segments and their structural joints.

Apart from holes that met threshold criteria, for the 22.6% of holes who exhibited higher permeabilities, 258 supplementary holes were drilled, tested and grouted in five stages. The average consumption rate (Q_g) of the primary stage was 48 lit/m (filtered mean 23.7 lit/m), and the rate of the supplementary stages was slightly reduced to 46 lit/m (filtered mean 23.7 lit/m). Moreover, a comparison of the consumption rate for all stages show a uniform distribution of values, of relatively low takes (<40 lit/m; Figure 6). As portrayed in the correlation graphs (overburden vs *CR*) there is an inverse exponential relationship between overburden and consolidation ratio; the greater the overburden, the lower the required grout volume. Moreover, there is a strong positive exponential relationship between the consolidation ratio (*CR*) and the consumption rate (Q_g). Thus, higher *CR* values, which indicate higher theoretical void spaces, correspond to anticipated increased grout consumption per meter of a grout-hole segment. Further to the overburden impact, and with respect to rock mass quality, there is a reliable exponential correlation between Q-value and D_f; a relationship that pinpoints a higher demand of supplementary drilled metres in order to address permeability issues in higher quality rock masses.

The estimation of *CR* and D_f are crucial for predicting grout consumption and planning the resources for a grouting programme. The detailed analysis of test and injection data with references to the geological and stress regime could provide valuable information towards a quantifiable approach. Notwithstanding, for the development of more accurate and reliable grouting pre-estimate relationships, the authors recommend further data analysis from other reference projects.

References

Barton, N., Suggested Methods for the Quantitative Description of Discontinuities in Rock Masses: Int. Soc. for Rock Mechanics. *Int. Jour. of Rock Mech. Min. Sci. Geom.,* Abstr. 15. 319-368. 1978

Basnet C.B., Panthi K.K. Evaluation on the Minimum Principal Stress State and Potential Hydraulic Jacking from the Shotcrete-Lined Pressure Tunnel: A Case from Nepal. *Rock Mech. Rock Eng*, 52, 2377-2399. 2019.

Brox, D. Hydropower tunnel failures: risks and causes. *Tunnels and Underground Cities: Engineering and Innovation meet Archaeology, Architecture and Art.* CRC Press. 2019.

Håkansson, U. *Rheology of fresh cement based grouts*. PhD Thessis, Division of Soil and Rock Mechanics, Royal Institute of Technology, Stockholm, Sweden. 1993.

Hencher, S.R. The Glendoe Tunnel Collapse in Scotland. *Rock Mech Rock Eng*. 52, 4033–4055. 2019.

NGI, *Using the Q-System; Rock Mass Classification and Support Design*, Oslo, Norway. 2022

Panthi, K.K. and Basnet, C.B. Design review of the headrace system for the Upper Tamakoshi project, Nepal. *International Journal on Hydropower and Dams*. 24 (Issue 1), 60-67. 2017.

Sapkota, S.; Christakis, R.; KC, J.; Raut, M. Combination of cementitious and chemical grouting in the transition zone of unlined and concrete-lined tunnel: a case from Upper Tamakoshi Hydroelectric Project, Nepal. *Proceedings of the 3rd European Regional Conference of IAEG,* Athens, Greece. 2021.

Shrestha, A. *Evaluation of deformation pressure on shotcrete lining at the headrace tunnels caused by squeezing and swelling of rocks*. MSc. Thesis, NTNU, Trondheim, Norway. 2021.

SOIL-WATER RETENTION AND DRAINAGE DURING SHEAR OF AN UNSATURATED GRANULAR MATERIAL

PAUL CHIASSON [1]

[1] *Department of Civil Engineering, Université de Moncton, Canada, paul.a.chiasson@umoncton.ca*

Abstract
The soil-water characteristic curve reveals that a first set of specimens of dense crushed sand and gravel with 8.9% fine particles content proves unable to maintain a saturated state under a positive matric suction. Capillary physics explains how this could result from the presence of millimetre size pores and why certain soils might display a null air-entry value. Unsaturated drained triaxial compression tests performed on a second set of samples confirm a relationship of the degree of saturation with the void ratio and matric suction while shearing. This defines a soil-water characteristic surface that is in turn used to analyze why loading induces the observed continuous outflow of water. Contrary to intuition, the results of this study show how the uninterrupted drainage during both contraction and dilation phase appears to remain compatible to the soil-water characteristic surface model. Furthermore, shearing of unsaturated materials that contract and then dilates creates a transitional wetting followed by drying cycle.

Key words
Soil-water characteristic surface, air-entry value, unsaturated soil, drained triaxial shear

1   Introduction

It stands established that drained shearing of dense saturated granular soils initially induces volumetric contraction and outflow of water. Further loading leads to volume expansion while water inflows into the sample. Khoury and Miller (2012) and Rahardjo et al. (2004), among others, report data where this one-to-one relationship between water flow and volume change no longer holds during drained shearing in an unsaturated state. They rather observe a continuous expulsion of water, even throughout the dilation phase. It appears that this phenomenon remains unexplained when writing this paper.

Ke et al. (2013) showed for three clean sands that at a set suction, a smaller void ratio yields a higher degree of saturation. Gallipoli et al. (2003) point out for their part that in a deformable soil, variations in the void ratio alters the size of the voids and of connecting pathways. This will necessarily lead to a change in the water retention curve. Using data from isotropic consolidations at constant matric suctions on a compacted Speswhite Kaolin, they confirmed that the degree of saturation rises as void ratio decreases. They also corroborated this in a drained unsaturated triaxial test at constant matric suction where the decreasing volume produced by the application of a stress difference q under constant net stress also conducted to an increasing degree of saturation. During both these types of volume contraction, the degree of saturation thus rose as the void ratio decreased. On this basis, they developed a model for a soil-water characteristic surface. It involves matric suction, the degree of saturation (which characterizes the soil's capillary capacity to partially fill voids with water) and the void ratio (that relates to the relative void size and interconnections). As for water drainage during loading, it isn't addressed.

This study aims to ascertain why drained triaxial shear of an unsaturated dense granular soil induces water outflow throughout both contraction and dilation phases. It evaluates the soil-water characteristic curve (SWCC) and examines the air-entry value of coarse materials for a first set of specimens that display large voids. It proceeds with reporting results obtained on a second set (exhibiting no macro

pores) from triaxial compression CD tests. These are performed after a desorption stage alone and after a cycle of desorption followed by sorption. Soil-water retention during shear is investigated and its link to the void ratio. It finally pays attention to the continuous water outflow throughout loading and changes in the degree of saturation (soil-water retention) and how this relates to matric suction and void ratio.

2   Methods

The studied crushed sand and gravel contains 8.9% of non-plastic fine particles. This well-graded soil gives coefficients of uniformity and curvature of 35 and 5.9. The triaxial shearing method in unsaturated state used a modified Bishop and Wesley triaxial cell such as described by Fredlund and Rahardjo (1993). Specimens manufacturing proceeded by a successive static compaction of five (5) 20 mm layers in a 50 mm diameter mould to attain the standard optimum proctor of 2100 kg/m3 in dry density at 7% water content (Figure b). These then sit on a 300 kPa HAEV (High Air-Entry Value) porous stone (saturated in advance) embedded in a pedestal and topped by a coarse-grained porous stone. Saturation starts by a slow water inflow by the base under a partial vacuum applied at the top. Valve closure follows when water exits into the upper drainage line. Successively increasing by small increments the back and cell pressures up to 500 kPa (the latter always higher by 10 kPa) ends this step. A Skempton coefficient (B) of 0.97 served to confirm saturation. The action of an isotropic net confinement stress then consolidates the saturated soil specimen. This is judged complete when the pore pressure attains the back pressure.

Desorption begins by applying air pressure (u_a) at the top end equal to the water back pressure (u_w) from the base. Subsequently decreasing the latter creates a matric suction (u_a-u_w) that dries the sample by water drainage through the base. The desorption-sorption cycle starts by desorption under a matric suction of 295 kPa. Following this, increasing the water pressure to an aimed value lowers the matric suction and induces water flow back into the specimen. During this desaturation operation called the equilibrium phase, the isotropic confinement stress remains unchanged. This axis-translation technique makes it possible to set the matric suction to a target value while maintaining the net confinement stress ($\sigma_3 - u_a$) constant under positive air and water pressures. Axial loading then proceeds at a constant strain rate of 0.01 mm/min up to 15% of total axial strain. A constant matric suction ($u_a - u_w$) and constant net confining stress ($\sigma_3 - u_a$) throughout loading characterizes the unsaturated CD triaxial test. Under a drainage condition by the base (water) and top end (air) of the specimen, excess pore water and pore air pressures created by shearing both dissipate during testing.

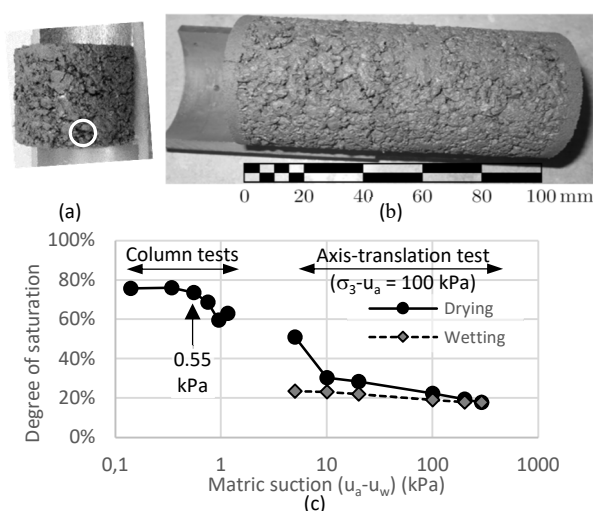**Figure 1.** Specimens for (a) measurement of soil-water retention (circled void at left has an approximate width of 6 mm) and (b) unsaturated triaxial shear; (c) Soil-water characteristic curve as determined by column tests ($\sigma_3 - u_a = 0$ kPa) and by axis-translation technique in the triaxial cell ($\sigma_3 - u_a = 100$ kPa).

Measurements of the SWCC at matric suctions above 5 kPa proceeded in the modified triaxial apparatus

by using the axis-translation technique under 100 kPa of net isotropic confinement pressure ($\sigma_3 - u_a$). The 50 mm diameter specimen had a reduced height of 40 mm (Figure a). This low height minimizes time to attain a constant water content. The equilibrium of the matric suction in the specimen is assumed to be achieved when the volume of water drained from the specimen becomes asymptotic over time. The closure of the drainage valve and the subsequent evaluation of the water pressure proved to stabilize at the targeted matric suction. This validated this method for determining the end of drainage.

Measurements for lower matric suctions used column tests. Material static compaction proceeded in a steel tube by a succession of 20 mm layers up to a total height of 120 mm. This permitted to apply precise matric suctions between 0.10 kPa and 1.1 kPa. Drying tests start by saturating the column under vacuum in an air- and water-tight cell and a slow water inflow from the base. Once saturation confirmed by reaching the targeted total mass, cell and specimen were then let to drain by the base soaking in water. Columns tests were extended up to 47 days to stabilize within 0.1 g of total setup mass, ensuring an error below 0.2% in degree of saturation.

3   Results

The following first presents the soil-water characteristic curve before proceeding with the results of the triaxial CD tests.

3.1 Measurements and interpretation of the soil-water characteristic curve

Desorption column tests immediately reveal an unsaturated state at a matric suction value of 0.14 kPa (Figure c). This 14 mm total water head corresponds to one of the lowest achievable matric suctions by this method that allows a reliable measurement of water content on a representative volume. Generally, conceiving a representative volume of material necessitates a specimen thickness of at least 20 mm. Since 0 kPa equates to the smallest attainable matric suction at the base, the top end develops 0.196 kPa. This gives a lower boundary of 0.098 kPa for the average matric suction.

The studied soil maintains approximately 74% saturation for the two subsequent measurements (Figure c). It then dries up abruptly beyond matric suctions of 0.55 kPa at a desaturation gradient of 25.3%/kPa. It falls to a degree of saturation of 61.3% at a matric suction of 1.05 kPa.

Attaining higher matric suctions in column tests requires higher specimens that increase their duration exponentially. A change of method therefore becomes necessary. This study used the axis-translation technique for this purpose. However, these tests were carried out under a net confinement stress which increases the air-entry value of unsaturated soils (Vanapalli, 2009). These latter measurements will therefore be translated to the right compared to those taken from column tests. This may explain a certain discontinuity in the data of the two methods as presented in Figure c.

The axis-translation test under a net confinement stress ($\sigma_3 - u_a$) of 100 kPa shows that the degree of saturation continues to drop abruptly to a residual value of about 30% at a matric suction of approximately 10 kPa (or less). The degree of saturation then decreases at a low rate on a logarithmic scale to attain 17.8% at a matric suction of 290 kPa. During subsequent sorption (wetting), the material absorbs water at an even lower gradient (Figure c) up to a water-entry value with a degree of saturation in the order of 23.5% and a matric suction below 5 kPa (500 mm of water head).

Between matric suctions of 0.14 kPa to 0.55 kPa, it is interesting to observe that water content in desorption columns rest on a sill below 100% saturation. In other words, not all the pores of the tested specimen seem capable of maintaining themselves in the saturated state. Although no one appears to report this observation, calculations based on water content data published by Zhao and Zhang (2014) give a degree of saturation sill value of 92%. Their material (90% coarse particles) displayed a double porosity. It contained 10% non-plastic fine particles, which compares to the 8.9% of this study.

Rigorously speaking, the true height of capillary rise depends on the Young-Laplace equation which defines matric suction (or Laplace pressure) $u_a - u_w$ in function of the air-water interface geometry by:

$$u_a - u_w = T_s \left(\frac{1}{r_1} + \frac{1}{r_2} \right) \tag{1}$$

In this equation, r_1 and r_2 define the principal radii of curvature at a point on the air-water interface while T_s corresponds to the surface tension (72.75 mN/m at 20 °C). By assuming it forms the surface of a spherical sector with a solid-liquid contact angle θ, the radius R of a capillary tube will correspond to the contractile skin's principal radii of curvature. Since the air pressure u_a applies on the air-water interface on both the inner side and outer side of a capillary tube, (1) becomes:

$$h \cong \frac{2T_s \cos \theta}{\gamma_w R} \tag{2}$$

Where γ_w corresponds to the unit weight of water. This latter expression, known as Jurin's law, defines the height of ascent h in a capillary tube as a function of its inner radius R. According to this law and a null contact angle, a capillary ascent of 5.4 mm should be observed in a tube of the same diameter. If this law applies to soils, only voids below this size may maintain saturation by capillarity. Jurin's equation, however, has its limits of appropriateness. Moving away from the wall of a large diameter tube, gravity takes over surface tension, and the contractile skin flattens. In this case, the earlier assumed spherical contractile skin overvalues true capillary ascent. The distance where gravity (the weight of the water column above the free surface) equals the Laplace pressure defines the capillary length l_{ca} (de Gennes et al., 2004). Jurin's law doesn't overestimate the height of the capillary rise when the radius of the tube falls much smaller than the capillary length ($R \ll l_{ca} = \sqrt{T_s/\gamma_w}$). A temperature of 20 °C gives a capillary length of 2.7 mm, meaning that the earlier discussed 5.4 mm diameter tube would yield a lower capillary ascent. It should rather be in the order of 4.7 mm according to the Prokhorov (1996) correction. Hence, a tube gives a height of capillary ascent equal to its diameter when the latter is of 5.1 mm. Assuming a soil has the same rise as a capillary tube, capillarity may maintain saturation of a 5.1 mm high soil column only if its maximum pore size falls smaller than 5.1 mm. This would give such a soil an air-entry value of 0.05 kPa. However, this defines an unattainable upper boundary limit. This maximum pore size should turn out much smaller, since the soil pore network bears no resemblance to tubes of circular cross-section. Lourenço et al. (2012) also reports that the shape of the contractile skin of water in soils adopts much more complex configurations than the concave and regular surface observed in a capillary tube. Hence, the relationship between the contractile skin's average radius of curvature and the pore size of a soil certainly differs from that with the diameter of a capillary tube. As a result, the maximum pore size capable of maintaining a state where water fully occupies it through capillarity would prove somewhat smaller than the diameter of a tube that yields a capillary rise equal to its height.

As equation (2) indicates, capillary rise also depends on the solid-liquid contact angle. The latter extends in a wetting sand from 60° to 80° and 30° to 80° for drying (Lu & Likos, 2004). In small tubes where Jurin's law applies (D < 2.5 mm), this reduces capillary rise by a factor of 0.17 to 0.87 for a contact angle of 80° to 30° respectively. To satisfy minimum volume representativeness, this study used column test of piled 20 mm segments in thickness to measure their water content and degree of saturation in function of the matric suction. For the subsample at the bottom of the column, assuming a 30° contact angle and that Jurin's equation applies, water may, at best, rise to the 10 mm mid-height and the 20 mm full height if pore sizes respectively correspond to 2.6 mm and 1.3 mm.

For the tested soil specimens, it appears that the matric suction of 0.55 kPa shown in Figure c draws a limit, where larger interconnected pores cannot maintain a greater degree of saturation by capillarity (they yield lesser capillary rise than their size). With the supposed 30° contact angle, Jurin's law gives for a matric suction of 0.55 kPa a diameter of 0.46 mm. Interestingly, more rigorous capillary pore size distribution computations based on a numerical integration procedure described by Lu and Likos (2004) produces a comparable result of 0.29 mm in size. Jurin's equation can thus serve to define a pore size

upper boundary linked to the air-entry value. For the studied soil, this upper boundary pore size corresponds to the air-entry value of its finer void matrix.

Visual inspection of specimens shows on the surface the presence of smaller millimetre size voids that interconnect larger voids ranging up to the order of 6 mm in width (Figure a and b). Arching of coarser particles against the steel mould throughout sample preparation seems the cause of the latter. According to the preceding discussion, the pore network appears likely to permit air penetration from top to bottom during drying. The resulting drainage would explain why the tested specimens cannot retain water at degrees of saturation higher than 74% (Figure c). This doesn't necessarily mean that they display a null air-entry value. Even 6 mm pore sizes should yield some capillary rise. Unfortunately, practical considerations impose a minimum sample thickness. To produce a soil-water characteristic curve requires to measure water volume (or mass) within a given total volume at a set matric suction. Exerting a matric suction at the level of the tested specimens' low air-entry value would require to prepare a sample with a height in the order of one to two millimetres. Considering the presence of particle sizes up to 6.3 mm in the material under study, this clearly proves unfeasible.

Hence, in the case of drying an initially saturated soil displaying a pore network unable to maintain its water content by capillarity, the air-entry value would mark a discontinuity in water content. The resulting SWCC should follow a step function, jumping from a saturated state to a degree of saturation somewhat below 100% when the matric suction crosses the air-entry value. This compares to the situation of the 100% degree of saturation of a set point somewhere under the contractile skin in a capillary tube. If the water level falls, the degree of saturation remains at 100% until the contractile skin attains the set point. It will then suddenly jump like a step function to a null value with a further infinitesimal drop of the water level.

The preceding arguments lead to postulate that certain soils may show a null air-entry value and a SWCC that follows a step function. In these soils, there exists an interconnection of "very" large pores characterized by very limited capacity to lift water by capillarity. This may turn out the case of clean uniform materials with particles of coarse gravel size or greater such as railroad ballast or rockfill. Whatever the air-entry value, an SWCC exhibiting a step function should have interesting repercussions on the hydraulic conductivity function. Since the air-entry value links to no single water content value, the same should be observed for the hydraulic conductivity when formulated as a function of the matric suction. For water flow computations, it should be possible to circumvent this difficulty by expressing it as a function of the degree of saturation, where there would exist a unique correspondence. Confirming these hypotheses needs further research. If they were to prove true, interesting consequences should result for problems such as the modelling of water flow in capillary barriers when matric suction reaches the air-entry value of the coarser layer.

3.2 Saturated triaxial tests

Three CD saturated triaxial tests at effective confinements of 25 kPa, 100 kPa and 200 kPa were performed to determine mechanical parameters such as the failure criterion and the volume change throughout shearing of the studied soil. In general, the material behaves under shearing as a dense granular soil and its failure envelope from the three CD saturated tests reveals zero effective cohesion (as with any granular material) and an effective friction angle of 43.1°.

3.3 Unsaturated CD triaxial tests in desorption

Shearing behaviour in the unsaturated state on the drying path was investigated through 15 CD triaxial tests. These were performed for matric suctions ranging from 5 kPa to 290 kPa under net confinements of 100, 150, 200 and 250 kPa. Among them, five (5) unsaturated triaxial loadings were carried out at a constant net confinement of 100 kPa under matric suctions of 5, 50, 100, 200 and 290 kPa (Figure presents the first three tests). Chiasson and Tamégnon (2023) used these same data to evaluate the hysteresis of the mechanical behaviour in drained loading performed after drying alone and after a drying and wetting cycle.

Shearing leads to total volume adjustments with initial contraction followed by expansion (Figure b). Water volume drains continuously during tests performed after initial drying (curves identified by Dxxx in Figure c), even through the dilation phase (except for the 100 kPa matric suction test which absorbs water beyond 4.5% axial strain). These variations to total and water volumes result by consequence into changes in the degree of saturation.

The degree of saturation during loading rises slightly for the first 0.5% to 1% axial strain (Figure d), meaning that the volume of voids in the unsaturated sample decreases faster than the volume of water retained in the pores. This constitutes an almost purely elastic stage where the plastic strain of the specimen remains low (little particle rearrangement). Beyond 0.5 to 1% of axial strain, the degree of saturation declines as axial strain increases. Above 7% axial strain, the rate of change in the degree of saturation dissipates, a sign that the material progresses towards a state of equilibrium even if it continues to deform (grains persist to move relatively to each other). At this stage, the rate of volume change also tends towards zero (Figure b).

Total and water volume changes plot a path in the degree of saturation to matric suction graph (Figure). The SWCC first heads slightly upwards then descends, passing through the value reached at peak shear strength and pursuing asymptotically towards a minimum. Loading thus creates a set of characteristic curves. It is worthwhile noting that a drained test at a constant matric suction doesn't imply a constant degree of saturation during shear. Forgetting this fact often occurs.

D: Drying path;   DW: Drying-wetting path;   xx: Matric suction
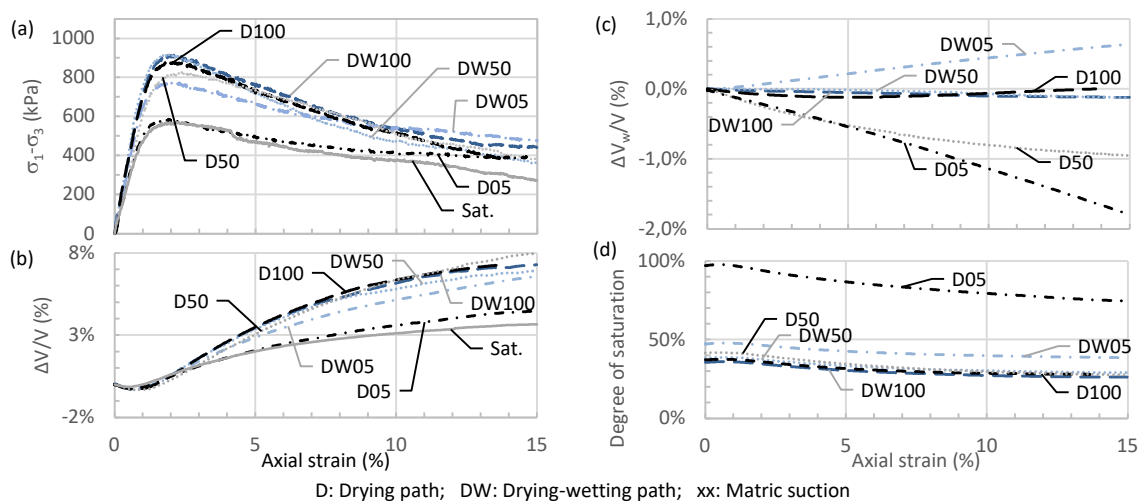
Figure 2. Saturated ($\sigma'_3 = 100$ kPa) and unsaturated on the drying path ($\sigma_3 - u_a = 100$ kPa) CD triaxial tests: (a) principal stress difference; (b) volumetric strain; (c) change in volumetric water content; (d) degree of saturation.

3.3 Unsaturated CD triaxial tests after a desorption-sorption path

Mechanical properties of the studied soil were determined on the desorption-sorption path using three (3) triaxial CD tests at matric suctions of 5, 50 and 100 kPa and submitted to a constant net confinement stress of 100 kPa. This confinement, identical to that employed on the desorption path, allows a comparative investigation of the effect of wetting (sorption). The desorption-sorption path follows in order: saturation, consolidation under confinement stress, drying under a matric suction of 295 kPa and wetting by decreasing the matric suction to the target value.

Following the desorption-sorption path, the studied soil shares several behaviours observed in saturated and unsaturated desorption loadings (Figure). As in the case of unsaturated triaxial tests on the drying path, the material after sorption shows a similar evolution in the degree of saturation during shearing. However, the degrees of saturation at failure fall lower than those measured on the drying path (Figure d). The primary distinction lies in a minute change in volumetric water content comparatively to that of the desorption path tests (Figure c). The change in the degree of saturation proves therefore mainly due

to total volume change.

Decreasing the applied matric suction on the desorption-sorption path gradually tends to shift from water discharge to absorption. For sorption at the higher 100 kPa matric suction, loading leads to a continuous, although very low, expulsion of water. This outflow declines when lowering the set matric suction and turns out close to null for a wetting matric suction of 50 kPa at axial strains of less than 4.5%. It even reverses into water absorption when shearing after initially wetting down to the lowest tested 5 kPa matric suction (DW05 in Figure c).
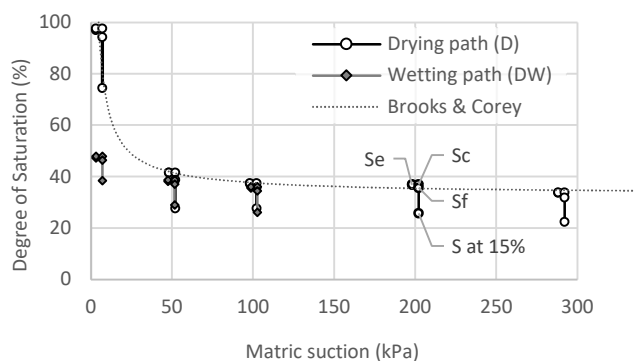

Figure 3. Degree of saturation paths in function of the matric suction during unsaturated shear after initial drying and initial drying-wetting. S_e, S_c, S_f and S at 15% represent values at equilibrium, maximum volume contraction, failure and 15% axial strain. Data points are slightly offset from their true matric suction to highlight the hydric trajectory throughout loading. An air-entry value of 4.7 kPa and a pore size distribution index of 0.86 gives the illustrated Brooks and Corey model.

3.4 Discussion of results

The characteristic curves presented in Figure c and Figure show that the column and axis-translation tests don't give the same results as those derived from the triaxial loadings. These differences may find an explanation in the preparation method of soil specimens. As earlier discussed, examination of sample photos reveals the presence of a network of large voids on their surface (Figure a and b).

Changes were introduced to sample preparation after noticing fissures on the high air-entry porous stone at the base pedestal following a preliminary triaxial test of the experimental program. This created an air pressure leak, hindering the application of the matric suction. Cracking was attributed to excessive concentration of the axial loading force at coarser grains contact points against the porous stone. The addition at the top and bottom of 5 mm thick fine particle soil layers fixed this problem. Subsequent study of photos of the modified specimens indicates that this change in their preparation for triaxial testing led to eliminate large voids at both extremities (Figure b). Examination of the samples after applying confining stress in the triaxial cell also showed that the membrane clung to their perimeter surface, which could have closed the bigger voids. In their absence, water retention would rise. This may explain the differences between results reported in Figure c and Figure . According to the latter figure, the specimens used for triaxial loading may feature an air-entry value in the order of a few kPa and a water-entry value under 5 kPa. Considering the steep desaturation gradient observed on samples in column tests (Figure c) that typically exhibit sands (Lu & Likos, 2004), the residual matric suction of triaxial specimens should be below 50 kPa. The modelled Brooks and Corey drying characteristic curve illustrated in Figure appears to confirm this.

3.4.1 Water drainage while shearing during both contraction and dilation phases

As observed for saturated shear tests, the material in the unsaturated state should intuitively drain during the volume contraction phase. Then absorb water throughout the subsequent dilation phase. Conversely, the contraction phase should decrease pore size, thus elevate capillary rise (or the degree of saturation) and yield water absorption while the dilation phase should act inversely. However, the findings don't appear to agree with either reasoning. In all but two tests (DW05 and D100 in Figure c), drainage occurs

in both the initial phase of contraction and pursues even so during the dilation phase. This behaviour appears contradictory and counter-intuitive.

As outlined in the introduction, evidence shows that a relationship exists between the SWCC and the void ratio where for a set matric suction, the higher the void ratio, the lower the degree of saturation. This should prove true for triaxial tests of this study. At the onset of loading up to the maximum volumetric contraction of the sample (from "e" to "c" along the black line of Figure as shown for the drained shear at 5 kPa matric suction), the degree of saturation rises as the void ratio decreases. The former reaches its peak when the latter attains its minimum. These results agree with the earlier underlined evidence. The observed increasing degree of saturation of the contraction phase corresponds to what a "wetting cycle" produces. From this point forward, further shearing generates dilation (Figure b). This increases the void ratio resulting in a similar inverse relationship where the degree of saturation declines (Figure). This decreasing volumetric water content indicates that the dilation phase engages a "drying cycle." To summarize, loading a soil that contracts and then dilates first generates wetting that reverses into drying. All tests of this study confirm the same trend.
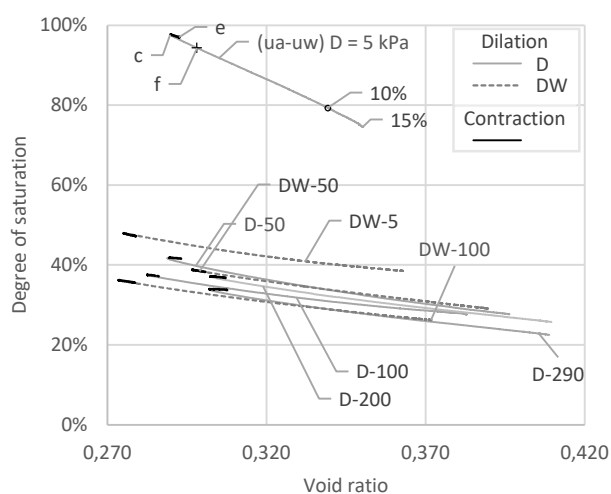

Figure 4 Degree of saturation in function of the void ratio during CD triaxial testing: shearing progresses from starting point "e" along the solid black line towards the maximum volume contraction point "c," then along the grey line (solid for shearing after drying path, dashed for after drying-wetting path) through the failure point "f" and ends at 15% axial strain.

During shear, the decreasing capillary retention created by the rising void ratio would explain why observed drainage occurs throughout dilation (moving along the solid grey line segment of Figure). Then why does drainage occur during the contraction ("wetting") phase? The answer may rest in the hysteresis of soil water retention. During the contraction phase, voids decrease in volume and increase capillary rise, as characterized by the increasing degree of saturation (black lines from "e" to "c" of Figure). On the other hand, contraction implies that the water volume occupies a larger part of the voids, yielding a degree of saturation that may exceed the retention capacity of the soil. Forcefully, this excess water (that pushes pore water pressure to rise and thus decreases suction) must drain to maintain equilibrium with the soil-water retention capacity and the set matric suction. This may explain why drainage also arises during the contraction phase of CD loadings. Wetting also means a smaller solid-liquid contact angle (Lu & Likos, 2004). Hence, for the same void ratio change during drained shearing, the absolute value of the retention increment should prove smaller for wetting (contraction phase) than during drying (dilation phase). Thus, while shearing under a constant matric suction, the water retention curves expressed as a function of the void ratio should display a steeper slope during dilation than for the contraction phase. Results of this study appear to confirm this hypothesis (Figure).

One final point regarding this topic deserves attention. The earlier presented paths of the degree of saturation during loading of Figure thus translate into curvilinear trajectories when displayed in function of the void ratio (Figure). As a result, drained shear tests follow a path on a surface defined in S-(u_a-u_w)-e

space (omitted due to lack of space). Many authors have observed and developed models for such a surface from isotropic consolidation data obtained under a constant matric suction (see those reported by Gallipoli and Bruno 2022). As hypothesized by Mašín (2010), it appears this study confirms that the water retention surface model applies to drained shear performed at a constant matric suction. However, this research highlights that dense materials express a non-monotonic hydric cycle with wetting followed by drying during shear. Hence, a transition model seems necessary to bridge from the wetting only surface to the drying only one.

4   Conclusion

Two types of specimens were prepared with the same sand and gravel an 8.9% silt content (SW-SM). The first displays large pores on their surface (up to 6 mm in width), creating what appears as a double porosity material. Column and axis-translation tests served to establish the soil-water characteristic curve. Measurements show an abrupt desorption gradient at a matric suction of 0.55 kPa and a residual value below 10 kPa. In sorption, the water-entry value is under 5 kPa. Interestingly, the samples turn out unsaturated during desorption even at the lowest measured matric suction of 0.14 kPa. Moreover, up to a matric suction of 0.55 kPa, they display a constant 74% degree of saturation. The analysis puts forward an explanation based on the existence of a maximum pore size capable of maintaining saturation by capillarity. Given the large voids of the studied specimens, this should lead to create an air-entry value under 0.05 kPa. This would explain the observed unsaturated state even at the lowest measured matric suction. This paper provides arguments on why practical considerations don't permit to determine a representative water content at such a low matric suction. It also appears likely that certain coarse grain soils (such as rockfill or riprap) with pores beyond the capillary length size should display a null air-entry value. This characteristic could offer interesting implications on the hydraulic conductivity in the unsaturated state and for groundwater flow such as in a capillary barrier.

The absence of a macro-porosity effect in the second specimen set (used in triaxial shear) seems to yield a single mode statistical void size distribution. They present an air-entry value in the order of 5 kPa, a residual matric suction below 50 kPa and a matric suction under 5 kPa for the water-entry value. Drained triaxial loadings performed at a constant matric suction gives no effective cohesion, a friction angle of 43.6° and a ϕ^b angle of 42.5 °.

Loading the granular material after desaturation by drying produces drainage during both contraction and dilation phases. This appears the result of the relationship between the void ratio and the soil-water retention capacity. As the soil contracts, the latter increases as void sizes decrease (implying wetting and a rising solid-liquid contact angle). Although the decreasing void ratio permits water to occupy a larger fraction of void space, it appears that it squeezes water volume towards exceeding the capillary retention capacity. This excess water needs to outflow, yielding drainage during contraction. As for the dilation phase, the increasing void size decreases capillary retention giving a smaller fraction of void space for water to occupy. Some water volume must thus exit to maintain equilibrium with the soil-water retention capacity. This would explain why drainage continues during dilation.

This study confirms that like with the matric suction (u_a-u_w), the degree of saturation inversely correlates to the void ratio and follows a path on a soil-water characteristic surface (SWCS) during shear. During the initial contraction phase, the water regime leaves the drying SWCS and moves along a transitional surface towards its wetting counterpart. Subsequent dilation then migrates the water regime back to the drying SWCS. Hence, performing shearing after initial drying on dense (with dilatancy) granular materials through constant matric suction CD tests permits observing their transitional SWCS and characterize their drying SWCS. Isotropic loading that contracts deformable ground, on the other hand, such as loose granular materials (or normally consolidated fine-grained soils) decreases the void ratio and causes soil-water retention capacity to rise. This equates to wetting. Such tests may thus prove well suited to model water retention while shearing loose soils since they contract and wet during loading. The cases of Kaolin Speswhite reported in the introduction falls in this latter category. This leaves to

investigate loading paths where soils contract and dry and where they dilate and wet. With this knowledge, any loading conditions (such as undrained, constant void ratio and constant water content tests) could be solved. This will require further research.

References

Chiasson, P., & Tamégnon, H. (2023). Mechanical properties hysteresis of unsaturated granular soil. *E3S Web of Conferences*, *382*, 04004. https://doi.org/10.1051/e3sconf/202338204004

de Gennes, P.-G., Brochard-Wyart, F., & Quéré, D. (2004). *Capillarity and Wetting Phenomena: Drops, bubbles, pearls, waves*. Springer New York. https://doi.org/10.1007/978-0-387-21656-0

Fredlund, D. G., & Rahardjo, H. (1993). *Soil Mechanics for Unsaturated Soils*. John Wiley & Sons.

Gallipoli, D., & Bruno, A. W. (2022). A methodology for the formulation of water retention models in deformable soils. *Acta Geotechnica*, *17*(3), 819–835. https://doi.org/10.1007/s11440-021-01271-0

Gallipoli, D., Wheeler, S. J., & Karstunen, M. (2003). Modelling the variation of degree of saturation in a deformable unsaturated soil. *Géotechnique*, *53*(1), 105–112. https://doi.org/10.1680/geot.2003.53.1.105

Ke, K., Tan, Y., Chen, C., & Lin, H. (2013). Characterizing the hydraulic properties of unsaturated sand considering various porosities and drying-wetting paths of the retention curve. *Hydrological Processes*, *27*(4), 592–604. https://doi.org/10.1002/hyp.9246

Khoury, C. N., & Miller, G. A. (2012). Influence of Hydraulic Hysteresis on the Shear Strength of Unsaturated Soils and Interfaces. *Geotechnical Testing Journal*, *35*(1), 135–149. https://doi.org/10.1520/GTJ103616

Lourenço, S. D. N., Gallipoli, D., Augarde, C. E., Toll, D. G., Fisher, P. C., & Congreve, A. (2012). Formation and evolution of water menisci in unsaturated granular media. *Géotechnique*, *62*(3), 193–199. https://doi.org/10.1680/geot.11.P.034

Lu, N., & Likos, W. J. (2004). *Unsaturated soil mechanics*. J. Wiley.

Mašín, D. (2010). Predicting the dependency of a degree of saturation on void ratio and suction using effective stress principle for unsaturated soils. *International Journal for Numerical and Analytical Methods in Geomechanics*, *34*(1), 73–90. https://doi.org/10.1002/nag.808

Prokhorov, V. A. (1996). Refinement of Rayleigh's equation for calculation of surface tension of a liquid from its capillary rise height. *Colloids and Surfaces A: Physicochemical and Engineering Aspects*, *116*(3), 309–316. https://doi.org/10.1016/0927-7757(96)03576-5

Rahardjo, H., Heng, O. B., & Choon, L. E. (2004). Shear strength of a compacted residual soil from consolidated drained and constant water content triaxial tests. *Canadian Geotechnical Journal*, *41*(3), 421–436. https://doi.org/10.1139/t03-093

Vanapalli, S. K. (2009). Shear strength of unsaturated soils and its applications in geotechnical engineering practice. *Unsaturated Soils: Theoretical and Numerical Advances in Unsaturated Soil Mechanics - Proceedings of the 4th Asia Pacific Conference on Unsaturated Soils*, 579–598.

Zhao, H. F., & Zhang, L. M. (2014). Effect of coarse content on shear behavior of unsaturated coarse granular soils. *Canadian Geotechnical Journal*, *51*(12), 1371–1383. https://doi.org/10.1139/cgj-2012-0292

EGOs & ON-SITE INNOVATIONS - INSIGHTS OF RANGIT-IV HE PROJECT, SIKKIM, INDIA

RADHENDRA NARAYAN SAHOO[1], PANKAJ RAWAT[2], SAURABH SINGH[3], PRAVEEN KUMAR SINGH[4], SANDEEP PRAKASH LAL[5]

[1] *NHPC Limited, India, radhendra.sahoo@gmail.com*

[2] *NHPC Limited, India, pankajrawat47@yahoo.com*

[3] *NHPC Limited, India, saurabhsingh@nhpc.nic.in*

[4] *NHPC Limited, India, praveensingh.1105@gmail.com*

[5] *NHPC Limited, India, sp1972lal@gmail.com*

Abstract

The certainty of uncertainties is the hallmark of Himalayan Geology. Intricate geological signatures attribute to occurrence of folds, faults/thrusts, shear zones, perennial nalas/gullies as lineaments etc. along with diverse climes; being the primary traits. Complex geology associated with brittle-ductile deformation poses greater challenge in tunnelling; leading to geological uncertainties. Such instances beyond DPR anticipations; if substantial in degree & difficult to handle/mitigate are tagged as Extraordinary Geological Occurrences (EGOs), which in turn lead to time and cost over-run of the project. Several EGOs were encountered during tunnelling in 120MW Rangit-IV Project viz. heavy underground seepage of 7000LPM, low-cohesive Coal band (8m thick), >2D Cavity, >1D Chimney, shear zones (>0.5D), high squeezing >5% radial tunnel closure, Gassy conditions (tunnel fire) and high tunnel temperature (upto 46°C) etc. Nevertheless, such EGOs were tackled conventionally, yet with certain on-site innovations. Of recent, EGOs are being quantified for sufficing contractual framework towards avoiding disputes between developer and executing agency. However, denotation of EGOs vis-a-vis their degree/dimension/extent are project-specific; yet limited. This paper is an attempt towards advocating a universal numerical assignment with due moderation for adverse geological conditions, thereby urging the need for framing an appropriate code/guidelines for EGOs.

Key words

EGO, Gassy tunnel, Squeezing, Cavity, Chimney, Shear Zone, Detailed Project Report (DPR)

1   Introduction

Rangit Stage-IV Hydroelectric Project located in Western Sikkim (Fig. 1) is a run-of-the river scheme which envisages construction of a 44m high concrete gravity dam with reservoir length of 2.1km and gross storage of 1.81Mcum at FRL to generate 120 MW (3x40MW) of power utilizing gross head of 123m. Construction of the Project started in June'2008; however, was stalled in Oct'2013 due to paucity of funds post cost overrun incurred by the previous developer. After 8 years of abandonment, the project was entrusted to NHPC Limited through National Company Law Tribunal (NCLT) from previous developer-JPCL for carrying out the balance excavation/construction works on as-is-where-is-basis.
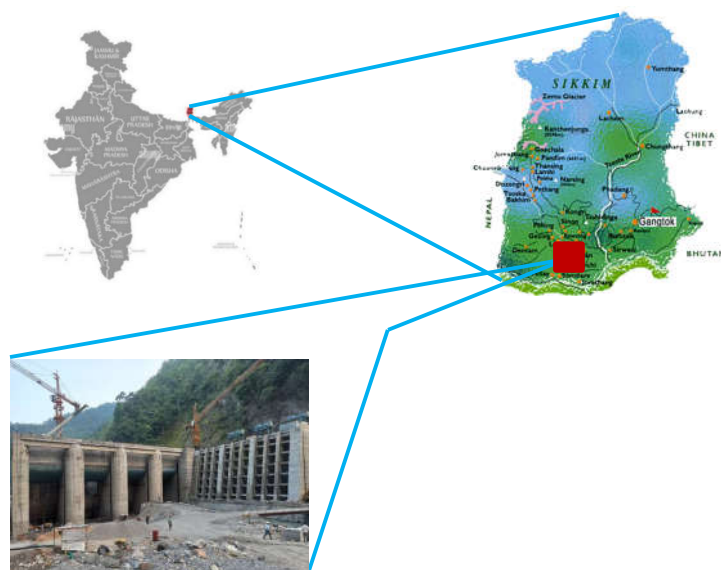
Figure 1. Location map of Project showing Rangit-IV dam.

Project envisages construction of 6488m long modified horse-shoe shaped Head Race Tunnel (7.3m excavated dia.) as water conductor system to convey water from Dam to a surface Powerhouse to harness hydropower. NHPC was entrusted to construct the balance HRT length of 2696.7m out of 6488m. Excavation is being carried out through 2 faces i.e. Face-2 from Adit-1 d/s & Face-3 from Adit-2 u/s. Additionally, a D-shaped Silt Flushing Tunnel (SFT) is also being constructed afresh having a length of 953.5m with 5.1m excavated dia.

Tunneling in this stretch of HRT & SFT encountered several adverse geological conditions/geological surprises which led to time & cost over-run. Such ground conditions were beyond speculations/anticipations as stipulated in Detailed Project Report (DPR) vis-à-vis their degree, dimension & extent in the tunnel; termed as Extraordinary Geological Occurrences (EGOs). Tunneling in young Himalayan mountains is a challenge due to its complex geology with numerous inter/intra fault-thrust systems and associated structural disturbances with intricate folding. Hence, EGOs are inevitable during construction even if adequate geo-explorations done during investigation; however, can be mitigated and tackled with regular short-interval geological analysis and monitoring, timely decision making with effective resourcefulness & on-site innovations.

2 Regional Geology

2.1 Topography

West Sikkim is characterized by rugged Himalayan terrain featuring steep slopes, deep gorges and narrow river valleys. Elevation varies significantly from around 300 metres in the lower areas to over 8,000 metres at the higher elevations. The area is home to mount Kanchenjunga, world's third highest peak at 8,586 metres. Dense forests cover the steep hillsides, interspersed with terraced fields. The topography is shaped by glacial action and intense river erosion. Rangit is the major N-S trending River system, which has several tributaries including Reshi Khola and Rammam River interspersed with many seasonal nalas/gullies. Rangit eventually joins the Teesta River at Melli, which further flows into the Brahmaputra River system. Climate varies from tropical to alpine zone. The annual rainfall varies from 2500mm to 600mm. Hence, altogether ascribe to a diverse climate prevailing in project area.

Rough inaccessible terrains, dense vegetation and limited rock exposures in Eastern Himalayan zone pose challenge in framing the layout of different structures in a hydropower project. Especially, the long

water conductor system (HRT/SFT) and underground excavation vis-à-vis tunnel design, alignment, shape, dia, and location of access tunnels/construction Adits.

2.2 Geology of the Project

The project area falls in Rangit Tectonic Window of Lesser Himalayan Fold-Thrust Belt and is characterized by complex geological structures, formed due to orogenic process between the Indian Plate and the Eurasian Plate. Terrain is represented by Gondwana, Buxa and Daling group of rocks. Gondwana rocks are represented by alternations of gritty Sandstone (micaceous), grey Sandstone, Carbonaceous Shale and Coal seams. Buxa is represented by mainly Dolomites and Limestones, whereas Daling Group of rocks are mainly Phyllites and Quartzites (Bhattacharyya and Mitra, 2009). The rocks are tectonically disturbed with a number of inter/intra-formational thrusts in the area which resulted in older formations overlying the younger ones (Fig. 2).

Environmentally, the project area receives frequent & heavy rainfall with varying intensity and duration mainly between mid-May to mid-October with higher relative humidity of the order of 63-90%.

2.3 Geology of HRT & SFT

N-S trending HRT having vertical cover ~70-955m is passing through Gondwana rocks comprising of alternate bands of medium strong-strong Grey Sandstone, weak Carbonaceous Shale & extremely weak low cohesive Coaly Shale/Coal bands of thickness ~1-8m having a cohesion=2Mpa & Φ=12°. Gradational variation in litho-units were also witnessed with presence of micaceous gritty sandstone, carbonaceous sandstone including siliceous-calc leachate hybrid rocks. The contacts between strata are in general crushed & sheared with calcite infillings at most places. Sandstone being intrinsically brittle, attributes to fracturization vis-à-vis closely spaced bedding joints. However, weak Shale/coaly shale being intrinsically ductile is commonly observed to be crumpled with presence of multiple shear seams/coal seams therein. Hence, due to the varying strength and competence (<5 to 80 MPa) of incumbent rock units, the tunnelling media does evince Mixed Ground Condition.

Further, a number of nalas and tributary seasonal run-off channels are also intersecting the hillmass above the HRT alignment. Structurally, Lensoid bodies of sedimentary rock units evinced with typical pinch & swell structures are encountered in HRT subjected under localised warping, drag folding and brittle-ductile deformation/fracturization. Few minor fault zones were also encountered in HRT conforming to the regional thrusting/intense folding in the area. In such tunneling media, so far HRT has negotiated in poor geology with 73% in Class-IV/V & 27% in Class-III rock as per RMR-Geomechanical classification (Bieniawski, 1989).

Similar rockmass conditions are also being encountered in the NW-SE aligned SFT within Gondwanas, under low vertical cover of the order of 37-135m. However, variation in lithounits was witnessed beyond anticipation with presence of weak friable sandstone, khaki shales in comparison to HRT geology, which negotiated through 60% in Class-IV/V rock and rest in Class-III rock. Rock support comprises of 100mm Shotcrete (SFRS) & 25Φ rockbolts, whereas in poor reaches-steel ribs ISHB-150 & Lattice girders (LGs) including PRH-cum-drainage holes, pre-drainage holes & pre-grouting are provisioned.
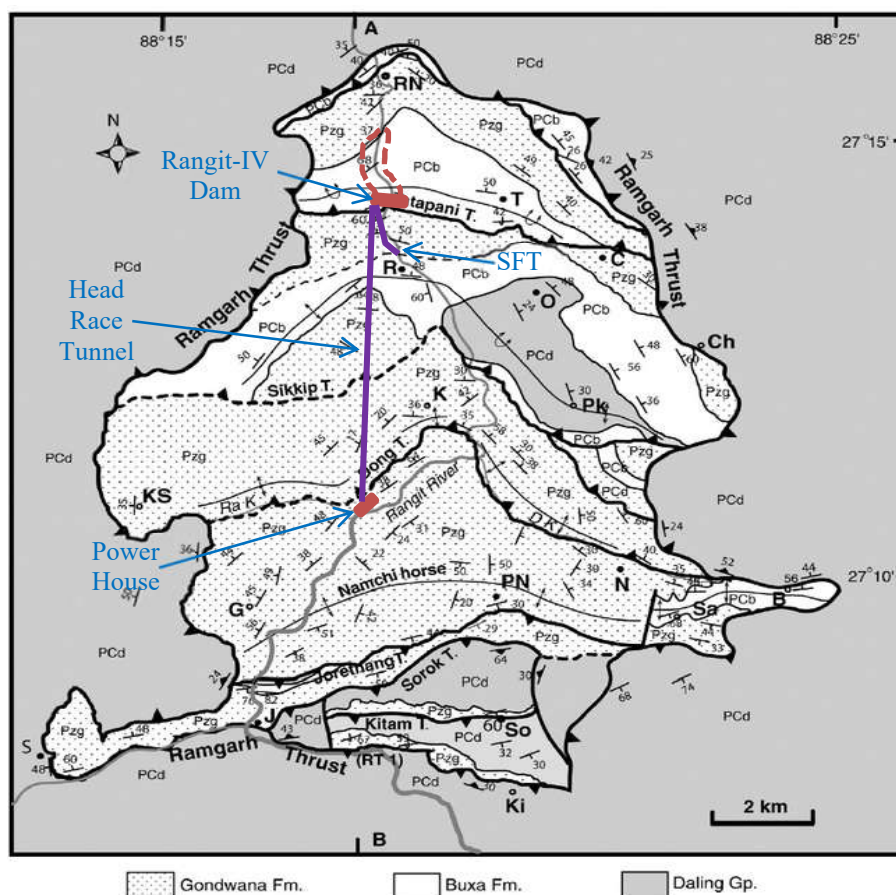
Figure 2. Geological map of the Rangit window showing thrust slices (Bhattacharyya and Mitra, 2009).

3   Extraordinary Geological Occurrences (EGOs)

3.1 The definition

"EGOs can be defined as geological uncertainties & unforeseen adverse site conditions which are substantial in degree/dimension beyond DPR anticipations, leading to time and cost over-run of the project". Such geological challenges are difficult to handle/mitigate, often demanding major changes in construction methodology and support optimization, which in turn badly affect the routine progress. Although geological uncertainties in surface works are not uncommon in complex Himalayan geological set-up, EGOs are rather referred to the events confining to underground/sub-surface works i.e. tunnelling. The common geological challenges in worldwide tunnelling are - substantial loosefall/spalling, cavity/chimney formation, rock bursting, squeezing ground conditions, thick shear/fracture zones, fold & fault zones, heavy ingress of water, silt laden running ground condition, geothermal conditions & gassy tunnel conditions etc.

3.2 What does it lack?

Almost all tunnelling projects, small to large, in Himalayan region do inevitably encounter EGOs. However, there is no clear-cut standard/guideline regarding degree/dimension/extent of such adverse geological condition so as to be tagged as EGOs. Therefore, project developers find it difficult to decide specific events of unforeseen geological conditions towards defining it as EGOs with respect to contractual obligations vis-à-vis allocation of time extension to the contractor and additional financial implications. Usually, DPRs and contract documents lack information regarding specific assignment of numerical threshold values/range of values to the adverse geological conditions for defining as EGOs.

3.3 Why prediction is difficult?

Rugged inaccessible terrains of Himalayas pose difficulty in first-hand, for carrying out detailed surface geological mapping. Further, structural complexity of the area with numerous inter/intra fault-thrust system and intricate multi-phases of folding pose added difficulty in projecting the surface geology to deep seated tunnel grade. Although standard codes mandate geotechnical investigation by core drilling of water conductor system in every kilometre along its alignment. However, core drilling in mid-portion of tunnel alignment is practically impossible due to incumbent high vertical and lateral cover in Himalayan terrain.

In case of Rangit-IV project, the geological complexities are attributed with mixed ground condition i.e. dissimilar lithounits having varying strength and competence; soft sediment deformation signatures viz. load, cast, ghost structures; prominent lensoid bodies of rock units evinced with typical pinch & swell structures; localised warping, drag folding and fault zones with abrupt truncation of strata. Intense fracturization and shear zones aided with abrupt seepage conditions have also posed difficult conditions for tunnelling.

Although, non-coring probe holes can infer geological strata ahead of face but practically the results remain non-conclusive in our case - with black colour return drill water & drill slush due to mixed ground condition of rockmass with alternate bands of sandstone, dark grey carbonaceous shale & pitch-black shiny crushed coal. Even geophysical tools such as Tunnel Seismic Prediction (TSP) tests had their own limitations in defining the exact geology ahead of face in view of mixed ground strata with lack of contrasting features. Even though, most stretch of tunnel had strike of strata near-parallel to drive direction; long-stretch geological prediction was practically difficult due to presence of abruptly truncating lensoid bands subjected under structural disturbances.

4   Factors considered for EGOs

DPR anticipated geology showed variations with respect to actual encountered geology in HRT as well as in SFT. The same is tabulated as under at Table-1.

Table 1. HRT Adverse Geology beyond DPR speculations/stipulations

DPR anticipations	Acutal encountered
Max. thickness of coal bands < 1m	Low cohesive Coal bands ~1-8m thick
Sandstones-hard, compact, moderately jointed	Sandstones- fractured & friable at places
Wedge failure and max. size of block for spalling was not mentioned.	Spalling incidences of wedges of the order of 1.5cum to max. size of 6.5cum encountered.
Thickness of Shear zones not mentioned.	>150mm Sheared lithocontacts (max. 1m)
No mentioning of tunnel squeezing/distress in soft rock strata under high or moderate cover	High squeezing ground conditions >200mm (more than 5% radial tunnel closure) encountered.
Full-face method of excavation was envisaged for HRT.	Heading-Benching adopted due to poor rockmass in HRT including multi-segmental-cum-mechanical excavation.
Anticipated seepage <10LPM contrary to Nala crossings above HRT alignment.	Heavy seepage of the order of ~125LPM (max. 550LPM) in HRT and ~7000LPM in SFT during monsoon season.
No speculations about encounterance of methane or any other harmful gases.	Harmful gases (Methane) ~4000-10000ppm encountered/ proportional to Coal band thickness at face/proximity.
No mentioning of Tunnel behaviour i.e. mix-ground conditions or mixed-face conditions in HRT vis-à-vis its effect in RMR computation.	Strata with varying strength & competence (Mix-ground condition), Localized warping (Mixed-face condition), Drag fold & associated faults.
No mentioning of large persistent Lensoid bodies.	Large persistent Lensoid bodies parallel to strike of the order of 6-42m, mostly 21m length.

The above actual encountered adverse incidences with their characteristic quantifiable scales formed the basis for formulating the factors with their numerical assigned threshold values for defining EGOs vis-à-vis time and cost over-run of the project. Accordingly, following considerations were taken into account.

- Cavity/chimney dimension ≥ 0.5D (D = Excavated dia. of tunnel)
- Sudden spalling of wedges > 1 cum size (considering wedge analysis & equipment size)
- Distress/squeezing ≥ 200mm (moderate squeezing ≥ 3% radial closure, IS15026 - 2012)
- Coal band thickness (low cohesive strata) ≥ 1 m
- Shear zone thickness >150mm
- Heavy ingress of water >500LPM
- Methane concentration (Gassy tunnel conditions) >5000 PPM (IS4756-2002)

Site photographs exemplifying different facets of adverse/unforeseen geological conditions (EGOs) encountered in the project are cited at Fig. 3 & 4.
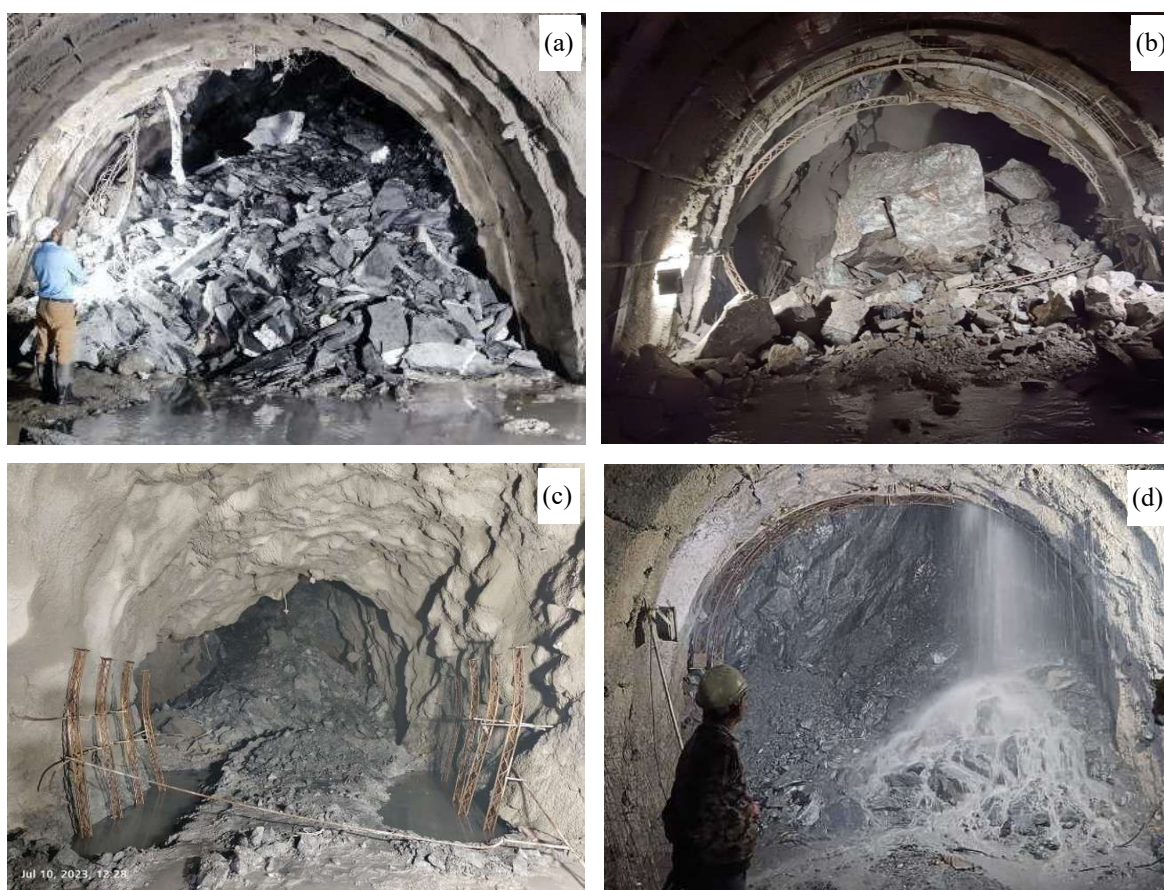
Figure 3. (a) Squeezing conditions in HRT face-2 in sandstone/shale rockmass with twisting & distortion of Lattice girders (LGs), spalling of shotcrete layers, rumbling/popping sound and consequent cavity formation; (b) Sudden spalling of 6.5cum of wedge block of gritty sandstone in HRT face-2, which was blasted out & demucked for revival of works at face; (c) Large cavity >1D height in HRT face-3 with kinematically aggravated longitudinal extent of 21m vis-à-vis long persistence of bedding joint; (d) Puncture of perched aquifers in sandstone with sudden gushing of ~1000LPM seepage and later on with max. 7000LPM seepage in SFT led to inundation of tunnel & halting of works.
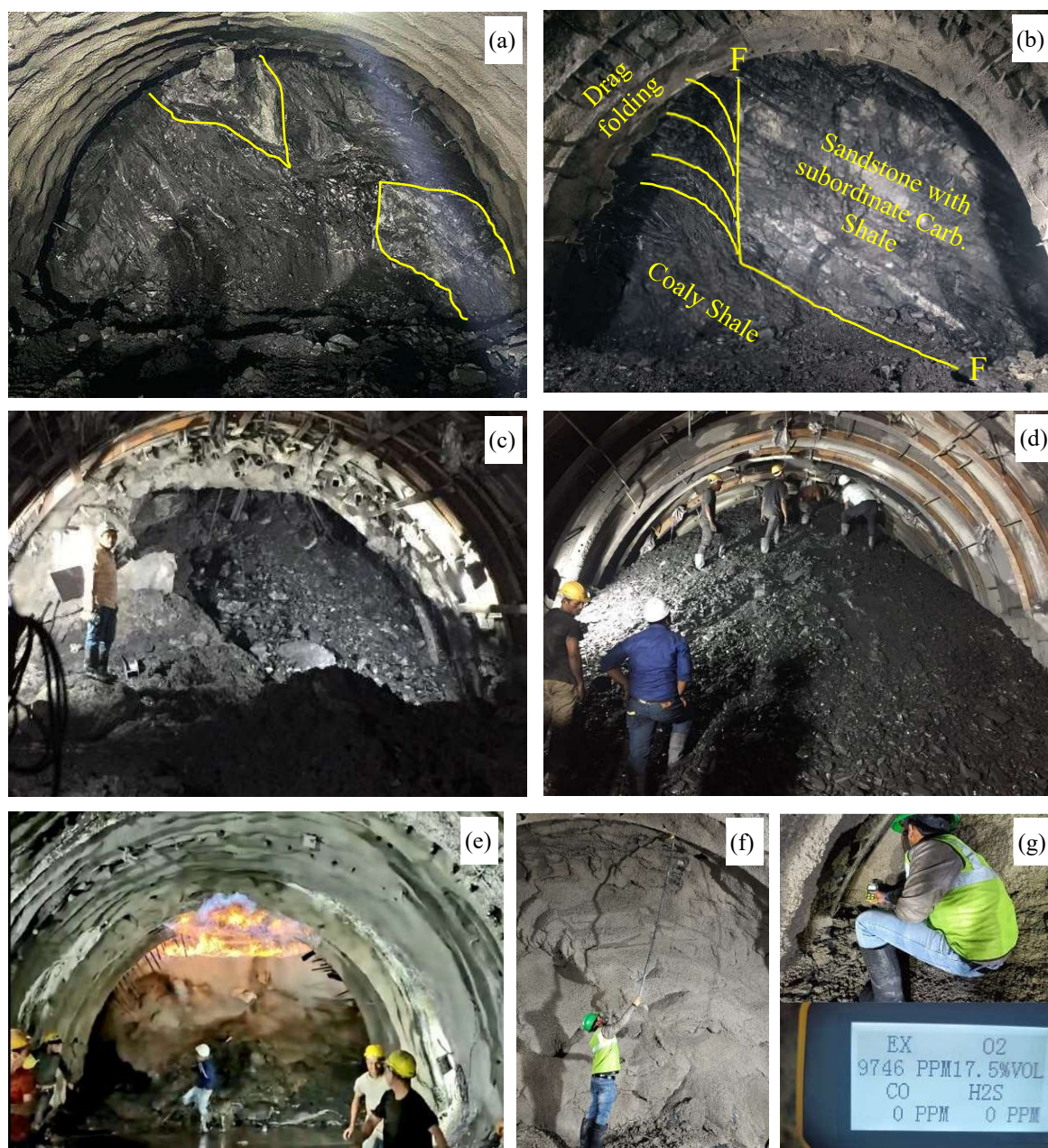
Figure 4. (a-b) Structural disturbances and soft sediment brittle-ductile deformation with features such as sandstone lensoid bodies & sheared coaly-shale, localized warping, fault & associated drag folding in HRT; (c-d) Ravelling ground with disposition of low-cohesive thick Coal strata at face and aggravated condition with seepage often leading to large cavities, squeezing with distortion of steel rib supports etc.; (e) Tunnel fire incidence in HRT face-2 with high methane concentration >5000ppm; (f-g) Provisional shotcreting at face in every blast cycle & regular monitoring of gases in tunnel at crown and Springing Level (SPL).

5   EGOs encountered in HRT & SFT

Several EGOs were encountered during tunnelling viz. heavy underground seepage of max. 7000LPM, low-cohesive Coal band (upto 8m thick), cavities of the order of >0.5D to 2D, chimney >1D, shear zones (max. 0.5D), high squeezing >5% radial tunnel closure (max. 1.8m), Gassy conditions (tunnel fire with Methane concentration ~4000-10000PPM) well corroborating and proportional with the disposition of Coal band thickness at face, which severely affected the progress of tunneling. The details of such incidences are enumerated below in Table 2.

Table 2. Details of Extraordinary Geological Occurrences (EGOs) in the Project

Sl. No.	Description of EGO	Total incidences		
		HRT Face-2	HRT Face-3	SFT
1.	Multi-stage loosefall/Cavity & chimney formation	9	11	2
2.	Distress/Squeezing conditions	8	1	1
3.	Thick Coal band/multi-segmental-cum-mechanical excavation	6	1	6
4.	Harmful gases (mainly methane) encounterance	120	0	0
5.	Sudden spalling of rock chunks >1 cum	1	1	0
6.	Heavy underground seepage	1	0	3

Accordingly, total 171 no. of incidences were encountered in a stretch of 3.4km of combined tunnelling in HRT & SFT, leading to a time over-run of 271 days.

6   Remedial measures and on-site innovations

Different EGOs were tackled differently with use of conventional support measures, on-site innovations based on available site resources and timely decision making with concerted team efforts. Site-specific methodology of remediation and treatment measures involved adoption of obtuse-face method of excavation leaving a rocky hump as toe support including mechanical-cum-multi-segmental approach in case of thick coal bands (Fig. 5). For squeezing condition, prompt additional support (steel ribs/LGs) behind affected zone to arrest further backward translation of distress followed by 76-89Φ PRH (varying lengths 4-12m) were done including provisional struts/steel pipes to restrain further tunnel closure.
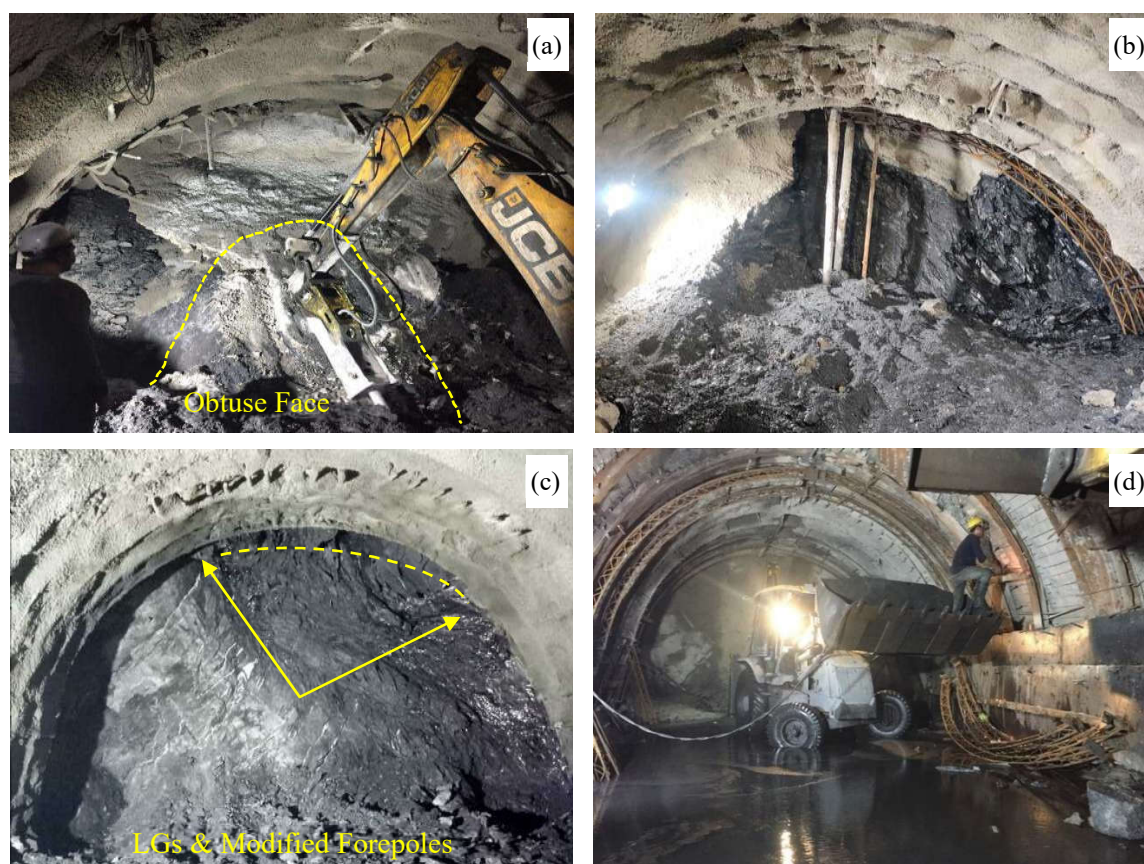

Figure 5. (a-b) Obtuse face method and multi-segmental-cum mechanical excavation method adopted for tackling weak rockmass/low-cohesive coal bands; (c) Unlike conventional 135° arc, forepoles with 32Φ bars/SDAs alternately with modified positioning as per disposition of weak strata; (d) Fusion of LGs with steel ribs as supplementary rock support mainly in distress zones.

Spalling due to wedge/slabbing was mitigated with 6m long, 32Φ rockbolts with larger bearing plates. Modified positioning of forepoles (differential clock position) with respect to weak bands/fractured zones was resort to prevent loosefalls, thereby reducing cycle time (Fig. 5). Further, SDAs were used as forepoles-cum-pre grouting ahead of face and for pre-lining consolidation grouting/backfill behind LGs.

Methane encounterance and tunnel fire incidence necessitated enhancement of existing blower ventilation system with secondary reverse exhaust booster fan for dilution, with 8m overlap against recirculation of harmful gases. Further, 2-4 inclined relief holes were drilled at face to expel accumulated gas above human height straight upto tunnel crown, so as not to affect people working near face. For catering seepage, systematic drainage holes (45Φ, 4-6m long) in heading zone upto 6m behind incumbent face including minimum 2 no. pre-drainage holes (76Φ, 4-8m long) were adopted vis-à-vis progress optimization maintaining effective cycle time. The heavy seepage as encountered with puncture of aquifers was catered with a number of 76-98Φ steel pipes and additional prompt deployment of dewatering pumps. Inter alia, non-stereotype approach with fusion of conventional steel rib supports with concrete backfill and flexible NATM- LGs encased in SFRS was also adopted as complementary and supplementary supports as per site condition depending upon the overbreak profile associated with different incidences. Onsite innovation also included false umbrella roofing with ISMC 100 channels for providing protective cover towards safe support installation works underneath it & at times fused as box channels for forepoling & concrete/shotcrete backfilling in large cavities. Another innovative approach was adopted by leaving rock buttresses of on either side of HRT below SPL as bench support, negating erection of additional vertical segments of steel ribs thereby saving substantial time.

Despite encounterance of poor geology & incidences of adverse geological conditions, an average progress of ~90m/month in HRT was achieved against previous developer's 67m/month. This could be accomplished with site optimizations and innovations in excavation methods as well as adoption of flexible NATM rock supports. With similar approach, average progress of 43m/month was achieved in SFT being excavated from one end only.

7   Conclusion

Elaborate integrated approach with modern geological, geotechnical and geophysical exploration tools can reduce the possible encounterance of unforeseen site conditions. However, EGOs are inevitable in complex Himalayan tunneling projects. Taking background cues from various projects, on many instances - ambiguities & disputes have arisen among the developers & executing contractors due to lack of clarity in contract provisions with reference to risk allocations vis-à-vis adverse geological conditions (EGOs). The main reasons being, non-quantification of characteristic attributes with threshold values of all possible EGOs & their well-defined boundary conditions.

Tunneling in Rangit-IV hydro project encountered many adverse geological incidences - from squeezing to translated cavities to heavy ingress of seepage including gassy tunnel conditions. Such events were duly tackled with on-site optimisation of support system, innovations & timely decision making. Individual incidences were categorised by assigning numerical threshold values for tagging under EGOs, which avoided contractual burping wrangles with contractor with respect to risk allocation, time extension and indirect cost implications.

Every project is unique in terms of its type, layout, set-up, climatic condition & above all - the geology, hence EGO considerations shall deem to be project-specific. However, contract provisions should have the necessary clarity of defining such incidences with their due quantifiable threshold limits so as to avoid any ambiguities. Hence, the current scenario demands the need for formulation of a standard and/or guideline for EGOs with all possible manifestations along with their numerical threshold values.

References

Bhattacharyya, K., Mitra, G., 2009. *A new kinematic evolutionary model for the growth of a duplex- an example from the Rangit duplex, Sikkim Himalaya, India*. Gondwana Research 16, 697-715.

Bieniawski, Z.T., 1973. *Engineering classification of jointed rock masses.* Trans S. Afr. Inst. Civ. Engrs 15, 335-344.

Bieniawski, Z.T., 1976. *Rock mass classification in rock engineering*. In Exploration for rock engineering, proc. of the symp., (ed. Z.T. Bieniawski) 1, 97-106. Cape Town: Balkema.

Bieniawski, Z.T., 1989. *Engineering rock mass classifications*. New York: Wiley.

CEA, 2022- *Guidelines for Formulation of Detailed Project Reports for Hydro Electric Schemes (Revision 6.0)*,
https://cea.nic.in/wp-content/uploads/hpa/2022/09/Guidelines_for_formulation_of_DPR_of_HE_schemes_Revision_6.0.pdf

GSI, 2012. *Guidelines for investigations and explorations required at detailed project report (DPR) stage of proposed hydroelectric projects, in Himalayan terrain*. Engineering project evaluation division, DGCO, Geological Survey of India, New Delhi.

IS4880 (Part II) – 1976 (Reaffirmed 2000) - *Code of practice for design of tunnels conveying water (Geometric design)*.

IS15026 – 2002 (Reaffirmed 2012) - *Tunnelling methods in rockmasses - Guidelines*

IS15662 – 2006 - *Geological Exploration for Gravity Dams and Overflow Structures – Code of Practice.*

IS4756 – 1978 (Reaffirmed 2002) – *Safety code for tunnelling work.*

Proctor, J Richard, 2002. *The San Fernando Tunnel explosion, California.* Engineering Geology, Volume 67, Issues 1–2, Pages 1-3. https://doi.org/10.1016/S0013-7952(02)00042-X

Rodríguez, Rafael., Lombardía, Cristobal, 2010. *Analysis of methane emissions in a tunnel excavated through Carboniferous strata based on underground coal mining experience.* Tunnelling and Underground Space Technology. 25. 456-468. https://doi.org/10.1016/j.tust.2010.02.010

SLOPE INSTABILITY AND ASSOCIATED GEOHAZARDS IN GISBORNE, NEW ZEALAND

MARTIN BROOK [1], MATT COOK [2], ARIANE POLA [3], JANKI PATEL [4], AYRTON HAMILTON [5], MURRY CAVE [6], MELANIE KAH [7], SATENDRA KUMAR [8]

[1-5, 7-8] School of Environment, The University of Auckland, Auckland 1010, New Zealand, m.brook@auckland.ac.nz

[6] Gisborne District Council, 15 Fitzherbert Street, Gisborne 4010, New Zealand, murry.cave@gdc.govt.nz

Abstract

Gisborne is a remote city on the northeast North Island of New Zealand, close to the Hikurangi Subduction Zone, subject to a range of geohazards. Landslide risk in recent years has been exacerbated by expansion of residential development into erosion-prone hillslopes surrounding the city. The hills are underlain by weak Neogene sediments and uplifted Pleistocene estuarine deposits. Sentinel-1 InSAR has revealed the pattern of slope displacement across Gisborne's steepland periphery from January 2016 to December 2021. Velocities in the line of sight were obtained from the stack of interferograms and projected along the direction of the maximum slope to correct for slope displacement. Ascending and descending datasets were combined to reveal the vertical and horizontal components of displacement. Activity at Gisborne landslides appears to be linked to rainfall-induced increases in soil moisture. Site investigations revealed the soils are smectite-rich and exhibit expansivity. In addition, small amounts of the toxic "asbestiform" mineral, erionite, have been detected in soil exposures in landslide scarplets. Despite clear evidence of the effects of tree removal, loading of slopes by construction activity, slope cutting, and installation of unconsented, inadequate retaining walls contributing to landslides, such activities continue to occur.
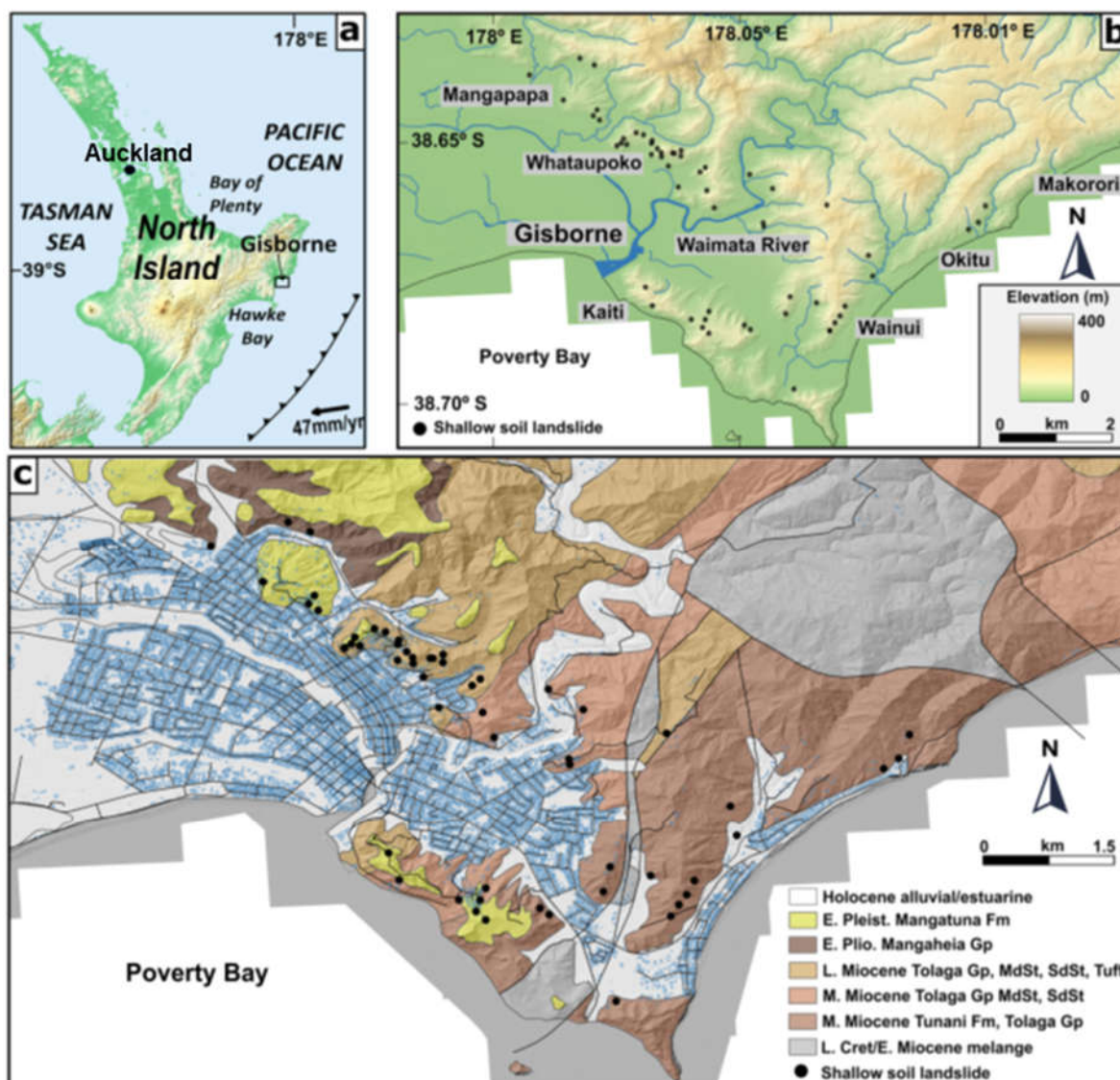
Key words

Landslides, Gisborne, rainfall, InSAR, landuse, erionite, geohazards

1   Introduction

In urban residential zones, landslides are a serious and complex natural hazard that occur in many countries globally, and can have social, economic and environmental impacts (Cruden 1990). The most common landslides in New Zealand are slides and flows in shallow soil and regolith, usually initiated by heavy rainfall (Crozier 2005). The scale of erosion can vary from individual landslides to multiple occurrence landslide events (MORLEs), whereby thousands of landslides are initiated in a single event, on a regional scale (e.g. Crozier 2005). Events of this magnitude make it extremely challenging to map landslides covering such large areas using conventional ground-based mapping methods and site-specific in situ monitoring such as extensometers and inclinometers. Therefore, remote sensing approaches, such as unmanned aerial vehicle (UAV) surveys, light detection and ranging (LiDAR) and interferometric synthetic aperture radar (InSAR), have been used in recent years. These approaches provide complementary data sets to traditional landslide mapping and monitoring techniques to maintain and update landslide inventories (Solari et al. 2020) and aid landslide susceptibility analysis.

The focus here is on Gisborne (Figure 1), on the northeast of New Zealand's North Island. The city of 38,000 people is situated on a landscape of steep slopes, narrow ridgelines and clay-rich soils, and is particularly susceptible to rainfall-triggered MORLEs (Cook et al. 2023). Such landslides are often triggered by extra-tropical cyclones, or slow moving "atmospheric rivers", which are long, narrow, and transient corridors of strong horizontal water vapor transport, typically associated with a low-level jet

stream ahead of the cold front of an extratropical cyclone (American Meteorological Society 2017). The landslides are often initiated as shallow slumps within Pleistocene estuarine and fluvial sediments, overlying weak, Pliocene and Miocene marine sediments (Cook et al. 2023). While shallow, they still damage houses and infrastructure (Figure 2).

Figure 1. (a) Location of Gisborne, close to the Hikurangi Subduction Zone; (b) elevation map with shallow landslide locations; (c) geology, landslides and residential property outlines (blue polygons).

In addition, the area is subject to earthquakes from the nearby Hikurangi Subduction Zone, tsunami, and mud volcano activity. A more recent emerging geological hazard reported here for the first time, and associated with landsliding, is the presence of the naturally occurring zeolite mineral, erionite, exposed in a landslide scarp. Erionite can form highly toxic mineral fibers, and when inhaled, can be orders of magnitude more toxic than asbestos fibers (Patel et al. 2022).

2   Methods

2.1 InSAR

The main methods for the detection of landslides across the Gisborne area here is Interferometric Synthetic Aperture Radar (InSAR), which is an active remote sensing imaging system that monitors surface displacement on a cm to mm scale accuracy (Ferretti 2014; Hu et al. 2014). By comparing the

phase component of repeated SAR acquisitions over the same area, at different times, we can generate interferograms which provide maps of range change between the ground and the satellite at spatial resolutions of metres to 10's of metres (Simons and Rosen 2007). This has emerged as a key remote sensing approach to allow large areas to be rapidly surveyed without putting people or equipment at risk and provide preliminary results to help target specific areas for further investigation. Furthermore, InSAR is most effective at detecting slow landslide processes moving at very slow (16 to< 1.6 m/year) to extremely slow (< 16 mm/year) velocities (as defined by Hungr et al. 2014), rather than detecting maximum velocity at failure.

Although InSAR is an effective instrument for landslide detection and analysis, it also presents some well-known limitations which can lead to the underestimation of the actual number of active or dormant landslides in an area (e.g., Bayer et al. 2018). These include: 1) Rapid movement such as earthflows and small-scale landslides can lead to complete coherence loss, and these can be challenging to detect depending on the satellite's spatial and temporal resolution. 2) The low density of coherent targets acquired over highly vegetated areas, especially for shorter wavelength SAR systems. 3) Another important factor to consider is decorrelation and noise in the phase from which deformation is obtained. While noise contained within the measured interferometric phase (e.g. atmospheric, topographic, and other noise components), are mostly removed during the processing of the interferograms, the processing method, filtering and other parameters will impact the LOS displacement results.

For the InSAR analysis in this study, the small baseline subset (SBAS) technique was used to identify landslide-related slope movements across the Gisborne area. Sentinel-1 single look complex images (12 or 24-day revisit cycle) from the interferometric wide-swath mode for descending and ascending orbit directions were used (e.g., De Luca et al. 2022). From the ascending track 8, 163 images were used to generate a stack of 487 interferograms, and from the descending track 175, 137 acquisitions were used to generate a stack of 409 interferograms. For most landslides the displacement direction coincides with the direction of the steepest slope, and the accepted method to delineate the actual component of landslide movement is to project the LOS velocity (V_{LOS}) along the direction of the slope (V_{SLOPE}; e.g., Notti et al. 2014).

2.2 Site Investigation and testing

To investigate the subsurface material properties, a range of field techniques have been used, including cone penetration test (CPT), shear vane, and ground penetrating radar (GPR). Laboratory investigations include Atterberg limits, index properties, shear strength. Mineralogy and geochemistry was assessed using X-ray diffraction (XRD) and scanning electron microscopy (SEM).

3 Results

The landslides (Figure 2) exhibited typical characteristics of previous rainfall-triggered landslides in the Gisborne region. They are mainly shallow (<2 m) slumps on slopes with initiation angles of 25–35°, that transition downslope into earthflows, with runout usually topographically constrained within existing gullies. Material types that fail include fill (e.g., Hill Road landslide), fluvial deposits (e.g., Owen Street landslide), residual soils, and colluvium (e.g., Gaddums Hill Road landslide).

Occasionally, the slope failures incorporated some highly-weathered rock (Richardson Avenue landslide). As an example, on the east-dipping slopes above the Wainui township (Figure 3), the InSAR line of sight (V_{LOS}) displacement time series of P2 shows a strong seasonal component (Figure 3c).

Peaks in the displacement occur during the Austral winter months (June–August). This can be attributed to the shrinkage of the clay soils in the dry summer months and swelling during the wet winter months. However, the overall trend indicates P2 is moving away from the sensor in a downslope direction. The average V_{SLOPE} in the area is −15 mm/year, and the maximum V_{SLOPE} in the area reaches up to −49

mm/year. In addition, at other sites measured in Gisborne, rates of ~70 mm year were measured via InSAR.
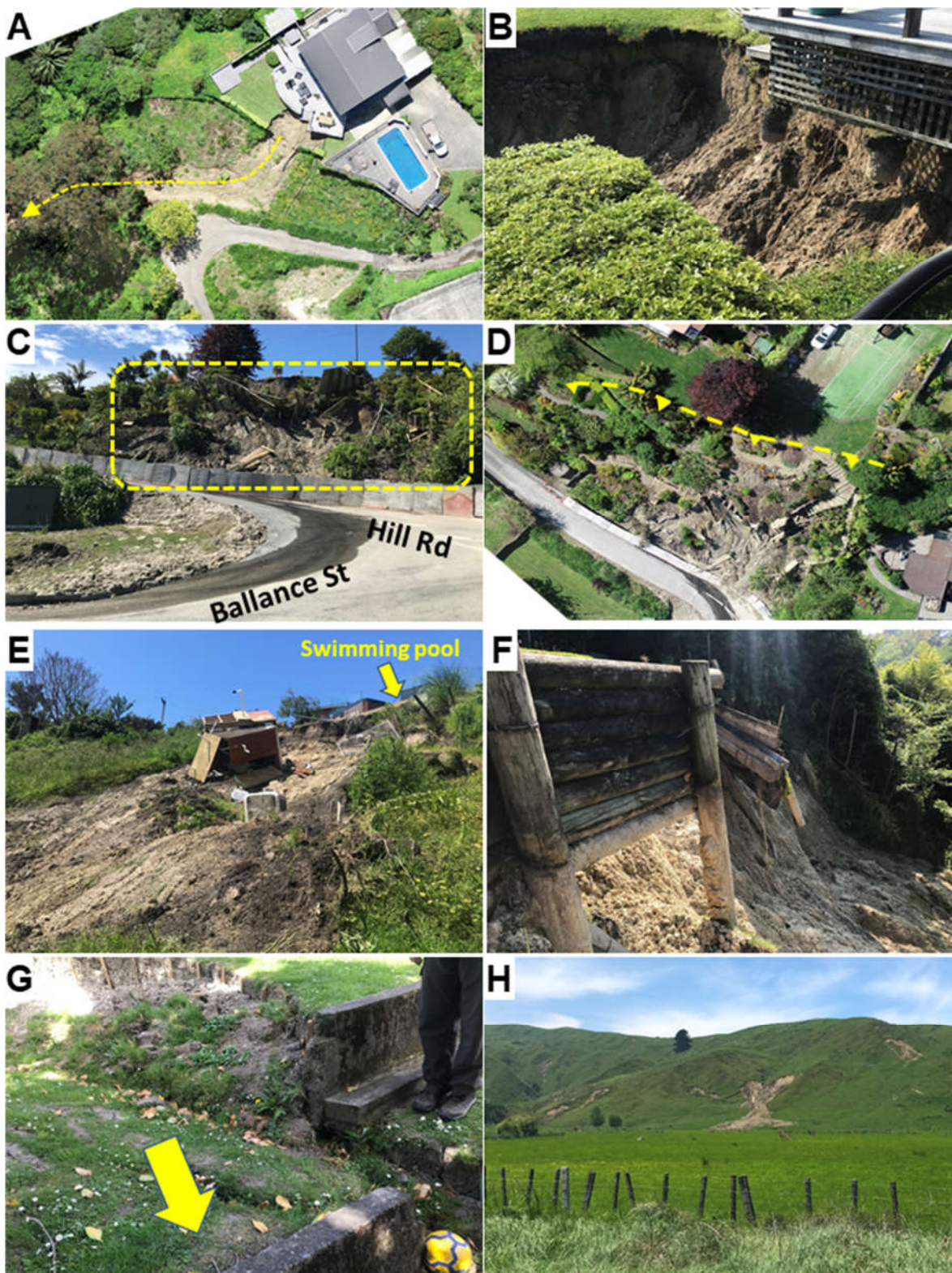

Figure 2. (A, B) Slump-flow at Clifford Street affecting deck and swimming pool; (C, D) Ballance Street fill/retaining wall failure; (E) Gaddum's Hill Road earthflow downslope towards 17 Darwin Road; (F) retaining wall failure at Owen Road; (G) scarplet and offset retaining wall, Argyll Street; (H) shallow earthflows at Wheatstone Road.
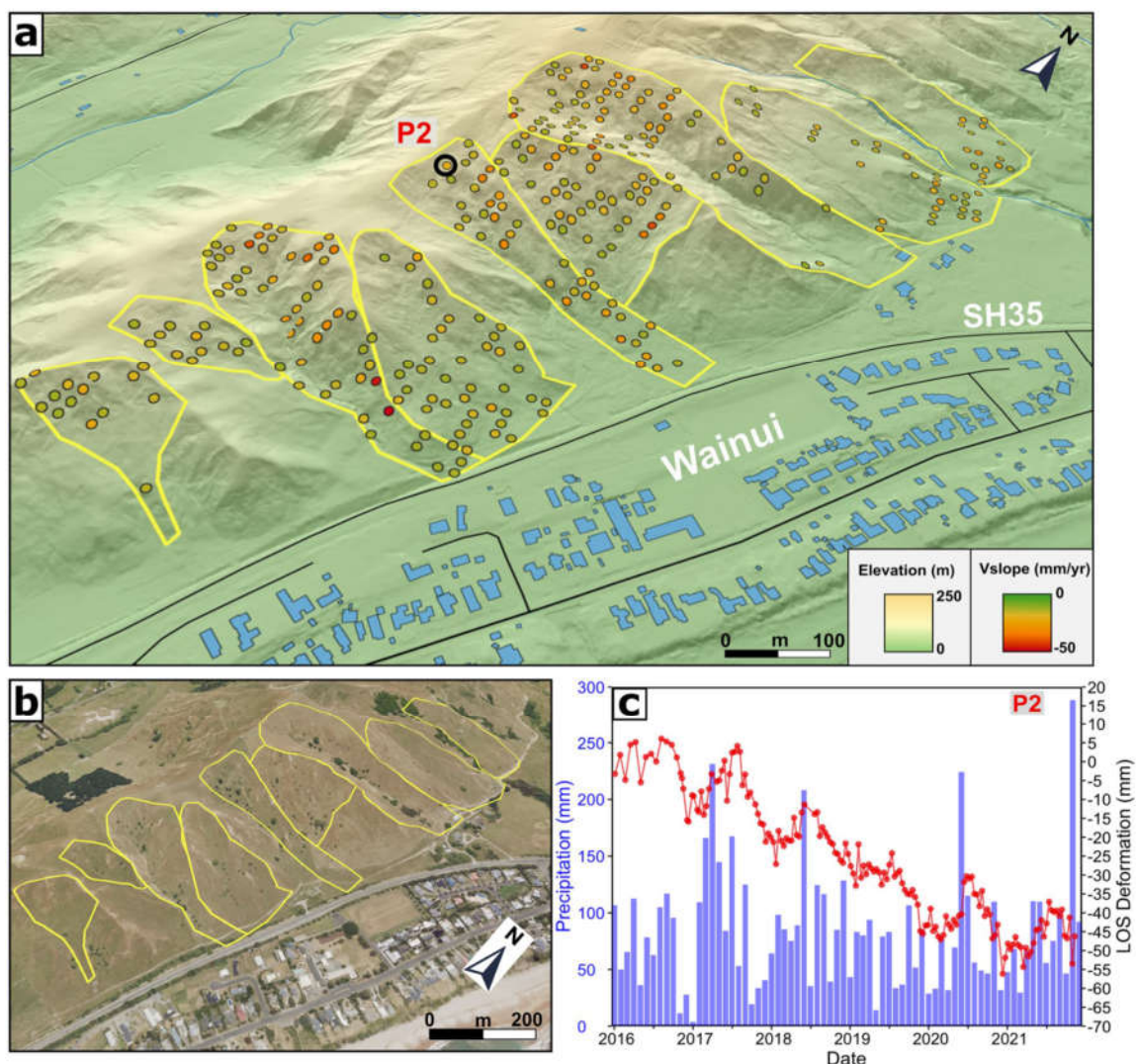
Figure 3. (a) Unstable slopes identified in using InSAR V$_{SLOPE}$ approach at Wainui, Gisborne. Negative values (red) indicate movement downslope; (b) aerial imagery showing exposed sediments; (c) displacement time series in the direction of the line of sight (LOS) from P2 highlighted in (a) and total monthly rainfall.

The hillshade (Figure 3a) shows multiple relict headscarps below the ridgeline, several scarplets are exposed further downslope, and exposed sediment can be seen in the aerial imagery (Figure 3b). Understanding the displacement rates and patterns is of particular interest as the shallow landslides are situated in an area of multiple residential properties under development along the ridgeline.

Example CPT data is shown for the Russell Street landslide in Figure 4, a deeper rotational slump affecting several houses. Three main soil behaviour types identified, with organic clays and clean sands 0-0.3 m depth: (1) from 0.3 m to ~7 m a clay unit is dominant with layers of silt and sand mixtures; (2) from ~7 m down to 9 m, silt mixtures are dominant layer; (3) from 9 m to the end of the CPT at 9.65 m the layer comprises of only sand mixtures. As the cone enters the clays and silts the cone resistance is ~1 MPa for clays and ~4 MPa for silts, and at 9 m, where the sand layer is reached, cone resistance increases to ~8 MPa. The clay layers exhibit low porewater pressures of near 0 kPa. Porewater pressure increases in the silt layers to ~100 kPa, and when the sand layer is reached at 9 m, porewater pressure significantly increases to > 800 kPa.
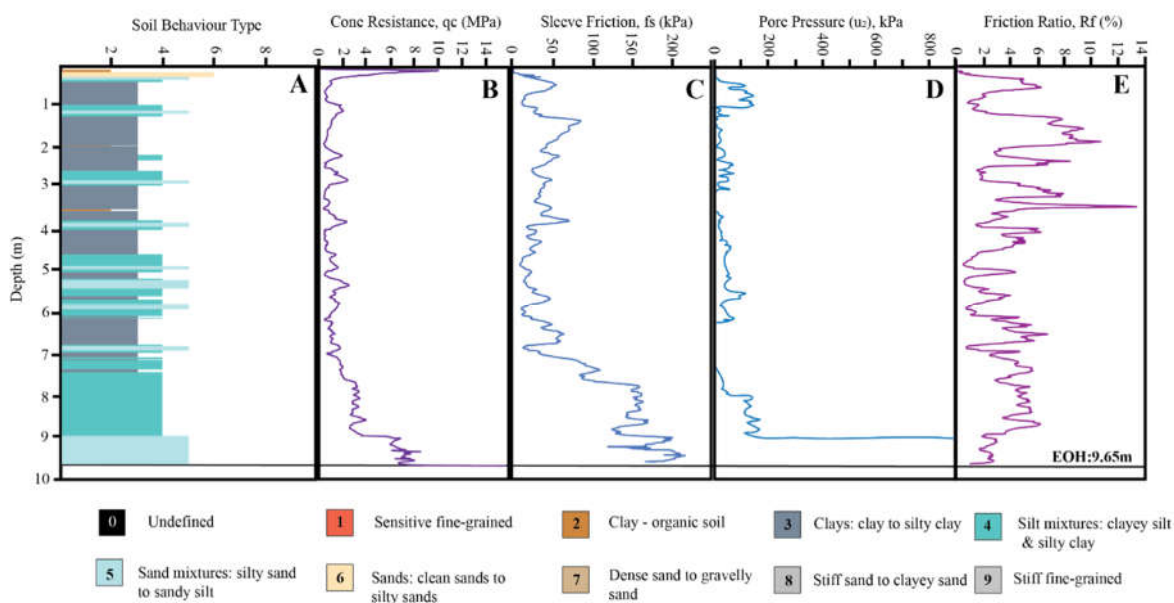
Figure 4. Example CPT results showing the subsurface soil characteristics at the middle of the Russell Street landslide.

Figure 5a shows a scanning electron microscopy (SEM) image of an erionite mineral fiber from a recently formed (2023) landslide scarp at Russell Street, Gisborne. Figure 5b also includes an energy-dispersive X-ray spectroscopy (EDS) plot that provides elemental information of the mineral fiber. The length of the erionite fiber (~5 μm) and diameter (~0.4 μm) means that it is close to respirable, according to the World Health Organization (WHO) guidelines. Indeed, WHO (1986) guidelines state that respirable fibers are particles with lengths >5 μm, diameters <3 μm, and aspect ratios ≥3:1. Given that such erionite fibers are a Group 1 carcinogen (Patel et al. 2022), this newly-identified geological hazard in Gisborne, and its geological provenance, is of significance.
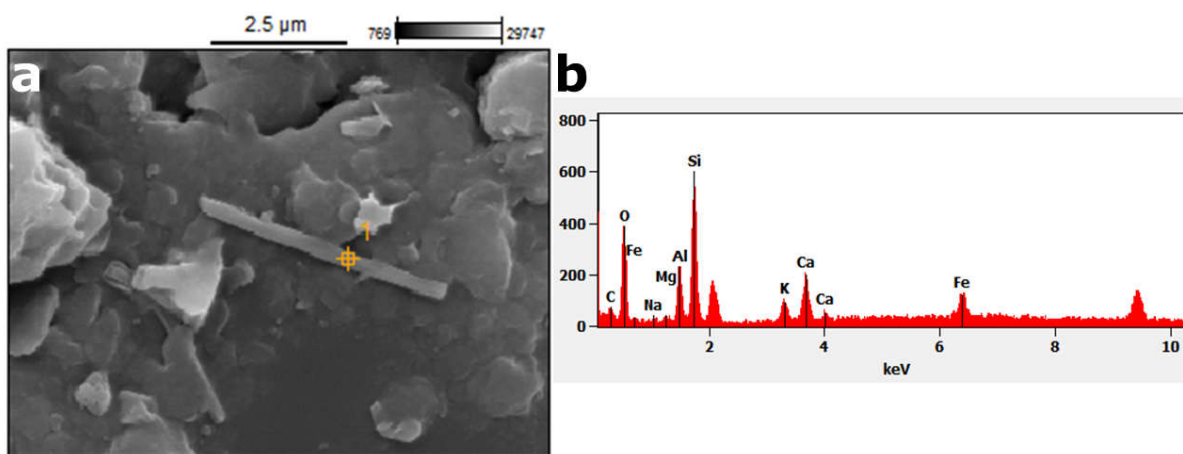
Figure 5. (a) SEM image of erionite fiber within Mangatuna Formation soils, with location of EDS target measurement marked; (a) EDS elemental counts of target measurement in (A).

4   Discussion

A range of site pre-conditioning factors can contribute to landslide activity and reactivation of 'dormant' landslides (Crozier, 2010). The latter are where the slope has failed in the past, and the slope materials are then at a residual strength, which is lower than their original, peak strength, and may be more

susceptible to failure (Stringer et al. 2021). Whether or not a slope fails in soil, rock or fill material is important, because soil and fill fail through the granular mass, while rock fails along defects such as joints and/or bedding planes.

Within the Gisborne area, as shown by site visits and Sentinel-2 optical imagery, shallow slumps and flows are common. Some of these are new failures, while others are more likely to be reactivated existing landslides. Generally, the observed landslides reported herein accord with previous observations of shallow landslides in the region, that typically occur within the highly-weathered Pleistocene Mangatuna Formation soils (e.g., Cook et al. 2022; Mazengarb 1997). In addition, however, several failures have been reported on 'fill' slopes, where slopes have been modified to accommodate construction activity, such as tennis courts or swimming pools. Such fill failures are not uncommon across New Zealand, often due to poor compaction and drainage management in urban and suburban areas (e.g., Brook, 2018).

Nevertheless, whether the landslide is within soil or fill, it is probably promoted by drainage and permeability contrasts that occur with the underlying Miocene Tunanui Formation mudstones (Cook et al. 2022). Such contrasts cause elevated groundwater tables during heavy, prolonged rainfall, as indicated by groundwater 'daylighting' out of exposed landslide headscarp exposures. The Mangatuna Formation soils have an effective friction angle of ~30°, but if soil have undergone 'strain-softening' through modification, loading or landsliding, they may be at a lower residual strength, making them susceptible to failure (e.g., Bromhead 1979). Hence, the residual friction angles of the soils are probably much lower than 30°, and close to typical slope angles.

Finally, while antecedent rainfall and soil moisture are important, slope failures often occur later summer when the ground has dried out, smectite-rich soils have shrunk, and fissures through the soil mass have opened up. This can result in slopes that are vulnerable to intense rainfall events, with water infiltrating deeper and faster into the subsurface, than when soils are much more moist, and fissures have narrowed (Cook et al. 2022).

5   Conclusions

This study focused on slow-moving shallow soil landslides driven by soil creep and the shrink-swell of clays, which in Gisborne often transition into fast-moving earth and mudflows during heavy rainfall events. The landslides are often associated with steep slopes affected by deforestation, overgrazing and undercut by roads, rivers and tracks. The InSAR analysis has shown a high consistency between areas of deformation and shallow soil failures observed in the aerial imagery and the field. Slope velocities increased rapidly, specifically, following ex-tropical cyclones since April 2017, and more generally following heavy rainfall events during winter months. Maximum velocities of ~70 mm/year in the V_{SLOPE} direction were detected by InSAR. Seasonal displacements due to shrinking and swelling of smectite-rich expansive soils also occurs, driven by wet and dry periods. In addition, a new geological hazard has been outlined for the first time here, the presence of the carcinogenic, naturally occurring zeolite mineral, erionite. This was identified in soils exposed in a fresh landslide scarp, but the risk to human health from erionite exposure is unknown, and is subject to ongoing research.

References

American Meteorological Society. Atmospheric river. Glossary of Meteorology. 2017, http://glossary.ametsoc.org/wiki/Atmospheric_river

Bayer, B., Simoni, A., Mulas, M., Corsini, A., Schmidt, D. Deformation responses of slow moving landslides to seasonal rainfall in the Northern Apennines, measured by InSAR. *Geomorphology. 2018,* 308:293–306. https://doi.org/10.1016/j.geomorph.2018.02.020

Bromhead, E.N. A simple ring-shear apparatus. *Ground Engineering*. 1979, 12, 40–44.

Cook, M.E., Brook, M.S., Hamling, I.J., Cave, M., Tunnicliffe, J.F., Holley, R., Alama, D. Engineering geomorphological and InSAR investigation of an urban landslide, Gisborne, New Zealand. *Landslides*, 2022, 19, 2423–2437.

Cook, M.E., Brook, M.S., Hamling, I.J., Cave, M., Tunnicliffe, J.F. and Holley, R. slow-moving shallow soil landslides in a vulnerable city using Sentinel-1 InSAR data. *Landslides*. 2023, 20, 427-446.

Crozier, M.J. Multiple-occurrence regional landslide events in New Zealand: Hazard management issues. *Landslides*. 2005, 2(4), 247–256.

Crozier, M. Landslide geomorphology: An argument for recognition, with examples from New Zealand. *Geomorphology*. 2010, 120, 3–15.

Cruden, D.M. Landslides: extent and economic significance. *Canadian Geotechnical Journal*. 1990, 27(3), 408.

De Luca, C., Casu, F., Manunta, M., Onorato, G. and Lanari, R. Comments on "Study of Systematic Bias in Measuring Surface Deformation With SAR Interferometry". *IEEE Transactions on Geoscience and Remote Sensing*. 2022, 60, 1–5.

Ferretti, A. Satellite InSAR Data: Reservoir Monitoring from Space (EET 9) (1st ed.). *EAGE*. 2014, 10.1109/MGRS.2015.2398392

Hu, J., Li, Z., Ding, X., Zhu, J., Zhang, L., Sun, Q. Resolving three-dimensional surface displacements from InSAR measurements: A review. *Earth Science Reviews*. 2014, 133:1–17. https://doi.org/10.1016/j.earscirev.2014.02.005

Mazengarb, C. *Slope instability and mud volcano hazard assessment, Gisborne District Council*. Client Report, 44692d. 13A. Institute of Geological & Nuclear Sciences, 1997.

Notti, D., Herrera, G., Bianchini, S., Meisina, C., García-Davalillo, J.C., Zucca, F. A methodology for improving landslide PSI data analysis. *International Journal of Remote Sensing*. 2014, 35(6), 2186–2214.

Patel, J., Brook, M.S., Kah, M., Hamilton, A. Global geological occurrence and character of the carcinogenic zeolite mineral, erionite: a review. *Frontiers in Chemistry*. 2022, 10:1066565. doi: 10.3389/fchem.2022.1066565

Simons, M., Rosen, P.A., Interferometric synthetic aperture radar geodesy. *Geodesy*. 2007, 3:391-446. 10.1016/B978-044452748-6.00059-6

Solari, L., del Soldato, M., Raspini, F., Barra, A., Bianchini, S., Confuorto, P., Casagli, N., Crosetto, M. Review of Satellite Interferometry for Landslide Detection in Italy. *Remote Sensing*. 2022, 12(8), 1351

Stringer, J., Brook, M.S., Justice, R. Post-earthquake monitoring of landslides along the Southern Kaikoura Transport Corridor, New Zealand. *Landslides*. 2021, 18, 409–423.

WHO. *Asbestos and other natural mineral fibres*. World Health Organization, Geneva, 1986.

ON AN ATYPICAL MORAINE OF THE SWISS PLATEAU AND THE PRESENCE OF A CONTINUOUS AQUIFER BETWEEN LAUSANNE AQUITANIAN GREY MOLASSE AND QUATERNARY DEPOSITS

FLAVIEN CHAPUIS [1], DANIELA ZAPATA FRANCO [2]

[1] *Lombardi SA Ingénieurs-Conseils, Fribourg, Suisse,* flavien.chapuis@lombardi.group

[2] *Lombardi Ingénierie SAS, Lyon, France,* daniela.zapatafranco@lombardi.group

Abstract

Switzerland's geology is divided into the Alps, the Plateau, and the Jura, with the Plateau separating the other two and forming the glacial foreland. The Plateau's stratigraphy typically features sub-horizontal molasse overlain by Quaternary glacial or periglacial deposits from the Würmian glaciation, with ground moraine being the quintessential morainic facies. This moraine, with low permeabilities, sometimes separates underlying aquifers in molasse discontinuities from those in superficial moraine and periglacial formations. This article discusses that topic encountered in northern Lausanne during the design of a shallow railway tunnel at the molasse and Quaternary deposits interface. The moraine's in-situ permeability values, pumping tests, and piezometric surveys are studied, aiming to answer whether a tight waterproofed separation between the Lausanne Aquitanian grey molasse and Quaternary deposits does exist. This case underscores the extreme heterogeneity of glacial and periglacial formations and the importance of careful study for structure design and environmental impact control.

Key words

Quaternary, hydrogeology, water table, moraine, molasse.

1   Introduction

1.1 Context

The Swiss Confederation, represented by the Federal Office of Transport, is financing the underground relocation of the Lausanne-Echallens-Bercher (LEB) railway, in the municipality of Étagnières, in the Canton of Vaud, 10 km north of Lausanne, Switzerland. Today, the LEB line can be considered as a commuter rail like the RER (*Réseau express régional*) lines in Greater Paris area, with a frequency already at 15 minutes; its ridership has been continuously increasing for several years due to the economic development of the Gros-de-Vaud region. The project in Étagnières is part of the development of the Swiss railway network (*Étape d'aménagement* PRODES 2035) and aims to increase the frequency of this line of the Lausanne metropolitan area's RER to 10 minutes to meet a predicted increase in traffic (+50% by 2030 and +100% by 2040).

The new underground crossing will be 1 km long, including 440 m of tunnel and 133 m of underground station. The tunnel is at a shallow depth (10 m) and intercepts the different geological formations found on the Swiss Plateau: Aquitanian molasse and glacial, periglacial and postglacial deposits from the Quaternary period. As part of the project design, geological and geotechnical investigations were carried out between January and August 2023 to characterise the different facies encountered and the hydrogeological conditions.

This article presents these tests, the results obtained, and the interpretation made, particularly regarding the "basal" moraine whose local particularities have shown that it is not sufficiently watertight: thus, it

does not make the roof of the molassic mass impermeable. This leads to the situation where an aquifer communication could exist between the Quaternary deposits and the molassic rock base, without it being possible to distinguish between perched lenticular aquifers present in the Quaternary deposits and a fissured aquifer in the molasse.

1.2 Geological survey carried out

In the spring of 2023, 20 cored boreholes (S21 to S27, S29 to S41) were drilled, complementing 14 others drilled in 2019 during an initial reconnaissance campaign. 11 of the boreholes were equipped with a piezometric tube, either screened in rock (S22, S24, S26, S34 and S35) or in unconsolidated materials (S27, S29 to S33). Figure 1 shows a location plan of the boreholes.

Figure 1. Situation of the drilled boreholes for both 2019 and 2023 surveys.

2   Geological context of the Swiss Plateau

2.1 Molasse

Switzerland is typically divided into three distinct geographical areas: the Jura, the Plateau, and the Alps. Regarding the Swiss Plateau, the substratum is composed of molasse; in the Lausanne and Gros-de-Vaud region, the molasse is a freshwater lower molasse, dated from the Aquitanian (Lower Miocene), called "Grey Molasse of Lausanne" (French: *Molasse grise de Lausanne*).

This molasse characteristically shows an alternation of sandstone and marl beds, sometimes indistinguishable. Generally, this rock formation consists of an alternation of thick sandstone beds with limestone cement and various layers with a more or less significant marly-clay component, including marlstone, marly sandstone, silty marl, more or less marl silts, and finally more or less clayey marls (Gencer *et al.* 2018).

In the Étagnières sector, the grey molasse shows a subhorizontal stratigraphy. Drilling has shown that the sandstone facies are weakly fractured, and the rock mass can be considered overall as quite massive. Only a few slightly open fractures (mm), sometimes oxidised, have been encountered in sandstone levels. The fractures can thus be considered as very spaced (more than 2 m) to locally moderately spaced (on the order of the meter). Their linear extension is generally several meters, sometimes up to a dozen meters. The fracturing is well observed in the sandstone levels. In the marls, it is marked rather by a tectonised matrix with lustrous surfaces.

2.2 Quaternary deposits

The Quaternary geology of the Swiss Plateau is dominated by glacial and periglacial deposits associated with the Quaternary glaciations, particularly the Würm glaciation. Morainic deposits are the most common in the region, with other periglacial or postglacial deposits interbedded within them. The formations encountered in the project are listed below:

—— Peat deposits: These were found in the S26 borehole and are 2.35 m thick. They consist of peaty silts and clayey silts with sand and organic matter and are generally very soft and compressible.

Figure 2. Former marsh: peaty facies at the top left and clayey facies in the rest of the cores (S26).

— Fluvio-glacial deposits: These periglacial deposits are present in the form of lenses with variable geometry and a thickness of 0.5 to 2.0 m within morainic deposits. They consist of gravelly sands and silty sands, sometimes limestone gravels, and are generally moderately compact. These fluvio-glacial materials are generally non-cohesive or slightly cohesive. Water inflows have been observed in several boreholes.

Figure 3. Fluvio-glacial deposits (S34).

— Glacio-lacustrine deposits: This second type of periglacial deposit is also present in lenses with variable geometry and metric thickness within morainic deposits. These materials are frequently associated with fluvio-glacial deposits. Glacio-lacustrine deposits are generally composed of clayey silts, varved, compressible, with a firm to hard consistency, becoming soft to very soft in the presence of water (often present in the overlying fluvio-glacial deposits). In the latter case, these materials are fluid.

Figure 4. Glacio-lacustrine deposits starting from 4.50 m (S09).

— Weathered moraine: This is sandy or silty moraine that has been altered and has a firm to very firm consistency, sometimes soft.
— Sandy moraine: The sandy moraine, more frequent in the southern half of the project, is composed of often silty sands with gravel. These materials have some cohesion, and their consistency can be described as very firm to hard. The presence of stones or blocks is possible. The thickness of the sandy moraine is generally 2 to 3 m.

Figure 5. Sandy moraine (S25).

— Silty moraine: The silty moraine is present mainly in the northern half of the project, often just above the rock, with a thickness of about 3 to 4 m. It is composed of generally gravelly silts, sometimes sandy, with a very firm to very hard consistency. This is not a typical basal moraine, which is why we have not named it as such.

Figure 6. Silty moraine (S25).

The longitudinal profile of the underground project established on the two different geological surveys is given hereafter (Figure 7):
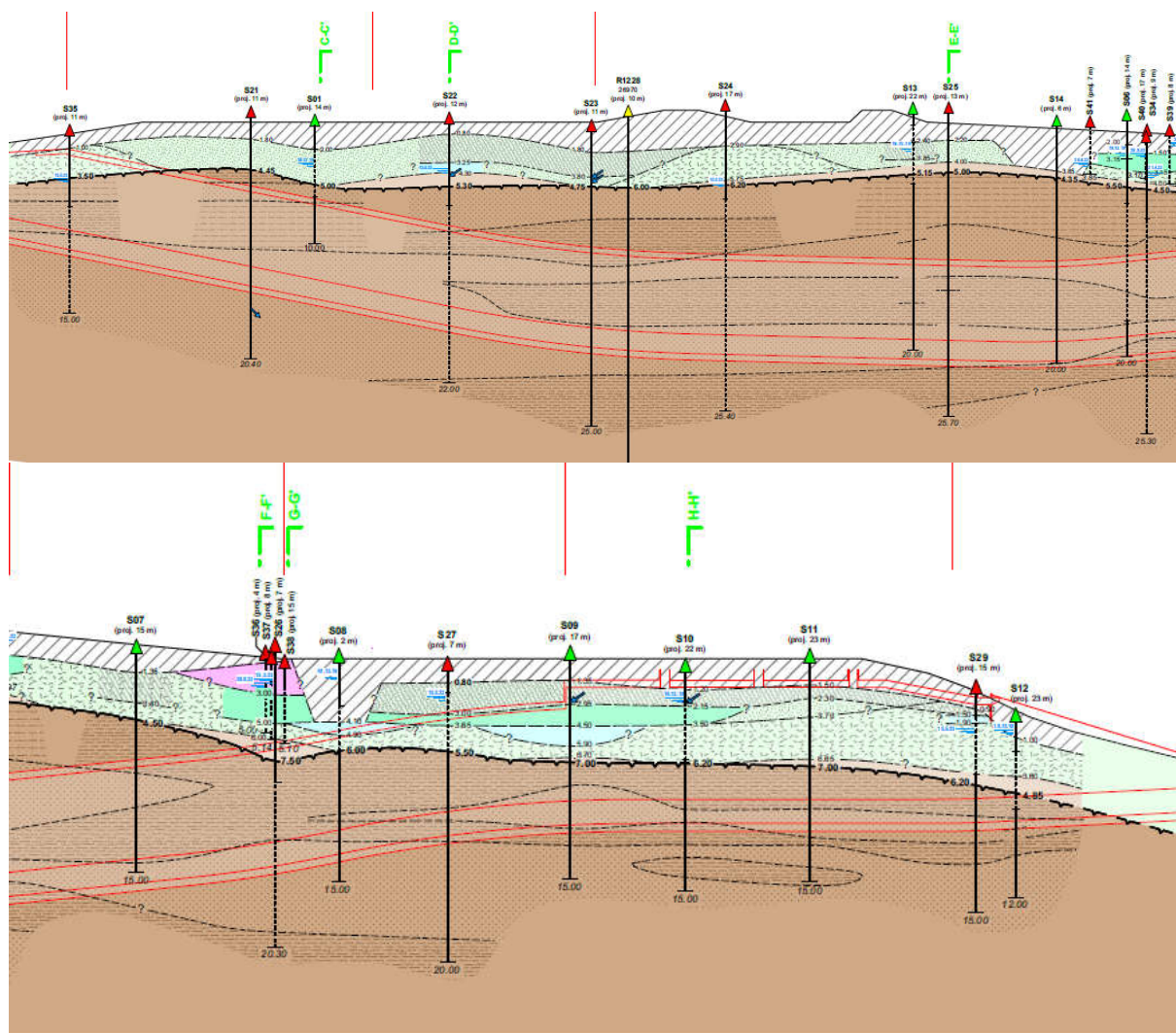
Figure 7. Longitudinal geological profile of the new tunnel and RER station in Étagnières.

2.3 Hydrogeological context of the Swiss Plateau

The glacial and periglacial facies exhibit quite different hydrogeological behaviours. The article by Parriaux and Nicoud (1993) provides a comprehensive synthesis on this subject regarding the formations encountered in the Northern Alps, based on several observations from glacial or periglacial terrains from the Swiss Plateau and Swiss and French Alpine valleys.

The basal moraine is generally considered to have low permeability ($k < 10^{-6}$ m/s) in its typical facies. According to Parriaux et Nicoud, in some rare cases, when the permeability is sufficiently low and the moraine has not been altered, it forms an impermeable layer between the underlying rock and the overlying deposits. Fluvio-glacial and glacio-lacustrine deposits, on the other hand, have typical permeabilities that are higher (from 10^{-2} to 10^{-4} m/s and from 10^{-3} to 10^{-4} m/s, respectively).

Several engineering projects have provided feedback on the complex hydrogeology at the interface between molassic formations and Quaternary deposits in the Lausanne region over the past 30 years. For example, in the extension of the LEB to the centre of Lausanne (Flon station) in 1995, Tappy (1995) reported that no significant and permanent aquifer flow was observed between the molasse and the basal moraine of the Rhone glacier. In another adjacent project to put the LEB underground in the heart of Lausanne, Hey (2020) reports that glacial and periglacial deposits most often form aquifer lenses, without communication with the molassic rock where only punctual water inflows were observed. Risch (2005) also reports the same observation during the construction of the second metro line in Lausanne: two aquifers exist, one perched in the Quaternary cover soils, the other in the discontinuities of the molasse, without them clearly joining together.

2.4 Objective

The objective of this study is to discuss the hydrogeology of the presented terrains based on various in situ tests. From a design perspective, it is crucial to determine whether there is communication between the rock base and the overlying soils to choose between a drained or non-drained tunnel. The literature review suggests that aquifer communication may exist, according to observations by Parriaux and Nicoud, as cases where the basal moraine acts as an impermeable layer are rare. However, feedback from previous projects indicates a separation of aquifers between the fractured aquifer and the lenticular aquifer in the Quaternary deposits. In this article, we aim to establish whether aquifer communication exists or not.

3   Methods

In order to clarify the hydrogeological conditions of the entire mass consisting of the rock mass and the loose soils, 10 in situ permeability tests were carried out: 3 Lefranc permeability reduction tests during drilling, and 7 drawdown-recovery tests in the boreholes. The tests were carried out in the unconsolidated soils and in the molassic rock.

Three short pumping tests, each lasting 5 to 6 hours, were carried out in spring 2023 in the piezometers S26, S24 then S34, all screened in the molasse, in order to evaluate the drawdown that would be caused by the draining effect of the project, particularly in loose soils. During each test, the pump flow rate was set (very low flow rate between 0.1 and 0.2 L/min) so that the piezometric level (PZ) was gradually lowered to 1 to 2 m below the level of the project raft (3 successive stages of 1.5 to 2 h). The PZ in nearby piezometers was measured every 30 minutes.

Additional pumping tests were carried out in August 2023 to try to clarify the hypothesis of the presence of a single aquifer and the permeability of the rock. For the pumping test in the piezometer S26 (screened in rock), pressure probes were installed in the observation piezometers S36, S37, S38 as well as S08 and S27 (all screened in loose soils). They measured the water levels every 5 minutes, during pumping and for 6 days after the pump was stopped. At the same time, manual control measurements were carried out.

For the pumping test in S34 (screened in rock), the pressure probes were placed in the observation piezometers S39, S40, S41 and S05 (screened in loose soils) as well as S26 (screened in rock). They measured the water levels every 5 minutes, during the 3 days preceding the pumping, during it and during the 3 days after its stoppage.

4 Results

4.1 Permeability tests

The water tests carried out during drilling, after piezometer installation or after pumping made it possible to evaluate the permeability of the encountered soils. The results are summarised in Table 1 below.

In the loose soils, the lowering tests carried out in the silty moraine indicate, as expected, low permeabilities of $5.5 \cdot 10^{-7}$ and $1.4 \cdot 10^{-6}$ m/s. The test carried out in the fluvioglacial alluvium (drilling S27) and partially in the silty moraine shows a permeability of the order of 10^{-5} m/s, which somehow represents a mean value between characteristic permeabilities of both formations, especially considering the values given by Parriaux et Nicoud (1993).

As for the rock base, the drawdown-recovery tests carried out after piezometer installation or after pumping indicate low permeabilities of the mass of the order of 10^{-6} m/s (values between $9.4 \cdot 10^{-7}$ and $2 \cdot 10^{-6}$ m/s). Water circulation will likely occur mainly in the sandstone levels and their fracture network (fissural permeability).

Table 1. Values of permeability measured in situ.

	Borehole	Formation	Technique	Permeability (m/s)
Loose soils	S27	Fluvio-glacial alluvium and silty moraine	Lefranc lowering during drilling	$1.2 \cdot 10^{-5}$
	S27	Sandy moraine, fluvio-glacial alluvium and silty moraine	Drawdown-recovery in piezometer	$3.5 \cdot 10^{-7} - 1.6 \cdot 10^{-6}$
	S24	Silty moraine	Lefranc lowering during drilling	$1.4 \cdot 10^{-6}$
	S34	Silty moraine	Lefranc lowering during drilling	$5.5 \cdot 10^{-7}$
Rock	S22	Molasse	Drawdown-recovery in piezometer	$9.4 \cdot 10^{-7}$
	S24	Molasse	Drawdown-recovery in piezometer	$1.2 \cdot 10^{-6}$
	S26	Molasse	Drawdown-recovery in piezometer	$1.5 \cdot 10^{-6}$
	S34	Molasse	Drawdown-recovery in piezometer	$2.0 \cdot 10^{-6}$
	S26	Molasse	Drawdown-recovery after pumping	$1.8 \cdot 10^{-6}$
	S34	Molasse	Drawdown-recovery after pumping	$1.8 \cdot 10^{-6}$

4.2 Pumping tests

The results form the pumping tests are presented below in Table 2.

Table 2. Results from the pumping tests.

Observation piezometer	Formation	Pumping borehole		
		S24	S34	S26
S24	Molasse	-15.4 m (pumping)	PZ still increasing	Unmeasured
S34	Molasse	Unmeasured	-18.4 (pumping)	PZ still increasing
S26	Molasse	Unmeasured	PZ still increasing	-12.0 m (pumping)
S02	Loose soils and top of molasse	0	Unmeasured	Unmeasured
S22	Molasse	PZ still increasing	Unmeasured	Unmeasured
S05	Loose soils	0	0	0
S08	Loose soils	Unmeasured	0	-0.08 m
S27	Loose soils	Unmeasured	0	0

Note that some piezometers showed an increase in water level during pumping tests (S34, S22 and S24). For S34 and S22, this can be explained by water levels that were in the process of rising following the drainage of the piezometers a few days before the pumping tests. Regarding S24, the water level was also in a phase of rising following the pumping test that was carried out the day before.

The results of the complementary pumping tests carried out in August 2023 are summarised in the following table (Table 3).

Table 3. Observations made during the complementary pumping tests.

Piezometers	Observations on the water table in the piezometers
S36	The water level decreases regularly and slowly before, during and after pumping due to a dry period. The rise observed during the measurement on 05.09.23 is due to the rains on 26, 27 and 28.08.23. The stop of pumping on 18.08.23 has no effect.
S37	Same as for S36. The measurements with the pressure probe show several "jumps" due to a displacement of the probe in the piezometer during manual measurements.
S38	The piezometric level is rising because its equilibrium with the water table took several weeks after the drilling was completed, due to very low permeability. The stop of pumping on August 18, 2023 has no effect.
S08	Same as for S36.
S27	Same as for S36. The difference of about 20 cm between the manual measurements and those with the pressure probe is due to a problem with the reference level 0 of the measurements with the probe. The peak on 12.08.23 is probably related to the rain of the day.
S39	The water level rises rapidly following the rains of August 26, 27, and 28, 2023, and then slowly decreases for about 2 weeks. The stop of pumping on September 1, 2023, does not induce any rise in the water level.
S40	Same as for S39.
S41	The water level rises quickly following the rains on August 26, 27, and 28, 2023, then decreases rapidly. No significant variation in the level during and after pumping.
S05	The water level rises after the rains of August 26, 27, and 28, 2023, and then decreases slowly. The stop of pumping on September 1, 2023, does not induce any rise in the water level.
S26	Same as for S41.

The monitoring of water levels in observation piezometers, whether using pressure probes or manual measurements, does not show any influence of pumping. The variations in piezometric levels are solely related to precipitation. These findings are summarised in table 3. This absence of influence can be explained by the low permeability of the rock (particularly the marl levels) and the unconsolidated soils. In S26, according to the water meter, only 730 litres of water were pumped during the nearly 8 days of pumping (very low pump flow rates of 0.1 to 0.2 L/min). This indicates that the radius of influence of the pumping around S26 was probably less than 1 metre and therefore explains why no influence was observed on the observation piezometers. In S34, the same finding was made (low volume of water pumped), although the exact value could not be recorded.

4.3 Sensitivity of the molasse permeability value

We wanted to numerically simulate the pumping test of borehole S26 in order to confirm the orders of magnitude of the permeability of the molasse with a 2D axisymmetric FEM on Plaxis. We took 624 m a.s.l. as the initial water table level, corresponding to the average level measured by the piezometers in the area.
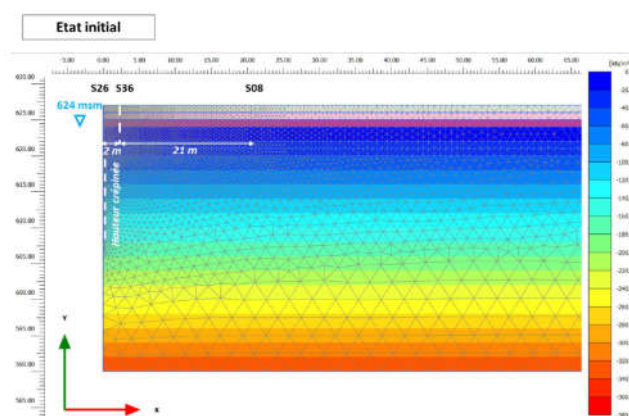
Figure 8. Initial state – Simulation of the pumping test in S26.

We simulated the pumping test by emptying the S26 piezometer and observing the cone of water lowering after 8 days (duration of the test). We carried out this exercise for different permeabilities of the molasse.
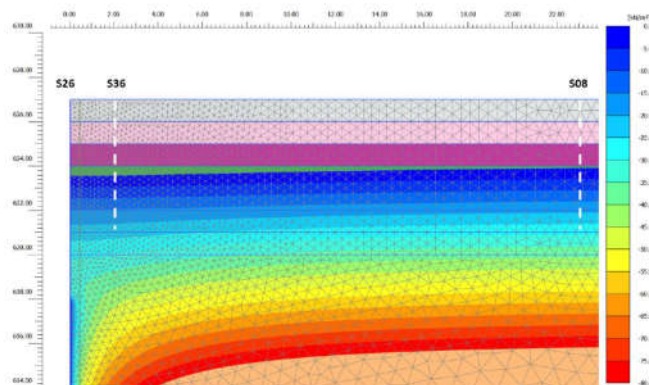
Figure 9. Simulation of the pumping test in S26 after 8 days, assuming $k = 10^{-6}$ m/s in the molasse.

With the permeability $k = 10^{-6}$ m/s, the piezometers S26 and S08 show a decrease in their level of 50 cm and 10 cm respectively. However, during the pumping tests, no effect was observed. Therefore, the permeability seems to be lower.

Figure 10. Simulation of the pumping test in S26 after 8 days, assuming $k = 10^{-7}$ m/s in the molasse.

With such a permeability ($k = 10^{-7}$ m/s), the piezometers S36 and S08 would have seen a decrease in their levels of 10 cm and 1 cm, respectively. However, no decrease was observed related to the pumping.

Figure 11. Simulation of the pumping test in S26 after 8 days, assuming $k = 10^{-8}$ m/s in the molasse.
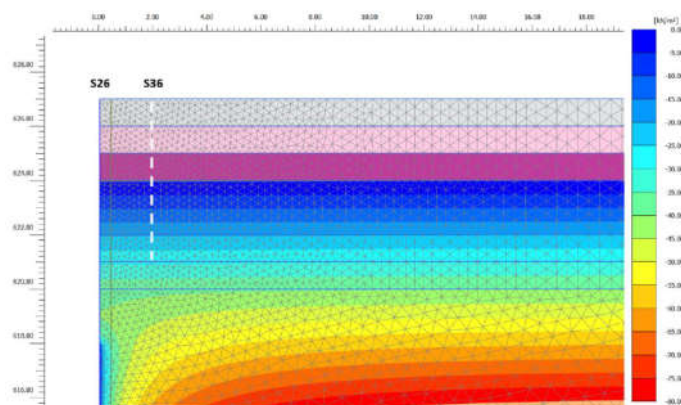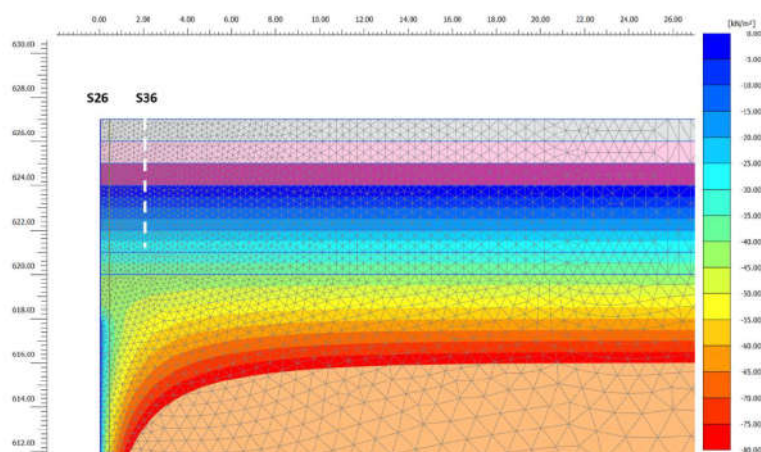
In this case ($k = 10^{-8}$ m/s), there would be no effect of pumping on the water levels of S36 and S08, as shown in the figure below. Thus, the permeability of the molasse would probably be between 10^{-7} and 10^{-8} m/s, lower than that indicated in the permeability tests conducted in situ, which is on the order of 10^{-6} m/s.

4.4 Discussion

Similar levels were observed in the piezometric measurements carried out in December 2019 (high water regime; precipitation between 155 and 163% of the monthly average at the MétéoSuisse station in Echallens for the months of October to December 2019) and in April-September 2023 (average to low water; 127% and 105% of the normal in March and April 2023, 56%, 66% and 86% in June, July and August 2023). These measurements indicate that the unconsolidated soils and the underlying rock mass contain a groundwater table with a piezometric level generally located between 1 and 4 meters deep, locally up to approximately 6 meters (S24 borehole). The variations of these levels depending on precipitation are proven by the measurements (particularly during the pumping tests of August 2023) and confirm that this is not just water pockets in isolated lenses, but rather a single aquifer.

The possibility of distinct aquifers has been ruled out, but this does not answer the question of whether the molassic rock and the Quaternary deposits actually communicate. The silty moraine observed on site

corresponds, in terms of depositional mode and in situ measured permeability, to the description of a classic basal moraine by Parriaux and Nicoud (1993). However, its lack of lateral continuity (incursions of sandy moraine, or even disappearance of the silty moraine in the southern part of the study area), as well as its sandier character compared to a typical basal moraine, suggest that it cannot guarantee complete sealing of the substratum. The absence of a thick and continuous layer of low-permeability deposits (basal moraine) at the top of the molassic rock, as well as similar piezometric levels in the unconsolidated deposits and in the molasse, indicate the probable presence of a single aquifer that can be considered continuous. However, despite this, pumping tests in piezometers screened in the molasse did not reveal a drawdown in the piezometers in the unconsolidated deposits, as if there were indeed a separation of groundwater into two aquifers. It may be thought that the very low permeabilities involved were an obstacle to visualising aquifer flows using pumping.

5   Conclusion

The present article aimed to highlight the difficulty, in the discussed case, of drawing a definitive conclusion, despite several geological surveys, regarding the aquifer communication between the molassic substratum and Quaternary deposits. The comparison between the geological synthesis at the scale of the northern slope of the Alps, feedback from tunnel projects in the Lausanne region, continuous piezometric measurements, and pumping tests has not yet provided a definitive answer to the question of the existence of a continuous aquifer along the new Étagnières underground crossing. This limitation poses a genuine engineering problem, and a choice had to be made. It was decided, in agreement between the project owner, the consulting engineer, and the experts checking the calculations, to assume that a single and continuous aquifer exists. This assumption, although very likely, remains the one that allows to control the geological risks to ensure the durability of the structure, and to avoid a drawdown of the aquifer with significant geotechnical (settlements) and environmental consequences. The construction of the tunnel will allow, through visual observation of the molasse and unconsolidated soils, to confirm or refute the assumption made. Finally, the article emphasized the sometimes-too-high value of direct permeability estimates from tests, which it is sometimes useful to compare with numerical simulations, even if the latter also have their biases.

References

Gencer, M.; Mathier, J.-F.; Noverraz, F. et Français, O. Description des propriétés mécaniques de la Molasse aquitanienne de Lausanne. *Revue française de géotechnique.* 2018, 154, 4.

Hey, O. Nouveau tunnel LEB – Défis d'un chantier en plein cœur de Lausanne. *Swiss Tunnel Congress – Fachtagung für Untertagbau.* 2020, 19, 117–130.

Parriaux, A.; Nicoud, G. De la montagne à la mer, les formations glaciaires et l'eau souterraine. Exemple du contexte Nord-alpin occidental. *Quaternaire*, 1993, 4, 2-3, 61-67.

Risch, C. Lots 1400/1500 : Partie souterraine de la station Ours et tunnels. *Mitteilungen der schweizerischen Gesellschaft für Boden- und Felsmechanik / Publication de la Société suisse de mécanique des sols et des roches*, 2005, 150, 43-52.

Tappy, O. Prolongement en souterrain de la ligne du LEB : travaux de génie civil. *Ingénieurs et architectes suisses*, 1995, 121, 1-2, 61-67.

INVESTIGATION WORKS AND REMEDIATION DESIGN OF A ROAD LANDSLIDE IN HRVATSKO ZAGORJE

KRISTINA VULIĆ [1], LOVORKA LIBRIĆ [2], MARIO BAČIĆ[3], STJEPAN MATIĆ[4]

[1] *University of Zagreb, Faculty of Civil Engineering, Croatia, kristina.vulic@unizg.grad.hr*

[2] *University of Zagreb, Faculty of Civil Engineering, Croatia, lovorka.libric@unizg.grad.hr*

[3] *University of Zagreb, Faculty of Civil Engineering, Croatia, mario.bacic@unizg.grad.hr*

[4] *Center of the Faculty of Civil Engineering, Croatia, stjepan.matic@unizg.grad.hr*

Abstract
The area of Hrvatska Zagorje is the most prone to landslides in the Republic of Croatia, with landslides occurring practically every day, caused either by natural or anthropogenic factors. Many of these landslides are activated along the network of state and local roads that pass through numerous cuttings mostly without any or with inadequate slope stabilization measures. Implementation of investigation works, and remediation design are all accompanied by numerous challenges. Designing effective landslide remediation measures requires a thorough understanding of geological, hydrological, and environmental factors influencing slope stability. This paper deals with investigation works and remediation design of a road landslide in Hrvatska Zagorje providing an overview of the landslide that occurred on the state road at the entrance to residential area Tkalci. The investigation works and remediation solution were implemented considering the spatial restrictions for remediation works (i.e. considering the proprietary and legal relations) and without any alternative road route which could be used during the implementation of remediation works. Also, a comprehensive overview of the results of stability analyses of the affected roadway in the cut have been carried out for different scenarios under static and seismic conditions, determining safety factors, and stress-deformation analyses to ascertain displacements and internal forces in the designed structure.

Key words
Road infrastructure, landslide, investigation works, remediation works, Hrvatsko Zagorje

1 Introduction

The area of Hrvatsko Zagorje is characterized by the frequent occurrence of landslides due to natural and anthropogenic influences. The transportation infrastructure in this area often runs through many cuts that lack adequate stabilization protection. This can lead to landslides, among other issues, due to weather-induced changes in slope geometry and the presence of seepage water, which can compromise the strength of the material in which the transportation infrastructure is built (Kim et al., 2018). Addressing landslide problems involves extensive investigation works and designing remediation solutions, both with numerous challenges. For an optimal remediation solution, a detailed understanding of the geological, hydrological, and meteorological impacts on slope stability is necessary. This knowledge is the basis for the proper dimensioning and implementation of stabilization measures, such as retaining walls, drainage systems, or other slope stabilization measures. This paper will provide an overview of the landslide situation that occurred on the state road in the Hrvatsko Zagorje area at the entrance to residential area Tkalci, with presentation of investigation work carried out at the site, and will provide a detailed insight into the chosen landslide remediation measure. The location in question is situated on the route of the state road between the residential area of Petrovsko and Tkalci. The

planned remediation is in the area of road subsidence, specifically around a landslide on the downhill slope at km 9+327 of the State Road DC206, as shown in Figure 1.
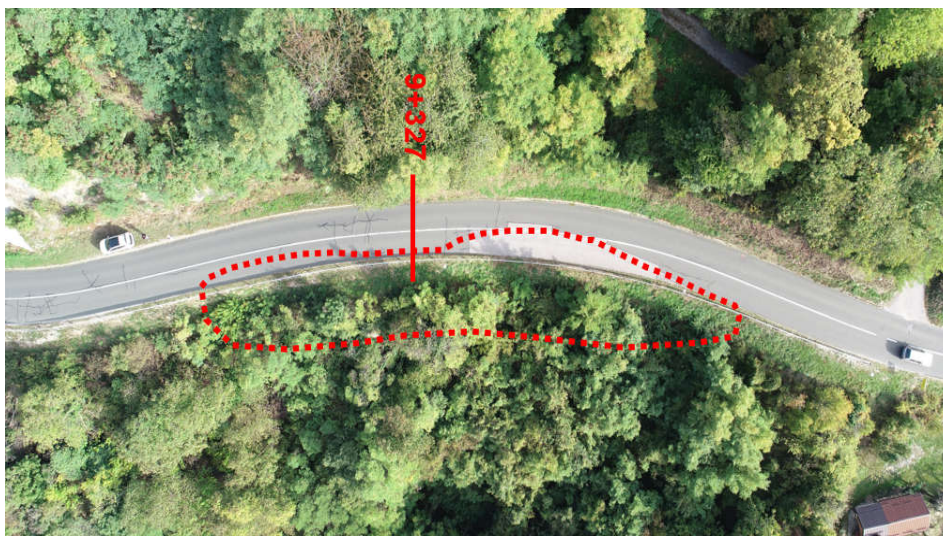
Figure 16. Area of instability and planned remediation, State Road DC206

The road is located at an altitude between 346 and 349 meters and has a width of 6.5 meters. At the location in question, there is a very steep slope of 8 meters on the uphill side, which is protected by a steel mesh and anchors. The downhill slope, covered with forest and dense vegetation, is also steep with a gradient of 30°, while along a smaller section of the road, the gradient reaches up to 50°. The landslide has affected approximately 80 meters of the road, with the most pronounced cracks appearing over a length of 30 meters. In this road section, significant shallow subsidence of the downhill lane has been observed, with visible cracks extending from the road axis towards the downhill slope.

An engineering visual inspection revealed that there was no rainwater drainage, instead, water is partially drained via curbs along the uphill edge of the road, directing water along the longitudinal gradient. Most of the rainwater flows down the slope, driven by the transverse gradient of the road. Surface drainage is further hampered by accumulated material in the narrow area next to the curbs. The accumulation of material on the uphill side is a result of water erosion and the washing away of cover material. Figure 2 shows a crack about 15 meters long, observed on the western part of the intervention area, located 1 meter from the edge of the road. The figure also shows a very steep slope covered with dense vegetation on the uphill side.

Figure 17. Western part of the road with developed crack about 15 meters long

It is predicted that shallow and slow sliding could occur on the mentioned site. As observed around the world, shallow landslides can be very destructive phenomena, with the potential for considerable loss of human life as well as property damage (Postance et al. 2017). Some examples of catastrophic translational landslides that occurred due to heavy rainfall include those at Mt. Umyeon in Japan, which resulted in 18 deaths and infrastructural damage (Lee and Park 2015), in eastern Liguria and northwestern Tuscany, which caused 13 casualties (Bartelletti et al. 2017), and in Macedonia, which is generally affected by landslides impacting infrastructure and the population (Peshevski et al. 2017; Haque et al. 2016). Therefore, appropriate landslide susceptibility, hazard, and risk assessments are needed in areas such as mentioned above or Hrvatsko Zagorje, which is prone to shallow landsliding, and any other locations affected by landslides around populated areas and infrastructure.

2   Geological and geotechnical conditions of the location

To gain a comprehensive understanding of the spatial distribution of engineering-geological environments at the site, as well as their physical-mechanical characteristics, the application of multiple soil investigation methods is required. Detailed engineering-geological investigations determine the morphological, geological, hydrogeological, and engineering geological characteristics of the location, including defining micro-locations for boreholes, inspection of drilled core, as well the selection of samples for laboratory testing.

Due to the very dense vegetation covering the terrain and hindering accessibility, no clear contours of the landslide or pronounced cracks were observed during the mapping of the downhill slope. It is presumed that shallow and slow sliding is occurring, affecting a narrow strip along the road for approximately 80 meters. The data on the distribution of individual lithological units were obtained through drilling, core determination, and geological mapping. An engineering geological map was developed, and it is shown in Figure 3. It is assumed that the sliding involves cover layers, specifically fill material and weathered rock. Leaning trees were occasionally observed on the slope, which occurs because of the very steep slope. The adverse morphological characteristics of the terrain and the action of rainwater, which flows over the slope, soaking the cover layers and reducing the shear strength of the material, are factors that contribute to the landsliding at this location. In the eastern part of the road, cracks and subsidence extend to its center, while in the western part of the area, the cracks are less pronounced, likely indicating road fill material sliding.

A total of two boreholes, were drilled to a depth of up to 14 meters, as shown in Figure 4. The exploratory drilling involved the identification and engineering description of the borehole core, standard penetration testing (SPT), and the collection of disturbed and undisturbed soil samples. The soil samples were transported to the laboratory for testing. Laboratory tests conducted included determining the natural moisture content of the soil, classification tests such as Atterberg limits and grain size distribution, as well as shear strength tests using the direct shear test and the determination of the compressibility modulus using the oedometer test.
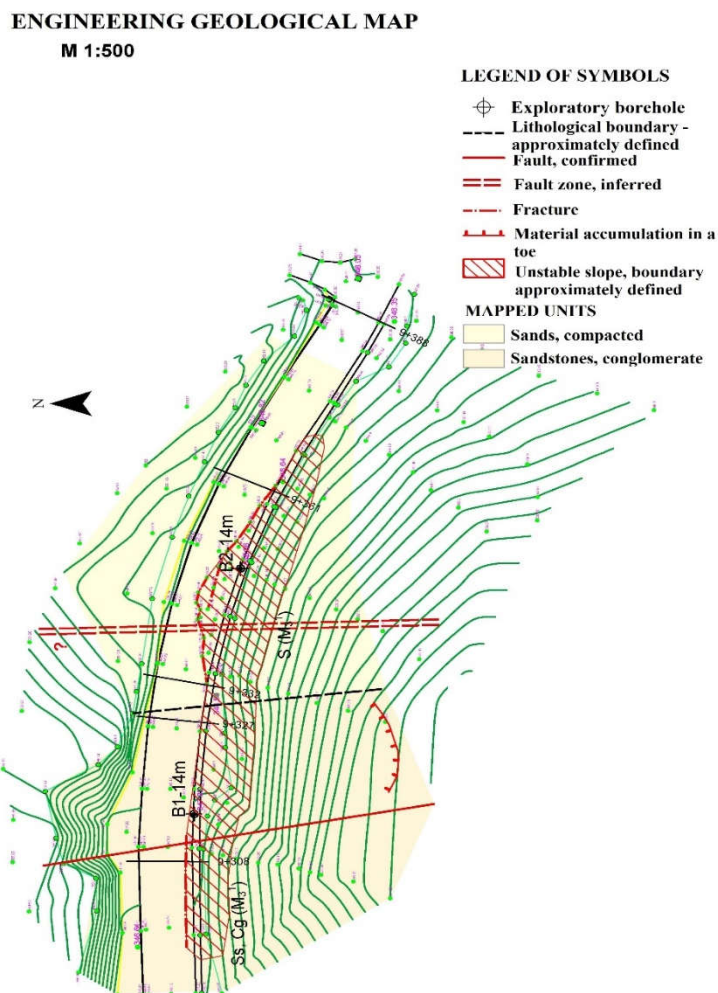

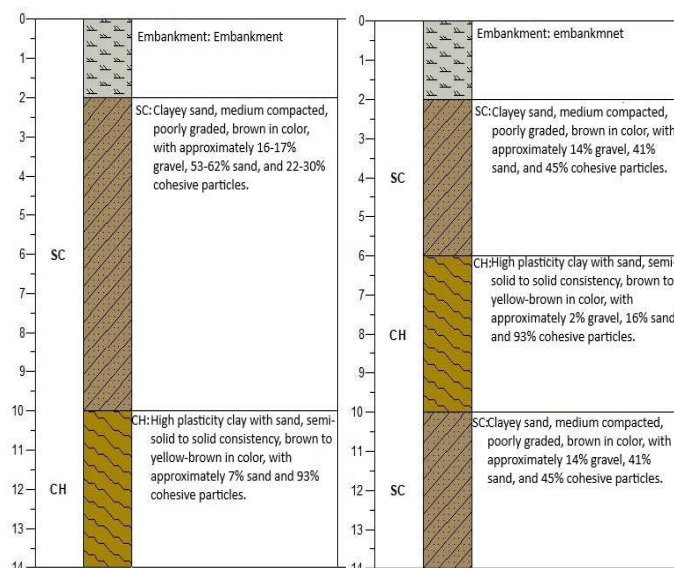**Figure 18** Engineering geological map of the area

Figure 19 Display of core samples from exploratory boreholes B1 (left) and B2 (right)

Based on the field determination and classification of the borehole core, considering the results of laboratory testing, the soil profile at the site was determined. The soil profile consists of an anthropogenic road fill layer of 2.0 meters thickness composed of non-cohesive material, gravel, and sand, gray brown in color. Beneath this layer, there is a deposit of clayey sand that is medium dense, poorly graded, and brown in color, consisting of gravel, sand, and cohesive particles in different percentages. Under clayey sand the soil transitions into a layer of highly plastic clay with a firm consistency, brown to yellow brown in color, containing gravel, sand, and cohesive particles. The clay exhibits high plasticity, which affects its stability and deformation characteristics. Under high plasticity clay there is another layer of clayey sand, which is also medium dense and poorly graded, brown in color.. The geotechnical properties of the soil profile show a unit weight of 18.0 kN/m³ in the upper and lower layers, with a slightly higher 21.0 kN/m³ in the clay layer. The cohesion of the clay is 7 kPa, with an internal friction angle of 20° and a compressibility modulus of 10 MPa. The clay's liquid limit is 56.7 %, while plasticity index is 37 %, and consistency index is 1.0, highlighting its significant plastic behavior and potential challenges for engineering applications.

3   Remediation design methodology

The optimal solution for stabilizing landslide has been selected, involving the installation of a pile wall in two rows that are connected by a cantilever wall as the pile head beam. Since the cantilever wall acts as the head beam rather than a retaining structure, the load is transferred to the piles, which then transmit it further into the deeper soil layers.

The chosen solution consists of two rows of piles with a diameter of Ø 60 cm and a length of 10 meters, along with a concrete cantilever wall with a base depth of 60 cm and a total wall height of 250 cm as shown in Figure 5. The two rows of piles are installed with the same diameter and length but with different spacing. The spacing for the front row of piles, in the zone of the roadway subsidence over a length of approximately 39 meters, is 1 meter, while the remaining piles of the first row are spaced 2 meters apart. The second, or rear row of piles, is installed with a spacing of 2 meters throughout its entire length. It should be noted that the remediation is implemented on the state road where usually there is no alternative route for traffic during the works. Therefore, road managers insist on implementing solutions during the traffic operation. In this case, to secure the safe implementation of works, as well the traffic operation along the one lane, the sheet pile wall is installed to secure the construction pit (Figure 5).
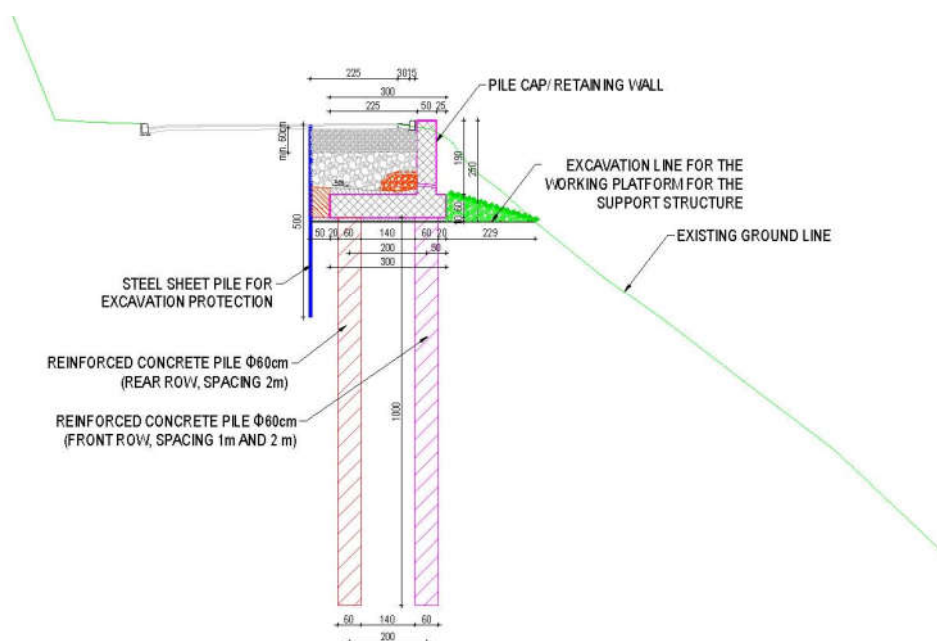
Figure 20. Cross-section with the planned landslide remediation solution

In preparing the geotechnical calculations according to the guidelines of HRN EN 1997-1:2012 Eurocode 7: Geotechnical Design and HRN EN 1998-5:2008 Eurocode 8: Design of Structures for Earthquake Resistance, and relevant Croatian national annexes, checks for both ultimate and serviceability limit states are conducted. Stability analyses of the affected roadway in the cut have been carried out for different scenarios under static and seismic conditions, determining safety factors and conducting stress-deformation analyses to ascertain displacements and internal forces in the structure.

When checking the stability of slopes and determining the safety factor of the sliding mass, the sliding mass is not predetermined; instead, it is necessary to find the one with the smallest safety factor, as this will be the critical sliding mass for evaluating slope stability (Burman, 2015). This safety factor is used as a measure of the stability of the entire slope. It follows that the practical application of the limit equilibrium method involves analyzing and finding the sliding mass with the smallest safety factor (Burman, 2015). During the stability analysis, following design situations were examined: current stability of the slope, pile installation and excavation for the retaining structure with installation of temporary sheet pile wall, installation of two rows of piles and the cantilever wall with backfilling and removal of the sheet piles, end of construction with operational vehicle loading, and application of seismic loading.

Stress-strain analyses are conducted for the ultimate limit state (ULS) for determining shear forces in structural elements, and as part of the serviceability limit state (SLS) for determining displacements. Stress-strain analysis is based on the finite element method, which is used to analyze stress and deformation relationships (Burman, 2015). For the described analysis, a hyperbolic constitutive model was used. The hyperbolic model analyzes soil behavior by checking if yielding or exceeding the shear strength occurs and assigns appropriate value of the soil stiffness.

For the purposes of conducting stress-strain analyses within the framework of ultimate and serviceability limit states at characteristic profile, the following design situations were considered: end of construction, operational conditions with traffic, sliding of the downhill slope (as a possibility), and seismic loading. Figure 6 shows the computational model with all elements of the planned remediation solution. The design situation in which the sliding of the downhill slope occurs after the implementation of the

remediation measures is analyzed, as these measures do not have impact on potential downhill sliding. This is a common situation when implementing remediation measures along the road infrastructure where the infrastructure managers usually own the land where the road itself is located and immediately next to it. This means that stabilization of whole downhill slope would include implementation of measures across the slope, which is usually considered too costly, as well not allowable since it is not land owned by the road managers. Therefore, the analyses should verify that the road and remediation solutions are stable and resistant to loads even in the case if downhill slope sliding occurs.
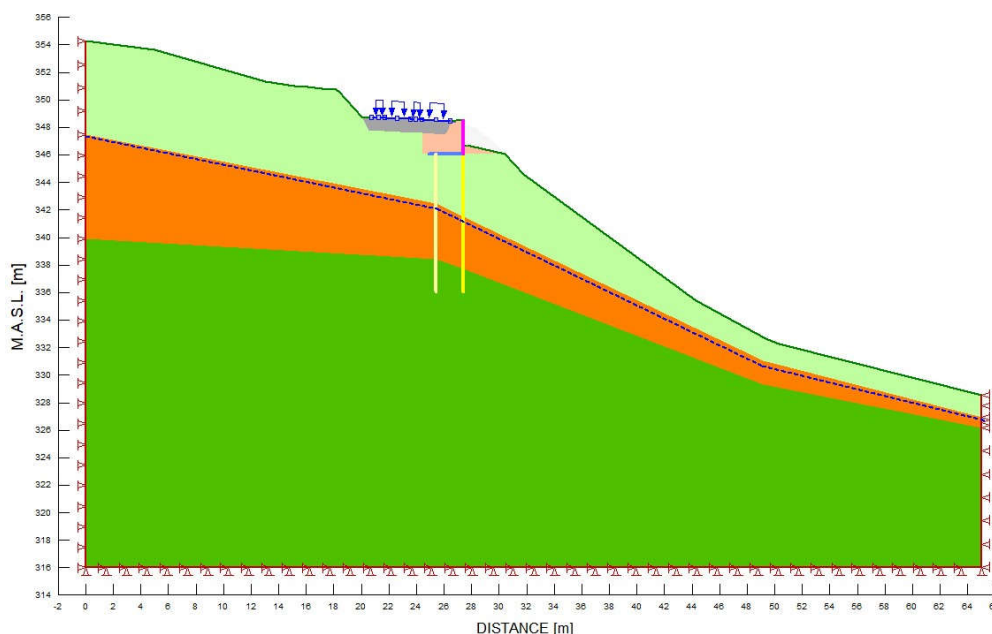
Figure 21 Computational model with elements of the planned remediation solution

For seismic load analyses, a design ground acceleration of $a_g = 0.19g$ was used. The design ground acceleration is relevant for a return period of 475 years. The design ground acceleration depends on the level of seismic risk and is determined based on appropriate seismological studies of the building location or according to adopted seismic maps. The maps with legends are an integral part of the National Annex to several standards HRN EN 1998-1:2011/NA:2011, Eurocode 8: Design of structures for earthquake resistance – Part 1: General rules, seismic actions, and rules for buildings.

4   Results and discussion

The stability analysis of the current (in situ) state showed a safety factor of 0.81. A safety factor less than 1 indicates a stability problem, which aligns with the observed subsidence of the roadway and the appearance of cracks, indicating active instability of the road and the downslope area. During the remediation works, the safety factor in all phases was satisfactory and greater than 1, as shown in Table 1. The same applies to both static and seismic conditions after construction and during exploitation, which signifies the stability of the proposed remediation solution.

Table 5. Factor of safety of Profile 1 for different scenarios

DESIGN SITUATION	Fs
In situ state (before remediation)	0,81
Excavation for the implementation of the remediation	1,12
End of construction and traffic	1,67
Earthquake conditions	1,55

During the stability analysis at the end of the remediation construction, a potential slip surface was observed on the downslope with a safety factor of 0.78, as shown in Figure 7. However, as explained earlier, the goal of the planned remediation solution is to ensure the safety of the road and there was no financial or property-legal justification to stabilize the downhill slope. However, the overall factors of safety of sliding surfaces which affect the road are well above the minimum required factors of safety, even in the case of downhill slope failure. This analysis, however, requires additional stress-strain analysis to check the internal forces and displacements of the structure in such a scenario.
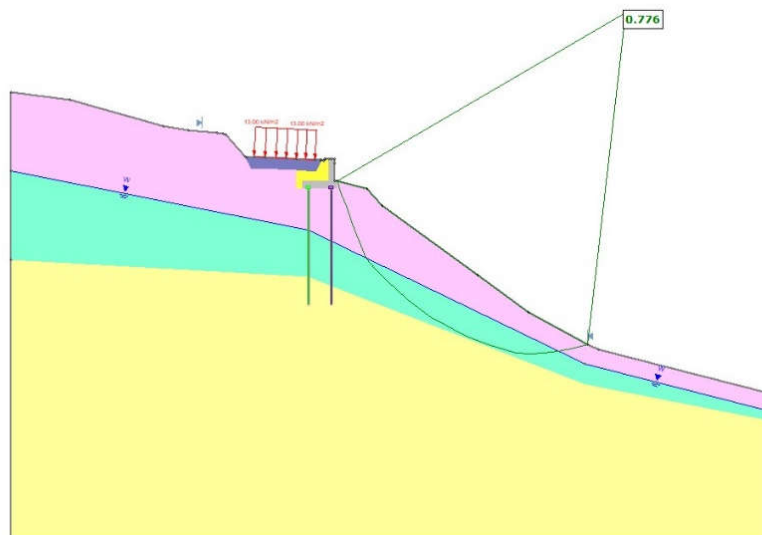
Figure 22 Potential slip surface on downslope with unsatisfactory factor of safety, Fs = 0,78

The analysis of serviceability limit states will be critical for determining the displacements of the structure, while the results of the ultimate limit state analysis are relevant for dimensioning the structural elements. As aforementioned, a model was created where a portion of the slope was "removed" to numerically verify the displacement conditions and the stress-strain relationship during potential landslides of the downslope beneath the road.

Analyzing the internal forces and displacements of the planned structure across different design scenarios showed that the critical values occur exactly in the scenario of a landslide beneath the road. Figure 8 presents the diagram of the internal forces of the pile wall for this critical design scenario. The displacements also have largest values in this scenario, and the structure was dimensioned specifically to accommodate these internal forces and. Figure 9 shows the displacements contours for the downhill slope sliding scenario with maximum displacement of 3.5 cm.
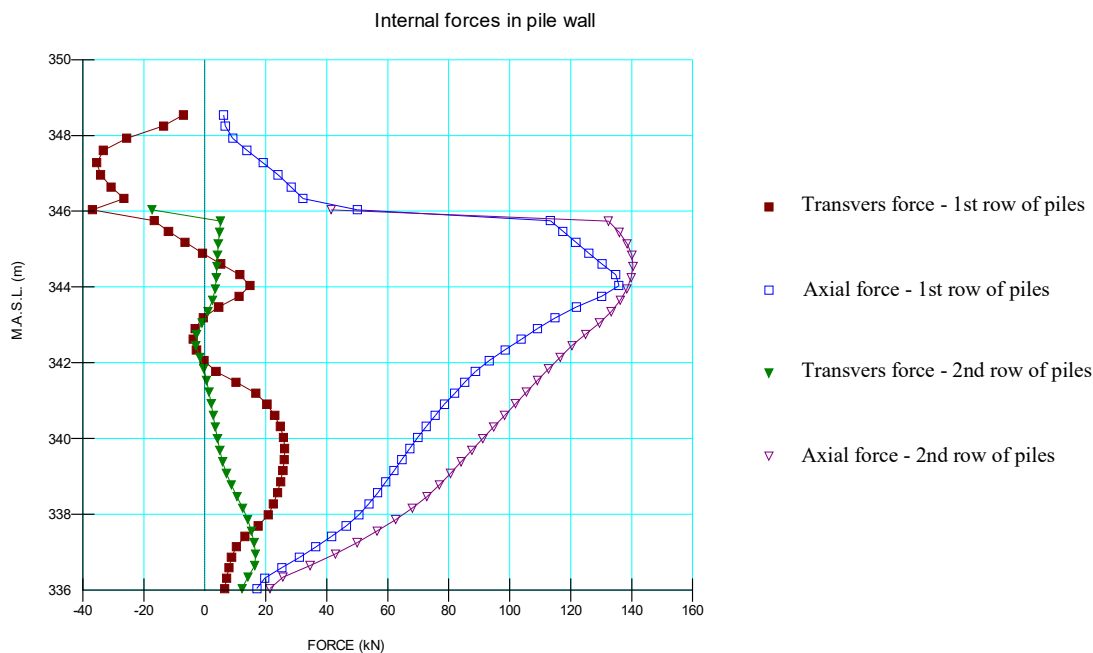
Figure 23 Transverse and axial internal forces of 1st and 2nd row of piles
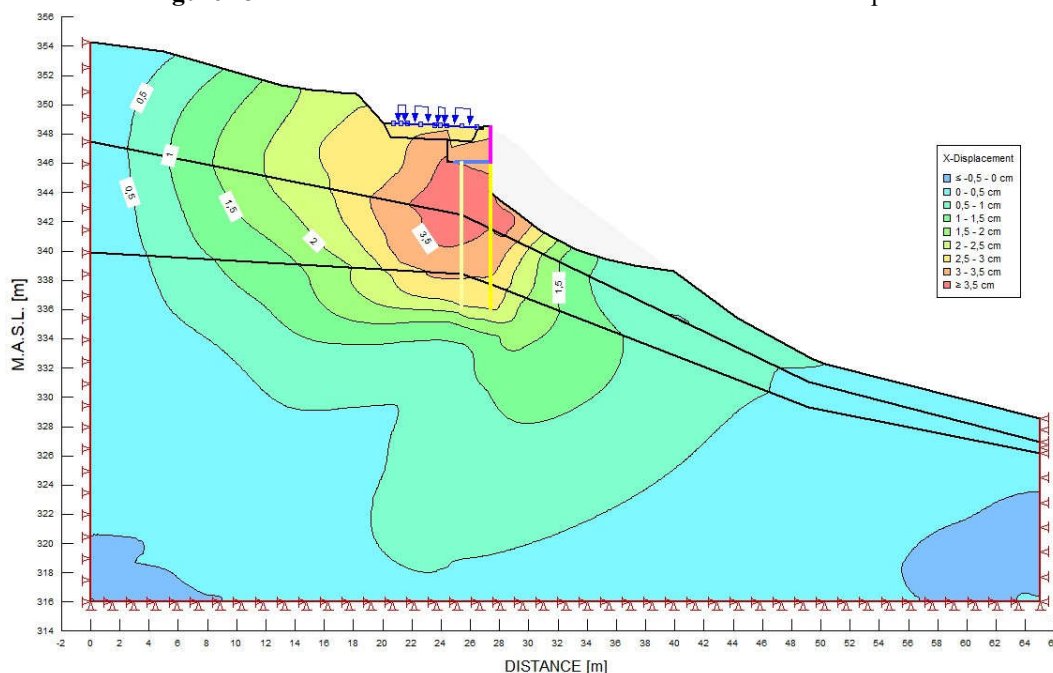
Figure 24 Contours of horizontal displacement

5   Conclusions

The geotechnical investigation and remediation design for the landslide along the state road DC206 have provided a comprehensive understanding of the site's stability issues and the effectiveness of the proposed solution. Detailed geotechnical and engineering-geological analyses were performed, including drilling, laboratory testing, and stability assessments, which were crucial in identifying the problematic areas and evaluating potential risks. The geotechnical findings revealed that the site is characterized by a complex subsurface profile, including layers of loose gravel, clayey sands and high plasticity clay. The stability analysis of the slope identified several design situations, including the existing slope state, conditions during excavation, and post-remediation scenarios under static and seismic loading conditions. The chosen remediation solution involves the construction of a two-row pile

wall with a cantilever concrete wall serving as the cap. The stability analysis showed that the factor of safety for the existing condition was below 1, indicating instability, which aligns with observed deformations and cracking in the road surface. However, the proposed solution ensures that the safety factor increases to acceptable levels both during construction and after the completion of the remediation works under static and seismic conditions. The analysis highlighted a potential sliding plane on the downhill slope with a low factor of safety in the post-construction scenario, which necessitates further examination of internal forces and displacements in the structural design to prevent damage due to potential sliding. The final design incorporates measures to address these concerns, ensuring that the constructed solution remains stable and resistant, thereby making the road in question safe and functional for operation. In summary, the integration of geological and geotechnical analyses, structural design, and remediation strategies ensures that the proposed solution effectively mitigates the risks associated with the landslide and provides a robust framework for maintaining the stability and safety of the road infrastructure.

References

Bartelletti C, Giannecchini R, D'Amato Avanzi G, Galanti Y, Mazzali A, *The influence of geological–morphological and land use settings on shallow landslides in the Pogliaschina T. basin (northern Apennines, Italy)*, Journal of Maps, 2017, 13(2): 142-152.

Burman, A., Acharya, S.P., Sahay, R.R., Maity, D., *A comparative study of slope stability analysis using traditional limit equilibrium method and finite element method*, Asian journal of civil engineering, 2015., vol. 16, no. 4, pp 467-492

Duncan, J.M., *State of art: limit equilibrium and finite element analysis of slopes*, 1996, J. Geotech. Engng, ASCE 122, no. 7, 577-596

Haque U, Blum P, Da Silva PF, Andersen P, Pilz J, Chalov RS, Malet JP, Jemec Aufli M, Andres N, Poyiadji E, Lamas CP, Zhang W, Peshevski I, Pétursson GH, Kurt T, Dobrev N, García-Davalillo JC, Halkia M, Ferri S, Gaprindashvili G, Engström J, Keellings D, *Fatal landslides in Europe*, Landslides, 2016, 13: 1545–1554.

Hungr O, Leroueil S, Picarelli L, *The Varnes classification of landslide types, an update*, Landslides, 2014, 11: 167-194.

Kim MS, Onda Y, Uchida T, Kwan Kim J, Song YS, *Effect of seepage on shallow landslides in consideration of changes in topography: Case study including an experimental sandy slope with artificial rainfall,* 2018, Catena, vol. 161, pp 50-62

Lee JH, Park HJ, *Assessment of shallow landslide susceptibility using the transient infiltration flow model and GIS-based probabilistic approach*, Landslides,2016, 13: 885-903.

Peshevski I, Peternel T, Jovanovski M, *Urgent need for application of integrated landslide risk management strategies for the Polog region in R. of Macedonia*, Proceedings of 4th World Landslide Forum, 29 May – 02 June 2017, Ljubljana, Slovenia. pp. 135-145

Postance B, Hillier J, Dijkstra T, Dixon N, *Comparing threshold definition techniques for rainfall induced landslides: a national assessment using radar rainfall. Earth Surface Processes and Landforms*, 2017, 43(2): 553-560.

Topic 7

Environmental Geology and Geotechnical Engineering for Natural Resource Management

PETROGRAPHIC, PHYSICAL AND MECHANICAL CHARACTERIZATION OF ROCKS FROM ANGOLA AS DIMENSION STONES

WIDNÉLIA LOPES[1], ISABEL FERNANDES[1,2], MATILDE COSTA E SILVA[3], AMÉLIA DIONÍSIO[3]

[1] *University of Lisbon, Faculty of Sciences, Portugal, nellyalopes@icloud.com*

[2] *IDL, Instituto Dom Luiz, Portugal, mifernandes@ciencias.ulisboa.pt*

[3] *CERENA, Instituto Superior Técnico, University of Lisbon, Portugal, matilde.horta@tecnico.ulisboa.pt; amelia.dionisio@tecnico.ulisboa.pt*

Abstract

Angola territory is composed of a wide diversity of rocks, with predominance of recent sedimentary rocks, in the East provinces, and metamorphic and igneous rocks outcropping in the Western region. The exploitation of dimension stone is a relevant industrial sector in the country, corresponding to thousands of cubic meters of stone produced each year and exported to countries all over the world. The selection of dimension stones is dependent on both their aesthetic features and physical-mechanical properties. Six samples of igneous rocks were studied both by petrographic analyses and by laboratory tests for the physical and mechanical characterization. Although these rocks are commercially known as "granites" they correspond to granite, granodiorite and gabbro. The laboratory tests performed aimed at the characterization of the colour and the determination of the open porosity, the water absorption, the unit volume, the ultrasonic pulse velocity, the dynamic deformation modulus, the linear thermal expansion coefficient, the flexural strength under concentrated load and the uniaxial compressive strength. The results obtained show that all the rocks are compact, with high unit weight, low porosity, high dynamic deformation modulus and high mechanical strength. Based on these parameters, some considerations are made concerning their adequacy as dimension stones.

Key words

Dimension stone, igneous rocks, physical-mechanical properties, petrographic assessment, applications.

1 Introduction

Natural stone is being used in construction since early antiquity (Siegesmund and Dürrast 2011). These stones are quarried and cut in different sizes and shapes to be used in the construction industry. Stones are described in what concerns mineral composition, texture, colour and geological framework or from a commercial perspective, focusing on colour and place of origin. Physical and aesthetic properties, and the absence of fractures are important characteristics that allow that large blocks are quarried aiming the use in sculptures and buildings (Yilmaz et al. 2011). Depending on their possible use, different laboratory tests must be performed which are generally classified in: visual tests, such as colorimetry and petrographic analysis; physical-mechanical tests to determine the porosity, the uniaxial compressive strength, the tensile strength, the flexural strength and the deformability. The relative importance of each property and the threshold values for each parameter depend on the application, e.g., as flooring, cladding, roofing, slabs or as a decorative element, exposed to internal or external environmental conditions. Granite, marble and limestone are among the most common rocks quarried as dimension stone. In particular, granular igneous rocks widely designated as "granites" and "black granite" (e.g., gabbro) usually show high load bearing capacity, resistance to foot traffic, resistance to weathering and

other environmental influences, as well as aesthetic properties and ability to obtain highly polished finish (Yilmaz et al. 2011). Aesthetical, strength and durability issues are very important when the stone is used as pavement and in façades. Nevertheless, some stones are better suited to a job than others and it is important that the selection is based on technological criteria (Shadmon 1996). The use as decorative material must fulfil several physical and technical parameters requested by users and controlled by national and international standards. The mineralogical composition, the texture and the degree of alteration have a great influence on the index properties, namely the unit weight, the porosity and the water absorption as well as on the compressive strength, tensile strength and durability. Aesthetic (texture and colour), physical (unit weight, porosity and water absorption) and mechanical properties (P-wave velocity, thermal conductivity, uniaxial compressive strength, flexural strength) must be assessed to define the quality and usability of the stones (e.g., ASTM C615, *Standard Specification for Granite Dimension Stone*).

Color is of paramount importance in ornamental stone. It is determined by the predominant coloration of its minerals and can be affected by the presence of friable, altered or soluble mineralogical constituents, which compromise the gloss and performance of the rocks (Iamaguti, 2001). The color perception is also affected by the stone finishing. Stone deterioration affects the use of stone either aesthetically (e.g., staining, discoloration), or in terms of physical-mechanical modifications (e.g., increase in porosity, water absorption, loss of mechanical strength), compromising the life cycle of the materials. Pires (2013) developed research to address natural stone degradation impact on facade dimensioning with stone from Portugal. This multi-analysis approach provided fundamental information regarding the intrinsic physical-mechanical behaviour of the studied stone and quantified the influence of several degradation effects on each stone intrinsic degradation curve with an impact on the cladding dimensioning.

Previous works show that the porosity influences the strength (e.g., Winkler 1997) and is dependent on grain contacts, fractures and microcracks as well as on the weathering degree. These characteristics can be assessed by the petrographic analysis of the rocks based on the study of thin section under optical microscopic to describe the texture, granularity, mineral composition, grain boundary features and degree of weathering. Tugrul and Zarif (1999) studied granitic rocks and found that there is a correlation between mechanical and petrographic parameters but not as much between petrographic features and the physical properties.

The main deposits of dimension stone in Angola are located in Huíla and Namibe provinces and they show a potential viability of these resources due to the occurrence of rocks susceptible to be used as dimension stone. Europe and Asia constitute important markets and Angola stones are highly appreciated and used as cladding, masonry and paving. The most widely known "granite" in the world is the Negro Granite (Black Granite) commercially known as Negro de Angola (CESO CI 2006), which is studied in this work. Stones are exposed to adverse environmental agents such as moisture, temperature fluctuations, salts, atmospheric contaminants and living organisms (fungi, algae, lichen, etc) and thus, stone decay takes many forms. The present work summarizes the preliminary study of six rocks aiming at characterizing their potential viability to be used as dimension stone, in particular as cladding.

2   Materials and Methods

Samples with a polished finish from different Angola natural stones were collected from four provinces of Angola, namely Cuanza Norte, Benguela, Huíla and Namibe.

A total of 12 thin sections of 0.030×25×50 mm was manufactured for the petrographic analysis. Also 36 prismatic specimens of 180×60×30 mm were prepared for the different laboratory test, corresponding to the six lithological types, i.e., six specimens per sample. The lithotypes are commercially known as Rosa HMA, Cinza HMA, Maria Teresa, Negro Cohiba, Negro Mingué and Negro Angola.

The methods used to characterize the rocks were selected based on the most relevant mineralogical-chemical and physico-mechanical characteristics for use as dimension stone, according with the European Standards (EN) and the standards of the American Society for Testing and Materials (ASTM). Chemical analysis of bulk rock was performed at Actlabs according to the Lithium Metaborate/Tetraborate Fusion method FUS-ICP (Inductively Coupled Plasma) method, to determine the oxides of the major elements, with detection limit of 0.01% and 0.001% for MnO and TiO_2.

Petrographic analysis was performed as indicated in EN 12407 (*Natural stone test methods - Petrographic examination*) on thin sections observed under a LEICA DM750P petrographic microscope, both in plane polarized light (PPL) and crossed polarized light (XPL). The photomicrographs were obtained by a Leica ICC50 HD camera.

The identification and semi-quantification of the mineralogical components was performed by X-ray diffraction using an XPERT-PRO diffractometer with CuKα radiation at 40 kV and 30 mA; a 2 theta step size of 0.1° and a scan step time of 50.0313s were considered. The diffractometer is provided with automatic divergence slit and graphite monochromator. The random powder method was used. The data obtained in this equipment were treated with X'Pert software - Philips Analytical.

The colour of the polished surfaces was quantified with a Minolta CM-700d spectrophotometer, at the CIELAB colour space. A total of 20 measurements for each sample were made, to obtain an average of 3 measurements, as recommended in Prieto et al. (2010) for plutonic stones with this grain size.

In what concerns the water absorption by total immersion quantification and the apparent density and open porosity determination, EN 13755:2008 (*Natural stone test method - determination water absorption at atmospheric pressure*) and EN 1936:2008 (*Natural stone test methods - Determination of real density and apparent density, and of total and open porosity*), were considered, respectively.

Thermal Linear Expansion Coefficient was determined according to EN 14581:2007 (*Natural stone test methods - Determination of linear thermal expansion coefficient,* method A) in a ventilated oven with an accuracy of 0.5°C, with the capability of increasing the temperature at a rate of 0.5°C/min and maintaining the temperature for two hours. A measuring device (Mitutoyo Digimatic Indicator) with an accuracy of 1/100000 of length. Adhesives, made from the blend of polyester bitumen (SILACA) and PEROXAN BP- Paste 50 PF, were applied to fix the measurement bases spaced 115 mm.

The ultrasonic pulse velocity was determined according to EN 14579:2007 (*Natural stone test methods - Determination of sound speed propagation*) using an Oscilloscope, Pulse Generator - BK PRECISION® 4011ª 5MHz Function Generator, with 50Hz range, a pair of transducers (the transducer arrangement was performed by indirect or surface transmission), and an amplifier. The P piezoelectric sensors, Nano-30, GE59 (with a sensitivity of 1v/bar) and the shear sensors SWC 37-0.5 were fixed to the rock samples with a couplant water-soluble organic substance of very high viscosity (Olympus SWC-2). The dynamic deformation modulus was obtained according to EN 14579:2007.

The flexural strength followed the indications in EN 13161:2013 (*Natural stone test methods - Determination of flexural strength under constant moment*). A Form Test machine was used to perform a three-point bending test on polished surface samples of 180×45×30 mm prisms.

After the flexural strength test, each specimen was cut in two parts to be used for the point load test in accordance with ISRM (1981). The specimens were cut to ensure that their dimensions respect the ratio of 0.3W<D<W and L> 0.5D, where W is the thickness, D the height and L the length, resulting in specimens of 50-50×45-47×30-35 mm. The tests were performed using a Tecnilab equipment. Compressive strength was obtained by the correlation suggested in ISRM (1981) between point load and uniaxial strength, using a coefficient of 22, following EN 1926:2006 (*Natural stone test methods - Determination of uniaxial compressive strength*).

3 Results

3.1 Chemical and mineralogical composition

These plutonic rocks are phaneritic, holocrystalline, differing in granularity and color. The dark samples (melanocratic), in which the mafic minerals predominate, namely Negro Cohiba, Negro Mingué and Negro Angola, are the ones with the coarsest granularity; the light-coloured (leucocratic) samples, composed mainly of felsic minerals, are the Rosa HMA and Cinza HMA; and the Maria Teresa, a mesocratic rock of intermediate composition, shows the finest granularity. Figure 1 presents the macroscopic description and the plot of the samples composition on the diagram $Na_2O + K_2O$ versus SiO_2 (Cox et al. 1979).
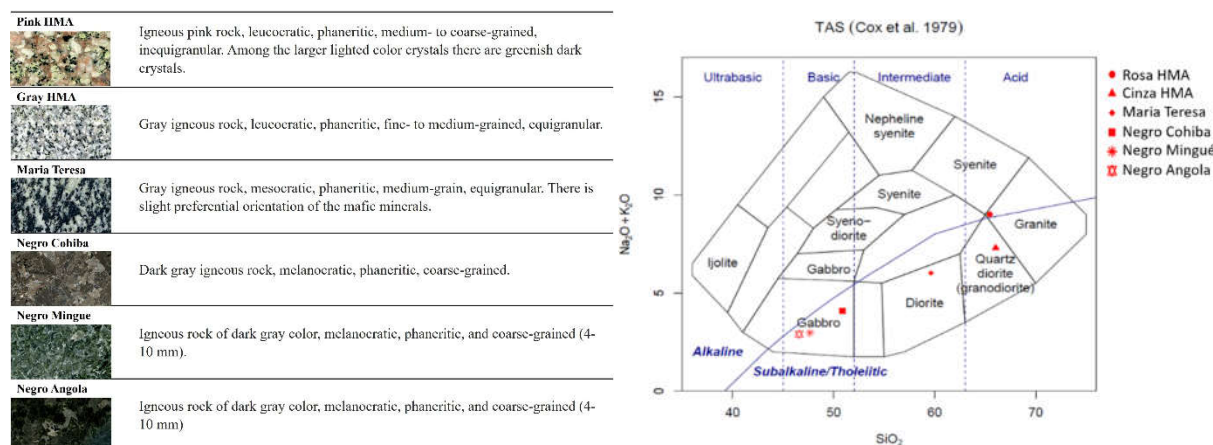

Figure 1. a) Designation and macroscopic description of the samples; b) $Na_2O + K_2O$ vs. SiO_2 (TAS) diagram with projection of the six samples analyzed (after Cox et al. 1979)

The *Cinza HMA* sample has the highest content of silica whilst *Negro Angola* sample shows the lowest. The sample with the highest alkali content ($Na_2O + K_2O$) is the *Rosa HMA,* and *Negro Mingué* presents the highest content in CaO. *Negro Angola* sample has the highest content in total iron and magnesium. From the chart it is concluded that these rocks belong to the subalkaline series, with the exception of the *Rosa HMA* sample which belongs to the alkaline series.

The mineralogical composition was obtained by the study of thin sections under optical microscope. Representative photomicrographs of the six samples are presented in Figure 2. *Rosa HMA* (Figure 2a) consists essentially of quartz, K-feldspar and plagioclase, with titanite, pyroxene, chlorite, biotite, amphibole, epidote, opaque minerals, apatite and zircon as minor components; it is classified as alkaline-granite. Quartz occurs as anhedral grains with sutured boundaries, undulatory extinction and subgraining, mainly along the boundaries of the larger crystals of the coarser crystals. Orthoclase is the dominant K-feldspar, forming the larger crystals in the rock, whilst the prismatic crystals of plagioclase (oligoclase-albite) occur in the same size of the matrix. The mafic minerals are associated with each other; they are anhedral, namely the biotite and chlorite plates, to euhedral, in particular the titanite crystals, which present well defined faces. Green amphibole (hornblende) and clynopyroxene are subhedral, usually occur together and in association with epidote. The feldspars show argilization and sericitization, which is much deeper in the plagioclase crystals, imprinting a dull appearance under natural light. Plagioclase shows compositional zoning, with more intense alteration of the cores of the crystals, sometimes with the formation of small subhedral grains of epidote. The biotite plates are usually chloritized. The presence of chlorite and of green amphibole imprints a greenish tonality to the agglomerates of mafic minerals, observed at hand specimen scale.

Cinza HMA (Figure 2b), classified as quartz-diorite, consists mainly of quartz, K-feldspar and plagioclase, containing also biotite, chlorite, epidote, titanite, alanite, amphibole, apatite, opaque

minerals, muscovite and zircon. Most of the minerals form anhedral crystals and inequigranular grains. Quartz exhibits straight borders and is mostly interstitial, with undulatory extinction. The larger crystals in the rock correspond to K-feldspar (orthoclase), some of which are slightly altered to clay minerals. Microcline (also K-feldspar) occurs in the interstitial spaces of the larger crystals of the main minerals. Zoned prismatic to elongated laths of plagioclase show intense alteration of the nucleus and clean boundaries. Some of the elongated plates of biotite are chloritized. The green-amphibole crystals present some well-defined faces and are associated with the plates of chlorite. Titanite occurs in skeletal crystals. *Maria Teresa* (Figure 2c), a darker equigranular rock, contains mainly plagioclase, K-feldspar, quartz, green amphibole (hornblende), pyroxene, biotite, garnet, apatite, opaque minerals. The rock is fine- to medium-grained diorite and the minerals occur in anhedral crystals. Plagioclase forms long prismatic laths, with slight sericitization, and K-feldspar is much less common, forming smaller crystals. Quartz is interstitial, occupying spaces in the boundaries of plagioclase and the mafic minerals. These minerals form clusters and define a slight preferential alignment in the rock. Orthopyroxene crystals are usually surrounded by chlorite and amphibole. In the rock, also garnet crystals are observed, in association with chlorite and amphibole. The *Negro Cohiba*, *Negro Mingué* and *Negro Angola* (Figure 2d, e, f) present similar mineral composition and texture and are classified as gabbro. They exhibit inequigranular subhedral texture, and are medium- to coarse-grained. The main component, plagioclase, occurs in tabular crystals, forming the largest crystals, which are sound (not altered) to slightly altered. The rocks contain variable percentages of anhedric crystals of olivine, pyroxene, amphibole, opaque minerals and biotite. In *Negro de Angola* a vermicular (wormlike) intergrowth of iron mineral (opaque minerals) in olivine can be observed (Figure 2f). In all the three samples, corona texture is observed, with pyroxene rimmed by amphibole of variable width. Some olivine and pyroxene crystals occur filling the interstitial spaces of the larger crystals of plagioclase.
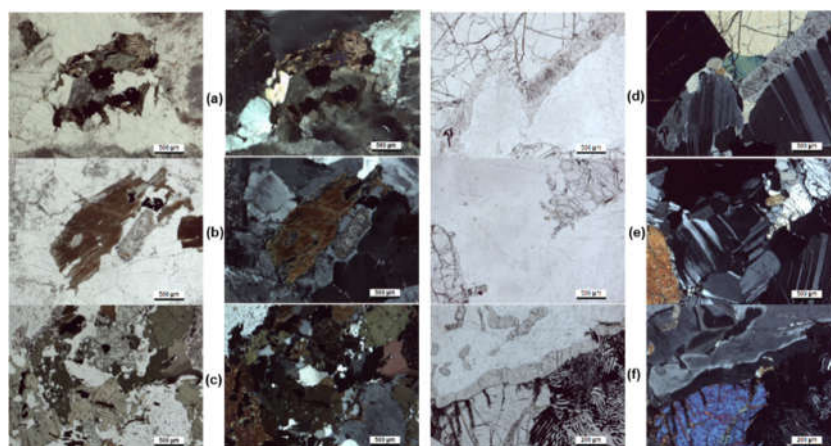
Figure 2. Photomicrographs obtained under the optical microscope: a) *Rosa HMA*; b) *Cinza HMA*; c) *Maria Teresa*; d) *Negro Cohiba*; e) *Negro Mingué*; f) *Negro Angola* (N //, on the left, and NX, on the right)

The results obtained by the X-ray diffraction are in line with the petrographic analysis performed, detailing some of the minerals present in the samples: in *Rosa HMA*, *Cinza HMA* and *Maria Teresa* the most common K-feldspar is microcline and the plagioclase corresponds to albite; there is pargasite in *Rosa HMA*; chlorite in *Cinza HMA*; and hornblende in *Maria Teresa*. For *Negro Cohiba*, *Negro Mingué* and *Negro Angola*, anorthite and forsterite were identified and the opaque minerals in *Negro Angola* correspond to magnetite.

3.2 Color

Finishing, in the present case study, is similar for all lithotypes. Average values of color coordinates measured for each sample are shown in Figure 3. As expected, based on mineralogical and textural description, CIELAB color parameters vary for each lithological type. Lowest luminosity mean values were recorded for the darker stones, namely *Negro Cohiba*, *Negro Mingué* and *Negro Angola* presenting values comprised between 25 and 45 CIELAB units. *Rosa HMA*, *Maria Teresa* and *Cinza HMA* present

L* values comprised between 50 and 60 CIELAB units. *Rosa HMA* is the lithotype that presents positive and higher values in a* and b* coordinates, with values comprised between 0-10 CIELAB units and 4-12 CIELAB units, respectively. *Cinza HMA* and *Maria Teresa* show similar values in terms of b* coordinates being most of values comprised between -2 and 6 CIELAB units. Darker lithotypes (*Negro Cohiba*, Negro Mingué and *Negro Angola*) have a range of variation in terms of b*coordinate narrower and closer to zero, with mean values varying from -1.6 to 1.5 CIELAB units. The chroma values, as expected, present higher values in *Rosa HMA* (values comprised between 5-10 CIELAB units), followed by *Cinza HMA* (values between 1 and 2.5 CIELAB units), *Maria Teresa* (values comprised between 0-2.5 CIELAB units), and little lower values for the darker lithotypes (values comprised between 0.6-1.5 CIELAB units). These results are in agreement with the mineralogical constitution of the lithotypes. Rocks that contain minerals such as quartz and/or K-feldspars present a lighter color, as observed in the samples *Rosa HMA*, *Cinza HMA* and *Maria Teresa*; the rocks that contain pyroxene or olivine in their mineralogical composition, which are minerals with a high content of iron and magnesium, present a darker color, as observed in samples *Negro Cohiba*, *Negro Mingué* and *Negro Angola*.
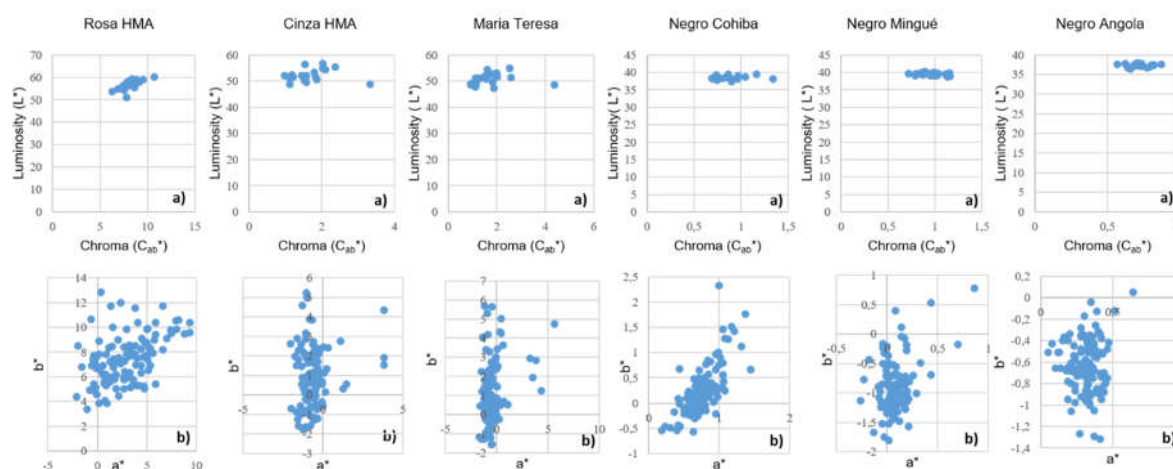
Figure 3. Luminosity versus Chroma a) and a* versus b* b) for the different lithotypes with polished finish

3.3 Physical and mechanical properties

The results obtained by the laboratory tests are summarized in Table 1. The highest values of water absorption at atmospheric pressure were obtained for *Cinza HMA* (0.26%) and *Maria Teresa* (0.23%), followed by *Rosa HMA* (0.14%) sample. The lowest values were observed in *Negro Mingué* (0.07%) *Negro Cohiba* (0.06%) and *Negro Angola* (0.06).

In what concern density, *Negro Mingué* presents the highest value (2.87 g/cm^3) and *Cinza HMA* have the lowest value, (2.67 g/cm^3). For the other samples the values obtained are: 2.69 g/cm^3 (*Rosa HMA*), 2.83 g/cm^3(*Maria Teresa*), 2.78 g/cm^3 (*Negro Cohiba*) and 2.80 g/ cm^3 (*Negro Angola*).

The open porosity values are in accordance with the water absorption values. The highest values were obtained for *Cinza HMA* (0.57%) and *Maria Teresa* (0.50%), followed by *Rosa HMA* (0.43%) sample. The lowest values were observed in *Negro Mingué* (0.26%), *Negro Cohiba* (0.20%) and *Negro Angola* (0.18%).

The average results for the coefficient of linear thermal expansion, *Rosa HMA* (granite) and *Cinza HMA* (granodiorite) show values between 7.61x10^{-6}/ºC and 6.17x10^{-6}/ºC, respectively. For the other rock types, the average values obtained are: 2.18x10^{-6}/ºC, for *Maria Teresa*, 12.2 x10^{-6}/ºC, for *Negro Cohiba*, 7.93x10-6/ºC, for *Negro Mingué* and 10.5x10^{-6}/ºC, for *Negro Angola*.

Based on the values obtained for the velocity of P waves, it is concluded that *Negro Cohiba* sample has the P-Wave highest velocity (5734.28 ms^{-1}), and the *Maria Teresa* sample has the lowest velocity

(3738.04 ms^{-1}). The other lithological samples present P wave velocities varying from 5374.91 ms^{-1}, for *Rosa HMA*, 3759.78 ms^{-1}, for *Cinza HMA*, 4378.47 ms^{-1}, for *Negro Mingué* and 5696.52 ms^{-1}, for *Negro Angola*.

Table 1. Average values obtained for the physical and mechanical properties

	Rosa HMA	Cinza HMA	Maria Teresa	Negro Cohiba	Negro Mingué	Negro Angola
Water absorption (%)	0.14	0.26	0.23	0.06	0.07	0.04
Apparent density (g/cm³)	2.69	2.67	2.83	2.78	2.87	2.80
Porosity (%)	0.43	0.57	0.50	0.0	0.26	0.18
Coefficient of linear thermal expansion (ºc^{-1})	7.61x10^{-6}	6.17x10^{-6}	2.18x10^{-6}	12.2x10^{-6}	7.93x10^{-6}	10.5x10^{-6}
Ultrasonic pulse velocity Vp (m/s)	5,374.91	3,759.78	3,738.04	5,734.28	4,378.47	5,696.52
Ultrasonic pulse velocity Vs (m/s)	2,989.97	2,721.93	2,630.92	3,176.39	2,836.52	3,293.94
Dynamic deformation Modulus (GPa)	61	38	40	72	53	76
Flexural strength (MPa)	72.73	38.33	40.08	43.05	32.94	44.27
Point Load (Is50) (MPa)	9.55	5.53	6.18	4.95	4.67	4.89
Compressive strength (MPa)	210.10	121.66	135.96	108.90	102.74	107.58

Negro Angola has the highest average S-wave velocity (3293.94 ms^{-1}), and *Maria Teresa* has the lowest average velocity (2630.92 ms^{-1}). The other samples present S-wave average velocities of 2989.97 ms^{-1}, for *Rosa HMA*, 2721.93 ms^{-1}, for *Cinza HMA*, 3176.39 ms^{-1}, for *Negro Cohiba* and 2836.52 ms^{-1}, for *Negro Mingué*.

The dynamic deformation modulus obtained varies from 38 GPa to 76 GPa, for *Cinza HMA* and *Negro Angola*, respectively. Values of 61 GPa, 40 MPa, 72 GPa and 53 GPa were obtained for *Rosa HMA*, *Maria Teresa*, *Negro Cohiba* and *Negro Mingué*, respectively.

In what concerns flexural strength, the average results obtained for each material show the highest value of 72.73 MPa, for *Rosa HMA*, and the lowest of 32.94 MPa, for *Negro Mingué*, with 38.33 MPa, for *Cinza HMA*, 40.08 MPa, for *Maria Teresa*, 43.05 MPa, for *Negro Cohiba*, and 44.27 MPa, for *Negro Angola*.

The results of the point load index were used to estimate the uniaxial compression strength (UCS) and to classify the samples according to the ISRM (1981) as very strong: *Cinza HWA*, *Maria Teresa* and *Rosa HMA* samples with the highest values (210.10, 135.96 and 121.66 MPa, respectively), *Negro Cohiba*, *Negro Mingué* and *Negro Angola* with 108.90, 102.74 and 107.58MPa, respectively.

5 Discussion

The selection of a dimension stone depends on the specific application and the properties that are required. Stone can be used in slabs or in blocks, in the interior or exterior, exposed to different environmental conditions. Mechanical properties and the durability are important, in particular for exterior use, as well as structural characteristics. However, abrasion resistance is of interest for foot traffic, but not for slabs in cladding. Correlations between the petrographic characteristics, such as grain size, shape of grains, degree of interlocking, type of contacts and mineralogical composition, and the mechanical properties have been studied (e.g. Tugrul and Zarif, 1999; Cowie and Walton, 2018) and therefore the petrographic analysis was included in this work, aiming at explaining the variations of the physical and mechanical results.

For the verification of the potential application of the stones covered in the present work, their nature as "granitic rock" was assumed and the information in ASTM C615:2005 and in Moura (2006) were followed. Table 2 presents the limits for each property and the verification of conformity of the results obtained in the respective tests.

From the petrographic study it is verified that the stones that show more intense alteration are Rosa and *Cinza HMA*, in special in the nucleus of the crystals of plagioclase. These are the samples that have lower apparent density values. Together with *Maria Teresa*, which is just slightly altered, these samples are the more porous, with values of porosity that are more than the double of the gabbro samples. Compared with the gabbro samples, the grain size of *Rosa HMA*, *Cinza HMA* and *Maria Teresa* are finer and the rocks exhibit some signs of deformation, with undulatory extinction of the crystals of quartz and bending of the mica plates. In addition, *Cinza HMA* and *Maria Teresa* show the lowest results for the elastic dynamic modulus due to low values of Vp.

As expected, open porosity increases with the increase of water absorption, which is the highest for *Cinza HWA*, with also the highest porosity. A linear relation between water absorption and porosity was obtained with a very high coefficient of determination (0.9582).

The analysis of the variation between water absorption and apparent density also shown a linear correlation, however, the coefficient of determination is very poor (0.2214). Water absorption increases with the decrease of apparent density. These physical properties are strongly related in the tested samples, following the observations in other studies with dimension stones (e.g. Ozcelik and Ozguven, 2014).

Table 2. Conformity of the values obtained for the physical and mechanical properties and the limits established in ASTM C615, Moura (2006, granitic rocks) and Frazão and Farjallat (1995) (* complies with Moura, 2006)

	ASTM C615	Moura (2006)	Frazão, Farjallat (1995)	Rosa HMA	Cinza HMA	Maria Teresa	Negro Cohiba	Negro Mingué	Negro Angola
Water absorption (%)	≤0.40	≤0.4	<0.4	V	V	V	V	V	V
Apparent density (g/cm³)	≥2.56	>2.56	>2.55	V	V	V	V	V	V
Porosity (%)	-	<1	<1	V	V	V	V	V	V
Coeff. of linear thermal expansion (°c⁻¹)	-	<9 x 10⁻⁶	-	V	V	V	X	V	X
Dynamic Deformat. Modulus (GPa)	-	-	>30	V	V	V	V	V	V
Flexural strength (MPa)	≥8.27	>10.5	>10	V	V	V	V	V	V
Comp. strength (MPa)	≥131	>100, blocks >80, slabs	>100	V	V*	V	V*	V*	V*

According to ASTM C615:2005 and Marques et al. (2014) the values of density, open porosity and water absorption obtained in these experiments are in accordance to those required for dimension stones used in exterior applications.

The darker rocks (gabbro and diorite) tend to absorb the sun's rays more intensely, dissipating less heat, reaching higher temperature and developing higher rates of expansion. These rocks are therefore recommended to cover buildings in temperate and cold climates (Filho 2002). However, as plot in Table 2, the values of the coefficient of linear thermal expansion are higher than the threshold required in

Moura (2006) for *Negro Cohiba* and *Negro Angola*. For hot climate these materials need to be further studied and, as precaution, they should be used in interior applications, such as interior walls, pavements and kitchen tops.

According to Vallejo et al. (2002) the dynamic modulus of granite varies between 10-84 GPa and diorite varies between 25-44 GPa. The values obtained in this study for granites and diorite are in accordance with the referred and are higher than to the minimum threshold suggested in Frazão and Farjallat (1995). The value recommended by ASTM C615:2005 for the flexural strength for exterior applications must be at least of 10 MPa; also requirements are stated in EN 1469 (*Natural stone products - Slabs for cladding – Requirements*) and EN 12057 (*Natural stone products - Modular tiles – Requirements*), depending on material and tiles thickness. All the values obtained are higher than the requested limits and therefore these materials are adequate to exterior applications.

According with ISRM (1981), the samples are classified as very strong. As shown in Tables 1 and 2, all the results comply with the minimum required in most of the recommendation (e.g. Moura, 2006, Frazão and Farjallat, 1995). However, following ASTM C615:2005, which is the most conservative standard, the only samples recommended for use in exterior applications as dimension stone are *Rosa HMA* and *Maria Teresa*.

5   Conclusion

Dimension stones from Republic of Angola are well known worldwide for their beauty and have been used for a wide range of finalities. The quality requirements for a dimension stone depend on the planned use, and specific physical and mechanical properties have to be verified to comply with the minimum values recommended by different standards. The most common properties to determine are apparent density, porosity, water absorption, coefficient of linear thermal expansion, compression strength and flexural strength (e.g., for the wind effect).

In the present work, also the ultrasonic pulse velocities Vp and Vs were obtained to determine the dynamic deformation modulus. Due to limitations related with the sample sizes, the compression strength was calculated based on the point load test on small samples.

The dimension stone samples analyzed in this work are commercially known as Rosa HMA, Cinza HMA, Maria Teresa, Negro Cohiba, Negro Mingue and Negro Angola. The results obtained are higher than the values established in standards for the use as dimension stone and it is assumed that these stones can be used in prefabricated floors and systems, stairs, ramps, including in external and internal works, interior and exterior floors, interior and exterior walls, façades and kitchen tops, suspended ceilings and various types of finishes, although some of these applications may require that other properties are analysed. Some of the samples show a compression strength value lower than the threshold in the ASTM C615:2005 standard for cladding. This standard is, however, the most conservative in comparison with the values pointed out in other publications, namely e.g., Frazão and Farjallat (1995) Moura (2006), for which values higher than 100 MPa are accepted. The compression strength was calculated based on the results of point load tests and further tests should be performed, using prisms for the compression tests to clarify this aspect.

Acknowledgements

References

CESO CI *Study on ornamental rocks in Angola*. International Consultants SA for the AIDA-ICEP-AIP-AEP Consortium, under the PRIME program. 2006.

Cowie, S.; Walton, G. The effect of mineralogical parameters on the mechanical properties of granitic rocks. *Engineering Geology*. 2018, 240: 204-225. https://doi.org/10.1016/j.enggeo.2018.04.021

Cox, K.G.; Bell, J.D.; Pankhurst, R.J. *The interpretation of igneous rocks*. Boston, George Allen and Unwin London. 1979.

Filho, C.C. *Aspects of Interest on Ornamental and Coating Rocks: Identification, Specification and Use*. KISTEMANN & CHIODI Consulting and Projects Ltda. 2002.

Frazão, E.B.; Farjallat, J.E.S. Características tecnológicas das principais rochas silicásticas brasileiras usadas como pedras de revestimento. *I Congresso Internacional da Pedra Natural*. Lisboa. 1995.

Iamaguti, A.P.S. *Manual of ornamental rocks for architects*. Institute of Geosciences and Exact Sciences of the Paulista State University. 2001.

ISRM *Rock characterization. Testing and monitoring. ISRM suggested methods*. Brown, E.T. (editor). Commission on Testing and Monitoring. International Society for Rock Mechanics. Pergamon Press. 1981.

Marques, J; Azevedo, M.R; Nogueira Neto, J.A.; Pereira, A.J.S.C.; Artur, A.C. Technological characterization of the Serra Branca monzogranite (Ceará, Brazil). *Geological Communications* 2014, 101, Special II, 799-802.

Moura, A.C. Qualidade Industrial e marcação CE. LNEG. 2006.

Ozcelik, Y.; Ozguven, A. Water absorption and drying features of different natural building stones. *Construction and Building Materials*. 2014, 63, 257–270

Pires, V. *Stone Materials and Cladding Fixing Systems - A Physical-Mechanical Behaviour Study*. PhD Thesis, IST, University of Lisbon, 2013.

Prieto, B.; Sanmartín, P.; Silva, B.; Martínez-Verdú, F. Measuring the color of granite rocks: a proposed procedure. *Color Research & Application* 2010, 35(5), 368-375

SGA *Notícia Explicativa da Carta Geológica à escala 1:100000*, Serviços Geológicos de Angola, Luanda. 1992.

SGA *Mapa síntese dos Serviços Geológicos de Angola*., Luanda. 1993.

Shadmon, A. *Stone: An Introduction*. Intermediate Technology Publications, 2nd edition. 1996.

Siegesmund, S.; Dürrast, H. (2011) Physical and Mechanical Properties of Rocks. In: Siegesmund, S.; Snethlage, R. (eds.), *Stone in Architecture*, 4th ed., Springer-Verlag Berlin Heidelberg. 2011, 97-225. https://doi.org/10.1007/978-3-642-14475-2_3.

Tugrul, A.; Zarif, I.H. (1999) Correlation of mineralogical and textural characteristics with engineering properties of selected granitic rocks from Turkey. *Engineering Geology*. 1999, 51, 303-317.

Vallejo, L.G.D.; Ferrer, M.; Ortuño, L.; Oteo, C. *Geological Engineering*. Prentice Hall, 2002.

Winkler, E.M. Stone in architecture: properties and durability. 3rd ed. Berlin, Springer-Verlag, 1997.

Yilmaz, N.G.; Goktan, R.M.; Yaşar, K. Relations between some quantitative petrographic characteristics and mechanical strength properties of granitic building stone. *Int. J. Rock Mechan. and Mining Sciences*. 2011, 48, 506-513

A METHOD OF DETERMINING UNSTEADY AIR PERMEABILITY OF ROCK

YOTA TOGASHI [1], MASAHIKO OSADA [2]

[1] *Graduate School of Science and Engineering Saitama University, Japan, togashi@mail.saitama-u.ac.jp*

[2] *Graduate School of Science and Engineering Saitama University, Japan, osada@mail.saitama-u.ac.jp*

Abstract
It is important for utilization of underground space or slope disaster prevention to determine the water transport in the rock mass including unsaturated zones. To precisely predict the two-phase flow of air and water in rock pore spaces, both the hydraulic conductivity and gas permeability must be accurately identified. Most existing methods estimate air permeability under steady-state conditions. There are still few methods for evaluating air permeability under unsteady state conditions. This study proposes a method of identifying the ever-changing permeability with time and pressure using a linearized governing equation for air permeability in porous media. To validate the method, we compared the exact solution derived with the results of air permeability laboratory tests on granite and conglomerate in previous studies. After confirming that the exact solution well represented the results of previous experiments, the unsteady air permeability of the rock was estimated from the results of the same experiments using the proposed method. As a result, it was confirmed that not only can the air permeability be identified with the same accuracy as the steady-state method, but also the unsteady air permeability, which varies with pressure, can be identified.

Key words
Air peameability, unsteady, unsaturated flow, rock, geological disposal, laboratory test.

1   Introduction

It is important for geological disposal of nuclear waste and large-scale collapse of rock slopes due to heavy rain fall to understand the properties of unsaturated rocks because the mechanical properties of rocks change significantly with water content (e.g. Chigira, 2015; Osada, 2014). The authors have been studying changes in the strength and deformation properties of sedimentary rocks associated with water content (Togashi and Imano et al., 2021; Togashi and Kikumoto et al., 2021; Kotabe et al., 2024) and water transport in the excavation disturbed zone (Osada et al., 2019; Togashi et al., 2022). To precisely predict the two-phase flow of air and water in rock pore spaces, both the hydraulic conductivity and gas permeability must be accurately identified. Most existing methods estimate the air permeability from the differential pressure under steady-state conditions (e.g. Sakaguchi et al., 1992). There are still few methods for evaluating air permeability under unsteady state conditions.

This study proposes a method of identifying the ever-changing permeability with time and pressure using a linearized governing equation for air permeability in porous media. This method is based on an exact solution of the linear diffusion equation. To validate the method, we then compared the exact solution derived with the results of air permeability laboratory tests on granite and conglomerate in previous studies. After confirming that the exact solution well represented the results of previous experiments, the unsteady air permeability of the rock was estimated from the results of the same experiments using the proposed method.

2 Methods

2.1 Non-liner partial differential equation of unsteady gas flow

Below, the governing equation of unsteady gas flow is derived according to the method of Katz (1959). The ideal gas law is as follows.

$$\rho = \frac{M}{RT}P \tag{1}$$

where *r*, *M*, *P*, *R* and *T* are density, amount of substance, air pressure, gas constant and temperature, respectively. Darcy's law is given by the following equation, where the flow velocity is *u*.

$$u = -\frac{K}{\mu}\frac{\partial P}{\partial x} \tag{2}$$

Here, *K* and *m* are intrinsic air permeability coefficient and viscosity coefficient. The following is the continuous equation.

$$\frac{\partial \rho u}{\partial x} = -\lambda\frac{\partial \rho}{\partial t} \tag{3}$$

where *l* is porosity. Substituting Eq. (1) into Eq. (2) to eliminate P and substituting Eq. (3) yields:

$$\frac{\partial \rho}{\partial t} = \frac{K}{\mu\lambda\gamma}\frac{\partial}{\partial x}\left(\rho\frac{\partial \rho}{\partial x}\right) \tag{4}$$

Here, $M / RT = g$ is set. The partial differential on the right side of this equation can be transformed as follows.

$$\frac{1}{2}\frac{\partial^2 \rho^2}{\partial x^2} = \frac{1}{2}\frac{\partial}{\partial x}\left(\frac{\partial \rho^2}{\partial x}\right) = \frac{1}{2}\frac{\partial}{\partial x}\left(2\rho\frac{\partial \rho}{\partial x}\right) = \frac{\partial}{\partial x}\left(\rho\frac{\partial \rho}{\partial x}\right) \tag{5}$$

The one-dimensional air permeability phenomenon is expressed by the following governing equation for density.

$$\frac{\partial \rho}{\partial t} = \frac{K}{2\lambda\mu\gamma}\frac{\partial^2 \rho^2}{\partial x^2} \tag{6}$$

Here, if Eq. (1) is assigned to *r* in Eq. (6) with $M / RT (= g)$ as a constant, the governing equation of the air permeability phenomenon for *P* is obtained and *g* disappears as follows.

$$\frac{\partial P}{\partial t} = \frac{K}{2\lambda\mu}\frac{\partial^2 P^2}{\partial x^2} \tag{7}$$

This equation is well known as the governing equation for the diffusion of porous media.

2.2 Simplification of the governing equation and exact solution for unsteady gas flow

As shown in Fig. 1, let the air pressures acting on $x = 0$ and $x = l$ be P_0 and P_l, respectively. If the difference between P_0 and P_l is small, the pressure in the analysis area is small, so it is assumed to liner relationships $P_2 \simeq (P_0 + P_l)P$. This means that the difference between P_2 and $(P_0 + P_l)P$ is small around $P = P_0 + P_l$. Based on this assumption, the governing equation of unsteady gas flow, Eq. (7), becomes the following linear diffusion equation.
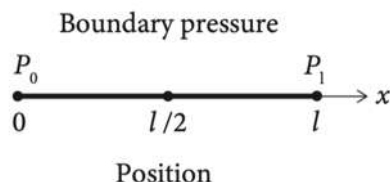
Boundary pressure

Figure 1. Problem setting of one dimensional gas flow.

$$\frac{\partial P}{\partial t} = G \frac{\partial^2 P}{\partial x^2} \tag{8}$$

It should be noted that $G = K(P_0 + P_l) / (2lm)$. By changing the variables as $h = x / 2(Gt)^{0.5}$, the infinitesimal increment of time, Dt and the square of the infinitesimal increment of coordinates, Dx^2, can be expressed as follows.

$$d\eta = -\frac{\eta}{2t} dt, \quad d\eta^2 = \frac{1}{4Gt} dx^2 \tag{9}$$

Substituting these small increments into Eq. (8) gives:

$$\frac{d^2 P}{d\eta^2} + 2\eta \frac{dP}{d\eta} = 0 \tag{10}$$

Equation (10) is a second-order homogeneous differential equation of variable coefficients, which is solved under the following boundary conditions.

$$x = 0 \quad (\eta = 0), \qquad P = P_0$$
$$x = l \quad (\eta = \alpha = \frac{l}{2\sqrt{Gt}}), \qquad P = P_l \tag{11}$$

When $dh = D$, Eq. (10) becomes a first-order linear differential equation as follows.

$$\frac{dD}{d\eta} + 2\eta D = 0 \tag{12}$$

When this equation is separated into variables, integrated on both sides and solved to obtain the equation for P, it becomes as follows.

$$P = c \int_0^{\eta} e^{-\eta^2} \, d\eta + F \tag{13}$$

where c and F are arbitrary constants of integration. From the boundary condition, $P(h = 0) = F = P_0$ and $c = (P_1 - P_0) / \int \exp(-h^2) \, dh$. The unsteady exact solution can be obtained by the following equation using the error function $\mathrm{erf}(x) = (2 / \pi^{0.5}) \int \exp(-t^2) \, dt$. Note that the interval of the integral sign in the sentence is $[0, x]$.

$$P = (P_l - P_0) \frac{\mathrm{erf}(\eta)}{\mathrm{erf}(\alpha)} + P_0 \tag{14}$$

2.3 Air permeability coefficient determination detection using un-steady exact solution

Here, we show how to specify the intrinsic permeability coefficient and unsaturated hydraulic conductivity using the exact solution of unsteady gas flow derived in the previous section. As shown in Fig. 1, a method for identifying the intrinsic air permeability coefficient K is shown by measuring the air pressure at the pressure boundary ($x = 0, L$) and the air pressure at one point inside the rock specimen ($x = L/2$). If the error function in the exact solution is expressed by a simple mathematical formula, the intrinsic air permeability coefficient K can be specified. The Taylor expansion of the error function is (Abramowitz et al. 1965):

$$\mathrm{erf}(x) = \frac{2}{\sqrt{\pi}} \sum_{n=0}^{\infty} \frac{(-1)^n x^{2n+1}}{n!(2n+1)} \tag{15}$$

By rearranging Eq. (14) and setting the ratio of the error functions to the symbol R, the following is obtained.

$$\frac{\mathrm{erf}(\eta)}{\mathrm{erf}(\alpha)} = \frac{P - P_0}{P_l - P_0} = R \tag{16}$$

At the position inside the specimen $x = l / 2$, $h = 0.5 \, l / (2 \, (Gt)^{0.5}) = 0.5 \, a$. Therefore, using the Taylor expansion of the error function up to the first-order term, the above equation becomes as follows.

$$R = \frac{\mathrm{erf}(\eta)}{\mathrm{erf}(\alpha)} = \frac{\eta - \frac{\eta^3}{3}}{\alpha - \frac{\alpha^3}{3}} = \frac{\frac{1}{2}\alpha - \frac{\alpha^3}{24}}{\alpha - \frac{\alpha^3}{3}} = \frac{12 - \alpha^2}{24 - 8\alpha^2} \tag{17}$$

By transforming this into an expression, expressing a^2 by R, and substituting $a = 1 / 2(Gt)^{0.5}$ following is obtained.

$$\alpha^2 = \frac{24R - 12}{8R - 1} = \frac{l^2}{4Gt} \tag{19}$$

Here, $G = K(P_0 + P_1) / 2lm$, so G is represented by R as follows.

$$G = \frac{K(P_0 + P_l)}{2\lambda\mu} = \frac{l^2}{4t}\frac{8R-1}{24R-12} \tag{20}$$

From the above, the following equation for finding K is obtained.

$$\begin{aligned} K &= \frac{2\lambda\mu}{P_0 + P_l}\frac{l^2}{4t}\frac{8R-1}{24R-12} \\ &= \frac{\lambda\mu}{P_0 + P_l}\frac{l^2}{2t}\frac{8\frac{P-P_0}{P_l-P_0}-1}{24\frac{P-P_0}{P_l-P_0}-12} \end{aligned} \tag{21}$$

P_0, P, and P_l are barometric pressure increments measured at the start, midpoint, and end points, respectively. In this way, if there are measurement data at three points, the intrinsic air permeability coefficient K can be explicitly obtained. In this equation, the back of the right side is the pressure ratio function, $f(R) = (8R-1) / (24R-12)$. The outline of this function is as shown in Fig. 2. $f(R)$ diverges at $R = 0.5$. On the other hand, if R deviates from 0.5, it shows a value close to constant ($f(R) \approx 1$). Based on these properties, in the next section, we verify the method for specifying Eq. (21). The conversion between the intrinsic permeability coefficient and the unsaturated permeability coefficient is also described. According to Taylor (1943), the relationship between the intrinsic permeability coefficient K [m²] and the unsaturated hydraulic conductivity k_w [m/s] is expressed by the following equation.

$$k_w = K\frac{\rho_w g}{\mu_w} \tag{22}$$
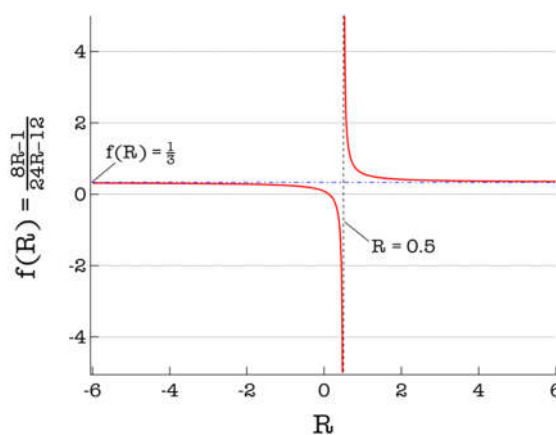
Figure 2. The nature of $f(R) = (8R-1) / (24R-12)$.

r_w [g/cm³], g [m/s²], and m_w [Pa · s] are water density, gravitational acceleration, and water viscosity coefficient, respectively. m_w at standard atmospheric pressure (0.1013MPa) and temperature of 20 degrees is 0.001016 Pa·s (e.g. Miyabe and Nishikawa 1968). When r_w and g are 1.0 g/cm³ and 9.81 m/s², and the unit of k_w is changed to m^2 (e.g. JAGH 2010), $k_w = 0.97K$ can be obtained. Therefore, under standard atmospheric pressure and temperature, the unsaturated hydraulic conductivity k_w and the intrinsic permeability coefficient K are almost equal.

3   Verification of the proposed method in laboratory air permeability test results

Here, we verify the proposed method for specifying the intrinsic air permeability coefficient using the results of previous experiments for unsteady gas flow. This test conducted under the same boundary conditions of the exact solution as described in previous section.

3.1 Air permeability coefficient determination detection using un-steady exact solution

As shown in Fig. 3, Sato and Ono (1987) permeated nitrogen gas from the upper end of a cylindrical rock specimen and measured changes in air pressure inside the specimen. In this experiment, the pressure at the lower end of the specimen is zero $P_l = 0$, and in this study, the experimental cases shown in Table 1 are taken up as verification of the proposed method. These rocks are sampled in Japan. The Granite is from Ibaraki prefecture, which has been often used as a research sample in Japan (e.g. Oda et al., 2002; Takemura and Oda, 2005). Here, the intrinsic air permeability coefficient is obtained from the measured values in the steady state by the following equation (Sakaguchi et al., 1992).

$$K_s = \frac{2Q\mu p_a}{A} \frac{l}{P_0^2 - P_l^2} \tag{23}$$

where K_s, Q, p_a, and A are intrinsic air permeability coefficient at steady state, the amount of air permeability, air pressure, and the cross-sectional area of the specimen, respectively. Other parameters are the same as above. The experimental results are shown in Fig. 4. This shows the time series change of the air pressure measured in the center of the specimen. The results of three tests in which the value of P_0 is changed are shown. The air pressure gradually rises to a constant value. Using these unsteady data, it is verified whether the intrinsic air permeability coefficient can be appropriately specified by Eq. (21).
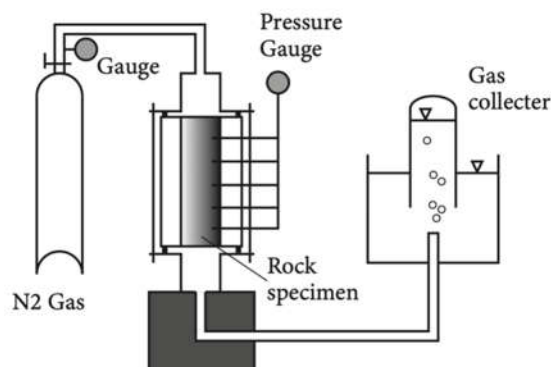
Figure 3. Laboratory air permeability test conducted by Sato and Ono (1987).

Table 1. Test cases of laboratory air permeability test by Sato and Ono (1987)

Rock type	Porosity l (%)	Specimen diameter (m)	Specimen height (m)	Case	P_0 (MPa)	K_s (m²)
				1	0.2	1.7×10^{-16}
Granite	0.92	0.2	0.2	2	0.3	2.0×10^{-16}
				3	0.38	3.8×10^{-16}
				1	0.33	5.4×10^{-18}
Conglomerate	0.94	0.052	0.2	2	0.48	8.2×10^{-18}
				3	0.57	8.8×10^{-18}

Figure 4. Unsteady gas flow of Japanese Granite (a) and Conglomerate (b) by Sato and Ono (1987): time series of *P* detected at the center of cylindrical specimen.

3.2 Identified intrinsic air permeability coefficient verification and its discussions

Figure 5 shows the results of determining the intrinsic air permeability coefficient *K* by Eq. (21) using the experimental results of unsteady pressure changes in Fig. 4. Here, the value of the air viscosity coefficient *m* is 1.81×10^{-11} MPa · s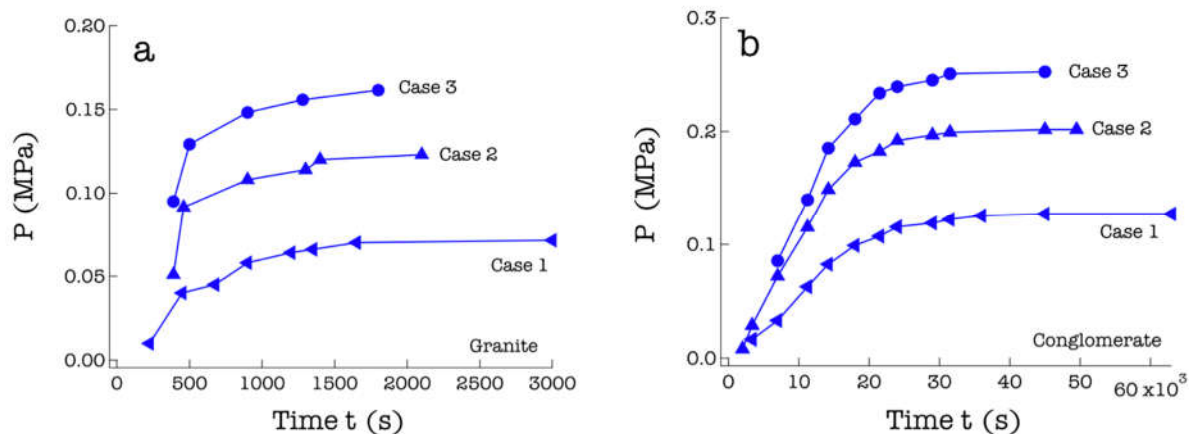. As the pressure ratio increases, *K* increases. This is the same tendency of the air permeability coefficient K_s specified in the steady state (in Table 1), and indicates that the larger the pressure, the easier it is for air to pass through. The value of *K* obtained from the unsteady data using the proposed method is a little smaller than the value of K_s obtained by waiting until the steady state is reached. The magnitude of the *K* and K_s values is almost the same as $10^{-16} - 10^{-17}$ m² for granite and 10^{-18} m² for conglomerate. Figure. 2 shows that the method of specifying *K* diverges around *K* = 0.5, but if *R* is greater than 0.55, it is possible to specify an appropriate *K* without diverging.
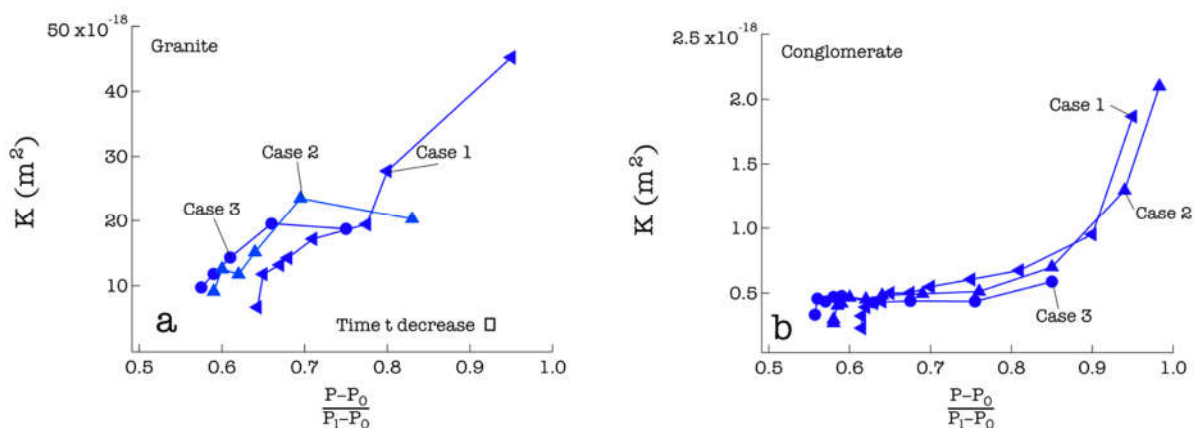

Figure 5. Relationships between identified intrinsic air permeability coefficient, K, and air pressure ratio $(P - P_0)/(P_1 - P_0)$ for Granite (a) and Conglomerate (b).

Figure 6. Comparison between experimental granite data of Fig. 4 (a) and exact solution (Eq. (14)) by using detected unsteady intrinsic air permeability coefficient, *K*.

Figure 6 compares the previous experimental results of granite in Fig. 4 with the exact solution, Eq. (14), calculated using the specified intrinsic air permeability coefficient, *K*. The figure shows an exact solution using the specified maximum, median, and minimum values of *K*. Similarly, Fig. 7 also shows a comparison of conglomerate. In all the results, the linearized unsteady exact solution using the intrinsic air permeability coefficient specified by the proposed method is in good agreement with the experimental results of Sato and Ono (1987). In particular, the exact solution using the smallest value of *K* shows a good match. This linearized exact solution assumed a small differential pressure. By this comparison, the exact solution can sufficiently express the actual phenomenon if the differential pressure $P_0 - P_1$ is about 0.57 MPa. Therefore, as stated above, the validity of both the exact solution of the linearized unsteady gas flow (Eq. (14)) and the method of specifying *K* using the unsteady data (in Eq. (21)) was shown.
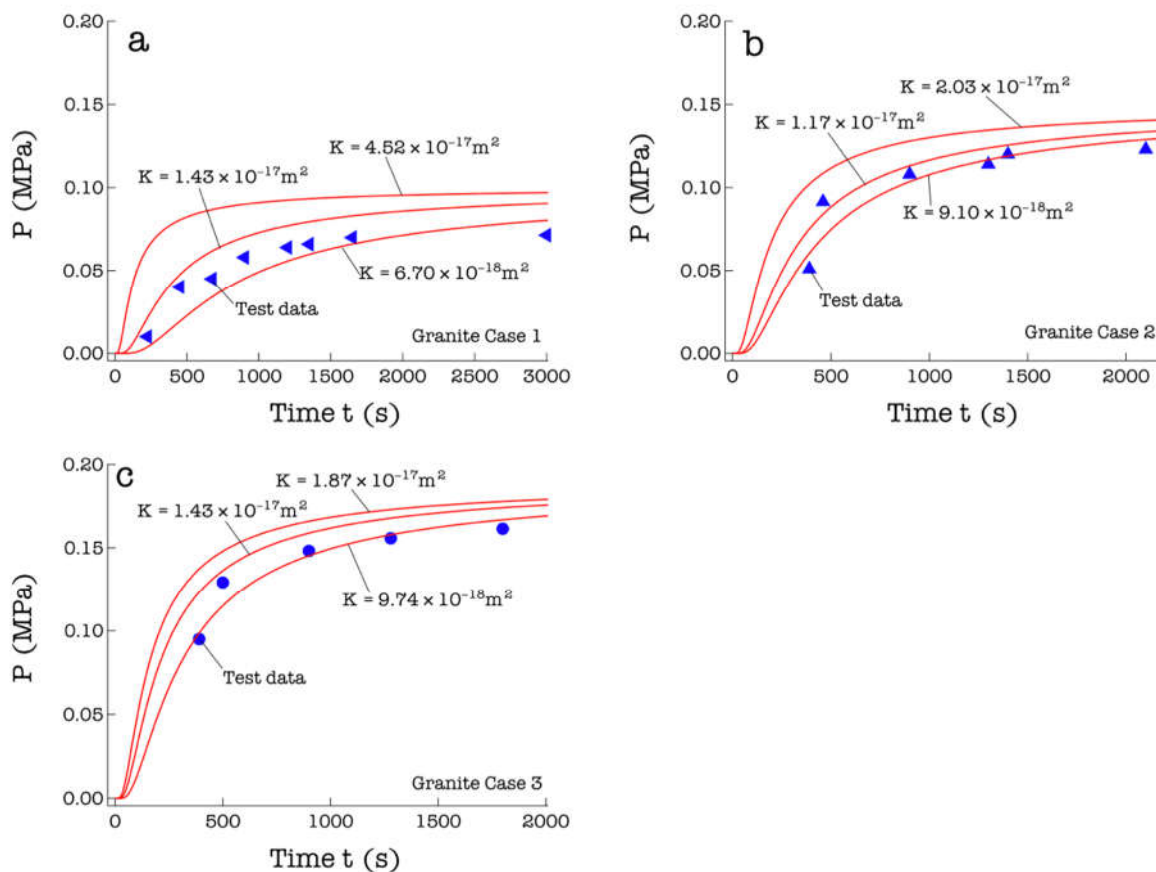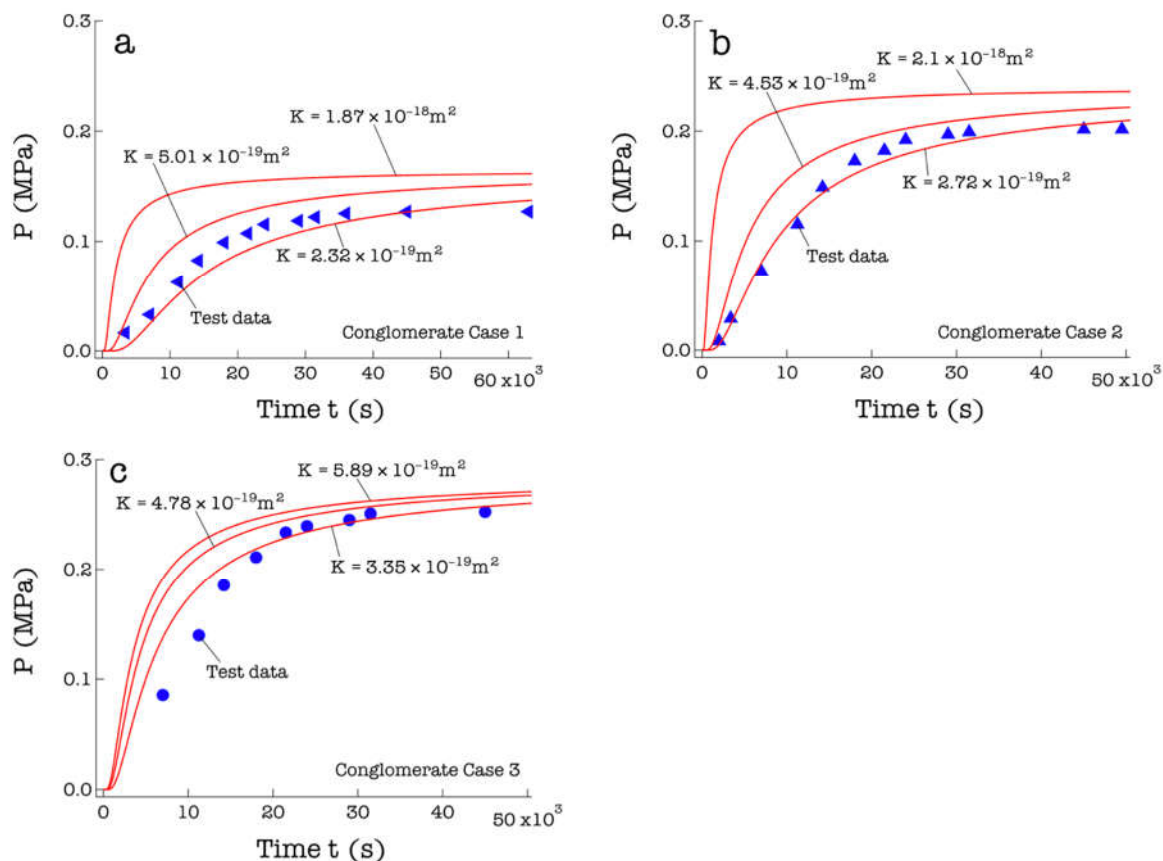
Figure 7. Comparison between experimental conglomerate data of Fig. 4 (b) and exact solution (Eq. (14)) by using detected unsteady intrinsic air permeability coefficient, *K*.

4   Conclusion

This study presents a new method to reasonably determine the unsteady air permeability using laboratory air permeability tests. Therefore, we show how to linearize the basic equation for air permeability with respect to air pressure by Katz (1959) and how to specify the air permeability explicitly from the linearized equation. The proposed method was applied using the results of previous air permeability tests to show that the identified unsteady air permeability coefficient is a reasonable value and that the linearized equations adequately represent the experimental pressure fluctuations. Future work includes further experimental investigations in the room and development of techniques to be applied to in-situ measurements.

References

Abramowitz, M.; Stegun, I.A.; Romer, R.H. *Handbook of mathematical functions with formulas, graphs, and mathematical tables*. USA, Dover Publications, p.297, 1965.

Bossart, P; Meier, P.M.; Moeri, A; Trick, T; Mayor, J. Geological and hydraulic characterisation of the excavation disturbed zone in the Opalinus Clay of the Mont Terri Rock Laboratory. *Engineering Geology*. 2002, 66, 19-38.

Chigira, M. Prediction of potential sites of deep-seated catastrophic landslides and its future research. *Jour Japan Soc Eng Geol*. 2015, 56(5), 200-209. (In Japanese)

Japanese Association of Groundwater Hydrology (JAGH). *Simulation of ground-water flow and solute transport*. Tokyo, Japan, Gihodo books, 2010. (In Japanese)

Kotabe, H.; Togashi, Y.; Hatakeyama, K.; Osada, M. Unsaturated strength of tage tuff and its water retention drying curve. *Journal of the Society of Materials Science, Japan*. 2024, 73(3), 212-219. (In Japanese)

Katz, D.L.V. *Handbook of natural gas engineering*. NewYork , McGraw-Hill, 1959.

Miyabe, K.; Nishikawa, K. Correlation of viscosity and thermal conductivity for water and water vapor. *Transactions of the Japan Society of Mechanical Engineers*. 1968, 34(265), 1567-1574. (In Japanese)

Oda, M.; Takemura, T.; Aoki, T. Damage growth and permeability change in triaxial compression tests of Inada granite. *Mechanics of Materials*. 2002, 34(6), 313-331.

Osada, M. Drying-induced deformation characteristics of rocks. *In Proc ISRM Int Sym 8th Asian Rock Mech Sym.* (ISRM Franklin lecture), Sapporo Japan, 3-19, 2014.

Osada, M.; Takemura, T.; Togashi, Y.; Goshima, S. Pore air pressure measurement at Mont Terri Rock Laboratory, Switzerland. *In Proc. 5th ISRM Young Scholars' Symposium on Rock Mechanics and International Symposium on Rock Engineering for Innovative Future*, Okinawa, Japan, P-31, 2019.

Sakaguchi, T.; Ito, Y.; Sato, K.; Shimizu, T. Fundamental study of gas seepage in rock and open-crack. Journal of JSCE. 1992, 445, 17-25. (In Japanese)

Sato. K.; Ono, M. Characteristics of unsteady gas seepage in rock and porous media. *In Proc. 18th domestic conference of rock mechanics, Japan*, Tokyo, Japan, 1987 186-190. (In Japanese)

Takemura, T.; Oda, M. Changes in crack density and wave velocity in association with crack growth in triaxial tests of Inada granite. *Journal of Geophysical Research: Solid Earth*. 2005, 110, B5.

Taylor, D.W. *Fundamentals of Soil Mechanics*. New York, John Wiley and Sons, pp.113-114, 1941.

Togashi, Y.; Imano, T.; Osada, M.; Hosoda, K.; Ogawa, K. Principal strain rotation of anisotropic tuff due to continuous water-content variation. *International Journal of Rock Mechanics and Mining Sciences*. 2021, 138, 104646.

Togashi, Y.; Kikumoto, M.; Tani, K.; Hosoda, K.; Ogawa, K. Determination of 12 orthotropic elastic constants for rocks. *International Journal of Rock Mechanics and Mining Sciences*. 2021, 147, 104889.

Togashi, Y.; Mizuo, K.; Osada, M.; Yamabe, T.; Kameya, H. Evaluating changes in the degree of saturation in excavation disturbed zones using a stochastic differential equation. *Computers and Geotechnics*. 2022, 143, 104598.

FEATURES OF THE ECOLOGICAL-GEOLOGICAL SYSTEM OF THE TUFF MASSIF OF THE PAUZHETSKY GEOTHERMAL REGION (KAMCHATKA)

VIOLETTA SHANINA [1]

[1] *Lomonosov Moscow State University, Russia, Violettav@inbox.ru*

Abstract

The purpose of the study is to fully characterize the ecological-geological system (EGS) of the tuff massif of the Pauzhetsky geothermal region, compiled on the basis of the author's own field research (six field seasons) and published literature data. Features of the lithotope: an outcrop of andesite-dacitic tuffs of the Upper Pauzhetian subformation was studied. The rocks are divided into groups: 1) silty tuffs: density 1.40-1.57 g/cm^3, porosity 42.2-48.2%, uniaxial compressive strength 8-11 MPa; 2) fine psephitic tuffs are dense ($\rho = 1.59$-1.80 g/cm^3), porous (33.8-42.7%); 3) pumice tuffs are characterized by the lowest density ($\rho = 0.98$-1.35 g/cm^3) and the highest porosity (n=49.8-63.5%). Features of the edaphotope: on the tuffs under consideration, volcanic layered ocher soils are developed; have a low density (0.6-0.8 g/cm^3). Features of the phytocenosis: forest and dwarf altitudinal zones occur. Features of the zoocoenosis: invertebrates include extensive complexes of arachnids, the diversity of the animal world is represented by species of mammals characteristic of Kamchatka. The EGS formed on the tuff massif of the Pauzhetsky geothermal region is a complex formation. The most important features of the EGS are mainly determined by its lithogenic base - rocks soils (andesite-dacite tuffs), which have specific properties.

Key words

ecological-geological system, Kamchatka, tuffs, Pauzhetsky geothermal region, andesite-dacitic

1 Introduction

A general classification of ecological-geological systems (EGS) was developed and first published in 2022 (Korolev, Trofimov, 2022). It identified the ecological and geological systems of rock massifs. And, if publications devoted to the EGS of dispersed soil massifs already exist (Korolev, Grigorieva, 2022), then for rocky soils there are very few such publications. The purpose of the study is to fully characterize the EGS of the tuff massif of the Pauzhetsky geothermal region (Kamchatka), compiled on the basis of the author's own field research (six field seasons) and published literature data.

2 Methods

Laboratory determination of composition, structure and physical properties. The mineral composition of the studied volcano-clastic rocks was determined in thin sections using a polarizing microscope, spot chemical analyzes of minerals and study the morphology of the pore space using a scanning electron microscope. To determine the composition of minerals a quantitative X-ray analysis is conducted. Chemical analysis of rocks is determined by X-ray crystal diffraction spectrometer. To study the physical and physico-mechanical properties of rock samples required preparations using stone-cutting machine to obtain rectangular parallelepipeds and also were polished. After preparation following properties are measured: bulk and mineral density, total porosity, open porosity, water absorption, propagation velocities of elastic waves (longitudinal and transverse), magnetic susceptibility, uniaxial

compression strength and tensile. The total porosity was determined by the ratio of the mineral density (ρ_s) and the bulk density of the rocks in the air-dry state (p) using the formula: $n=(\rho_s-p)/\rho_s$. All measurements are performed according to standard methods described in conventional textbooks and manuals.

3   Results

Let us consider the main features of the ecological-geological system of the tuff massif of the Pauzhetka geothermal region (Kamchatka) (Fig. 1, 2, 3), which is located in the south of Kamchatka in the Pauzhetka River valley within the internal zone of the Kuril-Kamchatka island arc and belongs to the southern segment of the East Kamchatka volcanic belt.

Figure 1. Scheme of the location of the ecological-geological system of the tuff massif of the Pauzhetsky geothermal region (https://yandex.ru/maps)
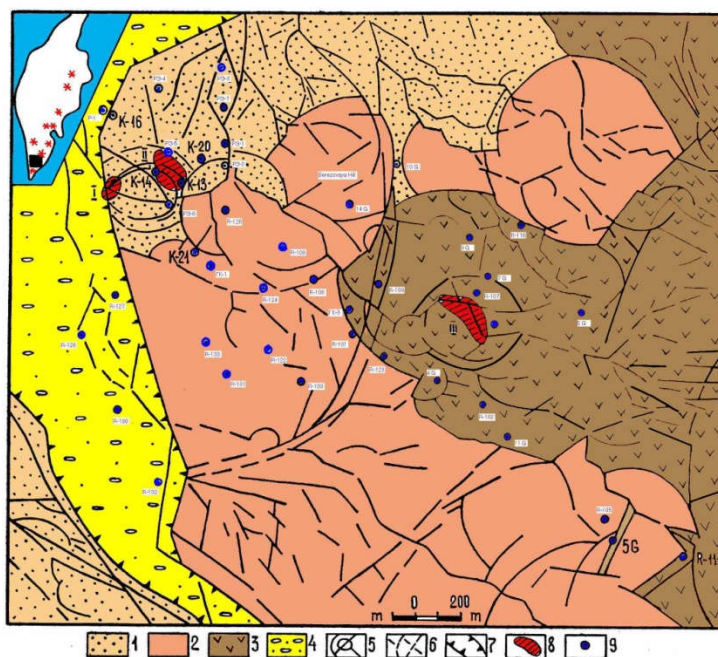
Figure 2. Schematic geological map of the Pauzhetka geothermal field (from The Structure of the Hydrothermal System, 1993). 1 - tuffs and tuffites of andesite-dacitic composition of the Upper Pauzhetka subsuite; 2 - lavas and extrusive bodies of dacite composition of Middle-Upper Quaternary age; 3 - andesite-basalts of Middle-Upper Quaternary age; 4 - modern alluvial deposits; 5-6 - tectonic structures: 5 - ring and their elements, 6 - "linear" and their elements; 7 - boundaries of the Pauzhetka Upper Quaternary graben; 8 - thermal fields: I - South, II - Upper, III - East; 9 - wells

Figure 3. General view of the ecological-geological system of the tuff massif of the Pauzhetsky geothermal region

Meteorological, hydrological and hydrogeological conditions. The climate is subarctic. The warmest month is August with an average temperature of 12.3 °C. The coldest month is January, with an average daily temperature of -6.3 °C. The average annual precipitation is 2056.1 mm. The minimum precipitation occurs in June, the maximum amount falls from October to December, most of it in the form of snow (Samkova, 2009b). Pauzhetka River (length 24 km, basin area 148 km²) originates on the slope of Kambalny volcano. It flows into the Ozernaya River on the left at a distance of 27 kilometers from its mouth. The width of the river in the middle reaches is 10 meters, the depth is 0.6 meters, the current speed is 2.5 m/s. Many streams flow into Pauzhetka, the largest of which is Lednikovy. The Pauzhetka thermal field in the Pauzhetka River valley has been studied in detail using exploratory drilling. Two pressure water-bearing complexes have been uncovered, confined to deposits of psephitic tuffs of the Pauzhetka suite (upper) and Paleogene-Neogene polymictic sandstones (lower). The upper water-bearing complex, with a thickness of 150-260 m, is isolated from groundwater by relatively impermeable siltstone tuffs. The area of the artesian slope, outlined by the distribution of psephitic tuffs in the western part of the Kambalny Ridge structure, is about 40 km²; the underground flow rate is at least 400 l/s (Structure of the hydrothermal system, 1993). According to the chemical composition, the waters of both horizons are chloride, sodium, and siliceous with a mineralization of 2.7–3.4 g/l (Belousov, Sugrobov, Sugrobova, 1976).

Features of the lithotope. Complete sections of the Pauzhetsky Formation are exposed by wells drilled at the Pauzhetsky springs and in the bedrock outcrops of the northern part of the Kambalny Range (Belousov, 1978). The upper 450 m of the sequence are represented by dacite and rhyolite tuffs of various granulometric compositions. On the right side of the stream, outside the zone of influence of hydrotherms, an outcrop of tuffs of the Upper Pauzhet subformation (N_2-Q_1pau_3) was studied. The exposed side of the stream represents a sequence of interlayered andesite-dacitic tuffs from fine to coarse clastics. According to their properties, the rocks are divided into three groups: 1) silty tuffs: density from 1.40 to 1.57 g/cm³, density of the solid component 2.70-2.72 g/cm³, porosity from 42.2% to 48.2 %, open porosity from 31.2 to 40.3%, hygroscopic humidity 0.7-3.6%, water absorption 20.5-27.1%, longitudinal wave speed 2.00-2.40 km/s, magnetic susceptibility 2.9-11.4*10^{-3} SI, uniaxial compressive strength 8-11 MPa; 2) fine psephitic tuffs are dense (ρ = 1.59-1.80 g/cm³), density of the solid component is 2.72-2.78 g/cm³, porous (33.8-42.7%); 3) pumice tuffs are characterized by the lowest density (ρ=0.98-1.35 g/cm³) and the highest porosity (n=49.8-63.5%) (Shanina, 2013), which is associated with the presence of pumice fragments.

Features of the edaphotope. On the considered tuffs of the Pauzhetsky geothermal region, volcanic layered ocher soils are developed (Samkova, 2009a), have a low density (0.6-0.8 g/cm³), crumbly, with high water permeability and a predominance of free humic acids and those associated with mobile sesquioxides humic acids and fulvic acids. Humus type is fulvate (0.7-0.9), humus content 15-20%. The presence of allophan and aluminum hydroxides determines the high sorption capacity. The edaphotope soils of the tuff massif of the Pauzhetsky geothermal region on aerial pyroclastic substrates are distributed outside the thermal fields.

Features of phytocenosis. The phytocenosis of the considered EGS of the tuff massif of the Pauzhetsky geothermal region contains forest and dwarf altitudinal belts. Forest vegetation is represented by stone birch forests on the slopes of the Kambalny Range (105-315 m above sea level). The elfin elfin belt (100 - 900 m above sea level) is composed of communities of alder and cedar elfin trees. Meadow vegetation is represented by large-grass hygromesophytic (shelomaynik) meadows, reed meadows, forb mesophytic and hygromesophytic meadows, subalpine meadows (in the dwarf belt) (Samkova, 2009b). The predominant plant communities are wormwood-geranium, wormwood-cinquefoil and burnet (Samkova, 2009a). Vascular plants include 112 species and subspecies belonging to 91 genera and 38 families (Samkova, 2009b). There are plants included in the Red Book of Russia - large-flowered slipper, rough bluegrass, Asian grasshopper, as well as rare plants of the Far East - Kamchatka lyubka, Daurian lily (Volcanoes of Kamchatka..., 2011).

Features of zoocenosis. The composition of the zoocenosis of the considered EGS of the tuff massif of the Pauzhetsky geothermal region is represented by both invertebrates and vertebrates. Among invertebrates, there are extensive complexes of arachnids of the families Clubionidae, Linyphiidae, Theridiidae, Tetragnathidae, Araneidae, Philodromidae, Eutichiuridae, Dictynidae, Thomisidae (Nenasheva, 2020) and insects (Fig. 4). Among insects, the species composition of caddisflies (Trichoptera) is especially representative, 10 species (Lobkova, Vshivkova, 2015). Insects of other orders are also numerous: hymenoptera, especially bees, dipterans, especially hoverflies, as well as bloodsucking (Tabanidae, Culicidae, Simulliidae, etc.) and butterflies. Predators predominate among beetles. There are also numerous vertebrate animals—birds and mammals—that live permanently or temporarily on the territory of the Pauzhetsky geothermal region. The diversity of the animal world is represented by mammal species characteristic of Kamchatka: brown bear, fox, sable, wolverine. The bird fauna includes 170 species, including the rare Buzzard subspecies Buteo lagopus kamtschatkensis (Lobkov, 2012), of which 34 are nesting (The trails of Southern Kamchatka, 2020).

Figure 4. Strelchatka caterpillar (Acronicta alni), Pauzhetsky geothermal region (Kamchatka)

4   Conclusion

The ecological-geological system formed on the tuff massif of the Pauzhetsky geothermal region is a complex formation. The most important features of the EGS are mainly determined by its lithogenic base - rocky soils (andesite-dacite tuffs), which have specific properties. The composition and properties of the lithotope largely determine the properties of the edaphotope and the species composition of phytocenoses and have less influence on the zoocenosis.

References

Belousov, V.I. *Geology of geothermal fields in areas of modern volcanism*. Moscow, Nauka, 1978.

Belousov, V. I., Sugrobov, V. M., Sugrobova, N. G. Geological structure and hydrogeological features of the Pauzhetka hydrothermal system / *Hydrothermal systems and thermal fields of Kamchatka*. Vladivostok: Far Eastern Scientific Center of the USSR Academy of Sciences, 1976. pp. 23-57.

Korolev, V.A., Grigorieva, I.Yu. The ecological-geological systems of loess soil massifs. *Engineering Geology World. 2022,* Vol. XVII, No. 2, pp. 42–64, https://doi.org/10.25296/1993-5056-2022-17-2-42-64.

Korolev, V.A., Trofimov, V.T. The development of a general classification of continental ecological–geological systems. *Moscow University Geology Bulletin*. 2022, Vol. 77, no. 2, p. 211–219.

Lobkov, E.G. Buzzard in Kamchatka / *Buzzards of Northern Eurasia: distribution, status of populations, biology*. Krivoy Rog: Center-Print, 2012.

Lobkova, L.E., Vshivkova, T.S. Caddisflies (Insecta, Trichoptera) of specially protected natural areas (SPNA) of the Kamchatka Territory. *Proceedings of the Kronotsky Natural Biosphere Reserve*. Issue 4. P.-Kamchatsky: Kamchatpress, 2015.

Nenasheva, E.M. *Spiders (Arachnida: Aranei) of natural parks of Kamchatka: fauna, ecology, zoogeography*. Petropavlovsk-Kamchatsky, KamchatSTU, 2020.

Samkova, T.Yu. Patterns of connection between the intensity of the modern hydrothermal process, the morphological structure of soils and the structure of vegetation cover using the example of thermal fields of the Pauzhetsky hydrothermal system. *In Proceedings of the 100th anniversary of the Kamchatka Expedition of the Russian Geographical Society*. P.-Kamchatsky, Russia, 2009a.

Samkova, T.Yu. *The influence of the hydrothermal process on vegetation (using the example of the Pauzhetsky hydrothermal system of Kamchatka)*. Ph.D. Thesis, IVIS FEB RAS, P.-Kamchatsky, Russia, 2009b.

Shanina, V.V. *Changes in the composition, structure and properties of volcanogenic rocks of the Pauzhetsky geothermal field, Koshelevsky and Krafla volcanoes under the influence of hydrothermal processes (according to field studies and laboratory experiments)*. Ph.D. Thesis, Lomonosov Moscow State University, Moscow, Russia, 2013.

The Structure of the Hydrothermal System. Moscow: Nauka, 1993.

The trails of Southern Kamchatka: a guide for responsible guides to the world of wild nature. Ed. A.V. Zavadskaya. Moscow, Pero, 2020.

Volcanoes of Kamchatka - a world heritage site. Institute of Geography RAS, 2011.

INVESTIGATION OF THE ABSORBING PROPERTIES OF MODIFIED SANDY SOIL TO CREATE A GEOCHEMICAL BARRIER FOR STORAGE LANDFILLS MUNICIPAL SOLID WASTE

ALEXANDRA KOVALEVSKAYA [1], TATYANA MALIKOVA [2], IRINA RODKINA [3]

[1] *Lomonosov Moscow State University (MSU), Russian Federation, alexa.kovalevskaya@mail.ru*

[2] *Lomonosov Moscow State University (MSU), Russian Federation, malikovatv@my.msu.ru*

[3] *Lomonosov Moscow State University (MSU), Russian Federation, irina-rodkina2007@yandex.ru*

Abstract
The study of the absorption capacity of sandy soil modified with clay soil and organic binder (starch) in relation to lead under dynamic sorption conditions was carried out. The behavior of the pH and Eh of the filtrate during the absorption of lead by the soil has been studied. It was revealed that the absorption of lead ions by the soil leads to a change in the pH of the filtrate. The value of the CEC and pH_{ZPC} of the modified soil is investigated. It is shown that the maximum amount of lead absorbed by the soil at the initial concentration of lead in a solution of 1,25 g/l is 1,96 mg/g.

Key words
geochemical barriers, Pb, dynamic sorption, pH, technical soil reclamation

1 Introduction

Technical soil reclamation is a science that develops the theory and methods of artificial improvement of the condition and properties of soils. At the same time, methods of technical reclamation can be used both in engineering and construction activities and to eliminate the ingress of hazardous chemical elements into the geological environment from landfills for storing solid household waste by creating geochemical barriers capable of retaining pollutants. One of the most dangerous pollutants is lead. At the same time, it is known that clay soils and organic substances have the greatest absorption capacity in relation to heavy metals, in particular lead, while sandy soils have practically no absorption capacity. Thus, the creation of a geochemical barrier based on sandy soil modified with clay soil and organic binder (starch) is quite promising.

Therefore, the purpose of this work is to study the absorption capacity of modified sandy soil in relation to lead. To achieve this goal, tasks were solved in the work:
1. Study of the physico-chemical properties of the studied sandy soil, clay soil and organic binder (starch);
2. Experimental study of the absorbing properties of modified sandy soil under dynamic sorption conditions;
3. Determination of the pH and Eh of the filtrate solution as the filtration process proceeds;
4. Processing and interpretation of the obtained results.

2   Methods

2.1   Creation of model soil samples

To study the absorbing properties of the modified sandy soil, a model soil was created based on Lyubertsy sand J_3v_2, kilic clay and organic binder (starch) in a ratio of 10:1:1 (100 g of sand, 10 g of clay, 10 g of starch). This ratio was chosen in order to establish the optimal (relatively fast) filtration time through the model soil, since the filtration time through sandy soil is less than the filtration time through both dusty soil (the particle size of which corresponds to the size of starch particles) and clay soil.

2.2   Preparation of lead nitrate solution

A solution of $Pb(NO_3)_2$ lead nitrate with a concentration of 2 g/l was used for the study. The solution was prepared by adding a sample of lead (II) nitrate $Pb(NO_3)_2$ to the volume of distilled water. In the experiment, a solution with a lead concentration of 1.25 g/l and a normality of 0.01 N was passed through the model soil. Despite the fact that the amount of lead 1.25 g/l is much higher than the maximum permissible concentration (MPC) for soils, this concentration is convenient for use in order to accelerate the filtration experiment and observe more visual results.

2.3   Collecting a filtration column and conducting a filtration experiment

A filtration column was used to study the absorption capacity of the model soil under dynamic conditions (figure 1).
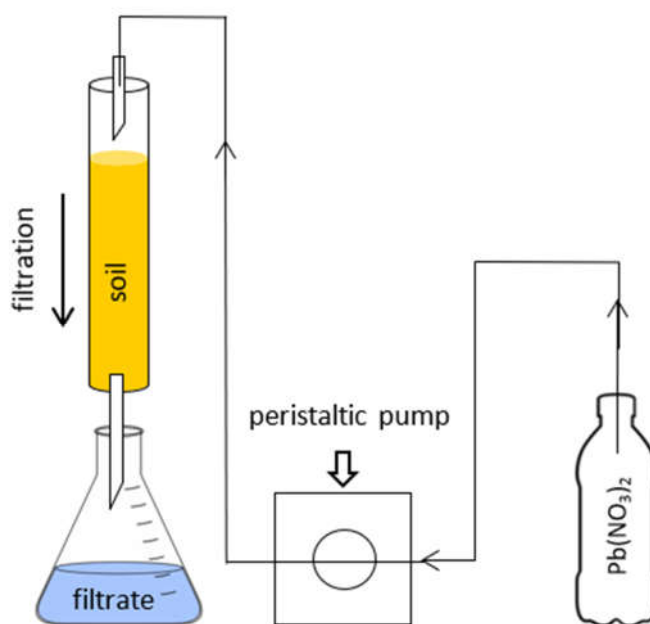
Figure 1. The general scheme of the filtration system.

The base area of column F was 7.07 cm^2, height – 13.5 cm, volume – 95.45 cm^3. A soil suspension was poured into each column to a height of 10 cm (the resulting volume of soil in the column is 70.7 cm^3) without compaction. On both sides, the column was closed with rubber stoppers with syringe nozzles. To prevent the particles from suffusing into the syringe nozzle, the soil was insulated with mesh filters and glass beads. The column with the sample was mounted on a tripod in an upright position. A peristaltic pump was used to filter the lead nitrate solution through the soil. A hose was connected to the

upper syringe nozzle, through which a $Pb(NO_3)_2$ solution was supplied using a pump. A receiving flask was supplied to the lower syringe nozzle, through which the solution filtered through the column (filtrate) was selected. The flow rate of solution Q during the experiment was estimated by measuring the volume of the solution passed through the soil per unit of time and was approximately 0.86 l/day (36 ml/hour), the filtration rate v was 1.22 m/day. The filtrate was selected as a volume of liquid equal to four pore volumes of the model soil accumulated in the flask. Steam volume refers to the maximum total volume of pores that can be filled with a solution. Thus, by selecting a filtrate whose volume is equal to the pore volume of the soil, taking into account numerous simplifications and assumptions, it is possible to accept the fact that the solution has passed through all the pores of the soil. Only sandy soil was used to assess porosity, since it was a large percentage of the total model soil compared to clay and starch. According to V.M. Shestakov, the porosity for sandy soil with a d60/d10 ratio equal to 2.4 (for Lyubertsy sand) is 35%. Therefore, for a soil volume of 70.7 cm^3, the pore volume is approximately 25 cm^3 or 25 ml. At a filtration rate of 1.22 m/day, a volume of 25 ml was selected in 42 minutes. Based on the first sampling attempts every 42 minutes and the subsequent pH values obtained, it was decided to select the filtrate by four pore volumes, that is, 100 ml every 2 hours and 48 minutes. Three parallel filtration experiments were carried out to ensure the accuracy of the obtained values.

2.4 Measurement of the pH and Eh of the solution by the potentiometric method

The determination of pH and Eh solutions was carried out potentiometrically on the pH-150 device in accordance with GOST R 51232-98: reference electrode EVP-1M4, measuring electrode ESL-45-11, the steepness of the electrode function 58.25.

2.5 Determination of the ground zero charge point

The zero charge point of the soil pH_{ZPC} – s the pH value at which the total charge of the surface of the soil particles is zero. By evaluating the difference between the pc and the pH of the solution, it can be concluded which ions (cations or anions) the soil will preferentially absorb. At $pH > pH_{ZPC}$ the soil particles are negatively charged, therefore the soil will be capable of preferential absorption of cations. At $pH < pH_{ZPC}$ the soil particles are positively charged, therefore the soil will preferentially absorb anions. In this work, pH_{ZPC} was determined for modified sandy soil both before and after the filtration process to compare the pH_{ZPC} values before and after lead ion sorption. To determine pH_{ZPC}, the method of acid-base titration of soil against the background of electrolyte solutions of different concentrations was used. HNO_3 acid and KOH alkali were used as titrants, and NaCl solutions with concentrations of 0.5 M, 0.1 M and 0.01 M were used as an electrolyte.

2.6 Determination of the soil cation exchange capacity

The cation exchange capacity (CEC) of a soil is a value that characterizes the ability of the soil to retain a certain amount of cations in an exchange form. Knowing the CEC of the soil, it is possible to estimate the total number of cations that can be displaced into solution from a unit mass of soil by a salt cation of a certain composition under standard conditions. In the work, the cation exchange capacity of the soil was determined for model soil (sand, clay, starch) and for sand modified only with kilic clay. The determination was carried out using a method based on saturation of the soil with sodium ion, followed by its determination by the gypsum method.

2.7 Determination of lead concentration in solutions

The concentration of lead in solutions was determined using the Quantum Z.ETA atomic absorption spectrometer, manufactured by NPO KORTEK, Moscow. The method of atomic absorption spectrometry (AAS) is based on the phenomenon of resonant absorption of light by free atoms (atomic vapor) of the element being determined.

3   Results

Based on the measurement results for three parallel filtration experiments, graphs of the dependence of pH and Eh on the number of selected filtrate pore volumes were constructed (figure 2 и 3, 1,2,3 – parallel experiments). The pH value of the initial solution was 5 units. In all parallel experiments, a dependence is observed: at first, the pH value fluctuates around 7-8 units, and then drops sharply to 5-6 units, which corresponds to the pH of the initial solution. Consequently, lead sorption was no longer carried out after the pH dropped to 5-6 units.

The Eh value in three parallel experiments ranges from 100-300 mV, and numerous areas of growth and decline of Eh are visible on the graph without a fixed pattern. The probable cause of such chaotic changes in the Eh value may be the activity of living organisms trapped in the solution or on the ground during the experiment.

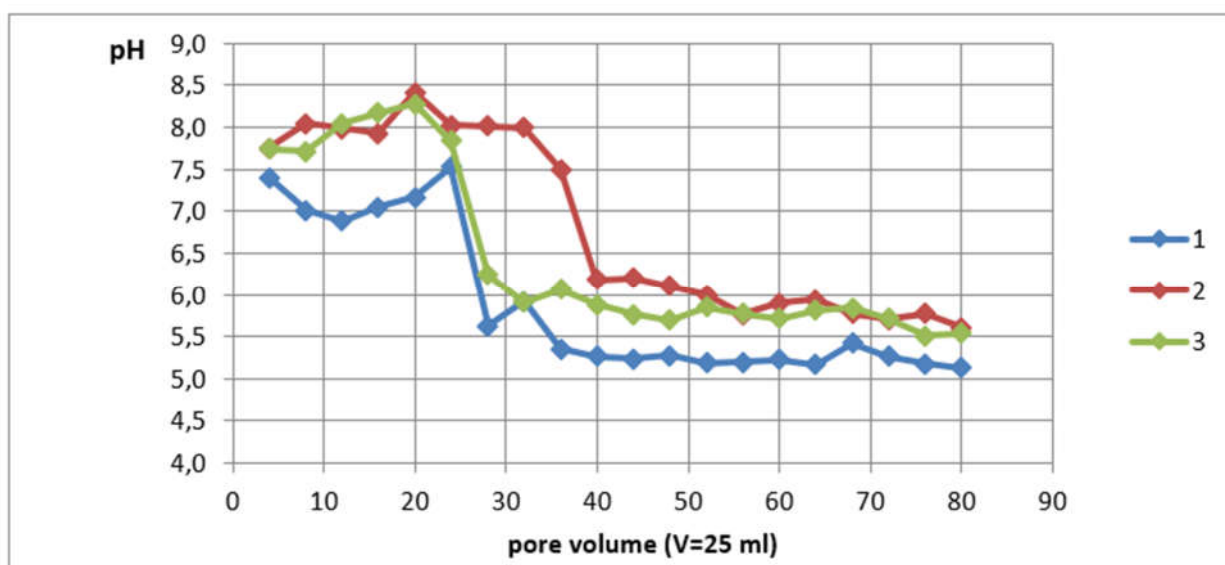**Figure 2.** The dependence of pH on the selected volume of filtrate.
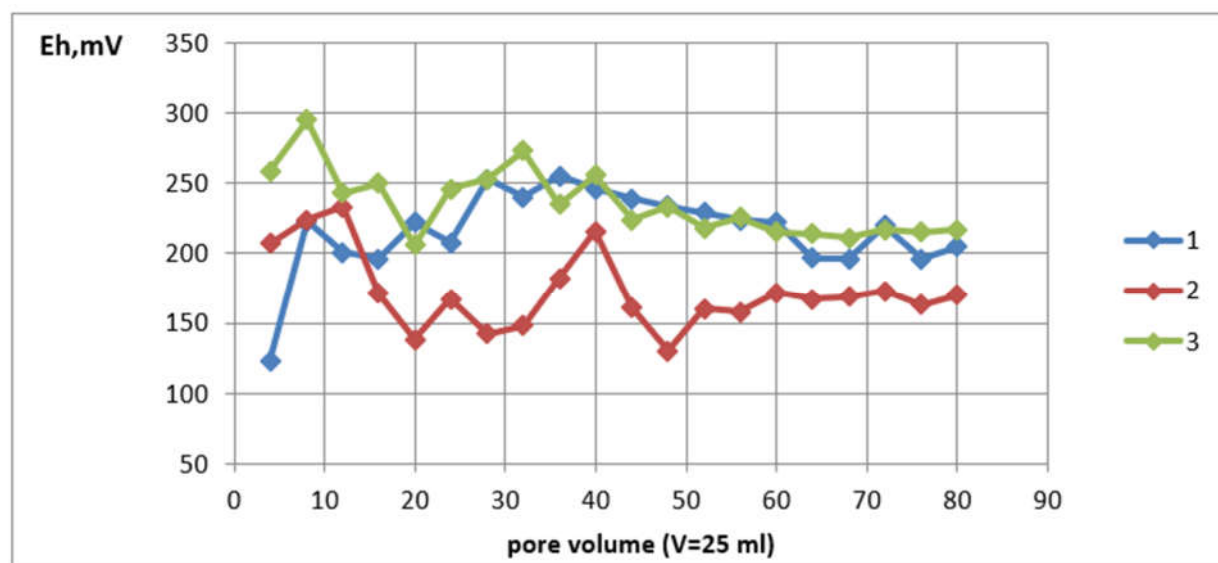
Figure 3. The dependence of Eh on the selected volume of filtrate.

The determination of the zero charge point of the soil showed that before the dynamic sorption process,

i.e. before the absorption of Pb ions by the soil, the pH_{ZPC} value was 8.5 units (figure 4). As the cations are absorbed by the soil, pH_{ZPC} shifts towards a more acidic medium and reaches a value of 6.25 after the dynamic sorption process (figure 5). Initially, the measured pH of the filtrate was 7-8 units, therefore, the pH of the surrounding solution was higher than pH_{ZPC} almost throughout the sorption process, that is, there was a predominant absorption of cations (namely Pb cations). After the filtrate reached pH 5-6 (less than 6.25 pH_{ZPC}), the predominant absorption of cations stopped, the sorption process was completed, which is confirmed by the final selected volumes of filtrate with pH 5-6.

Figure 4. The dependence of the titrant volume V [ml] on the pH of the solution (starting soil, pH 8.5), 0.01 M, 0.1 M, 0.5 M is the concentration of NaCl.

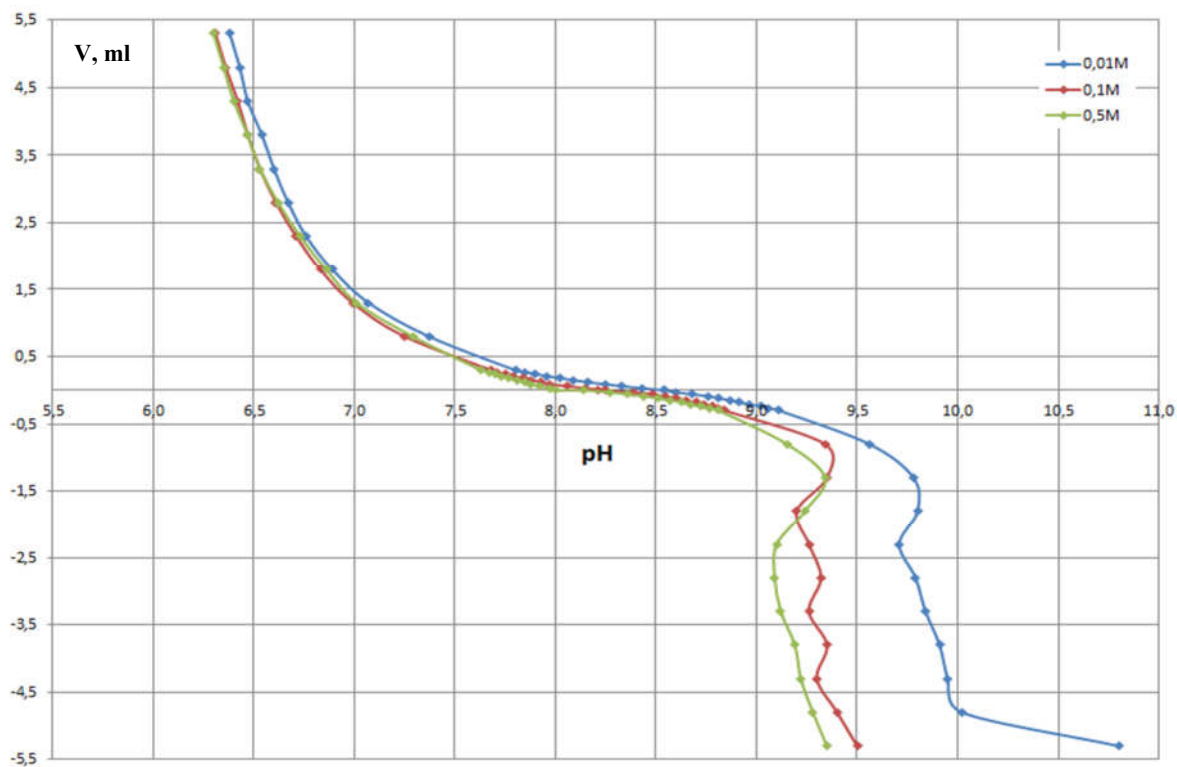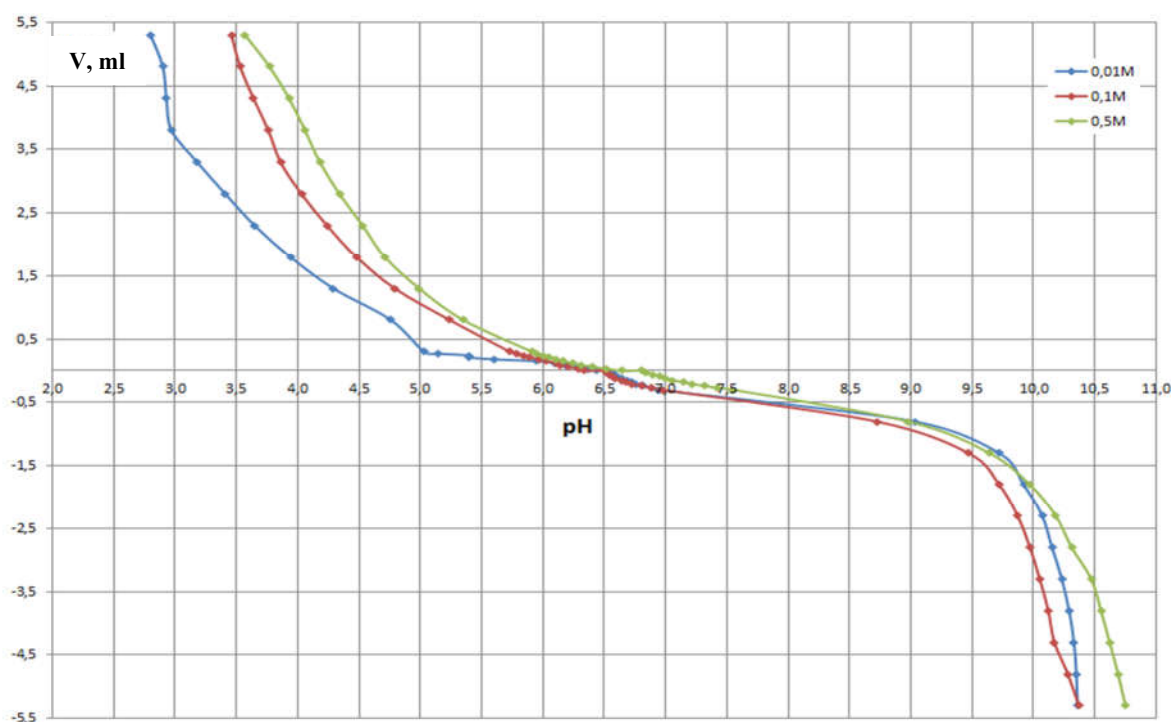**Figure 5.** The dependence of the volume of the titrant V [ml] on the pH of the solution (soil after sorption Pb, pH 6.25), 0.01 M, 0.1 M, 0.5 M is the concentration of NaCl.

The obtained values of the cation exchange capacity of 0.072 mg-eq/100g for a mixture of sandy and clay soil and 0.069 mg-eq/100g for a mixture of sandy soil, clay soil and starch do not allow us to draw an unambiguous conclusion about the effect of CEC on the absorption of lead by soil within the limits of this study. According to A.I. Kovalevskaya's static sorption of lead with clay soil and clay soil modified with starch, it was found that at a concentration of $Pb(NO_3)_2$ in a solution of 2 g/l, lead sorption with montmorillonite is about 70 mg/g, sorption with montmorillonite with starch addition is about 50 mg/g. The obtained values vary quite a lot, while the obtained CEC values for the same soils are similar (about 0.07 mg-eq/100g). Thus, considering that sandy soils are practically incapable of cation exchange, it can be concluded that the absorption of lead cations does not depend on the CEC values. Consequently, lead, when absorbed by the soil, is sorbed not in the exchange complex of the soil, but in other more durable centers. It is likely that the absorption of lead by the soil occurs either in intra-atmospheric complexes on the soil surface with the formation of strong covalent bonds between the soil and Pb ions, or lead is embedded in the soil structure itself, in particular in the structure of clay soil and starch (the absorption process occurs).

Table 1 shows the results of an experiment to study the absorption capacity of modified sandy soil under dynamic conditions with respect to lead. Based on the obtained values for the model soil, absorption curves were constructed – the dependence of the amount of lead absorbed by the soil and the pH of the filtrate on the number of selected pore volumes (figure 6,7,8).

Table 1. The results of an experiment to study the absorption capacity of modified sandy soil under dynamic conditions with respect to lead

| V (25ml)	pH			Eh			C, mg/g					
							sand+clay+starch			clay+starch		
	1	2	3	1	2	3	1	2	3	1	2	3
4	7,40	7,75	7,74	123	207	259	0,25	0,26	0,26	1,48	1,55	1,54
8	7,01	8,05	7,71	223	224	295	0,74	0,50	0,50	4,44	3,01	2,98
12	6,88	7,99	8,05	201	233	243	1,21	0,75	0,73	7,29	4,48	4,39
16	7,05	7,93	8,17	196	171	250	1,70	0,99	0,96	10,20	5,94	5,75
20	7,17	8,42	8,28	222	138	206	2,19	1,23	1,13	13,13	7,35	6,79
24	7,53	8,03	7,84	208	167	246	2,43	1,45	1,28	14,56	8,71	7,65
28	5,63	8,02	6,24	253	142	253	2,43	1,66	1,41	14,59	9,95	8,48
32	5,92	8,00	5,91	240	148	273	2,43	1,75	1,49	14,60	10,50	8,93
36	5,35	7,50	6,06	255	182	235	2,43	1,82	1,56	14,60	10,93	9,34
40	5,26	6,18	5,88	246	216	256	2,43	1,84	1,57	14,60	11,05	9,43
44	5,24	6,20	5,76	239	161	224	2,43	1,85	1,58	14,60	11,10	9,48
48	5,27	6,10	5,69	234	130	233	2,43	1,86	1,59	14,60	11,15	9,53
52	5,19	6,00	5,85	229	160	218	2,43	1,86	1,59	14,60	11,15	9,53
56	5,20	5,76	5,77	224	158	226	2,44	1,86	1,59	14,61	11,15	9,53
60	5,23	5,90	5,71	222	172	215	2,44	1,86	1,59	14,61	11,15	9,53
64	5,17	5,94	5,81	197	167	214	2,44	1,86	1,59	14,61	11,15	9,53
68	5,42	5,77	5,84	196	169	211	2,44	1,86	1,59	14,61	11,15	9,53
72	5,26	5,70	5,71	220	173	217	2,44	1,86	1,59	14,61	11,15	9,53
76	5,18	5,77	5,51	196	163	215	2,44	1,86	1,59	14,61	11,15	9,53
80	5,13	5,61	5,54	205	170	217	2,44	1,86	1,59	14,61	11,15	9,53
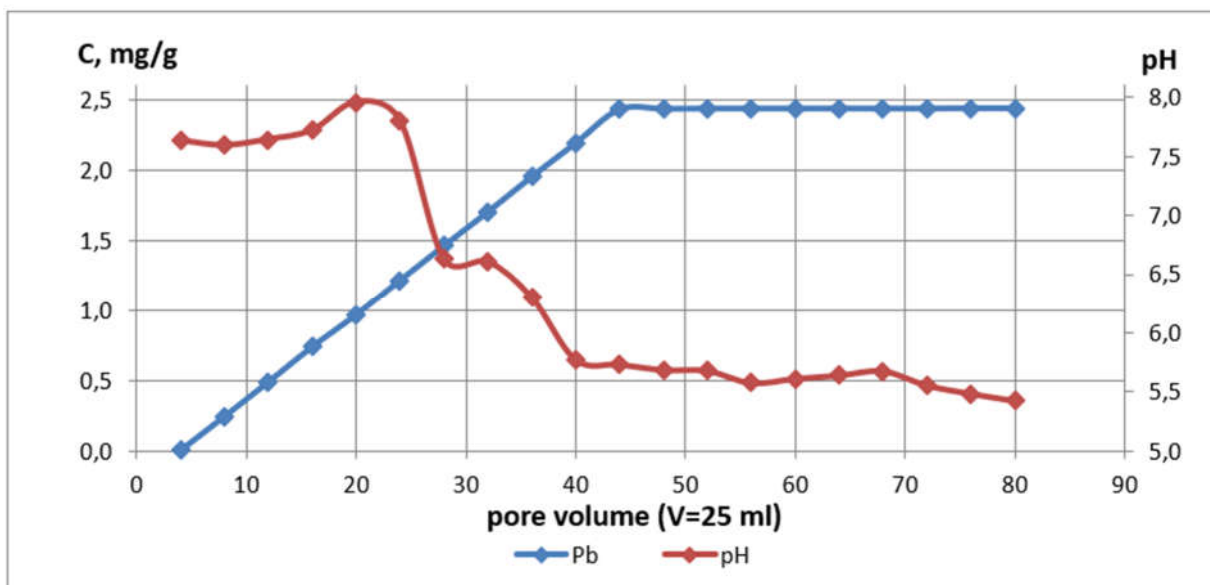
Figure 6. Graph of lead absorption by modified soil (1 parallel experiment).
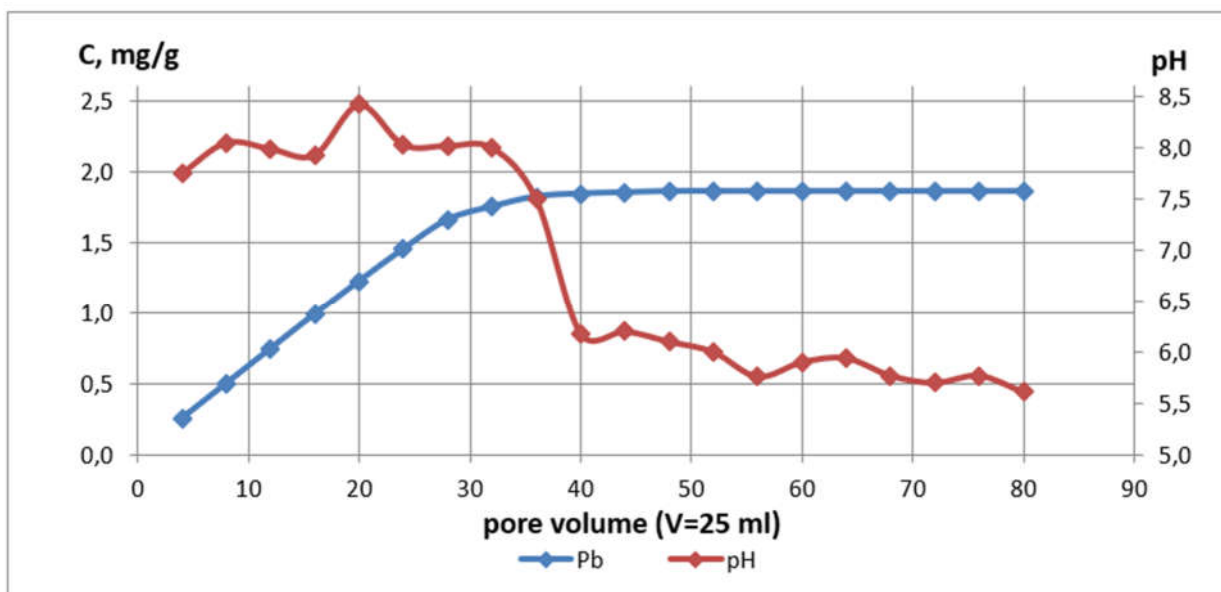
Figure 7. Graph of lead absorption by modified soil (2 parallel experiment).
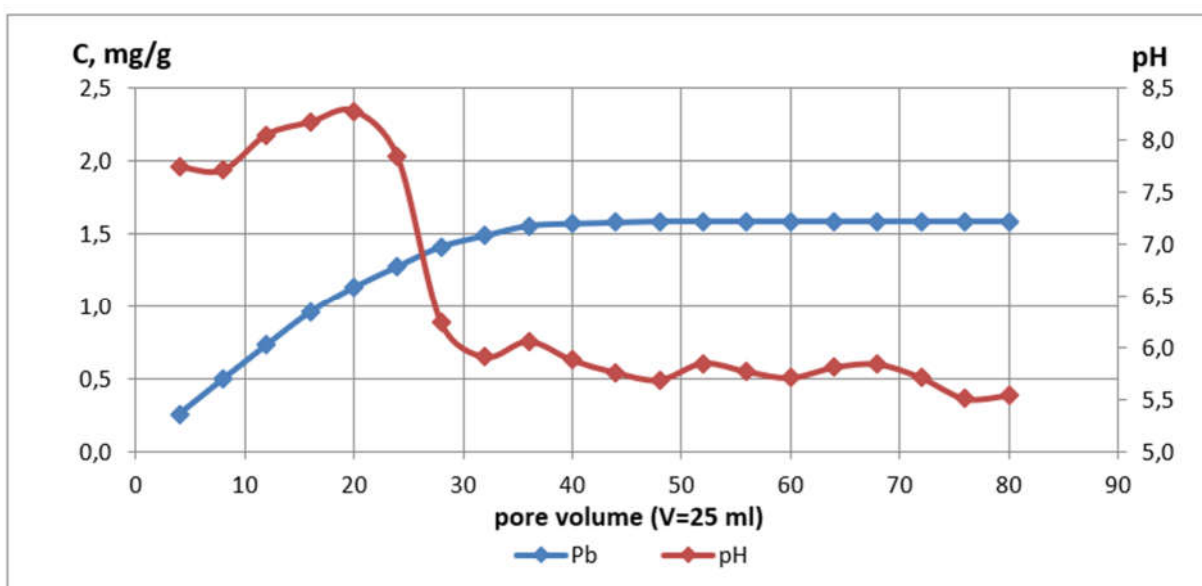

Figure 8. Graph of lead absorption by modified soil (3 parallel experiment).

As can be seen from the data obtained, the maximum possible value of lead absorbed by the model soil reaches 2.44 mg/g for the first, 1.86 mg/g for the second, 1.59 mg/g for the third parallel experiment. The average value of lead absorbed by the model soil for three experiments was 1.96 mg/g. The amount of lead absorbed by montmorillonite clay and starch (excluding sand) is 14.61 mg/g for the first, 11.15 mg/g for the second, 9.53 mg/g for the third parallel experiment. The average value of lead absorbed by clay and starch for three experiments was 11.76 mg/g. If we take into account the fact that the contribution of sandy soil to the Pb absorption process is quite low, then to assess the magnitude of the absorption capacity of clay and starch, we can rely on the research of A. I. Kovalevskaya on the absorption of Pb ions under static sorption conditions. Under static sorption conditions, at a concentration of Pb in the initial solution of 1.25 g/l, the absorption capacity of clay soil modified with starch was 48.24 mg /g, which is approximately 4 times higher than the values obtained by dynamic sorption. This difference may be related to the specifics of the present experiment:

1. Direct dynamic sorption with a fixed filtration rate, which means a shorter interaction time of the soil with the $Pb(NO_3)_2$ solution. The time of the dynamic sorption experiment was 56 hours, while for static sorption, sampling was carried out 3 weeks after the start of the experiment;

2. After carrying out the filtration processes, it was found that large aggregates were formed in the model soil by combining sandy and clay particles with starch, most pronounced after the second experiment. As a result, the absorption of lead ions took place over the surface area of the unit, including sand particles that are incapable of absorbing Pb, and not over the surface of clay particles and starch.

4   Conclusion

Thus, in this work, the absorption capacity of sandy soil modified with clay soil (montmorillonite) and organic binder (starch) in relation to lead was studied.

A relationship was revealed between the pH value of the solution and the amount of absorbed lead under dynamic sorption conditions (absorption of Pb ions by the soil leads to a change in the pH of the filtrate). Determination of the Eh values of the filtrate showed that the Eh value is probably influenced by living organisms.

The pH_{ZPC} value was obtained for the created model soil before (8.5) and after (6.25) lead absorption. At the same time, the obtained pH_{ZPC} values satisfy the general pattern of pH solution behavior.

According to the measurement of the cation exchange capacity, it was found that the absorption of lead cations does not depend on the value of the soil cation exchange capacity (0.072 mg-eq/100g for a mixture of sandy and clay soil and 0.069 mg-eq/100g for a mixture of sandy soil, clay soil and starch), therefore, the absorption of lead occurs with the formation of more durable complexes.

The maximum amount of lead absorbed by such a soil at an initial concentration of lead in a solution of 1.25 g/l is 1.96 mg/g. The maximum amount of absorbed lead without taking into account the mass of sand (absorption by clay and starch) is 11.76 mg/g, which is much less than the values obtained by studying the absorption capacity of similar soils under static sorption conditions (on average 48.24 mg/g according to A.I. Kovalevskaya). However, this study is significant because it has shown that a competent combination of sand, clay and starch can be used to create a model soil that plays the role of a protective barrier against Pb. Further research will allow us to find methods for creating protective barriers with greater absorption capacity.

References

Arinushkina E.V. Manual on chemical analysis of soils. Moscow: MSU, 1971.

Foo K.Y., Hameed B.H. Insights into the modeling of adsorption isotherm systems. // Chemical Engineering Journal. 2010.

Matthess G. Unsaturated Zone Pollution by Heavy Metals. // Pollutants in Porous Media. 2008.

Rodkina I.A. Soil composites with the addition of carbamide resin with a high sorption capacity to create a multilayer protective shield against lead: dissertation for the degree of Candidate of Geol.- a mineral.Sciences : 25.00.36. / Rodkina Irina Alekseevna; Moscow State University named after M.V.Lomonosov, Geol. fac., Kaf.engineer. and ecol.Geology. – M., 2010.

Shestakov V.M. Hydrogeodynamics. Moscow: Moscow State University, 1995.

Sokolova T.A., Trofimov S.Ya. Sorption properties of soils. Adsorption. Cationic exchange. Tula: Vulture and K, 2009.

Voronkevich S.D. Fundamentals of technical soil reclamation. M.: Scientific world, 2005.

APPLICATION OF GEOPHYSICAL INVESTIGATIONS FOR DETECTING THE GROUNDWATER SPRINGING IN THE SIRAČ LIMESTONE QUARRY, MINING FIELD ČELINA

JASMIN JUG [1], KRISTIJAN GRABAR [2], STJEPAN STRELEC [3], DRAGANA DOGANČIĆ [4]

[1] *Faculty of Geotechnical Engineering, University of Zagreb, Hallerova aleja 7, 42000 Varaždin, Croatia, jjug@gfv.hr*

[2] *SPP d.o.o., Koprivnička ulica 47, 42000 Varaždin, Croatia, krisitjan@spp.hr*

[3] *Faculty of Geotechnical Engineering, University of Zagreb, Hallerova aleja 7, 42000 Varaždin, Croatia,* sstrelec@gfv.hr

[4] *Faculty of Geotechnical Engineering, University of Zagreb, Hallerova aleja 7, 42000 Varaždin, Croatia, ddogan@gfv.hr*

Abstract

Natural resources, such as rock material, gravel and sand, are the most important mineral raw materials used in construction. Limestone rocks are exploited in the Sirač quarry Čelina, which is then processed into two types of products: crushed stone and stone aggregates. In 2021, during the excavation process, a new feature of water accumulation appeared on the quarry floor (208 m.a.s.l.) and water pools were formed, which tended to flow towards the northern part of the excavation floor. In the same year, an exploratory well with a depth of 50 meters was drilled near the place where the water appeared. Artesian water came to the surface from the mentioned well, which confirmed the presence of groundwater. Given that the inflow of water did not decrease over time, research had to be carried out with the aim of solving the problem so that the quarry could be properly managed as a natural resource of rock material. In addition to geological prospecting, three different methods of geophysical investigation were applied at the end of 2023 to detect the source and extent of groundwater springing: electrical resistivity tomography (ERT), multichannel analysis of surface waves (MASW) and ground penetrating radar (GPR). A fault zone was detected by interpreting the research results, which probably represents a groundwater aquifer. It was determined that the bedding planes of the Triassic carbonate rocks in the deposit have low water permeability therefore the fault zone allows drainage of seepage and groundwater. In addition, impermeable grey-green Triassic sedimentary elements of clastic rocks were identified in the sublayer of Triassic carbonates, which probably represents a barrier to the percolation and movement of groundwater.

Key words

limestone quarry, groundwater spring, exploratory well, geophysical investigations, fault zone.

1 Introduction

The complicated structure of the rock mass with its defects and inhomogeneity and the wide range of its applications cause challenges and problems in rock engineering and construction, which often involve considerations that are of relatively little or no concern in most other branches of engineering (Palmström, 1995). Together with sand and gravels, quarried rocks are essential raw materials for the construction industry. Construction rock material generally refers to rock blasted in quarries and commonly crushed and screened before use. Such rock is used mainly as aggregate for road surfaces, aggregates for concrete and asphaltic concrete, for constructing road bases and sub-bases, and as a basic raw material for producing building materials (e.g. plasters and adhesives).

All of the above also applies to the Sirač limestone quarry Čelina. However, during the exploitation and the progress of mining works in the aforementioned quarry, a problem arose in the water management activities (dewatering the quarry).

Generally, water in quarry excavations collects from precipitation or from groundwater seeping through fractures in quarry walls. Methods for calculating the groundwater inflow into the mining pit have mostly been worked out (Marinelli and Niccoli, 2000; Sobko et al., 2019). In addition to calculations, it is also possible to carry out hydrogeological modelling to assess the groundwater inflow into limestone mining pits (Surinaldu et al., 2011). Quarry operators pump out inflowing water from the excavation to allow for extraction (blasting and recovering the bedrock) on a dry quarry floor. Groundwater seeping into the excavation from water-bearing breaks (fractures) in the bedrock lowers the water table to the depth of the fracture break, releasing the water into the quarry. Except for the fractures, the bedrock prevents water movement (OSSGA, 2016). However, it is a general statement and it should be kept in mind that there are rocks that have a high primary permeability.

Problems with water management in the specific case (Čelina mining field) studied in this paper began in 2021. A new feature of water accumulation in the form of water pools appeared on the quarry floor (208 m.a.s.l.), where the water had a tendency to flow towards the northern part of the excavation floor (Figure 1.). Given that the inflow of water did not decrease over time, it was not possible to continue the management of the quarry as a natural resource of rock material. Such an unfavourable situation could have been prevented by carrying out detailed investigations before the quarry started working. Such extensive studies would assess the local impact on groundwater flow systems. However, considering that research was not carried out before, detailed geophysical and geological investigations were carried out at the end of 2023 to detect the source and extent of groundwater springing. In addition to geological prospecting, three different methods of geophysical investigation were applied: electrical resistivity tomography (ERT), multichannel analysis of surface waves (MASW) and ground penetrating radar (GPR). Input data for research planning was obtained from the results of exploratory drilling with a depth of 50 meters that was performed near the place where the water appeared. Artesian water came to the surface from the well, confirming groundwater's presence.

Figure 1. Panoramic photo of the research floor, 208 m.a.s.l.

The application of geophysical measurements for detecting the groundwater inflow in the quarry has already been recorded in the literature. Abd El-Gawad et al. (2018) applied geoelectrical measurements to detect groundwater seepage in a clay quarry. In order to detect the source and extension of the groundwater seepage, a geoelectrical resistivity technique in the form of vertical electrical soundings (VES, 1D method) was applied. About the above example, the research carried out in the Sirač limestone quarry, and presented in this paper, is upgrade of the application of geophysical research methods for the detection of groundwater inflow into the quarry, considering that several 2D geophysical methods are combined.

2   Methods

2.1 Geological investigations

All available geological reports and data, including satellite photographs, topographical maps, basic maps, legislative boundary maps, etc., were reviewed. Input data for research planning was obtained from the results of exploratory drilling with a depth of 50 meters that was performed in 2021 near the place where the water appeared. Exploratory drilling was performed by Kufner Group (2021) using a wireline system. Wireline core drilling is a special type of core drilling that is most commonly used for mining operations. Wireline coring allows rapid placement and withdrawal of the core barrel within the drill rods therefore the rods do not need to be removed to recover each individual core sample. Geological research was conducted in the field to collect additional data. These data were collected in the form of photographs, measurements and notes. Figure 2 shows the borehole log up to a depth of 25 m and other observations made during exploratory drilling and geological mapping.
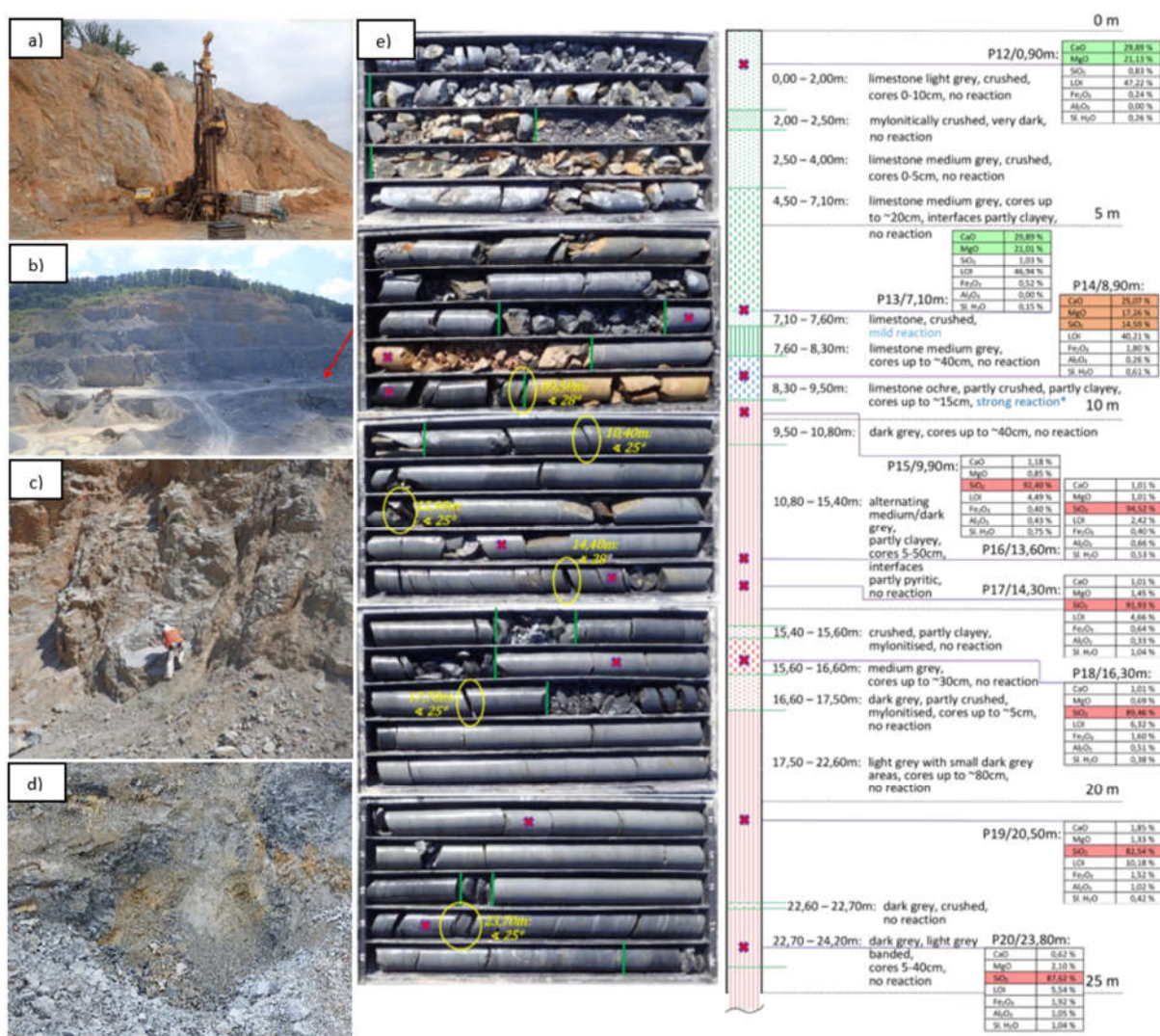

Figure 2. Input data for geological investigations: a) Drilling machine with wireline system; b) Exploratory well position marked with a red arrow; c) Geological maping; d) Cavern near a well location; e) Borehole log up to depth of 25 m (Kufner Group, 2021).

2.2 Geophysical investigations

The geophysical investigations were performed using three techniques: Electrical Resistivity Tomography (ERT), Multichannel Analysis of Surface Waves (MASW) and Ground Penetrating Radar (GPR). The position of the geophysical surveys is shown in Figure 3a.
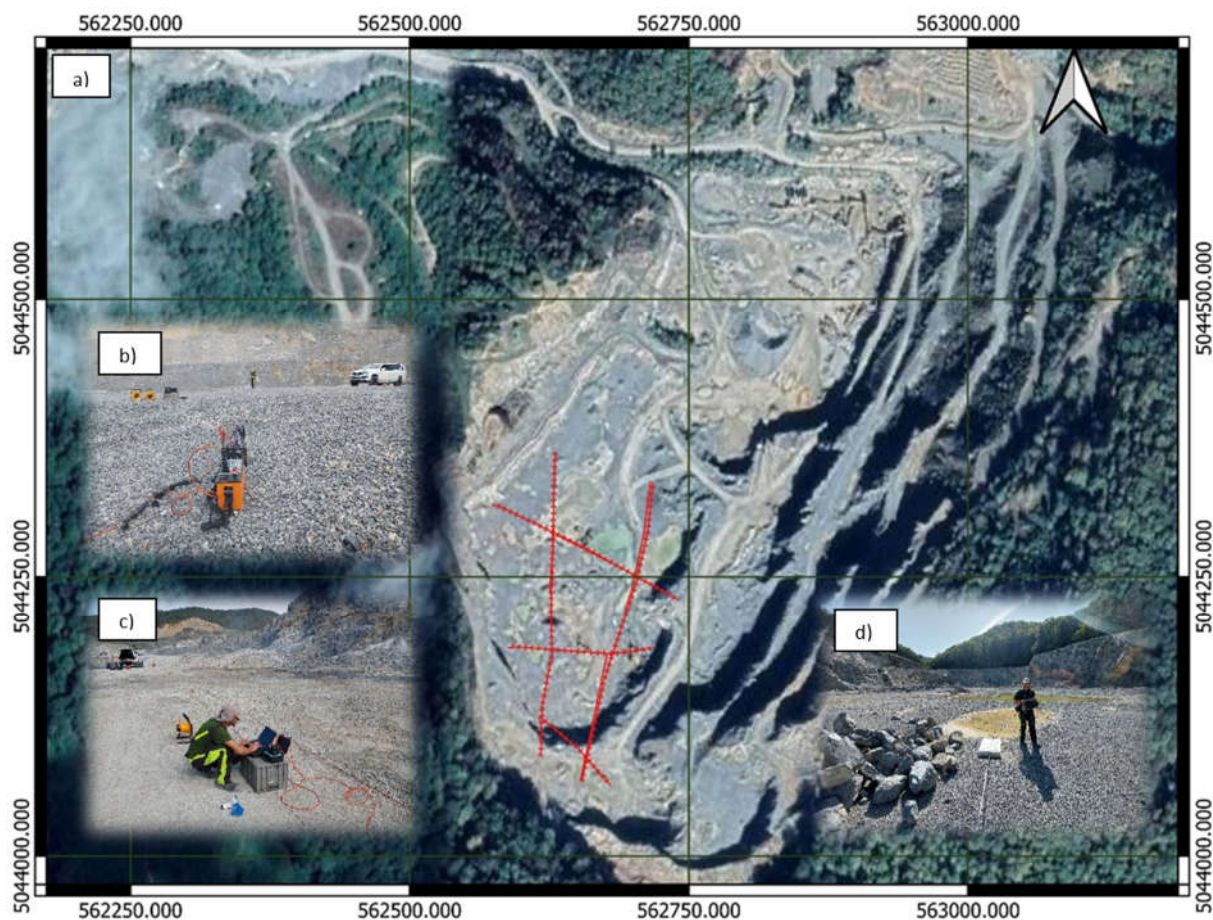

Figure 3. Geophysical investigations: a) Location of geophysical profiles on the satellite image from DGU Geoportal; b) ARES system for ERT; c) PASI GEA 24 investigation seismograph for MASW; d) ZOND12e GPR system.

2.2.1 Electrical Resistivity Tomography (ERT)

ERT is a geophysical technique that generates 2D pictures depicting electrical resistivity distribution in the subsurface (Strelec et al., 2017). The ARES system (Figure 3b) was used for field measurements (Czech manufacturer GF Instruments), a multi-electrode system used for 2D electric study. This technique utilises an array of electrodes interconnected by multicore cable to generate a linear depth profile, or pseudo section, of the resistivity variation along the survey line and at different depths. Loke (2011) describes this procedure. The analysis and interpretation of tomograms enable the detection of variations in resistivity, which can be caused by differences in lithological material or changes in water content within specific areas. The inversion of the resistivity profile was successfully performed via the RES2DINV software, which is based on Loke's methodology (2019).

2.2.2 Multichannel Analysis of Surface Waves (MASW)

MASW, first introduced in 1999 (Park et al., 1999), is a seismic exploration technique for mapping the

subsurface. The MASW technique initially detects seismic Rayleigh surface waves created by different seismic sources, analyses the velocities at which these surface waves propagate, and later indicates variations in shear wave velocity (v_S) below the surveyed zone. Foti et al. (2011) briefly described field techniques and data processing steps. The PASI GEA 24 investigation seismograph (PASI SRL) and 12 single-component geophones with a frequency of 4.5 Hz with a spacing of 5 meters are utilised for imaging in Sirač (Figure 3c). The collected data was analysed using the PC software SeisIMAGER 4.0.1.6. developed by OYO Corporation.

2.2.3 Ground Penetrating Radar (GPR)

Rock quality could be well investigated using electromagnetic techniques (Jug et al., 2020). Electromagnetic waves propagate through a medium of blocky limestone, thus reflecting inhomogeneity with different parameters, such as layer boundary. The receiving signal, however, in addition to the reflected wave, also contains a direct wave that travels the shortest distance directly from the transmitting to the receiving antenna. Therefore, the receiver's output signal combines the transmitter's pulse followed by reflected pulses. Field GPR profiling was done using the ZOND12e GPR system, Radar System, Inc. Latvia and a 300 MHz shielded antenna (Figure 3d), for which the expected investigation depth in the carbonate rock mass is 20 to 30 m. Acquiring was done with the Prism2 software.

3   Results

3.1 Results of geological investigations

As part of these detailed investigations, the lithological composition of the deposits was determined. In addition, tectonic elements (cracks and faults) were recorded. According to the basic geological map L33-95 Daruvar, the study area comprises Triassic and Jurassic deposits (Jamičić, 1989). The thickly layered grey dolomitic limestone (T_3) represents a lithological unit in which stone is exploited. Thinly layered clastites are locally found within these carbonate rocks. A sequence of grey-green clastites occurs in the base of the Triassic carbonates. During the investigations carried out in the southern part of the deposits on the terrain surface, a distinct fault zone extending NW-SE with a paraclase inclination of about 75° to the southeast was registered, which was later confirmed by the results of geophysical investigations. On already formed carbonate rocks of Triassic age, sedimentation continuously took place throughout the Jurassic (J) period, and thus thin-plate gray limestones were formed. In the quarry area, they were developed in the form of a narrow zone on the northern flank of the deposit. The mentioned deposits are not significant for the research presented in this paper. The described geological relationships are shown on a characteristic geological cross-section (Figure 4).
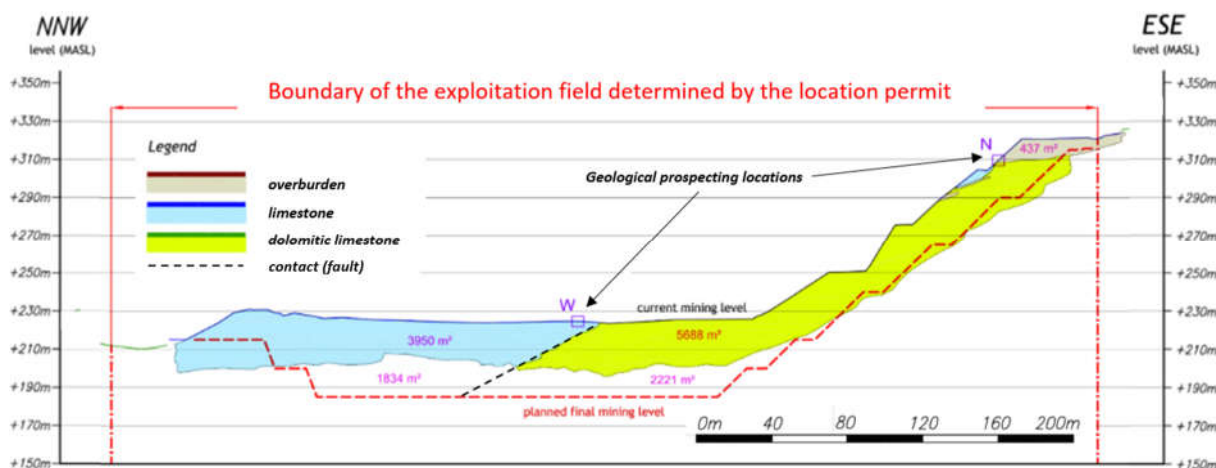

Figure 4. Characteristic geological cross-section - southern part of the Čelina mining field.

3.2 Results of geophysical investigations

3.2.1 Results of ERT investigations

In the Sirač quarry area, Čelina mining field, five 2D profiles were made by electrical resistivity tomography, with a length of 90 to 276 m and an interpretive depth of up to a maximum of 50 meters. The profiles were made using the Wenner electrode arrangement with an electrode spacing of 6 meters. The results of electrical resistivity measurements are shown in Figure 5.
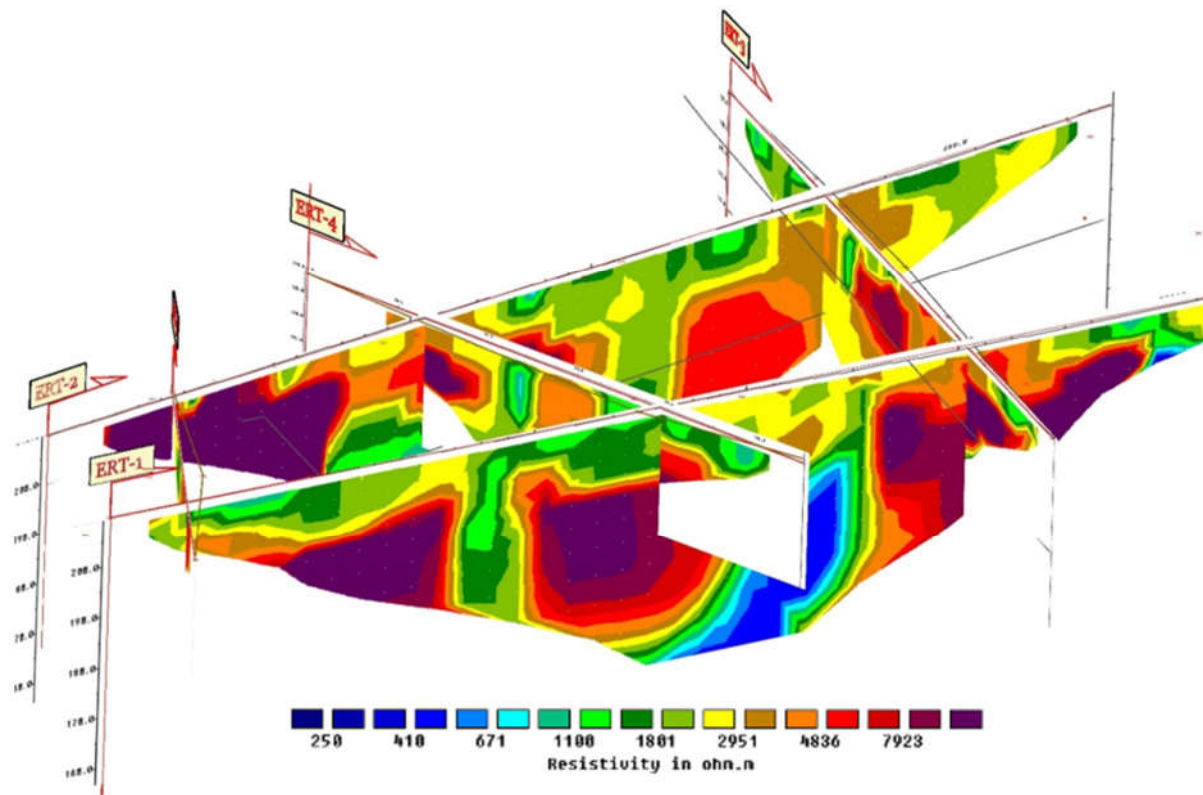

Figure 5. Results of ERT profiling in 3D view.

On the interpreted ERT profiles, based on electrical resistivities, it is possible to assume two lithological zones generally. Jurassic limestones and weathered rocks have lower resistivities, from 500 to 2000 Ωm (blue and green colour shades). According to these resistivities, younger limestones are represented in this zone, presumably saturated with water. The same resistivities can also represent a water-permeable zone as clastite in the fault area. Triassic dolomitic limestone has higher electrical resistance (red, yellow and brown colour shades), the resistivities range from 2800 to 10000 Ωm. According to the resistance of the rocks, it is more or less weathered. The mentioned materials on the tomography profiles alternate in depth and laterally.

3.2.2 Results of MASW investigations

The MASW data generated 2D shear wave velocity (v_s) profiles. Recorded seismograms were processed by the widely used MASW technique for picking the amplitude maximum in 2D spectral representations of the wavefield. A total of four seismic profiles were performed, each 115 meters long. Figure 6 shows the interpreted results of MASW-1 and MASW-2 profiling. The mentioned profiles follow the research line of the ERT-1 geoelectrical profile and are intersected by profiles ERT-3, ERT-4 and ERT-5. Seismic measurements detected lower shear wave velocities at the end of the MASW-1 profile and the beginning of the MASW-2 profile (v_s = 800-1400 m/s). Given that the mentioned area is surrounded by a more

compact rock mass (v_s = 1500-2200 m/s), it is obviously a discontinuous and weathered rock mass in the fault zone.
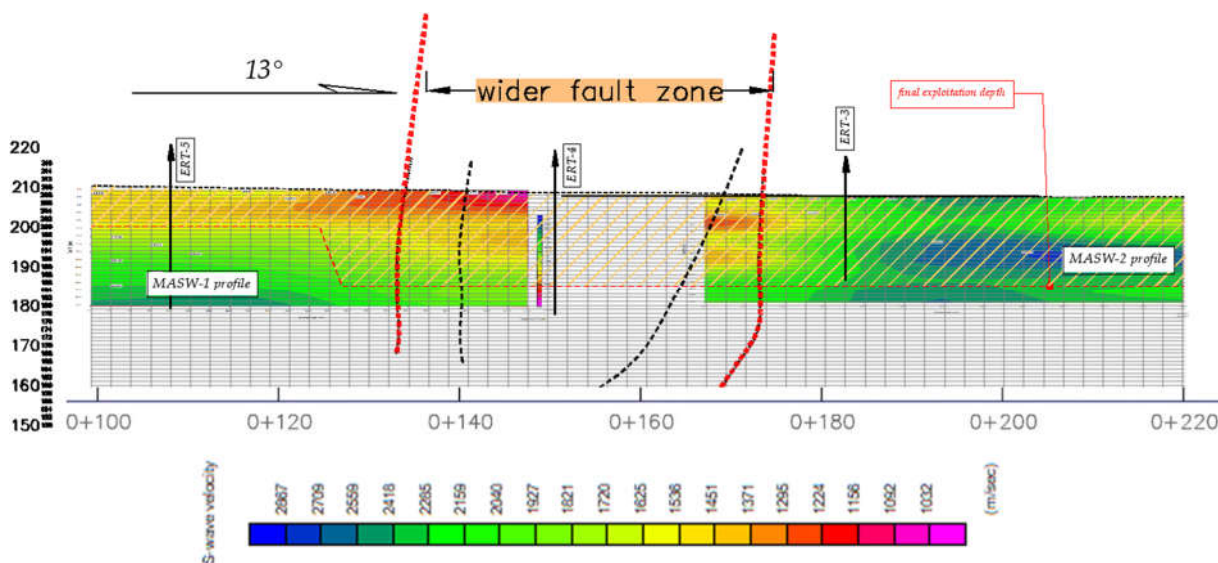
Figure 6. Results and interpretation of MASW profiling.

3.2.3 Results of GPR investigations

In the Čelina mining field, seven 2D profiles were made with ground penetrating radar, with an interpretive depth of up to a maximum of 20 meters. The section of the recorded GPR-2 radargram is shown in Figure 7, while the section of GPR-1 is shown in Figure 8 as a superimposed composite view with other geophysical investigation results. Detected crack systems within the investigated rock mass were interpreted on the radargrams. A dielectric permeability value of 6 was chosen for a time-depth conversion procedure in blocky limestones for all GPR recordings. The GPR-2 profile (Figure 7) also covers the fault zone detected by the MASW survey, and it is marked on the profile with black dashed lines. The main crack systems are also marked with dashed lines, and the depth and angle of the discontinuity are recorded.

Figure 7. Results and interpretation of GPR profiling, from station 0+100 to 0+220.

4   Discussion

Based on the interpreted geoelectrical models, a significantly reduced electrical resistance zone was identified in the ERT-1 profile in stations 0+1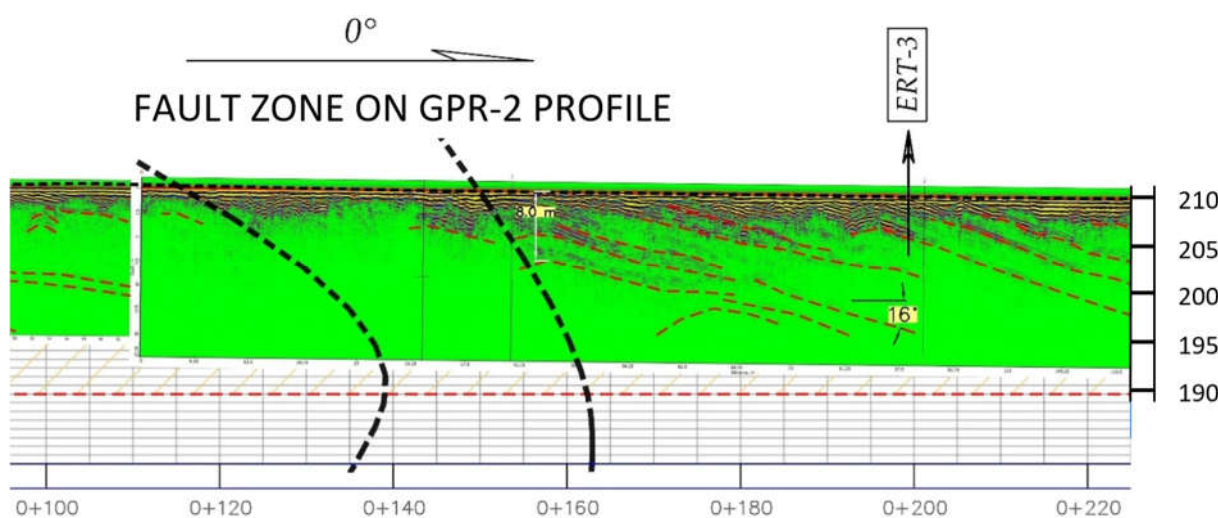40 to 0+165 m. Figure 8 shows that the mentioned anomaly is part of a wider disturbed zone from station 0+080 m to 0+165 m, which is additionally confirmed by the GPR radiogram recorded on the same geophysical profile. On the GPR radiogram, in the parts outside the disturbed zone, layer discontinuities with a layer inclination in the direction of the geophysical profile axis of 12° are visible, while inside the disturbed zone, the cracks are irregularly distributed and have approximately horizontal inclinations. For this zone, it can be assumed that it results from a fault, where the marginal areas along the fault wings are significantly eroded (Figure 8). In the hydrogeological sense, the detected fault zone represents a more significant weathering zone that can represent an accumulator, an underground water aquifer. It is known that the dolomitic rock in the reservoir has weakly permeable bedding planes. Therefore, the space of the fault enables the drainage of seepage and underground water. That is why it is recommended to drill a new well within the mentioned fault zone (Figure 9).
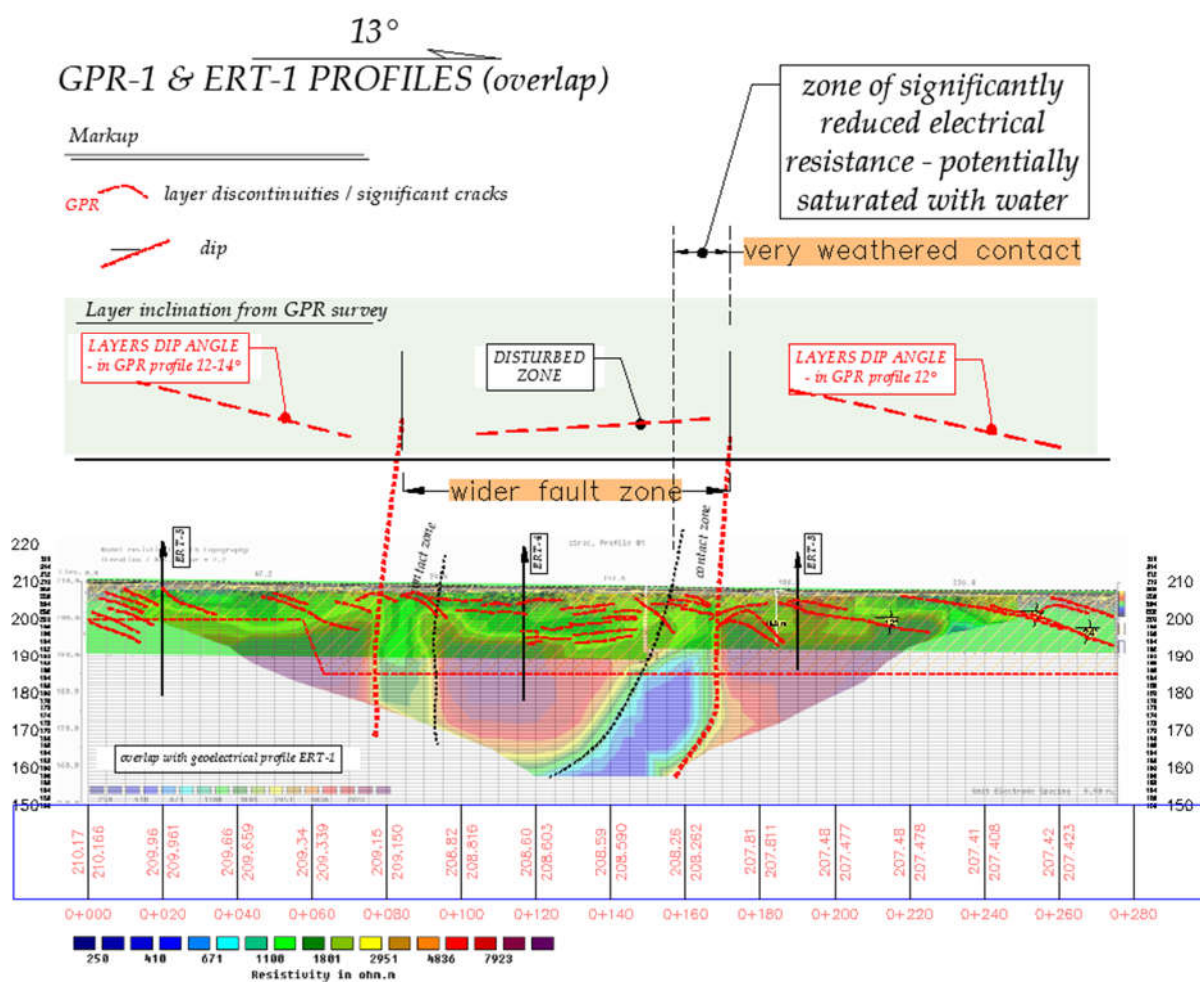
Figure 8. Composite ERT-1 electric tomography profile superimposed on GPR-1 georadar profile.

5   Conclusion

In the southern part of the Čelina exploitation field, geophysical surveys were carried out to locate the place of accumulation and discharge of underground water into the surface mine. Based on the results of the geophysical tests, a fault zone was detected, and the drilling of an exploration-exploitation well

is recommended. The drilling depth will not be designed in advance, but will be defined during drilling, depending on the structure of the aquifer.The recommended position of the well coincides with the location of the established rupture along the edge of the fault wing. The purpose of the exploratory well at the proposed micro-location is to confirm the presence of water within the fault contact. In the case of confirmation that these are permeabe water bearing rock bodies, the well would be equipped as a pumping well from which it would be possible to pump significant amounts of water. The assumption is that by pumping the well, the piezometric pressures within the aquifer around the well will be sufficiently reduced, resulting in a decrease in saturation and water spilling over a wider area of the disturbed fault zone.

Figure 9. Recommended position for drilling of an exploration-exploitation well.

References

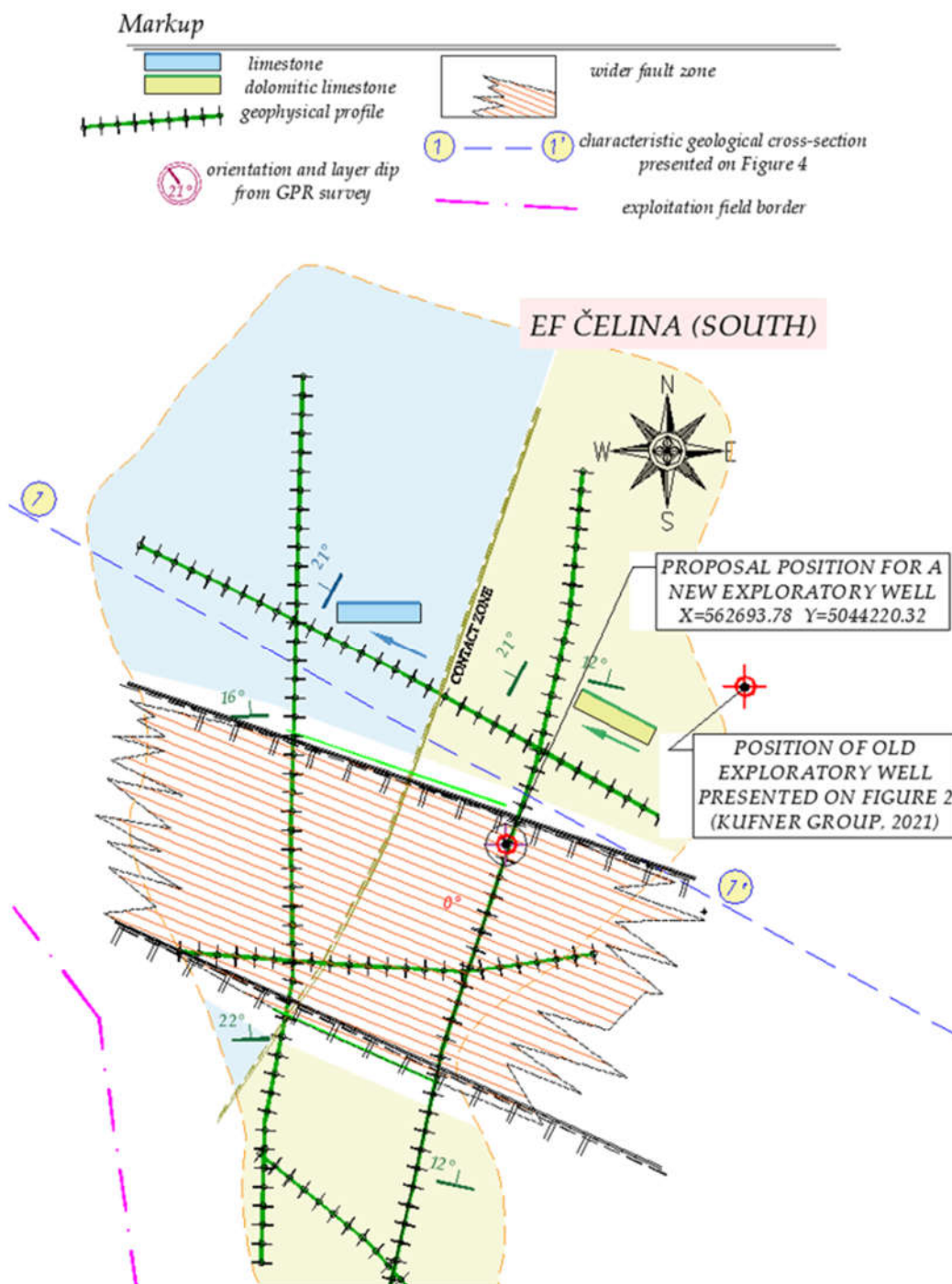Abd El-Gawad, A.M.S.; Helaly, A.S.; Abd El-Latif, M.S.E. Application of geoelectrical measurements for detecting the ground-water seepage in clay quarry at Helwan, southeastern Cairo, Egypt. *NRIAG Journal of Astronomy and Geophysics*. 2018, 7:2, 377-389, DOI: 10.1016/j.nrjag.2018.04.003.

Foti, S.; Parolai, S.; Albarello, D.; Picozzi, M. Application of Surface-Wave Methods for Seismic Site Characterization. *Surveys in Geophysics*. 2011, 32, 777-825.

Jamičić, D. *Basic geological map of Croatia M 1:100000, sheet L 33-95 Daruvar*. Institute for geological surveys from Zagreb (Croatia), 1989.

Jug, J.; Grabar, K.; Strelec, S.; Dodigović, F. Investigation of Dimension Stone on the Island Brač— Geophysical Approach to Rock Mass Quality Assessment. *Geosciences*. 2020, 10, 112. https://doi.org/10.3390/geosciences10030112.

Kufner Group. *Drilling campaign June/July 2021: Drilling core analysis for mining field Čelina*. Author: Martin Erich Lang. Sirač, Croatia, 2021.

Loke, M.H.; Chambers, J.E.; Kuras O. *Instrumentation, electrical resistivity. In Solid Earth Geophysics Encyclopedia*. 2nd ed. Editor: Gupta, H. Berlin, Germany, 2011. Springer. pp. 599-604.

Loke, M.H. *Rapid 2D resistivity & IP inversion using the least-squares method*. In RES2dINV program Manual. 4th ed. Geotomo software: Gelugor, Penang, Malaysia, 2019. pp. 74-82.

Marinelli, F.; Niccoli, W. Simple Analytical Equations for Estimating Ground Water Inflow to a Mine Pit. *Ground Water*. 2000, 38, 311-314. DOI: 10.1111/j.1745-6584.2000.tb00342.x.

OSSGA (Ontario Stone, Sand & Gravel Association). Water Managemet in Quarries. 2016 Available online: www.ossga.com (accessed on 6 May 2024).

Palmström, A. *RMi – a rock mass characterization system for rock engineering purposes*. Ph.D. Thesis, Oslo University, Norway, 1995, 400 p.

Park, C.B.; Miller, R.D.; Xia, J. Multichannel analysis of surface waves. *Geophysics*.1999, 64, 800-808.

Sobko, B.; Haidin, A.; Lozhnikov, O.; Jarosz, J. Method for calculating the groundwater inflow into pit when mining the placer deposits by dredger. *E3S Web of Conferences*. 2019, 123, 01025. DOI: 10.1051/e3sconf/201912301025.

Strelec, S.; Mesec, J.; Grabar, K.; Jug, J. Implementation of in-situ and geophysical investigation methods (ERT & MASW) with the purpose to determine 2D profile of landslide. *Acta Montanistica Slovaca*. 2017, 22/4, pp. 345-358.

Surinaldu, L.; Rao, V.; Ramesh, G. Assessment of groundwater inflows into Kuteshwar Limestone Mines through flow modeling study, Madhya Pradesh, India. *Arabian Journal of Geosciences*. 2011, 6. DOI: 10.1007/s12517-011-0421-5.

CHARACTERISTICS AND INTERLAYER SLIP STRUCTURE CONTROL OF COAL AND GAS OUTBURST IN BAIJIAO COAL MINE

WENQING SUN[1], QIHUA ZHAO[2], SHEQIN PENG[3], TIANHAI ZHANG[4], CHUNFU LIU[5]

[1] *State Key Laboratory of Geohazard Prevention and Geoenvironment Protection, Chengdu University of Technology, China;College of Engineering, Sichuan Normal University, China;College of Environment and Civil Engineering, Chengdu University of Technology, China, safety_sun@sicnu.edu.cn*

[2] *State Key Laboratory of Geohazard Prevention and Geoenvironment Protection, Chengdu University of Technology, China, zhqh@163.com*

[3] *State Key Laboratory of Geohazard Prevention and Geoenvironment Protection, Chengdu University of Technology, China, psq306@163.com*

[4] *College of Engineering, Sichuan Normal University, China, thzhang@sicnu.edu.cn*

[5] *Sichuan Coal Industry Group Limited Liability Company, China, 609168545@qq.com*

Abstract

In order to discuss the control effect of interlayer slip structure on coal and gas outburst in Baijiao Coal Mine. Based on the characteristics of stress and macroscopic deformation and destruction，In this paper，interlayer slip structures were classified into two categories (plastic deformation interlayer slip structures, fracture deformation interlayer slip structures) and four subcategories (plastic deformation interlayer slip structures, fracture deformation interlayer slip structures, sliding-damaged interlayer slip structures, derived interlayer slip structures). Combined with the types and distribution characteristics of coal and gas outburst in Baijiao Coal Mine，conclusions are drawn that interlayer slip structure makes coal thickness and coal seam spacing change dramatically, forms tectonic coal, and generates a large number of hidden faults. It makes the coal and gas outburst parameters change mutationally, and makes the coal and gas outburst concentrated and continuous. The interlayer slip structure area is also a concentrated area of coal and gas outburst.

Keywords

Coal and gas outburst, Interlayer slip structure, Characteristics, Impact, Baijiao Coal Mine

1 Introduction

Gas outburst refers to a geological phenomenon in which underground combustible gas is suddenly released under the action of ground stress. It is a common type of geological disaster in the construction of urban infrastructure such as coal mining, urban underground space development, subway, tunnel and underground pipeline construction, roads, Bridges and large buildings. Based on the study on the control of gas outburst by stratiform slip structure, this paper not only studies the engineering geological problems of coal mine safety, but also hopes to help geological and geotechnical engineers better evaluate the stability of underground rock strata through the mechanism of gas outburst, and provide reference and reference for the management and control of gas in the design, construction and operation of underground engineering.

The interlayer slip structure is very developed in the coal seam and its roof and floor[1],[2],[3],[4]. It causes solid staterheology[5],[6]and serious damage to coal seam and roof and floor[7],[8]. Scholars have done a lot of research on the basic characteristics of mine interlayer slip structure[9],[10],[11],[12], the

influence of interlayer slip structure on coal seamrheology[13],[14],[15],[16], the influence of interlayer slip structure on the change of coal thickness[17]and the control effect of interlayer slip structure on gas outburst[18],[19],[20],[21],[22],[23],[24] .

Baijiao coalmine located at the west end of the Gongchang Anticline, the west end and south wing of the Shuanghe Compound Anticline. It generally S-type toppling fan-shaped monoclinic structures (see Figure 1), small and medium-sized faults are developed in the field with NE-trending. Abroad and gentle anticline spreads in the central part, With NWW-NE undulating strike,dip direction NE , and dip angle 7~ 26°. The Upper Permian Xuanwei Formation is the main coal-bearing strata, thickness 130m. All of the 5- 14 layers of coal are anthracite. The coal layer belongs to the close distance coal seam group, with the B_2 and B_4 coal seams minable in the whole area, and B_3 coal seam locally minable. There are 5 districts in the second mining level of Baijiao Coalmine .
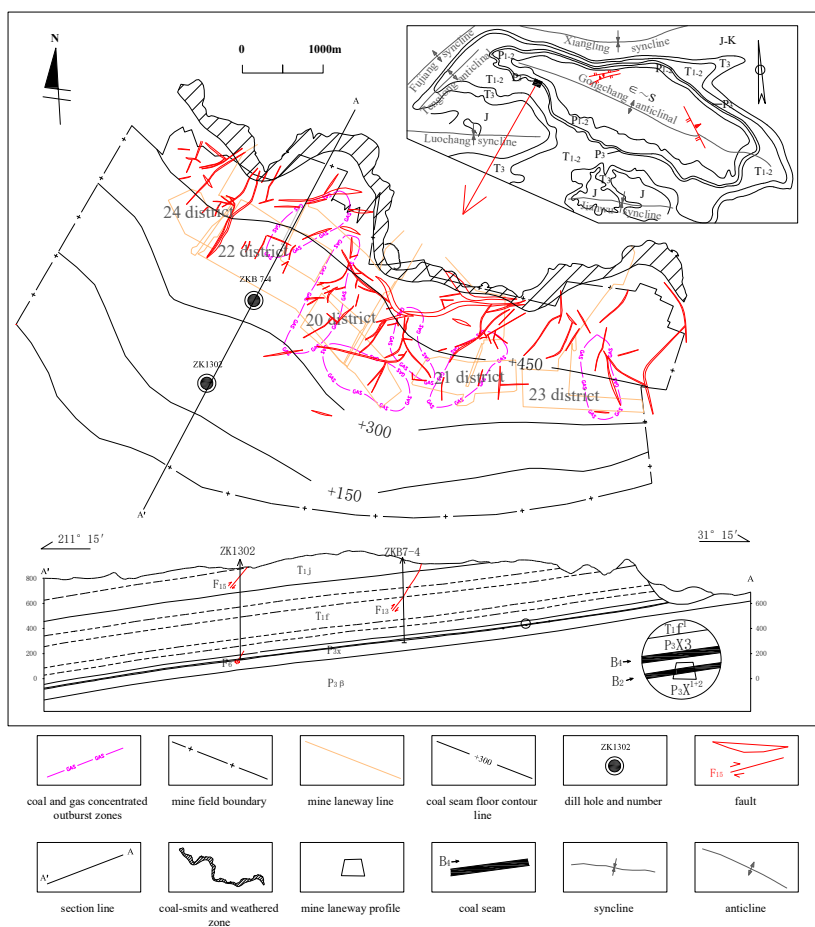
Figure 1. Geological survey and mining area distribution map of Baijiao Coal Mine

Baijiao coal mine, Located in the mountainous area of southwest China, has complicated geological structure, and interlayer sliding is common in coal measure strata. A lot of coal and gas outburst occurred in the process of coal mine production.Based on the study of the characteristics of coal and gas outburst, the characteristics of interlayer slip structure and their relationship, the paper summarizes the control effect of interlayer slip structure on coal and gas outburst. In order to provide scientific basis for preventing and reducing coal and gas outburst and coal mine safety production.

2   Methods
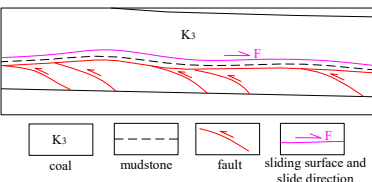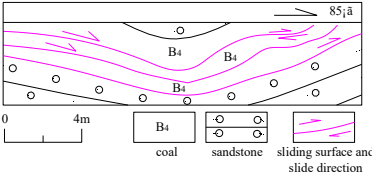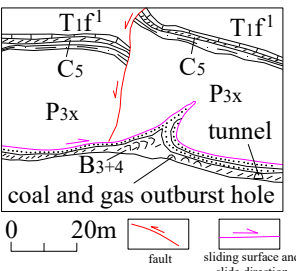
2.1 Baijiao coal mine interlayer slip structure

The interlayer slip structure is a special geological structure developed in the coal-bearing strata,

refers to the intra-layer crumpling, intra-layer faults and their derived structures caused by interlayer slip. It is an interlayer shear deformation and failure zone formed in the ' weak layer ' during the development of bending-slip folds.

The interlayer slip structure has caused drastic changes in coal thickness and coal seam spacing, formed a shear zone along the coal seam and deriving a large number of hidden faults in Baijiao coalmine. According to the characteristics of coal seam stress, macroscopic deformation and failure characteristics, the interlayer slip structure is divided in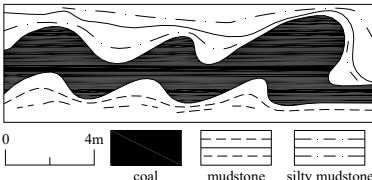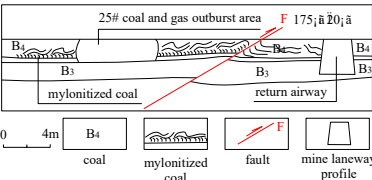to two categories : interlayer slip deformation structure and interlayer slip failure structure (see Table 1). and the interlayer slip deformation structure is divided into plastic deformation interlayer slip structure and rupture deformation interlayer slip structure, the interlayer slip failure structure is divided into sliding failure interlayer slip structure and derived interlayer slip structure.

Table 1. Type of interlayer slip structure in Baijiao coalmine

Type	Graphs	Features
plastic deformation interlayer slip structures	plastic deformation interlayer slip structures a	low damage degree of coal strata, Flow plasticity
	fracture deformation interlayer slip structures b	no sliding section, no relative isplacement, mylonitic coal seam is formated, Brittleness
fracture deformation interlayer slip structures	sliding-damaged interlayer slip structures c	a certain obvious sliding surface, coal rock is broken, Brittleness
	derived interlayer slip structures d e	independent fault systems, the coal seam and rock layer are damaged, Derivative structure

2.1.1 Plastic deformation interlayer slip structure

This kind of interlayer slip structure is mainly characterized by flow plasticity and low damage degree of coal strata (see Table 1.a). The soft coal strata between the hard strata are bent, resulting in plastic flow deformation. The whole form is banded similar to waves sliding along a certain direction without sliding surface, and the horizontal extension is not far. The horizontal fold in the layer can be formed when the sliding is strong.

2.1.2 Fracture deformation interlayer slip structure

This kind of interlayer slip structure is mainly characterized by brittleness, mylonitic coal seam is formated in the layer by coal rock deformation and coal structure failure. There is no sliding section, no relative displacement, and the roof and floor of the coal seam are complete. Such as the 14112 working face is atypical case (see Table 1.b).

2.1.3 Sliding-damaged interlayer slip structures

This kind of interlayer slip structure is mainly characterized by brittleness, the coal rock layer is staggered along a certain obvious sliding surface, and the coal rock is broken. The layer sliding surface is mostly developed along the layer, and the occurrence is basically consistent with the coal seam. The sliding zone is narrow while the coal thickness gradually changes and extends far, and the horizontal displacement is small in a short distance.

For example, a wavy shear zone along the coal seam is formed in B4 coal seam (see Table 1.c), where the coal thickness and seam spacing of "weak section" change greatly by interlayer shear action.

2.1.4 Derived interlayer slip structure

This kind of structure is a derivative structure, which is mostly manifested as a hidden fault. There are independent fault systems in the upper and lower layers of coal respectively match with the interlayer slip structure, and the coal seam and rock layer are damaged to varying degrees near the fault.

For example, There area group of small reverse faults at K3 bottom carbon plate in 1172 working face. When they extending to the interlayer slip surface, the faults no longer extend upward and disappear quickly, forming a special phenomenon of K3 coal seam floor complex and normal in the layer (see Table 1.d).

Another example is that there is a normal fault developed in the overlying Feixianguan Formationthe. The interlayer slip phenomenon is remarkable, the fault plane (belt) is closed and the fault disappears when he close to or enters the coal measure interlayer slip tectonic belt (see Table 1.e).

2.2 Gas dynamic phenomenon in Baijiao Coalmine

2.2.1 Types of coal and gas outburst in Baijiao Coal Mine

There are 229 coal and gas outbursts have occurred since June 1966 in Baijiao coalmine，including 211 medium and small outbursts (see Table2) . Large and extra-large outbursts mainly occur at the second mining level. The average amount of outburst coal is 164.93 t per time,and the gas is 12038.04 m^3 . The maximum amount of coal outburst is 2777 t, and the gas is 497513 m^3. The maximum distance of gas countercurrent is 1340 m. Rock cross-cut coal uncovering outbursts is not much but the strength is large. the coal and gas outburst in Baijiao Coalmine can be divided into four types : sudden dumping of coal, sudden pressing of coal, coal and gas outburst, gas ejection.

Table 2. Coal and gas outburst intensity statistics of Baijiao coalmine

coal and gas outburst scale	Outburst coal and rock quantity/T	Number of outbursts / times		
		excavation face	Mining Working Face	total
small outburst	＜100	120	39	159
medium outburst	100~500	46	6	52
Large outburst	500~1000	11	0	11
Extra-large outburst	≥1000	7	0	7
total		184	45	**229**

2.2.2 Distribution characteristics of coal and gas outburst in Baijiao coalmine

Coal and gas outburst in Baijiao coalmine has the characteristics of shallow initial outburst depth, independent layer in vertical direction and concentrated distribution in plane.

The initial outburst depth only 128 meters, the outburst frequency and intensity increase rapidly with the increase of buried depth. For example, Among the seven extra-large coal and gas outbursts, the second level (+ 450m ~ + 300m elevation) occurred six times, and the first level (above + 450m elevation) occurred only once.

Vertically, coal and gas outbursts have occurred in all mined coal seams. The first B4 mining coal seam with 156 outbursts(accounting for 68.1%) is the most likely to outbursts. The outburst strength of B2 coal seam is large once the outburst occurs, mostly at the most concentrated part of the ground stress and mining stress under the coal pillar of B4 coal seam.(for example, the 2074 conveyor lane occured 6 outbursts is excavated in the structural area and under the coal pillar, with an average strength of 494t and a maximum strength of 2266t. Where the coal thickness increases to 6m locally). The outburst risk enhance and strength Increase when the upper and lower coal seams change sharply or the coal spacing less than 1.0moreven combined. (for example,A large outburst occurs when the coal is uncovered in 20102 material return airway, with the outburst intensity 2777t and the gas emission 179.15m3 / t. That's because The B2 and B4 coal seams combined and folding broken seriously due to the interlayer slip structure, and coal thickness increases sharply.).

On the plane, the coal and gas outbursts mainly (89 %) occurred in 6 concentrated outburst zones (see Figure 1). Not only the outburst intensity is large, but also the points are dense (94 % of the outbursts above 100t occur in the concentrated zone). The outbursts concentrate at the bottom of valleys, cliffs and geological structures, and often approximately parallel to the fault zone.

3   Results

The interlayer slip effect is one of the main driving forces for the formation of ' tectonic coal ' in Baijiao Coal Mine, which leads to the destruction of coal structure, the decrease of strength, the increase of porosity and the increase of gas pressure. It has a certain control effect on the distribution of coal and gas outburst danger zone (zone), and is the culprit leading to coal and gas outburst.

3.1 Interlayer slip structure influence on coal seam texture and structure

3.1.1 Coal thickness and coal spacing changes

Affected by the interlayer slip structure, the coal thickness and spacing of Baijiao coalmine changed sharply and abruptly, the B4 coal seam thickness increased from 0.64 m to 4.20 m, and B4 ~ B3 coal seam spacing changed from 0.00 ~ 11.80 m(see table3).

Table 3. Coal seam thickness and spacing list of Baijiao coal mine

Coal seam number& parameter	coal seam thickness（m）				coal seam distance（m）		
	B_4	B_3	B_2	B_1	$B_4\sim B_3$	$B_3\sim B_2$	$B_2\sim B_1$
Min~Max	0.64~4.20	0~2.20	0.64~4.30	0.20~1.50	0~11.80	0.20~9.20	1.40~14.0
Average	1.10	0.92	2.04	0.50	3.50	2.50	6.00

Gas accumulate easyly near the coal ridge formed by the coal seam wrinkles and thickens. the tectonic stress concentrated due to a dramatically changes in layer spacing, and the outburst risk increases also . More than half of the coal and gas outbursts (119 times, accounting for 51.9 %) occurred in the high fluctuation region, or the transition area of coal thickness from thick to thin orthinto thick. And, the thickness is more than 2.0 m of large outburst and super large outburst.

For example, the interlayer slip structure starting from Fs27 normal fault (H =8 ~10m) and sliding along the top of B2 coal seamand bottom carbon extends to form a interlayer slip structure zone with a length of 1000 m and a width of about 80 ~ 100 min 2092 wind lane. The interlayer slip structure zone forming a serious coal and gas outburst zone where the distance between B2 and B4 coal seams changed from 10 m to combined layer, and the thickness increased. And there are 15 outbursts where the coal seam spacing decreased suddenly from 10.0 m to 2.0 m in about 100 m near the east wing of the 2092 mining working face(see B-B ' section in Fig. 2).
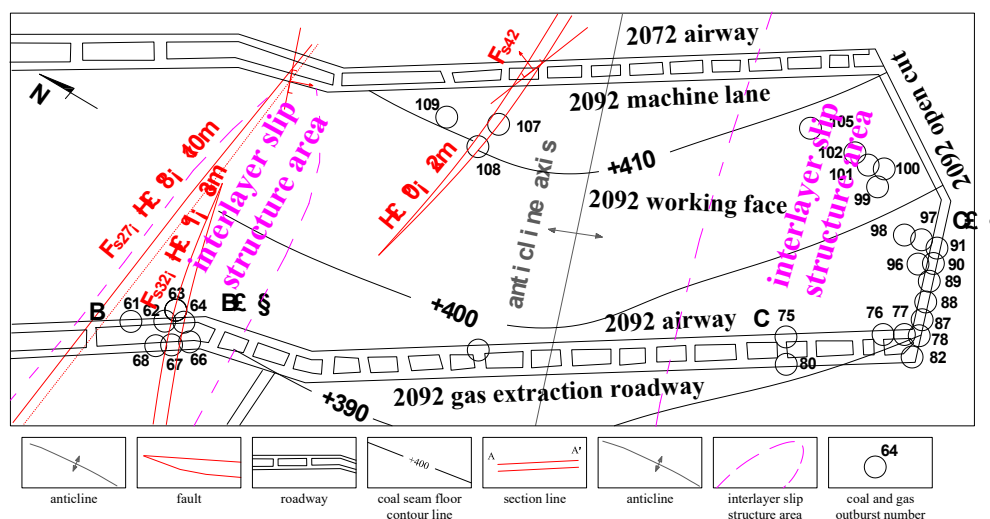
Figure 2. Interlayer slip structure and gas outburst of 2092 mining working face

3.1.2 Forming tectonic coal

In Baijiao coalmine,the coal fracture, the coal particles surface area and the gas adsorption capacity of coal increases exponentially as the tectonic coal is formed under the action of interlayer slip. The later in-situ stress causes the coal seam fracture smaller and the permeability decrease, forming a high gas area near the interlayer slip structure belt. For example, There are 118 times of coal and gas outburst occurs in soft coal stratification, and a gas outburst will occure when the soft coal layer thickness greater than 0.2-0.6m in Baijiao coalmine, the thicker the coal seam and the more structural coal is, the greater the outburst strength and outburst risk are. Coal and gas outburst is serious in the 14112 working surface as the interlayer slip structure forms a relatively stable mylonite layer in the coal seam(see Figure 3) .
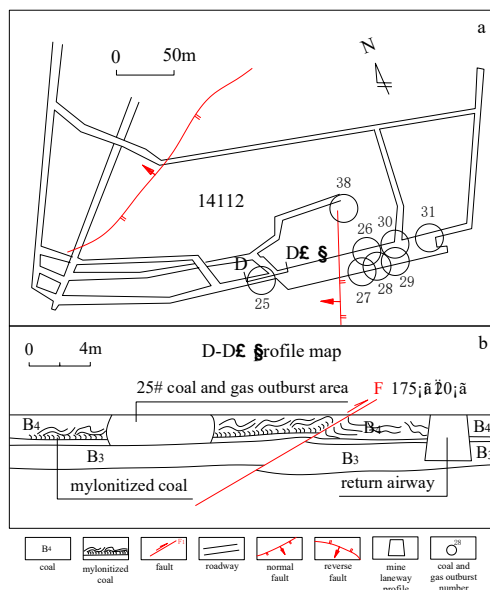
Figure 3. Coal and gas outburst in 14112 mining working face

3.1.3 The formation of hidden faults

In Baijiao coalmine, a large number of hidden faults are derived from the interlayer slip structure as the coal seam has small dip angle. The coal and rock mass is damaged to varying degrees near the fault. The derived faults are mainly compressive and torsional, which play a role in blocking the coal seam gas, and the gas is locally enriched, resulting in uneven gas distribution. For example, the coal and rock strata in the 2052 interlayer slip tectonic zone are seriously broken, and the coal and gas outburst are concentrated (see Figure 4). In particular, the coal structure damage is more serious and the fault surface (zone) close is more tighter near the inflection point of the overlying strata fault entering the interlayer slip zone, which often causes local gas accumulation (see Table 1.e).
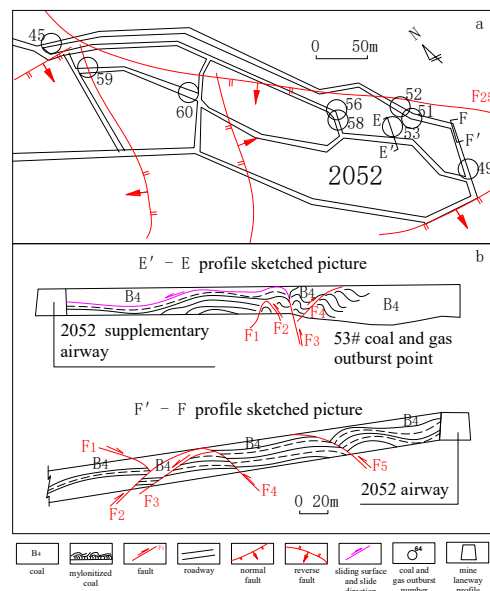
Figure 4. Buried fault and Coal and gas outburs in 2052 working face

3.2 Interlayer slip structure impact on coal and gas outburst

3.2.1 Abnormal parameters of coal and gas outburst

The risk of coal and gas outburst is usually characterized by parameters such as the initial velocity of gas emission ($\triangle P$), the firmness coefficient of coal (f), the wrinkle coefficient (K) and the comprehensive index (R). $\triangle P$ is the difference between the cumulative gas emission amount at 60s and the cumulative gas emission amount at 10s after the coal sample with a certain particle size and mass adsorbs gas under 0.1 MPa pressure and then releases gas to a fixed volume space. $\triangle P$ indicates the speed of gas emission from coal, reflecting the pore structure and microscopic damage degree of coal. The greater the $\triangle P$, the higher the risk. f is the breaking ratio formed by hammering a certain quality and particle size coal sample when a certain quality drop hammer falls freely from a certain height. fis a relative index. The smaller the f is, the lower the strength is, and the greater the outburst risk is. K is the ratio of the thickness of the soft medium layer to the total thickness of the coal seam. The higher the K value is, the more unstable the coal seam is , and the easier outburst it is; r is a comprehensive index, which reflects the permeability, damage degree, gas emission rate and rock stress state of the coal body in front of the working face.

It is easy to form cataclastic coal, granulated coal, mylonitic coal and other tectonic coal in the interlayer slip effect. The values of $\triangle P$, f, K and R in the interlayer slip zone are significantly different from those normal zone. Each parameter has obvious transition at the boundary of the normal zone, the coal-free zone, the thinning zone and the outburst zone (see Figure 5).

Figure 5. Characteristic of coal and gas outburst risk parameters at interlayer slip structure zone
（B-B´Geological section，2092 mining working face）

3.2.2 Coal and gas concentrated outburst

The interlayer slip structure belt controlles more than 70 % of coal and gas outbursts is usually also a coal and gas outburst belt. For example, the coal and gas outburst is mainly distributed in two concentrated zones in 2092 working face (see figure 2): One is a interlayer slip structure zone near the FS27 noirmal fault, with a length of 1000m and a width of about 80~100m. The coal and gas outburst occurred 17 times in this zone with an average strength of 441t (The 62 ~ 64 outburst characteristics are shown in table 4). Another one is a small interlayer sliding structure belt near the 2092 air roadway, open-off cut and working face.

Table 4. Characteristics of 62 ~ 64 coal and gas outburst in 2092 air roadway

number	Coal	Coal and rock/t	Gas emission quantity/m3	burial depth/m	geologic features
62	B_2	233	13770	438	B4 thinning, B2 thickening,Coal seam bedding disorder in fault fracture zone , gas content changes greatly.
63	B_4	21	491	475	Reverse fault, soft coal seam, structural disorder. CH4 anomaly
64	B_4	100	2338	475	Sudden thickening of coal seam, soft, CH4 anomaly. Sticking drill when drilling

3.2.3 Continuous outburst of coal and gas

There are more than 6 times continuous outbursts with a space about 10- 15m in the process of driving air roadway and gas channel in 14112 working face(see figure 4). Also, The coal body was continuously and suddenly pressed out 30 m along the strike during the initial mining period of the 2092 working face(see table 1), and there are about 17 coal and gas outbrust occurred continuously in the thinned zone of the intersliplayer near the Fs27 normal fault in the 2092 air roadway (see B-B ' section in figure 2), and 18 coal and gas outbrust occurred with 150 m in the wind roadway, open-off cut and mining face (see C-C ' section in figure 2).

4 Conclusion

1）The coal and gas outburst in Baijiao Coal Mine has the characteristics of shallow initial outburst depth, independent layer in vertical direction and concentrated distribution in plane. the coal and gas outburst in Baijiao Coalmine can be divided into four types : sudden dumping of coal, sudden pressing of coal, coal and gas outburst, gas ejection.

2）The interlayer slip structure of Baijiao coal mine is divided into two categories : interlayer slip deformation structure and interlayer slip failure structure . and the interlayer slip deformation structure is divided into plastic deformation interlayer slip structure and rupture deformation interlayer slip structure, the interlayer slip failure structure is divided into sliding failure interlayer slip structure and derived interlayer slip structure.

3）the interlayer slip structure causes sharply and abruptly changes in coal thickness and coal spacing, forming a shear zone along the coal seam, and deriving a large number of hidden faults, resulting in an increasing risk of coal and gas outburst.

4）The parameters such as ΔP,f, K and R have obvious transition at the boundary of the normal zone, the coal-free zone, the thinning zone and the outburst zone.
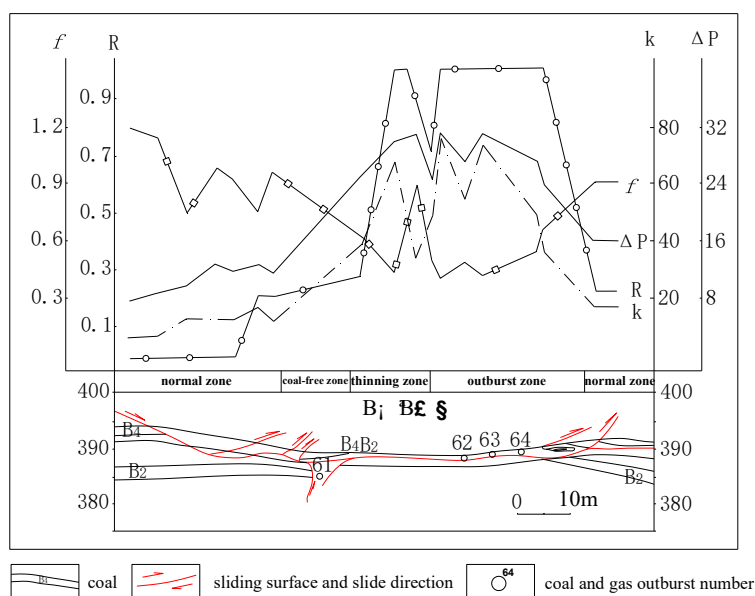
The interlayer slip structure area is also the concentrated area of coal and gas outburst. The interlayer slip structure causes the phenomenon of coal and gas outburst concentratedly and continuously.

References

[1] Evans H and Brown K M. Coal structures in outbursts of coal and firedamp conditions. *The Mining Engineer* 1973;132(148): 171-179.

[2] Hathaway TM and Gayer RA. Thrust-related permeability in the southwales coalfield. *Coalfield Methane and CoalGeol* 1996;109:121-132.

[3] Frodsham K and Gayer RA. Variscan compressional strctures within the main productive coal-bearing strata of SouthWales. *Journal of the Geologicak Society* 1997;154:195-332.

[4] Frodsham K and Gayer RA. The impact of tectonic deformation upon coal seams in the SouthWalescoalfield. :implications for the eprediction of outburst prone coals and sub-stand coals size-products. *International Journal of Coal Geology* 1999;38:297-332.

[5] Wang Guiliang, Zhu Yanming. On rheology of coal seam. *Journal of China University of Mining and Technology* 1988;17 (3):16-25. (in Chinese)

[6] Wang G L, Xu F Y, Long R S, Zuo D K. Mine structure prediction. Beijing: *Coal Industry Press*.

1993;28- 143.

[7] Shephred J, Rixon J K, Griffithis L. Outburst and geological structure in coal mines:areview. *International Journal of Rock Mechanics and Mining Sciences* 1981;18 (4):267-283.

[8] Hargraves A J. Instantaneous outburst of coal and gas:a review. *Journal of the South African Institute of Mining and Metallurgy* 1983;285 (3):1-37.

[9] Cao Yunxing, Peng Lishi, Hou Quanlin. Basic characteristics of faults along coal seam and their geological significance. *Geological Review* 1993;39 (6):522-528.

[10] Li Huoyin. Major and minor structural features of a bedding shearzone along a coal seam and related gas outburst, Ping-dingshancoal field, northern China. *International Journal of Coal Geology* 2001;47 (2):101- 113.

[11] Ju Yiwen, Jiang Bo, Wang Guiliang and Hu Chao. Characteristics of microcosm of interlayer-gliding tectonic coal-tectonite and their stress-finite strain analyses. *Chinese Journal of Geology* 2004;39(1):50-62.

[12] Ju Yiwen, Hou Quanlin, Jiang Bo, Wang Guiliang and Fang Aimin. Group patterns of interlayer-gliding structure and faults and deformation conditions in coak seams of the HaiZi mine,norther AnHui. *Chinese Journal of Geology* 2006;41(1):35-43.

[13] Wang Guiliang, Zhu Yanming. On rheology of coal seam. *Journal of China University of Mining and Technology* 1988;17 (3):16-25. (in Chinese)

[14] Wang Guiliang, Xu Fengyin. Restrictions of layer slip structureon formation and concentration of gas in Furong Mining Area. *Journal of China University of Mining and Technology* 1999;28 (1):9-13.

[15] Cao Yunxing, Peng Lishi. Basic types of coal faults and their controlling effect on gas outburst belt. *Journal of China Coal Society* 1995;20 (4):413-417.

[16] Ju YiWen, Jiang Bo, Wang GuiLiang, et al. Microscopic characteristics and stress-strain analysis of coal and rock mass in stratified slip structure. *Scientia Geologica Sinica* 2004;39 (1):50-62.

[17] Le Qilang, Yang Weimin, Qiu Desheng, et al. Distribution characteristics of thin coal belt in coal seam and its relationship with stratiform slip structure. *Coal Science and Technology* 2009;37

(11):106- 109.

[18] Farmer I W and Pooley F D. A hypothesis to explain the occurrence of outbursts in coal, basedon a study of West Wales outburst coal. *International Journal of RockMechanics and Mining Sciences* 1967; 4:189- 193.

[19] Alpern B. Tectonics and deposit in coalfields: a bibliographicalstudy and examples of application. *International Journal of RockMechanics and Mining Sciences* 1970;7 (1):67-76.

[20] Williams R J and Rogis J. Ananalysis of the geological factor sleading to outburst-prone conditions at collinsville, Queensland. In :*Australians Institute of Mining and Metallurgy. Ed. The Occurrence. Prediction and Control of Outbursts in coal mines Symposium.* Parkville victoria(Australia) 1980 :99- 109.

[21] Shepherd J, Rixon LK and Creasey J W. Analysis and prediction of geological structures associated with outbursts at Collinsville Queensland.bin: *Australian Institute of Mining and Metallurgy.ed. The Occurrence, Predictionand Control of Outbursts in Coal Mines Symposium.* ParkvilleVictoria(Australia) 1980 :157 - 171.

[22] Shepherd J Rixon LK and Griffiths L. Outbursts and geological structures in coalmines: A review. *International Jouranl of Rock Mechanics and Mining Sciences and Geomechanics Abstracts* 1981;18: 267-283.

[23] Bustin R M. The effect of shearing on quality of some coals inthe southeastern Canadian Cordillera Can. *Journal of the SouthAfrican Institute of Mining and Metallurgy* 1982;75:76-83.

[24] Li Kang, Zhong Dalai. Study on the relation between micro-structural characteristics of coal and gasburst. *Acta Geological Sinica* 2000;40 (5):27-34.

Topic 8

Advances in Geological Modelling
for Engineering Applications

KINEMATIC AND BLOCK THEORY ANALYSIS IN DOLOMITIC ROCKMASS FOR DAM-SITE STABILITY

SANJEEV REGMI[1], RANJAN KUMAR DAHAL [2]

[1] *Nepal Electricity Authority, Dudhkoshi Jalvidhyut Company Ltd, Kathmandu, Nepal, regmisanjeev@gmail.com*

[2] *Central Department of Geology, Tribhuvan University, Kirtipur, Kathmandu, Nepal, rkdahal@gmail.com*

Abstract

In the realm of dam-site slope stability assessments, an integrated approach utilizing both kinematic and block theory offers robust and comprehensive insights. Although, each theory possesses its advantage and limitations, the combined approach yields a more holistic understanding of potential failure mechanisms and formulating risk mitigation strategies. Kinematics analysis evaluates the potential movement of individual rock blocks within the rockmass, based on the orientation and properties of discontinuities whereas block theory analyses their stability due to exposed condition. This is the primary concern, ensuring the dam's slope whether rockmass could withstand without failure or excessive deformations that could compromise its integrity. This study is concentrated on dolomitic rock type and hence it considers the possible kartification dissolution, weathering and variable mechanical properties in such rock type. The geological model was prepared from geological study and eight scan lines were drawn on each bank of Dam-site of Tanahu Storage Hydroelectric Project. It was later verified with finite element analysis method. It was concluded that the maximum safe slope for dam-site slope is between 45 and 50 degrees. There was slope deformation on the right bank of the Dam-site after excavation. Hence, slope excavation should be conducted after considering safe slope for gaining required slope stability of the area.

Key words

Kinematic and Block Theory Analysis, dolomitic rock type, karst topography, finite element analysis method, maximum safe slope.

1   Introduction

In the realm of dam-site slope stability assessments, an integrated approach utilizing both kinematic and block theory offers robust and comprehensive insights (Liang et al., 1999), (Gurocak et al., 2008) and (Kulatilake et al., 2011). Block theory is a geometrically based set of analyses that determine where potentially dangerous blocks can exist in a geological material intersected by variously oriented discontinuities in three dimensions (Goodman, 1995) and (Wang & Ni, 2014). It applies ideally to hard, blocky rock in which blocks of various sizes may be potential sources of load and hazard during construction. The rockmass condition is the main intrinsic factor that determines the probability of failure of rock so the proper assessment of actual condition is vital in rock engineering and designing infrastructures (Jaeger, 1979). The geometry of dam, such as its slope angle and thickness, is main concern as it resist the hydrostatic pressure and other forces (Adamo et al., 2020). In other hand, geology of foundation of dam and permeability condition of ground are primary concerns during (Cambefort, 1977) (Warner, 2004) investigation period. All these factors plays crucial role in dam safety.

The mechanical and chemical properties of the bedrock affects the stability of slope highly (Wahlstrom, 2012). The fractured and jointed rockmass of dolomite is vulnerable to karst formation if rockmass gets exposed to ground water (Abdullatif, 2010) and Gauri & Bandyopadhyay, 1999). The proper investigation is required for the identification of rockmass properties and in-situ conditions. This works

includes studies of its geological factors like joint orientation, spacing, rockmass strength, deformability, weathering, erosion and groundwater conditions.

The aim of the present study is to apply integrated approach of kinematic and block theory for the slope assessment of dam-site in Tanahu Storage Hydroelectric Project. It is further verified by simulation works using Rocscience's Phase -2.

The project consists of a concrete gravity dam with a maximum height above foundation level of 140m. The project is located in Tanahu district of Gandaki state (State no 4) of Nepal as shown in Fig1. The major structures of the project are located on the right bank of the Seti River and Madi River. The dam-site of the project lies on the Hatisude and the powerhouse area lies on Bateni.
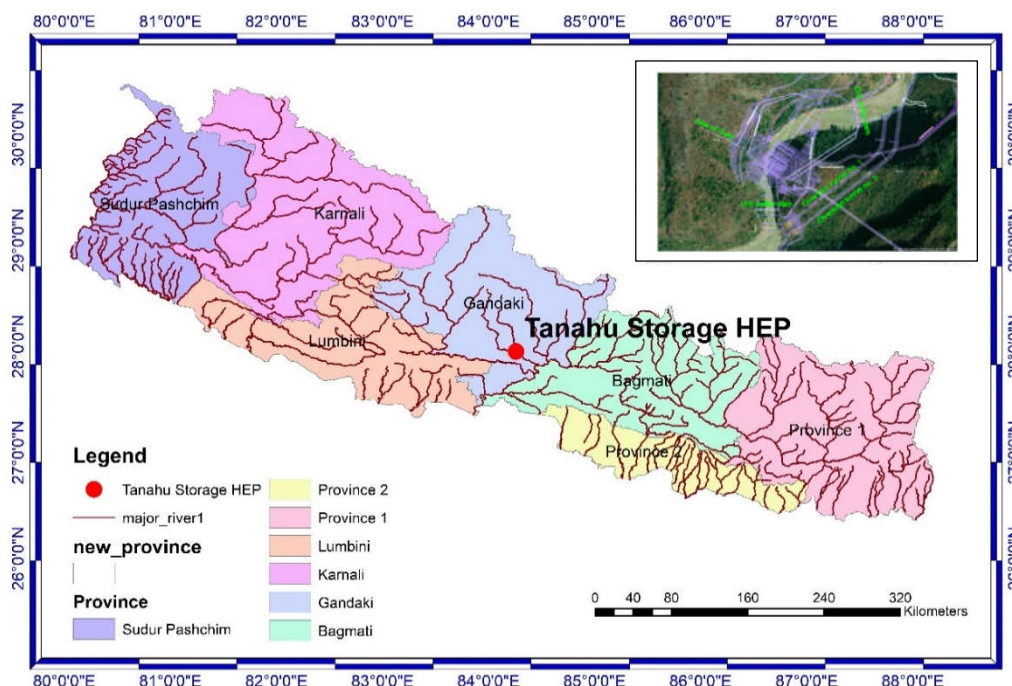
Figure 1. Location map of Tanahu Storage Hydroelectric Project

The predominant lithology of the area is Benighat Slate and Dhading Dolomite of Palaezoic to Precambrian belonging to Nawakot group. The massive dolomite is intercalated with thin bed of dark gray colored slate in dam-site area. The dam – axis is mainly consisting of thickly foliated, massive, yellowish colored, fractured, slightly weathered dolomite. Dolomite is well exposed along the Seti river bank on the dam-site area. The general trend of the bedrock is 340° to 10°. Benighat Slate which overlains the dolomitic rockmass, consists of dark bluish-gray to black, soft weathering, and highly cleaved slates and phyllites. The slate is abundant on the elevation of 500 amsl.
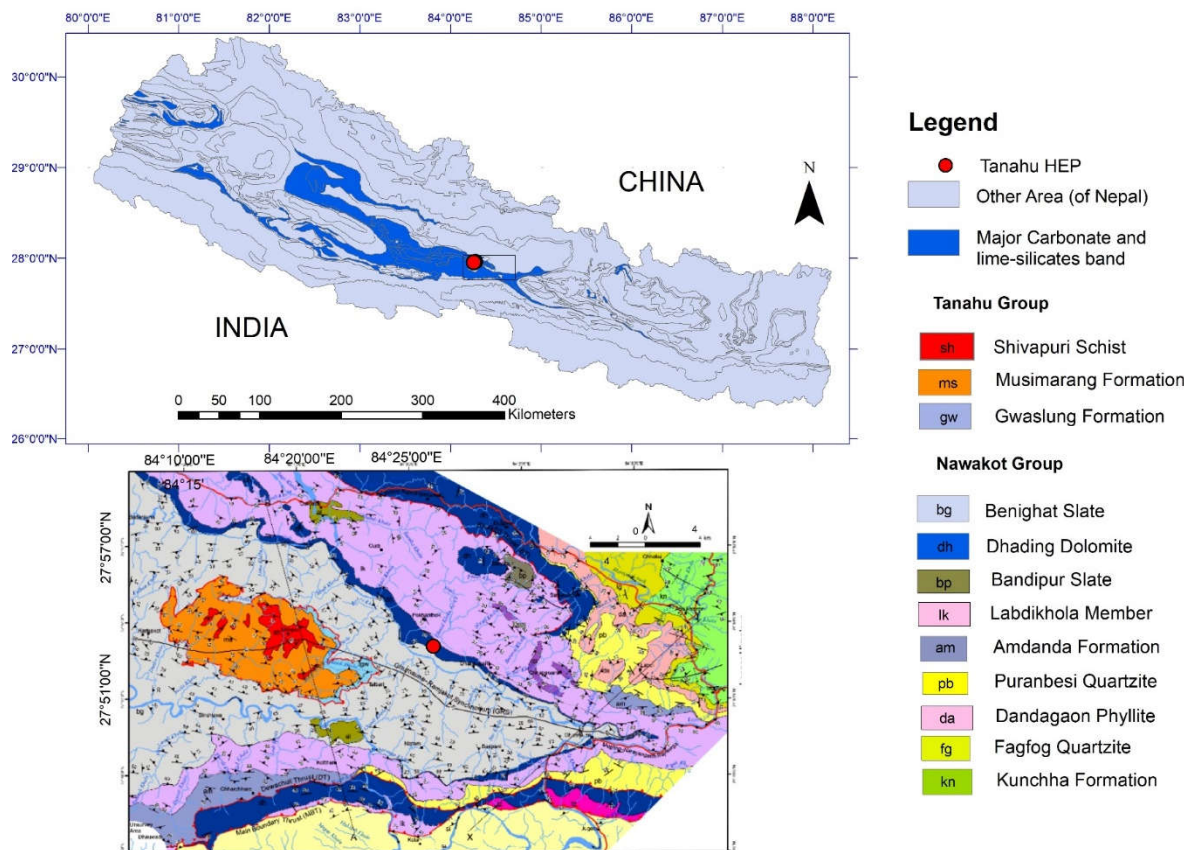
Figure 2. Regional Geological Map   of Damauli (after Dhital, 2014 and Paudyal and Paudyel 2013)

2   Methods

Block theory and kinematics analysis are applicable for finding out possible failures and determining Maximum Safe Slope Angle (MSSA) of rock slope (Goodman, 1976). In this study, altogether eight profiles with four profiles on each bank were taken on the hillslope of dam-site area. However, 50 joints for each scanline, which most represented the ground conditions, were processed utilizing a commercially available software DIPS 7.0 (Rocscience, 2017), based on equal angle stereographic projection and major joint sets and analysed with respect to the attitude of discontinuity. During this process, the blocks were categorized into finite (completely bounded by discontinuities) or infinite (extending to the rock mass boundary). The evaluation of potential blocks movements was analysed with respect to the orientation of discontinuities and the excavation geometry which provides insight to determine whether blocks could slide or fall under gravity or external forces. In addition, Phase-2 (Rocscience, 2017) was used to simulate the hillslope of the dam.

2.1 Kinematics Analysis

More than 500 representative joint-sets were collected from the study area for kinematic analysis of discontinuities. The analysis is related with the geometry of discontinuities in rockmass with respect to cut slope. The equal angle stereographic projection was applied during the analysis. Plane, wedge and toppling failure mode were identified. These failure modes were calculated on the different possible slope of cut direction with varaiable dip amount. The Table 1 shows the properties of selected scanline at the dam-site.

Table 1. Properties of selected Scanlines at the Dam-site

Scanline Number	Location	Rock face Dip Dir/Dip Amount(°)	Scanline trend/Plunge(°)	Rock Mass
LD-1	Weir	107/70	115/0	Fair
RD-1	Weir	300/52	295/0	
LD-2	Dam-Axis	115/56	110/0	Fair
RD-2	Dam-Axis	300/56	290/0	Fair
LD-3	U/S Dam-Axis	080/46	095/0	Fair
RD-3	Intake	265/55	270/0	Fair
LD-4	U/S Dam-Axis	128/35	115/0	Fair
RD-4	Diversion Inlet	240/45	260/0	Fair

2.2 Block Theory Analysis

The blocks that were formed due to joint's orientation, natural hillslope and cutslope were categorized into infinite block, finite (non-removable block), finite (removable block but stable without friction), finite removable block (stable with sufficient friction) and finite, removable block unstable without support). The factor of safety of block was analysed by SWEDGE (2017). There were three prominent discontinuities in selected eight scanlines. The aim of the block theory analysis is to find out the MSSA of the respective block of the scanline. The representative discontinuity is actually the mean of the discontinuity orientation and different cut slope direction that were determined as per possible cutslope for the selected scanline.
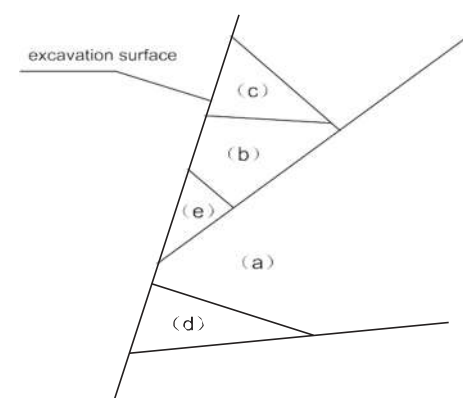
- •Infinite
- •Finite, nonremovable, tapered
- •Finite, removable stable without friction
- •Finite, removable, stable with sufficient friction
- •Finite, removable unstable without support

Figure 3. Types of blocks in a surface cut infinite (type V block), tapered (type IV block), stable (type III block), potential key block (type II block), and key block (type I block).

2.3 Finite Element Method

A continuum approach of Finite Element Method is the most used approach for numerical modelling of hillslope. In this approach, the rockmass is meshed applying elements of triangular or quadrilateral shape in 2D. The fixed boundary condition was adopted for the simulation except cutslope area. The failure criterion of intact rock which has been developed by Hoek-Brown (Hoek & Brown, 1980) was applied for simulation. The equation of the failure of intact rock is shown in Eq. (1):

$$\sigma 1 = \sigma 3 + \sqrt{mi\frac{\sigma 3}{\sigma c} + 1} \tag{1}$$

where σc is the Uniaxial Compressive Strength (UCS) of the material and mi is a material constant which defines the brittleness of intact rock. In this equation, $\sigma 1$ and $\sigma 3$ are major and minor principal stresses respectively, that act on the rockmass and are used to define the rock mass failure envelope in the Hoek –Brown failure criterion. This criterion allows simulation of varied stress-strain behaviour from simple elastic to elasto-plastic or time-dependent creep. This method can give information about the deformations at working stress levels and is able to monitor progressive failure including overall shear failure (Griffiths & Lane, 1999). Similarly, the Mohr Coulomb failure criterion was used for simulation of colluvial deposits. It is commonly used in geotechnical engineering to predict the behaviour of soils and rocks, but it can be also used for other materials. The criterion is based on the principal of maximum shear stress. According to this principle, a material will fail when the maximum shear stress on any plane within the material reaches a critical value. The Mohr - Coulomb failure criterion is expressed mathematically as shown in Eq. (2)

$$\Gamma = c + 6n * \tan(\varphi) \tag{2}$$

Where ɼ is the maximum shear stress on a plane within the material c, $6n\ and\ \varphi$ are cohesive strength of material, normal hear stress acting on the plane and the angle of friction between the particles of the material respectively. A Geological Strength Index (GSI) is used in conjunction with other parameters such as the rock quality (Q) and the rock mass rating (RMR) to evaluate the stability of a rock mass. A modification in the GSI approach was proposed for tectonically disturbed flysch rock masses (Hoek & Brown, 2019) and (Marinos & Hoek, 2000). In this study, the strength reduction method (SRM) was used to do this case study ((Fu & Liao, 2010) and (Hoek & Brown, 2019). The equations for calculating the rock mass with constants mb, s and a is in Eq. (3), Eq. (4) and Eq. (5).

$$m_b = m_i \exp\left(\frac{GSI-100}{28-14D}\right) \tag{3}$$

$$s = exp\left(\frac{GSI-100}{9-3D}\right) \tag{4}$$

$$a = \frac{1}{2} + \frac{1}{6}\left(e^{-GSI/15} - e^{-20/3}\right) \tag{5}$$

whereas D is a factor that depends upon the degree of disturbance to which the rock mass is subjected to blast damage and stress relaxation tests. In this study, the value of D is considered as zero.

3   Results

3.1 Kinematics Analysis

There are three different failures modes that have been identified in RD-2 region as shown in Table 2. The calculated final MSSA including and excluding toppling failure are between 45° and 60° and between 70° and 45° respectively at cut slope dip directions 95–290°. Similarly, the MSSA for plane sliding, wedge sliding and toppling failure and the final MSSA for the other seven regions were calculated, including and excluding toppling failure, selecting appropriate scanline orientation data from Table 2 with the kinematic analysis.

Table 2. MSSA for three basic failure modes under different possible cut slope dip directions at RD-2 region

Cut Slope Direction	MSSA for plane sliding			MSSA for Wedge			MSSA for Toppling			Dominant Mode		Final MSSA	
	D1	D2	D3	I1I2	I2I3	I3I1	T1	T2	T3	Including Toppling	Excluding Toppling	Including Toppling	Excluding Toppling
95	72	70	90	90	60	90	90	90	90	*D1,D2, I2I3*	*D1,D2*	60	70
110	72	70	90	90	50	90	90	90	90	*D1,D2, I2I3*	*D1,D2*	50	70
115	72	70	90	90	50	90	90	90	90	*D1,D2, I2I3*	*D1,D2*	50	70
125	72	70	50	90	45	90	90	45	90	*D1,D2, D3, I2I3,T2*	*D1,D2,D3*	45	50
260	72	70	50	90	45	90	90	90	90	*D1,D2,D3,I2I3*	*D1,D2,D3*	45	70
270	72	70	50	90	90	90	90	90	90	*D1,D2,D3,I2I3*	*D1,D2,D3*	50	50
280	50	50	60	90	90	90	90	90	90	*D1,D2,D3,I2I3*	*D1,D2,D3*	50	50
290	72	70	50	90	90	90	90	90	90	*D1,D2,D3,I2I3*	*D1,D2,D3*	50	50

Table 3. MSSA for three basic failure modes under different possible cut slope dip directions at LD-2 region

Cut Slope Direction	MSSA for plane sliding			MSSA for Wedge			MSSA for Toppling			Dominant Mode		Final MSSA	
	D1	D2	D3	I1I2	I2I3	I3I1	T1	T2	T3	Including Toppling	Excluding Toppling	Including Toppling	Excluding Toppling
95	90	90	90	90	90	90	90	90	90			90	90
110	90	90	90	90	90	90	90	90	90			90	90
115	90	90	90	90	90	90	90	90	90			90	90
125	90	90	90	90	90	90	90	90	90			90	90
260	90	90	90	90	77	90	90	90	90	*I2I3*		77	90
270	90	90	90	80	72	90	90	90	90	*I1I2, I2I3*		72	90
280	90	90	90	80	68	90	90	90	90	*I1I2, I2I3*		68	90
290	90	90	90	79	65	90	90	90	90	*I1I2, I2I3*		65	90

In Table 3, the MSSA is claculated for three different failure modes at LD-2 regions of dam-axis. The calculated final MSSA including and excluding toppling failure range between 65° and 90°.

Table 4. Percentage number of possible failure under each mode of instability for different slope regions

Region	Possible Cut-slope Dip Direction Range	Slope Ratio Vertical/Horizontal	Plane Sliding			Wedge Sliding			Toppling Failure		
			1:1	1:0.70	1:0.48	1:1	1:0.70	1:0.48	1:1 1:0.48	1:0.70	
		Slope Angle (°)	45	55	65	45	55	65	45	55	65
LD-1	90-100		0.00	2.00	3.00	0.00	7.69	13.97	7.84	13.73	13.73
LD-1	110-125		0.00	1.96	5.88	0.31	5.73	13.43	11.76	17.65	21.57
LD-2	90-125		0.00	0.00	1.89	0.00	0.22	0.80	18.87	18.87	18.87
LD-2	260-290		0.00	0.00	0.00	0.00	0.29	4.73	18.87	18.87	18.87
RD-1	260-270		0.00	0.00	3.92	0.00	1.26	4.23	27.45	29.41	33.33
RD-1	280-290		0.00	1.96	3.92	0.00	1.97	6.05	27.45	29.41	33.33
RD-2	260-270		0.00	0.00	0.00	0.00	0.00	0.43	14.29	14.29	14.29
RD-2	280-290		0.00	0.00	0.00	0.00	0.00	0.00	6.12	6.16	6.16
LD-3	90-100		0.00	0.00	7.14	0.13	3.12	6.12	12.50	17.86	26.78
LD-3	110-125		0.00	3.57	8.93	0.00	3.71	13.85	16.07	25.00	33.43
LD-4	90-100		0.00	2.53	3.80	0.10	2.24	4.97	11.39	18.98	20.25
LD-4	110-125		0.00	0.00	0.00	0.00	1.01	3.11	17.72	25.31	30.38
RD-3	260-270		0.00	0.00	0.00	0.00	0.08	0.41	14.00	14.00	14.00
RD-3	280-290		0.00	0.00	0.00	0.00	0.08	0.16	6.00	8.00	8.00
RD-4	260-270		0.00	0.00	4.00	0.08	0.49	2.70	30.00	32.00	36.00
RD-4	280-290		0.00	0.00	2.00	0.00	0.16	4.25	24.00	24.00	30.00

The percentage of the possible plane sliding, wedge sliding and toppling sliding for discontinuities were obtained using Dips software of rocscience. Toppling failure percentage is maximum that is 36% in RD-4 scanline at cutslope direction 280-290° and slope angle 65°. In RD-2, the percentage of toppling failure in cutslope angle 65°, 55° and 45° is 33.33%, 28.41% and 27.45% respectively (Table 4). The cut slope direction varies between 280° and 290° in RD-2.
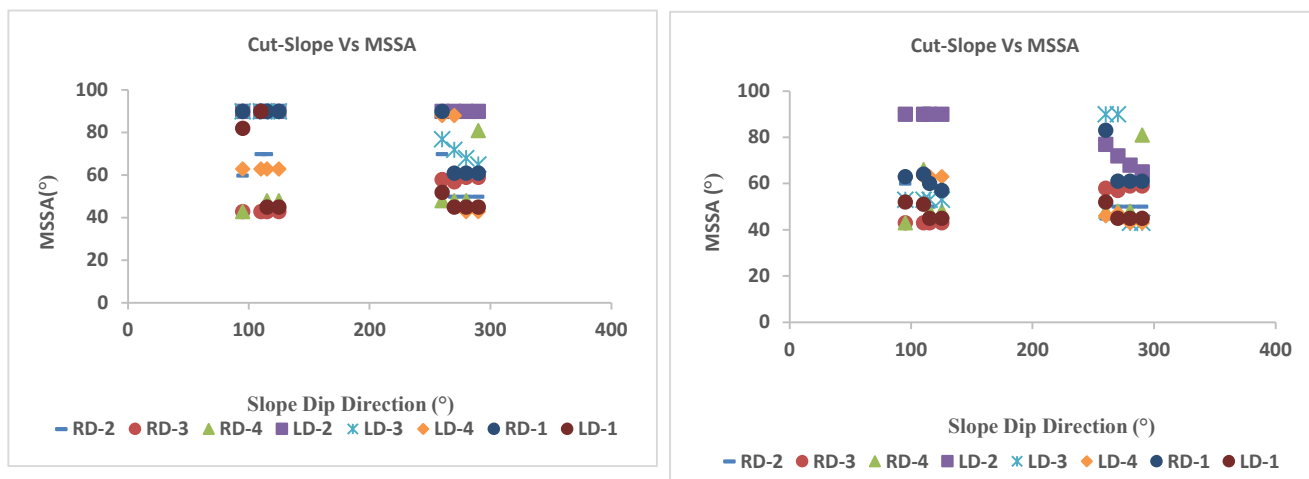

Figure 4. The relationship between MSSA (°) with Slope Dip Direction (°) including and exluding toppling failure.

The results given in Figure 4(a) and Figure 4(b) exhibits clearly that the final MSSA excluding toppling failure and including toppling failure is similar for slope direction between 95° and 125°. In the same region, the final MSSA including toppling failure is slightly lower in comparison to excluding toppling failure for slope direction between 260° and 290°. The final MSSA will range between 43° and 90° for wide range of slope direction between 95° and 290°, if other factors like the slope region, rock mass type and with or without toppling failure are not considered. The selected scanline with cut slope direction and cut slope angle for representative discontinuities the above results are obtained.

3.2 Block Theory Analysis

The block theory analysis was carried out in two region RD-2 and LD-2, which represents right and left slope of the Dam-site on three representative joint sets as tabulated in Table 2 only two discontinuities could be calculated at one time (Kulatilake et al., 2011). For the respective cutslope direction, key-block (type I block), sliding blocks and Type III block (stable block) were identified as shown in Table 5 and Table 6. In LD-2 region and RD-2 regions, possible slope direction ranges between 260° - 290° and 095° - 290° respectively. The factor of safety of key-blocks S23 and S12, which were formed in region LD-2 due to excavation, were greater than one and hence they were stable. Similarly, only one key - sliding block S23 was depicted in RD-2 which was unstable for the cutslope direction 095° and dip amount 70°. The clarity of three discontinuities is comparatively less than four and five discontinuities. It could be taken as the limitation of the study. However, analysis were carried out carefully so it actually represents the ground condition.

Table 5: Final failure modes and corresponding MSSA for different slope dip directions at LD2 region

Cut Slope Dip Dir. (°)	Discontinuity Combination	Key-block sliding mode	Potential key block	Type III block	Case MSSA	Final MSSA	Key block (sliding mode, safety factor)
260	*J1,J2,J3*	011(S23,77)		100	90	77	011(S23, >1)
	J1,J2 J3		110 (S12)	001	90		
	J1,J2,J3		101(S31)				
270	*J1,J2,J3*	110(S12,72)		100		72	110(S12, 3.4)
	J1,J2J3	011(S23,72)		001		72	011(S23, >1)
	J1,J2,J3		101(S31)		90		
280	*J1,J2,J3*	110(S12,68)		100		68	110(S12, 3.9)
	J1,J2,J3	011(S23,68)		001		68	011(S23,>1)
	J1,J2,J3		101(S31)		90		
290	*J1,J2,J3*	110(S12,65)		100		65	110(S12,3.3)
	J1,J2,J3	011(S23,65)		001		65	011(S23,>1)
	J1,J2,J3		101(S31)		90		

Table 6: Final failure modes and corresponding MSSA for different slope dip directions at RD2 region

Cut Slope Dip Dir. (°)	Discontinuity Combination	Key-block sliding mode	Potential key block	Type III block	Case MSSA	Final MSSA	Key-block (sliding mode, safety factor)
095	*J1,J2,J3*		110(S12)	100	70		
	J1,J2 J3	011(S23,60)		010			011(S23,0)
	J1,J2,J3		101(S31)		70		
110	*J1,J2,J3*			100	70		
	J1,J2J3	011(S23,50)		010	70	50	011(S23,>1)
	J1,J2,J3						
125	*J1,J2,J3*			100			
	J1,J2,J3	011(S23,45)		010,010	50, 45	45	011(S23,>1)
	J1,J2,J3			001			
260	*J1,J2,J3*		110(S12)	100	72		
	J1,J2,J3	011(S23,45)		010	70	45	011(S23,>1)
	J1,J2,J3		101(S31)	001	50		
270	*J1,J2,J3*		110(S12)	100	72		
	J1,J2,J3	011(S23,50)		010, 010	70, 90	50	011(S23, >1)
	J1,J2,J3		101(S31)	001	50		
280	*J1,J2,J3*		110(S12)	100	50		
	J1,J2,J3	011(S23,90)		010, 010	50	50	011(S23,>1)
	J1,J2,J3		101(S31)	001	60		
290	*J1,J2,J3*		110(S12)	100	72		
	J1,J2,J3	011(S23,90)		010, 010	70	50	011(S23,>1)
	J1,J2,J3		101(S31)	001	50		

3.3 Finite Element Analysis

The physical parameters of colluvial deposits, fractured rockmass and dolomite were carefully selected for simulation. The laboratory tests of the bedrock including UCS and Point Load Test (PLT) were extracted from the laboratory tests of samples and geotechnical investigation report of Tanahu Storage Hydroelectric project of Nepal Electricity Authority (Table 1). The simulation of Phase2 was carried out in the right bank of the dam-site in RD-2 region. After excavation, the strength factors of rockmass is reduced below 1 at the upper and bottom of hillslope.

Table 7: Physical and Mechanical Parameters used for Simulation

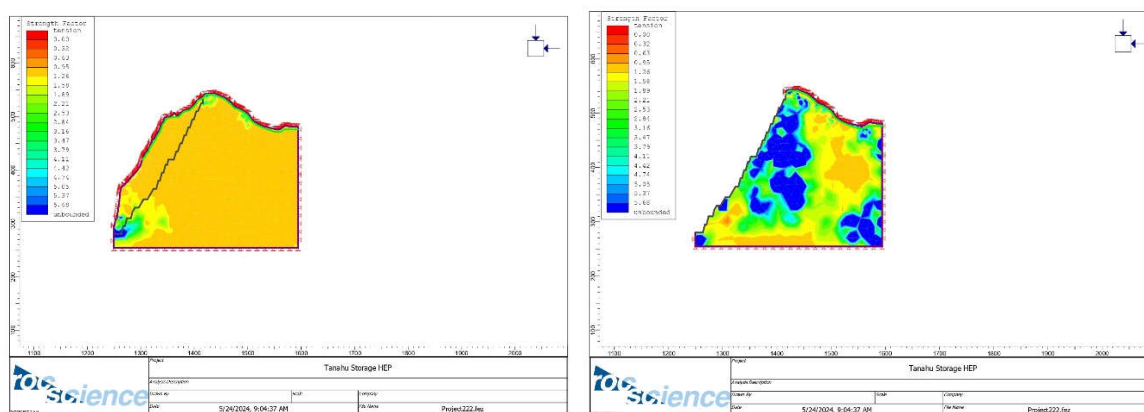|	GSI	Hoek - Brown Parmeters				Deformation Modulus (GPa)	Poisson's Ratio	Internal Friction Angle (°)	Cohesion (MPa)
		m_i	m_b	s	a				
Massive Dolomite	70	12	1.408	0.0067	0.501	15	0.2	50	3.8
Fractured Dolomite	60	10	0.57	0.0013	0.503	2.5	0.3	40	1.8

Figure 5. Strength Factor in the Right Bank of Hill-slope of Dam without excavation and with excavation

4 Conclusion

In this study, geological information were collected from field investigations, laboratory tests and other lithological information from report and literature. The dam-site belongs to Dhading Dolomite which is is characterized by thickly bedded structured to massive structured; rock is moderate to strong fracture. The predominant dip direction of discontinuities are NNE, NWW and SWW with dip amount varies between 25° and 65°. Three prominent discontinuities were thoroughly studied by identifying eight scanline from both sides of dam-site for kinematics and block theory analysis. The rock types encountered in left side is comparatively stronger, less fractured and more stable than right side. The friction angle of Dolomite is between 42° and 45°.

In this study, the output of MSSA from kinematics analysis matches with MSSA acquired from block theory analysis. The block theory analysis identifies two key blocks S12 and S23 for LD-2 region and final MSSA of cutslope direction 260°, 270°, 280° and 290° are 77°, 72°, 68° and 65° respectively. However, only one key block S23 is depicted for sliding mode. Along cut slope direction 095°, key block shows possible failure at dipping angle 60°. The final MSSA ranges between 45° and 50°. Toppling failure percentage is maximum that is 36% at RD-4 with cutslope 280-290° (dip direction) and slope angle 65°. The scanline RD-2 where we could observe displacement after excavation (Table 12) exhibits 33.33%, 28.41% and 27.45% toppling failure for cutslope angle 65°, 55° and 45° respectively for cut slope direction 280-290°.

The simulation of Phase2 was carried out in the left bank of the Dam-site in RD-2 scanline. After

excavation, the strength factor of hillslope is below 1 at the upper and bottom of hillslope. Hence, careful excavation with necessary support measures is required in regions namely RD-1, RD-2, RD-3 and RD-4.

Acknowledgements

References

Abdullatif, O. (2010). Geomechanical properties and rock mass quality of the carbonate Rus formation, Dammam dome, Saudi Arabia. *Arabian Journal for Science and Engineering*, *35*(2), 173.

Adamo, N., Al-Ansari, N., Sissakian, V., Laue, J., & Knutsson, S. (2020). Dam safety: General considerations. *Journal of Earth Sciences and Geotechnical Engineering*, *10*(6), 1–21.

Cambefort, H. (1977). The principles and applications of grouting. *Quarterly Journal of Engineering Geology and Hydrogeology*, *10*(2), 57–95.

Fu, W., & Liao, Y. (2010). Non-linear shear strength reduction technique in slope stability calculation. *Computers and Geotechnics*, *37*(3), 288–298.

Gauri, K. L., & Bandyopadhyay, J. K. (1999). *Carbonate stone: Chemical behavior, durability, and conservation*. John Wiley & Sons.

Goodman, R. E. (1995). Block theory and its application. *Geotechnique*, *45*(3), 383–423.

Griffith, A. A. (1924). *Theory of rupture*. 55–63.

Griffiths, D., & Lane, P. (1999). Slope stability analysis by finite elements. *Geotechnique*, *49*(3), 387–403.

Gurocak, Z., Alemdag, S., & Zaman, M. M. (2008). Rock slope stability and excavatability assessment of rocks at the Kapikaya dam site, Turkey. *Engineering Geology*, *96*(1–2), 17–27.

Hoek, E., & Brown, E. (2019). The Hoek–Brown failure criterion and GSI–2018 edition. *Journal of Rock Mechanics and Geotechnical Engineering*, *11*(3), 445–463.

Hoek, E., & Brown, E. T. (1980). Empirical strength criterion for rock masses. *Journal of the Geotechnical Engineering Division*, *106*(9), 1013–1035.

Hoek, E., & Diederichs, M. S. (2006). Empirical estimation of rock mass modulus. *International Journal of Rock Mechanics and Mining Sciences*, *43*(2), 203–215.

Jaeger, C. (1979). *Rock mechanics and engineering*. Cambridge University Press.

Kulatilake, P. H., Wang, L., Tang, H., & Liang, Y. (2011). Evaluation of rock slope stability for Yujian River dam site by kinematic and block theory analyses. *Computers and Geotechnics*, *38*(6), 846–860.

Liang, R., Nusier, b, OK, & Malkawi, A. (1999). A reliability based approach for evaluating the slope stability of embankment dams. *Engineering Geology*, *54*(3–4), 271–285.

Marinos, P., & Hoek, E. (2000). *GSI: a geologically friendly tool for rock mass strength estimation*. ISRM-IS.

NEA, 2014. Detailed Engineering Study of Tanahu (Upper Seti) Hydropower Project in Nepal

NEA, 2015. Final Report of Geotechnical Investigation.

NEA, 2021. Engineering Geological Report (Geological Assessment).

Um, J.-G., & Kulatilake, P. H. (2001). Kinematic and block theory analyses for shiplock slopes of the Three Gorges Dam Site in China. *Geotechnical & Geological Engineering*, *19*, 21–42.

Upreti, B. (1999). An overview of the stratigraphy and tectonics of the Nepal Himalaya. *Journal of Asian Earth Sciences*, *17*(5–6), 577–606.

Wahlstrom, E. (2012). *Dams, dam foundations, and reservoir sites* (Vol. 6). Elsevier.

Wang, S., & Ni, P. (2014). Application of block theory modeling on spatial block topological

identification to rock slope stability analysis. *International Journal of Computational Methods*, *11*(01), 1350044.

Warner, J. (2004). *Practical handbook of grouting: Soil, rock, and structures*. John Wiley & Sons.

EXPERIMENTAL AND NUMERICAL MODELING OF SOIL-VEGETATION-ATMOSPHERIC INTERACTION ON SLOPES AND EROSION CONTROL USING BIOPOLYMERS AND VEGETATION

JOSIF JOSIFOVSKI [1], BOJAN SUSINOV [2], ALEKSANDRA N. ATANASOVSKA [3]

[1] *Prof. Dr. University "Ss. Cyril and Methodius" in Skopje, Faculty of Civil Engineering, N. Macedonia, jjosifovski@gf.ukim.edu.mk*

[2] *Assist. Prof. Dr. University "Ss. Cyril and Methodius" in Skopje, Faculty of Civil Engineering, N. Macedonia, susinov@gf.ukim.edu.mk*

[2] *M.Sc. Skopje, N. Macedonia*

Abstract

The impact of climate change on the infrastructure creates serious challenges, especially affecting the stability and safety of the soil-cut slopes. The large temperature variations and more frequent intense rainfalls are the main contributing factors for soil instabilities, erosion, and landslides. This phenomenon is widely known as soil-atmospheric-vegetation interaction is studied. The hypothesis that intense rainfalls significantly impact slope stability has been investigated. Moreover, the application of biopolymers as a naturally-based solution and vegetation for erosion control has been tested. For this purpose, a holistic approach has been employed combining theoretical and experimental results.

The paper presents a unified methodology of physical and numerical modeling, laboratory and experimental tests, on soil slopes subjected to intense rainfalls with biopolymer-treated soil. The obtained results indicate that intense rainfalls significantly impact the stability of the surface layers where erosion occurs, leading to local instability which eventually can develop into a global failure and sliding. The results show that the biopolymer significantly reduces erosion and restricts the run-off water by infiltrating the ground, thus providing surface stability to the slopes and promoting vegetation growth. The tests confirm that the biopolymers significantly enhance the erosion resistance and stabilize the soil thus improving the slope stability.

Key words

Rainfall, Unsaturated soil, Erosion, Slope stability, Naturally-based solution, Biopolymer treatment.

1 Introduction

The influence of climate change in the infrastructure sector is becoming alarming and should not be ignored. Climate change creates several challenges for infrastructure projects regarding their lifespan and transport safety, especially on the soil-cut slopes. The high-temperature variations and intense rainfall are more often seen as triggering factors for instabilities, such as soil sliding and erosion of natural and engineering slopes. This soil-atmospheric-vegetation interaction phenomenon is neglected by engineers in the design process. The interaction is defined by soil wetting or drying due to the atmospheric, thermal, and hydraulic conditions.

Climate change can bring more frequent and intense rainfall that will cause increased soil water content in the surface layers. The soil water content is an important element for the soil stability but also for the vegetation dynamics largely depend on soil water availability, which, in turn, results from several complex and mutually interacting hydrologic processes (Chen et al. 2007). Different vegetation and soil types have different water infiltration capacities. Root systems make the soil more resistant to external

influences. Figure 1 shows slope erosion and local sliding of soil slope on the Miladinovci – Shtip highway in the central part of Macedonia after heavy rainfall on 29 May 2022 (Susinov and Josifovski, 2022). The nearest weather station measured 52 and 43 mm/h for two consecutive 12-hour periods. The national weather monitoring station measured 25.2 mm in one hour and 40.1 mm in 2 hours.

Figure 1. Slope exposed to intensive erosion on the Highway Miladinovci – Shtip, N. Macedonia.

To understand the unsaturated or partially saturated behavior of soils, it is necessary to introduce additional parameters, dependencies, and theories. Moreover, as a comprehensive solution of rainfall-induced slope instabilities, coupled hydro-mechanical analysis needs to be performed.

Natural soil improvement techniques can increase erosion resistance by improving mechanical and hydrological soil properties (Ham et al. 2018). Such is the biopolymeric material produced by microorganisms, algae, plants, etc., which is considered ecological and sustainable. In the past decade, natural polymers have been identified as highly effective polymers that stabilize soil surface structure and improve infiltration (Lentz et al. 1997). Natural polymers are water soluble and when mixed with soil, they can produce increased soil strength, improve cohesion, and reduce water permeability.

Figure 2 shows the erosion resistance model of polymer-treated soil. The gel-like structure of the polymer solution fills the pores and cavities, which reduces the potential for infiltration, and coats the grains, increasing the adhesion and strength (Ivanov et al. 2008). Soils treated with polymer solutions form a solid surface crust that prevents water infiltration and allows free surface runoff without soil erodibility (Cheng et al. 2015). Polymer-treated soils have an additional positive effect on vegetation, primarily due to the absorption and retention of moisture, which stimulates growth (Chung et al. 2018).
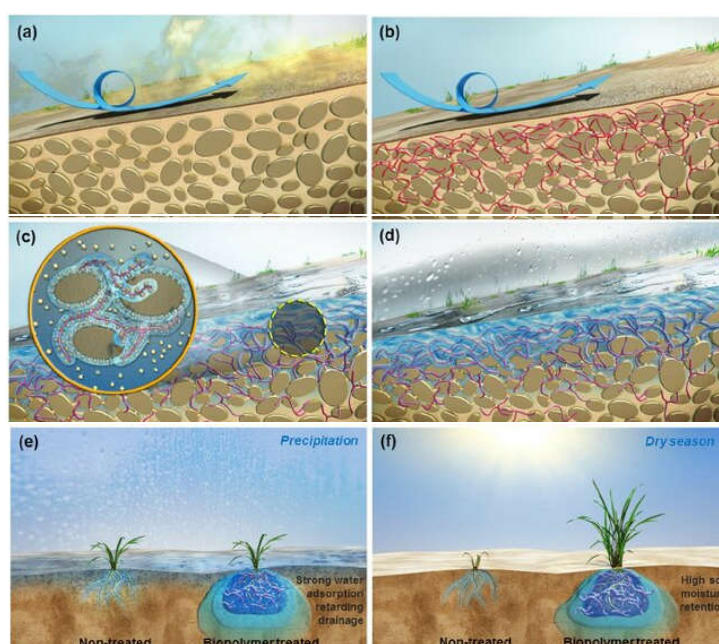

Figure 2. Erosion resistance model of biopolymer-treated soil.

In this study, a biopolymer binder is used as a naturally-based solution for erosion control. The effects are e examined through laboratory and experimental tests. Moreover, the physical and numerical modeling on an example of an ideal slope is employed to describe the complex interaction in the system between the hydraulic, thermal, and mechanical parts using an advanced fully coupled model.

2   Testing Methodology and Results

The testing methodology used in this study has been organized into three stages. In the first stage of the research, the material characteristics and biopolymer-treated soil characteristics are determined through laboratory tests. The biopolymer was applied in two concentrations of 1% and 2% mixed with the soil for a laboratory test and sprayed on the surface of the slopes in the experimental test. The composition and production details of the biopolymer can not be presented in this paper. In the second stage, several experimental tests were performed on a physical model for the untreated and biopolymer-treated slopes subjected to intense rainfall. The model was instrumented to measure several variables and soil characteristics during the testing. Finally, in the last research stage, employing all the previously gathered results a finite element numerical model was used to describe the complex soil-atmospheric-vegetation interaction.

2.1   Laboratory tests

In this study to determine the physical and mechanical properties of the soil around 60 laboratory tests have been performed. Figure 3 shows the grain size distribution curve of the soil of silty sand material that was tested.
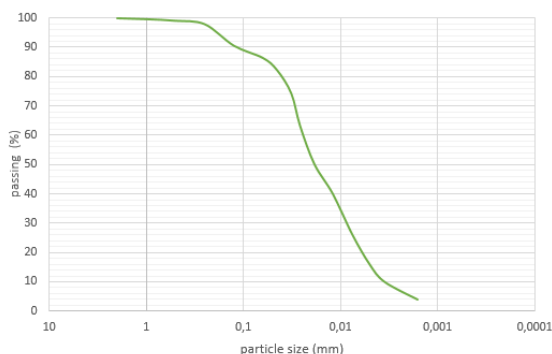

Figure 3. Grain size distribution curve.

The strength-deformation characteristics of the material were obtained through tests of Uniaxial Compressive Strength, Direct shear, Vane, and Oedometer tests. The water permeability has been determined for a pressure of 0.5 bar for saturated samples, Figure 4.

Figure 4. Soil samples from laboratory tests.

Table 1 presents the characteristic values of the material properties of silty sand soil.

Table 1. Physical properties of silty sand soil.

Natural moisture ω [%]	Unit weight γ [kN/m^3]	Specific gravity Gs [/]	Optimal moisture ω_{opt} [%]	Dry unit weight γ_d [kN/m^3]
23.62	18.82	2.67	17.60	15.20

The representative values of the resistance angle and cohesion have been determined as the average value of two series with three samples for untreated and biopolymer-treated soil. Table 2 presents the results of strength-deformation parameters, the angle of initial friction, and cohesion, where improvements of 9.52% and 7.5% are registered, respectively. The compressibility modulus is calculated for a normal stress of 240 kPa and represents an improvement of 36.64% compared with the modulus of untreated soil.

Table 2. Strength and deformation parameters.

Untreated soil			Polymer-treated soil		
ϕ [°]	c [kPa]	M$_v$ [kPa]	ϕ [°]	c [kPa]	M$_v$ [kPa]
29.2	25.9	4648	32.3	28.0	2945

The uniaxial compressive strength (UCS) was determined on samples with dimensions of 5.0 cm by 10.0 cm in series on 1, 7, 14, and 28 days. Tables 2 and 3, present the results of untreated and biopolymer-treated samples.

Table 3. UCS of untreated soil samples.

Day of Testing	Normal stress σ [kPa]	Strain ε [%]
1	435.3	4.0

Table 4. UCS of biopolymer-treated soil samples.

Day of Testing	Normal stress σ [kPa]	Strain ε [%]
1	257.1	3.5
7	1749.9	2.9
14	1132.4	2.6
28	2000.6	2.9

The volume of infiltrated water in the biopolymer-treated sample was 6.71 cm^3 /day, which is 6 times higher than the amount of the natural sample, 1.06 cm^3/day. Hence, biopolymer-treated soil has hydrophobic effects on the soil that allow free flow, unlike natural soil where the water is retained. Therefore, the water permeability coefficient tested for treated soil is 2.20 x 10^{-6} m/s and for the natural soil is 3.47 x 10^{-7} m/s.

2.2 Physical model test

The test has been performed on a large-scale physical model of an ideal slope subjected to intense rainfall with more than 30 mm/h (Susinov et al., 2019). An explanatory photo is shown in Figure 2. In particular, a large-scale model with the following dimensions 400 × 200 × 200 cm was instrumented with three sensors (volumetric water content, pore water pressure, suction) on five different locations in the slope. Additionally, the deformations were scanned by LIDAR equipment and camera, Figure 5.
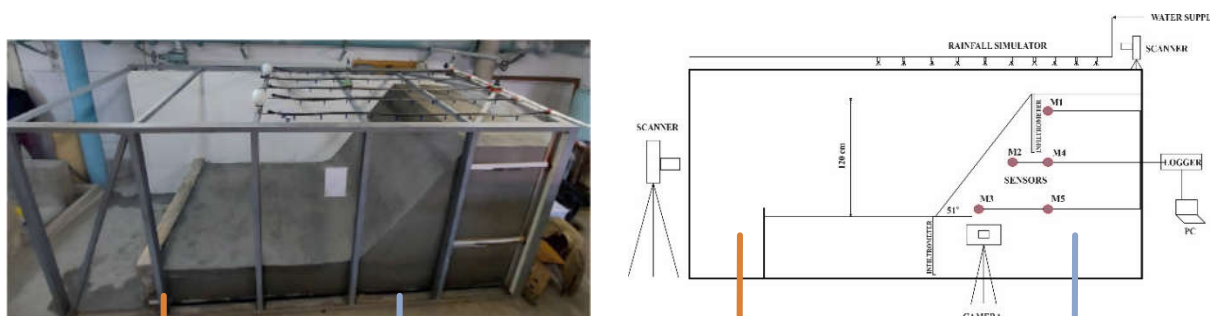
Figure 5. Photo of the physical model and schematic of the measuring equipment and sensors.

In the present study, a selected sandy soil material (Susinov and Josifovski, 2018) has been used with the following mechanical characteristics, unit weight $\gamma=18.2kN/m^3$, resistance angle $\varphi=30°$, and cohesion c=0 kPa. The hydraulic characteristics have been defined through the SWRC and permeability function obtained by specific hydraulic laboratory tests giving a relationship between the degree of saturation (S_r) – suction (ψ) and relative hydraulic conductivity (K_r) – suction (ψ). The results of the volumetric water content (VWC) and suction during the test are presented in Figure 6, respectively.
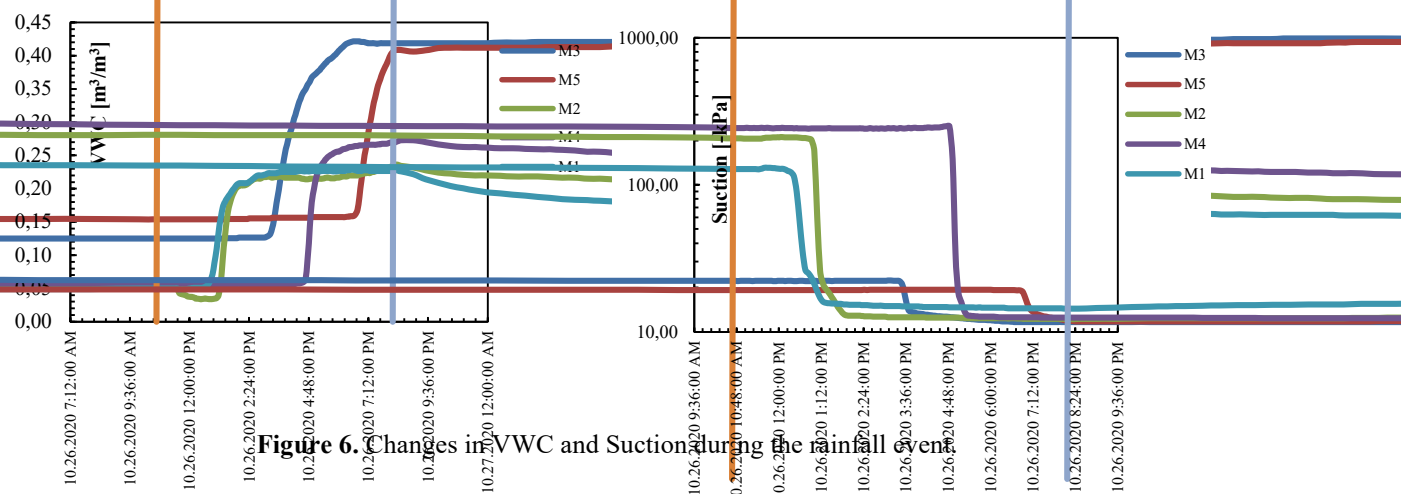

Figure 6. Changes in VWC and Suction during the rainfall event.

A change in VWC has been initially observed at the M1 and M2 sensors placed near the slope surface. Later they have lower values compared to those of the M3 and M5 sensors, which are placed near the phreatic level. The suction strongly depends on the VWC, thus the sensors placed in the upper half of the slope (M1, M2, and M4) show the highest initial suction. A significant drop in suction is observed when the infiltrated water reaches the sensor location.

2.3 Erosion resistance test

In the second stage of this study, an experimental test for erosion control on an inclined slope of biopolymer-treated and untreated soil slope was performed in an aluminum box with the following dimensions 50 × 50 × 10 cm, Figure 7. The rainfall was simulated through a system of sprinklers which were installed above the model and connected to the water supply system. Inside the box, the soil was instrumented with three types of sensors for volumetric water content, pore water pressure, and suction.
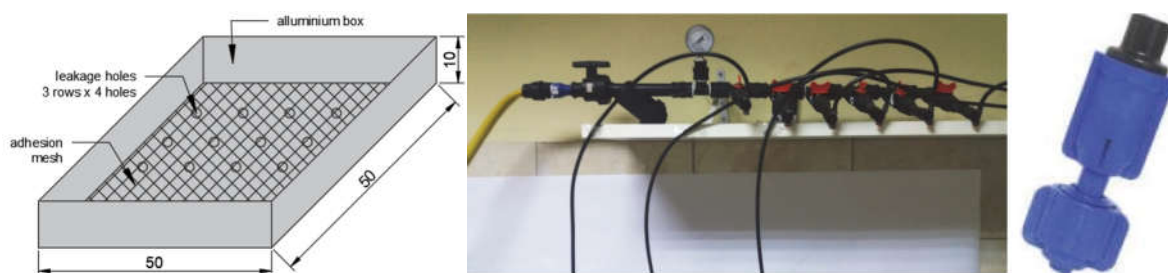
Figure 7. Test box and the sprinkler system.

The biopolymer solution has been applied by spraying evenly over the slope surface filling the pores and cavities in the soil and coating the grains with a biofilm creating a surface crust. The rainfall duration was 180 minutes, while every 60 minutes snapshots were made to register the changes on the surface of the slopes. In the beginning, there was no visual difference between the treated and untreated slope. The interaction between the biopolymer solution, soil, and water creates a specific soil rheology characterized by hydrophilic absorption, and binding of water molecules. In contact with water, the surface crust becomes a hydrophobic surface that allows surface water to flow freely with high resistance against the erosive forces of water visible in Figure 5 where practically no erosive changes were observed on the polymer-treated slope in 180 minutes (Nikolovska et al. 2022). After the soil was completely saturated, the water started to drain through the boreholes at the base, and movement paths of the eroded soil were observed on the surface. After 180 minutes, there was muddy water with fine fractions in the base of the slope, which was not the case with the treated slope. The erosion effects on a polymer-treated and untreated slope with an inclination of 1:1 is shown in Figure 8.
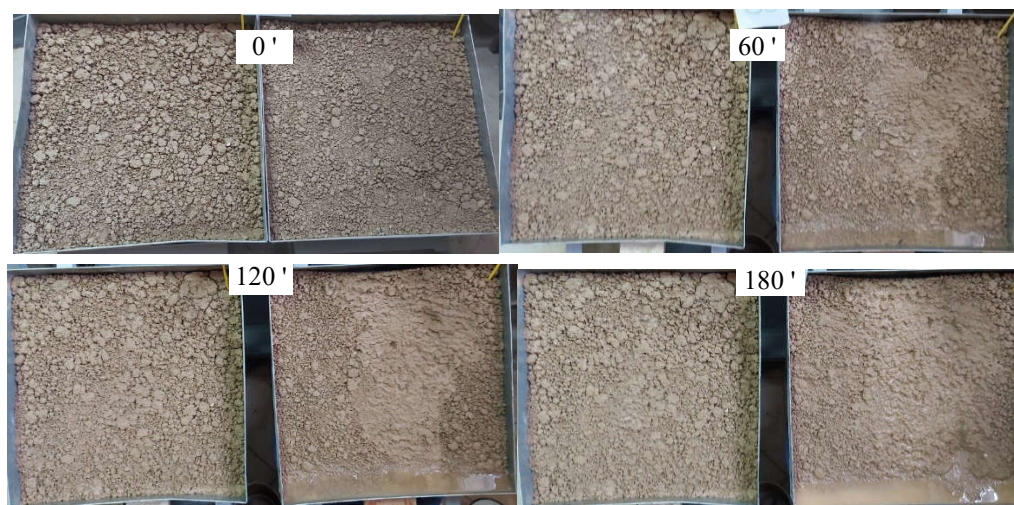

Figure 8. Erosion on polymer-treated slope (left side) and untreated slope (right side).

A series of tests on untreated and biopolymer-treated slopes with grown vegetation were also tested on 120 minutes of rainfall with an intensity of 12 l/h. During the rainfall, no erosion was observed, hence, the biopolymer-treated slope has a higher stability and resistance to erosive forces (Nikolovska et al. 2023). For precipitation duration of 3 h on an area of 1.0 m^2, a material with a weight of 1900 gr is eroded, which represents a loss of material of 9.5%, Figure 9.

Figure 9. Eroded soil in 180 minutes of rainfall for polymer-improved slope (left side) and natural slope (right side).

Moreover, the absorption capability of the biopolymer supports and stimulates vegetation growth. The biopolymer-treated slopes with vegetation were tested after 27 days of curing period. The curing period is needed for the vegetation roots to connect with the soil and hydrophobic layer, Figure 10.

Figure 10. Erosive changes of slopes with vegetation, polymer-improved slope (left side), and natural slope (right side)

Figure 11 presents the measured VWC and suction during the test on the inclined slope subjected to rainfall.
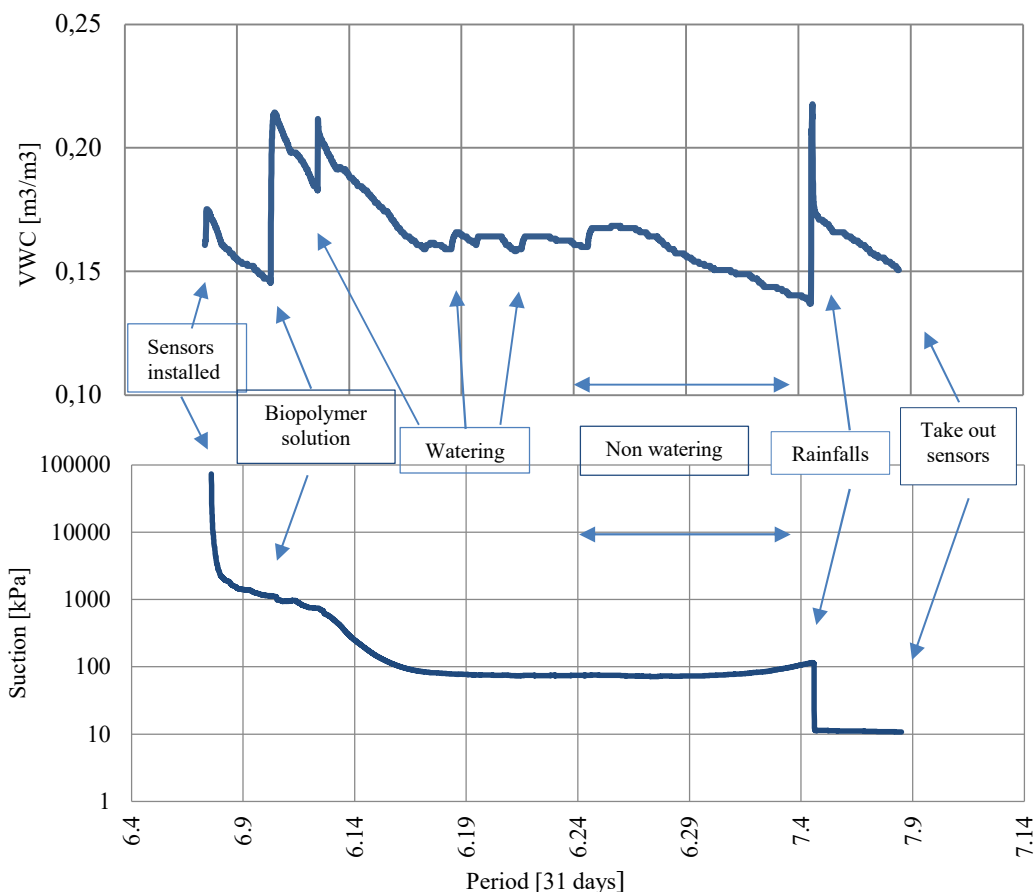
Figure 11. Results of Volumetric water content and suction for silty sand soil

During the wetting period, the volumetric soil moisture increases from 0.137 m^3/m^3 to 0.218 m^3/m^3, while in the dry periods decreases while the suction sharply decreases from 110.1 kPa to 11.3 kPa or reduces by almost 90%.

2.4 Numerical test

To simulate the soil-atmospheric-vegetation interaction, it is necessary to use unsaturated soil mechanics with a definition of constitutive both mechanical and hydraulic soil models. The most reliable and comprehensive solution would be to perform a transient analysis with the coupled flow-deformation calculation. A small-strain hardening soil model was used in definition of the mechanical behavior, and van Genuchten model for hydraulic. For the definition of the hydraulic model, the soil water retention curve – SWRC, and the suction-relative permeability function are both presented in Figure 12.
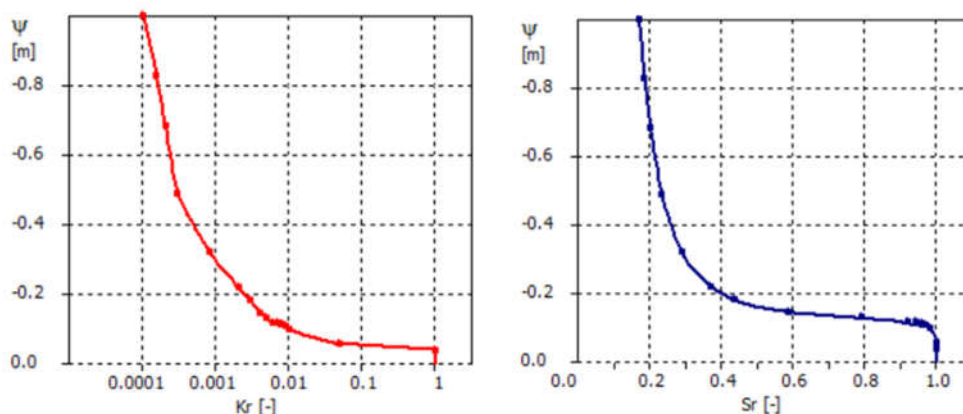
Figure 12. Used relationship for Spline model in Plaxis.

Based on the data measured on the physical model during the rainfall test, a calibration of a numerical model subjected to constant rainfall was performed using FEM analyses using the Plaxis software. Figures 13 and 14 present the results of the saturation and suction profiles before and after 3 hours of rainfall, respectively.
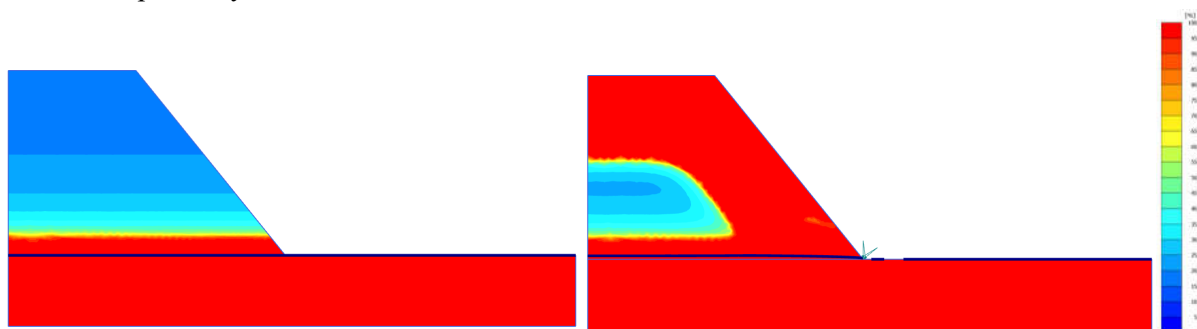

Figure 13. Degree of saturation before (left) and after (right) 3 hours of rainfall.
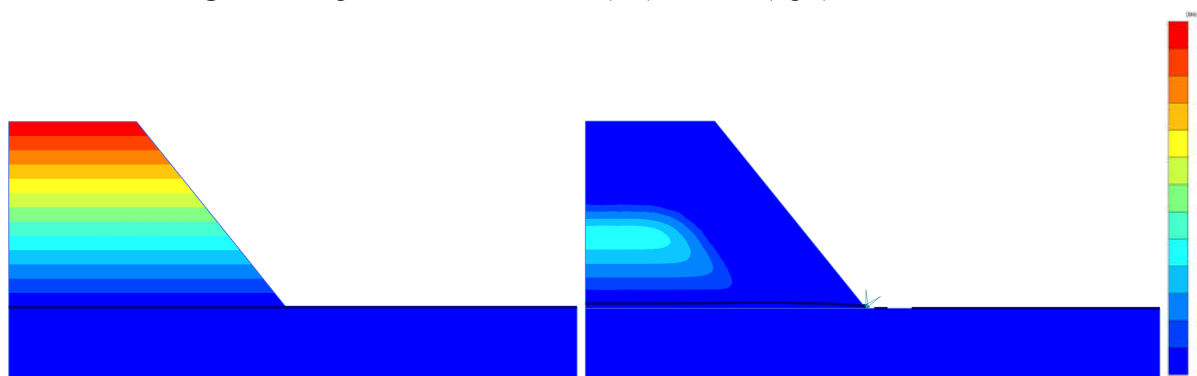

Figure 14. Suction before (left) and after (right) 3h rainfall.

The saturation changes immediately after the beginning of rainfall because of the infiltration. With time the saturation zone increases and the suction decreases as the infiltration increases. The maximum saturation and suction changes were observed on the slope surface where the rainfall influence is the highest (Fredlund et al., 2012). The minimum value of the initial saturation degree at the top of the slope is 16.89%. As infiltration increases, the unsaturated zone decreases and matches those of the physical model. At the end of the test, the minimum value level of the saturation degree is 24.2%. The calculated results show exceptional agreement with the measured ones, see Figure 15.
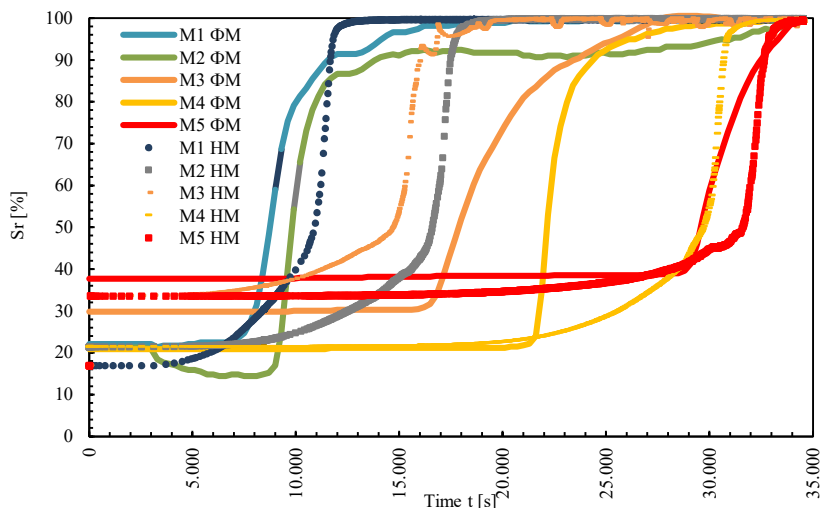
Figure 15. Comparison of S_r between the physical and numerical model.

The initial degree of saturation in the characteristic points M1, M2, and M4 is lower if compared to M3 and M5 due to the influence of the capillary effect. The saturation at points M1 and M5 at the top of the slope and the lower part compared over time show excellent matching. In points M2, M3, and M4, a minimal deviation in the results can be observed. A comparison between both models is also made regarding the deformations and the geometry of the potential failure surface. Hence, in Figure 16 the slope deformations with the ultimate global Factor of safety (FoS) are presented. The maximum calculated deformations are 6.62 cm and the minimum global FoS equals 1.037, which is very close to the slope limit equilibrium.
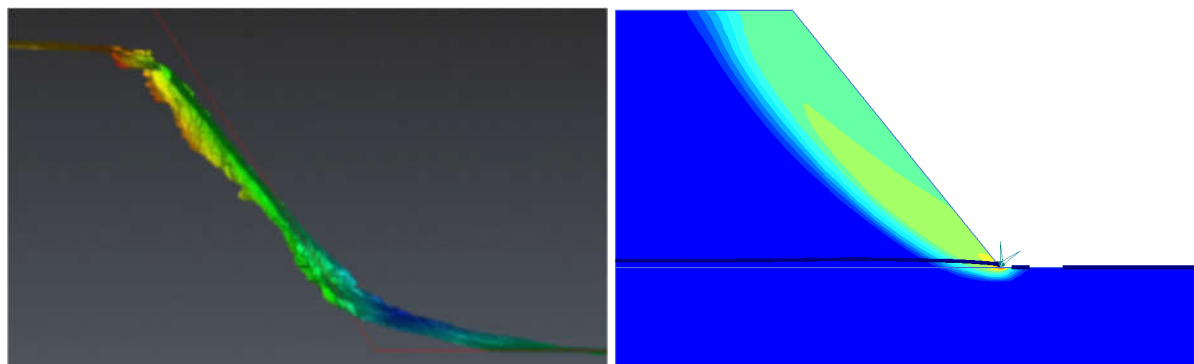

Figure 16. Slope deformation in physical (left) and numerical (right) models.

4   Conclusion

Nowadays, the consequences of climate change are becoming more visible, among other, it has a great impact on the stability of soil slopes. The increased precipitation and dry periods affect slopes and their stability causing erosion, development of cracks, and shallow (local) and even global instabilities and landslides. As a preventive measure, more recently, the use of natural microorganisms for soil improvement has attracted the attention of researchers. This research examines the stabilization with the natural polymer solution that forms a viscous gel matrix strengthening the bond between the soil particles. The results show that the polymer significantly reduces erosion and restricts the runoff water by infiltrating the ground, thus providing surface stability to the slopes and promoting vegetation growth. The laboratory tests have shown not just an increase in the cohesion of the treated soil, but also in the friction angle and modulus of compressibility by 20% to 50%. It is evident that biopolymers as an efficient, economical, and environmentally sustainable solution have great application potential.

Moreover, the study quantitatively evaluates the impact of precipitation intensity, frequency, and duration on slope stability. The obtained results from both physical and numerical modeling show that the intense short-term rainfall has significantly affected the stability of the slopes, caused erosion and reducing the slope stability by 30%. The results show that the biopolymer significantly reduces erosion and restricts the run-off water by infiltrating the ground, thus providing surface stability to the slopes and promoting vegetation growth. The tests confirm that the biopolymers significantly enhance the erosion resistance and stabilize soil thus improving the slope stability. The biopolymers stimulate the growth of the vegetation has additional beneficial effects. The study also highlights the importance of stability checks considering intense rainfall with short to medium duration recommending a probabilistic analysis to assess the risk of instabilities for projected rainfall intensities.

Acknowledgments

References

Chang I, Jeon M, Cho G-Ch (2015) Application of microbial biopolymers as an alternative construction binder of earth buildings in underdeveloped countries. International Journal for Polymer Science, Volume 2015, Article ID 326745, 9 p.

Chen L, Huang Z, Gong J, Fu B, Huang Y (2007) The effect of land cover/vegetation on soil water dynamic in the hilly area of the loess plateau, China. Journal of Soil Science, Catena, 70(2):200-208.

Chun G, Chang I (2018) Cementless soil stabilizer – biopolymer. The 2018 World Congress on Advances in Civil, Environmental, & Materials Research (ACEM18), Incheon, Korea, 29 p.

Josifovski, J. and Nikolovska, A. (2022). Biopolymer soil stabilization as protection from slope erosion and shallow sliding. EGU General Assembly 2022, EGU22-4236

Nikolovska, A. and Josifovski, J. (2023). Experimental and numerical soil stability analysis of biopolymer-treated slope. 2nd International conference of civil engineering ICCE 2023, Tirana Albania.

Nikolovska, A. Josifovski, and J. Susinov, B. and Abazi, S. (2022) Erosion of soil slopes under the influence of atmospheric actions and stabilization with natural polymer solutions. Second Macedonia Road Congress.

Nikolovska, A. and Josifovski, J. (2022). Biopolymer stabilization on soil slopes from surface erosion. Fifth symposium of the Macedonian Association for Geotechnics.

Nikolovska, A. Josifovski, J. Susinov, B. (2022) Atmospheric effects of soil erosion and slope stabilization with natural polymer solution. 17th International Symposium on Water Management and Hydraulic Engineering.

Susinov, B. and Josifovski, J. (2018). Investigation of the hydro-mechanical properties of silty sand material from Topolnica tailings dam, In ce/papers, Skopje, R. Macedonia, pp. 797-802.

Susinov, B. Josifovski, J. and Naumovski, M. (2019). Hydrological analysis of high-intensity rainfalls over Topolnica tailing dam, In Ss. Cyril and Methodius University, Scientific Journal of Civil Engineering Faculty – Skopje, Skopje, R. Macedonia.

Susinov, B. and Josifovski, J. (2022). Slope instabilities caused by atmospheric influences, In Macedonian Association for Geotechnics, Ohrid, Macedonia, pp. 669-678, ISBN 978-9989-2053-5-4.

Zhang, L., LI, J., Li, X., Zhang, J., Zhu, H. (2018). Rainfall-induced soil slope failure: stability analysis and probabilistic assessment, 1st ed., CRC Press, Boca Raton.

ANALYSIS OF THE SOIL PROPERTIES SPATIAL HETEROGENEITY BY MEANS OF ENGINEERING GEOLOGICAL MODELLING

GULMIRA AMANOVA [1,2,3], EUGENE VOZNESENSKY [1,2], PAVEL PATRIKEEV [3]

[1] *Sergeev Institute of Environmental Geoscience, Russian Academy of Sciences, Russia, 131597tupac@mail.ru*

[2] *Faculty of Geology, Lomonosov Moscow State University, Russia, eugene@geoenv.ru*

[3] *Atomenergoproekt, JSC, Russia, ilmarinnen@list.ru*

Abstract

The problem of soil properties heterogeneity in the massif and possible approaches of evaluating its regularities by means of three-dimensional numerical modeling of spatial fields of the studied parameters within the framework of geostatistical approach is considered. It can be demonstrated that the structure of geological parameters fields (a) differs for different stratigraphic-genetic complexes of soils and rocks, (b) can be simpler than the combination of engineering-geological units, (c) the proposed approach is able to identify and explain significant deviations from the normal or lognormal distribution in its upper and lower quartiles, presenting practically in any geological subdivisions of the section. These outbursts in the maximum and minimum ranges are themselves an additional characteristic of soil heterogeneity; they testify to the non-randomness of such "outbursts", their typicality. Unlike a formal approach of subdividing the soil profile into a set of engineering geological units the proposed differentiation is based initially on composing the geological model consisting of bodies with varying origin, age and lithology and separated by distinct boundary surfaces. Additional internal boundaries in these 3D bodies are, on the contrary, diffusive and based on the analysis of spatial fields of the studied soil parameters by means of appropriate geostatistical procedures.

Key words

heterogeneity, variability, soils, massif, geostatistics, parameter field, 3D modelling, engineering geological model

1   Introduction

One of the most important scientific problems of modern engineering geology is the problem of the nature of soil massif behaviour. The main components of our ignorance of this nature, which constitute the essence of this problem, include uncertainty of soil massif boundaries in space, impossibility of direct observation of geological processes occurring in soil massifs, uncertainty of correlation between the state and properties of the sample and the same soil in the massif, scale effect and heterogeneity of soil composition and properties in the massif. These summands define the main actual research tasks to overcome this scientific problem and require the development of an appropriate methodology. In this article, we will focus on the methodology of studying the heterogeneity of soil properties in their massifs.

The heterogeneity of soils is manifested in significant differences in their composition and properties between any two points, and the spatial heterogeneity of the considered attributes determines their variability which is characteristic for all soils. The heterogeneity and variability of soil properties within an arbitrary soil massif is caused by variations in such characteristics as composition, structure, texture, moisture, fracturing, weathering, soil stress state.
Back in the 60s of the last century, N.V. Kolomensky (1968) had postulated 3 types of variability of soil property parameters - discontinuously irregular, discontinuously regular and functional, examples of

which are also given in our work (Amanova, Voznesensky, 2023). Later these ideas were developed in the works of G.K. Bondarik (1971) and I.S. Komarov (1972), who introduced the concept of "geological parameter field". This field, its structure is the main characteristic of soil heterogeneity and spatial variability of properties in the massif. And it is exactly this field that is unknown to us.

For scientific understanding of the nature and regularities of soil heterogeneity it is necessary to construct and analyse the fields of soil properties parameters. And these so far unknown to us regularities definitely exist, because the formation of soils and rocks is a regular process, it is governed by the laws of physics, chemistry, geology and other natural sciences. And it is necessary to start with methodology.

2   Methodology

In general, it can be summarized as following. The main methodological tool is engineering-geological modeling. At the first stage a spatial geological model of the investigated soil massif is developed. For this purpose, software specialized for spatial modeling of geological objects is used. Next, the variability of soils is assessed by plotting the fields of each investigated geologic parameter. Geostatistics, machine learning, neural networks or other models and approaches can be used for this purpose. This information field can then be analyzed in 2D or 3D representation for each indicator of soil composition and properties. Then the incorporation of these parameter fields in the geological model of the considered array using specialized software will allow to obtain an engineering-geological model of the array, explicitly reflecting ground conditions including their continuous heterogeneity, instead of a combination of "bricks" - engineering geological units, which are assumed to be homogeneous, but are not in reality. The most important aspect of such a combination of the parameter field with the spatial model of the array is the preservation of its geological sense, for which certain rules for creating boundaries of different ranks in the model must be followed, and they are described below in this paper.

2.1 Formation of stratigraphic and genetic boundaries in the model

The procedure for development of a soil massif engineering-geological model includes a sequence of the following logical operations.

At the first stage, a geological model of soil and rock massif (as understood by G.A. Golodkovskaya and other authors) or its part is developed. This model implies the allocation of the main structural zones - geological and genetic complexes - according to the signs of unity of age and genesis. Geological boundaries between them, with the exception of consonants, become the main structural surfaces within the massif, and the boundaries are rigid, definite, interrupting all other boundaries, for example, facies boundaries. These surfaces fix in the model the fact of a jump-like change of rock formation conditions in time, and therefore all other boundaries of higher rank - for example, isolines of soil property fields - can undergo a rupture on them. This is fully consistent with the stratigraphic and geological-genetic approaches in geology.

At the second stage, "facies" - volumes of soils and rocks of the same composition with even closer age and genesis - are distinguished within the main structural zones, making it possible to reveal the structure of each geological and genetic complex in detail. The boundaries between different facies of the same age are, on the contrary, non-rigid, diffuse in the model and should not be transformed into the next generation of structural surfaces, reflecting a gradual change in the conditions of, for example, sedimentation within a single sedimentary cycle. This detailing of geological and genetic complexes in the geological model is necessary for understanding and subsequent correct interpretation of the already engineering-geological model.

At the third stage, the geological model of the massif is transformed into the engineering-geological model of the soil massif by superimposing the fields of variability of essential attributes of soils - their engineering-geological properties - on the main structural zones. The structure of variability fields of these properties should inevitably reflect the facies distribution to some extent, and the boundaries of

isofields of property parameters can either undergo a jump on the main structural surfaces, or correspond to the diffuse character of facies boundaries in the model and demonstrate a smooth change of parameters. Thus, when the values of the parameter in question are close to each other in the geological and genetic complexes of different age and genesis contacting on a rigid surface, its isofields can be characterized by smooth transitions.

2.2 Spatial data analysis

Patterns of soil properties heterogeneity in general can be studied using various approaches, including:
- geostatistical models considering the spatial autocorrelation of data points to estimate values at unsampled locations;
- machine learning and artificial intelligence algorithms like random forests, support vector machines, and neural networks can be trained to predict soil properties based on input variables;
- process-based models simulating the physical and chemical processes that influence soil development and behavior;
- digital soil mapping involving spatial information from various data sources and data analysis techniques to create high-resolution soil property maps to predict soil properties;
- ensemble modeling approach combining multiple models to improve predictive accuracy.

In this research we used geostatistical approach based on variogram analysis and methods of statistical simulations. To implement the aggregate data analysis, Petrel software by Schlumberger was chosen, which is originally developed for petroleum geology tasks and has in its arsenal tools of statistical analysis, which can be used for engineering and geological modelling as well.

A variogram is a function of the variation of a spatial variable depending on the distance between the points at which the values of this variable are directly determined. Any variogram reaches an asymptote value (plateau) (Figure 1). The distance at which the variogram reaches the threshold of such a plateau is called the correlation radius. If the correlation radius for a data set is equal to, for example, 1 km, it means that to calculate a parameter at a point where its value has not been directly observed, all directly determined values (in our case, based on drilling results) within a sphere radius of 1 km should be taken into account.
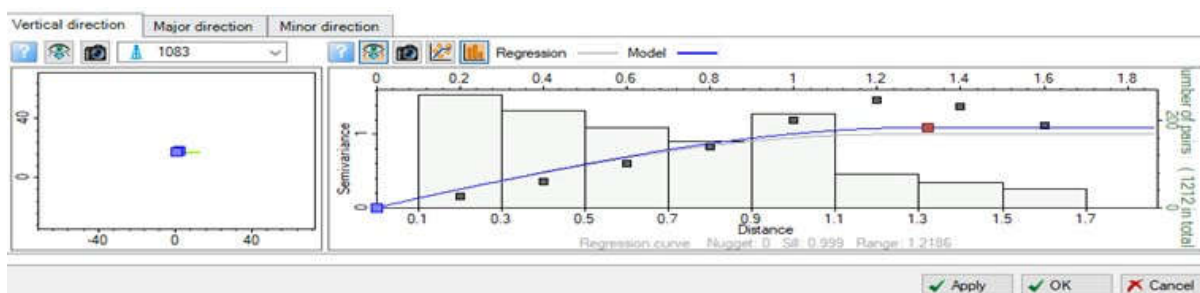

Figure 1. Example of a variogram for soil bulk modulus in Petrel variogram window.

Then within the specified correlation radius in the space between the tested points we can statistically develop parameter field for any indicator of soil composition and properties. We used Sequential Indicator Simulation (SIS) as a method for modelling lithological data, and Sequential Gaussian Simulation (SGS) for modelling soil properties parameters. SIS is a stochastic (cell-based) modelling algorithm that uses rescaled cells as a basis for relating the modelled lithological facies.

An approach known as Sequential Gaussian Simulation is often used to develop fields of continuous soil properties such as, e.g., porosity. The Sequential Stochastic Gaussian Simulation method assumes a joint normal distribution of the modelled random variable in the studied area. Real geological data, on

the contrary, are usually not normally distributed, so the SGS method requires their preliminary preparation. This involves converting the original borehole data to a normal distribution.

Thus, both SIS and SGS stochastic operations are applied to each geological and genetic complexes in geological model within their fixed structural boundaries. This logic provides the preservation of the geological sense of the resulting engineering geological model. The detailed flowchart of model development process is presented in Figure 2.
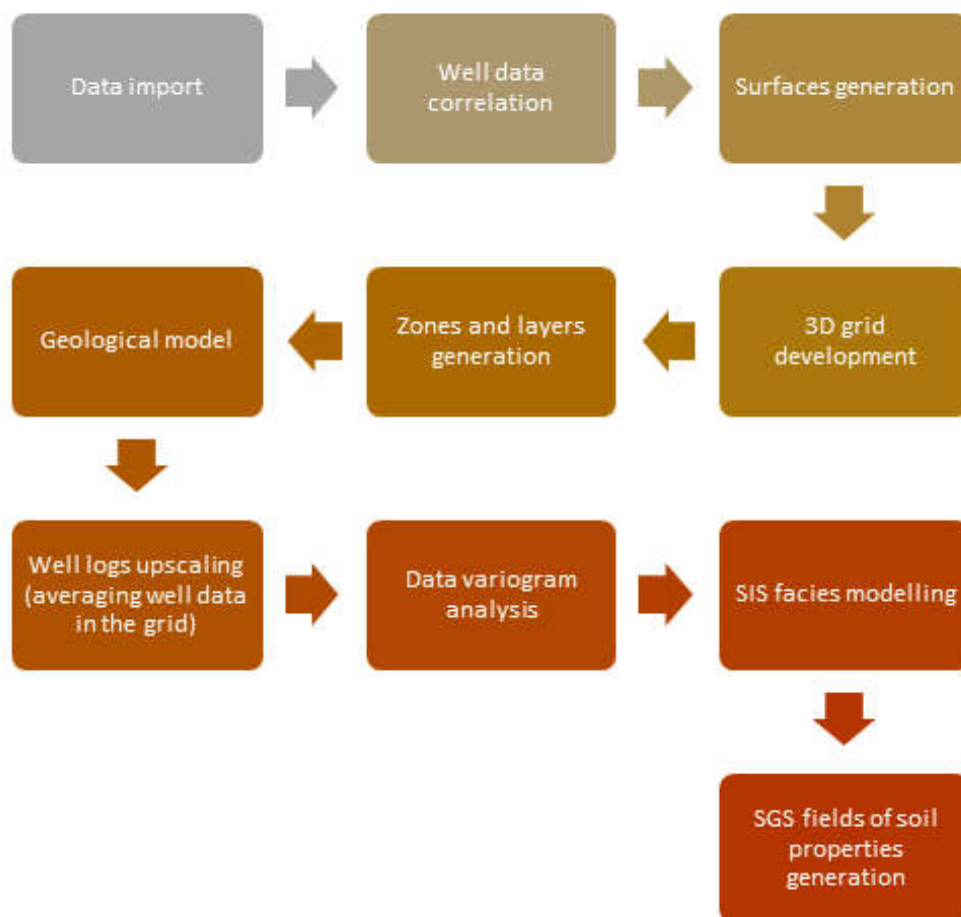

Figure 2. Modelling algorithm flowchart

About the resolution of the resulting model. In Petrel software rules of massif volume partitioning into cells should be set both laterally and vertically. If the model contains no faults, the cells have the same length and width. However, to correctly embed faults, it is necessary to modify the geometry of near-fault cells by "attracting" their vertices to the faults both horizontally and vertically. The horizontal resolution of the grid is determined by the increments of the horizontal projections of the cells and the correct choice of horizontal grid resolution - X and Y increments - is very important. It is usually desirable to have at least 2-3 cells between wells. For example, if the distance between wells is about 300 m, it is recommended to build a grid of cells no larger than 100 x 100 m. Grids in which several wells fall into the same or neighbouring cells should not be used and it is necessary to shift to smaller cells, if the wells are not too close to each other.

The model allows a certain smoothing. For example, lithological facies were modelled by averaging a set of stochastic SIS realizations and their subsequent smoothing. Smoothing is performed to remove noise (individual unrelated cells) while preserving values in well cells.

3   Results

The developed model is based on the following initial input data: geodetic survey data, engineering geological boreholes together with laboratory and field test results. Among the latter, the cone penetration test (CPT) data are of primary interest, since it provides such a massive, continuous and detailed distributed data set.

The object of modelling is the soil base of the nuclear industrial estate including different separate structures over a wide area. The site is located in the north-west of the European part of Russia. The structure of this massif up to a depth of 35 m is composed of Quaternary, mainly glacial and water-glacial soils on the top – loams, clays and quartz-feldspathic sands with gravel and pebble inclusions, as well as Cambrian sediments – sandstones and clays – at the bottom. There is a buried hollow in the site profile, associated with the pre-Valdaian palaeorelief stage and filled with younger sediments. In hydrogeological terms, water-bearing complexes confined to both Quaternary sediments and pre-Quaternary rocks are distinguished here. All Quaternary sediments represent water-bearing complexes and horizons. The groundwater level practically coincides with the day surface, hence all the considered soils are saturated in the massif, and all their properties, analyzed below, are characteristic for the saturated state. There is no permafrost.

Site investigations included more than 1500 boreholes of different depths. As a result of analysis of the data collected during engineering surveys, several dozens of engineering-geological units were identified in the massif profiles. At the same time, many of them are very similar to each other and, obviously, form single geological bodies, but differ in some features (e.g., variations in sand size), which, in fact, are a reflection of internal heterogeneity of these bodies. In general, the studied massif includes two quite homogeneous strata and a completely heterogeneous stratum of Quaternary sediments overlapping them. The formation has a rather complex structure, and in the geological profile appears as a set of numerous lenticular bodies. Some preliminary results discussing the variability of this massif are given in (Amanova, Voznesensky, 2023). Now we focus on the upper - the most variable and complexly composed - strata of Quaternary fluvio-glacial, alluvial and lacustrine-glacial sediments. For its detailed study 8 profiles were plotted using GeoSolution.Geology software. This software also allows to produce a set of structural surfaces – geological boundaries.

Consider the importance of these structural surfaces based on stratigraphic signs of age and genesis for correct representation of lithological facies in the model (Figure 3). Soil type is obtained from CPT data basing on the cone and friction sleeve resistances using standard geotechnical interpretation procedure and presented in this profile by sands, sandy silts, silts and clays, well corresponding with the direct soil description in the drill cores. In Figure 3a we observe overall random interlaying of facies replicating in general the shape of lower boundary of Quaternary deposits with the predominant occurrence of sands, which is not the case. Such chaotic interlacing, which is inconsistent with the geological regularities of formation of water and water-glacial origin strata, is an artefact of a simplified interpolation scheme that allows the inclusion of parameters of sediments formed at different time and in different conditions within the correlation radius of the variogram. The sharp-angled protrusions of the lower boundary and reflected higher in the strata are also not geologically meaningful and are related to the lack of actual data at individual points at the base of the strata.
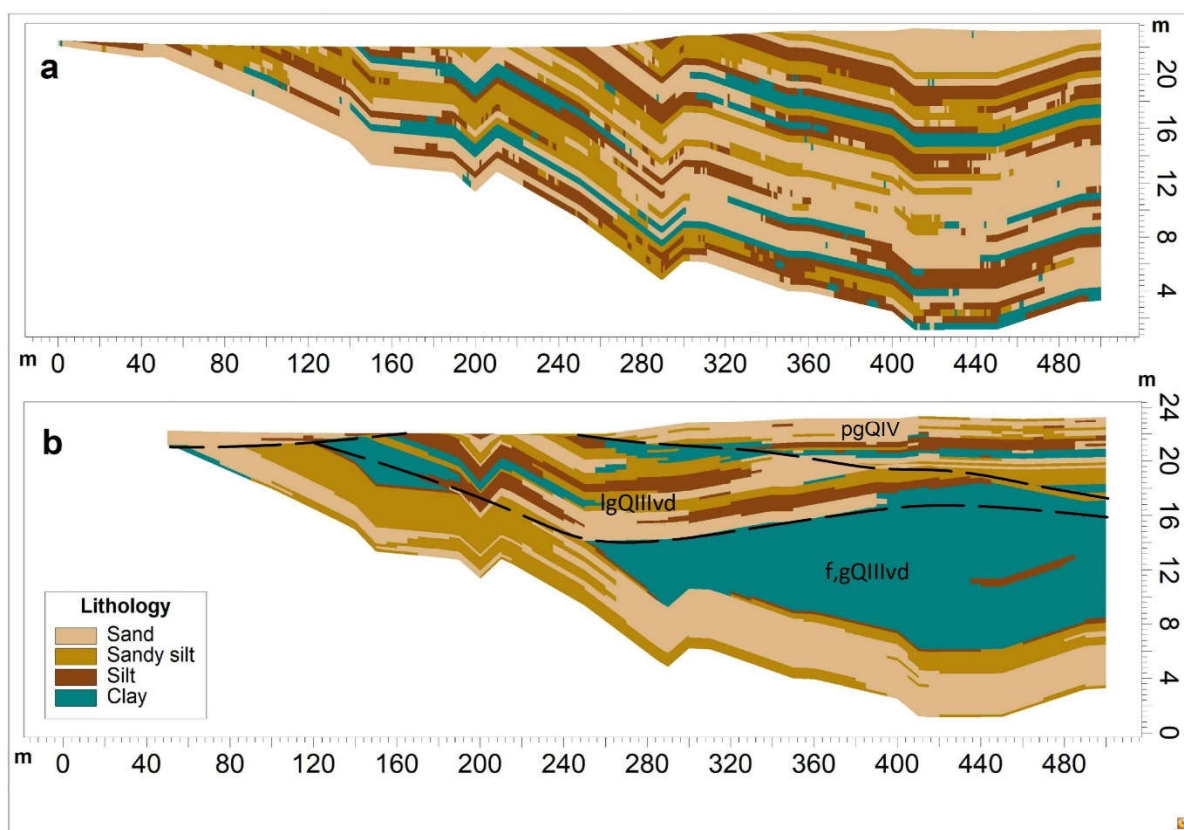
Figure 3. Spatial distribution of lithological facies in the model basing on CPT data: a – structural surfaces are ignored, b – geological boundaries are specified

On the contrary, in Figure 3b we observe geologically logic facies model with really observed soil lenses and predominance of clays in the central part of geological body. And diffusive boundaries of lithological facies are conformal to geological ones. Since soil properties depend primarily on composition, so the fields of their mechanical parameters (calculated for this model also from CPT data using generally adopted empiric relationships (Kulhawy, Mayne, 1990; Lunne, Robertson, Powell, 1997)) are expected to be also conformal to the facies spatial distribution.

This is what we really observe (Figure 4): on the top in Figure 4b there are mostly lacustrine-glacial sands and silt with bulk modulus generally below 150 MPa, whereas higher values – sometimes up to 350 MPa – occur in the lower fluvio-glacial clays and sands and the bottom. Interesting to note that in the upper Figure 4a, showing the modelling without taking into account structural surfaces, the distribution of the modulus is not just chaotic - the relatively thin (1-2 m thick) most rigid interlayers of loams and sands have been lost completely in this mess. We can also see that two different geological and stratigraphic complexes – upper lacustrine-glacial and lower fluvio-glacial – have different structure of parameter field, reflecting their deposition environment.
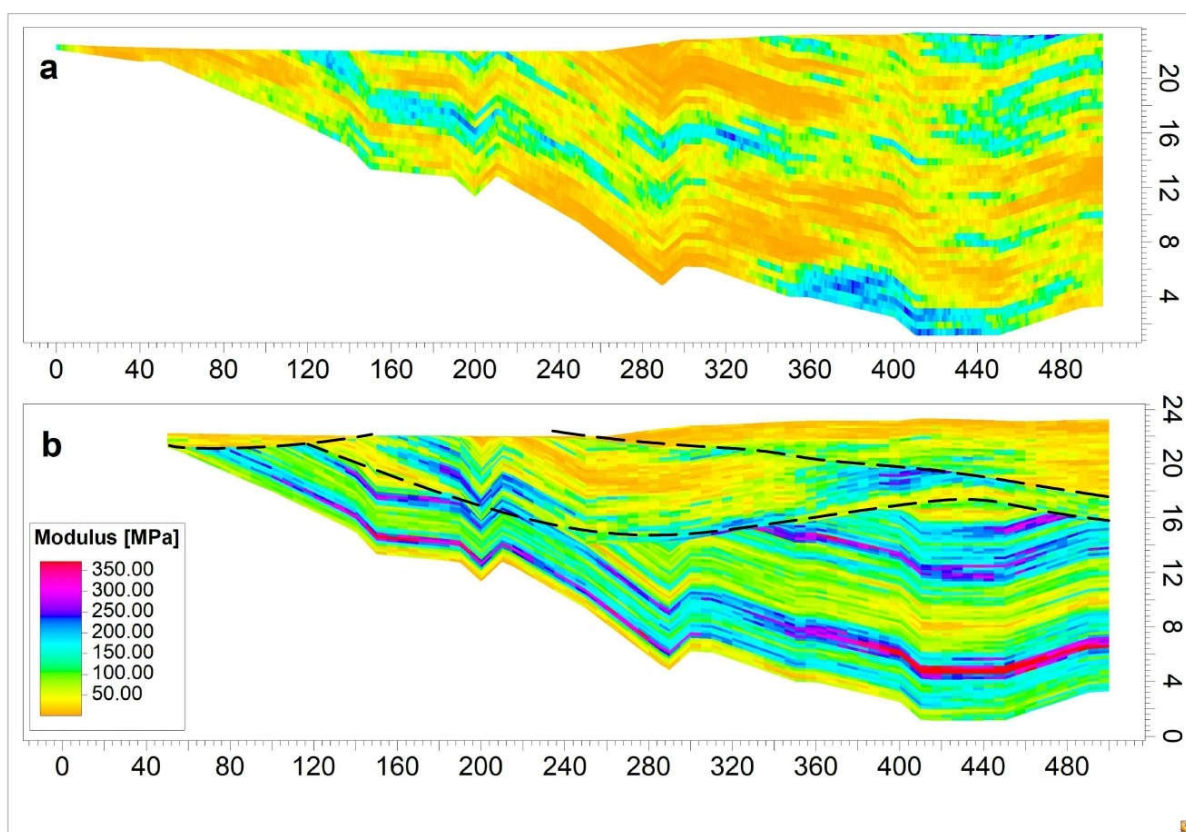
Figure 4. Spatial distribution of soil bulk modulus in the model basing on CPT data: a – structural surfaces are ignored, b – geological boundaries (black dashed lines) are considered

A similar situation is observed in the field of effective angle of internal friction (Figure 5): well-defined and generally conformal zones of this parameter for the model with fixed structural (geological) boundaries of stratigraphic and geological complexes (b) and haphazard distribution of "spots" with different values without this important consideration (a). It should be also noted that the structure of parameter field is also different for the soils of different origin. Considerably high absolute values for some facies (over 35°) should be attributed to possible drawbacks of empirical correlations used for parameter calculations and coarse particles occurrence locally influencing cone resistance.

Thus, correct representation of the real relationship of geological bodies of different age and genesis within the studied massif is an absolutely necessary condition for correct modelling and the very possibility of studying the heterogeneity of soil properties with the help of the generated model. Moreover, only this approach gives the possibility to investigate specific features of this heterogeneity for soils of different origin.

Analysis of the presented herein model reveals considerable differences in the patterns of soil properties variability. Fluvio-glacial deposits have a somewhat regular alterations of both modulus and angle of friction with depth, probably due to their formation by water streams with different amounts of suspended clastic material of different size. Such variability both in vertical soil profile or in any horizontal section may be attributed to the discontinuous irregular type ("saw-rule" type) after N.V. Kolomensky (1968). On the contrary, lacustrine-glacial deposits, sedimented mostly in a still water environment, demonstrate much less regular, diffusive variability, which in certain sections of their profile – both vertical and horizontal – can hardly be associated with any of the known variability type. Further numerical studies of parameter field variability patterns for soils of various origin within the obtained engineering geological 3D models is an interesting and very promising future scientific task.
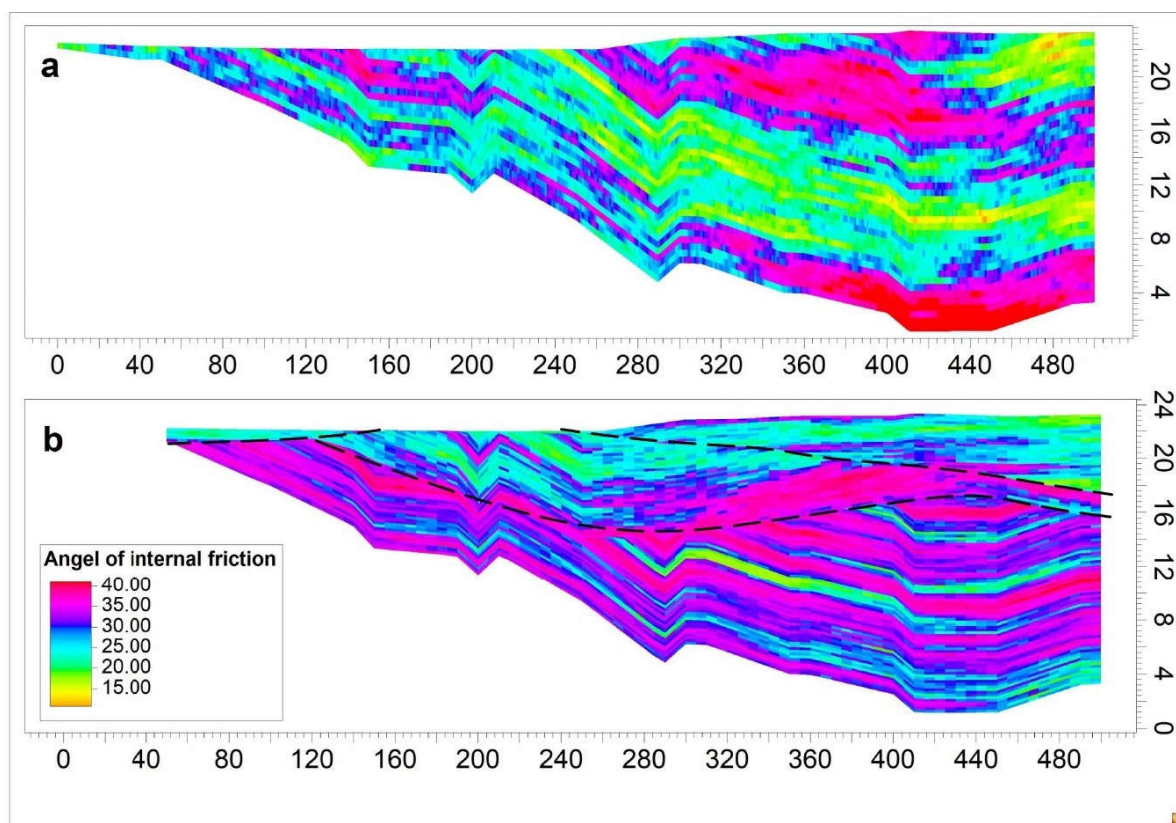
Figure 5. Spatial distribution of soil effective angle of internal friction in the model basing on CPT data: a – structural surfaces are ignored, b – geological boundaries (black dashed lines) are considered

Currently, in the practical field of engineering and construction activity this problem is circumvented by simplifying the real situation - by replacing a continuously inhomogeneous environment by its piecewise homogeneous model consisting of a set of engineering geological units (hereinafter referred to as EGU), all property indices of which are assumed to be constant within their boundaries, and on the basis of statistical processing of negligibly small sets of actual data. This approach was developed in 1960s for the possibilities of manual calculations and, in fact, has not changed so far. Many of the EGU boundaries are not unambiguous and abrupt in the geological space - on the contrary, they are often diffuse in nature, indicating gradual changes in some qualities of the soil, and only our subjective scheme of dividing the massif into EGU makes them some unambiguous lines on a profile or a map. Quantitative spatial analysis of soil massifs heterogeneity over large areas is complicated and requires a large volume of homogeneous and relatively uniformly distributed data. So, at present the solution of the above tasks seems to be expedient, primarily, for the bases of large and critical structures, the design of which requires the involvement of significant amounts of engineering geological information.

The development of the distribution fields of parameters allows not only to specify the geological boundaries of certain lithological facies, but also to identify deviations from their distribution law, which may be important for the operation of the structure, but are usually ignored in statistical processing. In addition, the fields of variation of parameters required for geotechnical calculations may not depend on the boundaries of the selected EGU, which opens up the possibility of improving this formal approach or even departing from it. Furthermore, the coupling of such engineering-geological model with the model (mechanical, thermal, hydraulic, etc.) of a foundation in the future will mean the emergence of a new type of geotechnical model of the structure base - with a continuous description of variations of key parameters instead of finite or boundary elements with discontinuous changes of corresponding parameters on their boundaries.

4   Conclusion

For scientific understanding of the nature and regularities of soil heterogeneity in a massif the parameters fields of soil properties should be generated and analysed. A methodology of such study based on engineering geological 3D modelling and geostatistical approach, including variogram analysis and methods of statistical simulations, is presented.

Correct allocation of the main structural zones within the model - geological and genetic complexes, separated by rigid, definite geological boundaries and diffusive, gradual boundary conditions between the facies is of crucial importance. The geological model of the massif is then transformed into its engineering-geological model by superimposing the fields of variability of essential attributes of soils - their engineering-geological properties - on the main structural zones.

The proposed methodology is demonstrated on the example of a variable and complexly composed strata of Quaternary fluvio-glacial, alluvial and lacustrine-glacial sediments within a single massif. Analysis of the presented model reveals considerable differences in the patterns of soil properties variability. Fluvio-glacial deposits have more or less regular alterations of both modulus and angle of internal friction with depth, probably due to their deposition by water streams with different amounts of suspended clastic material of different size and may be attributed to the discontinuous irregular type. Lacustrine-glacial deposits, sedimented mostly in a still water environment, demonstrate much less regular, diffusive variability, which hardly can be associated with any of the known variability type. Further numerical studies of parameter field variability patterns for soils of various origin within the obtained engineering geological 3D models is a very promising scientific task.

References

Amanova, G.S., Voznesensky, E.A. Engineering geological modelling of spatial heterogeneity of soils. *Gruntovedenie*, 2023, 2, 13-28. DOI:10.53278/2306-9139-2023-2-21-13-28

Bondarik, G.K. *Fundamentals of the theory of variability of engineering-geological properties of rocks*, Moscow, Nedra, 1971.

Kolomensky, N.V. *General methodology of engineering-geological research*, Moscow, Nedra, 1968.

Komarov, I.S. *Accumulation and processing of information in engineering-geological research*, Moscow, Nedra, 1972.

Kulhawy, F.H., Mayne, P.H. *Manual on estimating soil properties for foundation design*, Electric Power Research Institute, EPRI, 1990.

Lunne, T., Robertson, P.K., Powell J.J.M. *Cone Penetration Testing in geotechnical practice*, Great Britain, 1997.

APPLICATION OF MACHINE LEARNING FOR MODELLING SUBSURFACE SPATIAL MODEL USING GEOPHYSICAL AND BOREHOLE DATA – A CASE STUDY OF GUSIĆ POLJE 2 COMPENSATION BASIN FOR SENJ 2 HYDROELECTRIC POWER PLANT

MATIJA LOZIĆ[1], ANTONIA MIRČETA[2]

[1] *Elektroprojekt d.d., Croatia, matija.lozic@elektroprojekt.hr*

[2] *Elektroprojekt d.d., Croatia, antonia.mirceta@elektroprojekt.hr*

Abstract

Machine learning impacts everyday life in every field. This paper shows the application of machine learning in geoscience. Used machine learning model for classification and classification certainty estimation is ensembled from multilayer perceptrons each fitted in with different combination of variables. Used data consists of terrain data, borehole data, seismic refraction data and geoelectric data. Geophysics data was interpolated using IDW with a power parameter chosen based on a cross-validation process using mean squared error. Such prepared data was preprocessed and 49 data subsets were defined. Each multilayer perceptron was fitted in with the corresponding data subset using an optimal hyperparameter for that model. For ensemble learning classification max voting was used. Using a ratio of max voted class and number of votes certainty classification was estimated. Basic model metrics and prediction results are shown. Predictions are used for calculating robust orientational settlement map.

Keywords

Machine learning, Ensemble learning, Multilayer perceptron, Geostatistics, Inverse distance weighting (IDW), Modified Shepard's method, Geotechnical investigation, Subsurface spatial model, Gusić polje, Hydropower System Senj 2, settlement estimation.

1 Introduction

Geostatistics is a standard tool in geology used for analyzing and visualizing various types of data. It allows for the effective analysis of spatial variability and the creation of geological models.

By integrating multiple data sources such as boreholes, geophysical profiles, and remote sensing data, geostatistics provides a robust framework for subsurface characterization and natural hazard assessment. Techniques like kriging and inverse distance weighting are commonly used to interpolate and predict spatial models.

Pioneers of geostatistics in geology include Georges Matheron and Michel David. Georges Matheron is considered the founder of geostatistics, having developed the theoretical foundations and coined the term in the early 1960s. Michel David further advanced the field with his work on practical applications, particularly in mining geology. Their contributions have laid the groundwork for modern geostatistical methods used widely in geological and environmental studies.

This paper examines geostatistical methods combining machine learning to generate a subsurface spatial model. The main objectives of this study are to (1) provide a subsurface a spatial model (2) provide spatial certainty model and (3) create a settlement map of foundation soil after the construction water load.

Figure 1. The broader project area showing the existing Gusić polje basin and the designed Gusić polje 2 basin

The study area is located in central Croatia, in Ličko-Senjska County. The Senj Hydropower System (HPS) utilizes the water potential of the Lika and Gacka Rivers, situated between the Lička Visoravan plateau and the Adriatic Sea.

The Lika River, with a catchment area of approximately 1125 km² and an average annual flow rate of about 28.76 m³/s, is a torrential stream with flow rates ranging from 0 to 1300 m³/s. The Gacka River has a catchment area of 584 km² and an average annual flow rate of about 15.65 m³/s, with flow rates ranging from 3.5 m³/s to 149 m³/s.

The Senj HPS diverts water from the Lika River into the Gacka River and channels it through a common system for power generation in the Senj Hydroelectric Power Plant (HPP) with a maximum gross head of 437 meters. To reduce spillage losses, the second stage, HPP Senj 2, has been planned. The HPP Senj 2 project includes the construction of the Gusić Polje 2 Compensation Basin, featuring 3,664.06 meters of lateral embankments and a storage capacity of 2.87 million cubic meters for daily inflow regulation. The basin and embankments will be waterproofed using geomembrane techniques.

The existing Gusić Polje Compensation Basin of HPS Senj lies on the natural ground with karstic phenomena and is lined with clay. The new compensation basin, Gusić Polje 2, will be constructed adjacent to the existing one, connected via a culvert. Due to geological characteristics, settlements are expected. The surfaces to be covered include the slopes and bottom of the existing reservoir.

For this technical solution, calculating the settlements of the basin and embankments' foundation soil is essential. Various geotechnical investigations, geophysics, and exploratory boreholes have been conducted in the area over the years. Estimating the spatial distribution and thickness of strata in karst landscapes is challenging, requiring advanced estimation techniques.

Section 2 shows used raw data from geotechnical site investigations and terrain data. Section 3 presents data preprocessing. Sections 4 and 5 present model creation and evaluation by basic classification metrics. Section 6 is the results of predictions and section 7 is settlement calculations. Further in section 8 is an interpretation of results and section 9 discussion.

2.   Raw data

Raw data used in this paper are terrain data, boreholes data, geoelectric tomography data and seismic refraction data.

For project purposes terrain survey was conducted and a TIN model was built. Raw terrain data is a collection of TIN points on the grid. Grid parameters of collected points are shown below in Table 1.

The grid raster from which data was collected is raster used all along in this paper.

Table 1. Spatial variables boundary and step values

	min	max	step
x - Easting	390320	391500	10
y - Northing	4978340	4979420	10
z - Elevation	410.1	456.7	0.2
d - Depth	0	20	0.2

Borehole data was collected during site investigations. Drilling was performed in both soil and carbonate rock. During drilling in cohesive soil, undisturbed samples were taken, and a standard penetration test (SPT) was conducted approximately every 2 meters. Extracted cores were placed in labeled core boxes and photographed. They were then mapped by a geologist, who also conducted approximate uniaxial strength tests using a manual penetrometer. Characteristic soil and rock samples were selected for geotechnical laboratory testing. The groundwater level was measured and recorded post-drilling.
In all 92 boreholes were drilled. They essentially detected three materials: tuff, clay and limestone. To limestone material weathered zones were added.
Three types of stratigraphy can be concluded from core drillings. Stratigraphy one is when tuff is above clay and clay is above limestone, second stratigraphy is the absence of clay in the middle, and third stratigraphy is the absence of tuff on the surface.
Geoelectrical tomography was conducted to determine the depth and thickness of sediments in alluvial deposits, identifying lateral contacts in the underlying soil or rock due to lithological changes, creating vertical sections of materials and rocks along specified profiles, and locating fault zones.
A total of 9440 meters of geoelectrical tomography was performed across 16 profiles at the Gusić Polje 2 site using Wenner's electrode arrangement, with spacings of 2 and 5 meters. This setup provided interpretation depths of 24-60 meters. The profile locations matched those of the boreholes.
The results of the geoelectrical test are presented in a multicolored two-dimensional section of the deposit resistivity distribution (Table 2). The presentation also contains prognostic lithological determination based on resistance, geological mapping and core determination of boreholes in the research areas.

Table 2. Prognostic Lithological Determination Based on Geoelectrical Tomography Results

Resistance (Ωm)	Material
0 to 45	Clay, dust, fine rubble
45 to 100	Mixture of rubble, clay, and sands
100 to 600	Highly to moderately fragmented carbonate rock mass, cracks mostly filled with rubble and clay
600 to 7000	Poorly fragmented to compact carbonate rock mass, with fault zones possibly containing minor cracks and caverns
> 7000	Zone of possible cracks without filling, minor caverns

Geophysical investigations conducted in 1997 aimed to differentiate rock cover deposits in the subsoil using refraction seismic. Twenty-one profiles were surveyed with 135 geophones set along each profile and three shots per device. This geophone configuration enabled research to a depth of up to 40 meters. The refraction seismics identified four elastic environments based on primary elastic wave velocities:
1. Surface Complex: Velocities < 500 m/s, including various sediments and materials.
2. Cover Deposits: Velocities 600-1600 m/s, consisting of clays, weathered rock, and cavernous limestone.
3. Fractured Rock: Velocities 1480-2300 m/s, comprising fractured rock and zones of weaker rock.
4. Compact Rock: Velocities 2100-4000 m/s, including moderately fractured to compact rock.
5.

3.   Data preprocessing

The terrain data presented in Section 2 are discretized by depth at every 0.2 meters. At each point, a new elevation is calculated by subtracting the terrain surface elevation by depth, resulting in a data format as *{x, y, z, d}*. Borehole data, also presented in Section 2, are discretized by depth at every 0.2 meters, collecting the material in the corresponding interval. This data collection continues to a depth of 20 meters for each borehole. After processing, each discretized point contains variables *{x, y, z, d, and material}*. The material is encoded with integers as follows: Tuff – 1, Clay – 2, and Limestone – 3.

Geophysics data was spatially interpolated using Inverse Distance Weighting (IDW). IDW Power parameter was chosen based on a cross-validation process in a 70/30 ratio, observing mean absolute error and mean squared error of residuals between estimated and true values. Chosen power parameters were parameters obtained from averaging power parameters that produce a minimum of MAE and MSE functions. Interpolation was applied first on profile data and then on depth planes every 0.2 m on terrain data grid points and borehole data points.

Seismic refraction profiles interpolation was the exception, instead, IDW Modified Shepard's method was used, due to unfavorable data locations. A radius of influence of 35m was chosen. 35 m was a minimal value where data loss was acceptable. The cross-validation process of power parameter for IDW interpolation of seismic refraction depth planes data shows which is a good average power parameter. After the cross-validation process of the power parameter for IDW interpolation of geoelectric tomography profile data chosen power parameter was 3, and for depth planes was 5.

After the interpolation process in each point on the grid data takes form *{x, y, z, d, v, ohmm}*, the exception is borehole data which points have form *{x, y, z, d, v, ohmm, material code}*. From such formed data 49 data subsets were defined, each subset containing a different combination of variables.

The data was normalized to values between 0 and 1 using a simple min-max scaler. The minimum and maximum values were selected from the entire data domain. To define the training and testing datasets for model fitting, the boreholes were split into training and testing sets in a 70/30 ratio. The resulting train and test datasets had imbalanced classes. To address this, data containing dominant classes were removed until a class balance was achieved and applied to both the training and testing datasets.

4.   Multilayer perceptron

As weak learners multilayer perceptron for classification (MLPC) was chosen. MLPC is classified as supervised machine learning feedforward model, detailed description can be found in Gareth(2023). Model architecture is defined by its hyperparameters.

In this paper on each data subset different MLPC is used, with its own hyperparameters that are chosen by searching hyperparameter grid space observing accuracy on train set. Hyperparameters that was searched are: hidden layer size, activation function, l2.- regularization coefficient, Discrete value of each hyperparameter is presented in Table 3. To mitigated overfitting early stopping is used. As activation function of output layer softmax function is used. Output layer consists of three neurons, one for each class.

Table 3. Discrete values of multilayer perceptron hyperparameters

Number of hidden layers	form 1 to 3
Number of neurons in hidden layer	from 2 to 10
Activation function	['relu', 'tanh']
l2-regularization coefficient	[0.00001, 0.0001, 0.001, 0.01, 0.1]

Each MLPC model is fitted on train data using "optimal" hyperparameters and tested on test data. Basic metrics are conducted on train and test data to show how good a certain model is. Basic metrics contain for train dataset and test dataset accuracy, precision for each class, recall for each class and f1-score for each class.

Accuracy measures how many certain class is classified correctly. Expression for calculating accuracy:

$$Accuracy = \frac{(TP+TN)}{(TP+TN+FP+FN)} \qquad (1)$$

Precision measures how many predictions as certain class is actual class. Precision is calculated by expression:

$$Precision = \frac{TP}{(TP+FP)} \qquad (2)$$

Recall measures how many model correctly classified certain class compared to actual existing class in dataset

$$Recall = \frac{TP}{(TP+FN)} \qquad (3)$$

F1-score is harmonic mean of precision and recall. F1-score measures how well model balances between precision and recall.

$$F1score = 2 \cdot \frac{Precision \cdot Recall}{Precision+Recall} \qquad (4)$$

where:
TP – Number of true positives [1]
TN – Number of true negatives [1]
FP – Number of false positives [1]
FN – Number of false negatives [1]

Basic metrics of individual MLPCs for train and test data are shown in Table 4, also data subset parameters are introduced. Models on average had accuracy little below 70% on train and test data. The small difference between test and train accuracy indicates that there is no overfitting. For limestone class metrics show good performances, for tuff class fairly good, but for clay class metrics indicate poor performance, especially recall and consequently F1 score. This can be due to thick transitional zones of tuff and clay, weathered limestone discontinuities filled with clay and other reasons.

5. Model ensemble

To achieve a more robust estimator, model ensembling was employed, as detailed in Chollet (2017). The ensemble in this paper consists of 49 multilayer perceptron models from Section 4. The ensemble method used for the final classification was max voting, meaning the final classified class is the one with the most votes from all models.

The introduced model ensemble is also used for creating a certainty map according to (5) which can be found in Erharter(2021) that helps visualize which area of the site is less certain and prone to additional investigation. Additionally, certainty is used for determining and displaying material noisy boundaries and geological features, such as faults and weathering zones.

$$c = \frac{\left\{ max\left(\frac{\sum_n^1 \hat{y}}{n}\right) - \frac{1}{n_{classes}} \right\}}{1 - \frac{1}{n_{classes}}} \qquad (5)$$

where:
c – certainty
$\hat{y}$ – class classified from single weak learner
n – number of weak learners
$n_{classes}$ – number of classes

Table 4. Basic metrics on train and test data of multilayer perceptrons

Model	Data Subset parameters	TRAIN										TEST										
		Acc	Class 1 - Tuff			Class 2 - Clay			Class 3 - Limestone			Acc	Class 1 - Tuff			Class 2 - Clay			Class 3 - Limestone		
			P	R	F1	P	R	F1	P	R	F1		P	R	F1	P	R	F1	P	R	F1
1	v, ohmm	0.68	0.71	0.54	0.62	0.52	0.59	0.55	0.81	0.90	0.85	0.66	0.72	0.52	0.60	0.53	0.63	0.57	0.78	0.85	0.81
2	x, v	0.68	0.68	0.81	0.74	0.62	0.26	0.37	0.69	0.95	0.80	0.64	0.72	0.74	0.73	0.52	0.28	0.37	0.62	0.90	0.73
3	x, ohmm	0.46	0.43	0.68	0.53	0.90	0.06	0.11	0.46	0.62	0.53	0.41	0.51	0.48	0.49	0.39	0.11	0.18	0.37	0.66	0.47
4	x, v, ohmm	0.72	0.67	0.81	0.74	0.64	0.43	0.51	0.80	0.90	0.85	0.67	0.71	0.75	0.73	0.55	0.43	0.49	0.72	0.85	0.78
5	y, v	0.66	0.65	0.75	0.70	0.60	0.32	0.42	0.70	0.91	0.79	0.66	0.62	0.84	0.71	0.56	0.30	0.39	0.76	0.84	0.80
6	y, ohmm	0.45	0.37	0.82	0.51	0.47	0.25	0.33	1.00	0.27	0.43	0.42	0.37	0.91	0.52	0.45	0.13	0.20	1.00	0.22	0.36
7	y, v, ohmm	0.63	0.59	0.66	0.62	0.53	0.30	0.38	0.70	0.91	0.79	0.59	0.52	0.80	0.63	0.38	0.15	0.21	0.78	0.86	0.81
8	z, v	0.65	0.58	0.92	0.71	0.49	0.30	0.37	0.89	0.73	0.80	0.65	0.58	0.91	0.71	0.49	0.31	0.38	0.91	0.74	0.82
9	z, ohmm	0.66	0.60	0.95	0.73	0.62	0.27	0.37	0.79	0.78	0.79	0.71	0.62	0.96	0.75	0.73	0.34	0.47	0.84	0.83	0.84
10	z, v, ohmm	0.63	0.58	0.89	0.70	0.37	0.10	0.15	0.74	0.88	0.81	0.66	0.59	0.88	0.70	0.58	0.20	0.30	0.80	0.93	0.86
11	d, v	0.73	0.69	0.85	0.76	0.62	0.48	0.54	0.85	0.86	0.85	0.76	0.69	0.87	0.77	0.67	0.57	0.62	0.94	0.83	0.88
12	d, ohmm	0.75	0.71	0.83	0.76	0.64	0.58	0.61	0.90	0.85	0.87	0.77	0.72	0.84	0.78	0.67	0.67	0.67	0.97	0.81	0.88
13	d, v, ohmm	0.70	0.75	0.69	0.72	0.55	0.51	0.53	0.77	0.89	0.83	0.76	0.80	0.66	0.73	0.65	0.69	0.67	0.84	0.94	0.88
14	x, y, v	0.63	0.61	0.84	0.71	0.51	0.16	0.25	0.68	0.89	0.77	0.63	0.67	0.83	0.74	0.51	0.28	0.36	0.65	0.81	0.72
15	x, y, ohmm	0.47	0.43	0.66	0.52	0.59	0.13	0.21	0.49	0.62	0.55	0.44	0.47	0.71	0.57	0.38	0.03	0.05	0.40	0.59	0.48
16	x, y, v, ohmm	0.72	0.70	0.72	0.71	0.60	0.53	0.56	0.84	0.90	0.87	0.71	0.72	0.75	0.74	0.60	0.54	0.57	0.79	0.84	0.81
17	x, z, v	0.70	0.62	0.92	0.74	0.66	0.26	0.38	0.80	0.90	0.85	0.72	0.66	0.88	0.75	0.72	0.36	0.48	0.80	0.94	0.86
18	x, z, ohmm	0.54	0.50	0.76	0.61	0.31	0.15	0.20	0.69	0.70	0.69	0.59	0.66	0.67	0.67	0.50	0.35	0.41	0.58	0.76	0.66
19	x, z, v, ohmm	0.73	0.67	0.86	0.75	0.71	0.39	0.50	0.79	0.92	0.85	0.69	0.71	0.82	0.76	0.61	0.39	0.48	0.72	0.89	0.80
20	x, d, v	0.75	0.73	0.74	0.74	0.64	0.56	0.60	0.85	0.93	0.89	0.74	0.82	0.62	0.70	0.61	0.70	0.65	0.84	0.92	0.88
21	x, d, ohmm	0.75	0.81	0.68	0.74	0.59	0.76	0.66	0.90	0.80	0.85	0.78	0.89	0.71	0.79	0.63	0.84	0.72	0.91	0.79	0.85
22	x, d, v, ohmm	0.76	0.66	0.92	0.77	0.72	0.45	0.56	0.92	0.89	0.90	0.78	0.73	0.94	0.82	0.75	0.57	0.65	0.90	0.85	0.87
23	y, z, v	0.66	0.63	0.82	0.71	0.54	0.24	0.34	0.73	0.90	0.81	0.73	0.65	0.91	0.76	0.80	0.32	0.46	0.79	0.96	0.87
24	y, z, ohmm	0.57	0.48	0.75	0.59	0.52	0.30	0.38	0.76	0.65	0.70	0.53	0.43	0.89	0.58	0.55	0.15	0.24	0.89	0.57	0.69
25	y, z, v, ohmm	0.66	0.61	0.81	0.70	0.54	0.26	0.35	0.77	0.91	0.83	0.69	0.61	0.90	0.72	0.62	0.31	0.41	0.85	0.87	0.86
26	y, d, v	0.64	0.88	0.34	0.49	0.48	0.71	0.57	0.77	0.87	0.82	0.69	0.88	0.34	0.50	0.53	0.90	0.67	0.92	0.83	0.87
27	y, d, ohmm	0.73	0.74	0.80	0.77	0.59	0.60	0.60	0.87	0.78	0.82	0.74	0.74	0.81	0.77	0.60	0.71	0.65	0.97	0.69	0.80
28	y, d, v, ohmm	0.67	0.56	0.98	0.71	0.61	0.30	0.41	0.93	0.72	0.81	0.61	0.52	0.97	0.68	0.50	0.23	0.32	0.99	0.65	0.78
29	z, d, v	0.68	0.71	0.75	0.73	0.57	0.35	0.44	0.70	0.92	0.79	0.69	0.71	0.66	0.68	0.60	0.43	0.50	0.73	0.99	0.84
30	z, d, ohmm	0.73	0.72	0.78	0.75	0.60	0.54	0.57	0.84	0.86	0.85	0.77	0.74	0.78	0.76	0.66	0.69	0.67	0.94	0.84	0.89
31	z, d, v, ohmm	0.69	0.58	0.96	0.72	0.65	0.31	0.42	0.89	0.78	0.83	0.68	0.57	0.97	0.72	0.63	0.33	0.43	0.96	0.75	0.84
32	x, y, z, v	0.68	0.76	0.55	0.64	0.54	0.57	0.56	0.74	0.90	0.81	0.63	0.82	0.50	0.62	0.49	0.57	0.53	0.68	0.83	0.75
33	x, y, z, ohmm	0.51	0.86	0.40	0.55	0.42	0.26	0.32	0.45	0.85	0.59	0.52	0.89	0.47	0.62	0.53	0.16	0.25	0.42	0.95	0.59
34	x, y, z, v, ohmm	0.71	0.68	0.75	0.71	0.60	0.45	0.51	0.81	0.92	0.86	0.73	0.72	0.81	0.76	0.66	0.52	0.58	0.79	0.86	0.83
35	x, y, d, v	0.76	0.73	0.80	0.76	0.67	0.58	0.62	0.88	0.91	0.90	0.79	0.75	0.90	0.82	0.73	0.61	0.67	0.89	0.86	0.87
36	x, y, d, ohmm	0.70	0.65	0.82	0.73	0.66	0.36	0.47	0.78	0.92	0.84	0.73	0.68	0.93	0.79	0.81	0.41	0.54	0.77	0.87	0.82
37	x, y, d, v, ohmm	0.77	0.76	0.78	0.77	0.66	0.62	0.64	0.88	0.90	0.89	0.83	0.83	0.88	0.85	0.76	0.74	0.75	0.92	0.88	0.90
38	x, z, d, v	0.73	0.63	0.95	0.76	0.76	0.30	0.43	0.84	0.92	0.88	0.72	0.66	0.95	0.78	0.80	0.31	0.45	0.78	0.92	0.84
39	x, z, d, ohmm	0.74	0.71	0.80	0.75	0.66	0.48	0.56	0.81	0.92	0.86	0.74	0.83	0.82	0.82	0.67	0.52	0.59	0.72	0.90	0.80
40	x, z, d, v, ohmm	0.71	0.68	0.79	0.73	0.63	0.38	0.47	0.78	0.96	0.86	0.66	0.66	0.75	0.70	0.53	0.29	0.38	0.72	0.97	0.83
41	y, z, d, v	0.71	0.65	0.92	0.76	0.68	0.29	0.41	0.79	0.91	0.85	0.75	0.63	0.96	0.76	0.77	0.40	0.52	0.92	0.90	0.91
42	y, z, d, ohmm	0.70	0.68	0.83	0.75	0.60	0.40	0.48	0.79	0.88	0.83	0.70	0.59	0.91	0.72	0.65	0.31	0.43	0.91	0.89	0.90
43	y, z, d, v, ohmm	0.73	0.68	0.90	0.78	0.67	0.40	0.50	0.82	0.88	0.85	0.75	0.64	0.94	0.76	0.72	0.43	0.54	0.94	0.87	0.91
44	x, y, z	0.50	0.51	0.60	0.55	0.43	0.28	0.34	0.53	0.61	0.56	0.45	0.53	0.53	0.53	0.35	0.29	0.32	0.46	0.53	0.49
45	x, y, d	0.76	0.70	0.87	0.77	0.69	0.50	0.58	0.88	0.90	0.89	0.81	0.77	0.93	0.85	0.79	0.63	0.70	0.88	0.89	0.89
46	x, y, z, d	0.75	0.73	0.83	0.77	0.65	0.55	0.60	0.86	0.88	0.87	0.80	0.72	0.91	0.80	0.76	0.62	0.68	0.97	0.87	0.92
47	x, y, z, d, v	0.76	0.77	0.78	0.78	0.66	0.58	0.62	0.84	0.92	0.88	0.84	0.83	0.88	0.86	0.79	0.70	0.74	0.88	0.93	0.90
48	x, y, z, d, ohmm	0.77	0.77	0.78	0.78	0.65	0.62	0.64	0.86	0.89	0.88	0.87	0.88	0.89	0.89	0.80	0.83	0.81	0.94	0.89	0.91
49	x, y, z, d, v, ohmm	0.76	0.72	0.84	0.78	0.68	0.52	0.59	0.86	0.90	0.88	0.74	0.66	0.92	0.77	0.70	0.43	0.54	0.89	0.88	0.88
	Min	0.45	0.37	0.34	0.49	0.31	0.06	0.11	0.45	0.27	0.43	0.41	0.37	0.34	0.49	0.35	0.03	0.05	0.37	0.22	0.36
	Mean	0.68	0.66	0.78	0.70	0.60	0.40	0.46	0.79	0.84	0.81	0.69	0.68	0.80	0.72	0.62	0.44	0.49	0.80	0.83	0.80
	Max	0.77	0.88	0.98	0.78	0.90	0.76	0.66	1.00	0.96	0.90	0.87	0.89	0.97	0.89	0.81	0.90	0.81	1.00	0.99	0.00

Figure 2 shows the confusion matrix of the model ensemble, the matrix indicates good ensemble performance on tuff and limestone classes, but clay class remains problematic.
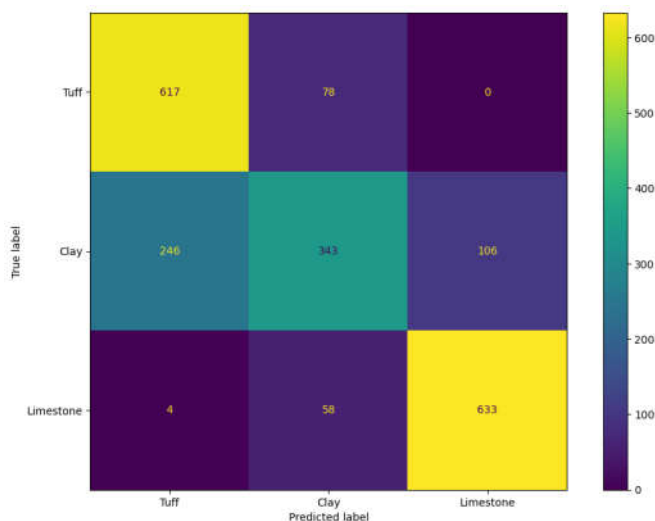

Figure 2. Confusion matrix of model ensemble prediction on all data

Table 5. Basic metrics of model ensemble

	Precsion	Recall	f1-score
Tuff	0.71	0.89	0.79
Clay	0.72	0.49	0.58
Limestone	0.86	0.91	0.88
Ensembe accuracy	0.76		

The model ensemble improved all average metrics from Table 5 by 3% to 12%. The most notable increase was observed in the clay class, which initially had the poorest metrics from individual classifiers, as well as in the overall ensemble classification. This indcates the usfullness of the ensemble method.

6   Results

The model ensemble for classification developed in the previous section was applied to the preprocessed input data. Below, we present some prediction results as examples of what can be generated from such a model.
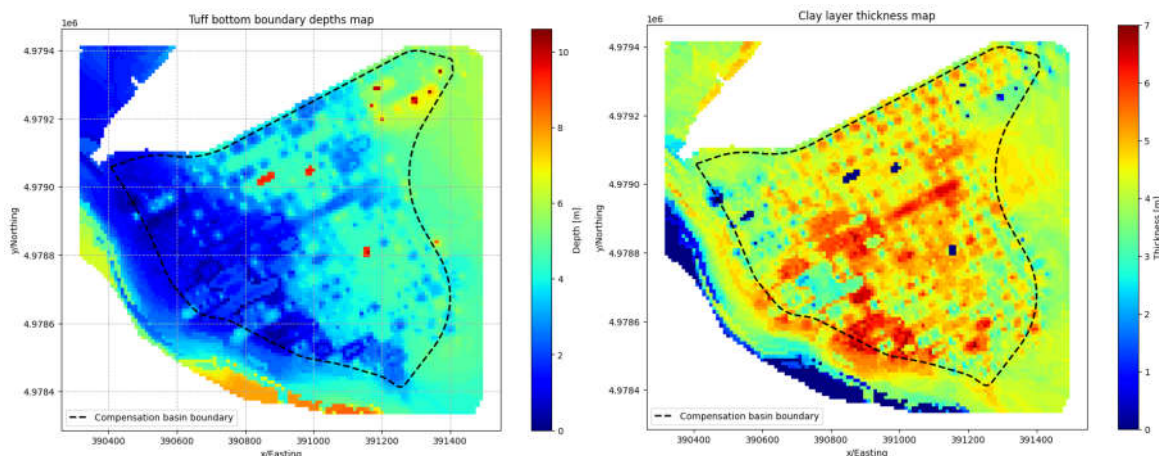
Figure 3. (left) Tuff layer bottom boundary map, (right) Clay layer thickness map
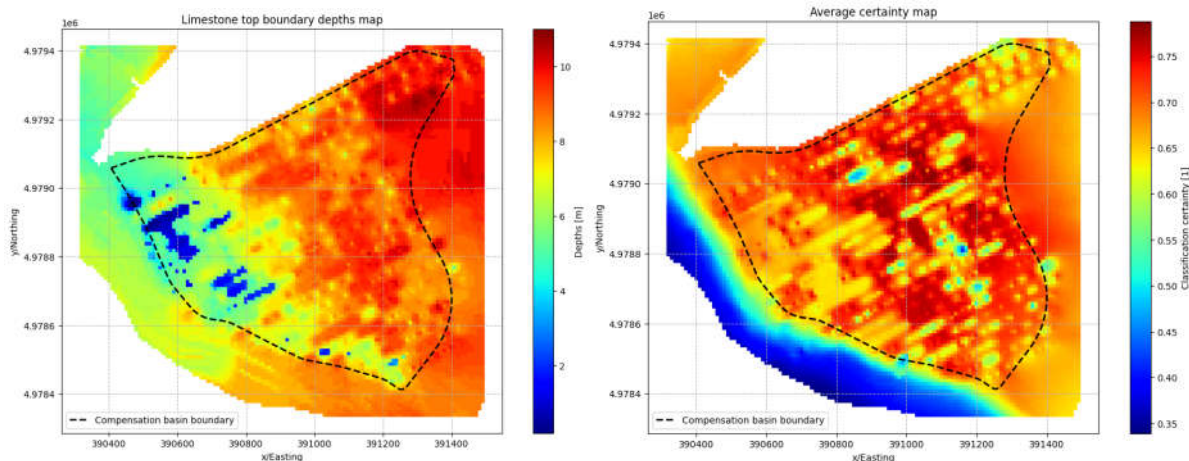
Figure 4. (left) Limestone surface depths, (right) Generated average certainty map
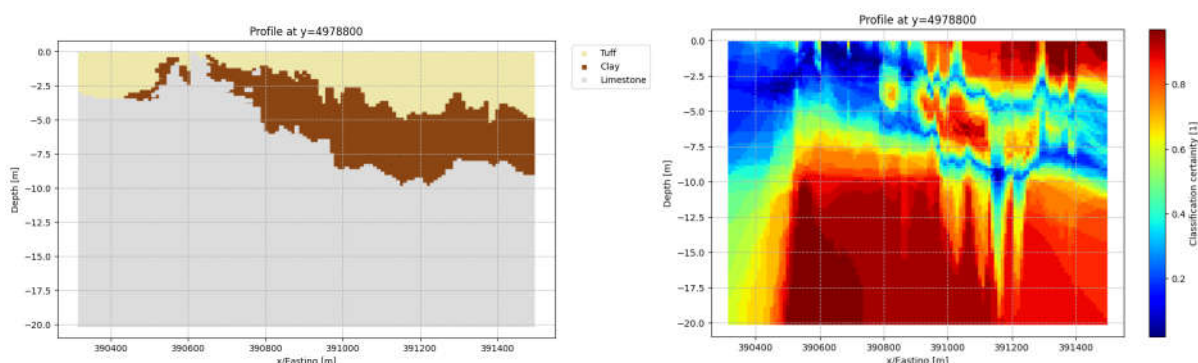
Figure 5. (left) Classification result profile at y= 4978800 on x-d plane , (right) Classification certainty profile at y= 4978800 on x-d plane
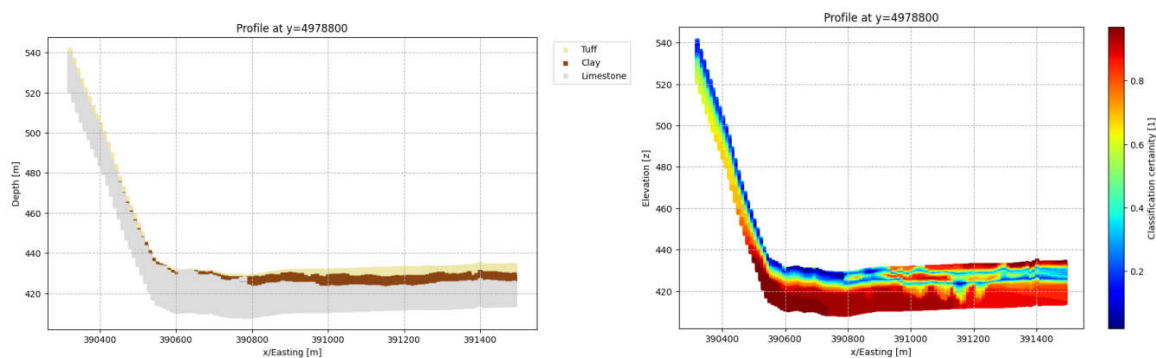
Figure 6. (left) Classification result profile at y= 4978800 on x-z plane, (right) Classification certainty profile at y= 4978800 on x-z plane

7   Settlement

A Settlement was calculated using the formula for soil deposits under a uniform load of the future hydrostatic pressure to 48kPa which is equivalent of 4.8m water column. Total settlement is the sum of deformations of individual soil layers, determined by stress changes and compressibility. The soil column is divided into layers with assumed uniform compressibility. Calculated settlement has an orientational purpose, just to show which area is more prone to settlement.

The expression for calculating the settlement is as follows:

$$s = \frac{\sigma}{E_s} H \tag{6}$$

where:

s - soil settlement,

σ - vertical load,

H - height of the soil layer,

E_s - oedometer modulus of deformation.

As previously mentioned, the subsurface spatial model was generated using data points on a 10 x 10 m grid. During the settlement map generation, each layer at each point was assigned a deformation modulus based on whether it was tuff or clay which is given below. The settlement for each layer at each point was calculated and summed to give the total settlement and the settlement map was created as shown in Figure 7.

Used oedometer modulus of soil deposits: Tuff - $E_s = 2\ MPa$ and Clay - $E_s = 10\ MPa$
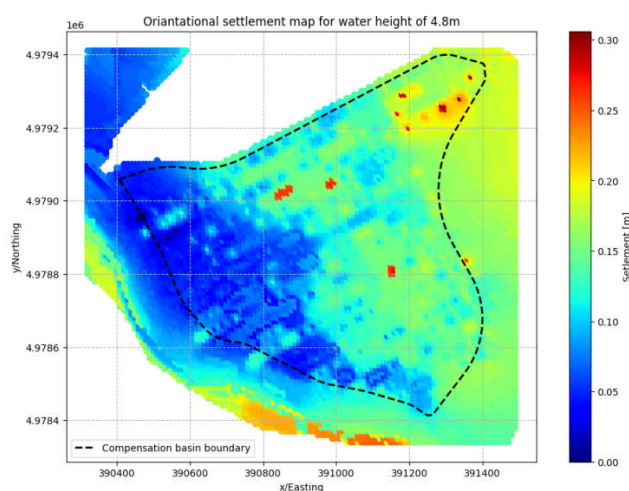
Figure 7. Settlement map

8   Interpretation of results

The results of this work include a spatial subsurface model, a spatial classification certainty model, and a settlement map, with this paper presenting only a glimpse of the findings. The aim is to demonstrate the value of the output from such models. In Figure 3(left), three areas with thick tuff deposits are observed, with tuff thickness increasing in the northeast direction, as does the clay, as shown in Figure 3(right). A limestone bedrock ridge is detected in the same direction, dividing the basin into two parts, as confirmed by the profile in Figures 5 and 6. The most intriguing aspect is the classification certainty of the profiles. At material boundaries, the certainty is almost 0, which is expected. However, the interesting parts are the low certainty zones in the limestone, which can be interpreted as fault zones or extremely weathered rock, essentially mixed limestone boulders with clay. These zones were added to the limestone as mentioned in Section 2. The average certainty map of the site highlights locations with low average certainty that are prone to additional investigations. Nevertheless, below the limestone layer, which has high certainty at bedrock locations, this high certainty significantly impacts the average values. The settlement map shows a resemblance to the tuff boundary depths map. This similarity is reasonable because tuff has five times more influence on settlement than clay.

9   Conclusion

This paper demonstrates the implementation of geostatistics and machine learning in geosciences for creating spatial subsurface models. Machine learning has an advantage over classical interpolation methods because it is better in generalization and can effectively deal with large high-dimensional, large datasets, can solve highly non-linear problems, and its computational complexity results are lower. After

preprocessing the raw data, multilayer perceptrons were fitted to different data subsets. While the overall metrics of the individual multilayer perceptron models were slightly above chance, combining them with the ensemble method resulted in a powerful and robust tool. The results presented in this paper highlight various applications of such a model. A spatial subsurface model was created, an average certainty map was generated, and information about soil deposits and the limestone surface was derived. Additionally, geomorphological features can be detected, although such claims require further validation. However, the model has its limitations. While it generalizes well, some specific information is lost. For instance, the model could not detect areas where tuff is directly above limestone or where clay is on the terrain surface, and it has a problem with correctly classifying clay. Nonetheless, these areas exhibit low certainty, demonstrating the effectiveness of the classification certainty model.

References

HE Senj 2, *Dno bazena i popratni nasipi, Geotehnički istražni radovi za izradu glavnog projekta, Elaborat za dno bazena i popratne nasipe*, INSTITUT IGH d.d., Zavod za projektiranje, Odjel za geotehnička istraživanja, Janka Rakuše 1, 10 000 Zagreb, Zagreb, veljača 2023.

HE Senj 2 – Glavni projekt, Kompezacijski bazen Gusić polje 2, Geološki radovi, Institut za geološka istraživanja – Zagreb, Sachsova 2, Zavod za hidrogeologiju i inženjersku geologiju, Zagreb, veljača 1998.

Kompezacijski bazen Gusić polje 2, Geofizička istraživanja, Moho d.o.o., Zagreb, svibanj 1997.,

HEP d.d. (Hrvatska elektroprivreda d.d.). Available online: www.hep.hr/projekti/hidroenergetski-sustav-senj-2/247 (accessed on 11 July 2024).

Chollet, F. (2017). *Deep learning with python*

Erharter, G. H., Oberhollenzer, S., Fankhauser, A., Marte, R., & Marcher, T. (Year). *Learning decision boundaries for cone penetration test classification.* Institute of Rock Mechanics and Tunnelling, Graz University of Technology, Graz, Styria, Austria; Institute of Soil Mechanics, Foundation Engineering and Computational Geotechnics, Graz University of Technology, Graz, Styria, Austria. Correspondence to G. H. Erharter (erharter@tugraz.at)

Garet, J. et al. (2023), *An Introduction to Statistical Learning* – with Applications in Python

Isaaks, E. H., & Srivastava, R. M. (1989). *Applied Geostatistics.* New York: Oxford University Press.

Davis, J. C. (2002). *Statistics and Data Analysis in Geology* (3rd ed.). Hoboken, NJ: Wiley.

Sever Z., *Hydroelectric power plants in Croatia*, Hrvatska elektroprivreda d.d., Elektrprojekt Consulting Engineers, Zagreb, February 2000.

EXCAVATION OF LARGE UNDERGROUND POWER HOUSE CAVERN & SURGE SHAFT IN ADVERSE GEOLOGICAL FEATURES LIKE SHEARED/FRACTURED ZONE: A CASE STUDY ON MANGDECHHU H.E. PROJECT, BHUTAN

SHRISH DUBEY [1], PRASHANT JAISWAL [2], PRADEEP KUMAR GARNAYAK [3], DEEPAK VERMA [4]

[1] NHPC Limited, India, shrish@nhpc.nic.in

[2] NHPC Limited, India, pjaiswal@nhpc.nic.in

[3] NHPC Limited, India, pradip333@rediffmail.com

[4] NHPC Limited, India, deepakverma33546@gmail.com

Abstract

The complex geological region and unpredictable nature of the Himalayas pose major challenges for construction of large underground structures. This paper presents the excavation of Power House Cavern & Surge Shaft of Mangdechhu Hydroelectric Project in poor geological features like sheared/fractured zones. The Cavern was proposed to be explored through a 410m long drift, however only 36.85m of Cavern was explored since the excavated drift got flooded with silt due to 'Aila' flood in May, 2009 and balance portion of cavern was investigated by two drill holes and Hydrofrac test was carried out to reveal the in-situ stress conditions. During the excavation of the central gullet of the underground caverns, a 1.5 m to 2.0 m thick sheared /fractured zone was encountered in oblique direction to the caverns. Due to its low dipping profile, this zone intersected both upstream and downstream walls of cavern and also partially affecting the crown of Transformer Cavern. This sheared/fractured zone could not be deciphered previously due to limited length of drift in the cavern. The geology of the caverns was again explored through additional vertical drill holes and both in-situ shear & deformability tests and laboratory tests were conducted for deciphering the rock mass properties of the sheared/fractured zone. Similarly, 152m deep Surge Shaft was explored by two drill holes revealing bedrock to be encountered at 15 to 18m below the ground level. The encountered strata comprised of highly fractured, highly weathered to decomposed rock mass with low in-situ strength.

Based on the numerical analysis of above structures, the excavation methodology and rock support system of Cavern and Shaft were updated and an elaborate instrumentation program was devised. This proved to be beneficial for the safe excavation of Power House Cavern & Surge Shaft in geologically challenging conditions, resulting in timely commissioning of Project.

Key words

Hydropower, Power House Cavern, Surge Shaft, Excavaion, Shear zone, Geological Challenges, Numerical Analysis, Instrumentation

1 Introduction

The Mangdechhu Hydroelectric Project is located in Trongsa Dzongkhag (District) of central Bhutan. The Black Mountains separate Western Bhutan from Central Bhutan. This region includes Trongsa and valleys of Bumthang including Chumey, Choekhar, Tang and Ura valleys.

Figure 1. Location Map of Mangdechhu Hydroelectric project, Bhutan

The project is a run-off the river project, located on the Mangdechhu River with an installed capacity of 720MW. The project comprises a 112m of high concrete gravity dam with length of 148m at the top. Two desilting chambers of 14m width, 17.7m height and 340m length have been provided to remove silt of particle size 0.2mm or above. A Head Race Tunnel of diameter 6.5m and 13.5km length carrying a total discharge of 118cumecs is provided. Restricted orifice type Surge Shaft of 13.5m diameter and 152m height is provided to accommodate the surge.

The Power House Cavern of size 155 x 23 x 50 m is separated from the Transformer Cavern of size 135.5 x 18 x 23m by 40m thick rock pillar. The Power House has four numbers of 180 MW vertical axis pelton turbine driven generating units. The Power House yields annual energy of 2925MUs in a 90% dependable year with 95% machine availability.
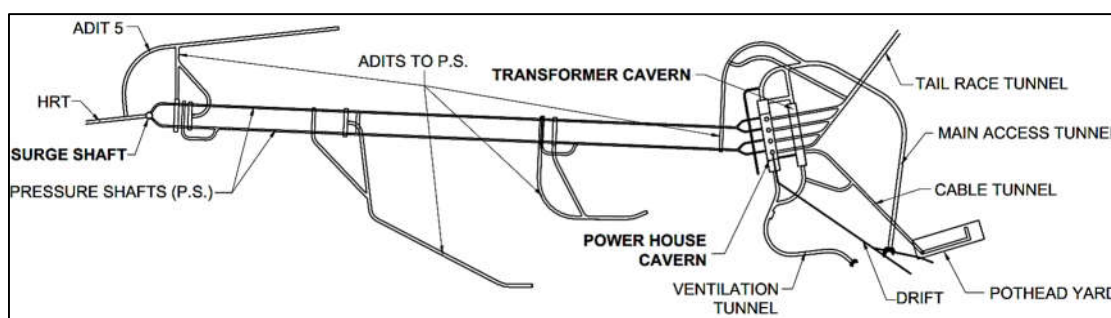
Figure 2. Poject layout of Surge Shaft & Power House Complex Area

2 Geological Set-up

2.1 Power House Cavern

The Power House cavern is located in chekha formation with super incumbent cover of about 150m-200m. The Chekha Formation consists of quartzite interbedded with biotite-muscovite-garnet schist.

Power House cavern is aligned almost parallel to direction of maximum horizontal principle stress. At Detailed Project Report (DPR) stage, Power House cavern was explored through a 410m long drift, covering only 36.85m of Machine hall length. Excavated Drift got flooded with silt due to Aila flood in May, 2009 and balance portion of drift could not completed. Thus, the balance portion of cavern was investigated by two drill holes. Rockmass at Power House Complex comprised of extremely strong to strong quartzite rock and medium strong to softer mica schist with occasional strong pegmatite, mafic and granite intrusions. The predicted rockmass was of Class-III (77%) and balance Class-II (23%) with minor Class-IV.

The rock mass was categorized based on Z. T. Bieniawski's Rock Mass Rating (RMR) classification, i.e Class-I (RMR 100-81), Class-II (RMR 80-61), Class-III (RMR 60-41), Class-IV (RMR 40-21) & Class-V (RMR below 20).

However, during central gullet excavation of the Power House & Transformer Caverns, a 1.5 m to 2.0

m thick sheared material band surrounded by fractured rock of 3 to 4 m width all around was encountered with orientation of N290-310/15-20° in oblique direction to the caverns with a low dip inclination, upwards and towards the drive. The low dipping profile of this zone led to its intersection with both walls (u/s & d/s) of the Power House Cavern and also partially affected the crown of Transformer Cavern. To determine detailed geological conditions to be encountered during excavation, 5 nos. of additional drill holes were drilled in the caverns along with 3-D logging of the excavated portion.
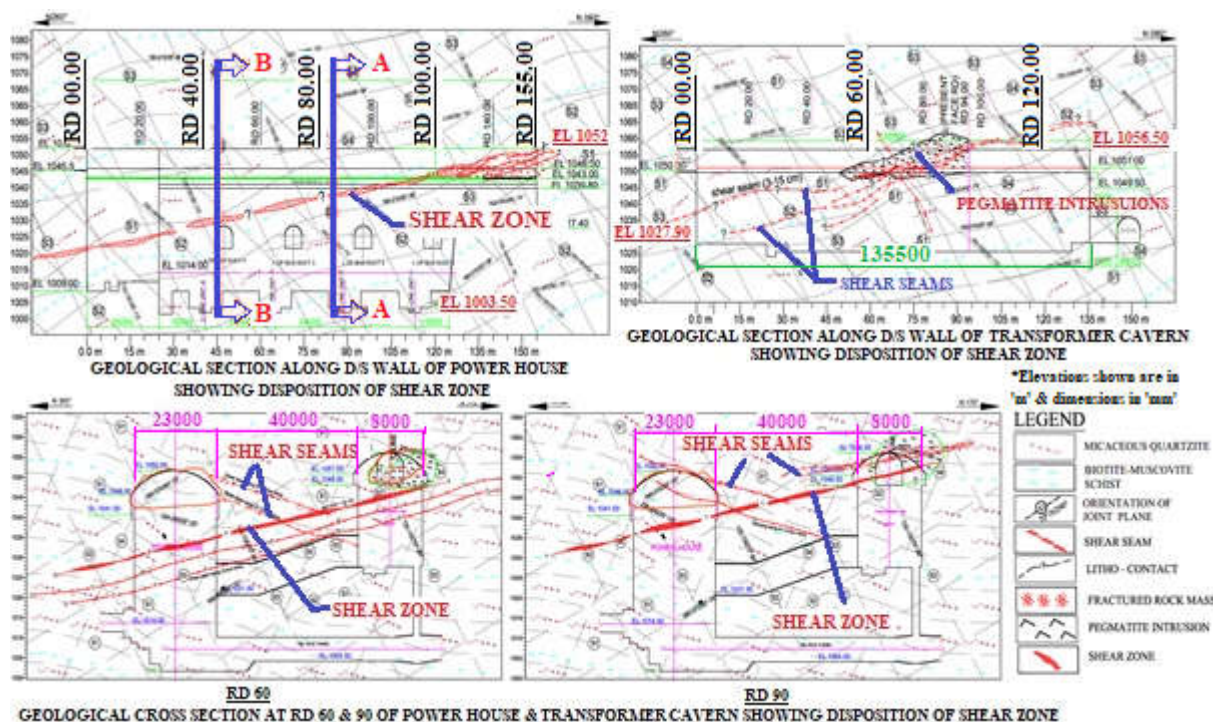
Figure 3. Power House & Transformer Cavern Geology

2.2 Surge Shaft

The Surge Shaft was proposed on the hill overlooking Trongsa-Gelephu highway & has a gentle slope. The drill holes for Surge Shaft, revealed 15 to 18m of overburden at the surface before encountering the bedrock. As such, about 10-13m shaft excavation in overburden was foreseen. The bed rock comprised of micaceous quartzites with bands or intercalations of mica schist and minor intrusions of granite and pegmatite. Rock strata also consisted of very poor mica schists which were weak to medium strong. Even though moderate or high permeability values were not obtained in drill hole, it was envisaged that fractured quartzite bounded by impervious mica schist might have some confined aquifers. This envision was further strengthened from the observations in adjacent area towards the east where the resistivity imaging had indicated water charged strata. In another drill hole, about 500m towards east, water table was encountered at 15m depth.

In view of the above challenging geological setup at Surge Shaft location, it was shifted by 20m towards upstream so that the shaft is placed in comparatively better geology, however the conditions at the shifted location were still challenging. The strong amphibolite band was dipping downwards from valley side towards the hill side. Hence, on shifting the shaft upstream, this band encountered the shaft at a lower level of excavation where the stresses would be high and thus it was expected that shifting the shaft upstream would reduce the stress distribution and displacement contours. Also, the shaft would get more side rock cover at the upstream location as compared to Detailed Project Report (DPR) location thereby increasing its overall stability.

The encountered strata at shifted location comprised of highly fractured, highly weathered to decomposed rock mass with low in-situ strength. The rock mass essentially comprised of Biotite schist with interfolial bands of Quartzite varying in thickness from 2 to 10cm and occasionally reaching up to

30cm. The rock mass was traversed by pegmatite and amphibolitic intrusions. A prominent amphibolitic intrusion was encountered between EL.1802 to 1790m which was represented by slightly strong and massive weathered amphibolites in SE and SW quadrant and extending midway up to the NE quadrant.
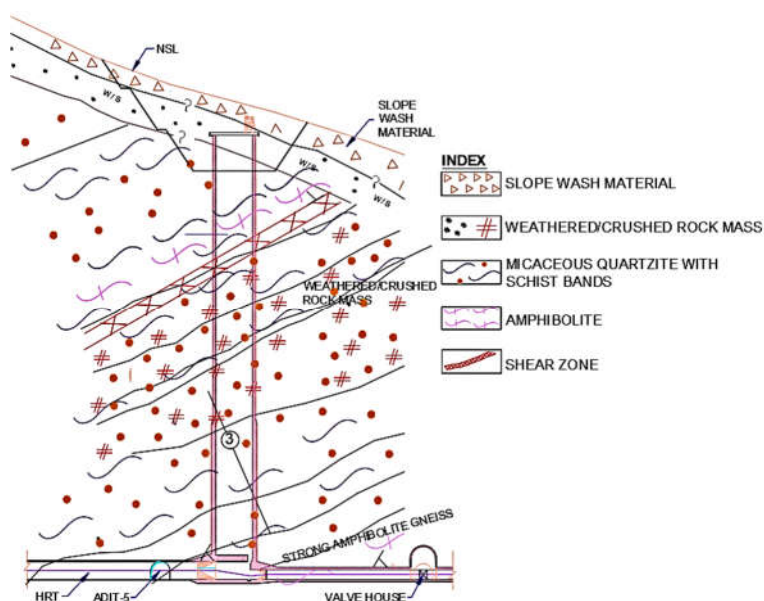

Figure 4. Surge Shaft Geology

3   In-Situ Stress Condition

During the geological exploration process, hydrofac test was carried to reveal the in-situ stress condition of Power House cavern. The maximum principal stress (σ_H) was about 8.38MPa with an orientation of N 70°E , where as the minor principal stress (σ_h) was about 5.59MPa. The horizontal stress to vertical stress ratio (k) was 1.47 corresponding to vertical stress of about 4.76MPa. The caverns are aligned in N 80°E which is almost parallel to maximum principal stress direction.

For analysis of caverns which are at sufficient depth below the ground surface, a constant vertical stress of 4.76 MPa along with 'k' value of 1.47 has been adopted. On the other hand, for open to air Surge Shaft, owing to its proximity to surface which tends to have higher 'k' values, gravity stresses varying with depth below the ground surface along with peak 'k' value of 1.76 has been adopted.

4   Rock Mass Parameters

In Power House drift, laboratory and in-situ deformability tests were carried out at Detailed Project Report (DPR) stage to assess the different strength parameters of Rockmass. In-situ deformability test results of rockmass by Goodman Jack method were as below:

Table 1. Deformation modulus of Rockmass by Goodman Jack method

Site	Ed, GPa	Ee, GPa	Ee/Ed
Vertical Borehole	11.65 – 20.90	36.42 – 47.45	2.03 – 4.07
Inclined Borehole	13.27 – 16.95	36.29 – 48.59	2.54 – 3.26

After encountering sheared/fractured zone during the excavation of central gullet, Plate Load Test & Direct Shear Test were carried out to assess the rock mass properties of shear/fractured zone material and disturbed rock mass. The summary of the results are listed below.

Table 2. Deformation modulus of Rock M ass by PlateLoad Test

In-Situ Deformability Parameters		
Rock Mass	Modulus of Deformability of Rock Mass (E_m) in GPa	Modulus of Elasticity of Rock Mass (E_{em}) in GPa
Class III	2.01 to 3.99	2.31 to 5.24
Shear Zone Area	0.46 to 1.24	0.49 to 1.36

Table 3. In-situ shear parameters of Rock Mass by Direct Shear Test

Rock Mass		Cohesion (C)		Friction Angle (Φ) in degrees
		Kg/cm^2	MPa	
Class III	Peak	3.8267	0.375	35.8°
	Residual	2.7918	0.274	34.2°
Shear Zone Area	Peak	3.6111	0.354	25.6°
	Residual	2.3538	0.231	25.3°

For analysis of Surge Shaft, the rock mass was divided into zones of different depths and based on the various rock mechanics tests and geological setup of rockmass, following properties were adopted:

Table 4. Properties for Surge Shaft at DPR location

Zone & Depth from surface	Rock Type	Cohesion (MPa)	Friction Angle (Φ) in degrees	Bulk Modulus (GPa)	Shear Modulus (GPa)	Tensile Strength (MPa)
Zone-I (10m)	Strong to Very Strong Amphibolite	1.2	67°	16	12	0.12
Zone-II (10 - 80m)	Fractured Quartzites with bands of Mica Schist	0.362	37°	0.9	0.7	0.03
Zone-III (80 – 200m)	Micaceous Quartzite with bands of Mica Schist	0.812	42°	3.5	2.56	0.08

Table 5. Properties for Surge Shaft at 20m upstream of DPR location

Zone & Depth from surface	Rock Type	Cohesion (MPa)	Friction Angle (Φ) in degrees	Bulk Modulus (GPa)	Shear Modulus (GPa)	Tensile Strength (MPa)
Zone-I (0-20m)	Micaceous Quartzite with bands of Mica Schist	0.812	42°	3.5	2.56	0.08
Zone-II (20 - 30m)	Strong to Very Strong Amphibolite Schist	1.2	67°	16	12	0.12
Zone-III (30 – 100m)	Fractured Quartzites with bands of Mica Schist	0.362	37°	0.9	0.7	0.03
Zone-IV (100 - 200m)	Micaceous Quartzite with bands of Mica Schist	0.812	42°	3.5	2.56	0.08

Various provisions of grouting and rock support were also considered along with above rock mass parameters in the analysis.

5   Numerical Analysis and Results

5.1 Power House & Transformer Cavern

Phase^2 Software of Rocscience was used to simulate numerical analysis of Power House and Transformer Cavern with shear zone. Shear zone plane traverses through the walls of both caverns at different locations including bus ducts. Sensitivity analysis of the caverns was carried out at different

locations to reveal the effect of shear/fractured zone on the stability of both caverns. In order to incorporate the in-situ shear parameters of class-III rockmass, a disturbed zone was modelled around the excavated periphery to consider the effect of disturbance due to blasting. Also, to include the effect of grouting done by 6m deep holes in Class-III rock & 20m deep holes in shear zone material, in-situ deformation modulus and shear parameters of these materials were enhanced upto respective hole depths. At the excavated boundary, the sheared material was planned to be scooped out upto a certain depth, backfilled with concrete thereby plugging the weak material inside the walls and the concrete plug shall be stitched into the wall with longer rock bolts. This methodology was also simulated in the model to check its effect on stability.
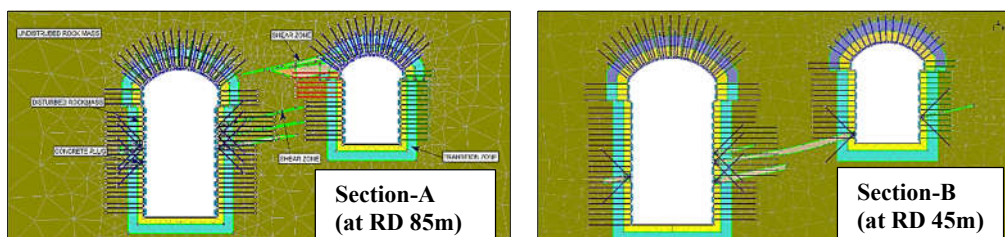
Figure 5. Numerical model of Powerhouse and Transformer Cavern depicting extent of shear zone

Deformations and stress distribution around underground caverns in non-homogeneous rock mass were determined. The behavior of rock mass was analyzed by elasto-plastic model considering the effect of weak zones like sheared/fractured zone. Effect of shear zone on the upstream wall of Power House cavern and downstream wall of Transformer cavern was quite less. The analysis revealed that position of shear zone in the rock pillar vitally affected the stability of both caverns and rock pillar itself. The extent of plastic zone in downstream wall of Power House cavern at RD 85m (section-A) & at RD 45m (Section-B) were about 15m and 13m respectively in the vicinity of sheared/fractured zone. The maximum deformation on the walls and crown were as below:

Table 6. Maximum Deformations in Power House & Transformer Cavern

Location	Section-A (RD 85)	Section-B (RD45)
Power House - Wall	45 mm	50 mm
Power House - Crown	24 mm	24 mm
Transformer Cavern - Wall	24 mm	17 mm
Transformer Cavern - Crown	26 mm	24 mm

The above deformations were within the permissible range of 0.1% of cavern dimension with provided rock support / enhancement measures.
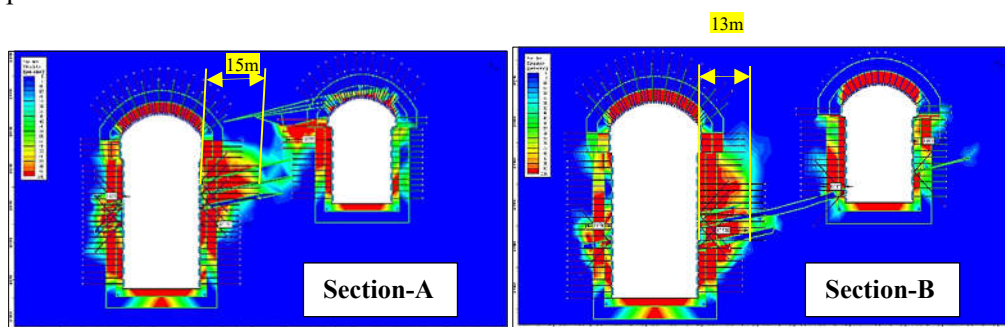
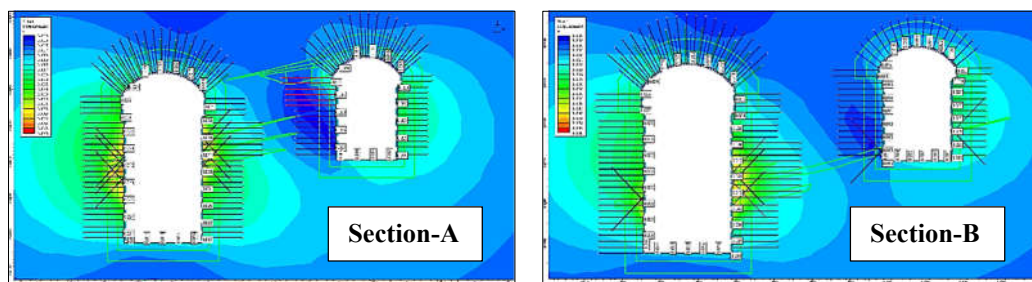**Figure 6.**Effect of shear zone on yielding of rockmass

Figure 7. Effect of shear zone on wall displacement

5.2. Surge Shaft

The Surge Shaft was analysed both at the Detailed Project Report (DPR) as well as shifted location to determine the actual effects of shifting the shaft upstream by 20m. Mohr-Coulomb plastic model of Surge Shaft without Rock supports and with rock supports were analysed. A 3D model was developed using the finite difference software FLAC3D to simulate the complex geometry of the Surge Shaft and its construction sequence. It is composed of 12000 zones, 12621 grid-points and 33220 structural elements. The Surge Shaft model was excavated in 16, each of 10m depth.
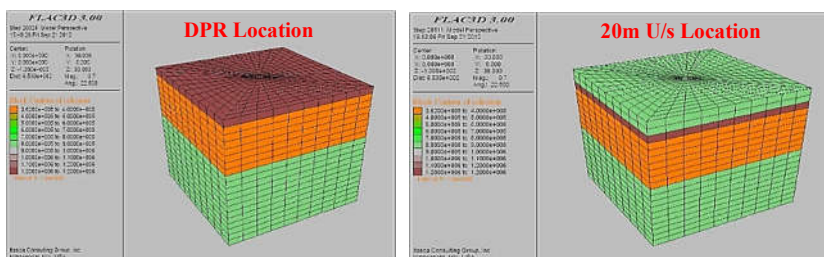
Figure 8. Models for Surge Shaft at DPR & 20m upstream
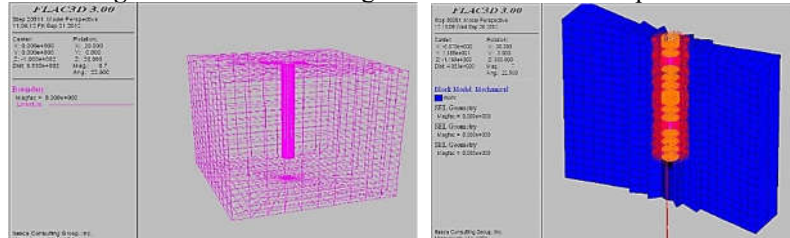
Figure 9. Surge Shaft – Meshing & Supported Model
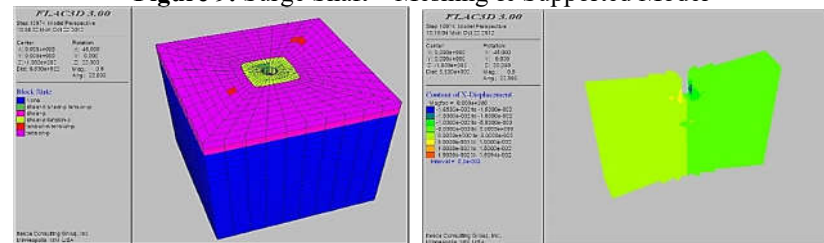
Figure 10. Surge Shaft – Results at DPR location for upto 40m depth of excvation

Table 7. Results for analysis at DPR location

Sl. no.	Depth of Excavation from top	Block state of Rock mass	Maximum horizontal displacement(mm)
1	10 m	Failure in Shear and Tension	4 mm
2	30 m	Failure in Shear	9 mm
3	40 m	Failure in Shear and Tension	16 mm

From the above results it was clear that failure in rock mass due to tension and shear continues even after supporting the excavated surface with pre-grouting, steel rib, rock bolts and shotcrete. Hence, the model was re-analysed at 20m upstream of DPR location.
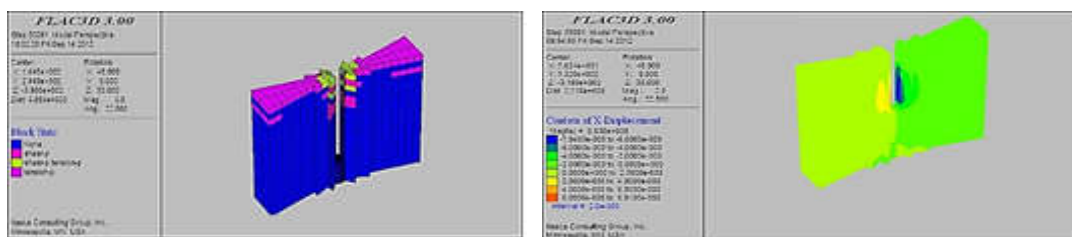
Figure 11. Surge Shaft – Results at 20m u/s of DPR location for upto 160m depth of excavation

Table 8. Results for analysis at 20m u/s of DPR location

Sl. no.	Depth of Excavation from Top	Block state of Rock mass	Maximum horizontal displacement(mm)
1	10m	No failure in shear and tension	1 mm
2	30m	No failure in shear and tension	2 mm
3	70m	No failure in shear and tension	6.2 mm
4	110m	No failure in shear and tension	8 mm
5	160m	No failure in shear and tension	8 mm

Above results show that shifting of Surge Shaft at 20m upstream of DPR location result in stable excavation with lower displacements.

6   Rock Support Measures

On the basis of numerical analysis and rock mass characteristics, the rock support system was reviewed for Power House and Transformer cavern. Also, the Surge Shaft was analyzed for shifted location in light of new geological conditions revealed. Based on the analysis, adequate support system for the treatment of the weak / shear zone and the methodology for the excavation of caverns & shaft were devised. The rock support system comprised of the following measures:

6.1. Power House & Transformer caverns

- The length of rock bolts at different locations was optimized on the basis of plastic / yield zone formed due to stress induced failures around the excavated caverns. On the downstream wall of the Power House cavern, 36mm diameter rock bolts of 18m length were installed at 1.5m spacing. At the upstream wall of Transformer cavern near the shear/fractured zones, 36mm diameter rock bolts of 12m length were used at 1.5m spacing. For areas on upstream and downstream walls of caverns which were not affected by shear zones, 36mm diameter rock bolts of 12m length were installed at 1.5m spacing were installed in Power House, while 36mm diameter rock bolts of 9m length were used at 1.5m spacing in Transformer cavern.
- Additional rock bolts in form of 36mm diameter, 12m long bolts at 3m spacing were installed alongside the previously installed 7.5m and 9m long rock bolts in the crown area.
- Thickness of steel fiber reinforced shotcrete (SFRS) was increased from 200mm to 250mm in the wall and crown portions of the caverns.
- Rockmass near the shear/fractured zone in the crown and wall was strengthened by consolidation grouting up to a depth of 6m. Similarly, consolidation grouting up to a depth of 20m was carried out along the shear/fractured zone.
- The exposed shear/fractured rock mass on the excavated surface was scooped out upto a maximum depth of 1.5 to 3m and filled with rich concrete of strength M30/A20 to form a concrete cladding which was stitched with competent bed rock using longer bolts of 36mm diameter and 18m length.
- Rock pillars between bus ducts were reinforced by stitching them with 32mm diameter bolts of 17m length in a staggered pattern. Holes for bots were drilled through one bus duct into adjacent bus duct, bolts were inserted and stressed from both sides which brought the rock pillar between them under

compression thereby stabilizing them.

- In the excavation methodology, bench height was reduced from 6m to 3m, along with controlled blasting and line drilling to reduce the damages due to blasting.
- Caverns were regularly monitored through an extensive network of geotechnical instruments.
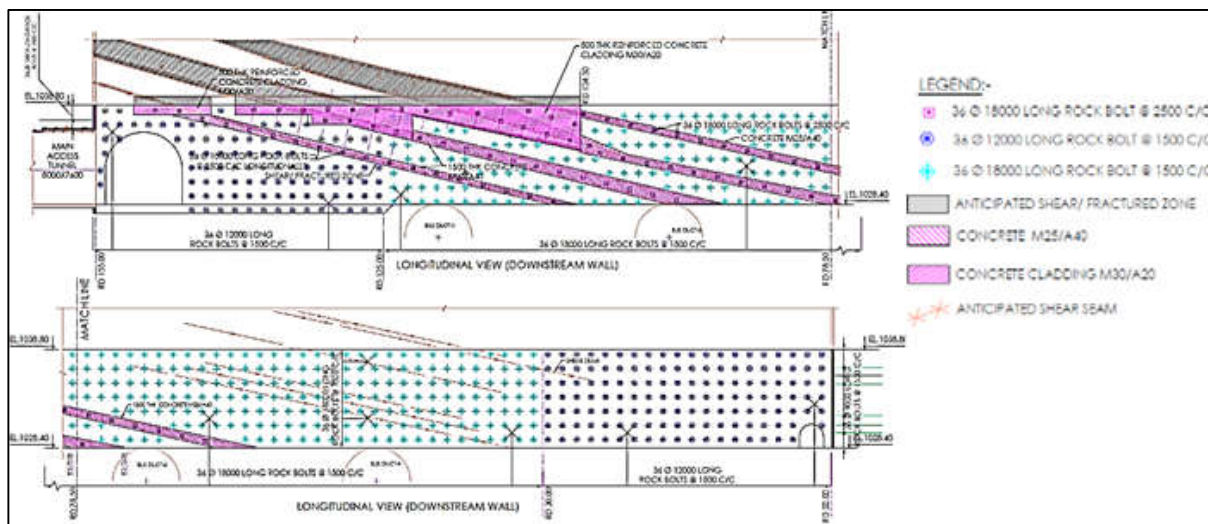

Figure 12. Rock support measures in the downstream wall of Power House Cavern

6.2. Surge Shaft

- Excavation methodology of Surge Shaft was changed from the use of raise borer (from the bottom to top) to full sinking method (from the top to bottom).
- Systematic pre-grouting and post-grouting of rock mass was done prior to excavation for improving the rock mass properties. Field tests were done before and after grouting validate improvement of rock mass properties.
- Simultaneously with the excavation, peripheral grouting was taken up radially in the form of two concentric rings around a zone, 4m and 7m away from the periphery of the shaft upto a depth of 100m.
- 200 mm thick steel fiber reinforced shotcrete (SFRS) was provided along with rock bolts of 32/36mm dia 6 to 12m length at 1.5m spacing to support the excavation.
- Steel ribs ISMB 250 at 500mm c/c spacing were provided upto a depth of 10m from the top of Surge shaft irrespective of rock class encountered. Ribs were also provided in poor rock mass and were embedded in SFRS for further strengthening.
- Consolidation Grouting was performed to prevent sudden rush of water during excavation.
- Pressure relief holes of 45mm dia, 5m length at 3m c/c spacing were provided above the steady state level of water in surge shaft.
- Control Blasting along with line drilling was used efficiently along with regular monitoring of excavation through geotechnical instruments.
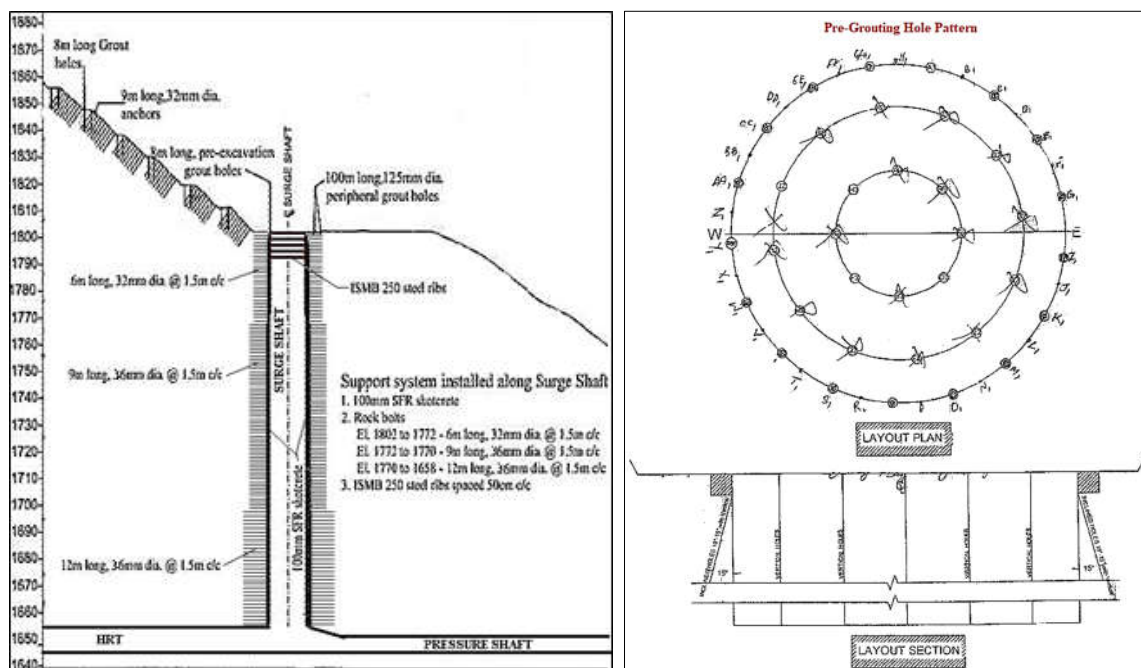
Figure 13. Rock support measures in Surge Shaft

7   Real Time Monitoring through geotechnical Instruments

Numerical analysis of the caverns & shaft revealed that deep seated movement were expected during excavation due to weak/shear/fractured zones. In order to monitor the behavior of excavated structures during excavation, an elaborate instrumentation program was designed comprising of load cell of capacity upto 100T, single (SPBX), multi-point (MPBX) bore hole extensometers of depth upto 20m, piezometers, tape convergence and survey target points. The actual loads and deformations obtained from these instruments were studied and numerical models were recalibrated such that their behavior matches the actual ground conditions right from the starting stages of excavation as soon as the receipt of instrumentation was started from site.

The readings of these instruments were plotted on graphs for each and every instrument installed at site and every fluctuation in the readings was co-related to ongoing activity (either construction activity or geological reason) at site. Accordingly, modifications in excavation methodology, benching sequence and rock support optimization were carried during the excavation based on the instrumentation readings. To understand the extent of successful incorporation of actual site data into numerical modeling and rightly predicting the future conditions to be faced in advanced stages of excavation, it can noted that the maximum deformations anticipated at wall and crown of Power House cavern were 50mm and 24mm respectively as per the calibrated numerical model which were in-line with maximum deformations observed at site were 43mm and 14mm.
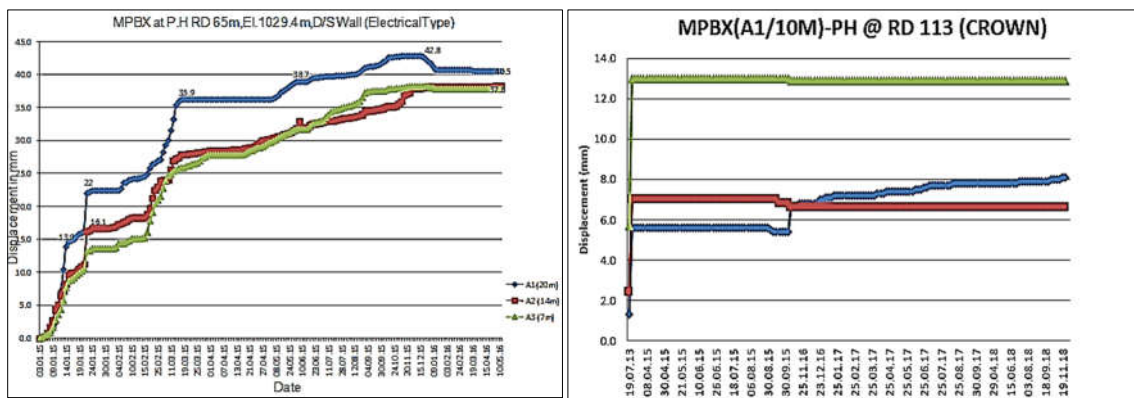

Figure 14. Displacement observed in Downstream wall and crown of Powerhouse Cavern
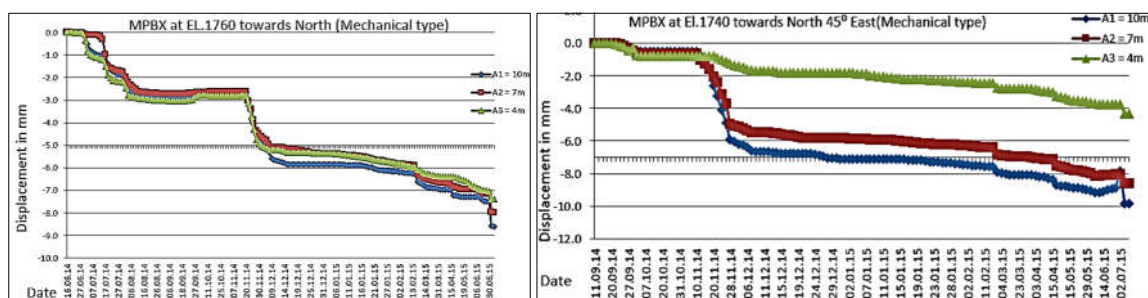
Figure 15. Load & Displacement observed in Surge Shaft

8   Conclusion

In complex Himalayan geology which is prone to geological surprises, prediction of geological conditions to be encountered and being ready for them beforehand plays a vital role in successful excavation of large underground cavities.

In case the geological features of project components could not be deciphered in early stages, detailed investigations are required during construction. Additional investigation results so obtained shall be incorporated in numerical models to revise the support requirements. A well planned instrumentation program for the validation of numerical studies of such large underground structures plays a vital role in safe and timely execution of works of such magnitudes.

Even in case additional costs are to be borne in these activities, the benefits of power generation due to early commissioning of the project surpass these initial costs.

References

Hoek, E.; Kaiser, P.K.; Bawden, W.F. *Support of Underground Excavations in Hard Rocks*.

Hoek, E.; Brown, E.T. *Underground Excavations in Rock*.

Hoek, E. *Rock Engineering*; *Support for very weak rock associated with faults and shear zone; Blast damage factor D; Putting numbers to geology – an engineer's viewpoint.*

Barton, N. *Rock engineering for large hydropower projects*. Lecture organized by ISRMTT, CSMRS & ISEG.

IS: 13365-1998 (Part 1 to 3) *Quantitative classification system of rock mass – guidelines*.

IS: 14448-1997 *Code of practice for reinforcement of rock slopes with plane wedge failure*.

EM 1110-2-3001 *U.S. Army Corps of Engineers - Planning and Design of Hydroelectric Power Plant Structures*.

SLOPE STABILITY ANALYSIS USING 3D LIMIT EQUILIBRIUM METHOD IN A FAULT CONTROLLED METAL MINE

C. OKAY AKSOY [1], G. GÜLSEV UYAR AKSOY [2], OZAN SAVAŞ [3]

[1]Dokuz Eylül University Mining Engineering Department, Turkey, okay.aksoy@deu.edu.tr

[2]Hacettepe University Mining Engineering Department, Turkey, gulsevaksoy@hacettepe.edu.tr

[3]GOA R&D Mining and Environment Technologies Ltd.Co Ankara/ Turkey, ozansavas@goamining.com.tr

Abstract

The effective management of slope stability risks stands as a cornerstone in ensuring the secure and cost-efficient operation of open-pit mines. Over time, a plethora of analytical methodologies have been devised to enhance the handling of these risks. Presently, while the overarching goal remains the eradication of all potential instabilities through the reduction of slope angles, it's evident that such an approach is economically unfeasible. Within open-pit mining operations, meticulous attention is demanded during the planning and production phases. The primary objective revolves around maximizing ore extraction while minimizing waste removal. Consequently, the accurate determination of bench heights, bench widths, and slope angles holds paramount importance. This study undertakes slope stability analyses utilizing the multiple limit equilibrium method within a field characterized by the aforementioned parameters. Identifying the most critical slip surfaces with the lowest safety coefficients among the array of potential slip scenarios forms a focal point of the investigation. Throughout the study, the outcomes are scrutinized utilizing diverse calculation methodologies, notably the Generalized Limit Equilibrium (GLE) and Bishop methods. Analysis is conducted using the "Plaxis 3D LE" software, ensuring comprehensive evaluation and validation of the results.

Key words
Slope stability, limit equilibrium, gle, bishop, open-pit

1   Introduction

The management of personnel, equipment, and ongoing production risks associated with slope instability is a critical responsibility of geotechnical and mining engineers in open pit mining. The primary objective of slope stability studies is to achieve economically viable and safe outcomes in ground structures, excavations, and embankments. This process begins with a comprehensive analysis of geotechnical, material, environmental, and economic parameters. Subsequently, it is essential to examine the dimensions, structure, and potential causes of the slope to determine the most appropriate slope stability analysis. This aspect of the field typically necessitates extensive research encompassing technical geology as well as soil and rock mechanics. A realistic slope analysis must incorporate numerous factors, such as topography, geology, material properties, and loading conditions. The primary variables influencing the stability of open pit slopes include slope geometry, the geomechanical properties of the material, and the engineering characteristics of the rock mass, such as faults, fractures, stratification, folds, cracks, groundwater conditions, and seismic activity. The incorporation of all these variables into the evaluation renders slope stability analyses inherently complex.

Failures in rock slopes primarily result from discontinuities within the rock mass. Therefore, the occurrence of such failures is contingent upon the interplay between the location and characteristics of these discontinuities and the position of the slope surface. Fault zones, frequently encountered within

open pits and among the largest geotechnical structures, play a crucial role in slope stability. While faults represent the most significant discontinuity structures, the material composition within fault zones, such as clay bands, also contributes to the formation of direct failure surfaces on slopes. Consequently, this complex scenario must be meticulously considered when analyzing the stability of open pits that contain faults. (Deliormanli and Ozdogan, 2023)

There are different methods used both in the evaluation of open pit slopes and in the evaluation of the stability of natural slopes. Among these methods, the most preferred methods are kinematic analysis, limit equilibrium analysis, numerical analysis and rock mass classification systems such as Slope Mass Rating (SMR) (Hoek and Bray, 1981; Hoek, 1999; Ulusay et al., 2001; Pantelidis, 2009; Alejano et al., 2011; Komurlu, 2022; Karaman, 2013).

In this study, 3D Limit-Balance Equation Slope Stability Analyses were performed according to the slope structure created by the company. Slope stability analyses were analyzed with the "Multiple Limit Equilibrium Method" calculated by Plaxis 3D LE program using analytical methods. In limit equilibrium methods, a slip surface is accepted and the equilibrium of the soil mass trying to slip is investigated and a safety coefficient is obtained. Among the slipping possibilities of the surfaces, the most critical slip surface that gives the lowest safety coefficient is found. During the study, two different calculation methods, GLE and Bishop, were used and the results were analyzed.

2   General Geology Of The Study Area

The pre-Tertiary rock assemblages of the Biga Peninsula are represented by Paleozoic aged Kazdağı metamorphics, Triassic aged Karakaya formation, Jurassic limestones and Upper Cretaceous aged ophiolitic melange. Tertiary rocks, which cover large areas in the region, begin with the Edincik and Beyçayır volcanites consisting of Middle Eocene aged andesitic lavas and pyroclastics. These two units are unconformably overlain by the Sahinli Formation consisting of basalt, basaltic andesite and associated volcaniclastics.

These units are unconformably overlain by the Fıçıtepe formation consisting of fine coal interbedded pebbles, sandstones and shales representing the delta plain and fluvial deposits. The Sahinli Formation and Fıçıtepe Formation are followed by the Soğucak Formation consisting of igneous limestone with a relationship that cannot be clearly traced. The Ceylan formation composed of turbiditic sediments and the Dededag volcanites were formed simultaneously with them in the region which started to deepen in the Upper Eocene. Dededag volcanites are divided into three members; Hacıbekirler member, Kazmalı tuff member and Korudere ignimbrite member. Ignimbirites, which constitute the dominant rock type, are widely distributed between Balıklıçeşme, Çan and Bayramiç districts of Çanakkale Province. Ignimbirites were developed as a product of submarine pyroclastic flows. Ignimbrites are overlain by the Beybaşlı Formation consisting of Upper Eocene aged sandstone, claystone and reefal limestone north of Beybaşlı village. The Beybaşlı formation is overlain by the Erdağ volcanite, which is thought to be Upper Eocene in age, with an abrupt contact. The Eocene volcano-sedimentary assemblages are unconformably overlain by Oligocene and Miocene aged andesitic, basaltic, rhyolitic and dacitic volcanites and lacustrine sediments in places. Following the Beyçayır volcanite of the Sahinli Formation, shallow marine sediments started to form in the region and this was accompanied by volcanism with a basic composition. Accordingly, volcaniclastic rocks were intensively deposited together with lavas. The unit presents a type section especially in the east of Lapseki district, around Şahinli village and was named Şahinli Formation.

The unit is cut by numerous basaltic dykes. Bilaller Member. The unit within the Sahinli Formation, consisting of volcanoclastics and turbiditic sediments in places and dominantly basalt and basaltic andesite composite lavas that cannot be separated from these sediments, is named as Bilaller Member. The rocks have hypocrystalline porphyritic texture and plagioclase and pyroxenes are the main phenocrysts. Plagioclases are semi-cored and polysynthetic twinned in places. Pyroxenes are in non-cored forms and are observed as bilaterally diluted. The paste consists of volcanic glass, plagioclase

microliths, pyroxene minerals and disseminated opaque minerals. Volcanic glass is heavily clayified and chloritized. The voids in the rock are filled with chlorite.

3   Methods

3D Limit-Balance Equation Slope Stability Analyses were performed according to the slope structure created by the company. Slope stability analyses were performed with the "Multiple Limit Equilibrium Method" calculated by Plaxis 3D LE program using analytical methods using rock mass properties. In limit equilibrium methods, a slip surface is accepted and the equilibrium of the soil mass trying to slide is investigated and a safety coefficient is obtained. Among the slipping possibilities of the surfaces, the most critical slip surface that gives the lowest safety coefficient is found. During the study, two different calculation methods, GLE and Bishop, were used and the results were analyzed.

Bishop method: This method considers the horizontal and vertical force balance and neglects the shear force between the slices.

Generalized Limit Equilibrium method (GLE): In the GLE approach, the safety numbers of the cohesion and friction components that make up the strength of soils are the same. The safety number is the same for all slices forming the shear circle under investigation. The force balance safety number Fs is calculated from the sum of the horizontal forces acting on all slices.

The results obtained as a result of these calculation methods and analysis methods are given below. The rock parameters used in the numerical model are given in Table 1.

Table 6. Rock parameters used in the analysis

	Unit Volume Weight (kN/m³)	**Cohesion (c) (kPa)**	**Internal Friction angle (⁰)**
Volcanic Rock	24.80	200	23
Fault 1	22	20	16
Fault 2	22.5	30	22

The digital elevation model of the open pit operation is given in Figure 1.
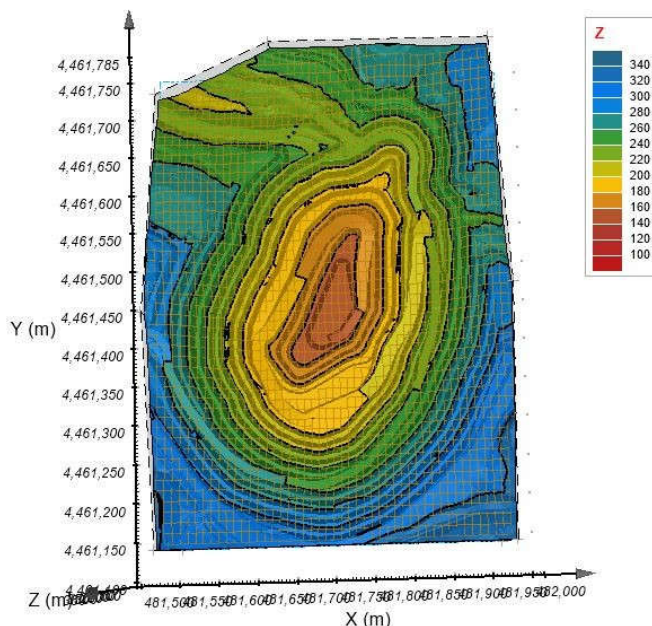
Figure 25. Digital elevation model of the open pit operation

The steps performed during the analysis phase are summarized below:

Using Plaxis Designer, the area to be studied on the hearth triangle model was determined and the volume definition process was performed. The quarry with the defined volume was transferred to Plaxis 3D LE application and material properties were defined for both the surface and the detected discontinuity elements. Contours were determined in the areas where we want to calculate the coefficient of safety FOS values on the quarry. For the determined contours, Bishop and GLE methods were examined and the solution process was started and took approximately 235 minutes.
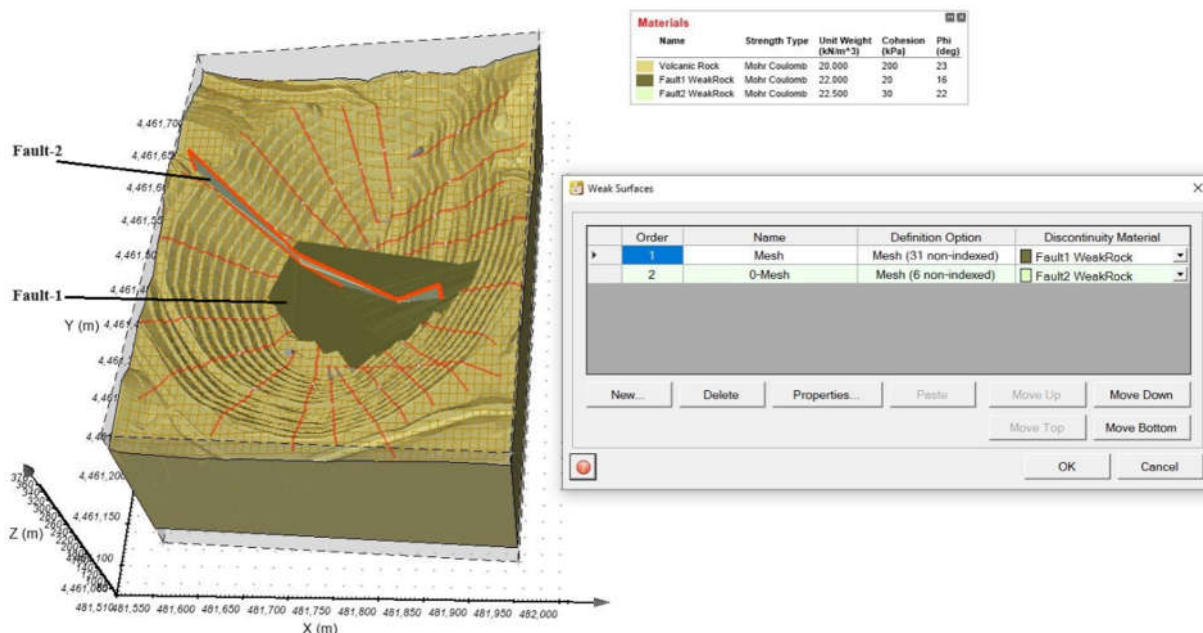
Figure 2. Contours determined on the quarry with defined faults and general view of the 3D design

In order to make a homogeneous analysis, contours (pink lines in Figure 2) were drawn at certain intervals throughout the quarry (22). Faults previously identified as a result of related studies on the quarry were defined as weak surface/discontinuity material on the program. For the area covered by each contour, coefficients of safety (CoS) were calculated using the limit-balance method, Bishop and

GLE approach. The results obtained for the open pit using these two calculation methods are given below.
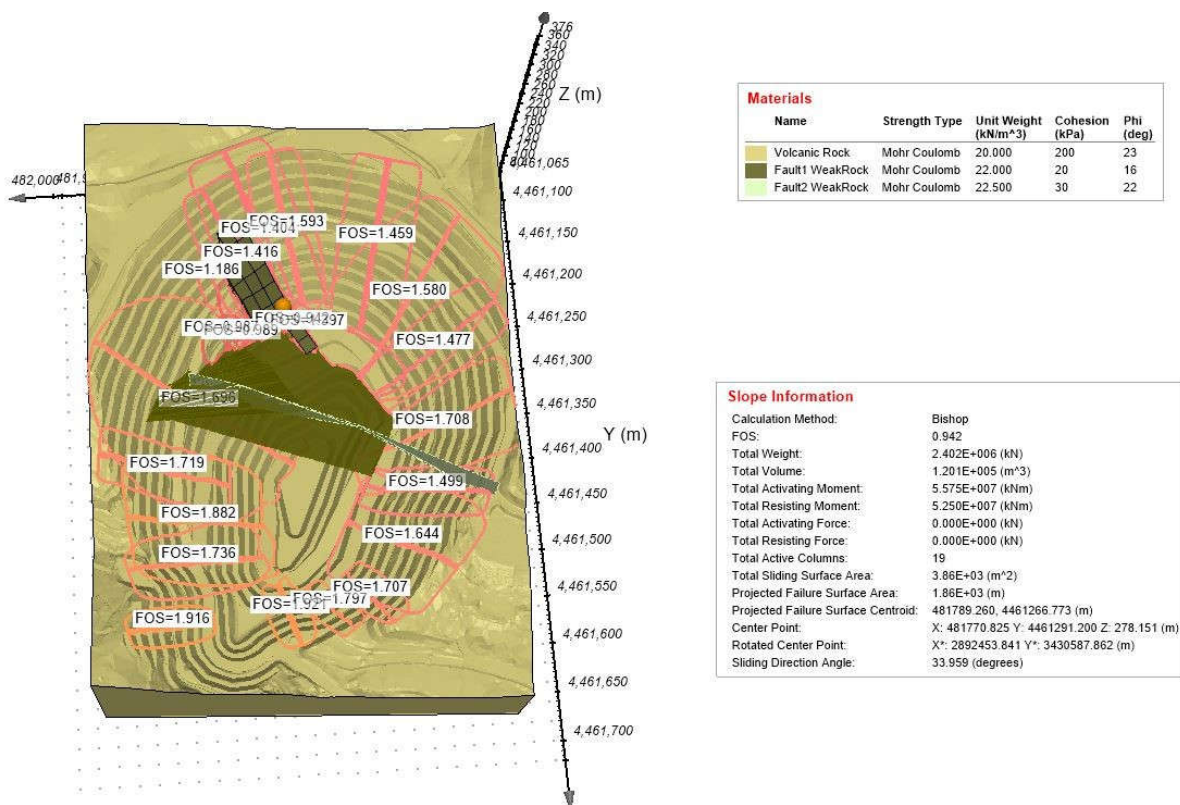
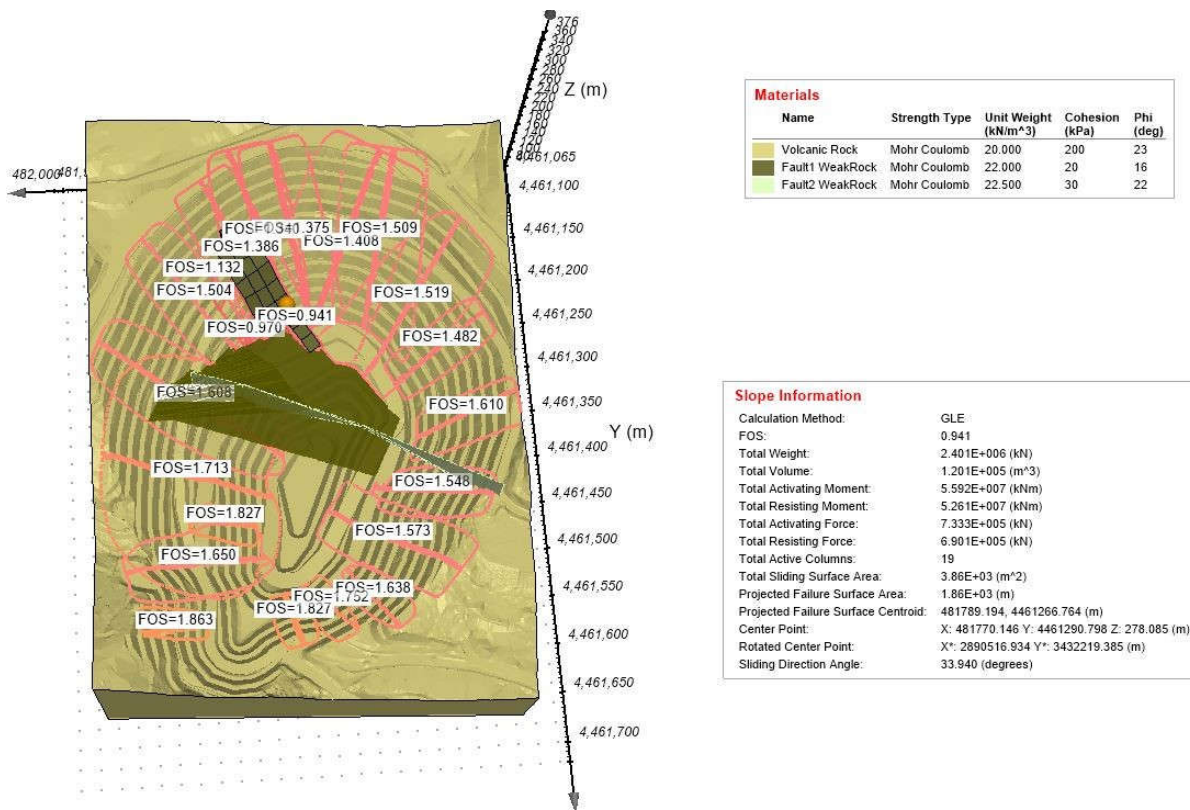**Figure 3.** Safety factor values calculated by Bishop's method and the lowest safety factor (0.942)

Figure 4. Safety factor values calculated by the GLE method and the lowest safety factor (0.941)
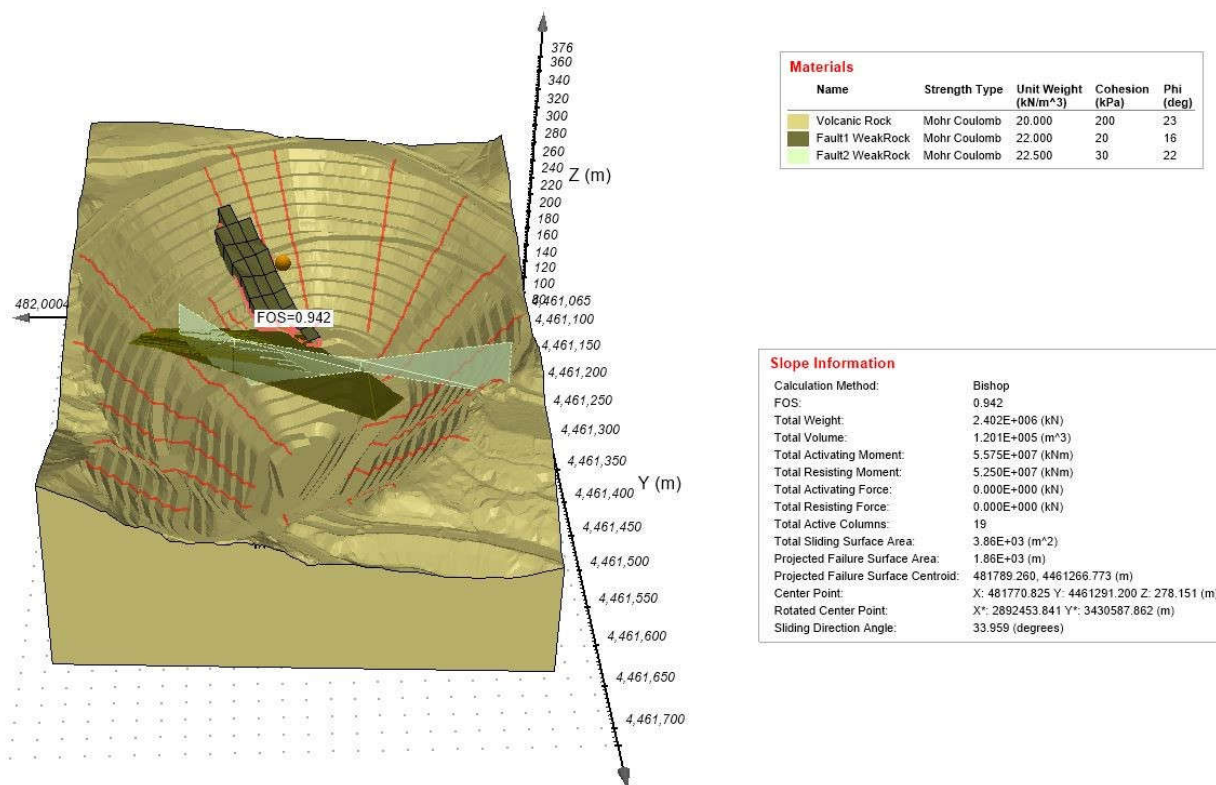
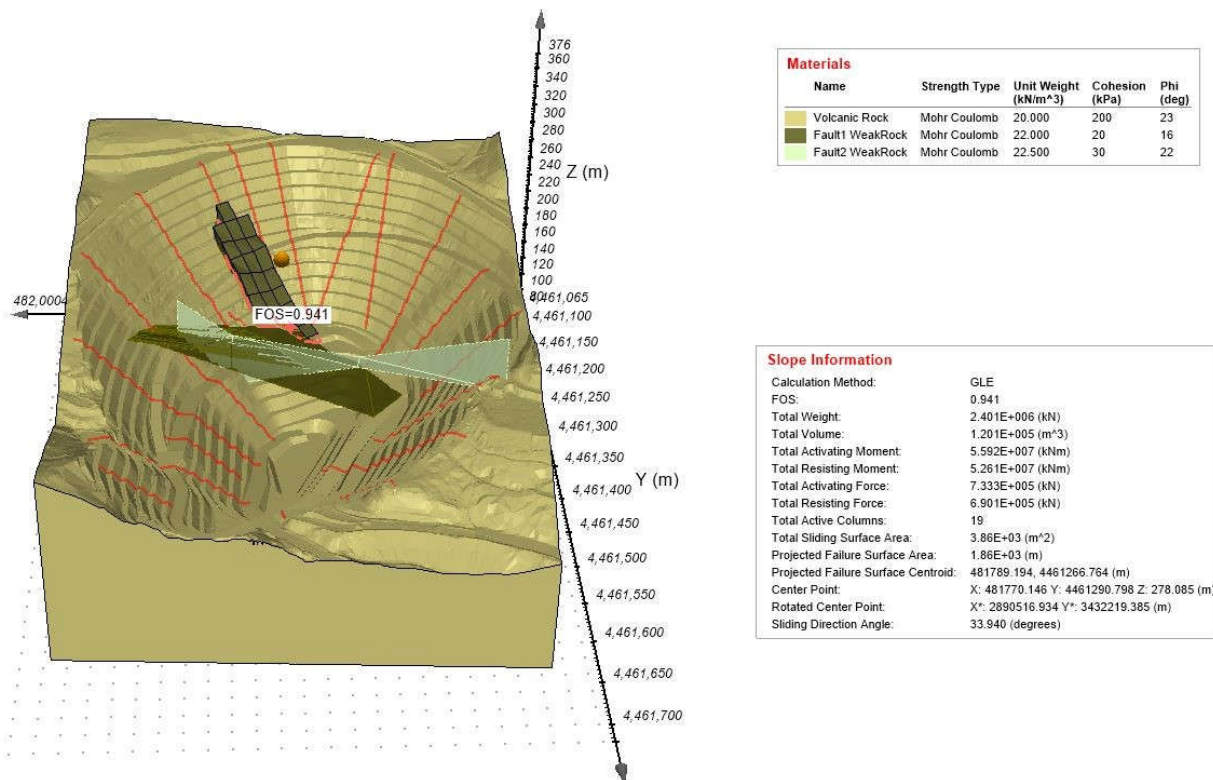**Figure 5.** Critical slip surface resulting from Bishop's method analysis

Figure 6. Critical slip surface resulting from GLE method analysis

Figures 5 and 6 show the critical slip surfaces determined by two different methods, bishop and gle. FOS values are written above the critical slip surfaces and highlighted with an orange dot.

4   Results

In this study, 3D Limit-Equilibrium Equation Slope Stability Analyses were performed according to the slope structure created by the company in order to evaluate the open pit slope stability. Slope stability analyses were analyzed with the "Multiple Limit Equilibrium Method" calculated by Plaxis 3D LE program using analytical methods.

In open pit slope stability analyses, the evaluation of faults together with rock mass properties provides more reliable and accurate results. The location, orientation, length and other geometric characteristics of faults can directly affect slope stability. Therefore, it is important to analyze faults in an integrated manner with rock mass properties. At this point, the fault surfaces that we directly identified were used in the analysis. It includes fault location, orientation, length and other geometric features.

In open pit slope stability analyses and analyses, it was seen that if the faults detected in the quarry are included in the analysis by determining the rock mass properties, the analysis gives much healthier results.

Within the scope of this study, Bishop and GLE methods were examined by using the 3D limit equilibrium method;

 - The lowest safety factor value obtained using the Bishop method was calculated as 0.942.
 - The lowest safety factor value obtained using the GLE method was calculated as 0.941.

The important point to be emphasized in this paper is that discontinuities and faults in the region should be included in the analysis of slope stability in open pit mining or in areas with any natural/artificial slope structure.

5   Conclusion

In the scenario where discontinuities and faults, which we define as weak surfaces, are not included in the analysis, it is observed that the average safety factor is around 1,400 - 1,700. This shows the importance of the fault plane in the quarry on the analysis in slope stability analysis in open pit mining.

In Figure 7, the slip surface detected by the program in the limit equilibrium analysis results is compared with the actual slip point detected in the quarry. The important factor here is that due to the heel left in front of the area where the wedging faults are located, the movement in this area was restricted and as a result, the forces accumulated here found their way from the heel edge area.
Figure 7.b is the visual sent by the company. The red lines indicated on the quarry surface are the areas of the quarry where slippage is currently observed. Comparing Figure 7, a and b proves that the results obtained from the analysis (critical slip surface) are in direct correspondence with the current situation.
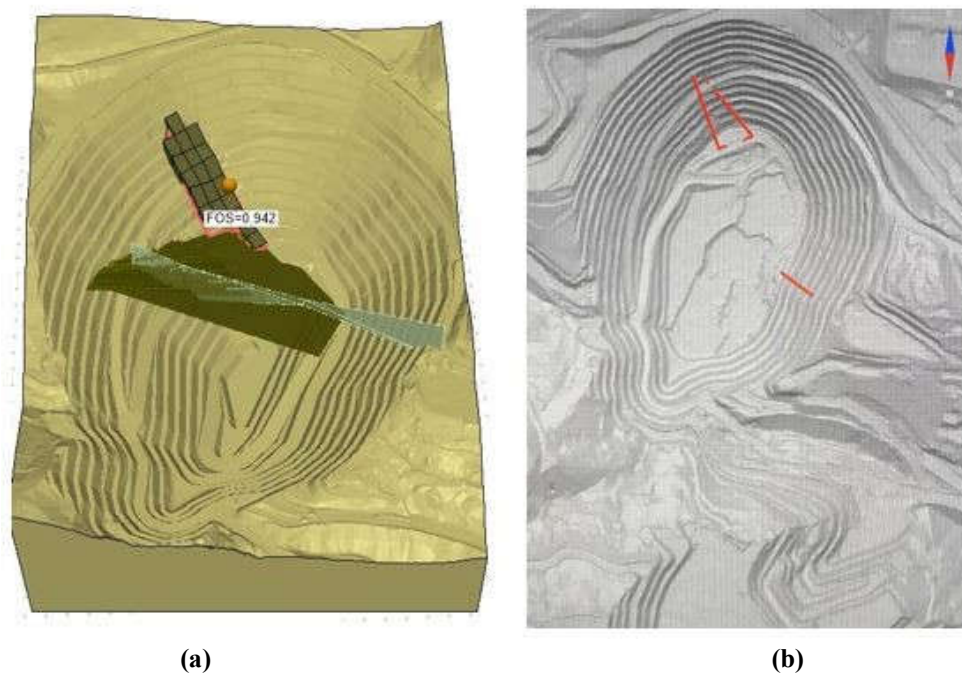
(a)   **(b)**

Figure 7. The slip surface detected by the program and the actual slip point detected in the quarry

References

Alejano, L.R., Ferrero, A.M., Oyanguren, P.R., Fernandes, M.I.A., 2011. Comparison of limit equilibrium, numerical and physical models of wall slope stability. International Journal of Rock Mechanics and Mining Sciences, 48, 16-26.

Deliormanli, A.H., Ozdogan, M.H., 2023. Stability Analysis in a Fault Controlled Open Pit, Journal of Underground Resources, MT Scientific, 23.

Hoek, E., Bray, J.W., 1981. Rock Slope Engineering. 3rd edition. London, Institute of Mining and Metallurgy. 385 p.

Hoek, E., 1999. Putting numbers to geology – an engineer's viewpoint. Quarterly Journal of Engineering Geology, 32, 1-19.

Karaman, K., 2013. Evaluation of Rock Slope Stability by Different Methods (Unye, Ordu) Journal of Geological Engineering 37 (1), 27-47.

Komurlu, E., 2022. Case studies on Q-slope method use for slope stability analyses. Studia Geo technica et Mechanica, 44, 190-197.

Pantalidis, L., 2009. Rock slope stability assesment through rock mass classification systems. International Journal of Rock Mechanics and Mining Sciences, 46, 315-325.

Ulusay, R., Gokceoglu, C., Sonmez, H., Tuncay, E., 2001. Causes, mechanism and environmental impacts of instabilities at Himmetoğlu coal mine and possible remedial measures, Environmen tal Geology, 40 (6), 769-786.

Topic 9

Geo-Aspects of Earthquake Engineering

REGULATING LIQUEFACTION RISK FOR RESIDENTIAL LAND DEVELOPMENT

CATHERINE ROH [1]

[1] *Auckland Council, New Zealand, Catherine.roh@aucklandcouncil.govt.nz*

Abstract

Management of natural hazard risks, such as liquefaction, was a grey area for New Zealand's residential land development sector. The "February 2011 Christchurch Earthquake" – second most populated city in New Zealand- was one such event. The earthquake, paired with significant liquefaction, saw over 400,000tonnes of silt brought up affecting over 600,000 homes and costing over NZD $40 billion in damages, making it New Zealand's costliest natural disaster at the time. Our engineering community were well aware it could happen, but the risk was not perceived to be significant enough for residential dwellings. Hence, in 2021, just over ten years following the Canterbury earthquake, the regulations governing how residential structures are designed changed. The Auckland Council responded by publishing liquefaction hazard maps and implementing the new rules at the Building Consent stage of new residential developments. This paper discusses the process set up including hazard maps and standard foundation designs and presents the challenges and outcomes in implementing the change in Auckland. The change signals a significant move in how we regulate liquefaction risk for residential land development in New Zealand. The change presents challenges around ensuring the effectiveness of the regulations to capture the liquefaction risk and design for it whilst managing costs to the developer such that they are not escalated disproportionately. Ongoing adaptation and refinement of the liquefaction rules, the process, liquefaction hazard map, and standard liquefaction resilient foundation guidance will be essential in addressing these challenges.

Key words
Regulation, Earthquake, Liquefaction, Residential Land Development, Hazard Map, Consenting, Local Authorities.

1   Introduction

1.1 Strategic Context

1.1.1   Snapshot of New Zealand (NZ)

Located in the South Pacific Ocean, New Zealand is a relatively isolated country with a population of just over 5 million and mixed economy operating on free-market principles. Auckland is the largest commercial and financial hub of New Zealand. It is also the most populated with over 25% of the NZ population living in Auckland. Please refer to Figure 1 below for the location of Auckland and Christchurch within New Zealand.

1.1.2   New Zealand Geology

New Zealand sits between two tectonic plates being the Australian and Pacific plates shown in Figure 1 below. As such the country is rendered with volcanic activity, geothermal areas, and numerous fault lines (denoted red in Figure 1). Constant movement and relatively recent geological history of New Zealand mean that the country is subject to risk of earthquakes, liquefaction, and lateral spreading.
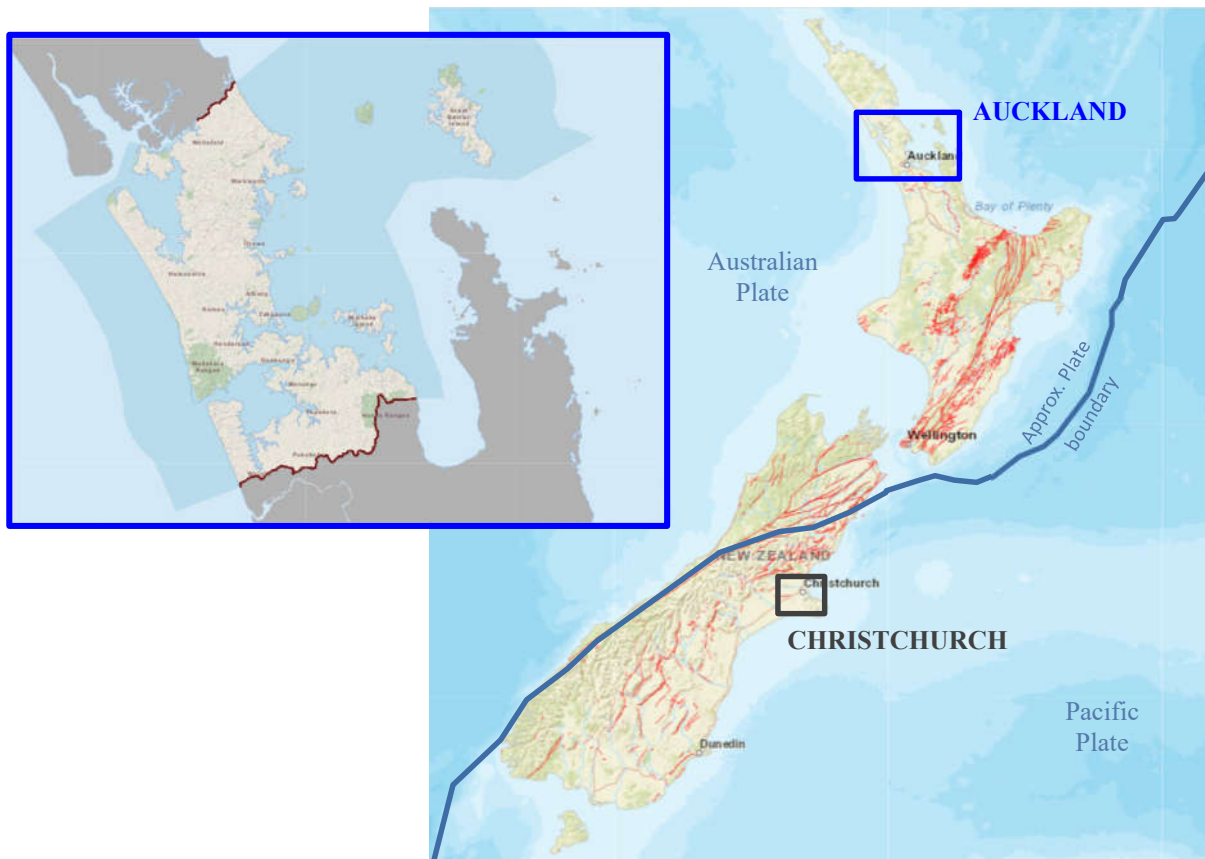
Figure 1. Map of New Zealand with active fault lines and the approximate plate boundary between the Australian and Pacific Tectonic Plates as shown in GNS Science [GNS.2024] (right) and close up of Auckland from Auckland Council website [Auckland Council.2024] (left)

As per Figure 2, the history of the land tells us that earthquakes with a magnitude of 7.0 or greater are always possible and have been occurring in general every 4 years Nationwide [Geonet.2024].
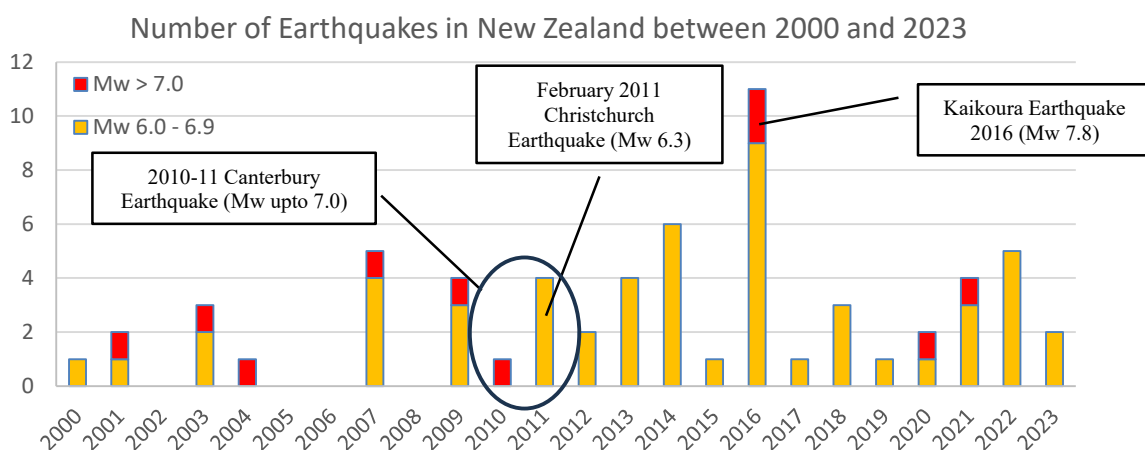

Figure 2. Graph showing the number of earthquakes with magnitude greater than 6.0 across New Zealand between 2000 to 2023 as per NZ geonet data [Geonet.2024]

1.1.3   Canterbury Earthquake

In 2010-11 a series of earthquakes and aftershocks occurred in the Canterbury region of New Zealand measuring magnitudes, Mw of up to 7.0 including the "February 2011 Christchurch Earthquake". Significant liquefaction saw over 400,000 tonnes of silt bought up affecting over 600,000 homes. Emergency works to remove debris and reinstate essential infrastructure to reopen the city centre spanned over years. The economic loss is estimated to be more than NZD $40billion in damages making it New Zealand's costliest natural disasters at the time [ICNZ.2024].
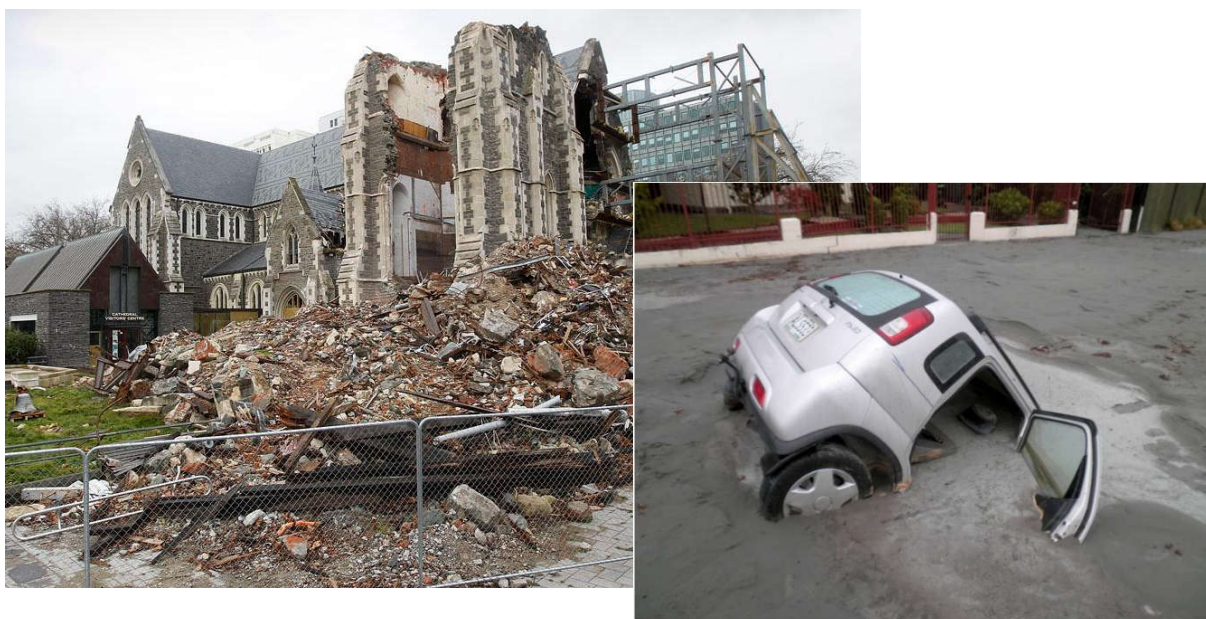
Figure 3. Photos from the 2010-11 Canterbury Earthquakes including this car (right) toppled into one of many large holes created by liquefaction (source: Stuff.co.nz and the Encyclopaedia of NZ)

1.1.4   Practice Prior to Regulatory Reform

In New Zealand, all residential dwellings are required to obtain a Building Consent to assess compliance with the NZ Building Act and Building Code. Acceptable Solution B1/AS1 in the NZ Building Code is widely cited as a means of compliance for the structural performance of residential building work, including foundations. This enabled liquefaction risk to be assessed by geo-professionals (i.e. Chartered Geotechnical Engineers or Professional Engineering Geologists) applying judgement without any regulations requiring minimum deep ground investigations.

Prior to the 2010-11 Canterbury earthquake, major fault lines were identified going through the wider Canterbury region. As such the city of Christchurch was identified as having a high seismic risk. The New Zealand Transport Agency bridge manual provided strict guidance on seismic design methodology and criteria for infrastructure projects [Waka Kotahi.2022]. However, the risk was not perceived to be significant enough for residential dwellings and the Building Act relied on professional judgement to assess the risk without regulations on deep ground investigations or standard liquefaction resistant foundation designs.

Following the 2010-11 Canterbury earthquake, the engineering community and government reacted to better manage the risk to building projects by producing several guidance documents and changes to the regulations within the Canterbury region. This helped fast track the rebuild and identify and manage high risk areas. Documents include:

- Standardised liquefaction resistant foundation designs [MBIE.2015].
- Liquefaction risk categorisation based on estimated liquefaction damage [MBIE, MfE.2017].
- Liquefaction hazard risk maps on the Christchurch City Council Website [CCC.2024].

In 2021, the above was implemented as a mandatory requirement nationwide. More formally, changes were made to the Building Code. These changes which came into effect on 29 November 2021 revoked this compliance pathway for building foundations on sites where liquefaction risk had been identified.

This called for action for individual local authorities including Auckland Council to undertake hazard mapping to identify liquefaction prone areas within Auckland and set up consenting processes to implement the regulatory reform.

2   Methods

2.1   Auckland Liquefaction Hazard Map

The liquefaction hazard mapping commenced in 2019 by Auckland Council in collaboration with the University of Auckland to assess and categorise the liquefaction risk within Auckland. The key outcome was to identify areas requiring further deep ground investigations to ascertain liquefaction risk.

The Ministry of Business Innovation and Employment (MBIE) Liquefaction Guidance [MBIE, MfE.2017] list four levels of detail of liquefaction assessment studies as per Table 1 below. Given the large extent of the study area and lack of required density of geotechnical investigation data across most of the region, the hazard mapping was undertaken in two phases; Level A basic desktop assessment followed by calibration of the assessment in Level B. [Brightman, C and R Roberts.2021].

Table 1. Overview of levels of detail of liquefaction assessment studies

LEVEL OF DETAIL	
Level A – Basic Desktop Assessment	**Auckland Liquefaction Hazard Map**
Level B – Calibrated Desktop Assessment	
Level C – Detailed Area-Wide Assessment	
Level D – Site-Specific Assessment	

Level A assessment was the high-level categorisation of the city based on geology, groundwater and seismic hazard data. Level B assessment involved calibration of the above level A assessment against nearby existing deep ground investigations and topographic data in areas where sufficient data was available within the publicly available New Zealand Geotechnical Database (NZGD) and Tonkin and Taylor Limited's in-house geotechnical database. More detailed Level C and D assessment were not undertaken as part of this Auckland Liquefaction Hazard Mapping. However, this is an area of work we may consider delivering in the future when the budget allows.

The resulting liquefaction hazard maps are available to the public via our Auckland Council geospatial system, "Geomaps". Where both level A and B assessments are available for the site, reference is made to Table 2 to determine which assessment level is applicable for the proposed works. The map is referenced in all our regulatory reviews to identify the level of liquefaction risk and associated deep ground investigation and liquefaction foundation design requirements.

As per Figure 4 below, the Auckland liquefaction hazard map (Assessment level B) shows the majority

of Auckland coloured blue or green denoting very low to low liquefaction vulnerability categories. Only a relatively small portion of Auckland concentrated along the low-lying areas are coloured grey or light orange denoting liquefaction damage is "undetermined" or "possible" vulnerability categories respectively.

This point is further emphasized when you compare the liquefaction hazard map of Auckland vs a high seismicity area such as Christchurch in Figure 4 below. Unlike Auckland, the majority of the Christchurch is coloured light orange, orange or red denoting medium to high liquefaction vulnerability.
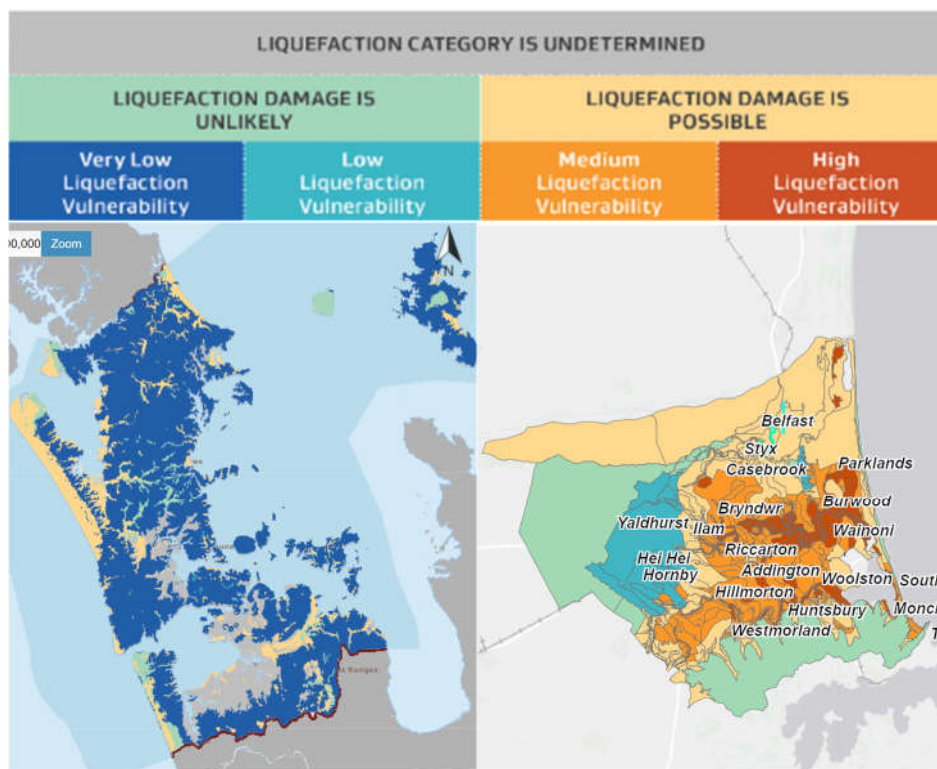
Figure 4. Liquefaction Hazard Map of Auckland Assessment Level B (left) and Christchurch (right) sourced from Auckland Council Public GiS Maps[Auckland Council.2024] and Canterbury Council maps [CCC.2024]

2.2 Minimum Deep Ground Investigation Requirement

A risk-based system was put in place whereby the level of deep ground investigations (assessment level) required to re-categorise the liquefaction hazard category is assessed as a function of:
- Scale of the proposed work plus;
- Liquefaction risk category as per Auckland Council Geomaps.

NZS1170 is the NZ Standard for structures and includes categorisation of structures into Importance Levels (IL) based on the consequence of the failure. ILs range from IL1 for minor structures (failure not likely to endanger human life) where the consequence of failure is low to IL5 exceptional structures where the consequence of failure is exceptional [NZS1170.2002]. IL1 structures such as in-ground swimming pools and sheds are not subject to these MBIE liquefaction requirements [MBIE,MfE.2017].

Large commercial/industrial buildings or residential buildings higher than 3 storeys are considered high risk and require specific investigation by suitably qualified and experienced geo-professionals. Designs must also be supported by a Producer Statement [EngNZ.2013].

Table 2 below shows the Assessment Level applicable for each development scenario (scale of proposed work) and liquefaction risk category combination. Assessment Level refers to the minimum deep ground investigation requirement, as shown in Table 3, ranging from no investigation required for level A applicable to sparsely populated rural areas (low scale) to a minimum of 2 deep ground investigations within or very close to the building footprint for Level D assessment applicable to small scale urban infill or greater scale development scenarios on high liquefaction vulnerability category areas.

Table 2. Assessment Level based on Development Scenario and Liquefaction Vulnerability Category [MBIE, Mfe.2017]

Development Scenario	Liquefaction Vulnerability Category			
	Liquefaction Category is Undertermined			
	Liquefaction Damage is Unlikely		Liquefaction Damage is Possible	
	Very Low	Low	Medium	High
Sparsely populated rural area	Level A	Level A	Level A	Level A
Rural-residential setting	Level A	Level B	Level B	Level B
Small-scale urban infill	Level B	Level B	Level B	Level D
Commercial or industrial development	Level B	Level B	Level C	Level D
Urban residential development	Level B	Level C	Level C	Level D

Notes: Refer to Table 3 below for deep ground investigation requirements associated with each Assessment Level.

Table 3. Indicative spatial density of deep ground investigation required by Assessment Level [MBIE, Mfe.2017]

Assessment Level	Avg Investigation Density	Average Sapcing Between	Minimum total number of investigations
Level A	0.01 to 1 per km	1 to 10 km	-
Level B	0.5 to 20 per km	220 to 1400 m	3 for each geological sub-unit
Level C	0.1 to 4 per Ha	50 to 320 m	5 if area >1 Ha 3 if area 0.25 – 1 Ha 2 if area < 0.25 Ha
Level D	2 to 40 per Ha	15 to 70m	2 within or very close to the building footprint

Notes: Deep ground investigations to characterise the ground to at least 10 – 15 m depth below ground level for residential or light commercial development [MBIE, Mfe.2017].

2.3 Standard Liquefaction Resistant Foundations

The standard liquefaction resistant foundations presented in the MBIE 'Repairing and rebuilding houses affected by the Canterbury earthquakes" version 3a Guidance documents [MBIE.2015] are divided into three categories; Technical Category 1 (TC1), Technical Category 2 (TC2) and Technical Category 3 (TC3) based on the estimated liquefaction ground damage.

- TC1 – Conventional NZS3604 foundations [NZS3604.2011].
- TC2 – Foundation options range between conventional NZS3604 foundations to ground improvements pending on shallow ground conditions.
- TC3 – Specific liquefaction design.

Experience from the 2010-11 Canterbury earthquake suggest the cost of these TC2 foundations are generally similar to conventional NZS3604 foundations given 300kPa ultimate bearing capacity can be demonstrated [MBIE,MfE.2017].

2.4 Compliance Pathway for Auckland Council

As mentioned previously, Importance level 1 (IL1) structures, as defined by NZ Standards [NZS1170.2002] are not subject to these MBIE liquefaction requirements. Where the MBIE liquefaction requirements apply, reference is made to the liquefaction vulnerability category from publicly available hazard maps.

Where the liquefaction vulnerability category is low or very low, no further assessment is required for liquefaction. Note when referring to the Auckland Council liquefaction hazard map, where both level A and B assessments are available, reference is made to Table 2 to determine which assessment level is applicable for the proposed works.

Where the liquefaction vulnerability category is undetermined or possible, then three options are available:
- Option 1 – undertake deep ground investigations as per MBIE liquefaction requirements [MBIE,MfE.2017] to re-categorise the liquefaction vulnerability category to very low, low, medium or high and design foundations accordingly. Note reference to nearby existing deep ground investigation results is acceptable.
- Option 2 – adopt standard liquefaction resistant foundation designs as per the standard liquefaction resistant foundation guidance [MBIE.2015].
- Option 3 – peer review by an external geotechnical consultant on Auckland Council's geotechnical panel.

Given Auckland is in a low seismic area (as defined by the hazard factor) [MBIE.2024], an alternative consenting pathway is available for low scale works, such as minor alterations or small-scale urban infill developments, that enables TC2 standard liquefaction resilient foundations to be adopted where the site is categorised as undetermined or possible liquefaction vulnerability within Auckland.

3   Results

3.1 Cost Implications to the Developer

One of the challenges of this regulatory reform is managing cost implications to the developer. Deep ground investigations are expensive relative to shallow hand auger borehole investigations traditionally associated with residential land development in Auckland.

Geotechnical investigation for a simple 2 lot subdivision on a 600m^2 full section, typical of a small scale urban infill project in Auckland, would cost in the order of NZD \$4,000 including reporting. The addition of one 15m deep machine borehole would incur additional costs in the order of NZD \$8,000 to \$15,000. Effectively, the addition of one deep ground investigation could increase the geotechnical investigation fee by more than two-fold.

As such, in the context of regulatory engineering for residential development, it is important that our review is risk based. This is to prevent costs to the developer escalating disproportionately to the risk.

3.2 Consideration of Scale of works in Auckland

MBIE liquefaction requirements make consideration to the scale of the project in several ways being:
- MBIE liquefaction requirements are not applicable to IL1 buildings [NZS1170.2011].

- Pathway for low scale urban infill and minor alteration projects to adopt TC2 foundations which includes the conventional NZS3604 foundation pending on shallow ground conditions.
- The minimum level of deep ground investigation required (assessment level) is a function of the liquefaction vulnerability category and scale of the project.
- Acceptance of reference to nearby existing deep ground investigations.
- Specific design and Producer statement(s) required for large commercial/industrial buildings or residential buildings higher than 3 storeys.

The above are working well to ensure what we require is proportional to the scale of the works proposed.

3.3 Consideration of Liquefaction Risk in Auckland

As per Figure 4, the liquefaction hazard map shows the majority of Auckland is categorized as having very low to low liquefaction vulnerability. As such, for the most of Auckland, no further liquefaction investigation and assessment is required.

Furthermore, in recognition of the low seismicity of the Auckland region (defined by the hazard factor z) [MBIE.2024], an alternate consenting pathway is available for low scale urban infill and minor alteration projects which enables TC2 foundations to be adopted where the liquefaction vulnerability category of the site is "possible" or "undetermined" within Auckland (low seismicity area). Experience from the 2010-11 Canterbury earthquake suggest the cost of these TC2 foundations are generally similar to conventional NZS3604 foundations given 300kPa ultimate bearing capacity can be demonstrated [MBIE,MfE.2017].

The result of the above is that for the majority of the Auckland region and for small scale urban infill or minor alteration projects within Auckland, the rule change is relatively inconsequential to the final foundation cost given 300kPa ultimate bearing capacity can be demonstrated.

3.4 Industry Feedback

Since its implementation in 2021, over 100 Building Consents have been assessed to date against the new MBIE liquefaction requirements at the time of preparing this paper. In the early days, there was considerable resistance to the changes by some geotechnical consultants blindsided by the change. MBIE liquefaction requirements are relatively new to the industry so sometimes it is just a matter of helping the consultant navigate the new rules and understand their options.

Three years in to implementing the changes, the industry has, for the most part, accepted the changes. There has been good uptake of our acceptance of nearby existing deep ground investigations to re-categorize the liquefaction vulnerability of the site with the NZGD platform frequently referenced by consultants for this data.

However, there are still discrepancies in how geotechnical consultants interpret and navigate the new rules. As the industry starts to test their boundaries, grey areas of note have and continue to emerge. Especially around the criteria for re-categorizing the liquefaction vulnerability category based on deep ground investigations and liquefaction assessment results and associated selection of standard liquefaction resistant foundations. For example, the MBIE liquefaction requirements [MBIE,MfE.2017] references the liquefaction induced settlement to define the degree of liquefaction damage. However, acceptable solutions MBIE Modules include more sophisticated assessment methodologies to define the degree of liquefaction damage. There is an opportunity for improvement here to incorporate/amalgamate the liquefaction damage criteria for the risk categorization with existing well-established liquefaction damage assessment methodologies, namely LSN and LPI analysis methodology of assessing the degree

of liquefaction damage presented in MBIE Module 3 [NZGD,MBIE.2021] to inform the liquefaction vulnerability category and associated standard liquefaction resistant foundations.

3.5 Next Steps

Some potential next steps include the following:

- The MBIE liquefaction requirements are relatively new to the industry. As such the need to increase exposure of this rule change to the industry has been highlighted. Auckland Council's next step in this space is to continue presenting the rules and regulatory expectations to the industry in the form of engineering forums and presentations.

- The MBIE liquefaction requirements and associated requirement for minimum deep ground investigations has meant that a sizable number of deep ground investigation data is now available to feed back into our liquefaction hazard map. We encourage the industry to actively share and grow the pool of data available on platforms such as The New Zealand Geotechnical Database (NZGD). With more deep ground investigations added to the pool of data, we envisage the liquefaction hazard map will be continuously refined with time.

- On going adaptation and refinement of the new MBIE liquefaction requirements [MBIE, MfE.2017] and standard liquefaction resistant foundation guidance [MBIE.2015] will be essential to ensure the effectiveness of this regulatory reform as our understanding of the MBIE liquefaction requirements mature.

- Since the new MBIE liquefaction rules were implemented, several local authorities including Auckland Council have and/or are in the process of producing liquefaction hazard maps and implementing the rule change for their respective local areas. The learnings shared between local authorities will prove to be invaluable.

- The current liquefaction hazard map for Auckland is limited to Level A and Level B assessments. Auckland Council may consider delivering hazard maps for Level C and Level D assessments subject to budget constraints.

4 Conclusion

Internationally, regulation of liquefaction risk for residential land development is not new. And there are plenty of examples worldwide of what success looks like in the residential field such as Japan [National Geographic. Jan 2024]. The NZ Transportation Agency has such regulations for our state highway infrastructure [NZTA Bridge Manual.2022]. With the new MBIE liquefaction rules we have now developed and deployed such a system for the residential space.

The MBIE liquefaction requirements are envisaged to capture liquefaction risk and design for it, creating more resilient buildings to house Kiwis (New Zealanders). The system is not perfect, but with further deep ground investigations and liquefaction assessments undertaken throughout the city, we envisage the liquefaction hazard map, MBIE liquefaction rules [MBIE,MfE.2017], standard liquefaction resistant foundation guidance [MBIE.2015] and the process to be refined with time. This will be essential to ensure the effectiveness of these regulations and address the evolving challenges of striking the right balance between adequately managing the risk and keeping costs to developers proportional to the risk.

Assets & Technical Advisory) and Regulatory Engineering (now Regulatory Engineering and Resource Consents) teams for creating the processes within Auckland Council to implement the change.

References

Auckland Council (Auckland Council Geomaps) Available online: https://geomapspublic.aucklandcouncil.govt.nz/viewer/index.html (accessed 10 June 2024)

Brightman, C and R Roberts (2021), *Auckland liquefaction assessment. Auckland Council technical report, TR2021/19*, Auckland Counicl. Novmeber 2021

Christchurch City Council (Christchurch City liquefaction information viewer, Vulnerability Map) Available online: https://apps.canterburymaps.govt.nz/ChristchurchLiquefactionViewer/ (accessed 14 June 2024)

Engineering New Zealand, New Zealand Institute of Architects and Incoporated, ACENZ. *Guidance on use of producer statements*, Engineering New Zealand, October 2013

GNS Science (NZ Active Faults Map) Available online: www.gns.cri.nz/data-and-resources/new-zealand-active-faults-map/ (accessed 15 June 2024)

Insurance Council of New Zealand (Canterbury Earthquakes Nga Ru o Waitaha) Available online: https://www.icnz.org.nz/industry/canterbury-earthquakes/#:~:text=Total%20economic%20losses%20for%20the,more%20than%20NZ%2440%20billion. (accessed on 15 June 2024)

Ministry of Business, Innovation and Employment, Ministry for the Environment, Earthquake Commission. *Planning and engineering guidance for potentially liquefaction-prone land Resource Management Act and Building Act aspects*, Ministry of Business, Innovation and Employment, September 2017.

Ministry of Business, Innovation and Employment. *Repairing and rebuilding houses affected by the Canterbury earthquakes, version 3a*, Ministry of Business, Innovation and Employment, April 2015.

GeoNet (Earthquake Statistics). Available online: www.geonet.org.nz/statistics_long (accessed on 06 June 2024)

Ministry of Business, Innovation and Employment (Z-values to determine seismic risk). Available online:www.building.govt.nz/managing-buildings/managing-earthquake-prone-buildings/how-the-system-works/z-values-seismic-risk. (accessed on 6 June 2024)

New Zealand Geotechnical Society, Ministry of Business, Innovation and Employment. *Earthquake geotechnical engineering practice MODULE 3: Identification, assessment and mitigation of liquefaction hazards, Revision 1,* New Zealand Geotechnical Society, November 2021.

National Geographic (Japan spent decades making itself earthquake resilient, January 2024) Available online: https://www.nationalgeographic.com/environment/article/japan-earthquakes-resilient-architecture-disaster-preparedness (accessed on 14 June 2024)

Statistics New Zealand (Popultation Estimates – DPE) available online: https://infoshare.stats.govt.nz/ViewTable.aspx?pxID=5097fc18-b993-4172-8284-67da8ecbac19 (accessed 14 June 2024)

Waka Kotahi NZ Trasnport Agency. *Bridge Manual SP/M/022.version 3, amendment 4*, Waka Kotahi NZ Transport Agency, May 2022.

COMPARATIVE SOIL LIQUEFACTION ASSESSMENT BASED ON MULTIPLE INVESTIGATIONS METHODS

MIHAELA STÃNCIUCU[1], ADRIAN M. DIACONU[2], IULIANA G. DOGARU[2], IRINA MIRCEA[1]

[1] *University of Bucharest, Romania, mihaela.stanciucu@unibuc.ro*

[2] *Geotesting CI, Romania, office@geotesting.ro*

Abstract

Submerged soils like loose sands or very soft clays are sometimes hard to evaluate for geotechnical purposes with classical methods like sampling and lab testing. In such soils, evaluation of liquefaction potential became very important, especially in large projects with hard geotechnical conditions where this issue is involved in almost all stages of design. The paper presents the results of the complex geotechnical evaluation of a site situated on the alluvial plain of the Danube, where simultaneous geotechnical investigations, boreholes with Standard Penetration Test measurements, laboratory analyses, and Cone Penetration Test were completed with geophysical survey (suspension of P-S waves).

Key words

liquefaction potential, safety factor against liquefaction, loose sands

1 Introduction

1.1. Geologic and seismic frame

Romania is a country with an active seismicity, in which more than 300 earthquakes with magnitude M>2.5 (Fig.1- a) occur annually, most of them are superficial and medium magnitude (Bala et al., 2003). The seismicity of Romania is divided into several epicentral areas: Vrancea, Fãgãraş - Câmpulung, Banat, Crişana, Maramureş and Dobrogea. Of these epicentre areas, the Vrancea seismic area is the most important, through the energy of the earthquakes produced, the expansion of their macro-seismicity area and the persistent and concentrated character of the epicenters.

The seismogenic areas bordering the investigated site are Vrancea, Central Dobrogea and Shabla-Cape Kaliakra (Bulgaria).

The Vrancea area represents the most complex seismogenic area being situated at the convergence of at least three tectonic plates: the Eastern European plate, the Moesic Platform and the Intra-Alpine Plate. From the point of view of the depth of the hypocenters, two distinct divisions are distinguished: an area generating normal crustal events up to 40km deep, located between the Peceneaga-Camena fault and the Intra Moesica fault, with moderate magnitude ($M_w < 5.6$), and an area that can generate 3-5 seismic events with $M_w > 7$ per century with intermediate epicentre depths of 70-180km. The strongest earthquake generated here is considered the event of 26.10.1802 ($M_w = 7.9$), followed by the 4 events of the last century 10.11.1940 ($M_w = 7.7$; h=150km), 04.03.1977 ($M_w = 7.4$; h=93km), 30.08.1986 ($M_w = 7.1$; h=131km), respectively 30.05.1990 ($M_w = 6.9$; h=91km) according to Bala et al., (2003) and Vãcãreanu et al., (2016). Almost 90% of seismic mechanisms are reverse fault type with NE-SW oriented planes, which gives the ellipsoidal character of the macroseismic field.

Central Dobrogea seismogenic zone is associated with Capidava-Ovidiu and Horia-Pantelimonu de Sus faults, both of which have transverse character. Between 1980-2010, this area generated 11 events with $M_w \geq 3$ and a maximum magnitude $M_w = 5$ (12.12.1986).

The seismogenic zone Shabla - Cape Kaliakra belongs geologically to the Moesian Platform and administratively to Bulgaria, being considered generators of normal crustal earthquakes. In the period 1980-2010, this area generated 15 events with $M_w \geq 4$, and the maximum magnitude $M_w = 7.2$ was recorded at the event on 31.03.1901.

From a geological point of view, the studied site conceals a complex structure of the preneogenic

foundation and quverture. The deep drilling performed in this county, as geophysical research has revealed the existence of several tectonic compartments, separated by large faults, oriented mostly NW-SE or N-S some limited to the Paleozoic-Mesozoic quilt, others reflecting down to the Neogenic quilt. Fig.1-b, (Oaie et al., 2016) gives the major structural-tectonic architecture of the graben-horst type resulting from the correlation of the above mentioned works, in which we consider that of interest for the front work are the following tectonic elements:

Figure 1. (a) Location of the sites on the seismic map of Romania (compilation after Popa et.al, 2022 and Văcăreanu et.al., 2016); (b) Tectonic map of Western sector of Black Sea (Oaie et al. , 2016); (c) Sketch of Holocene sedimentary structure of approximate 60m depth.

- the NW-SE directional fault system, seismically active, which is composed of: the Peceneaga-Camena transcrustal fault separating the eastern edge of the Moesic Platform from the North Dobrogean Orogen which is considered active at least in certain segments of the Danube's vicinity, and the profound fault of Saint George which represents the tectonic separation between the North Dobrogea Orogen and the Scythian Platform, being highlighted by numerous gravimetric and magneto-telluric studies, whose work is unanimously accepted and proven by numerous recent earthquakes;

- the NW-SE directional fault system, less active in current times which is composed of: the Voiteşti fault interpreted as a fracture induced by the flexure of the affected deposits, has an N-S direction starting from Tulcea to Kaliakra, it is considered as active in historical times and responsible for barring the intrusion of marine waters into dry territory, and the Danube fault at

the western border of Dobrogea developed in the N-S direction from the northern region of Bulgaria to the area of Fãlciu, on the Prut. It constitutes the deep boundary between the Dobrogea compartment, located at E and the foundation of the Romanian Plain which corresponds to the extension limit of Sarmatian and Pliocene. In the sectors where these regional tectonic accidents intersect, the Intramoesic Fault, The Capidava-Ovidiu Fault, the Peceneaga-Camena Fault and the Saint George Fault, it's recording a higher frequency of seismic events.

The area we refer to is situated at about 90 km distance from the Vrancea and 190km from Shabla seismogenic perimeter. Investigations has been made on two sites, which are located at the flat of Danube River, at 400 m (Site AJ) respectively 0 m distance (Site TJ) from the water course. From engineering perspective, the bedrock is located at more than 300m depth, being covered by shallow deposits consisting in Holocene deposits in fluvial facies which were investigated from surface to a maximum 120m depth. The specific sedimentary structure for this sandy fluvial system consists in (Einsele, 1992): large-scale facies such as floodplain deposits which are composed of small-scale bed types mainly cross-laminated fine sand, silt and mud with frequently peat thin lenses (layer 1), massive, fine sandy silts (layer 2) and gravel bars (layer 3). Figure 1-c contains a sketch of the sedimentary structure described above, with the position of both investigated sites.

1.2. Geotechnical and geophysical investigations

Three types of in situ investigations have been executed on both sites, at distances that do not exceed 50m one from other, which is:

- geotechnical boreholes in continuous rotary dry drilling system, with temporary metal casing protection, sampling system of A class according to ISO 22475-1:2007 and several undisturbed samples in thin Shelby tubes. In all boreholes Standard Penetration Test (*SPT*) has been executed at depth less than 30m.
- cone penetration tests (*CPTu* and *SCPTu*) performed with TE2 equipment types and application class 2 and 3 for *SCPTu* seismic velocities, according to ISO 22476-1:2012;
- geophysical survey (*CH*) for determination of the seismic velocity's profiles along the well depth, respectively "suspension of P-S waves".

The types and number of each investigation executed on both sites are presented in Table 1.

Table 1. Types and number of investigation

Site Investigation		Site AJ	Site TJ
Diameter of the area (m)		76	86
Geotechnical boreholes with SPT tests		4	4
Cone Penetration Tests	CPTu/ SCPTu	4	5
Geophysical survey	P-S	1	1

2 Assessment of liquefaction hazard

Liquefaction is one of the most damaging physical-geological processes associated with the seismic hazard that may damage all granular deposits as the fine ones, of low plasticity. The triggering mechanism depends on many factors that vary in space and time and may be separated into three classes: two related to the soil properties (general settings of soil layers and geomechanical features) and one defined by earthquake characteristics. The prelevation of undisturbed samples in very wet or submerged soils can be an extremely difficult task, sometimes impossible to resolve with usual tools, and thus, in consequence, the assessment of liquefaction hazard by in situ tests became of crucial importance especially in large projects with hard geotechnical conditions, like the one we discuss here.

Presently, assessment of liquefaction susceptibility may be performed in several different ways, (Anwar et al, 2016), either through: (i) probabilistic methods which evaluate the probability of liquefaction (PL), which is a quantitative measure of the severity of this possible phenomenon; (ii) artificial neural networks (ANN) which are conceptual models that estimates the relationships between the earthquake

characteristics and the soil with liquefaction potential or, more common, (iii) deterministic methods which provide an alternative verdict of "liquefiable" or "un-liquefiable" based on the computed values of the safety factor against liquefaction (F_{sliq}).

In this work we will approach the third method of research and we will assess the factor of safety against liquefaction (Fs_{liq}) as defined by Ishihara, (1993) and Seed and Harder, (1990):

$$Fs_{liq} = \frac{CRR}{CSR} = \frac{CRR_{7.5}MSF}{CSR}K_\sigma K_\alpha \tag{1}$$

where the significance of terms is: *CRR* - cyclic resistance ratio; $CRR_{7.5}$ - cyclic resistance ratio for an earthquake with 7.5 magnitude; *CSR* - cyclic stress ratio induced by the seismic shake; *MSF* - magnitude scaling factor; K_s - overburden stress correction factor and K_a - correction factor for sloping ground.

The estimation of both *CRR* and *CSR* may be done through numerous semiempirical correlations with in situ test results, some of those are presented in Table 2.

Table 2. List of most used relations involved in the calculation of Fs_{liq}

Parameter	Reference	Parameter	Reference	Site Investigation
CSR	Liao and Whitman,1986 Idriss, 1999 Cetin et al, 2004 Youd et al. 2001 Eurocode 8, Part 5	CRR	Seed et al., 1984 and Youd et al., 2001 Idriss and Boulanger, 2004 Japanese Bridge Code-JRA, 1990 Robertson and Wride, 1998 Andrus et al., 2000	SPT CPT CH

2.1. Assessment of CRR

Defined as "the capacity of the soil to resist liqefaction" (Youd et al. 2001), the cyclic resistance ratio may be assessed directly throught cyclic test in the laboratory conditions, or indirectly expresses from correlations of this parameter with the results of standard penetration tests (*SPT*), cone penetration tests (*CPT*) or shear-wave velocity measurements executed in various geophysical tests, such as cross-hole, down-hole, suspension of P-S waves (*CH*) or others. In what follows, due to the underconsolidate and loose state of sediments, very few undistorbed samples has been taken and we had chosen to perform comparative calculations of *CRR* based on *SPT* test, as on *CPT* and *CH* tests, which was executed on both selected sites.

2.1.1. Assessment of CRR based on SPT tests

SPT test is not only the older in situ test, but also the most widespread, so that the blow counts have been put in relation with *CRR* by numerous authors such as those listed in Table 2. The calculations of *CRR* based on *SPT* resistance, was expressed as functions of corrected and normalized values $(N_1)_{60}$ and of clean sand corrected N-value $(N_1)_{60cs}$.

a. In the first set of relations Seed et al., (1984) and Youd et al., (2001) expressed the cyclic resistance ratio for an earthquake with 7.5 magnitude, based on equation (2):

$$CRR_{7.5} = \frac{1}{34-(N_1)_{60cs}} + \frac{(N_1)_{60cs}}{135} + \frac{50}{[10(N_1)_{60cs}+45]^2} - \frac{1}{200} \tag{2}$$

According to Youd et al., (2001), $(N_1)_{60cs}$ may be obtained as a function of fine content (*FC*) from equation (3):

$$(N_1)_{60cs} = \alpha + \beta(N_1)_{60} \tag{3}$$

in which for *FC≤5%, a=0* and *b=1.0*; for *5%<FC <35%*, $\alpha = exp\left[1.76 - \left(\frac{190}{FC^2}\right)\right]$ and $\beta = \left[0.99 + \left(\frac{FC^{1.5}}{1000}\right)\right]$, and finally, for *FC ≥35% a=5.0* and *b=1.2*.

b. In the second set of relations, Idriss and Boulanger, (2004) express $CRR_{7.5}$ from equation (4):

$$CRR_{7.5} = exp\left(\frac{(N_1)_{60cs}}{14.1} + \left(\frac{(N_1)_{60cs}}{126}\right)^2 - \left(\frac{(N_1)_{60cs}}{23.6}\right)^3 + \left(\frac{(N_1)_{60cs}}{25.4}\right)^4 - 2.8\right) \tag{4}$$

in which $(N_1)_{60cs}$ has been calculated based on Idriss and Boulanger (2008), formulas (5):

$$(N_1)_{60cs} = (N_1)_{60} + \Delta(N_1)_{60}$$
$$\Delta(N_1)_{60} = exp\left(1.63 + \frac{9.7}{FC + 0.01} - \left(\frac{15.7}{FC + 0.01}\right)^2\right) \tag{5}$$

c. Finally, Japanese Bridge Code-JRA, (1990) attests that $CRR_{7.5}$ is affected by the median diameter of grain size distribution curve (D_{50}) as follows for 0.05mm $\leq D_{50} \leq$ 0.6mm (6):

$$CRR_{7.5} = 0.0882\sqrt{\frac{(N_1)_{60cs}}{\sigma'_v + 0.7}} + 0.255log\left(\frac{0.35}{D_{50}}\right) + R_3 \tag{6}$$

in which dimensionless coefficient $R_3=0$ for $FC<40\%$ and $R_3=0.004FC-0.16$ for $FC \geq 40\%$. We mention that in this third calculation, $(N_1)_{60cs}$ has been used based on Idriss and Boulanger (2004) formulas.

2.1.2. Assessment of CRR based on CPT tests

In international literature the main set of deterministic equations for the evaluation of *CRR* based on *CPT* tests, is given by Robertson and Wride (1998), by the following relations (7, 8).

$$CRR_{7.5} = 0.833\left[\frac{q_{c1Ncs}}{1000}\right]^3 + 0.05, \text{for } q_{c1Ncs} < 50 \tag{7}$$

$$CRR_{7.5} = 93\left[\frac{q_{c1Ncs}}{1000}\right]^3 + 0.08, \text{ for } 50 \leq q_{c1Ncs} < 160 \tag{8}$$

In the above relations, q_{c1N} [-] is the corrected and normalized penetration resistance expressed by (9), q_c [kPa] is the tip penetration resistance, p_a is approximatelly the atmospheric pressure 100 [kPa], σ'_{vo} [kPa] is the effective overburden effort, $(q_{c1N})_{cs}$ is the equivalent clean sand normalized penetration resistance (10), K_c is the granulometric correction of CPT (11), I_c is the index of the behavior of the soil (12), expressed on the basis of Q and F (13) and n take values from 0.5 for clean sands to 1 clays.

$$q_{c1N} = \frac{q_c}{\sqrt{\sigma'_v p_a}} \leq 254 \tag{9}$$

$$(q_{c1N})_{cs} = K_c q_{c1N} \tag{10}$$

$$K_c = -0.403I_c^4 + 5.581I_c^3 - 21.63I_c^2 + 33.75I_c - 17.88 \text{ for } I_c>1.64$$
$$K_c = 1, \text{ for } I_c<1.64 \tag{11}$$

$$I_c = [(3.47 - logQ)^2 + (1.22 + logF)^2]^{0.5} \tag{12}$$

$$Q = \left(\frac{q_c-\sigma_{vo}}{p_a}\right)\left(\frac{p_a}{\sigma'_{vo}}\right)^n, F = \left(\frac{f_s}{q_c-\sigma_{vo}}\right)100 \tag{13}$$

2.1.3. Assessment of CRR based on CH tests

Assessement of *CRR* based on shear-wave velocities came into research and practice since 1988, according to Seed and Idriss, (1988), and the most popular method of evaluation is attributed to Andrus and Stroke, (2000). In this method the *CRR* estimation is expressed as follows:

$$CRR = \left[0.022\left(\frac{V_{S1}}{100}\right)^2 + 2.8\left(\frac{1}{(V_{S1}^* - V_{S1})} - \frac{1}{V_{S1}^*}\right)\right]MSF \tag{14}$$

$$V_{S1}^* = V_{S1}\left(\frac{p_a}{\sigma'_v}\right)^{0.25} \tag{15}$$

where *Vs* is in situ measured shear wave velocity in m/s, and V_{S1}^* is limiting upper value of V_{S1} in m/s,

which is theoretically dependent on fine content, (*FC*).

2.2. Assessment of CSR

CSR defined as the average cyclic shear stress induced by shear waves normalized by the initial vertical effective stress (Seed and Idriss 1971), or "the seismic demand on a soil layer" (Youd et al., 2001), is usually expressed using the well-known formula:

$$CSR = 0,65 \left(\frac{a_{max}}{g}\right) \left(\frac{\sigma_v}{\sigma'_v}\right) r_d \tag{16}$$

where the significance of terms is: a_{max} - maximum horizontal ground surface acceleration, g [m/s²] - gravitational acceleration, s_v [kPa] - total overburden pressure at depth z [m], s'_v [kPa] - effective overburden pressure at depth z and r_d [-] is the stress reduction factor. The latest term, r_d, may be obtain through several analytical methods (Liao and Whitman, 1986; Idriss, 1999; Cetin et al, 2004), but in this application we used the relation of Youd et al. (2001)*,* wich is expressed as follows:

$$r_d = (131 - z)/131, \text{ for } z \leq 9.15\text{m};$$
$$r_d = (44 - z)/37, \text{ for } 9,15\text{m} \leq z \leq 23\text{m}; \tag{17}$$
$$r_d = (93 - z)/125, \text{ for } 23\text{m} \leq z \leq 30\text{m};$$

3. Results

As we presented in paragraph 1.1., both sites have a plane sedimentary unconsolidate structure, for which we performed calculations of Fs_{liq} till 30m depth in the worst scenario of an seismic event of M_w=7.5, in which case *MSF=1* in formula (1). Due to the close position of the locations towards the seimic area Vrancea, for the calculation of CSR we consider the value a_{max}=0.30g, according to Romanian Seismic Code. For both sites, the granulosity of sediments consists mainly in sands and silty sands, as presented in Figure 2, with fine contents varying from 1% to 80% and median diameter of granulometric curves from 0.01mm to 0.18mm.
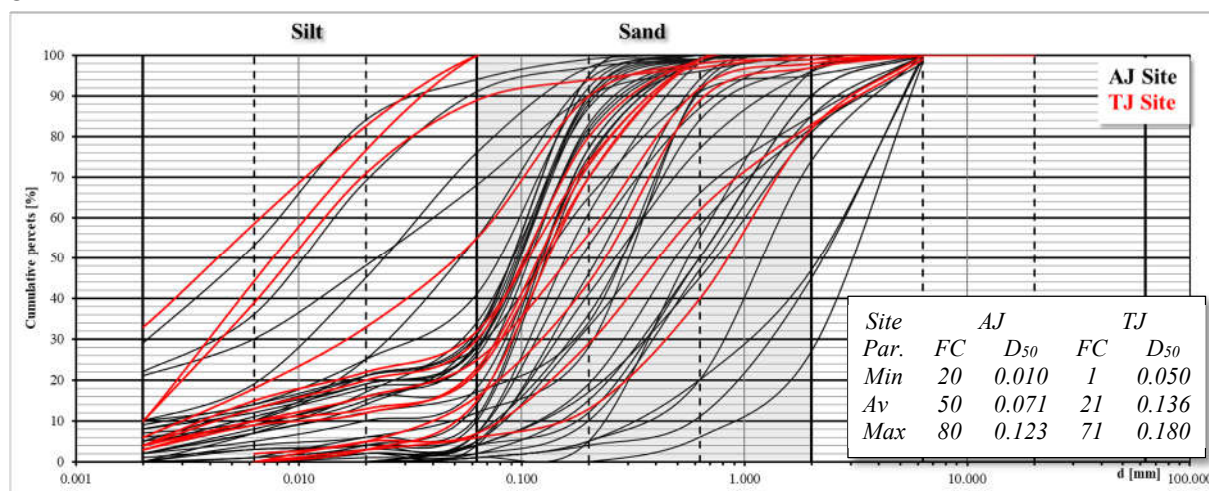

Figure 2. Grainsize distribution curves and specific parameters of investigated sites AJ and TJ.

3.1. Results of the assessment of liquefaction based on SPT tests

In order to estimate the liquefaction hazard based on SPT results we apply all variants of calculation of $CRR_{7.5}$ as described in paragraph 2.1.1. After normalization of *SPT* values, with the aim of calculation of the equivalent clean-sand corrected blow count $(N_1)_{60cs}$, we applied the relations (2÷6), which proved to offer similar results on the first 10m, and slightly to significant different from 10m to 30m depth. For both sites the variation in depth of F_{sliq} (calculated with Seed and Idriss, 1971*, CSR* formula) is presented in Figure 3. We also performed the same calculations using the *CSR* formula provided by Eurocode 8,

and results are compared with the previous. Differences in both sites reveals that the second calculation provides larger values of this parameter in the first 10m, and significant smaller below this depth.
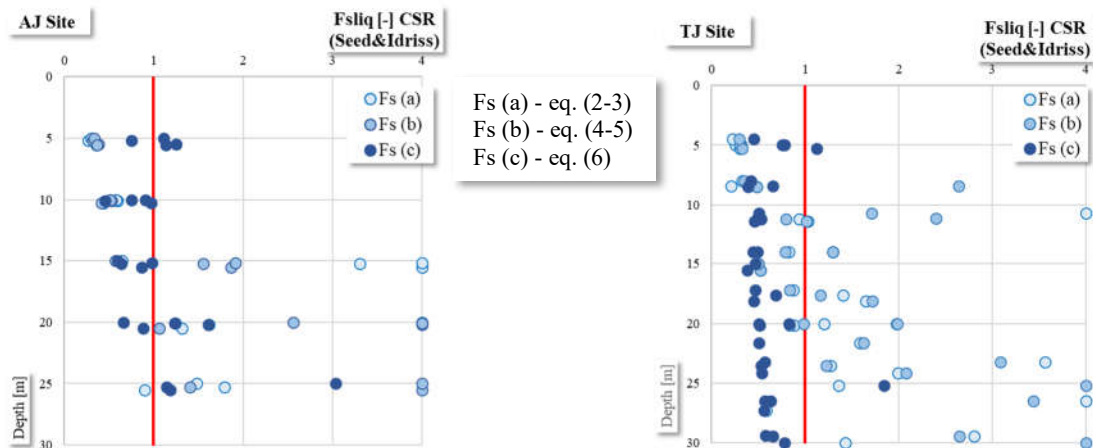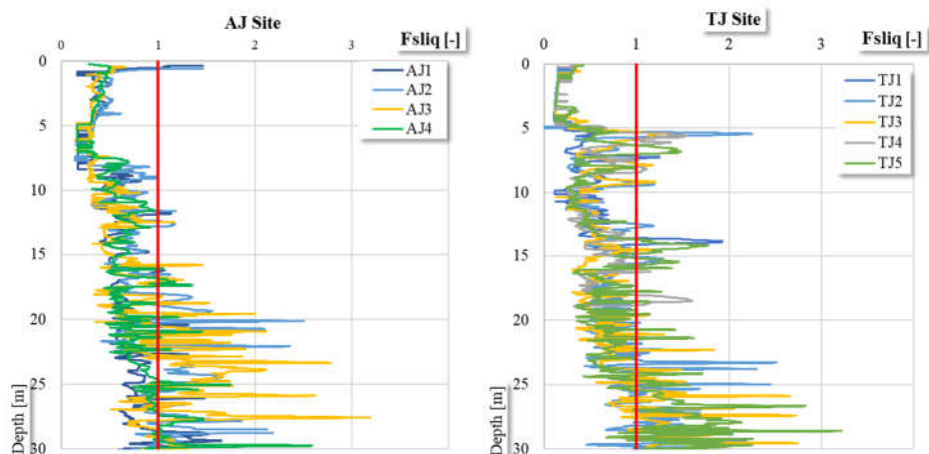

Figure 3. Assessment of factor of safety against liquefaction on AJ and TJ sites, based on *SPT* data.

## 3.2. Results of the assessment of liquefaction based on CPT tests

The assessment of $CRR_{7.5}$ based on *CPT* results was executed according to the procedure given by Robertson and Wride (1998) in equations 7÷13, for both sites, and the results are graphically represented in Figure 4.

Figure 4. Assessment of factor of safety against liquefaction on AJ and TJ sites, based on *CPT* data

3.3. Results of the assessment of liquefaction based on CH tests
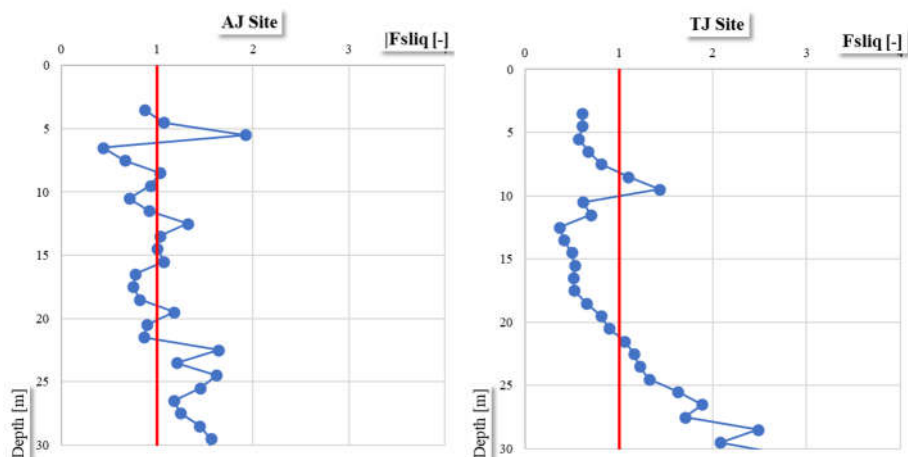
Figure 5. Assesment of factor of safety against liquefaction on A J and TJ sites, based on *CH* data

In the next step, in the purpose of estimation the resistance to liquefaction based on seismic measurements, Andrus and Stroke, (2000) procedure has been applyed on the basis of relations (9) and (10), for both sites, and the results are represented in Figure 5.

3.4. Comparison of results

Finally, after completing the evaluation of liquefiability by the three methods mentioned above, we proceeded to comparison of results. Starting from the reference level obtained from SPT test results (all three formulas), and we found for each site, that even if distances between locations are less than 80-90m, results of various methods do not resemble, except for investigations executed in the same borehole. In the last circumstances, the similitude of the curves of variation Fs_{liq} in depth is better if we relate to equations (4-5), given by Idriss and Boulanger (2004), as it can be visually observed in Figure 6.
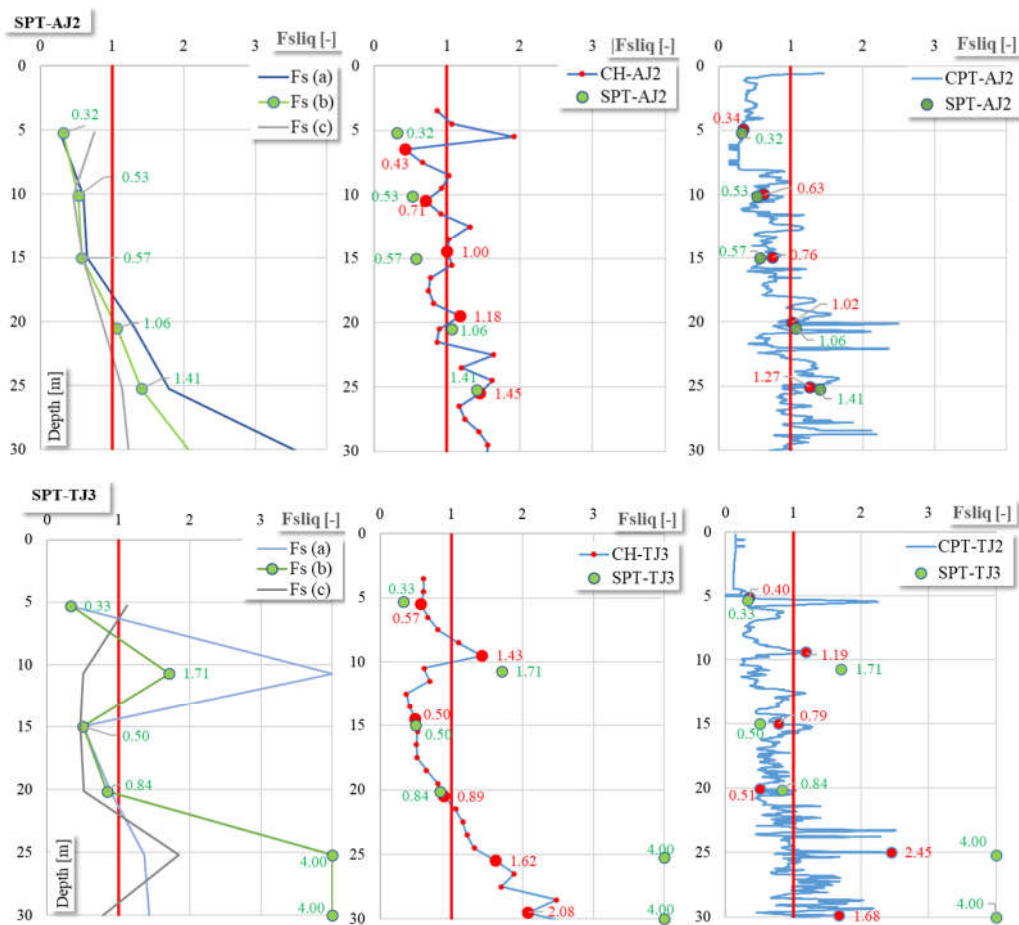
Figure 6. Comparison of safety factor against liquefaction obtained from *SPT*, *CPT* and *CH* tests

Differences obtained in the assessment of *CRR* through the mentioned methods may be explained by the following specific particularities of each method:

- both *SPT* and *CPT* are methods which pushed the soil in large deformations, over the limits of shear failure comparable with those produced by liquefaction, while *CH* measure the resistance of soils submitted to small efforts and deformations, significantly below the limits of equilibrium;

- another significant difference refers to the volume of soil tested: *SPT* and *CPT* are punctual tests which evaluate resistance over a small, limited volume of influence (4÷8 diameters of instruments according to Rogers, 2006), while *CH* test provides average strength properties of larger volumes, which can reach hundreds of meters in diameter depending on the power of the seismic source;

- finally, we conclude that the influence of granulosity over the assessment of *CRR* is variable:
  (i) in *SPT* assessment is very important, and thus for a prudent and correct application of all three formulas (2÷6), it should be associated with punctual laboratory analyses of grain size distribution of the soil executed at the level of measurement;
  (ii) in the absence of sample prelevation, the influence of granulosity on the values of CRR based on the *CPT* test is more discrete, thanks to the introduction of *Kc* and *Ic* parameters in formulas 7 and 8;
  (iii) in *CH* assessment, the influence of granulosity is implicit, as the measurements of shear waves velocities encompass in an overall mode the mechanical state of soil volume, and are strongly controlled by technical specifications of geophysical sensors.

4. Conclusions

- The comparative analysis of the results of Fs_{liq} calculations based on *SPT*, *CPT* and CH tests, reveals a good agreement only in close adjoining positions of investigations, inspite of the influence of the particularities of each method over results.

- Due to the strong influence of granulosity over the magnitude of *CRR* based on *SPT* test, we conclude that this method must be applyied only if each *SPT* measurements is accompanied by grain size distribution test executed in the same march as the penetration.

- Among the three methods of evaluation of *CRR* based on *SPT* test, those given by Idriss and Boulanger (2004), fits best with the similar calculations based on *CPT* and *CH* tests.

- Finally, due to the fact that all differences exposed above, transposed in terms of Fs_{liq} may conclude in divergent results regarding the liquefaction hazard, the interpretation and comparison of results must be limitted to in situ tests executed simultaneously at minimum distances, or if possible (for geophysical survey), in the same borehole.

References

Andrus, R.D. and Stokoe, K.H.II. Liquefaction resistance of soils from shear-wave velocity. *Journal of Geotechnical and Geoenvironmental Engineering*, 2000, ASCE 126:11, 1015-1025.

Anwar, A., Ahmad, S., Jamal, Y. and Khan, M.Z. Assessment of Liquefaction Potential of Soil Using Multi-Linear Regression Modeling, *International Journal of Civil Engineering and Technology*, 2016, 7(1), 373-415.

Bala A., Radulian M., and Popescu E. Earthquakes distribution and their focal mechanism in correlation with the active tectonic zones of Romania. *Journal of Geodynamics*, 36 (2003), 129–145.

Cetin K.O., Seed R.B., Der Kiureghian A., Tokimatsu K., Harder L.F. Jr, Kayen R.E., Moss R.E.S. SPT-based probabilistic and deterministic assessment of seismic soil liquefaction potential, *Journal of Geotechnical and Geoenvironmental Engineering*, 2004, ASCE, 130 (12), 1314-1340.

Einsele G. *Sedimentary Basins Evolution, Facies and Sediment Budget.* Springer - Verlag Berlin Heidelberg Eds., 1992, 628 pp

EN 1998-5: Eurocode 8: Design of structures for earthquake resistance – Part 5: Foundations, retaining structures and geotechnical aspects. 2004.

Idriss, I. M. An update to the Seed-Idriss simplified procedure for evaluating liquefaction potential in *Proceedings, TRB Workshop on New Approaches to Liquefaction*, Publication No. FHWA-RD-99-165, Federal Highway Administration, January 1999.

Idriss, I.M., and Boulanger, R.W. Semi-empirical procedures for evaluating liquefaction potential during earthquakes. In *Proceedings of 11th International conference on soil dynamics and earthquake engineering, and 3rd International conference on earthquake geotechnical engineering, vol. 1. Stallion Press*. , 2004, 32–56.

Ishihara, K. Liquefaction and Flow Failure during Earthquake. *Géotechnique*, 1993, 43, 351-415.

ISO 22475-1:2007. Geotechnical investigation and testing. Sampling methods and groundwater measurements. Part 1: Technical principles for the sampling of soil, rock and groundwater.

ISO 22476-1:2022. Geotechnical investigation and testing — Field testingPart 1: Electrical cone and piezocone penetration test

JRA-Specification for Highway Bridges: Part V- Seismic Design. Japan Road Association, Tokyo, 1990.

Liao, S.S.C. and Whitman, R.V. Overburden correction factors for SPT in sand. *Journal of Geotechnical Engineering*, 1986, Vol. 112, No. 3, 373-377.

Oaie Gh., Seghedi A., Rădulescu V. Natural marine hazards in the black sea and the system of their monitoring and real-time warning. *Geo-Eco-Marina* 22/2016, 5-28.

Popa, M., Chircea, A., Dinescu, R., Neagoe, C., Grecu, B., Borleanu, F. *Romanian Earthquake Catalogue* (ROMPLUS)", Mendeley Data, V2, doi: 10.17632/tdfb4fgghy.2. 2022.

Robertson P. K., Wride C. E. Evaluating cyclic liquefaction potential using the cone penetration test, *Can. Geotechnical Journal*, 1998, 35: 442–459.

Rogers, J.D. Subsurface Exploration Using the Standard Penetration Test and the Cone Penetrometer Test. Environmental & Engineering Geoscience, vol. XII, no.2, May 2006, 161-179

Seed, H.B. and Idriss, I.M. Simplified procedure for evaluating soil liquefaction potential. *Journal of Soil Mechanics and Foundations*. Div. ASCE, 1971, 97(SM9), 1249-1273.

Seed, H. B., Tokimatsu, K., Harder, L. F., Chung, R. M. The Influence of SPT Procedures in Soil Liquefaction Resistance Evaluations, Earthquake Engineering Research Center Report No. UCB/EERC-84/15, University of California at Berkeley, 1984.

Seed, R.B. and Harder, L.F. SPT-based analysis of cyclic pore pressure generation and undrained residual strength. In *Proceedings of the H. Bolton Seed Memorial Symposium*, Berkeley, Calif. Edited by J.M. Duncan. BiTech Pub- lishers Ltd., Vancouver. 1990, Vol. 2, 351-376.

Văcăreanu R., Radulian M. and Cioflan C.O. An Updated Probabilistic Seismic Hazard Assessment for Romania and Comparison with the Approach and Outcomes of the SHARE Project. Pure and Applied Geophysics, 2016, 173, 1881-1905.

Youd, T. L., Idriss, I. M., Andrus, R. D., Arango, I., Castro, G., Christian, J. T., Dobry, E., Finn, W. D. L., Harder Jr., L. F., Hynes, M. E., Ishihara, K., Koester, J.P., Liao, S. S. C., Marcusson III, W. F., Martin, G. R., Mtchell, J. K., Moriwaki,Y., Power, M. S., Robertson, P. K., Seed, R. B., and Stokoe II, K. H. Liquefaction resistance of soils: Summary report from the 1966 NCEER and 1998 NCEER/NSF workshops on evaluation of liquefaction resistance of soils. *Journal of Geotechnical and Geoenvironmental Engineering*, 2001, 124 (10), pp. 817-833.

LARGE SCALE ASSESSMENT OF THE LIQUEFACTION POTENTIAL USING THE CONE PENETRATION TESTING (CPT): EXAMPLE OF SISAK – MOSLAVINA COUNTY IN CROATIA

MEHO SAŠA KOVAČEVIĆ[1], DAVOR GARAŠIĆ[2], MARIO BAČIĆ[3], MARIJAN CAR[4]

1 University of Zagreb, Faculty of Civil Engineering, Croatia, meho.sasa.kovacevic@unizg.grad.hr

2 Center of the Faculty of Civil Engineering, Croatia, davor.garasic@unizg.grad.hr

3 University of Zagreb, Faculty of Civil Engineering, Croatia, mario.bacic@unizg.grad.hr

4 University of Zagreb, Faculty of Civil Engineering, Croatia, marijan.car@unizg.grad.hr

Abstract

On December 29th 2020, an earthquake with a magnitude of 6.2 on the Richter scale struck the area of central Croatia. During and after the earthquake, several geotechnical phenomena appeared that directly impacted buildings and infrastructure. The most widespread phenomenon that caused significant damages is liquefaction, which occurred on almost 1600 ha of the Sisak – Moslavina County's territory. As a phenomenon occurring during the strong seismic events in saturated non-coherent materials, it is characterized by turning the soil into a thick liquid, losing its strength and stiffness. As a part of large-scale investigations of the area in the post-seismic period, a Cone Penetration Testing (CPT) campaign was implemented to assess the probability of liquefaction occurrence. Considering the very large and statistically relevant number of collected data, the development of a map of a specific region of the county followed, by interpolating the obtained results. As such, this map can be directly compared to the previous liquefaction assessment efforts which relied only on the limited indicators, such as overall geology, distance from the adjacent rivers, the width of the valley and the elevation of the terrain above the flood water level.

Key words

liquefaction assessment, liquefaction probability, cone penetration test, Sisak – Moslavina County

1 Introduction

Liquefaction, a relatively rare phenomenon that occurs in water-saturated soils during earthquakes, often draws the attention of geotechnical experts in the aftermath of major seismic events. However, science is continuously striving to better understand the behaviour of soils under dynamic loading and to develop appropriate remedial measures. During liquefaction, relatively loose sand layers are suddenly and temporarily transformed into a dense liquid (Bačić et al., 2020), losing their shear strength and ability to support building foundations and near-surface infrastructure. For liquefaction to occur, two factors must occur simultaneously: saturated soil material, which is susceptible to liquefaction, and an earthquake of corresponding magnitude with maximum seismic acceleration (peak). It should be emphasized that soil that has liquefied once does not necessarily have sufficient resistance to liquefaction, i.e. liquefaction may occur again during subsequent seismic events. Furthermore, many studies (Ishihara and Okada, 1978; Suzuki and Toki, 1984; Olson et al., 2005; Wang et al., 2013) have shown that once soil has liquefied, it is most likely still susceptible to liquefaction, sometimes even more so during aftershocks than during the main shock.

A recent example of the large-scale liquefaction occurred as an aftermath of the strong 6.2 magnitude earthquake that shook the Sisak - Moslavina County in Croatia on December 29th 2020. The main impact was preceded by two foreshocks of magnitude 4.7 and 5.2, followed by a series of aftershocks, the strongest of which had a magnitude of 4.9. With stronger seismic activity continuing, a rapid assessment

of the liquefaction potential on large area was of paramount importance (Librić et al., 2022), especially on the inhabited locations, as well on the locations of surface and subsurface infrastructure, with focus on critical infrastructure such as educational and health institutions, transportation (evacuation) networks, flood protection system networks etc.

Since the liquefaction potential assessment required relatively fast and effective methods to be implemented, and considering the large area and many locations to be covered, an investigation campaign included a cone penetration test (CPT) method, Figure 1. Based on the analysed and interpreted results, a direct insight into the state of the soil from the aspect of dynamic instabilities (likelihood of liquefaction) was obtained. In view of the very large and statistically relevant amount of data collected, a map of the specific region of the county was developed by interpolating the results obtained. Thus, this map can be directly compared with the previous efforts to assess liquefaction on large-scale, which were based on limited indicators and relying mostly on existing geological maps and not on measured subsurface data.

Figure 1. Cone Penetration Testing in the area of Petrinja

2 Investigation method: cone penetration test (CPT)

In practice, methods based on the correlation of the occurrence of liquefaction with the results of in-situ penetration investigations are used for this purpose, namely the standard penetration test - SPT and the cone penetration test - CPT (Seed and Idriss, 1971), for which empirical so-called liquefaction diagrams are drawn up and periodically updated. The basis for the evaluation of the liquefaction potential is the calculation of the cyclic stress ratio (CSR):

$$CSR = 0{,}65 \times \frac{a_{max}}{g} \times \frac{\sigma_{v0}}{\sigma'_{v0}} \times r_d \tag{1}$$

where the r_d is stress reduction factor, a_{max} is peak horizontal ground acceleration, while σ_{vo} and σ'_{vo} represent total and effective vertical stress. The cyclic resistance ratio (CRR) can be determined based on the results of mentioned in-situ tests. The overall liquefaction assessment method compares these two parameters, CSR and CRR. If CSR > CRR, it can be concluded that the tested soil is susceptible to liquefaction. If the CRR value is higher, the probability of liquefaction occurring is lower.

The principle of the CPT, as method selected within this study, is to push a special probe into the soil at a certain speed, with constant measurement of the pressure resistance on the tip of the probe, q_c, and the friction on the probe sheath, f_s, which is activated when the probe is pressed between the sheath and the surrounding soil. Based on the three basic measured parameters (q_c, f_s, u_2), the type and profile of the soil, i.e. the type of soil behavior (SBT, Soil Behavior Type) was estimated using normalized and non-normalized classification diagrams, and the stiffness and strength parameters of the soil were estimated according to the existing correlations. The standard penetration speed is 20 mm/s. Test results are generally not sensitive to small deviations from the standard penetration speed (20 ± 2 mm/s). Most systems collect data at intervals of 25 to 50 mm, with 50 mm being the most common. In addition, CPT tests can also serve as an indicator of liquefaction potential, and this was utilized within presented study. The advantages of CPT testing are fast and continuous measurement, repeatability and reliability of measurement, economy, and productivity, and strong theoretical bases for interpretation. On the other hand, CPT can be of limited use in gravel and cemented soils, while no soil sample is taken during the investigation. Also, as noted by Bačić et al. (2024), the conventional liquefaction resistance assessment methods based on penetration tests, such as CPT, may overestimate the liquefaction potential in some soils, and this has been attributed to particle crushing and/or aging effects, but may also be due to the relationship inherent in a certain CPT-based procedure.

Based on the selected earthquake magnitude of 6.5 within this study (which roughly corresponds to the magnitude of the Petrinja 2020 earthquake) and the values for the horizontal ground acceleration (which correspond to the 475 - year return period design ground acceleration at the level of the bedrock at the site in question), the cyclic stress ratio (CSR) were calculated continuously by depth. Also, the cone penetration tip resistance (q_c) is continuously derived along the depth from the CPT test, enabling calculation of CRR. This provided calculation of the safety factor for liquefaction, continuously along the depth of each test. Based on the methodology proposed by Juang et al. (2002), the probability of liquefaction was also calculated as a function of the depth of each test:

$$PL = \frac{1}{\left[1 + \left(FS/A\right)^B\right]} \tag{2}$$

where A = 1.0 and B = 3.3 are selected as regression coefficient. Eventually, this enabled a classification of the soil in terms of liquefaction potential according to Table 1.

Table 1. Soil classes according to the probability of liquefaction

Probability of liquefaction	Class	Description
0.85 ≤ LP	5	The soil will almost certainly liquefy
0.65 ≤ LP < 0.85	4	It is very likely that the soil will liquefy
0.35 ≤ LP < 0.65	3	Liquefaction / non-liquefaction is equally likely
0.15 ≤ LP < 0.35	2	It is unlikely that the soil will liquefy
LP < 0.15	1	The soil will almost certainly not liquefy

In order to define all the required input for the mentioned calculation (in order: Soil Profile, Soil Bulk Weight, Percentage of Fine Particles, CSR, CRR, Liquefaction Safety Factor, Probability of Liquefaction Occurrence), the code was programmed in Python programming environment (Librić et.al., 2022).

3   Results and discussion

Given the vast number of investigated locations of buildings and infrastructure and thus the very large amount of data from the CPT tests carried out, a statistically relevant sample was obtained for the creation of a map of the liquefaction potential. It is important to note that when interpreting the data, the

thickness of liquefiable layer larger than half a meter was taken as a criterion for assigning a liquefaction potential class (Figure 2), as this conforms with some previous studies. The coordinates of all test locations were recorded and each coordinate was assigned a calculated liquefaction potential value from 1 to 5 (Table 2), based on the described methodology. A map of the liquefaction potential for selected region was created by interpolation with the QGis software.
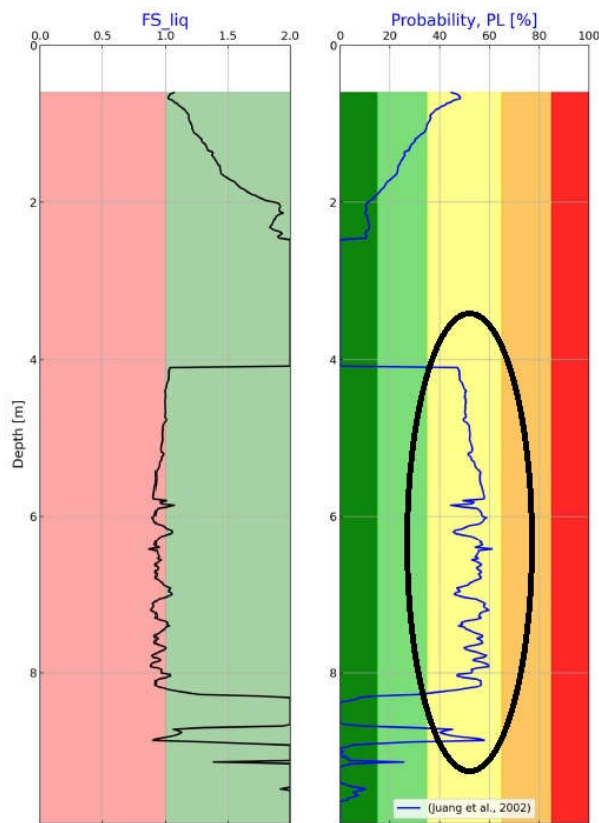

Figure 2. An example of liquefaction probability assessment along the depth

Table 2. An excerpt from the data sheet used for developing liquefaction map, with position (latitude and longitude) and CPT calculated liquefaction probability class as selected attributes

Location	Latitude	Longitude	Class
Ljudevita Gaja 49	45.444053	16.283117	4
Marina Držica 2	45.446430	16.290156	4
Mate Jerkovića 21	45.446303	16.320876	2
Matije Gupca 106	45.438123	16.262701	1
Matije Gupca 75	45.439006	16.266889	2

Figure 3 shows an excerpt from the susceptibility to liquefaction map for the area of the town of Petrinja (Krkač et al., 2021), which is used to compare with the results of this study. This map was developed mostly for the needs of spatial planning in the area, and uses several indicators, such as overall geology, distance from the adjacent rivers, the width of the valley and the elevation of the terrain above the flood water level. Authors of the mentioned map stress-out that the detailed geotechnical investigations are necessary in order to obtain relevant geotechnical data which would provide insight into the liquefaction susceptibility of the each particular site. On this map (Figure 3) the areas marked red represent high susceptibility, orange represents medium susceptibility and yellow represents low susceptibility to liquefaction.
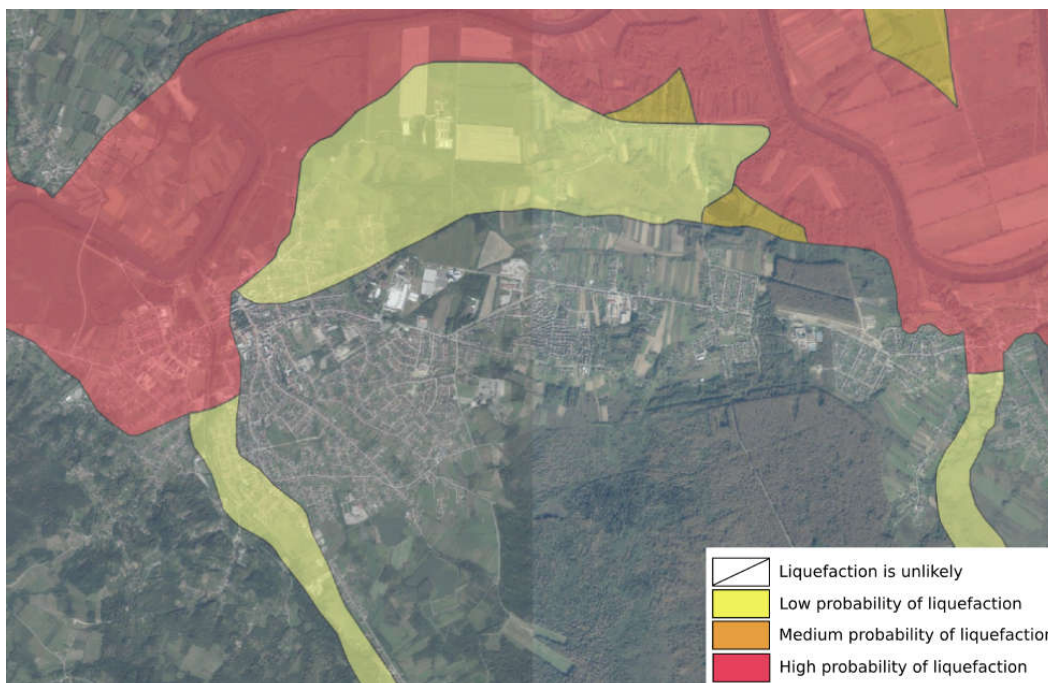
Figure 3. An excerpt from the preliminary susceptibility to liquefaction map for the area of the town of Petrinja, extracted from Krkač et al. (2021)

Figure 4 shows a map of the liquefaction potential for the area of the town of Petrinja calculated from CPT, following the methodology presented in the paper. Areas marked red represent the highest probability of liquefaction occurrence, or class 5. Orange represents class 4, yellow class 3, light green class 2 and dark green class 1. In order to create this part of the map, data from 121 CPT tests conducted in the Petrinja region were used.
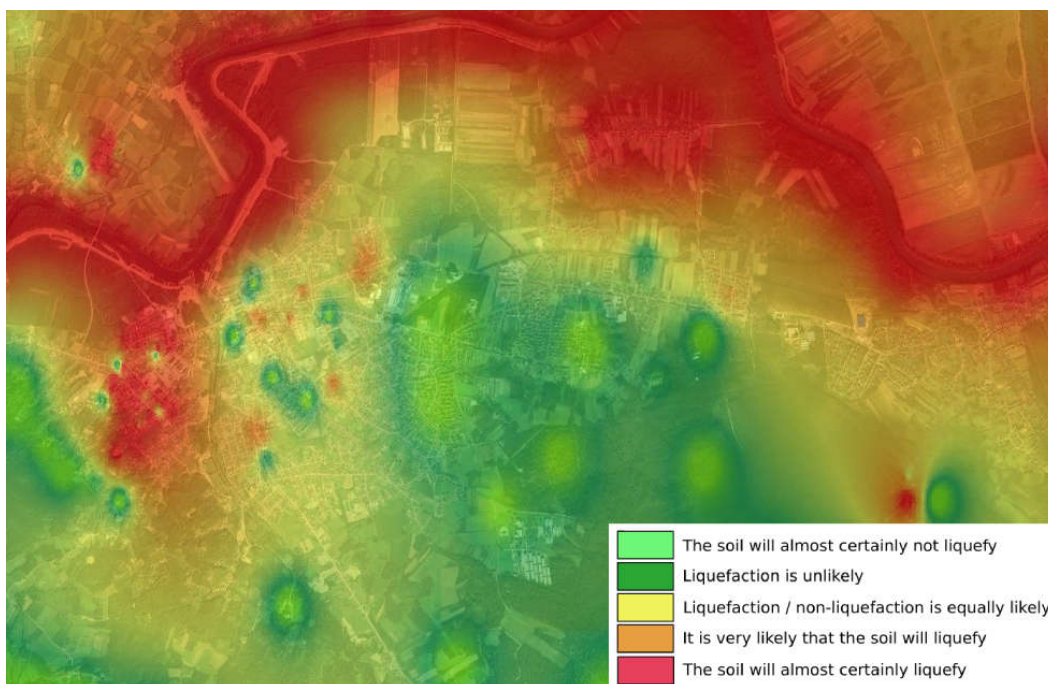
Figure 4. An excerpt from liquefaction potential map for the area of the town of Petrinja, following the CPT based methodology described in the paper

By overlapping both maps, high level of matching of liquefaction prone areas is visible. These are mostly located near the major rivers in the area. However, there are some deviations noticed, where the higher classes of liquefaction susceptibility where registered in areas of lower liquefaction potential according to the preliminary maps relying mostly on geological and overall position (location) indicators (Figure 5). These deviations can be attributed to the larger areas (such as 1 & 3 on Figure 5) or to some micro - locations (such as 2 & 4 on Figure 5) where there is possibility that liquefiable layers appear in form of isolated subsurface zones / lenses. Also, it should be noted that that the CPT results give a valuable information on the exact depth of the liquefiable layers, which is crucial information in case that liquefaction mitigation measures are to be implemented.
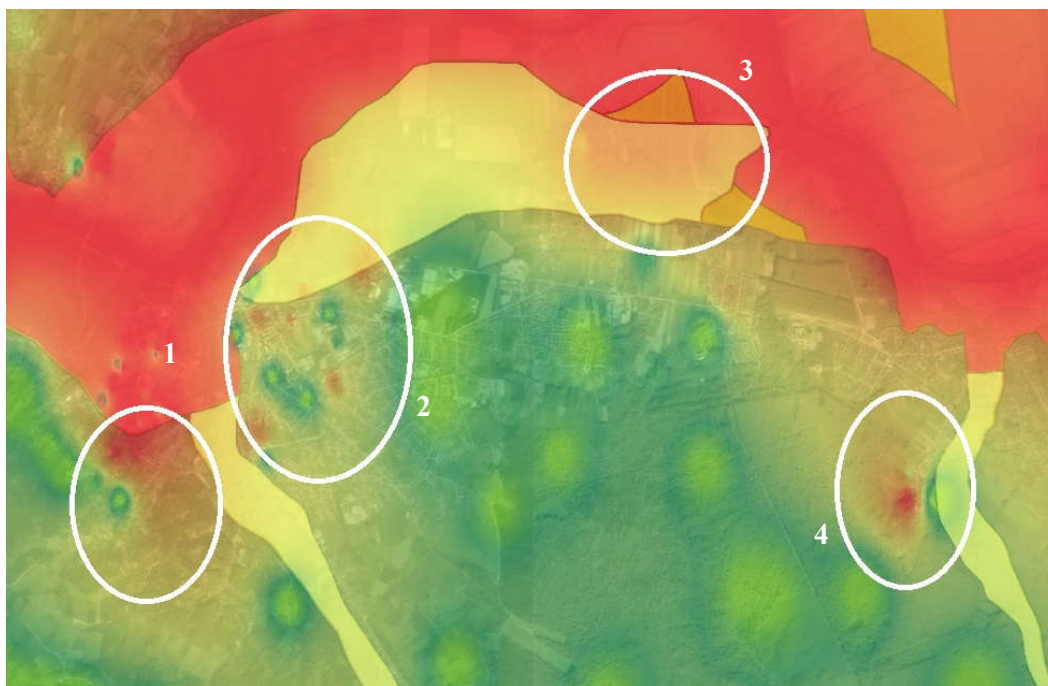
Figure 5. Overlapping the preliminary susceptibility map (Krkač, 2021) and the CPT-based map developed in this study

4   Conclusion

As part of the wider in-situ investigation campaign to determine the soil liquefaction potential after the Petrinja 2020 seismic event, numerous cone penetration tests (CPT) were conducted. The analysed and interpreted results provided a direct insight into the condition of the soil along the depth in terms of likelihood (probability) of liquefaction using the established procedure. This provided basis for the development of the liquefaction potential map by interpolating the results of 121 CPT tests on selected specific region of the Sisak – Moslavina county. Previous efforts to assess liquefaction potential in the area relied on limited indicators such as general geology, distance to adjacent rivers, the width of the valley and the elevation of the terrain above the flood water level. By comparing these two maps, it was shown that the results correlate well, but some deviations are also visible and stressed-out in the paper. Since the central Croatia is an area with a very complex geology, the deviations from general trends in individual micro locations are to be expected. It is therefore of paramount importance to conduct in-situ geotechnical investigations at each site in order to get reliable information on the probability of liquefaction occurrence and the depth of liquefiable layers. Only this can be used directly for the design and implementation of liquefaction mitigation measures. Since the research work in the earthquake-prone area has not been completed yet, the liquefaction potential map will continuously be updated.

Acknowledgements

References

Bačić, M., Ivšić, T., Kovačević, M. S.: Geotechnics as an unavoidable segment of earthquake engineering, GRAĐEVINAR, 72 (2020) 10, pp. 923-936, doi: https://doi.org/10.14256/JCE.2968.2020

Bačić, M., Kovačević, M. S., Rossi, N., Librić, L Assessing the Soil Liquefaction Susceptibility: A Comparative Study of CPT and MASW Techniques in the Aftermath of Road Failure, Proceedings of 8th International Conference on Road and Rail Infrastructure - CETRA 2024 / Lakušić, Stjepan (ed.). University of Zagreb, 2024. str. 783-790 DOI: https://doi.org/10.5592/CO/CETRA.2024.1540

Chen, C.J.; Juang, C.H. Calibration of SPT- and CPT-Based Liquefaction Evaluation Methods. Innovations and Applications in Geotechnical Site Characterization, 2000, https://doi.org/10.1061/40505(285)4

Ishihara, K.; Okada, S. Effects of stress history on cyclic behavior of sand. Soils and Foundations 18.4, 1978, 31-45.

Juang, C.H.; Rosowsky, D.V.; Tang W.H. Reliability-Based Method for Assessing Liquefaction Potential of Soils. Journal of Geotechnical and Geoenvironmental Engineering, 2002, Vol 125, Issue 8. https://doi.org/10.1061/(ASCE)1090-0241(1999)125:8(684)

Krkač, M.; Bernat Gazibara, S.; Damjanović, V.; Sinčić, M.; Jagodnik, V.; Peranić, V.; Jagodnik, P.; Mihalić Arbanas, S. Preliminary liquefaction vulnerability map and liquefaction inventory map - area of 16 municipalities/cities. Faculty of Mining, Geology and Petroleum Engineering, University of Zagreb; Faculty of Civil Engineering, University of Rijeka, 2021.

Librić, L.; Bačić, M.; Kovačević, M.S. Utilization of CPTU for evaluation of liquefaction probability below the flood protection embankment in Croatia, Proceedings of the 3rd International Conference on Natural Hazards and Infrastructure. 2022. pp. 1-8

Olson, S.M.; Green, R.A.; Obermeier S.F. Geotechnical analysis of paleoseismic shaking using liquefaction features: a major updating. Engineering Geology, Vol. 76, Issues 3–4, 2005, 235-261, ISSN 0013-7952, https://doi.org/10.1016/j.enggeo.2004.07.008

Seed, H. B.; Idriss, I. M. Analysis of liquefaction: Niigata earthquake, 1967. Proc., ASCE, 93(SM3), 83-108.

Suzuki, T.; Toki, S. Effects of preshearing on liquefaction characteristics of saturated sand subjected to cyclic loading. Soils and foundations, 24(2) 1984, 16-28

Wang, S.; Yang, J.; Onyejekwe, S. Effect of Previous Cyclic Shearing on Liquefaction Resistance of Mississippi River Valley Silt, Journal of Materials in Civil Engineering, 2013, 25, pp. 1415–1423

CORRELATING THE SPATIAL DISTRIBUTION OF LIQUEFACTION PHENOMENA WITH THE SURFICIAL GEOLOGY ON POINT BARS DEPOSITS; CASE STUDIES 2021 DAMASI, GREECE AND 2023, KAHRAMANMARAŞ, TÜRKIYE

MARIA TAFTSOGLOU[1], SOTIRIS VALKANIOTIS[1], GEORGE PAPATHANASSIOU[2], VASSILIS NTOUVARTZIS[2], DIMITRA RAPTI[3], RICCARDO CAPUTO[4]

[1] *Dept. Civil Engineering, Democritus University of Thrace, Greece,* mtaftsog@civil.duth.gr, svalkani@civil.duth.gr

[2] *School of Geology, Aristotle University of Thessaloniki, Greece,* gpapatha@geo.auth.gr, vasintou@geo.auth.gr

[3] *Dept. Chemical, Pharmaceutical and Agricultural Sciences, Ferrara University, Italy,* dimitra.rapti@unife.it

[4] *Dept. Physics and Earth Sciences, Ferrara University, Italy,* rcaputo@unife.it

Abstract

Liquefaction, a seismic threat to critical infrastructure, demonstrated its impact in the 2021 Damasi event in Greece and the 2023 Türkiye events. In both cases, extensive liquefaction phenomena were triggered in the floodplain and point bars of large meandering rivers. Considering that the identification of the paleoenvironmental features is a crucial step to assess the liquefaction susceptibility of an area, this research aims to statistically investigate the spatial distribution of liquefaction within point bars. Using historical and contemporary data, we were able to reconstruct the evolution of meandering fluvial systems in both cases and preliminary delineate the different types of lithofacies encountered in point bars; sand and mud prone. Afterwards, we compared the location of liquefaction related phenomena, ejecta and lateral spreading, with the predominant type of soil material within the point bars. As an outcome, it was concluded that more than 80% of the liquefaction phenomena, triggered by these two earthquake cases, reported on the upstream flow direction of point bars which is characterized as sandy like zone.

Key words

Liquefaction, point bar, lithofacies, geomorphology, remote sensing

1 Introduction

The occurrence of liquefaction phenomena and the induced failures are crucial issues that shoud be taken into account to ensure the stability of manmade structures and lifelines. During the last decade, major earthquakes in New Zealand, Italy, Greece and Türkiye demonstrated the severity of the liquefaction-induced damages. The outcomes that arose from these devoted studies strengthened the opinion that spatial distribution of these phenomena follows defined patterns and is strongly correlated with the depositional history of the sediments (Wotherspoon et al., 2012, Di Manna et al., 2012, Bastin et al., 2015, Papathanassiou et al., 2012; 2015; 2022, Civico et al., 2015, Taftsoglou et al., 2023, Abayo et al., 2023). In several cases it was concluded that most of the liquefaction effects were not randomly distributed over a floodplain but were concentrated in specific geomorphological areas where fine- and coarse-grained sediments of Holocene age sorted by fluvial or wave actions are deposited. In particular, old/ abandoned channels, point bars and coastal formations exhibited a notably higher density in liquefaction occurrences than other parts of a floodplain. Consequently, the reliability of a liquefaction susceptibility map is highly dependent by the scale and accuracy of the geological and geomorphological mapping of a floodplain.

Aiming to delineate the prone to liquefaction areas, many researchers used remote sensing techniques for compiling geomorphological maps (Papathanassiou et al., 2022, Taftsoglou et al., 2022; 2023).Thus,

the more likely to liquefaction geomorphological features are traced in detail, leading to a more reliable liquefaction susceptibility map.

Following this approach, this research focuses on the valleys of Piniada in Thessaly (Greece) and Orontes in Hatay (Türkiye), where the mainshocks of Mw=6.3 on 2021 and Mw=7.7 on 2023 occurred, respectively. As both valleys are covered by Quaternary fluvial deposits of Pinios and Orontes rivers, particular emphasis were placed on point bar formations where liquefaction phenomena i.e.ejecta and lateral spreading, were triggered by these two events. Taking into account the heterogeneity of the non-cohesive material accumulated on the inner part of the meander (point bars), the relationship between the distribution of liquefaction sites and the sand- and mud-prone sediments were examined. The delineation of different types of lithofacies was achieved by applying the method proposed by Russel et al., (2017) and correlated with the spatial distribution of manifestation with the predominant type of soil material, resulted to the evaluation of the total liquefaction density per heterogeneity type. As an outcome, it was concluded that most of liquefaction phenomena, triggered by these two earthquake cases, were triggered on the upstream flow direction of point bars, characterized as sandy like zone.

1.1 The case study of 2021 Damasi, Greece

On March 2021, a seismic sequence occurred in Thessaly, Central Greece, characterized by a Mw= 6.3 mainshock close to Damasi village and five Mw > 5.0 aftershocks. Considering the post earthquake documentation, extensive liquefaction manifestations were triggered in the floodplain of the Piniada Valley.

Defined as the central reach of Pinios River, Piniada Valley is located in between the western Karditsa and Eastern Larissa plain and represents an area of significant anomaly of the hydrographic network, as far as it allows the connection between these two basins since Early Quaternary age (Caputo et al., 2021). During the Late Quaternary, Piniada Valley was progressively filled by marshy-lacustrine deposits and finally by the eastwards prograding internal deltas of the Pinios River (Caputo et al., 2021). As a result of this complex geological evolution, the current Piniada Valley is characterized as an alluvial plain entirely covered by fluvial formations of abandoned channels, point bars and floodplain deposits (Fig.1). Documentation of liquefaction manifestations in Piniada Valley reported a 26.7m ground fissure as the longest one, while the total coverage of ejecta material was estimated as 0.0325 km^2 (Papathanassiou et al., 2022). Following the detailed geological mapping and the statistical analyses of the spatial distribution of liquefaction phenomena with the geomorphological features, it was shown that most of the liquefaction effects concentrated within specific areas that correspond to deposits formed as point bars and filled abandoned channels.

1.2 The case study of 2023 Türkiye earthquakes

During the 2023 earthquake doublet of Mw 7.7 and Mw 7.6 on East Anatolian Fault Zone (EAF), extensive liquefaction was observed at Amik Valley and specifically in Orontes (Asi) River. Being infilled with Plio-Quaternary sediments of more than 200–300 m thickness, Amik Plain extends for approximately 36 km long and 40 km wide and its drainage is controlled by Orontes, Karasu, and Afrin Rivers from the south, north, and east, respectively. In the past, the western central part of this valley was covered by Amik Lake, where through the last decades was completely drained by an artificial channel system into the Orontes River (Hazir et al., 2016).

As one of the most affected regions, due to liquefaction phenomena after the 2023 seismic events, Orontes River Valley presented a significant number of 560 sites of ejecta and lateral spreading effects in its meandering, delta and open valley zones (Taftsoglou et al., 2023).

For the purposes of this study, we focused on a segment of Orontes close to the South-East part of Amik Valley, delineating more than 0.161 km^2 of ejecta material and 0.544 km^2 of lateral spreading phenomena (Fig.2).
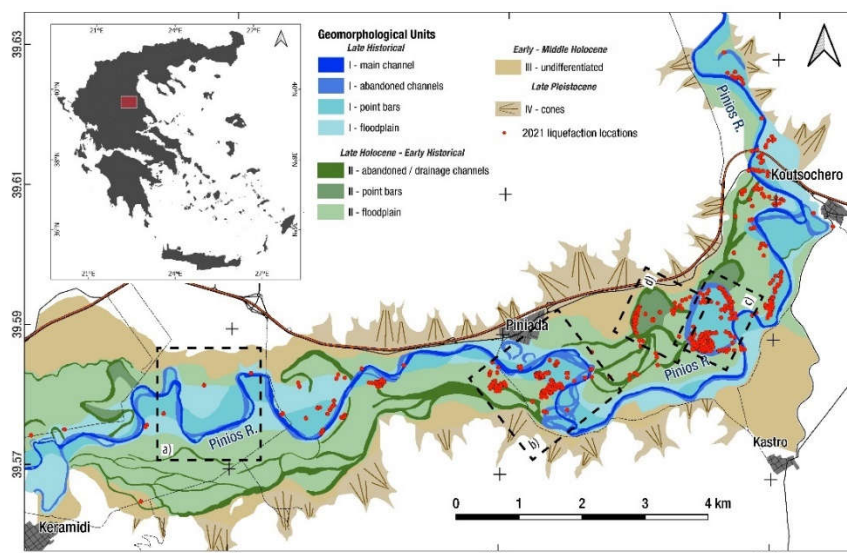
Figure 1. Surface geological map of the Piniada Valley-modified after Valkaniotis et al.(2024, in review). Red dots showing the liquefaction sites. Indexes (a-d) represent meanders where Russell criteria were applied.
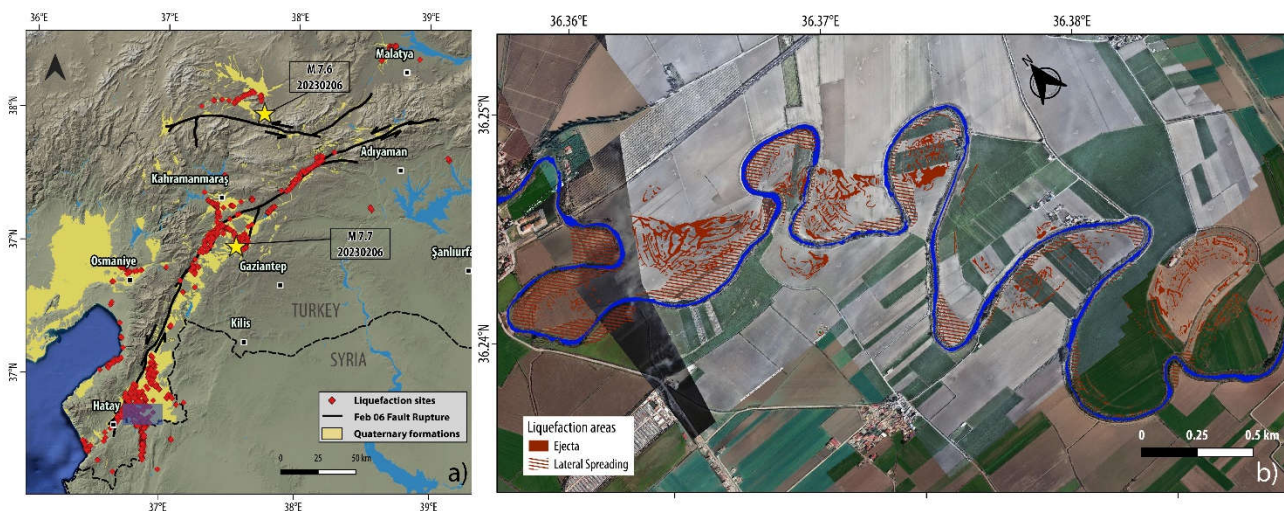

Figure 2. (a) Overview map of liquefaction and lateral spreading sites of the 2023 Türkiye / Syria earthquakes, identified and mapped using satellite imagery (Taftsoglou et al., 2023). Blue box indicates the area of figure b. (b) Liquefaction areas of ejecta and lateral spreading in the study area.

2   Methods

For the purposes of this study, the method proposed by Russell (2017) was applied for the cases of point bars at Piniada and Orontes Valley. Russel (2017) suggested that point-bar deposits are laterally discontinuous (Allen, 1965) and characterised by a complex distribution of lithofacies (Thomas, 1987, Tye, 2004, Miall, 2006, Durkin et al., 2015) comprised by alterations of mudstone and sandstone beds, while their sedimentology is strongly correlated with the evolution of a meander system and variations in channel geometry, channel orientation and channel position.

In addition, according to previous studies, the grain size of the deposited material in point-bar formations is influenced by the flow direction and speed of the meander, with the deposition of the finer grained materials occurs mostly in the downstream part and coarser deposits in the upstream part (Jackson, 1976, Fustic et al., 2012, Nardin et al., 2013). Furthermore, calibre of the sediment in a meander bend is

influenced by the different meander growth stages (expansion, translation and rotation), expressed as scroll bar morphologies and composed of genetically related sediments (Ghinassi et al., 2006). Furthermore, Smith et al., (2009) stated that when accretion occurs on the outer bank of meander, calibre of sediment may fine upstream, due to turning of scroll bars from concave to convex shapes and formation of the counter point-bar morphologies. Thus, counter point-bars can display the transition between the mud-prone and sand-prone beds.

In order to apply the methodology proposed by Russell et al., (2017), it is required to initial measure the meander shape and the episodes of meander growth in point bars features. In particular, it was measured the meander apex, the division of meander into the upstream and downstream part, the projection of the thalweg lines, the width of meander bend (mW) and the migration trajectory (tL) where scroll bars were visible. It should be noted that tracing of different meander generations was achieved in both cases using very high-resolution satellite images dated close to the seismic events (2021 and 2023), while in case of Piniada Valley 1945 historical aerial imagery was also used.

Through the first phase, the meander shapes developed after different growth stages were classified based on their geometrically shapes into four groups of 25 individual shapes: open asymmetric, angular, bulbous, open symmetric. Afterwards, thalweg line and apex for each meander were drawn separately, while locations in the downstream limbs where a riffle or cross-over once existed were characterized as inflection points and represented the transitional zones from sand- to mud-prone sediments (Smith et al., 2009).

Through the next step, meander thalweg lines were subdivided to heterogeneity types of Sand-I, Sand-II, Mud-I, Mud-II, according to the relative proportion of coarse to fine-grained material. Generally, for the open asymmetric, angular and open symmetric groups, Sand-I is mostly recorded on the upstream part, while Sand-II deposition occur after the upstream cross-over with its deposition influenced by the geometry and the growth of the meander. Sediments of Mud-I and Mud-II are mostly concentrated in downstream limbs, where counter point bars transforming from concave to convex forms. By contrast with the aforementioned groups, bulbous shaped meanders forming more than two inflection points and consequently can compound multiple zones of all relative heterogeneity types (Carter, 2003, Nanson et al., 1980). Combining this data with the ones regarding the direction or shifting of scroll bars and cross-cutting relationships, resulted in the compilation of a map for each investigated meander showing their relative heterogeneity types.

Having delineated the heterogeneity of point bars and compiled the relevant map, the liquefaction phenomena of ejecta and lateral spreading for Piniada and Orontes Valleys were plotted on these maps and correlated with the different lithofacies. In particular, the liquefaction density per heterogeneity type of sediment was calculated. In addition, it was investigated the correlation between the maximum distance of lateral spreading, from the free faces, with the different lithofacies of point bars.

3 Results

In order to examine the correlation between the density of liquefaction phenomena and the distribution of sand and mud rich deposits, we initially delineated the different lithofacies on selected point bars in Piniada and \ in Orontes Valley. For the purposes of this study three cases for both areas are discussed through the following paragraphs and the results are presented in Table 1 and Table 2.

The first examined meander of Piniada Valley is close to the Piniada village. Based on the 1945 historical aerial imagery, the delineated meander shape was classified as a compound of two distinct meanders of open asymmetric (S1i) and angular (S2c) type (a in Fig.3). According to the 2021 satellite image, the previous compound meander was transformed into a bulbous shape type (S3e) where four heterogeneity classes were traced after the projection of 1945 and 2021 heterogeneity thalweg lines. Following the 2021 earthquake sequence, liquefaction phenomena covered the coarser deposits of the upstream limb, with a number of 63.6% of the total records.

The second examined meander of Piniada valley is a cut-off form (b in Fig.3), which according to historical aerial imagery of 1945 was classified as a bulbous meander with a rounded apex and not overturned shape (S3a). Moreover, scroll bar morphologies indicated an extensional and rotational meander growth, where more than one major directional change occurred. However, due to the abandoned form of this meander since 1945, no alterations were detected in the recent 2021 image. Based on the 2021 liquefaction mapping, more than 70% of liquefaction sites was observed in areas of coarser material, with 63.3% and 9.4% corresponding in Sand-I and Sand-II types respectively.

The third area of interest in Piniada Valley is related to a cut-off meander (c in Fig.3) formed next to the previous one. Characterised as older cut-off feature, it was analysed separately and classified as an asymmetrical bulbous type (S3e). Regarding the liquefaction phenomena reported in this zone, post-event field observations document that the higher concentration of 87.5% was related to the area considered as Sand-II type.
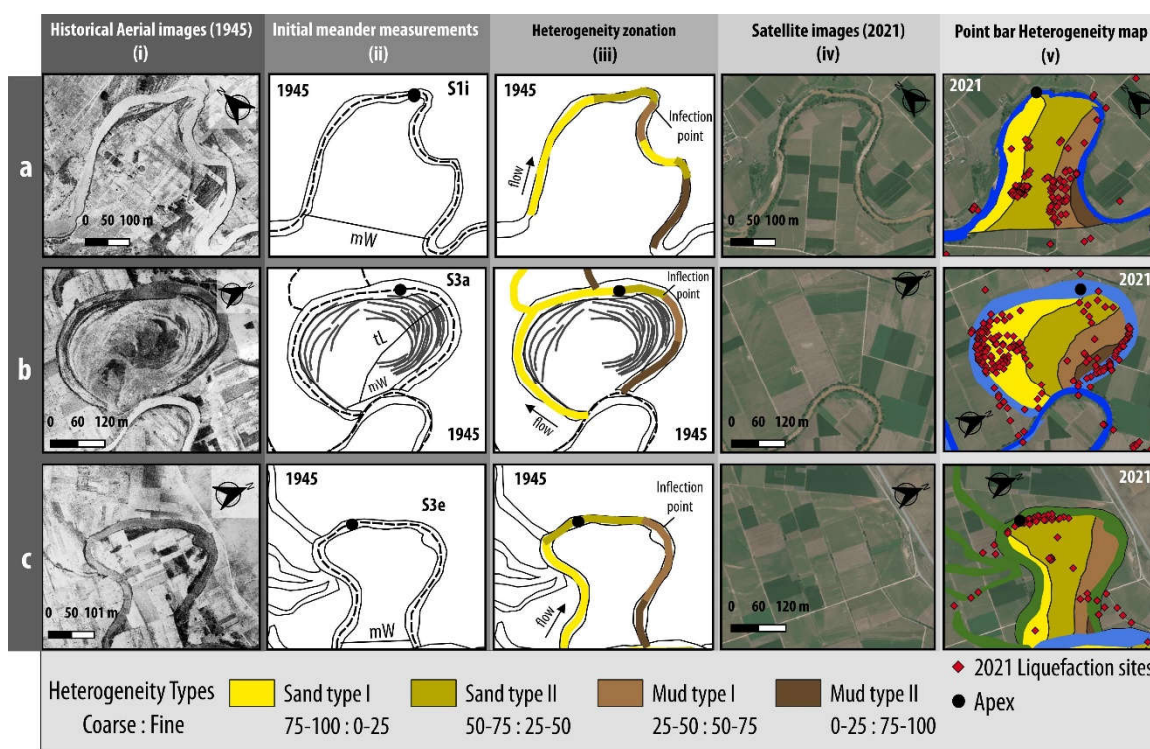
Figure 3. Assessment of heterogeneity types in four selected meanders (a-c) of the Piniada Valley based on the methodology proposed by Russell (2017) Columns (i-v) represent the different steps of the procedure for evaluating the sedimentary heterogeneity due to the Pinios River evolution from 1945 to 2021. Abbreviations of measurements in column (ii) stand for meander width (mW) and meander trajectory length (tL), while codes attributed to each meander shape refer to meander shape (S); parent group to which the meander belongs (1: open asymmetric, 2: angular, 3: bulbous, 4: open symmetric) and further qualifications of the meander shape ("a" to "i") (from Valkaniotis et al., 2024, in review, modified for the purposes of this study)

Following the same procedure with Piniada Valley, we focused on a segment of Orontes river close to the South-East part of Amik Valley. The delineated meander of first case (a in Fig.4) was classified as a bulbous shape (S3a). Tracing of the heterogeneity types in the thalweg of 2023 resulted in a map of four heterogeneity classes, with coarser materials covering the upstream limb and the areas of both apex, and finer sediments extending in the downstream part. According to the 2023 liquefaction manifestations, ejecta materials were detected only in Sand-I and Sand-II types (69.5% and 30.5%

respectively), while 82.2% of lateral spreading phenomena were observed in the same deposits (Table 1).

The second case study in Orontes river was also classified as a bulbous overturned shape (S3b) (b in Fig.4). Due to the projection of two downstream inflection points, the zonation of meander thalweg into heterogeneity types resulted in a map of multiple relative heterogeneity classes. Projection of liquefaction sites show that 40.2% and 51.6% of ejecta materials were detected in Sand-I and Sand-II deposits respectively.

Finally, the third case is a cut-off meander characterised as a bulbous shape with a rounded apex and an asymmetrical form (S3d) (c in Fig.4). Based on the 2023 satellite image, tracing of the heterogeneity types in the meander's thalweg classified the area into three heterogeneity classes of Sand-I, Sand-II and Mud-I. After the 2023 seismic events, 45.8% of the total ejecta material were detected mostly in the Sand-II deposits, while in this case 30.7% was found in Mud-I type.

Consequently, based on the analysis that took place in this study, most of liquefaction phenomena triggered by 2021 Damasi earthquake and 2023 Türkiye earthquakes are correlated with areas characterised as Sand-I and Sand-II types. As shown in Table 1, 72.7% of the total liquefaction sites in Piniada Valley were detected in sand prone zones, with the highest percentage concentrated in sediments of Sand-I type (38.4%). On the other hand, most of the liquefaction ejecta areas of Orontes case were hosted in the Sand-II material (62.7%).

Regarding the lateral spreading phenomena, 80.6% of them were recorded in the coarser grain size deposits (sands), coming in agreement with the outcomes of previous studies where the most prone to lateral deformations areas are the upstream segments (Abayo et al., 2023). In accordance with the expected maximum distance of triggering lateral spreading phenomena from the free face, as recommended by Honegger et al. (2006), Idriss and Boulanger (2008), Youd et al. (2002), Youd (2018), two buffer zones of 50m and 100m were delineated for Orontes river banks. Analyzing the mapped lateral spreading, it was shown that 88.8% of the phenomena were hosted in the former region (50m), while only 11.2% affected the latter one (Table 2).

It should be noted that mud prone areas of finer grain size characteristics should still be classified as likely to liquefaction. This aligns with numerous studies from the past 20 years, which have shown that non-cohesive, low-plasticity silty soils are susceptible to liquefaction (Bray and Sancio, 2006, Idriss and Boulanger, 2008).
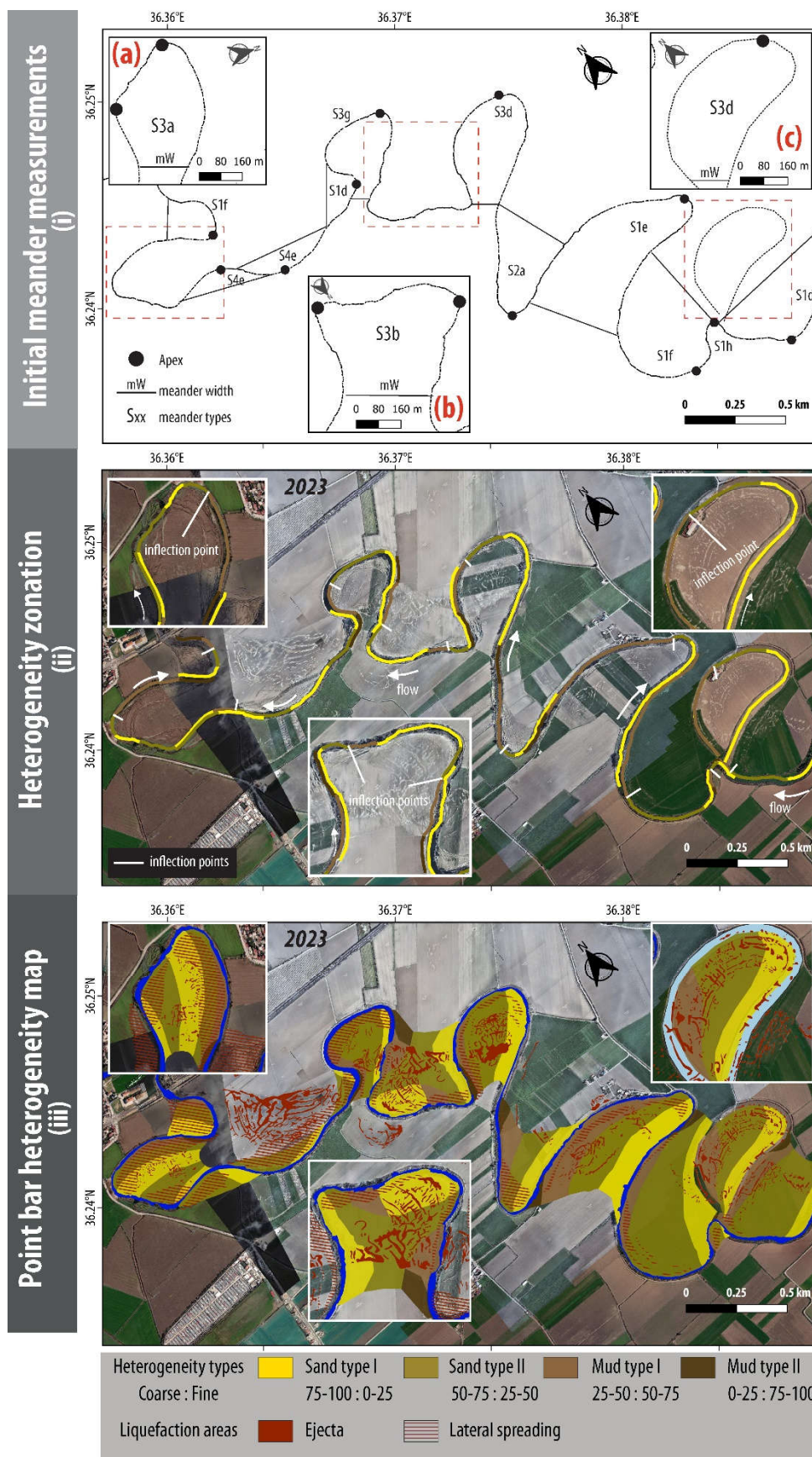
Figure 4. Assessment of heterogeneity types of the Orontes river based on the methodology proposed by Russell (2017). Columns (i-iii) represent the different steps of the procedure for evaluating the sedimentary heterogeneity. Index maps (a, b, c) represent the examples mentioned in this study.

Table 1. Correlation of the spatial distribution of liquefaction sites (%) triggered by the Damasi 2021 earthquake and 2023 Türkiye earthquakes with the relative heterogeneity types of each discussed meander. The total liquefaction percentage corresponds to the spatial distribution of liquefaction phenomena for all the examined cases of Piniada and Orontes Valleys (Fig.3, Fig.4).

		Heterogeneity Type			
		Sand-I	Sand-II	Mud-I	Mud-II
2021 Damasi earthquake	a	13.6	50	33	3.4
	b	63.3	9.4	10.1	17.3
	c	5.0	87.5	7.5	0
	Total liquefaction (%)	38.4	34.3	17.2	10.1
2023 Türkiye earthquakes	a	69.5	30.5	0	0
	b	40.2	51.6	8.2	0
	c	23.5	45.8	30.7	0
	Total liquefaction (%)	24.8	62.7	12.3	0.2

Table 2. Correlation of the spatial distribution of lateral spreading phenomena (%) triggered by 2023 Türkiye earthquakes with the relative heterogeneity types of Orontes River meanders (Fig.4).

		Heterogeneity Type				
	Buffer zones	Sand-I	Sand-II	Mud-I	Mud-II	Total % per buffer zone
Lateral Spreading (%)	50m	12.7	59.4	15.6	1.1	88.8
	100m	5.2	3.4	2.6	0	11.2
	Total % per Type	17.9	62.8	18.2	1.1	

4   Conclusions

The spatial distribution of liquefaction phenomena in Piniada and Orontes Valleys clearly indicates that one of the most susceptible to liquefaction geomorphological features are the point bars formations, which are formed by coarse sediments of sands deposited along the inner bank due to the decreasing flow of meander bend. However, the variable depositional processes along the whole meander results in a complex distribution of lithofacies with alterations between the ratio of coarser and fine materials, which can alterate the preferential behavior of the area to more or less likely to host liquefaction phenomena. Consequently, a detailed mapping of these heterogeneity types would be useful for preliminary geotechnical studies.

For the purposes of this study, point bar features were traced and classified into four heterogeneity classes of Sand-I, Sand-II, Mud-I and Mud-II, based on geological, geomorphological and remote sensing data. Comparison between the spatial distribution of different lithofacies with liquefaction manifestations indicated that most of the effects were triggered in deposits mainly consisted of sandy materials. In particular 72.7% and 87.5% of liquefaction phenomena occurred in Piniada and Orontes respectively, were hosted in Sand-I and Sand-II types of deposits. Highest densities of lateral spreading deformations (72.1%) were also recorded in the same materials in a distance less than 50m from the riverbed. Consequently, it is confirmed that point bar features can further be classified into distinct zones of liquefaction likelihood, improving the forecasting of soil behavior after seismic events and thus minimizing the relevant risk of a manmade environment especially in cases of structural linear works (pipelines, motorways etc.).

Funding

The research activities of D.R. are supported by a contract in the frame of the PON REACT EU Project by the Italian MUR; number 09-G-48651-15.

References

Abayo N.I.; Caba A.C.; Chamberlin E. and Montoya B. Fluvial geomorphic factors affecting liquefaction-induced lateral spreading. *Earthquake Spectra.* 2023. 39, doi: 10.1177/87552930231190655.

Allen J.R.L. A review of the origin and characteristics of recent alluvial sediments. *Sedimentology*, 1965. 5, 89-191, doi: 10.1111/j.1365-3091.1965.tb01561.x.

Bastin S.; Quigley M. and Bassett K. Paleoliquefaction in easter Christchurch, New Zealand. *Geological Society of America bulletin.* 2015, 12, 1348-1365.

Bray J.D; Sancio R.B. Assessment of the liquefaction susceptibility of fine-grained soils. *Journal of Geotechnical and Geoenvironmental Engineering*. 2006, 132: 1165–1177.

Caputo R.; Helly B.; Rapti D. and Valkaniotis S. Late Quaternary hydrographic evolution in Thessaly (Central Greece): The crucial role of the Piniada Valley. *Quaternary International*. 2021. 635, 3-19, doi: 10.1016/j.quaint.2021.02.013.

Carter D.C. 3-D seismic geomorphology: Insights into fluvial reservoir deposition and performance, Widuri field, Java Sea. *AAPG Bulletin*. 2003, 87, 909-934, doi: 10.1306/01300300183.

Civico, R.; Brunori, C.A.; De Martini, P.M.; Pucci, S.; Cinti, F.R.; Pantosti, D. Liquefaction susceptibility assessment in fluvial plains using airborne lidar: The case of the 2012 Emilia earthquake sequence area (Italy). *Natural Hazard Earth System Sciences*. 2015, 15, 2473–2483.

Di Manna P.; Guerrieri L.; Piccardi L.; Vittori E.; Castaldini D.; Berlusconi A.; Bonadeo L.; Comerci V.; Ferrario F.; Gambillara R.; Livio F.; Lucarini M. and Michetti A.M. Ground effects induced by the 2012 seismic sequence in Emilia: implications for seismic hazard assessment in the Po Plain. *Annales geophysicae*. 2012, 55(4), 697-703, doi: 10.4401/ag-6143.

Durkin P.R.; Hubbard S.M.; Boyd R.L. and Leckie D.A. Stratigraphic expression of intra-point-bar erosion and rotation. *Journal of sedimentary research,* 2015. 85, 1238-1257, doi: 10.2110/jsr.2015.78.

Fustic M.; Bennett B.; Huang H. and Larter S. Differential entrapment of charged oil - new insights on McMurray Formation oil trapping mechanisms. *Marine and Petroleum Geology*, 2012. 36(1), 50-69, doi: 10.1016/j.marpetgeo.2012.05.004.

Ghinassi M.; Ielpi A.; Aldinucci M. and Fustic M. Downstream-migrating fluvial point bars in the rock record. *Sedimentary geology*. 2006, 334, 66-96, doi: 10.1016/j.sedgeo.2016.01.005.

Hazir, I.; Akgul, M.A.; Alkaya, M.; Dağdeviren, M.F. From 27 January to 14 March 2012 Evaluation of Floods in Amik Plain of Hatay Province Using Geographic Information Systems. *In Proceedings of the the 4th National Flood Symposium*, Rize, Turkey, 23 November 2016. (In Turkish), 2016.

Honegger D.G.; Nyman D.J.; Youd T.L. Liquefaction Hazard Mitigation for Oil and Gas Pipelines. *In Proceedings of the 100th Anniversary Conference Commemorating the 1906 San Francisco Earthquake*, San Francisco, CA, EERI, 2006.

Idriss I.; Boulanger R. *Soil liquefaction during earthquakes*. Monograph MNO-12, EERI. 2008.

Jackson R.G. Sedimentological and fluid-dynamic implications of the turbulent bursting phenomenon in geophysical flows. *Journal of Fluid Mechanics*, 1976. 77(3), 531-560, doi: 10.1017/S0022112076002243.

Miall A.D. Reconstructing the architecture and sequence stratigraphy of the preserved fluvial record as a tool for reservoir development: a reality check. *AAPG Bulletin*. 2006. 90, 989-1002,

Nanson G.C. Point bar and floodplain formation of the meandering Beatton River, Northeastern British Columbia, Canada. Sedimentology, 1980, 27, 3-29, doi: 10.1111/j.1365-3091.1980.tb01155.x.

Nardin T.R.; Howard R.F. and Carter B.J. Stratigraphic architecture of a large-scale point-bar complex in the McMurray Formation: light detection and ranging and subsurface data integration at Syncrude's

Mildred Lake Mine, Alberta, Canada. In: Hein F.J., Leckie D.A. and Suter J.R. (Eds), Heavy oil and oil sand petroleum systems in Alberta and Beyond. *AAPG Bulletin.* 2013. 64, 273-311.

Papathanassiou G.; Caputo R. and Rapti-Caputo D. Liquefaction phenomena along the paleo-Reno River caused by the May 20, 2012, Emilia (northern Italy) earthquake. *Annales geophysicae*, 2012. 55(4), 735-742, doi: 10.4401/ag-6147

Papathanassiou G.; Mantovani A.; Tarabusi G.; Rapti D. and Caputo R. Assessment of liquefaction potential for two liquefaction prone area considering the May 20, 2012 Emilia (Italy) earthquake. *Engineering Geology.* 2015, 189, 1-16, doi: 10.1016/j.enggeo.2015.02.002.

Papathanassiou G.; Valkaniotis S.; Ganas A.; Stampolidis A.; Rapti D. and Caputo R. Floodplain evolution and its influence on liquefaction clustering: the case study of March 2021 Thessaly, Greece, seismic sequence. *Engineering Geology.* 2022, 298, 1-18, doi: 10.1016/j.enggeo.2022.106542.

Russell C.E. Prediction of sedimentary architecture and lithological heterogeneity in fluvial point-bar deposits. PhD thesis, University of Leeds, Leeds, UK, 2017.

Smith D.G.; Hubbard S.M.; Leckie D.A. and Fustic M. Counter point bar Deposits: lithofacies and reservoir significance in the meandering modern Peace River and ancient McMurray Formation, Alberta, Canada. *Sedimentology*, 2009. 56, 1655-1669.

Taftsoglou M.; Valkaniotis S.; Karantanellis S.; Goula E. and Papathanassiou G. Preliminary mapping of liquefaction phenomena triggered by the February 6 2023 M7.7 earthquake, Türkiye / Syria, based on remote sensing data. 2023, doi: 10.5281/zenodo.7668401.

Taftsoglou M.; Valkaniotis S.; Papathanassiou G.; Klimis N. and Dokas I.A. Detailed Liquefaction Susceptibility Map of Nestos River Delta, Thrace, Greece Based on Surficial Geology and Geomorphology. *Geosciences*, 2022. 12, 361, doi: 10.3390/geosciences12100361.

Taftsoglou M.; Valkaniotis S.; Papathanassiou G.; Karantanellis, E. Satellite Imagery for Rapid Detection of Liquefaction Surface Manifestations: The Case Study of Türkiye–Syria 2023 Earthquakes. *Remote Sensing*. 2023. 15, 4190. doi: 10.3390/rs15174190

Thomas R.G.; Smith D.G.; Wood J.M.; Visser J.; Calverley-Range E.A. and Koster E.H. Inclined Heterolithic Stratification-terminology, Description, Interpretation and Significance. *Sedimentary Geology* 1987. 53, 123-179.

Tye R.S. Geomorphology: An approach to determining subsurface reservoir dimensions. *AAPG Bulletin*. 2004. 88(8), 1123-1147, doi: 10.1306/02090403100.

Valkaniotis, S.; Rapti D.; Taftsoglou M.; Papathanassiou G.; Caputo R. Geomorphological mapping for liquefaction likelihood: the Piniada Valley, Greece, case study, *Bulletin of Earthquake Engineering* 2024. (under review)

Wotherspoon L.; Pender M. and Orense R. Relationship between observed liquefaction at Kaiapoi following the 2010 Darfield earthquake and former channels of the Waimakariri River. *Engineering Geology*. 2012, 125, 45-55, doi: 10.1016/j.enggeo.2011.11.001.

Youd T.L. Application of MLR Procedure for Prediction of Liquefaction-Induced Lateral Spread Displacement. *Geotechnical and Geoenvironmental Engineering*. 2018. ASCE, 144(6): 04018033.

Youd T.L.; Hansen C.M.; Bartlett S.F. Revised multilinear regression equations for prediction of lateral spread displacement, *Geotechnical and Geoenvironmental Engineering*. 2002. 128(12): 1007–017.

ASSESSMENT OF SOIL BEHAVIOR IN SEISMIC EXCITATIONS BY EXPLORING DIFFERENT APPROACHES

KEMAL EDIP [1], DAVOR STANKO [2], JULIJANA BOJADJIEVA [3], RADMILA SHALIC-MAKRESKA [4] AND VLATKO SHESHOV [5]

[1] *Ss. Cyril and Methodius University in Skopje, Institute of Earthquake Engineering and engineering seismology, N.Macedonia, kemal@iziis.ukim.edu.mk*

[2] *University of Zagreb, Faculty of Geotechnical Engineering, Croatia, dstanko@gfv.hr,*

[3] *Ss. Cyril and Methodius University in Skopje, Institute of Earthquake Engineering and engineering seismology, N.Macedonia, jule@iziis.ukim.edu.mk*

[4] *Ss. Cyril and Methodius University in Skopje, Institute of Earthquake Engineering and engineering seismology, N.Macedonia, r_salic@iziis.ukim.edu.mk*

[5] *Ss. Cyril and Methodius University in Skopje, Institute of Earthquake Engineering and engineering seismology, N.Macedonia, vlatko@iziis.ukim.edu.mk*

Abstract

In geotechnical earthquake engineering seismic site response analysis is a very complex task, which has gained an increasing importance for the last decades. This paper aims to numerically simulate the effect of an earthquake input in different types of soil layers in order to get the dynamic amplification factor. The methodology for correctly simulation of seismic waves propagation includes thorough theoretical background aided with different softwares (Shake, Strata,DeepSoil and Plaxis) which allow the simulation of soil as nonlinear material model or small strain linearly elastic material.

The verification of the model is done by comparison of numerical results in relation to two different soil profiles from Varazdin, Croatia and from Skopje, Macedonia. The proposed approach should demonstrate and illustrate the special points in taking into account the modelling of different layers. The earthquake input is given as acceleration signal which in case of low densities of soil material are prone to initiate higher amplifications. Finally, the advantages and limitations of the proposed numerical model are discussed in detail.

Key words

Site response analysis, SHAKE2000, Plaxis2d, Strata,DeepSoil

1   Introduction

In the last decades, earthquakes have shown the importance of site effects in the distribution of damages during seismic events. In 1985 a large earthquake with magnitude Mw=8.1 which occurred in Mexican subduction zone proved that the earthquake effects increased in soft soil areas composed mainly of clay layers in the Valley of Mexico (Chavez-Garcia and Bard 1994). The damage has been attributed to the amplification of seismic waves. In 1989 during the Loma Prieta earthquake the complex pattern of alluvial sediment thickness contributed to the variability of site response and presence of spectral resonance peaks at some sites (Hartzell, Carver and Williams 2001). In 2019 during the Durres earthquake with magnitude Mw=6.4 the effects of soil layers played important role in site amplification (Sheshov, Apostolska et al. 2021). The Earthquake in Zagreb, Croatia also showed that the site response amplification should be given importance (Markušić, Stanko et al. 2020, Atalić, Uroš et al. 2021).

In seismic zonation studies the local site amplification presents one of the most important factors which is not only correlated with soil thickness but also with soil properties such as shear wave velocities and

material damping as well as soil densities (Stanko, Gülerce et al. 2019). In the same time, the soil nonlinearity is to be considered during the destructive earthquakes. In modelling soil medium strain dependency of shear modulus and damping ratio should be evaluated with previous laboratory tests or the layer properties must be presented by measurement of shear wave velocities by geophysical models.

2   Model analysis

The site response analysis of soils to earthquake excitation is complex and depends on number of factors which cannot be obtained with certainty. In this work, two different soil profiles from Varazdin, Croatia and from Skopje, N.Macedonia have been selected in order to compare different soil responses from softwares Shake2000 (Ordonez 2000), Deepsoil(Hashash, Groholski et al. 2008), Strata (Rathje and Ozbey 2006) and Plaxis2D (García Ros, Jiménez Valera et al. 2022). The site from Skopje in the municipality of Kisela Voda (Bojadjieva, Dojchinovski et al. 2023) and Varazdin are shown below:

Figure 1. Mathematical model of analysis for Skopje and Varazdin models

The soil layers have been characterized by their shear wave velocity and unit weights. The soil layer materials in both models contain sand, clay and gravel without presence of groundwater. The numerical modelling of soil material has been done using small strain linear elastic models. Generally, the shear

behaviour of soils is expected to have effect on the response of the soil to earthquake excitation. As the soil layers depth increases the frequency of the layers increases which makes the upper layers more susceptible to strain increase.

In the analysis the following earthquakes time histories are used as input signals: ACC1: The North-South Center, USA, 1940, with a magnitude of M=6.7. It was selected as a representative event for earthquakes from neighbouring epicentres with magnitudes ranging from 6.5 to 7; ACC2: Bar N-S, recorded in the seismic records during the earthquake in Montenegro on April 15, 1979, with a magnitude of M=7.0. It was chosen as a representative event of a high-magnitude earthquake with a relatively broad frequency range of maximum amplitudes; ACC3: Ulcinj - Albatross N-S, recorded on a seismograph during the earthquake in Montenegro on April 15, 1979, with a magnitude of M=7.0; ACC4: Petrovac, Oliva N-S, recorded on a seismograph during the earthquake in Montenegro on April 15, 1979, with a magnitude of M=7.0. It was selected as a representative event of a high-magnitude earthquake with maximum amplitudes in the period range of 0.25-0.5 seconds; ACC5: Ulcinj - Olympic N-S, recorded on a seismograph during the earthquake in Montenegro on April 15, 1979, with a magnitude of M=7.0. It was chosen as a representative event of a high-magnitude earthquake with a relatively broad frequency range of maximum amplitudes.

The spectra from Earthquake inputs are shown in Fig.2 where it is clearly seen the difference in frequency content and amplification of the earthquakes which make the site response challenging.
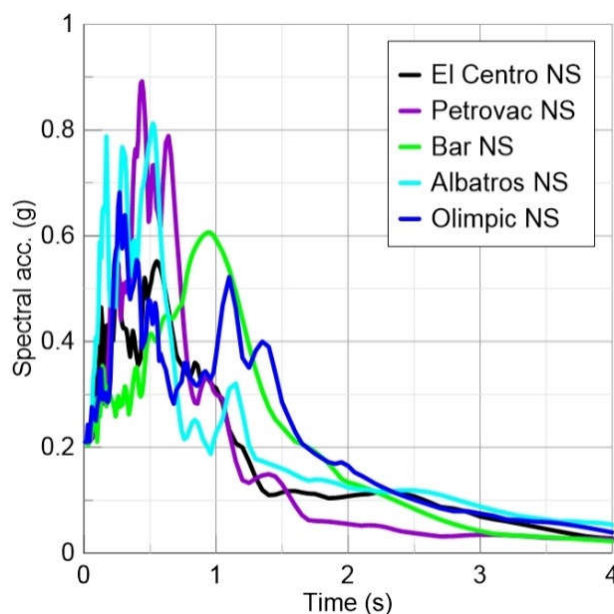

Figure 2. Spectra of input earthquakes with PGA of 0.21g

As can be seen from Fig.2 the spectra of input earthquake of Petrovac NS and Albatros NS have highest peeks and are expected to have greatest impact on the response analysis. On the other hand, the earthquake record of Olimpic NS has smaller but several peeks and is expected to have impact on different frequencies. The length of the records is approximately same and is around 30seconds.

3   Results
4

The cyclic loading due to earthquake which is imposed on soils can seriously affect the soil strength by lowering the shear stiffness and in the same time increasing the shear strain of the soil layers. Although the angle of friction is not affected by cyclic loading, the soil particle bonds are affected and strength reduction follows which enables alteration in the PGA during the excitation. The analysis of Skopje site comparing their peak ground acceleration is shown in Fig.3 below.
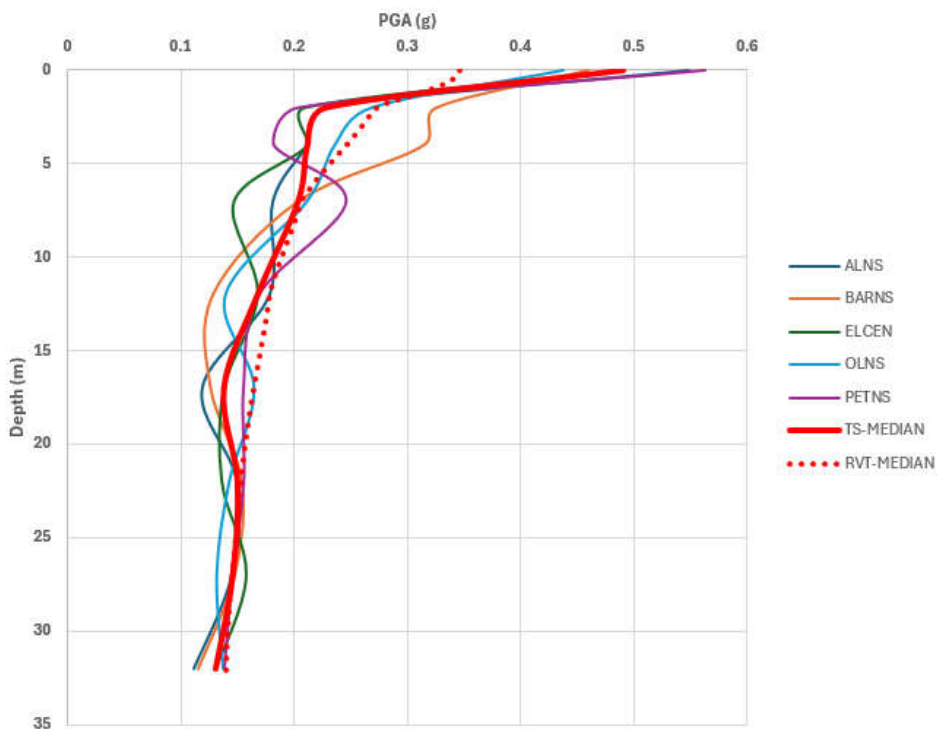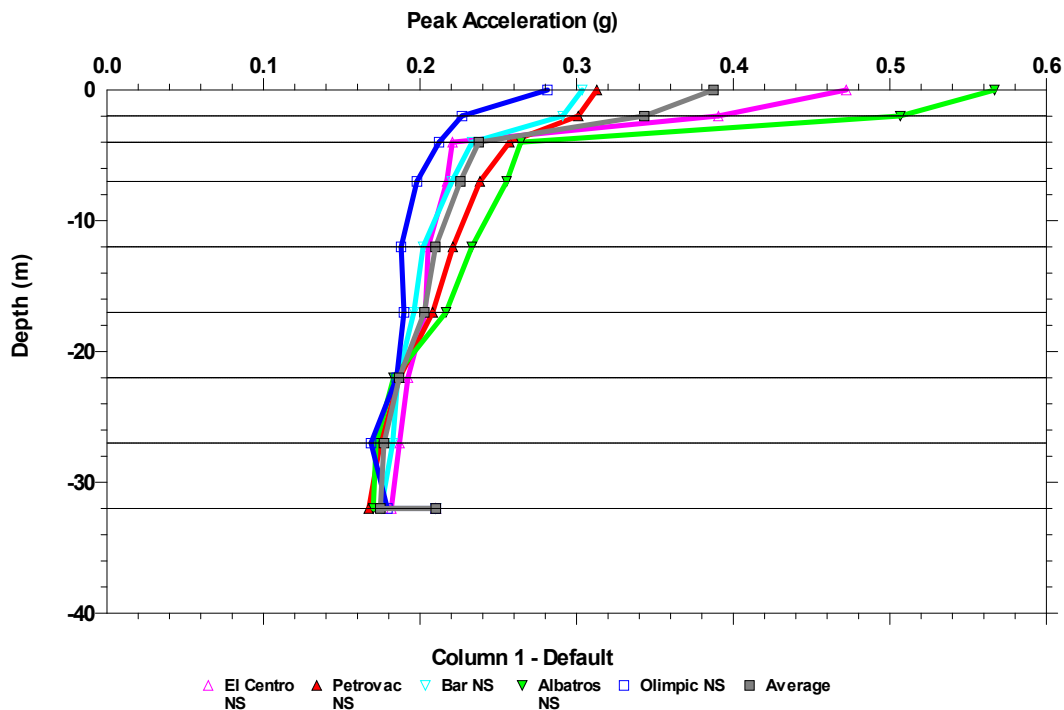
Figure 3. Comparison of Peak Ground Acceleration of Skopje model between Shake2000 and Deepsoil Softwares

As can be seen from Fig.3 the comparison is done with Shake2000 and Deepsoil Softwares. On the other hand, the comparison of results for the Varazdin model between the Shake2000 and Strata software are given in Fig.4.
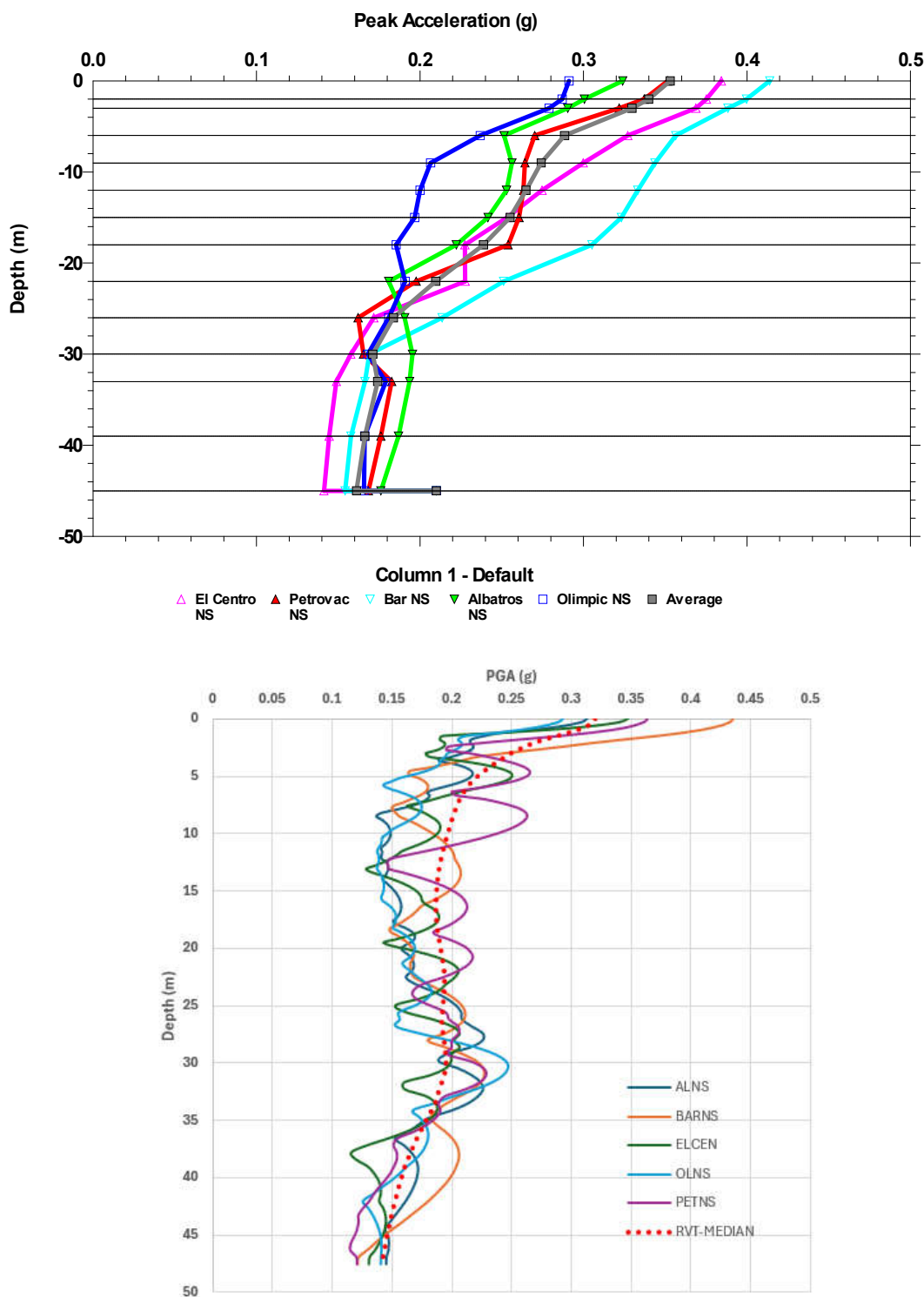
Figure 4. Comparison of Peak Ground Acceleration of Varazdin model between Shake2000 and Strata Softwares

As can be seen from Fig.3 and Fig.4, both sites show strength loss due to the earthquake excitations. The comparison of different softwares is in good accordance with each other. Here, it should be noted that the software work in 1d and the material definition is in small strain ranges. In order to compare the results with a 2d Software the Skopje model has been analysed using the Plaxis2d software with the Hardening soil Material model (Schanz, Vermeer and Bonnier 2019). Plaxis 2D is an advanced finite

element method software intended for analysing two dimensional problems of deformation and stability in geotechnical engineering. In defining the hardening soil model, the calibration of the model using the given shear wave velocity parameters have been done (Edip 2013). The output of the software is given in Fig.5 below.
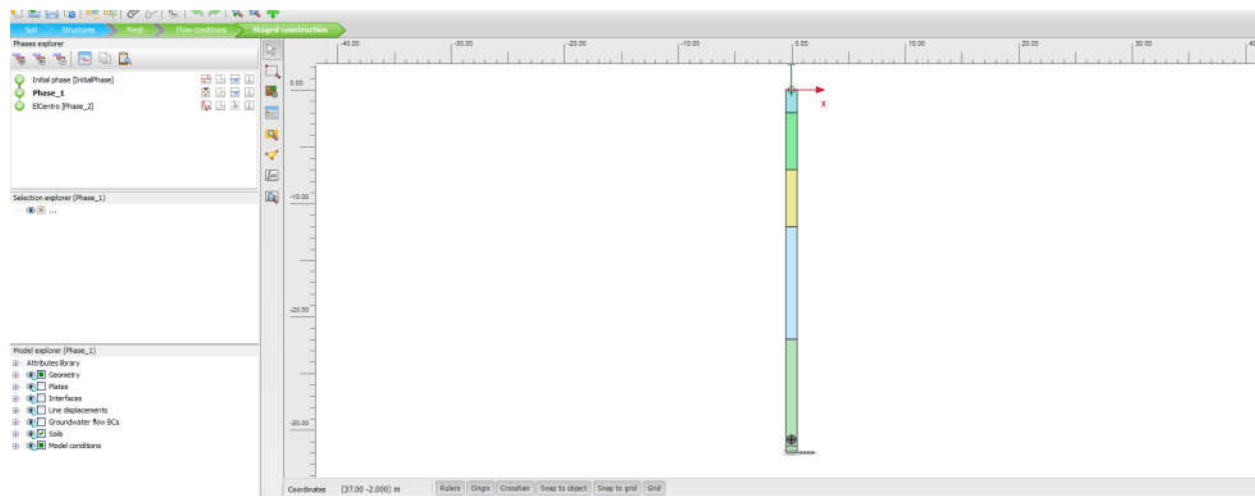

Figure 5. Modelling of horizontal layered soil profile in Plaxis 2d

As can be seen from the Fig.5 the modelling in Plaxis2d is straightforward and can be used in a simple manner when layers of soils are horizontal. In using 2d software the main point is to have big number of nodal points in order to obtain consistency in the analysis performed. In our case the meshing has been done using medium size of elements in order to have reasonable timing of analysis. Next the results of El Centro and Albatros earthquake records are given.
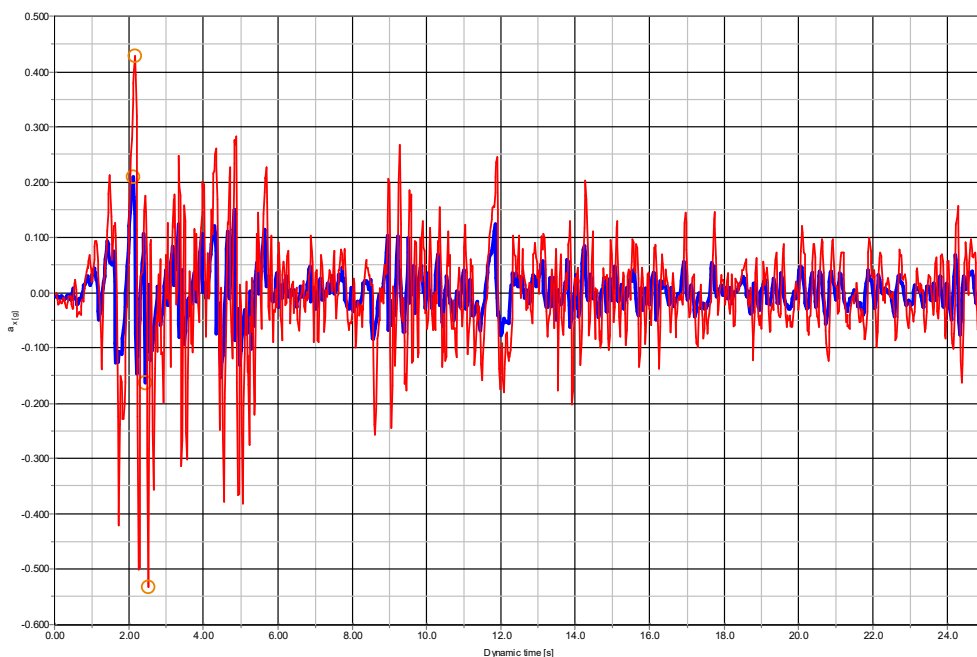

Figure 6. Output results of El Centro earthquake from Plaxis2D software
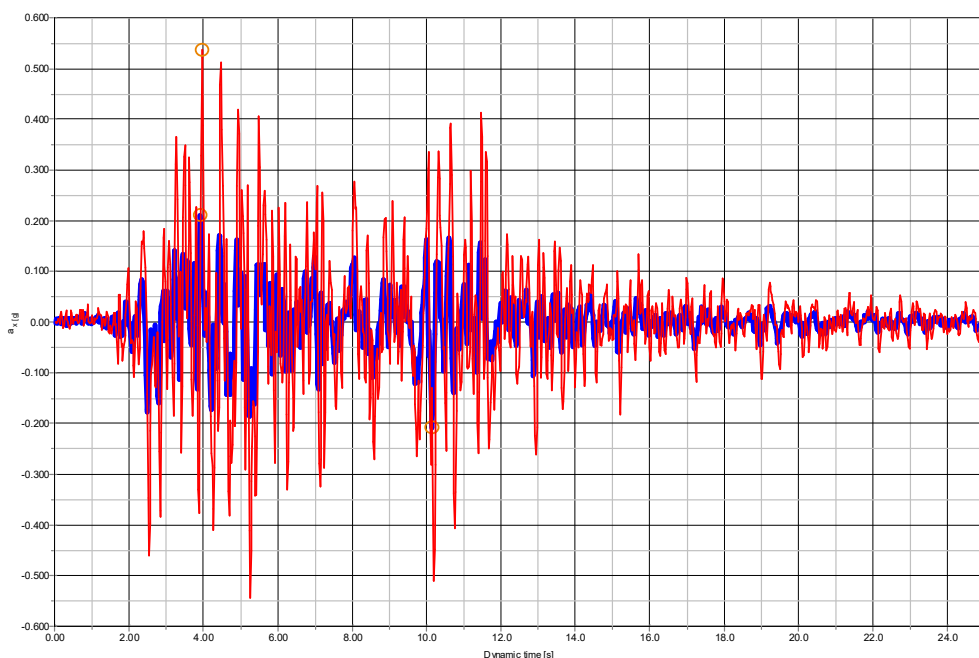
Figure 7. Output results of Albatros NS earthquake from Plaxis software

From Fig. 6 and Fig.7 the results show that the nodal values at bottom and top layers simulate the site response in a correct way. The maximum values obtained are in good correlation with the results from the Fig. 3. Namely, the values of El Centro earthquake record from the Shake2000 and Deepsoil software have similar values with Plaxis2d. On the other hand, the earthquake analysis with Albatros NS earthquake from site specific analysis has similar results of peak ground acceleration which are 0.55g and 0.56g. This proves the correctness of the 2d analysis by using the software Plaxis2D although further investigations are required in the material definition.

In order to obtain the effects of the soil profiles in the amplification of the earthquake inputs next the response spectra have been compared at the top layers for different earthquake records.
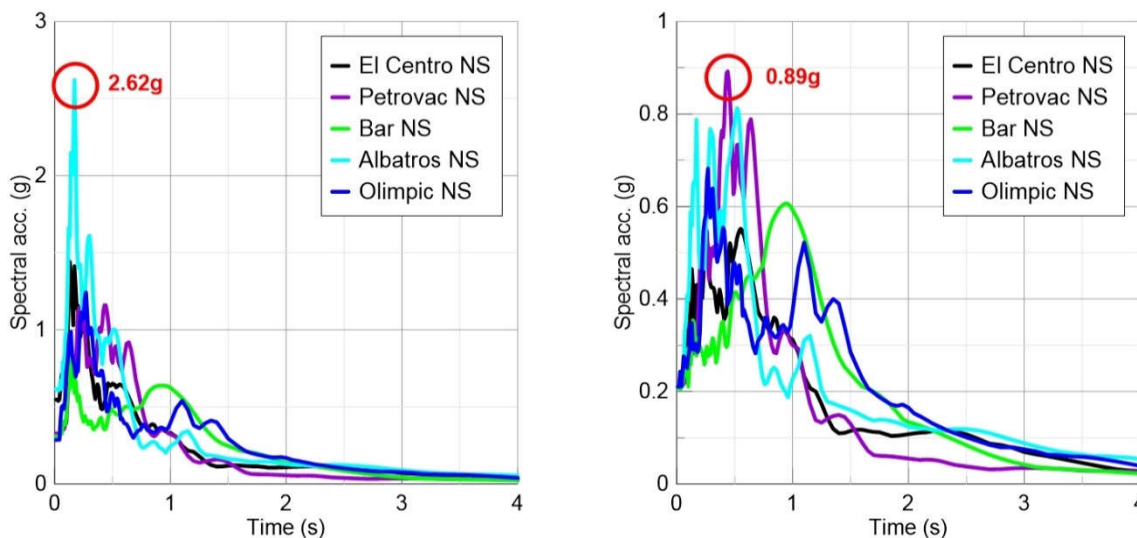

Figure 8. Response Spectra of input earthquakes at the top layer in Skopje model (left) and Varazdin model (right)

From Fig.8 it can be clearly seen that in selecting the earthquake recordings it is of important to capture

the features of rupture propagation, path and site effects which makes the selection of recorded accelerations important. For Skopje model comparison is done for Albatros NS earthquake among the softwares and following results are obtained.
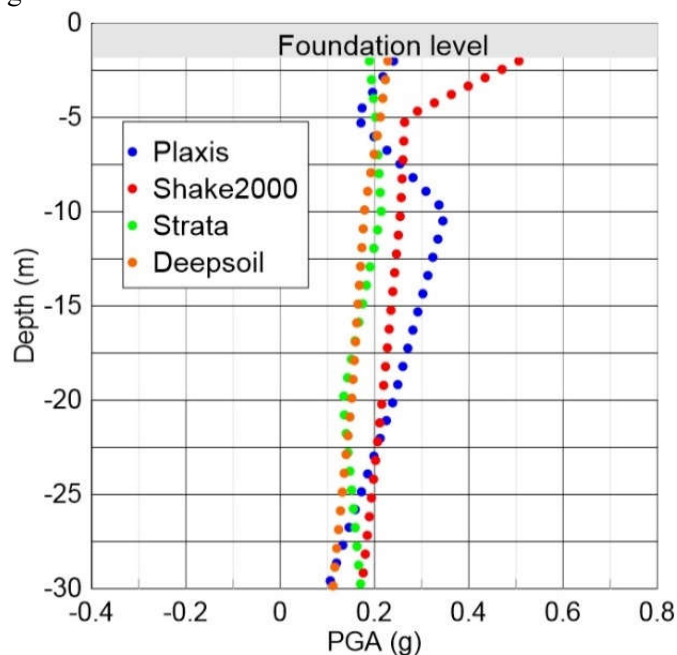

Figure 9. Comparison of different softwares for the Skopje model to Albatros earthquake input

As can be seen from Fig.9 the response of different sofwares are in general in agreement, although the results vary as the depth of the soil profile becomes small. The software Shake2000 has biggest values at the top layers due to the layer thickness assumptions. On the other hand, the Plaxis2d results vary in the depth of around -10m due to the fact that the integration meshing of the soil medium which need further increase in the number of elements which is not economically appropriate for this type of analysis.

4 Conclusion

In conclusion, the analyses which were performed in this work show that the site response analysis is of importance and should be considered when dealing with seismic response analysis. Stiffness of soil layers, foundations depth and vibration characteristics play important role and contribute to the overall safety and serviceability. Using different softwares, complete results have been obtained for input ground acceleration of 0.21g. Results show that the assumption of constant unit weight and shear wave velocity for soil layers can underestimate the variability of maximum horizontal acceleration. It can be concluded that the reliability of the results should be verified with on site measurements. This study's aim is to validate site response analysis by model and to investigate possible 2-D softwares seismic effects which can increase the ground motion amplifications due to local surface waves or possible 2-D resonance in deep valleys. These effects are strictly related to the geophysical properties of the local soil layers formations but are not compared and verified with experimental strong-motion data because they are missing in the selected sites. In fact, the soil strain increases and shear modulus reduction in upper layers of soil layers produce the shift toward higher natural periods and the amplitude attenuation from performed analysis.

References

Atalić, J., M. Uroš, M. Šavor Novak, M. Demšić and M. Nastev (2021). "The Mw5. 4 Zagreb (Croatia) earthquake of March 22, 2020: impacts and response." Bulletin of Earthquake Engineering **19**(9): 3461-3489.

Bojadjieva, J., D. Dojchinovski, V. Sheshov, R. Shalic-Makreska, K. Edip, M. Stojmanovska, T. Kitanovski, G. Chapragoski, M. Dimitrovski and D. Ivanovski (2023). Defining seismic parameters at location KP 763, KO Kisela Voda 2, Skopje, IZIIS 2023-34.

Chavez-Garcia, F. J. and P.-Y. Bard (1994). "Site effects in Mexico City eight years after the September 1985 Michoacan earthquakes." Soil Dynamics and Earthquake Engineering **13**(4): 229-247.

Edip, K. (2013). Development of three phase model with finite and infinite elements for dynamic analysis of soil media. PhD, Ss. Cyril and Methodius.

García Ros, G., J. A. Jiménez Valera, I. Alhama Manteca and M. E. Martínez Moreno (2022). "Resolution of geotechnical engineering problems with plaxis 2D."

Hartzell, S., D. Carver and R. A. Williams (2001). "Site response, shallow shear-wave velocity, and damage in Los Gatos, California, from the 1989 Loma Prieta earthquake." Bulletin of the Seismological Society of America **91**(3): 468-478.

Hashash, Y., D. Groholski, C. Phillips and D. Park (2008). "DEEPSOIL v3. 5beta, User manual and tutorial." University of Illinois, UC.

Markušić, S., D. Stanko, T. Korbar, N. Belić, D. Penava and B. Kordić (2020). "The Zagreb (Croatia) M5. 5 Earthquake on 22 March 2020." Geosciences **10**(7): 252.

Ordonez, G. A. (2000). "SHAKE2000: A computer program for the 1D analysis of geotechnical earthquake engineering problems." Geomotions, LLC, USA.

Rathje, E. M. and M. C. Ozbey (2006). "Site-specific validation of random vibration theory-based seismic site response analysis." Journal of geotechnical and geoenvironmental engineering **132**(7): 911-922.

Schanz, T., P. Vermeer and P. G. Bonnier (2019). The hardening soil model: Formulation and verification. Beyond 2000 in computational geotechnics, Routledge**:** 281-296.

Sheshov, V., R. Apostolska, Z. Bozinovski, M. Vitanova, B. Stojanoski, K. Edip, A. Bogdanovic, R. Salic, G. Jekic and T. Zafirov (2021). "Reconnaissance analysis on buildings damaged during Durres earthquake Mw6. 4, 26 November 2019, Albania: effects to non-structural elements." Bulletin of Earthquake Engineering: 1-23.

Stanko, D., Z. Gülerce, S. Markušić and R. Šalić (2019). "Evaluation of the site amplification factors estimated by equivalent linear site response analysis using time series and random vibration theory based approaches." Soil dynamics and earthquake engineering **117**: 16-29.

REMEDIATION OF THE EARTHQUAKE - INDUCED COLLAPSE SINKHOLES IN SISAK – MOSLAVINA COUNTY

MEHO SASA KOVACEVIC[1], MARIO BACIC[2], IVAN COSIC[3], TOMISLAV SKEGRO[4], IGOR TOMASEVIC[5]

[1] *University of Zagreb, Faculty of Civil Engineering, Croatia, msk@grad.hr,*

[2] *University of Zagreb, Faculty of Civil Engineering, Croatia, mbacic@grad.hr*

[3] *Brodska Posavina ltd, Croatia, ivan.cosic@brodska-posavina.hr*

[4] *Brodska Posavona ltd, Croatia, tomislav.skegro@brodska-posavina.hr*

[5] *Brodska Posavina ltd, Croatia, igor.tomasevic@brodska-posavina.hr*

Abstract

This paper presents the remediation works of surface openings in the Sisak - Moslavina County, whose activation was triggered by the M6.2 earthquake in December 2020 with an epicenter near Petrinja, Croatia. In addition to the immediate vicinity of residential buildings, openings are recorded near the transport infrastructure, on agricultural and non-agricultural land and in the forests of the municipality of Donji Kukuruzari. The aforementioned surface openings that occurred during and after the main impact were identified as collapse sinkholes. The lack of surface indicators and the sudden increase in the number of sinkholes in the period after the earthquake make this area very dangerous for its inhabitants. As part of the assessment of the condition and categorization of the collapse sinkholes, which preceded the development of a remediation design and remediation works, 143 collapse sinkholes were identified, two of which protrude with a large volume of 943 and 5014 m³. The paper presents the efforts to categorize the sinkholes to determine the remediation priorities, the development of a remediation design based on the inverse filter method with the use of materials of different grain sizes and geosynthetic materials, along with the remediation work and challenges involved.

Key words

collapse sinkhole, Petrinja earthquake, sinkhole categorization, inverse filter method

1   Introduction

During the strong 6.2 magnitude earthquake that shook Sisak – Moslavina County in Croatia on December 29, 2020, numerous geo-related problems occurred, including landslides, large-scale liquefaction, failure of geotechnical assets etc. In addition, numerous ground openings occurred south of the epicentre, especially in the villages of Mečenčani and Borojevići, leaving the authorities and the engineering community perplexed (Figure 1). Most of the openings occurred on agricultural and non-agricultural land, but some also occurred near buildings and infrastructure. The geology of this limited area is ≈10 km² and is characterised by karstic rocks covered by a 5–15 m thick proluvial soil layer deposited in the past by the Sunja River (Pollak, 2021).

Bačić et al. (2021) provide an insight into the formation of these openings and classify them as collapse sinkholes, where failure can develop in a short time, usually without any surface deformation prior to collapse. This type of sinkhole is formed when the soil-like material overlying the soluble karst rock is repeatedly wetted and dried, causing soil particles to dislodge through the channel draining the sinkhole and eventually form a structural arch in the ground. In this case, the aforementioned earthquake caused the arch material to collapse, resulting in sudden and dramatic sinkhole phenomena. For more details on the formation of this type of sinkhole, refer to Bačić et al. (2021) and Šumanovac & Pekaš (2023).
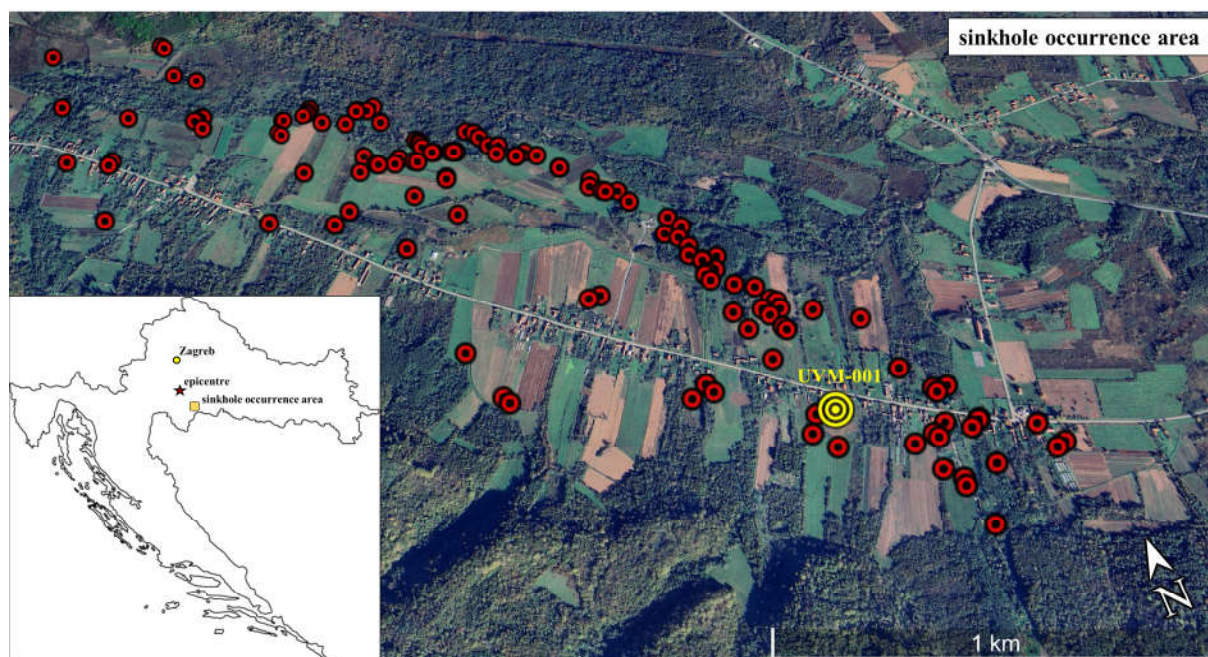
Figure 1. Locations of the occured sinkholes with the position of the largest sinkhole UVM-001

This paper focuses on the rapid assessment activities carried out in sinkhole occurrence area, which led to sinkhole categorization and served as a starting point for the development of the remediation design and the implementation of the remediation measures. While the general assessment methodology is explained, the planning and remediation design and work is demonstrated using the example of the largest collapse sinkhole (UVM-001) with a diameter of 25 m and a depth of 13 m (Figure 2).
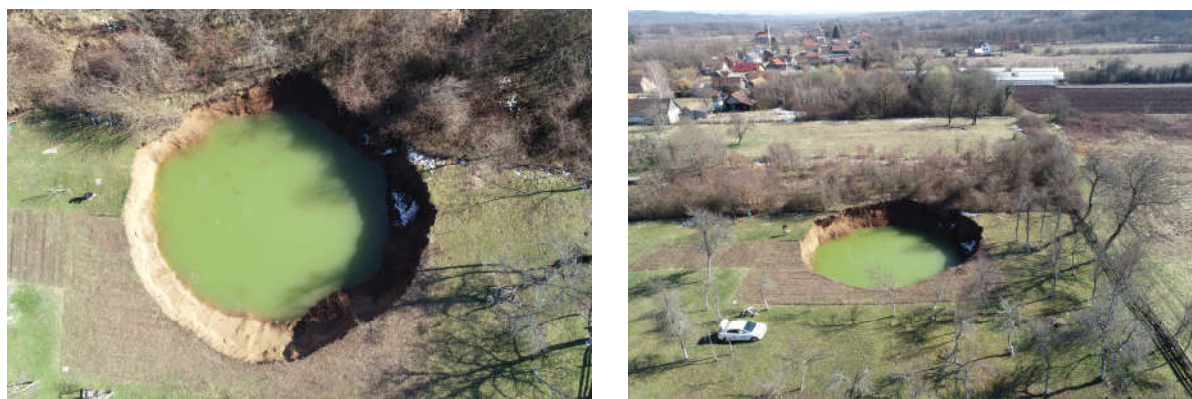

Figure 2. Largest sinkhole (UVM-001) occurred as a consequence of the Petrinja 2020 earthquake

2   Sinkhole categorization and remediation methodology

The sinkhole remediation activities financed by the European Union Solidarity Fund required careful planning and implementation. These activities were initiated by the Croatian Waters and the Faculty of Civil Engineering of the University of Zagreb, which prepared a document on the 'Assessment of the current state and categorization of sinkholes in the Sisak – Moslavina County' (FCEZG, 2022). The overall objective of this task was to create an inventory of sinkholes with an appropriate statistical analysis in terms of defined indicators that would serve as a basis for categorising sinkholes according to remediation priorities. However, given the large number of sinkholes, time constraints and the fact that most of these sinkholes are continuously expanding and pose an immediate threat, it was not

possible to carry out a comprehensive geotechnical survey campaign.

The general categorization methodology is shown in Figure 3. After the development of the categorization indicators (size, location based on land use pattern, presence of water in the sinkhole, etc.), the field work followed together with the survey campaign. The information thus obtained was subjected to a statistical analysis, followed by the preparation of an inventory of sinkholes with the identification of an optimal remediation method and a preliminary cost estimate. All this forms Phase I, followed by Phase II, in which a remediation design was developed for each sinkhole and the remediation work was carried out.
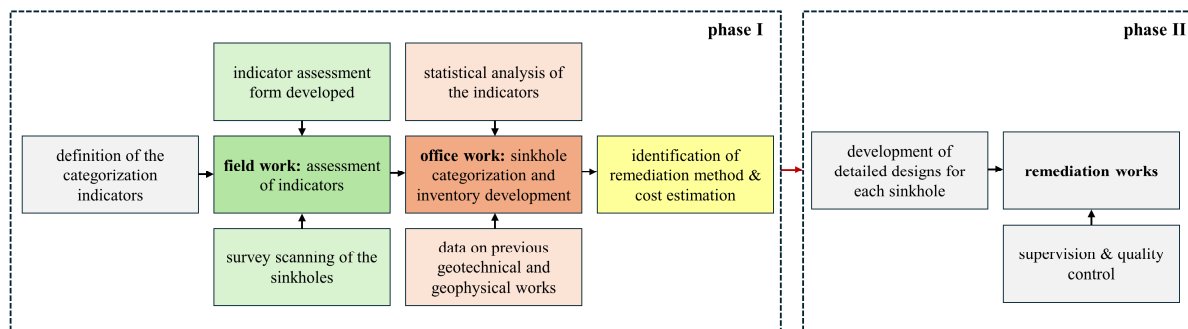

Figure 3. The general methodology for the categorization (phase I) and remediation (phase II) of sinkholes

A total of 143 sinkholes were detected by the end of 2021, two of them with very large volumes of 942.5 and 5014 m^3, while the other sinkholes all have a volume of less than 450 m^3, with most of them between 1 and 50 m^3. Figure 4 provides some statistical data on the sinkholes investigated, showing the volumes of the sinkholes based on the land use pattern and taking into account the size of the opening. The assessment indicates that sinkholes mostly occur in regular shapes, i.e. in the form of a hemisphere or truncated cones. Elongated forms (greater depths and smaller opening areas) also appear, but less often.
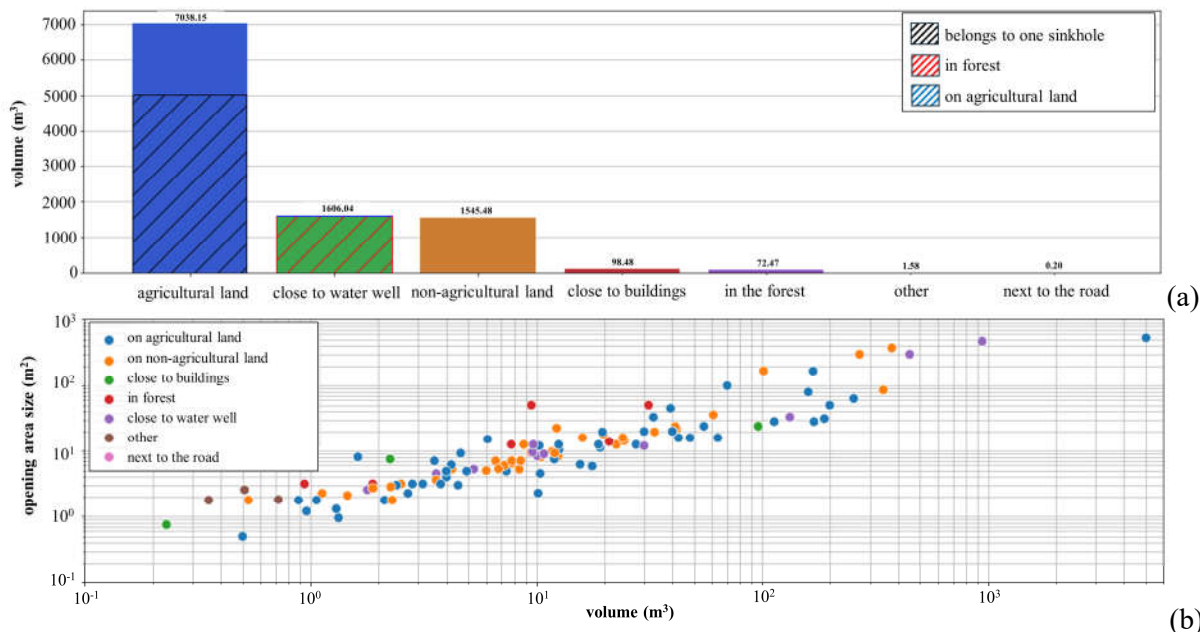

Figure 4. Volumes of the sinkholes based on the land use pattern (a) along with consideration of the opening size (b), modified from FCEZG (2022)

3   Geological and geotechnical conditions on the location of largest sinkhole

A number of scientists and practitioners from the fields of geotechnics, geology and geophysics participated in the data collection in order to gather as much data as possible to determine the causes of the occurrence of collapse sinkholes, but also to assess the risk of new sinkhole occurring, especially in times of increased seismic activity. All this was done in cooperation with the local community and civil defence authorities. Tomac et al. (2023) provide an overview of the geological and hydrogeological conditions of the area, noting that the Sunja River valley is a flat terrain covered by Holocene deluvial–proluvial deposits of low permeability, containing a certain amount of water and forming an aquitard underlain by karstified carbonates. The authors also present geotechnical and geophysical investigations carried out as part of the GEER (Geotechnical Extreme Events Reconnaissance) efforts. Geotechnical boreholes were drilled in predominantly clayey soils to a depth of 8.0 m and did not reach the depth of the bedrock. The clay samples obtained were used to carry out laboratory classification tests and conventional triaxial tests on saturated samples and to measure the soil water retention curve (SWRC). The MASW (Tomac et al., 2023) and HSVR (Ntambakwa et al., 2023) geophysical measurements were able to estimate the Holocene – weathered bedrock - compact bedrock boundaries to some extent. The higher resolution geophysical investigations were carried out by Šumanovac & Pekaš (2023), who conducted extensive geophysical campaigns using two-dimensional electrical tomography. The authors distinguish between two different geological models: GM-1, in which the layer base of the clastic surface deposits consists of lithothamnium limestones and calcarenites, which leads to the formation of underground cavities and collapse sinkholes, and GM-2, in which the layer base consists of clay deposits and no collapse sinkholes occur. Figure 5 shows one of the ERT profiles at the site of the largest sinkhole UVM-001, which shows that there are numerous larger and smaller subsurface voids in the upper parts of the lithothamnian limestones, therefore, the structure can be visually described as grid-like.
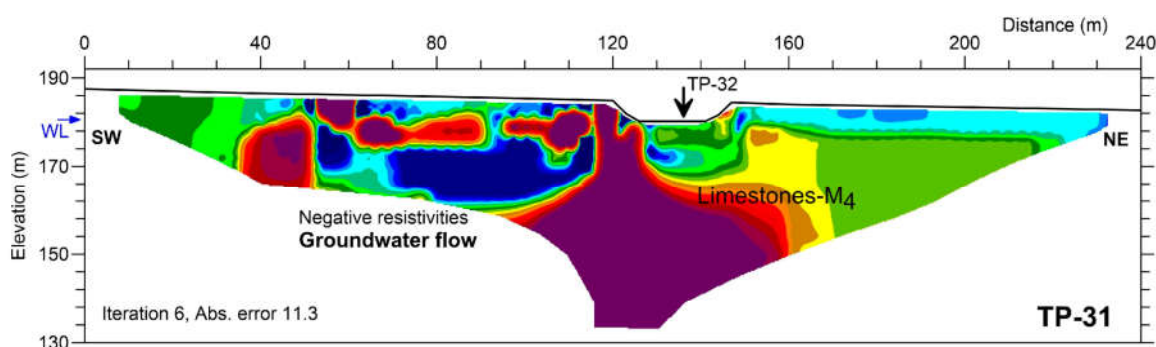

Figure 5. Electrical resistivity profile on the location of UVM-001 (Šumanovac & Pekaš, 2023)

4   Design and Remediation works

4.1 Remediation design: Inverse filter method

Categorization (FCEZG, 2023) proposed remediation of 102 sinkholes, while a detailed design was developed for each collapse sinkhole in order to take local characteristics into account. The inverse filter method proposed by Bačić et al. (2021) was considered as the optimal remediation method, as it is environmentally friendly and allows the continuation of natural water drainage. This is particularly important given the complex underground water flow and the proximity of the Pašino vrelo water well.

The remediation layout is given in Figure 6. The method consists of backfilling a sinkhole, including blocking the sinkhole throat with boulders, followed by the installation of upper granular layers with high permeability, each with finer particles than the one below. The backfill material consists of 300 -

500 mm and 500 – 800 mm boulders (Type 1), followed by 32 – 250 mm crushed stone (Type 2), over which 16 - 32 mm material (Type 3) is placed. The Type 2 and Type 3 materials are placed in 50 cm thick layers and compacted to 40 MPa.
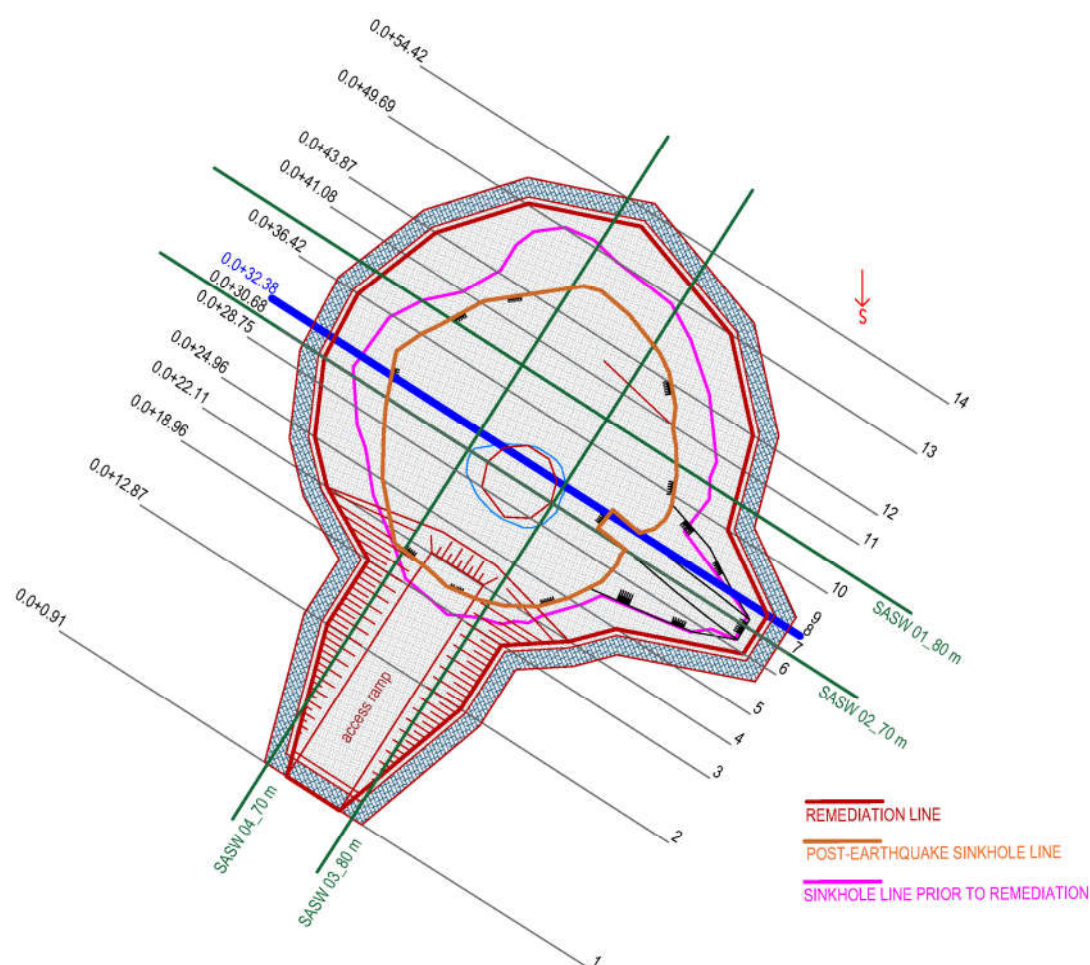

Figure 6. A layout of the remediation solution for UVM-001, modified from Brodska Posavina (2023)

After the initial excavation and reprofiling of the slopes, due to removal of loose slope material and to achieve sufficient compaction of the backfill material, the excavation area is lined with a geocomposite consisting of a non-woven geotextile with a mass of 300 g/m^2 (to prevent the penetration of fine soil particles into the backfill material during the water seepage) and biaxial geogrids with a tensile strength of 30/30 kN/m (to allow interlocking with the backfill material, increasing both the stiffness of the backfill and the contact shear strength along the slope). The geocomposite is placed in the surface trench and anchored to the ground with U-segments of reinforcing steel. The geogrids were also positioned at predefined heights to enable interlocking with the backfill material.

After backfilling the surface opening, the top layer of clay is installed in four 25 cm thick layers at a thickness of 1.0 m (on agricultural fields) or 0.5 m (on non-agricultural fields) and the surface is then weeded. The separating geotextile is laid on type 3 – clay cap boundary. The characteristic cross-section (blue line from Figure 6) is given on Figure 7.
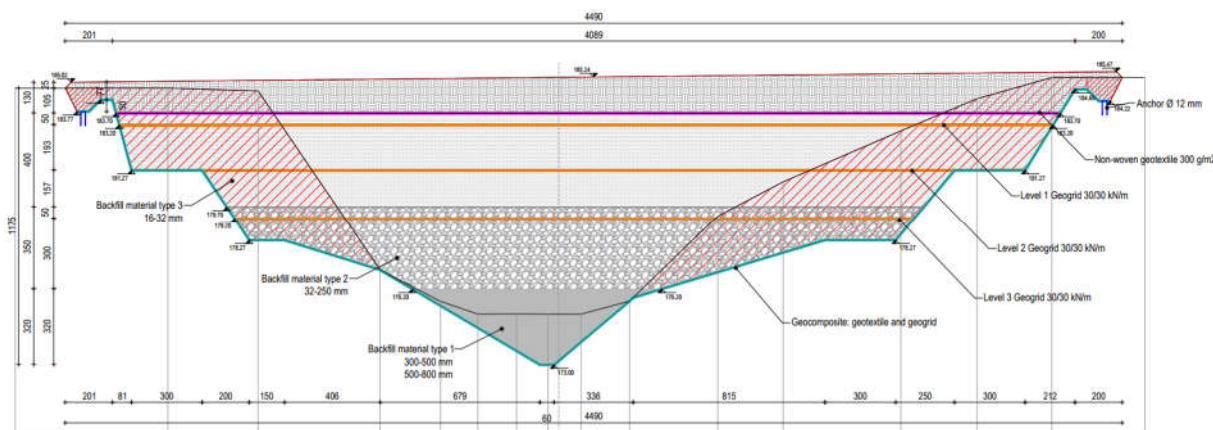
Figure 7. A cross-section of the remediation solution for UVM-001, modified from Brodska Posavina (2023)

4.2 Remediation works: phases and challenges

Due to its size (almost 50% of the volume of all the collapse sinkholes in the area) and complexity, the majority of the remediation work was focused on the largest collapse sinkhole, UVM-001. In order to carry out the planned work, the contractor started a trial water pumping operation to verify that the work could be carried out in dry conditions. It was found that water ingress was quite low due to the low permeability soil deposits. However, during this work, cracks appeared in the bottom of the sinkhole slopes and eventually slope sliding occurred, most likely due to the residual water in the soil reducing the shear strength and the loss of external water pressure, Figure 8. Slope sliding-induced sinkhole enlargement is depicted on Figure 6, compared to its initial size recorded just after the earthquake.
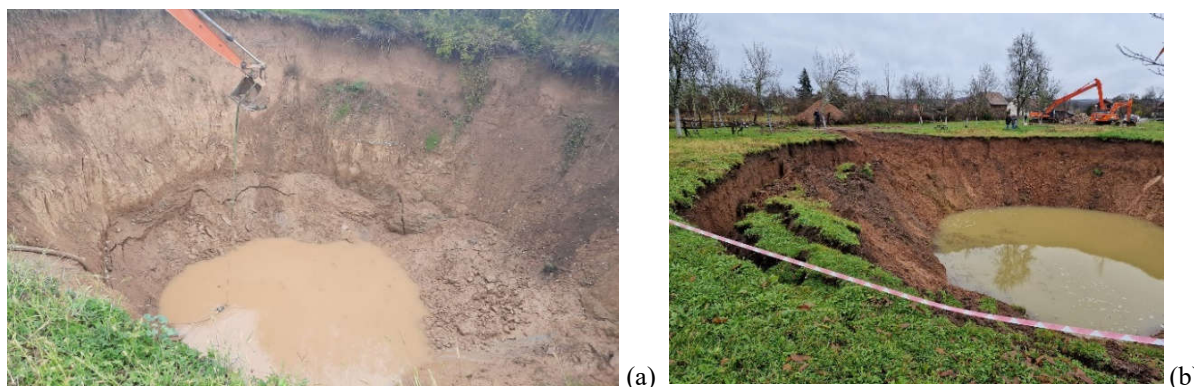
Figure 8. Trial pumping of sinkhole water (a) and the consequent collapse of the sinkhole slopes (b)

Work on the largest sinkhole began with the slope reprofiling (Figure 9a) in May 2023 and was completed in July 2023. However, it should be noted that the preparatory work started earlier, as the access road for the heavy machinery had to be built, as well the temporary disposal areas for the backfill material and geosynthetics. In addition, the underground telecommunications cable that runs along the site had to be relocated. After the geocomposite was installed (Figure 9b), backfilling began with Type 1 material (boulders), followed by Type 2 and Type 3 material (Figure 10).
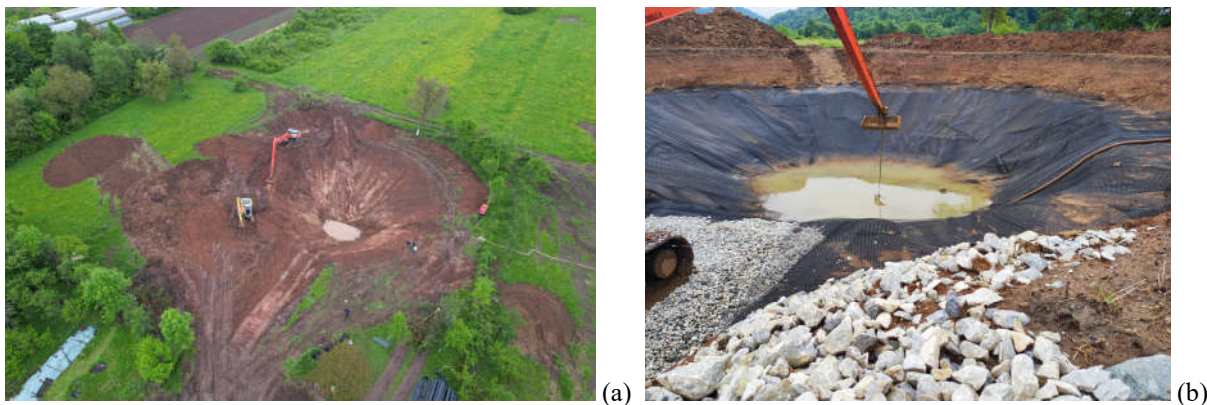
Figure 9. Reprofilling of the sinkhole slopes (a) and installed geocomposite on the excavation area (b)
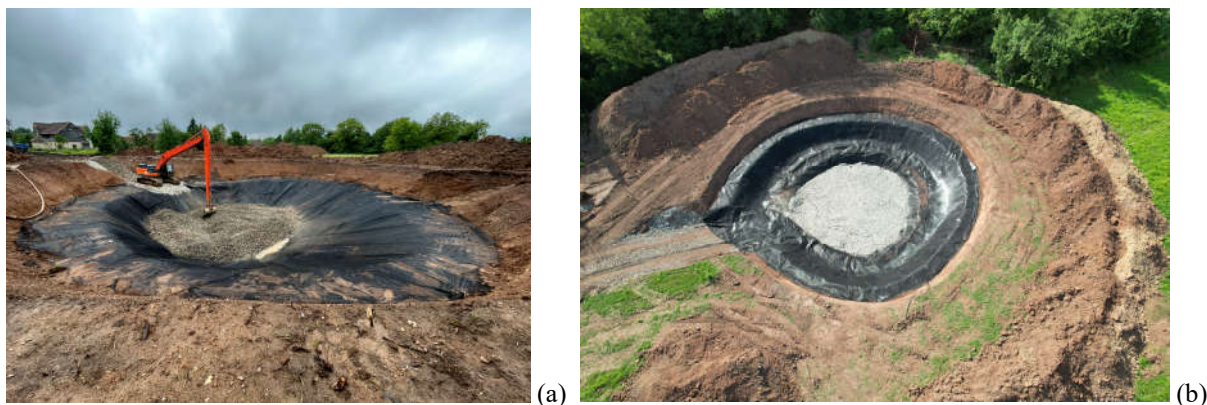
Figure 10. Backfilling works using long reach excavator (a) and aerial view of material type 2 placed and compacted (b)

During the backfilling work, several heavy rainfall events occurred, which prolonged and made the remediation work more difficult. However, the combination of the compaction of the backfill material and the installation of geogrids (Figure 11a) provided a solid foundation for the work of the heavy machinery (Figure 11b). This can be also considered as a large-scale load test which verified design solutions since no problems occurred regarding excessive deformation or settlements of backfill material Finally, a clay cap was installed (Figure 12a).
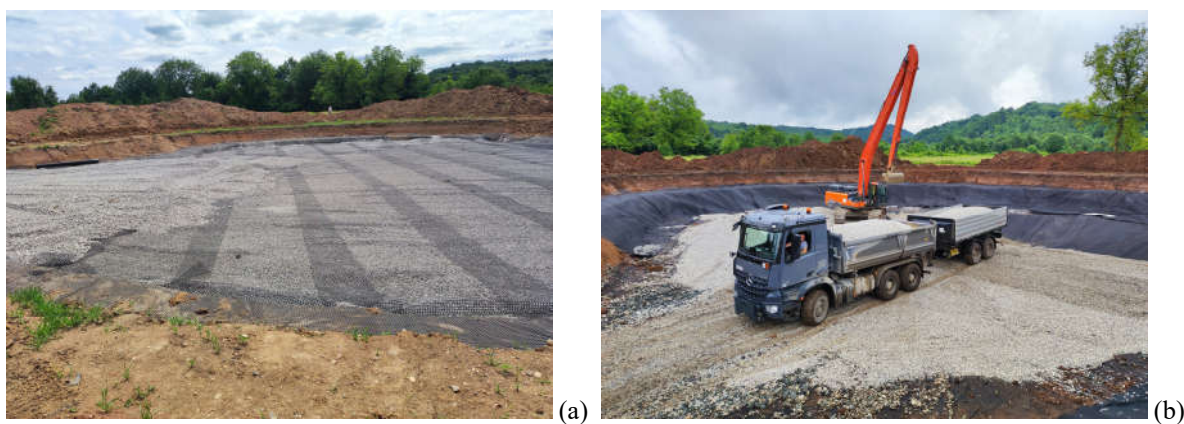
Figure 11. Installed biaxial geogrids (a) and heavy machinery inside the sinkhole (b)

(a)   (b)

Figure 12. Installation of final layer of clay cap (a) and the terrain surface after the remediation works with SASW control quality work being conducted (right)

Continuous supervision and control quality works have been carried out during the sinkhole remediation, which was particularly important given the many remediation phases and the large number of details. All the materials installed complied with the criteria set by the design. Quality control works were also carried out, including the plate load test to check the compaction of each layer and the geophysical method of spectral analysis of surface waves (SASW) to determine the stiffness over the entire backfill depth at the end of the work. Results of the one SASW profile, named SASW-02 (Figure 6), are shown in Figure 13. The required small – strain stiffness is higher than required by the design. It can be also seen that the backfill material (blue lines) exhibits larger shear wave velocities and small - strain stiffnesses than the surrounding soil (red lines) which is characterized by overconsolidated clayey materials. The monitoring network consisting of survey points was installed to measure the long-term settlement of the backfill material and this monitoring work will continue in the near future.

(a)   (b)
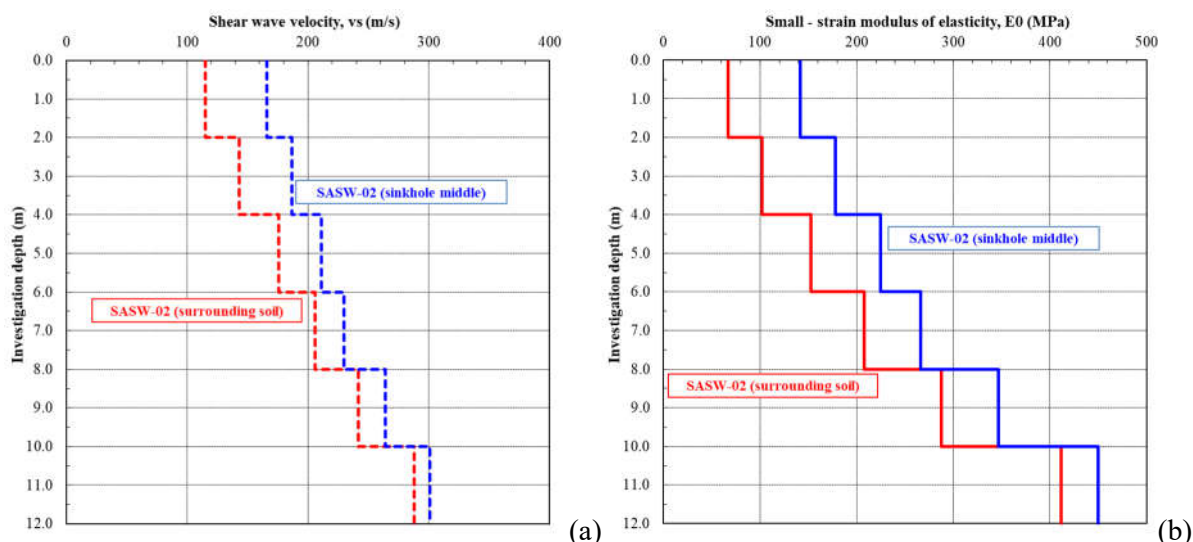
Figure 13. Excerpt from results of one SASW profile showing shear wave velocities (a) and small – strain stiffnesses (b) of the backfill material and the overconsolidated surrounding clayey material (CFCE, 2023)

5   Conclusion

In Sisak–Moslavina County, during and shortly after the strong earthquake of December 2020, numerous collapse sinkholes appeared, leaving the authorities and the engineering community perplexed. Numerous investigations were carried out to determine their origin and assess the risk of new

sinkholes occurring. The comprehensive efforts presented in this paper served to categorize sinkholes in order to identify remediation prioritizations. A detailed design for 102 sinkholes was developed, taking into account the specifics of the microsite, using the inverse filter method design solution, which consists of backfilling the sinkhole with materials of different grain sizes and incorporating geosynthetic materials. The remediation of sinkholes was a major challenge both in the categorization and design phase, as well during the remediation work, monitoring and quality control. All of these challenges required continuous collaboration between investors, designers, contractors and supervisors to successfully complete this project. In the end, the implementation of the remediation measures not only fulfilled the technical requirements set before the project itself, but also increased the level of safety for the population, agricultural land and infrastructure in this part of the Sisak – Moslavina County.

References

Bačić, M.; Kovačević, M. S.; Librić, L.; Žužul, P. Sinkholes induced by the Petrinja M6.2 earthquake and guidelines for their remediation. *In Proceedings of the 1st Croatian Conference on Earthquake Engineering - 1CroCEE*. Lakušić, S.; Atalić, A. (eds). Zagreb: University of Zagreb, Faculty of Civil Engineering, 2021., 341-351 doi: 10.5592/CO/1CroCEE.2021.237

Brodska Posavina ltd. *Remediation of collapse sinkhole UVM-001*. Detailed design 1935-26/22 UVM-001, 2023.

CFCE. Center of Faculty of Civil Engineering. *SASW report for the collapse sinkhole UVM-001*. Report no. UVM-71/2023, 2023.

FCEZG. University of Zagreb, Faculty of Civil Engineering. *Assessment of the existing condition and categorization of sinkholes in Sisak-Moslavina county*. Report no. GIZ-110-024/2022, 2022.

Ntambakwa, E.; Salković, I.; Tomac, I. Geophysical reconstruction of bedrock depth at the large sinkhole in the 2020 Petrinja earthquake. *In Proceedings of the 2nd Croatian Conference on Earthquake Engineering - 2CroCEE*. Atalić, J.; Šavor Novak, M.; Gidak, P. et al. (eds.). Zagreb: University of Zagreb, Faculty of Civil Engineering, 2023. 69-78 doi: 10.5592/co/2crocee.2023.85

Pollak, D.; Gulam, V.; Novosel, T.; Avanić, R.; Tomljenović, B.; Hećej, N.; Terzić, J.; Stipčević, J.; Bačić, M.; Kurečić, T. et al. The preliminary inventory of coseismic ground failures related to December 2020 – January 2021 Petrinja earthquake series. Geologia Croatica: journal of the Croatian Geological Survey and the Croatian Geological Society. 2021, 74 (2), 189-208. doi:10.4154/gc.2021.08

Šumanovac, F.; Pekaš, Ž. Modelling Cover-Collapse Sinkholes That Appeared after the M6.2 Petrinja Earthquake in Croatia Using Electrical Resistivity Tomography Data. *Sustainability*. 2023, 15, 1124. https://doi.org/10.3390/su15021124

Tomac, I.; Kovačević Zelić, B.; Perić, D.; Domitrović, D.; Štambuk Cvitanović, N.; Vučenović, H.; Parlov, J.; Stipčević, J.; Matešić, D. ; Matoš, B. et al. Geotechnical reconnaissance of cover-collapse sinkhole area following Petrinja 2020 earthquake. *In Proceedings of the 2nd Croatian Conference on Earthquake Engineering - 2CroCEE*. Atalić, J.; Šavor Novak, M.; Gidak, P. et al. (eds.). Zagreb: University of Zagreb, Faculty of Civil Engineering, 2023. 57-68 doi: 10.5592/co/2crocee.2023.84

DESIGN AND CONSTRUCTION FOR REHABILITATION OF EARTHQUAKE DAMAGED WATER PROTECTION LEVEES - METHODOLOGY AND SOLUTIONS

IVAN MIHALJEVIĆ[1], BERISLAV RUPČIĆ[1], MARKO KAIĆ[1], GORAN GRGET[1], LEO MATEŠIĆ[1]

[1] *Geokon-Zagreb d.d., Croatia, info@geokon.hr*

Abstract

After completing emergency measures for flood protection on the levees of the rivers Kupa, Sava and Petrinjčica, damaged by the earthquake, Croatian Waters Authorities (Hrvatske vode) assigned preparation of design documentation for rehabilitation. At each location, data on damage and from geotechnical investigations were collected. The damage included deep vertical cracks in the soil and embankments, in some cases with the expulsion of sandy material as a result of liquefaction, subsidence and loss of embankment integrity, and, in a smaller number of cases, landslides towards the riverbed. For each type of damage, its impact on the stability and safety of the levee was considered, and remedial measures were proposed. The measures to rehabilitate the foundation soil, culverts and embankments were then formed into complete solutions for the repair of damaged levees, taking into account the specifics of individual sections (state of construction and infrastructure, implemented intervention rehabilitation measures, etc.). The foundation soil under the embankment has increased its resistance to liquefaction, the embankments have been rehabilitated and strengthened against seismic load, while the damaged culverts have been replaced.

Key words

water protection levees, earthquake, liquefaction, emergency measures

1 Introduction

Croatian Waters Authorities (Hrvatske vode) and licensed contractors companies have within less than two months after the disastrous Petrinja earthquake Mw 6.4 from December 2020, conducted expert examinations and emergency remedial measures for 14 critically damaged location of water protection levees. Using box barriers (gabion type, earth filled barriers), second line of defences were built in the locations of Galdovo (740 m), Palanjek (250 m), Krnjica (530 m), Stara Drenčina (580 m). In order to access the locations it was necessary to build new access roads in total length of about 9 km.
After the earthquake, the composition and characteristics of the underlying soil had to be investigated, as well as the mechanisms that are led to damage.

Contracts with designers were concluded six months after the earthquake. In order to gain insight into levee damage, recordings and observations carried out by experts and volunteers in the days immediately after the earthquake, when there are traces of liquefaction and cracks in the soil and levees were "fresh" (Fig. 1a), proved to be invaluable. Subsequently, many cracks in the soil self-healed, or were hidden with grass growth by the time of designing, while traces of liquefaction have been washed away (Fig. 1b).

For liquefaction and related damages there were no experiences in the recent history of Croatia and surroundings region, which also represented a challenge for permanent rehabilitation solutions.
Designing the rehabilitation of damage to levees was led by international guidelines (Seismic Design Guidelines for Dikes, 2014) and published professional works (Sasaki et al., 2004). Designers were

looking for technical solutions that would be simple to implement, robust in application and safe for the final state of the performed rehabilitation.

Figure 1. Comparison of the levee crack: a) immediately after the earthquake and b) after 6 months

2 Geotechnical investigation works

At the locations of damaged levees, geotechnical investigation works were carried out, which consisted of geological and hydrogeological survey, geophysical field survey and exploratory drilling, as well as laboratory tests.

The geotechnical stratification of the underlying soil and the physical and mechanical parameters of the material were determined by exploratory boreholes. Special emphasis was placed on performing a larger number of static penetration tests (CPT), given that the determination of liquefaction potential relied on CPT tests (Boulanger and Idriss, 2014). Geophysical measurements were carried out with the aim of determining the thickness of the roof clay layer along the levee. Geophysical methods of seismic refraction, MASW (multichannel analysis of surface waves) and geoelectrical tomography were applied. In most locations, the composition of the foundation soil was determined, which consisted of roof clay layer and sand and gravel underneath (Figure 2).
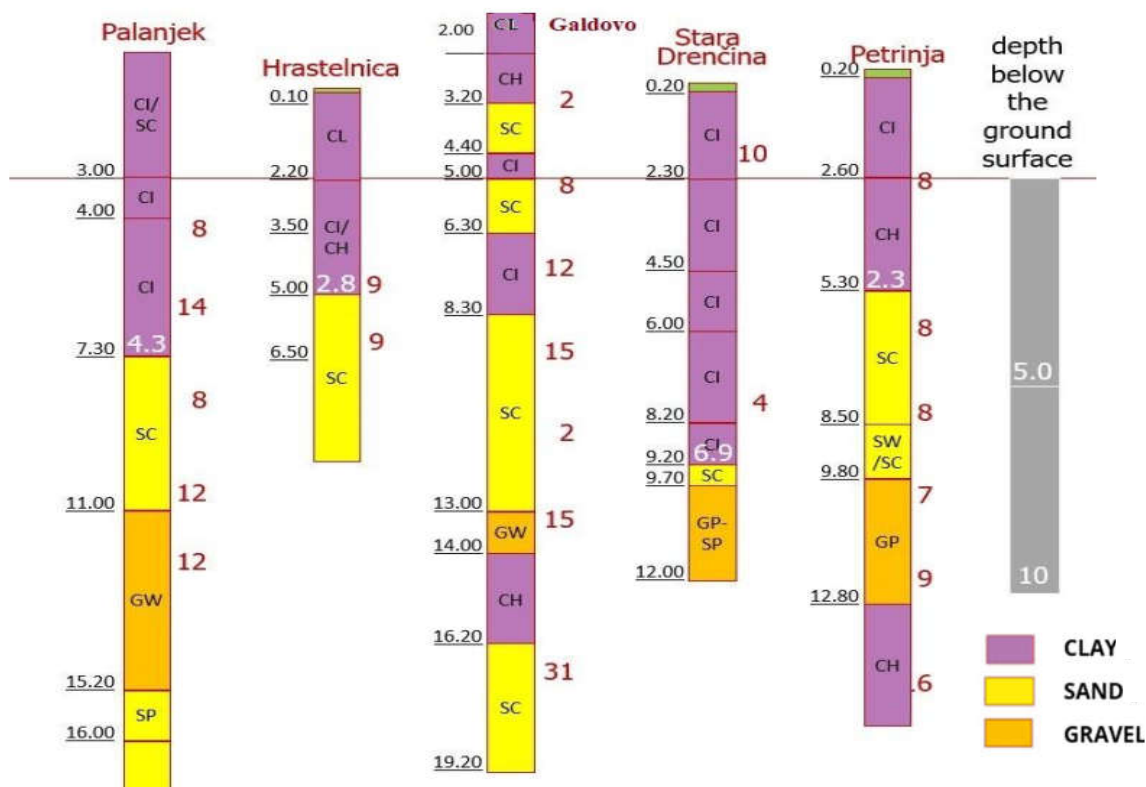
Figure 2. Geotechnical layering of embankment and subsoil by depth at damage locations with SPT values
(according to Mihaljević and Zlatović, 2023)

Seismological data were analysed from the official seismological maps of the Republic of Croatia. But the designers considered that the peak accelerations of the return periods were underestimated compared to the past earthquake, so based on the data of the Seismological Service at the Geophysics Department of the Faculty of Science in Zagreb (2021), the maximum values were defined for further design magnitude M_w 6.5 and horizontal acceleration a = 0.2 g. The soil is classified as soil type C and S2.

3 Analysis of liquefaction potential

In practice, procedures based on field correlations of the appearance of liquefaction with the results of in situ experiments, SPT and CPT (Seed and Idriss, 1971) are used to assess the liquefaction potential, for which empirical liquefaction diagrams are used.

The basis of the evaluation of the liquefaction potential is the calculation of the cyclic resistance ratio (CRR) to define the resistance of the soil to cyclic loading, and the cyclic stress ratio (CSR). If CSR is CRR, it can be concluded that the analysed soil is subject to liquefaction. If the CRR value is higher, the probability of liquefaction occurrence is low.

According to EC8, the formula for the required safety factor against the occurrence of liquefaction is:

$$F_s = \frac{CRR_{7,5} \cdot CM}{CSR} > 1,25$$

where is:
- CSR is the calculated shear cyclic stress ratio for a given earthquake,
- CRR7.5 is the cyclic resistance ratio for an earthquake of magnitude M=7.5,
- CM is the magnitude adjustment factor. (Magnitude Scaling Factor).

The liquefaction safety factor can be determined continuously by depth for each individual CPT test result. Based on the methodology proposed by Juang et al. (2002) also calculated the probability of

liquefaction according to the depth of each test. Chen and Juang (2000) proposed a soil classification with regard to liquefaction potential according to Table 1.

Table 1. Soil classes according to liquefaction probability

Probability of liquefaction	Class	Description
$0.85 \leq PL$	5	The soil will almost certainly liquefy
$0.65 \leq PL < 0.85$	4	It is very likely that the soil will liquefy
$0.35 \leq PL < 0.65$	3	Liquefaction / non-liquefaction is equally likely
$0.15 \leq PL < 0.35$	2	It is unlikely that the soil will liquefy
$PL < 0.15$	1	Almost certainly the soil will not liquefy
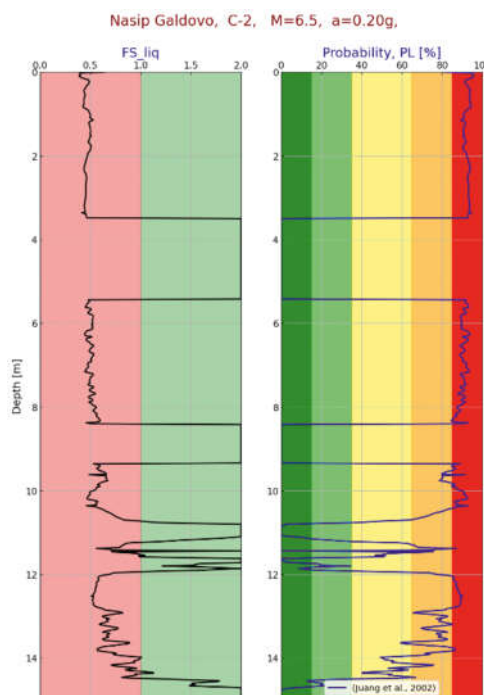
Figure 3. Safety factor against liquefaction and probability of liquefaction occurrence (Galdovo)

The analysis of the liquefaction potential at the locations of the damaged embankments was carried out according to the results of field CPTU tests, for an earthquake of magnitude M_w 6.5, with an assumed high level of underground water (Fig.3).

The results at the locations of most of the damaged embankments showed a high potential for the occurrence of liquefaction.

In addition to the appearance of liquefaction in the sandy layers of the foundation soil, the loss of strength under the seismic action was also observed in clays and silts under the name of cyclic softening. The phenomenon is caused by the increase of additional pore pressures, as a consequence of seismic action, which results in a temporary reduction or loss of strength in clays and silts. The phenomenon is comparable to the phenomenon of liquefaction in sands, except that there is no physical flow and movement of material, but instead large shear deformation occurs.

Taking that into account, high liquefaction potential in sands, or quasi-liquefaction potential, i.e. cyclic softening in clays and silts, is not surprising.

4. Rehabilitation methodology and solutions

Conceptualizing solutions for levee rehabilitation was approached by grouping according to the manifested type of damage, which is associated with the probable causes of its occurrence and the impact on the stability and safety of the levee.

4 main types of embankment damage were detected according to Table 2:

Table 2. Grouping types of levee damage with probable causes and impact on stability and safety

	Type of damage	Probable cause	Impact on the stability and safety
1)	Cracks in the levee that extend deep into the underlying soil	- Shear failure of clay soil layer caused by settlement, due to liquefaction of underlying sand layer	- Structural integrity of the levee body is compromised. - Open path for internal erosion and piping due to seepage.
2)	Settlement / sliding of the levee	- Liquefaction of sand layer in the foundation soil, accompanied with sand ejecta through cracks or in the watercourse.	- Loss of overflow height - possible overtopping - Questionable bearing capacity of foundation soil
3)	Cracks on the toe of the levee / with or without sand ejecta	- Shear failure of clay soil layer caused by seismic shaking - Shear failure of clay soil layer caused by settlement, due to liquefaction of underlying sand layer	- Open path for internal erosion and piping due to seepage. - Possible significant water flow on the protected side of the levee
4)	Structural damage of discharge pipe culverts in the levees	- Structural failure of pipes due to settlement	- Probable pipping - Functionality of discharge pipes is compromised

Variants of remedial measures were considered for each type of damage. The levees of a single section most often included several types of damage, so priority was given to solutions that could meet the requirements of repairing several types of damage and at the same time meet the criteria of simplicity, robustness and safety.

The limiting factor in the projects was the investor's request that the rehabilitation be carried out within the geometry of the existing levee and in the width of the existing cadastral parcels of the levee.
The chosen solution for levee that developed cracks and deformations and lost their integrity consisted of partial or complete removal of the clay embankment body and its reconstruction in the geometry that existed before the earthquake, while reinforcing the levee body by installing layers of geogrids (Sasaki et al., 2004).

A special challenge was represented by longitudinal, deep cracks along the toe of the embankment, which partially collapsed and self-healed after a certain time after the earthquake. The question arose whether it is necessary to treat them and in what way. It was concluded that they represent a permanent problem as places of possible seepage and internal erosion under the levee, and that they must be rehabilitated in the zone immediately next to the toe of the levee.

The idea of filling with coherent or incoherent materials was abandoned due to the unreliability of such a method, as well as the idea of injecting cracks, which would create unnatural inclusions in the soil, of different stiffness and questionable durability.

It was decided to excavate the foundation soil in the areas of the cracks near the toe of the levee to a minimum depth of 1.5 m and to install the clay material in a controlled manner, in order to ensure continuation of the soil conditions and safety from the hydraulic uplift.
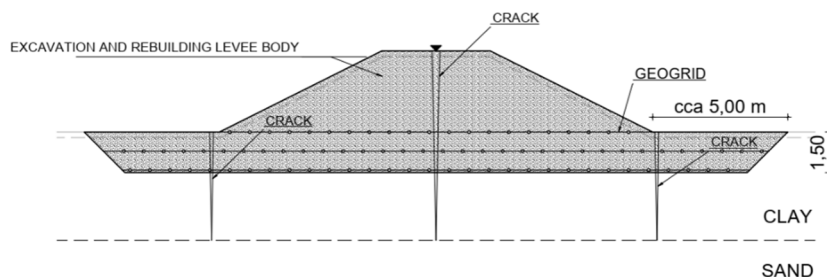
Figure 4. Solution for the repair of cracks and strengthening of levee against seismic loads

The results of the investigation showed that the underlying soil under the levee, even after the appearance of liquefaction in the past earthquake, is susceptible to liquefaction for new seismic actions and it is necessary to strengthen it.

On the parts of the levees that have experienced subsidence due to liquefaction, the foundation soil in the zone of the sand layer has been rehabilitated with a grid of jet-grouting columns, which have the role of increasing the resistance of the layer to seismic cyclic loading and, in the event of liquefaction, transfer the loads from the embankment and the overlying layer, as shown in Figure 5.
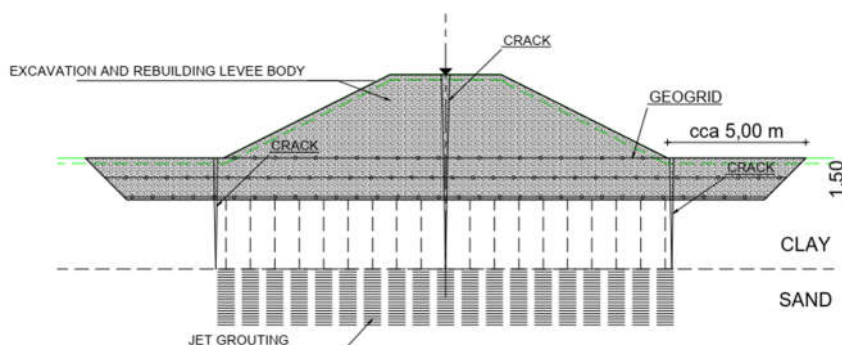
Figure 5. The solution for strengthening the sand layer under the levee with jet-grouting columns

In places of damaged pipe culverts, the solution consisted of excavation and removal of the culvert, improvement of the subsoil under the culvert with jet-grouting columns and construction of a new concrete culvert.

On the section of the damaged Sava levee near Galdovo, where the underlying soil is sandy, the improvement of the underlying soil by impulse compaction (rapid impact compaction - RIC) was chosen, as illustrated in Figure 6. With this improvement method the soil is compacted and brought to a denser state by a machine that strikes the surface of the foundation soil dozens of times per minute with a weight over a transfer plate. RIC was chosen because of its applicability to increase the density of granular soils and thereby reduce the likelihood of liquefaction.

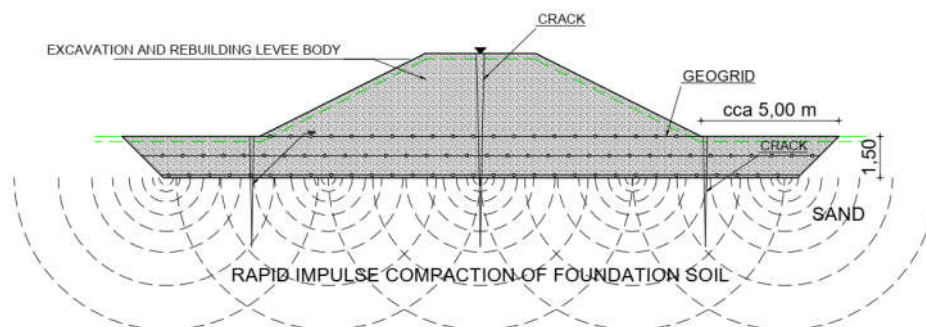**Figure 6.** The solution of strengthening the sand layer under the levee by impulse compaction

Control of the improvement by pulse compaction in terms of resistance to liquefaction is carried out by CPTU tests before and after the reclamation of the base soil. Although some limiting factors occurred during rehabilitation works (high water levels of river Sava resulting in high ground water levels) results showed that liquefaction potential has been significantly reduced.

On two sections of the left Kupa levee, where sliding and translational movement of the levee towards the riverbed occurred, the levee was relocated inland and reinforced, as shown in Figure 7.
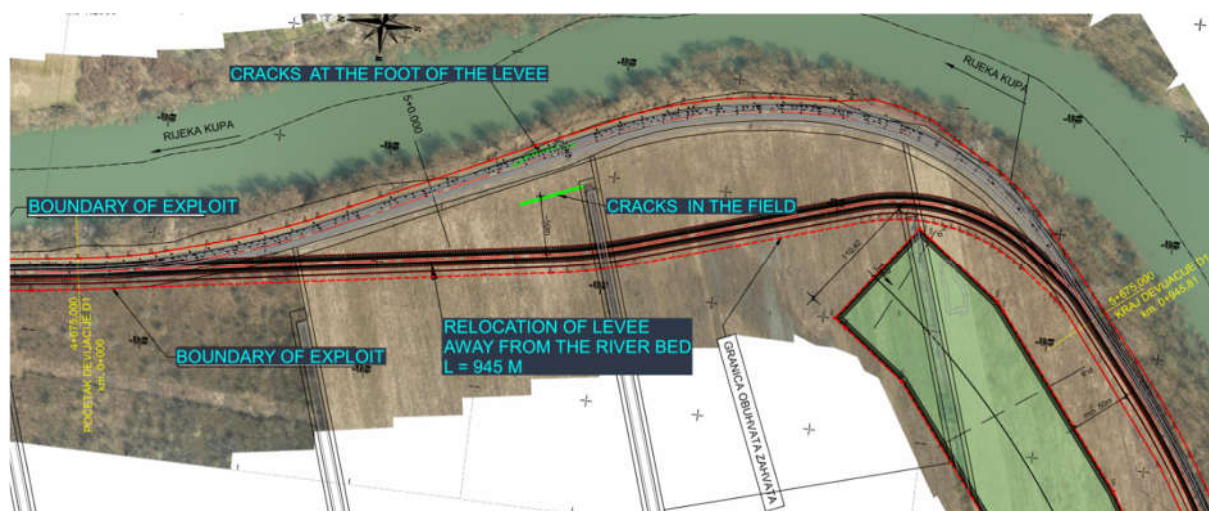

Figure 7. Relocation of the left Kupa levee damaged by sliding to the river bank (section Staro Pračno - Stara Drenčina), (*rijeka Kupa*= river Kupa)

5 Conclusion

For the permanent rehabilitation of levees damaged by the catastrophic Petrinja Mw 6.4 earthquake from 29.12.2020, geotechnical investigations were carried out and all available data on damage was collected. Damages were grouped according to type and probable causes, and their impact on the stability and safety of the levee was assessed.

Possible variants of rehabilitation measures by type of damage were considered. By combining the application of rehabilitation measures, complete solutions were formed that took into account the type of damage and the specifics of individual sections (state of construction and infrastructure, implemented interventional rehabilitation measures, etc.). Solutions were chosen that are easy to implement, robust in application and provide sufficient stability and security for design loads.

Table 3. Presentation of applied repair methods by type of damage

Type of damage	Rehabilitation measures
1), 3)	- Removal of the damaged levee, - Excavation of the foundation soil at the toe of the levee, - Reconstruction of the levee with geogrid reinforcement
2)	- Improvement of the sand layer of the soil with jet-grouting columns
2)	- Relocating the levee to a new location inland
2)	- Improvement of the sandy foundation soil by rapid impulse compaction
4)	- Removal of the damaged levee - Improvement of the foundation soil, - Removal of the damaged pipe culvert and construction of a new concrete culvert and building levee reinforced by geogrid

It is possible that in the upcoming period, under high water loads, residual damage which remained hidden, will manifest on unrehabilitated levee sections. Therefore, the importance of continuous levee

inspections is emphasized and projects for levee modernization and strengthening should be launched over time.

References

Boulanger, R.W.; Idriss, I.M., CPT and SPT based liquefaction triggering procedures, *Report No. UCD/CGM-14/01, Center for Geotechnical Modeling, Department of Civil and Environmental Engineering, University of California, Davis, CA, 134 pp.*, 2014

Chen, C. J.; Juang, C. H., Calibration of SPT- and CPT-Based Liquefaction Evaluation Methods, *Innovations and Applications in Geotechnical Site Characterization, doi:10.1061/40505(285)4*, 2000

Geokon-Zagreb d.d., Geotehnički istražni radovi za izvanredno održavanje l.o. savskog nasipa od n.km.r. 101+200 do n.km.r. 102+000 u naselju Galdovo; *Geokon-Zagreb d.d., Br. E-061-21-01, Zagreb*, 2021a

Geokon-Zagreb d.d., Projekt izvanrednog održavanja lijevoobalni savski nasip od n.km 101+200 do n.km 102+000 u naselju Galdovo, Sisačko-moslavačka županija; *Geokon-Zagreb d.d., Br. E-061-21-02, Zagreb*, 2021b

Juang, C.H., Jiang, T.; Andrus, R.D., Assessing probability-based methods for liquefaction evaluation, *Journal of Geotechnical and Geoenvironmental Engineering*, 128 (7), pp. 580-589, 2002

Mihaljević, I.; Zlatović, S. (), Embankments Damaged in the Magnitude Mw 6.4 Petrinja Earthquake and Remediation. *Geosciences 2023*, 13, 48. https://doi.org/10.3390/geosciences13020048, 2023

Ministry of Forests, Lands, and Natural Resource Operations – Flood Safety Division, *Seismic Design Guidelines for Dikes*, 2nd Edition, BC, Canada, 2014

Mihaljević, I., Zlatović, S., Čičak, M.: Croatian experience on urgent measures and remediation of levees after earthquake Mw 6.4 on December 2020, Proceedings from 13th Conference on Water Economy and Hydrotechnics, MACOLD 2023, Skopje, pp 59-68, ISBN 978-608-4953-02-9

Sasaki, Y.; Fukuwatari, T.; Tsuji, T.; Kano, S.; Sawada, S.; Uekuma, H., A Study on the Performance of a Reinforced Dike Section With Geogrid During the Tottori-Ken Seibu Earthquake, *International Conference on Case Histories in Geotechnical Engineering*. 36., 2004

Seed, H.B.; Idriss, I.M., Simplified procedure for evaluating soil Liquefaction Potential, *Journal of the Soil Mechanics and Foundation Division*, 97, pp. 1249-1273., 1971

Seizmološka služba, Preliminarni rezultati serije potresa kod Petrinje od 28. prosinca 2020. do 28. siječnja 2021., https://www.pmf.unizg.hr/geof/seizmoloska_sluzba/ mjesec_dana_od_glavnog_petrinjskog_potresa, 2021

Topic 10

In the Path of Progress AI Innovations in Landslide and Engineering Geological Research

LANDSLIDE SUSCEPTIBILITY MAP USING ViT ARCHITECTURES WITH PRE-SLIDE TOPOGRAPHIC DEM OF DEEP-SEATED LANDSLIDE EVENTS

TERUYUKI KIKUCHI [1], SHO FUKAYA [2],

[1] *Suwa University of Science, Japan, kikuchi_teruyuki@rs.sus.ac.jp*

[2] *Suwa University of Science, Japan, sho_fukaya@rs.sus.ac.jp*

Abstract

In landslide prediction, it is crucial to understand past landslides and prepare for similar future events. The development of automatic analysis methods using deep learning can enhance the sophistication and cost-effectiveness of screening. In this study, high-performing convolutional neural network (CNN) and Vision Transformer (ViT) architectures were applied for landslide detection, and their outcomes were compared for landslide susceptibility mapping in *Kii* Peninsula, Japan. Initially, 101 landslide and non-landslide points were identified and divided into training (70%) and validation (30%) datasets. Slope angle was used as an influencing factor. The CNN and ViT models were found to be almost equally accurate in the spatial prediction of landslides. Furthermore, the landslide susceptibility map was consistent with the trends in the distribution of gentle slopes and knick lines unique to the study area, demonstrating its potential as a powerful method for future landslide prediction.

Key words

Vision Transformer, Convolutional neural networks, Landslide susceptibility map, Deep-seated gravitational slope deformations, Slope Angle

1 Introduction

The prediction of landslides depends on the understanding of past cases and the assumption of similar future occurrences. Case studies of frequent slope hazards have revealed that landslide behavior varies depending on conditions such as local geology and topography, rainfall characteristics, and landslide progression. The multiregional and multifactorial nature of landslides is a major obstacle to a unified discussion. To date, no such system has been established.

Gravity deformation is a geomorphic feature associated with slope failure. This implies continuous deformation of the bedrock both near the surface and deep underground. Gravity deformation has been reported in glacial landforms in the European Alps, such as zagging and double mountain ridges (Zischinsky, 1966) and deep-seated gravitational slope deformations (DSGSD; Agliardi et al. 2001) are prime examples. Dramis and Sorisso-Valvo (1994) described DSGSDs as massive deformations, where small displacements cause gravitational deformation, with or without a slip surface. In their study in the Italian Pre-Alps, Crosta et al. (2006) numerically predicted that the upper slopes of large landslides are unstable and that potential instability factors, such as landslide sliding and flow, are present. This phenomenon is also frequent in Asian regions, with notable cases including Tsaoling in 1999 (Chigira et al., 2003; Evans et al., 2007) and the large-scale debris avalanche in southern Leyte, Philippines, in 2006. Many of these DSGSDs are not reactivations of old landslides, but have moved slightly before the event, providing precursor evidence.

Although the close relationship between topography and land subsidence is becoming clearer, land surface profiles obtained using Light Detection and Ranging (LiDAR) provide numerical information on the history of topographic features and deformations. However, interpretation by geomorphological and geological experts alone is not versatile and does not allow the simultaneous capture of a large area, leading to potential oversight. The aim of this study was to detect shared homogeneous topographic features using machine learning with pre-landslide LiDAR. Machine learning has often been used in landslide susceptibility maps (LSM) with grid data as a complementary method to multivariate analyses. Landslide location prediction using LSM was performed by Lee (2004) using a sigmoid function, whereas Dahal et al. (2008) predicted landslides using weight-of-evidence modelling conducted using eight factors. Convolutional neural networks (CNN) can outperform traditional support vector machine (SVM) methods owing to their high prediction rates and generalizability (Youssef et al., 2022). The network structure of CNNs is a major challenge for researchers, and attempts have been made to determine an optimal model using automatic search models (Kikuchi et al., 2023)
.

This study aimed to identify commonalities (e.g., DSGSD) specific to a particular region, given that multiregional and multifactorial factors can be attributed to landslides. To establish this, a comparison was made between CNN models, which have been extensively studied in landslide susceptibility modeling (LSM), and the Vision Transformer (ViT), which has been increasingly applied in the image processing field in recent years. Although few studies have focused on pre-disaster digital elevation model (DEM) images, we used a case study of the 2011 torrential rain disaster on Kii Peninsula in Japan. Specifically, the model was evaluated in a test domain. We believe that the results can assist researchers and local decision-makers with spatial information and erosion control to reduce landslide risk in the region.
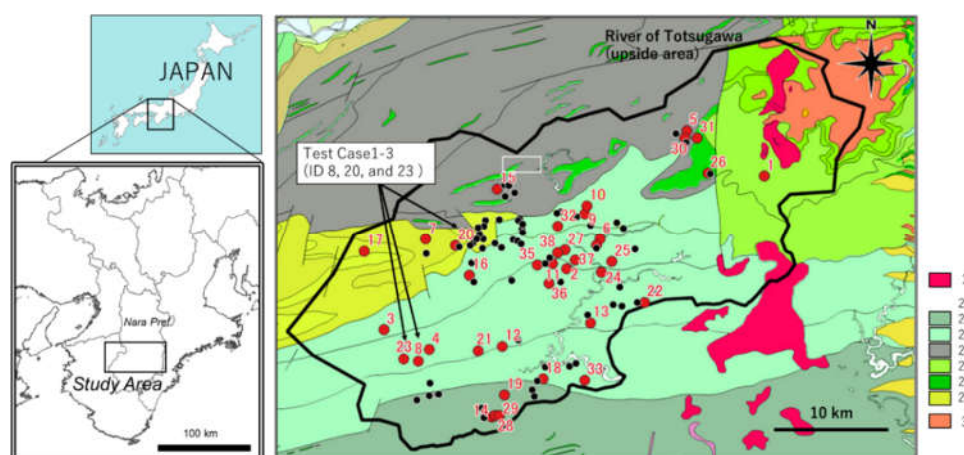
Figure 1. Study area and Geologic map showing the landslide location (Kikuchi et al, 2023).
Learning data used, red dots: slides (ID 1–38), black dots: non-slides (ID 39–101)
Legend 1: *Omine* Granitic Rocks; 2: *Hidakagawa* Group; 2a: *Ryujin* Formation; 2b: *Miyama*-Formation; 2c: *Hanazono* Formation; 2d: *Obadanigawa* Formation; 2e: Green stone; 2f: *Yukawa* Formation; 3: *Chichibu* terrane-*Daifugendake*-Formation.

2   Disasters and geomorphology

Typhoon Talas made landfall and crossed western Japan from 2–5 September 2011, bringing over 2,000 mm of rainfall to the Kii Mountains. Typhoons triggered more than 50 DLs(Deep sheeted landslides), which occurred when the total rainfall reached 600–1,200 mm (Chigira et al., 2013). Matsushi et al. (2012) studied rainfall and catastrophic landslides and noted that DLs occurred when cumulative rainfall exceeded 600 mm within 48–72 hours.

The Kii Mountains feature a ridgeline with uniform elevation, with Hakkeigadake (elevation 1,915 m) as the highest peak, as depicted in Figure 1. The elevation of the study area ranges from 220 to 1,915 m,

encompassing paleosurfaces in the southern and western parts of the Kumano-gawa basin. Gawa means river in Japanese. The study area constitutes the Shimanto Belt in the western Kii Peninsula and is a Cretaceous accretionary tectonic complex (Kimura, 1986). The upper reaches of the Totsu-gawa Formation, which is central to this study, lie within the northern belt and include the Hidaka-gawa Formation, which consists of five layers, beginning from the north: the Hanazono, Yukawa, Miyama, Ryujin, and Nyu-gawa formations (Hara and Hisada, 2007). The Hidaka-gawa Formation is predominantly underlain by the Shimanto Accretionary Complex of Cretaceous to Early Paleozoic age (containing a small amount of Miocene granite and sedimentary rocks). The Shimanto Accretionary Complex is composed of foliated mudstone, sandstone, acidic tuff, chert, and greenstone (Kumon et al., 1988; Hashimoto and Kimura, 1999).

3   Methods

The different datasets and data sources used for machine learning in landslide susceptibility mapping are described in this section. Four main phases were used. Various data sources were gathered to generate landslide susceptibility maps and extract landslide data. Modeling techniques were applied to the landslide susceptibility map generation, and a validation phase was conducted to test the accuracy and performance of the models (Figure 2).
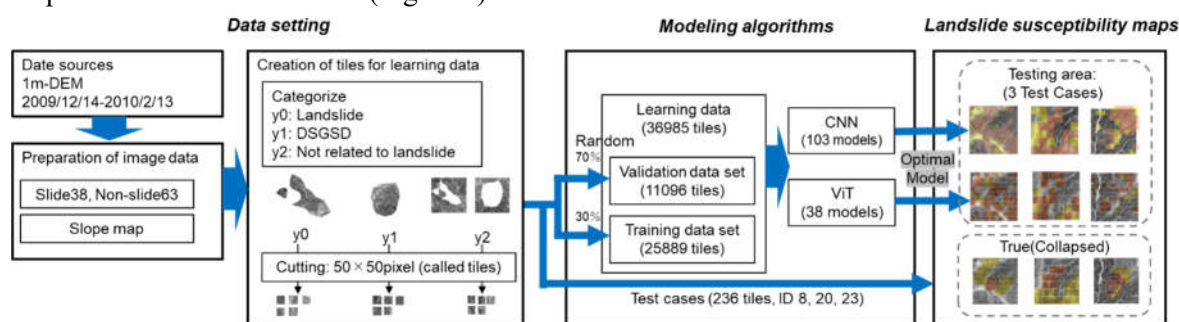
Figure 2. Schematic diagram of overall data sources, datasets, and model construction and process

3.1 Data Settings

In this study, supervised learning was used in areas where landslides have occurred. The training data comprised tiled pre-slide images of the landslide occurrence areas. Aerial laser surveys of the catchment areas before and after the disaster were conducted by the Kii Mountain Erosion Control Office, Kinki Regional Development Bureau, Ministry of Land, Infrastructure, and Transport. Measurements were taken in July 2009, before the disaster, and from December 2011 to February 2012, after the disaster. Measurements were taken as 1-m mesh DEMs using an airborne laser scanner. Thirty-eight landslide sites, each with a collapsed area exceeding 1,000 m^2, were used (Erosion Control and Disaster Prevention Division, Land Development Department, Nara Prefecture, 2012) (Figure 1; red circles). The data are summarized in Table 1.

Table 1. List of Learning Data

		Slide (y'0)	DSGSD (y'1)	Outside Landslide (y'2)	Total
Learning	training	14037	2966	8885	25888
	validation	6017	1272	3808	11097
Total		20054	4238	12693	36985
Test (Untrained area)		28	53	155	236

The pre-landslide topographic features at the landslide site include small scarps, flanks, terminal cliffs, gullies, and irregular undulations (Kikuchi et al. 2019), which are characteristic of the DSGSD (Figure 3a, b). Conversely, areas within the study area that did not collapse in 2011 were manually identified as having DSGSD. These are areas where no landslides have occurred but have the necessary geomorphic features for landslide development (Figure 3c, d). Sixty-three areas with these features were identified and extracted. The study data were then categorized into three groups: areas where landslides occurred in 2011 were classified as 'y1: landslides'. Area with DSGSD features but no landslides as, 'y1: DSGSD'. Landforms not included in y0 and y1 were classified as "y2: landforms not related to landslides". This classification was based on Kikuchi et al. (2023).
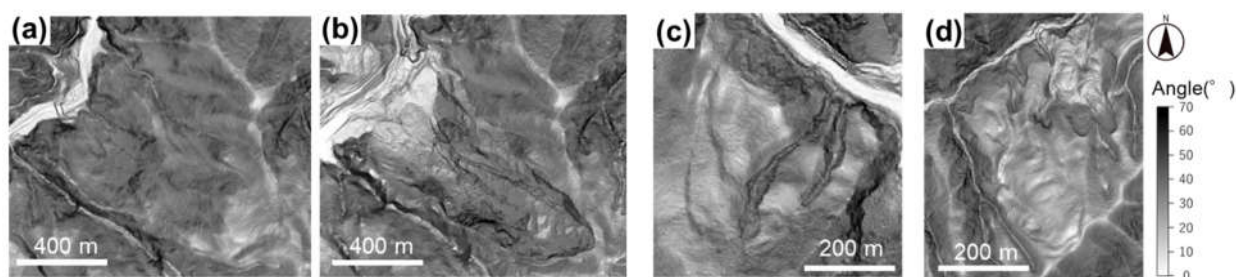

Figure 3. Images of the slope map: a: pre-collapse slope in the collapse study (y0) ; b: pre-collapse slope; c and d: terrain study (y1) without landslides, but with DSGSD.

3.2   Preparation of image data (Tiles)

To eliminate oversight and individual differences, the training data were not created from human-interpreted terrain features. Instead, an influential factor with objective features was created using various types of image analysis. In this study, the proven slope angle, a straightforward measure of terrain steepness, was employed. The slope angle is a topographic quantity that indicates the slope of each DEM mesh relative to the horizontal plane. Chigira et al. (2013) reported that small cliffs and irregular undulations are precursors to landslides. Kikuchi et al. (2019) obtained the following results: Landslides are often caused by small cliffs or irregular undulations. Seventy-one percent of the landslides occurred on slopes of 33-42°, whereas 68% of the DSGSDs occurred at 36-41°. Landslides occurred on gentler slopes than DSGSDs. These trends indicate that landslides have gentler slopes and more convex ridge and valley topography than DSGSDs; in the topographic wetness index (TWI), landslides clearly have a larger catchment area than DSGSDs. The concentrations at elevations of 750–800 m may have been due to the concentration of landslides around the transition line, as described by Tsou et al. (2017).

3.3   Creating tiles for learning data

Data were created by dividing the images into squares. The pre-landslide slope volume maps were sequentially cut into 50×50 pixel JPG images from the northwest corner. Fifty pixels correspond to 50 m, and 50×50 pixels correspond to 2500 m^2. The reason for using 50-pixel squares was that the minimum area of the landslide case was 1500 m^2. The tiles were replicated, one rotated by 90° and one with a mirror finish. The creation of rotated images results in the loss of information in the direction of the slide. Landslides and collapses have occurred on north-facing slopes. However, more emphasis was placed on increasing the training data by performing rotation, as it was necessary to determine the gravitational deformation characteristics of the mountain body rather than its directionality.

The tiles were randomly allocated for training and validation, as listed in Table 1. The final number of landslide tiles (y0) was 20,054. The 63 tiles labelled as DSGSDs (y1) and landslide outer terrain (y2)

were similarly processed. In total, 36,985 images were used for the training process, with 4,238 and 12,693 images, respectively. The final evaluation assessed the accuracy of the image analysis in the unknown domain using models from the training phase. By obtaining a confusion matrix, the analytical accuracies for each category (y0, y1, and y2) were compared and evaluated.

3.4   Modeling algorithms

Deep learning is an analytical technique that utilizes neural networks, which are multilayered structures modelled in a manner similar to neural circuits in the human brain. Image recognition has been used to create landslide susceptibility maps, and many case studies have been conducted. However, identifying gravity deformation in mountainous terrain poses a complex challenge. The DSGSD evidence often persists in landforms before landslides occur. Slight variations in land surfaces with complex histories present challenging areas that cannot be distinguished in a single image. This study compared CNNs, which are widely used as examples, with ViT, which is an increasingly adopted model in the image-processing field. The environmental conditions used in the analysis are listed in Table 2.

Table 2. Integrated development environment

Methods	CNN	ViT	ViT
Application	Neural Network Console	Jupyter lab	Google Colab
OS	Windows11(64bit)	Windows11(64bit)	Ubuntu V22.04.3
GPU	NVIDIA GeForce RTX 3060	NVIDIA GeForce RTX 3060	NVIDIA Tesla T4
CUDA	ver11.7	ver11.7	ver12.2
Python	3.9.1	3.9.1	3.10.2

3.4.1   Convolutional neural networks (CNN)

The analysis utilized a CNN, which is a highly effective method for image recognition. A CNN employs multiple convolutional layers within the neural network structure that generate feature values through convolution, and pooling layers that compress these features. The convolutional layers utilize kernels to effectively localize features in images and capture the relationships between a pixel of interest and its surrounding pixels. Based on previous studies, we utilized a two-dimensional (2D) CNN structure (CNN-2D) architecture that has been previously used for landslide detection (Ma et al., 2021).

3.4.2   Vision Transformer (ViT)

ViT, which is based on transformers, is a model developed for natural language processing. A CNN extracts features locally using kernels and has a limited receptive field for capturing the relationships between distant pixels. In contrast, ViT divides an image into patches and captures the relationship between patches using self-attention. ViT also performs processing by constructing word relationships, dividing an image into multiple small images (patches) and using these patches as words (tokens). This means that ViT can be more efficient than CNN by determining the "quality" of the dataset.

3.5   Creation of the artificial intelligence (AI) model

The artificial intelligence (AI) model involves two main phases: learning and evaluation. During the learning phase, the holdout method is used for learning and validation. Specifically, 70% of the tiles were used to develop weighted parameters and construct the model, referring to the model building method proposed by Kohavi (1995). In the validation phase, the remaining 30% of tiles were used to ensure the accuracy and effectiveness of the model. The resulting model is referred to as the "trained model."

3.5.1   Network structure of CNN

A search of the network structure of the CNN was performed for the best model using the autosearch model. Automatic search methods reveal new structures without the need for human coordination (Real et al., 2020). The results of this study not only reduce and streamline the human design burden, but also indicate the possibility of finding machine learning algorithms that do not use neural networks. A neural network console (Sony Corporation, Tokyo, Japan) was used in this study. This application allows automatic model building and parameter tuning using a graphical user interface (GUI). The search method uses Bayesian optimization (Wu et al., 2019) with network features and Gaussian processes to search for good networks faster than a random search. The initial model was LeNet (LeCun et al., 1989), which exhibited high character recognition rates.

3.5.2   Network structure of ViT

ViT does not require convolution. In natural language processing, words are divided into tokens. The vector corresponding to each token is represented by the following rule. These vectors are converted from words to vectors by the embedding layer, with one vector per token, and are input into the encoder (Dosovitskiy et al., 2021). The pre-training model of the TIMM library was used because it had few freely configurable parameters, and the setting of the parameters related to learning was performed by changing only the number of training sessions. The pre-training models in the TIMM library include various models in addition to the model size and patch size. In the learning stage, training was repeated several times. However, in this experiment, the model with the highest validation data evaluation was saved.

4   Results

4.1   CNN

An optimal model structure search was performed using CNN. A structural search was performed on 103 models based on LeNet in Figure 4. The prediction performance of the models was evaluated using a confusion matrix, which is a simple method for evaluating model prediction performance. As shown in Figure 5, the results of the optimal model applied correspond to model 57, with validation and test accuracies of 0.60 and 0.48, respectively, indicating it is a good and high-performing model. (Figure 4b).
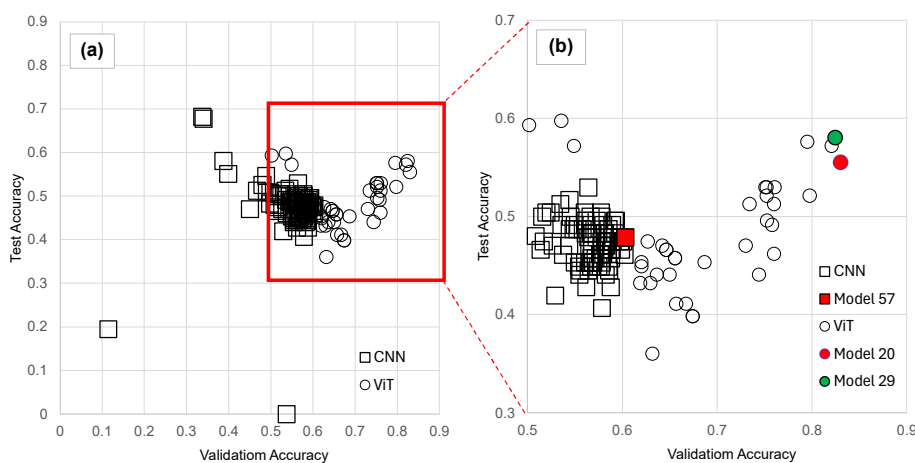

Figure 4 Accuracy from the automatic construction of the CNN and ViT model structures
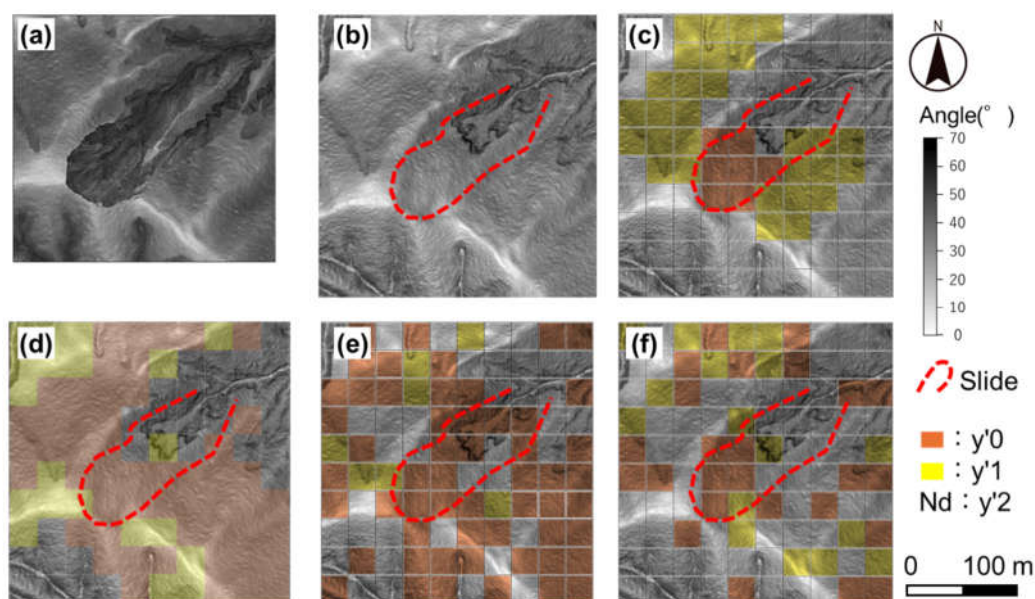
Figure-5 Analysis results of Test Case 1. a: post-collapse slope map; b: pre-collapse slope map; c: correct images for y0, y1, and y2; d: analysis results of model 57 for CNN; e: results of model 20 for ViT; f: results of model 29 for ViT.

4.2   ViT

In the ViT analysis, 38 different auto-model searches were performed with the parameters set manually, without an automatic optimal model structure search. The results are shown in Figure 4. Validation accuracy ranged from 0.50 to 0.83 and test accuracy from 0.36 to 0.60. The best accuracy was achieved by Model 20, which showed a validation accuracy of 0.83, 32 patches, a probability value of 0.25, and a random error of 0.6. The next best test accuracy was model 29 with 0.59, 32 patches, a probability value of 0.3, and random erasing of 0.6, with sharpness-aware minimization added to the process. Erasing was too low at 0.2 or too high at 0.8, and the effect of validation accuracy was reduced. Furthermore, changing the probability value had no significant effect (Figure 4b).

5   Discussion

The significance of the deep learning models used in this study was determined by testing whether topographic features specific to the collapse site could be determined in an untrained test area. Models 57 (CNN) and 20 (ViT), which had the lowest variation error, and 29 (ViT), which had the lowest test error, are discussed.

One tile automatically deciphered in this study encompasses a 50-m square of topographic data. The actual site of collapse is considered the result of a complex combination of extensive microtopographies. For performance evaluation in the test area, three of the 38 collapse locations were presented as test cases. Two of these locations were selected as shown in Figures 5 and 6 (See Figure 1 for the locations).
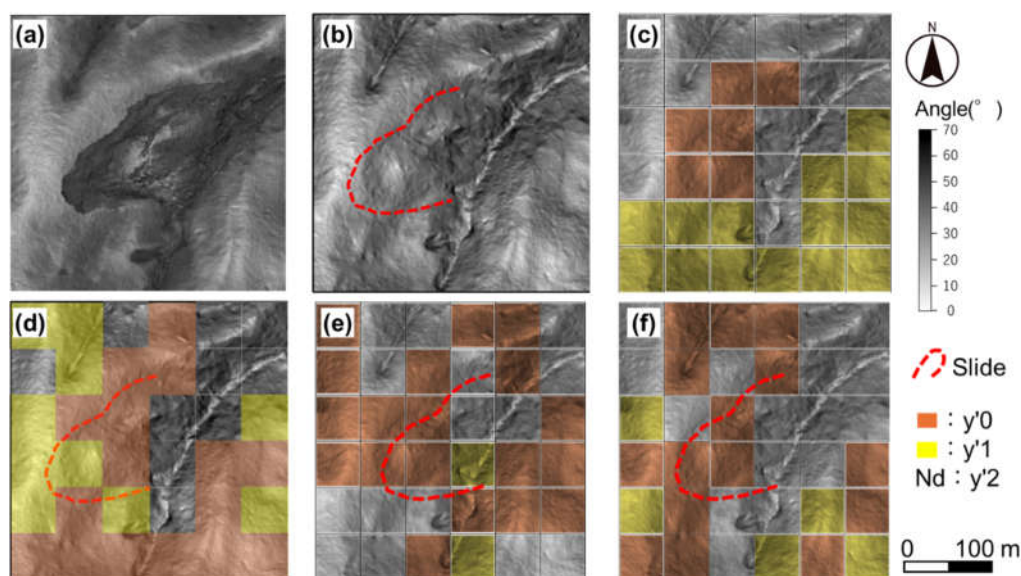
Figure 6 Analysis results of Test Case 2. a: post-collapse slope map; b: pre-collapse slope map; c: correct images for y0, y1, and y2; Red tiles indicate where the model judges the collapse (y'0), orange tiles indicate where the model judges the collapse as non-collapse (y'1), and colorless tiles are those judged to be unrelated to the mountain body gravity deformation (y'2). d: analysis results of model 57 for CNN; e: results of model 20 for ViT; f: results of model 29 for ViT.

5.1 Test Case 1

Test Case 1 (ID 8) collapsed in a north-easterly direction, originating from a northwest-southeast ridge. The collapsed area features a terminal collapse and multiple indistinct cliffs, likely caused by mountain gravity deformation. The intermittent formation of arcuate cliffs suggests the ongoing development of landslide landforms.

As shown in Figure 5(d), from the CNN, five of seven points accurately predicted the collapse (y'0), and the majority of the collapsed area was correctly identified. The extent of collapse conformed to the characteristics observed during training and validation.

Model 20 (Figure. 5(e)) by ViT accurately predicted five out of seven cases, with the majority of the collapsed area identified, showing a tendency towards selecting y'0 more frequently. However, Model 29 (Figure. 5(f)) correctly predicted four out of seven points, indicating less precision in selecting the majority of the collapsed area. In addition to the true value, the northeast slope of the ridge in the southeast direction from the collapse was selected as a collapse point (y'0). This decreases as the number of experiments increases, indicating the effect of the sophistication of the model.

5.2 Test Case 2

An example of Test Case 2 (ID 20) is illustrated in Figure 6. Test Case 2 was capped by a north-south ridge that collapsed in the northeasterly direction. The collapsed area exhibited a terminal collapse alongside indistinct small gullies and indistinct slip cliffs formed intermittently, suggesting that the landslide development history was in progress or that sliding had occurred.

As shown in Figure 6(d), five out of six points accurately predicted the collapse (y'0), and the majority of the collapse area was correctly identified. The point selected as y'0 formed a valley without large undulations and had a coherent catchment area near the ridge. The extent of collapse matches the

characteristics learned from the training and validation.

Model 20 (Figure 6(e)) from ViT correctly predicted the collapse in five out of six cases and was able to select most of the collapsed area with an overall preference for y'0. In contrast, Model 29 (Figure 6(f)) achieved four out of six points on the target, identifying most of the collapse area and selecting many surrounding landforms as collapses (y'0) in addition to the true value.

The collapse (y'0) decision was made outside the collapsed area. The reason why this area did not collapse during the 2011 rainfall is unknown, but the slope map shows that it had the characteristics learned from training and validation. Therefore, it should be considered as a "possible collapse site" in the event of similar heavy rainfall in the future rather than assuming it to be a misjudgment.

6 Conclusions

In this study, CNN automatic search models were utilized to identify better landslide susceptibility models, albeit within a specific domain, than deep learning models with multiple structures. The performance of ViT, which was applied for the first time in this study, is similar to that of conventional machine learning algorithms. However, there is room for consideration in the design of the model, such as the structure of the training data, the size of the input data. and the characteristics of the different layers. Notably, the validation accuracy of the optimal model using ViT outperformed that of CNNs in the validation accuracy, indicating equivalent performance to conventional machine learning algorithms, and the results show promise for future possibilities for ViT. However, the validation accuracy of only 88.7% can be explained as follows: the mesh cut is square; therefore, not all of the collapsed area consists of mountain-body gravity deformation. The teacher data objectively selected the extent of collapse, and it is likely that during the selection process, landforms unrelated to mountain gravity deformation were mixed within the extent of the collapse. In addition, many geotechnical engineers use more than one viewpoint to decipher data. Therefore, they should also have a multimodal viewpoint.

References

Agliardi, F.; Crosta, G; Zanchi, A. Structural constraints on deep-seated slope deformation kinematics. *Engineering Geology*, 2001, 59, 83–102. https://doi.org/10.1016/S0013-7952(00)00066-1.

Chigira M.; Tsou C.Y.; Matsushi Y.; Hiraishi N.; Matsuzawa M. Topographic precursors and geological structures of deep-seated catastrophic landslides caused by Typhoon Talas. *Geomorphology*, 2013, 201, 479–493. https://doi.org/10.1016/j.geomorph.2013.07.020.

Chigira M; Wang W.N.: Furuya, T; Kamai, T. Geological causes and geomorphological precursors of the Tsaoling landslide triggered by the 1999 Chi-Chi Earthquake, Taiwan. *Engineering Geology*, 2003, 68, 259–273. https://doi.org/10.1016/S0013-7952(02)00232-6.

Crosta, G.B.; Chen, H.; Frattini, P. Forecasting hazard scenarios and implications for the evaluation of countermeasure efficiency for large debris avalanches. *Engineering Geology,* 2006, 83, 236–253. https://doi.org/10.1016/j.enggeo.2005.06.039.

Dahal, R.K.; Hasegawa, S.; Nonomura, A.; Yamanaka, M.; Dhakal, S.; Paudyal, P. Predictive modelling of rainfall-induced landslide hazard in the Lesser Himalaya of Nepal based on weights-of-evidence. *Geomorphology*, 2008, 102, 496–510.https://doi.org/10.1016/j.geomorph.2008.05.041.

Dosovitskiy, A.; Beyer, L: Kolesnikov, A.; Weissenborn, D.; Zhai, X.; Unterthiner, T.; Dehghani, M.; Minderer, M.;Heigold, G.; Gelly, S.; Uszkoreit, J.; Houlsby, N. AN IMAGE IS WORTH 16X16 WORDS: TRANSFORMERS FORIMAGE RECOGNITION AT SCALE, Published as a conference paper at ICLR 2021 ,https://arxiv.org/pdf/2010.11929.pdf.

Dramis, F.; Sorriso-Valvo, M. Deep-seated gravitational slope deformations, related landslides and tectonics. *Engineering Geology*, 1994, 38, 231–243. https://doi.org/10.1016/0013-7952(94)90040-X.

Evans, S.G.; Guthrie, R.H.; Roberts, N.J.; Bishop, N.F. The disastrous 17 February 2006 rockslide-debris avalanche on Leyte Island, Philippines: a catastrophic landslide in tropical mountain terrain. *Natural Hazards and Earth System Sciences*, 2007, 7, 89–101. https://doi.org/10.5194/nhess-7-89-2007.

Hara, H.; Hisada, K. Tectono-metamorphic evolution of the Cretaceous Shimanto accretionary complex, central Japan: constraints from a fluid inclusion analysis of syn-tectonic veins. *Island Arc*, 2007, 16, 57–68. https://doi.org/10.1111/j.1440-1738.2007.00558.x.

Hashimoto, Y.; Kimura, G. Underplating process from melange formation to duplexing: example from the Cretaceous Shimanto Belt, Kii Peninsula, southwest Japan. *Tectonics,* 1999, 18, 92–107. https://doi.org/10.1029/1998TC900014.

Kikuchi, T.; Hatano, T.; Nishiyama, S. Verification of microtopographic features of landslide or non-landslide area in Typhoon Talus in 2011. *Journal of the Japanese Landslide Society,* 2019, 56, 141–152 (in Japanese with English abstract). https://doi.org/10.3313/jls.56.141.

Kikuchi, T.; Sakita, K.; Nishiyama, S.; Takahashi, K. Landslide susceptibility mapping using automatically constructed CNN architectures with pre-slide topographic DEM of deep-seated catastrophic landslides caused by Typhoon Talas. *Natural Hazards*, 2023, 117(1), 339–364.

Kimura, K. Stratigraphy and paleogeography of the Hidakagawa Group of the Northern Shimanto Belt in the southern part of Totsugawa village, Nara Prefecture, southwest Japan. *Journal of the Geological Society of Japan*, 1986, 92,185–203 (in Japanese with English abstract). https://doi.org/10.5575/geosoc.92.185.

Kohavi, R. A study of cross-validation and bootstrap for accuracy estimation and model selection. *In Proceedings of the International Joint Conferencee on Artificial Intelligence,* 1995, 14, 1137–1145.

Kumon, F.; Suzuki, H.; Nakazawa, K. Shimanto belt in the Kii Peninsula. *Modern Geology*, 1998, 12, 71–79.

LeCun, Y; Boser, B; Denker, J. S.; Henderson, D. Howard, R. E.; Hubbard, W.; Jackel, L. D. Backpropagation applied to handwritten zip code recognition. *Neural computation*, 1989, 1(4), 541–551.

Lee, S. Application of likelihood ratio and logistic regression models to landslide susceptibility mapping using GIS. *Environmental Management*, 2004, 34, 223–232. https://doi.org/10.1007/s00267-003-0077-3.

Ma, Z.; Mei, G.; Piccialli, F. Machine learning for landslides prevention: a survey. Neural Computing & Application, 2021, 33, 10881–10907. https://doi.org/10.1007/s00521-020-05529-8.

Matsushi, Y.; Chigira, M.; Yamada, M.; Hiraishi, N.; Matsuzawa, M. Location and timing of deep-seated landslides in Kii Mountains at the 2011 disaster: an approach from rainfall history. Characterization, prediction, and management of deep-seated catastrophic landslides. 2012 *Disaster Prevention Research Institute*, Kyoto University, 2012, 43–45 (in Japanese with English abstract). http://www.slope.dpri.kyoto-u.ac.jp/symposium/DPRI_20120218proceedings.pdf.

Real, E., Liang, C., So, D., Le Q. Automl-zero: evolving machine learning algorithms from scratch. In: International Conference on Machine Learning, 2020, 8007–8019. PMLR

Tsou, C.Y.; Chigira, M.; Matsushi, Y.; Hiraishi, N.; Arai, N. Coupling fluvial processes and landslide distribution toward geomorphological hazard assessment: a case study in a transient landscape in Japan. *Landslides,* 2017, 14, 1901–1914. https://doi.org/10.1007/s10346-017-0838-3.

Wu, J.; Chen, X.Y.; Zhang, H.; Xiong, L.D.; Lei, H.; Deng, S.H. Hyperparameter optimization for machine learning models based on Bayesian optimization. *Journal of Electron Science Technology*, 2019, 17, 26–40.

Youssef, A.M.; Pradhan, B.; Dikshit, A.; Al-Katheri, M.M.; Matar, S.S.; Mahdi, A.M. Landslide susceptibility mapping using CNN-1D and 2D deep learning algorithms: comparison of their performance at Asir Region, KSA. *Bulletin of Engineering Geology and Environment,* 2022, 81, 1–22. https://doi.org/10.1007/s10064-022-02657-4.

Zischinsky, Ü. On the deformation of high slopes. In: Proceedings of the 1st conference of International Society for Rock Mechanics, Lisbon, 1966, 2, 179–185.

LANDSLIDE SUSCEPTIBILITY MODELS AT A REGIONAL SCALE. THE CASE STUDY OF THE REGION OF EPIRUS IN GREECE

ZOE MISIRI [1], KATERINA KAVOURA [2], NIKOLAOS DEPOUNTIS [3],

[1] *University of Patras, Department of Geology, Greece, geo07060@ac.upatras.gr*

[2] *Hellenic Survey of Geology and Mineral Exploration (HSGME), Greece, aikavoura@eagme.gr*

[3] *University of Patras, Department of Geology, Greece, ndepountis@upatras.gr*

Abstract
The current study presents the results of a landslide susceptibility model applied in the Region of Epirus, Greece. For this purpose, a detailed record of 286 active landslides was created and the assessment of landslide susceptibility was based on the analysis of four predisposing factors (geology, slope angle, elevation, land use) and the application of the frequency ratio (FR) prediction model. FR is a statistical model of bivariate analysis that performs reliability tests on the results and is internationally accepted to quantitatively describe susceptibility. The final degree of landslide susceptibility was assigned through the landslide susceptibility index (LSI), which assumes that as the value of LSI increases, so does the susceptibility. In this way, five different susceptibility scenarios and associated maps were carried out for the study area, and all of them were evaluated for their ability to classify landslides in different susceptibility zones. Comparing the results, the most suitable model turned out to be the one in which all predisposing factors were included, as it had the highest percentage of landslides coinciding with the three highest susceptibility categories.

Key words
Landslide Susceptibility Index, Frequency Ratio, Regional scale, DEM, Land Use

1 Introduction

Landslides are quite common phenomena in Greece. According to the general landslide susceptibility map of Greece (Sabatakakis et al 2013) the largest part of Western Greece, that also includes the Region of Epirus, is characterized by "high" to "extremely high" susceptibility level. Some of the main predisposing factors that contribute to the occurrence of these landslides are geology, land use, elevation and slope angle. This study focuses on the investigation of the susceptibility of 286 active landslides in the Region of Epirus, as recorded in the field, with the evaluation based on the analysis of the relationship between the above four predisposing factors and landslide occurrence. The prediction model selected for this analysis was the Frequency Ratio (FR) and the final degree of susceptibility was assigned through the Landslide Susceptibility Index (LSI). Similar studies in Greece have been performed by Sabatakakis et al (2013), Ferentinou and Chalkias (2013), Kavoura and Sabatakakis (2020), and others. It is worth knowing that in the same Region, in the village of Metsovo, a pilot implementation of a permanent landslide early warning system has been set up (Depountis at al 2020).

2 Methods

2.1 Geological and geomorphological setting

The study area of the Region of Epirus extends over 9,203 km^2 and is characterized by a complex

geological structure due to the Alpine orogen tectonics. The study area is structured by the formations of the Geotectonic zones (from east to west) Sub-Pelagonic, Pindos, Gavrovo and Ionian as well as postalpine formations (Papanikolaou 2021). The eastern part of the area is geologically occupied by the Geotectonic zones that are mainly composed of flysch, while the western and central part of the area is mainly made of limestone. These formations are strongly tectonized and often covered by a weathered zone of varying thickness, with the result that most of the landslides occur within these formations. The highest altitudes are observed along the mountain massif of Pindos, while the lowest altitudes are mainly in the west and south of the research area. It is noted that the highest altitude in the mountain massif of Pindos is 2,629m and 65% of the landslides examined are recorded in areas with an altitude >600m.

2.2 Landslide inventory

Recently, the Laboratory of Engineering Geology of the University of Patras created an online geodatabase platform, named as Hellenic Landslide Platform (He.L.P), providing information on landslides that have been recorded throughout Western Greece. According to the He.L.P. platform in the Region of Epirus have been recorded 286 landslides (Fig1). The classification of these landslides was based on that of Cruden and Varnes (1996) in which we observe that earth and rock flows are the most common type of movement (39%) into the study area, followed by complex landslides (21%) and rotational landslides (15%).
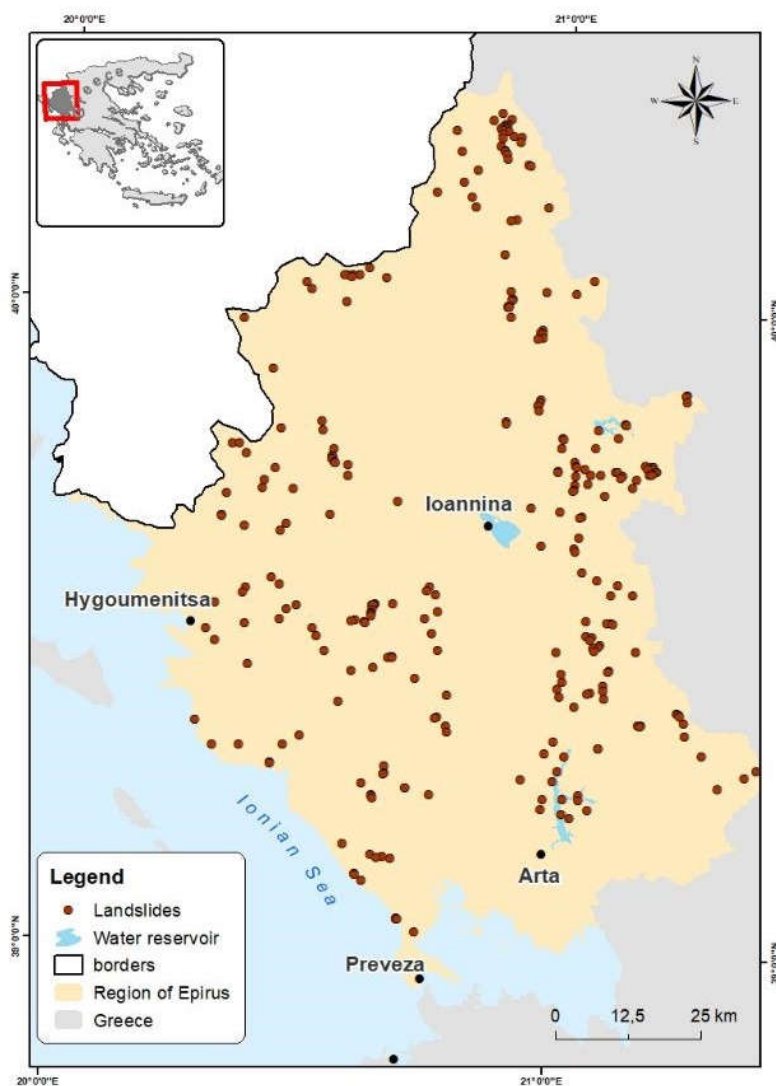
Figure 1. Landslide occurrences in the Region of Epirus, Greece

2.3 Predisposing factors

Four predisposing factors were chosen reflecting the general geological, geomorphological and environmental setting of the study area to access susceptibility. These predisposing factors were: a) Geology, based on an engineering geological mapping of a medium scale 1:50,000 (Fig2a), b) Elevation, in meters exported from a Digital Elevation Model (DEM) provided by the Greek Cadastral, with an accuracy of 5m (Fig2b), c) Slope inclination in degrees, calculated from a slope map with a pixel size of 5m (Fig2c), d) Land use, at an original scale of 1:100,000 provided by the Land Corine 2018 (Fig2d).

Figure 2. Landslise predisposing factors for the Region of Epirus, Greece a) Geology, b) Elevation, c) Slope inclination, d) Land use. The classes of all factors are presented in Table 2

2.4 Susceptibility model

In this work, the Frequency Ratio (FR) method was carried out for landslide susceptibility assessment. The FR model is a statistical approach based on the analysis between distribution of landslides and predisposing factors, in a specific area (Lee and Pradhan 2007). According to the method, the number of landslides in each c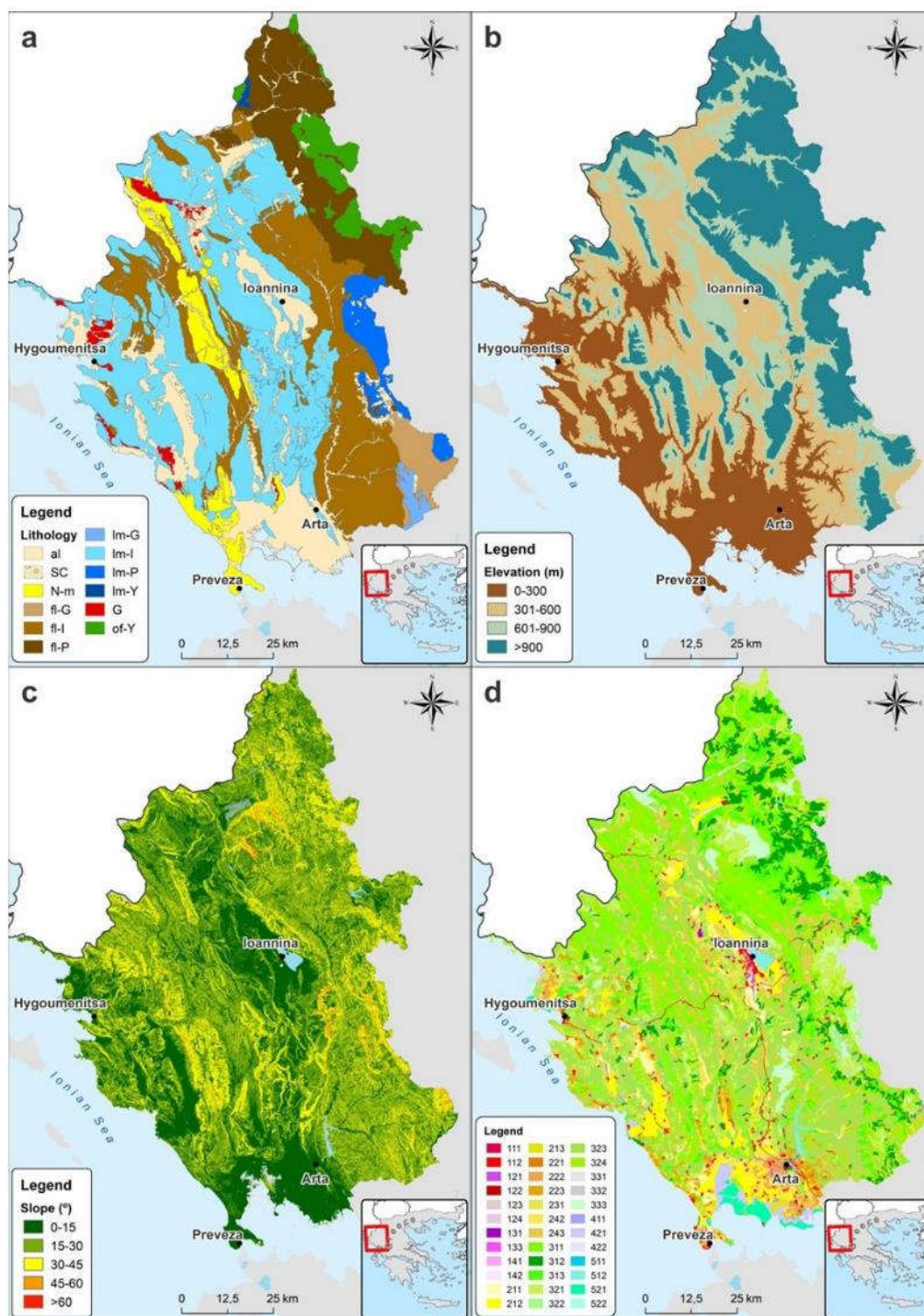lass of each factor is calculated and the frequency ratio for each factor class is found by dividing the frequency of landslides by the area of each class (Lee and Talib 2005). If the ratio (FR) is greater than one (1), then the relationship between a landslide and the factor's class is strong, whereas if the ratio is less than one (1), the relationship is weak. The FR values were calculated for each class of the participated factors, by using the following equation (Eq. 1):

$$FR = \frac{LF}{CA} \tag{1}$$

where LF is the relative frequency of landslides in a class of a factor and CA is the area (%) covered by the class of the same factor.

The Landslide Susceptibility Index (LSI) was estimated using equation 2 in the GIS environment:

$$LSI = \sum_{j=1}^{n} Wij \tag{2}$$

where n is the number of factors and Wij is the weight of each class i, of each factor j. The greater the index, the higher the landslide susceptibility.

This work provides an important opportunity to evaluate the reflection of the FR model, using different combination scenarios of four (4) predisposing factors. In the basic scenario (scenario 1) all factors participate, whereas in each subsequent scenario one factor is successively absent (Table 1).

Table 1. Suggested landslides susceptibility scenarios

Class	Scenario n.1	Scenario n.2	Scenario n.3	Scenario n.4	Scenario n.5
Geology	ü	ü	ü	û	ü
Land use	ü	û	ü	ü	ü
Elevation	ü	ü	û	ü	ü
Slope	ü	ü	ü	ü	û

3   Results

The FR model was applied to define weights for each factor, using the ratio of the percentage of landslides in a class of the selected factor to the percentage of the area of this class in the total area (Table 2).

Table 2. Classification of predisposing factors and their statistical weights

Factor	Class	Landslide frequency (Number)	(LF) %	Class area (CA) (km^2)	(CA) %	FR
Geology	Allouvial deposits (al)	21	7.34	1,357.92	14.82	0.50
(Fig.2a)	Scree (SC)	10	3.50	223.86	2.44	1.43
	Neogene formations (N-m)	23	8.04	517.24	5.65	1.42
	Flysch Gavrovo zone (fl-G)	9	3.15	209.70	2.29	1.37
	Flysch Ionian zone (fl-I)	103	36.01	1,914.35	20.89	1.72
	Flysch Pindos zone (fl-P)	72	25.17	961.32	10.49	2.40
	Limestones Gavrovo zone (lm-G)	0	0.00	70.35	0.77	0.00

	Limestones Ionian zone (lm-I)	37	12.94	3,129.2	34.15	0.38
	Limestones Pindos zone (lm-P)	4	1.40	289.38	3.16	0.44
	Limestones Sub-pelagonian (lm-Y)	0	0.00	16.25	0.18	0.00
	Evaporites (G)	1	0.35	119.6	1.31	0.27
	Ophiolites (of)	6	2.10	352.92	3.85	0.54
Elevation (Fig2b)	0 - 300 m	40	13.99	2,094.16	22.90	0.61
	300 - 600 m	64	22.38	2,481.38	27.14	0.82
	600 - 900 m	98	34.26	1,899.03	20.77	1.65
	> 900 m	84	29.37	2,668.93	29.19	1.01
Slope (Fig2c)	0° - 15°	58	20.28	3,204.51	35.50	0.57
	15° - 30°	115	40.21	3,644.41	40.37	1.00
	30° - 45°	80	27.97	1,956.88	21.68	1.29
	45° - 60°	31	10.84	202.39	2.24	4.83
	> 60°	2	0.70	18.89	0.21	3.34
Land use (Fig2d)	Continuous urban fabric (111)	0	0.00	5.79	0.06	0.00
	Discontinuous urban fabric (112)	5	1.75	102.85	1.12	1.57
	Industrial or commercial units (121)	0	0.00	22.46	0.24	0.00
	Road and rail networks (122)	2	0.70	28.57	0.31	2.26
	Port areas (123)	0	0.00	0.70	0.01	0.00
	Airports (124)	0	0.00	9.85	0.11	0.00
	Mineral extraction sites (131)	0	0.00	1.85	0.02	0.00
	Construction sites (133)	0	0.00	2.32	0.03	0.00
	Green urban areas (141)	0	0.00	4.22	0.05	0.00
	Sport and leisure facilities (142)	0	0.00	173.30	1.88	0.00
	Non-irrigated arable land (211)	0	0.00	333.55	3.62	0.00
	Permanently irrigated land (212)	0	0.00	11.33	0.12	0.00
	Rice fields (213)	0	0.00	0.93	0.01	0.00
	Vineyards (221)	0	0.00	95.54	1.04	0.00
	Fruit trees and berry plantations (222)	4	1.40	158.49	1.72	0.81
	Olive groves (223)	0	0.00	65.59	0.71	0.00
	Pastures (231)	8	2.80	405.17	4.40	0.64
	Complex cultivation patterns (242)	54	18.88	898.66	9.75	1.94
	Land principally occupied by agric.. (243)	38	13.29	1,419.01	15.40	0.86
	Broad-leaved forest (311)	23	8.04	593.79	6.44	1.25
	Coniferous forest (312)	16	5.59	520.75	5.65	0.99
	Mixed forest (313)	20	6.99	932.59	10.12	0.69
	Natural grasslands (321)	0	0.00	31.44	0.34	0.00
	Moors and heathland (322)	48	16.78	1,632.09	17.71	0.95
	Sclerophyllous vegetation (323)	56	19.58	1174.77	12.75	1.54
	Transitional woodland-shrub (324)	0	0.00	37.68	0.41	0.00
	Beaches, dunes, sands (331)	1	0.35	22.73	0.25	1.42
	Bare rocks (332)	9	3.15	297.93	3.23	0.97
	Sparsely vegetated areas (333)	0	0.00	14.06	0.15	0.00
	Inland marshes (411)	0	0.00	83.39	0.90	0.00
	Salt marshes (421)	0	0.00	9.21	0.10	0.00
	Salines (422)	2	0.70	46.93	0.51	1.37
	Water courses (511)	0	0.00	76.09	0.83	0.00

Water bodies (512)	0	0.00	1.20	0.01	0.00

At the end, the Landslide Susceptibility Index (LSI) for the relevant landslide susceptibility mapping was estimated using the weights that were derived from the bivariate statistical analysis (Fig3).
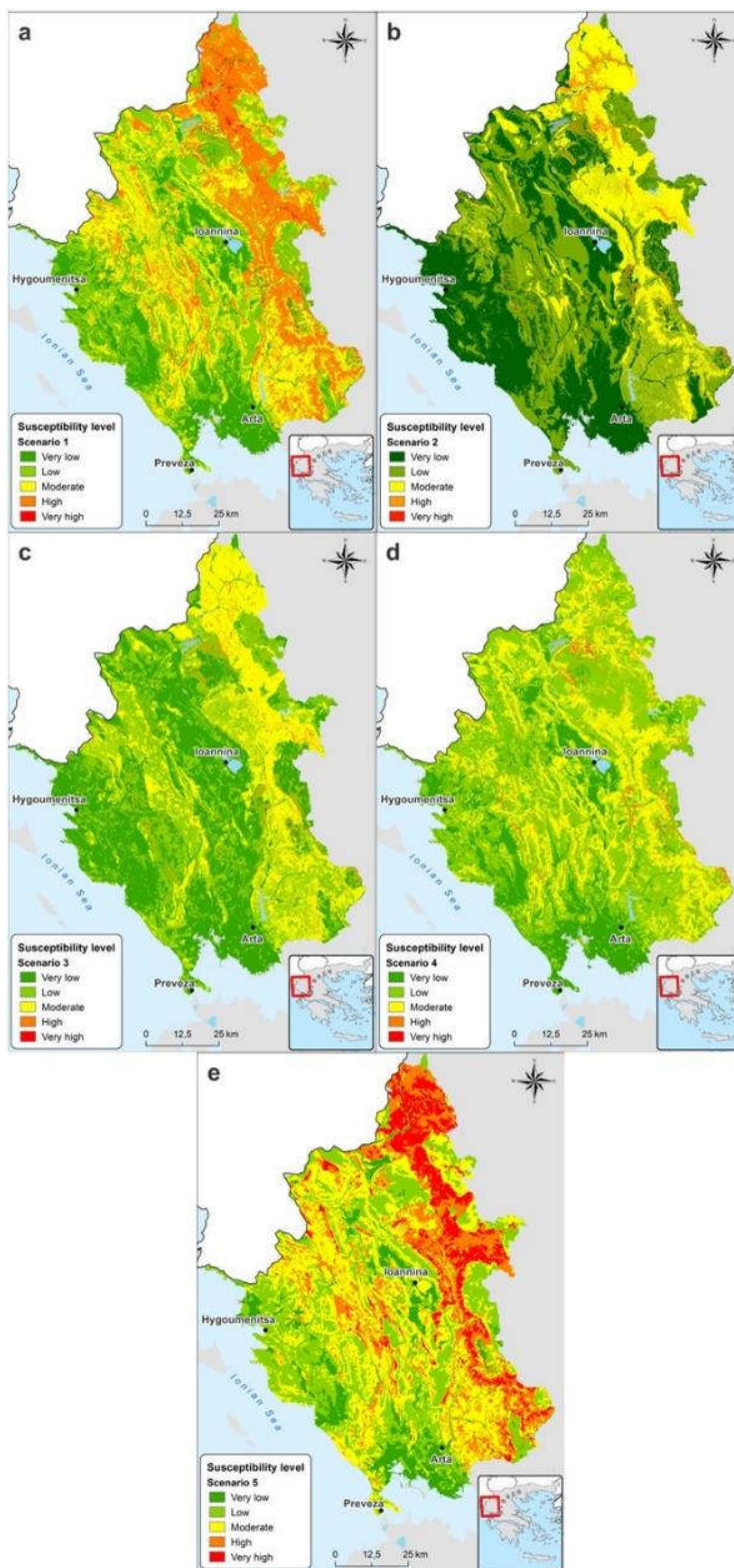

Figure 3. Lanslide Susceptibility Index mapping: a) scenario 1, b) scenario 2, c) scenario 3, d) scenario 4, e) scenario 5. The scenarios are presented in Table 1.

In all scenarios, the spatial distribution of LSI was categorized into very low, low, moderate, high and very high, susceptibility zones. After comparing the results, it turned out that scenario n.1, in which all factors are included, is the most suitable for the Region of Epirus, as it assigns up to 60% of landslides into the three most susceptible zones (Table 3). The final Landslide Susceptibility map created using the most suitable scenario n.1 is presented in Figure 3a.

Table 3. Percentage of landslides in susceptibility zones for each scenario

Class	Scenario n.1	Scenario n.2	Scenario n.3	Scenario n.4	Scenario n.5	Susceptibilty zone
1	1.7%	7.3%	7.3%	1.05%	0%	Very Low
2	12.9%	13.9%	29.0%	27.3%	14.0%	Low
3	25.5%	35.3%	49.6%	30.07%	29.0%	Moderate
4	48.2%	33.5%	8.4%	30.7%	22.4%	High
5	11.5%	9.7%	5.6%	10.8%	34.6%	Very High

4   Conclusion

The current study investigated the landslide susceptibility in the Region of Epirus, Greece. For this purpose, 286 active landslides recorded in the field were used as an inventory and four predisposing factors (geology, slope angle, elevation, land use) applied in a GIS framework in order to design four corresponding maps. Moreover, the frequency ratio (FR) equation was applied in the maps and the FR values were calculated for each class of the predisposing factors. The final degree of landslide susceptibility was assigned through the landslide susceptibility index (LSI), which assumes that as the value of LSI increases, so does the susceptibility. In this way, five different susceptibility scenarios were designed in a GIS framework and all of them were evaluated for their ability to classify landslides in the different susceptibility zones. In the basic scenario (scenario 1) all predisposing factors participate, whereas in each subsequent scenario one factor is successively absent. Comparing the results, the most suitable model turned out to be the one in which all predisposing factors were included, as it had the highest percentage of landslides coinciding with the three highest susceptibility categories.

In a next stage, the landslide susceptibility of the study area will be investigated in more detail by adding the precipitation factor with data derived from ERA5-Land. ERA5-Land is a gridded database with rainfall simulations derived from a subset of Global Climate Models (GCMs), developed under the CMIP6 projects, at a horizontal resolution of ~100 km and available for the continuous period 1971 - 2100 in the Copernicus Climate Data Store (C3S-CDS). For the region of Epirus, the GCMs of long-term climate projections/simulations will be downscaled to higher resolution (9-25km) using the gridded observation data with a spatial resolution 9-25km, available in C3S-CDS. This will improve the reliability of the susceptibility model in the study area, as rainfall is a predisposing and triggering factor in landslide occurrences.

References

CORINE Land Cover 2018 (vector/raster 100 m), Europe, 6-yearly. Assessed in 01.06.2024. https://land.copernicus.eu/en/products/corine-land-cover/clc2018

Cruden D.M.; Varnes, D.J. Landslide Types and Processes, Transportation Research Board, U.S. National Academy of Sciences, Special Report. 1996, 247: 36-75.

Depountis N.; Sabatakakis N.; Kavoura K.; Nikolakopoulos K.; Elias P.; Drakatos G. Establishment of an Integrated Landslide Early Warning and Monitoring System in Populated Areas. In: Casagli N., Tofani V., Sassa K., Bobrowsky P.T., Takara K. (eds) *Understanding and Reducing Landslide Disaster Risk. WLF 2020. ICL Contribution to Landslide Disaster Risk Reduction*. 2021, Springer, Cham. doi: 10.1007/978-3-030-60311-3_21

Ferentinou, M.; Chalkias, C. Mapping Mass Movement Susceptibility Across Greece with GIS, ANN and Statistical Methods. In: Margottini, C., Canuti, P., Sassa, K. (eds) *Landslide Science and Practice*. 2013, Springer, Berlin, Heidelberg.

He.L.P. (Hellenic Landslide Platform), University of Patras, Laboratory of Engineering Geology. https://patrasuni.maps.arcgis.com/apps/webappviewer/index.html?id=9ee309f77fca4790a64c716965c 99e88 ,available online, accessed on 7 July 2023.

Kavoura, K.; Sabatakakis, N. Investigating landslide susceptibility procedures in Greece. *Landslides.* 2020*,* 17, 127–145.

Lee S.; Talib A.T. Probabilistic landslide susceptibility and factor effect analysis. *Env Geol.* 2005, 47:982-990. doi: 10.1007/s00254-005-1228-z

Lee S.; Pradhan B. Landslide hazard mapping at Selangor, Malaysia using frequency ratio and logistic regression models. *Landslides.* 2007, 4 (1):33-41. doi: 10.1007/s10346-006-0047-y

Papanikolaou, D.I. The Geology of Greece. 2021, ISBN: 978-3-030-60730-2.

Sabatakakis, N.; Koukis, G.; Vassiliades, E.; Lainas, S. Landslide susceptibility zonation in Greece. *Natural Hazards.* 2013, 65(1)*,* 523-543.

MACHINE LEARNING LANDSLIDE SUSCEPTIBILITY MAPPING IN WESTERN GREECE WITH INSAR TIME-SERIES ANALYSIS

STAVROULA ALATZA[1,2], CONSTANTINOS LOUPASAKIS[1], ALEXIS APOSTOLAKIS[2,3], CHARALAMPOS KONTOES[2], MARTHA KOKKALIDOU[2], NIKOLAOS S. BARTSOTAS[2], CONSTANTINOS NEFROS[1]

[1] *National Technical University of Athens (NTUA), School of Mining and Metallurgical Engineering, Department of Geological Sciences, Greece,* kostasnefros@central.ntua.gr*,* cloupasakis@metal.ntua.gr

[2]*National Observatory of Athens, Institute for Astronomy, Astrophysics, Space Applications and Remote Sensing, Operational Unit "BEYOND Center of Earth Observation Research and Satellite Remote Sensing", Greece,* alatza@noa.gr*,* alex.apostolakis@noa.gr*,* kontoes@noa.gr*,* m.kokkalidou@noa.gr*,* nbartsotas@noa.gr

[3] *National Technical University of Athens, School of Electrical and Computer Engineering*

Abstract

The current study aims to investigate landslide susceptibility in Western and Central Greece and to enrich the existing knowledge in slow-moving deformation phenomena, mainly triggered by prolonged or excess precipitation events. For this purpose, SAR interferometry and Artificial Intelligence are implemented on Earth Observation data. Landslide susceptibility mapping was performed in a broad area within the most landslide prone geotectonic zones of Greece, extending from Crete Island up to the Greek - Albanian borders. These are the Ionios, Gavrovo and Pindos geotectonic zones. The variety of geological formations and morphological features, crucial infrastructure and the plethora of settlements provide a great variety of conditions and an exceptionally large landslide inventory. By exploiting a national scale inventory of Line-of-Sight surface displacements in Greece, the so-called InSAR Greece project, more than 3000 landslides were detected in Western Greece. Topographical, geological, meteorological, hydrological parameters and vegetation, were introduced to the model, as landslide contributing factors. The prediction problem was approached as a binary classification problem, whereby two classes were defined: (1) landslide and (2) no landslide for each assessed data point. The landslide prediction was solved by training robust classic machine learning algorithms using the aforementioned dataset. The annotation of the dataset was performed by experts in the field. A strict Machine Learning methodology was employed for training, tuning and testing the machine learning, comprising of 5-fold cross validation, hyperparameter tuning, feature ranking and selection and strict train validation dataset split to avoid spatial autocorrelation. XGBoost algorithm showed the best performance among the traditional ML algorithms, thus it was preferred for producing susceptibility maps. The exploitation of big volumes of EO data and AI, in landslide susceptibility mapping, can provide a valuable tool in risk reduction. Also, validation of susceptibility mapping with ground truth investigations, provides an additional advantage in establishing a landslide susceptibility system and in the adoption of mitigation measures.

Key words

XGBoost, landslide susceptibility, InSAR, machine learning.

1 Introduction

InSAR time-series analysis, has long been identified as an effective tool for landslides (LS) detection and monitoring (Aslan et al., 2020; Bekaert et al., 2020; Nefros et al., 2023; Kontoes et al., 2021; Smail et al., 2022). On the other hand, AI has rapidly demonstrated its efficacy in predicting LS -prone zones and providing early warning systems for LS. Numerous AI algorithms, predominantly tree-based

ensemble models, have been utilized in the field of LS susceptibility mapping. Support vector machines (SVM) (Lee et al., 2017), Random Forest (RF) models (Park et al., 2019), boost extreme gradient boosting (XGBoost) models (Can et al., 2021), are among the most commonly used ML models for LS detection and susceptibility mapping. Deep learning models have also demonstrated their efficiency in LS susceptibility studies (Zhang et al., 2024; Habumugisha et al.,2022).

Greece is listed among the most landslide-prone countries in the Mediterranean, due to its intense geomorphology. LS are considered among the most destructive natural hazards worldwide, often associated with seismic events or volcanic eruptions. In recent decades, extreme precipitation events intensified by the climate change, urban activities, and deforestation, along with seismic activity or volcanic eruptions, are considered as significant contributing factors for LS. In Greece Pindos, Gavrovo and Ionian are three of the most LS prone geotectonic zones. In Pindos geotectonic zone more than 40% of the total LS in Greece are recorded. On the contrary, in Gavrovo and Ionian zones, LS occurrences of 4% and 4.5%, are recored (Koukis et al., 2005; Sabatakakis et al., 2013). Intense tectonism, present at Pindos geotectonic zone (Delibasis et al., 1977), steep slopes, the highly susceptible flysch, in combination with high precipitation levels, enhance the frequency of slope failures. On the other hand, the smooth tectonic structures (Mountrakis, 2010) in the Gavrovo and Ionian geotectonic zones and the existence of limestones decrease the occurrence of LS in these zones. In the present study, the LS inventory is formed with landslides detected in Aitoloakarnania and Evritania prefectures, in Western and Central Greece (Figure 1), using InSAR time-series analysis and satellite image investigations from geotechnical experts. A strict ML methodology was employed for LS susceptibility mapping.
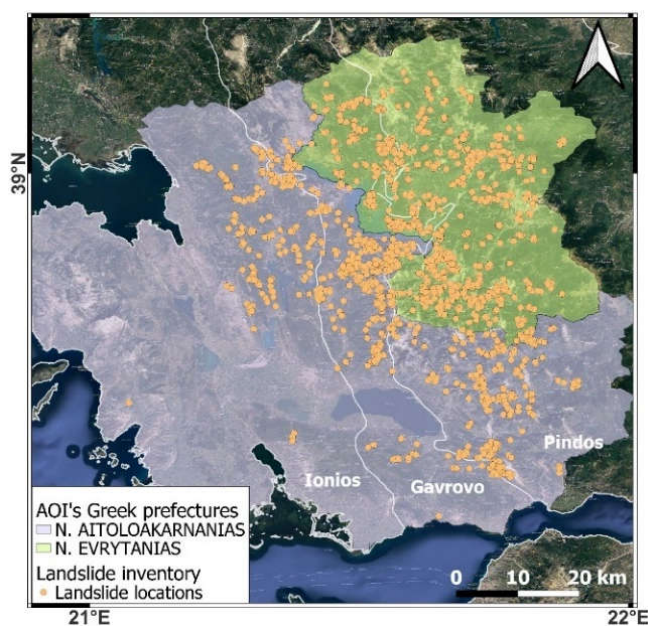

Figure 1. The study area and the landslides inventory.

As in most machine learning problems, the performance of ML models in landslide susceptibility studies heavily relies on the volume and accuracy of the dataset. An additional challenging aspect in ML studies, relates to the migration of the model to a larger scale. The present study exploits an exceptionally large LS inventory, with more than 3000 validated landslides created for LS susceptibility mapping in Western and Central Greece, using the XGBoost algorithm. The geotectonic zone index is added to the model as a contributing factor. By adapting the model to the special characteristics of each geotectonic zone, the migration of the model to a larger scale, will be facilitated, in future work. Finally, the exploitation of time-series InSAR techniques served as a valuable tool, in the creation of the LS inventory and also as a validation for the model's predictions, highlighting the significant potential of integrating remote sensing techniques and AI.

2   Dataset

2.1 LS locations

LS locations were derived from multiple sources, including landslides from Kontoes et al., (2021), enriched by 704 more landslides identified by satellite image investigations by geotechnical experts. 2146 slow-moving LS were derived by Line-of-Sight (LOS) displacements from the InSAR Greece project (Papoutsis et al., 2020). In InSAR Greece, LOS displacements were estimated for Greece's mainland, using Sentinel-1 SLCs from 2015 to 2019, with a parallelized version of the Stanford method for Persistent Scatterers Interferometry (Hooper et al., 2004). All LS locations introduced in the ML model, were finally validated by geotechnical expert. A total of 3224 LS forms an exceptionally large LS inventory in Aitoloakarnania and Evritania prefectures. It is worthwhile noting that one limitation of the PSI technique employed to identify LS locations, is the low presence of permanent scatterers in vegetated areas. Therefore, in the present study, LS locations derived from InSAR techniques are not detected in areas with dense vegetation.

The no-LS locations, were also derived from the Greece InSAR product. Permanent Scatterers with almost zero LOS displacement rates, were identified. To avoid misinterpretation of PS points as LS and no LS locations and to avoid data leakage because of spatial autocorrelation (Roberts et al., 2016) between close PS points during the training, buffers of several sizes, ranging from 200m to 1km, were tested around the LS and no LS locations. A buffer of 600m proved to be effective in avoiding labelling multiple PS points located in the same sliding slope, as different LS locations. Similarly, a buffer of 400m around each no LS PS point was applied to ensure that there is no spatial correlation in the final LS susceptibility map product. Therefore, 2753 no LS locations were introduced to the ML model. In the selection of non-LS points, two critical aspects were considered. First, the number of LS and non-LS points to have a ratio of almost 1:1. Second, the spatial distribution of LS and no LS locations to be homogeneous.

2.2 LS contributing factors

LS occurrence is triggered by both natural and anthropogenic factors. In Greece, geology (Sikodimou et al., 2018), earthquakes (Papathanassiou et al., 2021) and rainfall (Nefros et al., 2023), are considered significant LS contributing factors. In the present study, the LS contributing factors introduced to the model are summarized in Table 1. The LS contributing factors were selected based on the special characteristics of the study area (intense geomorphology, high precipitation rates, etc.) and literature review. These include, geomorphological and geological factors, hydrological and topography factors, climatological factors, land use/land cover and vegetation. The EU-DEM, with a 25m cell size, was employed for the estimation of the elevation factors. The same 25m pixel size was maintained in all computed raster layers. Among the geological factors, LS factor (Slope Length and Steepness factor), that is associated with soil erosion and surface lithology was also added. Land cover, as an indicator of natural or manmade elements in the study area, is also an important LS contributing factor. NDVI, as an indication of existence or absence of vegetation, was used as an LS contributing factor in the ML LS susceptibility model. Regarding the climate factors, precipitation is considered as a critical factor as the majority of the recorded LS in the study area, are triggered by extreme precipitation events. Snowmelt also poses a serious threat in slope stability. Hydrological factors which relate to soil moisture, surface roughness, slope erosion from water flow and sediment transportation, are also added as important LS contributing factors.

Table 1. LS contributing factors

Contributing Factors	Source
Elevation	
Aspect	EU-DEM (25m)
Slope	
LS factor (Slope Length and Steepness factor)	EUROPEAN SOIL DATA CENTRE (ESDAC)
Land use - Land cover	Copernicus Corine Land Cover 2018
Surface Lithology	EGDI 1:1 Million pan-european Surface Geology INSPIRE conformant National WFS services on GeologicUnit
Snow melt	ERA5 – LAND (spatial sampling of 9 km)
Precipitation	Climate Hazards Group InfraRed Precipitation with Station data (CHIRPS) from 2000 to 2020 (spatial sampling of 5 km)
Sediment transport index (STI)	
Topographic wetness index (TWI)	Calculated from the DEM (25m)
Terrain Ruggedness Index (TRI)	
Stream power index (SPI)	
Normalized difference vegetation index (NDVI)	MODIS data (1km)

3   Methods

Among the traditional machine learning algorithms tested to evaluate the dataset's potential, the XGBoost algorithm was preferred due to its superior performance in the study area. Another reason was the advantage of XGBoost compared to algorithms, like AdaBoost and Gradient Boosting, to prevent overfitting, owing to regularization techniques (Lasso-1, Lasso-2). Feature selection is an important part of a landslide classification problem, as uncorrelated factors may introduce noise to the model and negatively affect its performance. The selection of the final contributing factors, was determined after model training and feature importance estimation. Considering the different scales of the input features, a normalization of the dataset was applied, using a standard range from -1 to +1. To simplify data complexity, particularly for ensemble tree methods, and to ensure the dataset's compatibility with a wide range of ML algorithms, discretization followed by One Hot Encoding was applied in aspect, slope, LS factor, land use/land cover and geology factors. A 70% of LS and no LS locations was used as a train dataset and 30% was used as a test dataset for validation. To better support the generalization of the model a 5-fold cross validation was applied on the training dataset along with model hyperparameterization. The top performing model from cross validation was used for prediction on the test dataset. The final dataset and the split ratio are provided in Figure 2.
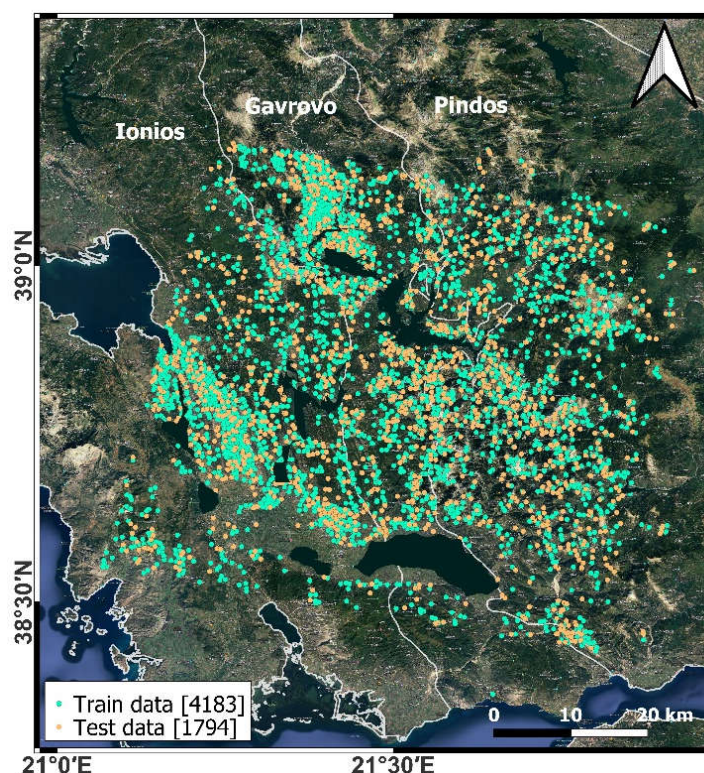
Figure 2. Dataset split ratio.

4   Results

Model evaluation is a critical aspect in every ML problem, especially in geological hazards applications, to ensure the reliability of the model's predictions. The XGBoost model used for LS predictions in the study area, was mainly evaluated based on precision, recall, F1 and Mathew's correlation coefficient (MCC) metrics. The MCC, is considered an important metric for the model's performance, owing to its ability to provide a high score, taking into account good results in all four components (Chicco et al., 2020) of the confusion matrix (Figure 3). Table 2 presents the model's evaluation metrics on the test dataset. The high MCC value of 0.75 in combination with the other metrics, verify the good performance of the model in landslide susceptibility predictions.

Table 2. XGBoost evaluation metric results on the test dataset

Score metric	Precision	Recall	F1	Support	Accuracy	MCC
No Landslide	0.94	0.78	0.85	827		
Landslide	0.83	0.96	0.89	967	0.88	0.75

According to the precision results shown in Table 2, 83% of the predictions were true positives and based on the recall, 96% of the identified landslides were actual events. The high F1 score verifies the ability of the model to effectively identify actual LS events and minimize false positive events. A confusion matrix was also used to assess the model's performance (Figure 3). Based on Figure 3, the model performed well in identifying True Negative events, which are no landslides and True Positive events that correspond to actual landslide events, in the test dataset.
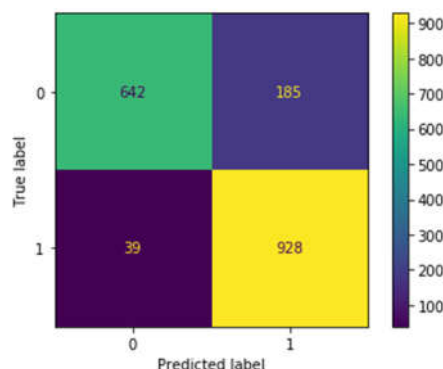
Figure 3. Confusion matrix

The final landslide susceptibility map, based on predictions on a grid with a cell size of 25m is presented in Figure 4. The landslide locations of the validation dataset are also added, as an indicator of the model's performance. As Figure 4 illustrates, the majority of landslides are presented in Gavrovo and Pindos geotectonic zones, where landslide occurrence is more frequent, due to the geotectonic evolution of the zones and the geotechnical characteristics of the geological formations.
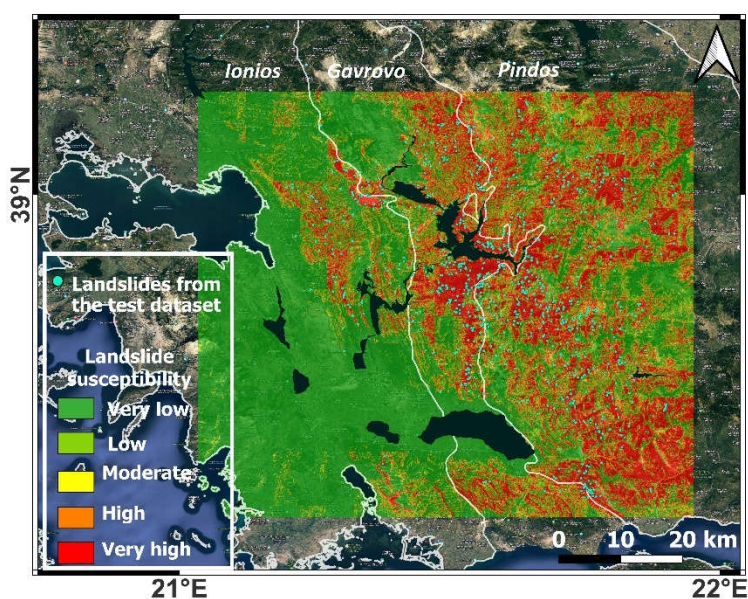

Figure 4. LS susceptibility map

5   Conclusions

This was a first attempt to demonstrate the potential of InSAR data, AI and ground truth investigations in establishing an LS susceptibility system in Greece. Using an originally created dataset LS susceptibility mapping with ML methodology was performed in a broad area in Western and Central Greece, within the most LS prone geotectonic zones, that is Ionios, Gavrovo and Pindos zones. Landslide locations from InSAR timeseries analysis in Greece and ground truth inspections formed an LS inventory of more than 3000 LS. Topographical, geological, meteorological, hydrological parameters and vegetation, were introduced to the LS susceptibility model, as landslide contributing factors. The XGBoost algorithm was used to perform LS susceptibility predictions and produce the LS susceptibility maps. The model demonstrates high performance with an accuracy of 88%, a precision of 83% in predicting landslide occurrences, and F1-scores of 0.85 for non-landslide events and 0.89 for landslide events. Also, the addition of the geotectonic zone index as a contributing parameter, is an

important factor to facilitate the model's predictions in new areas in Western and Central Greece, which will be included in future work.

References

Aslan, G.; Foumelis, M.; Raucoules, D.; De Michele, M.; Bernardie, S.; Cakir, Z. Landslide Inventory Mapping and Monitoring Using Persistent Scatterer Interferometry (PSI) Technique in the French Alps. *Remote Sensing*. 2020, 12(8), 1305, https://doi.org/10.3390/rs12081305. IF: 4.118.

Ballabio, C.; Sterlacchini, S. Support Vector Machines for Landslide Susceptibility Mapping: The Staffora River Basin Case Study, Italy. *Mathematical geosciences*. 2012, 44. 10.1007/s11004-011-9379-9.

Bekaert, D.P.S.; Handwerger, A. L.; Agram, P.; Kirschbaum, D. B. InSAR-based detection method for mapping and monitoring slow-moving landslides in remote regions with steep and mountainous terrain: An application to Nepal, *Remote Sensing of Environment*. 2020, 249 https://doi.org/10.1016/j.rse.2020.111983.

Can, R.; Kocaman, S.; Gokceoglu, C. A Comprehensive Assessment of XGBoost Algorithm for Landslide Susceptibility Mapping in the Upper Basin of Ataturk Dam, Turkey. *Appl. Sci*. 2021, 11, 4993. https://doi.org/10.3390/app11114993.

Chicco, D.; Jurman, G. The advantages of the Matthews correlation coefficient (MCC) over F1 score and accuracy in binary classification evaluation. *BMC Genomics*. 2020, 21, 6. https://doi.org/10.1186/s12864-019-6413-7

Delibasis, N.; Karydis, P. Recent earthquake activity in Trichonis region and its tectonic significance. *Ann. Geofis*. 1977, 30, 19 – 81.

Habumugisha, J.M.; Chen, N.; Rahman, M.; Islam, M.M.; Ahmad, H.; Elbeltagi, A.; Sharma, G.; Liza, S.N.; Dewan, A. Landslide Susceptibility Mapping with Deep Learning Algorithms. *Sustainability* 2022, 14, 1734. https://doi.org/10.3390/su14031734.

Hooper, A.; Zebker, H.; Segall, P.; Kampes, B. A new method for measuring deformation on volcanoes and other natural terrains using InSAR persistent scatterers. *Geophys. Res. Lett*. 2004, 31, L23611. https://doi.org/10.1029/2004GL021737.

Kontoes, C.; Loupasakis, C.; Papoutsis, I.; Alatza, S.; Poyiadji, E.; Ganas, A.; Psychogyiou, C.; Kaskara, M.; Antoniadi, S.; Spanou, N. Landslide Susceptibility Mapping of Central and Western Greece, Combining NGI and WoE Methods, with Re-mote Sensing and Ground Truth Data. *Land*. 2021, 10, 402. https://doi.org/10.3390/land10040402.

Koukis, G.; Sabatakakis, N.; Nikolaou, N., Loupasakis, C. Landslide hazard zonation in Greece. *In Proceedings of open symposium on landslide risk analysis and sustainable disaster management in the First General Assembly of International Consortium on Landslides*. 2005, 291-296.

Lee, S.; Hong, S.-M.; Jung, H.-S. A Support Vector Machine for Landslide Susceptibility Mapping in Gangwon Province, Ko-rea. *Sustainability*. 2017, 9, 48. https://doi.org/10.3390/su9010048.

Mountrakis, D. Γεωλογια και Γεωτεκτονικη Εξελιξη της Ελλαδας. UNIVERSITY STUDIO PRESS, Thessaloniki, 2010, 374.

Nefros, C.; Tsagkas, D.S.; Kitsara, G.; Loupasakis, C.; Giannakopoulos, C. Landslide Susceptibility Mapping under the Climate Change Impact in the Chania Regional Unit, West Crete, Greece. *Land* 2023, 12, 154. https://doi.org/10.3390/land12010154

Nefros, C.; Alatza, S.; Loupasakis, C.; Kontoes, C. Persistent Scatterer Interferometry (PSI) Technique for the Identification and Monitoring of Critical Landslide Areas in a Regional and Mountainous Road Network. *Remote Sensing.* 2023, 15, 1550. https://doi.org/10.3390/rs15061550.

Papathanassiou, G.; Valkaniotis, S.; Ganas, A. Spatial patterns, controlling factors, and characteristics of landslides triggered by strike-slip faulting earthquakes: case study of Lefkada island, Greece. *Bull Eng Geol Environ.* 2021, 80, 3747–3765. https://doi.org/10.1007/s10064-021-02181-x

Papoutsis, I.; Kontoes, C.; Alatza, S.; Apostolakis, A.; Loupasakis, C. InSAR Greece with Parallelized Persistent Scatterer In-terferometry: A National Ground Motion Service for Big Copernicus Sentinel-1 Data. *Remote Sensing.* 2020, 12, 3207. https://doi.org/10.3390/rs12193207

Park, S.; Kim, J. Landslide Susceptibility Mapping Based on Random Forest and Boosted Regression Tree Models, and a Comparison of Their Performance. Appl. Sci. 2019, 9, 942. https://doi.org/10.3390/app9050942.

Roberts, D; Bahn, V.; Ciuti, S.; Boyce, M.; Elith, J.; Guillera-Arroita, G.; Hauenstein, S.; Lahoz-Monfort, J.; Schröder, B.; Thuiller, W.; Warton, D.; Wintle, B.; Hartig, F.; Dormann, C. Cross-validation strategies for data with temporal, spatial, hierarchical, or phylogenetic structure. *Ecography.* 2016, 40. https://doi.org/10.1111/ecog.02881.

Sabatakakis, N.; Koukis, G.; Vassiliades, E.; Lainas, S. Landslide susceptibility zonation in Greece. *Nat. Hazards*. 2013, 65, 523–543.

Skilodimou, H.D.; Bathrellos, G.D.; Koskeridou, E.; Soukis, K.; Rozos, D. Physical and Anthropogenic Factors Related to Landslide Activity in the Northern Peloponnese, Greece. *Land.* 2018, 7, 85. https://doi.org/10.3390/land7030085.

Smail, T.; Abed, M.; Mebarki, A.; Lazecky, M. Earthquake-induced landslide monitoring and survey by means of InSAR, *Nat. Hazards Earth Syst. Sci.* 2022, 22, 1609–1625, https://doi.org/10.5194/nhess-22-1609-2022.

Zhang, Q.; Wang, T. Deep Learning for Exploring Landslides with Remote Sensing and Geo-Environmental Data: Frameworks, Progress, Challenges, and Opportunities. *Remote Sens.* 2024, 16, 1344. https://doi.org/10.3390/rs16081344.

Gold Sponsors

GEOTEHNIČKI RADOVI
TEL. 01/38 38 448
GRASA
KALINOVICA 3/III
ZAGREB
GRAĐEVINSKE SANACIJE

BRODSKA POSAVINA
D.D. ZA VODNOGOSPODARSKU DJELATNOST

Zagreb-Montaža

MONTERRA
PRVI KORAK STABILNOSTI

KARST
GEOTECHNICAL
ENGINEERING

P.G.P. d.o.o.

GEOKON

WWW.GEOKON.HR

INA

Bronze Sponsors

EA EURO-ASFALT

BRUGG
Geobrugg

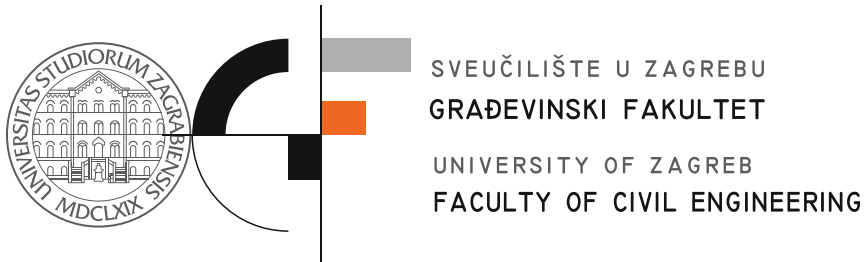MANING PROJEKT D.O.O.
GRADNJA, PROJEKTIRANJE, STRUČNI NADZOR GRAĐENJA

rocscience

Under the auspices of

REPUBLIKA HRVATSKA
Ministarstvo prostornoga uređenja,
graditeljstva i državne imovine

Coorganizers

SVEUČILIŠTE U ZAGREBU
GRAĐEVINSKI FAKULTET

UNIVERSITY OF ZAGREB
FACULTY OF CIVIL ENGINEERING

HGI 1909

HRVATSKI GEOLOŠKI INSTITUT
CROATIAN GEOLOGICAL SURVEY

HRVATSKO GEOLOŠKO DRUŠTVO
1951
Mente et Malleo

HRVATSKO GEOTEHNIČKO DRUŠTVO
CROATIAN GEOTECHNICAL SOCIETY
SOCIÉTÉ CROATE DE LA GÉOTECHNIQUE